

Case No. 84739

IN THE SUPREME COURT OF THE STATE OF NEVADA

Electronically Filed
Nov 08 2022 04:38 p.m.
Elizabeth A. Brown
Clerk of Supreme Court

ADAM SULLIVAN, P.E., NEVADA
STATE ENGINEER, et al.

Appellants,

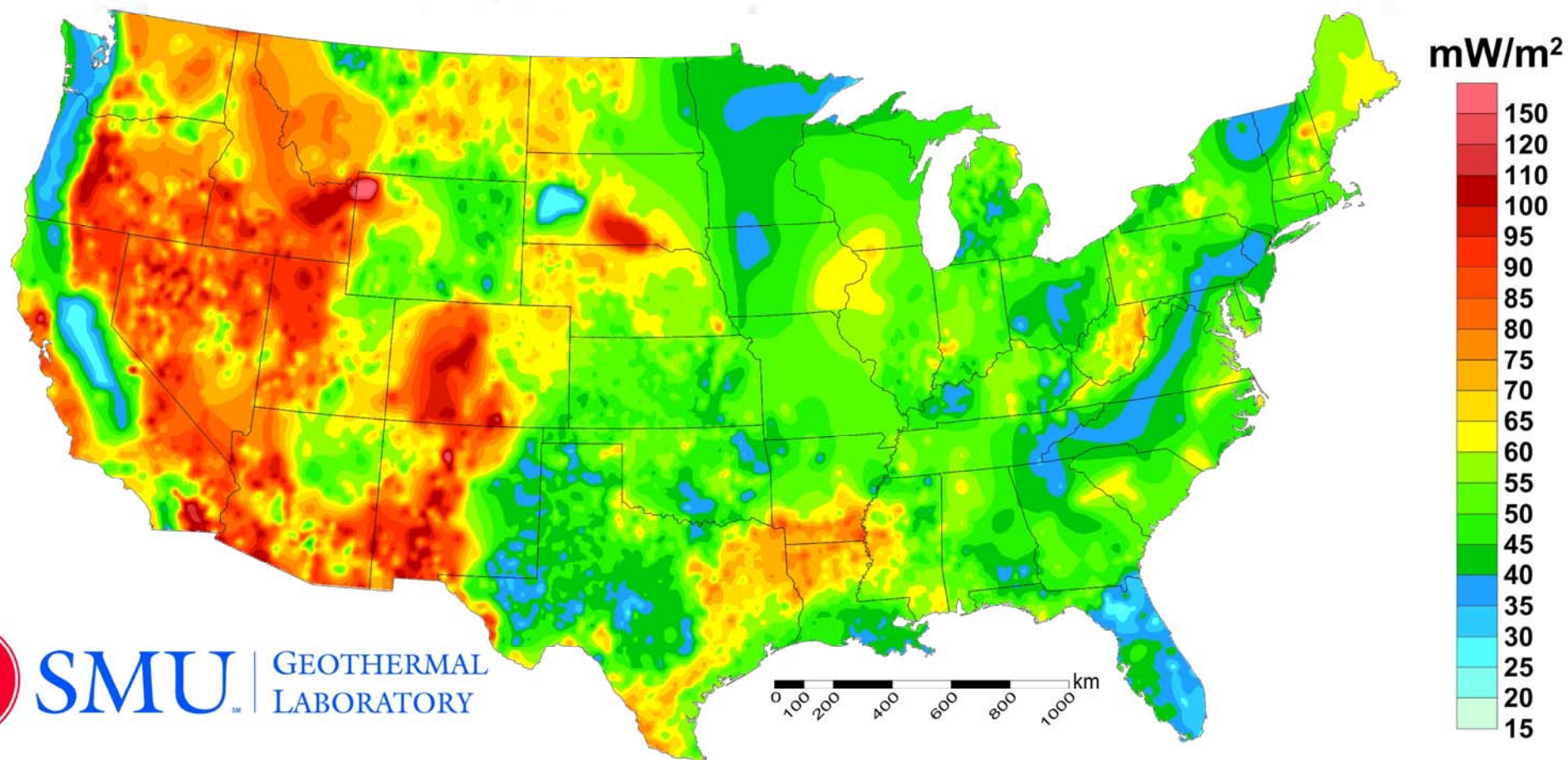
vs.

LINCOLN COUNTY WATER
DISTRICT, et al.

JOINT APPENDIX

VOLUME 19 OF 49

SMU Geothermal Laboratory Heat Flow Map of the Conterminous United States, 2011



Reference: Blackwell, D.D., Richards, M.C., Frone, Z.S., Batir, J.F., Williams, M.A., Ruzo, A.A., and Dingwall, R.K., 2011, "SMU Geothermal Laboratory Heat Flow Map of the Conterminous United States, 2011". Supported by Google.org. Available at <http://www.smu.edu/geothermal>.

SE ROA 36947

Guest Editorial/

It Is the Discharge

by John Bredehoeft

We all know the mantra *Keep It Simple*—the principle KISS. I have been thinking of another mantra for ground water—*It Is the Discharge*. Let me explain: In a recent conversation with one of my distinguished colleagues, he bemoaned our lack of understanding of ground water recharge. I keep thinking about that conversation. In a broad sense as hydrogeologists, we are hoping to understand how aquifer systems function, more particularly how much water is flowing through a particular system—the focus on recharge is simply one facet of the larger task. In studying the system, there are at least three aspects that we can focus on—(1) the recharge; (2) the aquifer itself as a transmission mechanism; and (3) the discharge from the aquifer.

One of the first principles of hydrogeology is that the recharge is balanced by the discharge before the system is perturbed. One tack commonly taken is to focus on the discharge and assume that recharge equals discharge. Of course, when we model a system in a virgin state, the mathematics demand conservation of mass, and the recharge, flow through the aquifer, and the discharge are balanced (or we do not have a solution to the problem). Often it is the capacity of the aquifer to transmit water that determines both the recharge and the discharge—the aquifer can accommodate only so much flow.

Generally, the recharge is the most difficult component of the ground water system to quantify, which brings me back to my colleague's comment—Shouldn't we be spending additional research effort to understand the recharge? My response is that it is more fruitful to examine the discharge. However, rarely do I hear hydrogeologists say that they are studying ground water discharge, especially in the academic community. Yet, the discharge is generally there to be observed—it occurs as springs, as base flow to streams, and as water for phreatophytes in the desert environment. There is a reason why hydrogeologists in Nevada still use the Maxey/Eakin method to estimate recharge, a method published in 1949—no one has come up with an improved procedure to estimate recharge even given 50+ years of further investigation. On the other hand, the methods of measuring phreatophyte discharge are greatly improved.

The Hydrodynamics Group, 127 Toyon Lane, Sausalito, CA 94965; (415) 332-0666; jbrede@aol.com; and member of Board of Directors AGWSE.

Copyright © 2007 The Author(s)

Journal compilation © 2007 National Ground Water Association.
doi: 10.1111/j.1745-6584.2007.00305.x

Furthermore, human activities that impact a ground water system ultimately impact the discharge. It is usually the ground water discharge that is captured during ground water development. The USGS (1972) in *Definitions of Selected Ground Water Terms* published the following definition of *capture*:

Water withdrawn artificially from an aquifer is derived from a decrease in storage in the aquifer, a reduction in the previous discharge from the aquifer, an increase in recharge, or a combination of these changes. The decrease in discharge plus the increase in recharge is termed capture.

Many aquifers can be analyzed mathematically as if they are linear systems; this includes all confined aquifers and even water table aquifers where the change in head, caused by a given stress, does not change the saturated thickness greatly. In this case, neither the recharge nor the discharge is of concern; rather, the changes in these quantities, caused by the stress—the capture, are of interest. In the linear mathematical system, if one knows (1) the geometry of the aquifer system, (2) its hydrologic properties (permeability and storage), and (3) the boundary conditions, one can determine the impact of a given stress on the system. Often it is the discharge that we end up capturing.

Even if the recharge is not of pragmatic concern, it still may be of interest—we would like to fully understand the ground water system. Other factors such as how contaminants are transported through the system sometimes depend upon the recharge.

I have no doubt that studying recharge will be high on the list of research topics for the future. I am also confident that the recharge is better understood through the discharge where there is an integrated and observable hydrologic signal, and that discharge is of much more pragmatic concern than recharge. Harold Thomas, the distinguished professor of Water Resources at Harvard, was working on the problem by studying stream hydrographs; unfortunately, he died before he could publish his ideas. I tried unsuccessfully to point out the importance of the discharge in commenting on a proposed National Academy of Sciences/National Research Council research agenda—my remarks had no impact. Still, my argument is—*It Is the Discharge*.

Editor's Note: Opinions expressed in the editorial column are those of the author(s) and do not necessarily reflect those of the National Ground Water Association or the staff of the journal.



Hydrologic Assessment of Kane Springs

Hydrographic Area (206): Geochemical Framework

**Presentation to the Office of
Nevada State Engineer**

**Prepared for: Lincoln County Water District
and Vidler Water Company, Inc.**

April 2006

SE ROA 36949

JA_8455

Hydrologic Assessment of Kane Springs Valley Hydrographic Area (206):
Geochemical Framework

Presentation to the Office of the Nevada State Engineer

Prepared for: Lincoln County Water District and Vidler Water Company

CH2M HILL

April 2006

The locations of the wells and springs in the hydrographic areas of the Colorado River Basin in Nevada for the 99 available chemical analyses are shown on Figure 1a through 1c and listed in Table 1. Subsequent base maps for individual parameters will use only figures 1a and 1c for illustration purposes. Green colored circles are spring locations and red inverted triangles are well locations. These data are used to determine the geochemical framework within which to characterize the Kane Springs Valley. The base of the chemical analyses is from Thomas, Calhoun and Apambire (2001) (all analyses with a site number), supplemented with chemical analyses from other sources noted in the "Sources" column and included in the references.

Total dissolved solids of groundwater from the Kane Springs Valley (KSV) is higher than the TDSS of the Coyote Springs Valley (CSV) but appears to become relatively rapidly attenuated within the CPV groundwater system. These relationships indicate relatively rapid mixing and dilution of groundwater moving from KSV into the CSV system. Figure 2a and 2b are maps showing the calculated total dissolved solids sum (TDSS) concentrations for each of the locations with sufficient water chemistry to calculate the TDSS. The TDSS was calculated by summing the silica, calcium, magnesium, sodium, potassium, bicarbonate, sulfate and chloride. TDSS generally increases relatively gradually south from Pahrangat Valley through the Coyote Springs Valley to the Muddy Springs Area. The KSV production well, KPW-1 has a TDSS of 653 mg/L. The downgradient CSV well CSVM-4 has 564 mg/L suggesting a relatively rapid decrease in TDSS in groundwater moving from KSV to CSV. At, and south of, the Muddy River Springs Area (MRSA) TDSS increases from between about 250 and 660 milligrams per liter (mg/L) in the CSV to between 500 and 4,000 mg/L. VF-2 Spring with a TDSS of 9,970 mg/L has the highest TDSS.

The temperature of the KSV well KPW-1 of 57 degrees Celsius (°C) indicates that the KSV has a high thermal gradient. The average temperature of the other 79 analyses ranges from 7 to 41.6°C with a mean temperature of 24.3°C. This next highest temperature (41.6°C) is from a sample of groundwater from CSV well CSVM-4 downgradient of KPW-1.

MAJOR ION CHEMISTRY OF GROUNDWATER

The major ion groundwater chemistry indicates three end-members water chemistry types: calcium-bicarbonate, sodium-bicarbonate and a mixture of calcium-sodium-sulfate water chemistry types. These water chemistry types for the end-members documenting mixing trends in both the springs and wells. Spring water chemistry forms more representative groups within the three end-members indicating more unique end-member representation than groundwater from the wells. Big Muddy Springs and associate springs in the MRSA are intermediate between all three end-members indicating they are a mixture of the three. In other words, the flow at MRSA do not originate from a single source but are a mixture of the three sources. Rogers and Blue Point Springs form a calcium-sodium-sulfate end-member. Groundwater from most of the wells indicates a mixing of the three end-members. Groundwater from only a few wells represent end-member water chemistry types indicating that most of the groundwater from wells are a mixture of water primarily between the regional carbonate aquifer and volcanics in the northern part of this segment of the Colorado River Basins. Beginning with the MRSA, this mixed groundwater continues to mix and is impacted by the evaporite-rich Muddy Creek Formation. The water chemistry reflects groundwater flowpaths presented in Eakin (1966). Northern and central CSV groundwater is primarily a mixture of recharge water from springs and regional carbonate aquifer groundwater in upgradient basins that includes groundwater from KSV. Regional carbonate groundwater from Pahanagat Valley appears to dominate the source of groundwater to CSV. Hidden Valley groundwater is very nearly the same type as the northern and central CSV. There is a water chemistry type trend that is compatible with two major groundwater flowpaths: one from central CSV through not only MRSA to Rogers and Blue Point springs but also one that moves from the central CSV through both Hidden and Garnet valleys.

Figure 3 shows the major ion relationships for all the analyses. Figures 4 and 5 are trilinear diagrams for all the springs and wells, respectively. Figure 6 illustrates the overlapping of well and spring data. Groundwater from the wells shows the mixing between the spring chemical types. Figure 7 shows the three-end-member distributions and their general associations. The calcium-bicarbonate type represents water primarily associated with calcite and carbonate rock. Regional carbonate aquifer groundwater from both the springs and wells forms a major part of this water chemistry type. Water from many mostly higher elevation springs are also represented in this type. The sodium-bicarbonate type represents water primarily in contact with and chemically reflects volcanic rocks. Groundwater from KSV Willow Springs and KPW-1 as well as CSV well CSVM-4 are indicative of this type. Gypsum in the evaporite-rich Muddy Creek Formation significantly impact groundwater within the boundary of this formation beginning with the MRSA and extending through the Rogers Blue Point springs in the Black Mountain Area. The sodium-chloride mineral, halite, is present in the Muddy Creek Formation in the extreme southern part of the Black Mountain Area and is probably responsible for the higher chloride in southern springs. Water from VF Spring 2 probably reflects a near boundary of halite associated with the groundwater.

Figure 8 is a trilinear diagram showing the average water chemistry types for the springs and groundwater from wells in each of the hydrographic areas. Groundwater from Pahrnagat Valley springs and wells, KSV springs and groundwater from KPW-1 are most

closely associated with northern and central CSV groundwater suggesting that these two valleys provide major sources of recharge to CSV. CSV springs are on a direct mixing line with KSV springs and are also a probable source of groundwater to the CSV mixed water chemistry type. Hidden Valley groundwater is closely associated with the CSV groundwater suggesting groundwater moves to Hidden Valley from CSV with little change in water chemistry. The average for MRSA groundwater includes CSV groundwater mixed with and/or impacted by association with the Muddy Creek Formation. Rogers and Blue Point springs represent the groundwater most impacted by evaporite minerals in the Muddy Creek Formation. Groundwater in Garnet Valley is more strongly influenced by the Muddy Creek Formation than Hidden Valley groundwater.

Major ion chemistry does not indicate the origin of water that is associated with either the volcanic rocks or the Muddy Creek Formation. In other words, it does not separate water from the regional carbonate aquifer that moves into and within the volcanic rocks and Muddy Creek Formation from localized sources of recharge water moving into and within these two major chemistry altering units. From the above water chemistry types on the trilinear diagrams, all of these conditions are probable within the groundwater system. The stable isotope, deuterium is capable of making these distinctions and provides a quantitative estimate of the mixture for each sample location.

DEUTERIUM

Deuterium is not only a naturally occurring stable isotope of hydrogen present in all water it is also an integral part of the water molecules themselves. It initially becomes part of the water molecules forming rain and snow that recharges the groundwater system. The deuterium value in parts per thousand (δD in permil units) depends on the storm tracks from the ocean to where it reaches the land surface and the elevation of the land surface where it infiltrates into the subsurface groundwater system. Deuterium is an excellent marker to track a specific water source because it does not participate in chemical reactions. It retains an essentially constant δD in the groundwater as groundwater moves along and through the various flowpaths. Deuterium in the groundwater packet of recharged water does not change by chemical reactions with the rock but the δD does change if the groundwater mixes with another groundwater with a different δD . The δD change is proportional to the volume and δD of the mixing water.

There have been many excellent groundwater investigations that include this area utilizing deuterium for estimating the groundwater exchanges as the regional carbonate groundwater moves through the basins (Winograd and Friedman, 1972, Kirk and Campana, 1990, Thomas et al., 1996; and Thomas et al., 2001 to name a few). Most recently Smith et al. (2002) concluded that geologically historical " δD values of groundwaters in southern Nevada fall within the range of present-day recharge." This conclusion supports a time independent nature of the δD indicating that recent and ancient deuterium values in water recharging the aquifers in this area have remained essentially the same over time therefore δD depend only on the dominant storm path contributing recharge and land surface elevation.

Figures 8 and 9 show the 88 deuterium analyses for the locations having deuterium data. The δD ranges from -109 permil in the northern Pahranaagat Valley spring water to -75 permil in the southern part of CSV. Overall, the δD becomes more positive to the south

indicating increasing mixing of recharge water with the regional carbonate groundwater. The KSV well KPW-1 has a δD close to the lowest Pahranaagat δD with -104 permil. A duplicate sample analyzed by SNWA reported a δD of -105 permil.

Figure 11 is a standard δD - δ oxygen-18 plot showing data points for all the springs and groundwater from wells. Many of the points fall near or on the global meteoric water line (GMWL) defined by [$\delta D=8(\delta^{18}O)+10$] based on worldwide precipitation data (Craig, 1961) indicating some degree of evaporation affecting the precipitation forming recharge to the groundwater system in this area. Only three locations fall to the right of the dashed line defined by [$\delta D=8(\delta^{18}O)+0$] used by Thomas et al., 1996 to "eliminate samples significantly affected by evaporation for use in estimating groundwater flow systems." The three samples are groundwater from the Hidden well SHV-1 very near the line, Pahranaagat Valley, Lone Tree Spring in the middle and US FWS Well also in Hidden Valley farthest from the line indicating significant evaporation has affected these waters. Figure 12 shows the average δD -oxygen-18 for each of the hydrographic area wells and springs. These average points also show a considerable amount of mixing of δD values.

Mixing between the regional carbonate aquifer and other recharge sources (annual recharge from precipitation and geologically historical water recharge) is indicated by the intermixture of springs and wells virtually over the entire δD range. If mixing did not occur then the δD plotted on Figures 11 and 12 would consist of essentially two clusters of points with the regional carbonate aquifer clustering around -109 permil plus or minus about 2 permil and the other waters clustering around about -87 permil. Some springs and wells do occur around these δD but by far most of the δD of both wells and springs plot between these two end-members indicating that they represent a mixture of the two.

Mixing naturally occurs between the regional carbonate groundwater and the other sources. Mixing is promoted by geological structures including faults, fractures, joints and karst features in the carbonate rocks. Mixing also occurs by pumping a well completed across two or more contributing depth intervals with different δD s. Figure 12 plots δD against the depth interval that contributed the δD in the California Wash area showing a shallow very high δD of about -70 permil but by a depth of about 400 feet the groundwater becomes considerably lighter with a range of values between -90 and -105 permil. The shallow groundwater is likely geologically recent recharge water and the deeper groundwater is probably the regional carbonate groundwater. Figure 13 shows what the δD of groundwater sampled from open-hole wells completed at deeper and deeper depths from the surface. Mixing between the geologically recent recharge water and the regional carbonate groundwater would occur from this pumped groundwater. The δD would significantly change toward that of the regional carbonate groundwater with completion depth of the well but it would not achieve the full δD signature even with full depth completion. Of course, a sample collected from a well completed over the entire depth during the earliest pumping time would likely have a recharge signature and the signature would become more like the regional carbonate groundwater as pumping continues.

Since the δD of the groundwater appears to be a mixture of regional carbonate groundwater and other waters the proportion of both groundwaters can be calculated by the simple mixing equation:

$$PRCGW = (\delta D_{Sample} - \delta D_{SGW}) / (\delta D_{RCG} - \delta D_{SGW})$$

indicating increasing mixing of recharge water with the regional carbonate groundwater. The KSV well KPW-1 has a δD close to the lowest Pahrnatat δD with -104 permil. A duplicate sample analyzed by SNWA reported a δD of -105 permil.

Figure 11 is a standard δD - δ oxygen-18 plot showing data points for all the springs and groundwater from wells. Many of the points fall near or on the global meteoric water line (GMWL) defined by [$\delta D=8(\delta^{18}O)+10$] based on worldwide precipitation data (Craig, 1961) indicating some degree of evaporation affecting the precipitation forming recharge to the groundwater system in this area. Only three locations fall to the right of the dashed line defined by [$\delta D=8(\delta^{18}O)+0$] used by Thomas et al., 1996 to "eliminate samples significantly affected by evaporation for use in estimating groundwater flow systems." The three samples are groundwater from the Hidden well SHV-1 very near the line, Pahrnatat Valley, Lone Tree Spring in the middle and US FWS Well also in Hidden Valley farthest from the line indicating significant evaporation has affected these waters. Figure 12 shows the average δD -oxygen-18 for each of the hydrographic area wells and springs. These average points also show a considerable amount of mixing of δD values.

Mixing between the regional carbonate aquifer and other recharge sources (annual recharge from precipitation and geologically historical water recharge) is indicated by the intermixture of springs and wells virtually over the entire δD range. If mixing did not occur then the δD plotted on Figures 11 and 12 would consist of essentially two clusters of points with the regional carbonate aquifer clustering around -109 permil plus or minus about 2 permil and the other waters clustering around about -87 permil. Some springs and wells do occur around these δD but by far most of the δD of both wells and springs plot between these two end-members indicating that they represent a mixture of the two.

Mixing naturally occurs between the regional carbonate groundwater and the other sources. Mixing is promoted by geological structures including faults, fractures, joints and karst features in the carbonate rocks. Mixing also occurs by pumping a well completed across two or more contributing depth intervals with different δD s. Figure 12 plots δD against the depth interval that contributed the δD in the California Wash area showing a shallow very high δD of about -70 permil but by a depth of about 400 feet the groundwater becomes considerably lighter with a range of values between -90 and -105 permil. The shallow groundwater is likely geologically recent recharge water and the deeper groundwater is probably the regional carbonate groundwater. Figure 13 shows what the δD of groundwater sampled from open-hole wells completed at deeper and deeper depths from the surface. Mixing between the geologically recent recharge water and the regional carbonate groundwater would occur from this pumped groundwater. The δD would significantly change toward that of the regional carbonate groundwater with completion depth of the well but it would not achieve the full δD signature even with full depth completion. Of course, a sample collected from a well completed over the entire depth during the earliest pumping time would likely have a recharge signature and the signature would become more like the regional carbonate groundwater as pumping continues.

Since the δD of the groundwater appears to be a mixture of regional carbonate groundwater and other waters the proportion of both groundwaters can be calculated by the simple mixing equation:

$$PRCGW = (\delta D_{Sample} - \delta D_{SGW}) / (\delta D_{RCG} - \delta D_{SGW})$$

present in today's spring waters from geologically historical regional carbonate groundwater when its water level could have been higher. Therefore, the estimated regional carbonate groundwater percentages are retained and shown for all samples to be conservative and eliminate bias.

The estimated percentages of regional carbonate groundwater in each water sample with a δD are listed in Table 1 and shown on Figures 15 and 16. These two figures assume a continuous regional carbonate groundwater flow from Pahranaagat Valley south through springs in the Black Mountain area using the same end members for the entire flowpath. Figure 17 shows the percentage of regional carbonate groundwater assuming that the δD end members of the regional carbonate groundwater and recharge water change (shift) to -105 and -79 permil, respectively, within and/or downgradient of the MRSA (southern part of the area). This shift in the δD end members results for the discontinuous groundwater flowpath causes the estimated regional carbonate groundwater percentages to be 10 to 15 percent higher than the estimates for the continuous groundwater flowpath.

Figure 18 shows the estimated percentages of regional carbonate groundwater in each well and spring sample for the continuous groundwater flowpath. As would be expected, groundwater from most wells have a higher percentage of the regional carbonate groundwater and most springs have higher percentages of recharge water. Most of the well samples form a trend line of increasing recharge from their high latitude locations to the lowest latitude. This trend line suggests an average increase in recharge of about 0.3 per mile along the groundwater flowpath. The cluster of springs at a latitude of about 36.4 are the Rogers, Blue Point and other springs in the Black Mountain area. They are considerably below the well trend line with an estimated average of about 40 percent regional carbonate groundwater.

Figure 19 separates out the springs for the continuous groundwater flowpath. Only the Pahranaagat Valley and MRSA (including Big Muddy Springs) are above 50 percent regional carbonate groundwater. Most of the springs approach and are parallel to that percentage but others like CSV and a couple of the very southern Black Mountain Area springs imply a trend of increasing recharge water along a groundwater flow to the south.

Figure 20 shows the estimated regional carbonate groundwater for the individual wells (continuous flowpath). The trend is toward increasing recharge with groundwater flow to the south in an envelope of all the wells. The single well sample in the Black Mountain Area contains virtually no estimated regional carbonate groundwater and, therefore is almost all recharge water. Figure 21 segments the upper tier of wells and springs by groups showing a consistent trend from Pahranaagat through CSV and MRSA to Garnet Valley. Rogers and Blue Point springs and other Black Mountain Area springs are below the trend.

Table 2 lists the average estimated percentages of regional carbonate groundwater in wells for the hydrographic areas, KPW-1, Big Muddy Spring and both Rogers and Blue Point Springs. Values are for the continuous groundwater flowpath except for Rogers and Blue Point Springs where the continuous and discontinuous groundwater estimates, respectively, are listed. There is a dominance of about 60 percent for most of the hydrographic areas suggesting that this is the average percentage of regional carbonate groundwater moving south from Pahranaagat Valley through Garnet Valley and California Wash. CSV has an estimated five percent more recharge water mixing with the regional carbonate

groundwater while Meadow Valley Wash has an estimated 22 percent more recharge water. However, the Rogers and Blue Point springs estimate is about 20 percent below the about 60 percent continuous groundwater flowpath that probably documents the major flowpath to

Table 2. Average percentage of regional carbonate Groundwater In wells of the hydrographic areas plus KPW-1 well, Big Muddy, Rogers Springs and Blue Point Springs.

Hydrographic Area/Well/Spring	Average Percent Regional Carbonate Groundwater
Pahanagat Valley	60
KPW-1	82
Coyote Springs Valley	55
Garnet Valley	58
Muddy River Springs Area	62
Big Muddy Spring	60
Meadow Valley Wash	38
California Wash	61
Rogers Spring	39 and 50
Blue Point Spring	42 and 53

the south. This relationship suggests that either Rogers and Blue Point springs are on a entirely different flowpath origin, for example the Virgin-River-Mesquite groundwater flowpath, a mixture of this different flowpath or are a weak secondary groundwater flowpath from the major MRSA flowpath. Given this ambiguity of the regional carbonate groundwater flow path to these two springs, the latter is included in this work. Therefore, the estimated regional groundwater percentages suggest two major groundwater flowpaths south of CSV, one through Garnet Valley moving south and a second moving through the MRSA into California Gulch flowing to the south but with the potential for a weak secondary flowpath that might include the Rogers Spring and Blue Point Spring to the east of this second major groundwater flowpath.

CARBON-14

Carbon-14 is a radionuclide that decays with a half-life of 5,370 years occurring as part of the carbon molecules that comprise the bicarbonate, carbonate and organic carbon in a water. Unlike deuterium, carbon-14 can be lost along groundwater flowpaths by carbonate precipitation or gained by dissolution of carbonate minerals and rocks as well as degraded organic carbon compounds. There are several geochemical models that approach accounting for these sources by using carbon-13 values and other techniques but there are insufficient data to approach modeling the carbon-14 date. Even the current geochemical models cannot really account for the relative amounts of mixing of groundwater with many different ages. The carbon-14 values typically reported in percent modern carbon (pmc) for the bulk groundwater in some cases can be, for example, almost all regional carbonate groundwater so that an apparent age calculated by using only the carbon-14 half-life may be near the true age of the groundwater. Alternately, and perhaps more usual, the bulk groundwater has a considerably more complex history that involves not only the products

of precipitation and dissolution reactions but also mixing between groundwaters of considerably variable ages. There are significant problems with age dates in southern Nevada as described by Winograd and Pearson (1976). This problem is still being worked on but at this point there is no readily available method that can give a consistently true "age" of any groundwater sample.

Figures 22 and 23 show the available carbon-14 values and their locations within the Colorado River Basin area. Table 3 lists a summary of carbon-14 data and the simple apparent age for hydrographic areas, KSV well KPW-1 as well as Big Muddy, Rogers and Blue Point springs. Most of the apparent ages are in the 14,000 to 35,000 years before present range. The KSV well, KPW-1, has one of the oldest apparent ages at 29,900 years. Assuming that the apparent ages are somewhat true, and in this case it may well be, it is not probable that KSV groundwater represented by KPW-1 with this age could represent a significant contribution to the flow at Big Muddy Springs. Again assuming that the apparent ages are somewhat true, the average apparent age for CSV of 20,800 years is essentially the same as MRSA which would support the above second major groundwater flowpath to the south.

Table 3. Carbon-14 percent modern carbon (pmc) values and apparent ages for hydrographic areas, KSV well KPW-1, major springs in Pahranaagat Valley as well as Big Muddy, Rogers and Blue Point springs.

Hydrographic Area/Well/Spring	Carbon-14 (pmc)	Apparent Age (Years Before Present)
Pahranaagat Valley, Major Springs	6.3-8.4	20,300-21,700
KPW-1	2.7	29,900
Coyote Springs Wells	4.2-17.9	14,200-26,200
Garnet Valley Wells	3	29,000
MRSA	8.4	20,500
Big Muddy Springs	7	22,000
Rogers Spring	1.6,2.4	30,900-34,200
Blue Point Spring	7.2,5.4	21,800-24,100

A longer travel time is estimated with the same assumption applied to travel time from CSV to Garnet Valley of 8,000 years. A similar assumption would mean a travel time from Big Muddy Springs to Rogers Spring on the order of about 10,000 years. The difference between Rogers Spring and Blue Point Spring apparent ages bring a common source to each spring into question. The difference could be a somewhat true age but may be related to either mixing differences between the water arriving at each spring or simply significantly more recent organ carbon present within the Blue Point Spring than Rogers Spring. The apparent ages indicate that the groundwaters within the Colorado River Basin flowpath are not young but are within the range of groundwater ages of groundwater in other basins in the southwestern U.S. Furthermore, travel time between hydrographic areas is probably on the order of thousands of years.

FLUORIDE

Fluoride is commonly elevated in groundwater associated with volcanic rocks. Figures 24 and 25 show the fluoride concentrations and their locations. Fluoride has an average concentration of 1.6 mg/L for the 63 analyses that include fluoride. Fluoride ranges from 0.1 to 6.1 mg/L with three analyses exceeding the current drinking water standard of 4.0 mg/L: groundwater from the KSV well KPW-1 with 6.1 mg/L; Little Ash Spring in the Pahranaagat Valley, 4.8 mg/L; and the CSV well CSVM-4 downgradient of KPW-1 with 4.6 mg/L. All of the remaining springs and wells have less than 3 mg/L. The fluoride concentrations support groundwater flow from both Pahranaagat and KSV into the CSV by an overall elevated concentration probably related to both volcanic rocks from the caldera complex and the tuffaceous sediments deposited within the basins during and following the development of the caldera complex. As shown on Figure 26, dissolved fluoride concentrations are generally controlled to less than about 2 mg/L by calcium both as a dissolved form and particularly within carbonate rocks by the precipitation of the calcium-fluoride mineral fluorite. Groundwater with less than about 100 mg/L calcium has the highest fluoride concentration. The elevated calcium concentrations above 400 mg/L include Rogers, Blue Point, Corral and VF-2 springs that also have highly elevated TDSS.

ARSENIC

An elevated arsenic concentration of 46 micrograms per Liter ($\mu\text{g/L}$) is reported for the KSV groundwater from KPW-1. There are too few arsenic data reporting arsenic concentrations to evaluate the arsenic concentrations throughout the area but the dissolved arsenic concentration is often elevated in water associated with volcanic rocks. Other groundwater samples analyzed for this investigation indicate that groundwater in the CSV probably ranges from about 10 to 20 $\mu\text{g/L}$. Bateman (1976) included additional arsenic concentrations in some groundwaters from this segment of the Colorado River Basin. Ash Spring in Pahranaagat Valley contained 30 $\mu\text{g/L}$; Little Ash Spring contained 20 $\mu\text{g/L}$; and groundwater from a well in Pahranaagat Valley is reported to contain 250 $\mu\text{g/L}$ (Alamo Farmstead System Well). Below CSV, Pederson Warm Spring in the Muddy Area contained 20 $\mu\text{g/L}$ and the Bhemer Well downgradient of Big Muddy Springs is reported to contain 2.8 mg/L (2800 $\mu\text{g/L}$) arsenic.

These relationships indicate a high probability that groundwater in this area contains dissolved arsenic concentrations in excess of the new arsenic drinking water standard of 10 $\mu\text{g/L}$ arsenic. The arsenic probably originates from the volcanic rocks and volcanic sediments through which the part of the groundwater flows.

SUMMARY

Groundwater from the KSV well KPW-1 is a relatively old and warm regional carbonate aquifer groundwater with a sodium-bicarbonate water chemistry type. Along with the age, this water chemistry type is unique for the regional carbonate groundwater in this area. It is both older than and has a higher TDSS than the CSV. However, these signatures are considerably attenuated within the CSV. The δD for this groundwater identifies this groundwater as being regional carbonate groundwater that is mixed with about 18 percent recharge water. A comparison of these chemical and isotopic relationships with Big Muddy Springs and particularly Rogers Spring and Blue Point Spring indicates that the

groundwater from KPW-1, assumed representative of KSV groundwater, is too strongly attenuated within CSV to be identifiable in these springs.

Mixing relationships between the regional carbonate groundwater and recharge water of younger age estimates a regional groundwater flowpath moving from the Pahrangat Valley south through the CSV that includes groundwater flow from KSV. Regional groundwater flow below CSV separates into two major groundwater flowpaths: one moving south through Garnet Valley and a second moving south through California Gulch. It is unclear if Rogers Spring and Blue Point Spring groundwater are on a weak secondary groundwater flowpath from the MRSA or from the Virgin River-Mesquite flowpath or a mixture of the two.

The regional groundwater appears to contain an average of about 60 percent regional carbonate groundwater and 40 percent recharge water as it moves through these hydrographic areas. Estimated percentages of regional carbonate groundwater indicate that the percentage of recharge water increases with distance below Pahrangat Valley. Big Muddy Springs is estimated to be comprised of 60 percent regional carbonate groundwater while Rogers Spring and Blue Point Spring are estimated to contain 60 percent recharge and only about 40 percent regional carbonate groundwater.

REFERENCES

Bateman, R.L., 1976, Inventory and Chemical Quality of Ground Water in the White River-Muddy River - Meadow Valley Wash Area, Southeastern Nevada: Desert Research Institute Project Report 40, January 1976, 19p.

Craig, H., 1961, Isotopic variations in meteoric waters: *Science*, Vol. 133, pp. 1702-1703.

Eakin, T.E., 1966, A Regional Interbasin Ground-Water System in the White River Areas, Southeastern Nevada: *Water Resources Research*, Vol. 2, pp. 251-271.

Eakin, T.E. and Moore, D.O., 1964, Uniformity of Discharge of Muddy River Springs, Southeastern Nevada, and Relation to Interbasin Movement of Ground Water: U.S. Geological Survey Professional Paper 501-D, pp. 171-176.

Johnson, M.E., 1, 2006, Drilling and Development of CSI Well No. 1 for Coyote Springs Investment LLC, Coyote Spring Valley, Clark County, Nevada: August 2005, p. 19.

Johnson, M.E., 2, 2006, Drilling and Development of CSI Well No. 2 for Coyote Springs Investment LLC, Coyote Spring Valley, Clark County, Nevada: November, 2005, p. 22.

Kirk, S.T. and Campana, M.E., 1990, A Deuterium-Calibrated Groundwater Flow Model of a Regional Carbonate-alluvial System: *Journal of Hydrology*, Vol. 119, pp. 357-388.

Smith, G.I., Friedman, I., Veronda, G. and Johnson, C.A., 2002, Stable isotope compositions of waters in the Great Basin, United States - 3. Comparison of groundwaters with modern precipitation: *Journal of Geophysical Research*, Vol. 107, 4402, pp. ACL 16-1 to 16-15.

Thomas, J.M., Calhoun, S.C. and Apambire, W.B., 2001, A Deuterium Mass-Balance Interpretation of Groundwater Sources and Flows in Southeastern Nevada: Desert Research Institute Publication No. 41169, May, 2001, 46p.

Thomas, J.M., Welch, A.H. and Dettinger, M.D., 1996, *Geochemistry and Isotope Hydrology of Representative Aquifers in the Great Basin Region of Nevada, Utah, and Adjacent States*: U.S. Geological Survey Professional Paper 1409-C, Washington D.C., 100p.

Univ. of Arizona, 2006, *Personal Communication*

URS, 2006, *Final Draft Groundwater Sampling Report, Coyote Spring Valley, Nevada*: URS Job No. 23444639, Prepared for Lincoln County Water and Vidler Water Company, March 10, 2006.

USGS, 1984, *Compilation of Selected Hydrologic Data from the MX Missile Siting Investigation, East-Central Nevada and Western Utah*: U.S. Geological Survey Open File Report 84-702, 123p.

Vidler, 2006, *Personal Communication*.

Winograd, I.J. and Pearson, Jr., F.J., 1976, *Major Carbon 14 Anomaly in a Regional Carbonate Aquifer: Possible Evidence for Megascale Channeling, South Central Great Basin*: *Water Resources Research*, Vol. 12, pp. 1125-1143.

Winograd, I.J. and Friedman, I., 1972, *Deuterium as a Tracer of Regional Ground-water Flow, Southern Great Basin, Nevada and California*: *Bulletin of the Geological Society of America*, Vol. 83, pp. 3691-3708.

Figure 1b

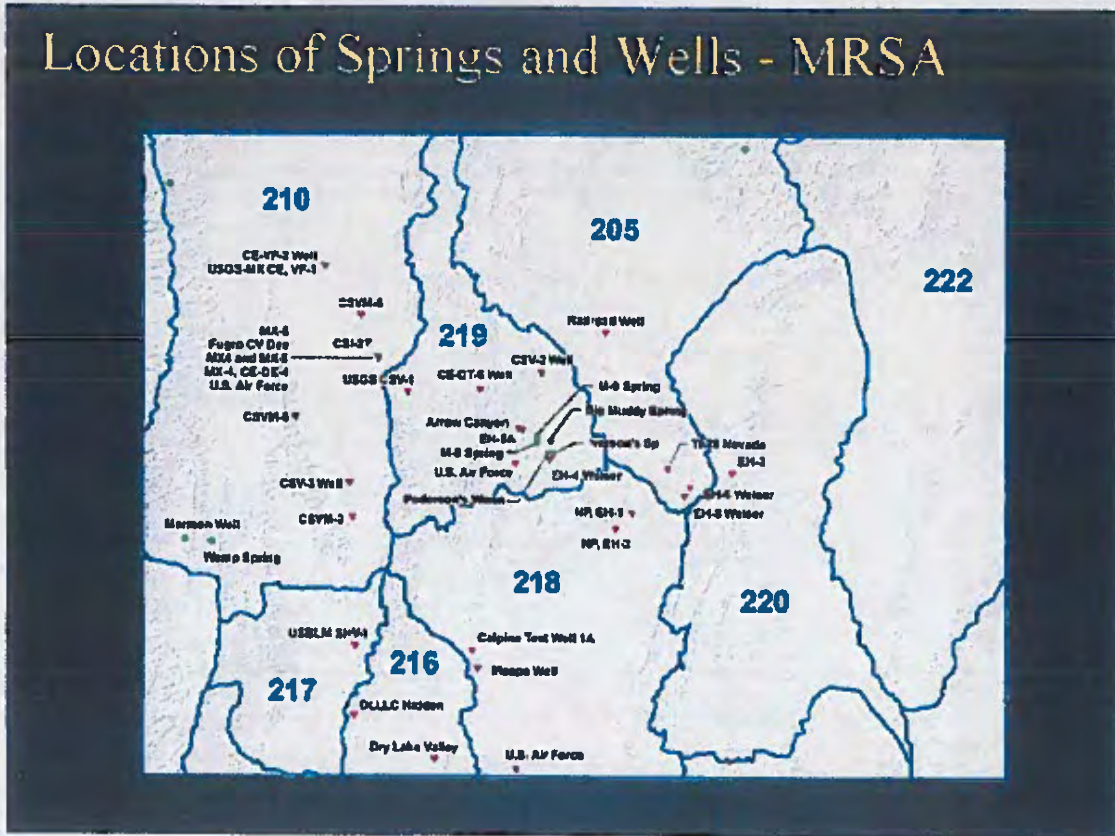


Figure 2a

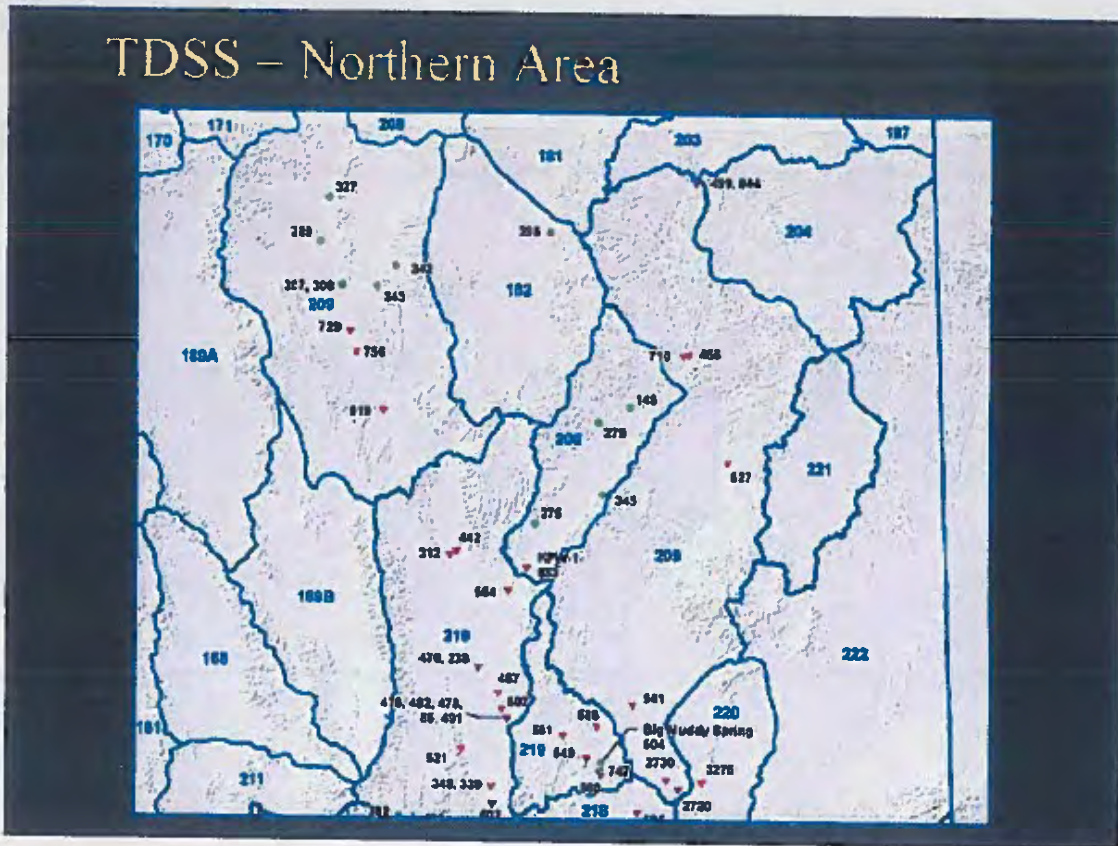


Figure 2b

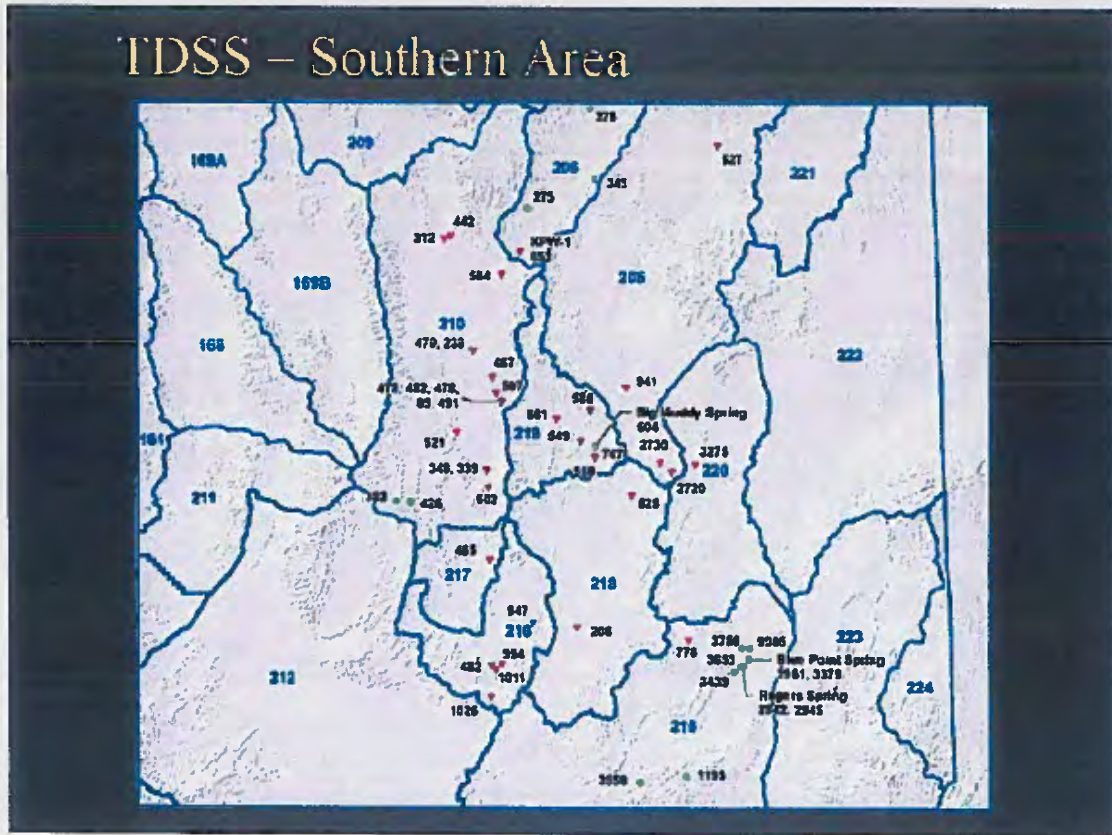


Figure 3

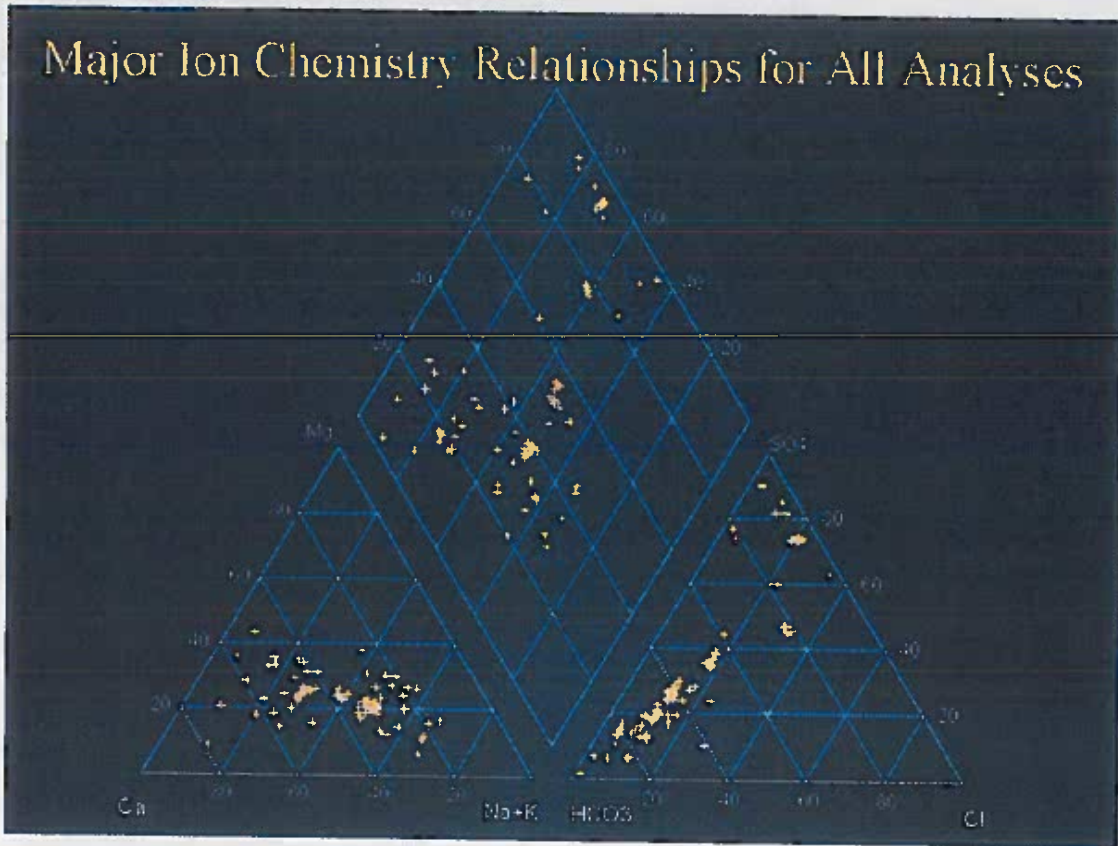


Figure 4

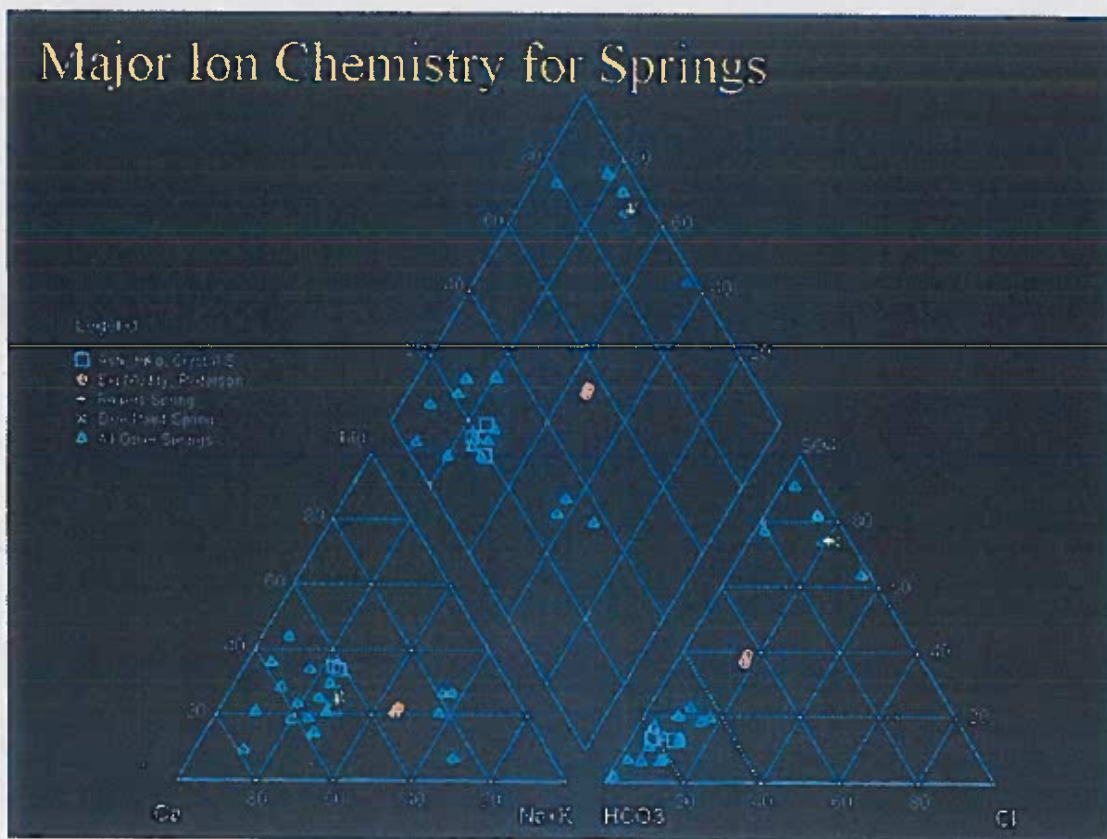


Figure 5

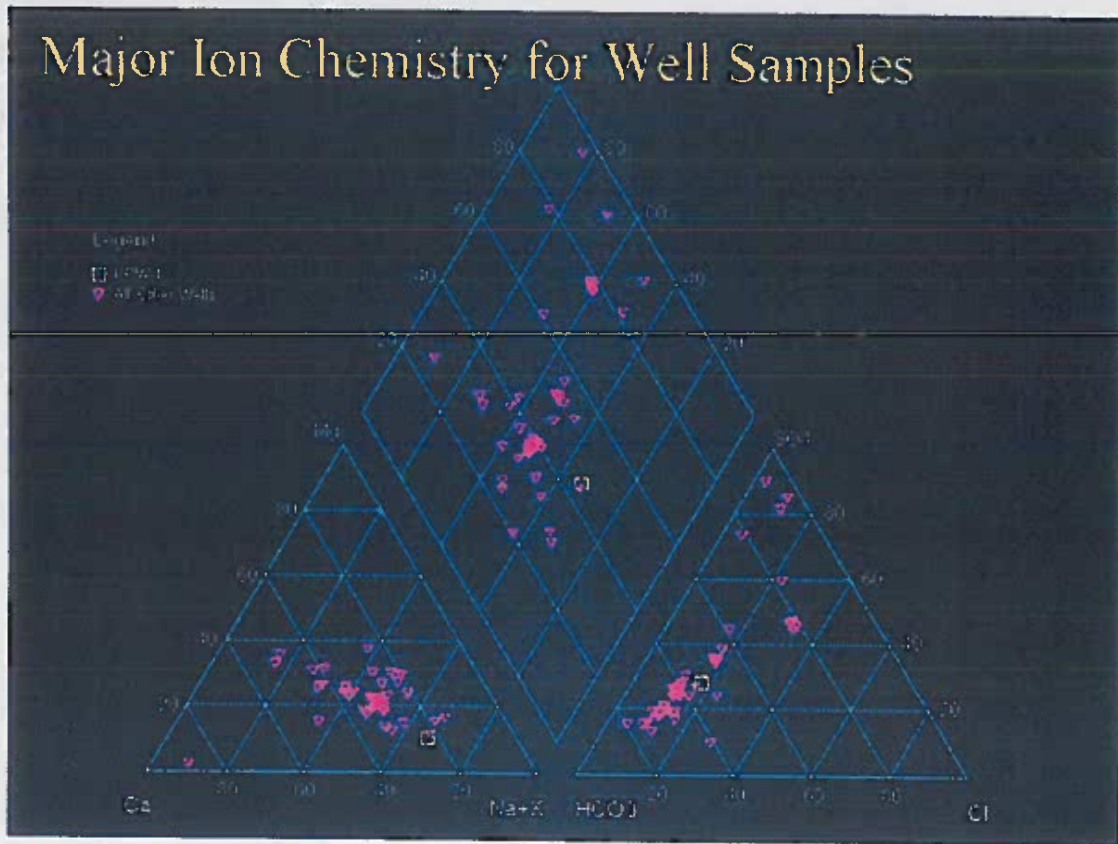


Figure 6

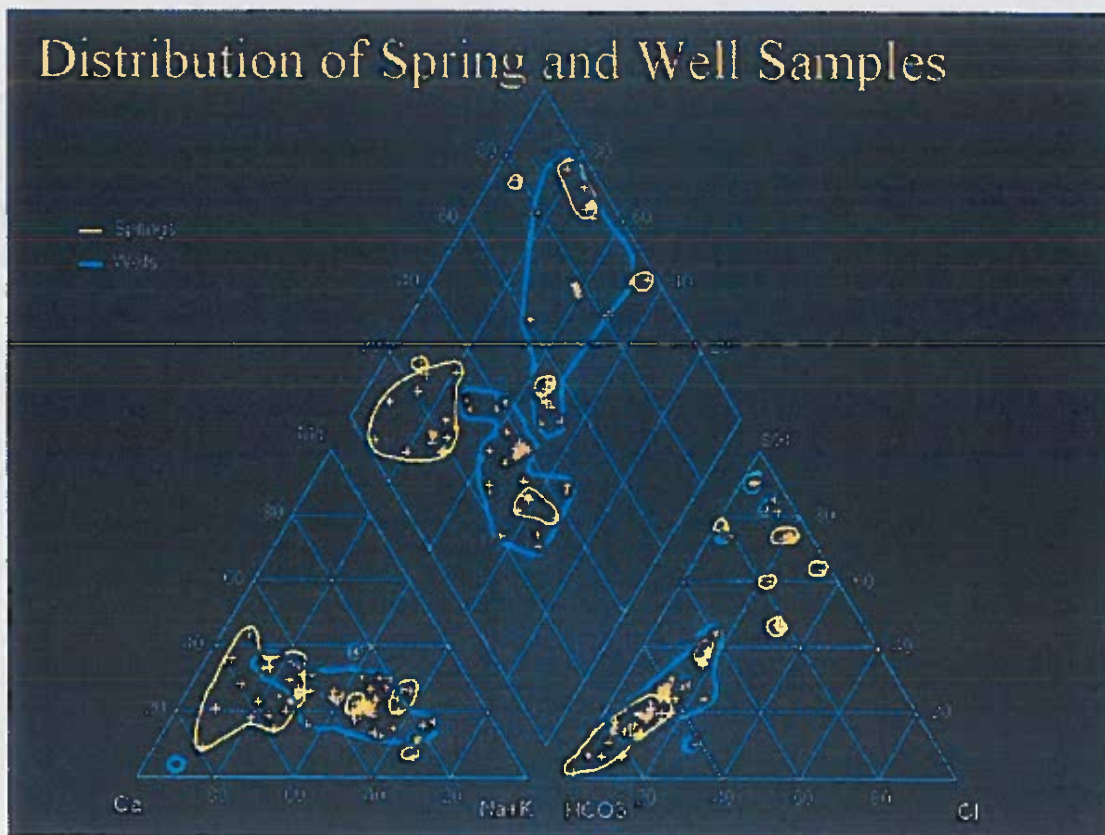


Figure 7

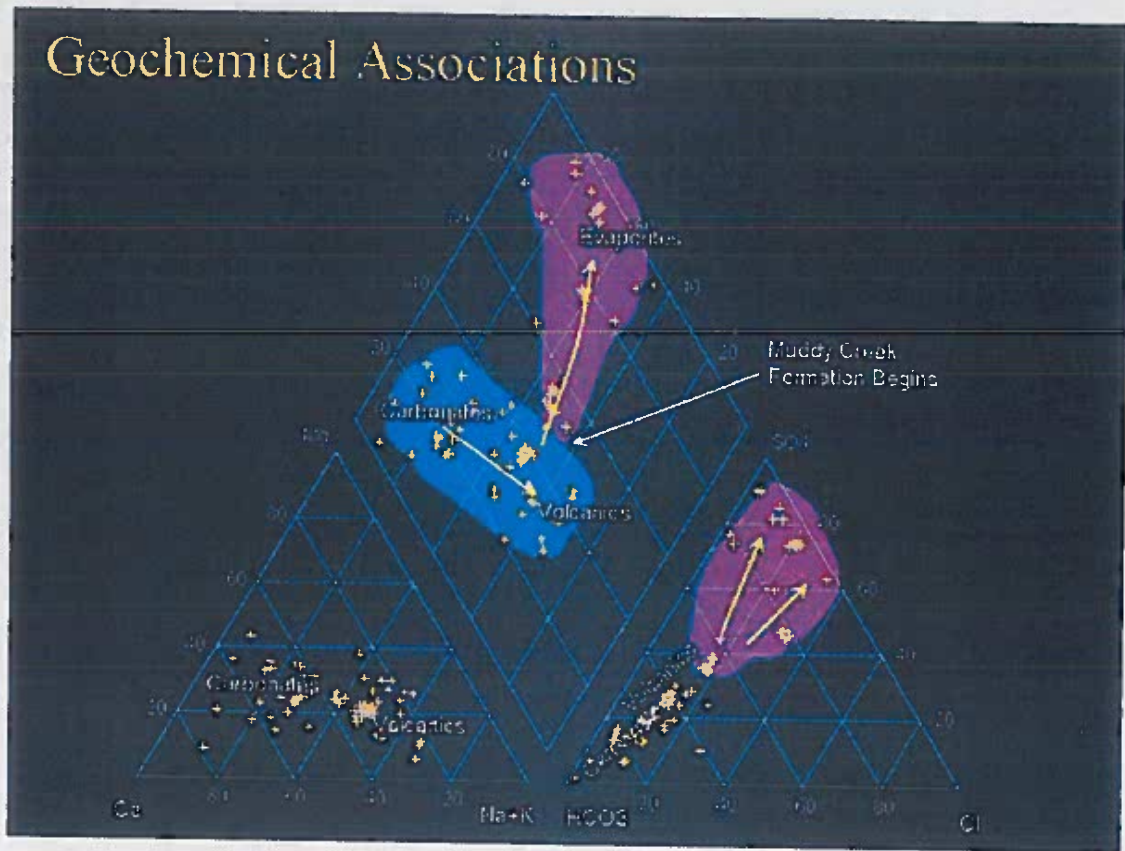


Figure 8

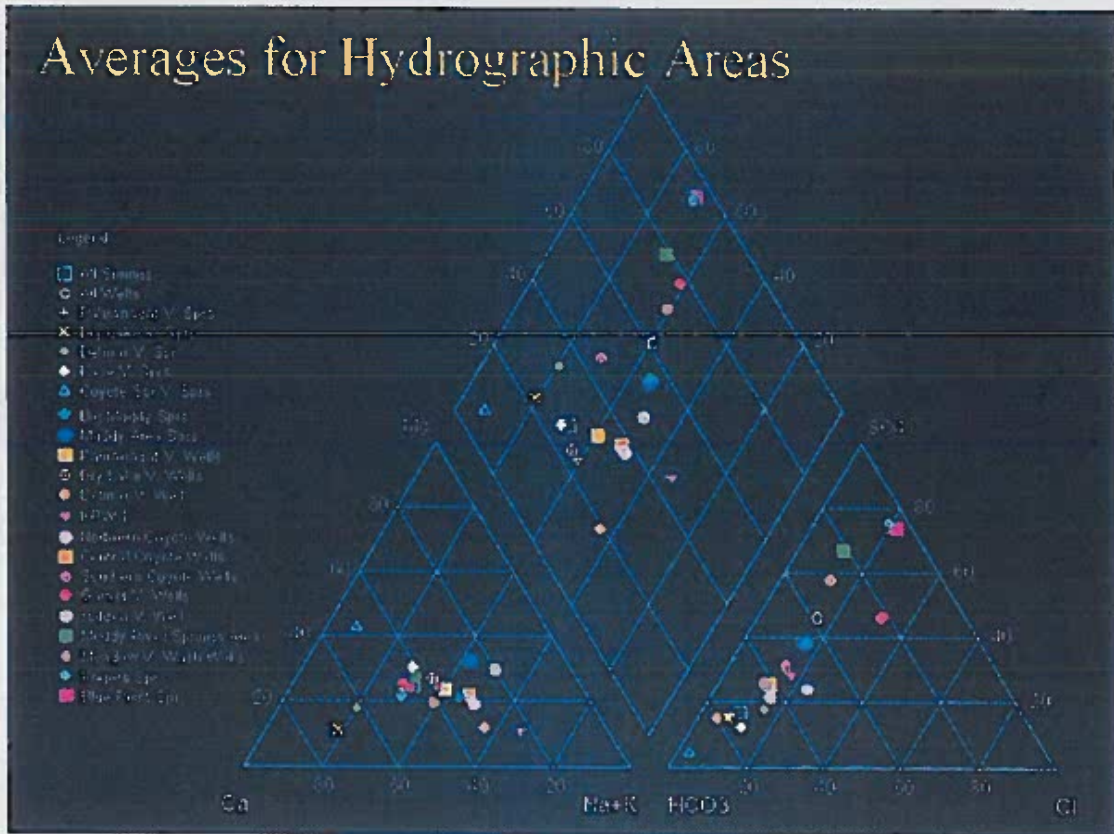


Figure 11

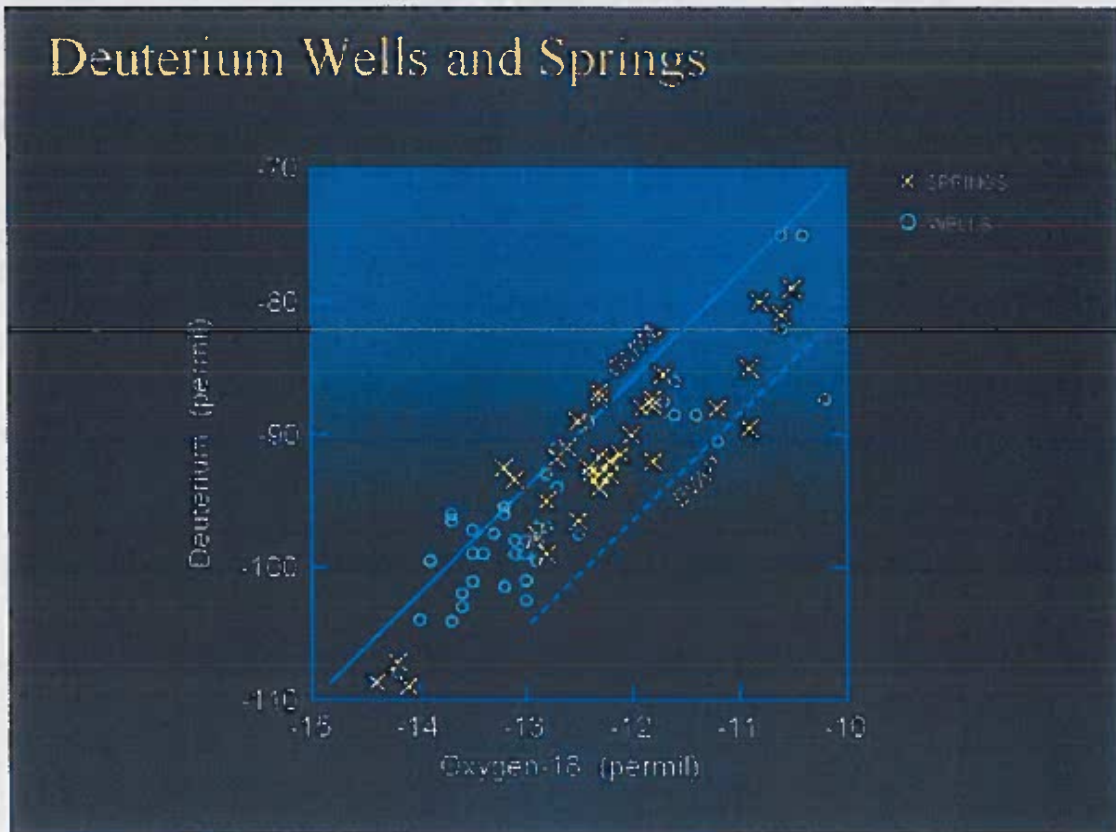


Figure 13

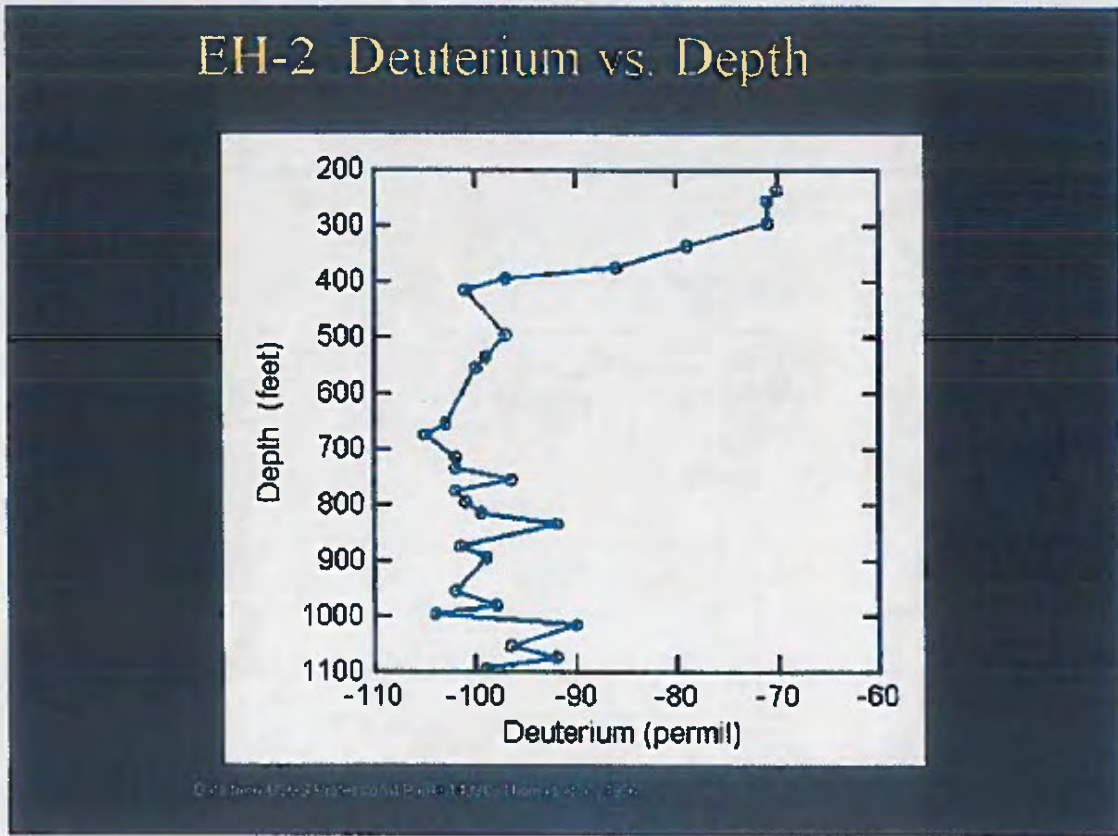


Figure 14

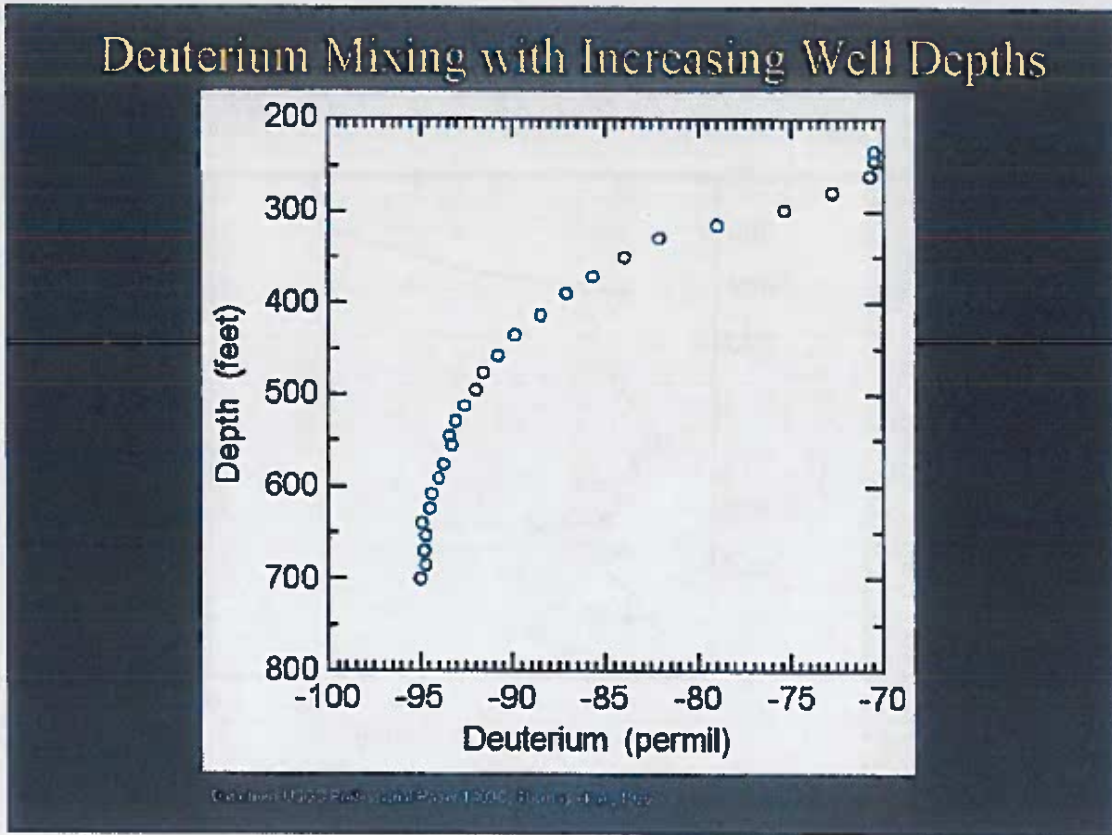


Figure 16

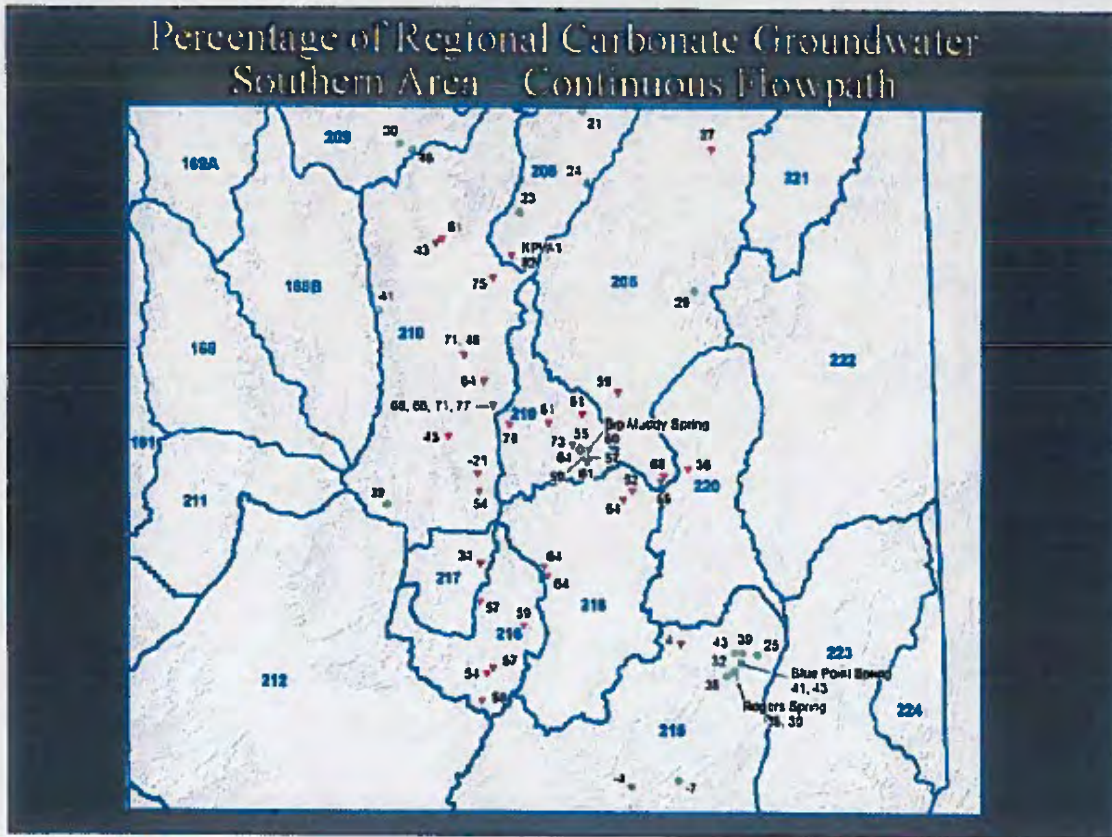


Figure 18

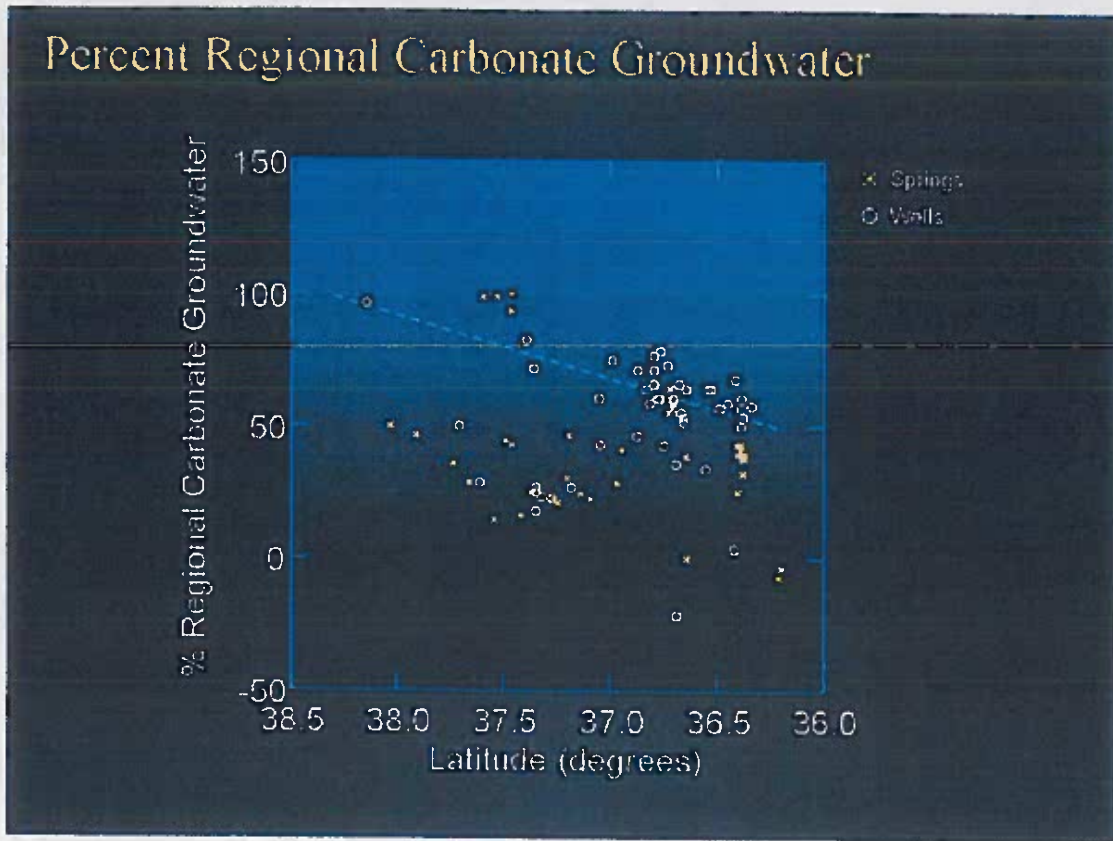


Figure 20

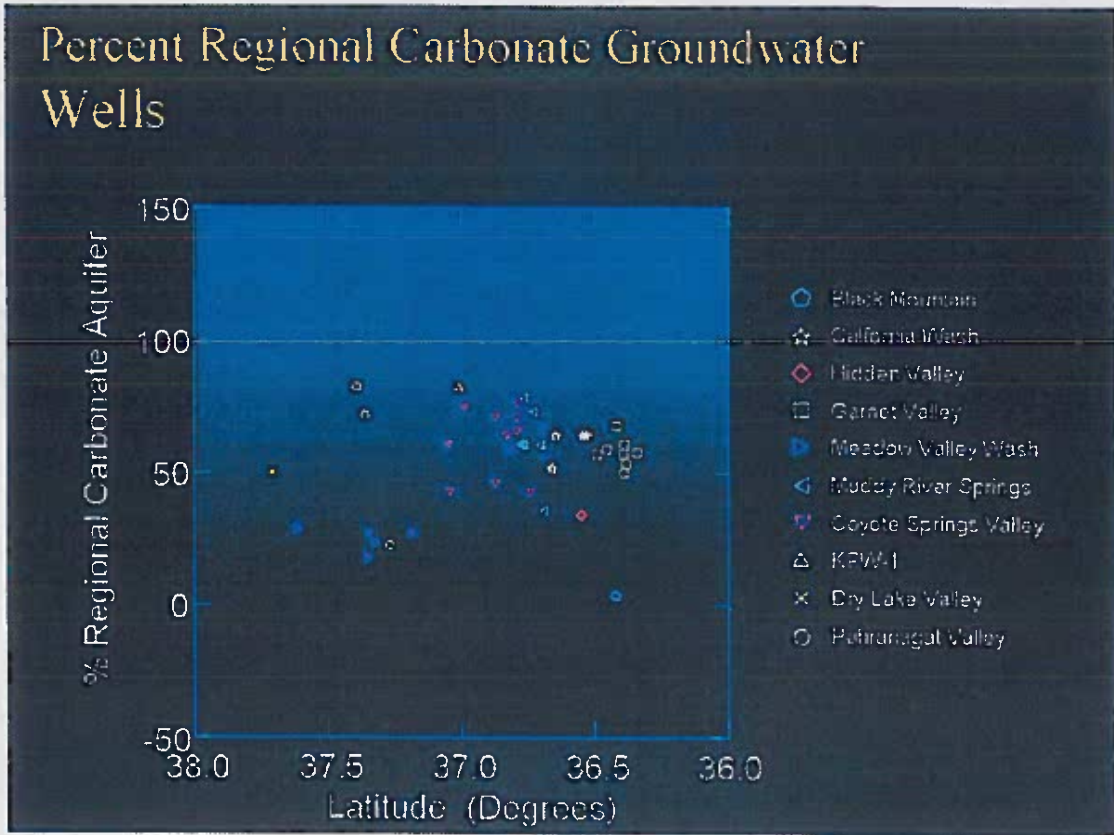


Figure 21

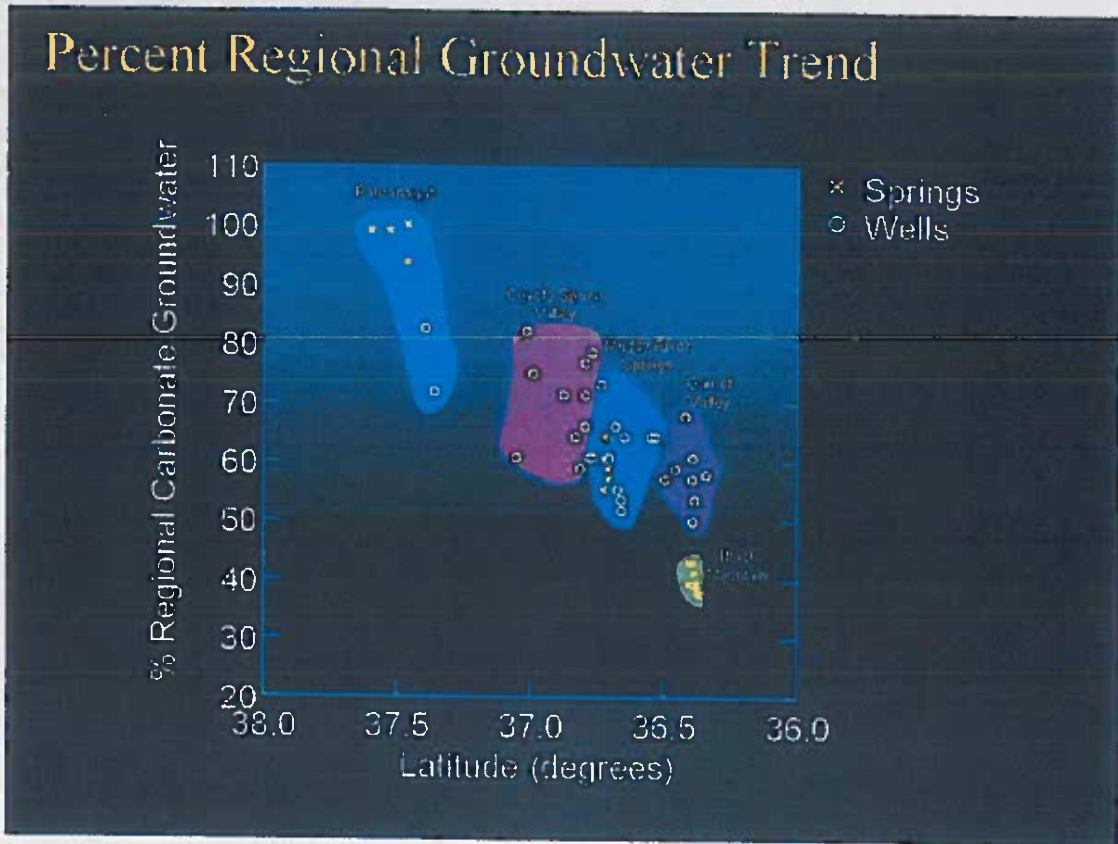


Figure 22

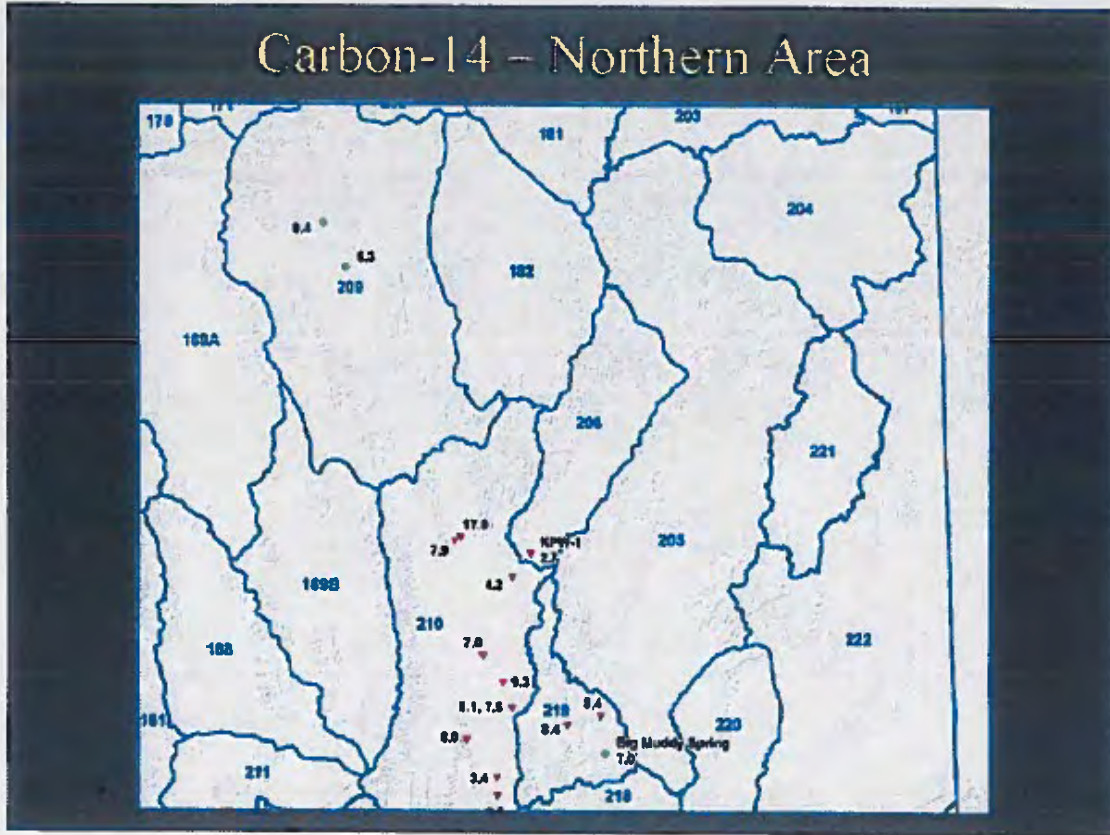
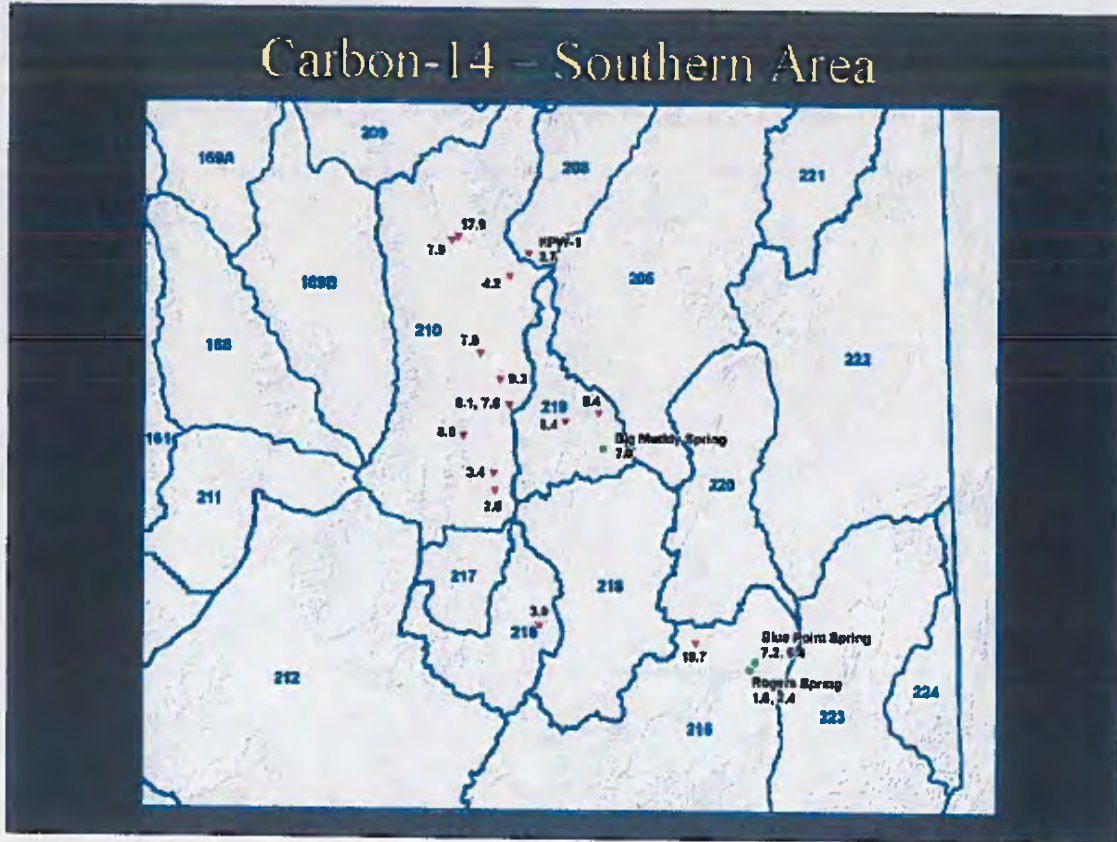


Figure 23



STRUCTURE AND DEVONIAN STRATIGRAPHY OF THE
TIMPAHUTE RANGE, NEVADA

Volume I

by
Alan K. Chamberlain
© Copyright, 1999

SE ROA 36992

JA_8498

A thesis submitted to the Faculty and Board of Trustees of the Colorado School of Mines in partial fulfillment of the requirements for the degree of Doctor of Philosophy (Geology).

Golden, Colorado

Date _____

Signed: _____

Alan K. Chamberlain

Approved: _____

Dr. John E. Warme

Professor and Thesis Advisor

Golden, Colorado

Date _____

Dr. Roger Slatt,
Professor and Head,
Department of Geology and Geological
Engineering

ABSTRACT

Sequences of Devonian rocks are advantageously exposed along a unique 40-mile-long east-west traverse in the greater Timpahute Range, southeastern Nevada. Study of these rocks casts light upon Devonian paleogeography, the Devonian Antler orogeny, an Upper Devonian cosmolite impact basin, this part of the Cretaceous Sevier fold-and-thrust belt, and the effects of Cenozoic extension. The greater Timpahute Range lies within the Timpahute Range 30' X 60' quadrangle and includes the region from Tempiute Mountain on the west to the Pahroc Range on the east.

Concealed major north-south trending normal faults caused by Cenozoic extension have been proposed to disrupt the Paleozoic rocks of the region. However, a structural interpretation using a new geologic map of the quadrangle requires no major north-south striking normal faults. Furthermore, the greater Timpahute Range is interpreted as a salient of stacked thrust sheets within the Sevier fold-and-thrust belt. The range is bounded on the north and south by thrust tear faults that may be related to basement fractures caused by the cosmolite impact.

Evidence for the Late Devonian cosmolite impact includes shocked quartz, iridium anomalies, ejecta spherules, and disturbed shallowing-upward sequences exhibiting intrasequence folding, brecciation, carbonate liquefaction, and graded bedding. Impact breccia thins radially from 510 feet at Tempiute Mountain to zero within 80 miles north and south of Tempiute Mountain, but within only 60 miles northeast and southeast of the impact site. Bed length measurements from a geometrically balanced cross section of the greater Timpahute Range show at least 64 miles of cumulative crustal shortening. When restored, the diameter of the concentric impact basin, centered near Tempiute Mountain, is 160 miles. A restored cross section suggests that the impact site is likely about 20 miles west of Tempiute Mountain.

Thrust sheets within the salient contain rocks of three contrasting facies above the cosmolite impact breccia marker: facies 1 is a peculiar, anoxic, deepwater, thin-bedded limestone characterized by soft-sediment slump folds and interbedded turbidites that may represent a crater fill that now is exposed in a proposed fenster on the west end of the range; facies 2 is a thick shallow-water quartz sandstone (as much as 1070 net feet thick) deposited on the west side of the impact basin that now is in an interpreted klippe in the middle of the range; facies 3 is a shallow-water platform carbonate deposited on the east side of the impact basin. It contains a large stromatoporoid reef.

Characterized by shallowing-upward cycles, a reference measured section for the carbonate platform facies 3 was correlated to surface and subsurface sections of the region using sequence characteristics and gamma-ray log patterns. Only 19 of 21 sequences are exposed in the reference section that lies in the footwall and east of the thrust sheet containing sandy facies 2. When viewed in order, isopach maps of the 21 sequences show a large (200 X 400 miles, unrestored) depression, the Sunnyside basin, the axis of which migrated from central Nevada to western Utah during the Devonian. A composite isopach map of the 21 sequences shows that the intrashelf Sunnyside basin is thickest and therefore centered over Sunnyside, 60 miles north of the Timpahute Range.

Quartz sandstone isolith maps show that Devonian quartz sandstones were deposited on the edges of the Sunnyside basin. It is proposed that sandstones on the west side were derived from the Devonian Antler orogenic forebulge. Sandstones on the east side were probably derived from the craton and more specifically from an east-west highland developed on the Uinta aulacogen in north-central Utah. Isopach patterns suggest that the highland or arch, herein called the Monitor-Uinta arch, extended into central Nevada.

Dolomite, a common constituent of much of the Great Basin Devonian, commonly occurs as penecontemporaneous dolomite caps on shallowing-upward cycles in facies 3. Sections of Upper Devonian strata near the edges of the Sunnyside basin are

more dolomitic than those within the basin. Dolomites, basinward of the sandy facies 2, are rich in the thin, stick-like stromatoporoid, *Amphipora*. Basinward of the *Amphipora*-rich dolomites are limestones rich in corals and bulbous and tabular stromatoporoids. A major unconformity, characterized by deep (100's feet) karst cavities, separates pervasively dolomitized Middle and Lower Devonian carbonates from Upper Devonian limestones. Of the three Upper Devonian facies in the greater Timpahute Range, only the facies 3 reference section contains significant dolomite as caps on shallowing-upward carbonate cycles, suggesting supratidal depositional environments in the shallower parts of the Sunnyside basin.

TABLE OF CONTENTS

ABSTRACT iii

LIST OF FIGURES xvii

LIST OF TABLES xx

LIST OF PLATES xxi

ACKNOWLEDGMENTS xxii

DEDICATION xvi

CHAPTER 1 1

INTRODUCTION 1

 Author’s Background Concerning Timpahute Range Research 4

 Purpose and Scope 5

 Format 8

 Location of the greater Timpahute Range 10

 Geologic Setting of the greater Timpahute Range 13

 Tectonic Setting 14

 Stratigraphic Setting 18

CHAPTER 2	26
RELATIONSHIP OF NEW RESEARCH TO PREVIOUS STUDIES	26
Mapping	27
Stratigraphy	27
Pre-Devonian Stratigraphy	28
Devonian Lithostratigraphy	31
Sevy Dolomite	32
“Oxyoke Formation”	33
Simonson Dolomite	34
Guilmette Formation	38
West Range Limestone	39
Pilot Formation	40
Regional Comparison	41
Younger Paleozoic Rocks of the Study Area	43
Sevier Synorogenic Sediments	44
Age of Thrusting	45
Distribution and Stratigraphy	48
Structure and Tectonics	49
Pre-Antler Orogeny	49
Monitor-Uinta Arch	52
Devonian-Mississippian Antler Orogeny	54
Mesozoic Sevier Orogeny	54
Sevier Fold-and-Thrust Belt	56
Sevier Fold-and-Thrust Belt in Nevada	57
Sevier Fold-and-Thrust Belt Analogue	58
Thrust Detachment	59

Tectonic Model of Thin-Skinned Deformation	60
Cenozoic Volcanism and Extension	64
Summary	65
CHAPTER 3	65
METHODS USED	65
Data Identification	66
Mappable Sequences	67
Measured Sections	74
Stratigraphic Terminology	75
Data Collection	76
Global Positioning Systems (GPS)	77
Aerial Photographs and Field Work Maps	78
Geographic Information System (GIS)	79
Gravity Data	79
Computer-aided Structural Cross Sections	81
Surface Gamma-Ray Logs	84
Gamma-Ray Logs vs. Fischer Plots	85
Gamma-Ray Field Data Acquisition	87
Data Analysis	87
Regional Correlations	88
Data Manipulation	90

CHAPTER 4	90
DEVONIAN SEQUENCES	90
Sequences	90
Devonian Sequences	91
Stratigraphic Sequences and the Geologic Map	92
Sequences and Sequence Boundaries	93
Mechanisms for Cycle and Sequence Development	99
Devonian Sequences at TMS	102
Sevy Dolomite	102
Characteristics of the Sevy Dolomite	104
Lower Contact	105
Upper Contact	105
Gamma Radiation	106
Environment of Deposition	107
“Oxyoke Formation”	108
Establishing the “Oxyoke Formation”	109
Characteristics	111
Thickness	112
Gamma Radiation	113
Sand Provenance	113
Environment of Deposition	114
Oxyoke Formation at Tempiute Mountain and Monte Mountain	115
“Oxyoke Formation” Sequences	115
“Oxyoke Formation” Sequence 1	116
“Oxyoke Formation” Sequence 2	116
Simonson Dolomite	118

Coarsely-Crystalline Sequence	120
Gamma Radiation	120
Structural Implications	121
Lower Alternating Sequence	121
Gamma Radiation	122
Brown Cliff Sequence	122
Gamma Radiation	123
Upper Alternating Sequence	123
Gamma Radiation	123
Regional Simonson Dolomite Unconformity	125
Guilmette Formation	129
Weathering Profile	129
Lithology and Texture	133
Color	133
Percentage of Limestone	134
Fossils	135
Bedding	137
Cycles	138
Cycle Thicknesses	140
Gamma Radiation	140
Guilmette Sequences	141
Fox Mountain Sequence	142
Summary of Descriptions	142
Fox Mountain, a Guilmette Formation Sequence	143
Fox Mountain Sequence Cycles	145
Distinguishing features of the Fox Mountain Sequence	146
Gamma Radiation	147

Interpretation of the Fox Mountain Sequence	148
Yellow Slope Sequence	150
Marker Beds	151
Cycle Thicknesses	151
Lithology, Texture, Erosional Profile, and Cycles	152
Gamma Radiation	152
Yellow Slope Sequence Interpretation	153
Sequence Dga	154
Gamma Radiation and Weathering Profile	154
Color, Texture, and Lithology	154
Typical Sequence Dga Cycle	155
Sequence Dga Cycles	155
Dolostone and Cycle Thicknesses	158
Subsequence Dga1	158
Subsequence Dga2	160
Sequence Dgb	161
Weathering Profile	162
Lithology, Color and Texture	163
Gamma Radiation	164
Subsequence Dgb2	166
Description and Fossils of the Dgb2 Breccia	167
Lower Contact of Dgb2 Breccia	168
Upper Contact of the Dgb2 Breccia	169
Distribution and Thickness of the Dgb2 Breccia	169
Origin of the Dgb2 Breccia	170
Reef Core vs. Reef Flank	171
Sequence Dgb3c	173

Sequence Dgb3f	173
Sequence Dgc	174
Sequence Boundary	174
Gamma Radiation	175
Depositional Indicators	175
Erosional Profile, Lithologies, Sequence Thicknesses, Textures, and Colors	176
Cycle Thicknesses	176
Sequence Dgd	
.....	177
Quartz Sandstone	177
Gamma Radiation	178
Sequence Dge	178
Gamma Radiation	178
Sequence Dgf	180
Sequence Dgg	180
Weathering Profile and Color	180
Gamma Radiation	181
The Uppermost Occurrence of <i>Amphipora</i>	182
West Range Limestone	183
Pilot Formation	184
Pilot Formation Sequence 1	185
Pilot Formation Sequence 2	186
Joana Limestone	187
Discussion	191

Dolomite at TMS	192
Finely-Crystalline Stratal Dolostone (Type 1)	194
Sevy Dolomite Finely crystalline Stratal Dolostone	194
Simonson Dolomite Finely crystalline Stratal Dolostone	195
Guilmette Finely-Crystalline Stratal Dolostone	196
Coarsely-Crystalline Stratal Dolostone (Type 2)	198
Pervasive Dolostone below the Simonson Dolomite Unconformity (Type 3)	
	199
Pervasive Dolomite in Paleozoic Rocks at TMS	200
Karsted Simonson Dolomite Unconformity	201
Sources of Dolomitizing Fluids	202
Timing of Dolomitization	203
Non-stratal Dolostone (Type 4)	205
Summary	207
Conclusions	208
CHAPTER 5	208
TIMPAHUTE RANGE STRUCTURAL ELEMENTS	210
Thrust Faults	213
Meadow Valley Mountain Thrust Sheet	213
Pahroc Thrust Sheet	217
Silver Canyon Thrust Sheet	218
Conclusions	219
Folds	220
Strike-Slip Faults	221
Strike-slip Faults as Thrust Tear Faults	221

Normal Faults	222
Extensional vs. Compressional Models	224
Conclusions	225
CHAPTER 6	225
STRATIGRAPHIC SIGNIFICANCE OF STRUCTURAL INTERPRETATIONS	225
Tectonic Model	226
Balanced Cross Section	227
Plate 4a and Plate 4b	228
Amount of Displacement	230
Facies Restoration and Devonian Paleogeography	232
Biostratigraphic Dislocations	233
Structural Implications of the “Oxyoke Formation”	234
Ely Springs Dolomite	235
Tertiary/Cretaceous Synorogenic Rocks	237
Conclusions	239
CHAPTER 7	239
DEVONIAN PALEOGEOGRAPHY	240
Sequence Correlations	243
Sunnyside Basin	250
Tempiute Basin	255
Devonian Sandstone	256
“Oxyoke Formation”	259
Guilmette Sandstones	259

Guilmette Sandstones in the Study Area	263
Regional setting of Guilmette Sandstones	265
Conclusions	266
CHAPTER 8	266
APPLICATIONS	266
Economic Applications	267
Oil and Gas Exploration	268
Sequence Boundaries in Exploration	268
Devonian Reefs	269
Devonian Porosity and Permeability	270
Sevy Dolomite Reservoir Potential	271
Roof Seal Potential	272
Mineral Exploration	273
Groundwater Exploration	273
Academic Applications	274
Structural Applications	274
Stratigraphic Applications	275
CHAPTER 9	275
CONCLUSIONS AND RECOMMENDATIONS	275
Conclusions	278
Recommendations	283

REFERENCES	283
APPENDICES	345
TABLE OF CONTENTS OF APPENDICES	345
APPENDIX A: ABBREVIATIONS	361
APPENDIX B: DEVONIAN CYCLES AT TMS	365
APPENDIX C: PETROLOGY	429
APPENDIX D: DIGITAL FIELD TRIP	461
APPENDIX E: DETAILED DESCRIPTIONS OF STRUCTURAL ELEMENTS OF THE TIMPAHUTE RANGE 30' X 60'	467
APPENDIX F: DEVONIAN DATA POINTS	559

LIST OF FIGURES

Figure 1 Index map showing the location of the Timpahute Range 30' X 60' quadrangle within the Sevier fold-and-thrust belt.	2
Figure 2 Sevier age thrust fault traces in eastern Nevada.	3
Figure 3 Index map showing the position of the Mail Summit 7.5' quadrangle (shaded gray) among the other 7.5-minute quadrangles (black lines) comprising the Timpahute Range 30' X 60' quadrangle.	9
Figure 4 Index map to the Mail Summit measured section (TMS) in the southwest part of the Mail Summit 7.5' quadrangle (stippled) and northern Mount Irish Se 7.5' quadrangle (hachured).	12
Figure 5 Topographic elements of the greater Timpahute Range	13
Figure 6 Pre-Antler orogeny tectonic setting and depositional profile from western Utah to central Nevada showing formational terminology from the Upper Cambrian through the Devonian.	15
Figure 7 Tectonic events at and since the Sevier orogeny in the eastern Great Basin. . .	17
Figure 8 Correlation diagram comparing the Devonian stratigraphy at TMS with the Paleozoic stratigraphy in the Egan and Pahrnagat ranges.	19
Figure 9 Index map showing parts of Nevada and Utah with location of southwest Mail Summit composite stratigraphic section, in the greater Timpahute Range near Hiko, Nevada, and other sections to which the TMS was correlated and used to make Plate 3	23
Figure 10 Time-rock transect and correlation chart illustrating Devonian nomenclature of the Sunnyside basin.	29
Figure 11 Distribution of outcrops of Mississippian Antler clastics in the Timpahute Range quadrangle as reported by Tschanz and Pampeyan (1970).	43
Figure 12 A correlation chart of surface to subsurface Middle and Lower Devonian	

sequences from Tempiute Mountain southeastward.	83
Figure 13 Composite stratigraphic column of southwest Mail Summit section	94
Figure 14 Legend for Figure 13	95
Figure 15 Distribution of Sevy Dolomite outcrops on the new geologic map of the Timpahute Range quadrangle.	104
Figure 16 Distribution of Simonson Dolomite outcrops on the new geologic map of the Timpahute Range quadrangle.	117
Figure 17 Generalized stratigraphic column of Middle and Upper Devonian Rocks in the Meadow Valley Mountains.	119
Figure 18 Distribution of Guilmette Formation outcrops on the new Timpahute Range quadrangle geologic map.	128
Figure 19 Histogram of percent dolomite within each cycle of the lower Guilmette Sequences at TMS	132
Figure 20 Histogram of percent limestone within each cycle of lower Guilmette sequences at TMS where Sequence Dgb3 is a stromatoporoid reef.	135
Figure 21 Histogram of cycle thickness and content of lower Guilmette Formation . .	139
Figure 22 Histogram of cycle thicknesses and content, Fox Mountain Sequence	145
Figure 23 Histogram of cycle thickness and content, Yellow Slope Sequence.	149
Figure 24 Histogram of cycle thickness and content, Sequence Dga1.	156
Figure 25 Histogram of cycle thickness and content of Sequence Dga2.	159
Figure 26 Histogram of cycle thickness and content of Sequences Dgb and Dgc	161
Figure 27 Histogram of cycle thickness and content, Sequences Dgbf and Dgcf.. . . .	163
Figure 28 Correlation chart comparing Guilmette cycles of Sequences Dgb3 and Dgc on a reef (Dgbc and Dgcc) with cycles on the reef flank (Dgbf and Dgcf) at TMS .	172
Figure 29 Distribution of Joana Formation outcrops on the new geologic map of the Timpahute Range 30' X 60' quadrangle.	187

Figure 30 Correlation of three measured sections in the greater Timpahute Range separated by Mesozoic thrust faults	190
Figure 31 Generalized diagenetic sequence for dolomites at TMS.	191
Figure 32 Generalized tectonic map of the Timpahute Range quadrangle	212
Figure 33 Diagrammatic stratigraphic cross section showing strata restored about Guilmette Sequence Dgb2 (Alamo Breccia) time..	231
Figure 34 North-south correlation of sections within the Silver Canyon (Gass Peak?) thrust sheet.	241
Figure 35 North-south correlation of sections between the Silver Canyon (Gass Peak?) and Pahroc (TMS) thrust sheets (Figure 2)	242
Figure 36 Isopach map of all 21 Devonian sequences of the Sunnyside basin	244
Figure 37 An unrestored isopach map of Guilmette Dgb2 breccia	247
Figure 38 Isopach map of unrestored Guilmette Sequence Dgb.	249
Figure 39 Crudely restored isolith map of the Guilmette Sequence Dgb2 breccia	253
Figure 40 An isopach map of “Oxyoke Formation” in the Sunnyside basin	258
Figure 41 Guilmette Formation net quartz sandstone isolith map, Timpahute area	261
Figure 42 An isolith map of the net quartz sandstone of the Guilmette Formation of the Sunnyside basin	264

LIST OF TABLES

Table 1 Paleozoic nomenclature in southeastern Nevada	20
Table 2 Wells and Measured Sections shown in Figure 9	24
Table 3 Criteria used to make facies assignments in the measured sections of the study area and beyond.	68
Table 4 Thickness, numbers of cycles, and significant features of Devonian sequences in southwest Mail Summit measured section, Timpahute Range, Nevada.	100
Table 5 Gamma radiation and weathering profile for the lower Guilmette Formation at TMS.	125
Table 6 Thicknesses and gross lithologies of the lower Guilmette Formation Sequences	130
Table 7 Color and texture of lower Guilmette Formation sequences expressed as percent of the sequence.	134
Table 8 Fossil occurrences in the lower Guilmette sequences at TMS	136
Table 9 Dolostone types, characteristics, distribution, inferred timing, and examples at TMS and in other parts of the study area.	193
Table 10 Bed length displacement scaled from a snip reconstruction model and the amount of slip for each thrust in Plate 4a	229
Table 11 Fossil occurrences in Devonian Guilmette rocks above Sequence Dgb2 breccia in three different thrust sheets of the greater Timpahute Range.	233
Table 12 Net Sandstone thickness of the Guilmette Formation in the Timpahute area and beyond providing data used to generate Figure 41	260

LIST OF PLATES

- Plate 1a** New geologic map and geologic cross section of the Timpahute, Nevada, 30' X 60' quadrangle.
- Plate 1b** Previously published geologic map of the Timpahute, Nevada, 30' X 60' quadrangle (after Tschanz and Pampeyan (1970) and digitized by Hess and Johnson, 1997).
- Plate 2a** Measured section of Devonian rocks at Mail Summit, Nevada, at 1"=50'
- Plate 2b** Measured section of Devonian Guilmette reef flank rocks at Mail Summit, Nevada, at 1"=20'
- Plate 2c** Measured section of Devonian Guilmette reef core rocks at Mail Summit, Nevada, at 1"=20'
- Plate 3** Isopach of the total Devonian rocks of the Great Basin.
- Plate 4a** Balanced structural cross section of the greater Timpahute Range (transect A-A' on **Plate 1a**).
- Plate 4b** Undisturbed profile (restored) of the greater Timpahute Range (transect A-A' on **Plate 1a**).
- Plate 5** A diagrammatic facies belt chart of the eastern edge of the Tempiute sub-basin, using terminology of Wilson (1975)
- Plate 6** Geologic map of sequences at Tempiute Mail Summit (TMS).
- Plate 7** Distribution of Pilot Formation outcrops on the new geologic map of the Timpahute Range quadrangle at an enlarged scale.
- Plates 8-14** Photomicrographs of thin sections from lower Guilmette sequences at TMS.

ACKNOWLEDGMENTS

I am grateful to those who reviewed and made recommendations for improvements to this manuscript: Dr. Dave Drowley (Amoco), Drs. Alton A. Brown and S. Judson May (Arco), Drs. Morris S. Peterson and Lehi F. Hinze (Brigham Young University), Dr. Gerald Friedman (Brooklyn College), Bruce Birge and Renae Wilkinson (Cedar Strat), Dr. Peter Verrall (Chevron, deceased), Dr. Steve Boyer (consultant, formerly University of Washington), Dr. William Jamison (consultant), Gerald G. Loucks (consultant), Bill Roberts (consultant), Dr. Dietrich H. Roeder (consultant, formerly University of Tennessee), Dr. John E. Welch (consultant), Joseph Kulik (Denver Earth Resources Library), Peter Hummel (Eagle Exploration), Dr. John Willott (Exxon), Karl E. Marlowe (Homestake), Dr. Eric Mountjoy (McGill University), James and Daniel Carpenter (Mobil), Dr. David Kopelman (Retired Prosecutor), Dr. Michael L. Morrison (Talisman), Drs. Kathryn M. Nichols and Norman J. Silberling (consultants, formerly USGS and Stanford University), and Rick Page (USGS).

Also thanks go to those who helped with field work and made helpful observations: Randy L. Chamberlain (Blue Eagle), Bruce Birge (Cedar Strat), Charles Gillespie (Tide Petroleum), Edgar Perez, Brian Ackman, Jane Estes, Anna J. Chamberlain and participants of several field trips to the greater Timpahute Range area. Chris Hansen and Greg Cameron (Cedar Strat) did much of the early field work. I picked the Devonian sequences and correlated them with surface and subsurface sections throughout the eastern Great Basin with the assistance of Bruce Birge. Also, many thanks go to participants of Cedar Strat's annual field conferences. Their comments were helpful.

I am thankful to the following for graciously providing data for this project: Martin A. Kopacz (Shell Western E&P Inc.) who gave me permission to use surface sections measured by Shell in the 1950's and 1960's. Ron Nowak (Maxus Energy

Corporation) provided cuttings, logs, and analyses for the Tikaboo Valley wells. Renee Davis (Helmrich & Payne) provided Total Organic Carbon data from the Mississippian Antler shales in a well in northern Railroad Valley. Anita Harris (USGS) graciously provided conodont dates for Guilmette equivalent rocks in the Reveille Range used in the isopach maps. Duane Harris (Harris-Hebrew Consulting, formerly with Shell Oil Company) provided helpful discussions, measured sections, and regional studies, and introduced me to much of the Great Basin stratigraphy. Dr. John Welch (Consultant, formerly with Shell Oil Company) also provided data and stimulating discussions on Great Basin stratigraphy. Dr. Gerald Waanders (Waanders Palynology) provided assistance and review of the Paleozoic biostratigraphy and Mississippian source rock quality, richness, and maturity and reviewed the dissertation. Dr. Alvin Smith, Professor of English at Saint Paul's College, Virginia, gave assistance on grammar and organization of the manuscript. Dr. Peter Jones (International Tectonic Consultants Ltd.) kindly provided the file to generate the balanced cross section using his *Thrustbelt* program.

I am grateful to the many companies that provided data or financial support. A partial list includes: Amoco, Anadarko, Anschutz, Arco (Vastar), BHP, Blair Petroleum, Chandler and Associates, Chevron, Connelley Exploration, Conoco, Diamond Shamrock, Exxon, Gary-Williams, Grace Petroleum, Hunt, Marathon, Maxus, Mobil, Moncrief, Moore McCormack, Occidental, Pawnee, Phillips, Pioneer, Shell, Sohio, Sinclair, Talisman, Texaco, Tide, Town Exploration, Union of Texas, and Unocal.

Nevada Bureau of Mines and Geology kindly gave me permission to photocopy all their well files up to 1990, and the Nevada Department of Minerals provided well completion reports from 1990 to 1998 and allowed me to photocopy all their well files and lithologic logs up to the present. Copyrighted data from regional measured sections and stratigraphic studies of wells incorporated into regional reservoir rock studies were

provided by Cedar Strat Corporation. Also, Cedar Strat Corporation provided the detailed 7.5' geologic maps and aerial photographs used to compile the Timpahute Range 30' X 60' geologic map.

A small amount of the work in the Nevada Test Site area was supported by a grant from the United States Department of Energy administered by the State of Nevada Nuclear Waste Projects office to evaluate the oil and gas potential of the proposed high-level nuclear waste repository at Yucca Mountain. Political pressures caused suspension of much of that grant. Part of this work was supported by NSF Grant EAR-906324 awarded to Colorado School of Mines, John E. Warme, Principal Investigator.

I am grateful to Drs. Lehi Hintze, Morris Peterson, Ken Hamblin, Myron Best and other professors at Brigham Young University who led undergraduate field camps and many field trips to the eastern Great Basin. I am also grateful to have been employed by Exxon Minerals, USA, where I learned to use scintillation equipment to generate gamma-ray data that can be used to suggest depositional environments and correlate well logs. Gulf Oil Company gave me the opportunity to work in the Big Horn Basin, Wyoming, where I first conceived of using scintillation counters to generate gamma-ray logs of outcrops to correlate from surface to subsurface sections. Marathon Oil Company gave me the experience of exploring the eastern edge of the Great Basin in central and western Utah. Placid Oil Company allowed me to develop surface gamma-ray log methods and gave me the resources to learn the Great Basin Paleozoic stratigraphy from experts who had worked for Shell Oil Company and measured Great Basin stratigraphic sections in the 1950's and 1960's.

I give thanks to Drs. J. Lintz, R.A. Schweickert, P.A. Cashman, and J.H. Trexler (University of Nevada, Reno) who encouraged me to attend a school more equipped and oriented to applying sequence stratigraphy to mineral and oil and gas exploration. I give

special thanks to those at the Colorado School of Mines who introduced me to the economic applications of sequence stratigraphy that has greatly enriched my eastern Great Basin stratigraphic data base.

Finally, I give thanks to my committee who have patiently given me the encouragement to finish this work and for carefully reviewing the manuscript. Many thanks go to Dr. John Warne who advised this work and spent many days in the field with me and who stimulated observations and interpretations. He worked hard and patiently to pull the geology from my head and get it on the written page. His generous investment of time for me will always be appreciated. Dr. Mark W. Longman (adjunct CSM professor and consultant) not only encouraged me to review current literature that guided my thinking and interpretations but also helped me with the carbonate petrology and carefully reviewed the dissertation. Dr. John B. Curtis (CSM professor and director Potential Gas Agency) encouraged me to relate this work to economic applications. Dr. Thomas L. Davis (CSM professor, Geophysics) encouraged me to relate the study area to the regional setting. Dr. Karl R. Nelson (CSM professor, Engineering) encouraged me to review the basic chemistry of dolomitization. The entire committee inspired me to reach for greater excellence in completing this dissertation.

Special thanks go to my wonderful wife, Yvonne, who willingly moved the Chamberlain family to the base of the greater Timpahute Range for seven years and encouraged me to finish this work. She and the family sacrificed greatly to see me complete this long-term dream.

DEDICATION

This dissertation is dedicated to my younger brother, Rex J. Chamberlain, who spent hundreds of hours with me hiking and exploring the Oquirrh Mountains, near Cedar Fort, Utah, where we were raised. He later helped me measure hundreds of thousands of feet of Paleozoic strata in the eastern Great Basin. Although his premature death prevents him from reaching his dream of earning a degree in geology, his shadow will always be present in the rocks of the everlasting hills.

This dissertation is also dedicated to my father, Don D. Chamberlain, who took me on many field trips looking for fossils and minerals. He unselfishly shared his love of geology and mountains with me. It was on those excursions into the hills that I learned to love my grandfather, Jim, who had worked in the old Mercur, Utah, gold mines. Jim died shortly before I was born. Those family bonds, coupled with my mother's careful instructions on prayer, gave me faith in the Creator of this wonderful earth. That faith has carried me over many cliffs and obstacles in the mountains and in life to reach for the impossible dream.

CHAPTER 1

INTRODUCTION

The Timpahute Range in western Lincoln County, Nevada, provides a unique opportunity to study a 40-mile long, continuous east-west exposure of Paleozoic rocks in this region of the Great Basin where most outcrops are subparallel to the north-south structural grain. Devonian rocks should reveal subtle, gradual changes in facies over long distances across the broad, featureless western North American continental shelf because they were believed to be deposited during a period of relative tectonic quiescence (Osmond, 1962; Niebuhr, 1979). However, abrupt contrasts in facies above a late Devonian impact breccia occur between thrust faults that segment the greater Timpahute Range. These contrasting facies from three thrust sheets of the greater Timpahute Range include: facies 1, a peculiar, anoxic, deepwater, rhythmic, thin-bedded limestone characterized by soft-sediment slump folds and some interbedded turbidites that may represent a crater fill that now is exposed in a fenster on the west end of the range; facies 2, a unique shallow-water quartz sandstone (as much as 1070 net feet thick) deposited on the west side of the impact basin and now is in a klippe in the middle of the range; and facies 3, a shallow-water platform carbonate deposited on the east side of the impact basin and lies on the east side of the range. These features and contrasts were revealed by a new geologic map (**Plate 1a**) of the Timpahute Range 30' X 60' quadrangle or Timpahute Range quadrangle (study area) which provides insight into this part of the Sevier fold-and-fault belt (**Figure 1**).

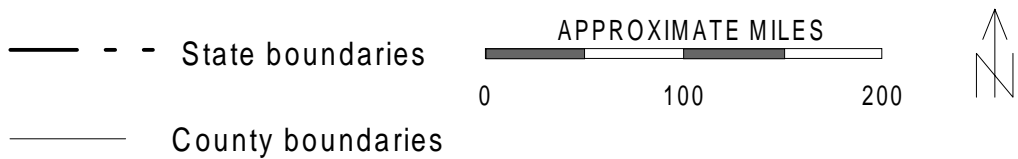
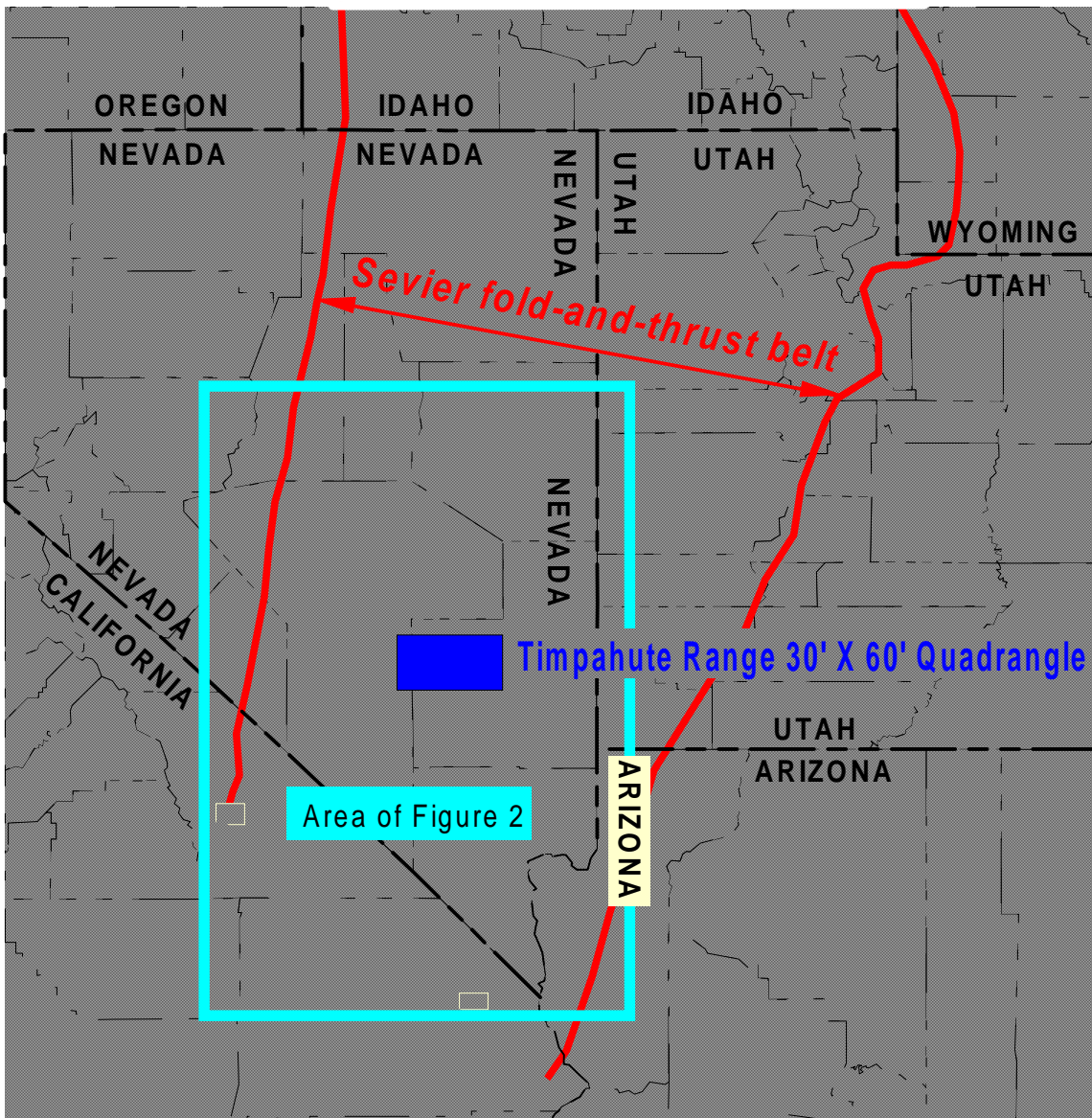


Figure 1 Index map showing the location of the Timpahute Range 30' X 60' quadrangle within the Sevier fold-and-thrust belt. Some data are from references cited in **Figure 2**.

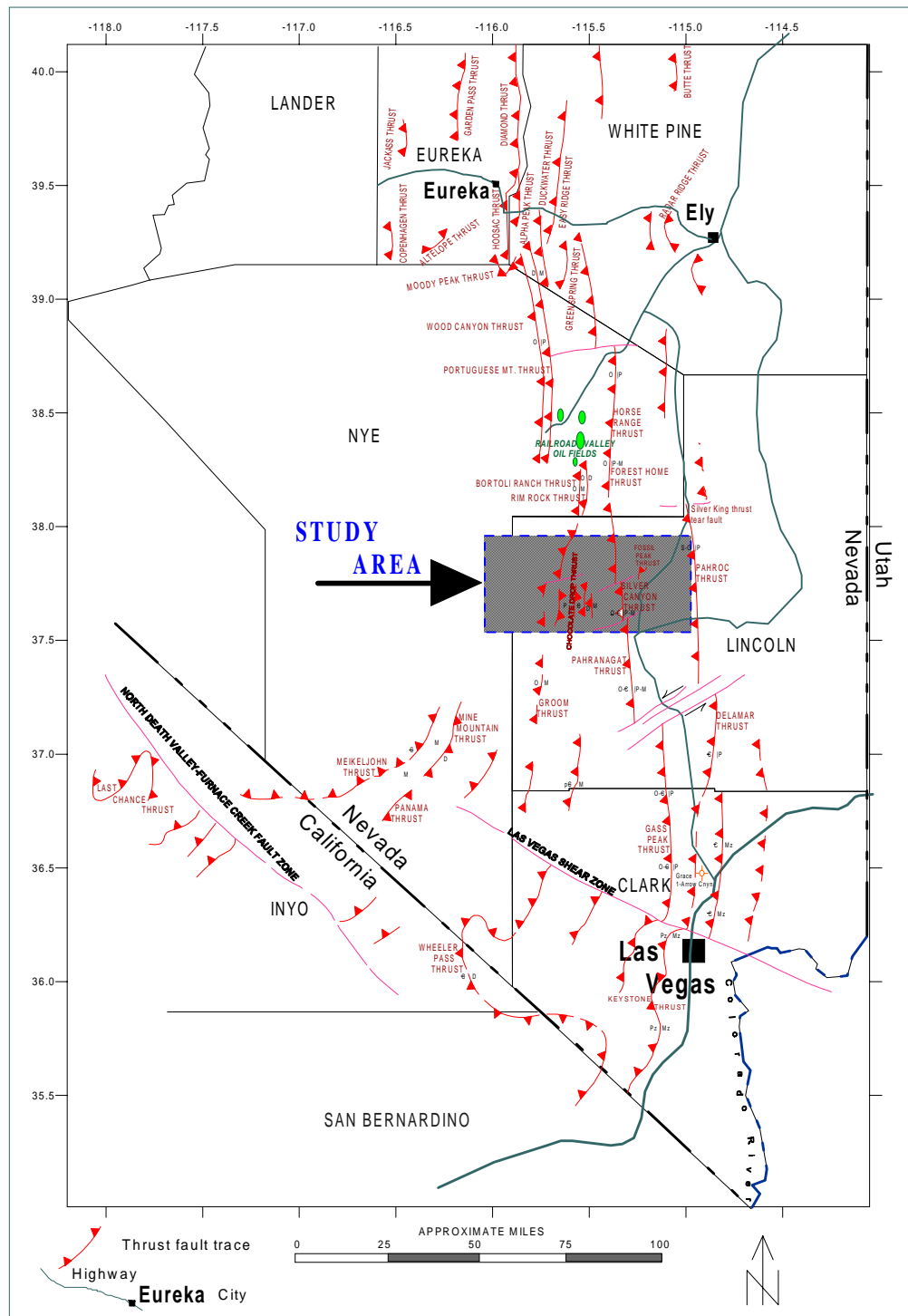


Figure 2 Sevier age thrust fault traces in eastern Nevada (from Hazzard, 1954; Burchfiel, 1961; Tschanz and Pampeyan, 1970; Kleinhampl and Ziony, 1984; Bartley et al., 1988; Cameron and Chamberlain, 1988; Carpenter et al., 1993; and proprietary mapping by the author). See **Figure 1** for index map.

Author's Background Concerning Timpahute Range Research

I have worked in the Great Basin region for more than 20 years, and much of that time in the Timpahute Range quadrangle. Considerable field and laboratory work was carried out before my specific dissertation research, and discussions and interpretations herein have necessarily evolved over many years, involved many projects, and included interaction with many geoscientists. Every effort has been made to document my sources of data and interpretations. Some data are proprietary and some interpretations are based in part on work completed before the onset of my doctoral program at the Colorado School of Mines.

I was raised near the southern Oquirrh Mountains, 40 miles southwest of Salt Lake City, Utah, and attended Brigham Young University, Provo, Utah, to complete my Bachelor's and Master's degrees in geology. My Masters' thesis, *Biostratigraphy of the Great Blue Formation*, included discovery of fossil-plant-bearing terrestrial valley-fill sequences interbedded with open-marine carbonates in the Mississippian proto-Oquirrh basin, north-central Utah, indicating marine and nonmarine cycles that were previously overlooked. This work continued beyond my Master's research (Chamberlain, 1987; 1990b, 1999).

Employment by Exxon Minerals USA (Michigan, Pennsylvania, and New York, 1976-1978) and Gulf Oil Company (Wyoming, 1978) resulted in pioneering applications of surface gamma-ray logs for the interpretation of depositional environments (Chamberlain, 1983). I worked for Marathon and Placid Oil Companies in the Great Basin of Utah and Nevada from 1979 to 1984 measuring and describing stratigraphic sections, conducting source- and reservoir-rock studies, and exploring for hydrocarbons. During this time I met many consultants who had previously worked for Shell Oil Company in a large research program that involved measuring and describing many stratigraphic sections. They shared first-hand knowledge of Paleozoic stratigraphy, structure, oil source- and reservoir-rocks, and geomorphology of the Great Basin.

In 1984, I founded Cedar Strat Corporation, and managed teams of geologists that remeasured many Shell Oil Company sections and many new ones. We successfully employed the surface gamma-ray log techniques to aid in surface to subsurface correlations. I directed studies on Mississippian source- and reservoir-rocks, on Devonian reservoir rocks, on individual wells and fields, and organized and led annual Great Basin field conferences.

In recent years I undertook detailed mapping projects in several areas, most intensely within the Timpahute Range quadrangle. This mapping was streamlined by incorporating GPS and GIS techniques, reported in Chapter 3. The results are presented in the map of **Plate 1a**.

From 1991 to 1999 my home was in Hiko, Nevada, within the study area. This location eased the logistics for field research, but complicated my access to libraries and research laboratories. As a result, this report is mainly based on new field work, which I believe must be the basis for most new understanding of the complicated geologic history of the Great Basin.

Purpose and Scope

This study provides the stratigraphic and structural data that constrain the restoration of the Devonian Sunnyside basin and allows a more accurate interpretation of its paleogeography (Chapter 7). The Sunnyside basin, named by Chamberlain and Birge (1997), is an intrashelf Devonian basin between the Antler forebulge (Carpenter et al., 1994) in central Nevada and the Utah hingeline in central Utah. Geologic mapping was limited to the Timpahute Range quadrangle and the study focuses mostly on Devonian sequences. A preliminary balanced cross section, restoration, and a surface geology

profile of the east-west transect A-A' from west of Tempiute Mountain (T4S R56E) to east of the Pahroc Range (T4S R62E) are provided (**Plates 4a** and **4b**). However, a rigorous structural analysis on the quadrangle is beyond the scope of this study.

This study illustrates the utility of applying the principles of “sequence stratigraphy” for geologic mapping of complex areas. Earlier workers using traditional lithologic formations were unsuccessful in accurately mapping the Timpahute Range quadrangle (**Plate 1b**). Twenty-one mappable Devonian sequences identified in Chapter 4 were used to map the structural elements presented in Appendix E, and to reconstruct the Devonian paleogeography in Chapter 7. Mapping the structural features in this complex region without knowledge of the order of sequences is untenable. Several obvious and accessible structural features had been described (e.g., Tschanz and Pampeyan, 1970; Armstrong and Bartley, 1993), but stratigraphic revisions on the new geologic map reveal significant structures--particularly folds, strike-slip faults, and thrust faults (Chamberlain and Chamberlain, 1990). Special attention has been paid in this study to the possible tectonic outcome of the Late Mesozoic Sevier orogeny on Paleozoic rocks in the Timpahute Range quadrangle, 100 miles west of the leading edge of the Sevier fold-and-thrust belt. Juxtaposition of different thrust sheets containing contrasting facies of Upper Devonian rocks in the Timpahute Range resulted from the Sevier compressional event. The overall goal of this research is to resolve these abrupt facies changes.

The specific goals of this research are threefold: 1) identify mappable sequences and interpret the Devonian strata using sequence stratigraphic concepts; 2) apply the mappable sequences to update the geology of the greater Timpahute Range on a map that shows the stratigraphy, folds, strike-slip faults, and thrust faults overlooked in previous mapping; and 3) reconstruct the Devonian paleogeography by evaluating the magnitude of deformation of this part of the Sevier fold-and-thrust belt using the new geologic map and correlations of Devonian sequences.

Realization of these goals is illustrated with plates 1 through 7. **Plate 1a** is a new

geologic map discussed in Chapter 5 and Appendix E. A profile of surface geology along transect A-A' along the bottom of the map provides some constraints used to construct **Plate 4a**. In comparing it with **Plate 1b**, a geologic map of the Timpahute Range quadrangle modified after Tschanz and Pampeyan (1970) with a similar scale and color scheme, significant revisions of the old mapping are readily apparent. **Plate 2a** is a stratigraphic section illustrating the cycles and sequences of the Devonian rocks at Mail Summit discussed in Chapter 4. **Plates 2b** and **2c** provide detail about Devonian reef and reef flank facies at Mail Summit. **Plate 3** is an isopach map of the Devonian system which shows the shape of the Sunnyside basin described and named by Chamberlain and Birge (1997). **Plate 4a** is a balanced retrodeformable cross section along the line of section labeled A-A' in the greater Timpahute Range on **Plate 1a**. Although normal faults occur on the line of section, they were too small to illustrate in the cross section. **Plate 4b** is the restored or undeformed section. This new structural model of the greater Timpahute Range resolves the abrupt facies changes in Upper Devonian sequences between thrust sheets and provides a more comprehensive guide to the structural style of the region. The model gives insight into structures concealed by Tertiary volcanics and valley fill in other parts of the Sevier fold-and-thrust belt. Restoration of stratigraphic sections to their original positions using the structural model is essential for correct interpretations of the Devonian paleogeography (Chapter 7).

Plate 5 is a diagrammatic facies belt chart after Wilson (1975) applied to the eastern edge of the Tempiute sub-basin. The Tempiute sub-basin is a basin at the south end of the Sunnyside basin created by a cosmolite impact (see Chapter 7). A cosmolite as used herein is an extraterrestrial body such as a meteorite or comet but of an uncertain composition. The facies belt chart lists microfacies characteristics and examples at Timpahute Mail Summit (TMS). **Plate 5** illustrates the correlation between microfacies in photomicrographs in Appendix C and the table of criteria to make facies assignments presented in Chapter 3. The microfacies helped refine facies assignments. Facies patterns and gamma-ray logs helped separate regional sequence boundaries from local

cycle boundaries. Twenty-one regionally mappable sequences were identified (Chamberlain and Warne, 1996). These regional correlatable sequences were used to make isopach maps and to make the new geologic map of the Timpahute Range quadrangle. **Plate 6** is a geologic map showing the distribution of Devonian sequences at the measured section in the southwest corner of the Mail Summit 7.5' quadrangle (TMS herein). **Plate 7** is a distribution map of Pilot outcrops within the Timpahute Range 30' X 60' quadrangle. A detailed biostratigraphic analysis of the sequences is beyond the scope of this study. Gamma-ray log patterns of sequences usually provide greater resolution for regional correlations than do conodont zones. Therefore, conodont and other fossil zones tied to surface gamma-ray logs would greatly enhance regional correlations.

Format

This report consists of nine chapters. Chapter 1 introduces the study area by presenting the format and purpose and scope of the study and describing the location and geologic setting of the study area. Chapter 2 provides a brief review of previous work in the study area. Chapter 3 introduces the methods used in the research. Chapter 4 consummated the first main research objective, which was to identify and interpret the mappable Devonian sequences in the study area. A well-exposed 5000-foot-thick composite stratigraphic section on the Mail Summit 7.5' quadrangle provided a useful reference section for Devonian depositional cycles and sequences across the eastern Great Basin and is called TMS (Timpahute Mail Summit measured section) in this report (**Figure 3**). Dolomite and dolomites, important components of the sequences, are discussed in Chapter 4. Recognition of the sequences was important in achieving research objective two, which was to make a geologic map of the Timpahute Range quadrangle. Defined sequences were used to make the geologic map and identify thrust sheets presented in Chapter 5 and structural elements described in Appendix E. The map

and correlation of the sequences at TMS to sections exposed in different thrust sheets in the greater Timpahute Range support the stratigraphic significance of structural interpretations in Chapter 6.

The sequences defined at TMS were correlated with other surface and subsurface sections of the region. These correlations provided the basis for sandstone isolith maps and the total Devonian isopach map presented in Chapter 7. Sequences at TMS provide clues to Devonian tectonic events in the region. For example, the “Oxyoke Formation” at TMS may be a record of the first siliciclastic pulse of the Devonian-Mississippian Antler

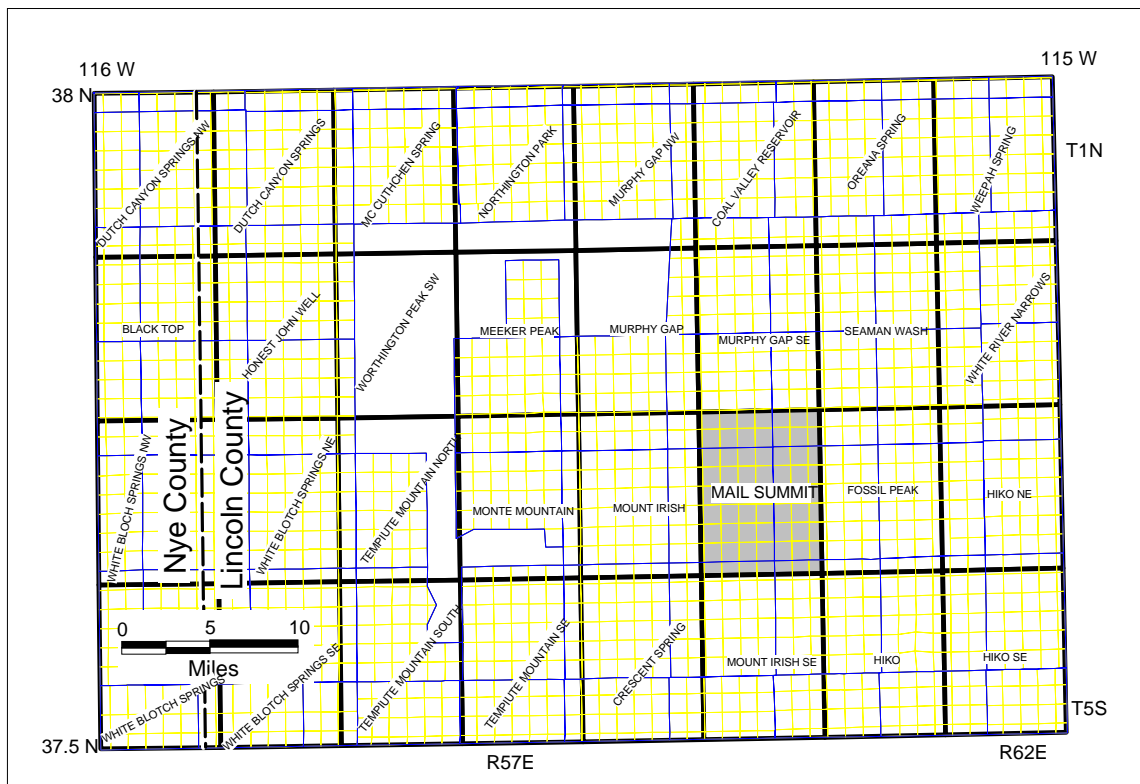


Figure 3 Index map showing the position of the Mail Summit 7.5' quadrangle (shaded gray) among the other 7.5-minute quadrangles (black lines) comprising the Timpahute Range 30' X 60' quadrangle. Surveyed townships and ranges are in blue and sections are in yellow. Several township and range values are indicated along two map edges. Digital land grid is from Premier Data Services, Denver (1997). Digital topographic index map was provided by Homestake Gold Company, Reno (1997). Degrees north latitude and west longitude are indicated on several map corners. See Chapter 3 for methods of constructing this and other maps from digital data bases.

orogeny. This and other tectonic events and features that affected the Devonian paleogeography are also presented in Chapter 7. The economic and academic applications of the stratigraphic sequences, the new geologic map and structural model, and the new paleogeographic interpretations of the Great Basin Devonian are discussed in Chapter 8. Conclusions and recommendations for further study comprise Chapter 9.

Appendices explaining abbreviations used in the text or sets of photographs and data too lengthy to be incorporated in the body of the text are provided for completeness. Appendix A provides an explanation for symbols and abbreviations used in maps, correlation charts and stratigraphic sections. Appendix B provides a detailed description of each cycle of TMS organized from the oldest sequence to the youngest. Appendix C provides descriptions of thin sections taken mostly from the lower Guilmette cycles. **Plates 8** through **14** contains selected photomicrographs of the thin sections. Appendix D is a CD-Rom originally presented as a poster session (Chamberlain et al., 1996; Chamberlain, 1998) and later published by SEPM (Hook et al., 1998). It is a digital presentation of a field trip in the Central Nevada Thrust Belt, and it contains annotated, animated, captioned, and plain digital images that compliment the text. Appendix E presents detailed descriptions of structural elements of the Timpahute Range 30' x 60' quadrangle geologic map. Appendix F is a table from a spreadsheet of control points of sections with the complete Devonian represented and used to label **Plate 3**.

Location of the greater Timpahute Range

The Timpahute Range 30' X 60' topographic quadrangle is covered in the 1:100,000-scale metric topographic map series by the United States Geological Survey published in 1988. It lies within western Lincoln County in southeastern Nevada, centered approximately 100 miles north of Las Vegas, from 37° 30' to 38° N latitude and 115° to 116° W longitude. This quadrangle is within the Sevier fold-and-thrust belt

(**Figure 1**). The Timpahute Range is in the southwest part of the Sunnyside basin (Chamberlain and Birge, 1997; **Plate 3**). It lies south of prolific oil wells in Railroad Valley that produce mainly from Devonian carbonates. It is northeast of the Nellis Air Force Bombing Range where access to rock outcrops is restricted by the United States Department of Defense.

The greater Timpahute Range provides an unique 40-mile-wide east-west band of nearly continuous Paleozoic outcrops (see **Plate 1**) in a region where usually only crestal exposures in north-south trending ranges are exposed between broad areas of Tertiary cover. It includes Tempiute Mountain, Monte Mountain, Mount Irish, Mail Summit, Fossil Peak, Hiko Range, and the southern end of the North Pahroc Range (**Figure 5**). Other ranges within the Timpahute Range quadrangle with significant outcrops of Paleozoic rocks include the Worthington, Golden Gate, Seaman, and Pahranaagat ranges. Extensive outcrops in the Timpahute Range quadrangle are especially favorable for study of Devonian strata in both north-south and east-west directions.

TMS (Timpahute Mail Summit measured section) is a composite measured section composed of three segments that mostly lie in the southern part of the Mail Summit 7.5' quadrangle (**Figure 4, Plate 6**). The lower parts of two of the segments lie in the northern part of the Mount Irish SE 7.5' quadrangle. However, because most of the section lies in the Mail Summit quadrangle, it is called TMS herein.

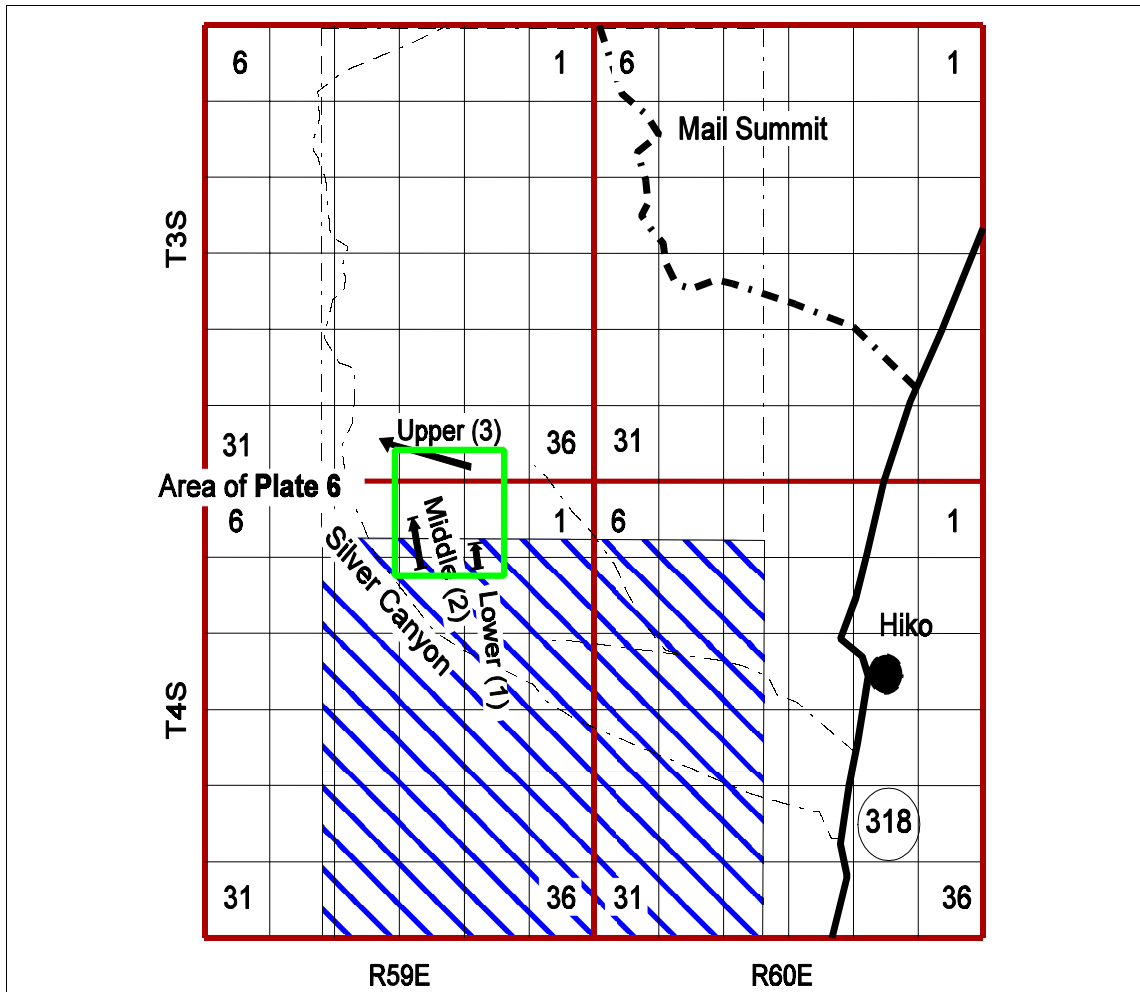


Figure 4 Index map to the Mail Summit measured section (TMS) in the southwest part of the Mail Summit 7.5' quadrangle (stippled) and northern Mount Irish Se 7.5' quadrangle (hachured). The solid black line is Nevada State highway 318, the heavy broken line is the Mail Summit county road, and the light broken lines are jeep trails. The lower, middle and upper segments of TMS composite measured section are indicated by arrows that point up-section. The green box shows the area covered by **Plate 6**, a geologic map of the sequences mapped at TMS and an example of the detail used to compile the geologic map of the Timpahute 30' X 60' quadrangle.

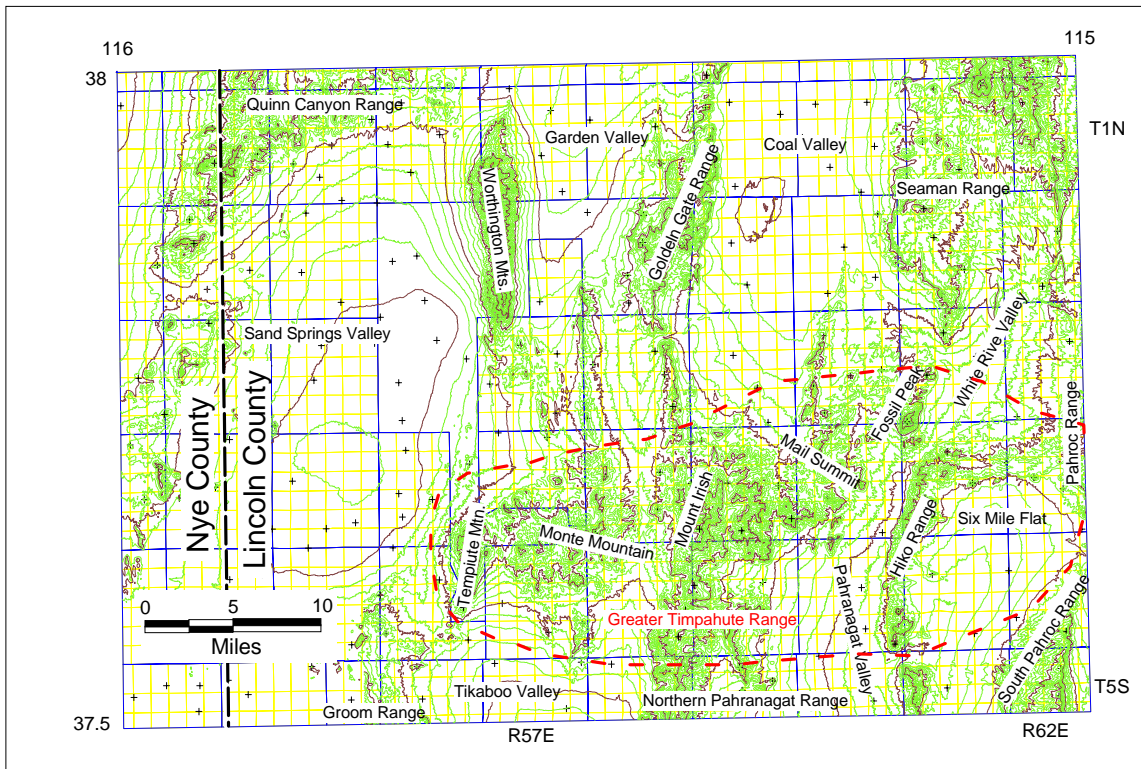


Figure 5 Topographic elements of the greater Timpahute Range (outlined in red dashed line) including Timpahute Mountain, Monte Mountain, Mount Irish, Mail Summit, Fossil Peak, Hiko Range, and the North Pahroc Range in the Timpahute Range quadrangle. Digital topography was downloaded from the United States Geological Survey web site. The small black crosses are elevation bench marks.

Geologic Setting of the greater Timpahute Range

The Timpahute Range lies in the Great Basin portion of the Basin and Range Physiographic Province. Deposition in the region was nearly continuous from Precambrian to Lower Triassic (Stewart, 1980). In this section, the tectonic setting that affected the Paleozoic rocks and their stratigraphic setting is discussed.

Tectonic Setting

North-south Precambrian rifting (Stewart and Poole, 1974) and east-west compression by the Mississippian Antler orogeny (Roberts, 1972) caused the north-south structural grain of the region that controlled or influenced all subsequent tectonic and depositional events. After the rifting and before the Antler orogeny, rocks in western North America were deposited on a passive margin. **Figure 6** is a diagrammatic cross section of the pre-Antler passive margin. A correlation chart and nomenclature of some units exposed in the study area will be presented later in this Chapter. Previous work that resulted in the evolution of **Figure 6** will be discussed in Chapter 2.

The greater Timpahute Range is perpendicular to the general north-south structural and physiographical grain of the Great Basin. It lies within the north trending Mesozoic Sevier fold-and-thrust belt that is responsible for much of the present-day regional structural grain and topography (**Figure 2**). Previous geologic mapping depicted the ranges in the study area as horsts and the valleys as grabens (Tschanz and Pampeyan, 1970). As a result, a fault-block model by Duey (1979) and Foster et al. (1979) has been used for oil exploration in the region. The fault-block model continues to be used in oil and gas exploration in Nevada (Bortz, 1998). However, the new geologic map shows that structures produced by east-west crustal shortening in the study area are also reflected by the topography (**Plates 1a, 4a**, Appendix E). Six thrust faults and their associated folds are exposed by Tertiary erosion in the greater Timpahute Range (**Plate 1a**). A seventh thrust fault, the Pahroc thrust fault, is exposed in the southern Delamar Range, 35 miles south-southeast of Hiko and beyond the area of **Plate 1**. It is interpreted to underlie much of the study area (**Plate 4a**). The ranges in the study area are generally anticlines and the valleys are synclines. Apparently they were not affected by an overprint of Cenozoic extension. Therefore, a lack of major normal faults with thousands of feet of displacement suggests that Cenozoic extension was minor in the Timpahute Range

quadrangle. Major north-south normal faults are reported in other areas in the Basin and Range Province (Effimoff and Pinezich, 1986).

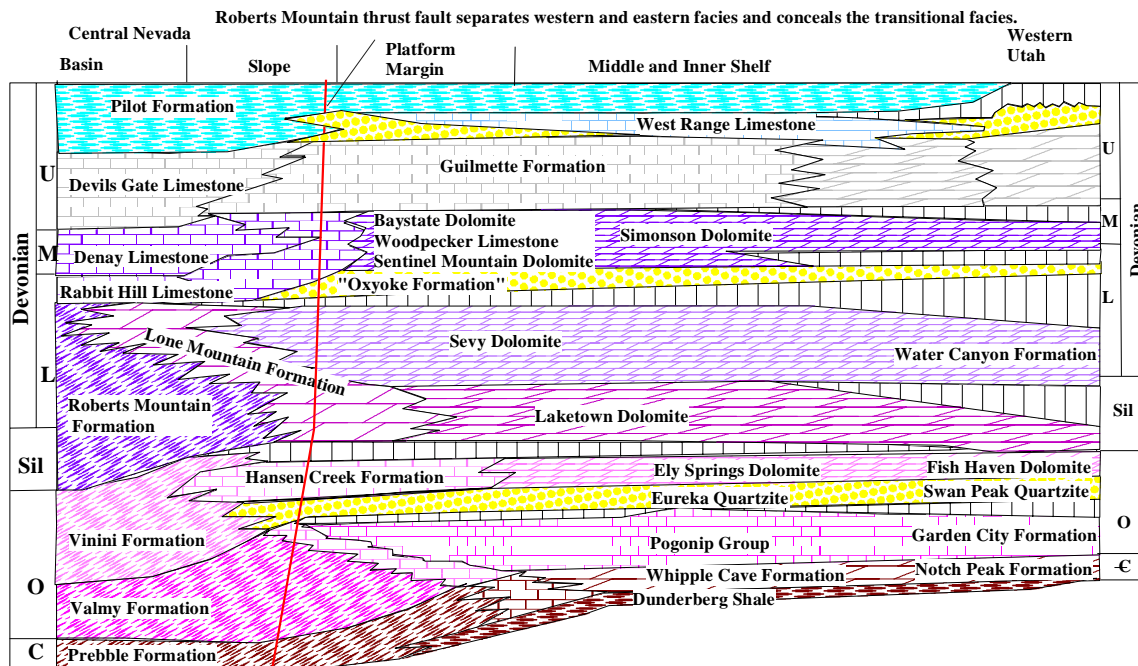


Figure 6 Pre-Antler orogeny tectonic setting and depositional profile from western Utah to central Nevada showing formational terminology from the Upper Cambrian through the Devonian. Modified after Cook and Taylor (1985) and Langenheim and Larson (1973). No attempt was made to include the effects of the Antler forebulge. The slope/margin area is diagrammatic as it lies in the same area as the Roberts Mountain thrust fault (red line) where the transition facies are concealed. Siliciclastic intervals are in yellow.

Lake beds or synorogenic sediments associated with the Sevier Orogeny represent the only possible Mesozoic strata preserved in the Timpahute Range quadrangle. Many compressional structures are masked by Tertiary volcanic deposits that filled paleovalleys and canyons with ash falls and flows. Paleotopographic high areas (anticlines) received little volcanic cover. A few north-south trending normal faults that could have had hundreds of feet of displacement likely formed during Cenozoic extension (**Plate 1a**). Two large displacement faults, the north Worthington and Hiko Narrows faults, could be normal faults associated with extension but are likely deeper thrust faults.

An extensive cover of Tertiary volcanic rocks and thick Tertiary valley fill conceal most of the structures in the region. Headward erosion by tributaries to the Colorado River has exhumed some Sevier-age structural elements from the greater Timpahute Range southward. Most of the compressional features remain buried below Tertiary strata north of the greater Timpahute Range. **Figure 7** summarizes the tectonic events of the Great Basin from the Late Mesozoic Sevier orogeny to the present.

Generally, lower Paleozoic strata thicken from east to west (many studies, and Cedar Strat proprietary measured sections, 1984-1989). West of the study area, deposition on the passive margin was interrupted by the Devonian-Mississippian Antler orogeny (Roberts, 1972). Carpenter (1997) suggested that the orogeny was initiated during Yellow Slope Sequence time in the Frasnian Stage of the Late Devonian (**Plate 2a**, Chapter 4). Carpenter et al. (1994) interpreted an Antler forebulge uplift, a positive area in central Nevada within and west of the Shoshone and Toiyabe ranges, 80 miles northwest of the study area. A forebulge is an upwarp or flexure of the lithosphere caused by tectonic loading (e.g., Roberts Mountain allochthon) that occurs in front of a thrust front. The upwarping or forebulge develops because of isostatic response to crustal loading and flexural downwarping and is predicted by flexural modeling (Giles, 1996). A backbulge basin (e.g., Sunnyside basin) occurs between the forebulge and the stable craton. It is a broader and shallower downwarp or backbulge basin than the downwarping of the foreland basin (Giles, 1996). The bulge coincides with the western side of the Sunnyside basin described in Chapter 7. The forebulge is defined by the increasing age eastward of subcropping miogeoclinal Cambrian and younger rocks beneath the Roberts Mountain thrust. When the Roberts Mountain allochthon overrode it in the Late Devonian, the Lower and Middle Devonian forebulge was an eroded paleohigh (Carpenter et al., 1994). Fossils, such as conodonts, and quartz sand that are insoluble in weak acids from early Paleozoic rocks were shed eastward into the Sunnyside basin and are the source of Devonian sandstones on the western edge. Paleozoic rocks within the

Sunnyside basin were subsequently deformed during the Mesozoic Sevier orogeny (Chapters 2 and 6).

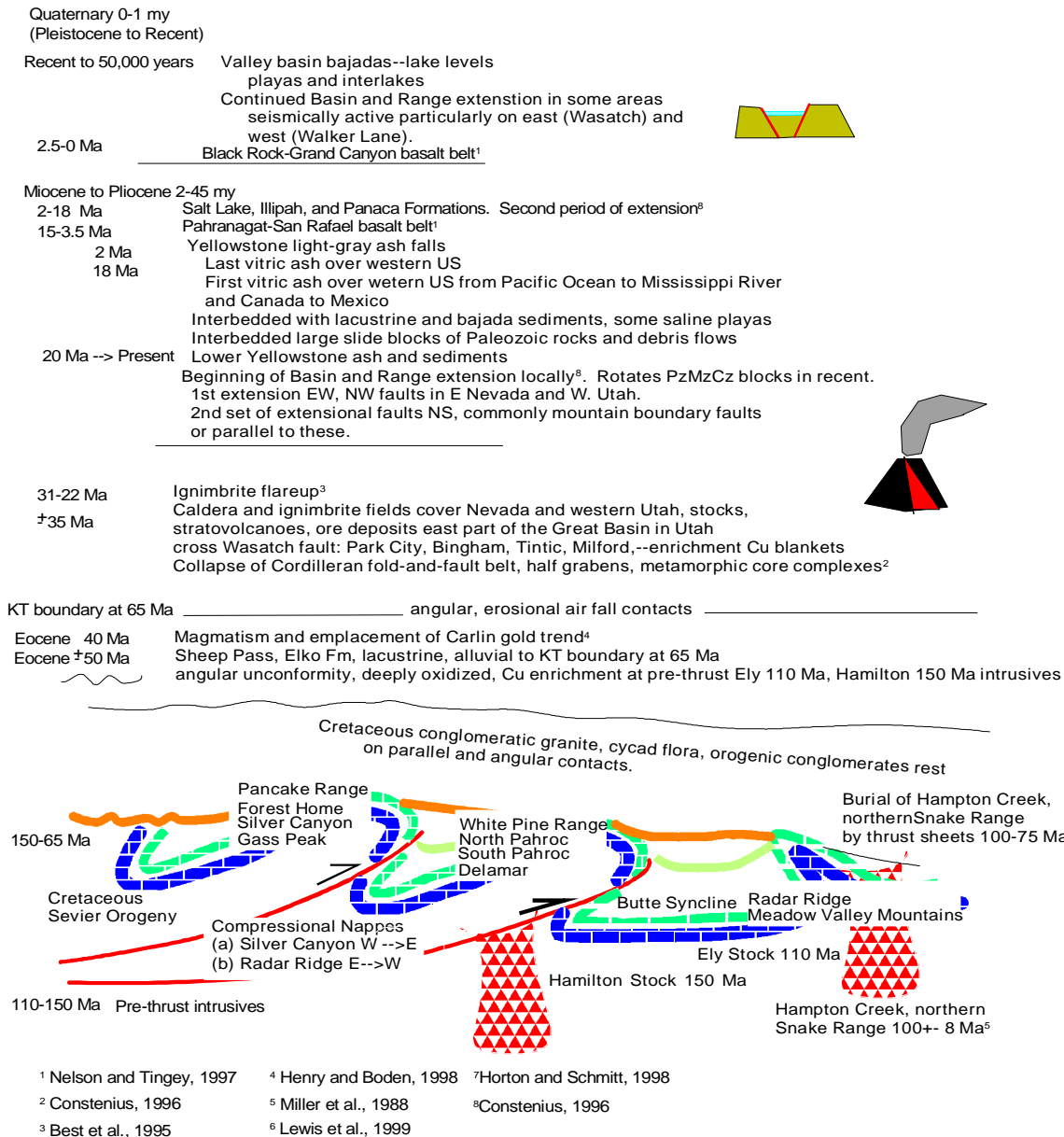


Figure 7 Tectonic events at and since the Sevier orogeny in the eastern Great Basin. Data are from proprietary mapping, Cedar Strat data files, J. Welch (1998, personal communication), and other references that are indicated by the superscript numbers. Lists of locations are examples of fold and thrust features. Dark blue represents older Paleozoic rocks. Green represents younger Paleozoic rocks. Pale green represents the base of Tertiary valley fill. Orange represents present-day surface. Patterned red represents pre-thrust intrusives.

Stratigraphic Setting

Devonian rocks form a significant part of the 15,000 to 20,000 feet of Paleozoic rocks exposed in ranges of the area (**Table 1**). These are summarized in **Figure 8**, a correlation chart that compares Devonian rocks exposed at TMS with the Paleozoic units exposed in the Pahrnatag Range 15 miles south of the study area (Stop #6, Appendix D) and those exposed in the Egan Range 65 miles north of the study area (Stop #13, Appendix D).

Table 1 lists the formations illustrated in **Figure 8** and compares the nomenclature used herein with that of other workers in the region. Some of these units were grouped for the new geologic map. For example, Cambrian units, including Lower Cambrian Prospect Mountain Quartzite, Middle Cambrian Chisholm Shale, Middle and Upper Cambrian Highland Peak Formation, and Upper Cambrian undifferentiated limestone and dolomite, and Dunderberg Shale, are grouped together on the geologic map in the restricted area of the Groom Range (**Plates 1a** and **1b**). Only the Upper Cambrian rocks are exposed in the greater Timpahute Range. Access to extensive outcrops of Lower and Middle Cambrian rocks exposed in the Groom Range, eight miles southwest of Tempiute Mountain, is restricted by the United States Department of Defense.

On the geologic map, the Mississippian Chainman Shale facies and the interfingering Scotty Wash Sandstone facies are grouped together as Mississippian Antler clastics (Mac). This was done to avoid confusion where Scotty Wash facies are below or interbedded with the Chainman Shale facies as in the Egan Range (**Figure 8**). In its type locality in the northern Bristol Range, 20 miles east-northeast of the study area, the Scotty Wash Sandstone overlies the Chainman Shale.

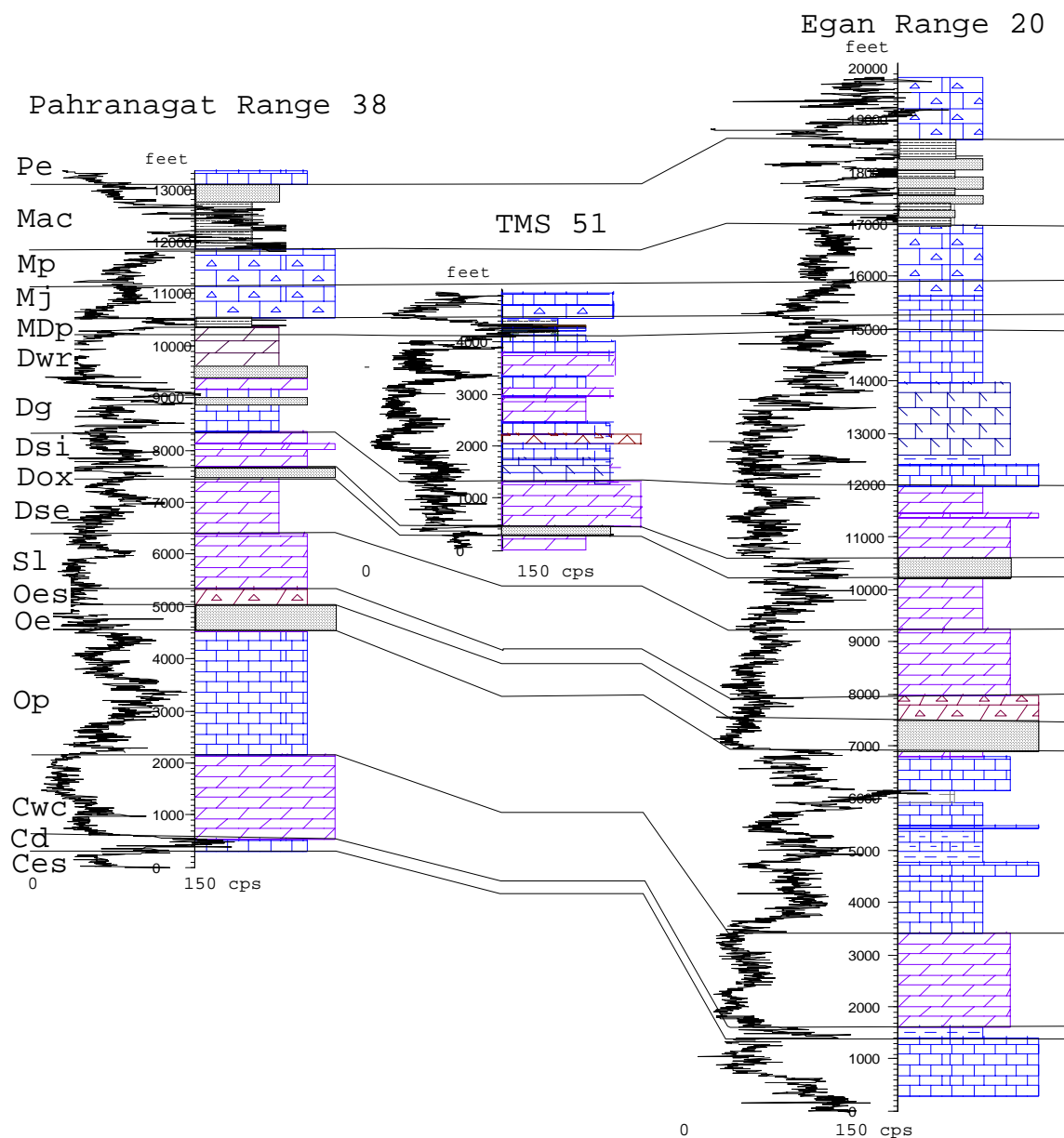


Figure 8 Correlation diagram comparing the Devonian stratigraphy at TMS with the Paleozoic stratigraphy in the Egan and Pahrnagat ranges. Numbers at the top of the stratigraphic columns are the section numbers listed in **Table 2** and **Figure 9**. See **Table 1** for abbreviations of the Paleozoic units. Gamma radiation varies from near 0 to over 150 counts per second. Placement of the gamma-ray scale varies between sections because the gamma-ray curve was placed to optimize amount of detail that is presented in the correlation diagram.

Table 1 Paleozoic nomenclature in southeastern Nevada with abbreviations used in **Figure 8**. Numbers in the column headers correspond to section numbers on **Figure 9** and **Table 2**. Rocks above the Ely Limestone were omitted from the table and figure.

Abbr.	Age	This paper TMS 51	Kellogg (1963) Egan Range 20	Reso (1963) Pahranagat Range 38
Dwr	Devonian	West Range Limestone	Lower and Middle West Range Formation	West Range Limestone
Dg		Guilmette Formation	Guilmette Formation	Guilmette Formation
Dsi		Simonson Dolomite	Simonson Dolomite	Simonson Dolomite
Dox		“Oxyoke Formation” (regionally mappable sandy, silty, and argillaceous dolomite)	sandstone lens (0- 25 feet thick) near top of Sevy Dolomite	Basal Simonson Dolomite sandstone and upper Sevy Dolomite calcareous siltstone and chert
Dse		Sevy Dolomite	Sevy Dolomite	Sevy Dolomite
Sl	Silurian	Laketown Dolomite	Laketown Dolomite	Laketown Dolomite
Oes	Ordovician	Ely Springs Dolomite	Fish Haven Dolomite	Ely Springs Dolomite
Oe		Eureka Quartzite	Eureka Quartzite	Eureka Quartzite
Op		Pogonip Group	Pogonip Group	Pogonip Group
Cwc	Cambrian	Whipple Cave Formation	Whipple Cave Formation	Desert Valley Formation
Cd		Dunderberg Formation	Dunderberg Formation	Dunderberg Shale
Ces		Emigrant Springs Formation	Emigrant Springs Formation	Highland Peak Formation

Table 1 (Continued) Paleozoic nomenclature in southeastern Nevada with abbreviations used in Figure 8 . Numbers in the column headers correspond to section numbers on Figure 9 and Table 2 . Rocks above the Ely Limestone were omitted from the table and figure.					
Abbr.	Age	This Paper TMS 51		Kellogg (1963) Egan Range 20	Reso (1963) Pahrnagat Range 38
Pe	Pennsylvanian	Ely Limestone		Ely Limestone	Bird Spring Formation
Mac	Mississippian	Scotty Wash Sandstone facies	Antler clastics	Scotty Wash Sandstone	White Pine Group. Langenheim and Larson (1973) included Scotty Wash in upper part
		Chainman Shale facies		Chainman Shale	
Mp		"Penoyer Limestone"		Joana Limestone	Joana Limestone
Mj		Joana Limestone			
MDp	Mississippian/ Devonian	Pilot Formation		Upper West Range Formation	Pilot Formation

Although it was not mapped separately on the final geologic map of the Timpahute Range quadrangle, the "Penoyer Limestone" was mapped separately on most of the field work maps (construction of field work maps is explained in Chapter 3). The slope-forming "Penoyer Limestone" is a mappable unit that lies above the cliff-forming Lower Mississippian Joana Limestone and is a useful field term. The "Penoyer Limestone" is composed of rhythmically bedded crinoid wackestones and mudstones that contain the trace fossil *Zoophycos*. It contrasts with the crinoidal grainstones and packstones of the underlying Joana Limestone and is more radioactive (**Figure 8**).

Surface gamma-ray logs, as shown in **Figure 8**, are valuable for regional correlations in frontier areas such as Nevada where few wells have penetrated the entire Paleozoic section. Note the similarity of the gamma-ray pattern for different units between the regional sections. Annotated unit thicknesses on the structural profile in the lower part of **Plate 1a**, constrain the structural cross section in **Plate 4a**.

Note in **Figure 8** how the Devonian rocks thicken northward toward the depocenter of the Sunnyside basin. Within the basin the sections are thicker and are mostly composed of coral and tabular stromatoporoid-bearing carbonates. They lack abundant *Amphipora*, a restricted platform and usually shallow-water fossil. In contrast, *Amphipora*-bearing carbonates and shallowing-upward cycles that imply shallow-water deposition in restricted marine conditions mostly occur in sections on the edges of the Sunnyside basin (**Plate 3**). Shoreward of the *Amphipora*-bearing carbonates are quartz sandstones. These changes in facies and a detailed discussion of the stratigraphic sequences and cycles in the Devonian rocks at TMS are presented in Chapter 4 and their paleogeographic significance is presented in Chapter 7.

The Devonian portion of the southwest Timpahute Range Mail Summit measured section, or TMS, is nearly 5000 feet thick. It lies in the footwall of the Silver Canyon thrust fault. The Silver Canyon thrust fault is near the middle of the greater Timpahute Range and in the northwest quadrant of the southeast quadrant of the Timpahute Range quadrangle (**Plate 1a**). TMS is a composite section consisting of three segments (**Figure 4**). Five formations comprise the Devonian at TMS. They are, in ascending order: the Lower Devonian Sevy Dolomite, Middle Devonian Simonson Dolomite, Late Devonian Guilmette Formation, very Late Devonian West Range Limestone, and Devonian-Mississippian Pilot Formation. Previous work on these formations and their previously mapped outcrop distributions are presented in Chapter 2 and **Plate 1b**. The newly mapped outcrop distribution of these formations and their sequences are presented in more detail in Chapter 4 and **Plate 1a**.

Devonian sequences of the TMS reference section were correlated to other sections in the region. **Figure 9** shows adjacent (inset) and regional surface and subsurface sections to which Devonian sequences in the TMS reference section were originally correlated (**Table 2**). Each measured section was measured at the same scale and detail as TMS but they are too voluminous to be included in this work. However,

sequence thicknesses and other data from these sections were used to construct regional isopach maps herein.

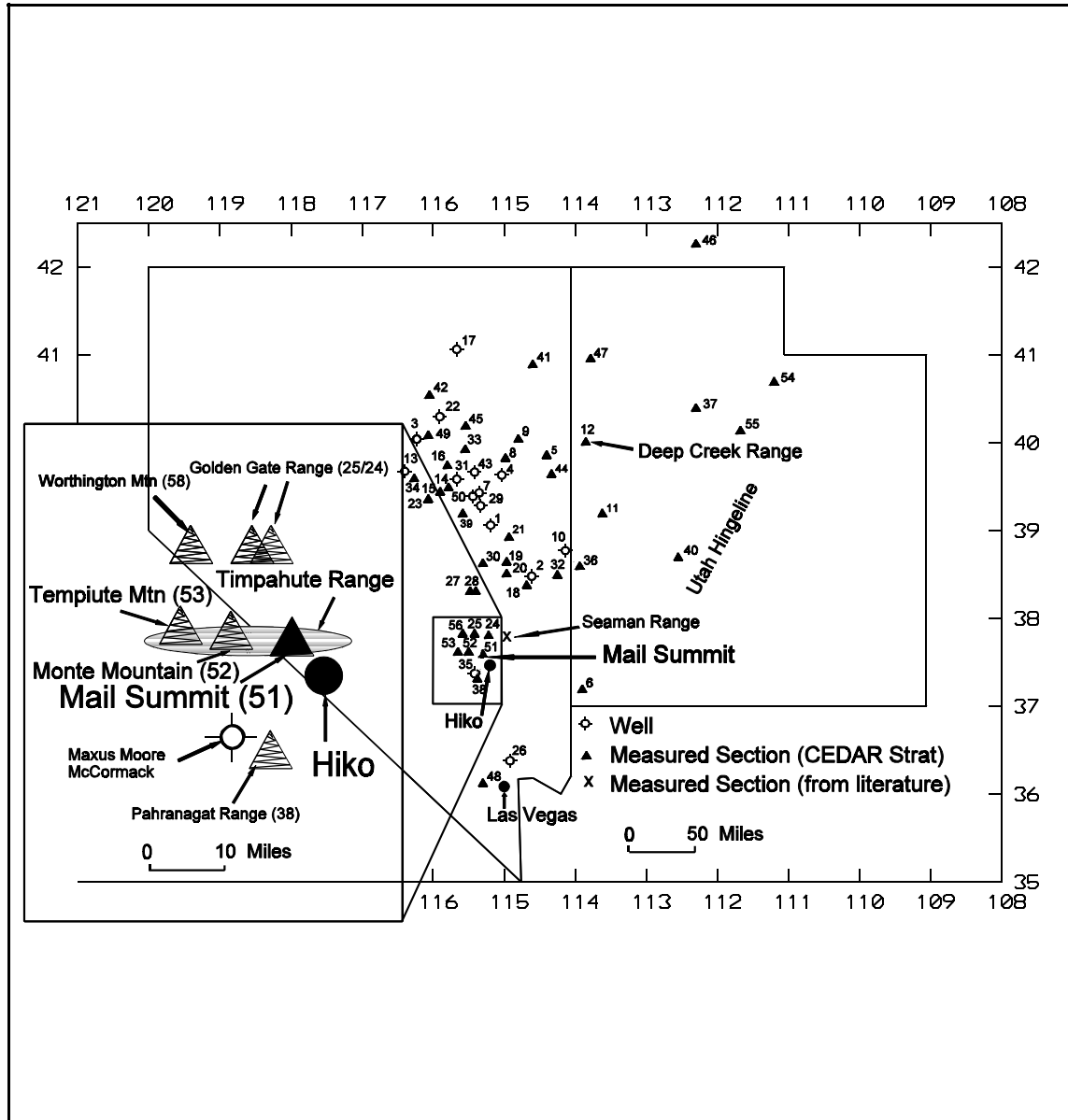


Figure 9 Index map showing parts of Nevada and Utah with location of southwest Mail Summit composite stratigraphic section, in the greater Timpahute Range near Hiko, Nevada, and other sections to which the TMS was correlated and used to make **Plate 3**. Degrees latitude and longitude are indicated on the edges. The scale in miles is approximate. The number and name of the sections are listed in **Table 2**.

Table 2 Wells and Measured Sections shown in **Figure 9**.

#	Well or Measured Section	#	Well or Measured Section
1.	American Hunter Exploration, Blackjack Spring	29.	GW, Moorman Ranch
2.	Amoco, Dutch John	30.	Horse Range
3.	Amoco, East Henderson	31.	Keith Walker, Fed
4.	Anadarko, Combs Peak	32.	Limestone Hills
5.	Antelope Range	33.	Little Bald Mountain
6.	Beaver Dam Mountains, Horse Canyon	34.	Lone Mountain
7.	Blair, White Pine	35.	Maxus Expl., Moore McCormack 6-1
8.	Cherry Creek Range, Egan Basin	36.	North Needles Range
9.	Cherry Creek Range, Goshute Canyon	37.	Oquirrh Mountains
10.	Commodore Resources, Outlaw Fed	38.	Pahranagat Range, Cutler Reservoir
11.	Confusion Range, Little Mile & ½	39.	Pancake Range, Green Spring
12.	Deep Creek Range	40.	Pavant Range, Dog Valley Peak
13.	Depco, Willow Wash	41.	Pequop Range, Independence Valley
14.	Diamond Range, Newark Mountain	42.	Pinion Range, Pine Mountain Klippe
15.	Diamond Range, Oxyoke Canyon	43.	Ram, Long Jevity-1
16.	Diamond Range, Rattlesnake Ridge	44.	Red Hills.
17.	Diamond Shamrock, Kimbark	45.	Ruby Range, Pearl Peak
18.	Dutch John Mountain	46.	Samaria Mountain, Idaho
19.	Egan Range, Ninemile	47.	Silver Island Mountain, Graham Peak
20.	Egan Range, Shingle Pass	48.	Spring Mountain, Lovell Canyon
21.	Egan Range, Water Canyon	49.	Sulphur Springs, Telegraph Canyon
22.	Exxon, Aspen Unit	50.	Tenneco Oil Co, Illipah-1
23.	Fish Creek Range, Bellevue Peak	51.	Timpahute Range, Mail Summit
24.	Golden Gate Range, Lower Plate	52.	Timpahute Range, Monte Mountain
25.	Golden Gate Range, Upper Plate	53.	Timpahute Range, Tempiute Mountain
26.	Grace Pet., Arrow Canyon-1	54.	Uinta Mountains, Hoyt Peak
27.	Grant Range, Forest Home Lower Plate	55.	Wasatch Range, Rock Canyon
28.	Grant Range, Forest Home Upper Plate	56.	Worthington Mountain

Regional sequence correlations were used to refine the TMS sequences (Chamberlain and Warne, 1996). Once the sequences were refined, they were used with additional sections (Appendix F) to construct **Plate 3**, a total Devonian isopach map of the eastern Great Basin. Dry-hole symbols on **Figure 9** show wells that penetrated a significant part of the Devonian section. Triangles depict the location of measured sections containing Devonian rocks. The Devonian rocks generally thicken from

approximately 500 feet east of the Utah hingeline to more than 6600 feet west of the hingeline. The Utah hingeline is a zone at the leading edge of the Sevier fold-and-thrust belt extending from southwestern Wyoming to southwest Utah where Paleozoic units are thick (1000's feet) to the west and thin (100's feet) to the east. Also shown in **Figure 9** is the location of the Seaman Range section (X) measured by Hurtubise (1989). Numbers on the map borders are degrees latitude and longitude. Nolan's (1935) type sections for the Devonian Sevy, Simonson Dolomite and Guilmette formations are in the Deep Creek Range, western Utah (**Table 2**, Number 12).

Most of the Devonian sections in the Sunnyside basin are similar to the TMS reference section. The Upper Devonian Guilmette Formation is composed of many shallowing upward cycles. However, the facies of the Upper Devonian sequences at TMS contrast sharply with the Upper Devonian sequence facies in other thrust sheets of the Timpahute Range. Examples include: 1) at Mail Summit (Number 51 on **Figure 9** and **Table 2**), reef-bearing carbonate rocks occur in the footwall of the Silver Canyon thrust; 2) at Monte Mountain (Number 52 on **Figure 9** and **Table 2**), thick quartz arenites dominate the hanging wall of the Silver Canyon thrust; 3) at Tempiute Mountain (Number 53 on **Figure 9** and **Table 2**), thin-bedded limestones comprise the hanging wall of the Tempiute Mountain thrust and footwall of the Chocolate Drop thrust (Chamberlain and Gillespie, 1993). Correlation charts showing these contrasts are presented in Chapters 4 and 8. The sharply contrasting facies are difficult to explain without taking into account evidences of post-Devonian crustal shortening in the greater Timpahute Range, probable east-west mixing of facies by the thrusting, and the presence of a Late Devonian impact crater and debris that were paleogeographically significant.

In this study, the lower Guilmette at TMS is described in more detail than other parts of the Devonian because it contains the impact breccia of Sequence Dgb2, and because it is unaltered, well exposed, and unstudied. Therefore, an understanding of the depositional setting immediately before and after the emplacement of the distinctive carbonate breccia is a primary focus of this study.

CHAPTER 2

RELATIONSHIP OF NEW RESEARCH TO PREVIOUS STUDIES

The geology of the Great Basin has been studied since the late 1800's (Hague and Emmons, 1877; King, 1870). This chapter, divided into three parts, contains reviews of mapping and the relationships between previous work on (1) stratigraphy and (2) structure in the region and the new research reported herein.

Mapping

Stewart and Carlson (1978) compiled the regional county geologic maps into a 1:500,000 scale map of Nevada. The digital (Hess and Johnson, 1997) regional geologic map for Lincoln County, which contains the Timpahute Range quadrangle, was originally published at a 1:250,000 scale by the United States Geological Survey (USGS) in 1970. It was a cooperative program with the Nevada Bureau of Mines and Geology (Tschanz and Pampeyan, 1970). Twenty-two man-months were allotted by the USGS to map the 10,649 square miles of the entire County, and much of the geology was mapped on Army Map Service 1:60,000-scale aerial photographs. The region lacked 7.5-minute topographic base map coverage until about the mid 1980's. Moreover, up to the time of the cooperative program, only about 7 percent of the region, mostly in mining districts, had been previously mapped. Other geologic mapping of Paleozoic rocks in the area includes the Seaman Range (DuBray and Hurtubise, 1994), northern Worthington Range (Martin, 1987), Golden Gate Range (Armstrong, 1991), and sketch maps of parts of the Timpahute and southern Worthington ranges (Taylor et al., 1994). Tingley (1991) provided a sample location map of the Timpahute Range quadrangle but no geologic mapping. Tschanz and Pampeyan (1970) focused their attention on the mining districts.

Stratigraphy

This section deals mostly with Devonian stratigraphy. However, earlier Paleozoic rocks are reviewed briefly. This section also briefly reviews younger Paleozoic rocks and Mesozoic and Cenozoic rocks of the study area. Earlier Paleozoic rocks were listed in Chapter 1 and **Table 1**. Also, cycle and sequence boundaries, mechanisms, regional comparisons, and their application to geologic mapping are discussed because they are important for understanding the stratigraphic framework.

Pre-Devonian Stratigraphy

No Precambrian rocks are exposed in the greater Timpahute Range and access to those mapped in the Groom Range, eight miles southwest of Tempiute Mountain, is restricted by the United States Department of Defense. However, much work has been done on the Precambrian rocks beyond the study area. Poole et al. (1992) summarized the stratigraphy from the latest Precambrian to latest Devonian time. The sequence of rocks is dominated by carbonates that lie on Precambrian and Lower Cambrian siliciclastics. Most of the early Paleozoic carbonates are dolomites except Ordovician limestones and minor Upper Cambrian limestones (**Figure 6** and **Figure 8**). Exposed Upper Cambrian rocks in the greater Timpahute Range are limestones. They are overlain by limestone beds of the Ordovician Pogonip Group, which are overlain by the Middle Ordovician Eureka Quartzite (**Figure 8, Table 1**). Excluding the limey Upper Ordovician Ely Springs Dolomite in the Silver Canyon thrust sheet, the lower Paleozoic rocks between Devonian Simonson unconformity and Eureka Quartzite are dolomites (Chapter 4). The tectonic setting and evolution of these rocks are discussed more fully in this chapter.

Devonian Lithostratigraphy

Nolan (1935) first applied the names Sevy Dolomite, Simonson Dolomite, and Guilmette Formation to Devonian strata in the Deep Creek Range, western Utah, 125 miles north-northeast of the study area (**Figure 9**, No. 12). Later, Nolan et al. (1956) established the Nevada Formation in the Eureka area, 100 miles north of the study area (**Figure 9**, No. 15 and **Figure 10**). The establishment of the Nevada Formation and other correlative units between scattered outcrops illustrates the confusion caused by mapping lithostratigraphic units. Members of the Nevada Formation roughly correlate with the uppermost part of the Sevy Dolomite through the lowermost Guilmette Formation. Because the Nevada Formation is based on lithologic changes that span several sequences, it is not useful for mapping or correlation purposes in the Sunnyside basin. Units correlative with the “Oxyoke Formation” represent different facies of the same sequences and all the units are grouped together into sequences of the “Oxyoke Formation.”

It appears to me that mapping and correlations in the Great Basin are difficult because narrow, north-south trending inselbergs of Paleozoic contain different facies. Scattered inselbergs only reveal fragments of the shelf to slope facies changes, and they are separated by broad, covered intervals. Furthermore, the thrust sheet fragments are tectonically shuffled. Puzzling facies changes between inselbergs commonly complicate lithostratigraphic correlations. As a result, dissimilar Devonian lithostratigraphic units were commonly given different names from inselberg to inselberg. Proliferation of Devonian nomenclature occurred mostly on the west side of the Sunnyside basin where structural deformation was the most intense (**Figure 10**).

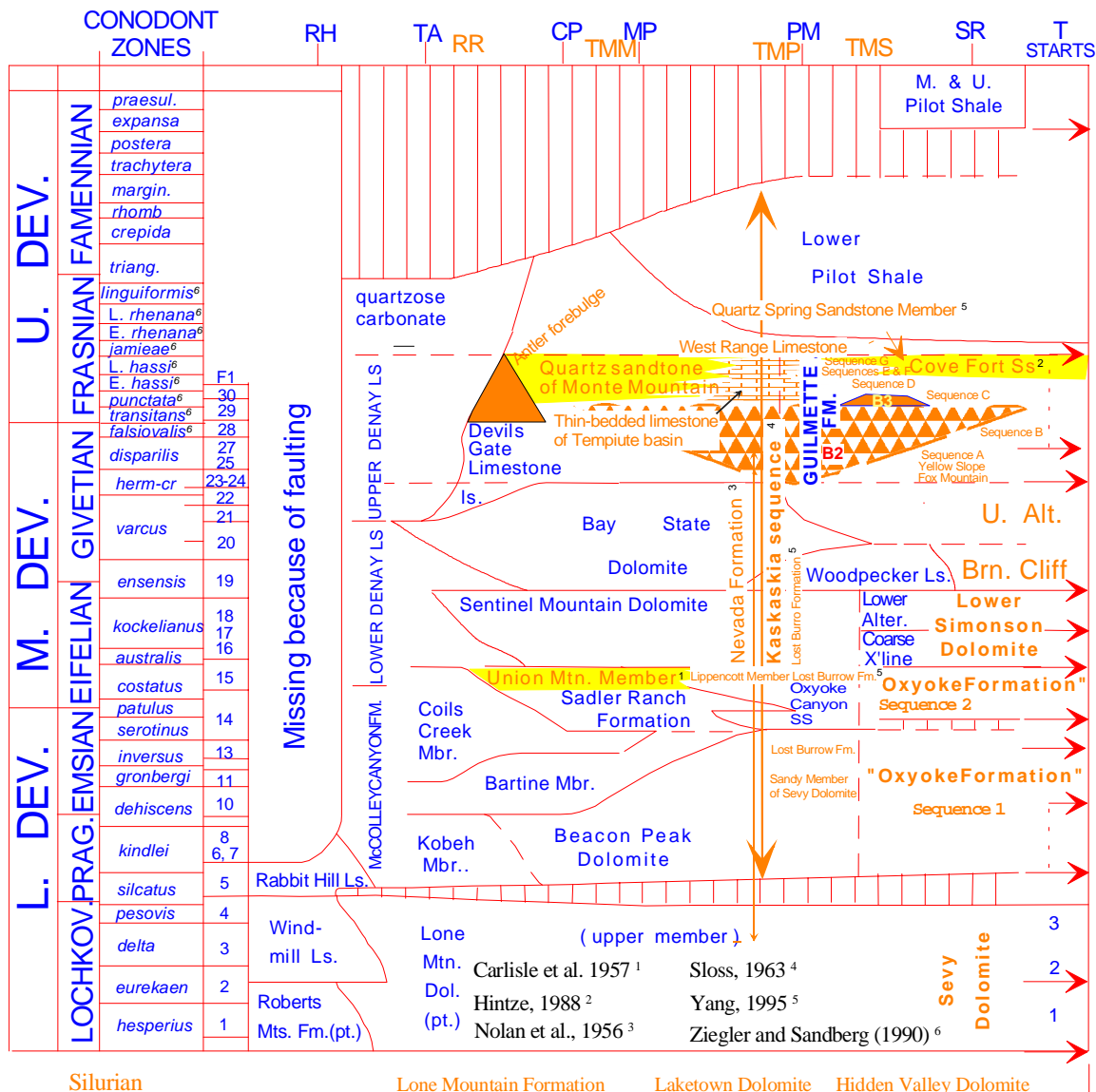


Figure 10 Time-rock transect and correlation chart illustrating Devonian nomenclature of the Sunnyside basin (after Johnson et al., 1985). Red arrows indicate beginning of transgressions (T starts). RH=Rabbit Hill, TA= northern Antelope Range, CP= Combs Peak, MP= Modoc Peak, PM= Phillipsburg Mine area, Diamond Range, SR=southern Ruby Range. Orange and yellow depict modifications. RR= Reveille Range; TMM=Timpahute Monte Mountain; TMP=Timpahute Tempiute Mtn.; TMS=Timpahute Mail Summit. Credits for Conodont zone changes and other modifications are indicated in superscript and listed above. Note the proliferation of units on the left side of the chart representing the western edge of the Sunnyside basin. Disruptions of the stratigraphic record caused by the Devonian Antler (orange triangle) and subsequent orogenies resulted in structural complexities. Rare exposures of Paleozoic rocks in thrust sheet fragments make correlation and mapping difficult, and thus an inflated nomenclature.

For example, between the very light-gray, slope-forming Sevy Dolomite and the darker gray, ledge-forming Simonson Dolomite is a sandy, brown-gray slope- and ledge-forming interval. It includes the Oxyoke Canyon Sandstone Member of the Nevada Formation (Nolan et al., 1956) which corresponds to the uppermost sequence of the “Oxyoke Formation” presented in Chapter 4. The “Oxyoke Formation” as defined in Chapter 4 is correlative with the McColley Canyon Formation (**Figure 10**). Limestones of the Bartine Member of the McColley Canyon overlie correlative beds of the Sevy Dolomite (LaMaskin and Elrick, 1997). They are lithologically dissimilar to the “Oxyoke Formation” in other locations. In **Figure 10**, Johnson et al. (1985) correlated the Coils Creek Member of the McColley Canyon Formation and the Sadler Ranch Formation with the Oxyoke Canyon Sandstone member of the Nevada Formation. In the Inyo Mountains, 120 miles southwest of the study area, rocks correlative with the “Oxyoke Formation” correspond to the lower Lost Burro Formation (Beck, 1981). In the Sulphur Springs Range, 145 miles north-northwest of the study area (**Figure 9**, No. 49 and **Table 2**), it is called the Union Mountain Member of the Nevada Formation (Carlisle et al., 1957).

This study simplified the Devonian nomenclature of the Sunnyside basin. The Sunnyside basin was introduced in Chapter 1 and will be discussed in more detail in Chapter 7. Instead of creating new stratigraphic units at each facies change, sequences of six Devonian formations were employed for regional correlations and mapping. Sequences from the work maps were combined into mappable formations to make **Plate 1a**. Construction of work maps is described in Chapter 3. **Plate 6** is an example of a geologic work map using sequences at TMS. This sequence stratigraphic approach resulted in a more accurate map of the Timpahute Range quadrangle and more accurate regional isopach maps. A comparison of the number and area of formation outcrops between old and new geologic maps illustrate the differences between mapping lithologic units (i.e., formations) vs. mapping sequences. Following is a discussion of previous work on each of the six formations: Sevy, “Oxyoke,” Simonson, Guilmette, West Range, and Pilot.

Sevy Dolomite Sevy Dolomite was the name given by Nolan (1935) to the dolomite exposures in Sevy Canyon, Deep Creek Range, Utah (**Figure 9**, No. 12). Later, Nolan et al. (1956) gave the name of Beacon Peak to the micritic, light-gray, slope-forming dolomite that overlies the Silurian Lone Mountain Dolomite (**Figure 10**). The lower Lone Mountain is probably partly equivalent to the Laketown Dolomite. The Beacon Peak is a member of the Nevada Formation in the Eureka area, Nevada, (**Figure 9**, No. 5). As Matti (1979) stated, the upper Sevy and Beacon Peak dolomites are correlative and lithologically identical. Sevy Dolomite has priority and Beacon Peak should be discarded. Johnson et al. (1985) placed the Sevy in the Lower Devonian (**Figure 10**). W.D. Roberts (1998, personal communication) collected Middle Devonian macrofossils from a limestone bed he placed in the upper part of the Sevy Dolomite in the Spotted range, 35 miles southwest of the study area. Access to the Spotted Range is now prohibited by the United States Department of Defense. His upper Sevy Dolomite is likely the “Oxyoke Formation” in this study. The digital geologic map (Hess and Johnson, 1997) of Tschanz and Pampeyan (1970) allowed me to compare their mapping with mine. The newly digitized geologic map of Tschanz and Pampeyan (1970) shows 48 outcrops of Sevy Dolomite that cover 24.46 square miles. In contrast, I show 68 outcrops covering 15.65 square miles using sequences on the new geologic map. Most of the difference is because Tschanz and Pampeyan (1970) combined the “Oxyoke Formation” with the Sevy Dolomite, and they mapped strata in the Hiko Range as Sevy Dolomite that is Guilmette Formation.

The Hidden Valley Dolomite, in the Inyo Mountains, California, 120 miles west-southwest of the study area, is approximately equivalent to the Sevy Dolomite or Laketown Dolomite. Tschanz and Pampeyan (1970) reported that fossils belonging to the *Spirifer kobehana* Zone occur in the upper 350 feet of the Hidden Valley Dolomite. Similar fossils were also found in the upper 65 feet of the Hidden Valley Dolomite at Quartz Spring by Beck (1981). These fossils are of Early Devonian Age and occur in rocks equivalent to the Sevy Dolomite.

“Oxyoke Formation” Previous investigators have been inconsistent in how they grouped and correlated the “Oxyoke Formation” and adjacent strata. As mentioned above, Nolan et al. (1956) established the “Oxyoke Formation” nomenclature naming the Oxyoke Canyon Sandstone Member of the Nevada Formation in the Eureka Mining District (**Figure 10**). Recognizing a faunal change between the argillaceous carbonate zone and the overlying quartzose carbonate zone, Johnson (1962) argued that the upper part of the Oxyoke Canyon Sandstone is correlative with the basal Simonson Dolomite east of the Diamond/Pancake ranges. The “Oxyoke Formation” in this study is possibly partly correlative with the basal part of the Coarse Crystalline Member of Johnson et al. (1989). However, the “Oxyoke Formation” was not mapped separately by Tschanz and Pampeyan (1970). They included rocks equivalent to the “Oxyoke Formation” in the Sevy Dolomite.

Southwest of the study area (120 miles) in the Inyo Mountains, California, Beck (1981) described the 164-foot thick sandy Lippincott Member of the Lost Burro Formation (**Figure 10**). It is probably partly correlative with the “Oxyoke Formation” at Mail Summit. Yang et al. (1995) divided the Lost Burro Formation into five units. The Lippincott lies above the Hidden Valley Dolomite and below their Unit 2 of the Lost Burro Formation.

Osmond (1962) described a persistent sandy interval between the Sevy and Simonson Dolomites and placed it at the top of the Sevy Dolomite. Hurtubise (1989), in his work in the Seaman Range, followed Osmond’s convention and described it as the Sandy Member of the Sevy Dolomite (**Figure 10**). He measured 101 feet of sandstone in the northern Seaman Range in contrast to 46 feet reported by Osmond (1954).

However, Osmond (1962), Hurtubise (1989), and other early workers used different criteria to pick the contacts. They did not have the benefit of sequence stratigraphic perceptions at the time. To resolve the above stated problems and conflicts, I have chosen to establish an informal unit of formational rank which I name the “Oxyoke Formation.” From **Figure 10**, it appears to range from upper Lower Devonian to lower

Middle Devonian. I propose the TMS to be the type section because it is easily accessible and because it and its contacts are well exposed. Though Tschanz and Pampeyan (1970) did not map “Oxyoke Formation” as a separate map unit (**Plate 1b**), I have found that it provides a key marker bed that reveals important structural details (**Plate 1a**).

The source for sandstone in the “Oxyoke Formation” is problematical. Osmond (1954) argued for wind blown sands from an emergent area in the east or southeast. Johnson (1962) argued for a source from an arch on the north. Paleocurrent directions from cross-bedding vary from a northwest transport direction at Fossil Peak (Hurtubise, 1989), southward in the Egan Range (Osmond, 1954; Reso, 1960)(**Figure 9**, No. 20 and **Table 2**), northeastward in the White Pine Range (Osmond, 1954)(**Figure 9**, No. 7 and **Table 2**), westward in the Grant Range (Osmond, 1954)(**Figure 9**, No. 27 and **Table 2**), south and southeastward in the Seaman Range and central Grant Range (Osmond, 1954), and southward in the Pahrnagat Range (Reso, 1960). Paleocurrent directions based on cross-bedding in the Hiko Range, however, vary from southwestward to northeastward. Herringbone cross lamination, bidirectional ripple marks, and cross-bedding all suggest that the sands--at least in this area--were deposited under the influence of tides. A new “Oxyoke Formation” sand provenance is proposed in Chapter 4 and discussed in Chapter 7.

Simonson Dolomite Nolan (1935) named the Simonson Dolomite after exposures in Simonson Canyon, Deep Creek Range, Utah (**Figure 9**, No. 12). Osmond (1954) subdivided the Simonson Dolomite into four members. His Coarsely crystalline, Lower Alternating, Brown Cliff Forming and Upper Alternating Members generally coincide with the sequences delimited in this study. As defined herein, the Simonson Dolomite lies within the Middle Devonian (**Figure 10**). The portion of the digital geologic map (Hess and Johnson, 1997) of Tschanz and Pampeyan (1970) of the Timpahute Range quadrangle shows 48 Simonson Dolomite outcrops covering 41.24 square miles. In

contrast, I mapped 78 Simonson Dolomite outcrops covering only 17.67 square miles. Part of the discrepancy between old and new mapping is caused by the difference in defining the Simonson Dolomite and Guilmette formations. Tschanz and Pampeyan (1970) combined the Fox Mountain Sequence of the Guilmette Formation with the Simonson Dolomite. They also mapped large parts of the Hiko Range as Simonson Dolomite that should have been mapped as Guilmette and younger units (**Plate 2a**).

Elrick (1995) suggested that these Middle Devonian carbonates of the eastern Great Basin were deposited along a low energy, westward-thickening, distally steepened ramp. However, isopach maps of Middle Devonian sequences suggest that the carbonates were deposited in the Sunnyside basin, an intrashelf basin (see Chapter 7). Devonian rocks thicken westward (as suggested by Elrick, 1995) to the axis of the Sunnyside basin. However, they thin westward from the axis toward the Antler forebulge (**Plate 3**). Devonian rocks west of Eureka, Nevada, lie below the Mississippian Roberts Mountain thrust (i.e., Lone Mountain, **Figure 9**, No. 34 and **Table 2**). These thick, open-marine rocks were likely deposited west of the Antler forebulge and then thrust into their present location by Sevier thrust faults.

Guilmette Formation The Guilmette Formation was also named by Nolan (1935) after exposures in Guilmette Gulch, Deep Creek Range, Utah (**Figure 9**, No. 12). The basis for originally separating the Simonson Dolomite from the overlying Guilmette Formation at its Deep Creek Range type locality was the change from sucrosic dolomite to limestone (Nolan, 1935). The dolomite breccia that Nolan described at the base of the Guilmette Formation may be related to a karst surface at the top of the Simonson Dolomite. It also could be related to a transgressive lag over it, both of which are described in Chapter 4. As defined in this study, **Figure 10** shows that the Guilmette Formation began in the upper Middle Devonian and ended in the lower Upper Devonian.

Unfortunately, subsequent workers have chosen to redefine the base of the

Guilmette Formation rather than use Nolan's original definition. Reso and Croneis (1959) proposed that the base of a yellow slope-forming bed (the upper Yellow Slope Sequence in this paper) be the base of the Guilmette Formation in the Pahranaagat Range. It is 40 to 90 feet above the highest bed in the Fox Mountain Sequence that bears the brachiopod *Stringocephalus* at TMS. The Fox Mountain Sequence herein is an interval between the major unconformity at the top of the Simonson Dolomite and at the base of the Yellow Slope Sequence. The sequence is present in some ranges. Following the convention of Reso and Croneis (1959), Tschanz and Pampeyan (1970) in their regional synthesis, Hurtubise (1989) in the Seaman Range, Ackman (1991) in the Worthington Range, and Estes (1992) in the Pahranaagat Range all placed the top of the Simonson Dolomite at the base of the yellow slope-forming bed. They included the *Stringocephalus*-bearing Fox Mountain Member with the uppermost part of the Simonson Dolomite. Sandberg et al. (1997) formally proposed the Fox Mountain as a new formation lying between the Guilmette Formation and the Simonson Dolomite. However, the boundaries of their Fox Mountain Formation are under debate and are different from the Fox Mountain Sequence herein (Chapter 4).

Hurtubise (1989) defined the base of the yellow slope-forming bed as the base of a stromatolite bed. He did not identify which stromatolite bed. Most sections contain several stromatolite beds that occur above the sequence boundary that separates the Yellow Slope Sequence from the Fox Mountain Sequences as defined herein. Sandberg et al. (1997) did not mention criteria for a sequence boundary between the Yellow Slope Sequence and the Fox Mountain Sequence nor the karsted sequence boundary between the Fox Mountain Sequence and the underlying Simonson Dolomite. The karst surface they describe between their lower and upper members is likely the sequence boundary or the top of the Simonson unconformity herein. Crinoids, occurring only in their upper member and my Fox Mountain Sequence, suggest open-marine deposition. The base of the Fox Mountain Sequence defined herein most likely marks the Taghanic onlap or Event 1 of Sandberg et al. (1997). Therefore, application of sequence stratigraphy and

recognition of the regional unconformity at the top of the type Simonson Dolomite returns us to Nolan's original definition of the lower contact of the Guilmette Formation as the change from underlying sucrosic dolomite to overlying limestone. A more detailed description of the Guilmette sequences, including the Fox Mountain, is presented in Chapter 4.

The number of Guilmette Formation outcrops and their distribution in the study area partly depends on how the Guilmette Formation is defined. The digital geologic map of Tschanz and Pampeyan (1970) shows 65 Guilmette outcrops covering 95.62 square miles in contrast my map that shows 142 Guilmette outcrops covering 89.07 square miles (Chapter 4). However, the large area Tschanz and Pampeyan (1970) mapped as undifferentiated Devonian and Mississippian in the Mail Summit 7.5' quadrangle (**Figure 3**), and the large area of Ordovician Pogonip Formation in the Monte Mountain 7.5' quadrangle they mapped as Guilmette, greatly increased the area they mismapped as Guilmette Formation. Nevertheless, they mismapped the Guilmette and younger beds in the Hiko Range as Simonson Dolomite (compare **Plates 1a** and **1b**).

Several workers have attempted to divide the Guilmette by lithology. In his work in the Pahranaagat Range area, Reso (1960) divided the Guilmette into two members above and below the top of a prominent carbonate breccia (Dgb2 Sequence in this paper). Hurtubise (1989) divided the Guilmette into two members above and below the top of the yellow slope-forming interval. Sandberg et al. (1997) formally proposed to make the Guilmette Sequence Dgb2 breccia facies the Alamo Breccia Member of the Guilmette Formation. In contrast, in this report I have divided the Guilmette into nine stratigraphic sequences (Chamberlain and Warme, 1996) that can be mapped and correlated throughout much of the Sunnyside basin (**Plate 3**). These sequences are described in detail in Chapter 4.

Dunn (1979) studied a reef sequence at TMS. She reported *Thamnopora* corals, ostracodes, styliolinids, *Tentaculites*, and foraminifers (e.g., *Tikhinella*) from beds herein assigned to Sequence Dgb3, Cycle 1 just below the reef (**Plate 2c**). TMS sequences are

described in Chapter 4 and cycles of the TMS sequences are described in Appendix B. Dunn (1979) reported that the high-energy assemblage of the reef (my Cycle 3, Sequence Dgb3) was characterized by tabular and massive stromatoporoids, tabulate corals *Thamnopora* and *Alveolites*, rhynchonellid and terebratulid brachiopods, crinoids, and gastropods. The reef was divided into three parts based on zonation of fauna within the reef. The first subdivision contains the rhynchonellid brachiopod *Hypothridina emmonsii*, terebratulid *Cranaena* sp., and the branching tabulate coral *Thamnopora* along with crinoids, horn corals and gastropods (Dunn, 1979). This subdivision probably included Sequence Dgb (reef core) Cycles 1 and 2 herein (**Plate 2c**).

Dunn's second subdivision probably extended near to sample MI-479 (Appendix C) at the 2,400-foot level in the TMS section (**Plate 2a**). **Plate 2a** shows the vertical position of samples from the TMS measured section. Dunn noted that this division contained many same fossils as in the lower subdivision with the addition of massive and tabular stromatoporoids and the colonial rugose coral *Pachyphyllum*. In addition, she listed the alga *Solenopora* sp. that would suggest the reef grew within the photic zone. Finally, *Renalcis* and *Sphaerocodium* algae and *Amphipora* stromatoporoids were noted in the middle or main subdivision. By comparing this reef with reefs in other parts of the world, she concluded that her tabular-massive stromatoporoid subdivision was constructed between storm and normal wave base. The uppermost subdivision contained more corals and fewer, thinner stromatoporoids and contained large colonies of the tabulate coral *Alveolites* that are rare in lower subdivisions, suggesting shallower water conditions.

Dunn (1979) pointed out that fossils from my Dgb3c at TMS (**Plate 2c**) were harder to identify than those of the reef flank equivalent beds due to the recrystallization of the reef core to coarsely-crystalline limestone. She listed the corals *Alveolites*, *Thamnopora*, and *Macgeea*, the mollusc (?) *Tentaculites*, the foraminiferans *Tikhinella*, *Nanicella*, *Elvania*, and *Multiseptada*, and the stromatoporoid *Trupetostroma*, as some fossils found in the reef flank equivalent beds. Dunn noted that the denser (thicker

stemmed) stromatoporoid *Stachyoides* predominates near the reef and the delicate *Amphipora* is more common away from the reef. Tabular stromatoporoids decrease in abundance away from the reef.

The Dgb3 reef is the famous structure mentioned by Reso (1960), discussed by Chamberlain and Warne (1996), Warne and Sandberg (1996), Sandberg et al. (1997) and Chamberlain and Birge (1997). A color oblique aerial photograph of the reef is shown in Chamberlain and Warne (1996, Figure 11). Digital images of reefs occurring in the Hiko Range are shown at Stop 16, in Appendix D.

West Range Limestone Westgate and Knopf (1932) established the West Range Limestone in the Pioche Mining District 25 miles east of the study area. They named it after rocks exposed in the West Range which they described as “blue-gray fine-grained limestones, in some places nodular, commonly weathering to a characteristic yellow color.” Kellogg (1963) in the Egan Range, Reso (1960, 1963) in the Pahrnagat Range, Hurtubise (1989) in the Seaman Range and Sandberg and Ziegler (1973) at Bactrian Mountain all recognized the West Range Limestone above the quartz sandstone at the top of the Guilmette Formation (**Table 1, Plate 1a**). Bactrian Mountain in the northern Pahrnagat Range is in T5S R59E on the south edge of the Timpahute Range quadrangle (**Plate 1**). Tschanz and Pampeyan (1970) did not map the West Range Limestone as a separate unit in their geologic map of Lincoln County. They probably grouped it with the Pilot Formation.

Johnson et al. (1991) suggested that the West Range Limestone intertongues with the Pilot Formation. It lies in the upper Frasnian (**Figure 10**). Sandberg et al. (1988) suggested that the Indian Ranch Tongue of the uppermost Guilmette Formation lies entirely within the Pilot Formation although it is “a time and lithogenetic equivalent of the West Range Limestone.”

Pilot Formation Spencer (1917) established the Pilot Formation in the Ely Mining District 100 miles north of the study area (**Figure 2**). Reso (1963) in the Pahrangat Range, Hurtubise (1989) at Fox Mountain (50 miles north-northeast of Hiko), and Sandberg and Ziegler (1973) at Bactrian Mountain also recognized the Pilot Formation between the West Range Limestone and overlying Joana Limestone. Tschanz and Pampeyan (1970) mapped 49 outcrops of Pilot Formation covering 10.9 square miles in the Timpahute Range quadrangle. In contrast, the new map shows 91 Pilot Formation outcrops that cover 5.85 square miles.

Sandberg et al. (1988) concluded that the lower member of the Pilot Formation was deposited in the Pilot Basin at the start of the *Ancyrognathus triangularis* conodont zone that lies above the *Mesotaxis asymmetrica (liguiformis)* in Sandberg et al., 1997) conodont zone of the upper Guilmette Formation. The *triangularis* zone began 364 Ma. (Sandberg and Ziegler, 1996). Johnson et al. (1985) placed the lower Pilot Shale at the end of the *Ancyrognathus triangularis* conodont zone (**Figure 10**). The *triangularis* zone ended 362.5 Ma. (Sandberg and Ziegler, 1996). Conodonts from the Dgb2 (Alamo Breccia) show the Alamo event occurred in the *punctata* zone (Warme and Sandberg, 1995) which ended three (Sandberg et al., 1997) or four (Sandberg and Zeigler, 1996) million years before the beginning of the *triangularis* zone. The Pilot Formation is divided into three members by major unconformities (Sandberg et al., 1997) but begins 356.5 Ma. In contrast, Carpenter (1997) suggested that the Yellow Slope Sequence could represent the earliest Pilot basin deposition. The Yellow Slope Sequence began about 371 Ma. (Sandberg et al., 1997).

According to Sandberg et al. (1988), the incipient Pilot basin is a small circular basin between the Utah/Nevada border and the Eureka area (**Figure 2**). It expanded slightly into westernmost Utah during the Lower *triangularis* Zone (Sandberg et al., 1988). In contrast, the Sunnyside basin began in Sevy Dolomite time and extended into Pilot Formation time and covered a much greater area than the Pilot basin (Chamberlain

and Birge, 1997). The Pilot basin of Sandberg et al. (1988) lies within the Sunnyside basin.

Regional Comparison According to earlier research, Devonian rocks exposed at TMS are lithologically, depositionally, and biostratigraphically similar to those in the Specter Range (60 miles south-southwest of the study area), Nevada (Burchfiel, 1964), and the Panamint Range (80 miles south of the study area), California (Zenger and Pearson, 1969), and to those as far north as Alberta, Canada (Reso, 1960).

The Middle and Late Devonian Lost Burro Formation, exposed in the Panamint Range, is composed of mostly dolomite in the lower part and limestone in the middle and upper parts (McAllister 1952). This pattern is found elsewhere, over much of the Devonian shelf throughout the region. According to Beck (1981), the lowermost part of the formation is marked by the 50-meter thick sandy Lippincott Member. Johnson et al. (1989) correlated the Lippincott to the Coarse Crystalline Member of the Simonson Dolomite. However, as mentioned above, part of the Lippincott is probably partly correlative with the “Oxyoke Formation” herein (**Figure 10**). According to Stevens (1986), the Lost Burro Formation was deposited on the western North American passive margin under subtidal to supratidal conditions. He suggested that similar thick platform Devonian carbonates found in the central and western parts of the Inyo Mountains-Angus Range region probably accumulated on a moderately channeled slope in deep water. Similar Devonian carbonates in the Panamint Range and the easternmost and southern Inyo Mountains were deposited on the western edge of the carbonate shelf near the continental slope (Armstrong, 1980).

Yang et al. (1995) divided the 1969-foot thick Lost Burro Formation into five units. Most of Yang et al. (1995)’s Unit 2 (459 feet) and the uppermost part (66 feet) of Unit 1 of the Lost Burro Formation is probably correlative with the Simonson Dolomite. It is correlative because it lies above the *Spirifer kobehana* Zone and below rocks of

Givetian age. An *Amphipora*-bearing bed near the middle of their Unit 2 is most likely correlative with the Simonson Dolomite Brown Cliff Sequence at TMS. Yang et al. (1995) described the upper part of the Lost Burro Formation as shallowing-upward cycles of predominantly stromatoporoid-bearing limestones and minor sandstones. The uppermost part of their Unit 2 (82 feet) and the lower part of their Unit 3 (443 feet) most likely correlate to the upper part of the Simonson Dolomite Upper Alternating Sequence and the Guilmette Fox Mountain Sequence at TMS because of its Givetian age. Because of the interbedded sandstones and Frasnian age, the upper parts of their Unit 3 (262 feet thick) most likely correlates to Guilmette Sequences Dge and Dgf of TMS. A regional unconformity and major sequence boundary cuts out lower and middle Guilmette sequences in many Nevada and Utah sections to the north and probably removed lower middle Guilmette sequences in the Panamint Range. Unit 4 of Yang et al. (1995) is 426 feet thick and probably correlates to Sequence Dgg at TMS. Their Unit 5 (66 feet), the Quartz Spring Sandstone Member, correlates to the sandstone at the top of Sequence Dgg at TMS (**Figure 10**). It probably correlates to the Cove Fort Sandstone and its equivalents in Utah and eastern Nevada (Langenheim and Larson, 1973). An isolith map of net Guilmette sandstones in Chapter 7 shows the distribution of Late Devonian quartz sandstones in the Sunnyside basin.

Younger Paleozoic Rocks of the Study Area

Although this study focuses on the Devonian rocks, the distribution of younger Paleozoic rocks is important to complete the geologic map. The Devonian Sunnyside intrashelf basin evolved into the Antler foreland basin in the Lower Mississippian. Synorogenic sediments shed off the Roberts Mountain allochthon filled the western side of the basin with siliciclastic sediments (Poole, 1974). Mississippian limestones with tongues of nonmarine valley-fill sediments filled the eastern side of the Mississippian

basin (Chamberlain, 1981). The Timpahute area lies between thick (more than 4000 feet) Mississippian carbonates on the east and correlative thick (more than 6000 feet) siliciclastics on the west (Cedar Strat proprietary measured sections, 1984-1989). Reso (1963) reported more than 1000 feet of Lower Mississippian limestone and more than 1000 feet of shales and sandstones in the Pahrnagat Range, five miles south of the study area. Tschanz and Pampeyan (1970) also estimated 1000 feet of Middle and Late Mississippian Antler siliciclastics in the Pahrnagat Range. At Tempiute Mountain, the Mississippian Antler clastics are 2220 feet thick (Cedar Strat proprietary measured section). The thickness and presence of Mississippian Antler clastics, and especially the shales, are important in the study area because they form one of the most important thrust detachment layers. As defined in Chapter 1, the Mississippian Antler clastics include Chainman shale and Scotty Wash sandstone facies.

The digitized map of Tschanz and Pampeyan (1970) shows 53 outcrops of Joana Limestone covering 38.02 square miles in the Timpahute Range quadrangle. In contrast, I show 101 Joana outcrops that cover 40.26 square miles, in Chapter 4. The biggest difference occurs in the Monte Mountain 7.5' quadrangle where they mistakenly took Joana Limestone for Pennsylvanian rocks. Tschanz and Pampeyan (1970) mapped 44 outcrops of Antler clastics (Chainman Shale and Scotty Sandstone) covering 11.66 square miles in the Timpahute Range quadrangle (**Figure 11**). In contrast, I show 46 Antler clastics outcrops that cover 9.9 square miles.

Reso (1963) reported 764 feet of Pennsylvanian (undifferentiated but probably Ely Formation) rocks in the Pahrnagat Range. Tschanz and Pampeyan (1970) noted that no complete section of Permian limestone exists in Lincoln County, but that in other sections in the region the Permian limestone is 2000 to 4500 feet thick. Rocks representing the uppermost Permian and Lower and Middle Mesozoic were not found in the study area.

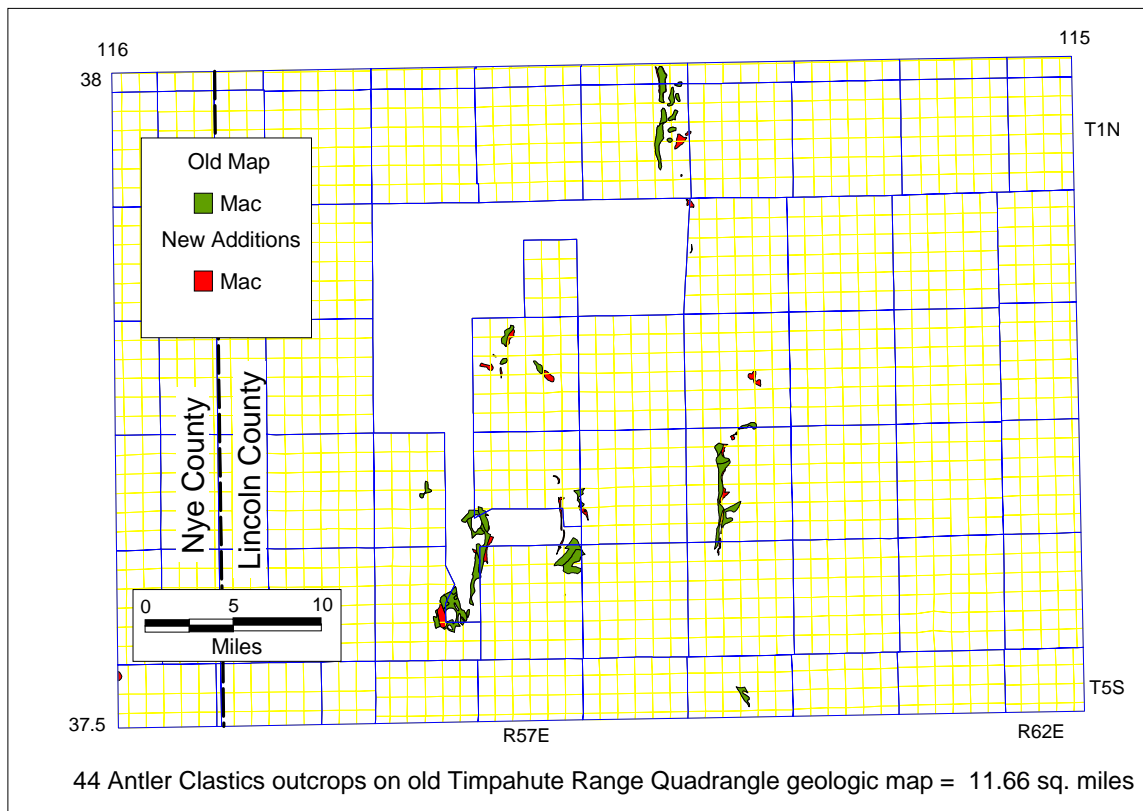


Figure 11 Distribution of outcrops of Mississippian Antler clastics in the Timpahute Range quadrangle as reported by Tschanz and Pampeyan (1970). Added Antler clastics outcrops from the new map are marked in red. Degrees latitude and longitude are marked at the corners of the map.

Sevier Synorogenic Sediments

Sevier synorogenic sediments are present in the study area and in much of the Nevada part of the Sevier thrust belt. They provide constraints on the age of thrusting and thus resolve controversy concerning the age of the Sevier orogeny. Their distribution and stratigraphy provide insight into the evolution of the Sevier orogeny.

Age of Thrusting The age of thrust faults in the region is controversial. Some believe that most of the thrusting in Nevada is likely pre-Cretaceous (e.g., W.J. Perry, 1991, personal communication), and others contend that most thrusting occurred in the Late Cretaceous.

Synorogenic strata exposed near the leading edge of the Sevier fold-and-thrust belt in northern Utah and southwestern Wyoming confirm a Late Mesozoic age for thrusting. The Sevier wedge in northeast Utah and southwest Wyoming was shortened by 60 miles in three major and one minor events from Neocomian(?) to Eocene time (Decals, 1994). These events resulted in an overall eastward progression of thrusting that was punctuated by several episodes of out-of-sequence and hinterland vergent thrusting (Decals and Mitra, 1995). An out-of-sequence thrust fault is a thrust fault that does not fit the predictive pattern of thrust faults in a sequence becoming younger in their vergent direction but cuts across or through older thrust faults. Hinterland vergent thrusts are backthrusts with a vergent direction opposite to the thrust faults in a normal sequence.

An isopach map of the Aptian-Albian Cedar mountain Formation at the leading edge of the Sevier fold-and-thrust belt in central Utah clearly shows that the Sevier orogeny there is Late Cretaceous (Currie, 1997). The Sevier thrust wedge of central Utah was emplaced between early Albian and Campanian time and persisted by out-of-sequence thrusting until Lower Eocene (Lawton and Trexler, 1991). Late Cretaceous (Albian-Cenomanian) synorogenic rocks associated with thrusting are found in outcrops from northern to southern Nevada. Some researchers suggest that these rocks provide constraints on timing of the Sevier deformation in the region (Vandervoort, 1987; Carpenter et al., 1993a, 1993b; Carpenter and Carpenter, 1994a, 1994b). Tertiary/Cretaceous rocks preserved in many ranges of eastern Nevada, including the study area, were probably associated with the Sevier fold-and-thrust belt (**Figure 1**).

Additional evidence of Cretaceous age thrusting comes from a well 180 miles on strike to the north. The Gary-Williams Company Three Bar Federal No. 36-C, C SW Sec

6 T27N R51E drilled from Ordovician Vinini Formation through Cretaceous strata and into upper Paleozoic strata (Well files, Nevada Bureau of Mines and Geology).

Two methods help date the Sevier orogeny. One is crosscutting relationships of dated igneous intrusions, and the other is dating of fossils and volcanics in the synorogenic sediments associated with thrusting. The Sevier thrust belt is best dated by the associated Cretaceous deposits in eastern Utah (L. Hintze, 1998, personal communication). Geochronological data from igneous intrusions and cross cutting relationships can also be used to date the Sevier orogeny. These relationships in the Clark Mountain area, at the southern end of the Sevier belt (**Figure 2**), suggest that thrusting was initiated in the Late Jurassic and continued to the Middle Cretaceous (Walker et al., 1995). However, Stamatakos et al. (1998) suggested that paleomagnetic and Paleozoic zircon fission-track data suggest that the Meiklejohn Peak thrust fault (near the Nevada/California border, 100 miles southwest of the study area) predates Jurassic-Cretaceous (Sevier) deformation. They suggested that the deformation may have resulted from a Permian or earlier contractional event. In the study area, the emplacement of the Freiburg intrusions (25.1 Ma., Taylor et al., 1993) that intrude the footwall and hanging walls of the Freiburg thrust fault suggests that the fault is Oligocene or older (**Plate 1a**, T1N R57E). An age date of the Troy Peak stock is 86.5 ± 4.6 Ma U/Pb on Zircon. It intrudes the recumbent limb of the Timber Mountain and associated thrust faults in the Grant Range. Therefore it gives an upper limit on time of formation (**Figure 2**) as Late Cretaceous (Taylor et al., 1993).

Distribution and Stratigraphy A newly discovered unit southwest of Monte Mountain between Paleozoic rocks and Tertiary volcanic rocks may provide insight on the age of the compressional structures of the region (Sec 5 T4S R58E, **Plate 1a**). The unit is Late Cretaceous or Lower Tertiary and is called Tertiary/Cretaceous (Chamberlain et al., 1992b). It probably predates Tertiary volcanics as it lacks fragments of Tertiary

volcanics within it. The Tertiary/Cretaceous strata contain lacustrine limestone beds similar to the Sheep Pass Formation in east central Nevada, the Flagstaff Limestone in central Utah (Fouch et al., 1991), and the Claron Formation in southwestern Utah (Goldstrand, 1992). Conglomerate underlies both the Claron Formation (Goldstrand, 1994) and the Tertiary/Cretaceous strata of the Timpahute region. It may be correlative with the conglomerates of the North Horn Formation that underlie and are coeval with the Flagstaff Limestone in central Utah (Fouch et al., 1979). A similar unit of limestone above conglomerate beds occurs in the Grant Range, 30 miles north of the study area. These beds were mapped as Sheep Pass on the Nye County Geological Map (Kleinhampl and Ziony, 1985).

Hurtubise (1989) described an outcrop of whitish weathering lime mudstone on the west side of the Seaman Range, thirty-five miles to the northeast of Monte Mountain. Palynomorphs suggest an Eocene age for the limestone. He correlated the outcrop in the Seaman Range with Winfrey's Member "B" from the Sheep Pass type locality in the Egan Range, 35 miles north-northeast of Hurtubise's location in the Seaman Range (Winfrey, 1960).

Limestones at Monte Mountain may yield an Eocene age (uppermost Refugian), similar to Hurtubise's (1989) assemblage. If they do, the underlying conglomerates could be correlated to Winfrey's Member A. If the beds are Sheep Pass age, then the Sheep Pass basin should be enlarged or another basin defined. It would reach at least thirty-five miles farther south than Hurtubise's newly discovered outcrops in the Seaman Range. I found similar limestones in the hanging-wall sheet of the Pahrnagat thrust near the top of Tikaboo Peak, twenty miles south-southeast of Monte Mountain. As with the Monte Mountain Tertiary/Cretaceous strata, they lie between the Paleozoic rocks and the overlying Tertiary volcanics.

Tschanz and Pampeyan (1970) described similar beds in the Pahroc (30 miles east of Monte Mountain), Groom (25 miles south-southwest of Monte Mountain), Pintwater (40 miles south of Monte Mountain), and Spotted (45 miles south-southwest of Monte

Mountain) ranges. According to their map, these rocks cover a significant portion of western Lincoln County. They suggested that the conglomerates are Cretaceous to Oligocene and the overlying limestone is Miocene or younger. These Tertiary/Cretaceous conglomerates and lacustrine limestones occur near thrust faults, were probably shed off from thrust fronts, and could provide important insight into timing of the thrust faults if they are genetically related to them. Tschanz and Pampeyan (1970) estimated that the thickest conglomerates exposed in the Spotted and Pintwater ranges are 5000 to 6000 feet thick. Access to these rocks is now restricted by the United States Department of Defense. These Tertiary/Cretaceous rocks that are closely associated with thrust faults along the four-hundred-mile-long Sevier fold-and-thrust belt in Nevada could provide insight into timing and thrust form. Others (e.g., Fouch et al., 1991) believed that there are no ramping thrust faults in the immediate region of these localities.

The Sevier fold-and-thrust belt in central Utah may have localized deposition of the Flagstaff Limestone, North Horn Formation and Colton Formation (Stanley and Collison, 1979). However, Fouch et al. (1991) suggest that the Sevier orogeny was over and no foreland basin in central Utah existed by the time of Flagstaff deposition. Goldstrand (1992) suggested that the correlative Pine Hollow and Claron formations were deposited during the Laramide Orogeny and are related to partitioning of the foreland basin into individual, internally drained basins. These basins derived sediment from surrounding structural highs during Lower Paleocene and Middle Eocene time. A contrast of depositional environments occurred between the west and east side of Lake Flagstaff. Western-derived lithic quartz sandstones show evidence of thinning over Sevier-age folds. They also show evidence of steep topography and high-energy along the west side of the lake. These sediments contrast with the shallow, vegetated, and episodically flooded east shore sediments. The phase of subsidence and infilling of a foreland basin east of the Sevier fold-and-thrust belt probably controlled the facies contrast. The Late Cretaceous to Lower Tertiary tectonic pulse of Elison (1991) probably controlled deposition of the North Horn Formation and associated units. This pulse

probably corresponds to the emplacement of Roeder's (1989) thick terrane such as the Silver Canyon thrust sheet. The thrust disrupted and reinvolved Roeder's (1989) thin terrane such as the Monte Mountain thrust sheet. The emplacement of Roeder's (1989) thin terrane could have been during one of two earlier Sevier tectonic pulses.

In contrast to the compressional synorogenic model supported by this research, some researchers (e.g., Newman, 1979) believed that the conglomerates in the Tertiary/Cretaceous beds were a result of erosion off normal fault horsts. Similarly, Constenius (1996) concluded that many valley fill deposits were deposited in Late Paleogene half grabens resulting from extensional collapse of the Cordilleran foreland fold-and-thrust belt. The new geologic map of the study area does not support these extensional collapse or horst and graben models (**Plate 1a**). However, the new geologic map shows more Late Cretaceous compressional features than do previously published geologic maps.

Structure and Tectonics

Paleogeographic reconstructions of this structurally complex region not only require a detailed analysis of stratigraphy but also an understanding of the structural elements and tectonic evolution. This section presents a brief discussion of tectonic events that influenced deposition and deformation of the Paleozoic rocks of the area. An emphasis is given to the Cretaceous Sevier orogeny because of its importance in paleogeographic reconstructions and its poorly understood effects on the rocks of the region.

Pre-Antler Orogeny

Rifting in the late Precambrian (<850 Ma) resulted in the western North American continental margin along which a thick wedge of strata accumulated during the late Precambrian and lower Paleozoic (Stewart and Poole, 1974). Most of the latest Precambrian (<850 Ma) to Late Devonian (>345 Ma) strata deposited east of the Sr 0.706 line were deposited in shallow-water conditions on the continental shelf. They were deposited during a time of relative tectonic stability (Stewart and Poole, 1974).

The 0.706 Strontium isotope line probably represents the rift edge in the Precambrian crust. It is a north-south line in central Nevada that divides older continental and newer oceanic crustal domains. It occurs where $^{87}\text{Sr}/^{86}\text{Sr} = 0.706$ in granitic rocks and is taken as the western edge of Precambrian crust at depth (Suppe, 1985). Oceanic sediments west of the line have $^{87}\text{Sr}/^{86}\text{Sr}$ ratios less than 0.706. They are interpreted as representing younger oceanic crust than the older continental rocks east of the line that have $^{87}\text{Sr}/^{86}\text{Sr}$ ratios above 0.706. Oceanic rocks deposited west of the $^{87}\text{Sr}/^{86}\text{Sr}$ 0.706 line were deposited in deepwater conditions. They are composed of chert, shale and volcanic rocks and were termed “western facies” by Merriam and Anderson (1942) and “siliceous facies” by Roberts (1972). These siliciclastic-rich oceanic rocks contrast sharply with the carbonate-rich eastern facies of the study area.

Stewart and Poole (1974) described the transition between western and eastern facies as abrupt. Crustal shortening during the Antler and Sevier orogenies probably account for the abrupt transition.

Monitor-Uinta Arch

Plate 3, an isopach map of the Great basin Devonian rocks, shows an east-west trend where the Devonian rocks are thinner with respect to correlative rocks north and

south. This east-west trend was a tectonic ridge or arch. Unconformities truncate some Devonian sequences on the arch. It coincides with the Precambrian Uinta aulacogen and may be genetically related to it. Some 25,000 feet of Precambrian shales and sandstones accumulated in the east-west trending Uinta aulacogen, north-central Utah (Hintze, 1988). An aulacogen is a tectonic trough, bounded by radially oriented convergent faults, that is open outward (Bates and Jackson, 1987). In other words, the two successful arms of a triradial fault system become the rift edge. Two arms of each of several such triple-rift systems will eventually link to form a single accreting plate boundary, along which an ocean will open (Sengör, 1987). The third, or failed arm, forms a tectonic trough into the continent from the ocean, 120° from the other two arms. The Uinta aulacogen may represent a failed arm of early crustal rifting. Rifting likely started at 600 Ma (Poole et al., 1992). The successful arms of the rifting separate the thick Paleozoic accumulations to the west from thin accumulations to the east. This thick and thin transition zone from southwestern Wyoming through southwestern Utah is called the Utah hingeline.

The aulacogenic behavior of the Uinta failed arm ceased before Cambrian time. However, a positive east-northeast trending arch coincides with the aulacogen during much or the lower Paleozoic, including the Devonian. Carpenter et al. (1994) recognized the positive area near the western edge of the pre-Antler continent and named it the Monitor arch. Isopach patterns in **Plate 3** suggest that the Monitor arch is an extension of the Uinta arch. Therefore, it is named the Monitor-Uinta arch herein. If this arch represents the uplifted aulacogen or failed arm, then the rift edge or successful arms in the Precambrian crust are likely reflected by the 0.706 Strontium isotope line. Nd isotope data provide the first evidence that the Monitor-Uinta arch was present in the region in the latest Proterozoic (Farmer and Ball, 1997). Pb, Sr, and Nd isotope data were used to distinguish mantle isotope signatures of Pacific Ocean mid-oceanic ridge basalts (MORB) from Indian Ocean MORB basalts in southeastern Australia (Zhang et al., 1999). Nd isotope data were used in western North America to identify the source areas of

siliciclastic detritus (Farmer and Ball, 1997). Mafic crust has higher Sm/Nd ratios and higher ϵ_{Nd} values than intermediate to felsic composition crust within each province.

The Uinta/Monitor aulacogen became a topographic low in Carboniferous time into which more than 4000 feet of Mississippian limestones and valley fill siliciclastics were deposited (Chamberlain, 1981, 1988c). More than 26,000 feet of Pennsylvanian and Permian rocks were deposited in the Oquirrh basin that developed about the aulacogen (proprietary measured section by the author, Wallsburg Ridge, Wasatch Mountains, Utah). However, Geslin et al. (1999) disputed the unusually thick section by attributing it to repetition of beds due to thrust imbricates. Erskine (1999) attributed the unusually thick section to normal sedimentary processes. I agree with Erskine. Gamma-ray patterns and patterns of decreasing Conodont Alteration Indices should be repeated if the section were tectonic thickened by thrust imbricates. I found no repetition of gamma-ray patterns and a consistent decrease in Conodont Alteration Indices (CAI) from the base to the top of the 26,000 foot section. Therefore, the Uinta-Monitor aulacogen changed from a positive arch in Devonian to a trough or graben structure in the Carboniferous. Similarly, the Peace River Arch, a northeast-southwest Precambrian crustal flexure in western Alberta, changed from a topographic high during the Devonian to a graben structure in the Carboniferous (Ross, 1991; Mossop and Shetson, 1994).

Longwell et al. (1965) provided strong evidence for several pulses of Cretaceous thrusting in the Spring Mountains, 120 miles south of the study area (**Figure 2**). They mapped the Keystone thrust fault that overrode the older Contact thrust fault. Matthews (1988) added detail that also suggested several pulses. An older sequence of Tertiary/Cretaceous strata provides information on thrust relationships in the southern Spring Mountains. The Keystone thrust sheet deformed (folded and faulted) rocks in Lavinia Wash and underlying older rocks of the Contact thrust sheet. The synorogenic Lavinia Wash rocks have a radiometric age of 120 Ma (Carr, 1980). Similarly, the Silver Canyon thrust deformed the Monte Mountain thrust (**Plate 1a** and **Plate 4**). See Stop #1, Appendix D, for digital images of the Keystone thrust fault in the Spring Mountains.

An isopach map of the Devonian clearly shows that the Monitor-Uinta arch has the same orientation and location of the Uinta aulacogen (**Plate 3**). Poole et al. (1992) named the eastern end of the arch, the Uinta uplift-Tooele arch. They suggested that it was a prong of the Transcontinental basement arch that extended from Colorado through northern Utah to eastern Nevada. The Monitor-Uinta arch affected deposition of Devonian quartz sandstones on the west and east edges of the Sunnyside basin (Chapter 7).

Other depositional troughs may have developed along the Proterozoic rift and may have influenced deposition of Devonian rocks in the region. South of the study area, in the Grand Canyon-Las Vegas area, more than 13,000 feet of middle and late Proterozoic rocks were deposited in a depositional trough that later became an “arch,” similar to the Monitor-Uinta arch (Poole et al., 1992).

Diamictite and volcanic rocks overlain by a thick (20,000 locally) terrigenous detrital late Proterozoic and Lower Cambrian rocks lie above the Proterozoic rocks (Poole et al., 1992). Carbonate rocks predominate the stratigraphic section between the Lower Cambrian terrigenous detrital rocks and the Middle Ordovician Eureka Quartzite (Cedar Strat proprietary measured sections; Poole et al., 1992). Barring Devonian sandstones and shales discussed in Chapter 4, the stratigraphic section between the Eureka Quartzite and the Mississippian Antler clastics is composed of carbonate rocks (**Table 1, Figure 8**). Carbonate deposition was probably related to a sea-level rise related to lithospheric cooling (Bond and Kominz, 1984).

Devonian-Mississippian Antler Orogeny

Recognizing the stratigraphic contrast between eastern carbonate facies and western siliceous facies, Kirk (1933) predicted the Roberts Mountains thrust. Merriam and Anderson (1942) first mapped the thrust fault in Nevada and employed the western

and eastern facies terminology. Kay (1952) was the first to suggest a mid-Paleozoic Age for the thrust. The Mississippian overlap deposits were documented by Dott (1955). Roberts et al. (1958), and Roberts (1972) first recognized siliceous marine rocks thrust eastward over Devonian and older shelf carbonate rocks along the leading edge of the Roberts Mountains thrust-and-fold belt in mountain ranges northwest of Eureka. Subsequent work provided evidence that the Roberts Mountain thrust movement occurred in Late Devonian to Lower Mississippian (Ketner, 1970, 1977; Smith and Ketner, 1968, 1975). Devonian and older rocks were moved 125 miles eastward in Nevada (Poole et al., 1992). In central Nevada, the Roberts Mountain allochthon consists of locally metamorphosed Middle Cambrian to Upper Devonian quartzo-feldspathic and orthoquartzite turbidites, chert and argillite, limestone, mafic volcanic rocks, and locally lowermost Mississippian strata (Johnson and Pendergast, 1981). Shelf strata are exposed in allochthon windows (Poole et al., 1992; Carpenter et al., 1994). Smith et al. (1993) concluded that the contractional orogeny resulting in the emplacement of deep basinal, submarine-fan, and mafic volcanic strata over autochthonous continental margin strata extended along the entire Cordillera from Nevada to the Yukon. Stewart and Poole (1974) described a persistent positive belt that coincides with the western side of the Sunnyside basin (Chapter 7). They suggested that this positive belt may account for local erosional truncation of lower Paleozoic strata. Carpenter et al. (1994) provided additional evidence of erosional truncation of lower Paleozoic rocks below the Roberts Mountains allochthon and suggested that the positive trend was a forebulge related to the Antler orogeny. They provided evidence that the Antler orogeny in Nevada was initiated as a forebulge in the Frasnian and that the orogeny continued into the Meramecian. It is likely the same as the Lower Silurian through middle Lower Devonian Toiyabe ridge of Matti and McKee (1977). This study provides evidence that the Antler forebulge was likely initiated in late Lower Devonian. It was probably the source area for Devonian sandstones on the western edge of the Sunnyside basin (Chapter 7).

Mesozoic Sevier Orogeny

King (1870) first noted compressive folds in the mountain ranges of the region, and Spurr (1903) first recognized thrusting in the Great Basin. Misch (1960) added detail to descriptions of thrust faults and folds in central northeast Nevada. Armstrong (1968) was the first to distinguish between Laramide and Sevier structures in western North America, and to synthesize faults and folds in the eastern Great Basin.

Sevier Fold-and-Thrust Belt Multiple working hypotheses (Chamberlin, 1897) exist regarding the structural interpretation of the Great Basin. One widely accepted hypothesis is that the geomorphology of the Great Basin is a result of normal faulted horsts and grabens created during Cenozoic extension. It is believed by some (e.g., Hamblin, 1985), that the crust was arched upward and pulled apart in the region forming a complex rift system from northern Mexico to southern Idaho and Oregon. If range-bounding faults extend to lower levels of the brittle crust, then the grabens are true rift valleys (Quennell, 1987). However, Quennell (1987) suggested that if the faults flatten at depth, the resulting graben may not be a true rift valley. Carpenter and Carpenter (1994b), from their work in southern Nevada, suggested that listric normal faults reactivating earlier thrust faults may be responsible for the modern basin-range physiography and extension of the crust. They concluded that rooted low-angle normal faults or detachments do not exist in their study area in the Muddy and Mormon Mountain area, 50 miles southeast of the Timpahute Range 30' X 60' quadrangle. They used seismic and well data to support their interpretations. In contrast, Wernicke (1981) and Axen et al. (1990) suggested that low-angle normal fault systems composed of mantle penetrating detachments controlled crustal extension in the area. They ignored well and seismic data. Broad playas separating inselbergs containing Paleozoic rocks in

the area invite unsupported speculations in their study area in contrast to the nearly continuous exposures of Paleozoic rocks in the Timpahute Range 30' x 60' quadrangle that constrain interpretations.

The ranges in the region have also been called fault-block mountains. Some suggest that the Basin and Range Province is one of the most extensive fault-block mountain systems in the world (e.g., Skinner and Porter, 1989; Carpenter and Carpenter, 1994b). However, large parts of the Basin and Range Province have not been mapped in detail. The valleys and ranges may have been formed by another process.

Another hypothesis is that the geomorphology of part of the Great Basin may be partly caused by compression during the Mesozoic Sevier orogeny (Chamberlain and Chamberlain, 1990). The orogeny resulted in a north-south belt of east-vergent thrust faults and folds that embodies much of the western Utah and eastern Nevada Great Basin (**Figure 1**). The new geologic map of the Timpahute Range quadrangle reveals few major normal faults that may be related to Cenozoic extension. However, it reveals many newly mapped folds and thrusts related to the earlier Sevier compressional event (**Plate 1a**, Chapter 5, Appendix E).

Other researchers have linked the Sevier fold-and-thrust belt to this region. Hintze (1988), for example, saw it as a segment of the 3,000-mile-long mountain chain that extends from southern California to Alaska. The Sevier fold-and-thrust belt is also part of the Cordilleran fold belt of King (1969). Tschanz and Pampeyan (1970) assumed that the major thrust faults in Lincoln County were Laramide age. In contrast, Chamberlain and Chamberlain (1990) identified the faults and folds exposed in the greater Timpahute Range as part of the Sevier fold-and-thrust belt (**Figure 2**). Cenozoic units, including Tertiary volcanic ash deposits, thin and pinch out over the ranges (anticlines) and thicken in the valleys (synclines). Typically, the underlying Paleozoic rocks dip toward the valleys and away from the ranges.

In addition, Sevier compressional features have been recognized in a narrow band from southern Nevada, through southwest and central Utah, to northeast Utah and

southwest Wyoming (Armstrong, 1968). Late Cretaceous to Early Tertiary Sevier thrusting shortened basement and cover rocks by more than 60 miles in northeast Utah and southwest Wyoming (Decals and Mitra, 1995). Assuming the same degree of shortening for the rest of the Sevier belt between southwest Wyoming and central Nevada, at least 200 miles of shortening would have occurred (See Chapter 5). Elison (1991) concluded that the western North American Cordillera from southeastern British Columbia to northern Nevada experienced 180 miles of east-west crustal shortening. The distance between central Utah and central Nevada (200 miles) is several times greater than the part of the thrust belt exposed in southwest Wyoming (40 miles) and contains many significant thrust faults in that distance (**Figure 2**).

In contrast, Dilles and Gans (1995) concluded that the western margin of the Basin and Range has moved progressively 60 miles westward during the Late Cenozoic and created the Walker Lane belt on the west side of the Great Basin. However, my research shows very little evidence of Cenozoic extension in the greater Timpahute Range area of the Great Basin.

Some workers have tried to divide the Sevier fold-and-thrust belt into smaller thrust belts and mix Sevier structures with other orogenies (e.g., Taylor et al., 1993). As used by Cameron and Chamberlain (1987, 1988) and Hook et al. (1998), the Central Nevada thrust belt is part of the Sevier fold-and-thrust belt only (**Figure 2**).

Sevier Fold-and-Thrust Belt in Nevada The band of compressional features accepted by the USGS as part of the Sevier fold-and-thrust belt has widened to include part of Lincoln County, Nevada (Page, 1993; Swadley et al., 1994). I believe that some workers such as Stewart and Poole (1974) erroneously correlated the north-south trending Gass Peak thrust fault, 24 to 98 miles south of the study area, to the Wah Wah thrust fault, nearly 100 miles to the east in western Utah (e.g., their figure 2). Structural features in the Sheep and Pahrnagat ranges strongly suggest that the Gass Peak continues northward

into the Timpahute 30' X 60' quadrangle. Others (e.g., Elison, 1991) placed westernmost Utah and northeastern and east-central Nevada, including the study area, west of the hinterland-foreland basin boundary. In his figure 1, Elison (1991) shows the hinterland-foreland basin boundary as a north-northeastward trending line in western Utah west of which are areas of Mesozoic metamorphism and where he shows a lack of east vergent thrust fault traces. However, abundant Sevier orogenic compressional features including thrust fault traces and associated syntectonic sediments occur as far west as the Pancake Range in Nye County and the Roberts Mountains and the Sulphur Spring Range in Eureka and Elko Counties, Nevada (Cameron and Chamberlain, 1987, 1988; Scott and Chamberlain, 1988a, b; Chamberlain, 1990c, 1991; Chamberlain and Chamberlain, 1990; Chamberlain et al., 1992a, 1992b; Carpenter and Carpenter 1994a, 1994b). This recent recognition of Sevier age compressional structures in central Nevada has important implications for petroleum and precious metal exploration (Chapter 8).

Sevier Fold-and-Thrust Belt Analogue The Canadian Rockies provide a thrust belt model that can help interpret the complex structure of the study area. Roeder (1989) suggested evidence to assume that the Nevada part of the Sevier fold-and-thrust belt has “a Dahlstrom geometry” similar to the Canadian Rockies. Similarities between the Nevada and Canadian Rockies portion of the thrust belt include: 1) Imbricate thrust sheets: a series of thrust sheets detached at a common deep horizon and that imbricately overlie one another in both thrust belts; 2) Total Displacement: total displacement in the Canadian Rockies is measured in tens of miles and stratigraphic displacement in thousands of feet (Gretener, 1972). In Nevada, total displacement is measured in tens of miles and stratigraphic displacement in thousands of feet; 3) Sedimentary wedge: Gretener (1972) pointed out the rapid thickening of the sedimentary section from Calgary to the Rocky Mountain Trench. Likewise, Paleozoic rocks thicken from hundreds of feet in central Utah to tens of thousands of feet in central Nevada (Cedar Strat proprietary

measured sections); 4) Progression of thrusting: Gretener (1972) noted that thrusting progressing outward or from west to east is well documented in the southern Canadian Rockies. Younger thrust faults are both younger and deeper. Folded thrust faults in the study area also suggest west to east progression of thrust faults; 5) Undeformed rocks at the leading edge of a thrust belt: Rocks east of the Canadian Rockies foothills are essentially undeformed (Dahlstrom, 1969). Similarly, Paleozoic rocks east of the leading edge of the Sevier fold-and-thrust belt, or Utah hingeline, are essentially undeformed. Differences between the Canadian Rockies and Nevada thrust belts include: 1) Precambrian basement. The Precambrian basement extends unbroken beneath the Canadian Rockies foothills structures (Dahlstrom, 1969). The nature of the Precambrian basement in the study area is unknown. It could be broken by Cenozoic normal faults. Metamorphic core complexes may provide windows into the Precambrian basement; 2) Cenozoic extension: Extensive Cenozoic extension is not known in the Canadian Rockies. Although little evidence for Cenozoic extension is found in the study area, much of the Great Basin is believed to have experienced considerable Cenozoic extension (Wernicke et al., 1988). Cenozoic extension is discussed further below in this chapter.

Thrust Detachment The exact decollements in the Sevier fold-and-thrust belt are not yet known. However, a series of finite element models of contractional deformation show that orogen evolution is strongly influenced by crustal architecture during the first 240 to 320 miles of shortening. Harry et al. (1995) provided evidence that major decollements develop at midcrustal and lower crustal levels, partition strain into upper crustal, lower crustal, and mantle strain domains, and extend throughout the width of the orogen. The most intense shortening occurs in the shallow crust as deformation propagates continentward (Harry et al., 1995). A crystalline basement is caught up in thrust sheets south of the Clark Mountains but may not be involved in Sevier thrusts north of the Clark Mountains (Walker et al., 1995). None of the thrust traces observed by me in the study

area involve crystalline basement rocks (**Figure 2**).

What previous research has not discovered, however, is the depth to the crystalline basement along the axis of the eastern Great Basin. No outcrops of crystalline basement occur in the study area. The depth to a crystalline basement can only be inferred from potential field data (i.e., gravity and magnetics, Appendix E). It can also be interpolated from surface outcrops of younger stratified rocks. Moreover, the western thickening of Paleozoic strata further frustrates attempts to find the depth to the crystalline basement. The problem is not unique to Nevada. Gwinn (1964) reported that the depth to basement along the structural axis of the Appalachian Basin was also imprecisely known.

The results of the Hunt Oil Company USA # 1-30 well (NE SE Sec 30 T1N R66E), near Pioche, Nevada (25 miles northeast of the study area), could provide insight into depth to basement. R. Fink (1997, personal communication) reported that the well penetrated nearly 9000 feet of Precambrian Prospect Mountain Quartzite before cutting into Mississippian Antler clastics. The nearest Mississippian Antler clastic outcrops are 15 miles on strike to the north, north of Bristol Pass. The fault in the well is most likely a low angle thrust fault. Tschanz and Pampeyan (1970) mapped thrust faults near Bristol Pass, 12 miles on strike north of the test. However, without the benefit of data from the Hunt well, Page and Ekren (1995) attributed the structures to a pre-Oligocene extensional decollement of younger on older rocks.

Tectonic Model of Thin-Skinned Deformation Rodgers (1949) pointed out two schools of thought concerning the Appalachian fold-and-thrust belt. One school follows the so-called thick-skinned thrusting theory and maintains that all major faults extend down to, and are supported by, a crystalline basement. The other school, following the so-called thin-skinned thrusting theory, supports the view that major bedding-plane thrust faults decouple the sedimentary cover and move it across the crystalline basement.

A similar controversy occurs in the Sevier fold-and-thrust belt because of a lack of regional seismic lines. Lack of control also originally retarded interpretation of the Appalachian fold-and-thrust belt. No regional seismic lines are available that clearly establish thin-skinned style of deformation for the Sevier fold-and-thrust belt. Nevertheless, inferences from a few scattered outcrops and several bore holes provide evidence that a north-south thin-skinned thrust belt runs through central Nevada (**Figure 2**, Cameron and Chamberlain, 1987). Moreover, balanced regional structural cross sections based on this evidence provide some additional information (**Plate 4**).

Conclusive evidence of the economic potential of the thrust belt may have to wait for regional seismic lines and additional bore holes deep enough to penetrate buried thrusts. Picha (1996) showed many examples of thin-skinned thrust belts, one of which is the eastern edge of the Sevier fold-and-thrust belt in southwest Wyoming, which involves the Cretaceous Fossil Basin source rocks. Although he discussed their economic potential, he did not mention the part of the thrust belt that involves the Mississippian Antler basin source rocks in Nevada. Thin-skinned thrusting in the Timpahute Range quadrangle is similar to productive thrust belts in other parts of the world. Chapter 8 includes discussions of the economic application of this research.

Cenozoic Volcanism and Extension

Before Cenozoic extension, the topographic evolution of the boundary between the eastern Basin and Range and the Colorado Plateau implies a topographic high in the Basin and Range that permitted drainage onto the plateau (Mayer, 1986). The boundary or transition zone between the Basin and Range and Colorado Plateau coincides with the leading edge of the Sevier fold-and-thrust belt.

Constenius (1996) concluded that the Cordilleran fold-and-thrust belt collapsed and spread west during a Middle Eocene to Early Miocene (ca. 49-20 Ma) episode of

crustal extension. He suggested two periods of extension. The first resulted in half grabens and was concurrent with the formation of metamorphic core complexes and regional magmatism. For example, Horse Camp basin, 75 miles north-northwest of Hiko, developed during Miocene time above a west-dipping detachment fault (Horton and Schmitt, 1998). Best et al. (1993) suggested that this localized extensional faulting in the Great Basin probably occurred before the ignimbrite flare-up (31 to 22 Ma) and that regional extension was minimal during most of the flare-up (**Figure 7**). Cenozoic listric normal faults causing the half grabens probably exploited Mesozoic thrust faults in some basins in Nevada (Effimoff and Pinezich, 1986).

A second period of extension (ca. 17-0 Ma) resulted in the Basin and Range overprint of earlier events (Constenius, 1996). A result of the second period of extension, among others, (Late Miocene to Holocene) is the development of Railroad Valley basin and exhumation the adjacent Horse Camp basin (Horton and Schmitt, 1998). Timing of the event is not precise. Bohannon (1983) concluded that the precise time of initiation of Basin and Range deformation in the Muddy Mountain area, 100 miles south-southeast of the study area, is difficult to pinpoint. Based on Cenozoic units found in some valleys, he suggested that the basin and range deformation might have begun as early as about 13 Ma locally. Guth et al. (1988) suggested that extension structures in the Sheep Range, 50 miles south of the study area, were formed about 13 Ma.

Associated with the second extensional event is basaltic volcanism in the transition zone between the Basin and Range and Colorado Plateau. Nelson and Tingey (1997) concluded that basaltic volcanism in the transition zone resulted from east-west extension and that the maximum thinning or extension of the lithosphere occurs near the transition zone (**Figure 7**). Earthquake studies in the transition zone led Arabasz and Julander (1986) to conclude that background seismicity is controlled by variable mechanical behavior and internal structure of individual horizontal plates within seismogenic upper crust.

Although the topographic high or crustal thickening is likely caused by stacked

imbricate thrust sheets, Mayer (1986) favored asthenospheric diapirism as the basic mechanism for continental rifting or Basin and Range extension. Similarly, Liu and Shen (1998) proposed a model that links the late Cenozoic uplift of the Sierra Nevada to ductile flow within the lithosphere induced by asthenospheric upwelling under the Basin and Range province. However, Okaya and Thompson (1986) pointed out that inflow of dense mantle material beneath a crust thinned by extension required by isostatically rising crust would result in elevations below sea level. Therefore they argued for igneous additions to the deeper crust of material of crustal density or of anomalously low mantle density. Rey and Costa (1999) argued for buoyancy-driven extension under low elevation conditions. In contrast, Jones et al. (1999) considered the hypothesis of low elevations at the time of Cenozoic extension suspect.

Furlong and Londe (1986) suggested that the specific mechanism for continental extension or rifting appears to differ from that of oceanic spreading centers. They pointed out that both pure and simple shear models proposed for the Basin and Range extension fall short in matching the observed elevation profile. They also pointed out that a uniform stretching mechanism obscures the evidences of simple shear. Pure shear involves uniform stretching and simple shear occurs along discrete low-angle shear zones. These zones of extreme extension involve metamorphic core complexes and are usually exposed in younger uplifted blocks but are older than faults responsible for the present Basin and Range topography (Okaya and Thompson, 1986). MacCready et al. (1997) suggested that the Ruby Mountain metamorphic core complex, 180 miles north of the study area, formed when Eocene-Lower Oligocene granitic magmas invaded middle crust rocks and resulted in highly extended upper crust rocks. Most metamorphic core complexes emerged during Oligocene to Miocene time (~36-16 Ma) (Rehig, 1986).

Liu and Shen (1998) concluded that the Basin and Range tectonic province (Great Basin) is one of the most extended continental regimes in the world. Metamorphic core complexes suggest 100% extension in the Great Basin (Rehig, 1986). Wernicke et al. (1988) concluded that their correlation of Early Mesozoic thrust faults suggests 155 to

186 miles of Neogene crustal extension in southern Nevada.

Cenozoic rocks deposited during the extensional and volcanic events conceal most of the Paleozoic rocks of the study area and provide a record of post-Paleozoic deformation (**Figure 7**). Tertiary/Cretaceous rocks associated with the Sevier fold-and-thrust belt that lie between the Cenozoic volcanic rocks and Paleozoic rocks are discussed elsewhere. At least sixty Tertiary calderas are responsible for thousands of cubic kilometers of ash-flow deposits that draped the pre-Oligocene Great Basin landscape (Best et al., 1993). In the study area, ash flows filled paleotopographic depressions and valleys such as footwall synclines or in prevolcanic strike valleys associated with folding and thrusting. In the Timpahute Range quadrangle and in the surrounding area, Oligocene volcanic rocks overlie folded Paleozoic rocks of various ages. Bartley et al. (1988) showed also an angular unconformity between Tertiary volcanics and Paleozoic rocks in the north Pahroc Range, 20 miles northeast of the study area. The angular discordance between the Oligocene volcanic rocks and the Paleozoic rocks implies that the Paleozoic rocks were folded and eroded before emplacement of the Oligocene volcanic blanket.

Though the study area is cut by abundant minor (10 to 100's feet of displacement) normal faults, no evidence of major (1000's feet of displacement) normal faults or reactivated thrust faults associated with Cenozoic extension were found in the study area (Appendix E). Edwards and Russell (1999) suggested that northern Cordilleran volcanic province of British Columbia is geologically similar to other extensional, continental volcanic provinces such as the Basin and Range and the East African rift system. They noted that all three regions have high surface heat flow values, are dominated by mafic rock, and are chemically bimodal. However, as with the study area, the northern Cordilleran volcanic province lacks pervasive extensional faulting. The Tertiary volcanics in the study area were buried by valley fill deposits eroded from the surrounding mountains (**Figure 7**). The present-day landscape of the study area is essentially a series of north-south trending inselbergs surrounded by an extensive lowland

erosion surface. Continuous, extensive east-west exposures of Paleozoic rocks are rare.

Summary

Previous investigators laid the stratigraphic and structural groundwork of an understanding of Great Basin Paleozoic rocks. Devonian formations defined beyond the Timpahute region were correlated to rocks in the study area. The reconnaissance map of Tschanz and Pampeyan (1970) generally differentiated Paleozoic rocks from Cenozoic rocks and grossly differentiated some Paleozoic rocks. Their map also provided a general view of some structural elements of the region.

The greater Timpahute Range (**Figure 3**), composed of forty miles of nearly continuous east west Paleozoic exposures, provides constraints on structural interpretations of the region. TMS is located near the center of the greater Timpahute Range. Devonian rocks in the range were deposited in the Sunnyside basin, an intrashelf basin on the western North American passive margin (**Figure 6**). Correlating Devonian sequences defined in the TMS reference section with other sections throughout the Sunnyside basin greatly simplified the formational terminology (**Figure 6**). The new map of the Timpahute Range 30' X 60' quadrangle sheds light on deformation of the Devonian rocks caused by the Sevier orogeny and subsequent tectonic events (**Figure 7**).

Earlier attempts to reconstruct the Devonian paleogeography of the study area were misleading because Sevier shortening was not documented, and thus was not taken into account. Conversely, attempts to map the structural features of the study area were incomplete because the identification and order of stratigraphic sequences were not recognized and used to solve structural problems. Therefore, structural and paleogeographic interpretations of the area needed reevaluation. This study illustrates the utility of mapping sequences for solving structural problems. It also illustrates the importance of understanding the structural complexities of the region to reconstruct the

paleogeography. Methods to provide accurate data that constrain a new structural model and paleogeographic interpretations of the study area are the subject of Chapter 3.

CHAPTER 3

METHODS USED

Having stated the goals of this research and reviewed previous work, the methods to achieve the goals are discussed. Methods of data identification, data collection, and data analysis are discussed in this chapter.

Data Identification

Mapped patterns of Paleozoic rocks in the eastern Great basin show a north-south structural grain (Stewart and Carlson, 1978). Either Mesozoic east-vergent crustal shortening or Cenozoic east-west extension, or both, were responsible for the north-south structural grain. Because of its anomalous east-west outcrop pattern of Paleozoic rocks, the greater Timpahute Range allows testing various structural models that may be responsible for the physiography of the region. These structural models can be tested by comparing and contrasting the stratigraphy of correlative units on the east and west sides of north-south trending faults. Therefore, an accurate geologic map and detailed stratigraphic sections are required to make the test.

Reconnaissance mapping revealed extensive Devonian outcrops and uncharted structural elements in the study area (Chamberlain and Chamberlain, 1990; Appendix E).

The Devonian section was chosen because measured sections throughout the region suggested little change in facies over much of the eastern Great Basin. A well-exposed section of Devonian rocks mostly on the southern edge of the Mail Summit 7.5' quadrangle was measured to provide a reference section to which the other sections could be correlated and to identify mappable sequences in the region. Construction of this stratigraphic framework resulted in identification of 21 regional correlatable and mappable sequences reported by Chamberlain and Warne (1996). These sequences were used to map more than 150 7.5' quadrangles in the region, 32 of which make up the Timpahute Range quadrangle (**Figure 3, Plate 1a**). Quadrangles mapped beyond the study area provided the locations of many thrust faults shown in **Figure 2** and allowed for testing structural models beyond the study area.

Mappable Sequences

Using bounding surfaces and associated facies such as Lowstand Surfaces of Erosion (LSEs) and Transgressive Surfaces of Erosion (TSEs), lithofacies, biofacies, inferred depositional processes, and gamma-ray response, I divided the Devonian section into 21 mappable rock sequences (**Figure 13**). Sequence criteria presented in Chapter 4 are useful in mapping complex structures in the region. After I mapped the sequences at larger scales (i.e., 1:12,000), I combined them into formations to produce the smaller scale map **Plate 1a**. **Plate 6** is an example of mapped sequences at TMS.

Sequence criteria presented in Chapter 4 were also useful in correlating sequences to other Great Basin surface and subsurface sections throughout the intrashelf basin and inner shelf. These correlations were used to make isopach maps of each sequence. Most of the sequences are composed of bundles of thinner (10's feet) cycles. Goldhammer et al. (1993) and Elrick (1995) used cycle stacking patterns to help define sequences. The use of cycle stacking patterns still holds promise as a tool for stratigraphic application.

However, gamma-ray responses of surface sequences may provide a more effective and practical means of correlation and chronostratigraphic analysis, especially when using subsurface information in the data set. Subsurface logging techniques have proven their worth because they have wide application in reconstructing major marine environments (Asquith, 1970).

Measured Sections

Helicopters were used to reconnoiter the region and choose possible stratigraphic sections to measure. Once a section was chosen, a traverse of the least structurally disrupted and best exposed section was chosen. This was done by creating a 1:24,000 scale reconnaissance geologic map of each 7.5-minute quadrangle, including the southwest Mail Summit 7.5' quadrangle (**Figure 4** and **Plate 1a**). Dirtbikes, motorcycles designed for cross-country, off-road use, greatly eased desert mapping by allowing quick, easy access to remote outcrops and terrain not accessible to four-wheel drive vehicles without disturbing environmentally sensitive terrains. Mounted with a clinometer adjusted for structural dip, a five-foot Jacob's Staff was used to measure section thicknesses. The outcrop profile, description, and gamma-ray measurements at 2.5-foot intervals were recorded on audio tape.

The outcrop profile is divided into four categories. These are: 1) covered slope (CS) where only scree shows the composition of the buried rocks; 2) partly covered slope (PCS) where some bedrock protrudes between covered areas; 3) ledges (LDG) where rocks are well exposed but can be easily negotiated; and 4) cliffs (CLF) where prominent outcrops can be climbed over with some difficulty and where near vertical rocks faces are prominent. The profile is portrayed graphically as a histogram (profile of the lithologic column) on **Plates 2a, 2b, and 2c**.

Outcrop descriptions included cycle boundaries, internal lithologies, colors,

textures, fossils, sedimentary structures, bedding, lateral and vertical changes and other significant information. A numerical value representing facies environment was assigned to each facies change while in the field. These data were used to construct a relative water-depth (relative sea-level) curve. Criteria used to make facies assignments are summarized in **Table 3** and illustrated in **Plate 5**. Approximately 500 thin sections of samples from the lower Guilmette sequences at TMS were used to confirm and adjust facies assignments made in the field. Selected photomicrographs of the thin sections are presented in Appendix C. Appendix B presents a detailed description of the cycles and sequences. **Plate 2a** presents these cycles and sequences graphically in a stratigraphic column.

Table 3 Criteria used to make facies assignments in the measured sections of the study area and beyond. The most characteristic properties are in bold type.		
Facies # (Plate 2a)	Interpreted Facies	Diagnostic Features/Depth Indicators
1	Supratidal	Usually dolomicrite , forms recessive slopes, very light-gray to yellow-gray , microcrystalline to very finely crystalline, stromatolitic, ripple, wavy or parallel laminations , mud-chip breccia, rip-up clasts, windblown (well sorted, frosted grains) silt and sand grains , paleokarst, solution breccias , vugs, paleosols, terra rosa, desiccation cracks , bird's-eyes, tepee structures ; laminated dolomicrites commonly cap shallowing-upward cycles and exhibits a higher gamma-ray log signature than adjacent more seaward strata. The most diagnostic features are the light color, laminations, dolomicrite, desiccation or karst features, scattered quartz silt and sand grains and a high gamma-ray log signature.

Table 3 Criteria used to make facies assignments in the measured sections of the study area and beyond. The most characteristic properties are in bold type.		
Facies # (Plate 2a)	Interpreted Facies	Diagnostic Features/Depth Indicators
1.5	Low supratidal	Usually dolomicrite , forms resistive slopes, darker (medium- to light-gray) than 1 but lighter than 2, thin bedded to weakly-laminated , ostracode grainstone, transitional between supratidal and intertidal strata. Forms the cap on shallowing-upward cycles where erosion has cut out high supratidal strata. Exhibits a higher gamma-ray log signature than intertidal rocks below but lower than supratidal rocks above. The most diagnostic features are weak laminations, light-gray color, and dolomicrite.
2	Intertidal	Commonly dolomicrite or dolomitic lime mudstone, characteristically partly covered intervals, mottled light- to very light-gray to medium dark-gray, microcrystalline or very finely crystalline to sucrosic, parallel-ripple or low-angle cross-laminations, low angle cross-bedding, channel and tidal flat quartz sandstone, shelly intraclast lags, rip-up clasts , vugs, sparse chert. Commonly lies between restricted-shelf and supratidal strata in a shallowing-upward cycle. May form base of a shallowing-upward cycle. Gamma-ray log signature is higher than low intertidal strata below but lower than supratidal strata above. Intraclast lags and mottles are the determining features.

Table 3 Criteria used to make facies assignments in the measured sections of the study area and beyond. The most characteristic properties are in bold type.		
Facies # (Plate 2a)	Interpreted Facies	Diagnostic Features/Depth Indicators
2.5	Low intertidal	Commonly dolomicrite or dolomitic lime mudstone, forms low ledges, dark gray to medium-light gray, brown-gray to medium gray, intraclast mudstone-wackestone, medium bedded, commonly mottled/burrowed . May form the base of shallowing-upward cycles but commonly occurs between restricted-shelf and subtidal strata. Gamma-ray log signature is lower than intertidal strata above but higher than restricted-shelf strata below. Relative cycle position and mottles/burrows are the determining factors.
3	Restricted subtidal- shelf	Limestone or dolomite, forms ledges, medium dark- to medium-light gray, <i>Amphipora</i> wackestone-packstone, low faunal diversity , some thin-shelled brachiopods, uncommonly gastropod-rich and rare stromatoporoids. Usually occurs between transgressive basal open-shelf and shallow intertidal strata. Gamma-ray signature may be lowest value in the cycle, but commonly underlying open-shelf strata exhibit slightly lower radiation. The presence of <i>Amphipora</i> and low faunal diversity provide the most diagnostic criteria.

Table 3 Criteria used to make facies assignments in the measured sections of the study area and beyond. The most characteristic properties are in bold type.

Facies # (Plate 2a)	Interpreted Facies	Diagnostic Features/Depth Indicators
3.5	Partially restricted subtidal-shelf	Limestone or dolomitic limestone, forms prominent ledges, medium light- to dark-gray or light brown-gray, small rounded stromatoporoids and <i>Amphipora</i> packstone-wackestone, burrowed/mottled mudstone, massive to medium bedded, dolomite/limestone, crinoids, rugose corals, grainstones, storm lags. Commonly forms the basal part of shallowing-upward cycles and emits less gamma radiation than adjacent strata. Small rounded stromatoporoids are the most significant criteria.
4	Open-shelf	Limestone (rarely dolomite), forms prominent ledges or cliffs, dark-medium gray, crinoid , coral (rugose or colonial) brachiopod, bryozoan, gastropod mudstone-wackestone-packstone, with bulbous-tabular stromatoporoids , rich faunal diversity , abundant fossil fragments. Commonly forms transgressive strata over the base of shallowing-upward cycles and usually exhibits a sharp decrease in gamma radiation. Crinoids, massive to tabular stromatoporoids and rich faunal diversity in limestone form the most important criteria.

<p>Table 3 Criteria used to make facies assignments in the measured sections of the study area and beyond. The most characteristic properties are in bold type.</p>		
Facies # (Plate 2a)	Interpreted Facies	Diagnostic Features/Depth Indicators
4.5	Deep open-shelf	<p>Limestone, with rare early-formed dolomite, forms thin ledges, medium dark gray, nodular lime mudstone, with uncommon crinoid or brachiopod fragments, burrowed, with chert stringers, massive to thick bedded. Rarely forms the lower part of shallowing-upward cycles. Hummocky crossbedding at the base of some cycles. Gamma-ray log pattern is similar to open-shelf carbonates. Crinoids and brachiopods, darker gray limestone than open-shelf strata, and chert stringers provide diagnostic criteria.</p>
5	Shelf edge	<p>Limestone, forms thin ledges or partly covered slopes, medium gray-black, lime mudstone, very thin- to thin-bedded, laminated, chert nodules and lenses, rare fossils, abundant load casts/soft sediment deformation. Rarely forms the base of shallowing-upward cycles. Gamma-ray radiation is higher than with open-shelf strata. This and the next three facies occur almost exclusively in the Guilmette Formation above Sequence Dgb at Tempiute Mountain. The black color and chert are diagnostic features.</p>

Table 3 Criteria used to make facies assignments in the measured sections of the study area and beyond. The most characteristic properties are in bold type.		
Facies # (Plate 2a)	Interpreted Facies	Diagnostic Features/Depth Indicators
5.5	Upper slope	Limestone, forms partly covered slopes, dark gray, no fossils , contains bedded chert . Gamma-ray log signature is relatively high but lower than the more shallow strata above. Rarely preserved between more basinward shelf slope strata and shoreward shelf-edge strata of 5. These and the two positions following are unique to the Tempiute Mountain section. Dark-gray limestone with bedded chert and lack of fossils are diagnostic features.
6	Slope	Limestone, forms covered slope with sparse prominent ledges, lime mudstone, rhythmic thin-bedded limestone with pale-red siltstone partings , isoclinally convoluted soft sediment deformation , sparse deepwater trace fossils. Gamma radiation is relatively low and is similar to the gamma-ray signature over open-shelf strata at the base of shallowing-upward cycles. Diagnostic features include, rhythmically, thin-bedded limestone and convolute, soft-sediment deformation.
7	Base of slope	Sandstone, forms thin ledges and partly covered slopes, light- to dark-gray, fine- to coarse-grained, lithic graywacke , deepwater sandstone (turbidites) and siltstone, interbedded thin-bedded unfossiliferous silty limestone, deepwater trace fossils. Occurs rarely in the Tempiute Mountain section above Sequence Dgb2 Guilmette Formation. A gamma-ray log signature is usually lower than overlying shelf-slope strata. Lithic graywacke is the most characteristic feature.

Lithologies were determined visually in the field using hydrochloric acid to detect the presence of calcium carbonate and a hand lens to detect the presence of quartz grains and other inclusions. Color was determined by comparing rock chips with the GSA rock-color chart (Goddard et al., 1984). Texture was assigned in the field using Dunham's (1962) classification and in thin section using Folk's (1962) classification. Where possible, the standard grain size scale for inclusions was used. I used the same criteria for crystal size where primary texture was obliterated by recrystallization.

Stratigraphic Terminology

In this report, I apply the most widely accepted sequence stratigraphic terms to describe and interpret the Devonian strata in Nevada (see Baum and Vail, 1988; Weimer, 1992). A sea-level Lowstand Surface of Erosion (LSE) is an unconformity or a significant hiatus formed during a relative lowstand of sea level that forms a sequence boundary of any scale. In carbonate rocks, LSEs are signaled by zones of karst, paleosols, or erosion. A Transgressive Surface of Erosion (TSE) is a hiatus within or at the base of every sequence. It is formed by intertidal to submarine erosion of the seabed during episodes of a sea-level rise and landward shifts of the shoreline. It commonly represents minor erosion, transgresses time surfaces, and may be a sharp surface or rendered vague by bioturbation. A Maximum Flooding Surface (MFS) is formed during sea-level transgression and highstand. It represents a surface or interval of deepest marine conditions with sediment starvation over much of the shelf. A Condensed Section (CS) represents beds accumulated during a sea-level highstand above the MFS where the rate of deposition is low over a wide area. It commonly consists of pelagic shale or lime mudstone. It may be lacking benthic fossils, have a depauperate benthic fauna, or contain "deep water" ichnofacies assemblages, hardgrounds, lags that shifted about during

periods of zero net deposition. It should have an enhanced nautiloid, conodont, and acritarch fauna (E. Brown, 1998, personal communication).

The base of a unique sequence (Guilmette Sequence Dgb2, Chapter 4) related to a Devonian cosmolite impact does not fit LSE or TSE criteria for erosional sequence boundaries. High-pressure phenomena associated with the impact created a carbonate breccia fluidized zone between strata. Because the fluidized zone was created by processes more closely related to impact tectonic processes than erosional processes associated with changes in relative sea level, a new sequence boundary term is applied herein. A Disrupted Surface of Erosion or DSE connotes impact tectonic disruption of already deposited beds in contrast to TSE and LSE that connote erosion and deposition associated with sea-level changes. A DSE occurs as a thin (one inch to several feet thick) zone of Dgb2 at the base of Dga2 at TMS. Possible tectonic processes forming a DSE could include shearing between beds, shock pressure that liquefies the carbonate, or carbonate breccia liquefaction between beds under extreme high pressure and short duration conditions (see Appendix C for examples of liquified carbonate rocks in thin sections from the base of Guilmette Sequence Dgb2).

Data Collection

Data were collected using a variety of modern techniques, equipment, and software all designed to increase accuracy and efficiency. This section briefly reviews the technology used to measure the Devonian sequences and map the geology of the study area.

Global Positioning Systems (GPS)

A Pathfinder Pro global positioning system was used to assure accuracy in locating field stations to make geologic maps. Pathfinder Pro is a trademark of Trimble Navigation, Limited. The global positioning system affords precise locations (within a meter). It allows field attributes such as attitudes (dip and strike) of the strata, lithology, stratigraphic sequence, inclusions, and other descriptions to be recorded onto a hand-held computer in the field at each station. These field attributes are recorded along with location coordinates found by recording at least 25 satellite signals with a roving Pathfinder Pro receiver. These data are stored in a tabular form that could easily be used for additional analysis. Satellite positions were simultaneously recorded using a Trimble Navigation 4600LS Surveyor receiver at a precisely located base station in Hiko. Post-field processing and differentiation using the satellite signals from the base station and roving unit provided accurate sub-meter positions of field stations. The digital data were downloaded directly onto digitized 7.5-minute quadrangles formatted with *MapInfo*, a type of Geographic Information System (GIS) software. *MapInfo* is a trademark of MapInfo Corporation.

Accurate positioning provides a great advantage for field methodology because it reduces controversy over fault angles, location of formation contacts, and sample locations. It also provides for repeatability of results: Future investigators can use Global Positioning Systems to navigate to precisely the same location where geologic observations were made or where samples were taken. Furthermore, a Global Positioning System eliminates errors in transposing data from field notes to the final geologic map. As a result, interpretation controversies concerning some fault attributes can be eliminated and field data can rapidly and accurately be added to the geologic map. Approximately three times more area can be precisely mapped in the same amount of time than using less precise, cumbersome, and outmoded methods of the past such as mapping on aerial photographs without GPS support.

Aerial Photographs and Field Work Maps

Besides using GPS methods, geology of the Timpahute 30' X 60' quadrangle was mapped on 1:24,000-scale, color aerial photographs taken by Intrasearch Incorporated and on field work maps. Photograph stereo pairs were used to plan traverses, pick outcrops for study, and identify critical relationships to investigate. Mapping in the field was done directly on 1:24,000, or where needed, 1:12,000 or 1:6,000 work maps generated from digitized United States Geological Survey topographic quadrangles overprinted with digitized published geologic maps (e.g., Hess and Johnson, 1997). Colored field work maps were plotted using a Hewlett-Packard DesignJet 7500C plotter. Much of the detailed, 1:24,000 topographic data have become available only in the mid 1980's. Though much of the Timpahute Range quadrangle was mapped on large scale (1:12,000 or 1:6000) work maps using the 1:24,000 topographic base maps, only the smaller scale (1:75,000) compilation using the 1:100,000 topographic base map is necessary for the scope of this study.

Field notes made on the field work maps were compared with the images on color aerial photographs and then compiled onto a master map using *MapInfo*. Contacts, faults and other features were drawn directly onto the photographs with erasable ink. Predictions of trends were made on the photographs before going back to the field. The trends were confirmed or corrected after being field checked. The color aerial photographs allowed me to distinguish subtle differences between formations and identify areas of hydrothermal alteration. Hydrothermally altered areas commonly are associated with major fault systems. I discovered several, mostly concealed, outcrops in the pediments by using the color photographs. Also, color imagery allows for easy identification of jeep trails, subtle changes in vegetation related to underlying bedrock, and other subtle features that are not clearly visible on black and white imagery.

Geographic Information System (GIS)

Field data were readily downloaded into *MapInfo* from the Geographic Positioning System for quick generation of accurate, colored geologic maps. Digitized topographic base maps were prepared by using a line trace program that converted scanned raster images of U.S. Geological Survey topographic quadrangles into vector maps. The vector maps were imported into *MapInfo* using the Universal Transverse Mercator NAD 27, Zone 11 for the United States coordinate system. The digitized geologic map of Lincoln County was prepared by the Nevada Bureau of Mines and Geology. The scale of the vector 1:250,000 geologic map was changed to fit over the vector 7.5' topographic maps. Geologic features including fault and formation contacts were manipulated with *MapInfo*. Precisely pinpointed and oriented dip symbols and labels were created at each station using a complementary program, *Vertical Mapper*. Each attribute such as faults, attitudes, geologic attributes, geographic attributes, hydrology, cultural attributes, elevation contours, and labels were placed in separate layers within the mapping program. By putting attributes in each layer, maps that emphasized different features or various combinations of them could be easily generated. Because any part of the maps could be enlarged to any scale, much of the mapping was done with greater precision than the normal 1:24,000, namely at 1:12,000 or 1:6,000. Generating ancillary larger-scale maps, such as 1:24,000 or larger, using geology from published maps or new data was advantageous.

The geologic map made for this study was made by using the vector U.S. Geological Survey Timpahute Range 30' X 60' 1:100,000-scale topographic map. The digital format allowed for quick changes and productions of maps at any scale. **Plates 1a** and **1b** are the same scale (1:75,000) and have the same color scheme to compare new and old geologic maps.

Gravity Data

Digital gravity data (Ponce, 1997) was contoured using *Surfer*, a contouring program. *Surfer* is a trademark of Golden Software, Inc. The digital contour map was reformatted for *MapInfo* and was used to create figures in Appendix E. Talisman Oil Company provided a much more refined digital contour map used to overlay the Timpahute 30' X 60' geologic quadrangle map during the interpretation phase of this study. However, because it cluttered the map, the gravity and magnetic map layers were turned off to produce **Plate 1a**.

Computer-aided Structural Cross Sections

Dahlstrom (1969) suggested that the first step to construct a balanced cross section is to establish a pair of reference lines at either end of the section in areas of no interbed slip. His example in the Alberta foothills extends eastward into the undeformed Alberta plains. However, the portion of the Sevier fold-and-thrust belt in the study area lies more than 100 miles west of the correlative undeformed rocks in central Utah. Much of the intervening area is covered. Therefore, a balanced cross section of the study area is not possible using the method and ground rules outlined by Dahlstrom (1969). Roeder (1989) noted that his cross sections of the Timpahute Range and northward are open thrust systems and cannot be balanced. Furthermore, Mukul and Mitra (1998) noted that the assumptions that deformation within an individual thrust sheet are limited to flexural slip for line balancing and plane strain for area balancing breaks down into internal sheets where beds are penetratively deformed as in the Sheeprock thrust sheet, central Utah. Therefore, they stated that balanced cross sections constructed across the entire fold-and-thrust belt and their restoration will not be completely accurate.

Dahlstrom (1969) suggested that other ground rules will apply to other structural provinces beyond the Canadian Rockies foothills. Fortunately, the distinctive Guilmette Dgb2 breccia provides such a marker that allows for more accurate construction of balanced cross sections and restorations of the greater Timpahute Range (see Chapter 7). **Plate 4a**, constrained by the geologic map and distribution of the Guilmette Dgb2 breccia, exhibits a balanced cross section of the Timpahute Range that is probably more accurate than would otherwise be possible.

The new geologic map provides a spatial model of the structure and geology of the region. Verification of geometric balance of vertical models such as **Plate 4a** can be facilitated using computer programs such as *GeoSec*. *GeoSec* is a trademark of GeoScience Corporation. These programs take advantage of the vector topographic and geologic data and allow rapid construction of vertical profiles annotated with formation contacts, faults, and apparent dip directions of any desirable transect. These profiles are used to construct balanced structural cross sections and restorations. The software insures geometric precision and allows structural restoration in dimensions. Fermor (1999) suggested that in many areas of the Alberta Foothills structural restoration in only two dimensions is apparently invalid. However, the geologic models depend on both the operator's experience and the accuracy of the available data.

Plate 4a, a geometrically balanced structural cross section of the greater Timpahute Range, was constructed using the software program *Thrustbelt*. *Thrustbelt* is a trademark of International Tectonic Consultants, Limited. **Plate 4b** is the restored cross section. The program used a process of forward modeling.

First, thicknesses of stratigraphic units from sections along the line of transect were acquired. The line of transect is generally along A-A' on **Plate 1a**. Bends in the transect, minor faults and intrusives were ignored as they contribute little to the structural model. Thicknesses of units were compiled from Cedar Strat and Shell proprietary measured sections, published sections, and new measured sections for this study. Some thicknesses are noted on the geologic profile on the lower part of **Plate 1a**. The thrust

fault angle through different strata was assumed. For dense carbonates, the angle was assumed to be greater (25°-30°) and for less competent shaly intervals it was assumed to be much less (5°-10°).

Second, based on the facies and thicknesses of the stratigraphic units, an undeformed stratigraphic cross section was assumed. The original positions of the stratigraphic sections within the cross section were partly determined from a previous structural cross section model by Chamberlain and Chamberlain (1990) using a snip-reconstruction or rigid body cut and paste restoration. The cross section was modeled after other cross sections in the Great Basin by Roeder (1989).

Third, the cross section was created through successive iterations until it matched the geologic map (surface geology, topography, well tops, etc.). Although the geologic interpretation may be flawed, the section is geometrically balanced and is a possible solution. The computer program helps to quickly eliminate impossible or geometrically unbalanced cross sections.

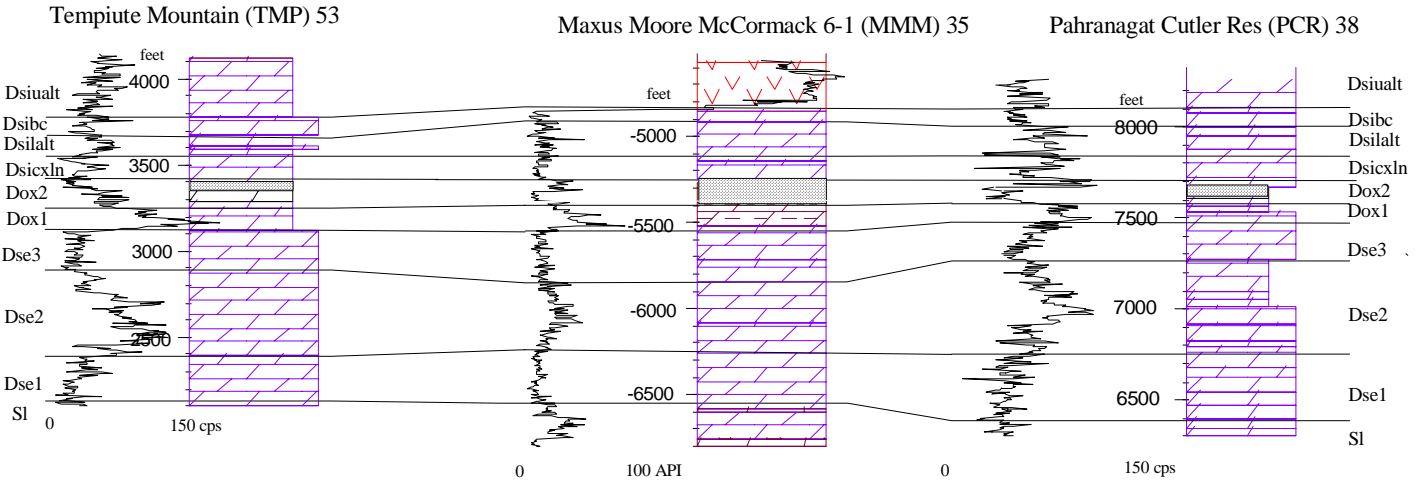
A more rigorous modeling program, *GeoSec* mentioned above, could be used to restore stratigraphic sections to their undeformed position. *Thrustbelt* used in this study employs only the vertical slip kinematic algorithm. In contrast, *GeoSec* uses many algorithms such as the fault propagation model, fault bend model, etc. that takes into an account flexural slip. However, such a rigorous analysis is beyond the scope of this study.

Surface Gamma-Ray Logs

Surface gamma-ray logs were employed in this study to aid the correlation of stratigraphic sequences between structural sheets and subsurface sections (**Figure 12**). They provide much more resolution in local regions than correlations based on conodont zones. However, conodont zones provide worldwide correlations and show time gaps

between sequences where zones are missing. Furthermore, conodonts can be used as independent depth (paleoenvironment) indicators and thermal alteration indicators (Conodont Alteration Indices). Nevertheless, gamma-ray patterns of sequences can provide more correlation resolution in the Sunnyside basin. For example, most of the Guilmette is represented by the *diparilis*, *falsiovlais*, *transitans*, *punctata*, *hassi*, and *jamieae*, conodont zones (**Figure 10**). Surface gamma-ray patterns of ten major regional correlatable Guilmette sequences and more than twenty subsequences greatly refine correlations in the Sunnyside basin. Most sequences were broken down into regionally correlatable subsequences. Each sequence and subsequence is marked by a unique gamma-ray pattern that can be correlated to sections within the eastern Great Basin. The major advantage of using sequences over conodont zones in correlations is that they can be identified on outcrops and in well logs. Furthermore, well cuttings may be too fine or not plentiful enough to yield diagnostic conodont faunas. Also, extracting conodonts from dolomitized intervals is difficult. However, gamma-ray logs are easy to obtain from wells and outcrops. Gamma-ray sequence correlation methods were perfected during the study. A future study could focus on correlations of conodont zones with sequences (Chapter 9).

Figure 12 A correlation chart of surface to subsurface Middle and Lower Devonian sequences from Tempiute Mountain southeastward (see **Figure 9** for section locations) illustrates the utility of using gamma-ray logs.



Surface gamma-ray logs provide a powerful correlation tool in frontier areas especially where surface and subsurface (wells) sections need to be correlated (Chamberlain, 1983). They provide physical measurements that tie exposures of stratigraphic sequences to seismic reflectors for use in seismic stratigraphy. **Figure 12** provides an example of surface and subsurface correlations in the Timpahute Range region (**Figure 9**). Sequences tied with gamma-ray logs can be tied to sonic and neutron density logs, which in turn are tied to seismic reflectors.

Correlations based on gamma-ray profiles can help where facies change between sections. For example, the gamma-ray spikes at the base and the top of the “Oxyoke Formation” allow correlation between sections, despite lateral changes in lithology. These gamma-ray spikes may be due to periods of greater amounts of radioactive dust falling from the atmosphere. These dusty periods likely occurred during periods of drought and high winds and could be possibly related to distant volcanic activity. Gamma-ray spikes most commonly occur at the top of cycles that contain evidence of subaerial exposure. Admittedly the correlatable gamma-ray spikes are subtle. Nevertheless, they can provide reliable markers for correlations. Examples of additional correlation charts using gamma-ray logs are presented in the summary of Chapter 4 and in Chapter 7.

Gamma-Ray Logs vs. Fischer Plots A Fischer plot is a graph in which cumulative cycle thickness of peritidal carbonates is corrected for linear subsidence and plotted versus time using an average cycle period (Read and Goldhammer, 1988). Whether Fischer Plots are useful guides to sea-level history and correlation between sections is controversial. Sadler et al. (1993) defended the usefulness of Fischer plots to track the cumulative departure from mean cycle thickness through a vertical sequence of continuous shallowing-upward units. However, Drummond and Wilkinson (1993) argued for the lack of a direct correlation between multiple-frequency eustatic sea-level

variations and meter-scale cycle stacking hierarchies. The assumption that each individual cycle represents a single sea-level rise explicit in using Fischer Plots as guides to sea-level history may be flawed. Multiple autocyclic shallowing-upward cycles may originate during any single rise in sea level. Elrick (1995) concluded that Fischer plots are of limited use as a correlation tool for Devonian Great Basin carbonates. Thus, the gamma-ray curve provides an alternative, and practical, means for overcoming limitations of using Fischer plots and other stacking techniques for correlations. The value of gamma-ray profile correlations has been repeatedly proven by oil industry geologists.

Gamma-Ray Field Data Acquisition Consistent gamma-ray measurements were made by holding a scintillation counter waist high and recording the average counts per second from the digital display (Chamberlain, 1983). The count rate is set at one second intervals. I found that taking measurements at a consistent interval simplifies construction of gamma-ray logs. For most of my work in the eastern Great Basin, a five-foot Jacob's Staff, mounted with a Brunton compass (clinometer), provided a convenient interval for measuring thicknesses of strata. The clinometer was set to correct for tectonic tilt of the strata and allowed measurement of the section in five-foot increments of true stratigraphic thickness.

Having two-man teams was helpful. One member of the team measured the interval, provided the tally of measured intervals and recorded the gamma-ray counts per second. The other described the strata in the five-foot interval. If the sections were reconnaissance sections, then the team could measure and record the data continuously as they moved up through the section. For detailed sections, as in this work, each five-foot interval is marked on the outcrop with biodegradable tree paint. The marked section allows for detailed description and study of the strata.

The Scintrex BGS-4, with its digital display, was the easiest to use, and it gave gamma-ray logs the best resolution. The Scintrex BGS-4 is a trademark of the Scintrex

Corporation. Fluctuating intensity of gamma radiation makes the Mount Sopris model with its analogue meter difficult to use. Mount Sopris is a trademark of Mount Sopris Corporation. The BGS-4 has a large enough iodide crystal to provide satisfactory resolution. For most work, only one measurement is needed. Others prefer to average three to five measurements (R.M. Slatt, 1997, personal communication). The reason for holding the scintillation counter waist high is to get an average measurement for the five-foot interval measured with a Jacob's Staff. The intensity of gamma radiation from the rocks is a mass effect. The closer the scintillation counter is held to the rocks, the higher the reading. This higher reading dampens the resolution of the gamma-ray log. Poor-quality logs result from inconsistencies in the distance the scintillation counter is held from the rocks. For shorter intervals, the scintillation counter is held closer to the outcrop. However, gamma-ray character can be sacrificed at the expense of an attempt to construct more accurate logs if the detector is held too close to the outcrop when measuring greater intervals of rock. Carefully collected, measurements can provide enough resolution to identify cycles in a gamma-ray log if the cycles are thicker than the interval measured.

I have found that calibrating the scintillation counters is not necessary if measurements are taken by the same instrument during a brief period. The reason for this is that only the relative changes in gamma-ray counts are necessary to create a correlatable gamma-ray profile. It would be necessary to calibrate the instruments if different segments of the measured interval were measured by different scintillation counters or if portions of the measured interval were measured between long periods.

A hand-held tape recorder simplified data collection in the field. By this method I could dictate a thorough description more quickly than by taking notes manually. If station number, a measured interval tally, gamma-ray measurement and lithologic descriptions are systematically dictated, the data can be transcribed onto spreadsheets for data manipulation and log construction.

Data Analysis

Most of the data were analyzed using a computer. Measured sections were put on a spread sheet to aid in efficient data manipulation and presentation. Mapping was compiled from GPS data using a GIS to make presentation maps. The following section provides more detail on how the stratigraphic data were analyzed.

Regional Correlations

Diagnostic features and water depth indicators listed in **Table 3** were used to help identify and group sets of shallowing-upward cycles into sequences in the regional correlations. I used significant features listed in **Table 4** (Chapter 4) to identify and differentiate sequences as I mapped. I found these sequences to be indispensable tools for mapping complex structures in the study area and beyond. The TMS reference section with its gamma-ray profile was also useful in correlating surface sections with other surface and subsurface sections at a higher level of detail and precision than otherwise possible (e.g., **Figure 12**). Also, by correlating sections in loops, miscorrelations could be detected and adjusted and significant sequence boundaries properly defined. Thus, the sequences of the Mail Summit reference section were refined. Examples of additional correlation charts are in the summary of Chapter 4 and in Chapter 7.

Predictable gamma-ray patterns were especially helpful in correlating the sections. At TMS and other sections in the Sunnyside basin, a genetic relationship between gamma-ray inflections and rocks associated with different depositional settings seems to occur. Wilson and Pilatzke (1987) suggested that gamma-ray inflections were caused by an increase of wind-blown, radioactive detrital grains that occur at the top of Devonian Duperow cycles in the Williston Basin. Altschuld and Kerr (1982) also noted increased radioactivity associated with supratidal dolomite and anhydrite at the top of shallowing-

upward cycles that cause high radioactive reading on logs. Similarly, the Mission Canyon Formation in North Dakota displays argillaceous and sandy dolomite marker beds, as noted by Harris et al. (1966). Swart (1988) showed that uranium concentrations in a core taken from Miocene and Pliocene rocks, island of San Salvador, Bahamas, are higher at dissolution surfaces than in adjacent strata. Chan (1999) suggested that a surface gamma-ray log of a paleosol in the Mahogany member of the Triassic Ankareh Formation, north-central Utah could correlate to subsurface well logs. She showed the sharp gamma-ray decrease from the Mahogany member to the Gartra Grit. She also illustrated a gamma-ray spike at a paleosol at the top of the Mahogany member. Similar gamma-ray spikes occur at sequence boundaries in the Great Basin Devonian rocks.

In contrast to higher gamma radiation over dolomite caps at the top of shallowing upward cycles, gamma radiation is typically much lower over carbonates interpreted to have been deposited in open-marine conditions. Because these patterns are so predictable, it is likely that the radioactive particles were deposited during the Devonian. Uranium and the associated thorium mineralization in Devonian rocks of the Sunnyside basin have not yet been detected.

Data Manipulation

Stratigraphic field data were transcribed onto a spreadsheet for further data manipulation and preparation for graphic output. Common spreadsheet programs such as *Excel* or *Lotus 1-2-3* provided a simple way to format the data. *Excel* is a trademark of Microsoft Corporation and *Lotus 1-2-3* is a trademark of Lotus Corporation. Once the data are in a spreadsheet, statistical values for different lithologic characteristics such as gamma-ray intensity, color, texture, weathering profile, lithologies, etc. can be easily calculated and presented in detailed descriptions and graphics of cycles, sequences and formations. Statistics, such as average gamma radiation, standard deviations, etc.

presented in detailed descriptions of the lower Guilmette Formation in Chapter 4, were calculated in this manner. Because all the Cedar Strat proprietary sections were prepared in this manner, it greatly helped correlations of Devonian sequences throughout the Sunnyside basin.

Text editor programs such as *Word Perfect* were used to format the data for the graphics program, *Logger*. *Word Perfect* is a trademark of Corel Corporation and *Logger* is a trademark of Rockware Corporation. *Logger* was used to make combined gamma-ray logs and lithologic logs. A paper printout of the measured section at a large scale (e.g., one inch to 10 feet) allowed detailed correlation of the gamma-ray log with the outcrop description. A final printout at smaller scales (e.g., one inch to 200 feet) compressed the gamma-ray log and emphasized subtle, but significant, changes. These helped to discriminate sequence boundaries (**Plate 2a**). The gamma-ray log is compressed much more (e.g., one inch to 2000 feet) and the lithology greatly generalized in **Figure 8**.

CHAPTER 4

DEVONIAN SEQUENCES

The first objective of this research was to give a more detailed account of the Devonian sequences found in the study area and identify regionally correlatable sequences to be used to map the Timpahute Range quadrangle. Topics in this chapter include Devonian sequences, their relationship to the geologic map, sequence boundaries, and mechanisms for cycle and sequence development. It contains descriptions of each Devonian sequence at TMS and how they correlate to other sections in the region. Diagenesis and the occurrence of dolomite in the section are briefly discussed at the end of the chapter.

Sequences

This section contains a brief discussion concerning the importance of recognizing Devonian sequences at TMS in constructing the geologic map and it provides examples of how sequences helped reveal overlooked geologic features. It also contains the framework for recognizing sequence boundaries at TMS and includes a review of some mechanisms for cycle and sequence development.

Devonian Sequences

Recognition of stratigraphic sequences was essential for constructing an accurate geologic map to constrain a reasonable structural interpretation of the complexly

deformed rocks in the Timpahute Range quadrangle. In this study, emphasis was placed on mapping Devonian sequences, which are widespread throughout the quadrangle. Obscured by the massive appearance of the thick (100's feet) formations in the Timpahute Range, many significant structural features were overlooked or misidentified. Division of the TMS Devonian formations into mappable sequences provided a way to enhance structural resolution. This higher resolution was necessary to map structural features overlooked in previous mapping using entire formations. Some formations were misidentified on previous maps.

Stratigraphic Sequences and the Geologic Map Using the stratigraphic order of Paleozoic sequences in mapping helped reveal important structural relationships. For example, few workers have recognized the overturned rocks in the Monte Mountain and Penoyer Springs footwall synclines (e.g., Taylor et al., 1993). Though Tschanz and Pampeyan (1970) showed the overturned fold on their map, Taylor et al. (1994) did not discuss the overturned Silver Canyon footwall syncline. It is understandable that the overturned rocks were overlooked because top and bottom indicators such as geopetal structures are rare. However, the order of shallowing-upward cycles in sequences reveals the up section sense of the beds and could be applied to geologic mapping.

Other subtle features were understandably overlooked. For instance, Taylor et al. (1993) published a geologic sketch map of the Penoyer Springs area that did not show the strike-slip displacement of the south Penoyer Springs and Tunnel Spring faults (see **Plate 1a**). In Appendix E, which contains discussions and illustrations of these faults, a map shows that the south Penoyer Springs fault offsets the Pilot Formation 1.3 miles and the Tunnel Springs fault offsets the Penoyer Springs thrust fault 1.4 miles. Armstrong and Bartley (1993) made conclusions about the lateral thrust termination in the southern Golden Gate Range without recognizing key units and faults at the thrust termination in Baseline Canyon discussed in Appendix E. They mismapped West Range Limestone and

Joana Limestone as Guilmette Formation at the Baseline Canyon fault that intersects their thrust fault termination. DuBray and Hurtubise (1994) reversed the thrust fault interpretation of the Fossil Peak thrust by Tschanz and Pampeyan (1970) without recognizing key beds involved in the faulting. It is shown in Appendix E that they mismapped Silurian Laketown Dolomite as Sevy Dolomite and that they did not map a thin exposure of Eureka Quartzite in fault contact with the Laketown Dolomite. Also, they overlooked the Fossil Peak footwall anticline highlighted by Devonian Sequences (Appendix E). Martin (1987) and Tschanz and Pampeyan (1970) did not recognize key stratigraphic and structural relationships and mistakenly changed the stratigraphic displacement at the north end of Freiburg Mountain from Ordovician on Devonian to Ordovician on Ordovician. Recognition of Devonian sequences in the footwall east of Worthington Peak improved the accuracy of the geologic map in this area. The revised map turns the fault eastward instead of westward and places Ordovician on Devonian rocks (Appendix E). Dunn (1979) interpreted the Guilmette Sequence Dgb2 breccia in the Mail Summit 7.5-minute quadrangle as local reef talus, but did not recognize the significance of its lateral continuity across many other ranges in the area (Warne et al., 1993; Warne and Kuehner, 1998). Therefore, detailed knowledge of the order, boundaries, and genesis of Paleozoic sequences is essential to making a geologic map that constrains structural and paleogeographic interpretations.

Sequences and Sequence Boundaries A sequence, as used in this paper, is a bundle of one or more conformable depositional cycles bounded by discrete bedding surfaces or boundaries that are widely traceable (Chamberlain and Warne, 1996). For practical purposes, the mappable sequences were grouped together into formations to produce **Plate 1a**. **Plate 6** is an example of a geologic map showing Devonian sequences at TMS. The sequences typically produce unique gamma-ray patterns that simplify regional correlations. Many preserved bedding surfaces or erosional surfaces represent significant

unconformities or their correlative conformities (Mitchum et al., 1977). Reid and Dorobek (1993), and many others, used this definition to study carbonate strata. They suggested that sequence-bounding unconformities show evidence of subaerial erosional truncation or subaerial exposure and represented significant depositional hiatuses. Many sequence bounding unconformities in TMS are karstified. Karstification can represent minor exposure with the removal of several inches of strata. It can also represent a significant drop in relative sea level resulting in karst cavities, extensive breccia, removal of tens to hundreds of feet of section, and freshwater phreatic diagenetic alteration 100 feet or more below the unconformity. Only the major karst intervals or dissolution surfaces (DIS) are illustrated in the TMS stratigraphic column (**Figure 13**).

Mechanisms for Cycle and Sequence Development The driving forces that create stratigraphic cycles and sequences, and particularly carbonate cycles and sequences, are not completely understood. Earlier work (e.g., Vail et al., 1977) attributed the mechanism for sequence generation to eustatic sea-level change. Others argued for tectonic or other forces (e.g., Wilkinsen et al., 1998). Many papers deal with the driving forces of cycles at all scales arguing all sides of the question. For example, Yoshida et al. (1996) found no independent evidence for eustasy controlling deposition of the siliciclastic Mesaverde Group of the Book Cliffs, Utah. However, the Mesaverde Group is one of one of the best-described and best-known instances of high-frequency successions in North America. New evidence from Yoshida et al. (1996) suggested that tectonism involving changes in intraplate stresses originating from thrust-belt compression may be the major mechanism for sequence generation in foreland basins. The researchers found no evidence of climatically induced changes in sediment supply for the Mesaverde Group. They saw no need to invoke eustasy as a mechanism to control sequences.

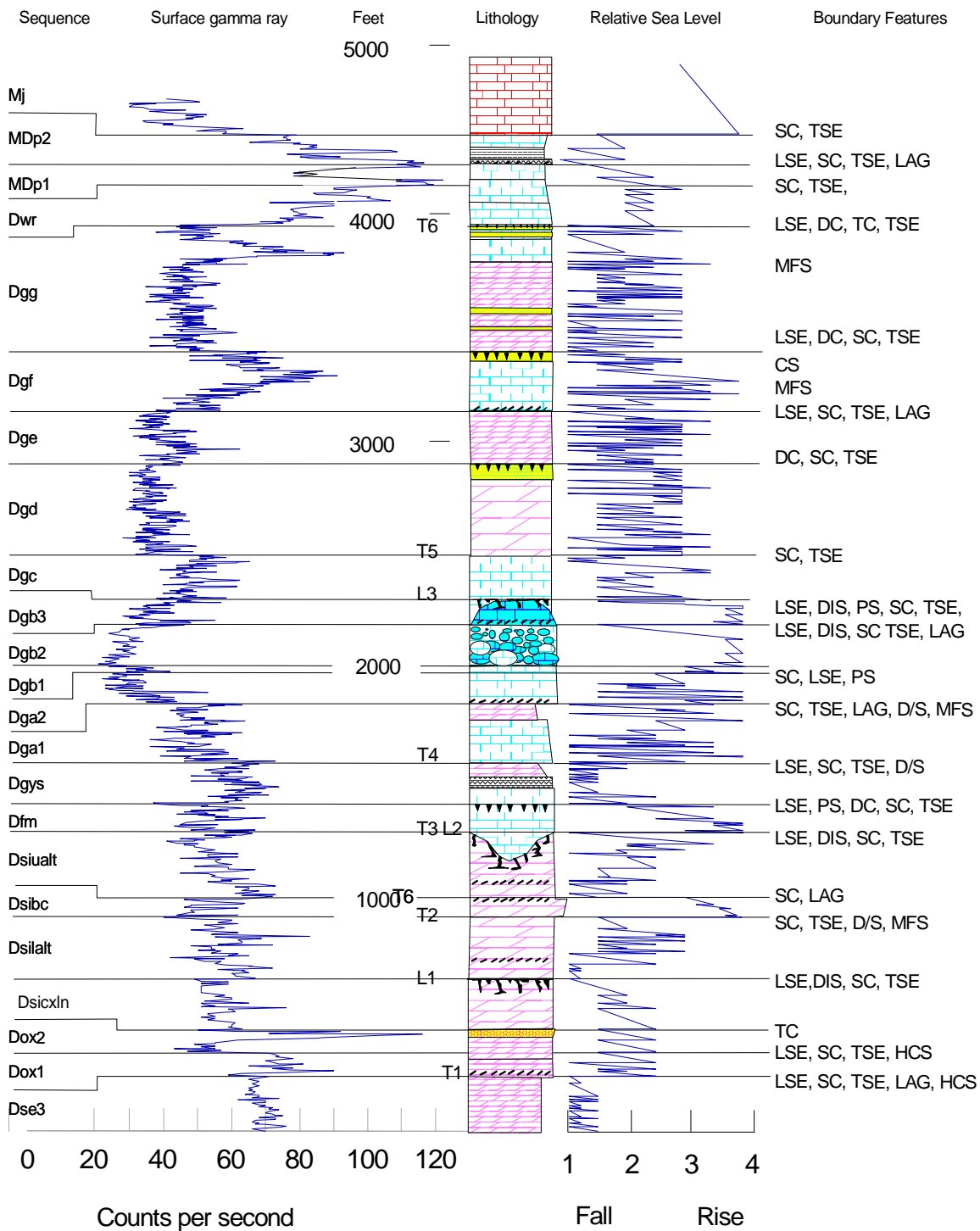


Figure 13 Composite stratigraphic column of southwest Mail Summit section, TMS, showing sequences, surface gamma-ray log, sea-level lowstand and transgressive events (L1 to L3, T1 to T3), stratigraphic column, relative sea-level curve, and sequence-boundary features (Chamberlain and Warme, 1996). See **Figure 14** for the legend.

LEGEND		BOUNDARY FEATURES	
Symbol	Sequence		
Mp	"Penoyer Limestone"	CS	Condensed Interval
Mj	Joana Limestone	HCS	Hummocky Cross-stratification
MDp2	Sequence 2, Pilot Formation	MFS	Maximum Flooding Surface
MDp1	Sequence 1, Pilot Formation	 LAG	Lag Deposit, Rip-up Clasts
Dwr	West Range Limestone	D/S	Deep over Shallow
Dgg	Sequence G, Guilmette Formation	TSE	Transgressive Surface of Erosion
Dgf	Sequence F, Guilmette Formation	SC	Sharp Contact
Dge	Sequence E, Guilmette Formation	TC	Transitional Contact
Dgd	Sequence D, Guilmette Formation	LSE	Low stand Surface of Erosion
Dgc	Sequence C, Guilmette Formation	 DIS	Dissolution Surface (Karst)
Dgb3	Sequence B3, Guilmette Formation (reef)	PS	Paleosol
Dgb2	Sequence B2, Guilmette Formation (breccia)	 DC	Desiccation Cracks
Dgb1	Sequence B1, Guilmette Formation		
Dga2	Sequence A2, Guilmette Formation		
Dga1	Sequence A1, Guilmette Formation		
Dgys	Yellow Slope Sequence, Guilmette Formation		
Dgfm	Fox Mountain Sequence, Guilmette Formation		
Dsiualt	Upper Alternating Sequence, Simonson Dolomite		
Dsibc	Brown Cliff Forming Sequence, Simonson Dolomite		
Dsilalt	Lower Alternating Sequence, Simonson Dolomite		
Dsicxln	Coarsely Crystalline Sequence, Simonson Dolomite		
Dox2	"Oxyoke Formation" Sequence 2		
Dox1	"Oxyoke Formation" Sequence 1		
Dse3	Sequence 3, Sevy Dolomite		
Dse2	Sequence 2, Sevy Dolomite		
Dse1	Sequence 1, Sevy Dolomite		
		LITHOLOGY	
			Limestone
			Cherty Limestone
			Stromatolite Beds
			Stromatoporoid Reef
			Karsted Limestone
			Dolostone
			Karsted Dolostone
			Calcareous Siltstone
			Sandstone
			Desiccation Cracks in Sandstone
			Carbonate Breccia

Figure 14 Legend for **Figure 13** describing and defining Devonian sequences, features at sequence boundaries, and symbols. See **Figure 4**, **Figure 9**, and **Plate 6** for location of TMS.

In another system in another part of the world, Satterley (1996) suggested that Late Triassic eustatic sea-level fluctuations were ineffective in controlling sedimentation of the Dachstein Limestone, Austria. He suggested that vertical facies patterns are best explained by aperiodic fault-controlled downdropping.

On the other hand, Yang et al. (1995) suggested that Milankovitch climatic

forcing was responsible for cycle periodicity of the Lost Burro Formation rocks in the Panamint Range over a large, low-latitude Devonian carbonate platform. However, in their work on the Virgilian and Wolfcampian Cisco Group in north-central Texas, Yang et al. (1998) pointed out the importance of distinguishing the roles of autogenic versus allogenic processes to establish a high-resolution (meter-scale) chronostratigraphy of any sedimentary record. An allocyclic Cisco record in the lower platform contains abundant autocyclic imprints because allogenic controls on cyclic sedimentation were accomplished through local autogenic processes. Elrick (1995) suggested that the cycles in the Great Basin Simonson Dolomite formed in response to glacio-eustatic sea-level oscillations. Similarly, McLean and Mountjoy (1994) attributed parasequence cycles in the Canadian Devonian Cairn Formation to high-frequency sea-level oscillations, but Wilkinson et al. (1996) concluded that meter-scale cyclicity was more apparent than real. They also suggested that perceptions of repeated and eustatically driven platform flooding were largely incorrect, and that much of the presumed stratigraphic order in peritidal carbonates reflected random migration of sedimentary subenvironments. From their work on the peritidal Upper Cambrian and Conococheague Formations, Virginia, Wilkinson et al. (1998) concluded that the frequency of stratigraphic recurrence of 265 shallowing-upward cycles is random. They believed that in most epicratonic peritidal sequences meter-scale variations in carbonate deposition are randomly controlled and are not related to recurrent intrabasinal or extrabasinal mechanisms that force rhythmic sediment accumulation. Furthermore, Wilkinson et al. (1999) showed that Phanerozoic peritidal sequences exhibit exponential thickness frequency distributions and that thickness distribution is independent of facies type. In other words, numbers, sizes, and compositions of carbonate units in the Phanerozoic imply a less deterministic relation between environment of accumulation than the lateral/vertical distribution of different stratal elements in cratonic peritidal sequences. The linkage between sea-level change and sequence shape and size relies on deterministic conjectures. In contrast, Gupta and Allen (1999) speculated that high-frequency episodic fluctuations in relative sea level of

the French Early Tertiary Alpine foreland basin are a consequence of glacioeustatic sea-level oscillations of > 0.5 m.y. duration. These oscillations are superimposed upon a steady relative sea-level rise resulting from the background flexural subsidence. Their conclusion is based on data from which sediment supply can be eliminated as a variable. They analyzed the paleoshoreline features preserved along the Eocene Nummulitic Limestone Formation basal unconformity of the basin in southeastern France.

Sami and James (1994) inferred that small, meter-scale cycles in the Proterozoic upper Pethei Group, northwest Canada, were mainly autogenic, having formed in an aggradational tidal island model. They interpreted the formation-scale and decameter-scale cycles as controlled by changes in eustasy and subsidence rates. Along similar lines, Goldhammer et al. (1993) claimed those cycles in the Lower Ordovician Diablo Platform, west Texas, were probably driven by a combination of high-frequency, eustatic sea-level oscillations and autocyclic progradation.

Rankey and Walker (1994) suggested that carbonate platform cycles on the Cambrian Iapetan passive margin in the southern Appalachians are caused by autocyclic aggradation and progradation unrelated to sea-level fluctuations. In their model, the carbonate-producing mechanism shifts laterally to a more favorable location when the shallowing-upward cycle reaches its upper limits and the mechanism shuts off.

Another possible mechanism for cycle development involves tectonic activity. McLean and Mountjoy (1994), for example, attributed episodic longer-term regional development of Canadian Devonian sequences superimposed on a high-frequency cyclicality to episodes of tectonic loading related to the Antler orogeny. This hypothesis is important for the current research because Devonian rocks in the eastern Great Basin were deposited in the Sunnyside basin (**Plate 3**), next to and east of the region of the Antler orogeny.

In summary, agreement on the mechanisms for cycle and sequence development has not been reached. A combination of mechanisms could account for the cycles and sequences in the Sunnyside basin. Autocyclic mechanisms may have controlled

development of cycles because cycles are not correlative throughout the basin. Some of these carbonate autogenic processes include variations in carbonate production and dispersal, intensity and frequency of tropical storms and monsoons, thermohaline circulation patterns, and ambient ocean chemistry and temperature as a control on cycles within the sequences. Tectonic or eustatic controls may have controlled regionally correlatable sequences. Tectonic pulses of the active Antler Orogeny likely affected relative sea-level changes in the adjacent Sunnyside basin. However, until more precise methods of dating the emplacement of the Antler thrust sheets can be made, the driving mechanisms for sequence development in the Sunnyside basin remain undetermined. Erosion at sequence boundaries precludes making useful conclusions of cycle stacking patterns between sequences in the Sunnyside basin because much of the record is missing.

In this report, the Sunnyside basin is identified and interpreted as the incipient Antler foreland basin that began to form in the Early Devonian. Episodic tectonic pulses of the incipient Antler orogeny may be responsible for some large-scale sequences in the Great Basin Devonian. Sequences defined in this study are correlatable throughout the Sunnyside basin. However, the composition, thickness, and number of shallowing-upward cycles within the sequences are highly variable across the Sunnyside basin. Similarly, Lehmann et al. (1998) found that composition, thickness and number of meter-scale cycles within their sequences of the Early Cretaceous carbonates and evaporites are highly variable across the Cupido and Coahuila platforms, northeastern Mexico. They attributed the cycle variability to interacting processes that created variable physiographic and oceanographic conditions across the platforms that complicated the sedimentary record generated by Milankovitch-driven sea-level changes.

Devonian Sequences at TMS

Table 4 provides a convenient reference for the thicknesses, numbers of cycles and significant features that locally distinguish each sequence. **Figure 13** is a composite stratigraphic column illustrating the surface gamma-ray log, generalized lithology, relative sea-level curve, and sequence boundary characteristics for sequence at TMS. It was constructed from three segments (**Figure 4** and **Plate 6**). Segment 1 starts in the Sevy sequence 3 and ends at the top of the Simonson Brown Cliff Sequence. Segment 2 starts at the top of the Brown Cliff Sequence and ends in Guilmette Sequence Dgd. Segment 3 starts near the top of Guilmette Sequence Dgb2 and ends in the Mississippian “Penoyer Limestone” (**Table 1**).

Overlap from the top of Sequence Dgb2 to the lower part of Sequence Dgd in segments 2 and 3 was intentional. In segment 2, Sequence Dgb3 is a stromatoporoid reef. This section is called reef core herein and a letter “c” is added to the sequence designation. For example, Dgbc is Sequence Dgb where Dgb3 is the stromatoporoid reef. On the other hand, Sequence Dgb3 in segment 3 is on the reef flank. A letter “f” is added to the sequence designation. For example, Dgbf is Sequence Dgb where Dgb3 is on the reef flank. **Figure 14** is a legend for symbols and abbreviations in **Figure 13**, **Table 4**, and **Figure 28**.

Table 4 Thickness, numbers of cycles, and significant features of Devonian sequences in southwest Mail Summit measured section, Timpahute Range, Nevada.			
Seq. Abbrev.	Thickness in Feet	Cycles	Significant Features
Dga2	145	8	Shallowing-upward cycles that successively deepen upward, predominantly limestone, open-marine fauna, ledges and slopes
Dga1	250	12	Shallowing-upward cycles that successively deepen upward, predominantly dolomite, open-marine fauna, ledges and slopes
Dgys	182	10	Yellow, silty dolomite, stromatolites, and cycles capped by thin beds of very fine-grained quartz sandstone, ostracodes, forms slopes
Dgfm	135	4	Open shelf fauna, brachiopod <i>Stringocephalus</i> , resistant cliffs.
Dsiualt	285	12	Shallowing-upward cycles that successively deepen upward giving the dolomite an alternating dark and light band appearance, karst breccia, ledges
Dsibc	85	4	Open shelf fauna (corals, stromatoporoids), dark brown-gray dolomite cliff
Dsilalt	265	12	Alternating intertidal-supratidal or dark and light bands of dolomite ledges
Dsicxln	225	4	Coarsely crystalline dolomite capped by karsted interval, light-gray to light-gray brown cliffs
Dox2	95	2	Quartz sandstone with hummocky cross-bedding at base overlain by sandy dolomite, ledge
Dox1	100	4	Burrowed, silty dolomite with flat-pebble conglomerate at base, light-brown slope
Dse3	240+	12+	Light-gray, fine-grained, laminated dolomite, slopes, base concealed
Total	4370	189+	

Table 4 Continued			
Seq. Abbrev.	Thickness in Feet	Cycles	Significant Features
MDp2	115	2	Silicified stromatolites and laminated black chert, slope
MDp1	130	2	Silty limestone capped with fossil bone-bearing sandstone, slope
Dwr	153	4	Silty, burrowed limestone, partly covered slopes
Dgg	567	29	Carbonate cycles capped by thick (>10 feet) quartz sandstone beds
Dgf	267	16	Slightly deeper cycles and contains more limestone than in adjacent sequences
Dge	235	17	Carbonate cycles capped by thin (<10 feet) quartz sandstone beds
Dgd	406	23	<i>Amphipora</i> dolopackstone, dark-gray ledges and cliffs
Dgc	188	6	Silty limestone with abundant gastropods & burrows, slope
Dgb3	97	3	Stromatoporoid and coral reef facies, light-gray cliffs
Dgb2	179	1	Graded bed of carbonate breccia, open-marine fauna, brown-gray cliffs
Dgb1	26	2	Abundant corals, stromatoporoids, and <i>Amphipora</i> , limestone cliffs

Although some sequence boundaries do not exactly coincide with formation contacts, the sequences are grouped into formations wherever possible. Characteristics of each formation, including lithology, weathering profile, gamma-ray character, distribution of the formation in the study area, cycle attributes and tectonic significance, are described in this chapter. Then each sequence is described. Detailed descriptions of each cycle within each sequence are presented in Appendix B. Photomicrographs and their descriptions from the lower Guilmette sequences are presented in Appendix C.

Recorded in the measured section are three major Devonian sea-level lowstand events (L1-L3, **Figure 13**) that produced regionally and economically significant karst intervals, and six major sea-level transgressions (T1-T6, **Figure 13** and **Plate 2a**). Bounding surfaces and internal features were interpreted for their relative sea-level changes and paleoenvironmental significance, and the results were used to create a relative sea-level curve. Criteria used to classify sequences are presented in **Table 3**, Chapter 3.

Sevy Dolomite

Three mappable sequences comprise the Sevy Dolomite in the Sunnyside basin. Isopach maps of the sequences suggest that the center of the Sunnyside basin in Sevy Dolomite time was near Eureka, Nevada (see **Figure 2** for location of Eureka, Nevada). Only 240 feet of Sequence 3 are exposed at TMS. However the Sevy Dolomite is 980 feet thick in the Tempiute Mountain section where all three sequences are exposed (No. 53, **Figure 9**; **Figure 12**; see summary of this chapter for another correlation chart involving the Tempiute Mountain measured section). In the study area and areas east of the Diamond Range, the Sevy Dolomite lies unconformably on Silurian Laketown Dolomite. It lies unconformably on top of the Silurian Lone Mountain Dolomite in the Diamond Mountain vicinity (**Figure 9**, Nos. 14, 15, 16, 23, and 34).

Characteristics of the Sevy Dolomite

The Sevy Dolomite is a 500 to 1,600-foot-thick, monotonously repetitive, micritic to finely-crystalline, laminated, light-to very light-gray, dense dolomite that occurs throughout the study area (**Plate 1a**). Typically, the sequence boundary at its base occurs

at the change from cliff-forming, dark-gray, chert-bearing, fossil-rich Silurian Laketown Dolomite to the slope-forming, fossil-poor, laminated, light-gray Devonian Sevy Dolomite. Reso and Croneis (1959) reported Lower Devonian (Oriskany) fossils in the Sevy Dolomite in the Pahrangat Range, five miles south of the study area. Tschanz and Pampeyan (1970) suggested that the Lower Devonian fossils occur considerably below the Oxyoke Canyon Sandstone Member of the Nevada Formation west of Eureka. They occur above the *Halysites*-bearing dolomites of the underlying Silurian Laketown Dolomite. *Halysites* corals are marker fossils of the Laketown Dolomite.

On fresh surfaces, the color of the Sevy Dolomite varies much more than it does on weathered surfaces. Fresh color ranges from light gray to dark gray, to light olive gray to light brownish gray. The light olive gray to light brown gray is typical for most of the section throughout most of the region. The darker grays are generally limited to the uppermost part of the sequence. However, sections in Elko and northernmost White Pine counties in Nevada and Silver Island Mountains in northwestern Utah (**Figure 9**, Nos. 41, 42, 45, and 47) are different. In these sections, the darker grays are prevalent throughout the formation. Most of the rocks in the formation contain thin stromatolitic laminations. Osmond (1954) described the sequence as uniformly micritic. The outcrops that I observed show the average grain size to be closer to very finely crystalline.

The Sevy Dolomite maintains its lithologic character from southern Nevada to southern Idaho and central Utah. It is easily recognized in the field by its micritic to very finely-crystalline grain size, extensive laminated beds, distinctive very light gray-weathering color and its slope-forming weathering profile (**Table 4**). **Figure 15** illustrates the distribution of 68 outcrops of Sevy Dolomite covering 15.65 square miles in the Timpahute Range quadrangle.

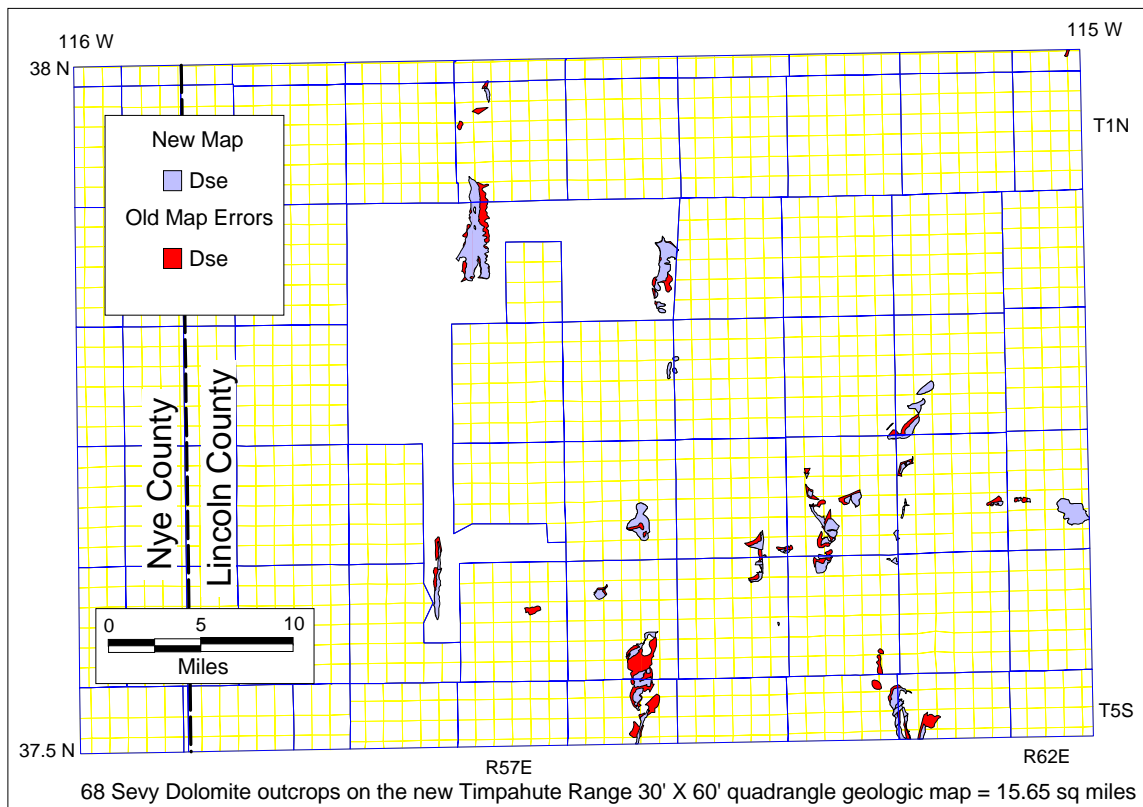


Figure 15 Distribution of Sevy Dolomite outcrops on the new geologic map of the Timpahute Range quadrangle. Areas erroneously mapped as Sevy Dolomite on the old geologic map are marked in red. Degrees N latitude and W longitude are marked at the corners of the map. Surveyed township and range lines are blue and section lines are yellow.

Lower Contact As noted by Osmond (1962), the surface between the Silurian Laketown Dolomite and the Devonian Sevy Dolomite is a regional unconformity that can be readily recognized in some sections. In other sections, the unconformity is obliterated by recrystallization and dolomitization. This lower contact is picked in the measured sections at an abrupt decrease in fossils and bedded chert and where gamma radiation decreases. Locally a thin sandstone bed or sandy dolomite bed occurs at the base of the Sevy Dolomite, as Osmond (1962) reported. This boundary may also be subtle and occur on partly covered slopes.

Upper Contact Sharp in most measured sections, the upper contact of the Sevy Dolomite is picked at the unconformity between light-gray, supratidal, finely-crystalline stratal dolomite and light yellow-gray beds containing the first occurrence of “Oxyoke Formation” detrital sand grains. This erosion contact is overlain by breccia clast beds and sandy dolomite that is probably related to transgressive marine flooding and sedimentary reworking. Light gray clasts in the light yellow matrix are from the underlying Sevy Dolomite. A sharp increase in gamma radiation also marks the contact. Even without an obvious increase of siliciclastic grains in the carbonate beds, the increase in gamma radiation at the base of the overlying “Oxyoke Formation” is generally present.

In contrast to other workers who place the second order Kaskaskia sequence of Sloss (1963) at the base of the Sevy Dolomite, I place it at the top. I believe the unconformity at the top of the Sevy Sequence is the base of the Kaskaskia (**Figure 10**). The unconformity is marked by a more distinctive change in lithology and reflects a greater facies shift than the unconformity at the base of the Sevy Dolomite. Most of the Devonian strata at Mail Summit are incorporated in the Kaskaskia sequence of Sloss (1963) and as refined by Wheeler (1963). The paucity of fossils disallows placement of the lower Kaskaskia sequence boundary more precisely.

Gamma Radiation

Gamma-ray logs help divide the Sevy Dolomite into three regionally correlatable sequences: lower, middle and upper. Gamma radiation is lower over Sevy Sequence 1 and Sequence 3 and higher over Sevy Sequence 2 (**Figure 12**). Sevy Sequence 1 is between 50 and 70 CPS (Counts Per Second) in the Tempiute Mountain measured section and is constantly about 20 API units in the Moore McCormack well. Sevy Sequence 2 is mostly between 70 and 110 CPS at Tempiute Mountain and 20 to 30 API units in the

Moore McCormack well. Sevy Sequence 3 is mostly 60 CPS at Tempiute Mountain, 20 API units in the Moore McCormack well, and 90 CPS in the TMS.

Environment of Deposition

Although the occurrence of fossils in the Silurian Laketown Dolomite suggests deposition in open-shelf conditions, I agree with Osmond (1962) who believed that the generally fossil-poor Sevy Dolomite originated mainly as a primary evaporitic dolomite in a supratidal setting. Most of the Sevy Dolomite is composed of the supratidal finely-crystalline stratal dolomite facies. This dolomite facies and other dolomite occurrences at TMS are described later in this chapter. Anhydrites have not been found in measured sections and wells listed in **Table 2** and in Appendix F. However, other characteristics common to sabkhas such as absence of fossils, thin pebble conglomerates, stromatolitic laminae, desiccation cracks, and other diagenetic modifications such as dolomite replacement to form finely-crystalline stratal dolomite, tepee structures, and disrupted bedding strongly indicate supratidal conditions and indirectly suggest hypersaline conditions.

The paleogeography of the eastern Great Basin during much of Sevy Dolomite time is interpreted as a vast sabkha, extending for hundreds of miles in width and perhaps a thousand miles or more along depositional strike. Just west of the Diamond Range, 100 miles north of the study area, was a narrow area of intertidal conditions next to an area of subtidal conditions (**Figure 9**, Nos. 14, 15). Correlative intertidal beds include the Beacon Peak, upper part of Lone Mountain, Wenban Limestone, Rabbit Hill, and the upper part of Roberts Mountain Formation, as Matti (1979) pointed out (**Figure 10**). Telescoping of the section by thrusting during the Sevier orogeny in the Diamond Range area is probably responsible for what now may be a very narrow, abrupt outer shelf (Chamberlain and Birge, 1997). Many workers have reported thrust faults in the area

(Nolan, 1962; Nolan et al., 1971; Nolan et al., 1974; Roeder, 1989; Carpenter et al., 1993; Camilleri, 1999). Outer shelf deposits now lie next to sections with supratidal and subtidal deposits. Thrust fault restorations suggest that they were probably deposited west of Sunnyside basin and have been subsequently thrust into their present position. Relative sea-level changed little during Sevy Dolomite time; most cycles begin in high intertidal conditions and end in high supratidal conditions.

In the Silver Island Mountain section (**Figure 9**, No. 47) in northwestern Utah, the typical Sevy Dolomite lithotype is missing. A local fossiliferous, medium dark-gray weathering dolomite, similar to the Lone Mountain Formation, occurs at the same stratigraphic interval. The interval contains a few beds of typical Sevy Dolomite lithology just beneath the Simonson Dolomite. This suggests the development of a marine embayment on the shelf. The presence of this lithotype at this location could also be due to tectonic transport from the west by the Sevier thrusting event. Also it could be the result of tectonic transport from the northwest by pre-Sevier thrusting (N. Silberling, 1998, personal communication). Farther north and east, at Samaria Mountain in southern Idaho (**Figure 9**, No. 46), the Lower Devonian Water Canyon Formation exhibits typical Sevy Dolomite-like stratigraphy. Other workers have previously correlated the Water Canyon Formation with the Sevy Dolomite (Hintze, 1988). However, more data are needed to better define the paleogeography of the Samaria Mountain area.

“Oxyoke Formation”

The “Oxyoke Formation” at TMS is 195 feet thick and is composed of two sequences. It is a distinctive light-brown argillaceous and sandy interval between the light-gray Sevy and medium dark-gray Simonson Formations, and thus, an important regional marker bed. The lower contact at TMS is sharp and is marked by a regional LSE cut into the top of the Sevy Dolomite and merged with a TSE and associated rip-up clasts

above the unconformity. It is distinct at TMS where light-gray dolomite is overlain by light-brown argillaceous dolomite of “Oxyoke Formation” Sequence 1. Forming a prominent brown cliff, sandstones of “Oxyoke Formation” Sequence 2 are the first prominent occurrences of regionally distributed quartz sandstones in the Paleozoic rocks above the Ordovician Eureka Quartzite. Sandstones become interbedded with coarsely-crystalline dolomite near the top of the sequence. The uppermost occurrence of quartz sandstone marks the upper contact with the base of the Simonson Dolomite Coarsely-Crystalline Sequence. Sharp inflections on the gamma-ray log mark the lower and upper contacts at TMS.

Establishing the “Oxyoke Formation”

Inconsistencies in correlating the argillaceous and sandy interval between the Sevy and Simonson Formations were discussed in Chapter 2. Osmond (1962), Hurtubise (1989), and other early workers each used different criteria to pick the contacts. They did not use sequence stratigraphic concepts to do so. I have chosen to establish the “Oxyoke Formation” as a mappable unit bounded by unconformities between the Sevy and Simonson formations to avoid these inconsistencies. Establishing the “Oxyoke Formation” avoids confusion over arbitrary contacts based on facies variations.

The “Oxyoke Formation” is not to be confused with the Oxyoke Canyon Sandstone Member of the Nevada Formation of Nolan et al. (1956). The type section of the Oxyoke Canyon Sandstone Member of the Nevada Formation is in Oxyoke Canyon, Diamond Range (**Figure 9**, No. 15). It correlates with “Oxyoke Formation” Sequence 1 in **Figure 10**. However, the “Oxyoke Formation” as employed here is composed of two sequences: Sequence 1 that correlates to the Oxyoke Canyon Member of Nolan, and Sequence 2. A reference section of the “Oxyoke Formation” is TMS (**Figure 9**, No. 51, **Table 2**, and **Figure 13**).

Characteristics

The “Oxyoke Formation” is a distinctive grouping of facies assemblages and lithologies between the Sevy and Simonson Dolomites. It contains types of strata found in neither the underlying Sevy Dolomite nor the overlying Simonson Dolomite. The “Oxyoke Formation” includes sandstone beds, sandy dolomites, and other beds above the Sevy Dolomite unconformity and below the Simonson Dolomite Coarsely-Crystalline Sequence. It includes both the cherty argillaceous member and the sandy member described by Osmond (1954), Reso (1960) and Hurtubise (1989). At TMS and in much of the Sunnyside basin, the argillaceous member generally corresponds to Sequence 1 and the sandy member to Sequence 2. However, Sequence 1 may be mostly quartz sandstone with dolomite cement as at the type locality of the Oxyoke Canyon member of the Nevada Formation (**Figure 9**, No. 15) and at other western sections. In some eastern sections, Sequence 2 lacks quartz sandstones.

At TMS, the lower part of the lowermost shallowing-upward cycle of the 100-foot thick “Oxyoke Formation” Sequence 1 is a hummocky cross-stratified, light yellow-gray, sandy, finely-crystalline dolomudstone. Several inches of thin, light-gray Sevy Dolomite rip-up clasts that lie parallel to the bedding in sandy dolomudstone suggest a major transgressive surface and mark the basal contact of the “Oxyoke Formation” Sequence 1. Normally, the significance of an unconformity is determined by the number of missing faunal zones. However, the paucity of fossils in the supratidal beds of the Sevy Dolomite preclude identifying the unconformity based on missing fossils. Therefore, other physical evidence such as the transgressive lag, irregular contact, missing Sevy Dolomite cycles on regional correlations must be used to find the significance of the unconformity. The transgressive intraclast packstone lag is overlain by a burrowed light yellow-brown weathering dolomudstone with quartz sand and black chert nodules two to three inches in diameter (**Plate 2a**). Intensity of burrowing decreases upward. Near the top of Sequence 1, the dolomites become more laminated.

“Oxyoke Formation” Sequence 2 contains persistent quartz sand intervals that are about five to 60 feet thick in most sections in much of the Sunnyside basin. At TMS, a 54-foot thick quartz sandstone bed forms a prominent brown cliff in the 95-foot thick sequence. The sandstone weathers medium yellow-brown and is cross-bedded, fine- to medium-grained and is poorly cemented with dolomite. Throughout the Sunnyside basin, quartz grain size ranges from medium sand to silt size. Fine- to medium-grained sand is most common. Sandstones commonly are subordinate to quartz-sand dolomites and may be missing altogether. In sections that contain no distinct quartz sandstone, the “Oxyoke Formation” is characteristically a silty dolomite bearing quartz sand grains. At localities where the base and top of the sequence are difficult to find, the gamma-ray log signature is diagnostic.

In the type locality of the Oxyoke Canyon member of the Nevada Formation or “Oxyoke Formation” Sequence 1 (**Figure 9**, No. 15), the trough cross-bedded sandstone is light olive-gray on a fresh break. It is medium- to coarse-grained in contrast to “Oxyoke Formation” sandstones in sections farther east. Nolan et al. (1956) reported a transgressive bed containing many casts of large crinoid columnals near the base of the unit at Phillipsburg mine, 15 miles north of the type locality (**Figure 9**, No. 16). Fossils are lacking in the unit in sections farther east.

Throughout the Sunnyside basin, horizontally laminated and ripple laminated beds are common, and these may contain dolomite interlaminations. Many sandstone beds have sedimentary structures such as horizontal planar laminations and hummocky cross-stratification that suggest a lower shoreface environment. Typically, the sandstones grade up to fine-grained sandstones with desiccation cracks suggesting a tidal flat origin. Near the top of the unit, interbeds of dolomite are coarsely crystalline. Sparse quartz-sandy laminae and floating quartz grains occur in the upper part of many sections where carbonate beds dominate. The quartz grains are subrounded to rounded, well-sorted, and fine- to medium-grained. Laminae of quartz grains commonly appear as discrete lenses within cross-bedded dolomite.

Seventeen feet of upward thickening, finely-crystalline, quartz sand-bearing dolomite beds that weather medium yellow-brown lie on top of the sandstone interbed at TMS. The upper contact of the “Oxyoke Formation” is marked by an irregular surface of erosion and where sand content abruptly decreases zero. The less radioactive Coarsely-Crystalline Sequence of the Simonson Dolomite overlies the upper beds of the “Oxyoke Formation” at TMS. See Appendix B for a more detailed description of the “Oxyoke Formation” sequences and cycles at TMS.

Thickness

The “Oxyoke Formation” is 285 feet thick at Tempiute Mountain (53), 195 feet thick in the reference section at TMS (51), 430 feet thick at Monte Mountain (52), 285 feet thick in the Maxus Moore McCormack well (35), and 230 feet thick at Cutler Reservoir, Pahrnagat Range (38)--see **Figure 9** and **Table 2** for surface and subsurface section locations. It thickens to a maximum of about 580 feet in Oxyoke Canyon, Diamond Range, Sec. 20 T18N R54E. The sandy member of Hurtubise (1989) at Fossil Peak, Sec. 30 T2S R61E, is 139 feet thick and at Timber Mountain, Sec.10 T2N R62E, it is 101 feet thick. Hurtubise (1989) measured 22 feet of net sand within the sandy member at Timber Mountain section but did not provide a figure for net sand at Fossil Peak, which probably ranges between 50 and 150 feet. Sandy beds are absent in the “Oxyoke Formation” of the Pequop Range (**Figure 9**, No. 41), Cherry Creek Range (**Figure 9**, Nos. 8 and 9), Ruby Range (**Figure 9**, No. 45), and the Silver Island Mountains (**Figure 9**, No. 47). Nevertheless, the distinctive gamma-ray signature persists in these sections that appear to have a higher silt and clay content than the underlying and overlying formations. An isopach map of the “Oxyoke Formation” and a discussion of quartz sandstones in the Sunnyside basin are presented in Chapter 7.

Gamma Radiation

In contrast to the smooth, nearly constant line of low radiation over the upper part of the Sevy Dolomite, the gamma-ray log exhibits sharp fluctuations over the more radioactive, argillaceous, and sandy “Oxyoke Formation.” The lower contact of the “Oxyoke Formation” is easy to pick and correlate on gamma-ray logs because of the sharp rightward inflection caused by an increase in gamma radiation and in cuttings. Higher radiation is typical of the argillaceous “Oxyoke Formation.” **Figure 12** provides an example of the correlation from surface to subsurface sections. In the Maxus Exploration Moore McCormack well (**Figure 9**, No. 35)--a well near the study area (Sec 6 T7S R58E) that penetrated Devonian rocks--the 285-foot-thick “Oxyoke Formation” exhibits the sharp rightward gamma-ray inflection at its base. As with the surface gamma-ray on nearby outcrops, the “Oxyoke Formation” produces more radiation than the underlying Sevy Dolomite and the overlying Simonson Dolomite. It is highest over argillaceous “Oxyoke Formation” Sequence 1 and lower over sandy Sequence 2 (**Figure 12**).

The anomalously low gamma radiation of “Oxyoke Formation” Sequence 2 at TMS is probably due to the abundance of medium to coarse quartz sand grains that dilute the finer-grained, more radioactive particles. Similarly, in the type locality of the Nevada Formation Oxyoke Canyon Member at Oxyoke Canyon near Eureka, Nevada, the gamma-ray signature of the light gray sandstone is less pronounced than in the adjacent dolomites of the Sevy Dolomite below and Simonson Dolomite above (Cedar Strat proprietary measured section, 1985).

A pronounced upward decrease in gamma radiation marks the top of the “Oxyoke Formation” in most sections (**Plate 2a**). In some sections the upward decrease in gamma radiation is gradational with the overlying Coarsely-Crystalline Sequence of the Simonson Dolomite.

Sand Provenance

As stated in Chapter 2, the source of the sandstone in the “Oxyoke Formation” is problematical. Osmond (1954, 1962) and Poole et al. (1992) suggested an easterly source for the sand. However, this study proposes an alternative source area. Introduced in Chapter 2, the Antler forebulge was likely the source area for “Oxyoke Formation” quartz sandstones in the western side of the Sunnyside basin. The quartz sandstones in the “Oxyoke Formation” coarsen and thicken westward toward the Antler forebulge where unconformities on the west flank of the Sunnyside basin have cut out older Paleozoic rocks including Eureka sandstones. For example, in the Toquima Range, a window through the Roberts Mountain allochthon of Ordovician rocks reveals that Mississippian rocks unconformably lie on Cambrian rocks (Cedar Strat proprietary measured section). Measured sections of the region suggest that the Ordovician Eureka Quartzite was at least 400 feet thick about the forebulge. Eureka sandstones eroded off the forebulge were recycled and were redeposited in the back-bulge Sunnyside basin during the Devonian. The implications of the distribution of quartz sandstones in the Sunnyside basin and the regional tectonic features affecting Devonian paleogeography are presented in Chapter 7.

Environment of Deposition

Burrows in silty dolomudstone above the hummocky cross-stratified sandy dolomudstone at the base of Sequence 1 suggest a shallowing-upward from above storm wave-base in open-shelf conditions to low-intertidal conditions (**Plate 2a**). J. Warne (1999, personal communication) reported *Zoophycus* at Six Mile Flat, nine miles northeast of Hiko, suggesting quiet water. The abundance of burrows decreases upward to laminated dolomudstone. This suggests a shallowing-upward cycle to supratidal conditions at the top of Sequence 1.

Overlying the laminated dolomudstones of Sequence 1 is a cliff-forming sandstone interbed containing hummocky cross-stratification in the lower part of “Oxyoke Formation” Sequence 2. The hummocky cross-stratification was probably deposited above storm wave-base in open-shelf conditions. These sandstones were overlain with a clean, well-sorted, bidirectional trough cross-bedded sandstones that were probably deposited as upper shoreface sandstones. Above the shoreface sandstones, tabular cross-bedded sandstones suggest beach or intertidal conditions. Above the sandstone interbed, quartz sand content decreases gradually upward for 35 feet to the top of the “Oxyoke Formation.” The upper contact of the “Oxyoke Formation,” marked by a leftward flexure in gamma radiation, is the uppermost occurrence of quartz sandstone at TMS. Although bedding is obliterated by dolomitization, the higher gamma radiation at the top of the “Oxyoke Formation” could be a result of supratidal dolomite typical of many shallowing-upward cycles of the Devonian at TMS.

Oxyoke Formation at Tempiute Mountain and Monte Mountain

The “Oxyoke Formation” at Tempiute Mountain and Monte Mountain displays some variability of the unit. It is composed of four shallowing-upward cycles at Wildcat Wash, Tempiute Mountain (**Figure 9**, No. 53; see **Plate 1a** for measured section location), where its base is less conspicuous than at TMS because it lacks rip-up clasts at the contact. I place the basal contact where dark-gray weathering dolomite overlies light-gray weathering dolomite. It coincides with a significant increase in gamma radiation (**Figure 13**). A 52.5-foot quartz arenite occurs near the top of the “Oxyoke Formation.” It is pale red gray on a fresh and weathered surface. Cemented with dolomite, its fine sand grains are trough crossbedded. It overlies a 60-foot bed of quartz sand-bearing dolomite. A sharp upper contact marks the change from sandstone to dark weathering, laminated dolomite of the Simonson Dolomite Coarsely-Crystalline Sequence. Gamma

radiation is low over the sandstone and begins to increase over the dolomite above the sandstone (**Figure 13**). About a mile south of Wildcat Wash the “Oxyoke Formation” is shattered, liquified, and jammed upward into a set of dikes and sills associated with the cosmolite impact (Warme and Kuehner, 1998).

The “Oxyoke Formation” at Monte Mountain (No. 52, **Figure 9**) has one thick (35-foot) quartz arenite and three thin (5- to 10-foot) ones near the base. Approximately 100 feet of sandy dolomite beds occur near the top of the interval. Eleven shallowing-upward cycles produce a serrated gamma-ray pattern at Monte Mountain.

“Oxyoke Formation” Sequences

Two sequences, containing six shallowing-upward cycles, occur in the 195-foot thick “Oxyoke Formation” at Mail Summit. They are described briefly below and in detail in Appendix B.

“Oxyoke Formation” Sequence 1 “Oxyoke Formation” Sequence 1 at TMS is 100 feet thick and comprised of four of the six “Oxyoke Formation” cycles. The lower boundary of Sequence 1 is a merged LSE and TSE. It separates the underlying ledge-forming, laminated, quartz-free, light-gray Sevy Dolomite from the overlying slope-forming, light-yellow-brown, sandy, hummocky cross-stratified, intraclast (flattened rip-up clasts) packstone that grades upward to finely-crystalline, black chert nodule-bearing, burrowed “Oxyoke Formation” dolomudstone. In cuttings, the Sevy Dolomite and the “Oxyoke Formation” could be confused unless the silty and cherty nature of the “Oxyoke Formation” is observed. A minor rightward gamma-ray spike followed by a prominent leftward gamma-ray inflection marks the base of Sequence 1 (**Figure 13**). All four of the Sequence 1 cycles are shallowing-upward cycles and are interpreted as beginning in

restricted-marine to intertidal conditions and culminating in low-intertidal to supratidal conditions.

“Oxyoke Formation” Sequence 2 “Oxyoke Formation” Sequence 2 is 95 feet thick and is composed of two cycles at TMS. The lower cycle is a light orange-brown quartz sandstone cliff that creates a regionally recognizable but intermittent stratigraphic marker. Hummocky cross-stratification at the base of the cycle suggests a second major deepening event within the “Oxyoke Formation.” Medium yellow-brown, fine- to medium-grained, crossbedded, poorly dolomite-cemented quartz sandstone comprises the rest of the cycle. Quartz sand content decreases upward, and the cycle appears to shallow upward. The second cycle is composed of finely-crystalline, medium dark-gray dolomite that contains upward-thickening sandy beds. Superficially, the transition upward from sandy “Oxyoke Formation” beds to the overlying Coarsely-Crystalline Sequence of the Simonson Dolomite seems gradual. However, a significantly sharp leftward gamma-ray inflection was used to define the boundary (**Figure 12** and **Figure 13**). In other sections, the contact between the sandy, light-brown “Oxyoke Formation” and the sand-free, medium-gray Simonson Dolomite is sharp on the outcrop and gamma-ray log.

Simonson Dolomite

The Simonson Dolomite at TMS is 860 feet thick and is composed of four sequences (**Table 4**), which coincide with the four members of the Simonson Dolomite identified by Osmond (1954): Coarsely crystalline, Lower Alternating, Brown Cliff, and Upper Alternating. It is characteristically banded with light-gray and dark-brown bands

that are one to tens of feet thick. The bands represent upward shallowing cycles. Elrick (1995) interpreted the banded dolomites of the Simonson Dolomite as peritidal cycles. However, the broad shelf and the Antler forebulge probably dampened the effects of tides. Two major karst surfaces, one at the top of the Coarsely-Crystalline Sequence and the other at the top of the Upper Alternating Sequence, make the Simonson Dolomite a potentially attractive hydrocarbon exploration target (**Figure 13** and Stop #7, Appendix D). The economic potential of this interval is discussed in Chapter 8. Pervasive dolomitization of the Simonson Dolomite is discussed in later in this chapter. **Figure 16** shows the distribution of the 78 Simonson Dolomite outcrops that cover 17.67 square miles in the Timpahute Range quadrangle.

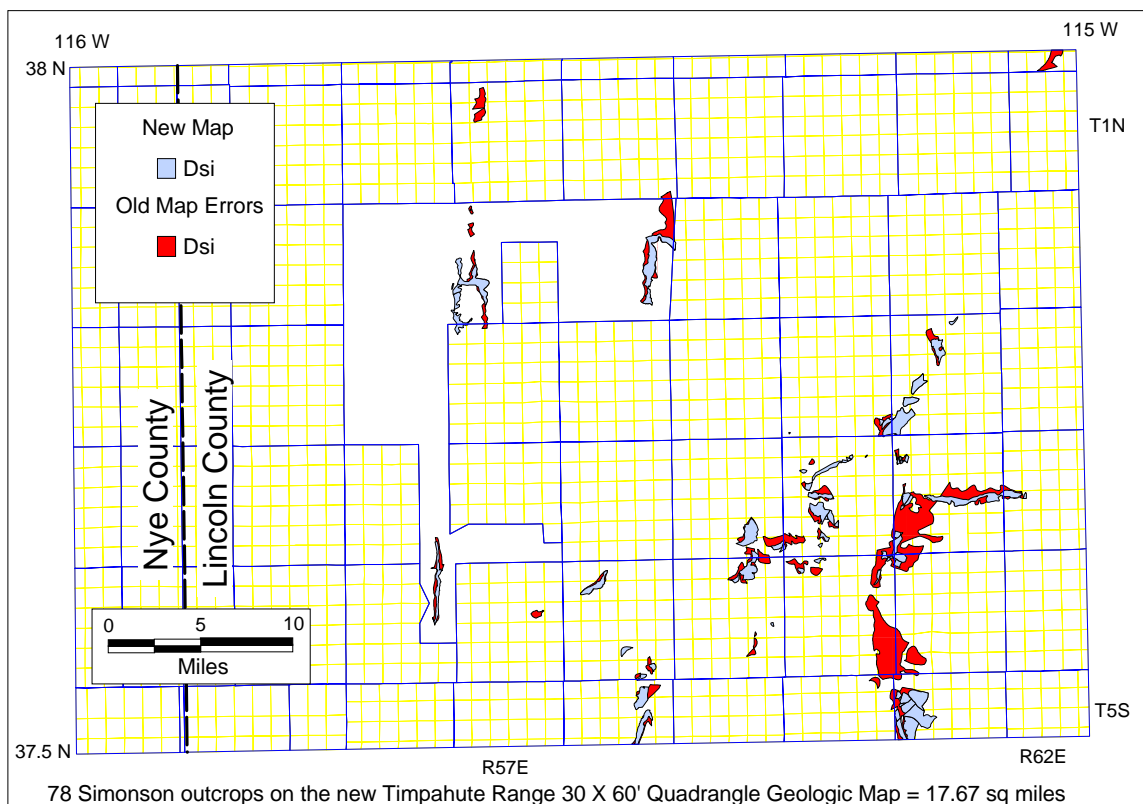


Figure 16 Distribution of Simonson Dolomite outcrops on the new geologic map of the Timpahute Range quadrangle. Areas erroneously mapped on the old geologic map as Simonson Dolomite are marked in red. Degrees N latitude and W longitude are marked at the corners of the map. Surveyed township and range lines are blue and section lines are yellow.

Coarsely-Crystalline Sequence

Comprising four cycles, the Coarsely-Crystalline Sequence is 225 feet thick at TMS. Recrystallization of the dolomite to a very coarsely-crystalline texture has obliterated most primary depositional features in this basal member of the Simonson Dolomite (**Table 4**). Shallowing-upward cycles are subtle. Regionally, the base of the Coarsely-Crystalline Sequence appears to interfinger with the top of the “Oxyoke Formation.” At TMS, the base of the sequence is picked at a leftward flexure in the gamma-ray log coincident with a significant decrease in quartz grain content as described in the “Oxyoke Formation” section above. The top of the sequence is marked by a regional unconformity that separates coarsely-crystalline, karsted dolomite below from cyclic finely-crystalline dolomite above (**Figure 17**). Solution-collapse breccias and drusy cavity fillings occur tens of feet below the top of the unconformity. Intensity of karsting, width of fractures filled with white coarsely-crystalline dolomite, and crystal coarseness all increase to the upper sequence boundary, and must be related to the exposure surface there (**Figure 13**).

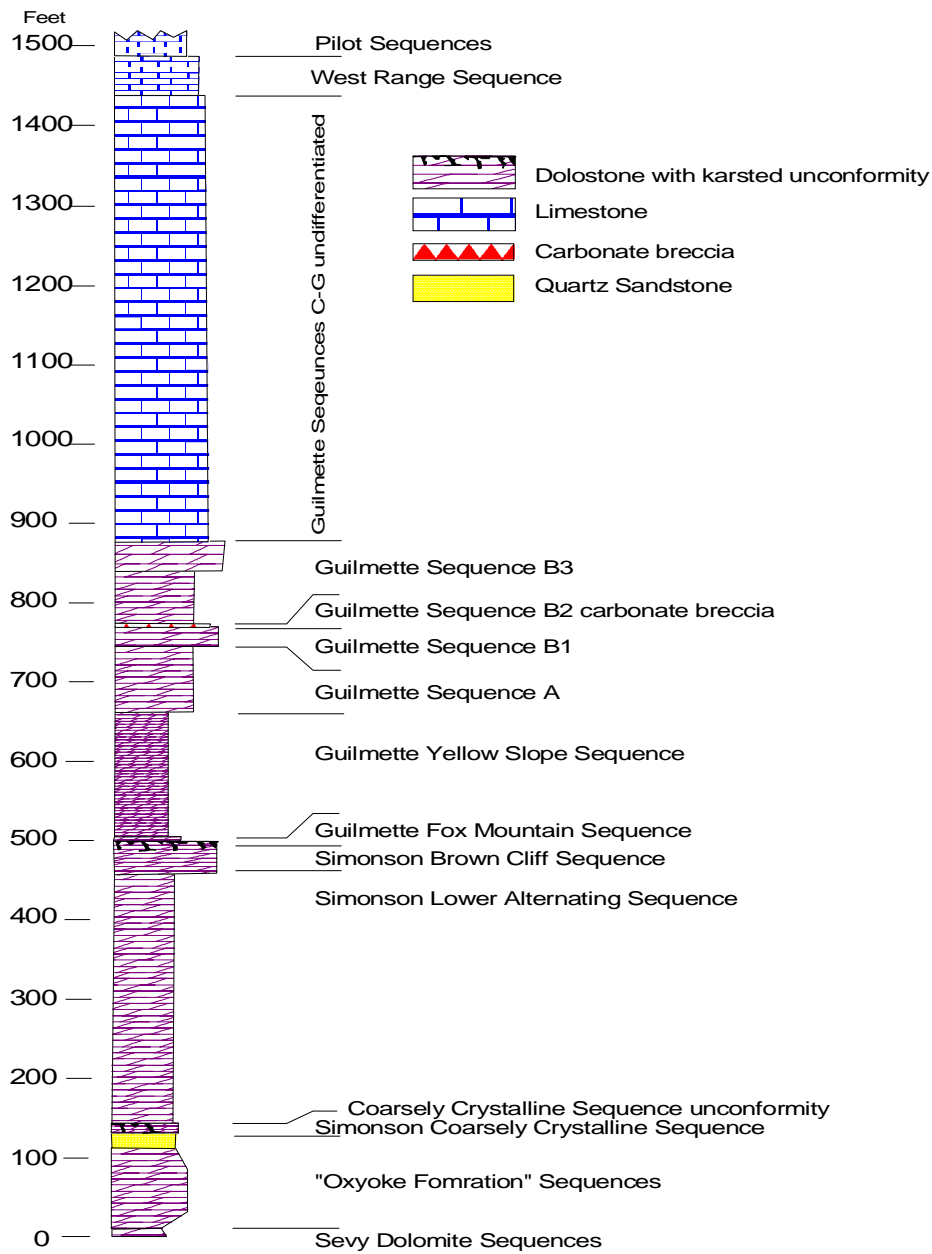


Figure 17 Generalized stratigraphic column of Middle and Upper Devonian Rocks in the Meadow Valley Mountains, Longitude 114° 44' W, Latitude 37° N, Lincoln County, Nevada showing unusually thin Guilmette Sequence Dgb2 and thin Simonson Coarsely-Crystalline Sequence.

Gamma Radiation A slight rightward gamma-ray inflection marks the top of the upper karsted surface of the sequence and correlates to other wells and sections (**Plate 2a**). The gamma radiation of the sequence is generally weak and forms a smooth pattern. Within the sequence, gamma radiation of each cycle gradually increases upward then abruptly decreases at the base of the succeeding cycle.

Structural Implications If the Monte Mountain (TMM) section in the Silver Canyon thrust sheet is restored west of the Tempiute Mountain (TMP) section, the thickness of the Coarsely-Crystalline Sequence thickens progressively eastward to TMS. The depth of karsting also increases eastward from the study area and suggests that the Monte Mountain section was less emergent than the Tempiute Mountain section during the sea-level drop that produced the LSE at the top of the sequence.

In a section measured in the Meadow Valley Mountains about 50 miles southeast of Mail Summit, karst cavities associated with the LSE penetrate downwards into the “Oxyoke Formation” (**Figure 17**). Geopetal structures containing pale-red, laminated silty dolomite parallel to tectonic dip, the proximity of the karsting to the unconformity, and persistence of karsting in the same beds along structural strike, all distinguish Devonian karsting from recent karsting of this interval. In the Meadow Valley section, most of the Coarsely-Crystalline Sequence is missing and only 12.5 feet are remaining due to the unconformity. Overlying the unconformity is the Lower Alternating Sequence.

Therefore, the unconformity at the top of the Coarsely-Crystalline Sequence progressively cuts out more of the sequence eastward and the depth of karsting below the unconformity increases eastward. This regular eastward thinning of the Coarsely-Crystalline Sequence can be used to help restore thrust sheets.

Lower Alternating Sequence

The Lower Alternating Sequence is 265 feet thick and is composed of 12 cycles (**Plate 2a**). A transgressive lag above the merged LSE and TSE marks the base of the Lower Alternating Sequence (**Figure 13**). Twelve prominent shallowing-upward cycles form the sequence. Each cycle is tens of feet thick and exhibits an alternating light and dark appearance at TMS. These cycles contain minor cycles (<10 feet thick). Subtidal, medium-gray to dark-gray, burrowed, medium-crystalline dolomite intervals that commonly contain *Amphipora* make up the lower part of the major cycles. They shallow upward to supratidal, light-gray, fossil-poor, finely-crystalline dolomite, some with tepee structures. Successive cycles become bathymetrically deeper, and become subsequently thinner to the middle of the sequence and then thicken to the top (**Figure 13**). Gamma radiation increases abruptly at the base of the sequence and gradually decreases upward (**Plate 2a**). Minor fluctuations superimposed on the upward decrease in gamma radiation roughly track the twelve shallowing-upward cycles, with each cycle marked by a subtle decrease at the base and a gradual increase upward.

Gamma Radiation A sharp increase in gamma radiation marks the base of the sequence and a sharp decrease in gamma radiation marks the top of the sequence (**Plate 2A**). Generally, the base of each of the ten cycles that comprise the sequence is marked by a sharp decrease in gamma radiation. Gamma radiation gradually increases upward within the cycles. A gamma-ray spike at the top of cycle 8 is higher (> 80 cps) than any other gamma-ray measurement in the Simonson Dolomite.

Brown Cliff Sequence

The Brown Cliff Sequence is 85 feet thick and comprised of four cycles. It lies above a regionally significant, undulating surface that cuts into the top of the Lower Alternating Sequence. The surface represents a merged LSE and TSE. This lower sequence boundary is directly overlain by an MFS. Recrystallization has largely masked a transgressive lag in the Brown Cliff Sequence above the erosional surface (**Plate 2a**). The Brown Cliff Sequence was probably deposited in more open marine conditions than any of the Simonson Dolomite sequences above or below. It is the first sequence above the Silurian to contain abundant marine fossils such as corals, large stromatoporoids and brachiopods. Though the Brown Cliff Sequence at TMS does not contain large reefs, Devonian reef building peaked during the Givetian worldwide (Webb, 1998). However, in other parts of the Sunnyside basin, Lower Givetian reefs were formed in the Brown Cliff Sequence. Givetian reefs are found in the Limestone Hills, 60 miles northeast of the study area and in the Meadow Valley Mountains, 40 miles south-southeast of the study area (Cedar Strat proprietary measured sections, 1985). Fossils are scarce in sequences between the Brown Cliff and the base of the Guilmette Formation at TMS.

Gamma Radiation The Brown Cliff-Forming Sequence contains more open-shelf fossils and exhibits weaker gamma radiation than any other sequence in the Simonson Dolomite. A sharp gamma-ray leftward inflection at the base of the sequence is regionally correlatable (**Figure 13**). Typically, gamma radiation decreases over fossiliferous, thickly bedded, darker-gray carbonates at cycle bases interpreted to be deposited in more open-shelf conditions. Gamma radiation increases toward cycle tops that consist of thinly-bedded, lighter-gray, fossil-poor carbonates interpreted to be deposited in more restricted to supratidal conditions. Slight increases in overall gamma radiation from base to top follows the same pattern of shallowing-upward cycles in other

parts of the TMS. Thus, the gamma-ray pattern calibrated with fossil distributions suggests that the Brown Cliff-Forming Sequence is a shallowing-upward sequence.

Upper Alternating Sequence

The Upper Alternating Sequence is 285 feet thick and consists of 12 cycles at TMS (**Table 4**). A merged LSE and TSE marks its base (**Plate 2a**). Thin sections display ghosts of intraclasts near the base of the sequence, suggesting a TSE lag. Above the TSE, a pronounced lack of open-shelf fossils and increase in gamma radiation abruptly occurs. Depositional environments of this sequence are similar to the Lower Alternating Sequence. *Amphipora* in the lower, darker part of some cycles suggests intertidal conditions. Lighter-gray, fossil-poor, and the more finely crystalline upper parts of the cycles suggest supratidal conditions.

Gamma Radiation A sharp increase in gamma radiation marks the base of the Upper Alternating Sequence (**Plate 2a**). The general decrease in gamma radiation of each succeeding cycle upward supports the upward-deepening interpretation made from changes in lithology and biofacies (**Figure 13**). Gamma-ray spikes at the tops of internal shallowing-upward cycles may be due to concentrated, wind-blown radioactive detritus. A gamma-ray spike at the top of the sequence at TMS is probably caused by radioactive debris concentrated along the karsted interval.

Regional Simonson Dolomite Unconformity Extensive karsting at the top of the Simonson Dolomite marks the most persistent exposure surface of the Great Basin Devonian section (**Figure 13**). The regional unconformity, marked by karsting hundreds

of feet deep, separates the calcareous Guilmette Formation from the underlying dolomitic Simonson Dolomite. However, the lower Guilmette that lies on the unconformity can be dolomitized as in the Meadow Valley Mountains where the unconformity cuts down into the Simonson Dolomite Brown Cliff Sequence (**Figure 17**). This LSE at the top of the Simonson Dolomite occurs in most outcrops and wells of Devonian rocks in eastern Nevada and western Utah (**Figure 9**).

The light and dark bands of the Upper Alternating Sequence become faded upward toward bleached dolomites below the unconformity. The bleached karsted Simonson Dolomite contrasts sharply with the darker gray limestones of the Fox Mountain and younger sequences on aerial photographs and outcrops. The karsted upper Simonson Dolomite is 55% dark-gray, 30% light-gray, and 15% medium-gray in contrast to 69% dark-gray carbonates in the overlying Guilmette Formation. Pervasively dolomitized, the Simonson Dolomite is easily distinguished from overlying limestone beds of the Guilmette Formation. Furthermore, the karsted, porous, and permeable Simonson Dolomite weathers into partly covered slopes and ledges whereas the Fox Mountain and younger sequences form ledges and cliffs (**Plate 2a, Table 5**).

Evidence for karsting includes karst breccia, drusy dolomite-lined cavities, dolomite crystal coarseness increasing upward, white dolomite spar-filled fractures that widen upward, bleaching, and geopetal structures filled with laminated yellow-gray, silty dolomite (Stop #7, Appendix D). At TMS, some karst cavities in the Simonson Dolomite are filled with Guilmette limestone that suggest that the transgression of the Guilmette sea must have been rapid. Some karst cavities, filled with dolomite breccia, occur as deep as 200 feet below the karst surface at TMS. The basis for separating the Simonson Dolomite from the overlying Guilmette Formation at its Deep Creek Range, Utah, type locality is presented in Chapter 2.

Table 5 Gamma radiation and weathering profile for the lower Guilmette Formation at TMS. For gamma radiation, the average, maximum, minimum, and standard deviation in counts per second are presented. The average weathering for each sequence is presented from most resistant (cliff) to least resistant (covered slope). Note that the Yellow Slope Sequence emits the highest average radiation and that Sequence Dgb2 is more cliffy than the other sequences. The method for determining sequence values is explained in Chapter 2.

SEQUENCE	GAMMA RADIATION Counts Per Second				PROFILE PERCENT(%)			
	AVE	MAX	MIN	STD	CLF	LDG	PCS	CS
SEQUENCE Dgcc	46	53	41	3.3	0	0	22	78
SEQUENCE Dgcf	46	64	36	8.8	0	31	43	26
SEQUENCE Dgb3c	24	41	18	5.4	44	49	7	0
SEQUENCE Dgb3f	38	57	28	7.2	3	92	5	0
SEQUENCE Dgb2	27	34	21	3.3	100	0	0	0
SEQUENCE Dgb1	30	37	24	3.9	60	20	10	10
SEQUENCE Dgbc	26	41	18	4.9	72	23	4	1
SEQUENCE Dgbf	33	57	32	7.3	65	32	2	1
SEQUENCE Dga	43	64	22	10.0	36	46	7	21
SEQUENCE Dga2	32	53	22	6.5	50	40	8	2
SEQUENCE Dga1	49	64	36	6.4	32	42	9	17
YELLOW SLOPE	62	74	48	5.5	0	26	49	25
FOX MOUNTAIN	53	70	37	7.6	13	58	27	2

Key: AVE: Average; MAX: Maximum; MIN: Minimum; STD: Standard Deviation; CLF: Cliff; LDG: Ledge; PCS: Partly Covered Slope; CS: Covered Slope

Guilmette Formation

Of the five TMS Devonian formations, the Guilmette Formation, which is 2,677 feet thick and consists of nine sequences and five subsequences, is the most lithologically variable (**Table 2**). It contains limestone, dolomite, siltstone, sandstone, reefs, and

breccia. For convenience it was divided into two parts. The lower Guilmette Formation is composed of the Fox Mountain and Yellow Slope Sequences and Sequences Dga, Dgb, Dgc, and the upper Guilmette Formation is composed of Sequences Dgd, Dge, Dgf, and Dgg. All nine sequences are present at TMS (**Figure 13**), though the Fox Mountain Sequence is missing at Monte Mountain, and Sequence Dgb lies directly on the Simonson Dolomite at Tempiute Mountain.

Superficially, the Guilmette appears to be a massive carbonate with little internal character. However, a detailed analysis of the Guilmette sequences reveals a unit with enough internal character that it can be used to unravel complex structural relationships. Each sequence contributes an important part of the stratigraphic and structural picture. For example, the thickness of the Fox Mountain sequence suggests where within the Sunnyside basin each section was deposited before they were dislocated by Mesozoic thrusting. Sections with a thick Fox Mountain sequence such as at TMS and the Worthington and Golden Gate ranges were deposited near the center of the Sunnyside basin. In contrast, in the Silver Canyon thrust sheet, the Fox Mountain sequence is absent in the Monte Mountain (TMM) section and very thin at the Down Drop Mountain section deposited on the west edge of the Sunnyside basin. It is also thin in the Meadow Valley section (**Figure 17**) deposited on the east side of the basin.

Some Guilmette sequences are excellent marker beds and help delineate structural features. A good Guilmette marker bed in eastern Nevada is the nonresistant Yellow Slope Sequence (**Plate 2a**). It is easily recognized in the field and on areal photographs. Above the Yellow Slope Sequence are the well-developed, preserved and exposed cycles of Sequence Dga. Their upward shallowing nature helps restore deposition orientation in structurally complex areas.

Sequence Dgb, containing reefs and breccia, is easily identified in the field because it weathers into massive cliffs, whereas Sequence Dga and the rest of the Guilmette weathers into ledges and slopes. The unique concentric nature of the distribution of the Sequence Dgb2 impact breccia constrains restoration of thrust sheets

containing the breccia. Above Sequence Dgb at TMS, the section is mostly shallow-water, cyclic carbonates that are predominantly dolomite with some limestone and minor sandstone beds higher in the section. These post-impact beds also constrain restoration of thrust sheets. Equivalent beds are predominantly quartz sandstone at Monte Mountain and deeper-water, thin-bedded limestone at Tempiute Mountain. The distribution of these post-impact sequences makes little sense without the thrust reconstruction presented in Chapter 5. Therefore, the Guilmette sequences in the Timpahute Range 30' X 60' quadrangle hold important keys to understanding this part of the Sevier fold-and-thrust belt. **Figure 18** illustrates the locations of 142 Guilmette outcrops that cover 89.07 square miles in the Timpahute Range quadrangle.

In this study, the lower Guilmette at TMS is described in more detail than other parts of the Devonian because it contains the impact breccia of Sequence Dgb2. Therefore, an understanding of the depositional setting immediately before and after the emplacement of the distinctive carbonate breccia is a primary focus of this study. Also, the shallowing-upward cycles in the lower Guilmette are unaltered (not pervasively dolomitized), well-exposed, and were overlooked in previous studies. They provide an unusual opportunity to study carbonates and carbonate environments. They provided the opportunity to test the usefulness of surface gamma-ray logs in cycle and sequence analysis. As a result, they were used to calibrate surface gamma-ray patterns in other sections throughout the Sunnyside basin. Microfacies analysis of thin sections from the lower Guilmette cycles and sequences provided additional detail and further calibrated the TMS cycles and sequences (**Plate 5**). Therefore, TMS is the reference section of Devonian sequences in the Sunnyside basin.

This section summarizes and compares the characteristics of the lower Guilmette sequences. These characteristics consist of general descriptions of weathering profile, color, gamma-ray patterns, lithology and texture, sequence and cycle thicknesses, fossil occurrences, and thickness patterns of cycles and are graphically presented in Tables 5-8 and Figures 20-22. Percentages were calculated from the number of measured increments

of a particular characteristic divided by the total number of measured increments in the sequence (Chapter 2). Following this section summarizing the lower Guilmette sequences, a description of each Guilmette sequence is presented. Descriptions of each cycle within each sequence can be found in Appendix B.

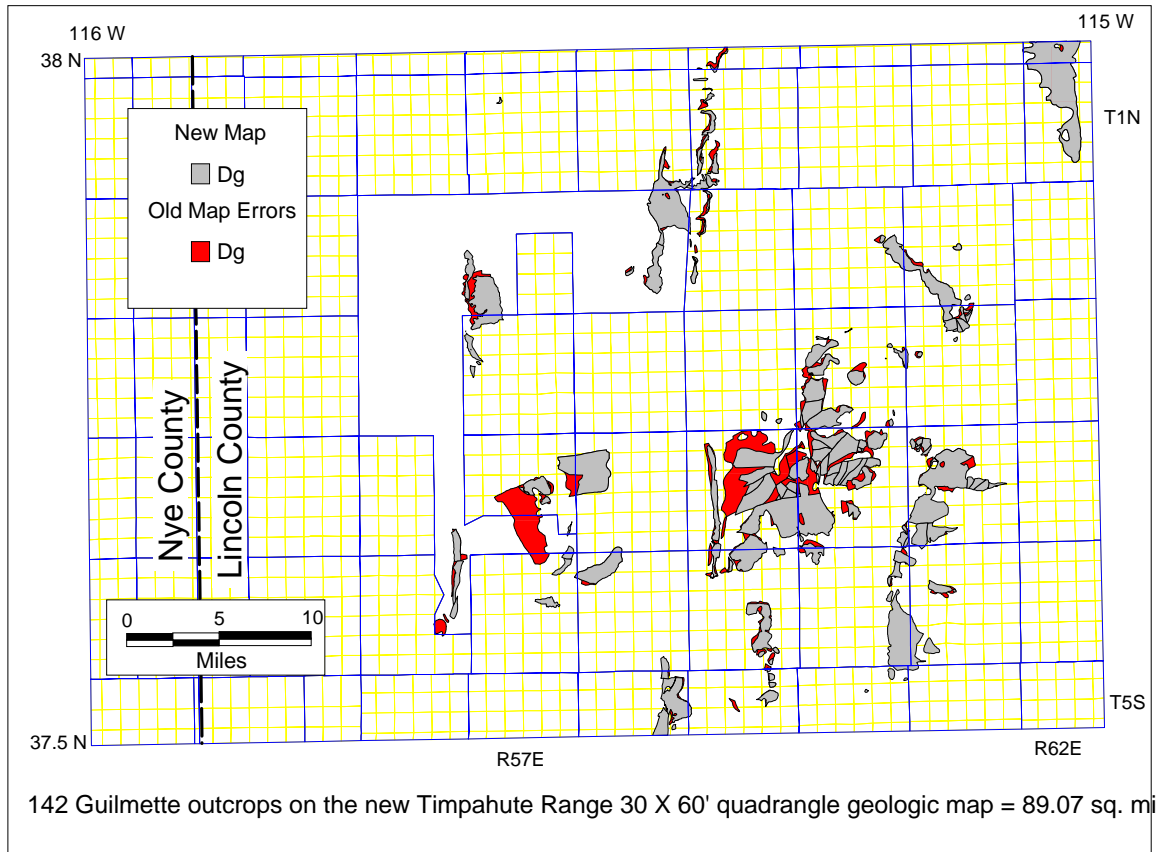


Figure 18 Distribution of Guilmette Formation outcrops on the new Timpahute Range quadrangle geologic map. Areas erroneously mapped as Guilmette on the old geologic map are marked in red. Degrees N latitude and W longitude are marked at the corners of the map.

Weathering Profile

Whereas the 135-foot-thick Fox Mountain Sequence is mostly cliffs (71%) and ledges, nearly 75% of the 182-foot-thick Yellow Slope Sequence weathers into covered and partly-covered slopes. Where present, the resistant Fox Mountain forms prominent ledges and cliffs (**Plate 2a, Table 5**). Ledges and cliffs make up 82% of the 395-foot-thick Sequence Dga, 95% of the 420-foot-thick Sequence Dgbc (reef core), and 97% of the 302-foot-thick Sequence Dgbf (reef flank). Sequence Dgc forms a 45-foot-thick slope above Dgbc and at Dgcf, forms a 188-foot-thick interval of ledges, partly covered slopes, and covered slopes above Dgbf (**Figure 4**). **Table 5** summarizes the weathering profiles of the lower Guilmette sequences.

Lithology and Texture

Table 6 summarizes thicknesses and lithologies of the lower Guilmette Formation sequences. Except the Yellow Slope Sequence and Sequence Dga1, limestone predominates in the lower Guilmette sequences. The percent of limestone in each sequence increases upward from the Yellow Slope Sequence to Sequence Dgc. The distribution of dolomite in the lower Guilmette sequences is significant because most of the dolomite occurs as finely-crystalline caps on the shallowing upward cycles. Sequences that contain a greater proportion of supratidal dolomite caps, such as the Yellow Slope Sequence, contain more dolomite than those composed mostly of open-marine carbonates such as Sequences Dgb1, Dgb3f, and Dgcc that contain almost no dolomite.

Table 6 Thicknesses and gross lithologies of the lower Guilmette Formation sequences. The method for determining the gross lithology percent is explained in Chapter 2. Sequence Dgb3c is thicker than Sequence Dgb3f. The greater thickness could have been caused by accelerated growth and reef development at Dgb3c and lack of reef development at Dgb3f. Data in the table indicate that the percent of dolomite decreases upward from the Yellow Slope Sequence.

SEQUENCE	THICKNESS in FEET	LITHOLOGY PERCENT (%)				
		LS	DOL	SS	BRC	SLTS
SEQUENCE Dgcc	45	100	0	0	0	0
SEQUENCE Dgcf	188	72	20	3	0	5
SEQUENCE Dgb3c	228	90	10	0	0	0
SEQUENCE Dgb3f	97	100	0	0	0	0
SEQUENCE Dgb2	179	0	0	0	100	0
SEQUENCE Dgb1	26	100	0	0	0	0
SEQUENCE Dgbc	420	52	5	0	43	0
SEQUENCE Dgbf	302	41	0	0	59	0
SEQUENCE Dga2	145	75	25	0	0	0
SEQUENCE Dga1	250	50	50	0	0	0
SEQUENCE Dga	395	59	41	0	0	0
YELLOW SLOPE	182	39	58	3	0	0
FOX MOUNTAIN	135	93	7	0	0	0
KEY: LS: LIMESTONE; DOL: Dolostone; SS: SANDSTONE; BRC: BRECCIA; SLTS: SILTSTONE						

A histogram of dolomite percentages in each cycle of the lower Guilmette Formation illustrates the distribution of dolomite in the section (**Figure 19**). Lithologies vary from 100% dolomite in Yellow Slope Sequence Cycle 7 and Sequence Dga1 Cycle 5, to 100% limestone in Fox Mountain Sequence Cycle 4 (**Table 6**). Dolomitization of 58% of the Yellow Slope Sequence is probably associated with early peritidal

dolomitization. This finely-crystalline stratal dolomite contrasts with the medium- to coarsely-crystalline pervasive dolomite of the underlying Simonson Dolomite that is probably related to the regional unconformity at the top of that formation. The occurrences and significance of dolomite at TMS are discussed in more detail in later in this chapter.

Five sets of cycles in which the percentage of dolomite decreases upward occur in the lower Guilmette sequences (**Figure 19**). They are Fox Mountain Sequence Cycles 1 through 4, Yellow Slope Sequence Cycles 3 through 5, Yellow Slope Sequence 9 through Sequence Dga1 Cycle 3, Sequence Dga1 Cycles 5 through 11, and Sequence Dga2 Cycles 2 through 4. Two sets of cycles in which the percentage of dolomite increases upward include Yellow Slope Sequence Cycles 5 through 7 and Sequence Dga2 cycles 4 through 7. Repeated patterns of dolomite content in the histogram suggest that most of the dolomite in the reference section be related to selective early dolomite diagenesis at cycle tops. Most of the dolomite forms finely-crystalline stratal dolomite caps on shallowing upward cycles. These occurrences of dolomite contrast to later dolomitization associated with unconformities, faulting and porous zones.

Other than a small percent of sandstone in the Yellow Slope Sequence and in Sequence Dgcf, lower Guilmette sequences lack sandstone. Siltstone is a minor constituent in Sequence Dgcf, but is lacking in the other lower Guilmette sequences.

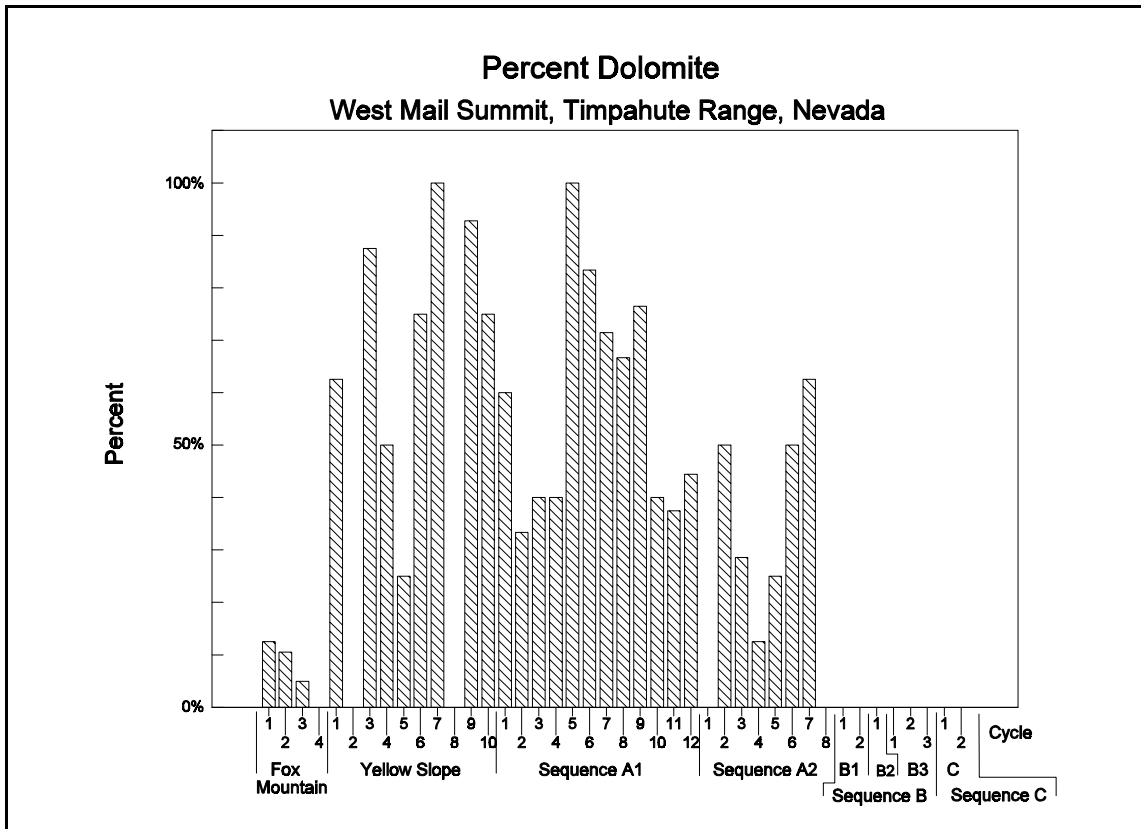


Figure 19 Histogram of percent dolomite within each cycle of the lower Guilmette Sequences at TMS where Sequence Dgb3 is a stromatoporoid reef illustrates the abundance of dolomite in the Yellow Slope and Dga1 Sequences and the lack of dolomite in the Fox Mountain, Dgb, and Dgc Sequences.

Table 7 summarizes the depositional textures of the lower Guilmette Formation Sequences. Texture coarsens upward from 72% mudstone in the Yellow Slope Sequence to 2% mudstone in the overlying Sequence Dgbc. Packstone predominates in five of the 13 lower Guilmette sequences listed in **Table 7**. Wackestone predominates in four of the sequences, mudstone in three of the sequences and boundstone in two of the sequences.

Color

Table 7 summarizes the colors of the lower Guilmette sequences. The percent of dark-gray carbonates increases upward from 55% in the Simonson Dolomite to 69% in the Fox Mountain. In contrast, only 21% of the Yellow Slope is dark gray. However, the percent of dark-gray carbonates increases upward again from 36% in Sequence Dga to 45% and 62% in Sequence Dgbc and Dgbf respectively. Light-gray carbonates increase upward from 35% in Sequence Dga to 43% in Sequence Dgb reef core but decrease to 9% in Sequence Dgb reef flank. Medium-gray carbonates decrease from 29% in Sequence Dga to 12% Sequence Dgbc and 28% Dgbf.

Percentage of Limestone

A histogram of the percentage of limestone in each cycle illustrates the higher concentration of calcium carbonate in the Fox Mountain Sequence and in Sequences Dgb and Dgc with respect to the other sequences (**Figure 20**). Three sets of cycles in which the percent limestone increases upward occur. They are Fox Mountain Sequence Cycles 1 through 4, Yellow Slope Sequence Cycle 7 through Sequence Dga1 Cycle 4, and Sequence Dga1 Cycle 5 through Sequence Dga2 Cycle 5. One set of cycles shows an upward decrease in percentage of limestone from Sequence Dga2 Cycle 4 through Sequence Dga2 Cycle 7. Sequences Dgb and Dgc are all limestone except local non-stratal dolomite associated with fractures and porous zones. The cyclic pattern of the percentage of dolomite and the percentage of limestone suggests that dolomitization at the tops of shallowing-upward cycles occurred penecontemporaneously with deposition (**Figure 21**). Because dolomite-rich zones at the top of cycles occur at the same interval in other sections, it is likely that the zones were selectively dolomitized before Mesozoic thrusting and Cenozoic extension of the eastern Great Basin.

Table 7 Color and texture of lower Guilmette Formation sequences expressed as percent of the sequence. The table indicates the unique abundance of pale yellow-brown rocks in the Yellow Slope Sequence and the muddy nature of the Yellow Slope Sequence and Sequence Dgc.

SEQUENCE	COLOR PERCENT (%)				TEXTURE PERCENT (%)				
	LGY	MGY	DGY	PYB	MU D	WAC	PAC	GRN	BND
SEQUENCE Dgcc	71	0	29	0	100	0	0	0	0
SEQUENCE Dgcf	42	40	18	0	74	36	0	0	0
SEQUENCE Dgb3c	86	7	7	0	0	2	3	5	90
SEQUENCE Dgb2	14	18	68	0	2	0	98	0	0
SEQUENCE Dgb1	0	50	50	0	0	21	79	0	0
SEQUENCE Dgbc	43	12	45	0	0	2	53	2	43
SEQUENCE Dgb3f	2	42	53	3	0	10	5	17	68
SEQUENCE Dga2	12	38	50	0	24	39	33	4	0
SEQUENCE Dga1	48	25	27	0	31	47	17	5	0
SEQUENCE Dga	35	29	36	0	28	44	23	5	0
YELLOW SLOPE	21	14	21	44	72	14	5	6	3
FOX MOUNTAIN	0	31	69	0	13	82	4	1	0
KEY: LGY: Light Gray; MGY: Medium Gray; DGY: Dark Gray; PYB: Pale Yellow Brown; MUD: Mudstone; WAC: Wackestone; PAC: Packstone; GRN: Grainstone; BND: Boundstone									

Fossils

Table 8 summarizes the occurrences of fossils in the lower Guilmette Formation. Fossil content changes from predominantly corals at the top of the Simonson Dolomite to brachiopods and gastropods in the Fox Mountain Sequence. Ostracodes, calcispheres and stromatolites commonly occur in the Yellow Slope Sequence. *Amphipora* and corals are

more common in Sequence Dga. Tabular and bulbous stromatoporoids are more common in Sequence Dgb. Sequence Dgc is heavily burrowed, contains abundant gastropods, and contrasts sharply with the *Amphipora*-bearing beds of Sequence Dgd in the upper Guilmette Formation.

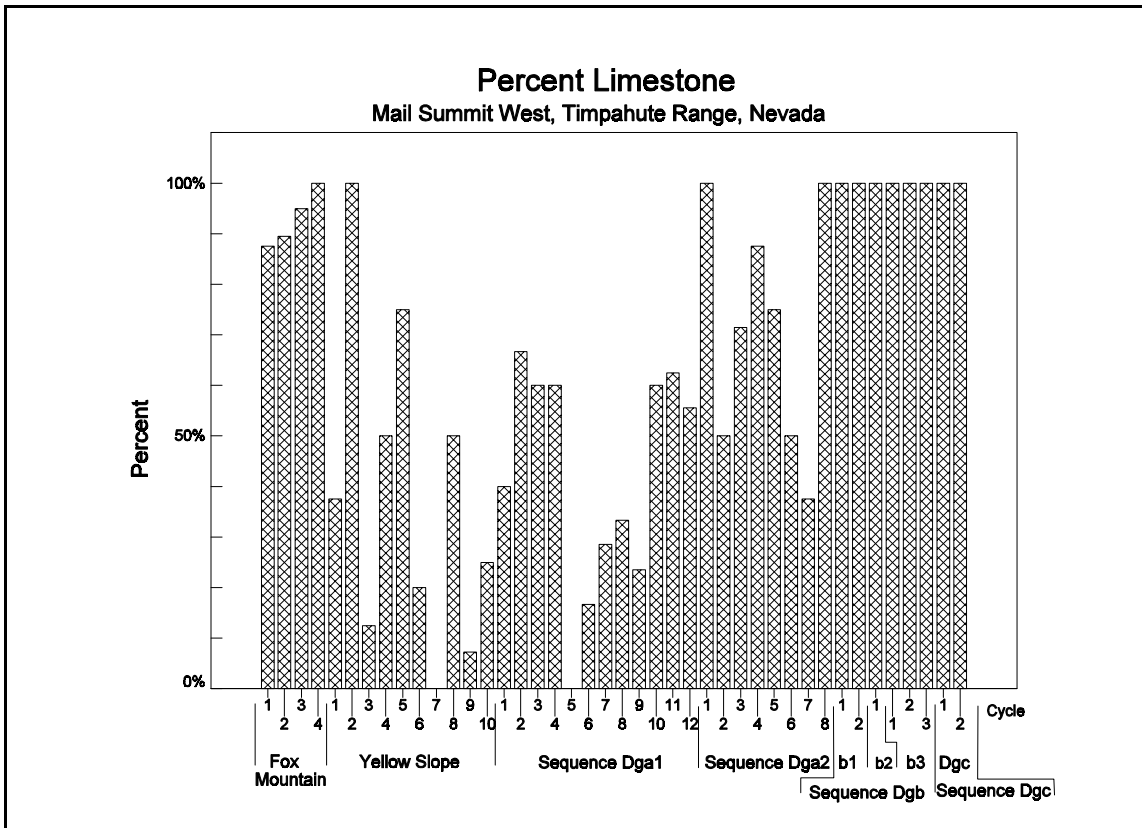


Figure 20 Histogram of percent limestone within each cycle of lower Guilmette sequences at TMS where Sequence Dgb3 is a stromatoporoid reef. The highest percentages of limestone occurs in the Fox Mountain Sequence and in Sequence Dgb.

Bedding

Bedding in the five basal sequences of the Guilmette Formation varies from massive for the sedimentary breccia and reef in Sequence Dgb to stromatolitically

laminated for the Yellow Slope Sequence. Sequence Dga is characterized by prominent shallowing-upward cycles whereas the Fox Mountain Sequence is characterized by subtle shallowing-upward cycles. Burrowed limestone beds help distinguish Sequence Dgc from the adjacent sequences.

Table 8 Fossil occurrences in the lower Guilmette sequences at TMS ranked by abundance. Data in the table indicate that the abundance of fossil assemblages with an affinity for open-marine conditions increased from the Yellow Slope Sequence to Sequence Dgb3 at TMS.

Formation Sequence	<i>Amphipora</i>	Bulbous Stromatoporoids	Tabular Stromatoporoids	Corals	Ostracodes	Brachiopods	Burrows	Stromatolites	Calcspheres	Echinoderms	Gastropods	Barren
Dgcc	N	N	N	R	R	R	C	N	N	N	C	C
Dgb3f	C	A	C	C	R	C	R	R	R	R	R	R
Dgb3c	C	A	A	A	R	C	R	R	R	C	R	R
Dgb2	C	C	C	C	R	C	R	R	R	N	R	R
Dgb1	C	C	R	C	R	C	R	R	R	N	R	R
Dgbf	C	A	A	A	R	C	R	R	R	R	R	R
Dgbc	C	A	A	A	A	R	C	R	R	R	R	R
Dga2	C	C	R	C	R	C	C	R	R	N	C	R
Dga1	C	C	R	C	R	C	C	R	R	R	C	R
YS	N	N	N	R	C	R	R	C	C	N	R	C
FM	R	R	N	C	R	C	C	R	R	C	C	R

A = Abundant, C = Common, R = Rare, N = None
 FM = Fox Mountain, YS = Yellow Slope,

Cycles

Four major shallowing-upward cycles and two minor cycles compose the Fox Mountain Sequence. Three of the cycles are limestone with a dolomite cap. It appears that open-marine limestones truncate intertidal carbonates. Perhaps serving as a dolomite cap of a large-scale cycle involving the Fox Mountain Sequence, the Yellow Slope Sequence is made of at least ten shallowing-upward cycles. Because open-marine fauna is lacking in the Yellow Slope Sequence, it is likely that the bases of the cycles are no deeper than intertidal. However, the tops of the cycles contain mudcracks filled with quartz sand grains characteristic of supratidal conditions. Two of the cycles are capped by very fine-grained quartz sandstones.

The lower parts of most of the 20 cycles of Sequence Dga contain open-marine fauna. Most of the cycles are capped by laminated, unfossiliferous dolomite. Only two minor shallowing-upward cycles occur below the sedimentary breccia in Sequence Dgb1. The sedimentary breccia or Dgb2 and overlying reef or Dgb3c form the rest of Sequence Dgb in the reef core measured section. All of Sequence Dgb appears to have been deposited in open-marine conditions. Karsting at the top of the Sequence Dgb3c marks an LSE between Sequences Dgb and Dgc. A pale red paleosol occurs at the unconformity and in some karst cavities 20 feet below the unconformity. Geopetals of laminated dolomitic siltstone within some karst cavities have the same attitude as strata above and below suggesting they were deposited before Mesozoic tilting. Burrowed, slope-forming limestone of Sequence Dgc lies above Sequence Dgb and marks another sequence of restricted-marine conditions.

Cycle Thicknesses

A histogram of thickness and content of cycles of the lower Guilmette Formation Sequences (**Figure 21**) provides insight into the nature of bundling of the cycles. It reveals a pattern in which groups of cycles thicken upward from the base of the Fox Mountain Sequence to Cycle 10 of Sequence Dga (UTK1, UTK2, UTK3, and UTK4). An exception to the upward thickening pattern is an upward-thinning pattern from Yellow Slope Sequence Cycle 3 to Yellow Slope Sequence Cycle 8 (UTN1). Above Sequence Dga Cycle 10, two groups of cycles thin upward to the top of Sequence Dgc. One group begins with Sequence Dga1 Cycle 10 (UTN2) and the other group begins with Sequence Dga2 Cycle 7 (UTN3). Admittedly, the trend lines marking bundles of upward thickening and thinning cycles are subjective and may be grouped and interpreted differently by other workers. If bundle thicknesses are related to sequence boundaries, perhaps they could be changed to reflect that relationship. However, the histogram show that there is no relationship.

An upward increase in cycle thickness or upward thickening probably represents an increase of accommodation space caused by an increase in the rate of relative sea-level rise. A comparison of the percentage of dolomite in **Figure 19** with the set of upward thickening Fox Mountain Sequence Cycles 1 through 4 illustrates that the percentage of dolomite decreases as cycle thickness increases upward. As the rate of relative sea-level rise increases, more accommodation space becomes available for open-marine carbonate deposition. Apparently this leaves less time for the formation of supratidal dolomite caps before the next transgression.

A major facies shift occurs at the base of the Yellow Slope Sequence with a greater percent (62%) of dolomite in Cycle 1 than any of the Fox Mountain cycles. The sequence is mostly composed of a set of upward-thinning cycles in which dolomite predominates. An upward decrease in cycle thickness or upward thinning suggests an upward decrease in accommodation space cause by a decrease in the rate of a sea-level

rise. A slower rate of relative sea-level rise should provide a greater proportion of supratidal dolomites at the top of shallowing-upward cycles.

Two other facies shifts marking sequence boundaries are seen in the histogram of cycle thicknesses (**Figure 21**). Much of Sequence Dga1 is composed of a set of upward thickening cycles (UTK4) in which the percent of dolomite also increases. Another facies shift occurs at the base of Sequence Dga2, which is mostly a set of upward thinning cycles (UTN2). A greater facies shift occurs at the base of Sequence Dgb1. Sequence Dgb and Dgc cycles never shallow enough to preserve supratidal finely-crystalline stratal dolomite caps.

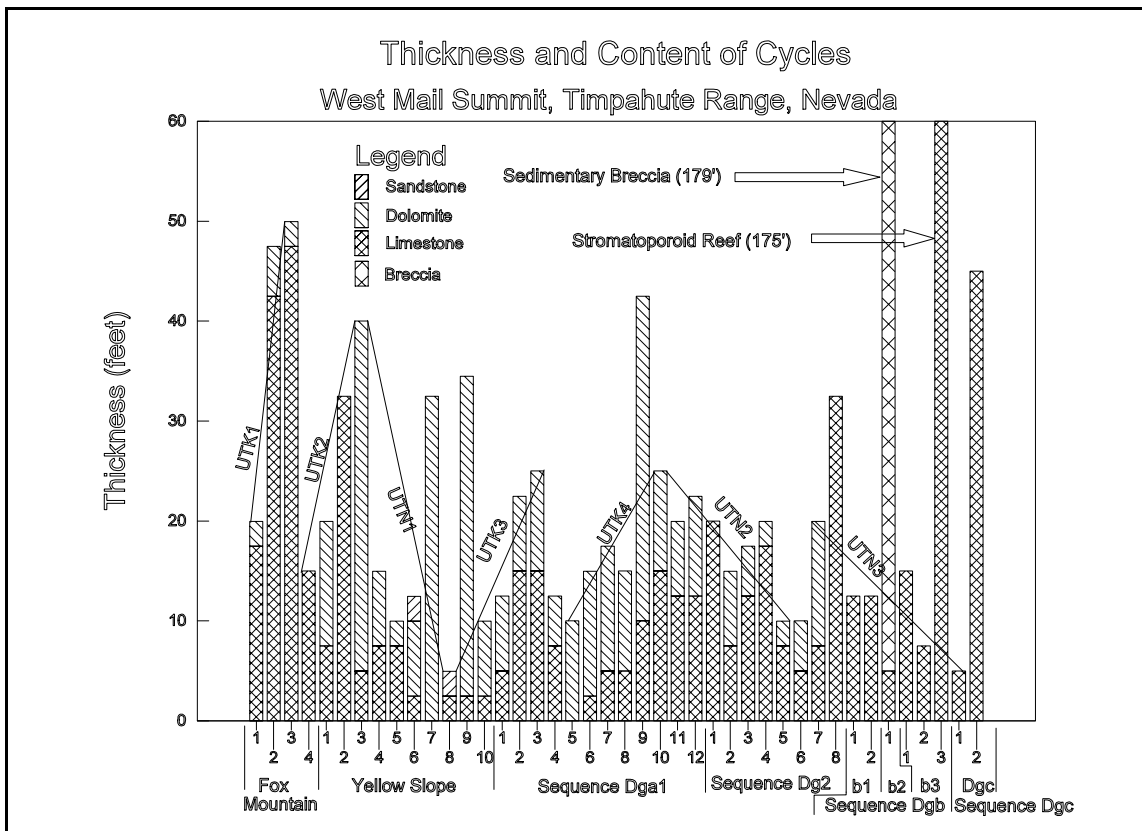


Figure 21 Histogram of cycle thickness and content of lower Guilmette Formation suggest possible upward thickening (UTK) and upward thinning (UTN) trends at TMS where Dgb3c is a stromatoporoid reef. The sedimentary breccia (Dgb2) and reef (Dgb3c) were truncated at 60 feet to emphasize the other cycles in the lower Guilmette Sequences.

Gamma Radiation

Table 5 summarizes the gamma radiation and weathering profile for lower Guilmette Formation sequences. Gamma radiation increases from about 38 CPS over the Simonson Dolomite Upper Alternating Sequence to an average of 53 CPS over the Fox Mountain Sequence. The radiation continues to increase to an average of 62 CPS over the Yellow Slope Sequence and then decreases to an average of 43 CPS over Sequence Dga and an average of 26 CPS over Sequence Dgbc or 33 CPS over Sequence Dgbf. Karsting at the top of the Sequence Dgb3 reef marks an LSE that merges with a TSE at the base of Sequence Dgc. Bioturbated and silty Sequence Dgc forms a regional rightward gamma-ray inflection that can be correlated with outcrops and wells throughout eastern Nevada and western Utah. Over Sequence Dgc, average gamma radiation increases to 46 CPS.

Guilmette Sequences

The general characteristics and features of the lower Guilmette sequences were described above. All nine Guilmette sequences are described individually and in detail in this section. Again, emphasis is on the lower Guilmette sequences. Additional descriptions of each cycle and sequence are presented in Appendix B and **Plate 2a**.

Each sequence is composed of one or more cycles. Though cycle boundaries are marked by unconformities or hiatuses, almost no facies shift occurs at the cycle boundaries. On the other hand, major facies shifts mark sequence boundaries. Regionally correlatable gamma-ray log patterns accompany the sequence boundaries. However, gamma-ray patterns of cycles are not regionally correlatable.

Under each sequence described in this section a description may include color, texture, weathering profile, fossils, cycle thicknesses and patterns, and other features.

Next, the gamma-ray patterns of the sequence are described. Finally, for some sequences, a brief interpretation of depositional conditions is presented.

Fox Mountain Sequence

Overlying the regional unconformity at the top of the karsted, light brown-gray Simonson Dolomite is the transgressive 135-foot-thick cliff-forming Fox Mountain Sequence comprising four cycles that consist of medium dark-gray limestone and (**Figure 13** and **Plate 2a**). It represents the first occurrence of a significant amount of undolomitized limestone on the eastern Nevada Devonian shelf. Where the Fox Mountain Sequence is missing, by erosion or by nondeposition on adjacent topographic highs as at other measured sections, younger sequences overlie the Simonson Dolomite unconformity (see correlation charts that compare Timpahute Mountain with Mail Summit sections in the discussion in this chapter and in Chapter 7).

An abrupt deepening of the Fox Mountain Sequence above the Simonson Dolomite unconformity is illustrated by the relative sea-level curve in **Figure 13** and **Plate 2a**. The sequence is composed of four shallowing-upward cycles, mentioned above and described in Appendix B. The lower parts are composed of open-marine, medium dark-gray, burrowed, brachiopod, echinoderm, gastropod lime wackestones and upper parts of supratidal, medium-gray to light-gray, laminated dolomites. The lower two cycles have more open-shelf limestone than the upper two cycles. A regional LSE at the top of the Fox Mountain is marked with a pale-red siltstone paleosol, desiccation cracks, and a change from open-marine to restricted-marine fossils. As **Figure 13** shows, gamma radiation generally mirrors the relative sea-level curve. Open-shelf limestones of Fox Mountain cycle bases emit less gamma radiation than their supratidal dolomite tops.

Summary of Descriptions Tables in the previous section summarize some characteristics of the Fox Mountain Sequence. **Table 5** shows that the Fox Mountain sequence weathers into mostly ledges with some partly covered slopes. The table also shows that the gamma radiation over the Fox Mountain is lower than over the Yellow Slope Sequence but higher than the rest of the lower Guilmette sequences. Generally, the cycle bases are more resistant than the cycle tops. The weathering histogram in **Plate 2a** illustrates the weathering profile of the ledgy Fox Mountain Sequence. **Table 6** shows that the sequence is 135 feet thick and is predominantly limestone. **Table 7** shows the wackestone texture and the dark-gray appearance of the Fox Mountain Sequence. Texture descriptions were refined by thin-section analysis (Appendix C).

Brachiopods, crinoids, and gastropods typically occur at the base of the Fox Mountain cycles whereas the cycle tops generally lack fossils (see Appendices B and C). *Amphipora* is rare (**Table 8**).

Fox Mountain, a Guilmette Formation Sequence The controversy over whether to place the Fox Mountain Sequence in the Simonson Dolomite or Guilmette Formation was presented in Chapter 2. As explained in Chapter 2, the Fox Mountain Sequence is different from the Fox Mountain Formation proposed by Sandberg et al. (1997). They propose that their Fox Mountain Formation be composed of two members. Their lower member is composed of karsted dolomite that grades downward to the upper alternating member of the Simonson Dolomite. Their upper member is composed of open-marine limestone. I place the lower contact at the Simonson unconformity sequence boundary. The karsted interval below the unconformity may be the same as the lower dolomitized and karsted Fox Mountain member of Sandberg et al. (1997). Because this karsted interval is a diagenetic front, it has no definite boundary with the unaffected part of the Upper Alternating Sequence of the Simonson Dolomite. At TMS, the Fox Mountain Sequence is composed of four upward shallowing cycles. The lower parts of the cycles

contain crinoids, corals, and brachiopods deposited in open-marine conditions. The upper parts of the three lower cycles consist of finely-crystalline stratal dolomite deposited in supratidal conditions. My upper sequence boundary is marked by desiccation cracks and a thin exposure interval or paleosol on the uppermost Fox Mountain Sequence. Strata above this unconformity are rich in restricted-marine to supratidal fossils such as ostracodes and stromatolite bed. Sandberg et al. (1997) include part of the lower Yellow Slope Sequence into their Fox Mountain Formation. I regard the Fox Mountain Sequence as lower Guilmette Formation because: 1) the most pronounced regional sequence boundary in the Devonian occurs at the top of the Upper Alternating Sequence of the Simonson Dolomite; 2) the regional exposure surface separates fine-grained Fox Mountain limestones from underlying coarsely-crystalline, karsted, and pervasively dolomitized Simonson Dolomite carbonates; 3) the inconsistent occurrence of the Fox Mountain Sequence, which may be hundreds of feet thick in some sections near the middle of the Sunnyside basin and absent in others on the edges of the basin (**Figure 13**; see correlation charts in the discussion near the end of this chapter and in Chapter 7); and, 4) the pronounced geomorphic expression of the Fox Mountain cliffs (where present) above karsted Simonson Dolomite slopes and ledges are easily recognized in the field and on aerial photographs.

Fox Mountain Sequence Cycles The lower three Fox Mountain Sequence cycles are capped by laminated, light-gray dolomite that represents supratidal conditions (**Figure 22**). Cycle 1, a 20-foot-thick cycle, begins in open-shelf conditions and ends in restricted-shelf conditions. The lower 27 feet of Cycle 2 are composed of medium-dark limestone that contains an open-shelf fauna. A sharp decrease (leftward inflection) in gamma radiation marks the base of Cycle 2. Cycle 3, the thickest of the shallowing-

upward cycles (50 feet), forms a complete (i.e., an open-marine base and supratidal cap) cycle as do Cycles 1 and 2. The lower parts of the cycles were probably deposited in partly restricted open-shelf conditions whereas their upper parts were deposited in peritidal conditions.

An erosional surface and missing facies (i.e., the supratidal cap is missing) suggest that the top of Cycle 4 was truncated by erosion before deposition of the Yellow Slope Sequence. Average thickness of the cycles is 34 feet (**Table 6**). Cycle thickness increases from 19 feet for Cycle 1 to 49 feet for cycle 2 and 52 feet for cycle 3. A histogram of cycle thicknesses illustrates the upward cycle thickening (**Figure 22, Plate 2a**). If the cycles are of similar duration and if no strata are missing, then the histogram suggests an upward increase of accommodation space or an increase in the rate of relative sea-level rise. This increase in the rate of relative sea-level rise is repeated at least four times, to the middle of Sequence Dga (UTK1-4, **Figure 21**). A relative sea-level lowering at the top of the Fox Mountain Sequence could have resulted in erosion of the top of Cycle 4 (base of UTK2, **Figure 21**). In other sections, karst cavities occur tens of feet below the Fox Mountain unconformity. In Chapter 9, it is suggested that an isopach map of the depth of karsting could provide a rough estimate of paleotopography at the end of Fox Mountain time.

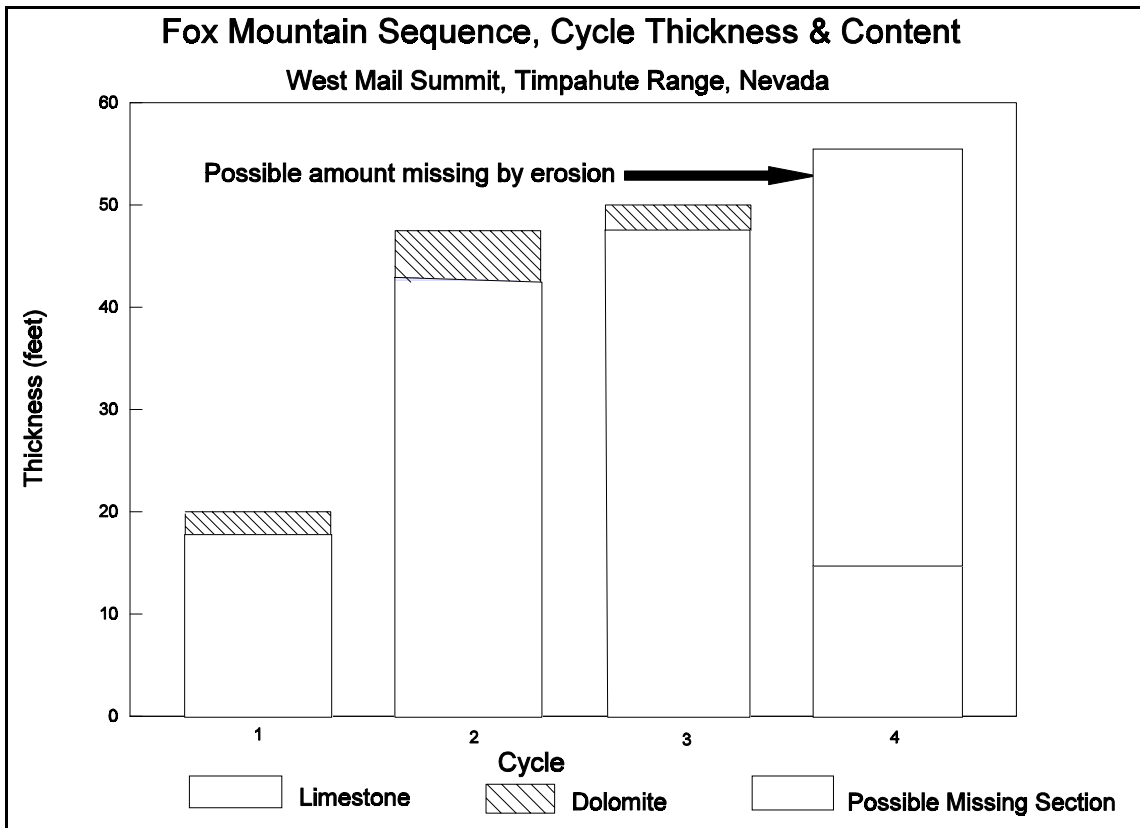


Figure 22 Histogram of cycle thicknesses and content, Fox Mountain Sequence shows a pattern of upward thickening cycles and could be a clue to the amount of section missing at the unconformity at the top of the sequence.

Distinguishing features of the Fox Mountain Sequence The Fox Mountain can be distinguished from earlier Devonian rocks in the study area because it is the first mainly limestone formation above the Ordovician Eureka Quartzite, except the limey Ordovician Ely Springs Dolomite in the Silver Canyon thrust sheet. Also, the Fox Mountain limestones are finely crystalline whereas the underlying Simonson Dolomite is medium to coarsely crystalline. Fox Mountain Sequence Cycles can be distinguished from cycles of younger Guilmette sequences by their resistance to weathering and distinctive fauna (**Table 4**). Two cycles in the cliff-forming Fox Mountain Sequence typically contain crinoids. Crinoids are rare in the rest of the Guilmette Formation. Crinoids occur in the Fox Mountain Sequence of the study area as a thin bed in Cycle 3 and as Middle

Devonian two-holed crinoid columnals in Fox Mountain Cycle 2. However, crinoid columnals do occur locally above the Dgb2 breccia in the Hiko and Pahrangat ranges. Crinoids occur throughout the Guilmette equivalent rocks in the Reveille Range, Sec. 35, T2N R51½ E. Elrick (1986) reported crinoids in the Guilmette in the Goshute Range, T30N R68E. Besides crinoids, the highest known occurrence of the distinctive brachiopod *Stringocephalus* occurs in the Fox Mountain Sequence. It also occurs in the Simonson Dolomite Brown Cliff Sequence. Because of the affinity of *Stringocephalus*-bearing beds, Hurtubise (1989) and Tschanz and Pampeyan (1970) assigned the Fox Mountain limestone to the Simonson Dolomite.

Fox Mountain cycles are thicker than some Sequence Dga cycles (34 feet vs. 20 feet). Fox Mountain cycles thicken upward. They are more radioactive than the underlying Simonson Dolomite but are less radioactive than the overlying Yellow Slope Sequence. Changes in radioactivity occur at the two regional unconformities that bound the Fox Mountain sequence. Besides the sharp increase in radiation, a paleosol that partly fills mudcracks at the top of the Fox Mountain separates the sequence from the overlying Yellow Slope Sequence at TMS and in the Worthington Range. The Fox Mountain unconformity cuts out most of the Fox Mountain at Dondrop Mountain, 16 miles south-southeast of Monte Mountain, and all of the Fox Mountain Sequence at Monte Mountain and the Meadow Valley Mountains (45 miles southeast of Hiko).

Gamma Radiation Average gamma radiation over the sequence is 53 CPS with a maximum of 70, a minimum of 37, and a standard deviation of 7.6 (**Table 5**). In contrast, average gamma radiation over the upper Simonson Dolomite is 41 CPS with a maximum of 61, a minimum of 25, and a standard deviation of 8.7. Intervals of higher gamma radiation reflect concentrations of windblown siliciclastic detritus. Typically, sand grains that occur with siltstone at the top of some upward shallowing cycles are frosted and trough-cross bedded. Desiccation cracks provide evidence that the beds were periodically

subaerially exposed. Devonian supratidal flats in Nevada could have concentrated wind-blown siliciclastics. A potential source area could have been the Antler forebulge uplift, parts of which were subaerially exposed during lower Guilmette time (Chapters 2 and 8).

Other possibilities for increased windblown siliciclastic detritus include a change in prevailing wind direction or a more narrow shelf. However, no evidence of a change in the ocean-land shape resulting in a change of prevailing wind direction is found. Because the Guilmette is more widespread than the underlying Simonson Dolomite, it seems unlikely that the exposed shelf suddenly became reduced with time. Most likely the radioactive dust is from the Antler forebulge, the same area that eventually served as the source for mature quartz sandstones in the upper Guilmette Formation and was probably the source for the “Oxyoke Formation” sandstone below.

Interpretation of the Fox Mountain Sequence The Fox Mountain at Mail Summit was probably deposited in a topographic low near the center of the Sunnyside basin where marine limestone predominated. Other sections in the study area that lie near the center of the basin include the Golden Gate and Worthington ranges. In contrast, sections deposited on the edges of the Sunnyside basin either lack the Fox Mountain sequences such as at Monte Mountain or an unusually thin Fox Mountain Sequence as in the Meadow Valley Mountains (**Figure 17**).

Downdrop Mountain and Monte Mountain both lie within the Silver Canyon thrust sheet. The structural model presented in Chapter 5 and Devonian paleogeography presented in Chapter 7 suggests that the Silver Canyon thrust sheet was deposited on the west side of the Sunnyside basin and west of Tempiute Mountain. Thin Fox Mountain Sequence at Downdrop Mountain and no Fox Mountain Sequence at Monte Mountain suggest an eastward thickening of the Fox Mountain Sequence toward the center of the Sunnyside basin.

Similarly, thin Fox Mountain Sequence in the Hiko Range and in the Meadow Valley Mountains suggest an eastward thinning of the Fox Mountain Sequence (**Figure 17**). Probably more of the Fox Mountain Sequence was cut out by the Fox Mountain Sequence unconformity on the flanks of the Sunnyside basin than in the center of the basin. However, it is possible that more Fox Mountain Sequence was deposited in the center of the basin than on the basin flanks. Thin sections from the lower parts of TMS Fox Mountain cycles contain open-marine fauna including echinoderms, brachiopods, and corals (Appendix C). Therefore, the lower parts of Fox Mountain Sequence cycles in the center of the Sunnyside basin are interpreted to be deposited in open-shelf conditions (Appendix B). The upper parts of the cycles are fossil-poor, burrowed, and are composed of stratal finely-crystalline dolomite. They are interpreted to be deposited in low-intertidal conditions.

Yellow Slope Sequence

The Yellow Slope Sequence, 182 feet thick at TMS and comprising 10 cycles, is easily identified on aerial photographs and in the field (**Table 4, Figure 23, Plate 2a**). It erodes into a conspicuous, yellow slope between dark-gray cliff- and ledge-forming sequences above and below. It is predominantly (44%) pale-yellow brown (**Table 7**). The supratidal, silty dolomite cycles of the Yellow Slope Sequence mark an abrupt facies shift from predominantly open-shelf limestones of the Fox Mountain (**Plate 2a**). The TSE at the base of the Yellow Slope Sequence merges with a mud-cracked LSE at the top of the Fox Mountain Sequence. **Figure 13** illustrates the decrease in the rate of relative sea-level rise and the increase in gamma radiation at the sequence boundary (**Plate 2a**).

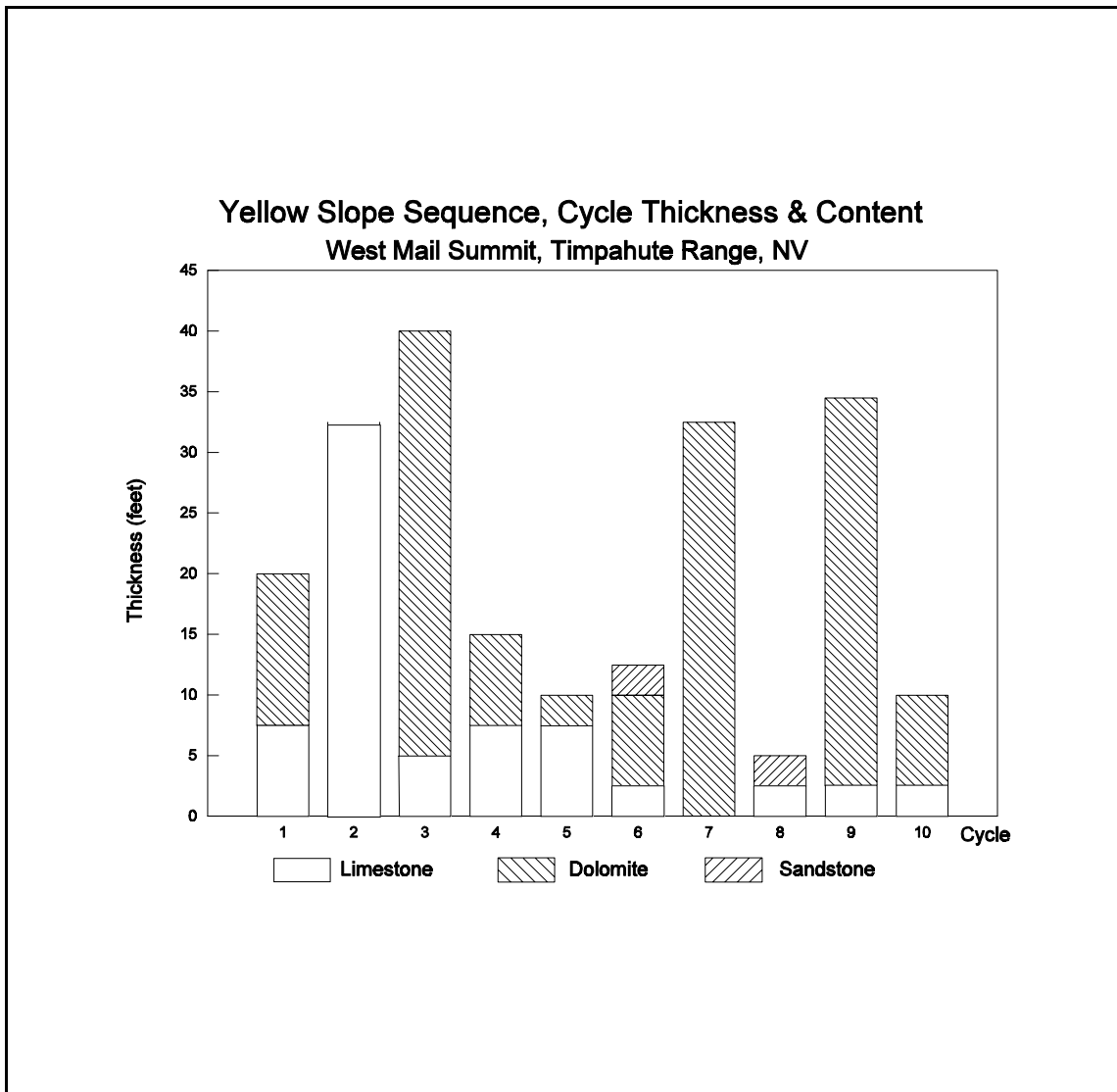


Figure 23 Histogram of cycle thickness and content, Yellow Slope Sequence. Most of the sequence is set of upward thinning cycles. Limestone content also decreases upward.

Another significant facies shift occurs at the sequence boundary that marks the top of the Yellow Slope Sequence. The TSE at the base of Sequence Dga represents the first major transgression within the Guilmette. Here medium-dark-gray, burrowed, intraclast, brachiopod, pelletal lime bioclastic wackestone overlies medium-gray, laminated, lime mudstone. Barren, pale yellow-brown to light-gray, silty, laminated dolomudstone lies

just below the mudstone whereas coral lime wackestone lies just above the wackestone. As seen on **Plate 2a** and as discussed in the section on gamma radiation, a sharp leftward inflection on the gamma-ray profile marks the Dga1 transgression.

Marker Beds The Yellow Slope Sequence is a prominent marker bed of the lower Guilmette Formation in southeastern Nevada (**Table 4, Plate 2a**). Early location of this marker bed helped in mapping and planning measured sections. At TMS, it is comprised of ten shallowing-upward cycles presented in more detail in the section on lithology and texture hereafter (**Figure 23**).

Although tops of other shallowing-upward cycles in other sequences are marked by yellow-gray, silty, laminated dolomudstone, beds of large, digitate stromatolites occur only in Yellow Slope Sequence Cycle 2 at TMS. Cycle 2 stromatolite beds serve as prominent regional marker beds within the Yellow Slope Sequence, as noted by Hurtubise (1989). He chose the base of a stromatolite bed as the base of Guilmette Formation as presented in Chapter 2. However, several stromatolite beds occur in many sections and at different levels above the base of the Yellow Slope Sequence. Therefore, although columnar stromatolites serve as excellent marker fossils for the Yellow Slope Sequence, the base of a stromatolite bed serves as a poor boundary between mappable units. Much of the sequence is laminated, but the stromatolites in Cycle 2 are uniquely diagnostic at TMS. Columnal stromatolites are thought to have formed by mucilaginous surfaces of cyanobacterial mats selectively trapping sediments (Ginsburg, 1991). At TMS, they form dark-gray, cyanobacterial boundstones with some columns reaching three to four feet high. Ostracodes and calcispheres are more abundant in the Yellow Slope Sequence than in any other Guilmette sequence (MI-316, Appendix C). The presence of the unique stromatolites alone is not adequate evidence for an intertidal zone or restricted circulation conditions because stromatolites can be found in normal marine settings (Ginsburg, 1991). However, no open-marine fossils such as crinoids, corals, or

stromatoporoids have yet been detected in the Yellow Slope Sequence, which contains desiccation cracks at the tops of finely-crystalline stratal dolomite caps. Therefore, the sequence is interpreted to represent restricted subtidal to supratidal conditions. The lower parts of these cycles contrast with open-marine conditions of the lower parts of cycles in adjacent sequences, because they lack open-marine fossils.

Cycle Thicknesses Thickness patterns reveal that the average thickness of the ten Yellow Slope cycles is 18 feet in contrast with 34 feet for average cycle thickness in the underlying Fox Mountain and 21 feet for average cycle thickness in the overlying Sequence Dga1. Generally, cycles at the lower and upper parts of the sequence are thicker, and their bases were deposited in deeper water than cycles in the middle of the sequence. A histogram of cycle thickness versus cycle number shows that the first three Yellow Slope Sequence Cycles thicken upward (**Figure 23**). Thickening upward suggests an increase in accommodation space that in turn reflects an acceleration of relative sea-level rise (UTK2, **Figure 21**). The last three cycles, combined with the first three cycles of Sequence Dga, show another upward thickening trend (UTK3, **Figure 21**). Hematite/goethite/limonite(?) stains in fractures and stylolites have been detected in seven of the ten cycles (Appendix C).

Lithology, Texture, Erosional Profile, and Cycles The Yellow Slope Sequence can be readily differentiated from the underlying Fox Mountain and the overlying Dga1 Sequence based on lithology and texture. Yellow Slope Sequence Cycle 1 is a shallowing-upward cycle of limestone with a dolomite cap. It contains abundant ostracodes and rare large calcispheres in contrast to the brachiopod wackestone of the underlying Fox Mountain Sequence.

Most of the Yellow Slope Sequence eroded into covered slopes (25%) and partly-covered slopes (49%). Only 26% of the sequence forms resistant ledges (**Table 5**).

Seven of the Yellow Slope Sequence Cycles are capped by supratidal, fossil-poor, laminated, silty and sandy, pale yellow-brown to yellow-gray dolomudstone. Several exhibit desiccation cracks (**Plate 2a**). Nine of the ten cycles have a transgressive limestone base that is commonly marked by a leftward inflection in the gamma-ray log. These transgressive limestones are medium- to dark-gray, intertidal, calcisphere lime mudstone. Thin (less than 5 feet thick), yellow-gray, fine-grained, dolomitic, quartz sandstone interbeds cap the sixth and eight cycles in the section and contain intertidal ostracode lime mudstones (MI-316, Appendix C).

These thin beds of sandstone are the first occurrence of conspicuous quartz grains above the “Oxyoke Formation,” as noted by Chamberlain and Warne (1996). Concentrations of quartz siltstone and sandstone in the Yellow Slope Sequence are probably due to wind-blown detrital grains trapped by moisture on peritidal flats. Except sparse, scattered quartz grains, the next occurrence of quartz sandstone in the section is at the tops of several shallowing-upward cycles in Sequence Dgd, nearly 1,000 feet above the Yellow Slope Sequence (**Plate 2a**).

Gamma Radiation The Yellow Slope Sequence emits higher gamma radiation than other Devonian sequence at TMS (**Plate 2a**). Its average gamma radiation is 62 CPS (**Table 5**). It ranges from a minimum of 48 to a maximum of 74 CPS. This is possibly due to wind-blown silt and sand.

The standard deviation of 5.5 CPS is lower than that of the adjacent sequences. The standard deviation radiation of the Sequence Dga of 10.0 CPS and that of the Fox Mountain is 7.6 CPS. At the base of the sequence, gamma radiation increases sharply above the LSE at the top of the Fox Mountain Sequence. An equally sharp decrease in gamma radiation occurs at the TSE marking the base of Sequence Dga above. **Plate 2a** illustrates these changes in gamma radiation.

Yellow Slope Sequence Interpretation Desiccation cracks, stromatolites, and abundances of ostracodes suggest that the Yellow Slope Sequence was deposited in shallow water. Most of the Yellow Slope Sequence is composed of stratal finely-crystalline dolomite caps interpreted to be deposited in supratidal conditions. On a larger scale, the Yellow Slope Sequence is a shallow-water, dolomite cap on the shallowing-upward Fox Mountain Sequence with the Dga1 Sequence boundary marking the overlying transgression.

Though the thickness of the Fox Mountain varies greatly depending on its position in the Sunnyside basin, the thickness of the Yellow Slope Sequence remains nearly constant throughout the basin. It is 182 feet thick at TMS, 140 in the Golden Gate and Worthington ranges, and 150 at Monte Mountain. Apparently the Fox Mountain unconformity leveled the Devonian paleogeography making it possible for the supratidal Yellow Slope Sequence to be distributed uniformly over much of the Sunnyside basin. The uniform thickness of the Yellow Slope Sequence even persisted over the Monitor-Uinta arch, an east-west positive feature that affected deposition of all the Devonian sequences (Chapter 7). Forming a vast sabkha that extended from western Utah to central Nevada (120 miles unrecovered) and most of the length of Nevada (250 miles), the Yellow Slope Sequence was deposited in similar conditions as the Sevy Dolomite. The main differences are that the Yellow Slope cycle bases are typically limestone, some cycles contain fossils including ostracodes, and two cycles are capped by thin sandstone units.

Sequence Dga

Sequence Dga is 395 feet thick and contains 20 shallowing-upward cycles grouped into two subsequences in the TMS, but the subdivision was not always recognized in other sections (**Figure 9**). Sequence Dga1 is predominantly dolomite and

Sequence Dga2 is predominantly limestone (**Table 6, Plate 2a**). The sequence boundary at the base of Sequence Dga is marked by a conspicuous facies shift from predominantly yellow-weathering ostracode-bearing dolomite to cycles of multifauna coral, *Amphipora*, stromatoporoid lime wackestones and light-gray dolomicrites. Another facies shift from multifauna coral, *Amphipora*, stromatoporoid wackestones to single-fauna stromatoporoid wackestones and a regional gamma-ray spike marks the top of the sequence.

Gamma Radiation and Weathering Profile A regionally correlatable leftward gamma-ray inflection marking a TSE over an LSE separates the sequence into two subsequences Dga1 and Dga2. A regionally correlatable slight decrease in gamma marks the top of the sequence. Average gamma radiation over Sequence Dga is 43 CPS (**Table 5**). It decreased from 49 CPS over Sequence Dga1 to 32 CPS over Sequence Dga2.

Sequence Dga becomes more resistant upward from the Yellow Slope Sequence that is 74% covered and partly covered slopes (**Table 5**) to Sequence Dgb that is 95% cliffs and ledges. Sequence Dga1 lies between the covered and partly covered slopes of the Yellow Slope Sequence below and the cliffs and ledges of Sequence Dgb above. It is 74% cliffs and ledges whereas Sequence Dga2 is 90% cliffs and ledges (see weathering histogram on **Plate 2a**).

Color, Texture, and Lithology **Table 7** summarizes the color and texture of the lower Guilmette sequences at TMS. The average dolomite content decreases from 58% in the underlying Yellow Slope Sequence to 41% in Sequence Dga and to 5% in Sequence Dgb above (**Table 6**). Limestone predominates in Sequence Dga (59%).

Subsequences Dga1 and Dga2 also reflect this upward decrease in dolomite content. Sequence Dga1 is 50% dolomite whereas Sequence Dga2 is only 25% dolomite (**Figure 19**).

Typical Sequence Dga Cycle The lower part of a typical shallowing-upward cycle in Sequence Dga is a coral-stromatoporoid open-shelf, medium dark-gray limestone above a TSE/LSE. It grades upward to a supratidal, laminated, light-gray dolomudstone facies bounded by an LSE at the top. *Amphipora* is an important constituent between the basal limestone and the dolomite cap.

Sequence Dga Cycles Depending on the amount of strata removed at the next TSE, some cycle tops are composed of light-gray, laminated dolomudstone. Eight of the 12 cycles in Sequence Dga1, but none of the cycles in Sequence Dga2, shallow up to light-gray, rarely mud-cracked, laminated dolomicrite facies. Either a TSE\LSE truncated supratidal strata or transgression occurred before the shallowing-upward sequence was completed in the partial cycles. Incomplete cycles in Sequence Dga2 are probably due to general deepening, and cycles only shallowed to intertidal environments before the next transgression. However, a histogram of cycle thickness for Sequence Dga1 and Dga2 illustrates that after Sequence Dga1 Cycle 9, cycles get thinner upward until Sequence Dga2 Cycle 6 (**Figure 21**). This thinning upward suggests an upward decrease in accommodation space caused by a decrease in the rate of relative sea-level rise. A similar decrease in accommodation space or a decrease in the rate of relative sea-level rise occurs from Sequence Dga2 Cycle 7 to Sequence Dgb3 Cycle 2 reef (see UTN2 and UTN3 in **Figure 21**).

Dolostone and Cycle Thicknesses A histogram of the dolomite percentage for each cycle of Sequences Dga1, Dga2, and Dgb1 provides some interesting patterns (**Figure 19**). **Figure 24** illustrates two sets of thickening upward cycles in Sequence Dga1. Cycles 1, 2, and 3 thicken upward. **Figure 19** illustrates that the percent of dolomite in these cycles progressively decreases upward. Cycles 5 through 9 also thicken upward and the percent of dolomite decreases upward. The percent of dolomite continues to decrease upward to Sequence Dga2 Cycle 1 where no dolomite is preserved. The uppermost cycles in Sequence Dga1 and most of the Cycles in Dga2 form a set of upward thinning cycles (UTN2 on **Figure 21**). Dolomite percent decreases in Cycles 2 to 4 and increases from 4 to 7. This increase in percentage of dolomite is abruptly truncated at Sequence Dga2 Cycle 8, above which no supratidal dolomite occurs in cycles of Sequences Dga or Dgb. Sequences Dgc and Dgd lack shallowing-upward cycles with supratidal caps such as those in Sequence Dga1. An increase in dolomite thickness from the base of Sequence Dga to Cycle 9 is partly caused by an increase in accommodation space resulting from an increase in the rate of relative sea-level rise (UTK4 **Figure 21**).

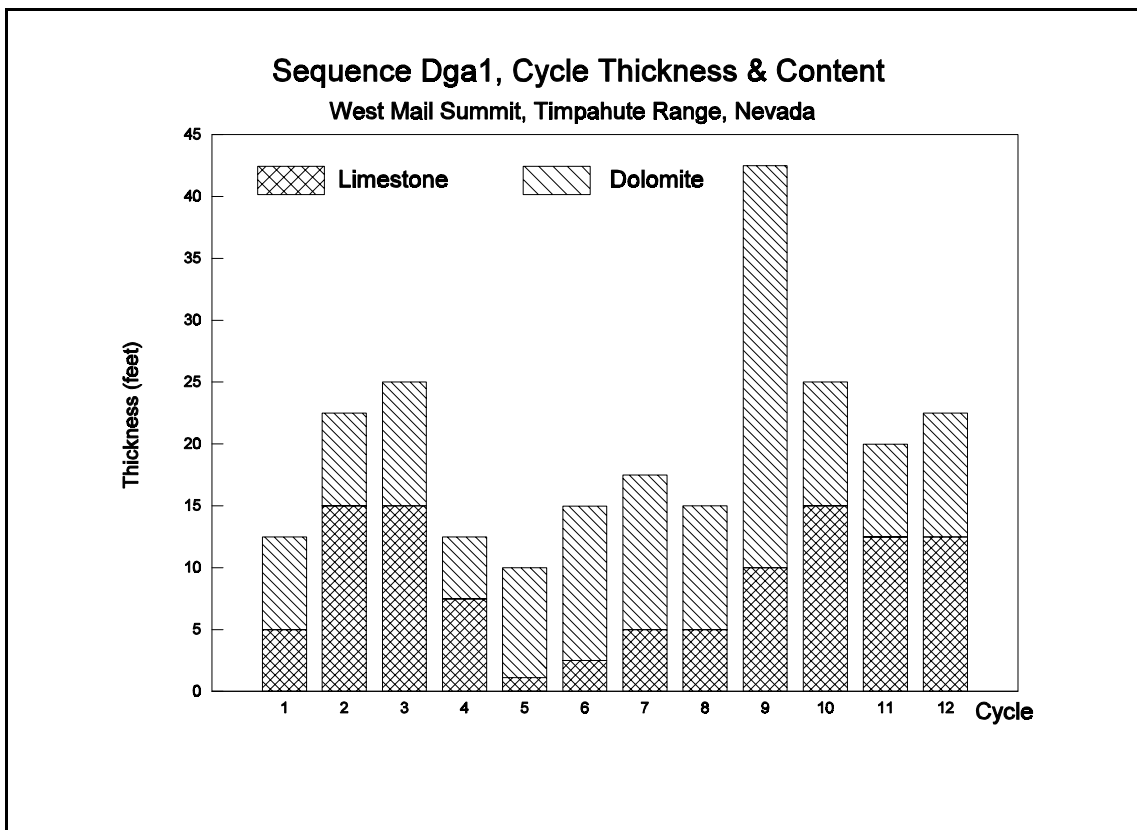


Figure 24 Histogram of cycle thickness and content, Sequence Dga1. Two sets of upward thickening limestone cycles with dolomite caps characterize the sequence (cycles 1-3 and cycles 5-10). The first set is part of the upward thickening trend that begins with cycle 8 in the Yellow Slope Sequence (UTK3 in **Figure 21**) and the second is UTK3 in **Figure 21**. Cycles 11 and 12 are part of the upward thinning trend that continues to cycle 6 in Sequence Dga2 (UTN2 in **Figure 21**).

A decrease in the rate of sea-level rise resulted in less accommodation space and thinner cycles upward in Sequence Dga1 Cycle 10 through Sequence Dga2 Cycle 6 (UTN2 **Figure 21**). Less dolomite was preserved as dolomite caps in Sequence Dga because of the facies shift from predominantly supratidal environment to more open-marine environment at the top of the Yellow Slope Sequence. A cycle thickness increase from Sequence Dga1 Cycle 5 to Sequence Dga1 Cycle 10 reflects another increase in the rate of relative sea-level rise. However the percent of dolomite decreases upward suggesting that, although accommodation space was available, deepening occurred faster

than carbonates could build up to supratidal conditions, or at least more deposition in open-marine conditions took place than in supratidal conditions. As a result, less supratidal dolomite is preserved at the top of the cycles. This pattern of decreasing amounts of dolomite preserved as dolomite caps continues upward to Sequence Dga2 Cycle 8 where no dolomite is preserved. This upward decrease in dolomite content may represent a local, deepening event superimposed on a general shallowing-upward pattern (UTN2 and UTN3 **Figure 21**).

Microfacies analyses and megascopic fossils show an overall deepening of cycles within Dga (compare photomicrograph descriptions for Wilson's (1975) microfacies in Appendix C with **Plate 5**). This deepening includes the sedimentary breccia Dgb2 and stromatoporoid reef Dgb3. Supratidal dolomite cycle caps of equivalent age (i.e., within the same sequence) are found shoreward in the Sunnyside basin. Correlative beds could have been the source for light yellow-gray, laminated dolomite clasts within the overlying Sequence Dgb2 sedimentary breccia. These dolomite caps are not preserved in beds next to the Dgb2 breccia at TMS. A thin lens of breccia associated with the overlying Dgb2 breccia sequence was emplaced or liquidized as a single bed and will be discussed later in this chapter.

Subsequence Dga1 Subsequence Dga1 is 250 feet thick and is composed of 12 cycles (**Plate 2a, Figure 24**). A conspicuous facies shift separates the ostracode- and calcisphere-bearing Yellow Slope Sequence from the coral-, stromatoporoid-, and brachiopod-bearing Sequence Dga1 (**Figure 23**). Generally, the lower parts of the sequence cycles are composed of open-shelf, medium dark-gray to medium-gray, burrowed stromatoporoid, coral, brachiopod, *Amphipora* lime wackestone. Supratidal, light-gray, laminated dolomudstones with rip-up clasts cap most of the Sequence Dga1 cycles. **Plate 2a** illustrates the cycle thicknesses and contents. With few exceptions, Sequence Dga1 cycles exhibit a general upward-deepening trend from supratidal Yellow

Slope Sequence Cycles to open-shelf Sequence Dga2 cycles and a general upward decrease in gamma radiation from the underlying Yellow Slope Sequence (**Figure 13**).

A sharp leftward gamma-ray inflection marks the TSE/LSE at the base of the sequence. Within the sequence, each cycle begins with a sharp leftward gamma-ray inflection at the limestone base followed by a gradual increase in gamma radiation and dolomite content to the cycle top (**Plate 1a, Figure 13**).

Subsequence Dga2 Subsequence Dga2 is 145 feet thick and comprised of eight cycles. A TSE/LSE at the base of Sequence Dga2 separates equal amounts of dolomite and limestone strata containing common open-shelf fossils of Sequence Dga1 from the overlying predominantly limestone strata characterized by abundant open-shelf fossils (**Table 6, Plate 2a**). **Figure 25** illustrates cycle thicknesses and composition of Sequence Dga2. A thin (1-2 foot) bed of distinctive Dgb2 carbonate breccia occurs 20 feet above the base of Sequence Dga2 and 392 feet from the top of Dgb2. It will be discussed later.

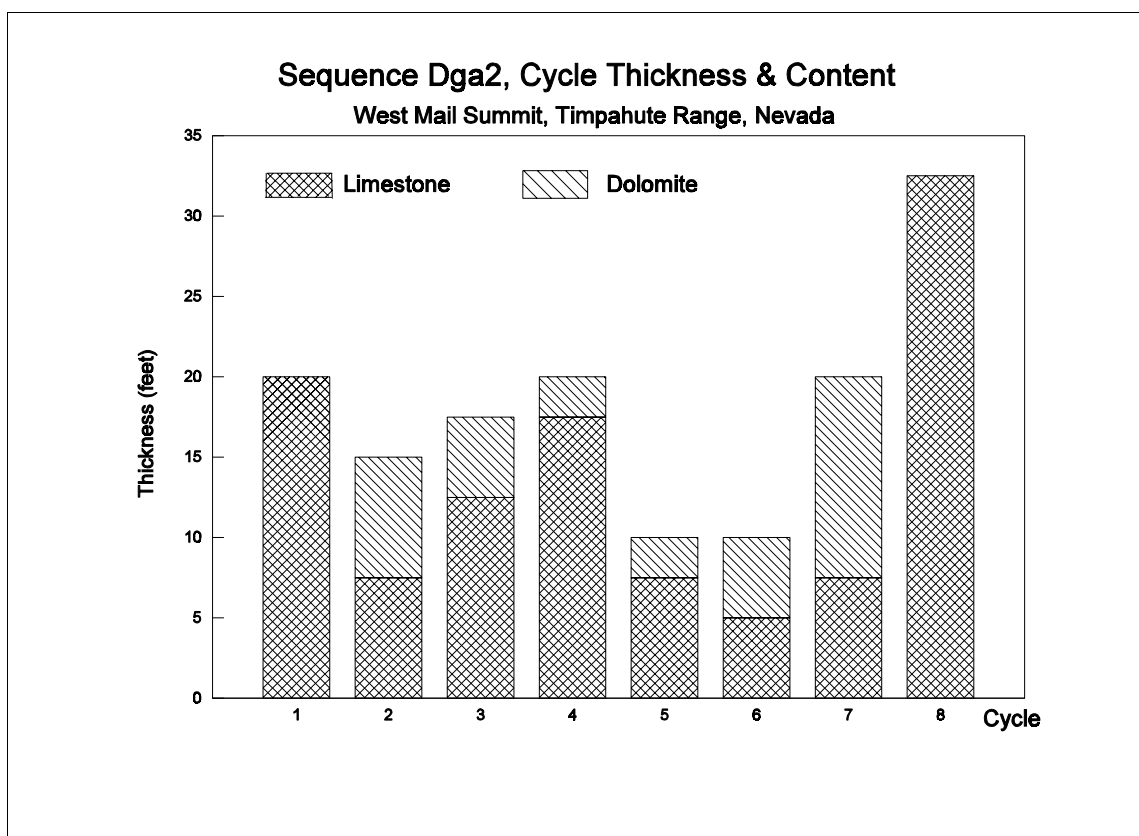


Figure 25 Histogram of cycle thickness and content of Sequence Dga2 shows two sets of possible upward thickening cycles from cycle 2 to 4 and from cycle 5 to 8. However, cycle thicknesses and contents are probably random. Except for cycle 7, dolomite content tends to decrease as the cycles become thicker. Compare with **Table 9** which shows the percent of dolomite increasing from cycle 4 to cycle 7. The only dolomite from cycle 8 to Sequence Dgd is late diagenetic dolomite associated with fractures or porous parts of the Dgb2 breccia matrix.

Each shallowing-upward cycle in Sequence Dga2 shows a more pronounced change from the base to the top than in underlying Guilmette sequences. Generally, the base of each cycle is marked by an open-shelf, medium dark-gray to medium-gray, stromatoproid, coral, brachiopod lime wackestone to packstone. Seven of the eight

cycles are capped with subtidal, laminated, commonly burrowed, light yellow-gray, fossil-poor dolomite (**Plate 2a**). Two cycles are capped by an extensively burrowed, medium-gray, lime fossil wackestone of a restricted-shelf environment.

A regionally correlative abrupt decrease in gamma radiation occurs at the base of Sequence Dga2 (**Figure 13**). The weak gamma radiation is interpreted to be caused by carbonate dilution of radioactive detritus in open-shelf conditions. Gamma radiation continues to decrease upward to a distinctive gastropod lime wackestone at the top of Sequence Dga2, above which gamma radiation abruptly increases.

Sequence Dgb

Though Sequence Dgb can be correlated to more remote outcrops such as the Egan Range (**Figure 9**), a sedimentary breccia, Subsequence Dgb2 restricted to the Timpahute region, divides the 301 foot-thick sequence into three subsequences, Dgb1, Dgb2 and Dgb3 at TMS (**Plate 2a**). **Figure 26** illustrates cycle thicknesses and composition of Sequence Dgb and overlying Sequence Dgc cycles where Sequence Dgb3 is a stromatoporoid reef. The distinctive sedimentary breccia (Dgb2) forms the middle part of Sequence Dgb. It provides an excellent marker bed in the Timpahute area. At TMS, Subsequence Dgb2 consists of an apparently single graded bed of sedimentary packstone megabreccia. It contains huge clasts up to hundreds of feet long at the base and mudstone at the top (Warme et al., 1993). Employing the grain-size classification of Blair and McPherson (1999), grain size decreases from “blocks” and “slabs” in the lower part to clay in the upper part. A thin layer of the megabreccia occurs tens of feet below the graded bed near the base of Sequence Dga2 at or just above the Dga2 gamma-ray marker bed at TMS and at other localities. It is described in a later section. Two shallowing-upward cycles below the sedimentary megabreccia comprise Sequence Dgb1. Two thinner cycles and the thick stromatoporoid reef cycle above the megabreccia comprise

Sequence Dgb3 (**Plate 2a**). Prominent rightward gamma-ray inflections at the base and top of Sequence Dgb are regionally correlative (**Figure 9, Figure 13**). Sequence Dgb emits less radiation, as low as 21 CPS, than any other sequence in the TMS. Except for the gamma-ray spike between Sequences Dgb2 and Dgb3, radiation increases steadily from the base to the top of Sequence Dgb (**Plate 2a**).

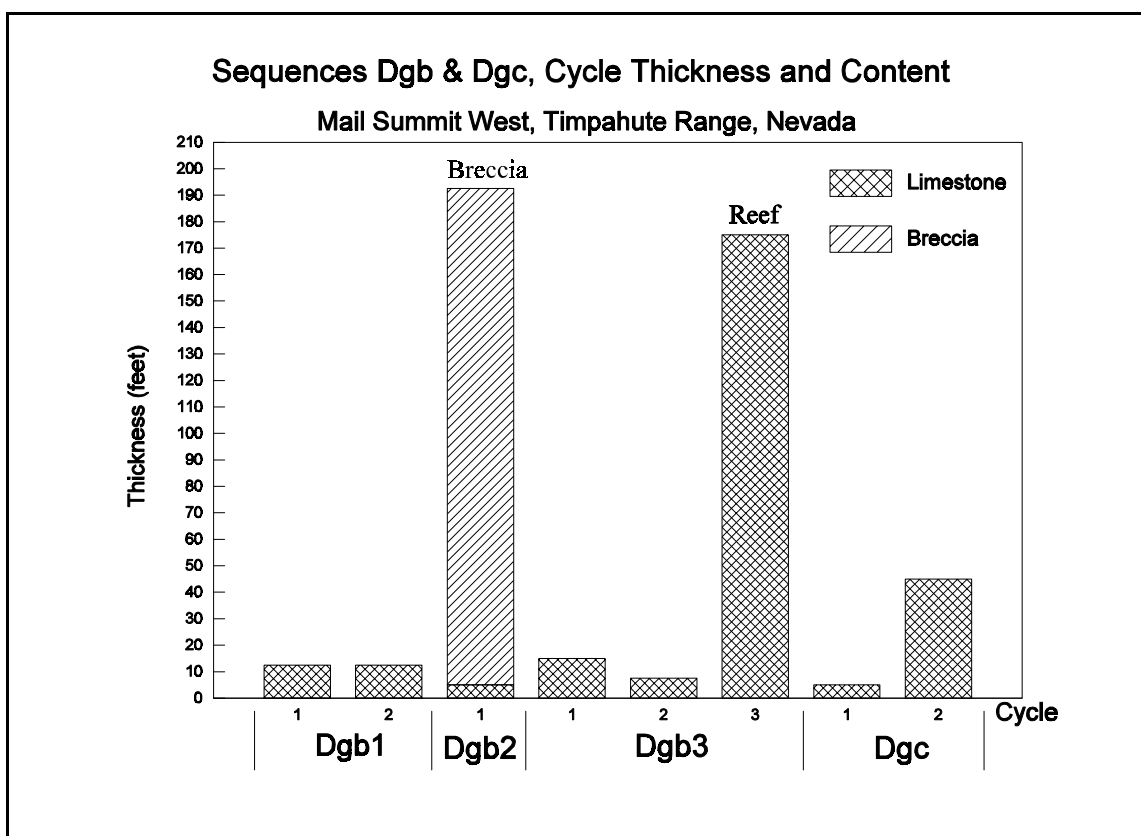


Figure 26 Histogram of cycle thickness and content of Sequences Dgb and Dgc where Dgb3 is a stromatoporoid reef at TMS. The reef and Dgb2 breccia comprise most of Sequence Dgb and only two Sequence Dgc cycles overlap the reef. Cycles in the Sequence Dgb2 interval were obliterated by the Dgb2 breccia event and were replaced with breccia of the shattered cycles.

Weathering Profile **Table 5** and **Figure 28** summarize the weathering profile of

Dgbc and Dgbf. Most of the cliffy Dgbc profile is due to the 179-foot-thick Sequence Dgb2 breccia that forms 100% cliffs. It is also due to the 215-foot-thick Sequence Dgb3 measured on the reef core that forms 93% cliffs and ledges.

Lithology, Color and Texture **Figure 26** illustrates the thickness and composition of cycles in Sequence Dgbc and **Figure 27** illustrates the thickness and composition of cycles in Dgbf. **Table 6** and **Figure 28** summarize the lithologic components of the sequences.

Color of Sequence Dgb is summarized in **Table 7**. Sequence Dgb2 is another useful marker bed in the Timpahute region. Its dark gray cliff typically separates dark and light-gray cyclic beds of Sequence Dga and light-gray, cliff-forming reefy beds of Sequence Dgb3c. The lateral variability in color could be a pitfall to correct mapping and interpretation. For example, beds equivalent to the light gray reef are medium gray about a mile away and could be mistaken for a different sequence.

Significant lateral textural variations in Sequence Dgb occur between the two TMS sections. Textures for Sequence Dgb are summarized in **Table 7**. The lack of mudstone in Sequence Dgb suggests that it was deposited in a higher energy environment than sequences above or below.

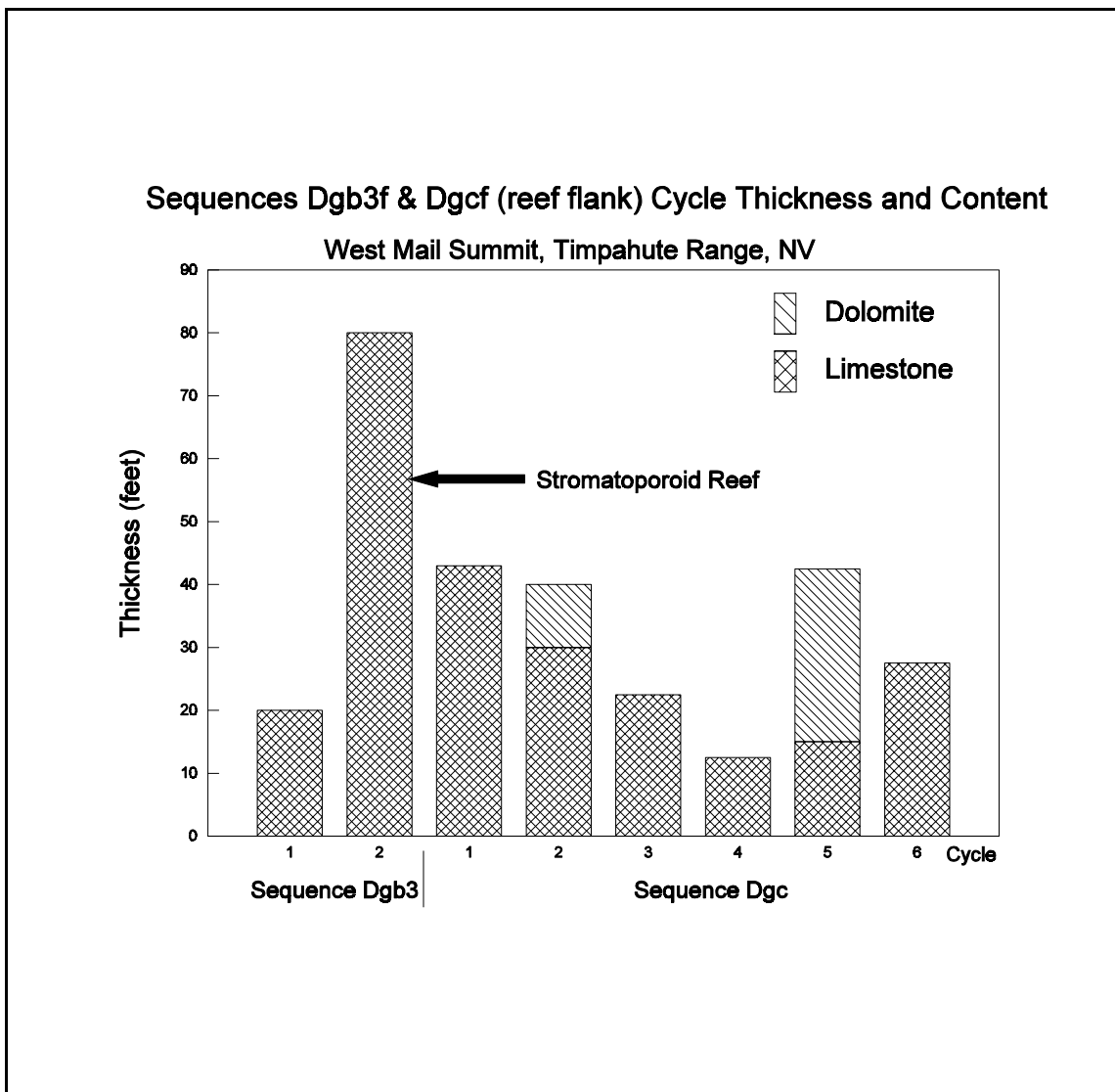


Figure 27 Histogram of cycle thickness and content, Sequences Dgbf and Dgcf. Six cycles, four of w against the reef, comprise Sequence Dgc on the reef flank (see **Figure 28**).

Gamma Radiation Commonly, gamma radiation is higher over mudstones that contain more fine-grained detritus and less over higher energy boundstones and grainstones. This is the case with Sequence Dgb (**Plate 2a**). Gamma-ray response generally reflects the particle size of the matrix being measured. Because Sequence Dgb lacks mudstone with fine-grained detritus, it emits little gamma radiation. Average

gamma radiation over Sequence Dgbc is thus only 26 CPS, less than that of any of the lower Guilmette sequences. In contrast, Dgbf has an average of 38 CPS. On the reef flank, increased percentages of fine-grained matrix results in higher gamma-ray intensity. Gamma radiation over Dgb1 is higher than over the rest of Sequence Dgbc and reflects higher content of mud-size matrix. Gamma radiation for Sequence Dgb is summarized in **Table 5**.

A low-intensity and featureless gamma-ray pattern over most of Sequence Dgb2 suggests that the entire sequence was deposited under uniform conditions. Average gamma radiation over Dgb2 is 27 CPS. Compositionally, Sequence Dgb2 is the most homogeneous of any of the Guilmette sequences. Therefore, the composition of its radioactive components remains uniform. B2 has the lowest standard deviation (3.3 CPS) of the three b subsequences. However, the texture of Sequence Dgb2 is highly heterogenous. A gamma radiation spike at the top of the sequence may reflect settling of impact dust after the event responsible for the megabreccia.

The Dgb2/Dgb3 contact is marked by a gamma-ray radiation decrease from the Dgb2 breccia to the overlying reefy Dgb3 strata in both the reef and reef flank segments of the measured section (**Figure 28**). The blocky, low-intensity, surface gamma-ray log response over the Dgb3 Cycle 3 in both sections is typical of an open-shelf depositional environment. However, the gamma-ray pattern for the reef is nearly a straight line whereas the reef flank facies produces a more undulating gamma-ray signature over shallowing upward cycles. Gamma radiation in both segments increases upward (**Figure 13**). A sharp, rightward gamma-ray inflection at the top of the Dgb3 Cycle 3 reef marks an LSE and a paleosol zone manifested on the outcrop as yellow-gray beds of silty dolomite. Above this unconformity, higher background radiation persists through Sequence Dgc up to the base of Sequence Dgd. This increase in background radiation is seen in surface and subsurface sections throughout the region (**Figure 9** and **Figure 13**).

Subsequence Dgb2 Dgb2 breccia is a unique rock body in the study area that deserves special treatment. In this section the evolution of understanding the breccia is presented along with a brief description of the breccia and its contacts. The distribution of the unique rock body has application to thrust reconstruction. Its unique origin provides a classic opportunity to study the effects of a cosmolite impact on a carbonate shelf.

Evolution of Understanding the Dgb2 Breccia Previously described by Reso (1960), Estes (1991) and Yarmanto (1992) in the Pahranaagat Range, Dunn (1979) at TMS, Cedar Strat geologists (1985) at Tempiute Mountain, and in the Golden Gate, Grant, and Worthington ranges, and Hurtubise (1989) and Ackman (1991) in the Worthington Range, Guilmette Subsequence Dgb2 breccia is a unique unit in the southern part of the Sunnyside basin. Its close association with reefs in the Pahranaagat and Mount Irish ranges caused Reso (1960), Dunn (1979), and Estes (1992) to conclude that it is reef talus. Cedar Strat geologists first recognized the regional distribution of the breccia and concluded that it was caused by slumping of steep carbonate banks into an intrashelf basin (Devonian Reservoir Study 1996, a Cedar Strat proprietary study). Warne et al. (1993) concluded that it was caused by a cosmolite impact. Warne and Sandberg (1995) developed a classification scheme to describe the breccia. Their A unit was the obviously graded matrix near the top of the unit consisting of boulder, in some places to mud size grains. B is the main body of the breccia matrix consisting of cobble to boulder size clasts with a matrix of finer breccia. C consists of large clasts or slabs near the base of the breccia separated from the underlying strata by their Unit D, a megabreccia sill of fluidized carbonate rocks. Not all these elements are present in all sections. Chamberlain and Warne (1996) recognized the cyclic nature of the gamma-ray patterns and illustrated four subtle cycles in the breccia. Kuehner (1997) recognized subtle graded beds in the breccia. Some of his graded beds may be the same as the gamma-ray fluctuations and

sea-level changes on **Figure 13** and **Plate 2a** that represent subtle cycles. Sandberg et al. (1997) formalized the breccia as the Alamo Breccia Member of the Guilmette Formation. Warne and Kuehner (1998) suggested that the breccia exhibits up to five subtle graded beds and proposed that each formed by a tsunami generated by the impact. Chamberlain (1999) used the distribution of the breccia to reconstruct the Sevier fold-and-thrust belt in the Timpahute Range 30' X 60' area.

Description and Fossils of the Dgb2 Breccia In the distance, the cliffy, dark gray nature of the breccia is easily recognized in many locations. Up close the breccia matrix is typically composed of medium gray clasts in a light gray matrix. At TMS, the dark-gray, massive cliffs of Sequence Dgb2 contrast sharply with the cyclic or banded sequences below and the light-gray stromatoporoid reef above (Figure 11 in Chamberlain and Warne, 1996). As reported by Warne et al. (1993), the breccia appeared to consist of a single graded bed of sedimentary packstone megabreccia. It contains huge clasts exceeding one thousand feet in length at the base and grades to mud at the top. Clasts are typically light-gray to medium light-gray limestone, in contrast to the commonly dolomitized fine-grained matrix that gives the outcrop a dark-gray appearance (Figure 10 in Chamberlain and Warne, 1996). The clasts are fragments of shallowing-upward sequences entrained into the breccia. If the strata between the thin breccia sill of Sequence Dga (Unit D of Warne and Sandberg, 1995) and the main breccia mass are included, then some clasts may be several miles long.

Fossils present in the Dgb2 breccia clasts at TMS include colonial corals, solitary corals, brachiopods, and clasts and matrix contain abundant stromatoporoids including *Amphipora*. MI-407 (two feet from the base of the cycle) is partially dolomitized (30%) coral, brachiopod, intraclast lime grainstone (See Appendix C for photomicrograph and descriptions of thin sections). MI-408 (seven feet from the base of the cycle) is dolomitized (80%) coral, intraclast, *Amphipora*, stromatoporoid, brachiopod packstone.

In the middle of the breccia, a chaotic interval of medium dark-gray, stromatoporoid, coral, and intraclast lime grainstone (open-marine) is medium brown-gray, with increasing stromatoporoids, corals, and intraclast matrix dolograins upward. Stromatoporoids are less abundant, and some clasts are flat. MI-421 (72 feet from the base of the breccia mass) is a brachiopod, calcisphere, coral, pelletal lime grainstone. MI-429 (112 feet from the base of the breccia mass) is an intraclast coral, gastropod, pelletal lime grainstone.

Lower Contact of Dgb2 Breccia The base of Sequence Dgb2 varies from section to section due to its catastrophic nature of emplacement. It is generally defined as the first occurrence of a megabreccia matrix above shallowing-upward carbonate cycles of Sequence Dga. The base of the breccia is an erosional, undulating surface regionally and locally. At TMS the lower part of the breccia matrix (Sequence Dgb2) is a chaotic sequence of a medium dark-gray, dolomitized matrix, abundant coral, and *Amphipora* lime grainstone. However, a thin (1 to 10-foot) bed or a sedimentary “fluidized zone” of megabreccia, genetically related to Dgb2, commonly occurs tens of feet below Dgb2. It may represent a potential surface-of-detachment for the Sequence Dgb2 sedimentary megabreccia and is designated as Unit D by Warne and Sandberg (1995). It is a carbonate diamictite of fluidized bedrock. If it is fully detached, then all of Sequences Dga2 and Dgb1 above this level are a great clast of the megabreccia at TMS. It would be classed as a medium to coarse monolith (Blair and McPherson, 1999). At southwest Mail Summit (TMS), this unusual megabreccia bed occurs at or above the Dga2 gamma-ray marker bed, 20 feet above the base of Sequence Dga2, or 392 feet below the top of Dgb2. Apparently, the megabreccia “fluidized zone” was either fluidized or liquified at this horizon by the same catastrophic event responsible for the formation of Dgb2 megabreccia. Its sequence boundary is neither an LSE nor a TSE but is a DSE, a new term herein. As defined in Chapter 3, a DSE is a Disturbed Surface of Erosion caused by

other processes other than changes in relative sea-level. Because the liquified zone does not look like the surrounding bedrock, it is likely that the clasts within the zone were “loosed” and “transported,” and thus, satisfy the definition of erosion (Bates and Jackson, 1987). Zones of fluidized or liquified carbonates are described in thin sections from the top of Sequence Dga (MI-401, Appendix C), Sequence Dgb1 (MI-405 and MI-406, Appendix C), and from the base of Sequence Dgb2 (MI-407, Appendix C). An unusual abundance of circular structures in MI-400, MI-401, MI-402, MI-403, and MI-425 could be impact-related spherules described by Warne and Kuehner (1998). The liquified carbonates could have been caused by liquefaction processes briefly reviewed by Warne and Kuehner (1998).

At Monte Mountain, ten miles west of TMS, Dgb2 lies on a thin (145feet) Sequence Dga. The thin megabreccia fluidized zone or liquified carbonate also occurs at Monte Mountain. Farther west, at Tempiute Mountain, the Dgb2 breccia cuts down into the top of the Simonson Dolomite. The thin liquified layer is missing there.

Kuehner (1997) reported an anomalously thin (20 feet thick) Dgb2 breccia at Six Mile Flat. However, in a section less than two miles northwest of his section (Sec 10, T7N R61E), a thin layer of Dgb2 liquified carbonate lies about 200 feet below the top of the main breccia body. It is likely that the breccia fluidized zone was overlooked at Six Mile Flats.

Upper Contact of the Dgb2 Breccia A karstified surface of dissolution marks the upper contact of Sequence Dgb2 in some sections. It is characterized by silty terra rosa filling fractures and cavities found in the upper 20 feet of the sequence. The size and number of the fractures and cavities decrease downward. Attitudes of some strata within some cavity fillings are parallel to tectonic dip caused by Mesozoic folding. MI-440 (167 feet from the base of the sequence) is dolomitized (95%) intraclast packstone containing subvertical and subhorizontal fractures partially filled with coarsely-crystalline white

dolomite and calcite. This regional exposure surface at the top of the Dgb2 breccia suggests that the event responsible for the breccia was followed by a period of local exposure and carbonate dissolution. Open-marine carbonates above the karsted interval show that the exposed areas were drowned under the transgressive sea.

Distribution and Thickness of the Dgb2 Breccia This lithologically unique rock body is distributed over more than 10,000 square miles in western Lincoln County, east-central Nye County and northern Clark County, Nevada. After palinspastic thrust fault restoration, this breccia could have been distributed over more than 20,000 square miles. In sections beyond the breccia occurrence, Sequence Dgb is a more ordinary succession of carbonate shelf strata (**Figure 9**, **Table 2**, and **Plate 3**).

The Tempiute cosmolite created the 160-mile diameter Tempiute basin that is assumed to be concentric about Tempiute Mountain before Mesozoic thrusting (Chamberlain, 1999). Warne et al. (1993) noted that it is thickest at the west end of the greater Timpahute Range. It thins radially. It is 510 feet thick at Tempiute Mountain (Cedar Strat proprietary measured section, 1985). In the Forest Home hanging wall thrust sheet (**Figure 2**), eastern Grant Range, 50 miles north of Tempiute Mountain, it is 20 feet thick (Cedar Stat proprietary measured section, 1985; No. 28, **Figure 9**). Guilmette Sequence Dgb2 at TMS is 179 feet thick from the base of the matrix to the graded bed at the top. It is 392 feet thick from a liquified interval near the base of Guilmette Sequence Dga2 to the top.

Origin of the Dgb2 Breccia Warne and Sandberg (1995) recounted mounting evidence that the Dgb2 megabreccia is a massive debris slide triggered by a Late Devonian cosmolite impact. That model assumed that the Tempiute Mountain section is on the shelf edge. However, as shown in Chapter 7, after thrust restoration the Tempiute Mountain section is interpreted to be deposited in the southern end of the Sunnyside basin

and to contain depositional environments that become shallower westward toward the Antler forebulge. The depositional environment of the breccia is problematical, but the thickness of the unit and the size and grading of clasts suggest open-marine conditions. I believe the impact of the Tempiute cosmolite created the Tempiute basin and was responsible for the distribution of Dgb2 breccia. Warne and Kuhner (1998) summarized evidence for the Late Devonian cosmolite impact including shocked quartz, iridium anomalies, ejecta spherules, and disturbed shallowing-upward sequences including intrasequence folding, brecciation, carbonate liquefaction, and graded bedding

Clasts within the breccia are fragments of shallowing-upward cycles of Sequence Dgb. Evidence of earlier Devonian sequences being involved in the breccia only occur at Tempiute Mountain. No evidence suggests that earlier Paleozoic rocks were involved in the breccia other than Ordovician conodonts reported by Warne and Sandberg (1996). I believe it likely that the conodonts are part of the recycled insoluble residues eroded from early Paleozoic carbonates on the Antler forebulge and redeposited in the Sunnyside basin. T. Hutter (1998, personal communication) found recycled early Paleozoic microfossils in Devonian rocks throughout the Sunnyside basin. The Antler forebulge and Sunnyside basin are discussed in Chapter 7.

Reef Core vs. Reef Flank **Figure 28** compares the overlapping sections where Sequence Dgb3 is a stromatoporoid reef (reef core) and where it is composed of reef flank facies (reef flank). The middle segment on **Figure 4** and **Plate 6** was measured where Subsequence Dgb3 is mostly a stromatoporoid reef (**Figure 26, Plate 2a**). Sequences Dgb and Dgc and Subsequence Dgb3 in the middle reef section are designated Dgbc, Dgcc and Dgb3c respectively in **Table 5, Table 6** and **Table 7**. The upper segment on **Figure 4** was measured where Subsequence Dgb3 is composed of off-reef facies (**Figure 27, Plate 2b**). Sequences Dgb and Dgc and Subsequence Dgb3 in the upper off-reef segment are designated Dgbf, Dgcf, and Dgb3f respectively in **Table 5, Table 6** and

Table 7. Correlative strata of the two sections exhibit different thicknesses, and erosional and weathering characteristics (**Figure 28**). Whereas the reef facies is a massive recrystallized body, the Dgb3f facies is more cyclic and less recrystallized. Also, the gamma-ray pattern for the reef is nearly a flat line whereas the reef flank facies produces a more undulating gamma-ray signature over shallowing upward cycles. Sequence Dgbc is 420 feet thick (**Plate 2a**). Sequence Dgbf is 302 feet thick (**Plate 2a**).

Sequence Dgb3c Sequence Dgb3c is 228 feet thick at TMS and is composed of three cycles (**Figure 28**). The base is marked by an LSE overlain by a transgressive lag that makes a sharp contact with the underlying Sequence Dgb2. Cycles 1 and 2 contain corals, crinoids and other open marine fossils (see Appendix B for more details). The uppermost cycle, Cycle 3, is a coral-stromatoporoid boundstone reef and is much thicker than the lower two cycles (**Figure 28**). The reef is a classic lens-shaped, open-shelf, stromatoporoid reef with associated flank beds (Figure 11 in Chamberlain and Warne, 1996). It is composed of recrystallized limestone with some dolomite patches and forms a prominent, light-gray cliff above the medium-gray Dgb2 megabreccia cliffs. The exposed thickness of the lenticular reef is 165 feet thick in the center. It can be traced laterally for about 500 feet.

At the base of the reef, stromatoporoids are tabular and are up to six feet in diameter whereas in the middle and upper part of the reef stromatoporoids are bulbous, decreasing in diameter upward (12 inches to two inches diameter). A photomicrograph shows MI-456 is light-gray, dolomitized (<1%), recrystallized, stromatoporoid lime boundstone with tiny authigenic quartz crystals. A subvertical stylolite provides no visual porosity but shows evidence of lateral compression. MI-479 is a light-gray, recrystallized, stromatoporoid, lime boundstone. Details of the reef architecture and biostratigraphy have previously been documented by Dunn (1979).

Terra rosa and karst pockets characterize the LSE exposure surface at the top of the reef and at the top of Sequence Dgb3 on the reef flanks (**Figure 13**). Some karst cavities just below the exposure surface contain pale yellow-gray, laminated dolomudstone. The structural attitude of the dolomudstone is parallel to tectonic dip caused by Mesozoic folding.

Other stromatoporoid reefs of Sequence Dgb3, such as the one at Mail Summit, occur in the study area (Stop 16, Appendix D). They could serve as economically important hydrocarbon reservoirs in the region. Economic considerations are presented in Chapter 8.

Sequence Dgb3f Sequence Dgb3f is 97 feet thick and is composed of three cycles in the upper segment of TMS (**Figure 4** and **Figure 28**). Cycles 1 and 2 at the reef flank are similar to those in the middle segment of the measured section at the reef core. Cycle 3 is a 77-foot-thick shallowing-upward cycle of medium dark-gray, stromatoporoid coral lime packstone at the base (open-shelf) that becomes a burrowed, gastropod wackestone at the top (restricted shelf from 2,305 to 2,307 feet, **Plate 2a**). It is correlative with the 165 foot-thick stromatoporoid reef Guilmette Sequence Dgb3c, Cycle 3. The upper sequence boundary separates burrowed Sequence Dgcf rocks that lack marine fossils from underlying Sequence Dgb3f rocks that are rich in gastropods and other marine fossils.

Sequence Dgc

Two sections were measured TMS to compare and contrast Sequence Dgc strata deposited above the two different Dgb3 facies (**Figure 28**). Dgcf was measured in the

upper segment at TMS where Dgb3 is reef flank facies (**Figure 4, Plate 6**). Dgcc was measured in the middle segment where Dgb3 is stromatoporoid reef facies. Sequence Dgcf is 188 feet thick and comprised of six cycles. Dgcc is 55 feet thick and comprised of two cycles.

Sequence Boundary The unconformity marked by a paleosol on a dissolution surface at the top of Sequence Dgb3 forms the major sequence boundary between Dgb3 and overlying Sequence Dgc (**Figure 13**). Above the unconformity, a TSE marks the base of Sequence Dgc, a silty, burrowed, gastropod lime wackestone (**Table 7, Plate 2a**).

Except for the uppermost part, the base of each shallowing-upward cycle in Sequence Dgc begins with sediments deposited in shallower water than the base of each previous cycle. The lower part of most of the cycles is composed of medium-gray, burrowed limestone. The upper part of each cycle consists generally of fossil-poor, medium to light-gray limestone, which was deposited in shallow-water conditions. Each successive cycle has more fossil-poor, light-gray limestone (**Figure 28**, see Appendix B for more details).

Gamma Radiation An abrupt gamma-ray increase at the base of Sequence Dgc is conspicuous and is correlatable on measured sections and well logs throughout the eastern Great Basin (**Figure 13, Figure 9, and Table 2**). The average gamma radiation of Sequence Dgc, 46 CPS, is almost twice that of the average gamma radiation of Sequence Dgb with an average of 26 CPS. The distinctive gamma-ray rightward inflection occurs because Sequence Dgc is more silty than adjacent sequences. Gamma radiation intensity increases upward from the open-shelf to slightly restricted-shelf bases to the more restricted-shelf tops of the shallowing-upward cycles. Gamma radiation of Sequence Dgc in the middle and upper segments of TMS is summarized in **Table 5**.

Depositional Indicators The most characteristic features of Sequence Dgc rocks are the intensity of burrowing and the abundance of gastropods (**Table 4**). Sequence Dgc rocks lack open-marine fossils such as corals, stromatoporoids, and brachiopods and lack supratidal dolomites typical at the tops of shallowing-upward cycles of Sequence Dga below and Sequences e through g above. A dolomite cap on Cycle 5 of Sequence Dgcf is an exception and was probably deposited in supratidal conditions. The sandy limestone on dolomite and siltstone at the top of Sequence Dgc Cycle 2 was deposited in low-supratidal conditions.

Erosional Profile, Lithologies, Sequence Thicknesses, Textures, and Colors

Sequence Dgc tends to erode into a weathering profile of partly-covered to covered slopes (**Plate 2a** and **Table 5**). Typically, Sequence Dgc forms a saddle between the limestone cliffs of Sequence Dgb below and the dolomite ledges of Sequence Dgd above. **Table 5** summarizes the weathering profiles.

All of Sequence Dgcc is limestone and Dgcf is 72% limestone, 20% dolomite, 5% terrigenous siltstone, and 3% quartz sandstone (**Table 6**). Though the cumulative thickness of Sequence Dgb3 and Sequence Dgc in the two sections is similar, there is, nevertheless, a striking difference in the thickness of Sequence Dgc (**Plate 2a, Figure 26** and **Figure 27**). Cumulative thickness of Sequences Dgb3c and Dgcc is 260 feet and that of Dgb3f and Dgcf is 285 feet. Sequence Dgcc is only 45 feet thick. However, Dgcf is 188 feet thick.

Sequence Dgcc is 100% mudstone and Sequence Dgcf is 74% mudstone and 26% wackestone. Sequence Dgc mudstone contrasts with *Amphipora* wackestone of Sequence Dgd above and stromatoporoid packstones and boundstones of Sequence Dgb below. **Table 7** summarizes the sequence colors.

Cycle Thicknesses There are only two cycles in Sequence Dgcc. In contrast, six cycles with an average thickness of 31 feet make up Sequence Dgcf, approximately a mile away (**Figure 28**, **Figure 26**, and **Figure 27**). The thickest Sequence Dgcf cycle is 42.5 feet and the thinnest cycle is 13.5 feet. Similarly, Sequence Dgcc cycles average 28 feet thick, ranging from a maximum of 45 feet to a minimum of 10 feet. Cycle thickness can be used to distinguish Guilmette sequences. For example, the average Sequence Dgcf cycle is thicker (31 feet) than the average cycle of Sequence Dga (20 feet).

Figure 27 illustrates that Sequence Dgcf cycles become thinner from Cycle 1 (43.5 Feet) through Cycle 4 (15 feet) and then thicken at Cycle 5 (42.5 feet). If the upward-thickening trend continued to Cycle 6, then erosion at the top of Cycle 6 could have removed 20 or 30 feet of supratidal dolomites. Because Sequence Dgcc is mostly (78%) a covered interval, it is unclear if it consists of more than two cycles (**Plate 2a**). All six cycles of Sequence Dgcf may merge into the two cycles of Sequence Dgcc. If they do, they thin over the reef core. Otherwise, Cycles 1 through 4 are missing over the reef core by onlap and Cycles 5 and 6 on the reef flank correlate to Cycles 1 and 2 on the reef core as shown in **Figure 28**. Cycles 1 through 4 on the reef flank represent a period of shallowing-upward or slowing of relative sea-level rise that would result in less accommodation space. Cycles 5 and 6 on the reef flank and Cycles 1 and 2 on the reef core represent a period of accelerated sea-level rise, creating more accommodation space upward. A deepening of sea level at the top of the shallowing upward Cycle 6 (reef flank) resulted in a merged LSE/TSE responsible for truncating the upper part of Cycle 6 on the reef flank and Cycle 2 on the reef core.

Sequence Dgd

Sequence Dgd is 406 feet thick and comprised of 23 cycles. *Amphipora*-rich dolowackestone-packstone characterizes Sequence Dgd (**Table 7**). The medium dark-

gray to medium brown-gray *Amphipora* wackestone-packstone facies suggests deposition in a restricted-shelf lagoon environment, an interpretation that concurs with Niebuhr (1979). A merged LSE/TSE marks the sharp basal contact of this sequence. Above the transgressive lag deposit associated with the TSE is an oncolite-bearing bed. Except for a few minor (10 feet thick or less) limestone intervals and several thin (less than 5 feet thick) quartz sandstone beds, 90% of Sequence Dgd is an *Amphipora*-rich dolopackstone that generally shallows upward (**Plate 2a**).

Quartz Sandstone Most of the cycles in Sequence Dgd are capped by thin, laminated, light-gray dolomite (**Plate 2a**). Four of the cycles are capped by thin sandstone beds less than five feet thick. The light-gray, medium-grained, well-sorted, dolomite-cemented, quartz sandstones are trough crossbedded. Commonly the crossbedding shows a prevailing southwest current direction. Some sandstones have desiccation cracks. Other than a few scattered medium-sized quartz grains and rare thin (1' thick) sandstone beds in the Yellow Slope Sequence, sandstone in cycle 16, near the middle of Sequence Dgd, contains the first occurrence of medium-grained quartz sand above the “Oxyoke Formation” sandstone.

Though quartz sandstone makes up a small part of the Guilmette at TMS, it predominates in the Monte Mountain Section above the Dgb2 breccia (**Figure 9**, No. 52). One massive sandstone unit, truncated at the base by the Monte Mountain thrust fault, is at least 700 feet thick (Stop 14, Appendix D). Net sandstone for the formation at Monte Mountain is 1,070 feet. The sandstone bodies are composed of well-sorted, well-rounded, frosted, fine to medium quartz grains (Chapter 7).

Gamma Radiation A prominent, regionally persistent, gamma-ray leftward inflection marks the base of Sequence Dgd, which lies on the unconformity at the top of

Sequence Dgc. **Figure 13** illustrates a slight increase in gamma radiation from the base to near the middle of the sequence. The gamma-ray pattern is generally smooth over the sequence except local inflections at cycle tops caused by concentrations of wind-blown radioactive dust. A regionally persistent gamma-ray leftward inflection occurs in the middle part of the sequence.

Sequence Dge

Sequence Dge is 235 feet thick and comprised of 17 cycles. Whereas Sequence Dgd is predominantly dolomite, Sequence Dge is a mixture of dolomite, limestone, quartz sandstone, and siltstone (**Plate 2a**). Denoting another merged LSE and TSE sequence boundary, the dolomite at the base of Sequence Dge directly overlies an unconformity at the top of Sequence Dgd. In some sections north of the study area, the unconformity cuts out much of Sequence Dgd.

Gamma Radiation A regionally correlatable gamma-ray rightward inflection marks the base of Sequence Dge (**Figure 13**). Cycles within the sequence are marked with a leftward gamma-ray inflection at the base and a gradual gamma radiation increase toward the top. Gamma-ray spikes are common where terrigenous grains are concentrated at the tops of some cycles.

Sequence Dgf

Sequence Dgf is 267 feet thick and comprised of 15 cycles. The sharp basal contact of Sequence f occurs where an LSE truncates the uppermost light-gray, laminated

dolomite of Sequence Dge and is merged with a TSE. A six-inch lag deposit of light-gray, finely-crystalline dolomite clasts in medium dark-gray dolomite overlies the TSE. The sequence is predominantly limestone, except the uppermost 65 feet, which is composed of predominantly dolomite (**Table 6**). Medium-gray to medium dark-gray, medium to thin-bedded, locally *Amphipora*-bearing, lagoonal, burrowed limestones form the lower part of most cycles. Many cycles are capped by either supratidal, light-gray, laminated dolomudstone with tepee structures or one- to two-foot thick supratidal, light yellow-gray, fine-grained quartz sandstone beds. Many supratidal caps contain intervals of desiccation cracks.

The sequence is erosionally nonresistant, because 61% is partly-covered slopes, 15% are covered slopes and only 24% are ledges. Light colors dominate as 33% of the sequence is medium light-gray, 26% is light-gray, 4% is pale yellow-gray, 13% is medium-gray, and only 24% is medium dark-gray.

The rightward gamma-ray inflection at the base of Sequence Dgf is regionally correlative (**Figure 13**). As observed in other cycles, gamma radiation is generally higher over light-gray, unfossiliferous, laminated, finely-crystalline dolomite interpreted to have been deposited in supratidal conditions. Gamma radiation is lower over thick-bedded, open marine fossil-bearing limestone interpreted to have been deposited in open-shelf conditions. However, cycles 9, 10, and 11 not only provide the highest gamma-ray responses in the sequence, but also contain the uppermost occurrences of open-marine fauna in the TMS section including corals, bulbous stromatoporoids, and brachiopods. The higher gamma-ray response associated with open-marine carbonates is probably due to a higher influx of detrital material. Above cycle 9, the detrital material shut off the carbonate factory. Detrital influx from the incipient Antler orogeny and more restrictive circulation is probably responsible for the paucity of abundant open-marine macrofossils observed between Sequence Dgf cycle 11 and the Mississippian Joana Limestone at TMS.

Sequence Dgg

Sequence Dgg, with its 567-foot-thickness and its 29 cycles, is the most variable sequence of the Guilmette Formation in cycle lithologies and thicknesses. At TMS, the section is 59% dolomite, 24% quartz sandstone, and 17% limestone.

A regionally correlatable leftward gamma-ray inflection (lower gamma radiation) marks the base of Sequence Dgg (**Figure 13**). Otherwise, the contact between the light brown-gray dolomite of Sequence Dgf and that of Sequence Dgg is indistinguishable in the field. Indicators of a sequence boundary or unconformity are yet to be found in the covered interval. The covered interval probably formed on a nonresistant paleosol developed on the top of Sequence Dgf.

The top of the Guilmette Formation in many sections on the edge of the Sunnyside basin is marked by a prominent sandstone bed, representing the uppermost part of the uppermost cycle. This sandstone probably correlates to the Cove Fort Sandstone in other sections of western Utah. Hintze (1988) showed the Cove Fort Sandstone at the top of the Guilmette Formation in western Utah sections.

Weathering Profile and Color Most (57%) of Sequence Dgg is resistant and forms ledges. Nevertheless, 39% of the sequence erodes into partly-covered slopes and 4% is covered. In contrast to earlier sequences, Sequence Dgg lacks cliffs. The sequence weathers to shades of gray and brown-gray. It is 42% light-gray, 36% medium-gray, 11% brown-gray, and 11% light brown-gray.

Gamma Radiation The sequence has a variable gamma-ray log response. It has a standard deviation of 10.3 CPS, higher than the standard deviation of Sequence Dga (**Table 5**). Average gamma radiation of the sequence is 49 CPS. It ranges from a

minimum of 32 CPS to a maximum of 92 CPS. The abrupt decrease in gamma radiation at the base of the sequence provides a leftward inflection that is regionally recognizable. Another regionally correlative gamma-ray spike occurs at the top of the sequence. Gamma radiation intensity in Sequence Dgg is low compared with subjacent Sequence Dgf (average of 49 in Dgg versus 61 CPS in Dgf) and superjacent West Range Limestone Sequence (average of 49 CPS in Dgg versus 82.6 CPS in West Range Limestone (**Figure 13**)).

The Uppermost Occurrence of *Amphipora* The uppermost occurrence of *Amphipora* in TMS Devonian occurs in the lower part of Sequence Dgg Cycle 25 (see **Plate 2a**). The last occurrence of rugose corals at TMS occurs in Sequence Dgf Cycle 11 and the last occurrence of stromatoporoids occurs in Sequence Dgf Cycle 5 (Appendix B). The lack of reef-building stromatoporoids and corals and the last occurrence of *Amphipora* could represent the Frasnian-Famennian boundary. Sandberg et al. (1997) also placed the Frasnian-Famennian above the cyclical carbonate rocks and within the sandy member in their time-rock chart of the north Pahrnagat Range and Mount Irish Range. They place it much lower in their Tempiute Mountain section. However, if their top of the Dgb2 breccia is the same as TMS herein, then using their thicknesses, the boundary is in Sequence Dgd. Either the measured thicknesses are different or Sequences Dgc-Dgg are unusually thin at TMS and the section needs to be recorrelated. It would have been most helpful if Sandberg et al. (1997) would have added a surface gamma-ray log to their chart so that the sections could be correlated directly. It is recommended in Chapter 9 that conodont zones of the region be tied to surface gamma-ray logs to tighten and refine sequence correlations of the region. The extinction of most reef-building stromatoporoids and corals at the Frasnian-Famennian boundary correlates to the collapse of North American stromatoporoid-dominated reefs (Webb, 1998). *Amphipora* does not occur in the uppermost cycles of Sequence Dgg in other sections throughout the

Sunnyside basin where the uppermost part of the sequence is preserved. Therefore, the Frasnian-Famennian boundary probably occurs at the top of Sequence Dgg Cycle 25.

West Range Limestone

The West Range Limestone is 153 feet thick at TMS and comprised of one sequence and four cycles (**Plate 2a**). The basal contact of the sequence is marked by a transgressive erosional surface over the unconformity at the top of Sequence Dgg. In some sections north of the study area, the unconformity cuts out much of Sequence Dgg. The West Range Limestone consists of intertidal lime mudstones. They overlie the uppermost intertidal to supratidal quartz sandstone bed of Sequence Dgg (**Figure 13**). The West Range Limestone is readily eroded into recessive, partly-covered slopes. It is typified by light-gray, burrowed lime mudstone that contains few macrofossils. It is commonly mottled or burrowed, silty, argillaceous, partly laminated, and thin-bedded.

If the Monte Mountain (TMM) section is restored to west of Tempiute Mountain (TMP) as proposed in Chapter 5, then the West Range Sequence regularly thins westward. It is 153 feet thick at TMS, 125 feet thick at TMP, and 58 feet thick at TMM.

The West Range Limestone has a higher gamma-ray intensity than the underlying Guilmette. The highest gamma-ray count in the West Range Limestone is 106 CPS and the lowest is 61 CPS. The average is 82.6 CPS. The standard deviation is 10.7 CPS. A sharp, distinct, rightward gamma-ray inflection marks the base of the sequence on surface and subsurface logs (**Figure 13**).

The top of the West Range Sequence herein is defined by a sequence boundary with a sharp rightward gamma-ray inflection. It is different from the lithologic formation boundary by Sandberg and Ziegler (1973) who did not employ principles of "sequence stratigraphy" to their measured section at Bactrian Mountain. They included the upper part of the West Range Sequence in their Pilot Formation.

Pilot Formation

The Pilot Formation is 245 feet thick and comprised of two sequences at TMS. **Plate 7** illustrates the distribution of 91 Pilot Formation outcrops in the Timpahute Range 30' X 60' quadrangle that cover 5.85 square miles. The poorly exposed Mississippian-Devonian Pilot Formation occurs above the cyclic Devonian carbonates (**Plate 2a, Figure 13**). The Mississippian-Devonian boundary lies within the Pilot Formation. The sequence boundary could be the unconformity at the top of Sequence 1. Sandberg and Ziegler (1973) pointed out that erosion at the unconformity cuts out eight conodont zones in the Pilot Formation at Bactrian Mountain, on the north end of the Pahranaagat Range, seven miles south of the TMS section. The Pilot Formation manifests a unique gamma-ray signature with the highest radioactivity of all the Devonian system. It has a high clay content and probably high concentrations of radioactive potassium. In measured sections and well cuttings of the Mississippian Antler clastic shales, those which exhibit higher radiation are also higher in Total Organic Carbon or TOC (Chamberlain, 1988c). Similarly, the high organic carbon in the siliceous stromatolites and black siltstone is probably the source of the high gamma radiation in the Pilot Formation.

At the beginning of this chapter, it was proposed that the sequence boundary at the top of the Sevy Dolomite is probably the base of the Kaskaskia sequence of Sloss (1963) and the Piankasha Holostrome of Wheeler (1963). The Kaskaskia or Piankasha is one of several major continental sequences bounded by continent-wide unconformities. It began in the Early Devonian and ended in the Late Devonian. The top of the Kaskaskia or Piankasha may correspond to the sequence boundary between Pilot Formation Sequences 1 and 2. Wheeler called the missing interval at the unconformity the Acadian Hiatus. Most of the sequences described in this chapter lie in the Kaskaskia sequence (**Figure 10**).

Sandberg and Ziegler (1973) reported 426 feet of Pilot Formation at Bactrian Mountain in the study area, 60 miles south of the southern edge of the Pilot basin of Sandberg et al. (1988). Pilot Sequences are thickest (815 feet) in the Confusion Range

(No. 11, **Figure 9**), are absent in the Forest Home footwall thrust sheet (No. 27, **Figure 9**), and 233 feet thick in the Forest Home hanging wall thrust sheet (No. 28, **Figure 9**). Pilot Sequences in the Pancake Range, near the Pilot basin of Sandberg et al. (1988), are 365 feet thick (Cedar Strat files). The sequences thin over the Monitor-Uinta arch and thicken to 230 feet at Pearl Peak (No. 45, **Figure 9**) and 275 feet in the Pequop Range (No. 41, **Figure 9**) north of the arch (Cedar Strat files). Sandberg et al. (1988) neither show the thinning of the Pilot Formation over the Monitor-Uinta arch, nor do they mention the shuffling of sections caused by Sevier thrusting. Therefore, their paleogeographic maps may be misleading.

Correlation charts in Chapter 6 illustrate the thicknesses of Pilot Sequences in different thrust sheets in the Timpahute Range. It is 300 feet thick at Tempiute Mountain, 117 feet thick at Monte Mountain, and 245 feet thick at TMS. If the Silver Canyon thrust sheet is restored to west of Tempiute Mountain, then a consistent thinning of the Pilot Sequences occurs from near the center of the Sunnyside basin at Tempiute Mountain to Monte Mountain on the west and TMS on the east.

Pilot Formation Sequence 1

Pilot Formation Sequence 1 at TMS is 130 feet thick and is comprised of two cycles (**Plate 2a**). It consists of most of the West Range Limestone upper unit and all of the Pilot Shale lower unit of Sandberg and Ziegler (1973). It lies in the lower *marginifera* conodont zone (**Figure 10**). The base of Sequence 1 occurs where recessive limestones of the West Range Limestone abruptly give way to mostly covered intervals. These slopes, bearing fragments of light-gray, silty limestone, produce an increased gamma-ray measurement. The top of the sequence is marked by a thin, ferruginous, fossil fish plate-bearing quartz sandstone only five to ten feet thick that overlies ten feet of pale-yellow, calcareous siltstone. This may be correlative with the planar, crossbedded, coarse-

grained, quartz sandstone, containing abundant abraded fish bones and teeth, conodonts, and phosphatic pellets between sequences three and four of Giles (1994) in the Confusion Range, western Utah. However, Giles (1994) placed a regional unconformity below the sandstone.

The Pilot Formation Sequence 1 is more radioactive than the underlying West Range Limestone. Furthermore, two of the highest gamma-ray spikes in the TMS occur in Pilot Formation Sequence 1 (**Figure 13**). The first occurs at the base of Cycle 1, and the second occurs near the top of Cycle 2 in the ferruginous sandstone. Although thick cover commonly masks the base of the sequence, the contact can be picked on the surface gamma-ray log where an abrupt gamma-ray intensity increase occurs. This provides an example of the usefulness of surface gamma-ray logs for interpreting changes in lithology otherwise hidden by scree or soil.

Pilot Formation Sequence 2

Pilot Formation Sequence 2 at TMS is 115 feet thick and comprised of 2 cycles. As mentioned above, the major unconformity that cuts out eight conodont zones in the Pilot Formation at Bactrian Mountain (Sandberg and Ziegler, 1973) may be the sequence boundary between Sequences 1 and 2. The ferruginous quartz sandstone at the top of Sequence 1 is overlain by the pale-red, cherty siltstone of Sequence 2. Its base lies in the Middle *costatus* conodont zone of Sandberg and Ziegler (1973) at Bactrian Mountain (**Figure 10**). Black, laminated, silicified stromatolite beds of cycle 1 are capped by a 2.5-foot-thick bed of bioturbated sandstone (**Table 6**). The second cycle is a silty limestone that is commonly covered.

The ferruginous sandstone at the top of Sequence 1 produces a gamma-ray peak in contrast to the abrupt gamma-ray leftward inflection at the base of Sequence 2 (**Figure 13**). The gamma-ray spike mentioned in the first paragraph of this section on the Pilot

Formation is associated with silicified stromatolites that occur at the top of Cycle 1. Gamma radiation abruptly decreases at the base of Cycle 2, and continues to decrease gradually to the base of the overlying Joana Limestone where a distinct gamma-ray leftward inflection at a sharp erosional break occurs (**Plate 1a**).

Joana Limestone

The Mississippian Joana Limestone (note that only the base of the formation is shown in **Plate 2a**) represents a major transgression over the uppermost Pilot Formation Sequence 2 Cycle 2. The Joana Limestone contains abundant bedded chert and open-marine fossils including crinoids and corals in contrast with the uppermost Pilot Formation that lacks bedded chert and open-marine fossils. Joana Limestone sequences from the base to the top include: (1) ledge-forming, silty lime wackestone; (2) prominent, cliff-forming crinoid grainstone; (3) prominent, cliff-forming crinoid grainstone banded with chert; and (4) cliff-forming crinoid grainstone. The formation is mostly a medium-gray weathered, massively bedded crinoid packstone. **Figure 29** illustrates the distribution of 101 Joana Formation outcrops in the Timpahute Range 30' X 60' quadrangle that cover 40.25 square miles.

Although the Joana Limestone-Pilot Formation contact is generally covered with scree from the from overlying Joana Limestone, it can be picked at a pronounced decrease in gamma radiation. This gamma-ray shift is an abrupt change to some lowest values measured in the TMS (**Figure 13**). The leftward gamma-ray inflection at the erosional break is interpreted to be a merged LSE and TSE that separates Pilot Formation slopes from overlying Joana cliffs. Gamma radiation generally increases upward to the top of the Joana Limestone.

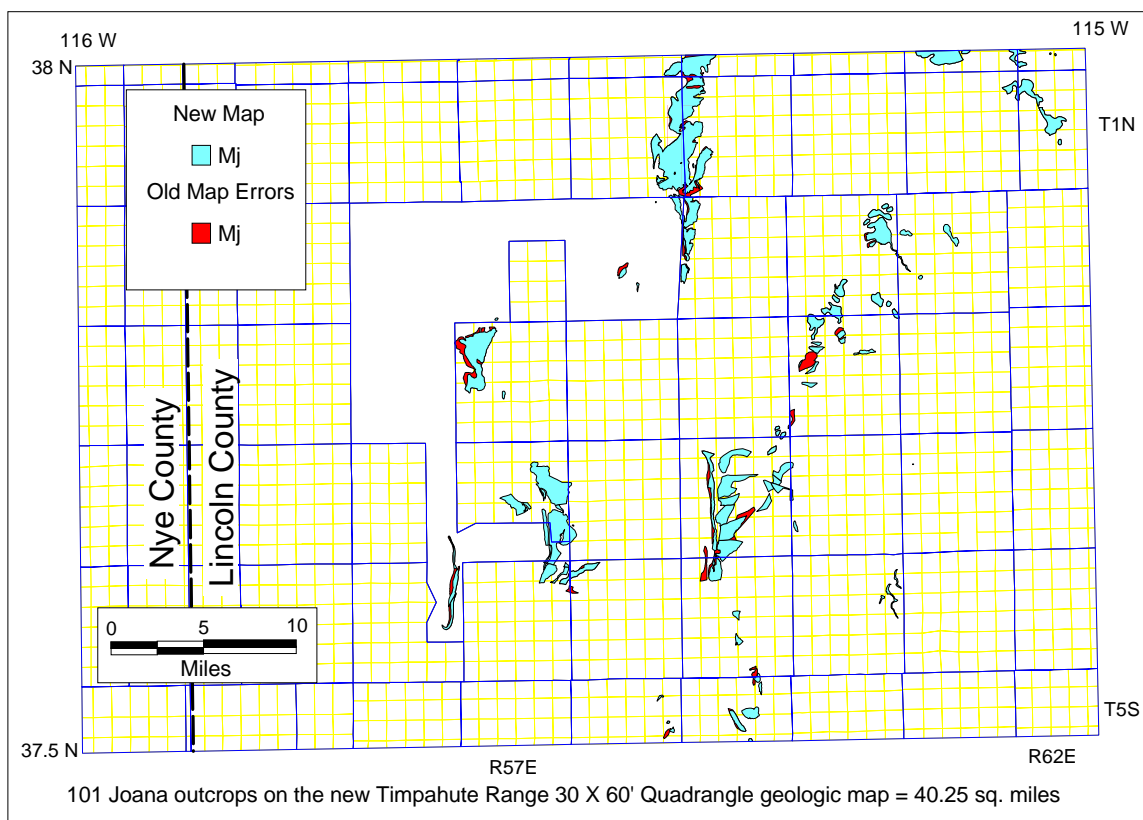


Figure 29 Distribution of Joana Formation outcrops on the new geologic map of the Timpahute Range 30' X 60' quadrangle. Areas erroneously mapped on old map as Joana are marked in red. Degrees N latitude and W longitude are marked at the corners of the map. Blue lines are surveyed townships and ranges and the yellow lines are surveyed sections.

Discussion

Devonian sequences at TMS serve as a reference section for the rest of the Sunnyside basin and fulfill the first objective of this research, namely to give an account of the 21 mappable Devonian sequences at TMS (**Figure 13**). These regionally correlatable sequences at TMS were correlated to more than 500 other Great Basin surface and subsurface sections measured and described in Nevada and western Utah (**Figure 9, Plate 3**). However, **Table 2** and Appendix F lists only those sections and wells where the complete Devonian interval is represented or where no Devonian rocks

were deposited. All Cedar Strat sections listed in the tables were measured at the same scale and detail as TMS. They all contain surface gamma-ray logs for correlating. Cuttings from most of the wells listed in the tables were described by Cedar Strat. These descriptions, combined with gamma-ray logs, were used for correlations. Many other sections are described in the literature or in proprietary studies. Though they lacked the detail and surface gamma-ray logs, less exact correlations based on lithologic and fossil descriptions were made using these other sections. They did provide additional control points. Most of the surface and subsurface sections are composed of only parts of the Devonian interval because of faulting, cover, erosion, or not drilling deep enough. A spreadsheet of all the data points, sequence thicknesses, thicknesses of sandstones and other information provided a method of organizing the data set. Every section that contained one or more sequences was added to the spreadsheet. Data from the spreadsheet were used to construct isopach and isolith maps presented in Chapter 7. As each isopach map of each of the 21 sequences was made, errors in correlation were detected and corrected. The final product was an isopach map of the total Devonian (Chapter 7, **Figure 9, Plate 3**). Viewed in order, the 21 isopach maps reveal the evolution of the Sunnyside basin. This evolution aided in inferences and interpretations. For example, unconformities cut out some sequences over the Monitor-Uinta arch. These unconformities provided some basis for determining the sequence boundaries at TMS. However, a detailed analysis of the evolution of the Sunnyside basin is beyond the scope of this study.

Facies of sequences in most sections and wells throughout the Sunnyside basin are similar to TMS. However, abrupt contrast occurs in facies of post Guilmette Sequence Dgb2 in sequences from different thrust sheets in the greater Timpahute Range. For example, post Sequence Dgb2 facies at TMS are composed of limestone to dolomite shallowing upward cycles. Correlative rocks in the Silver Canyon thrust sheet are uniquely predominantly quartz sandstones and those in the Tempiute Mountain thrust sheet are uniquely predominantly thin-bedded limestones. The contrasting facies are

illustrated by an east-west correlation chart (**Figure 30**). Gamma-ray log patterns of the sequences allow correlation of these sequences of different facies. Concentrations of greater amounts of wind-blown radioactive dust were not facies sensitive and left their chronostratigraphic imprints in the rock record. These imprints, much like bentonite beds in the Cretaceous Rocky Mountain seaway, mark the sequences with unique gamma-ray patterns that are regionally correlative. Because these patterns are not facies sensitive, sequences with sharply contrasting facies can be correlated between the thrust sheets.

Small, meter-scale, shallowing-upward cycles at TMS were probably controlled by local depositional systems involving autocyclic aggradation. These small-scale cycles can be traced laterally only locally. Cycle thicknesses and stacking patterns seem random and unpredictable. In contrast, the sequence and formation-scale cycles were probably controlled by changes in eustasy and subsidence rates. They are predictable and can be traced regionally. Some sequence boundaries are subtle on the outcrop but all the boundaries have recognizable gamma-ray signatures. Other sequence boundaries such as the change from light-gray dolomudstone to argillaceous dolomite at the Sevy Dolomite/"Oxyoke Formation" contact are more obvious on the outcrop. The unconformity at the top of the Simonson Dolomite is a regionally correlatable sequence boundary.

The upper parts of most of the cycles that make up the Guilmette sequences are dolomudstone and all the sequences below the Simonson Dolomite unconformity are pervasively dolomitized. However, thin-bedded limestones above the Dgb2 breccia in the Timpahute Mountain (west Pahroc) thrust sheet are not dolomitized. Less dolomite occurs in the sandy Silver Canyon thrust sheet than in the reefy east Pahroc thrust sheet. The dolomite occurrences and possible dolomitization mechanisms are the subject of the next section.

Dolomite at TMS

Much of the Devonian section in the study area has undergone diagenetic transformation to dolomite, particularly in the Sevy and the Simonson formations. However, classifying Devonian dolomite types in the study area is limited to dolomite fabrics, field relationships, and limited petrography. Using these data, a paragenetic sequence is suggested (**Figure 31**). Fabric refers to size and mutual relationships of crystals, whereas texture refers to shape of crystals (Friedman and Sanders, 1967). Other workers have developed crude paragenetic sequences based on limited data. Fischer (1988) classified dolomites of the Cambrian Metaline Formation, northwest Washington, based on crystal fabric.

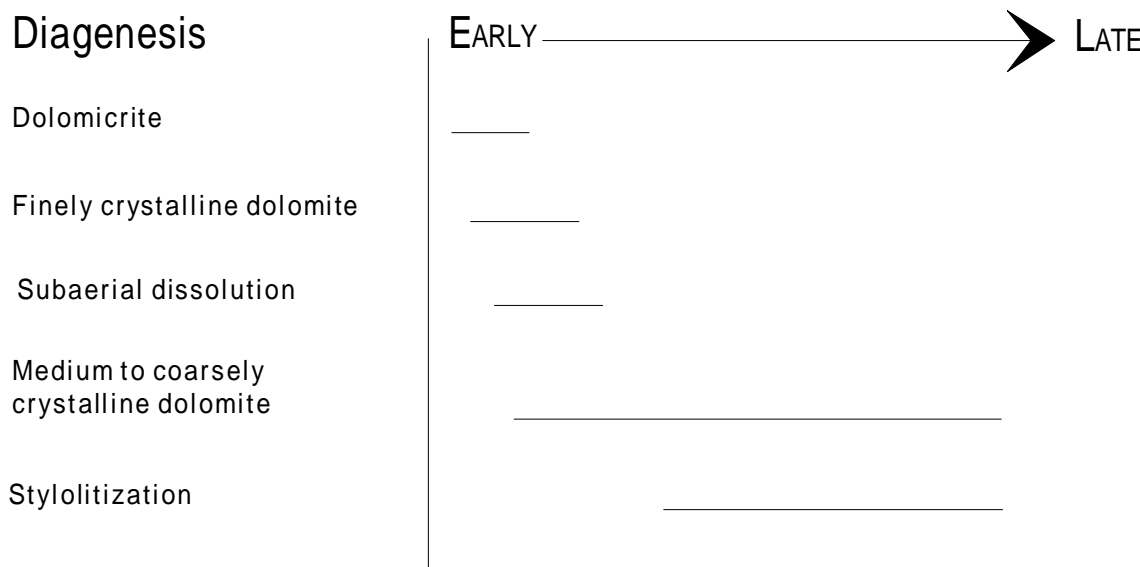


Figure 31 Generalized diagenetic sequence for dolomites at TMS. Micrite caps on shallowing-upward cycles were probably diagenetically altered to stratal finely-crystalline dolomite penecontemporaneously. Porous zones created by subaerial dissolution during low sea-level stands channeled dolomitizing fluids resulting in medium to coarsely-crystalline dolomite. Regional burial and tectonism resulted in later-stage stylolitization.

At least four types of dolomite or dolomite facies occur in the study area. They are: 1) finely-crystalline stratal, 2) coarsely-crystalline stratal, 3) pervasive, and 4) non-stratal dolomite. All four types are considered to be replacement dolomites.

Dolomitization of the cycle caps to finely-crystalline stratal dolomite probably occurred penecontemporaneously and the other types occurred later. Besides the dolomite bodies, Devonian sandstones discussed in Chapter 7 are cemented with dolomite. The four principal types of dolomite fabrics or dolomite facies at TMS are summarized in **Table 9**.

Pervasive dolomite is most important below the Simonson unconformity. TMS was intentionally picked to avoid secondary dolomitization and alteration associated with faults. Therefore, finely-crystalline stratal dolomite is most important in the Guilmette cycle caps above the Simonson unconformity.

Finely-Crystalline Stratal Dolostone (Type 1)

Most of the Sevy Dolomite and much of the Simonson Dolomite is composed of finely-crystalline, stratal dolomite. However, some of it has been modified to fine- to coarsely-crystalline fabrics. In the Guilmette Formation, finely-crystalline stratal dolomite is mostly restricted to the upper part of many shallowing-upward cycles. The finely-crystalline fabric provides some light on the diagenetic sequence. Shukla (1988) suggested that penecontemporaneous dolomites are more finely crystalline than diagenetic dolomites. Fischer (1988) also interpreted his finely-crystalline fabric type A dolomite as a penecontemporaneous dolomite formed by supratidal processes.

Table 9 Dolostone types, characteristics, distribution, inferred timing, and examples at TMS and in other parts of the study area.				
TMS dolomite type	Characteristics	Distribution	Timing	Example
1. Finely crystalline stratal dolomite	Finely crystalline, laminated, unfossiliferous, upper part of shallowing-upward cycles.	Restricted to upper parts of local carbonate cycles	Very early- syn-depositional.	Cycle tops in the Guilmette, Simonson Dolomite, and Sevy Dolomite
2. Coarsely crystalline stratal dolomite	Coarsely crystalline, crystal coarseness and size of fractures filled with coarsely-crystalline dolomite increase upward toward sequence boundaries. Unaltered patches of limestone. Commonly contains zebra dolomite.	Local (not correlative with other sections in the basin) to regional (correlative with other sections in the basin)	Intermediate, restricted to sequence boundaries suggesting dolomitization before deposition of overlying unit.	Dolostone zones below some Guilmette Dgd, Dge, Dgf, and Dgg sequence boundaries
3. Pervasive dolomite below the Simonson Dolomite unconformity at upper contact of the Simonson Dolomite	Finely to coarsely-crystalline dolomite, dolomitization complete. Associated with karst breccia and coarse dolomite-filled fractures that increase in abundance and thickness upward to major sequence boundaries.	Regional, associated with major LSE and karsting	Intermediate, restricted to below the Simonson Dolomite unconformity suggesting dolomitization before Guilmette deposition	All carbonate rocks below the Simonson Dolomite unconformity and above the upper Pogonip Group limestones except in the Silver Canyon thrust sheet.
4. Non-stratal dolomite	Frequency of zebra dolomite and fractures filled with sparry, saddle? dolomite crystals and coarseness of crystals increase toward faults.	Local, near faults or selective porous zones	Very late, cuts across all other dolomite types and sequence facies.	Dolostone associated with the Silver Canyon thrust fault and some normal faults and porous intervals that have no obvious association with faults

Sevy Dolomite Finely crystalline Stratal Dolostone The Sevy Dolomite is composed of finely-crystalline dolomite that I interpret to have been deposited in mostly supratidal conditions at TMS (Chapter 4). Evidence of supratidal conditions includes lack of fossils, laminated dolomudstone, light-gray color (suggesting an oxidizing environment), tepee structures, desiccation cracks, and fenestral textures. The Sevy Dolomite is composed of many shallowing-upward cycles. Bases of the cycles were deposited in low tidal flat conditions and the tops of cycles were deposited in high supratidal conditions. The dolomite in the Sevy Dolomite cycles is similar to the finely-crystalline stratal dolomite in the Guilmette cycle caps.

Simonson Dolomite Finely crystalline Stratal Dolostone The succession of alternating light and dark layers (1-10's feet thick) that form the cycles within the Simonson Dolomite gives it a banded appearance. The banded layering is interpreted as a repetition of the alternating lower and upper parts of shallowing-upward cycles. Rarely *Amphipora* occurs in the darker, coarser-crystalline dolomite in the lower part of the shallowing-upward cycles. *Amphipora* suggests open-shelf to restricted marine near-shore conditions. The upper part of the shallowing-upward cycles consists of unfossiliferous, light-gray, fine- to medium-crystalline dolomite. Tepee structures and fenestral texture suggest that it was probably deposited in highly restricted to supratidal conditions. The dolomite was probably penecontemporaneously altered to finely-crystalline stratal dolomites in supratidal conditions. Capillary upward movement of sea water becomes concentrated by evapo-transpiration in supratidal environments (Friedman and Sanders, 1967).

Finely crystalline stratal dolomites probably occurred in the upper parts of shallowing-upward cycles of the Coarsely-Crystalline Sequence between the “Oxyoke Formation” and the Lower Alternating Sequence. Primary bedding and sedimentary structures in this interval have been obliterated by dolomitization and recrystallization.

The alteration may be associated with an unconformity at the top of the Coarsely-Crystalline Sequence. Upward-shallowing cycles in this sequence are similar to the Lower and Upper Alternating Sequences above the unconformity. The main difference is that they are recrystallized to coarsely-crystalline dolomite below the unconformity and they are not recrystallized to coarsely-crystalline dolomite above the unconformity. The unconformity apparently separates an earlier diagenetic event from a later one.

Guilmette Finely-Crystalline Stratal Dolostone Most of the upward-shallowing cycles in the Guilmette at TMS are capped by finely-crystalline stratal dolomite. An example of a shallowing-upward cycle with a dolomite cap is Cycle 9 in the Guilmette Yellow Slope Sequence (Appendix B). Three feet above the base of the cycle is an intraclast, ostracode, pellet lime packstone (see MI-317, Appendix C). At the top of the 20-foot cycle is a silty, laminated dolomudstone (see MI-320.95, Appendix C). This is an unfossiliferous, silty, light-gray dolomite that weathers gray-yellow. Based on evidence for desiccation and subaerial exposure, calcium carbonate was probably deposited in sabkha conditions and penecontemporaneously converted to dolomite in this and other shallowing-upward cycles. Evidences for supratidal conditions are listed in **Table 3**.

Some workers favor evaporative processes for diagenetic transformation to dolomite. Friedman and Sanders (1967), Sun (1994), and Friedman (1995) concluded that most dolomite in the rock record formed under hypersaline conditions. Though evidence of hypersalinity is sparse in the Devonian rocks in Nevada, Niebuhr (1979) found evidence of pseudomorphs after salt crystals in the finely-crystalline stratal dolomites of the Guilmette 75 miles north of the study area. However, indirect evidence such as exposure and deflation surfaces, solution-collapse breccias, zebra dolomite, tepee structures, desiccation cracks, and replacement chert nodules suggest that elevated salinity was likely at the time of deposition or shortly afterwards.

Zebra dolomite and tepee structures at TMS look like those illustrated by Beales and Hardy (1980) in the Mississippi Valley-type ore deposits. Zebra dolomite that is parallel to bedding and associated with the upper part of shallowing-upward cycles could be associated with dissolved evaporite deposits as discussed by Beales and Hardy (1980). However, the creation of zebra dolomite by evaporative processes was not proven by Beales and Hardy (E. Mountjoy, 1998, personal communication). Zebra dolomite that is closely associated with non-stratal dolomite near faults is most likely to have formed under hydrothermal burial processes.

Examples of dolomudstone forming the upper parts of shallowing-upward cycles at TMS include MI-329.8, MI-334, MI-342, MI-344, and MI-383.6 in Appendix C. These photomicrographs exhibit common wispy laminations, mud-size grains, 100% dolomite, absence of fossils, and sparse burrows.

Coarsely-Crystalline Stratal Dolostone (Type 2)

The same processes may be responsible for both coarsely-crystalline stratal dolomite (Type 2) and pervasive dolomite (Type 3). They differ in the intensity of dolomitization. No limestone remnants occur in the pervasively dolomitized rocks below the Simonson Dolomite unconformity. Limestone remnants commonly occur in coarsely-crystalline stratal dolomites in the Guilmette above the unconformity. Several intervals at TMS are composed of stratally confined coarsely-crystalline dolomite. They include: from oldest to youngest 1) Guilmette Sequence Dgd cycles 3, 7, 9, 10, 14, 17, 22, and 23; 2) Guilmette Sequence Dge cycles 3, 12, and 13; 3) Guilmette Sequence Dgf cycle 7; and 4) Guilmette Sequence Dgg cycles 9, 20, and 23. Zebra dolomite is common in these intervals of coarsely-crystalline stratal dolomite and is probably genetically related to it. Zebra dolomite consists of bands of white sparry dolomite separated by bands of dark-gray finely-crystalline dolomite. Cavities lined with drusy dolomite in the white sparry

dolomite are common (see Beales and Hardy, 1980, Figures 2E and 3A-E, for examples of zebra dolomite). These intervals typically occur just below dissolution surfaces in the upper parts of sequences and cycles that contain karst breccia.

Typically, coarsely-crystalline drusy dolomite crystals line karst cavities, many of which are partly open. Terra rosa and hematite staining at cycle boundaries provide additional evidence of exposure and indirectly suggest periods of erosion. These periods of erosion could result in elevated salinity of ephemeral pools trapped on a low-relief exposure surface. If evaporite minerals formed in these pools, then the residual fluids could contribute to the dolomitization of the underlying karst zone.

Dunham and Olson (1980) provided evidence that dolomitization of the Ordovician Hansen Creek Formation carbonate platform was an early diagenetic process related to the Ordovician-Silurian paleogeography of the region. As with the Hansen Creek Formation, the shallowing-upward cycles in the Guilmette represent transgressions and regressions of the shoreline that controlled the western limit and seaward extent of the freshwater phreatic aquifer system. Similar to the Hansen Creek example, dissolution surfaces or karst zones developed at some Devonian sequence boundaries. Therefore, based solely on field evidence, I propose a similar model for the coarsely-crystalline, strata-bound dolomite at TMS. Dolomitization by brines resulted in intervals of coarsely-crystalline, strata-bound dolomite.

Coarsely-crystalline stratal dolomite intervals in the Guilmette commonly are associated with several feet of breccia and zebra dolomite. Breccias associated with cycle and sequence boundaries are likely karst breccias. They are regionally correlative. Other strata-bound breccia bodies may be a result of solution collapse. The solution collapse breccia occurs locally, is not associated with unconformities, and is not regionally correlative. Coarsely crystalline stratal dolomite intervals associated with cycle and sequence unconformities contain white, sparry dolomite that fills most of the fractures and voids in the karst zone. Open voids are lined with drusy dolomite. Subvertical fractures in the karst zone widen upward and are truncated by the unconformity. They do not

continue into the base of the overlying cycle. The coarseness of the dolomite crystallinity increases upward to the unconformity. Primary structures become more obliterated upward to the unconformity. Without fluid inclusion work, the origin of the coarsely-crystalline stratal dolomite is unknown.

Pervasive Dolostone below the Simonson Dolomite Unconformity (Type 3)

Carbonate rocks between the top of the Ordovician Pogonip Group and the regional unconformity at the top of the Simonson Dolomite were pervasively dolomitized in the Fossil Peak and Tempiute Mountain thrust sheets (see **Table 1** for Paleozoic nomenclature). In the Silver Canyon thrust sheet, carbonate rocks are pervasively dolomitized from the top of the Ordovician Ely Springs Dolomite to the top of the Simonson Dolomite. The significance of the anomalous occurrence of undolomitized limestone in the Ely Springs Dolomite of the Silver Canyon thrust sheet is discussed under structural interpretations in Chapter 6. The Silver Canyon thrust juxtaposed an Ely Springs limestone facies with a dolomite facies that probably experienced different paleogeographic and diagenetic histories.

The Simonson Dolomite unconformity truncates the Upper Alternating Sequence, which consists of shallowing-upward cycles that resemble those found in the overlying Guilmette. Pervasively dolomitized rocks below the top of the Simonson Dolomite are more coarsely crystalline and occur more regionally than finely-crystalline stratal dolomite cycle caps of the Guilmette Formation. Vuggy, coarsely-crystalline dolomite occurs in the karsted interval below the unconformity at the top of the Simonson Dolomite (Stop 7, Appendix D; Chamberlain and Warne (1996) Figure 4). Dolomites occur in the Guilmette above the unconformity. However, the pervasively dolomitized rocks differ from coarsely-crystalline stratal dolomites of the Guilmette in that no limestone remnants are preserved below the Simonson Dolomite unconformity. This

section on pervasive dolomite contains discussions including: 1) pervasive dolomite in Paleozoic rocks at TMS; 2) karsted Simonson Dolomite unconformity; 3) possible sources for dolomitizing fluids; and, 4) timing of dolomitization.

Pervasive Dolomite in Paleozoic Rocks at TMS The Simonson Dolomite unconformity divides the Paleozoic section at TMS and Tempiute Mountain and most sections in the Sunnyside basin from predominantly dolomite below (at least down to the top of the Pogonip) to predominantly limestone above the unconformity.

Ely Springs Dolomite (**Table 1**) is correlative with the Ordovician Hansen Creek and Vinini Formations in the Eureka area. Because of the lack of associated evaporite minerals or their traces, Dunham and Olson (1980) concluded that models involving hypersalinity were inadequate to account for the origin of regionally extensive replacement-dolomite formations. They provided evidence that dolomitization of the carbonate platform was an early diagenetic process related to the Ordovician-Silurian paleogeography of the region. Finney, et al. (1999) noted that the embayed platform margin Hansen Creek Formation in the Monitor Range (35 miles southwest of Eureka) is composed of lime mudstone rich in a diverse open-marine fauna. It lies in a facies between off-platform to basin Vinini Formation shales and limestones at Roberts Mountains (40 miles north-northwest of Eureka) and the shallow-marine pervasively dolomitized Hansen Creek Formation at Lone Mountain (25 miles west-northwest of Eureka). Similarly, dolomitization of the Ordovician-Devonian carbonate platform was also likely an early diagenetic process related to the paleogeography of the Timpahute region.

The Simonson Dolomite unconformity marks the last regionally extensive, pervasive, replacement- coarsely-crystalline Paleozoic dolomite (Type 3) in this part of the Great Basin. Its regional occurrence contrasts with the irregularly distributed late diagenetic products in the Western Canada Sedimentary Basin. These products include

coarse-crystalline replacement dolomites, minor occurrences of late-diagenetic saddle dolomite, and thermochemical sulfate reduction products formed during intermediate to deep burial (Mountjoy et al., 1997).

Karsted Simonson Dolomite Unconformity A regional major zone of karstification occurs immediately below the post-Simonson Dolomite unconformity (Chapter 4). This 20 to 100-foot thick zone is characterized by bleaching, karst breccia, upward thickening fractures filled with a dolomite spar and lined with coarsely-crystalline drusy dolomite crystals, and laminated cave deposits (Stop #7, Appendix D). Typically, the laminated cavity-filling cave deposits are pale-red, silty dolomite with angular carbonate fractures, and contain some small-scale cross bedding. Because the bedding of most of these cavity-filling sediments is parallel to the present-day tectonic dip, they must have been deposited before Mesozoic folding.

Simonson Dolomite unconformity karst differs from the zone of hydrothermal dissolution vugs, caverns, and breccia that host Mississippi Valley-type ore deposits in Devonian rocks at Pine Point, Northwest Territories, Canada. The Simonson Dolomite karst zone does not contain saddle dolomites, sulfide minerals, late-stage calcite, or pyrobitumen that Qing and Mountjoy (1994) attribute to hydrothermal fluids. At Pine Point, the hydrothermal dissolution zone follows a regional conduit and occurs both above and below the Watt Mountain unconformity. In contrast, the regional Simonson Dolomite unconformity karst zone is restricted to the strata immediately below the unconformity. Some karst cavities near the top of the Simonson Dolomite contain unaltered limestone from the overlying Fox Mountain Sequence. Furthermore, the Sulphur Point Formation below the Watt Mountain unconformity comprised of reef and shallow subtidal packstones, grainstones, floatstones and boundstones that could have had 5 to 10% porosity before dolomitization (Qing and Mountjoy, 1994). In contrast, the shallowing-upward cycles of the Upper Alternating Sequence below the Simonson

Dolomite unconformity are composed of wackestones and mudstones. They probably had very little porosity before karsting and dolomitization.

Some karst breccias in this interval extend several hundred feet below the unconformity. The upward thickening fractures filled with a dolomite spar and the coarsely-crystalline dolomite are truncated at the unconformity in most sections in the Sunnyside basin. Laminated cave deposits, described above, occur throughout the karsted zone. Bleached dolomites in the karst zone are distinct on the outcrop and on aerial photographs. The 100-200 foot bleached zone grades downward into the darker, underlying, non-karsted dolomites. Fluids moving through the well-developed pore system created in karsted carbonates is postulated to be related to the pervasive dolomitization below the unconformity. Large-scale and basin-wide process(es) involved in the dolomitization of the pre-Guilmette strata in the Great Basin could be similar to the processes involved in dolomitization of the Leduc in western Canada as discussed by Dix (1993).

Sources of Dolomitizing Fluids Almost no evaporite minerals occur in the Devonian carbonate section of the eastern Great Basin. Only two reports suggest anhydrite in Devonian rocks and both occur as cement in two wells: the Shell Oil Company Sunset Canyon #1 Unit well (Sec 21 T22S R4W, Millard County, Utah) and Tide Petroleum Baseline Canyon Unit #2 well (NE SW SW Sec 21 T1N R59E, Lincoln County, Nevada; Cedar Strat well files).

To the northeast of the Great Basin region, however, thick evaporite accumulations of the Prairie Formation were deposited in the Elk Point basin of western Canada and the Williston basin, Montana and North Dakota (Loucks, 1977). Also, a salt (halite) unit in the upper Duperow (Frasnian), the Flat Lake Evaporite, is locally preserved in northeast Montana and in southern Saskatchewan (Burke and Stefanovsky, 1984; Weinzapfel and Neese, 1986). It may have been deposited over a much wider area and

then subsequently removed. Similarly, the cycle cap breccias at the top of Guilmette cycles may be evidence of evaporites removed. No direct evidence of evaporites has been found. However, indirect evidence of removed evaporite minerals includes zebra dolomite at the top of shallowing-upward cycles, desiccation cracks, tepee structures, and salt casts in finely-crystalline dolomite.

The Williston basin Middle Devonian evaporites were deposited about the time of deposition and dolomitization took place in the Simonson Dolomite. The Simonson Dolomite is Emsian to Givetian (Johnson et al., 1989) and the Prairie Evaporite is Eifelian to Givetian according to the northern Rockies/Williston basin Region COSUNA chart by the American Association of Petroleum Geologists. The southwestern depositional edges of the Prairie Evaporite basin are not preserved because of periodic episodes of subsurface salt dissolutions from Late Devonian to the present (Horita et al., 1996). Thus, the Simonson Dolomite could have also contained evaporites that were not preserved.

Timing of Dolomitization There is an abrupt lithologic change across the Simonson Dolomite/Guilmette unconformity regionally. This abrupt change from pervasive dolomite to predominately limestone above the unconformity suggests that pervasive dolomitization in the Simonson Dolomite occurred before deposition of the overlying Guilmette. Unaltered limestone infiltration from the overlying Fox Mountain limestone into the aquifer provides the key to timing of dolomitization. The Fox Mountain lies between the karsted aquifer of the upper Simonson Dolomite and the aquitard of the Guilmette Yellow Slope Sequence. If dolomitization of the Simonson Dolomite occurred after deposition of the Guilmette Fox Mountain Sequence, then dolomitizing fluids should have also altered the overlying Fox Mountain limestones, provided they were porous and permeable. Preferential Cenozoic karsting of the Fox Mountain suggests that the limestone is still porous and permeable. Leviathan Cave in the Worthington Range is a good example of selective Cenozoic karsting of the Fox

Mountain limestone. Simonson Dolomite unconformity dolomitizing fluids should have been confined to carbonates below the Yellow Slope Sequence aquitard. In most stratigraphic sections of the Sunnyside basin, the Fox Mountain is limestone and not dolomite. This suggests that the dolomitizing fluids responsible for pervasive regionally correlatable dolomitization must have been restricted to Simonson Dolomite carbonates and older carbonates. Most dolomites in Devonian rocks above the unconformity occur locally as finely-crystalline stratal dolomite caps on upward shallowing cycles or as non-stratal dolomite associated with faults. Some dolomites, above the unconformity, occur as coarsely-crystalline stratal dolomite associated with minor unconformities.

The extensive, pervasive dolomite below the Simonson Dolomite unconformity occurs regionally throughout the Sunnyside basin. Similarly, extensive replacement dolomitization affected much of the Western Canada Sedimentary Basin during shallow burial and resulted in early-diagenetic porous matrix dolomites (Mountjoy, et al, 1997). In contrast to the regionally distributed pervasive dolomite below the Simonson Dolomite unconformity, the other three types of dolomite are more irregularly distributed.

Non-stratal Dolostone (Type 4)

In the Guilmette Formation, non-stratal dolomite occurs locally in zones from several feet to tens of feet wide. It occurs near major faults and fractures. Typically it cuts across strata. Commonly, this Type 4 dolomite exhibits “zebra” structures or zebra dolomite near faults. Zebra dolomite is an altered rock that exhibits alternating light and dark bands. The light bands are composed of coarsely-crystalline dolomite crystals or dolomite spars and the dark bands are composed of finely-crystalline dolomite crystals. Zebra dolomites in non-stratal dolomites are the most intensely altered carbonates at TMS. Similarly, Fischer (1988) also noted that zebra dolomite is found in his intensely altered fabric D dolomite of the Metaline Formation, northeast Washington. In the

Metaline Formation, Zebra dolomites occur in association with lead-zinc mineralization. Fischer (1988) interpreted it as an advanced diagenetic alteration. Emsbo et al. (1999) also noted that the Roberts Mountains Formation is pervasively dolomitized adjacent to vertical faults and that the resulting dolomite exhibits zebra texture. They suggested that basinal brines moved upward along synsedimentary faults where they dolomitized the Silurian-Devonian Roberts Mountains Formation and deposited barite and base-metal sulfides in fractures and cavities. Similarly, the non-stratal dolomite at TMS is probably attributable to a late stage hydrothermal alteration event. Some early-formed, east-west faults in the Silver Canyon footwall sheet are mineralized with jasperoids and are associated non-stratal dolomite containing zebra dolomite. The intensity of alteration along these faults decreases to no observable alteration about a mile from the Silver Canyon thrust fault. Intensity of dolomitization and abundance of zebra dolomite decreases away from the faults. Non-stratal dolomites are interpreted to be caused by late dolomitization along Mesozoic and Cenozoic fractures and faults. Dissolution or alteration of calcite and replacement by dolomite was the result of hydrothermal fluids or deep-basin brines moving along the fractures.

A non-stratal style of local dolomitization is evident in the outcrops of the Guilmette at Timber Pass, Seaman Range (Hurtubise, 1989), and in the northern Pahroc Range. Hurtubise (1989) suggested that dolomitization was related to the east-west Tertiary Timber Pass fault. Hurtubise and Dubray (1988) suggested that secondary dolomitization along this fault is evidence for a deep-seated crustal structure they called the Silver King lineament. They showed that the intensity of dolomitization in the Guilmette decreases away from the fault. Similarly, local dolomitization of the Guilmette limestones in the northern Pahroc Range, seven miles east of the study area, is probably related to the Late Mesozoic Pahroc thrust fault (Chapter 5 and Appendix E). Non-stratal dolomite also occurs in the Joana Limestone near a thrust contact at Hancock Summit, two miles south of the study area (Stop 6, Appendix D). This type of dolomite also occurs near Hiko Narrows (**Plate 1a**) where much of the Guilmette Formation is

dolomitized near faults. The intensity of dolomitization decreases away from the faults. Dolomitization may extend 100's of feet from larger faults such as at Hiko Narrows and only 5-10 feet from minor faults in the Hiko Range.

Much of the late dolomitization along fractures and faults in the Mail Summit section could be related to mineralization of the Pahranaगत (Mount Irish) mining district. Mineralization probably occurred about the time of Late Mesozoic Sevier compression and before Early Tertiary volcanism. Mineralized veins and fractures in dolomitized carbonates along the Silver Canyon thrust do not penetrate the overlying Tertiary volcanic rocks. Devonian carbonates in the fault bounded overturned western limb of the Silver Canyon syncline are pervasively dolomitized but they are not pervasively dolomitized in the upright, eastern limb (Appendix E).

Most of the thin sections in this study were taken from lower Guilmette sequences at TMS (Appendix C). All of them were stained with potassium ferricyanide. None of them developed a bluish hue typical of iron-rich crystals. TMS was selected to avoid faults. Therefore, the section lacks non-stratal dolomite except the dolomitized matrix of the lower part of Sequence Dgb2 breccia that may have been fed from nearby faults. Furthermore, none of the thin sections exhibit saddle dolomite that might be found in dolomite-filled fractures associated with non-stratal coarsely-crystalline dolomite. Also, the lack of pyrite in the thin sections suggests that bacterial sulfate reduction did not play a major role in the origin of dolomites in the section, a criterion used by Holail et al. (1988) for dolomite in the Upper Cretaceous of Egypt.

Summary

At least four types of dolomite occur in the Devonian section at TMS. Finely crystalline stratal dolomite (Type 1) at the top of shallowing-upward cycles is the most common type of dolomite in the Devonian rocks at TMS. The abundance of finely-

crystalline stratal dolomite decreases upward from the Sevy Dolomite to the Guilmette Formation. Finely crystalline stratal dolomite forms most of the Sevy Dolomite, about half the Simonson Dolomite, and is restricted to the upper parts of shallowing-upward cycles in the Guilmette Formation.

Stratal dolomite (Type 2) occurs locally below cycle boundaries that are not regionally correlatable. The upper part of Cycle 3, Guilmette Sequence Dgd at TMS is an example.

Pervasive dolomites below the Simonson Dolomite unconformity (Type 3) are widespread and predictable. The unconformity marks a major sequence boundary and a major lithologic change from pervasive dolomite below to predominately limestone above. Unaltered (undolomitized) limestone infiltrating into aquifer cavities from the overlying Fox Mountain Sequence shows that regionally correlative pervasive dolomitization below the unconformity took place before deposition of the Fox Mountain limestones.

Non-stratal dolomites (Type 4) are associated with faults. Their occurrence is irregular and they are not regionally correlatable. Dolomitized Guilmette in the fault-bounded overturned west limb of the Silver Canyon syncline is an example of this type of dolomite.

These four dolomite types can be roughly separated into penecontemporaneous dolomite and diagenetic dolomite. Penecontemporaneous dolomites are enriched in Sr and are more finely crystalline than diagenetic dolomite (Nichols and Silberling, 1980; Shukla, 1988). Type 1 or finely-crystalline stratal dolomite is penecontemporaneous and is probably more enriched in Sr than the other three types that are diagenetic dolomites. However, Sr analysis is beyond the scope of this study. Of the different processes or models of dolomitization discussed below, penecontemporaneous dolomites were likely formed from either primary precipitation, evaporative processes, marine water pumping, or seepage reflux. Diagenetic dolomites could have resulted from either mixing processes, large-scale basin-wide processes, burial compaction, tectonics and sedimentary

loading, or hydrothermal processes.

Conclusions

Many processes of dolomitization could explain the four dolomite fabric types at TMS. Capillary compaction is most likely the dolomitization process forming the finely-crystalline stratal dolomite upward-shallowing cycle caps at TMS. Hydrothermal processes probably resulted in the non-stratal coarsely-crystalline dolomite associated with faults. However, until they are thoroughly analyzed, the processes, timing, and sequences of dolomitization of TMS carbonates are unknown. Even with the availability of trace element, fluid inclusion, and detailed petrographic analyses, distinguishing conclusively between alternate processes and combinations of processes may be difficult (Zenger and Dunham, 1988). However, the Great Basin with its widely distributed outcrops offers an opportunity to resolve some “dolomite problems.”

CHAPTER 5

TIMPAHUTE RANGE STRUCTURAL ELEMENTS

Structural elements including thrust faults, folds, strike-slip faults, and normal faults of the greater Timpahute Range are summarized in this chapter and described in Appendix E. They set the stage for restoring thrust sheets containing measured sections (Chapter 6) and reconstructing the Devonian paleogeography (Chapter 7). The second goal of this study is to provide a new geologic map of the greater Timpahute Range. Upon completion, the new map illustrated the structural elements separating the sharply contrasting Upper Devonian facies of the study area. It is beyond the scope of this study to provide a detailed analysis of the structural elements, but this study provides constraints for a future comprehensive structural analysis recommended in Chapter 9.

As a step toward the new analysis I have generated a geometrically balanced structural cross section (**Plates 4a and 4b**). It shows that the greater Timpahute Range is composed of a stack of at least three main thrust sheets--Meadow Valley Mountain, Pahroc, and Silver Canyon--separated by two main thrust faults--Pahroc-Delamar and Silver Canyon-Chocolate Drop. The Penoyer Springs and Monte Mountain thrust faults are splay thrusts riding on the Silver Canyon thrust fault. The Fossil Peak, Tempiute Mountain, and an unnamed (5 on **Plate 4a**) thrust faults are splays on the Pahroc thrust fault. The Pahroc thrust fault may be a splay off another unnamed thrust fault (8 on **Plate 4a**). See thrust faults in Appendix E for detailed descriptions of these features.

Structural elements on the new Timpahute Range 30' X 60' geologic map include twelve thrust faults, 21 folds, thirteen strike-slip faults, but only five significant north-south striking normal faults in the Paleozoic rocks. These structural elements are named, classified, and described in Appendix E. They are indexed in a table of contents for Appendix E (page 345). In this chapter, the structural elements are grouped and discussed

in four categories: 1) thrust faults, 2) folds, 3) strike-slip faults, and 4) normal faults.

Names for all the structural elements on **Plate 1a** are new except the Freiberg thrust fault and the Seaman Wash fault both named by Tschanz and Pampeyan (1970) and the Golden Gate thrust fault and Garden Valley anticline named by Armstrong (1991). These names are used herein but names of other structures used by Tschanz and Pampeyan (1970) were discarded to avoid confusion with structural elements that were incorrectly mapped or which I interpreted differently. Two unnamed thrust faults shown on **Plate 4a**, but not exposed or mapped in the study area, were inferred on the cross section to explain the attitude of the overlying beds. Because of discontinuous outcrops, some of the twelve separately mapped thrust faults may represent structures that connect or that were connected before being offset by other faults.

Mappable stratigraphic sequences introduced in Chapter 4 were used to map the study area and helped refine structural elements presented in this chapter. As mentioned in Chapter 3, stratigraphic sequences along with other field attributes were recorded at each station. Stations are precise locations in the field where geologic attributes are measured and described. They are shown on my geologic maps as dip and strike symbols. Methods of plotting stations, tracing faults and formation contacts, and constructing map compilations are described in Chapter 3. Some stations are not shown on the maps because the symbols overlap. A table of approximately six thousand stations with all their field attributes would be impractical to include in this study (approximately 300 pages). Stratigraphic sequences mapped on large-scale (1:12,000 or 1:24,000) work maps described in Chapter 3 were grouped into formations to compile the small-scale map (approximately 1:80,000) **Plate 1a**, a composite of 24 7.5' quadrangles (**Figure 3**). **Plate 6** is an example of a map compilation from large-scale work maps (approx. 1:1,000) which also shows mapped sequences and section segments at TMS. Therefore, **Plate 1a**, a revised geologic map of the Timpahute Range 30' X 60' quadrangle, is a generalized geologic map illustrating the main structural elements that separate measured sections of contrasting Upper Devonian facies.

Thrust Faults

Thrust faults provide the greatest evidence for crustal shortening of the greater Timpahute Range. Chapter 1 shows how the thrust faults in the study area fit into the Sevier fold-and-thrust belt. Three main imbricated thrust sheets containing contrasting Upper Devonian stratigraphy make up the Paleozoic rocks of the greater Timpahute Range (**Figure 32**). They are from lower to upper: 1) Meadow Valley Mountain, 2) Pahroc, and 3) Silver Canyon. A thrust sheet is the package of rock above a thrust fault (Marshak and Mitra, 1988). Three contrasting Upper Devonian facies help distinguish the thrust sheets. Upper Devonian rocks of the Meadow Valley thrust sheet are not exposed in the map area. However, where they are exposed in the Meadow Valley Mountains and Pahroc Range, to the southeast and east of the study area, respectively, they are mostly dolomitized. The exposed part of the Pahroc sheet at Tempiute Mountain is composed of thin-bedded limestone (facies 1), and the exposed part east of the Silver Canyon thrust fault is composed of cyclic carbonates and reefs (facies 3). Separating the two Pahroc sheet facies is the Silver Canyon thrust sheet composed of thick quartz sandstones (facies 2). These facies and the significance of their structural position are discussed more fully in Chapter 7. Bounding the Silver Canyon thrust sheet are two east-west striking faults, the North Penoyer Springs and Reed Spring faults (Strike-Slip Faults, Appendix E). They are likely thrust tear faults.

Fortunately, erosion has cut through the Silver Canyon and Pahroc sheets at Tempiute Mountain, thus revealing a small sliver of the unnamed thrust sheet below the Tempiute Mountain thrust sheet (**Figure 32**). Only Mississippian shales and fusulinid-bearing Pennsylvanian-Permian rocks are exposed in the fenster. This fenster revealing the thrust sheet below the Pahroc and Silver Canyon thrust sheets is illustrated on the geologic profile on **Plate 1a** and on the structural cross section **Plate 4a**. The Tempiute Mountain thrust fault, a splay off the Pahroc thrust fault, separates the Pahroc and the unnamed thrust sheet (thrust faults, Appendix E). On the west end of the Timpahute

Range, the Chocolate Drop thrust fault separates the Pahroc and Silver Canyon thrust sheets. The Chocolate Drop and Silver Canyon thrust faults are probably the same thrust fault (geologic profile, **Plate 1a** and 3, 3a, and 3b on **Plate 4a**).

Lying on the Meadow Valley thrust sheet on the eastern greater Timpahute Range and below the Silver Canyon thrust sheet in the middle and western greater Timpahute Range is the Pahroc thrust sheet. In the greater Timpahute Range, it is divided into west and east segments by the overlying Silver Canyon thrust sheet (**Figure 32**). Upper Devonian strata in the Silver Canyon thrust sheet are composed of more than 1000 feet of quartz sandstones (facies 2). Exposed in a fenster of the Silver Canyon thrust sheet at Tempiute Mountain is a western segment of the Pahroc thrust sheet (**Plate 1a**). It contains a unique Upper Devonian thin-bedded limestone facies (facies 1) that is correlative with the thick sandstone facies in the Silver Canyon thrust sheet. In contrast, correlative strata in the eastern exposures of the Pahroc thrust sheet contain stromatoporoid reefs and lack thick sandstones (facies 3). Unconformities cut out many Devonian sequences in the Meadow Valley thrust sheet below the Pahroc thrust sheet (**Figure 17**). The three contrasting facies from different greater Timpahute Range thrust sheets were introduced in Chapter 1 and are discussed in Chapters 4 and 7. **Plate 4b** illustrates the location of the three facies after thrust restoration.

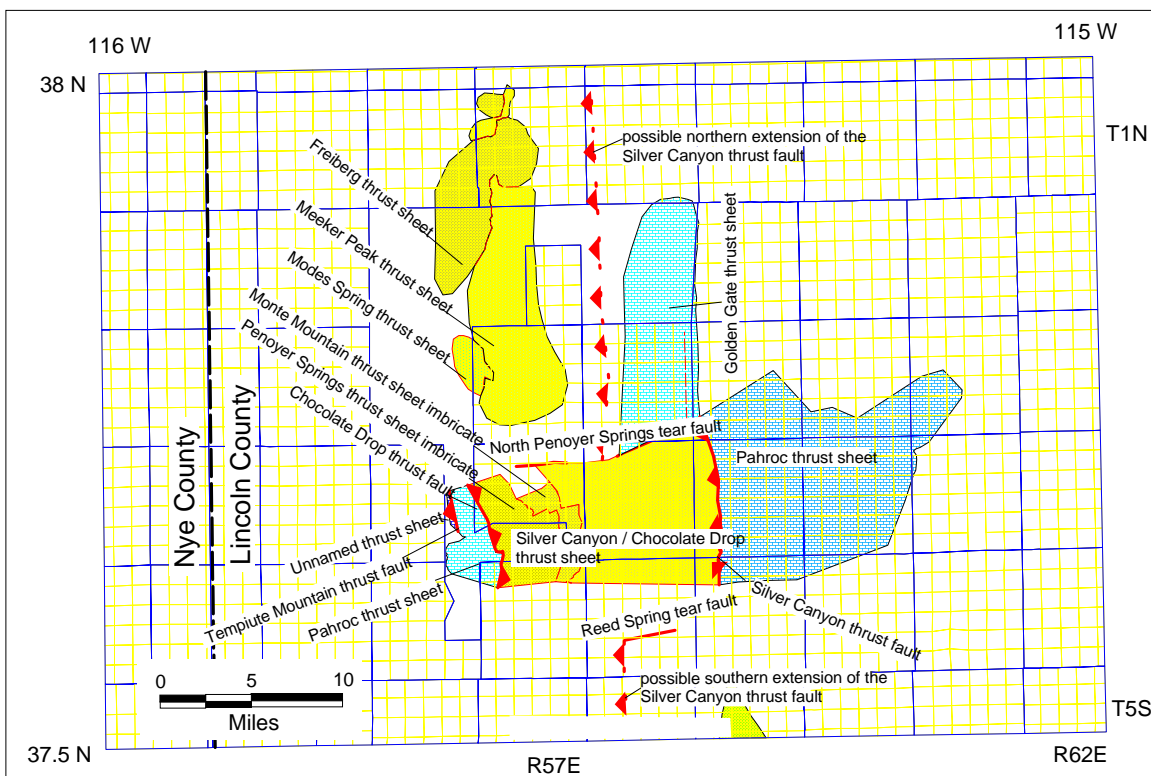


Figure 32 Generalized tectonic map of the Timpahute Range quadrangle showing the major thrust sheets and some of their imbricate sheets that make up the greater Timpahute Range. The sandy (facies 2) Silver Canyon thrust sheet (yellow) and its imbricates (darker yellow) contrast sharply with the reefy (facies 3, east) Pahroc and thin-bedded limestone (facies 1, west) Pahroc thrust sheet (light blue bricks). Thin red lines separate imbricate thrust sheets within the Silver Canyon thrust sheet. Only a small sliver of an unnamed thrust sheet (dark blue bricks--see label) is exposed in a fenster of the Silver Canyon and Pahroc thrust sheets on the west end of the greater Timpahute Range.

The uppermost thrust sheet, the Silver Canyon thrust sheet, is well-exposed in the middle of the greater Timpahute Range and in the Worthington Range to the north. A deep (>30,000 feet) test on Mount Irish should cut two and perhaps three thrust sheets (**Plate 1a**).

Meadow Valley Mountain Thrust Sheet

The Meadow Valley Mountain thrust sheet is exposed in the North Pahroc Range, five miles northeast of the study area, and in the Meadow Valley Mountains, 25 miles southeast of the study area (**Figure 2**, Pahroc thrust fault, Appendix E, and **Plate 4**). Western dipping Paleozoic rocks of the Meadow Valley Mountain thrust sheet steepen westward in the North Pahroc Range (Cedar Strat proprietary geologic map, 1996). Unfortunately the trace of the thrust fault, or the normal fault of Taylor (1989), between the Seaman and North Pahroc ranges is buried by Tertiary volcanic rocks.

At Pahroc Summit, 14 miles east-northeast of Hiko, folded Paleozoic rocks in the Pahroc thrust sheet attest to an underlying thrust detachment (see Pahroc Spring anticline, Appendix E). However, the Pahroc thrust fault is concealed by Tertiary volcanic rocks in and next to the study area. The Pahroc thrust fault is the inferred northern extension of the Delamar thrust fault. Only in the southern Delamar Mountains, 35 miles south-southeast of the study area, has headward erosion by Colorado River tributaries exhumed the Delamar/Pahroc thrust fault.

A footwall syncline in the Meadow Valley Mountain thrust sheet in the southern Delamar Mountains suggests yet another thrust detachment below the Pahroc thrust fault. Therefore, the Pahroc thrust sheet is another imbricate in a stack of thrust sheets. Additional regional mapping, deep well bores, and seismic data will likely reveal deeper thrust detachments. However, the upper three thrust sheets are the main focus of this study.

Pahroc Thrust Sheet

Lying on the Meadow Valley thrust sheet and partly concealed by the overlying Silver Canyon thrust sheet, the Pahroc thrust sheet contains the TMS (facies 3) and the

Tempiute Mountain (facies 1) measured sections (**Plate 1a**). Exposures of the Pahroc thrust sheet are found east of the Silver Canyon thrust fault and west of the Chocolate Drop thrust fault (**Figure 32**). TMS, with its Upper Devonian stromatoporoid reef, lies about 1.5 miles east of the Silver Canyon thrust fault. The Tempiute Mountain measured section containing thin-bedded limestones lies 1.9 miles west of the Chocolate Drop thrust.

Folded Paleozoic rocks in the Pahroc thrust sheet suggest an underlying detachment. Its western exposure contains the Tempiute Mountain anticline. Folds of the eastern exposure include Silver Canyon syncline, Mail Summit anticline, Fossil Peak anticline, folds in the Hiko Range, and Pahroc Spring anticline (Appendix E). Fusulinid-bearing Permian-Pennsylvanian limestones on the eastern edge of the western exposure of the Pahroc thrust sheet near the Chocolate Drop thrust fault are vertical to overturned. These folded rocks provide evidence of an underlying detachment below the greater Timpahute Range. Folds in the Golden Gate and Seaman ranges north of the greater Timpahute Range also suggest a thrust fault detachment beneath the Pahroc thrust sheet.

The main stratigraphic differences between rocks of the Meadow Valley Mountain thrust sheet and the Pahroc thrust sheet include abrupt changes in the thickness of the Sequence Dgb2 breccia and the content of quartz sandstone in the Upper Devonian Guilmette Formation. The breccia is more than 100 feet thick in the hanging wall Pahroc thrust sheet (Hiko and Delamar ranges) and is less than 10 feet thick in the Meadow Valley Mountain thrust sheet (Meadow Valley Mountain (**Figure 17**) and North Pahroc Range). Quartz sandstone thickens from zero sandstone in the Meadow Valley Mountain thrust sheet to 10's of feet in the Pahroc (Delamar-Arrow Canyon) thrust sheet, to 100's of feet in the Pahrnagat thrust sheet. The Pahrnagat thrust sheet possibly correlates to the Silver Canyon thrust sheet (**Figure 32**).

In the northern Arrow Canyon Range (114.88 W Longitude; 36.76 N Latitude, 62 miles south-southeast of Hiko), the Dgb2 breccia is 3 feet thick. In the Delamar Range (114.98 W Longitude, 37.05 N Latitude, 40 miles south, southeast of Hiko) it is 260 feet

thick. Thicknesses of the Ordovician Eureka Quartzite in both ranges are similar (164 feet in the north Arrow Canyon Range and 142 feet in the southern Delamar Range, Shell Oil Company proprietary measured sections). Webb (1958) reported 132 feet of Eureka Quartzite in the northern Arrow Canyon Range. If the two sections correlate and belong to the same thrust sheet, then the thickness of breccia decreases from 260 to 3 feet in approximately 22 miles. However the thickness of the Eureka Quartzite in the Meadow Valley Mountains, ten miles east of the Delamar Range, is approximately 20 feet (A Cedar Strat proprietary map). Therefore, the Meadow Valley Mountains lie in another thrust sheet, footwall to the Delamar-Arrow Canyon thrust sheet. If the breccia decreases in thickness linearly between the Delamar and Arrow Canyon ranges, then the same rate of decrease could be applied between the Delamar and Meadow Valley Mountain sections. Applying that rate of decrease (5.8 feet per mile), depositional or restored distance between the Delamar Range and the Meadow Valley Mountains should be approximately 44 miles. If the above assumptions in correlations and rate of change of thicknesses hold, the amount of crustal shortening on the Pahroc thrust fault is approximately 44 miles, based on Dgb2 stratigraphic considerations. Cumulative thrust slip on the Pahroc and underlying unnamed (8 on **Plate 4a**) thrust faults on **Plate 4a** is 20 miles. Other concealed thrust faults taking up addition displacement could lie between the Pahroc and Meadow Valley ranges. Therefore, crustal shortening between the ranges is at least 20 miles and could possibly be more.

The Ordovician Eureka Quartzite can also be used to estimate shortening on the Pahroc thrust fault (**Plate 1a** and Appendix E). It is approximately 120 feet thick in the east Arrow Canyon Range (Longwell et al., 1965) and 150 feet thick in the Delamar Range (Tschanz and Pampeyan, 1970), 22 miles away. Therefore, it thins an average of 1.36 feet per mile. The Eureka Quartzite is approximately 20 feet thick in the Meadow Valley Range sheet. If the thickness decreases linearly, then the Eureka Quartzite in the Delamar Range was deposited 96 miles from the Meadow Valley sheet, based on Eureka Quartzite stratigraphic considerations. However, crustal shortening was probably less

than 96 miles on the Pahroc thrust fault. More accurate stratigraphic sections with gamma-ray logs and correlations based on sequences as presented herein should improve the estimates of crustal shortening.

Splay thrust faults in the Pahroc thrust sheet include the Fossil Peak thrust fault, Hiko Spring klippe, and the Golden Gate thrust fault. The Fossil Peak thrust sheet and the Hiko Spring klippe may both belong to the Fossil Peak thrust fault (Thrust Faults, Appendix E). The Golden Gate thrust fault superficially appears to terminate south of the Baseline Canyon fault in the Golden Gate Range (**Plate 1a** and Thrust Faults, Appendix E). However, folds north of the east-west trending Baseline Canyon fault and footwall splay thrust faults east of the Golden Gate thrust fault suggest that shortening on the Golden Gate thrust fault was taken up by other structures (see Golden Gate thrust fault, Golden Gate anticline, Golden Gate syncline, Garden Valley anticline and Baseline Canyon fault in Appendix E).

A group of east-west normal faults is restricted to the Pahroc thrust sheet east of the Silver Canyon thrust fault in the greater Timpahute Range (see Mail Summit faults, Appendix E). They are lacking in the overlying Silver Canyon thrust sheet. Another east-west striking fault cutting the Pahroc thrust sheet is the Wildcat Wash fault. It occurs 1.4 miles west of the Chocolate Drop thrust fault. South (1.3 miles) of Wildcat Wash fault, the Tempiute Mountain fault could have strike-slip displacement (Appendix E).

North of the greater Timpahute Range, the Pahroc thrust sheet, exposed in the Golden Gate Range, is also cut by east-west normal faults. However, similar faults are lacking in the Worthington Range interpreted to be part of the Silver Canyon thrust sheet. Another east-west trending fault in the Pahroc thrust sheet, the Crystal Springs Canyon fault, could have strike-slip displacement plus dip slip displacement (see Crystal Springs Canyon fault in Appendix E). Two east-west striking faults, the North Penoyer Springs and Reed Spring faults, are likely thrust tear faults. Other east-west striking faults in the Pahroc thrust sheet include: northeast Tikaboo Valley faults, faults north of Bactrian Mountain, and Logan Canyon fault.

Three significant north-south trending normal faults in the study area cut rocks of the Pahroc thrust sheet: Hiko Narrows, Coal Valley Reservoir, and Mail Summit faults. However, the Hiko Narrows fault could be a thrust fault revealing rocks in a fenster of a lower thrust sheet (see Hiko Narrows fault in Appendix E). The Coal Valley Reservoir fault, is likely a listric normal fault on the west side of Coal Valley with several hundred feet of displacement (see Coal Valley Reservoir fault in Appendix E). The west Mail Summit fault is exposed 2.9 miles east of the Silver Canyon thrust fault (**Plate 1a**). It also has several hundred feet of displacement. North-south trending normal faults with thousands of feet of displacement were not detected in the study area (see discussion of normal faults below and description of normal faults in the Timpahute Range 30' X 60' quadrangle in Appendix E).

Silver Canyon Thrust Sheet

Exposures of the Silver Canyon thrust sheet in the middle of the greater Timpahute Range lie between the Chocolate Drop thrust fault on the west and the Silver Canyon thrust fault on the east (**Plate 1a; Figure 32**). North of the greater Timpahute Range, the Silver Canyon thrust sheet is exposed in the Worthington Range (**Figure 32**).

Folds within the Silver Canyon thrust sheet attest to underlying thrust detachments. Folds include Mount Irish anticline, Monte Mountain syncline, Penoyer Springs syncline, north Timpahute anticline, and the Worthington Mountain doubly plunging anticline (Appendix E).

Splay thrust faults within the Silver Canyon thrust sheet include Penoyer Springs and Monte Mountain thrust faults in the greater Timpahute Range and the Freiberg and Modes Spring thrust faults in the Worthington Range (Appendix E). The north Worthington fault may be a fenster into a deeper thrust sheet or it could be a normal fault (see Appendix E). Penoyer Springs and Monte Mountain thrust faults have footwall

synclines. Footwall synclines are absent, however, in the Worthington Mountains. East-west striking strike-slip faults are generally restricted to the Silver Canyon thrust sheet. They include six faults: south Penoyer Springs, Tunnel Spring, Monte Spring, Chocolate Drop, south Timpahute Range and Logan Canyon faults (Strike-Slip Faults, Appendix E).

In the greater Timpahute Range, the Silver Canyon thrust sheet is bounded on the north and south by faults interpreted as thrust tear faults. Therefore, the greater Timpahute Range portion of the Silver Canyon thrust sheet moved eastward approximately two miles with respect to the northern or southern portions of the thrust sheet. Two miles is the measured distance between the north and south sides of the Logan Canyon fault (**Plate 1a**).

Thick (1000+ feet) Upper Devonian quartz sandstone (facies 2), abnormally thin (~200- feet) Sequence Dgb2 breccia, and limey Ordovician Ely Springs Dolomite distinguish the strata of the Silver Canyon thrust sheet from the underlying Pahroc thrust sheet. An isolith map of the Devonian quartz sandstones was used to estimate the 30 miles of crustal shortening on the Silver Canyon thrust fault (Chapter 7). Also, in Chapter 7, isolith maps of the Dgb2 breccia were used to estimate about 100 miles of relative cumulative crustal shortening of the three thrust sheets of the greater Timpahute Range.

Conclusions

Newly mapped thrust sheets in the Timpahute 30' X 60' quadrangle geologic map explain the abrupt change in Upper Devonian facies separated by thrust faults. Approximately 62 miles of structural shortening shuffled the thrust sheets and required thrust restoration to accurately interpret the Devonian paleogeography. Unique stratigraphic components such as the distribution of the Dgb2 breccia and Upper Devonian quartz sandstone provide tools to aid in thrust reconstruction.

Figure 32 is a conceptual tectonic map of the study area summarizing the major thrust sheets of the greater Timpahute Range. Cenozoic cover conceals most of the thrust sheets and thrust fault traces in the Paleozoic rocks. Strike-slip faults on the north and south sides of the greater Timpahute Range are probably thrust tear faults that separate contrasting stratigraphic facies of the different thrust sheets. The Silver Canyon thrust sheet in the greater Timpahute Range moved eastward approximately two miles with respect to portions of the sheet north and south of the greater Timpahute Range. Tempiute Mountain is a fenster in the Silver Canyon thrust sheet revealing a western segment of the Pahroc thrust sheet. A second fenster on the west side of Tempiute Mountain in the Pahroc thrust sheet reveals a sliver of an unnamed thrust sheet. Folding in exposures of the Meadow Valley thrust sheet east of the Pahroc thrust fault suggest another, deeper detachment. Therefore, the greater Timpahute Range is interpreted to be composed of a stack of at least three thrust sheets: Meadow Valley Mountain, Pahroc, and Silver Canyon.

This stack of thrust sheets probably has ridden eastward on yet deeper detachments. Other than minor splay thrust faults, all the thrust faults in the study area glide on Carboniferous strata and especially on Mississippian shale (**Plate 4a**). The master detachment probably involves Lower Cambrian or older rocks on Carboniferous or younger rocks. Probably all of the exposed thrust faults in the study area are merely thrust fault splays of a large system (Sevier orogenic belt?).

Folds

Twenty-one folds in the study area testify of the intensity of crustal shortening of this part of the Sevier fold-and-thrust belt. See Folds, Appendix E for a detailed description of each fold. The new map showing these folds contrasts sharply with previous mapping that shows only four folds in the study area (**Plate 1a** and **Plate 1b**).

Broken recumbent footwall synclines, an important signature of the region's structure style, provide strong evidence of deeper thrust faults. The study area represents only a small sample of the Sevier fold-and-thrust belt in Nevada. Many uncharted folds occur beyond the study area. All these folds attest to the amount of crustal shortening. However, newly mapped thrust faults discussed above provide a stronger witness to the amount of crustal shortening that occurred in this part of the Sevier fold-and-thrust belt. Without an understanding of the amount of crustal shortening accurate reconstruction of Devonian paleogeography is not possible.

Strike-Slip Faults

Little work has been done to date on strike-slip faults within the Timpahute Range quadrangle. More than thirteen strike-slip faults are documented on the Timpahute Range quadrangle geologic map (Appendix E, **Plate 1a**). Most of them are newly mapped and all of them are newly named. All the strike-slip faults, except the Tempiute Mountain and Reed Spring faults, have sinistral strike-slip displacement. The most obvious ones with the most strike-slip displacement include Logan Canyon, Tunnel Springs and South Penoyer Springs faults. Dip-slip normal displacement on these faults is measured in hundreds of feet and strike-slip displacement is measured in thousands of feet or miles. Dip-slip normal displacement probably took place along pre-existing zones of weakness caused by the strike-slip displacement. As Tschanz and Pampeyan (1970) point out, strike-slip displacement may be related to tear faults.

An important diagnostic feature of these strike-slip faults is that, despite highly divergent domains of structural dip, the sense of displacement remains the same along their trace. The diagnostic features that are sporadically observed include slickensides, dikes, hydrothermal alteration zones, discontinuities in structural grain, and outcrop patterns. Descriptions of the newly named faults appear in Strike-Slip Faults, Appendix

E.

This study documents several strike-slip faults. Most of them are east-west trending or parallel with thrust fault movement. Strike-slip faults, confined to a single thrust sheet, could be tear faults created synchronously with thrust fault emplacement. Some exhibit dip-slip movement and could have been reactivated during Cenozoic extension. Faults most likely having dip-slip displacement are described in normal faults of Appendix E.

Strike-slip Faults as Thrust Tear Faults In 1964, Gwinn stated that abrupt changes in structure and stratigraphy or outcrop patterns along strike-slip faults in the Appalachians are probably caused by tear-faults. Strike-slip faults in the Timpahute Range quadrangle may be tear faults. As mentioned above Tschanz and Pampeyan (1970) suggested that the Arrowhead Mine fault, twenty miles south of the study area, could be a tear fault. Some sets of faults in the study area are confined to certain thrust sheets. This implies they formed synchronously with formation of the thrust sheet in the Late Mesozoic. Four strike-slip faults described in this section are restricted to the Silver Canyon thrust sheet. The Mail Summit faults presented in the section on normal faults are restricted to the Fossil Peak thrust sheet. The Reed Spring fault may be a right-lateral tear fault on the south edge of the Silver Canyon thrust sheet. The Penoyer Springs fault may be a left-lateral tear fault on the north side of the Silver Canyon thrust sheet.

Normal Faults

Continuous outcrops in the greater Timpahute Range provide an opportunity to study the results of Cenozoic extension in this region of the Great Basin. These faults and

fractures greatly enhance the reservoir qualities of the rocks of the region. However, only eight faults with significant displacement or features were documented, as described in detail in Appendix E.

Five of the eight significant normal faults in the study area strike north-south, parallel with the structural grain of the region. Two of the five have 10,000 feet or more stratigraphic displacement and may be thrust faults. Stratigraphic displacement on the other three is 2000 feet or less. No classical Basin and Range normal faults with tens of thousands of feet of displacement are found in the study area. Either the study area is a unique area that has escaped regional Cenozoic extension or the region has been misinterpreted to have been severely affected by Cenozoic extension.

Geologic mapping beyond the study area revealed few possible Basin and Range normal faults constrained by outcrop data. Many published classical Basin and Range normal faults are shown in valleys where they are unconstrained by outcrops. Some have used seismic data to justify their interpretation of a classical Basin and Range faults such as on the east side of Eagle Springs field in Railroad Valley (Effimoff, and Pinezich, 1986; Dolly, 1979; Vreeland and Berrong, 1979). No mention is made of the westward steeply dipping Paleozoic rocks in the pediment and at the foot of Grant Range on the east end of the seismic lines. If a normal valley-bounding fault occurs as suggested by Bortz and Murray (1979), then it is subparallel to bedding in Paleozoic rocks. Clearly, all Great Basin inselbergs containing Paleozoic rocks need to be mapped more carefully before sweeping interpretations of this complex region are made.

Extensional vs. Compressional Models

Mayer (1986), using topographic constraints to model lithospheric stretching or crustal thinning of the Basin and Range province, concluded that the thinning resulted in “a topographic pattern characterized by normal-fault-bounded mountain blocks separated

by alluvial valleys superimposed on a broad regional uplift.” The most widely accepted model of Tertiary Basin and Range extension in the region of the study area emphasizes north-south trending faults of major displacement (thousands of feet) bounding the ranges (horsts) and valleys (grabens). Effimoff and Pinezich (1986) concluded, from their study of selected basins in the region, that the basins are bounded by listric normal faults with displacements of 10,000 to 15,000 feet.

Taylor (1989) attributed the tilted Paleozoic rocks in the North Pahroc Range, 10 miles northeast of the study area, to normal faults. Though he misidentified several key outcrops, Hurtubise (1989) found no evidence for thrust faults in the Seaman Range, from Fossil Peak to Black Cliff, 25 miles north. He also attributed tilting in Paleozoic rocks to normal faults caused by Cenozoic extension. However, Bartley et al. (1988) described the area from the Seaman Range to the Golden Gate Range, five miles north of the study area, as an area of minor normal faults caused by Cenozoic extension. North-south normal faults related to Cenozoic extension are rare in the study area. Most of the exposed normal faults cut across the north-south structural grain in the study area. The few normal faults that are subparallel with the north-south structural grain have stratigraphic displacement of no more than several hundred feet. An exception is the Hiko Narrows fault exposed in Sec 7 T3N R61E with about 5000 feet of stratigraphic displacement (See Fossil Peak thrust in Appendix E). Normal north-south trending faults with tens of thousands of feet of displacement are not recognized in the study area. In contrast, thrust faults with tens of miles of displacement are documented in the study area. Significant normal faults in the study area with their locations and approximate throws are listed in Appendix E.

Some normal fault models depict 20-40,000 feet of vertical stratigraphic separation and many miles of horizontal extension. Axen et al. (1993), for example, speculated that a major normal fault is situated just east of the study area, between the Seaman and North Pahroc ranges, and is concealed by Tertiary volcanics and sediments. They concluded that the ranges in the region of the Timpahute Range quadrangle were

extended during the Tertiary. However, I find no evidence in my mapping that supports their conclusion. Furthermore, it is shown in Appendix E that steep gradients in an isostatic gravity contour map supporting their postulated normal fault are lacking. In contrast to their model, I postulate that a major thrust fault (Pahroc/Delamar thrust fault) is situated just east of the study area. As with the postulated normal fault, it is concealed by Tertiary volcanics. However, the Pahroc Spring anticline, exposed through a window of volcanic rocks and exposures of the Delamar thrust fault to the south, supports the crustal shortening model. The current study provided the opportunity to test, within the Timpahute Range quadrangle, both models and their inherent ramifications.

Conclusions

New mapping clearly shows more compressional structural elements in the Paleozoic rocks of the Timpahute Range quadrangle than was previously known. The new mapping combined with well and gravity data (Appendix E) dispute the existence of published hidden normal faults believed to have been caused by Cenozoic extension. No classic, north-south trending Basin and Range normal faults were found cutting the greater Timpahute Range. Therefore, the region likely underwent more Late Mesozoic compressional deformation and much less Cenozoic extension than was previously thought. **Plate 4**, a structural cross section, constrained by the new mapping, shows significant displacement between thrust sheets. Therefore, paleogeographic reconstructions based on unrestored locations for measured sections are misleading. The stratigraphic significance of structural interpretations in Chapter 6 sets the stage for paleogeographic reconstructions based on restored sections (Chapter 7).

CHAPTER 6

STRATIGRAPHIC SIGNIFICANCE OF STRUCTURAL INTERPRETATIONS

The magnitude of the Sevier-age compressional event on the Paleozoic rocks of the study area estimated in this chapter, shows how the newly mapped folds and faults on **Plate 2a** contribute to a new tectonic model. The new model helps explain contrasting post-Guilmette Formation Sequence Dgb facies in juxtaposed thrust sheets. The new geologic map of the greater Timpahute Range, with its more detailed analysis of Great Basin thrust styles, also provides constraints for a more accurate tectonic model. It will be shown in Chapter 7 that knowledge of the assumed original distribution of Dgb2 breccia provides a unique opportunity to restore thrust sheets with a greater degree of confidence and further constrains the structural model. This new tectonic model is illustrated by a geometrically balanced structural cross section of the greater Timpahute Range (**Plate 4a**) and its restoration (**Plate 4b**). The tectonic model is supported by other data including biostratigraphic dislocation, structural implications of the “Oxyoke Formation,” contrasting facies in the Ordovician Ely Springs Dolomite between structural sheets, and the distribution of Tertiary-Cretaceous synorogenic rocks

Tectonic Model

A tectonic model of the greater Timpahute Range is supported by a balanced cross section (**Plate 4**). Restoration of the cross section shows that cumulative displacement of thrust faults within the greater Timpahute Range is approximately 63 miles. An explanation of the distribution of contrasting facies in different structural sheets is shown

by the model. It also provides new opportunities for oil and gas exploration and helps predict the location of the Dg2 breccia impact site.

Balanced Cross Section

An advantage of a balanced cross section is that it helps isolate possible geometric solutions and eliminate impossible ones. Normally, balanced cross sections in eastern Nevada are impossible to construct because of the lack of constraint or control that ties the deformed region to an undeformed region (Chapter 3). However, because of its unique nature, the distribution of the Dgb2 breccia may provide the constraint necessary to construct a balance cross section of the greater Timpahute Range (Chapter 7). **Plate 4a**, a cross section along A-A' of the greater Timpahute Range geologic map, was made using *Thrustbelt*, a software program described in Chapter 3.

Fundamental parameters needed to construct a balanced cross section included spacing and scales. Spacing affects the smoothness of the appearance of lines in the cross sections. Centimeters were used as the unit of measurement to construct **Plate 4a** and **Plate 4b** because they were easier to use than English measurements. Distances and elevations on the 30' X 60' Timpahute Range topographic quadrangle are in meters. The metric system simplified relating distances and thicknesses on the cross section. Horizontal and vertical scale factors were kept constant to avoid vertical exaggeration.

Once the fundamental parameters were established, geologic parameters were added. First, a stratigraphic section was made by building up layer by layer, starting at the lowest layer of interest, the Upper Cambrian. Rocks of the Upper Cambrian are the oldest exposed in the greater Timpahute Range (**Plate 1a**). A topographic profile of the greater Timpahute Range transect A-A', showing the surface geology and formation thicknesses that constrain the structural cross section, **Plate 4a**, lies below the geologic map on **Plate 1a**. Formation thicknesses were taken from measured sections and wells (Well Data,

Appendix F) in the region. The base of each formation was entered from oldest to youngest along with its x-coordinate on the stratigraphic cross section.

An angle in degrees, compared with the base of each rock unit at which a hypothetical fault would cut through the unit, was specified. A higher angle (25°) was chosen for more massive, resistant units (Laketown, Sevy, Simonson, and Ely formations). A lower angle (20°) was assigned to more platy, less resistant units (Pogonip, Guilmette, and Joana formations. Because of its shaley nature, the lowest angle (15°) was assigned to the Mississippian Antler clastics. The differences in thrust fault angle can be seen on **Plate 4b**.

Each fault is described as to the unit it is rooted in, its position in the cross section, the layer to which it climbs and the x-coordinate of the ramp of the next sub-fault, and the direction and amounts of movement along the fault plane. These fault parameters were changed and tested until a satisfactory solution was found and thrust fault traces and units matched the topography, geology, and faults on the geologic map (**Plate 1a**). Any of the 50 or so iterations are geometrically possible but the final solution, **Plate 4a**, most closely matches the new geologic map. The model could always be improved with additional mapping and more rigorous structural analysis.

Plate 4a and Plate 4b

Plate 4a illustrates the deformed Paleozoic rocks along transect A-A' (**Plate 1a**). Rocks above the erosional profile have been removed by erosion. The erosional profile is shown by the thick, solid line that begins on the left-hand side at 16.5 kilometers above the base of the section. Several topographic features along the erosional profile are labeled for reference. Sea level is the horizontal, straight line below the erosion profile at 15 kilometers above the base of the section. A legend for rock units is on the right-hand end of both **Plate 4a** and **Plate 4b**. The darkest gray unit, Mississippian Antler clastics, is the

last prominent shale unit in the Paleozoic rocks and contains the main thrust detachments. It is also the main source rock in Nevada (Poole and Claypool, 1984). How much compression to cause the folds and faults in the greater Timpahute Range can be seen on the left-hand end of **Plate 4a**. The missing rock units above the Upper Cambrian were moved 104 kilometers or about 64 miles to the east.

Thrust faults are labeled consecutively from left to right on **Plate 4b**. The oldest faults are on the left and the youngest are on the right. In the deformed area, they are curved, solid, dark-gray lines that separate wedges of different formations. Left of the deformed area on **Plate 4a**, the faults root in the Upper Cambrian and are parallel to bedding. Right of the deformed area, the faults lie within the upper detachment in the Carboniferous. Undoubtedly, thrust faults east and west of the greater Timpahute Range will further complicate the cross section and will show more compression in this region of the Sevier fold-and-thrust belt.

Amount of Displacement

The cumulative amount of thrust displacement shown on **Plate 4b** is 105 kilometers or about 64 miles. Thrust faults east and west of the greater Timpahute Range were not taken into account on **Plate 4a**. Another model using “snip reconstruction” and thrust displacement within and beyond the greater Timpahute Range estimated 98 miles (**Table 10**) of cumulative compression (Chamberlain and Chamberlain, 1990). Snip restoration is a technique of thrust fault restorations introduced by D. Roeder to Esso in 1967 (D. Roeder, 1998, personal communication). Each thrust slice is snipped or cut from a cross section and laid out in sequence like a puzzle to preserve area of the beds. Bed-length measurement from **Plate 4a** suggests that the Silver Canyon thrust fault have a displacement of approximately 22 miles. Snip reconstruction of the Chocolate Drop-Silver Canyon thrust fault suggested that the fault have about 28 miles of lateral

displacement (Chamberlain and Chamberlain, 1990). **Table 10** lists the approximate displacement of faults estimated from snip reconstruction and from **Plate 4a**.

Table 10 Bed length displacement scaled from a snip reconstruction model and the amount of slip for each thrust in **Plate 4a**.

Thrust Fault	Approximate Displacement snip reconstruction	Approximate Displacement Plate 4a
Pahroc	50 miles	18 miles
Silver Canyon	28 miles	22 miles
Tempiute Mountain splays	12 miles	9 miles
Penoyer Springs	3 miles	3 miles
Fossil Peak	3 miles	9 miles
Monte Mountain	2 miles	2 miles
Unnamed thrust fault		1 miles
Cumulative displacement	98 miles	64 miles

Much of the compressional displacement of the greater Timpahute Range was taken up by folding. Most of the thrust faults in the greater Timpahute Range along transect A-A' (**Plate 1a**) are characterized by an anticline with a gentle west back limb and a steep east forelimb in the hanging wall sheet. They are also characterized by a broken recumbent syncline in the footwall. Typically, a footwall thrust fault places the recumbent limb on Mississippian Antler shales (Chainman facies, **Table 1**). Unless Pennsylvanian rocks are included, the upper sandy facies (Scotty Wash facies) of the Antler clastics are usually sheared off by thrust faults. The shales extend for an unknown distance under the thrust faults. Examples of this style of thrust faults include the Golden Gate (Stop 10,

Appendix D), Penoyer Springs (geologic profile, **Plate 1a**), Monte Mountain (Stop 14, Appendix D and Appendix E), and Silver Canyon thrust faults (a geologic profile, **Plate 1a**). Examples of older Paleozoic rocks thrust over Pennsylvanian rocks include the Chocolate Drop (geologic profile, **Plate 1a**) and Pahroc thrust faults (Stop 2, Appendix D, and Appendix E). In all these examples, Mississippian organic-rich, oil-prone source rocks are placed advantageously below potential reservoir rocks. The economic significance of this thrust style is discussed in Chapter 8.

Facies Restoration and Devonian Paleogeography

On the cross section, prominent geographic features are labeled along the present-day erosional surface for correlating the cross section with the geologic map (**Plate 1a**). Three of these features associated with measured sections in **Figure 30** include Tempiute Mountain (TMP or 53 on **Figure 9**), Monte Mountain thrust (TMM or 52 on **Figure 9**) and Mail Summit three miles east of Mount Irish (TMS or 51 on **Figure 9**). Without a structural reconstruction, the spacial distribution of facies represented by these sections is puzzling. However, restoration of the thrust model to its prethrust configuration (**Plate 4b**) allows reconstruction of a probable Devonian basin and depositional model (Chapter 7). The thrust restoration places the three stratigraphic sections with contrasting upper Guilmette facies in a spacial relationship that is more reasonable than their present post-thrust positions. It also causes the Tempiute impact basin to become more concentric.

The new tectonic model suggests that the source for the siliciclastics at Monte Mountain was an emergent region to the west. The emergent region is likely the Antler forebulge of Carpenter et al. (1994). Erosion of Ordovician Pogonip limestones from the forebulge is the likely source of the recycled Ordovician conodonts in Sequence Dgb2 impact breccia reported by Warme and Sandberg (1996). It is also the likely source of recycled early Paleozoic microfossils in Devonian rocks throughout the Sunnyside basin (T. Hutter, 1998,

personal communication). Conodont paleontologists have yet to take advantage of Devonian sequences defined in this work. A restricted basin of deeper-water mixed siliciclastics and carbonates at Tempiute Mountain lies between the sandy emergent region on the west and the reef-bearing carbonate platform at Mail Summit to the east (**Figure 33**). The paleogeography of the Sunnyside basin was similar to the paleogeography of the Late Pennsylvanian Oquirrh-Wood River basin of southern Idaho where shallow-marine siliciclastics filled the basin from the west and the bioclastic limestone facies filled the basin from the east (Geslin, 1994, 1998).

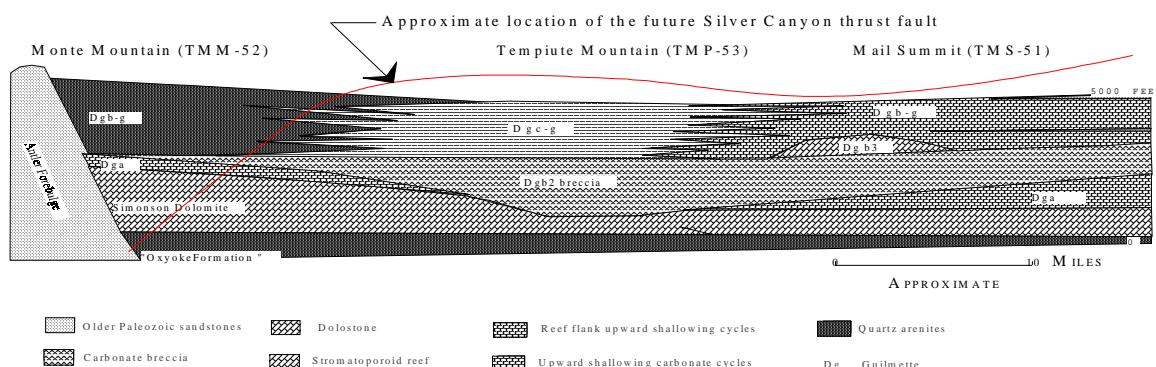


Figure 33 Diagrammatic stratigraphic cross section showing strata restored about Guilmette Sequence Dgb2 (Alamo Breccia) time. TMM is an abbreviation for Timpahute Range, Monte Mountain measured section. TMP is an abbreviation for Timpahute Range, Tempiute Mountain measured section. TMS is an abbreviation for Timpahute Range, Mail Summit measured section. The number after the section abbreviation is the number of the section on **Figure 9**. The future Silver Canyon thrust fault shown as a red line indicates how western Monte Mountain facies is placed between Tempiute Mountain and Mail Summit facies. Subsequent movement and erosion created the present relationship as seen in the geologic profile (**Plate 1a**) and the balanced cross section (**Plate 4**).

Bed-length restoration of the structural cross section (**Plate 4b**) suggests that the Monte Mountain (TMM) hanging wall lies about two miles west of Monte Mountain footwall (**Figure 33** and **Table 10**). Displacement is the amount the thrust fault had to be shifted to fit the model. It can also be scaled off **Plate 4a**. Evidence that the rocks of the TMM hanging wall were closer to the siliciclastic source area than the rocks of the TMM footwall include

thicker and coarser sandstones and lack of *Amphipora*-bearing interbeds in the TMM hanging wall in contrast to thinner and finer grained sandstones and *Amphipora*-bearing interbeds in the footwall. Section restoration shows that both sections at TMM originated not east of TMP, but west (see faults one and two on **Plate 4b** and **Figure 33** for the restored Tempuete basin). Bed-length restoration (**Plate 4b**) suggests that TMM originated at least twenty miles west of TMP. The distance is measured between fault cut offs on **Plate 4a** and is the amount the fault was shifted to fit the model.

TMP is more basinward than TMM or TMS, contains basinal carbonates (facies 1), and lacks abundant well-sorted sandstones (facies 2) or reefs (facies 3). About twenty miles east of TMP, the reef of TMS was constructed in up-dip, shallow basin margin carbonates. The reef was discussed in Chapter 4. A schematic cross section illustrates the principal depositional environments of the Devonian Guilmette and the relative positions of the three measured stratigraphic sections (**Figure 33**). The provenance and distribution of quartz sandstones shed off the Antler forebulge are discussed in Chapter 7.

Figure 33 shows the Dgb2 impact breccia to be thicker at TMP than at TMM on the west and TMS on the east. Warme and Kuehner (1998) suggested that the thicker breccia at TMP is a crater fill. Thickness of the crater fill thins radially and provides another structural tool in this part of the Sevier thrust belt (Chapter 7).

Biostratigraphic Dislocations

Biostratigraphic dislocations across the Silver Canyon thrust fault support the notion of significant shortening. Fossil occurrences above the Sequence Dgb2 breccia in the greater Timpahute Range are summarized in **Table 11**. Megalodonts are common in Devonian carbonates in the hanging wall of the Silver Canyon thrust plate (TMM) and are rare in the footwall (TMS). They are absent in the Tempuete Mountain thrust sheet (TMP). Stromatoporoid reefs are conspicuous in the Devonian rocks of the footwall (TMS) and are

absent in the Silver Canyon hanging wall (TMM) and at Tempiute Mountain (TMP). *Amphipora* is abundant at TMS and is common in the carbonate facies of TMM. They are absent at TMP. Corals are abundant at TMS but are rare at TMM and absent at TMP. Crinoids are rare at TMS and absent at TMM and TMP. Perhaps crinoids are lacking at TMM and TMP because those sections were in restricted marine conditions on the west side of the Sunnyside basin.

Table 11 Fossil occurrences in Devonian Guilmette rocks above Sequence Dgb2 breccia in three different thrust sheets of the greater Timpahute Range.

Fossil	TMM	TMP	TMS
Corals	R	N	A
Amphipora	C	N	A
Stromatoporoids	R	N	A
Stromatoporoid Reefs	N	N	C
Megalodonts	A	N	R
Crinoids	N	N	R
N= None or Absent R= Rare C= Common A= Abundant TMM= Timpahute Monte Mountain TMP= Tempiute Mountain TMS= Timpahute Mail Summit			

Structural Implications of the “Oxyoke Formation”

An isopach map of structurally unrestored sections of the “Oxyoke Formation” in Chapter 7 gives an anomalous thickness of 430 feet at Monte Mountain (TMM), in the middle of the greater Timpahute Range. This section is in the hanging wall of the Silver Canyon and Chocolate Drop thrust faults. East of Monte Mountain, in the footwall of the Silver Canyon thrust fault (TMS), the “Oxyoke Formation” is 195 feet thick. West of Monte Mountain, in

the footwall of the Chocolate Drop thrust fault (TMP), the “Oxyoke Formation” is 285 feet thick. If the structural reconstruction of the greater Timpahute Range presented in Chapter 5 is correct, and the Monte Mountain section was deposited west of Tempiute Mountain, then the “Oxyoke Formation” thickened progressively to the west (**Plates 1 and 4**). If the Monte Mountain section was deposited between the other two sections, then some sort of depression caused a thicker “Oxyoke Formation” section in the middle of the greater Timpahute Range. All three sections appear to have been deposited in shallow water making it difficult to resolve the depositional position using “Oxyoke Formation” facies distributions alone.

Ely Springs Dolomite

An independent argument that supports this new structural model is found by examining the Ordovician Ely Springs Dolomite in the different structural sheets. See **Figure 8** and **Table 1** to see the position of the Ely Springs Dolomite in the stratigraphic column. In the Silver Canyon sheet (TMM), the formation contains open-marine limestones in contrast to the sections exposed in the Silver Canyon footwall (TMS) and in the Chocolate Drop footwall (TMP) at Tempiute Mountain (**Plates 1 and 4**). In those sections, and in most sections of Ely Springs Dolomite in this part of Nevada, the formation is pervasively dolomitized (Cedar Strat proprietary measured sections, 1984-1989).

However, Reso (1960) noted that the Ely Springs Dolomite contains more limestone in the hanging wall of the Pahrnagat thrust fault than in the footwall, 15 miles south-southwest of Mount Irish. I correlated his Pahrnagat hanging wall thrust sheet to the Silver Canyon hanging wall thrust sheet. However, my interpretation shows that the Silver Canyon thrust sheet in the Timpahute salient traveled farther east than the Pahrnagat thrust sheets. A structural salient is part of a thrust fault, bounded by thrust tears, that moved farther than the rest of the thrust fault. The Pahrnagat hanging wall thrust sheet is exposed 18 miles south of Silver Canyon. Pervasive dolomitization of the Ely Springs is related to the

Ordovician-Silurian paleogeography. Ordovician rocks in the Silver Canyon sheet, containing more open-marine fossils including crinoids and corals, were deposited more seaward and, being less emergent, were less affected by dolomitizing processes than equivalent rocks to the east, higher on the shelf and containing fewer abundant open-marine fossils.

An argument that paleogeography controlled dolomitization of equivalent rocks comes from outcrops west of Eureka, Nevada (**Figure 2**). The Ely Springs Dolomite is equivalent to the Hanson Creek Formation in the Eureka area. Duhnam and Olson (1980) argued that dolomitization of the Hansen Creek was related to paleogeography of the region. Similarly, Ely Springs Dolomite in the Silver Canyon thrust sheet is composed of open-marine limestone (abundant open-marine fossils) in contrast to restricted-marine dolomites (less open-marine fossils) in the Pahroc and Meadow Valley Mountain thrust sheets. Therefore, it is likely that Ordovician rocks in the Silver Canyon thrust sheet were deposited seaward or west of Ordovician rocks at Tempiute Mountain.

Tertiary/Cretaceous Synorogenic Rocks

The newly discovered Late Cretaceous or Early Tertiary rock unit (TKs) southwest of Monte Mountain that lies between Paleozoic rocks and Tertiary volcanic rocks (Chamberlain, et al., 1992b) was introduced in Chapter 2. It may provide insight into the age of formation of Late Mesozoic to Early Tertiary structures in the region. As presented in Chapter 2, the upper lacustrine limestone beds of the unit probably correlate to the Lower Eocene lacustrine Sheep Pass Formation in Nevada and the Flagstaff Limestone and Claron Formation in Utah. The underlying conglomerate beds may correlate to Late Cretaceous conglomerates of the Newark Canyon Formation in central Nevada or the North Horn Formation in central Utah.

The Sevier fold-and-thrust belt produced folds in Paleozoic rocks. Erosion cut down and exposed the folded Paleozoic rocks before deposition of the Monte Mountain

Tertiary/Cretaceous strata. Because of folding in the Monte Mountain footwall, the Tertiary/Cretaceous strata lie on younger Paleozoic rocks westward. Where they overlie resistant Mississippian Joana Limestone in the footwall sheet of the Monte Mountain thrust fault, they are 300 feet thick. However, the unit is about 500 feet thick where it lies over the nonresistant Mississippian shales and sandstones. In contrast, the Tertiary/Cretaceous strata are less than 100 feet thick where they lie over Mississippian carbonates of the Monte Mountain hanging wall thrust sheet. Tertiary/Cretaceous strata lying on breached structures of Paleozoic rocks are not unique to the greater Timpahute Range. Eocene lacustrine limestones lie on Mississippian shales in the breached Illipah anticline in the White Pine Range, 120 miles to the north. I have mapped similar beds in the Grant, Pancake, and Egan ranges. Sparse well and outcrop data in central Nevada suggest that the Tertiary/Cretaceous strata thin and pinch out over Mesozoic anticlines and are thicker in synclines. The distribution of the Tertiary/Cretaceous strata along the Sevier fold-and-thrust belt is similar to the distribution of the Tertiary/Cretaceous strata over folds in central Utah.

Interbedded with and below the limestone beds at Monte Mountain are conglomerate beds with limestone clasts containing *Receptaculites*, a marker fossil found near the top of the Ordovician Pogonip Formation. The conglomerate also contains clasts of Eureka Quartzite and other Pogonip units. Erosion has exposed the nearest outcrops of *Receptaculites*-bearing Ordovician rocks in the Penoyer Springs plate 1.3 miles to the west.

Interbedded with cross-bedded sandstone, the well rounded, exotic clasts are in stream deposits. Imbrication of the clasts and cross-bedding suggests a paleocurrent direction of 165° at Monte Spring (see Monte Spring fault, **Plate 1a**). Exotic clasts shed from thrust sheets are not unique to the Monte Mountain locality, but also occur to the south and north. Carpenter and Carpenter (1994a, b), for example, described exotic clasts in Albian synorogenic beds in the Muddy Mountains, 90 miles south-southeast of the greater Timpahute Range. They found Ordovician clasts but no Ordovician outcrops. I found clasts of Ordovician Eureka Quartzite and *Receptaculites*-bearing limestone in a Tertiary/Cretaceous conglomerate unit ninety miles north of the study area at Big Louis Spring in the Pancake Range (near Wood Canyon thrust

fault, **Figure 2**). There, nearly flat-lying Ordovician-bearing conglomerates lie unconformably on steeply-dipping Mississippian strata. The Tertiary/Cretaceous rocks are overlain by a thrust sheet of Devonian Guilmette Formation (Cedar Strat proprietary map, 1997). Volcanic rocks conceal the thrust klippe in most of the area. The clasts must have come from the nearest outcrops of Eureka Quartzite in the Moody Peak thrust sheet six miles to the west (**Figure 2**). I believe that the Late Mesozoic to Early Tertiary compressional event allowed Tertiary/Cretaceous strata rocks to be deposited in interthrust and foreland basins. The Monte Mountain Tertiary/Cretaceous basin may be similar to the Axhandle piggyback basin of central Utah. That basin contains Cretaceous to Tertiary North Horn conglomerates overlain by Eocene Flagstaff lacustrine limestones (Talling et al., 1995). Unfortunately, the most widespread area of exposed Tertiary/Cretaceous strata near the study area is in the restricted area of the Nellis Bombing Range (Tschanz and Pampeyan, 1970). Map patterns on their map show that the Tertiary/Cretaceous strata are closely associated with thrust faults. A detailed study of these strata may shed more light on the timing and style of this part of the Sevier fold-and-thrust belt. It is recommended that the United States Department of Defense remove restrictions and allow access to study these rocks (Chapter 9).

Conclusions

A cumulative bed-length reconstruction of all the thrust faults in the greater Timpahute Range suggests at least 64 and possibly 98 miles of horizontal displacement in this part of the Sevier fold-and-thrust belt. It was pointed out in Chapter 2 that workers in other parts of the thrust belt suggested similar amounts of displacement. Elison (1991) concluded that the western North American Cordillera from southeastern British Columbia to northern Nevada experienced 180 miles of east-west crustal shortening. The magnitude of crustal shortening strongly affected the position of thrust sheets containing Devonian rocks and had a strong impact on interpreting the Devonian paleogeography.

My structural interpretation of the greater Timpahute Range improves significantly the stratigraphic analysis of this area, and the stratigraphic interpretation adds rigor to the structural model. Together, the merging of the structural (Chapter 5) and stratigraphic (Chapter 4) data illustrates the complexities of this part of the Sevier fold-and-thrust belt. The combination of the structural and stratigraphic analysis aids the paleogeographic interpretation of the Devonian rocks in Chapter 7. The new structural model and recognition of Devonian sequences herein also have economic implications (Chapter 8).

CHAPTER 7

DEVONIAN PALEOGEOGRAPHY

In the previous chapters the groundwork was laid for reconstructing the Devonian paleogeography of the study area. Chapter 4 provided the basis for dividing the Devonian into mappable sequences and contains sequence descriptions. In Chapter 5 and Appendix E the sequences are used to document structural features shown on **Plate 1a**. A structural model based on new mapping and distribution of contrasting sequence facies appears in Chapter 6. In the present chapter results of the previous chapters are combined and synthesized into an interpretation of the Devonian paleogeography.

The 21 mappable sequences at TMS introduced in Chapter 1 were identified and refined by correlating them to other sections and wells in the region (Chapter 4, **Figure 9**). An east-west correlation chart through the greater Timpahute Range was presented in Chapter 4. Other examples of some of these correlations are provided in this chapter. Formation names from previous work, introduced in Chapter 2, were retained wherever possible. Methods used to construct surface gamma-ray logs and isopach maps used in this chapter were presented in Chapter 3.

After correlating and refining sequences between sections listed in **Table 2**, correlations between sections and wells listed in Appendix F provided additional control to construct isopach maps. An isopach map of each sequence was constructed, two of which are shown in this chapter. A comparison of the isopach maps from the oldest to the youngest sequence shows that the center of the Sunnyside basin, described in Chapter 1, migrated from central Nevada in Lower Devonian (Sevy Dolomite Sequences) to western Utah in Late Devonian (Pilot Formation Sequences). All of the sequences were combined into a composite isopach map for the total Devonian (**Plate 3**). The map shows the form

of the Sunnyside basin with the basin center near Sunnyside, Nevada, 54 miles north of Hiko. The axis of the Sunnyside basin trends north-northeast and intersects the basin center.

Sequence Correlations

Three contrasting facies of Upper Devonian rocks from different thrust sheets in the greater Timpahute Range were introduced in Chapter 1. Structural elements of the thrust sheets were introduced in Chapter 5, illustrated on **Plate 1a**, and described in detail in Appendix E. The Chocolate Drop thrust fault separates facies 1 (thin-bedded limestone of the western exposure of the Pahroc thrust sheet) from the overlying facies 2 (sandy Silver Canyon thrust sheet). Facies 2 is separated from facies 3 (reefy, cyclic carbonates of the eastern exposure of the Pahroc thrust sheet) by the Silver Canyon thrust fault (**Plate 1a**). These contrasting facies are illustrated in **Figure 30**. The uniqueness of the Silver Canyon thrust sheet sandy facies is also illustrated by north-south correlation charts (**Figure 34** and **Figure 35**). Tear faults separate the Silver Canyon thrust sheet in the Pahrnagat and Golden Gate ranges from the Silver Canyon thrust sheet in the greater Timpahute Range (**Plate 1a** and **Figure 32**). **Figure 34**, a correlation chart from the Pahrnagat Range (correlative with the Silver Canyon thrust sheet) through Monte Mountain (Silver Canyon thrust sheet) and to the Golden Gate Range (Pahroc thrust sheet) shows the Guilmette sequence thicknesses to be more similar than those in a correlation chart from the Pahrnagat Range through TMS (Pahroc thrust sheet) and to the Golden Gate Range (**Figure 35**). This is because the Silver Canyon thrust sheet and the correlative Pahrnagat Range section are more genetically related than sections in the Pahroc thrust sheet.

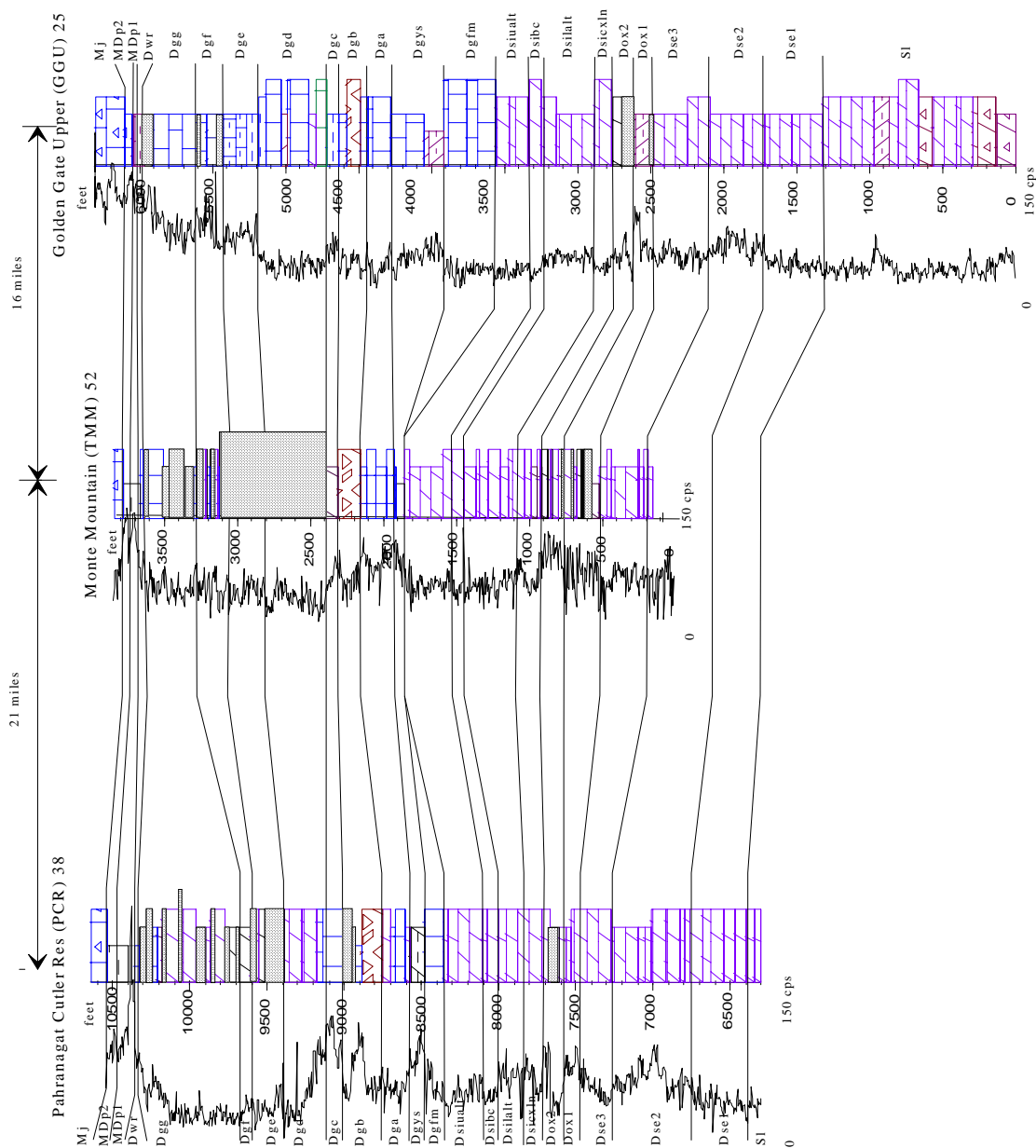


Figure 34 North-south correlation of sections in the region showing the northward thickening of the pre-b2 breccia units toward the Sunnyside basin and the uniform thickness of the post-b2 breccia units within the Silver Canyon (Gass Peak?) thrust sheet (**Figure 2** for Gass Peak thrust in Clark County). See **Figure 9** for locations of sections.

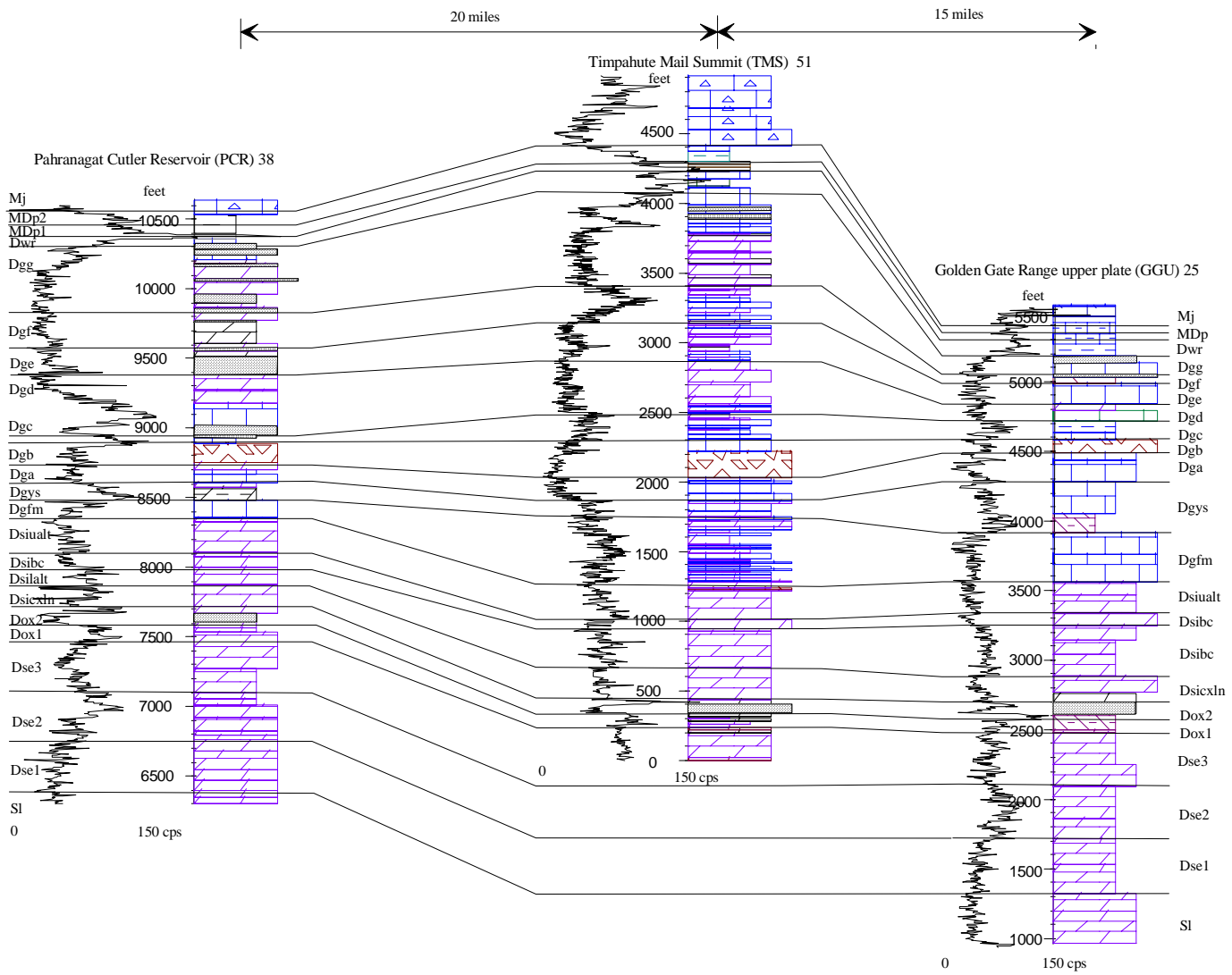


Figure 35 North-south correlation of sections in the region showing the northward thickening of the pre-b2 breccia units toward the Sunnyside basin and the nonuniform thickness of the post-b2 breccia units between the Silver Canyon (Gass Peak?) and Pahroc (TMS) thrust sheets (Figure 2). See Figure 9 for locations of sections

The trend of sandy facies thrust over reefy facies can be followed southward to the Gass Peak thrust fault that may be correlative with the Silver Canyon thrust fault (**Figure 2**). The Pahrangat Range is in the hanging wall of the Gass Peak thrust fault and contains a Guilmette sandy facies above Sequence Dgb. It contrasts with the footwall exposed in the southern Delamar Range, 25 miles south of the study area, that lacks the sandstone facies.

Sunnyside Basin

Plate 3 and **Figure 36** provide an example of an unrestored regional isopach map of the total Great Basin Devonian. Isopach maps of each of the 21 Devonian sequences were composited to make the total Great Basin Devonian isopach map (Chapter 4). The map implies an intrashelf basin centered near Sunnyside, 60 miles north Hiko. Therefore, the basin is named the Sunnyside basin (Chamberlain and Birge, 1997). The greater Timpahute Range lies on the southwest flank of the basin.

The Sunnyside basin is a northeast-southwest trending Devonian intrashelf basin about 400 miles long and 200 miles wide before structural restoration (**Figure 36**). Devonian strata thicken from approximately 500 feet near the basin edges to more than 6,600 feet in the basin (**Figure 8**). The steepest contour gradient is on the southeast flank of the basin between the Meadow Valley Mountains in south central Lincoln County, Nevada, and Blue Mountain in the Wah Wah Range, western Utah (**Plate 3** for locations). It lies within the area of known Sevier-age thrust faults. Contours on the western edge of the basin, western Eureka and Nye Counties, Nevada, also show steep gradients. The steep gradients are probably due to crustal shortening. Along the northeast structural strike within the basin, contour gradients are gentle, and probably more representative of original depositional trends. Restoration of the thrust sheets causes the steep gradients to flatten.

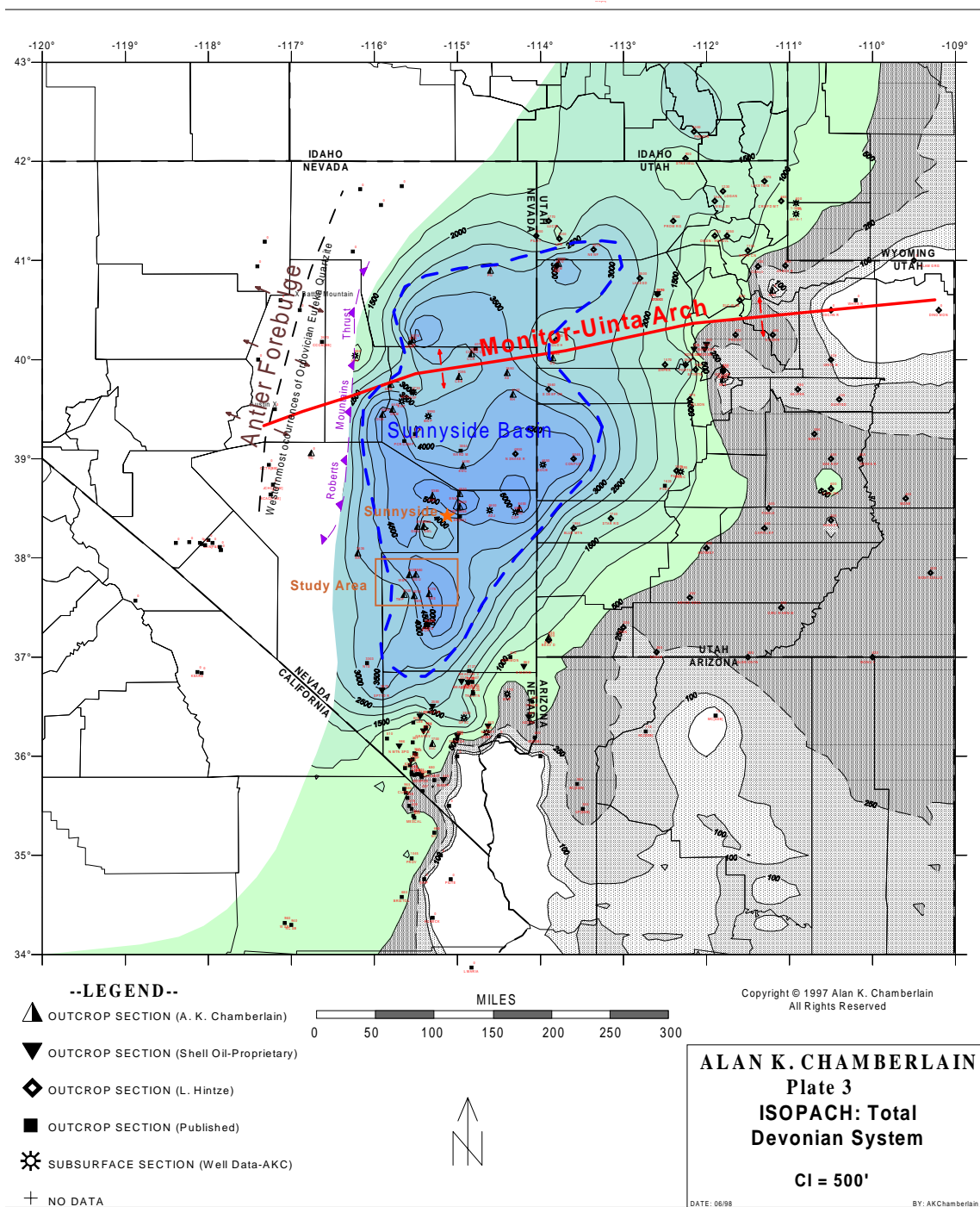


Figure 36 Isopach map of all 21 Devonian sequences of the Sunnyside basin shows the configuration of the basin, some Paleozoic tectonic features including the Antler forebulge, Utah hingeline, and Monitor-Uinta arch, and the steep gradient on the southeast side of the basin caused by Mesozoic Sevier crustal shortening. The blue dashed line is the outline of the unrestrained Sunnyside basin.

As mentioned in Chapter 6, at least 64 and possibly 98 miles of crustal shortening occurred in the greater Timpahute Range. Chapter 5 presented evidence of deeper thrust faults. They probably carried the Timpahute Range eastward some unknown distance. Elison (1991) estimated 180 miles of cumulative crustal contraction of the Cordilleran fold-and-thrust belt (see Chapter 6). If this cumulative displacement was restored then the northeast trending steep isopach gradient would flatten significantly. Furthermore, the size of the Sunnyside basin would approach the size of the Williston basin. As LeFever (1996) pointed out, the Williston basin is also approximately 300 by 600 miles in size. However, the Williston basin is a cratonic basin and the Sunnyside basin is an intrashelf basin. Strata of equivalent ages are much thicker in the Sunnyside basin than in the Williston basin, and the Sunnyside basin strata lack the evaporate-bearing strata of the Williston basin.

Guilmette rocks on the east side of the Sunnyside basin are characterized by reefs, bioherms, and other organic buildups. Thick quartz sandstones occur along the edges of the basin, shoreward of the organic buildups. Guilmette rocks on the west side (i.e., Pancake Range) of the basin are characterized by thick strata bearing *Amphipora*. Westward of the *Amphipora* wackestones are quartz sandstone beds. These mature quartz sandstones were probably derived from erosion of older Paleozoic rocks on the Antler forebulge. Evidence of a forebulge associated with the Antler Orogeny is found in fensters in the Roberts Mountain allochthon between Battle Mountain and Austin (Carpenter et al., 1994). Thousands of feet of lower Paleozoic rocks, including the Eureka Quartzite, were removed by erosion and shed eastward into the Sunnyside basin. Webb (1958) showed the upper sandstone member of the Eureka Quartzite thickening toward the study area. He also showed thickening of the highest two members of the Eureka Quartzite (up to 500') toward the Antler forebulge. An example of a fenster in the Roberts Mountains allochthon is in the Toquima Range (TIC), north-central Nye County, where a thin section of Devonian rocks lies on Ordovician Pogonip rocks (**Figure 36, Plate 3**). In other fensters, the Roberts Mountain allochthon lies directly on Cambrian and Lower Ordovician

carbonates (Carpenter et al., 1994). Younger strata, including the Eureka Quartzite, have been removed. Most of the eroded strata were carbonate rocks. Consequently the insoluble residues from these older rocks in Sunnyside basin Devonian rocks testify to the erosional event. Devonian quartz sandstones that thicken westward are probably residues of the eroded Eureka Quartzite. Erosion of the lower Paleozoic rocks from the Antler forebulge was arrested by emplacement of the Roberts Mountain thrust sheet in Late Devonian and Lower Mississippian. Erosion of the allochthon resulted in a thick wedge of Mississippian Antler siliciclastics that attest to the emplacement of the Roberts Mountains allochthon that followed the development and eastward migration of the Antler forebulge.

An isopach of Guilmette Dgb2 breccia (Alamo Breccia) shows a sub-basin within the southwestern end of the Sunnyside basin that was probably created by the cosmolite impact at Tempiute Mountain (**Figure 37**). I named this impact basin the Tempiute basin (Chamberlain, 1999). Devonian strata in this part of the Sunnyside basin should be thinner and composed of shallowing-upward cycles with abundant *Amphipora* and supratidal, fine-grained stratal dolomite cycle caps. However, *Amphipora* and shallowing-upward cycles capped with supratidal dolomite are absent in the Tempiute basin. Instead, the unique thin-bedded limestone facies 1, commonly exhibiting soft-sediment deformation and containing rare thin quartzose turbidite sandstone beds, fill the Tempiute impact basin. No other section or well in the region exhibits these unique facies (facies 1).

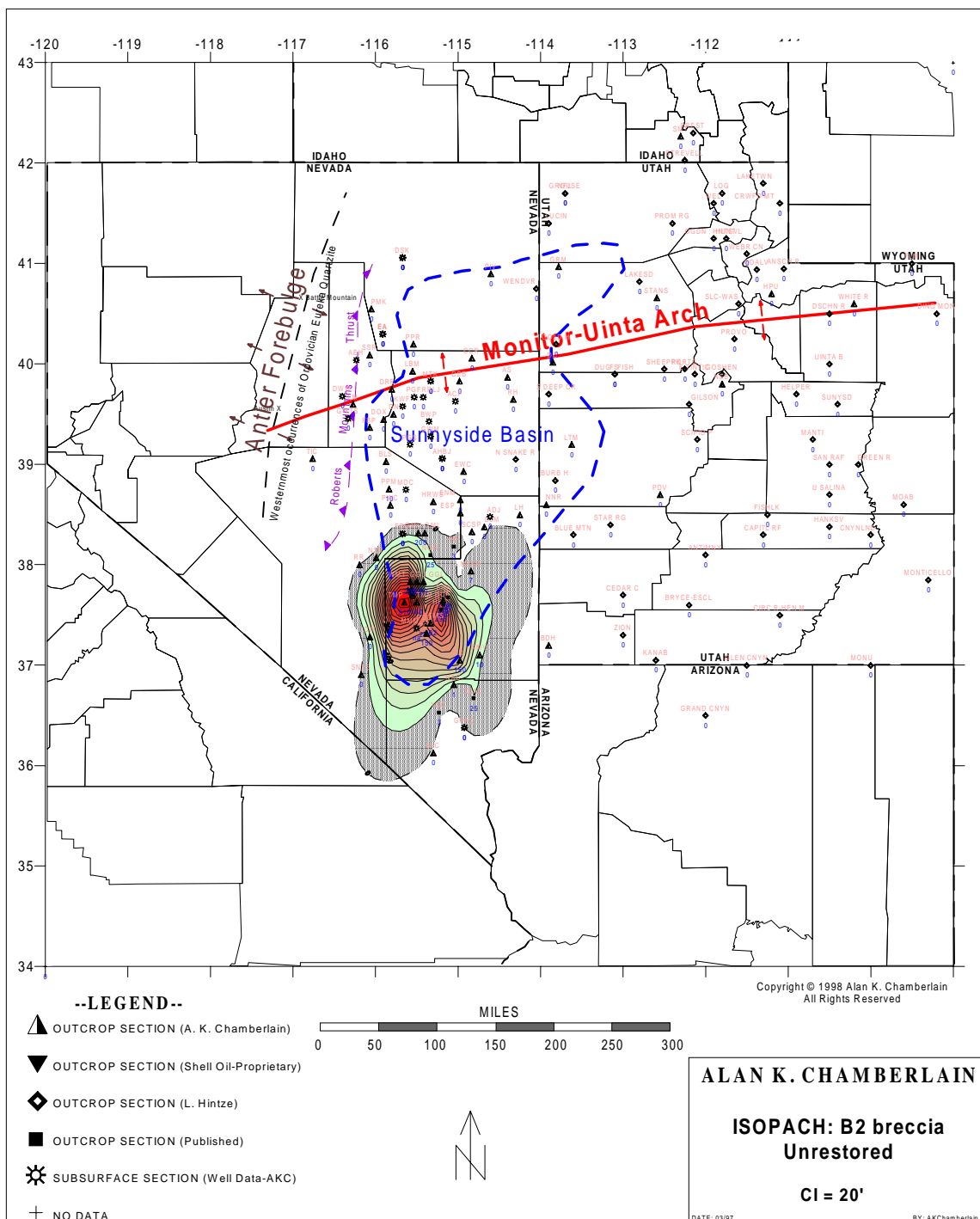


Figure 37 An unrestored isopach map of Guilmette Dgb2 breccia shows the form of the unrestored Tempiute basin in the Sunnyside basin. It shows an oval pattern 160 miles long and 60 miles wide with two pods of thicker breccia separated by a ridge of thinner breccia. The blue dashed line is the outline of the unrestored Sunnyside basin.

The isopach of Sequence Dgb also shows that the thickest Sequence Dgb is in the Egan Range, near Sunnyside (**Figure 38**). **Figure 34** and **Figure 35** show this northward thickening in sequences below Sequence Dgb. Being continuous with the north-northeast trending axis of the Sunnyside basin, another thick area occurs in southwestern White Pine County. It occurs in an area of known Sevier thrust and strike-slip faults. If the sections containing thinner Sequence Dgb strata west of Sunnyside were restored to the west, then the Sunnyside basin axis and the southwest White Pine thick area would converge into a single basin (**Plate 3**). Because the axis of the Sunnyside basin appears to have moved eastward with time, the axis of the basin during Sequence Dgb2 time is farther to the west than the average basin axis in **Figure 36**. This would imply that the Antler forebulge migrated from central Nevada toward western Utah during the Devonian. Giles (1994) concluded that the Pilot basin reflected the flexural downwarping of the Antler back-bulge basin. She suggested that the flexural features remained fixed throughout the history of the Pilot basin and that the forebulge moved eastward across eastern Nevada into western Utah during the Early Mississippian. Giles (1996) suggested that the Lower Mississippian Joana Limestone shows a retrograde stratigraphic pattern interpreted to have been forced by lithospheric flexural subsidence during the Antler orogeny. The relationships all suggest that the Antler forebulge migrated eastward from central Nevada in Early Devonian to western Utah in Early Mississippian.

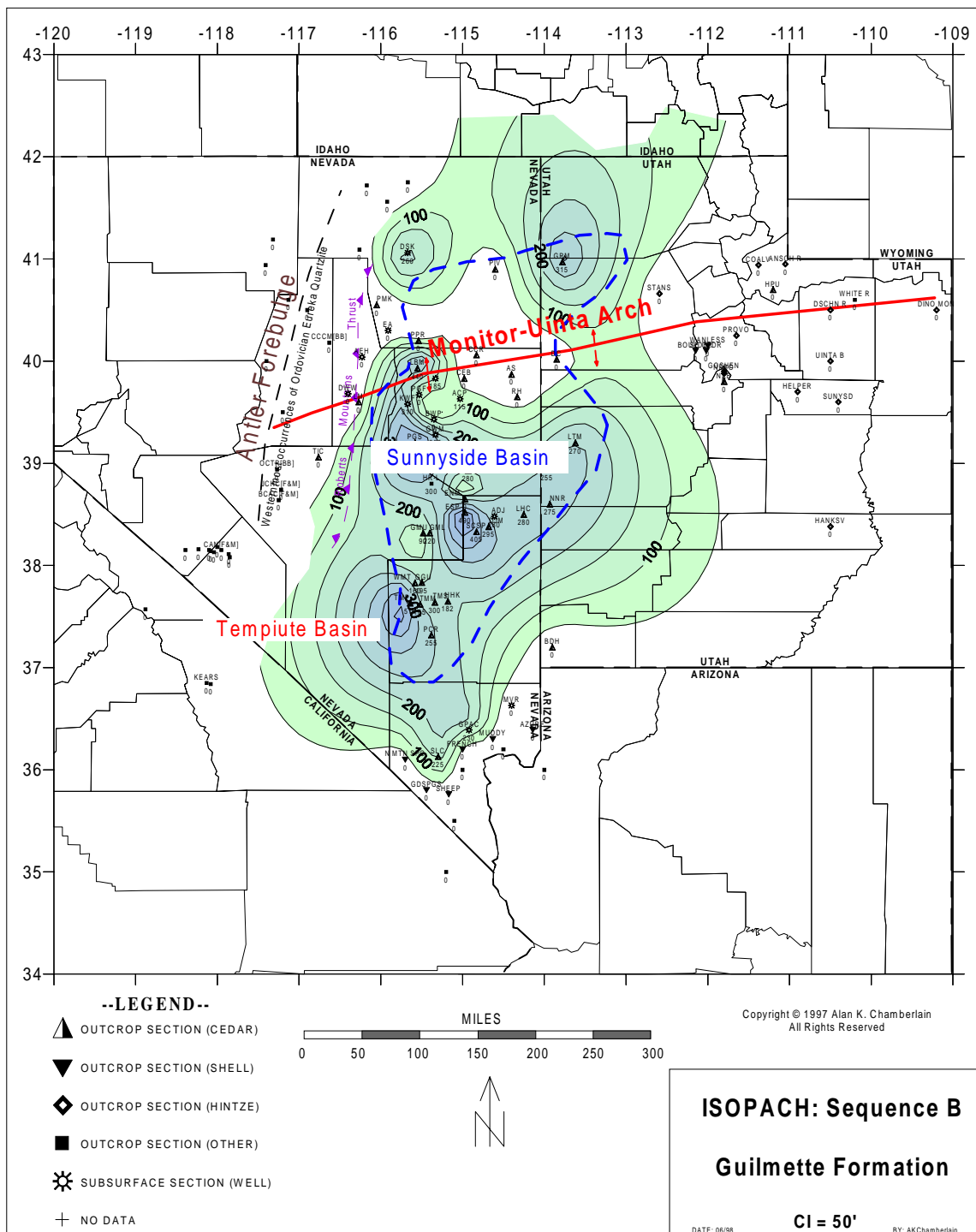


Figure 38 Isopach map of unrestrained Guilmette Sequence Dgb shows contours closing on the Dgb2 breccia basin (Tempiute basin) in the southern end of the Sunnyside basin. The blue dashed line is the outline of the unrestrained Sunnyside basin.

Generally, Sequence Dgb thins northward to the Monitor-Uinta arch. The thinning of Sequence Dgb near the Monitor-Uinta arch suggests that the arch was a positive area during Sequence Dgb time. North of the arch, Sequence Dgb thickens again. The blue dashed line in the isopach maps, **Figure 36**, **Figure 37**, **Figure 38**, **Figure 39**, **Figure 40**, **Figure 41** and **Plate 3**, represents the unrestored outline of the Sunnyside basin.

Tempiute Basin

The subbasin discussed above within the southern end of the Sunnyside basin was likely created by a Devonian cosmolite impact that disrupted Sequence Dgb strata and is named Tempiute basin herein. The impact likely created a concentric basin, similar to other terrestrial impact basins including: Chesapeake Bay (Johnson et al., 1998), Bosumtwi, Ghana (Reimold et al., 1998), Morokeng, South Africa (Koeberl et al., 1997a), Popigai, Russia (Koeberl et al., 1997b), and Chicxulub, Yucatan Peninsula, Mexico (Hildebrand et al., 1991) and many others. However, subsequent tectonic events have deformed some impact basins such as the Sudbury structure, Canada (Fueten and Redmond, 1997; Ames et al., 1998). Mesozoic thrusting deformed the Tempiute impact basin. Well-preserved impact basins, such as Chicxulub, exhibit distinct topographic rings and predictable morphology including a central uplift, terrace zone of slumped blocks, and inward-facing asymmetric scarps (Morgan and Warner, 1999). These morphologic features are yet to be found in the deformed Tempiute impact basin.

Within the Tempiute basin, a central crater is marked by an abrupt thickening of the impact breccia (**Plate 4b**). An unrestored isolith map of the Tempiute basin shows two thick areas, delimiting the central crater, within the basin (**Figure 37**). The ridge between the two lows is caused by thinner (126-200 feet) Dgb2 breccia in the Silver Canyon thrust sheet than in the thicker Pahroc (east) thrust sheet (392 feet) and in the Pahroc (west) thrust sheet (510 feet). The isolith contours should have produced a concentric pattern.

However, the unrestored distribution of the breccia forms a large oval pattern 160 miles long in the longest dimension (north-south) and 60 miles wide in its shortest dimension (east-west). Its size can be compared with other terrestrial impact craters. The Chesapeake Bay (Johnson et al., 1998) and Popigai (Koeberl et al., 1997b) craters are about 60 miles in diameter, Chicxulub (Hildebrand et al, 1991) is about 160 miles in diameter, and the Morokeng (Koeberl et al., 1997a) is approximately 210 miles in diameter. Lunar mare crater counts, the terrestrial impact flux, and astronomical observations of asteroids and comets provided data to predict 11 continental craters with 155-186 miles of diameter (Glikson, 1999). Only three craters of this rank are reported in literature (Glikson, 1999). Timpahute may be the fourth.

According to the emerging structural model presented in Chapter 6, the Tempiute Mountain section was deposited in an intrashelf basin west of the reef-bearing TMS section and east of the Monte Mountain sandstone facies. In other words, the Monte Mountain section (TMM), which is now between TMS and TMP, was probably originally deposited west of TMP (**Plate 4b**). Thrust restoration suggests that TMP facies 1 of the central crater were probably deposited approximately 30 miles to the west (**Plate 4b**). Post impact strata at TMS are deepwater, rhythmic, thin bedded limestones (facies 1) that are unique in the region. They intertongue with the shallowing-upward cycles of TMM (facies 2). Evidence of the intertonguing is found by comparing post impact sequences in the Monte Mountain hanging wall, to the Monte Mountain footwall and the northernmost exposures of the sequences in the Pahrnagat Range (NPR, T5N R58E Sec 5, **Plate 1a**). Thick-bedded, sandy, burrowed limestone and dolomite lies immediately above the Dgb2 breccia at TMM hanging wall. The carbonates are more limey, less sandy and thinner bedded in the TMM footwall. Correlative beds at NPR are rhythmically, thin-bedded limestone and are similar to those at TMP. Therefore the rocks in the Silver Canyon thrust sheet deepen eastward toward the restored position of TMP. Cycles at NPR contain a greater proportion of deeper-water facies than those at Down Drop Mountain (DDM) which is nearer the edge of the Tempiute basin. For example, the abundance of

Amphipora, which suggest restricted marine conditions, increases from NPR to DDM. All these sections, TMM, NRP, and DDM lie within the Silver Canyon thrust sheet.

Thicknesses and the number of tongues of deepwater, thin-bedded limestones in the sequences and especially cycles in Sequence C increase eastward, toward the Tempiute basin and decrease toward the edge of the basin. Similarly, basinal post impact strata of the Chesapeake Bay impact structure, Virginia, intertongues with offshore shoal deposits (Johnson et al., 1998). From assumptions within this study, it appears that the TMM section was likely deposited on the west edge of the Sunnyside intrashelf basin.

Restoration of the sections places TMP near the axis of the Sunnyside basin with the sandy TMM on the west side and the reefy TMS on the east side. This restoration provides for a thicker Dgb2 breccia near the center of the circular impact crater and a consistent thinning radially. Similarly, the Exmore Breccia of the Chesapeake Bay impact structure thins rapidly from 984 feet in the annular trough to zero outside the outer rim (Johnson et al., 1998).

Providing an ideal chronostratigraphic bed, the unique nature of the single-event Dgb2 breccia can be used to unshuffle thrust sheets not only in the Timpahute region but beyond. The cosmolite impact crater was most likely circular. The impact ejecta blanket and associated disturbed seabed rocks were probably distributed radially. Channel-like occurrences of the breccia in the Golden Gate hanging wall thrust sheet and in the south Seaman Range could be associated with ejecta rays or breccia-filled grooves radiating from the impact crater. In the southern Golden Gate range thick (100's feet) of breccia occur between ridges of undisturbed Sequence Dgb. In the southern Seaman Range, thinner (10's feet) of breccia occur between intervals of undisturbed Sequence Dgb. See **Figure 37** and **Figure 39** for isolith maps of the breccia. In the third dimension, these bodies of breccia may be channels or valleys cut into undisturbed Sequence Dgb. They thicken and widen toward Tempiute Mountain.

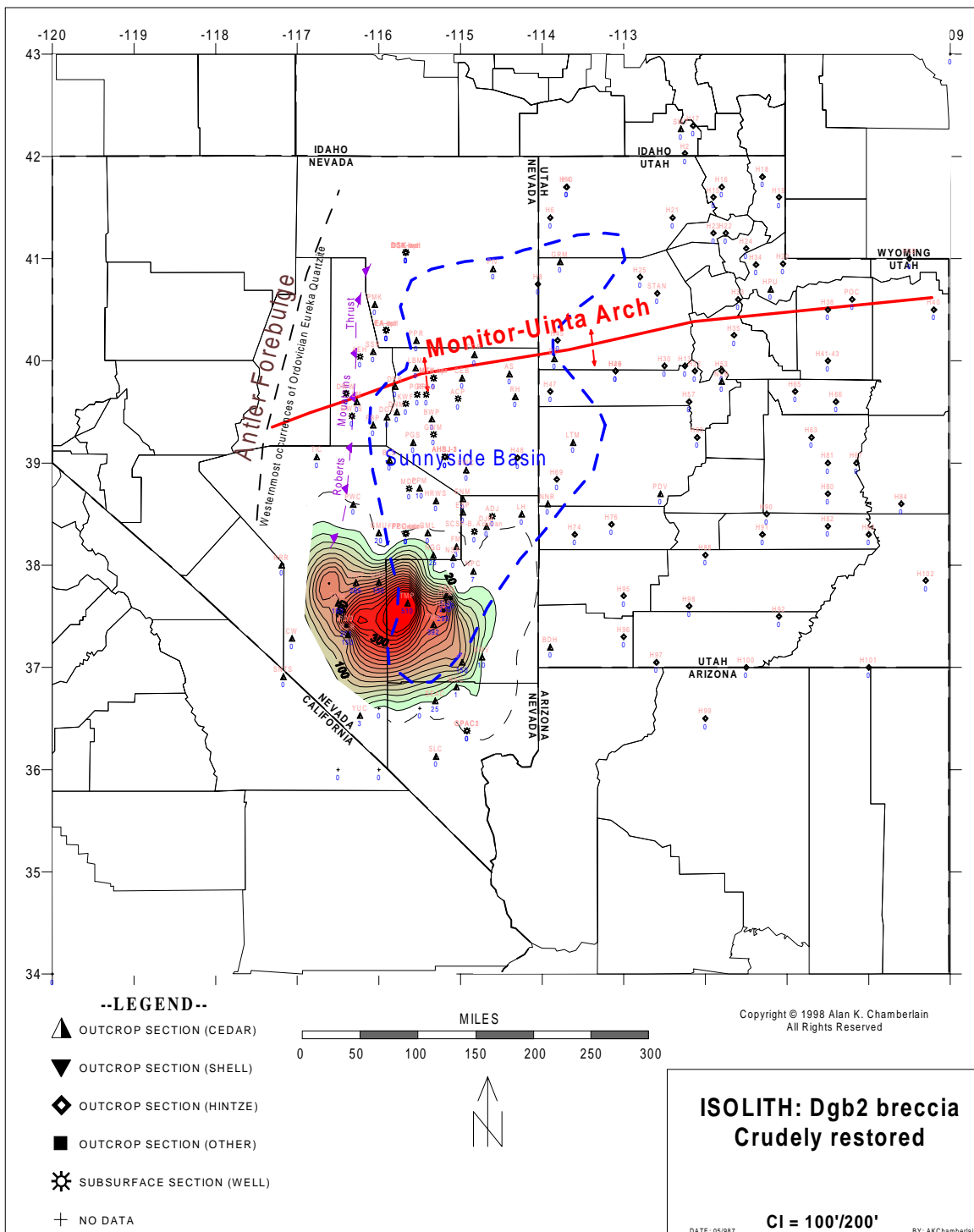


Figure 39 Crudely restored isolith map of the Guilmette Sequence Dgb2 breccia shows a more concentric distribution of the breccia in the Tempiute sub-basin. The restoration eliminates the ridge of thinner breccia between pods of thicker breccia. The blue dashed line is the outline of the unrestored Sunnyside basin.

SE ROA 37271

Once the Silver Canyon thrust sheet is restored west of Tempiute Mountain, a consistent thinning of the breccia occurs radially from the circular impact site. Beyond the major changes in thickness across the Silver Canyon and Chocolate Drop thrust faults, other major changes in thickness occur across the Pahroc, Forest Home, and Wood Canyon thrust faults (**Figure 2**). The breccia is more than 100 feet thick in the hanging wall of the Pahroc/Delamar thrust sheet in the southern Delamar, Hiko, and southern Seaman ranges (**Figure 5**). However, it is about 10 feet thick in the footwall sheet exposed in the northern Meadow Valley and northern Pahroc ranges (**Figure 17**). The breccia is absent in Sequence Dgb exposed in a fenster of the Forest Home thrust sheet 20 miles north of the study area (Stop 12, Appendix D). Nevertheless, it is about 8 feet thick in the Forest Home hanging wall thrust sheet (**Figure 2**). In the Pancake Range, 40 miles northwest of the study area, the breccia is about 6 feet thick in the Portuguese Mountain thrust sheet, footwall to the Wood Canyon thrust fault. It is absent in the Wood Canyon hanging wall thrust sheet (**Figure 2**).

Thrust fault restorations using the structural model presented in Chapter 6 provide constraints on the circular Tempiute sub-basin created within the Sunnyside basin by the cosmolite impact (Chamberlain, 1999). An isolith map of the present-day distribution of the breccia manifests an ellipsoidal areal distribution (**Figure 37**). The Tempiute sub-basin, in which Dgb2 breccia is found, extends from the southern Arrow Canyon Range on the south to Portuguese Mountain on the north, a distance of about 160 miles. In contrast, the east-west distribution covers only about 60 miles from west of Tempiute Mountain to east of the Pahroc Range. The compressed, ellipsoidal shape was likely due to, or accentuated by, the Sevier orogeny. A knowledge of the assumed distribution of breccia before thrusting provides a unique opportunity to restore thrust sheets with a greater degree of confidence and could help predict the center of the impact.

A crudely restored isolith map was made by moving sections west of the Gass Peak/Silver Canyon thrust one degree, or about 55 miles, to the west (**Figure 39**). Cumulative shortening of the Silver Canyon, Monte Mountain and Penoyer Springs thrust

faults is approximately 50 miles (**Table 11**). Restoration of the Pahroc thrust sheet would move the Tempiute basin an additional 50 miles to the west. Cumulative shortening of the entire greater Timpahute Range, including the Pahroc thrust fault, is approximately 100 miles (Chapter 6). Because the traces of some thrust faults extend more than 200 miles along the north-south structural strike, then 100 miles of east-west crustal shortening is reasonable. Though maximum displacements are not linearly related to thrust lengths, worldwide three-dimensional seismic surveys show length exponents vary from 0.8 to 1.55 (Fermor, 1999).

The crudely restored isolith map (**Figure 39**) shows a more concentric basin than the unrestored isolith map (**Figure 37**). Although these isopach maps are constructed with limited preliminary control, refined maps with many more control points could be adjusted until the breccia basin is perfectly concentric. As pointed out in Chapter 3, without additional constraints for this unique region, accurate balanced cross sections and restorations cannot be constructed. Distribution of the Dgb2 breccia provides the additional constraints needed to make accurate balanced cross sections in the area. It could be a powerful tool to restore the sections and obtain accurate values for crustal shortening for each thrust sheet. Accurate balanced cross sections constrained by those values would greatly improve the structural model and provide a better template for structural analysis along strike.

Devonian Sandstone

Quartz sandstone in the Devonian rocks of Nevada have largely been overlooked. Ryan and Langenheim (1973) attempted to describe and interpret sandstones in the Upper Devonian regionally. They cite many workers who mentioned local sandstone occurrences, but they were first to put the sandstones into a regional setting. In my

analysis, the Upper Devonian sandstones and sandstone intervals of the Middle Devonian “Oxyoke Formation” are also put into a regional setting.

As mentioned in Chapter 2, provenance of Devonian sandstones is problematic. C. Sandberg (1998, personal communication) suggested that the source of the Devonian sandstones in the study area was the Stansbury uplift in north central Utah. According to Sandberg et al. (1988) the Stansbury uplift was initiated after the Pilot basin formed in the Famennian. However, most of the Guilmette sandstones were deposited below the Pilot Formation in the study area and are Frasnian. Sandberg and Ziegler (1973), at Bactrian Mountain within the study area, documented the base of the West Range Limestone in the Middle *crepida* conodont zone at the base of the Famennian. This implies that the sandy beds of the Guilmette lie well below Stansbury siliciclastics. This chapter shows that a probable Antler forebulge bordered the west side of the Sunnyside basin and was the likely source area for the mature sandstones there. Sandstones along the eastern edge of the Sunnyside basin were derived from highlands in northeastern and east-central Utah. The distribution of Devonian sandstones also provides another tool for restoring structural cross sections in the study area.

“Oxyoke Formation”

Carbonate deposition predominated between deposition of the Ordovician Eureka Quartzite to the Devonian “Oxyoke Formation” in the Sunnyside basin. The “Oxyoke Formation” recorded the first pulse of the Antler forebulge as containing the first significant quartz sandstone above the Eureka Quartzite. Sandstone beds of the “Oxyoke Formation” consist of mature quartz grains. They generally overlie argillaceous dolomite beds. A detailed description of the “Oxyoke Formation” sequences and cycles are presented in Chapter 4 and in Appendix B.

An isopach of the “Oxyoke Formation” shows that the formation increases in thickness on the western side of the Sunnyside basin (**Figure 40**). It is thickest near the intersection of the Sunnyside basin and the western extension of the Monitor-Uinta arch. Hurtubise (1989) described the Timber Mountain strike-slip fault as a major fault cutting the northern end of the Seaman and Golden Gate ranges with sinistral movement. Isopach contours show a sinistral offset of thicker “Oxyoke Formation” in the axis of the Middle Devonian Sunnyside basin (**Figure 40**). Thrust restoration of the Timpahute area westward would place the north-south trending thick or basin axis south of the fault in line with the thick or basin axis north of the fault. It would also place the Timpahute area closer to sandstone source areas on the Antler forebulge. The structural model (**Plate 4a**) that supports this thrust restoration is presented in Chapter 6 (**Plate 4b**).

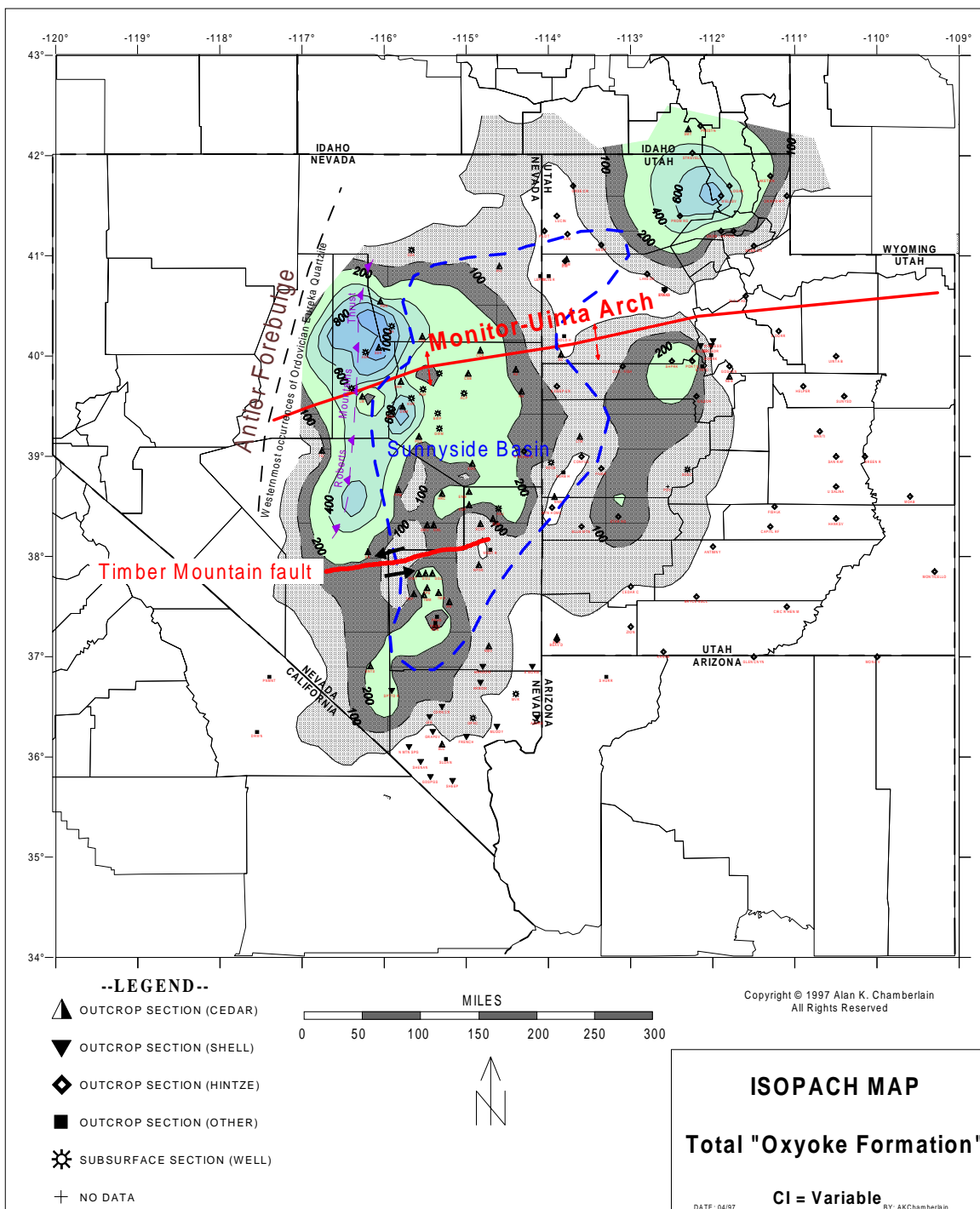


Figure 40 An isopach map of “Oxyoke Formation” in the Sunnyside basin shows that the basin axis was farther west during Oxyoke time than during younger Devonian time (**Figure 38**). It also suggests that the western extent of the Monitor-Uinta arch was a source area for quartz sandstones and that the Timber Mountain strike-slip fault offsets the basin axis. The blue dashed line is the outline of the unrestored Sunnyside basin.

Guilmette Sandstones

Siliciclastic rocks above the “Oxyoke Formation” next occur in the Yellow Slope Sequence of the Guilmette. Carpenter et al. (1994) and Carpenter (1997) recognized the importance of these siliciclastic rocks and suggested that rocks equivalent to the Yellow Slope Sequence represented the initial filling of the backbulge basin east of the Antler forebulge. Occurrence of quartz sand grains in the Yellow Slope Sequence is persistent in much of the Sunnyside basin and a careful study of them may provide insight into the paleogeography of the Sunnyside basin. However, thick sandstone occurrences above Sequence Dgb were the main topic of Ryan and Langenheim (1973) and are the subject of this section. This discussion begins with the Guilmette quartz sandstones in the study area, then includes the regional setting of the study area sandstones within the Sunnyside basin.

Guilmette Sandstones in the Study Area A number of conspicuous features that differ across the Silver Canyon thrust fault suggest eastward displacement of tens of miles. First, an abrupt change in the volume and characteristics of Guilmette sandstones occur across the thrust fault (**Table 12** and **Figure 41**). Reef-bearing rocks (facies 3) occur in Guilmette Sequence Dgb east of the thrust, and thick (up to 860 feet) quartz sandstone units (facies 2) make up Sequences Dgb through Dgg in the hanging wall west of the thrust.

Table 12 Net Sandstone thickness of the Guilmette Formation in the Timpahute area and beyond providing data used to generate **Figure 41**.

LONG LAT	NET FEET	SECTION	SECTION NAME
-115.42 37.83	75	GGL	GOLDEN GATE RANGE, LOWER PLATE
-115.50 37.83	100	GGU	GOLDEN GATE RANGE, UPPER PLATE
-115.38 37.32	320	PCR	PAHRANAGAT RANGE, CUTLER RESERVOIR
-115.37 37.34	330	PCR	PAHRANAGAT RANGE, CARBONATE RIDGE
-115.36 37.40	830	PHS	PAHRANAGAT RANGE, HANCOCK SUMMIT
-116.20 8.05	0	RR	REVEILLE RANGE
-114.83 38.33	20	SCSP	SCHELL CREEK, SIDEHILL PASS
-115.35 37.63	150	TMS	TIMPAHUTE RANGE, MAIL SUMMIT
-115.65 37.63	40	TMP	TIMPAHUTE RANGE, TEMPIUTE MOUNTAIN
-115.52 37.63	1070	TMM	TIMPAHUTE, MONTE MOUNTAIN
-115.48 37.69	965	TPS	TIMPAHUTE PENOYER SPRINGS
-115.58 37.83	190	WMT	WORTHINGTON MOUNTAIN

Net Guilmette quartz sandstone in the Silver Canyon thrust sheet (TMM) is 1,070 feet thick in contrast with 150 feet in the Pahroc (east) thrust sheet (TMS). Note the unusual thickness for the sandstone in the Silver Canyon thrust sheet in **Figure 41**. Sandstone bodies in the hanging wall are lenticular, occur throughout the Guilmette, exhibit bidirectional cross bedding, and are interbedded with *Amphipora*-bearing carbonates. They are interpreted as tidal deposits in channels and flats. Thin sandstone units of the Pahroc thrust sheet, by contrast, mostly occur in the uppermost Guilmette.

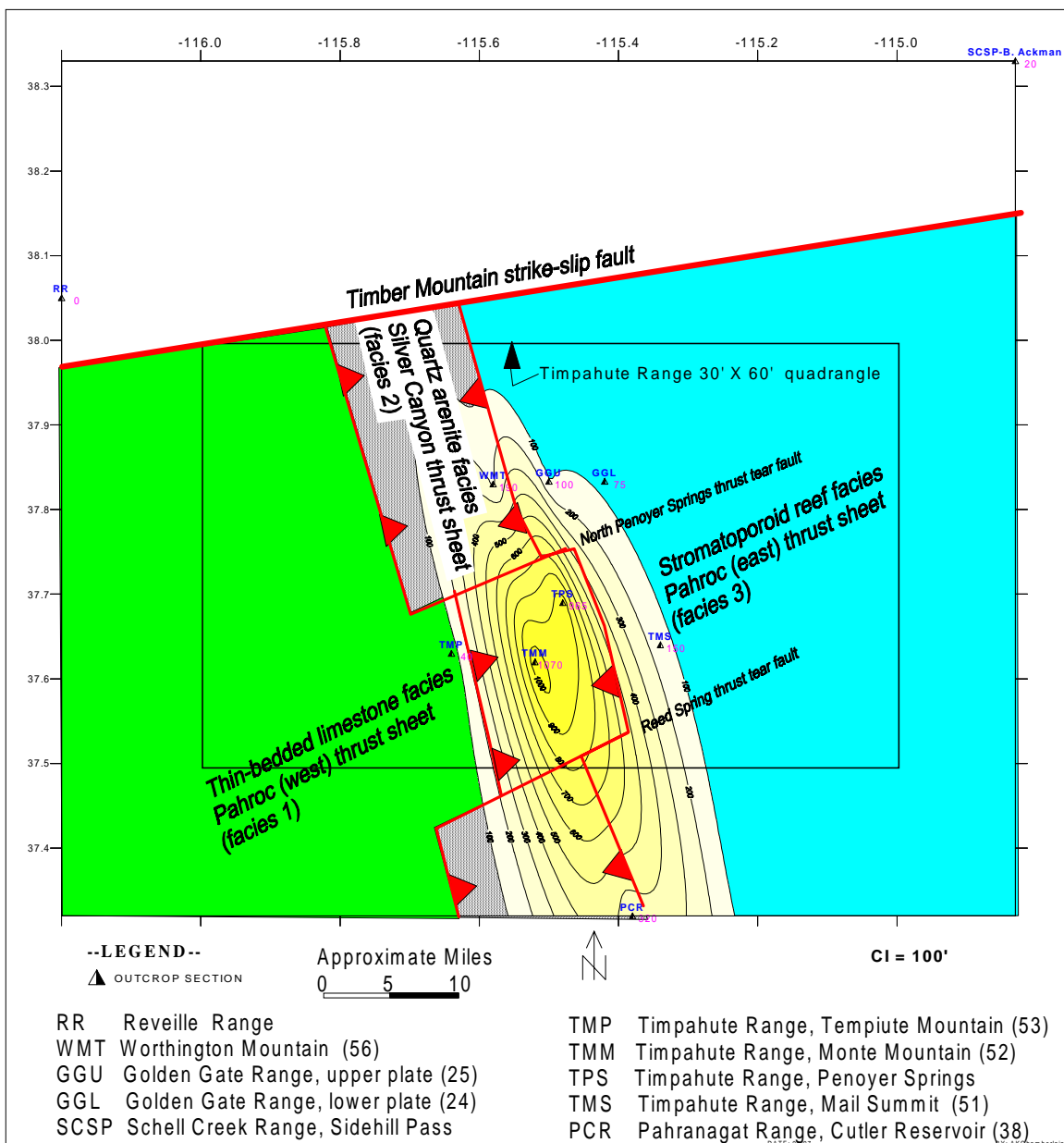


Figure 41 Guilmette Formation net quartz sandstone isolith map in the Timpahute area shows the abrupt changes in sandstone thicknesses between structural plates. Compare with the generalized tectonic map showing the structural plates of the greater Timpahute Range (**Figure 32**). Sections with capital letters are from Appendix F and **Table 2**. The value adjacent to the triangles are net sandstone thicknesses in feet. Thrust faults and thrust sheets are schematic. See Timber Mountain strike-slip fault on **Figure 38**.

Composite sandstone thickness in the Guilmette Formation increases northward from the southern Pahrnagat Range to the Timpahute Range and then rapidly decreases to zero sandstone north of the Timber Mountain fault. Thickness of the sandstones increases from 320 feet in the Pahrnagat Range to more than a thousand feet at Monte Mountain. North of the greater Timpahute Range, quartz sandstone thickness decreases rapidly to no sandstone in the southern Egan Range, 60 miles north-northeast of Hiko (**Figure 8**, **Figure 9**, No. 20 and **Table 2**). If the original thickness trends were gradual, then the present abrupt trends could be due to thrust tear faults that bound the north and south sides of the Silver Canyon thrust sheet in the Timpahute salient. Structural salient is defined in Chapter 6. These thrust tear faults may be related to basement fractures caused by the cosmolite impact. Glikson (1999) suggested a potential correlation between mega-impacts and crustal magmatic and tectonic episodes. Cedar Strat measured 190 feet in the Worthington Range and 100 feet in the Golden Gate Range of net quartz sandstones (proprietary measured sections, 1986, 1987). I measured 40 feet of net quartz sandstone in the Guilmette Formation in the western exposure of the Pahroc thrust sheet at Tempiute Mountain. In the Pahrnagat Range, south of the study area, Estes (1992) reported 830 feet of net Guilmette sandstone near Hancock Summit and Downtop Mountain. Similar thicknesses were reported for Downtop Mountain (Shell Oil Company and Cedar Strat proprietary measured sections). Reso (1960) reported 330 feet west of Badger Spring, six miles south of Hancock Summit.

The change in net sandstone thickness between the central Pahrnagat Range and Monte Mountain, a distance of 23 miles along structural strike, is 740 feet or an average of 32 feet per mile. Assuming the same gradient, net sandstone thickness would decrease to 150 feet, the thickness at Mail Summit, nine miles from Monte Mountain. If the gradient were similar between Monte Mountain and Mail Summit, Monte Mountain should be restored 29 miles west of Mail Summit. Approximate crustal shortening estimated by balancing bed lengths in a snip reconstructed structural cross section is 28 miles and the amount of slip on the Silver Canyon thrust fault on **Plate 4a** is 22 miles (**Table 10**).

Regional setting of Guilmette Sandstones An isolith map of net sandstone (**Figure 42**) of the Guilmette Formation in the Sunnyside basin sheds light on possible source areas for the sandstones. Generally quartz sandstones are thickest on the edges of the Sunnyside basin. Some thickest sandstones occur where the Monitor-Uinta arch intersects the edges of the Sunnyside basin. Thick uppermost Devonian sandstones are focused in the Stansbury uplift area in north central Utah. The sandstones become thinner southwestward, parallel with the Utah hingeline. Another area of thick uppermost Devonian sandstones occurs near the Utah/Nevada border at latitude 38.75°. Isolith contours suggest that another positive area could have occurred in an east-west belt in central Utah. Sand moving westward from eastern and central Utah would have been trapped at the edge of the Sunnyside basin near the Nevada border. The sandstones are mature. Ryan and Langenheim (1973) suggested that the sandstones must have moved from the environment of maturation to the site of deposition. The maturation of the sandstones could be a result of recycling sandstones from earlier mature sandstones such as the Eureka Quartzite.

Thick middle Upper Devonian sandstone occurrences in the Silver Canyon thrust sheet in the Timpahute region occur on the southwest edge of the Sunnyside basin. These sandstones are described in Chapter 4 and in Appendix B. Generally they are composed of mature, fine- to medium-grained, well-sorted, well-rounded, and frosted quartz grains. They occur in lenticular channels tens to hundreds of feet wide and tens of inches to tens of feet deep. They exhibit planar crossbedding and are rippled. Ryan and Langenheim (1973) reported a predominant current direction from the northeast for Guilmette sandstones exposed in the Arrow Canyon Range, 62 miles south-southeast of Hiko. Mudcracks are common at the top of the sandstone beds in the study area.

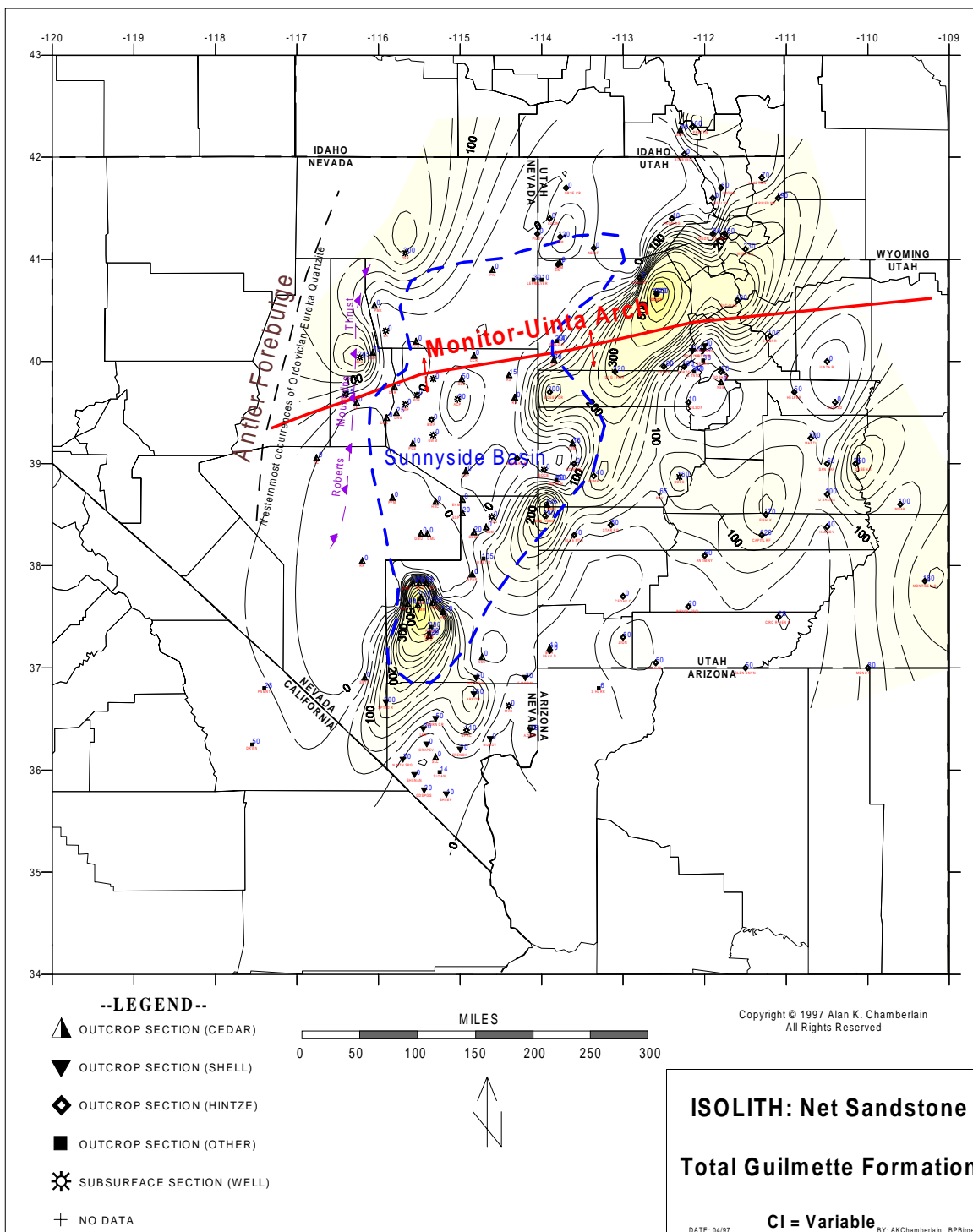


Figure 42 An isolith map of the net quartz sandstone of the Guilmette Formation of the Sunnyside basin, Nevada and Utah shows that sandstones are concentrated along the edges of the Sunnyside basin (see Appendix F for data locations). The blue dashed line is the outline of the unrestrained Sunnyside basin.

Thrust restoration of the greater Timpahute Range would place the thick quartz sandstones even closer to the Antler forebulge, a likely source of the mature sandstones. The steep gradient on the north side of the Timpahute sandstone accumulation is probably due to strike-slip displacement along the north Penoyer Spring tear fault and more especially along the Timber Mountain fault four miles north of the study area.

On the northwest edge of the Sunnyside basin, another sandstone thick occurs below the Mississippian Roberts Mountain allochthon near the Monitor-Uinta arch. The source area for these mature sandstones is likely from erosion of lower Paleozoic sandstones such as the Eureka Quartzite on the Antler forebulge.

Conclusions

Isopach maps of correlated Devonian sequences reveal the form of the Sunnyside basin, an intrashelf basin with restored dimensions similar to the Williston basin. The Sunnyside basin may be a precursor to the Antler foreland basin. It was bordered on the west by the Antler forebulge. Recycled sandstones, and perhaps insoluble residues including conodonts, from lower Paleozoic rocks were eroded from the forebulge and were deposited in the Sunnyside basin. Thick accumulations of the "Oxyoke Formation," with the first significant accumulations of quartz sandstone above the Eureka Quartzite near the Antler foreland bulge, may record the first pulse of the Antler orogeny.

Amphipora-bearing facies is more common on the west side of the basin and coral and stromatoporoid-bearing facies is more common on the east side of the basin. Thick, mature, quartz sandstone beds accumulated on the edges of the basin. A cosmolite impact created the Tempiute basin, a sub-basin in the south end of the Sunnyside basin, during Sequence Dgb time. The oval-shaped sub-basin is more concentric when sections are restored closer to their prethrust locations (Chamberlain, 1999).

CHAPTER 8

APPLICATIONS

This study has academic applications dealing with stratigraphy and structure. It also has economic implications for oil and gas, mineral, and groundwater exploration.

Economic Applications

The new structural model presented in this report suggests considerable displacement on thrust faults in the study area thus creating viable structural targets for oil and gas. Most of the thrust faults place porous middle and lower Paleozoic carbonates on Mississippian source rocks (Chamberlain et al., 1992a). Devonian carbonates, with karsted regional unconformities, reefs, sandstones, breccias, and fractures may be the best reservoir rocks in the region (Chamberlain 1986a, b). Skarns in Devonian and Mississippian rocks associated with intrusives at Tempiute are enriched with tungsten and other metals. Silver and molybdenum mineralization favors the fractures and hydrothermal alteration associated with the Silver Canyon thrust fault. An understanding of the regional Devonian paleogeography will not only help predict reservoir and host rock trends but help predict gold occurrences. Devonian rocks in the Great Basin contain significant amounts of syngenetic gold (Emsbo et al., 1999). This section briefly reviews some economic applications of this research.

Oil and Gas Exploration

In the Golden Gate Range, organically rich, thermally mature Mississippian source rocks containing 4-6% Total Organic Carbon (TOC)(Chamberlain, 1990a) occur within the oil-generation window ($R_o > 0.65$)(Scott and Chamberlain, 1986; Chamberlain, 1998b). Specifically, these rocks lie in the footwall of the Golden Gate thrust fault. Devonian reefs and karsted intervals below unconformities occur in the hanging wall of large fault folds (Stop 10, Appendix D). Open fractures, perpendicular to the underlying source rocks, could have served as conduits for fluids migrating into the porous beds above. Before erosion, thousands of feet of Mississippian shales and thin beds of anhydrites draped the structure and could have served as effective regional seals over the now breached Golden Gate structure. Therefore, the Golden Gate anticline serves as a model for traps along the central Nevada Oil and Gas Fairway, a north-south trending region in east central Nevada where organic-rich Mississippian source rocks are thermally mature (Scott and Chamberlain, 1986; Chamberlain, 1988d, Chamberlain, 1999). Pine Valley, containing the Blackburn Oil Field (210 miles north, northwest of Hiko), marks the northern end of the fairway. The Nevada Test Site marks the southern end of the fairway (Trexler et al., 1999). All of the existing oil production in Nevada lies within this trend (Chamberlain, 1988a). The well exposed and well preserved Golden Gate anticline provides an excellent opportunity to study sources, reservoirs, traps, and seals that could exist in similar, unbreached structures along the fairway. The structural model presented in Chapter 5 (**Plate 4**) could serve as a template to find structures like the Golden Gate feature along strike, where they are concealed by Tertiary volcanics and valley fill.

The axis of the 15-mile-long Worthington Mountain doubly-plunging anticline is convex eastward, analogous to the giant 14-mile-long Whitney Canyon-Carter Creek Gas Field (Bishop, 1982) and the giant five-mile-long Anschutz Ranch East Field (Lelek, 1982) in the Utah-Wyoming thrust belt. The Worthington Mountain anticline provides another model for folded structures in this part of the Sevier thrust belt. It also provides an

example of a folded thrust fault. Such structures could have contained significant quantities of hydrocarbons if they are not breached. Similar, unbreached structures along the Central Nevada Oil and Gas Fairway (Chamberlain, 1988b, Chamberlain et al., 1999) could contain significant hydrocarbon reserves.

Sequence Boundaries in Exploration Recognition of sequence boundaries not only provides a practical basis for correlating strata, but also guides explorationists to intervals of potential economic significance. For example, a sequence boundary expressed as a karst surface at the top of the Simonson Dolomite separates dolomites below from varied lithologies of limestone, dolomite, sandstone, megabreccia, and siltstone above. The karsted, coarsely-crystalline dolomite below the unconformity has favorable reservoir properties. Reservoir properties include interconnecting coarsely-crystalline dolomite pores, interconnecting vugs and karst cavities, and fractures that interconnect karst cavities, vugs, and coarsely-crystalline dolomite pores (Stop 7, Appendix D). Thus, it is a major hydrocarbon exploration target and could correlate to the reservoir rocks at the Grant Canyon oil field 65 miles north-northwest of Hiko.

Hulen et al. (1994) described the Grant Canyon and closely associated Bacon Flat reservoirs as vuggy, brecciated, Paleozoic dolomites. They suggested an early period (Devonian?) of fracturing followed by dissolution that could be karsting related to the regional unconformity. A later event (Tertiary?) of major brecciation and fracturing followed by dissolution described by Hulen et al. (1994) could suggest a period of reactivation of the karsted interval that enhanced the reservoir porosity.

Devonian Reefs Reefs in the Devonian Guilmette Formation are similar to those in the hydrocarbon-producing reef trend in the Alberta Basin of Canada. The reefs in the Hiko Range, up to 3,000 feet long and more than 100 feet thick (Stops 5 and 16, Appendix

D), are composed of stromatoporoids and corals. Porosity in the reefs has been enhanced by episodes of karstification and diagenetic alteration.

Devonian Porosity and Permeability Much of the Devonian section in the Timpahute area is dolomitized. Dolomitization could have either improved or destroyed porosity and permeability. Porosity in the pervasively dolomitized carbonates below the Simonson Dolomite unconformity could be similar to that of the Mississippian Burlington-Keokuk Formation in Iowa, Illinois and Missouri. Within the Burlington-Keokuk, three pervasively dolomitized microfacies comprise up to 70% of the formation and contain > 80% of the formation's pore volume (Choquette et al., 1992).

Permeability is the hardest characteristic of potential oil reservoirs to evaluate without knowledge of how the fluids interacted with the rock at burial temperatures and pressures (Longman, 1982). Outcrops provide some information about permeability, but without more exploratory drilling and testing, fluid/rock interactions at burial temperatures and pressures and subsequent diagenetic alterations are poorly known. The paucity of Devonian penetrations hinders testing various hypotheses of diagenesis of the rocks and predicting porosity and permeability trends. Compensated neutron-density logs in mature oil provinces such as the Williston basin provide the ability to trace different carbonate units through their complex facies changes across that basin. They also help distinguish limestones, dolomites, anhydrites, and even partly-dolomitized limestones and determine porosity with remarkable accuracy (Longman, 1982). Lacking these logs, surface gamma-ray logs and descriptions of outcrops in the Great Basin provide the basic information to begin to understand the complex history of Devonian sedimentation (Chamberlain, 1983).

Descriptions of porous and permeable zones such as the karst interval below the Simonson Dolomite unconformity and dolomitized reefs in Sequence Dgb provide some empirical data that may help quantify porosity and permeability in the rocks. Furthermore, descriptions and measurements of fracture patterns such as those associated with the crest

of large thrust fault structures may further help quantify permeability for migration paths and reservoirs. Locally, fractured reservoirs may have developed because of the cosmolyte impact into Devonian seas during Sequence Dgb time. Reservoirs in other regions that could have developed as fossil meteorite or cosmolyte impacts include Viewfield field in Saskatchewan and Red Wing Creek and Newporte fields in North Dakota. In each case, a highly disturbed and brecciated crater is surrounded by a structurally high rim of highly fractured rock (Longman, 1982). The impact responsible for the Guilmette Dgb2 breccia Sequence could have also produced a similar crater.

Although most exploration is focused on structural traps, stratigraphic traps could play an important role in successful oil and gas exploration in the Great Basin. Commonly, porous dolomites in the Guilmette grade laterally into tight limestones. Porous, coarsely-crystalline Simonson Dolomites grade into tight, finely-crystalline dolomite. Development of an exploration model is partly dependent on dolomitization mechanisms. Possible mechanisms of dolomitization and descriptions of Devonian dolomite occurrences in TMS are reviewed in Chapter 4.

Sevy Dolomite Reservoir Potential For petroleum exploration, the Sevy Dolomite may be the poorest Devonian reservoir target in Nevada, as it lacks any visual porosity. The density of the Sevy Dolomite is an obvious attribute noticed by most field geologists. However, the correlative Beacon Peak Member of the Nevada Formation is likely the primary reservoir unit at the Blackburn Field in Pine Valley (Scott and Chamberlain, 1988a, b). Fenestral vugs do occur in the Sevy Dolomite locally. These tiny (<0.2" diameter) vugs are neither persistent, abundant, nor interconnected. They would provide a poor reservoir unless somehow enhanced in the subsurface. In areas where interstitial anhydrite is present in the Sevy Dolomite, hydrocarbon accumulation could occur because: 1) anhydrite can be diagenetically removed differentially creating secondary intercrystalline porosity; and (2) where the anhydrite remains intact, the Sevy Dolomite

may act as a competent roof seal on the underlying Laketown Dolomite or on the footwall of any age where the Sevy Dolomite occurs in a hanging wall plate.

Roof Seal Potential All the Yellow Slope Sequence Cycles have low permeability and lack visual porosity. The tight, laminated, dolomudstones may provide a hydrocarbon roof seal above the unconformity at the top of the Fox Mountain Sequence. A thin-section of a core from Grant Canyon No. 3 at 3,961.9 feet has a striking resemblance to a Cycle 3 thin-section (MI-301 in Appendix C). It is likely they are both of the Yellow Slope Sequence because of the similarity in the stratigraphic sequence and the rare occurrence of detrital quartz grains in a dolomicrite of the lower Guilmette Formation. Nearly five hundred thin sections taken at 2.5 foot intervals of the lower Guilmette at TMS revealed no detrital sand grains between the “Oxyoke Formation” and Sequence Dgd above Dgb2 breccia except in the Yellow Slope Sequence. Therefore, the main producing reservoir at Grant Canyon is likely just below the major unconformity at the top of the Simonson Dolomite. Large cavities were encountered while drilling. This suggests that part of the prolific production from Grant Canyon may be due to karsting. Karst cavities associated with the unconformity were probably reactivated and enlarged before being charged with oil. The impermeability of the overlying Yellow Slope Sequence could be responsible for the roof seal of some oil at the Grant Canyon oil field. If the Yellow Slope Sequence functions as a reservoir seal over karsted reservoirs at the tops of the Simonson Dolomite and Fox Mountain sequences at Grant Canyon, then this model may serve as an exploration target in other prospective areas. Hulen et al. (1994) suggested that karst is not important at Grant Canyon Field. In other localities including Lake, White Pine, Coal, and Long valleys, drill stem tests and wireline logs show that the karst interval below the Simonson Dolomite unconformity is very porous; they commonly produce water with minor oil shows (Cedar Strat well files).

Mineral Exploration

Correlative with Upper Devonian Guilmette rocks in the Timpahute Range, Upper Devonian Slaven Chert rocks in the Robert Mountains allochthon, north-central Nevada, host the world's largest resources of barite in sedimentary exhalative deposits (Emsbo et al., 1999). Auriferous sedimentary exhalative deposits are hosted in the underlying autochthon. They could be the source of gold in the world-class Carlin gold trend (Emsbo et al., 1999). Therefore, a better understanding of Great Basin Devonian depositional systems could have economic significance.

The structural model presented herein provides insight into the distribution of precious metals in the greater Timpahute Range. Geochemical analyses of several hundred jasperoid occurrences in the Timpahute Range show elevated gold values in the footwall of the Chocolate Drop thrust fault (Cedar Strat proprietary data). Gold production at the old Tempiute Mining District in the late 1800's complement these analyses (Tschanz and Pampeyan, 1970). Geochemical analysis of jasperoids in the Silver Canyon thrust sheet provide only trace amounts of precious metals and their associated pathfinding elements. Pathfinding elements include Cu, As, Pb, Sb, Mo, and Zn. For example, no pathfinding elements occur in unaltered carbonates, but trace concentrations of precious metals and precious metal pathfinder elements occur in jasperoids near the Penoyer Springs thrust fault footwall contact. Higher concentrations were found in footwall jasperoids near the Silver Canyon thrust fault. Silver production came from mines along the Silver Canyon thrust fault in Silver Canyon during the late 1800's (Tingley, 1991). Silver production matches the elevated values near the thrust fault. Thus, a knowledge of structural relationships can guide exploration companies to appropriate areas for further evaluation.

Groundwater Exploration

Devonian rocks in the study area provide the major aquifer for the region. Hiko Spring and Crystal Springs both occur in the Guilmette Formation where east-west structures intersect the north-south structural grain. Hiko Spring is in the axis of the east-west trending Hiko syncline where Dgb2 breccia is in thrust fault contact with the Pilot Formation (Appendix E). The porous Dgb2 breccia serves as the aquifer in the hanging wall plate and the Pilot Formation serves as an aquitard or floor seal. The artesian spring flows about 2700 gallons per minute (E. Hansen, 1998, personal communication).

Crystal Springs flows from fractured upper Guilmette rocks near the projected position of the Crystal Springs Canyon fault (Appendix E). It flows about 5400 gallons per minute. About four miles south of the study area, Ash Springs flows about 8000 gallons per minute (B. Tanner, 1998, personal communication). Both are artesian springs.

Results of this study provide additional information on the structure and stratigraphy of this regionally important Devonian aquifer. This information coupled with well data and geophysical data could help identify potential targets for water exploitation.

Academic Applications

Results of this work have structural academic applications. For example, the concentric Tempiute basin constrains the construction of retrodeformable balanced cross sections. Also, results of this work have stratigraphic academic applications. For example, exposed stratigraphic sequences can be tied to seismic stratigraphy by correlating between surface and subsurface gamma-ray logs and tying well data to the seismic lines. Furthermore, geologic maps based on sequences rather than formations and members depict complex structures more accurately and clearly.

Structural Applications

Construction of retrodeformable balanced cross sections should involve undoing the total displacement field. However, Mukel (1998) pointed out that most restorations only account for translation and rotation components and ignore the penetrative internal deformation of thrust sheets. He also pointed out that the most accurate restorations are obtained by retrodeforming the deformation profile incrementally using strain history of the thrust sheet as a guide. Incremental strain data are not always available. Estimates of spacial variability of strain in a thrust sheet causes the cross section to be less accurate. However, the restored concentric Tempiute basin constrains assumptions and estimates of the spatial variability of strain in the thrust sheets. Thrust restoration of the Dgb2 basin provides a unique opportunity to test various thrust models. If the assumptions about the strain variations that lead to the retrodeformable balanced cross section that most closely restores the concentric Tempiute basin are regarded as correct (**Plate 4a**), they could be used to construct other cross sections in this part of the Sevier fold-and-thrust belt.

Stratigraphic Applications

Devonian sequences in the study area have characteristic gamma-ray patterns that are regionally mappable in surface and subsurface sections. As a result, surface gamma-ray logs tie exposed sequences to well logs that can be tied to seismic data. Thus, sequence stratigraphy can be tied to seismic stratigraphy with surface gamma-ray logs.

Furthermore, this study shows the utility of mapping sequences instead of formations and members in structurally complex areas (**Plate 6**). Therefore, structural stratigraphy, the application of sequence stratigraphy to solve structural problems, greatly refined the structural detail of the study area.

CHAPTER 9

CONCLUSIONS AND RECOMMENDATIONS

Twelve conclusions summarize this research. Because of the scope and limitations of this study, 19 recommendations suggest directions for future work.

Conclusions

1. A well-exposed 5,000-foot-thick composite stratigraphic section, comprised of 21 mappable sequences in the greater Timpahute Range, provides a new and more detailed reference section for Devonian depositional cycles and sequences across the eastern Great Basin. A knowledge of these sequences is indispensable for mapping this complex region. For example, recognition of overturned beds associated with thrust faults in the study area was eased by applying detailed knowledge of stratigraphic sequences and shallowing-upward patterns of the carbonate cycles.
2. The Simonson Dolomite unconformity, a karsted sequence boundary, divides the pervasively dolomitized Paleozoic rocks below from undolomitized rocks above in most of the Sunnyside basin.
3. Guilmette sequences can be distinguished regionally on surface gamma-ray logs. Surface gamma-ray logs provide a way to tie exposed sequences to wells. From the wells the sequences could be tied into seismic data. Thus, exposed sequence stratigraphy can be tied to seismic stratigraphy.

4. The most common occurrence of dolomite in Devonian rocks exposed on the southwestern part of the Mail Summit and northwestern part of the Mount Irish SE 7.5' quadrangles is the finely-crystalline stratal dolomite that caps most of the shallowing-upward cycles. They are most obvious in the Guilmette Formation where the dolomite cycle caps lie on limestone bases. In the Simonson Dolomite, they are the light bands between the alternating dark bands. Most of the Sevy Dolomite is composed of finely-crystalline stratal dolomite.

5. Isopach maps of Devonian sequences and isolith maps provide insight to Devonian paleogeography. A composite isopach map of all the Devonian sequences reveals the unrestored shape of the Sunnyside basin, an intrashelf basin, that is a precursor of the Mississippian Antler basin. A sandstone isolith map shows that quartz sandstones were deposited on the edges of the basin. It also suggests that the Antler forebulge was the probable source area for Devonian quartz sandstones on the west side of the basin. Additionally, the forebulge was probably the source of Cambrian, Ordovician and Silurian conodonts and other microfossils found in Devonian carbonates of the Sunnyside basin.

6. The Sunnyside basin lies between the Antler forebulge in central Nevada and the Utah hingeline in central Utah. Sequence isopach maps show that the axis of this Antler backbulge basin migrated eastward from around Eureka, Nevada, in Early Devonian Sevy Dolomite time to western Utah by Early Mississippian Pilot Formation time.

7. Thinning of Devonian sandstones and sequences shown by regional isolith and isopach maps, and unconformities cutting out lower Paleozoic rocks beneath the Devonian-Mississippian Roberts Mountains allochthon, imply an active tectonic high on the western side of the Devonian Sunnyside basin. These maps and unconformities suggest that the "Oxyoke Formation" resulted from a siliciclastic pulse marking the onset of the Antler Orogeny.

8. The methods used to produce the new geologic map for the greater Timpahute Range took advantage of mapping, contouring, and graphic software and satellite global positioning systems. Other methods and resources that proved useful include surface gamma-ray logging, recently available low-altitude color aerial photography, and 7.5-minute topographic base maps. The application of these methods and tools and others described in Chapter 3 provide a new, more effective way to acquire geologic data and annotate and animate images and document and express the geologic data and interpretations to others. Such technology coupled with GIS mapping led to a new level of mapping efficiency, viewing, and geologic interpretation.

9. The new geologic map of the Timpahute Range quadrangle reveals many newly identified compressional features in Paleozoic rocks associated with of the Sevier compressional event (Appendix E). Thrust restoration suggests at least 30 miles of east-west crustal shortening on the Silver Canyon thrust and at least 63 miles of cumulative crustal shortening along the length of the greater Timpahute Range. When restored, the Tempiute impact crater becomes more concentric.

10. The new geologic map of the Timpahute Range quadrangle reveals abundant compressional elements of the Mesozoic Sevier fold-and-thrust belt, but failed to reveal major north-south trending faults associated with Cenozoic extension. Models of Cenozoic extension should probably be revised.

11. The new structural cross section of the greater Timpahute Range provides a template that can be used to decipher structural complexities along strike where thrust fault relationships are hidden by Tertiary cover. For example, Cenozoic cover in Coal, Garden and Sand Springs valleys conceal all but the crests of the Golden Gate and Worthington ranges north of the greater Timpahute Range. However, by projecting thrust faults northward from the greater Timpahute Range and adjusting for strike-slip faults, the

Freiburg thrust fault probably correlates to the Penoyer Springs thrust fault. It is likely that a thrust fault, correlative with the Monte Mountain thrust fault, is concealed in the Freiburg thrust footwall. The outcrop of Guilmette Formation exposed below the north Worthington fault, described in Appendix E, may be a small window into the thrust fault correlative with the Monte Mountain thrust fault.

12. Application of data and interpretations presented herein may lead to new mineral and hydrocarbon discoveries and to a better understanding of the regional Devonian carbonate groundwater aquifer. Three major sea-level lowstand events that produced regionally and economically significant karst intervals occur in the reference section of Devonian rocks at TMS.

Recommendations

1. Detailed analysis of the Sevy Dolomite could reveal the source of dolomitizing fluids and the potential for preserved evaporites in the subsurface. It may be worth further study to learn if the Sevy Dolomite becomes sufficiently anhydritic to serve as a competent reservoir roof seal for the Laketown Dolomite.
2. Additional research, including measured sections, isotope studies, and petrographic analysis, on the “Oxyoke Formation” and Guilmette quartz sandstones could test the hypothesis that some of these sandstones were derived from the Antler forebulge and provide additional insight into the evolution of the Antler orogeny. The sandstones may be important hydrocarbon reservoir rocks in some areas.

3. Detailed stratigraphic analysis of the Devonian sequences of the TMS has led to the identification of regional karsted intervals associated with major sequence boundaries. Additional work on these karsted intervals, occurring in many sections of the region, could provide attractive targets for hydrocarbon exploration. Additional work could include more measured sections, well log analyses, petrographic analyses, etc.
4. In Chapter 4, it was suggested that an isopach map of the depth of karsting could provide a rough estimate of the paleotopography at the end of Fox Mountain time. Such a map could serve as a potential reservoir trend map for hydrocarbon exploration.
5. An isopach map and facies maps of Fox Mountain Sequences would provide additional insight into the paleotopography and nature of the Guilmette transgression.
6. The unique structural grain in eastern Nevada provides an opportunity to compare and contrast cycles over large (10's miles) distances along strike. A series of closely spaced measured sections could provide insight into the processes and causes of carbonate cycles in the Sunnyside basin.
7. This study provides the criteria for recognizing Devonian sequences in the Sunnyside basin. Using these criteria, a systematic study of recycled pre-Devonian microfossils in the sequences could shed light on the unroofing of the Antler forebulge. Of particular interest is Sequence Dgb in and beyond the Tempiute impact basin.
8. A more rigorous approach using Guilmette Dgb2 breccia isolith maps to restore thrust faults could refine the tectonic model and may provide insight into constructing retrodeformable internal thrust belt cross sections in the region.

9. Documentation of the reef at TMS and the reefs in the Hiko Range and their position in the Sunnyside basin could lead to the discovery of additional reefs on outcrops and hidden reefs buried beneath valley fill and Sevier thrust sheets. Some reefs may be important hydrocarbon reservoirs.

10. Isopach maps of each sequence provide clues to the evolution of the Sunnyside basin centered north of the study area. Further research and mapping of this basin will result in better facies maps that can be used to predict hydrocarbon reservoir rocks, depositional trends, and tectonic imprint on the rocks.

11. A rigorous analysis of coalescing sequence boundaries from the middle to the eastern edge of the Sunnyside basin would provide insight into the evolution of the basin and the effects of relative sea-level changes on the Devonian strata. Such analyses should provide trends of unconformities. Hydrocarbon reservoir rocks or seals may have formed at the unconformities

12. This study has laid the groundwork for a comprehensive analysis of dolomite in Devonian rocks of the region. Regional isotope and trace element trends could lead to a better understanding of the dolomitizing events and should provide additional information about the tectonic and diagenetic history of the region. Fluid inclusions could provide clues on timing and fluid conditions of the dolomitizing events. Identification of dolomitization processes and timing could lead to better predictions of possible hydrocarbon reservoirs and subtle mineralization trends.

13. Rigorous structural modeling that includes gravity, magnetic, seismic and new surface mapping could add insight into the region's complex structural evolution and could result in economic benefits.

14. A corollary study that will complement this work is a detailed gravity profile of the greater Timpahute Range. A rigorous structural analysis coupled with a detailed gravity and magnetic survey of the exposed greater Timpahute Range may provide a refined structural template that could help interpret the structure in fewer exposed areas along strike.

15. A more detailed study of fracture patterns within the study area should reveal additional fault patterns related to the Dgb2 impact event, Cretaceous compression, and Cenozoic extension of this part of the Sevier fold-and-thrust belt.

16. The surface gamma-ray technique developed in this study can be applied to other regions of the world to tie exposed stratigraphic sequences to sequence and seismic stratigraphy. Future work on the Great Basin Devonian rocks would benefit from detailed surface gamma-ray logs. For example, the gamma-ray signature of a sequence from where conodonts or other microfossils were collected could be correlated to gamma-ray logs of wells and outcrops where sample quality is inadequate to provide fossil zones. The definition of sequences, formations and members should include their gamma-ray signature as I suggested in 1983.

17. The technique of integrating a Global Positioning System (Trimble Pathfinder) with a Geographic Information System (*MapInfo*) used to make the geologic map of the Timpahute Range quadrangle has worldwide applications for rapid precision mapping. Additional mapping and sample collection in the Great Basin would be greatly enhanced with GPS and GIS techniques.

18. Data and interpretations presented herein may be helpful in evaluating the natural resource potential of several wilderness study areas in and near the study area. For example, extensive mapping of Nellis Air Force bombing range and the Nevada test site

should yield information on Mississippian source rocks, Devonian sequences including the Guilmette Formation Sequence Dgb2 (Alamo Breccia), Mesozoic thrust faults and associated synorogenic strata, and possible hydrocarbon and mineral prospects, when the areas are declassified and made accessible to researchers. Independent evaluation of the region may result in interpretations that contrast with those of federal geologists. For example, Barker (1999) concluded that the Nevada Test Site lacks oil and gas potential. In contrast, Trexler et al. (1999) provided evidence for oil and gas potential. Neither considered the additional potential by projecting thrust faults from the Timpahute quadrangle south, along strike to the Nevada Test Site. With further evaluation, significant hydrocarbons may be found in the Nevada Test Site region (Chamberlain, 1991).

19. All the text and figures of this dissertation fit on one compact disk. Availability of this dissertation in digital form and a comment form for suggestions and comments can be found at www.cedarstrat.com. Because it is in digital form, it is easily updated as suggestions, comments, and new data and technology become available.

REFERENCES

Ackman, B.W., 1991, Stratigraphy of the Guilmette Formation, Worthington Mountains and Schell Creek Range, southeastern Nevada: unpublished M.S. thesis, Colorado School of Mines, Golden, 207 p.

Albright, G.R., 1991, Late Devonian and Early Mississippian paleogeography of the Death Valley region, California: *in* Cooper J.D., and Stevens, D.H., eds., Paleozoic paleogeography of the western United States-II: Pacific Section Society of Economic Paleontologists and Mineralogists, v. 67, p. 253-269.

Altschuld, N., and Kerr, S.D.Jr., 1982, Mission Canyon and Duperow reservoirs of the Billings Nose, Billings County, North Dakota: *in* Christopher, J.E., and Kaldi, J., eds., Fourth International Williston Basin symposium: Special Publication Number 6, Saskatchewan Geological Society, p. 103-112.

Ames, D.E., Watkinson, D.H., and Parrish, R.R., 1998, Dating of a regional hydrothermal system induced by the 1850 Ma Sudbury impact event: *Geology*, v. 26, p. 447-450.

Arabasz, W.J., and Julander, D.R., 1986, Geometry of seismically active faults and crustal deformation within the Basin and Range-Colorado Plateau transition in Utah, *in* Mayer, L., ed., Extensional tectonics of the southwestern United States: a perspective on processes and kinematics: Geological Society of America Special Paper 208, p. 75-96.

Armstrong, J.A., 1980, Correlation of Devonian rocks in southwestern Nevada--southeastern California with reference to central Nevada: unpublished Master's thesis, California State University, Fresno, 112 p.

Armstrong, P.A., 1991, Displacement and deformation associated with a lateral thrust propagation: an example from the Golden Gate Range, southern Nevada: unpublished M.S. thesis, University of Utah, Salt Lake City, 162 p.

Armstrong, P.A., and Bartley, J.M., 1993, Displacement and deformation associated with a lateral thrust termination, southern Golden Gate Range, southern Nevada, U.S.A.: *Journal of Structural Geology*, v. 15, p. 721-735.

Armstrong, R.L., 1968, Sevier orogenic belt in Nevada and Utah: *Geological Society of America Bulletin*, v. 79, p. 429-458.

Arthur, M.A., and Garrison, R.E., 1986, Cyclicality in the Milankovitch band through geologic time: an introduction: *Paleoceanography*, v. 1, p. 369-372.

Asquith, D.O., 1970, Depositional topography and major marine environments, Late Cretaceous, Wyoming: *American Association of Petroleum Geologists Bulletin*, v. 54, p. 1184-1224.

Axen, G.J., Taylor, W.J., and Bartley, J.M., 1993, Space-time patterns and tectonic controls of Tertiary extension and magmatism in the Great Basin of the western United States: *Geological Society of America Bulletin*, v. 105 p. 56-76.

Axen, G.J., Wernicke, B.P., Skelly, M.F., and Taylor, W.J., 1990, Mesozoic and Cenozoic tectonics of the Sevier thrust belt in the Virgin River Valley area, southern Nevada, *in* Wernicke, B.P., ed., *Basin and Range extension tectonics near the latitude of Las Vegas, Nevada: Geological Society of America Memoir 176*, p. 123-153.

- Baer, J.L., 1962, Geology of the Star Range, Beaver County, Utah: Brigham Young University Studies v. 9, pt. 2, p.29-52.
- Baer, J.L., R.L Davis, and George, S.E., 1982, Structure and stratigraphy of the Pavant Range, central Utah: *in* Nielson, D.L., ed., Overthrust belt of Utah, 1982 Symposium and Field Conference: Utah Geological Association Publication 10, p.31-48.
- Baker, W.H., 1959, Geologic setting and origin of the Grouse Creek pluton, Box Elder County, Utah: unpublished Ph.D. thesis, University of Utah, 150 p.
- Barker, C.E., 1999, Middle Devonian-Mississippian stratigraphy on and near the Nevada Test Site: implications for hydrocarbon potential: discussion: American Association of Petroleum Geologists, v. 83, p. 519-522.
- Barosh, J.P., 1960, Beaver Lake Mountains, Beaver County, Utah: Utah Geological and Mineral Survey Bulletin 68, 89 p.
- Bartley, J.M., Axen, G.J., Taylor, W.J., and Fryxell, J.E., 1988, Cenozoic tectonics of a transect through eastern Nevada near 38° N. latitude, *in* Weide, D.L., and Faber, M.I., eds., This extended land, geological journeys in the souther Basin and Range: Geological Society of America Cordilleran Section Field Trip Guide, p. 1-20.
- Bates, R.L., and Jackson, J.A., 1987, Glossary of geology: American Geological Institute, third edition, 788 p.

Baum, G.R., and Vail, P.R., 1988, Sequence stratigraphic concepts applied to Paleogene outcrops, Gulf and Atlantic basins, *in* Wilgus, C.K., ed., Sea-level changes: an integrated approach: Society of Economic Paleontologists and Mineralogists Special Publication 42, p. 309-328.

Beales, F.W., and Hardy, J.L., 1980, Criteria for the recognition of diverse dolomite types with an emphasis on studies on host rocks for Mississippi Valley-type ore deposits: *in* Zenger, D.H., Dunham, J.B., and Ethington, R.L., eds. Concepts and models of dolomitization: Society of Economic Paleontologists and Mineralogists Special Publication 22, p. 197-213.

Beck, A.S., 1981, Stratigraphic analysis, Lippincott member, Lost Burro Formation, California-Nevada: unpublished Master's thesis, California State University, Fresno, 149 p.

Bereskin, S.R., 1982, Middle and Upper Devonian stratigraphy of portions of southern Nevada and southeastern California: *in* Powers, R.B., ed., Geologic studies of the Cordilleran thrust belt: Rocky Mountain Association of Geologists, p.751-764.

Berry, W.B.N., 1977, Great Basin Devonian western assemblage rocks, *in* Murphy, M.A., Berry, W.B.N., and Sandberg, C.A., eds., Western North America: Devonian: University of California, Riverside, Campus Museum Contribution 4, p. 204-219.

Best, M.G., Scott, R.B., Rowley, P.D., Swadley, W.C., Anderson, R.E., Gromme, C.S., Harding, A.E., Deino, A.L., Christiansen, E.H., Tingey, G., and Sullivan, K.R., 1993, Oligocene-Miocene caldera complexes, ash-flow sheets, and tectonism in the central and southeastern Great Basin, *in* Lahren, M.M., Trexler, J.H.Jr., and Spinosa, C., eds., Crustal evolution of the Great Basin and the Sierra Nevada: Cordilleran/Rocky Mountain sections

of the Geologic Society America Field Trip Guide, p. 285-312.

Beus, S.S., 1965, Devonian faunule from the Jefferson Formation, central Blue Springs Hills, Utah-Idaho: *Journal of Paleontology*, v. 39, p. 21-30.

Beus, S.S., 1980, Late Devonian (Frasnian) paleogeography and paleoenvironments in northern Arizona, *in* Fouch, T.D., and Magathan, E.R., *Rocky Mountain Paleography Symposium 1 Paleozoic Paleogeography of the west-central U.S.: Rocky Mountain section of the Society of Economic Paleontologists and Mineralogists*, p. 55-69.

Bick, K.F., 1959, Stratigraphy of Deep Creek Mountains, Utah: *American Association of Petroleum Geologists Bulletin*, v.43, p.1064-1069.

Biller, E.J., 1976, Stratigraphy and petroleum possibilities of lower Upper Devonian (Frasnian and lower Famennian) Strata, southwestern Utah, U.S. Geological Survey open-file report 75-343, 105 p.

Bishop, R.A., 1982, Whitney Canyon-Carter Creek gas field southwest Wyoming: *in* Powers, R.B.I., ed. *Geologic Studies of the Cordilleran thrust belt: Rocky Mountain Association of Geologists*, p. 591-599.

Bissell, H.J., Rigby, J.K., Proctor, P.D., and Moyle, R.W., 1959, Geology of the southern Oquirrh Mountains and Five-Mile Pass--northern Boulder Mountain area, Tooele and Utah Counties, Utah: *Utah Geological Society Guidebook*, no. 14, 262 p.

Blair, T.C., and McPherson, J.G., 1999, Grain-size and texture classification of coarse sedimentary particles: *Journal of Sedimentary Research*, v. 69, p. 6-19.

Blue, D.M., 1960, Geology and ore deposits of the Lucin Mining District, Box Elder county, Utah, and Elko County, Nevada: unpublished M.S. thesis, University of Utah, 162 p.

Bohannon, R.G., 1983, Mesozoic and Cenozoic tectonic development of the Muddy, North Muddy, and northern Black Mountains, Clark County, Nevada, *in* Miller, D.M., Todd, V.R., and Howard, K.A., eds., Tectonic and stratigraphic studies in the eastern Great Basin: Geological Society of America Memoir 157, p. 125-148.

Bond, G.C., and Kominz, M.A., 1984, Construction of tectonic subsidence curves for the early Paleozoic miogeocline, southern Canadian Rocky Mountains; Implications for subsidence mechanisms, age of breakup, and crustal thinning: Geological Society of America Bulletin, v. 95, p. 155-173.

Bortz, L.C., 1998, Blackburn oil field, Pine Valley, Nevada--a case history update: Nevada Petroleum Society Newsletter, v. 13, issue 2, p. 1-2.

Bortz, L.C., and Murray, D.K., Eagle Springs oil field, Nye County, Nevada, *in* Newman, G.W., and Goode, H.D., eds., Basin and Range Symposium: Rocky Mountain Association of Geologists and Utah Geological Association, p. 441-453.

Boucot, A.J., and Potter, A.W., 1977, Middle Devonian orogeny and biogeographical relations in areas along the North American rim, *in* Murphy, M.A., Berry, W.B.N., and Sandberg, C.A., eds., Western North America: Devonian: University of California, Riverside, Campus Museum Contribution 4, p. 210-219.

Boyer, S.E. and Elliot, D., 1982, Thrust systems: American Association of Petroleum Geologists Bulletin, v. 66, p. 1196-1230.

Brown, H.J., 1991, Stratigraphy and Paleogeographic setting of Paleozoic rocks in the San Bernardino Mountains, California *in* Cooper, J.D. and Stevens, C.H., Paleozoic paleogeography of the western United States-II: Pacific Section Society Economic Paleontologists and Mineralogists, v. 1, p. 193-208.

Buelter, D.P., and Guillemette, R.N., 1988, Geochemistry of epigenetic dolomite associated with lead-zinc mineralization of the Viburnum trend, southeast Missouri: a reconnaissance study, *in* Shukla, V., and Baker, P.A., eds., Sedimentology and geochemistry of dolostones: Society of Economic Paleontologists and Mineralogists Special Publication 43, p. 85-93.

Burchfiel, B.C., 1961, Structure and stratigraphy of the Specter Range quadrangle, Nye County, Nevada: unpublished Ph.D. thesis, Yale University, 197 p.

Burchfiel, B.C., 1964, Precambrian and Paleozoic stratigraphy of Specter Range Quadrangle, Nye County, Nevada: American Association of Petroleum Geologists Bulletin, v. 48, p. 40-56.

Burke, R.B., and Stefanosvsky, G.L., 1984, Porosity types, geometry and interpore minerals of the lower Duperow Formation, Billings nose area, Williston Basin, North Dakota: *in*: Christopher, J.E., and Kaldi, J., eds., Fourth International Williston Basin symposium: Special Publication Number 6, Saskatchewan Geological Society, p. 92-100.

Calkins, F.C., and Butler, B.S., 1943, Geology and ore deposits of the Cottonwood American Fork District, Utah: U.S. Geological Survey Professional Paper 201, 150 p.

Cameron, G., and Chamberlain, A.K., 1987, Reevaluation of late Mesozoic thrusting in east-central Nevada: American Association of Petroleum Geologists Bulletin v. 71, p. 536.

Cameron, G., and Chamberlain, A.K., 1988, Delineation of late Mesozoic thrust belt in east-central Nevada: Geological Society of America, Cordilleran Section, 84th annual meeting. Abstracts-with-Programs, Geological Society of America, v. 20, p. 148.

Camilleri, P.A., 1999, Reevaluation of metamorphic “klippen” in the Diamond Mountains, Nevada and the implications for Mesozoic (?) Shortening and Cenozoic extension: Rocky Mountain Association of Geologists, *The Mountain Geologist*, *in press*.

Carlisle, D., Murphy, M.A., Nelson, C.A., and Winterer, E.L., 1957, Devonian stratigraphy of Sulphur Springs and Pinyon ranges, Nevada: American Association of Petroleum Geologists Bulletin, v. 41, p. 2175-2191.

Carpenter, D.G., and Carpenter, J.A., 1994a, Fold-thrust structure, synorogenic rocks, and structural analysis of the north Muddy and Muddy Mountains, Clark County, Nevada: southern Nevada, southwest Utah, and northwest Arizona: *in* Dobbs, S.W., and Taylor, W.J., eds., Structural and stratigraphic investigations and petroleum potential of Nevada, with special emphasis south of the Railroad Valley producing trend: Nevada Petroleum Society Conference Volume II, p. 65-94.

Carpenter, D.G., Carpenter, J.A., Dobbs, S.W., and Stuart, C.K., 1993, Regional structural synthesis of the Eureka fold-and-thrust belt, east-central Nevada: *in* Gillespie, C.W., ed., Structural and stratigraphic relationships of Devonian reservoir rocks, east central Nevada: 1993 Field trip Guidebook, Nevada Petroleum Society, Reno, Nevada, p. 59-72.

Carpenter, J.A., 1997, Antler tectonic system and global analogs in the Mediterranean and Asia: American Association of Petroleum Geologists Annual Convention, Abstracts with programs, p. A17-A18.

Carpenter, J.A., and Carpenter, D.G., 1994b, Analysis of basin-range and fold-thrust structure, and reinterpretation of the Mormon Peak detachment and similar features as gravity slide systems: southern Nevada, southwest Utah, and northwest Arizona: *in* Dobbs, S.W., and Taylor, W.J., eds., Structural and stratigraphic investigations and petroleum potential of Nevada, with special emphasis south of the Railroad Valley producing trend: Nevada Petroleum Society Conference Volume II, p. 15-52.

Carpenter, J.A., Carpenter, D.G., and Dobbs, S.W., 1993a, Structural analysis of the Pine valley area, Nevada: *in* Gillespie, C.W., ed., Structural and stratigraphic relationships of Devonian reservoir rocks, east central Nevada: 1993 Field trip Guidebook, Nevada Petroleum Society, Reno, Nevada, p. 9-49.

Carpenter, J.A., Carpenter, D.G., and Dobbs, S.W., 1993b, Fault reactivation and deactivation in the Basin-Range, western United States: *in* Gillespie, C.W., ed., Structural and stratigraphic relationships of Devonian reservoir rocks, east central Nevada: 1993 Field trip Guidebook, Nevada Petroleum Society, Reno, Nevada, p. 73-87.

Carpenter, J.A., Carpenter, D.G., and Dobbs, S.W., 1994, Antler Orogeny: Paleostuctural analysis and constraints on plate tectonic models with a global analogue in southeast Asia: *in* Dobbs, S.W., and Taylor, W.J., eds., Structural and stratigraphic investigations and petroleum potential of Nevada, with special emphasis south of the Railroad Valley producing trend: Nevada Petroleum Society Conference Volume II, p. 187-240.

Carr, M.D., 1980, Upper Jurassic to Lower Cretaceous (?) Synorogenic sedimentary rocks in the southern Spring Mountains, Nevada: *Geology*, v. 8, p. 385-389.

Castonguay, S., and Price, R.A., 1995, Tectonic heredity and tectonic wedging along an oblique hanging wall ramp: the southern termination of the Misty thrust sheet, southern Canadian Rocky Mountains: Geological Society of America Bulletin, v. 107, p. 1304-1316.

Chafetz, H.S., and Zhang, J., 1998, Authigenic euhedral megaquartz in a Quaternary dolomite: Journal of Sedimentary Research, v. 68, p. 994-1000.

Chamberlain, A.K., 1981, Biostratigraphy of the Great Blue Formation: Brigham Young University Geology Studies. v. 28, p. 8-17.

Chamberlain, A.K., 1983, Surface gamma-ray logs: a correlation tool for frontier areas: American Association of Petroleum Geologists Bulletin, v. 68, p. 1040-1043.

Chamberlain, A.K., 1986a, A new Paleozoic play in East Great Basin: American Association of Petroleum Geologists Bulletin, v. 70, p. 1034.

Chamberlain, A.K., 1986b, New Paleozoic play in East Great Basin: Oil and Gas Journal. v. 84, no. 38, p. 52-54.

Chamberlain, A.K., 1987, Depositional environments and hydrocarbon occurrence of Mississippian Antler basin, Nevada and Utah: American Association of Petroleum Geologists Bulletin v. 71, p. 1002-1003.

Chamberlain, A.K., 1988a, Petroleum exploration in Nevada, then and now: Geological Society of America, Cordilleran Section, 84th annual meeting; Abstracts with Programs, 20, p. 149.

Chamberlain, A.K., 1988b, A Mississippian thermal maturation map of the eastern Great Basin illustrates regions of thermal and tectonic events: Geological Society of America, Rocky Mountain Section, 43rd annual meeting; Abstracts with Programs, v. 22, p. 5-6.

Chamberlain, A.K., 1988c, Three lobes of higher organic content may be related to three Mississippian Antler basin delta systems, Utah and Nevada: Geological Society of America, Rocky Mountain Section, 43rd annual meeting; Abstracts with Programs, v. 22, p. 5.

Chamberlain, A.K., 1988d, Depositional environments and hydrocarbon occurrence of the Mississippian Antler basin, Nevada and Utah: Geological Society of America, Cordilleran Section, 84th annual meeting; Abstracts with Programs, v 20, p. 149.

Chamberlain, A.K., 1990a, Three lobes of higher organic content may be related to three Mississippian Antler basin delta systems, Utah and Nevada: American Association of Petroleum Geologists Bulletin, v. 74, p. 1319.

Chamberlain, A.K., 1990b, Stigmaria; indicator for erosional surfaces of low sea level stands in the Mississippian Antler basin, Utah and Nevada: American Association of Petroleum Geologists Bulletin, v. 74, p. 1319.

Chamberlain, A.K., 1990c, A Mississippian thermal maturation map of the eastern Great Basin illustrates regions of thermal and tectonic events: American Association of Petroleum Geologists Bulletin, v. 74, p. 1318.

Chamberlain, A.K., 1991, Yucca Mountain, high-level nuclear waste repository over a billion barrel oil field?: American Association of Petroleum Geologists Bulletin, v 75, p.3, p. 551.

Chamberlain, A.K., 1998, Rapid precision mapping: American Association of Petroleum Geologists National Convention, Salt Lake City Abstracts with Programs, p. 82.

Chamberlain, A.K., 1999, Thrusted Devonian Tempiute meteorite crater, Nevada: American Association of Petroleum Geologists National Convention, San Antonio, Texas, Abstracts with Programs, p. A23.

Chamberlain, A.K., and Birge, B.P., 1997, Devonian Sunnyside Basin, Nevada: American Association of Petroleum Geologists Abstract Volume, p. A19.

Chamberlain, A.K., and Chamberlain, R.L., 1990, Monte Mountain Thrust, additional confirmation of the central Nevada thrust: American Association of Petroleum Geologists Bulletin v. 74, p. 626.

Chamberlain, A.K., Chamberlain, R.L., and Roeder, D., 1992a, Oil and gas exploration of the central Nevada thrust belt: American Association of Petroleum Geologists, 1992 annual convention; Abstracts with Programs, p.18-19.

Chamberlain, A.K., Chamberlain, R.L., and Roeder, D., 1992b, Tertiary/Cretaceous syntectonic sediments of the central Nevada thrust belt: American Association of Petroleum Geologists, 1992 annual convention; Abstracts with Programs, p. 19.

Chamberlain, A.K., and Gillespie, C.W., 1993, Evidence of late Mesozoic thrusting, Timpahute Range, south-central Nevada, *in* C.W. Gillespie, ed., Structural and stratigraphic relationships of Devonian reservoir rocks, east-central Nevada: 1993 Field trip Guidebook, Nevada Petroleum Society, Reno, Nevada, p. 139-155.

- Chamberlain, A.K., Graham, A.T., and Connelly, M.S., 1999, Channel sandstones, Mississippian Antler basin, Nevada: American Association of Petroleum Geologists National Convention, San Antonio, Texas, Abstracts with Programs, p. A22-23.
- Chamberlain, A.K., Hook, S.C., and Frost, K.R., 1996, Digital field trip to the Central Nevada thrust belt: American Association of Petroleum Geologists 1996 annual convention; Abstracts with Programs, p. 25.
- Chamberlain, A.K., and Warne, J.E., 1996, Devonian sequences and sequence boundaries, Timpahute Range, Nevada: *in* Longman, M.W., and Sonnenfeld, M.D., eds., Paleozoic Systems of the Rocky Mountain Region: Rocky Mountain Association of Geologists and SEPM (Society for Sedimentary Geology), p. 63-84.
- Chamberlin, T.C., 1897, The method of multiple working hypotheses: *Journal of Geology*, v. V, p. 837-848.
- Chan, M.A., 1999, Triassic loessite of north-central Utah: stratigraphy, petrophysical character, and paleoclimate implications: *Journal of Sedimentary Research*, v. 69, p. 477-485.
- Choquette, P.W., Cox, A., and Meyers, W.J., 1992, Characteristics, distribution and origin of porosity in shelf dolostones: Burlington-Keokuk Formation (Mississippian), U.S. mid-continent: *Journal of Sedimentary Research*, v. 62, p. 167-189.
- Coats, R.R., 1987, Geology of Elko County, Nevada: Nevada Bureau of Mines and Geology Bulletin 101, 112 p.

Cohenour, R.E., 1959, Sheeprock Mountains, Precambrian and Paleozoic stratigraphy, igneous rocks, structure, geomorphology, and economic geology: Utah Geological and Mineral Survey Bulletin 63, 201 p.

Compton, J.S., 1988, Sediment composition and precipitation of dolomite and pyrite in the Neogene Monterey and Sisquoc Formations, Santa Maria basin area, California, *in* Shukla, V., and Baker, P.A., eds., Sedimentology and geochemistry of dolostones: Society of Economic Paleontologists and Mineralogists Special Publication 43, p. 53-64.

Constenius, K.N., 1996, Late Paleogene extensional collapse of the Cordilleran foreland fold-and-thrust belt: Geological Society of America Bulletin, v. 108, p. 20-39.

Cook, H.E., and Taylor, M.E., 1985, Paleozoic carbonate continental margin: facies transitions, depositional processes and exploration models--the Basin and Range Province: American Association of Petroleum Geologists Field Seminar, 177 p.

Cornwall, H.R., and Kleinhampl, F.J., 1960, Preliminary geologic map of the Bare Mountain Quadrangle, Nye county, Nevada: U.S. Geological Survey Map MF-239.

Costain, J.K., 1960, Geology of the Gilson Mountains and vicinity, Juab County, Utah: unpublished Ph.D. dissertation, University of Utah, 139 p.

Cowell, P.F., 1986, Structure and stratigraphy of part of the northern Fish Creek Range, Eureka County, Nevada: unpublished MS thesis, Oregon State University, Corvallis, 96 p.

Crosby, G.W., 1959, Geology of the South Pavant Range, Millard and Sevier Counties, Utah: Brigham Young University Research Studies, Geology Series v.6, n.3, p.59.

Currie, B.S., 1997, Sequence stratigraphy of nonmarine Jurassic-Cretaceous rocks, central Cordilleran foreland-basin system: *Geological Society of America Bulletin*, v. 109, p. 1206-1222.

Dahlstrom, C.D.A., 1969, Balanced cross sections: *Canadian Journal of Earth Sciences*, v. 6, p. 743-757.

Dahlstrom, C.D.A., 1977, Structural geology I the eastern margin of the Canadian Rocky Mountains: *in* Heisey, E.L., Lawson, D.E., Norwood, E.R., Wach, P.H., and Hale, L.A., eds., *Rocky Mountain thrust belt geology and resources: Wyoming Geological Association 29th annual field conference in conjunction with Montana geological Society and Utah Geological Society*, p. 407-439.

Decals, P.G., 1994, Late Cretaceous-Paleocene synorogenic sedimentation and kinematic history of the Sevier thrust belt, northeast Utah and southwest Wyoming: *Geological Society of America Bulletin*, v. 106, p. 32-56.

Decals, P.G., and Mitra, G., 1995, History of the Sevier orogenic wedge in terms of critical taper models, northeast Utah and southwest Wyoming: *Geological Society of America Bulletin*, v. 107, p. 454-462.

Decker, R.W., 1953, *Geology of southern Centennial Range, Elko County, Nevada*: Unpublished Ph.D. dissertation, Colorado School of Mines, 150 p.

Dilles, J.H., and Gans, P.B., 1995, The chronology of Cenozoic volcanism and deformation in the Yerington area, western Basin and Range and Walker Lane: *Geological Society of America*, v. 107, p. 474-486.

Dix, G.R., 1993, Patterns of burial and tectonically controlled dolomitization in an Upper Devonian fringing-reef complex: Leduc Formation, Peace River Arch area, Alberta, Canada: *Journal of Sedimentary Research*, v. 63, p. 628-640.

Dolly, E.D., 1979, Geologic techniques utilized in Trap Spring field discovery, Railroad Valley, Nye County, Nevada, *in* Newman, G.W., and Goode, H.D., eds., Basin and Range Symposium: Rocky Mountain Association of Geologists and Utah Geological Association, p. 455-467.

Donovan, J.T., 1951, Devonian rocks of the Confusion Basin and vicinity, *in* Guidebook to the geology of Utah, Intermountain Association of Petroleum Geologists guidebook second annual field conference, Geology of the Canyon, House and Confusion Ranges, Millard County, Utah, (Guidebook to the Geology of Utah, no. 6), p.47-53.

Dott, R.H., 1955, Pennsylvanian stratigraphy of Elko and northern Diamond Ranges, northeastern Nevada: *American Association of Petroleum Geologists*, v. 39, p. 2211-2305.

Drummond, C.N., and Wilkinson, B.H., 1993, Carbonate cycle stacking patterns and hierarchies of orbitally forced eustatic sea level change: *Journal of Sedimentary Research*, v. 63, p. 369-377.

DuBray, E.A., and Hurtubise, D.O., 1994, Geologic map of the Seaman Range, Lincoln and Nye Counties, Nevada: U.S. Geological Survey, Miscellaneous Investigation map I-2282.

Duey, H.D., 1979, Trap Spring oil field, Nye County, Nevada: *in* Newman, G.W., and Goode, H.D., eds., Basin and Range Symposium and Great Basin field Conference: Rocky Mountain Association of Geologists and Utah Geological Association, p. 469-476.

Dunham, J.B., and Olson, E.R., 1978, Diagenetic dolomite formation related to Paleozoic paleogeography of the Cordilleran miogeocline in Nevada: *Geology*, v. 33, p. 556-559.

Dunham, J.B., and Olson, E.R., 1980, Shallow subsurface dolomitization of subtidally deposited carbonate sediments in the Hanson Creek formation (Ordovician-Silurian) of central Nevada: *in* Concepts and models of dolomitization, Zenger, D.H., Dunham, J.B., and Ethington, R.L., eds., Society of Economic Paleontologists and Mineralogists Special Publication 22, p. 139-161.

Dunham, R.J., 1962, Classification of carbonate rocks according to depositional texture: *in* Ham, W.E. ed., Classification of carbonate rocks: American Association of Petroleum Geologists, Memoir 1, p. 108-121.

Dunn, M.J., 1979, Depositional history and paleoecology of an Upper Devonian (Frasnian) bioherm Mount Irish, Nevada: unpublished M.S. thesis, State University of New York at Binghamton, 133p.

Eardley, A.J., 1944, Geology of the north-central Wasatch Mountains: Geological Society America Bulletin, v.55, p.819-94.

Edwards, B.R., and Russell, J.K., 1999, Northern Cordilleran volcanic province: a northern Basin and Range?: *Geology*, v. 27, p. 243-246.

Effimoff, I., and Pinezich, A.R., 1986, Tertiary structural development of selected basins: Basin and Range Province, northeastern Nevada, *in* Mayer, L., ed., Extensional tectonics of the southwestern United States: a perspective on processes and kinematics: Geological Society of America Special Paper 208, p. 31-42.

Einsele, G., 1982, Limestone-marl cycles (periodites): diagnosis, significance, causes- a review, *in* Einsele, G., and Seilacher, A., Cyclic and event stratification: Springer-Verlag, New York, p. 8-53.

Ekren, E.B., Rogers, C.L., and Dixon, G.L., 1973, Geologic and Bouguer Gravity Map of the Reveille Quadrangle, Nye County, Nevada, U.S. Geological Survey Map I-806.

Elison, M.W., 1991, Intracontinental contraction in western North America: continuity and episodicity: Geological Society of America Bulletin, v. 103, p. 1226-1238.

Elrick, M., 1986, Depositional and diagenetic history of the Devonian Guilmette Formation southern Goshute Range, Elko, County, Nevada: unpublished MS thesis, Oregon State University, Corvallis, 109 p.

Elrick, M., 1995, Cyclostratigraphy of Middle Devonian carbonates of the eastern Great Basin: Journal of Sedimentary Research, v. B65, p. 61-79.

Elrick, M., 1996, Sequence stratigraphy and platform evolution of Lower-Middle Devonian carbonates, eastern Great Basin: Geological Society of America Bulletin, v. 108, p. 392-416.

Emsbo, P., Hutchinson, R.W., Hofstra, A.H., Volk, J.A., Bettles, K.H., Baschuk, G.J., and Johnson, C.A., 1999, Syngenetic Au on the Carlin trend: implications for Carlin-type deposits: Geology, v. 27, p. 59-62.

Erken, E.B., Bucknam, R.R.C., Carr, W.J., Dixon, G.L., and Quinlivan, W.D., 1976, East-trending structural lineaments in central Nevada: U.S. Geological Survey, Professional Paper 986, p. 16.

Erskine, M.C., 1999, The Oquirrh basin revisited: reply: American Association of Petroleum Geologists, v. 83, p. 367-369.

Estes, J.E., 1992, Stratigraphy of the Devonian Guilmette Formation, Pahrnagat Range, Lincoln County, Nevada: unpublished M.S. thesis, Colorado School of Mines, Golden, 94 p.

Farmer, G.L., and Ball, T.T., 1997, Sources of Middle Proterozoic to Early Cambrian siliciclastic sedimentary rocks in the Great Basin: a Nd isotope study: Geological Society of America Bulletin, v. 109, p. 1193-1205.

Farr, M.R., 1992, Geochemical variation of dolomite cement within the Cambrian Bonneterre Formation, Missouri: evidence for fluid mixing: Journal of Sedimentary Research, v. 62, p. 636-651.

Felix, C.E., 1956, Geology of the eastern part of the Raft River Range, Box Elder County, Utah, *in* Guidebook to the geology of Utah, n.11: Utah Geological Society, p. 76-97.

Ferguson, H.G., 1952, Paleozoic of Western Nevada: Washington Academy of Science Journal, v.42, n.3, p.72-74.

Ferguson, H.G., and Muller, S.W., 1949, Structural geology of the Hawthorne and Tonopah Quadrangles, Nevada: U.S. Geological Survey Professional Paper 216, p.55.

Fermor, P., 1999, Aspects of the three-dimensional structure of the Alberta Foothills and Front Ranges: Geological Society of America Bulletin, v. 111, p. 317-346.

Finney, S.C., Berry W.B.N., Cooper, J.D., Ripperdan, R.L., Sweet, W.C., Jacobson, S.R., Soufiane, A., Achab, A., and Noble, P.J., 1999, Late Ordovician mass extinction: a new perspective from stratigraphic sections in central Nevada: *Geology*, v. 27, p 215-218.

Fischer, H.J., 1988, Dolomite diagenesis in the Metaline Formation, northeastern Washington State, *in* Shukla, V., and Baker, P.A., eds., *Sedimentology and geochemistry of dolostones: Society of Economic Paleontologists and Mineralogists Special Publication 43*, p. 209-219.

Flügel, E., 1982, *Microfacies analysis of limestones*: translated by Christenson, K., Springer-Verlag, Berlin-Heidelberg-New York, 633 p.

Folk, R.L., 1962, Spectral classification of limestone types: *in* Ham, W.E., ed., *Classification of carbonate rocks: American Association of Petroleum Geologists, Memoir 1*, p. 62-84.

Foster, N.H., 1979, Geomorphic exploration used in the discovery of Trap Spring oil field, Nye County, Nevada, *in* Newman, G.W., and Goode, H.D., eds., *Basin and Range Symposium: Rocky Mountain Association of Geologists and Utah Geological Association*, p. 477-486.

Foster, N.H., Howard, E.L., Meissner, F.F., and Veal, H.K., 1979, The Bruffey oil and gas seeps, Pine Valley, Eureka County, Nevada: *in* Newman, G.W., and Goode, H.D., eds., *Basin and Range Symposium and Great Basin field Conference: Rocky Mountain Association of Geologists and Utah Geological Association*, p. 531-540.

Fouch, T.D., Hanley, J.H., and Forester, R.M., 1979, Preliminary correlation of Cretaceous and Paleogene lacustrine and related nonmarine sedimentary and volcanic rocks in parts of the eastern Great Basin of Nevada and Utah, *in* Newman, G.W., and Goode, H.D., eds., Basin and Range Symposium and Great Basin field Conference: Rocky Mountain Association of Geologists and Utah Geological Association, p. 395-312.

Fouch, T.D., Lund, K., Schmitt, J.G., Good, S.C., and Hanley, J.H., 1991, Late Cretaceous(?) basins in the region of the Egan and Grant ranges, and White river and Railroad valleys, Nevada: their relation to Sevier and Laramide contractional basins in the southern Rocky Mountains and Colorado Plateau, *in* Flanigan, D.M.H., Hansen, M., and Flanigan, T.E., eds., Geology of White River Valley and western Egan Range, Nevada: Nevada Petroleum Society 1991 Field trip Guidebook, p. 15-23.

Frank, J.R., Cluff, S., Bauman, J.M., 1982, Painter Reservoir, East Painter Reservoir and Clear Creek fields, Uinta County, Wyoming: *in* Powers, R.B., ed., Geologic Studies of the Cordilleran thrust belt: Rocky Mountain Association of Geologists, p. 601-611.

Friedman, G.M., 1990, Dolomite is an evaporite mineral: evidence from the rock record and from sea-marginal ponds of the Red Sea: *in* Concepts and models of dolomitization, Zenger, D.H., Dunham, J.B., and Ethington R.L., eds., Society of Economic Paleontologists and Mineralogists Special Publication 22, p. 69-80.

Friedman, G.M., 1995, A reappraisal of dolomite abundance and occurrence in the Phanerozoic--discussion: *Journal of Sedimentary Research*, v. A65 p. 244-245.

Friedman, G.M., and Sanders, J.E., 1967, Origin and occurrence of dolostones *in* Chilingar, G.V., Bissell, H.J., and Faribridge, R.W., eds., Carbonate Rocks: Elsevier Publishing Company, New York, 267-348.

Fuerten, F., and Redman, D.J., 1997, Documentation of a 1450 Ma contractional orogeny preserved between the 1850 Ma Sudbury impact and the 1 Ga Grenville orogenic front, Ontario: Geological Society of America Bulletin, v. 109, p. 268-279.

Furlong, K.P., and Londe, M.D., 1986, Thermal-mechanical consequences of Basin and Range extension, *in* Mayer, L., ed., Extensional tectonics of the southwestern United States: a perspective on processes and kinematics: Geological Society of America Special Paper 208, p. 23-30.

Geslin, J.K., 1994, Carbonate pseudomatrix in mixed siliciclastic-carbonate turbidite from the Oquirrh-Wood River basin, southern Idaho: Journal of Sedimentary Research, v. A64, p. 55-58.

Geslin, J.K. 1998, Distal ancestral Rocky Mountains tectonism: evolution of the Pennsylvanian-Permian Oquirrh-Wood River basin, southern Idaho, Geological Society of America Bulletin, v. 110, p. 644-663.

Geslin, J.K., Link, P.K., Mahoney, J.B., and Burton, B.R., 1999, The Oquirrh basin revisited: Discussion: American Association of Petroleum Geologists Bulletin, v. 83, p. 362-366.

Giles, K.A., 1994, Stratigraphic and tectonic framework of the Upper Devonian to lowermost Mississippian Pilot Formation Basin in east-central Nevada and Western Utah: *in* Dobbs, S.W., and Taylor, W.J., eds., Structural and stratigraphic investigations and petroleum potential of Nevada, with special emphasis south of the Railroad Valley producing trend: Nevada Petroleum Society Conference Volume II, p. 165-185.

Giles, K.A., 1996, Tectonically forced retrogradation of the Lower Mississippian Joana Limestone, Nevada and Utah: *in* Longman, M.W., and Sonnenfeld, M.D., eds., Paleozoic Systems of the Rocky Mountain Region: Rocky Mountain Association of Geologists and SEPM (Society for Sedimentary Geology), p. 154-164.

Ginsburg, R.N., 1991, Controversies about stromatolites: vices and virtues: Controversies in Modern Geology, Academic Press, p. 25-36.

Glikson, A.Y., 1999, Oceanic-impacts and crustal evolution: *Geology*, v. 27, p. 387-390.

Goddard, E.N., Trask, P.D., DeFord, R.K., Rove, O.N., Singewald J.T.Jr., and Overbeck, R.M., 1984, Rock-Color Chart: National Research Council and The Geological Society of America.

Goldhammer, R.K., Lehmann, P.J., and Dunn, P.A., 1993, the origin of high-frequency platform carbonate cycles and third-order sequences (Lower Ordovician El Paso Gp, West Texas): Constraints from outcrop data and stratigraphic modeling: *Journal of Sedimentary Research*, v. 63, p. 318-359.

Goldstrand, P.M., 1992, Evolution of Late Cretaceous and Early Tertiary basins of southwest Utah based on clastic petrology: *Journal of Sedimentary Research*, v. 62, p. 495-507.

Goldstrand, P.M., 1994, Tectonic development of Upper Cretaceous to Eocene strata of southwestern Utah: *Geological Society of America Bulletin*, v. 106 p. 145-154.

Goodwin, P.W., and Anderson, E.J., 1985, Punctuated aggradational cycles: a general hypothesis of episodic stratigraphic accumulation: *The Journal of Geology*, v. 93, p. 515-533.

Granger, A.E., 1953, Stratigraphy of the Wasatch Range near Salt Lake City, Utah: U.S. Geological Survey Circular 296, 14 p.

Gretener, P.E., 1972, Thoughts on overthrust faulting in a layered sequence: *Bulletin of Canadian Petroleum Geology*, v. 20, p. 583-607.

Gupta, S., and Allen, P.A., 1999, Fossil shore platforms and drowned gravel beaches: evidence of high-frequency sea-level fluctuations in the distal Alpine foreland basin: *Journal of Sedimentary Research*, v. 69, p. 394-413.

Guth, P.L., Schmidt, D.L., Deibert, J., and Yount, J.C., 1988, Tertiary extensional basins of northwestern Clark County, Nevada, *in* Weide, D.L., and Faber, M.I., eds., This extended land, geological journeys in the souther Basin and Range: Geological Society of America Cordilleran Section Field Trip Guide, p. 239-254.

Gwinn, V.E., 1964, Thin-skinned tectonics in the plateau of northwestern Valley and Ridge provinces of the central Appalachians: *Geological Society of America Bulletin*, v. 75, p. 863-900.

Hague, A., and Emmons, S.F., 1877, Descriptive geology: U.S. Geological Exploration, 40th Parallel Rport, v. 2.

Hamblin, W.K., 1985, *The Earth's dynamic systems a textbook in physical geology*, fifth edition: MacMillian Publishing Company, New York, 576 p.

Hanson, A.M., 1949, Geology of the southern Malad Range and vicinity in northern Utah: unpublished Ph.D. thesis, University of Wisconsin, 150 p.

Harland, W.B., Cox, A.V., Llewellyn, P.G., Pickton, C.A.G., Smith, A.G., and Walters, R., 1982, a geologic time scale: Cambridge university Press, 131 p.

Harris, L.D., and Milcici, R.C., 1977, Characteristics of thin-skinned style of deformation in the southern Appalachians, and potential hydrocarbon traps: U.S. Geological Survey Professional Paper 1018, 40 p.

Harris, S.H., Land, C.B.Jr., and McKeever, J.H., 1966, Relation of Mission Canyon stratigraphy to oil production in north-central North Dakota: American Association of Petroleum Geologists Bulletin, v. 50, p. 2269-2276.

Harry, D.L., Oldow, J.S., and Sawyer, D.S., 1995, The growth of orogenic belts and the role of crustal heterogeneities in decollement tectonics: Geological Society of America Bulletin, v. 107, p. 1411-1426.

Hazard, J.C., 1954, Revision of Devonian and Carboniferous section, Nopah Range, Inyo County, California: American Association of Petroleum Geologists Bulletin, v.38, p.878-885.

Hazard, J.C., 1954, Rocks and structure of the northern Providence Mountains, San Bernardino County, California: California Division Mines Bulletin 170, Chapter IV, Contribution 4, p 27-36.

Henry, C.D., and Boden, D.R., 1998, Eocene magmatism: the heat source for Carlin-type gold deposits of northern Nevada: Geology, v. 26, p. 1067-1070.

- Hess, R.H., and Johnson, G., 1997, County digital geologic maps of Nevada, scale 1:250,000: Nevada Bureau of Mines and Geology Open File 97-1, 1 CD disk.
- Hewett, D.F., 1956, Geology and mineral resources of the Ivanpah Quadrangle, California and Nevada: U.S. Geological Survey Professional Paper 275, p.172.
- Hildebrand, A.R., Penfield, G.T., Kring, D.A., Pilkington, M., Camargo, A.Z, Jacobsen, S.B., and Boynton, W.V., 1991, Chicxulub Crater: a possible Cretaceous/Tertiary boundary impact crater on the Yucatan Peninsula, Mexico: *Geology*, v. 19, p. 867-871.
- Hintze, L.F., 1988, Geologic History of Utah: Brigham Young University Geology Studies Special Publication 7, 202 p.
- Hoffman, M.E., and Balcells-Baldwin, R.N., 1982, Gas Giant of the Wyoming thrust belt: Whitney Canyon-Carter Creek field: *in* Powers, R.B., ed., *Geologic Studies of the Cordilleran thrust belt: Rocky Mountain Association of Geologists*, p. 613-618.
- Holail, H., Lohmann, K.C., and Sanderson, I., 1988, Dolomitization and delolomitization of Upper Cretaceous carbonates: Bahariya Oasis, Egypt, *in* Shukla, V., and Baker, P.A., eds., *Sedimentology and geochemistry of dolostones: Society of Economic Paleontologists and Mineralogists Special Publication 43*, p. 191-207.
- Hoggan, R.D., 1975, Paleoecology of the Guilmette Formation in eastern Nevada and western Utah: *Brigham Young University Geological Studies*, v.22, pt.1, p.141-198.
- Hook, S.C., Chamberlain, A.K., and Frost, R.K., 1998, Digital field trip to the central Nevada thrust belt: *Society for Sedimentary Geology (SEPM) Continuing Education Digital Field Trip No.1*.

Horita, J., Weinberg, A., Das, N., and Holland, H.D., 1996, Brine inclusions in halite and the origin of the Middle Devonian Prairie Evaporites of western Canada: *Journal of Sedimentary Research*, v. 66, 956-964.

Horton, B.K., and Schmitt, J.G., 1998, Development and exhumation of a Neogene sedimentary basin during extension, east-central Nevada: *Geological Society of America Bulletin*, v. 110, p. 163-172.

Hose, R.K., and Blake, M.C.Jr., 1976, Geology and mineral resources of White Pine County, Nevada: *Nevada Bureau of Mines and Geology Bulletin* 85, 105 p.

Hose, R.K., Repenning, C.A., and Ziony, J.I., 1960, Generalized geologic map of a part of the Confusion Range, Utah: *U.S. Geological Survey Open File Report*, 150 p.

Hulen, J.B., Goff, F., Ross, J.R., Bortz, L.C., and Bereskin, S.R., 1994, Geology and geothermal origin of Grant Canyon and Bacon Flat oil fields, Railroad Valley, Nevada: *American Association of Petroleum Geologists Bulletin*, v. 78, p. 596-623.

Humphrey, F.L., 1960, Geology of the White Pine Mining District, White Pine County, Nevada: *Nevada Bureau of Mines Bulletin* 57, 119 p.

Humphrey, J.D., and Quinn, T.M., 1989, Coastal mixing zone dolomite, forward modeling, and massive dolomitization of platform margin carbonates: *Journal of Sedimentary Petrology*, v. 59, p. 438-454.

Humphrey, J.D., and Quinn, T.M., 1990, Coastal mixing zone dolomite, forward modeling, and massive dolomitization of platform margin carbonates-Reply: *Journal of Sedimentary Petrology*, v. 60, p. 1013-1016.

Hurtubise, D.O., 1989, Stratigraphy and structure of the Seaman Range, Nevada, with an emphasis on the Devonian System: unpublished Ph.D. dissertation, Colorado School of Mines, Golden, 443 p.

Hurtubise, D.O., 1994, Silver King lineament, the missing link of a 50 km east-trending structure in the southern Great Basin: *in* Dobbs, S.W., and Taylor, W.J., eds., Structural and stratigraphic investigations and petroleum potential of Nevada, with special emphasis south of the Railroad Valley producing trend: Nevada Petroleum Society Conference Volume II, p. 127-139.

Hurtubise, D.O., and DuBray, E.A., 1988, Stratigraphy and structure of the Seaman Range and Fox Mountain, Lincoln and Nye Counties, Nevada: U.S. Geological Survey Bulletin 1988-B, 31 p.

James, N.P., 1984a, Carbonate slopes, *in* Walker, R.G., ed., Facies Models: Geological Association of Canada Geoscience Canada, Reprint Series 1, p. 245-257.

James, N.P., 1984b, Reefs, *in* Walker, R.G., ed., Facies Models: Geological Association of Canada Geoscience Canada, Reprint Series 1, p. 224-257.

James, N.P., 1984c, Shallowing-upward sequences in carbonates, *in* Walker, R.G., ed., Facies Models: Geological Association of Canada Geoscience Canada, Reprint Series 1, p. 213-228.

Johnson, G.H., Kruse, S.E., Vaughn, A.W., Lucy, J.K., Hobbs, C.H.III, and Powers, D.S., 1998, Postimpact deformation associated with the late Eocene Chesapeake Bay impact structure in southeastern Virginia: *Geology*, v. 26, p. 507-510.

Johnson, J.G., 1962, Lower Devonian-Middle Devonian boundary in central Nevada: American Association of Petroleum Geologists Bulletin, v.46, p.542-545.

Johnson, J.G., 1977, Status of Devonian studies in western and arctic North America, *in* Murphy, M.A., Berry, W.B.N., and Sandberg, C.A., eds., Western North America: Devonian: University of California, Riverside, Campus Museum Contribution 4, p. 1-15.

Johnson, J.G., Klapper, G., and Sandberg, C.A., 1985, Devonian eustatic fluctuations in Euramerica: Geological Society of America Bulletin, v. 96, p. 567-587.

Johnson, J.G., and Murphy, M.A., 1984, Time-rock model for Siluro-Devonian continental shelf, western United States: Geological Society of America Bulletin, v. 95, p. 1349-1359.

Johnson, J.G., and Pendergast, A., 1981, Timing and mode of emplacement of the Roberts Mountain allochthon, Antler orogeny: Geological Society of America Bulletin, v. 92, p. 648-658.

Johnson, J.G., and Sandberg, C.A., 1989, Devonian eustatic events in the western United States and their biostratigraphic responses, *in* McMillan, N.J., Embry, A.F., and Glass, D.J., Devonian of the World: Canadian Society of Petroleum Geologists, Calgary, Memoir 14, v. 1, Regional Syntheses, p. 171-178.

Johnson, J.G., Sandberg, C.A., and Poole, F.G., 1989, Early and Middle Devonian paleogeography of western United States, *in* McMillan, N.J., Embry, A.F., and Glass, D.J., Devonian of the World: Canadian Society of Petroleum Geologists, Calgary, Memoir 14, v. 1, Regional Syntheses, p. 161-182.

Johnson, J.G., Sandberg, C.A., and Poole, F.G., 1991, Devonian lithofacies of the western United States, *in* Cooper J.D, and Stevens, C.H., eds., Paleozoic Paleogeography of the western United States II: Pacific Section Society of Economic Paleontologists and Mineralogists, p. 83-105.

Johnson, M.S., and Hibbard, D.E., 1957, Geology of the Atomic Energy Commission, Nevada Proving Grounds Area, Nevada: U.S. Geological Survey Bulletin, 1021-k, p. 333-384.

Jones, C.H., Sonder, L.J., and Unruh, J.R., 1999, Lithospheric gravitational potential energy and past orogenesis: implications for conditions of initial Basin and Range and Laramide deformation: Reply: *Geology*, v. 27, p. 475-476.

Jones, B, and Hunter, I.G., 1994, Messinian (Late Miocene) karst on Grand Cayman, British West Indies: an example of an erosional sequence boundary: *Journal of Sedimentary Research*, v. B64, n. 4, p. 531-541.

Jordan, D.W., 1991, Outcrop gamma-ray logging: truck-mounted and hand held scintillometer methods are useful for exploration, development, and training purposes: 66th Annual Technical Conference and Exhibition of the Society of Petroleum Engineers, p. 841-852.

Kay, M., 1952, Late Paleozoic orogeny in central Nevada: *Geological Society of America Bulletin*, v. 63, p. 1269-1270.

Kellogg, H.E., 1959, Stratigraphy and structure of the southern Egan Range; unpublished Ph.D. thesis, Columbia University, 150 p.

Kellogg, H.E., 1960, Geology of the Southern Egan Range, Nevada; *in* Boettcher, J.W. and Sloan, W.W. Jr., Guidebook to the Geology of east-central Nevada: Intermountain Association of Petroleum Geology and Eastern Nevada Geological Society, 11th Annual Field Conference, Salt Lake City, Utah, p.189-197.

Kellogg, H.E., 1963, Paleozoic Stratigraphy of the Southern Egan Range, Nevada; Geological Society of America Bulletin. v. 74, p.685-708.

Kendall, G.W., Johnson, J.G., Brown, J.O., and Klapper, G., 1983, Stratigraphy and facies across Lower Devonian-Middle Devonian boundary, central Nevada: American Association of Petroleum Geologists Bulletin, v.67, p. 2199-2207.

Kennedy, M.J., 1996, Stratigraphy, sedimentology, and isotopic geochemistry of Australian Neoproterozoic postglacial cap dolostones: deglaciation, $\delta^{13}\text{C}$ excursions, and carbonate precipitation: Journal of Sedimentary Research, v. 66 p. 1050-1064.

Ketner, K.B., 1970, Limestone turbidite of Kinderhook age and its tectonic significance, Elko County, Nevada: U.S. Geological Survey Professional Paper 700-D, p. D18-D22.

Ketner, K.B., 1977, Deposition and deformation of lower Paleozoic western facies rocks, northern Nevada, *in* Stewart, J.H., Stevens, C.H., and Fritsche, A.E., eds., Paleozoic paleogeography of the western United States: Society of Economic Paleontologists and Mineralogists, Pacific Section, Pacific Coast Paleogeography Symposium 1, p. 251-258.

King, C., 1870, U.S. Geological Exploration 40th Parallel Report, v 3, p. 451-473.

King, P.B., 1969, Tectonics of North America-a discussion to accompany the tectonic map of North America: U.S. Geological Survey Prof. Paper 628, 95p.

Kirk, E., 1918, The stratigraphy of the Inyo Range: *in* Knopf, A., A geologic reconnaissance of the Inyo Range and the eastern slope of the southern Sierra Nevada, California: U.S. Geological Survey Professional Paper 110, p.19-48.

Kirk, E., 1933, The Eureka quartzite of the Great Basin region, *American Journal of Science*, 5th ser., v. 26, p. 27-43.

Kleinhampl, F.J., and Ziony, J.I., 1984, Mineral resources of northern Nye County, Nevada, Nevada Bureau of Mines and Geology Bulletin 99B, 243 p.

Kleinhampl, F.J., and Ziony, J.I., 1985, Geology of northern Nye County, Nevada, Nevada Bureau of Mines and Geology Bulletin 99A, 172 p.

Kuehner, Hans-Cristian, 1997, A genetic model of the Devonian Alamo Breccia, southeastern Nevada: unpublished Ph. D. dissertation, Colorado School of Mines, Golden, 321 p.

Koeberl, C., Armstrong, R.A., and Reimold, W.U., 1997a, Morokweng, South Africa: a large impact structure of Jurassic-Cretaceous boundary age: *Geology*, v. 25, p. 731-734.

Koeberl, C., Masaitis, V.L., Shafranosky, G.I., Gilmour, I., Langenhorst, F., and Schrauder, M., 1997b, Diamonds from the Popigai impact structure, Russia: *Geology*, v. 25, p. 967-970.

LaMaskin, T.A., and Elrick, M., 1997, Sequence stratigraphy of the Middle to Upper Devonian Guilmette Formation, southern Egan and Schell Creek Ranges, Nevada: Geological Society of America Special Paper 321, p. 89-112.

Langenheim, R.L. Jr., 1956, Mississippian stratigraphy in eastern Nevada: Geological Society America Bulletin, v.67, p.1714.

Langenheim, R.L. Jr., 1960a, Early and Middle Mississippian Stratigraphy of the Ely Area: in Intermountain Association Petroleum Geologists, Guidebook 11th Annual Field Conference, Geology of east-central Nevada, 1960, p.72-80.

Langenheim, R.L. Jr., 1960b, Preliminary report on the geology of the Ely No.3 Quadrangle, White Pine County, Nevada, in Guidebook to the geology of east-central Nevada: Intermountain Association of Petroleum Geologists, p.148-156.

Langenheim, R.L. Jr., 1960c, The Pilot Shale, West Range Limestone, and the Devonian-Mississippian boundary in eastern Nevada: Illinois Academy of Science, v.53, n.3-4, p.122-131.

Langenheim, R.L. Jr., Carss, B.W., Kennerly, J.B., McCutcheon, V.A., and Waines, R.H., 1960, Paleozoic section in the Arrow Canyon Range, Clark County, Nevada (abs): Geological Society America Bulletin, v.71, p.2064.

Langenheim, R.L. Jr., Carss, BW, Kennerly, J.B., McCutcheon, V.A., and Waines, R.H., 1962, Paleozoic section in Arrow Canyon Range, Clark County, Nevada: American Association of Petroleum Geologists Bulletin, v.46, p.592-609.

Langenheim, R.L. Jr., and Larson, E.R., 1973, Correlation of Great Basin stratigraphic units: Nevada Bureau of Mines and Geology, Bulletin 72, 36 p.

Langenheim, R.L. Jr., and Tischler, H., 1960, Mississippian and Devonian paleontology and stratigraphy, Quartz Spring area, Inyo County, California: California University Publications, Geologic Science, v.38, n.2, p.89-150.

Lawton, T.F., and Trexler, J.H.Jr., 1991, Piggyback basin in the Sevier orogenic belt, Utah: implications for development of the thrust wedge: *Geology*, v. 19, p. 827-830.

LeFever, R.D., 1996, Sedimentology and stratigraphy of the Deadwood-Winnipeg interval (Cambro-Ordovician, Williston Basin: *in* Longman, M.W., and Sonnenfeld, M.D., eds., *Paleozoic Systems of the Rocky Mountain Region*: Rocky Mountain Association of Geologists and SEPM (Society for Sedimentary Geology), p. 11-28.

Lehmann, C., Osleger, D.A., and Montañez, I.P., 1998, Controls on cyclostratigraphy of Lower Cretaceous carbonates and evaporites, Cupido and Coahuila platforms, northeastern Mexico: *Journal of Sedimentary Research*, v. 68, p. 1109-1130.

Lelek, J.J., 1982, Anschutz Ranch East field, northeast Utah and southwest Wyoming: *in* Powers, R.B., ed., *Geologic studies of the Cordilleran thrust belt*: Rocky Mountain Association of Geologists, p. 619-631.

Lewis, C.J., Wernicke, B.P., Selverstone, J., and Bartley, J.M., 1999, Deep burial of the footwall of the northern Snake Range decollement, Nevada: *Geological Society of America Bulletin*, v. 111, p. 39-51.

Link, P.K., 1983, Glacial and tectonically influence sedimentation in the upper Proterozoic Pocatello Formation, southeastern Idaho, *in* Miller, D.M., Todd, V.R., and Howard, K.S. eds., *Tectonic and stratigraphic studies in the eastern Great Basin*: Geological Society of America Memoir 157, p. 165-181.

Liu, M., and Shen, Y., 1998, Sierra Nevada uplift: a ductile link to mantle upwelling under the Basin and Range province: *Geology*, v. 26, p. 299-302.

Longman, M.W., 1982, Carbonate diagenesis as a control on stratigraphic traps (with examples from the Williston Basin): American Association of Petroleum Geologists Education course note series #21, 159 p.

Longwell, C.R., 1928, Geology of the Muddy Mountains, Nevada: U.S. Geological Survey Bulletin, 798, 152 p.

Longwell, C.R., 1952, Basin and Range geology west of the St. George Basin, Utah: Guidebook to the Geology of Utah, Intermountain Association of Petroleum Geologists, n. 7, p.27-42.

Longwell, C.R., Pampeyan, E.H., Bowyer, B., and Roberts, R.J., 1965, Geology and mineral deposits of Clark County, Nevada: Nevada Bureau of Mines Bulletin 62, 218 p.

Loucks, G.G., 1977, Geologic history of the Devonian northern Alberta to southwest Arizona, in Heisey, E.L., Lawson, D.E., Norwood, E.R., Wach, P.H., and Hale, L.A., eds., Rocky Mountain thrust belt geology and resources: Wyoming Geological Association 29th annual field conference in conjunction with Montana geological Society and Utah Geological Society, p. 119-134.

Lu, F.H., and Meyers, W.J., 1998, Massive dolomitization of a late Miocene carbonate platform: a case of mixed evaporative brines with meteoric water, Nijar, Spain: *Sedimentology*, v. 45, p. 263-277.

Lumsden, W.W.I. Jr., 1964, Geology of the southern White Pine Range and northern Horse Range, Nye and White Pine Counties, Nevada: unpublished Ph.D. dissertation, University of California, Los Angeles, 249 p.

MacCready, T., Snoke, A.W., Wright, J.E., and Howard, K.A., 1997, Mid-crustal flow during Tertiary extension in the Ruby Mountain core complex, Nevada: Geological Society of America Bulletin, v. 109, p. 1576-1594.

Machel, H.G., Cavell, P.a., and Patey, K.S., 1996, Isotopic evidence for carbonate cementation and recrystallization and for tectonic expulsion of fluids into the Western Canadian Sedimentary Basin: Geological Society of America Bulletin, v. 108, p. 1108-1119.

Machel, H.G., and Mountjoy, E.W., 1987, General constraints on extensive pervasive dolomitization--and their application to the Devonian carbonates of western Canada: Bulletin Canadian Petroleum Geology, v. 35, p. 143-158.

Machel, H.G., and Mountjoy, E.W., 1990, Coastal mixing zone dolomite, forward modeling and massive dolomitization of platform margin carbonates-Discussion: Journal of Sedimentary Petrology, v. 60, p. 1008-1012.

Marshak, S., and Mitra, G., 1988, Basic methods of structural geology: Prentice Hall, New Jersey, 446 p.

Martin, M.W., 1987, The structural geology of the Worthington Mountains, Lincoln County, Nevada: unpublished M.S. thesis, University of North Carolina, 112 p.

Matthews, V., 1988, Reinterpretation of the relations between the Keystone, Red Spring, Contact, and Cottonwood faults; eastern Spring Mountains, Clark County, Nevada: *The Mountain Geologist*, v. 25, p. 181-191.

Matti, J.C.D., 1979, Depositional history of middle Paleozoic carbonate rocks deposited at an ancient continental margin, central Nevada: unpublished Ph.D. dissertation, Stanford University, 486 p.

Matti, J.C., and McKee, E.H., 1977, Silurian and Lower Devonian paleogeography of the outer continental shelf of the Cordilleran miogeocline, central Nevada, *in* Stewart, J.H., Stevens, C.H., and Fritsche, A.E., eds., *Paleozoic paleogeography of the western United States: Society of Economic Paleontologists and Mineralogists, Pacific Section, Pacific Coast paleogeography symposium I*, p 181-215.

Mayer, L., 1986, Topographic constraints on models of lithospheric stretching of the Basin and Range province, western United States, *in* Mayer, L., ed., *Extensional tectonics of the southwestern United States: a perspective on processes and kinematics: Geological Society of America Special Paper 208*, p. 1-14.

Mayo, E.B., 1931, Fossils from the eastern flank of the Sierra Nevada, California: *Science*, v. 74, p. 514-515.

McAllister, J.F., 1952, Rocks and structure of the Quartz Spring area, northern Panamint Range, California: California Department of Natural Resources, Division of Mines, Special Report 25, 38 p.

McAllister, J.F., 1974, Silurian, Devonian, and Mississippian formations of the Funeral Mountains in the Ryan quadrangle, Death Valley region, California: U.S. Geological Survey Bulletin 386, 35 p.

McKee, E.H., 1968, Geology of the Magruder Mountain area, Nevada-California: U.S. Geological Survey Bulletin 1251-H, 40 p.

McKee, E.H., 1976, Geology of the northern part of the Toquima Range, Lander, Eureka, and Nye Counties, Nevada: U.S. Geological Survey Professional Paper 931, 49 p.

McLean, D.J., and Mountjoy, E.W., 1994, Allocyclic control on Late Devonian buildup development, southern Canadian Rocky Mountains: *Journal of Sedimentary Research*, v. B64, p. 326-340.

McNair, A.H., 1951, Paleozoic stratigraphy of part of northwestern Arizona: *American Association of Petroleum Geologists Bulletin*, v.35, p.503-541.

McNair, A.H., 1952, Summary of the Pre-Coconino stratigraphy of southwestern Utah, northwestern Arizona and southeastern Nevada, in *Guidebook to the geology of Utah*, n. 7: Utah Geological and Mineral Survey, p.45-51.

Merriam, C.W., 1940, Devonian stratigraphy and paleontology of the Roberts Mountains region, Nevada: *Geological Society of America Special Paper* 25, 114 p.

Merriam, C.W., and Anderson, C.A., 1942, Reconnaissance survey of the Roberts Mountains, Nevada: *Geological Society of America Bulletin*, v. 53, p. 1675-1728

.

Meyers, W.J., Lu, F.H., and Zachariah, J.K., 1997, Dolomitization by mixed evaporative brines and freshwater, Upper Miocene carbonates, Nijar, Spain: *Journal of Sedimentary Research*, v. 67, p. 898-912.

Miller, E.L., Gans, P.B., Wright, J.E., and Sutter, J.F., 1988, Metamorphic history of the east-central Basin and Range Province: tectonic setting and relationship to magmatism, *in* Ernst, W.G., ed., *Metamorphism and crustal evolution of the western United States*, (Rubey Volume VII): Englewood Cliffs, New Jersey, Prentice-Hall, p. 649-682.

Miller, G.M., 1959, The Pre-Tertiary structure and stratigraphy of the southern portion of the Wah Wah Mountains, southwestern Utah: unpublished Ph.D. thesis, University of Washington, Seattle, 150 p.

Miller, M.G., and Friedman, R.M., Early Tertiary magmatism and probable Mesozoic fabrics in the Black Mountains, Death Valley, California: *Geology*, v. 27, p. 19-22.

Misch, P., 1960, Regional structural reconnaissance in central-northeast Nevada and some adjacent areas observations and interpretations: *Intermountain Association of Petroleum Geologists and Eastern Nevada Geological Society Guidebook Geology of East Central Nevada*, p. 17-42.

Mitchum, R.M., Vail, P.R., and Thompson, S. III, 1977, Seismic stratigraphy and global changes of sea level, Part 2: The depositional sequence as a basic unit for stratigraphic analysis *in* Payton, C.E., ed., *Seismic Stratigraphy--Applications to Hydrocarbon Exploration*: American Association of Petroleum Geologists Memoir 26, p. 53-62.

Morgan, J., and Warner, M., 1999, Chicxulub: the third dimension of a multi-ring impact basin: *Geology*, v. 27, p. 407-410.

Morris, H.T., and Lovering, T.S., 1961, Stratigraphy of the East Tintic Mountains, Utah: U.S. Geological Survey Professional Paper 361, 145 p.

Mossop, G., and Shetsen, I., 1994, Geological Atlas of the Western Canadian Sedimentary Basin: Canadian Society of Petroleum Geologists and Alberta Research Council, 510 p.

Mountjoy, E.W., Qing, H., and McNutt, R.H., 1992, Strontium isotopic composition of Devonian dolomites, Western Canada Sedimentary Basin: significance of sources of dolomitizing fluids: *Applied Geochemistry*, v. 7, p. 59-75.

Mountjoy, E., Whittaker, S., Williams-Jones, A., Qing, H., Drivet, E., and Marquez, X., 1997, Variable fluid and heat flow regimes in three Devonian dolomite conduit systems, Western Canada Sedimentary Basin: isotopic and fluid inclusion evidence/constraints: *in* Basin-wide diagenetic patterns: integrated petrologic, geochemical, and hydrologic considerations: SEPM (Society of Sedimentary Geology) Special Publication No. 57, p. 119-137.

Mukul, M., 1998, A spatial statistics approach to the quantification of finite strain variation in penetratively deformed thrust sheets: an example from the Sheeprock thrust sheet, Sevier fold-and-thrust belt, Utah: *Journal of Structural Geology*, v. 20, p. 371-384.

Mukul, M., and Mitra, G., 1998, Finite strain and strain variation analysis in the Sheeprock thrust sheet: an internal thrust sheet in the Provo salient of the Sevier fold-and-thrust belt, central Utah: *Journal of Structural Geology*, v. 20, p. 385-405.

Nelson, R., 1959, Stratigraphy and structure of the northernmost part of the northern Snake Range and the Kern Mountains in eastern Nevada and the southern Deep Creek Range in western Utah: unpublished Ph.D. thesis, University of Washington, Seattle, 165 p.

Nelson, S.L., 1994, Lower and Middle Devonian carbonate platform and outer-shelf basin deposits from the southern end of Railroad Valley, Nevada: *in* Dobbs, S.W., and Taylor, W.J., eds., Structural and stratigraphic investigations and petroleum potential of Nevada, with special emphasis south of the Railroad Valley producing trend: Nevada Petroleum Society Conference Volume II, p. 157-164.

Nelson, S.T., and Tingey, D.G., 1997, Time-transgressive and extension-related basaltic volcanism in southwest Utah and vicinity, *Geological Society of America Bulletin*, v. 109, p. 1249-1265.

Newman, G.W., 1979, Late Cretaceous(?)–Eocene faulting in the east central Basin and Range, *in* Newman, G.W., and Goode, H.D., eds., Basin and Range Symposium: Rocky Mountain Association of Geologists and Utah Geological Association, p.245-257.

Niebuhr, W.W., 1979, Biostratigraphy and paleoecology of the Guilmette Formation (Devonian) of eastern Nevada: unpublished Ph.D. dissertation, University of California, Berkeley, 246 p.

Nichols, K.M., and Silberling, N.J., 1980, Eogenetic dolomitization in the pre-Tertiary of the Great Basin: *in* Zenger, D.H., Dunham, J.B., and Ethington, R.L., Concepts and models of dolomitization, eds. Society of Economic Paleontologists and Mineralogists Special Publication 22, p. 237-246.

Nolan, T.B., 1935, The Gold Hill mining district, Utah: U.S. Geological Survey Professional Paper 177, 172 p.

Nolan, T.B., 1943, The Basin and Range Province in Utah, Nevada, and California: U.S. Geological Survey Professional Paper 197-D, 196 p.

Nolan, T.B., 1962, The Eureka mining district, Nevada: U.S. Geological Survey Professional Paper 406.

Nolan, T.B., Merriam, C.W., and Williams, J.S., 1956, The stratigraphic section in the vicinity of Eureka, Nevada: U.S. Geological Survey Professional Paper 276, 77 p.

Nolan, T.B., Merriam, C.W., and Brew, D.A., 1971, Geologic map of the Eureka quadrangle, Eureka and White Pine Counties, Nevada: U.S. Geological Survey Map I-612.

Nolan, T.B., Merriam, C.W., and Blake, M.C. Jr., 1974, Geologic map of the Pinto Summit quadrangle, Eureka and White Pine Counties, Nevada: U.S. Geological Survey Map I-793.

North, F.K., 1988, The state of the system and economic survey of the whole Devonian: *in* McMillan, N.J., Embry, A.F., and Glass, D.J., Devonian of the World: Canadian Society of Petroleum Geologists, Calgary, Memoir 14, v. 1, Regional Syntheses, p. 1-14.

Okaya, D.A., and Thompson, G.A., 1986, Involvement of deep crust in extension of Basin and Range province, *in* Mayer, L., ed., Extensional tectonics of the southwestern United States: a perspective on processes and kinematics: Geological Society of America Special Paper 208, p. 15-22.

Olson, R.H., 1956, Geology of Promontory Range, *in* Geology of parts of northwestern Utah: Utah Geological Society, p.41-75.

Osmond, J.C., 1953, Mottled carbonate rocks in the Middle Devonian of Eastern Nevada: Geological Society America Bulletin, v.64, p.1460.

Osmond, J.C., 1954, Dolomites in Silurian and Devonian of east-central Nevada: American Association of Petroleum Geologists Bulletin, v. 38, p.1911-1156.

Osmond, J.C., 1962, Stratigraphy of Devonian Sevy Dolomite in Utah and Nevada: American Association of Petroleum Geologists Bulletin, v. 46, p. 2033-2056.

Paddock, R.E., 1956, Geology of the Newfoundland Mountains, Box Elder County, Utah: unpublished MS thesis, University of Utah, Salt Lake City, 101 p.

Page, W.R., 1993, Stratigraphy and structure of the Paleozoic rocks in the southern Delamar Mountains, Lincoln County, Nevada: unpublished M.S. thesis, Colorado School of Mines, Golden, 95 p.

Page, W.R., and Ekren, E.B., 1995, Preliminary geologic map of the Bristol Well Quadrangle, Lincoln County, Nevada: U.S. Geological Survey Open-File Report 95-580, 27 p.

Page, W.R., Swadely, W.C., and Scott, R.B., 1990, Preliminary geologic map of Delamar three SW quadrangle, Lincoln County, Nevada: U.S. Geological Survey Open-File Report 90-336, 17 p.

Paulsen, T., and Marshak, S., 1998, Charleston transverse zone, Wasatch Mountains, Utah: structure of the Provo salient's north margin, Sevier fold-thrust belt: Geological Society of America Bulletin, v. 110, p. 512-522.

Perkins, R.F., 1955, Structure and stratigraphy of the lower American Fork Canyon--Mahogany Mountain area, Utah County, Utah: Brigham Young University Research Studies, Geology Series, v.2, n.1, 38 p.

Perry, W.J.Jr., and Sando, W.J., 1982, Sequence of deformation of Cordilleran thrust belt in Lima, Montana region, *in* Powers, R.B., ed., Geologic studies of the Cordilleran thrust belt: Rocky Mountain Association of Geologists, v. 1, p. 137-144.

Peterson, J.A., and MacCary, L.M., 1987, Regional stratigraphy and general petroleum geology of the U.S. portion of the Williston basin and adjacent areas: *in* Longman, M.W., ed., Williston Basin: Anatomy of a cratonic oil province: Rocky Mountain Association of Geologists, p. 9-43.

Petersen, M.S., 1956, Devonian strata of central Utah: Brigham Young University Research Studies, Geology Series, v.3, n.3, 37 p.

Picha, F.J., 1996, Exploring for hydrocarbons under thrust belts-a challenging new frontier in the Carpathians and elsewhere: American Association of Petroleum Geologists, v. 80, p. 1547-1564.

Ponce, D.A., 1997, Gravity data of Nevada: U.S. Geological Survey Digital Data Series DDS-42.

Poole, F.G., 1974, Flysch deposits of Antler foreland basin, western United States, in Dickinson, W.R., ed., *Tectonics and sedimentation: Society of Economic paleontologists and Mineralogists Special Publication 22*, p. 58-83.

Poole, F.G., and Claypool, G.E., 1984, Petroleum source-rock potential and crude-oil correlation in the Great Basin, *in* Woodward, J., Meissner, F.F., and Clayton, J.L., eds., *Hydrocarbon source rocks of the greater Rocky Mountain region: Rocky Mountain Association of Geologists*, p. 179-228.

Poole, F.G., Sandberg, C.A., and Boucot, A.J., 1977, Silurian and Devonian paleogeography of the western United States, *in* Stewart, J.H., Stevens, C.H., and Fritsche, A.E., eds., *Paleozoic paleogeography of the western United States: Society of Economic Paleontologists and Mineralogists, Pacific Section, Pacific Coast Paleogeography Symposium 1*, p. 39-65.

Poole, F.G., Stewart, J.H., Palmer, A.R., Sandberg, C.A., Madrid, R.J., Ross, R.J. Jr., Hintze, L.F., Miller, M.M., and Wrucke, C.T., 1992, Latest Precambrian to latest Devonian time: Development of a continental margin, *in* Burchfiel, B.C., Lipman, P.W., and Zoback, M.L., eds., *The Cordilleran Orogen: Conterminous U.S.: Boulder, Colorado, Geological Society of America, The Geology of North America*, v. G-3, p. 9-56.

Quennell, A.M., 1987, Rift Valleys: *in* Seyfert, C.K., ed., *the encyclopedia of structural geology and plate tectonics: Van Nostrand Reinhold Company, New York*, p. 671-688.

Rankey, E.C., and Walker, K.R., 1994, Gradual establishment of Iapetan “passive” margin sedimentation: stratigraphic consequences of Cambrian episodic tectonism and eustasy, southern Appalachians: *Journal of Sedimentary Research*, v. B64 p. 298-310.

Read, D.L., and Zogg, W.D., 1988, Description and origin of the Devonian dolomite reservoir, Grant Canyon field, Nye County, Nevada, *in* Goolsby, S.M., and Longman, M.W., eds., Occurrence and petrophysical properties of carbonate reservoirs in the Rocky Mountain region: Rocky Mountain Association of Geologists, Denver, p. 229-240.

Read, J.F., and Goldhammer, R.K., 1988, Use of Fischer plots to define third-order sea-level curves in Ordovician peritidal cyclic carbonates, Appalachians: *Geology*, v. 16, p. 895-899.

Rehig, W.A., 1986, Processes of regional Tertiary extension in the western Cordillera: insights from the metamorphic core complexes, *in* Mayer, L., ed., Extensional tectonics of the southwestern United States: a perspective on processes and kinematics: Geological Society of America Special Paper 208, p. 97-122.

Reid, R.K., and Dorobek, S.L., 1993, Sequence stratigraphy and evolution of a Paleozoic foreland carbonate ramp in the Mississippian Mission Canyon Formation and stratigraphic equivalent, Montana and Idaho: *in* Loucks, R.G and Sarg, J.F., eds., Carbonate sequence stratigraphy: recent developments and applications: American Association of Petroleum Geologists Memoir 57, p. 327-352.

Reimold, W.U., Brandt, D., and Koeberl, C., 1998 Detailed structural analysis of the rim of a large, complex impact crater: Bosumtwi Crater, Ghana: *Geology*, v. 26, p.543-546.

Reso, A., 1960, The geology of the Pahrangat Range, Lincoln County, Nevada: unpublished Ph.D. dissertation, Rice University, Houston, Texas, 656 p.

Reso, A., 1963, Composite columnar section of exposed Paleozoic and Cenozoic rocks in the Pahranaगत Range, Lincoln County, Nevada: Geological Society of America Bulletin, v. 74, p. 901-918.

Reso, A., and Corneis, C.G., 1959, Devonian system in the Pahranaगत Range, southeastern Nevada: Geological Society of America Bulletin, v. 70, p. 1249-1252.

Rey, P.F., and Costa, S., 1999, Lithospheric gravitational potential energy and past orogenesis: implications for conditions of initial Basin and Range and Laramide deformation: Comment: Geology, v. 27, p. 475-476.

Riciputi, L.R., Machel, H.G., and Cole, D.R., 1994, An ion microprobe study of diagenetic carbonates in the Devonian Nisku formation of Alberta, Canada: Journal of Sedimentary Research, v. A64, p. 115-127.

Rigby, J.K., 1958, Geology of the Stansbury Mountains, eastern Tootle County, Utah, *in* Guidebook to the geology of Utah, n.13: Utah Geological Society, 134 p.

Rigby, J.K., 1959, Stratigraphy of the southern Oquirrh Mountains, Lower Paleozoic succession, *in* Guidebook to the geology of Utah, n.14: Utah Geological Society, p.9-36.

Rigby, J.K., 1960, Geology of the Buck Mountain-Bald Mountain area, southern Ruby Mountains, White Pine County, Nevada: *in* Intermountain Assoc. Petroleum Geologists, Guidebook 11th Ann. Field Conference, Geology of east-central Nevada, 1960, p.173-180.

Rinehart, C.D., Ross, D.C., and Huber, N.K., 1959, Paleozoic and Mesozoic fossils in a thick stratigraphic section in the eastern Sierra Nevada, California: Geological Society America Bulletin, v.70, p.941-946.

Roberts, R.J., 1949, Structure and stratigraphy of Antler Peak Quadrangle, north-central Nevada: Geological Society America Bulletin, v.60, p.1917.

Roberts, R.J., 1972, Evolution of Cordilleran fold belt: Geological Society of America Bulletin, v. 83, p. 1989-2004.

Roberts, R.J., Hotz, P.E., Gilluly, J., and Ferguson, H.G., 1958, Paleozoic rocks of north-central Nevada: American Association of Petroleum Geologists Bulletin, v.42, p.2813-2857.

Roberts, R.J., Montgomery, K.M., and Lehner, R.E., 1967, Geology and Mineral Resources of Eureka County, Nevada: Nevada Bureau of Mines and Geology Bulletin 64, 152 p.

Roeder, D., 1989, Thrust belt of central Nevada, Mesozoic compressional events, and the implications of petroleum prospecting, *in* Garside, L.J., and Shaddrick, D.R., eds., Compressional and extensional structural styles in the northern Basin and Range seminar proceedings: Reno, Nevada Petroleum Society and Geological Society of Nevada, p. 21-34.

Roeder, D., Gilbert, O.C., and Witherspoon, W.D., 1978, Evolution and macroscopic structure of the Valley and Ridge thrust belt, Tennessee and Virginia: Studies in Geology 2, University of Tennessee Department of Geology Sciences, 25 p.

Rodgers, J., 1949, Evolution of thought on structure of middle and southern Appalachians: American Association of Petroleum Geologists Bulletin, v. 33, p. 1643-1654.

Ross, D.C., 1961, Geology and mineral deposits of Mineral County, Nevada: Nevada Bureau of Mines Bulletin 58, 98 p.

Ross, D.C., 1962, Preliminary geologic map of the Independence Quadrangle, Inyo County California: U.S. Geological Survey Mineral Field Studies Map MF254.

Ross, G.M., 1991, Precambrian basement in the Canadian Cordillera: an introduction: Canadian Journal of Earth Sciences, v. 28, p. 1133-1139.

Rush, R.W., 1951, Stratigraphy of the Burbank Hills, Western Millard County, Utah: Utah Geological and Mineral Survey Bulletin 38, 23 p.

Rush, R.W., 1956, Silurian rocks of western Millard County, Utah: Utah Geological and Mineral Survey Bulletin 53, 66 p.

Ryan, J.F., and Langenheim, R.L. Jr., 1973, Upper Devonian sandstone in Arrow Canyon Quadrangle, Clark County, Nevada: American Association of Petroleum Geologists Bulletin, v.57, p.1734-1742.

Sadler, P.M., Osleger, D.A., and Montañez, I.P., 1993, On the labeling, length, and objective basis of Fischer plots: Journal of Sedimentary Research, v. 63, p. 360-368.

Sami, T.T., and James, N.P., 1994, Peritidal carbonate platform growth and cyclicity in an early Proterozoic foreland Basin, Upper Pethei Group, northwest Canada: Journal of Sedimentary Research, v. B64, p. 111-131.

Sandberg, C.A., Morrow, J.R., and Warme, J.E., 1997, Late Devonian Alamo impact event, global Kellwasser events, and major eustatic events, eastern Great Basin, Nevada and Utah, *in* Link, P.K. and Kowallis, B.J., eds., Proterozoic to recent stratigraphy, tectonics, and volcanology, Utah, Nevada, southern Idaho and central Mexico: Brigham Young University Geology Studies, v. 42, part 1, p. 129-160.

Sandberg, C.A., and Poole, F.G., 1977, Conodont biostratigraphy and depositional complexes of the Upper Devonian cratonic-platform and continental-shelf rocks in the western United States, *in* Murphy, M.A., Berry, W.B.N., and Sandberg, C.A., eds., Western North America: Devonian: University of California, Riverside, Campus Museum Contribution 4, p. 144-182.

Sandberg, C.A., Poole, F.G., and Johnson, J.G., 1988, Upper Devonian of western United States, *in* McMillan, N.J., Embry, A.F., and Glass, D.J., Devonian of the World: Canadian Society of Petroleum Geologists, Calgary, Memoir 14, v. 1, Regional Syntheses, p. 183-220.

Sandberg, C.A., and Ziegler, W., 1973, Refinement of standard Upper Devonian conodont zonation based on sections in Nevada and West Germany: *Geologica et Paleontologica*, v. 7, p. 97-122.

Sandberg, C.A., and Ziegler, W., 1996, Devonian conodont biochronology in geologic time calibration: *Senckenbergiana lethae*, v. 76, p. 259-265.

Sandberg, C.A., Ziegler, W., Dreesen, R., and Butler, J.L., 1988, Late Frasnian mass extinction: Conodont event stratigraphy, global changes, and possible causes, *Courier Forschungs-Institute Senckenberg*, v. 102, p. 263-307.

- Satterley, A.K., 1996, Cyclic carbonate sedimentation in the Upper Triassic Dachstein Limestone, Austria: the role of patterns of sediment supply and tectonics in a platform-reef-Basin system: *Journal of Sedimentary Research*, v. 66, p. 307-323.
- Schaeffer, M.E., 1960, Stratigraphy of the Silver Island Mountains, *in* Guidebook to the geology of Utah, n.15: Utah Geological Society, p.15-111.
- Scott, C.H., Chamberlain, A.K., 1986, Mississippian source rock maturation and richness, eastern Nevada: *American Association of Petroleum Geologists Bulletin*, v. 70; p. 1055.
- Scott, C.H., and Chamberlain, A.K., 1988a, Blackburn Field, Nevada; a case history: *Geological Society of America, Abstracts with Programs*; v. 20, p. 229.
- Scott, C., and Chamberlain, A.K., 1988b, Blackburn Field Nevada: a case history: *in* Goolsby, S.M., and Longman, M.W. eds., Occurrence and petrophysical properties of carbonate reservoirs in the Rocky Mountain region: 1988 Rocky Mountain Association of Geologists, Denver, Colorado, p. 241-250.
- Sengör, A.M.C., 1987, Aulacogen: *in* Seyfert, C.K., ed., the encyclopedia of structural geology and plate tectonics: Van Nostrand Reinhold Company, New York, p. 18-25.
- Sharp, R.P., 1942, Stratigraphy and structure of the southern Ruby Mountains, Nevada: *Geological Society America*, v.53, p.647-690.
- Shukla, V., 1988, Sedimentology and geochemistry of a regional dolostone: correlation of trace elements with dolomite fabrics, *in* Shukla, V., and Baker, P.A., eds., Sedimentology and geochemistry of dolostones: Society of Economic Paleontologists and Mineralogists Special Publication 43, p. 145-157.

Simpson, R.W., Jachens, R.C., and Blakley, R.J., 1986, A new isostatic residual gravity map of the conterminous United States with a discussion on the significance of isostatic residual anomalies: *Journal of Geophysical Research*, v. 91, p. 8348-8372.

Skinner, B.J., and Porter, S.C., 1989, *The dynamic Earth an introduction to physical geology*: John Wiley & Sons, New York, 541 p.

Skipp, B., and Hiatt, M.H., Jr., 1977, Allochthons along the northeast margin of the Snake River Plain, Idaho: *in* Heisey, E.L., Lawson, D.E., Norwood, E.R., Wach, P.H., and Hale, L.A. eds., *Rocky Mountain Thrust Belt Geology and Resources: Wyoming Geological Association-Montana Geological Society-Utah Geological Society Joint Field Conference*, p. 499-515.

Sloss, L.L., 1963, Sequences in the cratonic interior of North America: *Geological Society of America Bulletin*, v. 74, p. 93-113.

Smith, M.T., Dickinsen, W.R., and Gehrels, G.E., 1993, Contractional nature of the Devonian-Mississippian Antler tectonism along the North American continental margin: *Geology*, v. 21, p. 21-24.

Smith, J. Jr., and Ketner, K.B., 1968, Devonian and Mississippian rocks and the date of the Roberts Mountains thrust in the Carlin-Pinon range area, Nevada: *U.S. Geological Survey Bulletin* 1251-I, 18 p.

Smith, J. Jr., and Ketner, K.B., 1975, Stratigraphy of Paleozoic rocks in the Carlin-Pinon range area, Nevada: *U.S. Geological Survey Professional Paper* 867-A, 87 p.

Snyder, D. B., 1983, Interpretation of the Bouguer gravity map of Nevada: Caliente sheet: Nevada Bureau of Mines and Geology, Report 37, 8 p.

Spencer, A.C., 1917, The geology and ore deposits of Ely, Nevada: United states Geological Survey Professional Paper 96, 189 p.

Spurr, J.E., 1903, Descriptive geology of Nevada south of the fortieth parallel and adjacent portions of California: U.S. Geological Survey Bulletin 208, 229 p.

Staatz, M.H., and Osterwald, F.W., 1959, Geology of the Thomas Range fluorspar district, Juab County, Utah: U.S. Geological Survey Bulletin 1069, 97 p.

Stamatakos, J.A., Ferrill, D.A., and Spivey, K.H., 1998, Paleomagnetic constraints on the tectonic evolution of Bare Mountain, Nevada: Geological Society of Geology Bulletin, v. 110, p. 1530-1546.

Stanley, K.O., and Collison, J.W., 1979, Depositional history of Paleocene-Lower Eocene Flagstaff Limestone and coeval rocks, central Utah: American Association of Petroleum Geologists Bulletin, v. 63, p. 311-323.

Stevens, C.H., 1986, Evolution of the Ordovician through Middle Pennsylvanian carbonate shelf in east-central California: Geological Society of America Bulletin, v. 97, p. 11-25.

Stewart, J.H., 1980, Geologic Map of Nevada: Nevada Bureau of Mines and Geology Special Publication 4, 136 p.

Stewart, J.H., and Carlson, J.E., 1978, 1:500,000 scale geologic map of Nevada, U.S. Geological Survey and Nevada Bureau of Mines and Geology.

Stewart, J.H., and Poole F.G., 1974, Lower Paleozoic and uppermost Precambrian Cordilleran miogeocline, Great Basin, western United States, *in* Dickenson, W.R., ed., Tectonics and sedimentation: Society of Economic Paleontologists and Mineralogists, Special Publication, n. 22, p. 28-57.

Stewart, S.A., 1996, Influence of detachment layer thickness on style of thin-skinned shortening: *Journal of Structural Geology*, v. 18, p. 1271-1274.

Stokes, W.L., 1979, Stratigraphy of the Great Basin region, *in* Newman, G.W., and Goode, H.D., eds., Basin and Range Symposium: Rocky Mountain Association of Geologists and Utah Geological Association, p. 195-220.

Suek, D.H., and Knaup, W.W.I, 1979, Paleozoic carbonate buildups in the Basin and Range Province *in* Newman, G.W., and Goode, H.D., eds., Basin and Range Symposium: Rocky Mountain Association of Geologists and Utah Geological Association, p.245-257.

Suppe, J., 1985, Principles of structural geology: Prentice-Hall, New Jersey, 537 p.

Swadley, W.C., Page, W.D., Scott, R.B. and Pampeyan, E.H., 1994, Geologic map of the Delamar three SE Quadrangle, Lincoln County, Nevada: U.S. Geological Survey Map GQ-1754.

Swart, P.K., 1988, The elucidation of dolomitization events using nuclear-track mapping, *in* Shukla, V., and Baker, P.A., eds., Sedimentology and geochemistry of dolostones: Society of Economic Paleontologists and Mineralogists Special Publication No. 43, p. 11-23.

Talling, P.J., Lawton, T.F., Burbank, D.W., and Hobbs, R.S., 1995, Evolution of latest Cretaceous-Eocene nonmarine deposystems in the Axhandle piggyback Basin of central Utah: Geological Society of America Bulletin v. 107, p. 297-315.

Taylor, W.J., 1989, Geometry of faulting, timing of extension and their relationship to volcanism, near 38° N latitude, eastern Nevada: Unpublished dissertation, University of Utah, Salt Lake City, 204 p.

Taylor, W.J., Bartley, J.M., Fryxell, J.E., Schmitt, J., and Vandervoort, D.S., 1993, Mesozoic central Nevada thrust belt, *in* Lahren, M.M., Trexler., J.H., and Spinosa, C., eds., Crustal evolution of the Great Basin and the Sierra Nevada: Geological Society of America Cordilleran/Rocky Mountain Section Field Trip Guidebook, p. 57-96.

Taylor, W.J., Dobbs, S.W., Nelson, S.L., and Armstrong, P.A., 1994, Generation of four-way closure through multiple tectonic events: structures of the Timpahute Range, southern Nevada: *in* Dobbs, S.W., and Taylor, W.J., eds., Structural and stratigraphic investigations and petroleum potential of Nevada, with special emphasis south of the Railroad Valley producing trend: Nevada Petroleum Society Conference Volume II, p. 141-156.

Tingley, J.V., 1991, Mineral resources of the Timpahute Range 30' x 60' quadrangle: Nevada Bureau of Mines and Geology Report 46, 40 p.

Trexler, J.H.Jr., Cole, J.C., and Cashman, P.H., 1999, Middle Devonian-Mississippian stratigraphy on and near the Nevada Test Site: implications for hydrocarbon potential: reply: American Association of Petroleum Geologists, v. 83, p. 523-524.

Tschanz, C.M., and Pampeyan, E.H., 1970, Geology and Mineral Deposits of Lincoln County, Nevada: Nevada Bureau of Mines and Geology Bulletin 73, 188 p.

Vail, P.R., Mitchum, R.M., and Thompson, S. III, 1977a, Seismic stratigraphy and global changes of sea level, Part 3: Relative changes of sea level from coastal onlap, *in* Payton, C.E., ed., *Seismic Stratigraphy--Applications to Hydrocarbon Exploration: American Association of Petroleum Geologists Memoir 26*, p. 83-97.

Vail, P.R., Mitchum, R.M., Todd, R.G.Jr., Widmier, J.M., Thomson S. III, Sangree, J.B., Bubb, J.N., and Hatlelid, W.G., 1977b, Seismic stratigraphy and global changes of sea level, *in* Payton, C.E. ed., *Seismic stratigraphy--Applications to hydrocarbon exploration: American Association of Petroleum Geologists Memoir 26*, p. 49-212.

Vandervoort, D.S., 1987, Sedimentology, provenance, and tectonic implications of the Cretaceous Newark Canyon Formation, east-central Nevada: unpublished M.S. thesis, Montana State University, Bozeman, Montana, 145 p.

Vreeland, J.H. and Berrong, B.H., 1979, Seismic exploration in Railroad Valley, Nevada, *in* Newman, G.W., and Goode, H.D., eds., *Basin and Range Symposium: Rocky Mountain Association of Geologists and Utah Geological Association*, p. 557-569.

Waines, R.H., 1961, Devonian sequence in the north portion of the Arrow Canyon Range, Clark County, Nevada (abs.), *Geological Society America Special Paper 68*, p. 62.

Waines, R.H., 1965, Devonian Stromatoporoids of Nevada: unpublished Ph.D. dissertation, University of California, Berkeley, 505 p.

Waite, R.H., 1953, Age of the "Devonian" of the Kearsarge area, California (abs.): *Geological Society America Bulletin*, v.64, p.1521.

Walker, J.D., Burchfiel, B.C., and Davis, G.A., 1995, New age controls on initiation and timing of foreland thrusting in the Clark Mountains, southern California: Geological Society of America Bulletin, v. 107, p. 742-750.

Walker, J.P., 1982, Hogback Ridge field, Rich County, Utah: thrust-belt anomaly or harbinger of further discoveries? *in* Powers, R.B., ed. Geologic Studies of the Cordilleran thrust belt: Rocky Mountain Association of Geologists, p.581-590.

Wang, K., Orth, D.J., Atreep, M.Jr., Chatterton, B.D.E., and Geldsetzer, H.H.J., 1991, Geochemical evidence for a catastrophic biotic event at the Frasnian/Famennian boundary in south China: *Geology*, v. 19, p. 776-779.

Warne, J.E., Chamberlain, A.K., and Ackman, B.W., 1991, The Alamo Event; Devonian cataclysmic breccia in southeastern Nevada: Geological Society of America, Cordilleran Section, 87th annual meeting, Abstracts with Programs; v. 23, p. 108.

Warne, J.E., and Kuehner, Hans-Christian, 1998, Anatomy of an anomaly: the Devonian catastrophic Alamo impact breccia of southern Nevada: *International Geology Review*, v. 40, p. 189-216.

Warne, J.E., and Sandberg, C.A., 1995, The catastrophic Alamo breccia of southern Nevada: record of Late Devonian extraterrestrial impact: *Courier Forschungsinstitut Senckenberg*, v. 188, W. Ziegler Commentuative Volume.

Warne, J.E., and Sandberg, C.A., 1996, Alamo megabreccia: record of a Late Devonian impact in southern Nevada: *GSA Today*, v. 6, n. 1, p.1-7.

Warne, J.E., Yarmanto, Chamberlain, A.K., and Ackman, B.W., 1993, The Alamo event: cataclysmic Devonian breccia, southeastern Nevada: *in*: Gillespie, C.W., ed., Structural and stratigraphic relationships of Devonian reservoir rocks, east central Nevada: 1993 Field trip Guidebook, Nevada Petroleum Society, Inc., Reno, NV, p. 157-170.

Warner, M.A., 1982, Source and time of generation of hydrocarbons in the Fossil Basin, western Wyoming thrust belt: *in* Powers, R.B., ed., Geologic studies of the Cordilleran thrust belt: Rocky Mountain Association of Geologists, p. 805-815.

Webb, G.E., 1998, Earliest known Carboniferous shallow-water reef, Gudman Formation (Tn1b) Queensland, Australia: implications for Late Devonian reef collapse and recovery: *Geology*, v. 26, p. 951-953.

Weimer, R.J., 1992, Developments in sequence stratigraphy: foreland and cratonic basins: *American Association of Petroleum Geologists Bulletin*, v. 76, p. 965-982.

Weinzapfel, A.C., and Neese, D.G, 1986, Gooseneck field, north Williston Basin: *in*: Noll, J.H. and Doyle, K.M., eds., Rocky Mountain oil and gas fields: 1986 symposium, Wyoming Geological Association, Casper, WY, p.61-82.

Wernicke, B.P., 1981, Low-angle normal faults in the Basin and Range Province: Nappe tectonics in an extending orogen: *Nature*, v. 291, p. 645-648.

Wernicke, B., Snow, J.K., and Walker, J.D., 1988, Correlation of Early Mesozoic thrusts in the southern Great Basin and their possible indication of 250-300 km of Neogene crustal extension, *in* Weide, D.L., and Faber, M.I. eds., This extended land, geological journeys in the souther Basin and Range: Geological Society of America Cordilleran Section Field Trip Guide, p. 255-268.

Westgate, L.G., and Knopf, A., 1932, Geology and ore deposits of the Pioche District, Nevada: U.S. Geological Survey Professional Paper 171, 79 p.

Wheeler, H.E., 1963, Post-Sauk and pre-Absaroka Paleozoic stratigraphic patterns in North America: American Association of Petroleum Geologists Bulletin, v. 47, p. 1497-1526.

Wilkinson, B.H., Diedrich, N.W., and Drummond, C.N., 1996, Facies successions in peritidal carbonate sequences: Journal of Sedimentary Research, v. 66, p. 1065-1078.

Wilkinson, B.H., Diedrich, N.W., Drummond, C.N., and Rothman, E.D., 1998, Michigan hockey, meteoric precipitation, and rhythmicity of accumulation on peritidal carbonate platforms: Geological Society of America Bulletin, v. 110, p. 1075-1093.

Wilkinson, B.H., Drummond, C.N., Diedrich, N.W., and Rothman, E.D., 1999, Poisson processes of carbonate accumulation on Paleozoic and Holocene platforms: Journal of Sedimentary Research, v. 69. P. 338-350.

Willden, R., and Kistler, R.W., 1979, Precambrian and Paleozoic stratigraphy in central Ruby Mountains Elko County, Nevada, *in* Newman, G.W., and Goode, H.D., eds., Basin and Range Symposium: Rocky Mountain Association of Geologists and Utah Geological Association, p. 221-243.

Williams, J.S., 1948, Geology of the Paleozoic rocks, Logan Quadrangle, Utah: Geological Society America Bulletin, v.59, p.1121-1164.

Williams, J.S., 1955, Resume of Paleozoic stratigraphy, Ordovician to Pennsylvanian, of the Green River Basin area, Wyoming, *in* Guidebook Tenth Annual Field Conference: Wyoming Geological Association, p.43-47.

Wilson, J. L., 1975, Carbonate facies in geologic history: Berlin-Heidelberg-New York, Springer-Verlag, 471 p.

Wilson, J.L., and Pilatzke, R.H., 1987, Carbonate-evaporite cycles in lower Duperow formation of the Williston Basin, *in* Longman, M.W., ed., Williston Basin: Anatomy of a cratonic oil province, Rocky Mountain Association of Geologists, p. 119-146.

Winfrey, W.M.Jr., 1960, Stratigraphy, correlation, and oil potential of the Sheep Pass Formation, east-central Nevada: *in* Boettcher, J.W. and Sloan, W.W. Jr., Guidebook to the Geology of east-central Nevada: Intermountain Association of Petroleum Geology and Eastern Nevada Geological Society, 11th Annual Field Conference, Salt Lake City, Utah, p.126-133.

Winterer, E.L., and Murphy, M.A., 1958, Silurian reef complex and associated facies, central Nevada: Geological Society America Bulletin, v.69, p.1711.

Wire, J.C.D., 1961, Geology of the Currant Creek District, Nye and White Pine Counties, Nevada: unpublished MA thesis, University of California, Los Angeles, 154 p.

Woodhead, J.D., Herst, J.M., and Simonson, B.M., 1998, Isotopic dating of an Archean bolide impact horizon, Hamersley basin, Western Australia: *Geology*, v. 26, p. 47-50.

- Xun, Z., and Fairchild, I.J., 1987, Mixing zone dolomitization of Devonian carbonates, Guangxi, south China, *in* Marshall, J.D., ed., Diagenesis of sedimentary sequences: Geological Society Special Publication n. 36, p. 157-170.
- Yang, W., 1989, Facies analysis of the middle member of Devonian Lost Burro Formation, Death Valley, California: *Journal of Natural Science, California State University, Fresno*, v. 4, p. 31-35.
- Yang, W., Harmsen, F., and Kominz, M.A., 1995, Quantitative analysis of a cyclic peritidal carbonate sequence, the Middle and Upper Devonian Lost Burro Formation, Death Valley, California--a possible record of Milankovitch climatic cycles: *Journal of Sedimentary Research*, v. B65, p. 306-322.
- Yang, W., Kominz, M.A., and Major, R.P., 1998, Distinguishing the roles of autogenic versus allogenic processes in cyclic sedimentation, Cisco Group (Virgilian and Wolfcampian), north-central Texas: *Geological Society of America Bulletin*, v. 110, p. 1333-1353.
- Yarmanto, 1992, Sedimentology and stratigraphic setting of a Devonian carbonate breccia, northern Pahranaagat Range, Nevada: unpublished M.S. thesis, Colorado School of Mines, Golden, 218 p.
- Yoshida, S., Willis, A., and Miall, A.D., 1996, Tectonic control of nested sequence architecture in the Castlegate Sandstone (Upper Cretaceous), Book Cliffs, Utah: *Journal of Sedimentary Research*, v. 66, p. 737-748.
- Young, J.C.D., 1955, Geology of the southern Lakeside Mountains, Utah: *Utah Geological and Mineral Survey Bulletin* 56, 110 p

Zhang, M., O'Reilly, S.Y., and Chen, D., 1999, Location of Pacific and Indian mid-ocean ridge-type mantle in two time slices: Evidence from Pb., Sr, and Nd isotopes for Cenozoic Australian basalts: *Geology*, v. 27, p. 39-42.

Zenger, D.H., and Pearson, F.E., 1969, Stratigraphy and petrology of the Lost Burro Formation, Panamint Range, California: California Department of Natural Resources, Division of Mines, Special Report 100, p. 45-65.

Ziegler, W., and Sandberg, C.A., 1990, The Late Devonian standard conodont zonation: *Courier Forschungsinstitut Senckenberg*, v. 121, p. 1-115.



ELSEVIER

Earth and Planetary Science Letters 170 (1999) 181–196

EPSL

www.elsevier.com/locate/epsl

The correlation between $^{18}\text{O}/^{16}\text{O}$ ratios of meteoric water and surface temperature: its use in investigating terrestrial climate change over geologic time

Henry C. Fricke*, James R. O'Neil

Department of Geological Sciences, University of Michigan, Ann Arbor, MI 48109-1063, USA

Received 12 June 1998; revised version received 24 March 1999; accepted 6 April 1999

Abstract

Correlations between mean annual temperature (MAT) and the weighted average oxygen isotope composition of yearly precipitation ($\delta^{18}\text{O}_{\text{pt}}$) are well-known, but the utility of modern relations to make reliable estimates of temperature change over geological time is uncertain. This question has been addressed by using seasonal subsets of the global data base of temperature and isotopic measurements to represent two different climate modes. A comparison of middle- to high-latitude $\delta^{18}\text{O}_{\text{pt}}$ /temperature relations for each climate mode reveals (1) a significant offset between them, and (2) a difference in the strength of their correlations. The offset in relations is due to differences in temperature and water vapor budget in the tropics, and can lead to serious underestimates of temperature change. Differences in the strength of correlations arise from the influence of climate mode-specific, non-temperature factors on $\delta^{18}\text{O}_{\text{pt}}$. The overall result is that no single relation can be used in all cases to make unambiguous temperature estimates using a temporal record of $\delta^{18}\text{O}_{\text{pt}}$ values. One way to overcome these problems is to reconstruct $\delta^{18}\text{O}_{\text{pt}}$ /temperature relations for the time periods being investigated. If an appropriate proxy for $\delta^{18}\text{O}_{\text{pt}}$ is available, it may also be possible to estimate temperature *without* relying on $\delta^{18}\text{O}_{\text{pt}}$ /temperature relations. A promising alternative to these options is to use records of $\delta^{18}\text{O}_{\text{pt}}$ to test predictions of global climate models, an approach that may allow a reliable and more complete reconstruction to be made of climate change over geologic time. © 1999 Elsevier Science B.V. All rights reserved.

Keywords: O-18/O-16; meteoric water; isotope ratios; seasonal variations; paleoclimatology; climate; paleotemperature

1. Introduction

Over the last several decades, investigation of the stable isotope systematics of precipitation has added a great deal to our understanding of the source and transport of moisture in the atmosphere. One

of the most important contributions resulting from this research was the identification of a good correlation between mean annual surface temperature and the weighted oxygen isotope composition of precipitation ($\delta^{18}\text{O}_{\text{pt}}$) at mid- to high-latitude regions, whereby higher temperatures correspond to higher $\delta^{18}\text{O}_{\text{pt}}$ values [1–3]. Although this relation is not perfectly understood, it is generally agreed that $\delta^{18}\text{O}_{\text{pt}}$ /temperature covariance is consistent with continual lowering of $^{18}\text{O}/^{16}\text{O}$ of vapor in the air mass due

*Corresponding author. Present address: Geophysical Laboratory, Carnegie Institution of Washington, Washington, DC 20015, USA. Fax: +1 202 686 2410; E-mail: fricke@gl.ciw.edu

to preferential incorporation of ^{18}O into condensate during adiabatic processes of cooling [1–5]. The air masses lose water as they move along surface temperature gradients from tropical to polar latitudes, inland from the sea, or to higher elevations. It should be stressed that, while the temperature of the air mass controls condensation, it is exchange between condensate and water vapor at the warmer temperatures of the cloud base that provides the most reasonable physical basis for the relation between surface temperature and $\delta^{18}\text{O}_{\text{pt}}$ values [5].

In contrast to phenomena occurring at higher latitudes, there is no correlation between surface temperature and $\delta^{18}\text{O}$ values of precipitation in the tropics [1–3]. Tropical regions are characterized by converging air masses that are forced to move vertically rather than horizontally. As a result they are cooled predominately by convection in atmospheric towers, while surface temperature gradients remain negligible. Although temperature does not correlate with $\delta^{18}\text{O}_{\text{pt}}$ in the tropics, a negative correlation has been observed between the amount of rainfall and $\delta^{18}\text{O}_{\text{pt}}$ values at tropical island locations, and is termed the *amount effect* [1]. It is caused by gradual saturation of air below the cloud base as precipitation proceeds, an effect that diminishes any shift to higher $\delta^{18}\text{O}_{\text{pt}}$ values caused by evaporation during precipitation [1], and by the preferential loss of ^{18}O from an air mass as rainout continues.

The oxygen isotope composition of past precipitation can be measured directly on ice cores, ground waters, fluid inclusions, or estimated by measuring the oxygen isotope ratio of a proxy material such as skeletal remains of animals, lake sediments, and soil minerals that formed in equilibrium with surface or ground waters. Because other kinds of geochemical climate records are lacking for terrestrial environments, the $\delta^{18}\text{O}_{\text{pt}}$ /temperature relation for middle- to high-latitude precipitation has garnered a great deal of attention as a possible tool for investigating terrestrial climatic conditions from the Mesozoic to the present [6]. Nevertheless, it remains difficult to make quantitative climatic interpretations of a temporal record of $\delta^{18}\text{O}_{\text{pt}}$ values. Factors other than temperature are affected by climate change, and they too can have a local influence on how $\delta^{18}\text{O}_{\text{pt}}$ changes over time. For example, during the Holocene–glacial transition, a change in the position of boundaries

between air masses played a predominant role in determining $\delta^{18}\text{O}_{\text{pt}}$ at some high latitude locations [7,8]. Even if it *could* be ascertained that temperature was the underlying cause of variations in $\delta^{18}\text{O}_{\text{pt}}$ over time in a given location, many observations lead to the conclusion that the present-day relation between temperature and $\delta^{18}\text{O}_{\text{pt}}$ may not be the appropriate one to use in estimating temperature change over time [9–13].

The goal of this paper is to consider those problems associated with the $\delta^{18}\text{O}_{\text{pt}}$ paleothermometer from the perspective of global changes in climate, and to discuss ways to overcome them. The global perspective is provided by using seasonal subsets of isotopic and temperature data from a global network of collection stations to represent the conditions that prevail under fundamentally different global climate modes. Although changes in season are not completely analogous to longer-term changes in climate mode, the stable isotope systematics of summer and winter precipitation are well documented and provide a simple model for identifying understanding which factors influence the relation between $\delta^{18}\text{O}_{\text{pt}}$ and temperature thus allowing a more sensible interpretation to be made of $\delta^{18}\text{O}_{\text{pt}}$ data. An analysis of the seasonal data indicates that it should be possible to use records of $\delta^{18}\text{O}_{\text{pt}}$ from proxy data as a quantitative paleothermometer over geologic time by reconstructing $\delta^{18}\text{O}_{\text{pt}}$ /temperature relations in that region for time periods in the past. In addition to their potential as a paleothermometer, records of $\delta^{18}\text{O}_{\text{pt}}$ may also prove ideal for testing predictions of climate change made using global climate models.

2. Methods

Monthly averages of temperature and $\delta^{18}\text{O}_{\text{pt}}$ from the global network of weather stations operated by the IAEA–WMO (International Atomic Energy Agency–World Meteorological Organization) [14] are grouped by season to create average values at each locality for summer and winter (Table 1). Values for each season are then compared in order to determine the nature of global patterns in temperature and $\delta^{18}\text{O}_{\text{pt}}$ under climate conditions, or modes, that are distinctly warmer and cooler than the mean annual conditions that exist at present. Patterns con-

Table 1
Summer and winter averages for global climate and isotope data

Station	Latitude (°)	Winter oxygen ($\delta^{18}\text{O}$)	Summer oxygen ($\delta^{18}\text{O}$)	Winter temperature (°C)	Summer temperature (°C)
Tropics					
Addis Abada	9	0.39	-1.22	15.58	15.87
Alice Springs*	23.8	-3.71	-4.41	12.21	27.87
Asuncion*	25.27	-3.5	-6.3	19.4	28.7
Bamako	12.63	no rain	-4.58	25.75	27.5
Bangkok	13.73	-2.06	-5.51	26.63	28.63
Barbados Is.	13.07	0.8	-1.82	25.57	27.28
Barranquilla	10.88	-5.2	-4.08	26.53	27.93
Belem*	1.43	-0.77	-2.16	25.89	25.8
Bogata	4.7	-4.95	-10.57	12.88	13.14
Bombay	18.9	-0.2	-1.23	25.1	28
Brasilia*	15.85	-1.78	-5.15	19.1	21.65
Cayenne	4.83	-1.14	-3.83	25.17	25.25
Ceara Minim*	5.8	-1.34	-1.23	24.45	26.28
Corrientes*	24.47	-3.51	-7.84	15.66	25.85
Culaba*	15.6	-5.87	-0.89	24.1	26.7
Dar es Salaam*	6.88	-1.21	-2.16	23.82	27.33
Darwin*	12.43	-2	-4.51	25.68	28.87
Djajapura*	2.53	-4.93	-5.5	25.17	27.07
Djakarta*	6.18	-4.62	-5.93	26.8	26.58
Entebbe	0.05	-1.57	-2.37	20.85	21.95
Fortaleza*	3.72	-1.82	-1.57	25.59	26.99
Geneina	13.48	no rain	-1.41	22.71	27.4
Guilin	25.21	-8.2	-2.9	9	27.8
Hong Kong	22.32	-2.45	-7.02	16.15	25.01
Howard AFB	8.92	-1.12	-5.94	27.06	27.07
Izobamba*	0.37	-11.39	-8.83	10.93	11.21
Jedda	21.3	-1.28	no rain	24.14	30.78
Kano	12.05	no rain	-3.56	22.38	26.72
Karachi	24.9	-0.83	-3.44	17.87	29.36
Khartoum	15.6	no rain	-1.44	23.22	31.82
Kinshasa*	4.37	-2.03	-3.42	22.3	24.73
Kuming	25.05	-11.7	-3.92	19.7	8.9
Ko Samui	9.28	-3.35	-3.39	26.83	28.28
Ko Sichang	13.17	-5.25	-5.27	26.59	29.97
Luang P.	19.88	-3.1	-7.48	21.64	28.01
Madung*	5.22	-5.04	-8.76	26.78	26.25
Malange	9.55	-0.67	-4.65	22.85	22.34
Manaus*	3.12	-2.82	-4.19	26.9	26.35
Manila	14.52	-3.11	-6.18	25.3	27.5
Maracay	10.25	-2.13	-3.54	23.52	24.47
Menongue*	14.67	0.21	-6.34	16.65	21.26
Muguga*	1.22	-1.53	-2.54	n.m.	n.m.
N'djamen	12.13	no rain	-2.56	24.28	27.7
Ndola*	13	no rain	-6.59	18.09	22.67
P. Velho*	8.77	-3.72	-6.82	24.7	25.4
Pretoria*	25.73	-0.55	-3.53	12.25	21.94
Rio D.*	22.9	-2.58	-4.76	21.57	26.13
Salvador*	13	-1.54	-0.89	23.76	26.23
Salta*	24.78	-2.03	-5.64	11.11	18.47
San Gabriel	0.13	-2.77	-3.87	25.87	24.83
San Juan Is.	18.43	-1.05	-1.57	25.42	28.17

SE ROA 37365

Table 1 (continued)

Station	Latitude (°)	Winter oxygen ($\delta^{18}\text{O}$)	Summer oxygen ($\delta^{18}\text{O}$)	Winter temperature (°C)	Summer temperature (°C)
San Salvador	13.7	-3.44	-6.47	22.27	23.88
Shillong	25.57	-1.71	-5.93	12.25	21
Singapore	1.35	-6.21	-6.76	25.6	26.63
Ushulala*	54.78	-12.07	-10.11	2.2	9.68
Veracruz	19.2	-0.61	-3.97	21.86	28.22
Windhoek*	22.57	-1.15	-4.02	14.25	22.99
Yap Is.	9.49	-3.41	-6.4	26.84	27.07
Middle latitudes					
Adana	36.98	-6.21	-2.75	10.44	26.91
Adelaide*	34.93	-4.83	-3.74	12.06	21.9
Alexandria	31.2	-4.23	no rain	9.01	25.38
Amman, Jor.	31.98	-5.75	no rain	n.m.	n.m.
Ankara	39.95	-11.12	-4.13	1.2	21.65
Antanan*	36.88	-3.18	-8.53	14.41	20.2
Antalya	36.88	-6.08	-3.9	10.34	27.12
Astrakhan	46.25	-11.6	-5.85	-3.17	27.22
Athens	37.9	-6.96	-2.67	10.49	25.43
Atikokan	48.75	-22.79	-9.53	-16.44	15.8
Barcelona	41.38	-6.21	-3.06	9.69	22.37
Bahrain	26.27	-0.05	no rain	17.92	33.5
Batumi	41.39	-10.19	-6.56	8.03	22.4
Beer Shava	31.15	-5.63	no rain	12.46	25.47
Beja, Port.	38.01	-5.94	-4.19	10.64	23.68
Berlin	52.07	-10.6	-7.03	0.68	17.39
Bern	46.92	-12.66	-7.12	0.32	17.26
Bet Dagan	32	-5.1	no rain	13.06	25.57
Brest	52.07	-13.66	-7.23	-2.04	17.3
Brisbane*	27.43	-4.12	-3.42	16.22	24.95
Buenos Aires*	34.58	-4.35	-3.09	11.06	23.33
Cape Grim*	40.68	-5.07	-2.78	10.28	15.11
Changsha	28.1	-4.63	-8.03	6.32	28.3
Chicago	41.78	-12.34	-3.09	-3.64	22.63
Chihuahau	28.63	-9.25	-5.6	10.42	24.97
Coshocton	40.37	-11.4	-4.7	n.m.	n.m.
Crete	35.2	-6.83	no rain	13.28	30.6
Edmonton	53.57	-27.06	-13.85	-12.12	16.47
Faro	37.01	-4.87	-1.57	12.85	22.85
Flagstaff	35.13	-10.93	-3.63	-1.21	16.75
Fuzhou	26.09	-4.75	-6.85	12.53	28.92
Genoa	44.42	-6.16	-3.73	7.6	21.29
Gibraltar	36.15	-4.62	-2.17	13.6	22.98
Gimli	50.62	-24.81	-10.24	-16	18.08
Goose Bay	53.32	-19.91	-12.45	-13.47	13.5
Gorki	56.13	-15.68	-9.31	-8.2	17.44
Grimsel	46.57	-16.83	-10.3	-5.04	8.42
Groningen	53.21	-9.1	-6.3	2.65	16.56
Guiyang	26.35	-4.26	-9.5	5.5	24.59
Guttane, Swit.	46.65	-16.03	-8.6	-1	14.25
Har Kanan	32.97	-6.83	no rain	8.85	23.73
Hatteras	35.07	-4.84	-3.49	7.98	24.84
Kabul	34.67	-10.57	-1.12	-0.56	22.92
Kalinin	56.54	-16.76	-8.38	-7.81	16.4

SE ROA 37366

JA_8872

Table 1 (continued)

Station	Latitude (°)	Winter oxygen ($\delta^{18}\text{O}$)	Summer oxygen ($\delta^{18}\text{O}$)	Winter temperature (°C)	Summer temperature (°C)
Kataia*	35.07	-5.36	-3.64	12	18.76
Keyworth	52.52	-8.7	-5.6	7.61	20.63
Kirov	58.39	-16.77	-9.91	-10.83	16.79
Konstanz	47.68	-12.78	-6.98	0.72	17.8
Krakow	50.07	-12.92	-7.15	-1.38	17.07
L'vov	49.49	-14.05	-7.77	-2.33	16.54
La Suela*	30.58	-5.5	-4.76	12.15	23.63
Leige	50.7	-8.73	-5.05	n.m.	n.m.
Lista	58.1	-7.55	-5.35	1.12	13.68
Ljubljana	46.04	-11.67	-6.9	0.17	19.29
Loncaro, Swit.	46.17	-12.17	-5.9	3.86	20.1
Malan*	33.97	-3.57	-1.92	12.05	20.05
Meiringe, Swit.	46.73	-15.24	-7.83	0.19	15.7
Melbourne*	37.82	-5.66	-4.16	10.52	20.08
Mendoza*	32.88	-10.8	-3.5	8.2	23.8
Minsk	52.52	-14.46	-8.81	-5.21	19
Moskova	55.75	-16.3	-7.69	-7.37	17.92
Najing	32.05	-7.4	-9.64	2.86	26.39
Nanuncun*	34.03	-9.8	-3.69	6.95	22.37
New Dehli	28.58	-0.87	-3.83	15.59	31.37
Odessa	46.48	-11.91	-6.76	-0.31	19.89
Ottawa	45.32	-16.91	-7.83	-9.05	19.35
Perm	58.01	-18.23	-3.53	-12.11	16.4
Perth*	31.95	-3.97	-1.79	13.96	23.83
Petzenkirchen	48.15	-13.63	-6.39	0.08	17.43
Pohang	36.03	-6.13	-8.47	1.99	23.51
Porta, Port.	41.09	-6.25	-4.04	9.29	23.11
Porto Alegre*	30.08	-4.17	-5.29	14.83	24.11
Puerto Monte*	41.47	-6.88	-5.17	6.62	13.8
Quiqihar	47.23	-23.77	-9.51	-15.9	21.19
Rhodes	36.38	-4.97	no rain	11.15	26.1
Riga	56.97	-11.45	-8	-4.44	15.77
Rjazan	54.37	-15.1	-7.2	-7.66	18.27
Rostov	47.25	-11.42	-4.97	-2.88	20.93
Ryori	39.02	-9.2	-8.2	0.33	18.94
Sant. del. Sst*	27.78	-2.9	-5.07	12.28	25.91
Santiago*	33.45	-8.73	no rain	8.78	21.25
Saratov	51.34	-15.39	-7.26	-7.54	21.31
Shijiazuang	38.02	-11.21	-7.53	-0.74	25.77
Sidi Barani	31.63	-5.76	no rain	19.67	24.69
Simcoe	42.85	-15.72	-6.35	-5.31	20.26
St. Agathe	46.05	-13.7	-8.11	-11.57	19.23
St. Petersburg	59.58	-13.94	-10.01	-5.84	16.4
Stuttgart	48.83	-10.77	-5.87	1.25	17.72
Taastrap	55.67	-11.15	-7.49	n.m.	n.m.
Teheran	35.68	-6.49	-1.57	4.66	28.04
The Pas	53.97	-26.14	-13.41	-17.78	16.74
Thonon-Bains	46.22	-11.87	-6.41	2.46	18.9
Tianjin	39.55	-11.78	-7.66	-0.58	27.93
Tokyo	35.68	-8.46	-6.98	6.04	24.72
Truro	45.37	-12.66	-7.02	-4.7	17.58
Tunis	36.83	-5.01	1.39	11.85	26.39
Ulan Bator	47.45	-14.83	-7.48	-17.9	15.66

SE ROA 37367

Table 1 (continued)

Station	Latitude (°)	Winter oxygen ($\delta^{18}\text{O}$)	Summer oxygen ($\delta^{18}\text{O}$)	Winter temperature (°C)	Summer temperature (°C)
Valentia	51.93	−8.9	−5.76	7.05	14.47
Victoria	48.25	−10.89	−8.51	4.97	16.42
Vienna	48.64	−13.65	−6.68	0.57	19.17
Volgada	59.17	−17.56	−9.69	−10.72	15.39
Waco	31.62	−6.39	−2.03	8.88	29
Wallingford	51.37	−8.12	−5.21	7.34	21.08
Wirzburg	49.8	−9.97	−6.29	0.81	17.56
Wynard	51.77	−25.85	−13	−14.08	15.15
Xian	34.3	−7.64	−5.75	1.47	25.16
Yinchuan	38.3	−15.51	−6.32	−5.53	22.2
Zagreb	45.49	−11.88	−6.28	1.87	22.01
Polar latitudes					
Amderma	69.46	−19.54	−11.91	−18.63	5.1
Archanglsk	64.58	−18.61	−9.44	−12.09	14.3
Barrow	71.3	−21.41	−13.72	−25.94	2.35
Bethel	60.78	−14.81	−10.36	−14.3	11.36
Ft. Smith	60.02	−25.92	−15.06	−23.48	14.78
Groennedal	61.22	−13.22	−11.39	−4.26	7.29
Halley Bay*	75.5	−26.09	−14.58	−27.65	−6.15
Isfjord	78.07	−10.39	−8.28	−11.78	3.51
Murmansk	68.58	−15.73	−3.45	−10.61	11.38
Nord	81.6	−29.64	−17.22	−29.93	1.2
Pechora	65.07	−20.37	−10.94	−17.14	13.48
Prins Christian	60.02	−12.56	−9.72	−3.81	5.99
Reykjavik	64.13	−8.1	−7.6	0.1	10
Scoresbury	70.5	−15.67	−10.01	−15.6	1.7
Thule	76.52	−30.37	−18.87	−23.67	3.06
Whitehorse	60.72	−22.64	−18.02	−15.42	12.77

Temperature and $\delta^{18}\text{O}_{\text{pt}}$ for summer and winter seasons for all IAEA weather stations with at least three years of isotopic data [10]. The mean monthly data for December, January, and February are averaged to represent winters in the northern hemisphere and summers in the southern hemisphere, while data for June, July, and August represent the opposite season. A single asterisk ‘*’ indicates that a given locality is located in the southern hemisphere. The weather stations are also separated spatially into tropical, middle latitude, and polar zones with approximate boundaries at 25° and 60° latitude.

structured in this way may not accurately represent conditions prevailing during periods in the past when *mean annual* climate was different, but they do provide a heretofore unavailable means of investigating the effects of global changes in temperature and insolation in an empirical rather than theoretical manner.

All IAEA–WMO stations with at least three years of $\delta^{18}\text{O}_{\text{pt}}$ data are included in this study. Including shorter records greatly increases the geographic area represented by the data set, but also increases the possibility that these records are inappropriate because of the inclusion of years with anomalous temperature and $\delta^{18}\text{O}_{\text{pt}}$. The months of June, July, and August are defined as *summer* in the northern

hemisphere and *winter* in the southern hemisphere, while December, January, and February define *winter* in the northern hemisphere and *summer* in the southern hemisphere. These months were chosen to facilitate comparison with previous work on seasonal differences in temperature and $\delta^{18}\text{O}_{\text{pt}}$ values [11,15], and to isolate seasonal extremes in climate variables and $\delta^{18}\text{O}_{\text{pt}}$ values from the generally ‘transitional’ seasons of spring and fall. Seasonal extremes, however, may not coincide exactly with these months at all localities. Near the equator in particular, the position of the boundary between northern and southern hemisphere air masses (intertropical convergence zone) is highly variable, so designating the months

of June, July and August as winter or summer may not be as meaningful for stations at low latitude.

The IAEA–WMO stations have also been assigned to groups defined by ranges of latitude in an effort to isolate isotopic and temperature differences between tropical, middle-latitude, and polar air masses. It should be noted that air mass boundaries are by nature diffuse and variable in position, so there may be regional differences in circulation patterns that cannot be distinguished. Nevertheless, as a first-order approximation, 25° latitude will be considered the boundary between tropical and mid-latitude air masses, and 60° latitude will be considered the boundary between mid-latitude and polar air masses. These latitudes roughly correspond to the bands of high and low atmospheric pressure, respectively, that characterize the three Hadley cells associated with idealized atmospheric circulation.

3. Results

Once the IAEA–WMO data are assigned to different climate modes and latitudinal bands, they can

be plotted in a number of ways. Of interest for this study are latitudinal gradients in temperature and $\delta^{18}\text{O}_{\text{pt}}$ under summer and winter climate modes, and the resulting $\delta^{18}\text{O}_{\text{pt}}$ /temperature relations. Latitudinal temperature gradients are illustrated in Fig. 1. As expected, summer temperatures are always higher than winter temperatures, but the *magnitude* of this difference (seasonality) increases with latitude because high latitude regions undergo more extensive heating and cooling in response to seasonal changes in insolation than do the tropics. The result is that the latitudinal temperature gradient for summer conditions of $\sim 0.22^\circ\text{C}/^\circ$ latitude is about half the $\sim 0.44^\circ\text{C}/^\circ$ latitude range observed for winter conditions. Another important feature of Fig. 1 is the dependence of the temperature/latitude relation on geographic location. Temperatures vary irregularly in the tropics whereas, at higher latitudes, there is a systematic decrease in temperature with latitude.

It is evident from Fig. 2 that trends in $\delta^{18}\text{O}_{\text{pt}}$ with latitude are similar to those with temperature. There is no systematic variation of $\delta^{18}\text{O}_{\text{pt}}$ values in the tropics while at higher latitudes $\delta^{18}\text{O}_{\text{pt}}$ decreases regularly with distance from the equator. In addition,

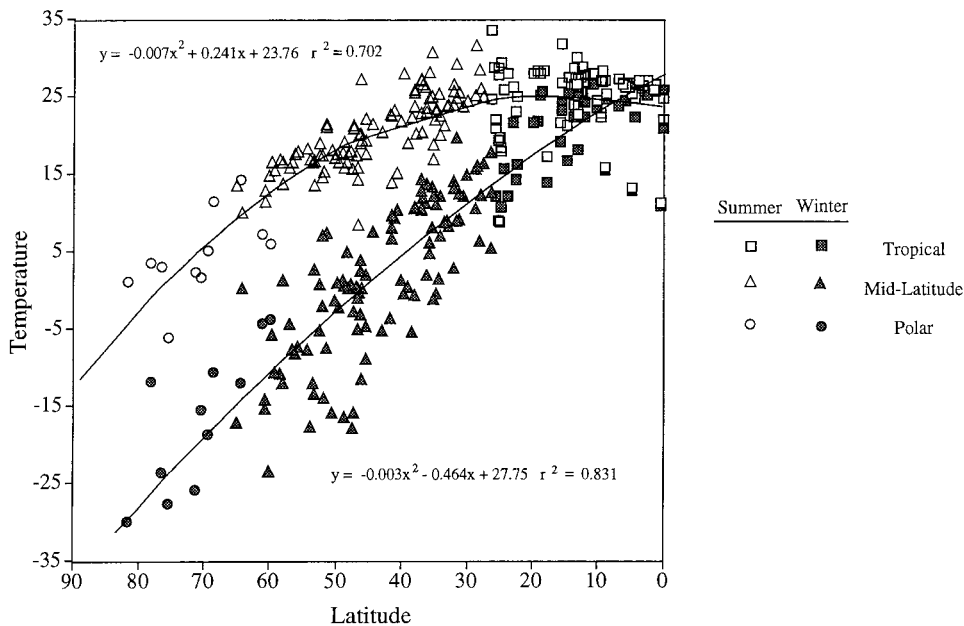


Fig. 1. Latitude versus temperature for summer and winter climate modes. Each point represents averages for an individual IAEA/WMO station. Trends for both modes are characterized by flat slopes in the tropics that become steeper with increasing latitude, and by similar correlation coefficients. Temperatures are uniformly higher and global temperature ranges are smaller under summer climate conditions.

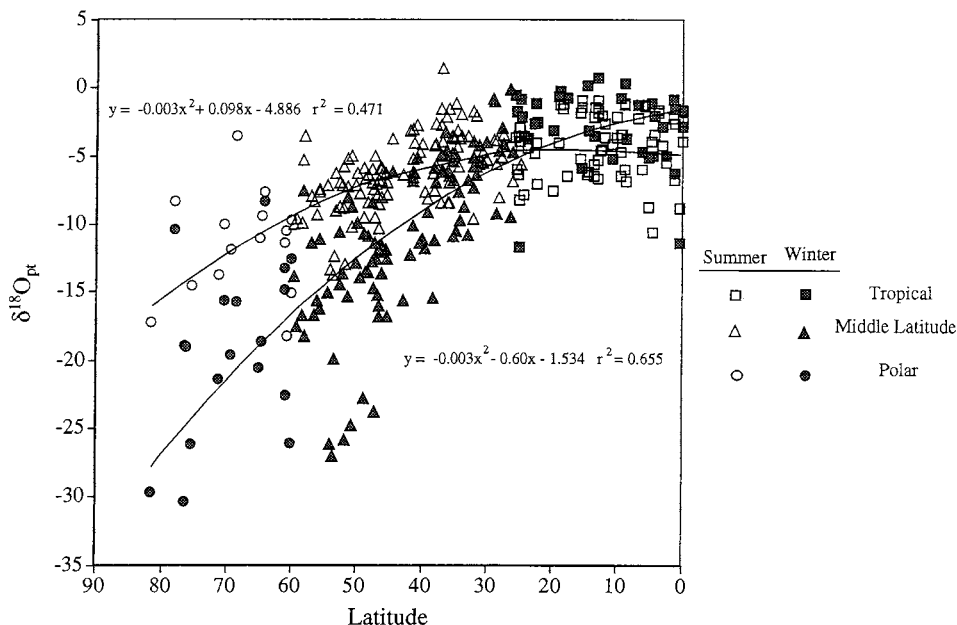


Fig. 2. Latitude versus $\delta^{18}\text{O}_{\text{pt}}$ value of precipitation for summer and winter climate modes. Each point represents averages for an individual IAEA/WMO station. Trends are similar to those in Fig. 1 except for the crossover in trends for summer and winter climate modes, and the weaker correlation for summer relative to winter climate conditions. These features demonstrate the influence of air mass rainout and evapotranspiration on $\delta^{18}\text{O}_{\text{pt}}$ in the tropics and extra-tropics, respectively.

gradients in $\delta^{18}\text{O}_{\text{pt}}$ with increasing latitude are shallower for summer than for winter climate modes. The similarities in latitudinal temperature gradients emphasize the role of air mass cooling in forming condensate that preferentially incorporates ^{18}O , thus lowering the $\delta^{18}\text{O}_{\text{pt}}$ of subsequent precipitation. In contrast to behavior at higher latitudes, however, $\delta^{18}\text{O}_{\text{pt}}$ values in the tropics are *lower* in summer than they are in winter. The resulting inversion of $\delta^{18}\text{O}_{\text{pt}}$ /latitude trends is a reflection of the *amount effect*, and is due to the greater amount of precipitation that falls in the tropics in summer relative to winter ([3], fig. 19). Lastly, the correlation between $\delta^{18}\text{O}_{\text{pt}}$ and latitude depends strongly on climate mode, with the summer correlation being worse than the winter correlation. Poorer correlations probably arise from the influence of local factors other than temperature on $\delta^{18}\text{O}_{\text{pt}}$, and will be discussed below.

The global relation between temperature and $\delta^{18}\text{O}_{\text{pt}}$ is expressed most clearly by comparing the two variables directly, as has been done for weighted $\delta^{18}\text{O}_{\text{pt}}$ and mean annual temperature in the past [1–3]. What is new in the plot shown in Fig. 3 is a

view of this same relation as it exists for different climate modes, as represented by data for summer and winter seasons. Although not shown, the mean annual relation lies between, and parallels, those for summer and winter climate conditions. Three important aspects of this plot are (1) the relatively invariant slope of the $\delta^{18}\text{O}_{\text{pt}}$ /temperature relations at mid- to high-latitudes regardless of climate mode, (2) the significant offset between $\delta^{18}\text{O}_{\text{pt}}$ /temperature relations under summer and winter climatic conditions, and (3) the weaker correlation that exists under summer compared to winter conditions. The constant slope implies that any steepening or shallowing of gradients in the temperature/latitude trend outside of the tropics is effectively mirrored by similar modifications of gradients in the $\delta^{18}\text{O}_{\text{pt}}$ /latitude relation. Thus the role of temperature change in controlling air mass condensation, and hence $\delta^{18}\text{O}_{\text{pt}}$ change on a global scale, is reemphasized. The offset between $\delta^{18}\text{O}_{\text{pt}}$ /temperature relations, however, indicates that *absolute* $\delta^{18}\text{O}_{\text{pt}}$ values at each locality are determined by factors that are unique to a given climate mode. Lastly, $\delta^{18}\text{O}_{\text{pt}}$ /temperature relations with dif-

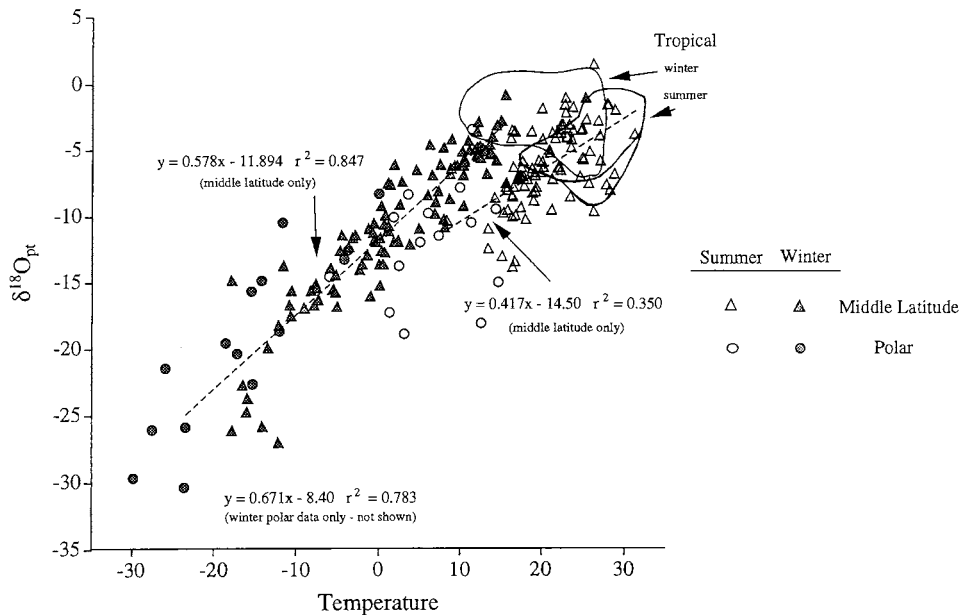


Fig. 3. $\delta^{18}\text{O}$ value of precipitation versus temperature for summer and winter climate modes. Each point represents averages for an individual IAEA/WMO station. Stations from tropical latitudes (individual data points not shown) and the six higher-latitude stations affected by the Asian monsoon are not included in calculating the slope and intercept of $\delta^{18}\text{O}_{\text{pt}}$ /temperature relations. Relations for summer and winter climate modes have similar slopes, but are significantly offset due to the existence of different intercepts. As in Fig. 2, the correlation for summer climate mode is weaker than for winter due to non-temperature factors such as evapotranspiration, which may also account for the relatively high values for precipitation at polar stations.

ferent correlation coefficients indicate that factors other than temperature influence $\delta^{18}\text{O}_{\text{pt}}$ to varying degrees depending on climate mode.

4. Problems using a single $\delta^{18}\text{O}_{\text{pt}}$ /temperature relation as a paleothermometer

In general, the relations between latitude, temperature, and $\delta^{18}\text{O}_{\text{pt}}$ (Figs. 1–3) indicate that surface temperature plays an overriding role in determining $\delta^{18}\text{O}_{\text{pt}}$ values on a global scale. Therefore any temporal change in climate mode that modifies latitudinal gradients in temperature will also modify global condensation patterns and hence $\delta^{18}\text{O}_{\text{pt}}$ at any given latitude (Fig. 2). In order to use this covariance as a quantitative paleothermometer, however, it is necessary to evaluate $\delta^{18}\text{O}_{\text{pt}}$ /temperature relations that can vary systematically with climate mode, and the influence of factors other than temperature on $\delta^{18}\text{O}_{\text{pt}}$.

4.1. Offset of $\delta^{18}\text{O}_{\text{pt}}$ /temperature relations with climate mode

4.1.1. Effects on estimating past temperatures and temperature change

One consequence of having climate-dependent relations between $\delta^{18}\text{O}_{\text{pt}}$ and temperature is that no single relation can be used unambiguously to infer absolute temperature *for all time periods* in the geological past. This restriction is particularly serious for ‘Icehouse’ and ‘Greenhouse’ time periods when the global distribution of heat and moisture, and hence intercepts of $\delta^{18}\text{O}_{\text{pt}}$ /temperature relations, would likely have been very different from what they are at present (Fig. 3). For example, the mid-Cretaceous is characterized by warmer ocean temperatures and shallower latitudinal temperature gradients than at present [16], and it has been noted by previous authors [9] that the present-day weighted $\delta^{18}\text{O}_{\text{pt}}$ /MAT relation is probably not valid for inferring temperatures at this time, especially in polar regions.

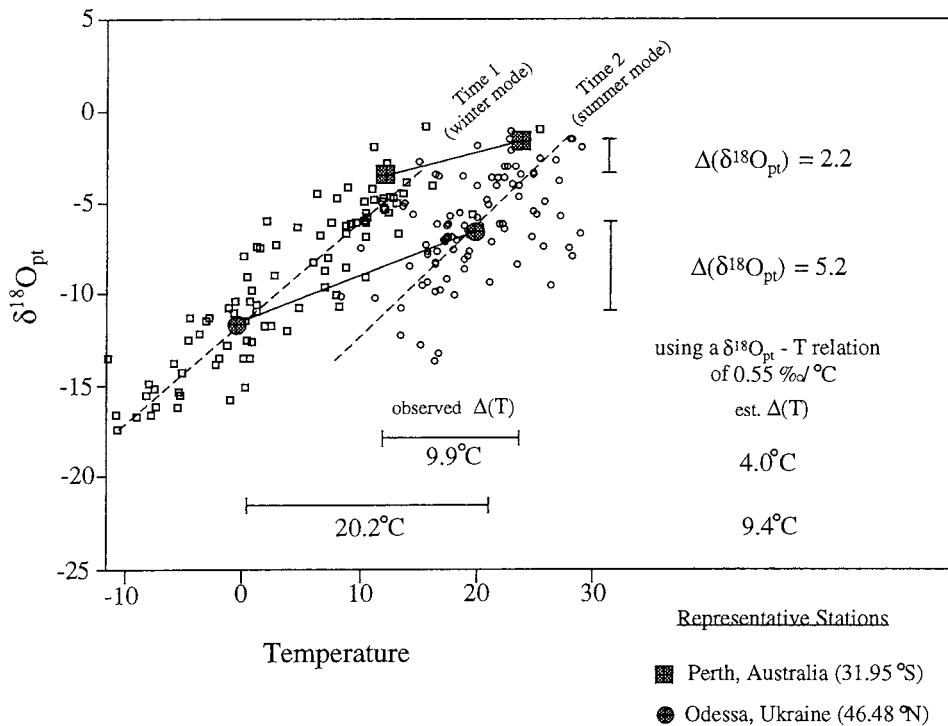


Fig. 4. Effect of two different $\delta^{18}\text{O}_{\text{pt}}$ /temperature relations on paleotemperature estimates. Summer and winter data for precipitation at two representative middle-latitude localities (Perth, Australia, 31.95°S; Odessa, Ukraine, 46.48°N) are plotted along with the $\delta^{18}\text{O}_{\text{pt}}$ /temperature relations for summer and winter climate modes. If a hypothetical temperature change over time takes place during a climate change from winter to summer conditions (or visa versa), and it is assumed that the slope of $\delta^{18}\text{O}_{\text{pt}}$ /temperature relations do not change, the estimates of temperature change are almost half of those actually observed. This difference arises because the *temporal* $\delta^{18}\text{O}_{\text{pt}}$ /temperature relations (solid lines) are shallower than *spatial* $\delta^{18}\text{O}_{\text{pt}}$ /temperature relations (dashed lines).

Variable $\delta^{18}\text{O}_{\text{pt}}$ /temperature relations also affect paleothermometry by making it difficult to quantify the amount of temperature change *over time* if there is a dramatic modification in climate mode. This difficulty arises because a comparison of data representing climate modes with offset $\delta^{18}\text{O}_{\text{pt}}$ /temperature relations results in an underestimate of temperature change. To illustrate this point, temperature and $\delta^{18}\text{O}_{\text{pt}}$ data for two representative middle-latitude stations (Perth, Australia and Odessa, Ukraine) are plotted along with global $\delta^{18}\text{O}_{\text{pt}}$ /temperature relations for summer and winter climate modes (Fig. 4). Proxy records of weighted $\delta^{18}\text{O}_{\text{pt}}$ covering a dramatic global change from cooler to warmer mean annual climate conditions at these localities would record changes of +2.2‰ and +5.2‰, respectively (vertical bars in Fig. 4). Using only the slope of the $\delta^{18}\text{O}_{\text{pt}}$ /temperature relation, which has a rela-

tively constant value of $\sim 0.55\text{‰}/\text{°C}$, these temporal changes in $\delta^{18}\text{O}_{\text{pt}}$ are interpreted to represent increases in temperature of 4.0 and 9.5°C, respectively. These estimates, however, are only about *half* of the 9.9 and 20.2°C changes in temperature that are actually observed at each locality (horizontal bars, Fig. 4). Similarly, estimates of temperature decrease made in the same manner will be too low.

The apparent underestimation of temperature change over time compared to temperature change over space using $\delta^{18}\text{O}_{\text{pt}}$ has been observed at both seasonal [10,11] and geologic time scales [12], and it can be used to question the validity of the $\delta^{18}\text{O}_{\text{pt}}$ paleothermometer. It is clear from Fig. 4, however, that the reason seasonal temperature change is underestimated is that *temporal* $\delta^{18}\text{O}_{\text{pt}}$ /temperature relations are shallower than *spatial* $\delta^{18}\text{O}_{\text{pt}}$ /temperature relations. The two types of

relations are very different because temporal $\delta^{18}\text{O}_{\text{pt}}$ /temperature relations are site-specific, being created by comparing data for different climate modes (solid lines in Fig. 4), while the spatial $\delta^{18}\text{O}_{\text{pt}}$ /temperature relations represent global conditions for each specific climate mode (dashed lines, Fig. 4). A similar argument was presented by Boyle [13], who showed that ice core $\delta^{18}\text{O}_{\text{pt}}$ records from Greenland will underestimate glacial/interglacial temperature change relative to borehole thermometry records if an offset in $\delta^{18}\text{O}_{\text{pt}}$ /temperature relations for the two periods is not taken into account. Lastly, it can be inferred from Fig. 4 that no matter what the offset in $\delta^{18}\text{O}_{\text{pt}}$ /temperature relations over time, the extent to which temperature change is underestimated at a given latitude will remain relatively constant as long as the slopes of the $\delta^{18}\text{O}_{\text{pt}}$ /temperature relations do not vary significantly.

4.1.2. Causes of offsets in $\delta^{18}\text{O}_{\text{pt}}$ /temperature relations

Beyond discussing the effects of offset $\delta^{18}\text{O}_{\text{pt}}$ /temperature relations on paleothermometry, it is important to understand why the offset occurs between summer and winter climate modes. A primary reason for the offset is the seasonal change in insolation that results in higher surface temperatures at all latitudes in the summer. The importance of temperature in controlling the relative position of $\delta^{18}\text{O}_{\text{pt}}$ /temperature relations has been illustrated by using temperature-dependent Rayleigh equations to model progressive condensation from low to high latitudes [1,9,13]. A change in the initial condensation temperature will result in an offset in the position of global $\delta^{18}\text{O}_{\text{pt}}$ /temperature relations so that it remains exponential in nature, but is shifted in the same direction as observed for data representing summer and winter climate modes.

A change in the atmospheric water vapor budget in the tropics can also result in an offset in $\delta^{18}\text{O}_{\text{pt}}$ /temperature relations between climate modes. This parameter is important because the tropics are the ultimate source of much of the moisture that ultimately reaches higher latitudes. Therefore any difference in the amount or initial $\delta^{18}\text{O}$ value of moisture in tropical air masses will necessarily affect the nature of the $\delta^{18}\text{O}_{\text{pt}}$ /temperature relation at higher latitudes. For example, the amount of water vapor in tropical air

masses is different in glacial and non-glacial periods [17] and $\delta^{18}\text{O}_{\text{pt}}$ varies between summer and winter climate modes (Fig. 2). Both of these factors are tied to changes in precipitation/evaporation ratios, air mass rainout, etc. These aspects of the tropical water vapor budget are quite important because their effects on $\delta^{18}\text{O}_{\text{pt}}$ are not related directly to changes in surface temperature, but rather to changes in atmospheric circulation patterns and the intensity of convective cooling. As a result, offsets in $\delta^{18}\text{O}_{\text{pt}}$ /temperature relations at higher latitudes can be modified by conditions in the tropics that are independent of temperature changes at the surface.

Lastly, a change in the $\delta^{18}\text{O}$ value of ocean water in the tropics can cause an offset in $\delta^{18}\text{O}_{\text{pt}}$ /temperature relations because the initial $\delta^{18}\text{O}$ value of water vapor formed in tropical source areas is significantly controlled by the $\delta^{18}\text{O}$ of the tropical oceans. Although unlikely to be an important variable seasonally, $\delta^{18}\text{O}$ of the oceans have varied by at least $\pm 1\text{--}2\text{‰}$ over geologic time scales.

4.2. Influence of factors other than temperature on local $\delta^{18}\text{O}_{\text{pt}}$ values

The second major problem in interpreting temporal records of $\delta^{18}\text{O}_{\text{pt}}$ are the factors other than temperature that influence $\delta^{18}\text{O}_{\text{pt}}$ on a local scale, and their relative impact on climate mode. In addition to the position of air mass boundaries mentioned above [7,8], there are several other factors whose effects are discernible in Figs. 2 and 3. For example, evaporation of water from the surface (i.e. large lakes [18] and near-shore ocean water) and the transpiration of moisture by plants affects local $\delta^{18}\text{O}_{\text{pt}}$ values by sending moisture back into overlying air masses [19–21]. This recycling of precipitation influences the isotopic and mass balances of overlying air masses, and thus modifies local $\delta^{18}\text{O}_{\text{pt}}$ values that would be appropriate to the closed-system condition inherent to idealized Rayleigh condensation. The result is poorer correlations between latitude, temperature, and $\delta^{18}\text{O}_{\text{pt}}$ that are observed during summer when higher temperatures and more plant growth increase rates of evaporation and transpiration, respectively (Figs. 2 and 3). In addition, systematically higher $\delta^{18}\text{O}_{\text{pt}}$ values for stations in polar latitudes (Fig. 3) are likely the result of evaporation from

the oceans near the low pressure bands at $\sim 60^\circ$ latitude that introduces local moisture with relatively high $\delta^{18}\text{O}$ values to overlying air masses moving in from lower latitudes. Although more common in the tropics, the *amount effect* can also influence $\delta^{18}\text{O}_{\text{pt}}$ values at higher latitudes, as is evidenced by the systematically lower $\delta^{18}\text{O}_{\text{pt}}$ values for stations in coastal China that are in the path of the Asian monsoon. Lastly, evaporation of precipitation as it falls to the surface shifts the remaining liquid water to higher $\delta^{18}\text{O}_{\text{pt}}$ values, and is a common phenomenon in arid regions. This factor accounts for very high $\delta^{18}\text{O}_{\text{pt}}$ values at warm, arid locations [5].

Focusing on the seasonal data, it is clear that the relative importance of these factors in influencing $\delta^{18}\text{O}_{\text{pt}}$ at a given locality depends on the climate mode. As already noted, $\delta^{18}\text{O}_{\text{pt}}$ /temperature correlations vary with climate mode due to changes in evapotranspiration and, from Figs. 2 and 3, it can be seen that evaporation of precipitation and monsoonal air circulation do not affect $\delta^{18}\text{O}_{\text{pt}}$ values to the same degree under summer and winter climate conditions. The implication of these observations is that any temporal change in weighted average $\delta^{18}\text{O}_{\text{pt}}$ at a given locality may reflect a change in temperature, a change in the relative influence of other non-temperature factors, or a combination of effects. In the absence of outside information, it is thus impossible to make a completely unambiguous interpretation of a temporal record of $\delta^{18}\text{O}_{\text{pt}}$ for a single locality.

5. Reconstructing $\delta^{18}\text{O}_{\text{pt}}$ /temperature relations over geologic time

The fact that the present-day relation between weighted average $\delta^{18}\text{O}_{\text{pt}}$ and mean annual temperature cannot be used to make quantitative estimates of temperature change over all of geologic time is unfortunate, but there are other ways in which paleoclimatic information can be obtained using appropriate records of $\delta^{18}\text{O}_{\text{pt}}$. The most basic method involves reconstructing global $\delta^{18}\text{O}_{\text{pt}}$ /temperature relations for the time periods being investigated, for example with direct measurements of preserved waters or of proxy materials.

5.1. Empirical reconstructions

$\delta^{18}\text{O}_{\text{pt}}$ /temperature relations can be reconstructed by comparing records of $\delta^{18}\text{O}_{\text{pt}}$ from at least two localities that cover a wide range of latitude in combination with independent estimates of temperature from one of those localities. A hypothetical illustration of how this sampling strategy works is presented in Fig. 5. Temporal records of past $\delta^{18}\text{O}_{\text{pt}}$ at localities A and B are used to reconstruct latitudinal gradients in $\delta^{18}\text{O}_{\text{pt}}$ for time periods 1 and 2 that are characterized by a cooler and a warmer climate mode, respectively (Fig. 5, panel 1). Using these records, and assuming that the slopes of global $\delta^{18}\text{O}_{\text{pt}}$ /temperature relations have relatively constant values of $\sim 0.55\text{‰}/^\circ\text{C}$ regardless of climate mode (Fig. 3), then it is possible to reconstruct global $\delta^{18}\text{O}_{\text{pt}}$ /temperature relations for time periods 1 and 2 if an independent estimate of temperature is available from one of the localities. These temperatures can be inferred from geological, biological, and geochemical evidence at a given latitude. For example, terrestrial floral and faunal reconstructions or the $\delta^{18}\text{O}$ of planktonic foraminifera from latitudinally-equivalent marine sediments, could be used to anchor the position of the $\delta^{18}\text{O}$ data (Fig. 5, panel 2).

An obvious challenge lies in bringing together temporal records of $\delta^{18}\text{O}_{\text{pt}}$ from a wide range of latitudes. The relative difficulty of making such a comparison will depend on the proxy for $\delta^{18}\text{O}_{\text{pt}}$ that is being used, with certain materials like soil carbonate being less common over time and space than materials like biogenic apatite that is found in animal fossils. Comparing records of $\delta^{18}\text{O}_{\text{pt}}$ from different but related localities is profitable because it has the additional and very important advantage of reducing ambiguities otherwise associated with trying to interpret a temporal record of weighted $\delta^{18}\text{O}_{\text{pt}}$ values from a single locality. As mentioned above, these ambiguities stem from the possible influence of factors other than temperature on $\delta^{18}\text{O}_{\text{pt}}$ at any given place. By comparing $\delta^{18}\text{O}_{\text{pt}}$ records from a number of sites, however, the scale of investigation is changed from a site-specific scale where it may be difficult to distinguish the role of factors such as air mass boundaries and evapotranspiration on $\delta^{18}\text{O}_{\text{pt}}$, to a global scale where their effects are more likely to

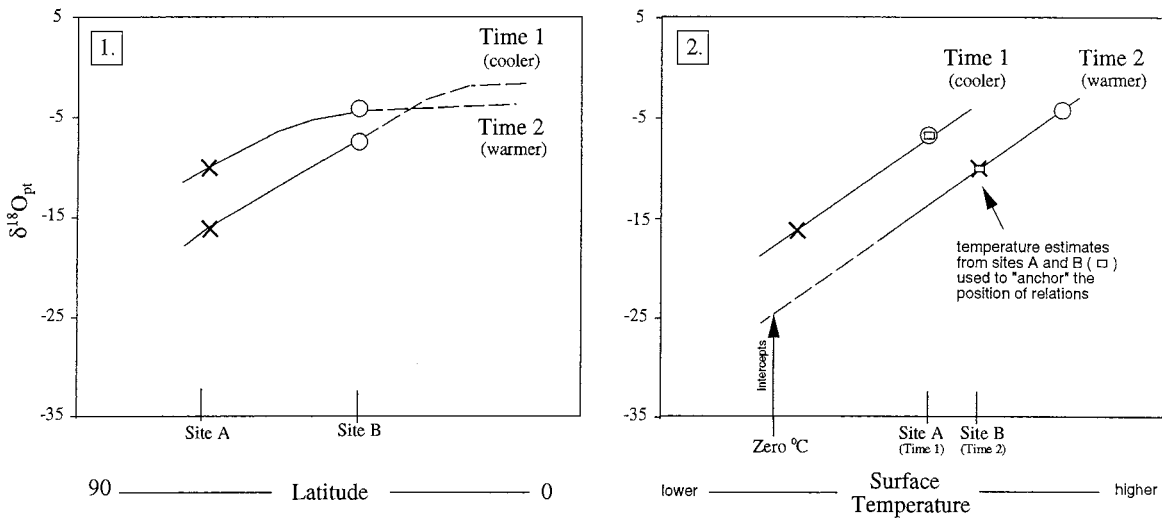


Fig. 5. Comparing $\delta^{18}\text{O}_{\text{pt}}$ records from a wide range of latitudes allows reconstructions to be made of $\delta^{18}\text{O}_{\text{pt}}$ /temperature relations. In panel 1, weighted $\delta^{18}\text{O}_{\text{pt}}$ values from two different times and two different localities (sites A and B) are plotted versus paleolatitude. In this manner $\delta^{18}\text{O}_{\text{pt}}$ /latitude gradients can be reconstructed for times 1 and 2 when global climate was significantly different. Using independent temperature estimates from the latitudes of sites A and B, and assuming that the $\delta^{18}\text{O}_{\text{pt}}$ /temperature relation has a constant slope of $\sim 0.55\text{‰}/\text{°C}$, it is possible to reconstruct $\delta^{18}\text{O}_{\text{pt}}$ /temperature relations and their intercepts for times 1 and 2 (panel 2).

stand out as anomalies in a global pattern, and can be interpreted as such.

The major drawback to this empirical method of reconstructing $\delta^{18}\text{O}_{\text{pt}}$ /temperature relations is that it relies on 'outside' estimates of temperature from the very same kinds of proxy records the relations are aimed to replace. If these independent temperature estimates themselves are poorly quantified, as is the case for estimates based on sedimentology, then the usefulness of reconstructed $\delta^{18}\text{O}_{\text{pt}}$ /temperature relations will be diminished.

5.2. Model reconstructions

Another method of reconstructing $\delta^{18}\text{O}_{\text{pt}}$ /temperature relations relies on theoretical calculations of global condensation that assume Rayleigh conditions [1,9,14] rather than on empirical data, but it is not without problems of its own. As in the case of empirical reconstructions, the use of model equations requires some knowledge of surface temperatures, in particular tropical temperatures, for each time period of interest [14]. In addition, it is necessary to have an estimate of the $\delta^{18}\text{O}$ value of tropical ocean water in order to get the most accurate results

using the theoretical models. More importantly, it has been noted that Rayleigh equations are only an approximation of the complex global condensation process [5], and thus may not be completely accurate in any case. For example, the exponential Rayleigh equations cannot reproduce the global $\delta^{18}\text{O}_{\text{pt}}$ /temperature trends that form as the result of decoupling between atmospheric processes occurring in tropical and extra-tropical regions (Fig. 3).

6. Additional ways of using estimates of $\delta^{18}\text{O}_{\text{pt}}$ to study climate in the past

In the above discussion we reviewed the difficulties involved in using $\delta^{18}\text{O}_{\text{pt}}$ /temperature relations as quantitative paleothermometers over geologic time, and noted that the approach to resolving these problems will depend on the paleoenvironmental and isotopic data available for a given time period or region. There are, however, alternative ways in which paleoclimatological information can be obtained using oxygen isotope data that do not rely on reconstructing $\delta^{18}\text{O}_{\text{pt}}$ /temperature relations in the past.

6.1. Direct estimates of temperature using biogenic apatite as a proxy for $\delta^{18}\text{O}_{\text{pt}}$

One way to estimate temperature without relying on $\delta^{18}\text{O}_{\text{pt}}$ /temperature relations is to utilize equations that describe oxygen isotope fractionation between water (precipitation) and different mineral phases that form in equilibrium with it. A novel example of this approach involves the measurement of $\delta^{18}\text{O}$ values of a *single* substance that forms under *different* conditions in *different* surficial environments [22]. In particular, $\delta^{18}\text{O}$ of apatite coming from mammalian fossils can be used to determine the $\delta^{18}\text{O}$ of ingested water (precipitation) because the apatite forms at the constant body temperature of the animal ($\sim 37^\circ\text{C}$). Combining this information with $\delta^{18}\text{O}$ values of associated fish fossils and using the phosphate paleothermometer of Longinelli and Nuti [23], it is then possible to estimate the temperature of river water, which mirrors that of air temperature. Oxygen isotope analyses of mammalian tooth enamel and fresh water fish scales were recently used in this manner to infer temperature change during the early Paleogene [24], and the widespread occurrence of biogenic apatite over time and space may make this sampling strategy a reasonable alternative to reconstructing $\delta^{18}\text{O}_{\text{pt}}$ /temperature relations.

6.2. Using $\delta^{18}\text{O}_{\text{pt}}$ to validate GCM predictions

A quite different approach to using records of $\delta^{18}\text{O}_{\text{pt}}$ to study terrestrial paleoclimatology does not rely on $\delta^{18}\text{O}_{\text{pt}}$ to estimate temperature, or any other climate variable. Instead, records of $\delta^{18}\text{O}_{\text{pt}}$ are used to test predictions of global climate models (GCM) which are in turn used to elucidate the nature of climate change (for a review see [25]). The goal of integrating oxygen isotope systematics with GCMs is to predict the spatial distribution of $\delta^{18}\text{O}_{\text{pt}}$ in the past by accounting for oxygen isotope fractionations that accompany phase changes that take place as water 'moves' through the hydrologic cycle during a climate simulation. A comparison of the predicted distribution with the actual distribution obtained from records of $\delta^{18}\text{O}_{\text{pt}}$ then provides a much-needed check on the ability of GCMs to replicate complex changes in climate over geologic time. This

method is appealing because, in contrast to focusing on a single variable such as temperature, GCM predictions have the potential to provide a much more complete picture of how several climatic variables like vegetation cover, ocean/atmospheric circulation patterns, $p\text{CO}_2$, heat transfer, the hydrologic cycle, etc., interact to produce a change in climate.

Attempts to reproduce modern patterns in $\delta^{18}\text{O}_{\text{pt}}$ using GCM model predictions have been relatively successful indicating that the potential exists for combined GCM-isotope investigations of terrestrial paleoclimate [26,27]. More recent efforts have focused on comparing model predictions and proxy records of $\delta^{18}\text{O}_{\text{pt}}$ for the last glacial maximum [28,29]. Continued study of these well-characterized time periods should help refine the model-isotope approach to studying terrestrial climate change over a much broader range of geologic time.

7. Conclusions

Separating the global data base of temperature and isotopic measurements into climate modes defined by summer and winter climate conditions, provides a simple model for understanding how global relations between $\delta^{18}\text{O}_{\text{pt}}$ and temperature can be offset relative to one another as a result of differences in temperature and air mass rainout in the tropics. It is not always possible to use the well known weighted $\delta^{18}\text{O}_{\text{pt}}$ /MAT relation to make accurate interpretations of a temporal record of $\delta^{18}\text{O}_{\text{pt}}$ values, especially if climate mode in the geologic past was radically different from that at present, or if climate change over time was extreme. While there is a strong relation globally between $\delta^{18}\text{O}_{\text{pt}}$ and temperature regardless of the source area and transport history of air masses, there are a number of factors other than temperature that can mask the $\delta^{18}\text{O}_{\text{pt}}$ /temperature relation on a local/regional scale. The effect of these factors can vary depending on climate mode, making the interpretation even more ambiguous.

At present, there are three ways to circumvent problems associated with the $\delta^{18}\text{O}_{\text{pt}}$ paleothermometer in terrestrial environments. One may compare $\delta^{18}\text{O}_{\text{pt}}$ records from localities that cover a wide range of latitudes with independent estimates of temperature to reconstruct global $\delta^{18}\text{O}_{\text{pt}}$ /temperature rela-

tions for different time periods in the past. Under certain favorable conditions, it may also be possible to estimate temperature using records of $\delta^{18}\text{O}_{\text{pt}}$ without relying on any $\delta^{18}\text{O}_{\text{pt}}$ /temperature relation. The most profitable use of $\delta^{18}\text{O}_{\text{pt}}$ records may lie in their ability to test the accuracy of climate-change predictions produced using global climate models. [CL]

References

- [1] W. Dansgaard, Stable isotopes in precipitation, *Tellus* 16 (1964) 436–468.
- [2] Y. Yurtsever, J.R. Gat, Atmospheric waters, in: J.R. Gat, R. Gonfiantini (Eds.), *Stable Isotope Hydrology — Deuterium and Oxygen-18 in the Water Cycle*, IAEA, Int. Atomic Energy Agency Tech. Rept. Ser., 1981, pp. 103–142.
- [3] K. Rozanski, L. Araguás-Araguás, R. Gonfiantini, Isotopic patterns in modern global precipitation, in: P.K. Swart, K.C. Lohmann, J. McKenzie, S. Savin (Eds.), *Climate Change in Continental Climate Records*, Am. Geophys. Union, *Geophys. Monogr.* 78 (1993) 1–36.
- [4] H. Craig, L.I. Gordon, Deuterium and oxygen-18 variations in the ocean and the marine atmosphere, in: E. Tongiorgi (Ed.), *Proceedings of a conference on stable isotopes in oceanographic studies and paleotemperatures*, Consiglio Nazionale della Ricerca, Pisa, 1965, pp. 9–130.
- [5] J.R. Gat, Oxygen and hydrogen isotopes in the hydrologic cycle, *Annu. Rev. Earth Planet. Sci.* 24 (1996) 225–262.
- [6] P.K. Swart, K.C. Lohmann, J. McKenzie, S. Savin (Eds.), *Climate Change in Continental Climate Records*, Am. Geophys. Union, *Geophys. Monogr.* 78 (1993).
- [7] T.W.D. Edwards, B.B. Wolfe, G.M. MacDonald, Influence of changing atmospheric circulation on precipitation $\delta^{18}\text{O}$ -temperature relations in Canada during the Holocene, *Quat. Res.* 46 (1996) 211–218.
- [8] R. Amundson, O. Chadwick, C. Kendall, Y. Wang, M. DeNiro, Isotopic evidence for shifts in atmospheric circulation patterns during the late Quaternary in mid-North America, *Geology* 24 (1996) 23–26.
- [9] R.T. Gregory, C.B. Douthitt, I.R. Duddy, P.V. Rich, P.H. Rich, Oxygen isotopic composition of carbonate concretions from the lower Cretaceous of Victoria, Australia: implications for the evolution of meteoric waters of the Australian continent in a paleopolar environment, *Earth Planet. Sci. Lett.* 92 (1989) 27–42.
- [10] J.R. Lawrence, J.W.C. White, The elusive climate signal in the isotopic composition of precipitation, in: H.P. Taylor, J.R. O'Neil, I.R. Kaplan (Eds.), *Stable Isotope Geochemistry: A Tribute to Samuel Epstein*, The Geochemical Society, Special Publication, 1991, pp. 169–185.
- [11] K. Rozanski, L. Araguás-Araguás, R. Gonfiantini, Relation between long-term trends of oxygen-18 isotope composition of precipitation and climate, *Science* 258 (1992) 981–985.
- [12] K.M. Cuffey, R.B. Alley, M. Stuiver, E.D. Waddington, R.W. Saltus, Large arctic temperature change at the Wisconsin–Holocene glacial transition, *Science* 270 (1995) 455–458.
- [13] E.A. Boyle, Cool tropical temperatures shift the global $\delta^{18}\text{O}$ - T relationship, *Geophys. Res. Lett.* 24 (1997) 273–276.
- [14] IAEA/WMO, Global Network for Isotopes in Precipitation — the GNIP Database, Release 1, URL: <http://www.iaea.org/programs/ri/gnip/gnipmain.htm>, 1997.
- [15] C. Sonntag, K. Rozanski, K.O. Munnich, H. Jacob, Variations of deuterium and oxygen-18 in continental precipitation and groundwater and their causes, in: A. Street-Perot et al. (Eds.), *Variations in the Global Water Budget*, D. Reidel, Dordrecht, 1983, pp. 107–124.
- [16] B.T. Huber, D.A. Hodell, C.P. Hamilton, Middle–Late Cretaceous climate of the southern high latitudes: Stable isotopic evidence for minimal equator-to-pole thermal gradients, *Geol. Soc. Am. Bull.* 107 (1995) 1164–1191.
- [17] W. Broecker, Mountain glaciers: Recorders of atmospheric water vapor content?, *Global Biogeochem. Cycles* 11 (1997) 589–597.
- [18] M.V. Machavaram, R.V. Krishnamurthy, Earth surface evaporative process: A case study from the Great Lakes region of the United States based on deuterium excess in precipitation, *Geochim. Cosmochim. Acta* 59 (1995) 4279–4283.
- [19] E. Salati, A. Dall'olio, E. Matsui, J. Gat, Recycling of water in the Amazon Basin, an isotopic study, *Water Resources Res.* 15 (1979) 1250–1258.
- [20] H. Jacob, C. Sonntag, An 8-year record of the seasonal variation of ^2H and ^{18}O in atmospheric water vapor and precipitation at Heidelberg, Germany, *Tellus* 43B (1991) 291–300.
- [21] R.D. Koster, D.P.d. Valpine, J. Jouzel, Continental water recycling and H_2^{18}O concentrations, *Geophys. Res. Lett.* 20 (1993) 2215–2218.
- [22] Y. Kolodny, B. Luz, O. Navon, Oxygen isotope variations in phosphate of biogenic apatite, I: fish bone apatite, *Earth Planet. Sci. Lett.* 64 (1983) 398–404.
- [23] A. Longinelli, S. Nuti, Revised phosphate–water isotopic temperature scale, *Earth Planet. Sci. Lett.* 19 (1973) 373–376.
- [24] H. Fricke, W. Clyde, J. O'Neil, P. Gingerich, Evidence for rapid climate change in North America during the latest Paleocene thermal maximum: oxygen isotope composition of biogenic phosphate from the Bighorn Basin (Wyoming), *Earth Planet. Sci. Lett.* 160 (1998) 193–208.
- [25] J. Jouzel et al., Validity of the temperature reconstruction from water isotopes in ice cores, *J. Geophys. Res.* 102 (1997) 26471–26487.
- [26] S. Joussaume, J. Jouzel, R. Sadourny, A general circulation model of water isotope cycles in the atmosphere, *Nature* 311 (1984) 24–29.
- [27] J. Jouzel, R. Koster, R. Suozzo, G. Russell, J. White, W.

- Broecker, Simulations of the HDO and H₂¹⁸O atmospheric cycles using the NASA GISS general circulation model: Sensitivity experiments for present-day conditions, *J. Geophys. Res.* 96 (1991) 7495–7507.
- [28] S. Joussaume, J. Jouzel, Paleoclimatic tracers: An investigation using an atmospheric general circulation model under ice age conditions 2. Water isotopes, *J. Geophys. Res.* 98 (1993) 2807–2830.
- [29] J. Jouzel, R.D. Koster, R.J. Suozzo, G.L. Russell, Stable water isotope behaviour during the last glacial maximum: A general circulation model analysis, *J. Geophys. Res.* 99 (1994) 25791–25801.

Chemical and physical characteristics of springs discharging from regional flow systems of the carbonate-rock province of the Great Basin, western United States

Ronald L. Hershey · Steve A. Mizell · Sam Earman

Abstract The regional carbonate aquifer in the carbonate-rock province of the Great Basin, USA, covers thousands of square kilometers. It is a significant potential source of water for growth in this arid area. Few wells penetrate the carbonate aquifer, so information on water quantity and quality is derived in large part from 'regional springs' that discharge from regional interbasin flow systems. For this study, springs in the carbonate-rock province were sampled; their physical, chemical, and isotopic characteristics were compared to those of known regional springs to identify previously unrecognized regional waters using both examination of the data and multivariate statistical analysis. Criteria for comparison included temperature, discharge, ^3H activity, carbon isotope values, and ratios of major and trace ions. Of the 18 springs selected for detailed chemical and isotopic sampling, five springs—Hot, Littlefield, Petrified, Saratoga, and Warm (a)—were identified as regional, and one (Monte Neva Hot) was identified as a possible regional spring. Regional springs

provide an easy, low-cost means of investigating aquifer properties; identification of regional springs thus increases the ability to understand the regional carbonate aquifer. The techniques applied in this study can also be used in other regional aquifer systems with diverse and complex geology.

Keywords Arid regions · Carbonate rocks · Hydrochemistry · Regional aquifer · USA

Introduction

The carbonate-rock province of the Great Basin in the western USA (Fig. 1) is an area where carbonate rock types predominate in bedrock outcrops (Mifflin 1968). The province extends from the Utah–Idaho border to west of the Nevada–California border, a distance of approximately 950 km. The province encompasses western Utah, eastern and southern Nevada, and a small portion of southeastern California. Extensional faulting has created numerous topographic basins, many of which have closed surface-water drainage. However, in locations where there is carbonate rock, groundwater flows between the basins. These interbasin flow systems define the regional carbonate aquifer of the Great Basin. In Nevada, groundwater flow in the regional carbonate aquifer is from north to south. In southern Nevada, the regional carbonate aquifer splits into two major flow systems. One extends north to south along the east side of Nevada, with discharge occurring at the Colorado River; the second extends northeast to southwest from the south-central part of Nevada with discharge occurring in Ash Meadows, Nevada and Death Valley, California (Thomas et al. 1996).

Because much of the area underlain by the regional carbonate aquifer is sparsely populated, the aquifer has been targeted as a source of water for growing metropolitan areas including Las Vegas, Nevada, which has had the fastest growth rate of any major metropolitan area in the USA since at least 1970 (Rappaport 2003; UNLV Center for Business and Economic Research 2008). Although

Received: 8 January 2009 / Accepted: 15 December 2009

© Springer-Verlag 2010

Electronic supplementary material The online version of this article (doi:10.1007/s10040-009-0571-7) contains supplementary material, which is available to authorized users.

R. L. Hershey
Division of Hydrologic Sciences,
Desert Research Institute,
2215 Raggio Pkwy, Reno, 89512 NV, USA

S. A. Mizell
Division of Hydrologic Sciences,
Desert Research Institute,
755 E. Flamingo Road, Las Vegas, 89119 NV, USA

S. Earman (✉)
Earth Sciences Department,
Millersville University, PO Box 1002, Millersville, PA 17551, USA
e-mail: sam.earman@millersville.edu
Tel.: +1-717-8712086
Fax: +1-717-8714725

Hydrogeology Journal

Published online: 03 February 2010

DOI 10.1007/s10040-009-0571-7

SE ROA 37379

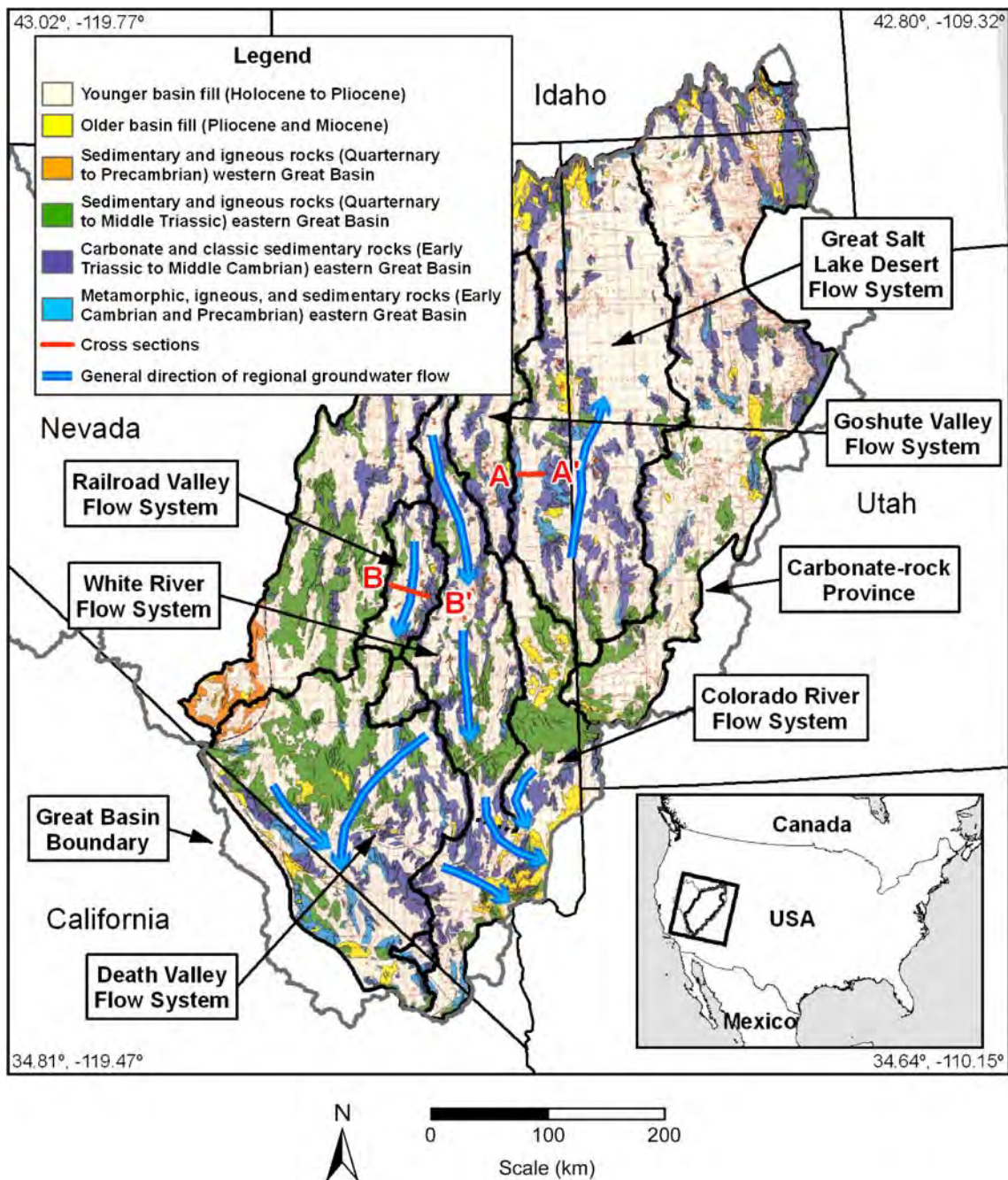


Fig. 1 Location, generalized geology (Plume 1996), regional groundwater flow systems (Harrill et al. 1988), and general direction of regional groundwater flow (Harrill et al. 1988) in the carbonate-rock province (Thomas et al. 1986) of the Great Basin, western USA

interest in the water of the regional carbonate aquifer is high, data on the quality and quantity of water are relatively limited because the carbonate aquifer is often deep below the ground surface and relatively few wells penetrate the aquifer. Springs in mountain blocks and some springs on valley floors are considered 'local' in that they discharge water from relatively small (basin-scale or smaller) catchments, often from aquifers composed of alluvium or volcanic rock; regional springs, which tend to be located on basin floors, discharge through basin fill sediments from the underlying carbonate aquifer.

The current set of springs recognized as being regionally sourced is based on a limited set of physical and chemical characteristics. This study was conducted to identify additional chemical and physical characteristics of springs discharging from the regional carbonate aquifer of the Great Basin and to use these characteristics to identify regionally sourced springs that had not been previously recognized. The results of this study advance the knowledge of the extent of the regional carbonate aquifer and the locations of its natural discharge zones, identify additional water sources that may be useful for monitoring the long-term effects of

development of the regional carbonate aquifer, and develop techniques that can be applied to other geologically diverse regional aquifer systems.

Physiography, geology, hydrogeology, and climate of the carbonate-rock province

The carbonate-rock province lies within the Great Basin and adjacent areas. The Great Basin is the largest division of the Basin and Range physiographic province of the western United States (Hunt 1967) and is defined as “that portion of the geologic Basin and Range with no drainage to the sea” (Fiero 1986). Topography in the carbonate-rock province is dominated by N–S trending mountain ranges, which generally form long, narrow valleys. Many of these valleys are topographically closed. Carbonate rocks are prominent in the ranges of the eastern and southern portions of the Great Basin (Hunt 1967; Plume 1996). Figure 1 illustrates the generalized geology of the carbonate-rock province of the Great Basin.

Geologic characteristics of the carbonate-rock province that influence modern groundwater movement began to form in the late Precambrian. From the late Precambrian into the early Mesozoic, what would become the eastern Great Basin was continental shelf where clastic and carbonate sediments were accumulating. Simultaneously, the future western Great Basin was continental slope and rise where deep marine sediments and lavas were deposited, forming sedimentary and volcanic rock units (Fiero 1986; Stewart 1980; Sweetkind et al. 2007). During the Antler (Late Devonian and Mississippian) and Sonoma (Early Triassic) orogenies, the deep marine deposits were thrust over the shelf deposits, creating highlands that became sources of clastic material deposited in the surrounding basins. As a result, the eastern two-thirds of the Great Basin is characterized by alternating sedimentary sequences that are dominated either by clastic rocks with minor carbonate rocks or by carbonate rocks with minor clastic rocks. Generally, the overall thickness of carbonate-rock sequences exceeds that of clastic-rock sequences (Plume 1996). A period of continental deposition dominated the region from the Middle Triassic into the late Tertiary as a result of the westward shift of the continental margin during the Triassic and Jurassic (Plume 1996). Extensional faulting began to form the present-day basin-and-range characteristics of the Great Basin in the Oligocene, and by the late Pliocene, the present distribution of mountains and basins was established (Plume 1996). Basin-fill sediments, consisting of clay-to-boulder-size materials, collected in the basins that were formed from about middle Miocene (or earlier) through the Holocene. Volcanic rocks deposited between the Eocene and Pleistocene, and possibly into the Holocene, can be found in nearly every mountain range of the Great Basin; they also underlie, and are interbedded with, basin-fill deposits in much of the area (Plume 1996).

Structural development of the region was dominated by tectonic compression during the Paleozoic, Mesozoic, and

possibly the early Cenozoic eras and by tectonic extension since the Tertiary. The Antler, Sonoma, and Sevier (Jurassic to early Tertiary) orogenies produced major thrust fault features (Coney and Harms 1984; Morris 1983; Tooker 1983; Wernicke et al. 1988). During the extensional period (Oligocene to Holocene), geologic structure was dominated by normal faulting, which formed fault-block mountains and basins (Coney and Harms 1984; Gans et al. 1987; Hamilton 1988). High-angle and listric normal faults and detachment faults are found throughout the Great Basin. Because of scale, specific structural features of the eastern Great Basin could not be indicated clearly on the geologic map shown in Fig. 1; interested readers are referred to Plume (1996) and Sweetkind et al. (2007) for concise summarizations of the region’s geology and structure and to other referenced works for specific information about the geologic structure of the eastern Great Basin.

Plume (1996) describes six hydrogeologic units in the Great Basin (Fig. 1). These are: (1) basin-fill deposits of Pliocene-to-Holocene age, (2) basin-fill deposits of Miocene-to-Pliocene age, (3) sedimentary and igneous rocks of late Precambrian-to-Quaternary age in the western Great Basin, (4) sedimentary and igneous rocks of Middle Triassic-to-Quaternary age in the eastern Great Basin, (5) carbonate and clastic sedimentary rocks of Middle Cambrian to Early Triassic age in the eastern Great Basin, and (6) metamorphic, igneous, and sedimentary rocks of late Precambrian and Early Cambrian age in the eastern Great Basin. He identifies two aquifer systems in the eastern Great Basin: the basin-fill aquifers, which occur in the two basin-fill sedimentary units, and the carbonate-rock aquifers, which occur in the carbonate and clastic sedimentary rocks of Middle Cambrian to Early Triassic age.

The basin-fill aquifers are bounded by consolidated rock units that define the structural basins (Fig. 2). These aquifers may be: confined by impermeable consolidated rocks of the structural basin, hydraulically connected to adjacent basin-fill aquifers through basin-fill deposits or permeable consolidated rocks, or hydraulically connected to the carbonate-rock aquifer (Plume 1996). The carbonate-rock aquifers are laterally bounded by the extent of the carbonate-rock province. Quartzite and shale units, or poorly permeable or impermeable carbonate rock that underlies the permeable units at depth, define the bottom of these aquifers (Plume 1996). In the carbonate-rock aquifers, water is stored and transmitted in fractures and joints, which may have been widened by solution (Plume 1996). Drilling circulation loss and bit-drop problems in some deep test wells may suggest karst features in the carbonate rock units (Mifflin 1968). However, the extent of karst development in the carbonate-rock province is limited, primarily because of the aridity and thin soils of the region (Dettinger 1995).

Structural deformation of the carbonate-rock province can enhance groundwater flow or create barriers to flow depending on the permeability of the fault zone or juxtaposed rock units relative to permeability of adjoining

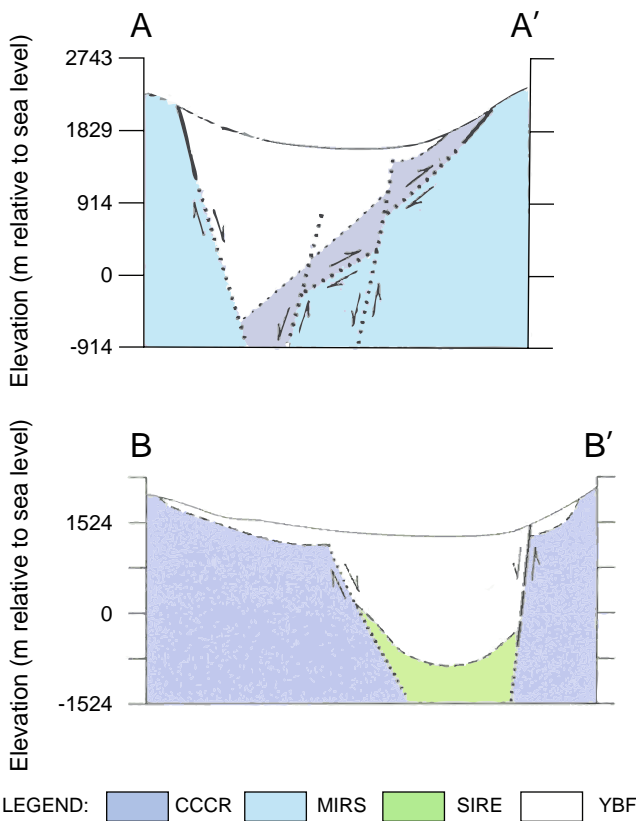


Fig. 2 Example cross-sections showing the general geology and structure (Plume 1996) of basins in the carbonate-rock province (Thomas et al. 1986) of the Great Basin, western USA. *CCCR* carbonate and clastic sedimentary rocks, *MIRS* metamorphic and igneous rocks; *SIRE* sedimentary and igneous rocks, *YBF* younger basin fill (Holocene to Pliocene)

aquifers (Bredehoeft et al. 1992). Faults oriented parallel to the maximum component of the present stress field are under tension and tend to be conduits for flow; those that parallel the minimum component of the stress field are under compression and tend to be barriers to flow (Anna 1986; Faunt 1997). Faunt (1997) describes both effects in the discharge zone of the Death Valley flow system. In addition, continuity of carbonate rock, despite the structural deformation, gives rise to the potential for regional groundwater flow systems (Anderson et al. 1983; Dettinger 1995).

Early investigators performing water-resource assessments of topographic basins in the carbonate-rock province recognized that discharge in some basins was greater, and in other basins far less, than the basin's estimated recharge (Carpenter 1915; Eakin 1962, 1963a, 1963b; Maxey and Eakin 1949). These workers recognized the need for underflow of groundwater to balance recharge and discharge estimates; at about the same time, Tóth (1962, 1963) illustrated the theoretical basis for regional flow. Eakin (1966) appears to be the first to apply the concepts of regional flow in his appraisal of the White River flow system (Fig. 1). Delineation of this interbasin flow system was based on the distribution and quantity of estimated groundwater recharge and discharge, uniformity of discharge from large springs, regional hydraulic gradients, hydraulic properties of

major rock groups, and the chemical character of water discharging from large springs. He identified numerous springs in the White River interbasin groundwater flow system that were characterized by relatively uniform flow, reasonable uniformity of chemical composition, and increases in concentrations consistent with aquifer rock type and flow path length.

Mifflin (1968) delineated interbasin flow systems in Nevada using fluid potential, groundwater temperature, spring discharge, water chemistry, and ^3H activity. He determined that groundwaters discharging with temperatures between 18 and 27 °C were associated with interbasin flow systems or were near major geologic structures. Because dissolved constituents in spring water reflect the rock that water flows through and concentrations tend to increase with longer flow paths, he determined that the relative proportions of equivalent concentrations (molar concentration multiplied by ionic charge) of $(\text{Na}^+ + \text{K}^+)$ and $(\text{Cl}^- + \text{SO}_4^{2-})$ could be used to delineate the size and extent of groundwater systems. Mifflin also used ^3H activity and $(\text{Na}^+ + \text{K}^+)$ to classify springs from three different flow systems, "small-local," "local," and "regional." Significant amounts of ^3H were found in springs with less than 3.8 ppm $(\text{Na}^+ + \text{K}^+)$, indicating short flow paths and recent groundwater recharge (small-local), while springs with no measurable ^3H and more than 8 ppm $(\text{Na}^+ + \text{K}^+)$ indicate long flow paths and insignificant recent groundwater recharge (regional). Thirty-nine springs were identified as regional on the basis of these criteria.

Viability of interbasin flow is controlled by the hydraulic connection of aquifer and confining units across the basin boundaries (Sweetkind et al. 2007). Harrill et al. (1988) describe 10 regional flow systems located entirely within the carbonate-rock province and four more that border on the carbonate-rock province. Some of these regional flow systems are shown in Fig. 1. The Colorado River flow system, which includes the White River flow system, encompasses 33 topographic basins. Prudic et al. (1995) and Plume (1996) reduced the number of regional flow systems within the carbonate-rock province to five.

Stratigraphic thickness of the carbonate rocks in the carbonate-rock province ranges from 1,525 to 9,150 m (Dettinger et al. 1995; Plume 1996; Sweetkind et al. 2007). However, the effective hydrogeologic thickness may be less because of structural deformation and variations in primary permeability (Plume 1996). Transmission of water through the carbonate rocks is dependent upon intergranular, fracture, and solution porosity (Dettinger and Schaefer 1996; Sweetkind et al. 2007). Sweetkind et al. (2007) tabulated hydraulic conductivity values ranging from 0.01 to 82,420 cm/day from 67 documented tests. Regional water movement through the aquifer is greatly influenced by conditions at the structural boundaries of hydrographic basins. Where relatively permeable rocks are juxtaposed by a fault, water may move across boundaries of hydrographic basins, but where a permeable zone is juxtaposed against a low-permeability zone, cross-boundary movement of water is inhibited (Sweetkind et al. 2007).

In the flow systems of the carbonate-rock province, recharge is commonly derived from precipitation on mountains which define the flow system boundaries. The higher mountains receive larger amounts of precipitation and generate the greater portion of recharge. Since recharge areas are scattered along the flow systems, recharge from multiple locations influences the water chemistry of the flow system. From the recharge areas, water may move directly into the volcanic or carbonate-rock aquifers or through the basin-fill aquifer, then to the consolidated-rock aquifers. Near the southern end of the Colorado River flow system, water may also flow through evaporite deposits rich in gypsum and anhydrite. The different rock types each have an influence on the chemistry of the groundwater and are discussed in more detail in the following. The length of flow path or residence time in the

various rock types further influences the concentration of specific constituents in the water chemistry.

Local climate conditions in the carbonate-rock province are dependent on latitude, elevation, and current atmospheric conditions. Generally, temperatures are cooler in the north and increase toward the south. The average annual minimum and maximum temperatures at valley locations in northern portions of the province are near -1 and 17 °C, respectively, whereas in the south these values are 12 and 27 °C (Western Regional Climate Center 2008). Extreme temperatures are as much as 16 °C above or below the averages. Average annual precipitation ranges from near 241 mm in northern valley locations to about 101 mm in southern locations. These precipitation amounts may easily increase by a factor of two or more at higher elevations.

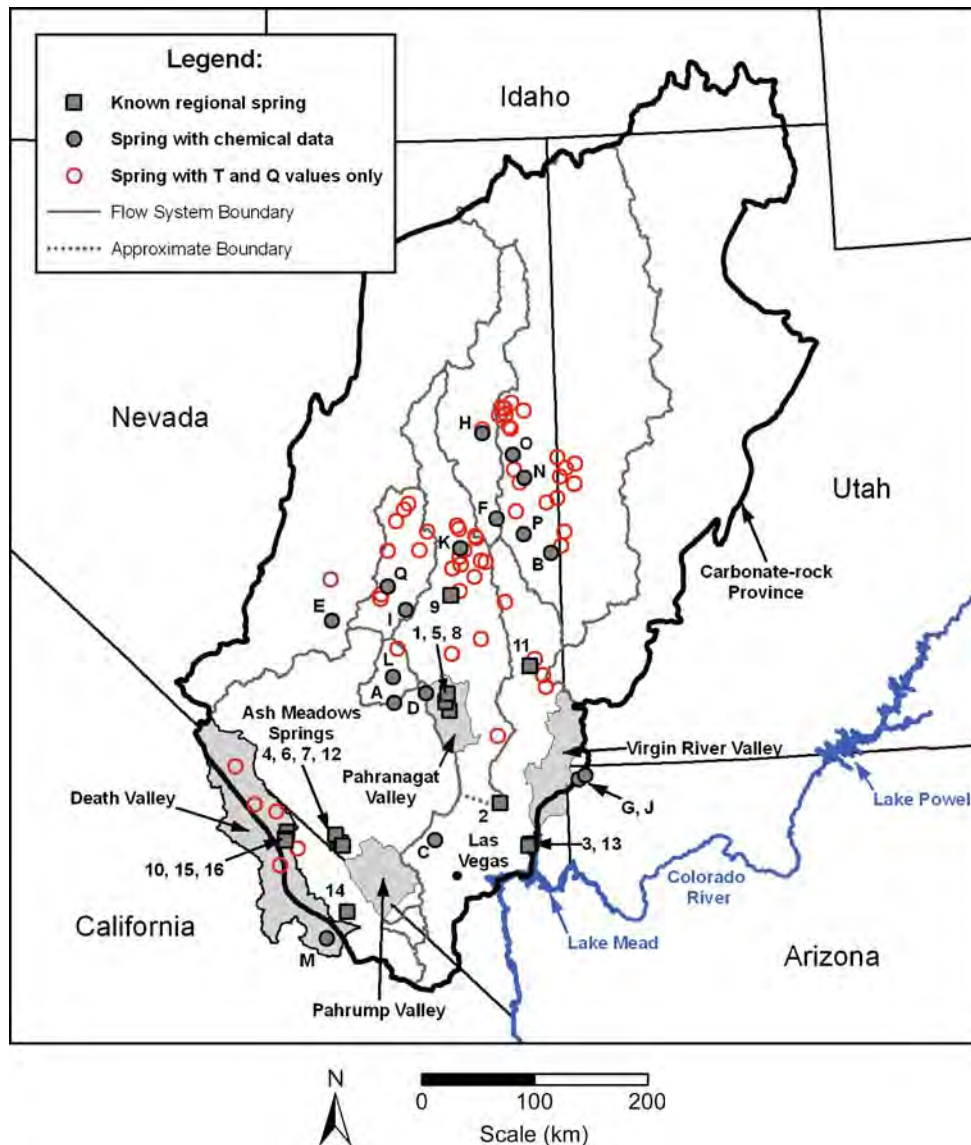


Fig. 3 Location of groundwater samples listed in Tables 1 and 2, geographic locations described in the text, and regional groundwater flow systems (Harrill et al. 1988) in the carbonate-rock province (Thomas et al. 1986) of the Great Basin, western USA. Known regional springs are represented by *grey squares with numerals* (Table 1), other springs with chemical data are represented by *grey circles with letters* (Table 2), and springs with only temperature (*T*) and discharge (*Q*) data are unlabeled and represented by *red open circles*

Table 1 Listing of physical, chemical, and isotopic data for known regional springs in the study area and springs other than known regional springs. All values (except pH) are in units of mg/L, unless otherwise noted. Chemical and isotope data for Ash Spring and Blue Point Spring, and isotope data for Point of Rocks Spring are average values reported by Thomas et al. (1996); chemical data for Point of Rocks Spring are from the Nevada Bureau of Mines and Geology (2009); all other data are from this study. δD and $\delta^{18}O$ values are relative to VSMOW; $\delta^{13}C$ values are relative to VPDB. All location data are provided in UTM Zone 11 coordinates, using the North American Datum of 1927

ID	Spring name	Sample date	UTM north	UTM east	Field EC ($\mu S/cm$)	Field pH	Temp. ($^{\circ}C$)	Discharge (L/s)	Ca ²⁺ (mg/L)	Mg ²⁺ (mg/L)	Na ⁺ (mg/L)	K ⁺ (mg/L)	Field HCO ₃ ⁻ (mg/L)	Field CO ₃ ⁻ (mg/L)	SO ₄ ²⁻ (mg/L)
Known regional springs															
1	Ash Spring	-	4147631	659926	460	7.2	36	32	46	15	29	7.7	259	0	33
2	Big Muddy Springs	3/5/92	4066293	704217	917	7.4	32	189	62.9	27.2	98.5	11.9	259	0	164
3	Blue Point Spring	-	4029995	731061	3,800	7.0	30	19	510	170	360	23	160	0	2,300
4	Crystal Pool	3/17/92	4030607	560737	700	7.3	31	126	46.2	21.4	76.1	9.60	305	0	84.6
5	Crystal Spring	5/12/92	4155244	656343	479	7.5	27	288	44.7	22.3	24.2	5.35	250	0	32.0
6	Devils Hole	7/9/92	4031120	563498	692	7.2	34	-	48.6	20.4	67.7	8.80	294	0	74.4
7	Fairbanks Spring	3/17/92	4038175	558967	661	7.5	27	120	48.1	21.0	69.7	7.68	310	0	78.8
8	Hiko Spring	12/18/91	4162546	657702	486	7.5	27	95	47.1	23.3	25.7	7.54	262	0	34.8
9	Hot Creek Spring	5/20/92	4249349	661012	547	7.3	32	440	57.5	22.4	24.7	4.99	285	0	42.4
10	Nevares Springs	4/17/92	4040454	516168	1,025	7.4	39	18	42.7	20.6	145	12.3	344	0	162
11	Panaca Spring	5/20/92	4187455	730656	397	7.8	29	60	30.9	10.0	36.8	6.92	180	0	26.6
12	Point of Rocks Spring	-	4028514	565236	-	7.2	32	60 ^a	49	21	69	7.7	310	0	80
13	Rogers Spring	3/19/92	4028539	729654	3,630	7.0	30	32	423	143	291	22.7	161	0	1,620
14	Tecopa Hot Springs	5/4/92	3969819	569462	3,700	8.2	42	19	4.55	1.47	783	17.6	708	0	520
15	Texas Springs	4/17/92	4034597	514685	967	7.9	31	12	34.5	18.7	147	12.0	344	0	147
16	Travertine Springs	4/17/92	4033057	515186	974	7.5	34	46	34.5	18.8	145	12.1	339	0	146
Other Springs															
A	April Fool	12/18/91	4154365	611330	763	7.3	13	0.1	78.6	51.1	28.1	3.73	417	0	110
B	Big	6/19/92	4287063	749501	378	7.7	18	234 ^a	46.6	19.9	5.54	1.53	240	0	7.27
C	Corn Creek	3/5/92	4033682	647244	488	7.6	22	6.3	45.8	33.7	6.51	2.07	291	0	16.9
D	Crescent	12/18/91	4163104	638877	577	7.3	12	0.05	93.6	11.0	20.5	2.91	368	0	14.8
E	Hot	5/12/92	4227408	556165	1,347	6.5	59	43 ^a	70.6	22.8	191	25.1	702	0	91.9
F	Kious	6/19/92	4317541	701552	440	7.6	14	1.8	52.8	7.69	27.2	1.62	271	0	13.8
G	Littlefield	7/22/92	4087048	774078	3,243	6.6	27	75	432	121	288	33.1	465	0	1,300
H	Monte Neva Hot	5/28/92	4393017	688616	595	6.6	76	95	66.1	19.5	16.7	6.25	311	0	24.5
I	Ox	5/12/92	4237122	621221	492	7.6	12	3	62.8	25.5	8.33	1.18	319	0	13.0
J	Petrified	7/22/92	4090520	779801	3,318	7.3	26	N/A	437	122	284	32.8	449	0	1,280
K	Ruppess Boghole	5/20/92	4291063	669425	465	7.7	16	1.3 ^a	59.9	24.5	6.27	1.28	300	0	21.4
L	Sand	12/17/91	4177373	609993	332	9.3	19	0.1	15.5	10.8	36.8	11.4	126	30	21.9
M	Saratoga	5/4/92	3946865	551414	4,625	7.7	28	13	31.8	34.7	977	34.9	427	0	1,020
N	South Millick	6/18/92	4353631	726060	432	7.7	13	19	52.4	22.6	8.64	1.35	262	0	14.6
O	Unnamed (east of Piermont Creek)	6/18/92	4373818	715407	137	6.9	15	0.1 ^a	15.8	3.83	6.08	1.22	54	0	9.50
P	Unnamed (north of Shoshone)	5/27/92	4304021	725273	269	7.8	12	19.8 ^a	35.9	11.6	2.60	0.73	182	0	4.08
Q	Warm (a)	5/12/92	4257712	605567	749	6.9	64	1.3 ^a	68.3	15.1	68.2	15.8	468	0	46.3

^aLocations where discharge was measured at one orifice in a 'spring group' with multiple orifices

Field and laboratory methods

It is well established that regional springs discharging from the carbonate-rock aquifer regional flow systems (Fig. 1) have large and consistent discharge, and consistent temperature, water chemistry, and isotopic signatures (e.g., Eakin and Moore 1964; Mifflin 1968; Winograd and Thordarson 1975; Harrill et al. 1988; Thomas et al. 1996; Rose and Davisson 2003); therefore, a single sampling campaign as conducted for this study over only several months of one year adequately captures the characteristics of regional springs. However, it is recognized that seasonal and annual variations in 'small-local' and 'local' springs are not captured in a single sampling campaign and that there is a possibility, although small, that a non-regional spring could be incorrectly characterized as a regional spring in this study.

As an initial reconnaissance tool, discharge and temperature were measured at 95 waters in the carbonate-

rock province—Fig. 3 (see Table 1 of ESM). Based on the initial results, 34 springs (Fig. 3) were sampled to determine the concentrations of major ions and selected trace metals, the δD and $\delta^{18}O$ of the waters, the $\delta^{13}C$ of dissolved carbon, and activities of ^{14}C and 3H (Table 1). Springs sampled were selected based on their availability for sampling, ease of access, spatial distribution across the province, and location near a basin's floor. Sixteen of the springs sampled were previously identified as known regional springs (Mifflin 1968) in the central and southern portions of the regional flow system. The remaining 18 springs were not previously identified as regional, but appeared likely to be regional based on their temperature and discharge rate. The physical, chemical, and isotopic characteristics of the known regional springs formed the basis of comparison for assessing the likelihood that other springs might be supported by regional groundwater flow. Springs are referred to in the text by name. However, for easy identification in figures, a numeral

Cl ⁻ (mg/L)	F ⁻ (mg/L)	SiO ₂ (mg/L)	NO ₃ ⁻ (as N, mg/L)	Ba ²⁺ (mg/L)	Li ⁺ (mg/L)	Sr ²⁺ (mg/L)	TDS (mg/L)	δD (‰)	δ ¹⁸ O (‰)	¹⁴ C (pmc)	δ ¹³ C (‰)	³ H (pCi/L)	Position in flow system
8	0.9	30	-	-	-	-	429	-108	-14.1	6.3	-6.7	<10	Intermediate
60.1	2.1	29.1	0.43	0.04	0.14	0.99	716	-97	-13.2	9.7	-5.9	<10	End
500	1.4	18	-	-	-	-	4,042	-93	-12.4	7.2	-5.3	-	End
23.7	1.7	27.3	0.09	0.07	0.090	0.94	597	-102	-13.7	11.2	-5.7	<10	Intermediate
8.8	0.35	24.6	0.27	0.08	0.03	0.23	413	-109	-15.4	6.2	-7.7	<10	Intermediate
20.7	1.8	22.9	0.18	0.080	0.09	0.85	561	-103	-13.4	2.8	-6.8	<10	Intermediate
21.4	1.7	22.7	0.04	0.06	0.09	0.84	582	-103	-13.8	4.6	-4.9	<10	Intermediate
9.4	0.60	32.4	0.29	0.11	0.04	0.34	444	-109	-13.8	N/A	N/A	<10	Intermediate
9.6	0.99	26.8	0.10	0.12	0.06	0.36	475	-119	-15.6	4.5	-5.1	<10	Intermediate
35.6	3.3	26.4	0.07	0.04	0.15	1.07	793	-103	-13.6	3.6	-7.8	<10	End
16.0	1.5	47.7	0.63	0.08	0.06	0.3	357	-107	-14.4	23.1	-9.0	<10	Intermediate
21	1.4	23	-	-	-	-	582	-104	-13.6	-	-	-	Intermediate
327	1.4	16.8	0.27	0.02	0.58	4.38	3,011	-92	-12.4	3.0	-2.3	<10	End
423	3.0	86.9	0.07	0.03	0.22	0.11	2,548	-98	-12.7	2.2	-6.3	<10	End
35.7	3.6	31.2	0.14	0.04	0.16	1.06	775	-101	-13.6	3.4	-5.6	<10	End
35.2	3.6	31.6	0.15	0.04	0.16	1.09	767	-102	-13.7	3.5	-7.9	<10	End
15.6	0.60	27.7	0.07	0.05	0.03	0.47	733	-98	-12.7	N/A	N/A	11	N/A
5.1	0.15	10.6	0.35	0.12	0.01	0.13	337	-111	-14.9	29.8	-9.5	11	N/A
6.1	0.16	18.4	0.96	0.07	0.01	0.26	422	-93	-13.1	14.1	-8.4	<10	N/A
10.7	0.24	61.3	0.34	0.17	0.02	0.32	584	-95	-12.6	N/A	N/A	16	N/A
31.0	3.3	50.1	<0.01	0.13	0.66	2.18	1,191	-114	-14.3	<0.5	-2.3	<10	N/A
34.0	0.70	17.5	0.53	0.03	0.01	0.18	427	-110	-14.5	83.1	-12.4	11	N/A
394	1.3	14.4	0.16	0.02	0.54	4.63	3,054	-97	-12.3	7.8	-5.8	<10	N/A
3.4	0.13	49.9	<0.01	0.38	0.07	0.22	498	-125	-16.6	4.7	-1.5	<10	N/A
4.0	0.09	14.1	0.40	0.02	0.01	0.1	449	-107	-14.3	66.1	-9.9	15	N/A
390	1.2	15.7	0.59	0.02	0.54	4.75	3,018	-97	-12.4	8.9	-2.6	<10	N/A
3.2	0.21	17.4	0.45	0.09	0.010	0.34	435	-114	-15.1	28.4	-8.2	<10	N/A
3.6	1.7	35.4	0.05	0.11	0.09	0.29	314	-107	-14.3	N/A	N/A	<10	N/A
672	2.6	38.3	0.89	0.02	0.370	2.76	3,242	-88	-10.4	30.3	-7.3	<10	N/A
8.5	0.09	10.5	0.39	0.11	0.01	0.2	381	-116	-15.2	56.8	-10.3	21	N/A
9.2	0.06	3.7	0.21	0.05	<0.005	0.06	104	-121	-16.1	N/A	N/A	86	N/A
1.3	0.06	11.8	0.30	0.02	0.01	0.23	251	-111	-15.1	46.8	-9.3	23	N/A
11.1	1.8	44.0	<0.01	0.23	0.240	0.61	740	-121	-15.4	<1.0	-2.3	<10	N/A

is used to represent known regional springs and a letter is used to identify other sampled waters; the numerals or letters associated with each water source are given in Table 1. Springs with only temperature and discharge data are identified by two letters (see Tables 1 and 2 in ESM).

Because of the range of discharges observed, several measurement methods were used. Where available, discharge was measured using a flume or weir. In many locations, less precise methods of measurement were used such as collecting discharge in a bucket or beaker over a specific period of time or measuring the channel cross-sectional area and velocity of the flow away from the spring; at some locations, it was necessary to visually estimate discharge because of very low flow volumes. Where springs emanated from multiple orifices and/or diffuse seepage areas, discharge was measured only at the sample collection point. In these instances, the reported discharge underestimates the total discharge of the spring area. Temperature

measurements were made using a thermometer placed in the spring discharge as close to the orifice as possible. Electrical conductivity (EC), pH, and alkalinity were measured in the field.

Water samples for chemical analysis were collected in clean HDPE bottles that were triple rinsed with sample water prior to filling. All samples were filtered through a 0.45- μ m filter. Reagent-grade HNO₃ was added to the cation and trace metal samples until the pH of the sample was less than 2. Samples were stored and transported under cool conditions. Stable isotope samples were collected in clean, triple field rinsed glass bottles with a Poly-Seal lid. Samples for ¹⁴C analysis were collected in 50 L HPDE carboys. Samples for ³H analysis were collected in 1 L glass bottles.

Chemical analyses were conducted at the Desert Research Institute's US Environmental Protection Agency (EPA) certified Water Analysis Laboratory in Reno, Nevada, USA following standard US EPA methods for

chemical analyses of water; stable isotopic analyses were conducted at the Desert Research Institute's Stable Isotope Laboratory in Las Vegas, Nevada. $\delta^{18}\text{O}$ samples were prepared by reacting water with guanidine hydrochloride to yield CO_2 ; δD samples were prepared using the zinc-reduction method to form H_2 . Carbon isotope samples were treated to precipitate dissolved carbonate species by adding sodium hydroxide and strontium chloride. The precipitated carbon for $\delta^{13}\text{C}$ analysis was converted to CO_2 gas by acid hydrolysis using 100% phosphoric acid. $\delta^{18}\text{O}$, δD , and $\delta^{13}\text{C}$ samples were analyzed on a gas-ratio mass spectrometer, with values for $\delta^{18}\text{O}$ and δD reported relative to VSMOW (Vienna Standard Mean Ocean Water) and $\delta^{13}\text{C}$ values reported relative to VPDB (Vienna PeeDee Belemnite). The activity of ^3H samples was determined by liquid scintillation counting at the Desert Research Institute's Enriched Tritium Laboratory in Reno, Nevada; the water samples for ^3H determination were electrolytically enriched prior to analysis. ^{14}C analyses were conducted at Krueger Enterprises Inc., Geochron Laboratories Division, Cambridge, Massachusetts.

Discharge and temperature

Spring discharge and temperature are easily observed conditions that have been used for preliminary identification of regional springs in the carbonate-rock province (Mifflin 1968). Large and consistent discharge suggests a supporting groundwater system that is recharged over a large area where natural small-scale variations in recharge are smoothed. Warm water temperatures suggest deep groundwater flow paths under a normal geothermal gradient or contact with a localized geologic heat source. Many regional springs are found on valley floors where faulting has juxtaposed low permeability non-carbonate rock with the regional carbonate aquifer (Winograd and Thordarson 1975; Dettinger et al. 1995; Dettinger and Schaefer 1996) forcing the regional carbonate groundwater to the surface. In contrast, springs discharging from local systems are likely to have shallow flowpaths and smaller recharge areas, suggesting lower temperatures and discharges. Thus, regional springs are likely to have relatively high temperatures and discharge rates compared to local springs. Of course, exceptions to this generalization occur, but examining discharge and temperature is a reasonable first-pass screening method.

The ranges of spring discharge (Q) and temperature (T) for the springs sampled for this study are shown in Fig. 4. The known regional springs sampled for this study (Mifflin 1968) have discharges greater than 10 L/s and temperatures greater than 25 °C; six springs other than the known regional springs were observed to discharge at temperatures in excess of the T/Q criterion—Hot [E], Littlefield [G], Monte Neva Hot [H], Saratoga [M], Moorman [BE], Warm (b) [BZ]. As this study was designed to initially survey as many springs as possible in the area of interest, only the first four of these springs were among the 18 selected for additional detailed

sampling and analysis. There are also a number of springs that meet either the temperature or discharge portion of this criterion, but fail to meet the other.

Spring chemistry and isotopic composition

In the regional carbonate aquifer, groundwater usually exhibits chemical characteristics consistent with interaction with carbonates. Regional carbonate aquifer groundwater is at saturation with respect to calcite and at, or above, saturation with respect to dolomite—calculated saturation indices (SI) for important minerals are listed in the electronic supplementary material (see Table 2 in ESM); karst features (e.g., Winograd and Thordarson 1975), along with carbonate mineral SI indicate incongruent dissolution of calcite and dolomite. As groundwater moves along a flowpath, concentrations of ions such as SO_4^{2-} and Ca^{2+} increase because of the dissolution of minor minerals like gypsum (Thomas et al. 1996; Winograd and Thordarson 1975), which is under-saturated in the regional carbonate aquifer (see Table 2 in ESM). Na^+ and K^+ are often derived from the dissolution of volcanic rocks—under-saturated primary silicate minerals (see Table 2 in ESM)—and increase in concentration in the regional carbonate aquifer by mixing with waters from volcanic aquifers. Cl^- concentrations may also increase by mixing with groundwaters that have undergone evaporation or by dissolution of sedimentary rocks formed in the oceans (Hem 1992).

Major dissolved ion contents for the known regional springs are plotted on a Piper diagram (Fig. 5) showing the chemical composition of groundwater in the central and southern portions of the regional carbonate aquifer. Known regional springs are grouped by both geographic location within the regional carbonate aquifer and by similarity in major-ion composition. Illustrated flow directions are from Harrill et al. (1988) and are shown in Fig. 6. Figure 7 shows the changes in major-ion composition along the regional carbonate aquifer with Stiff diagrams. Groundwater in the central portion of the regional carbonate aquifer (group I) tends to have anion chemistry dominated by HCO_3^- ; cation composition is mixed, and Ca^{2+} is found in higher proportion than in groups II, III, IV and V. As groundwater flows downgradient toward the end of the regional aquifer, the proportions of ($\text{Na}^+ + \text{K}^+$) and ($\text{Cl}^- + \text{SO}_4^{2-}$) increase relative to ($\text{Ca}^{2+} + \text{Mg}^{2+}$) and ($\text{HCO}_3^- + \text{CO}_3^{2-}$), showing the influence of dissolution of minor minerals like gypsum (under-saturated, see Table 2 in ESM) and halite (or connate Cl^-) in either the regional carbonate aquifer or in local geologic units near the springs, mixing with local volcanic groundwaters (under-saturated primary silicate minerals, see Table 2 in ESM), mixing with local evaporated shallow groundwaters (groups II–VI), and precipitation of carbonate minerals such as calcite (regional groundwater stays near saturation with respect to calcite regardless of position in the flow systems, see Table 2 in ESM).

Spring discharge in the central portion of the regional carbonate aquifer at Hot Creek (9) and at the Pahranaagat Valley springs ([1], [5], and [8]; group I) are of nearly

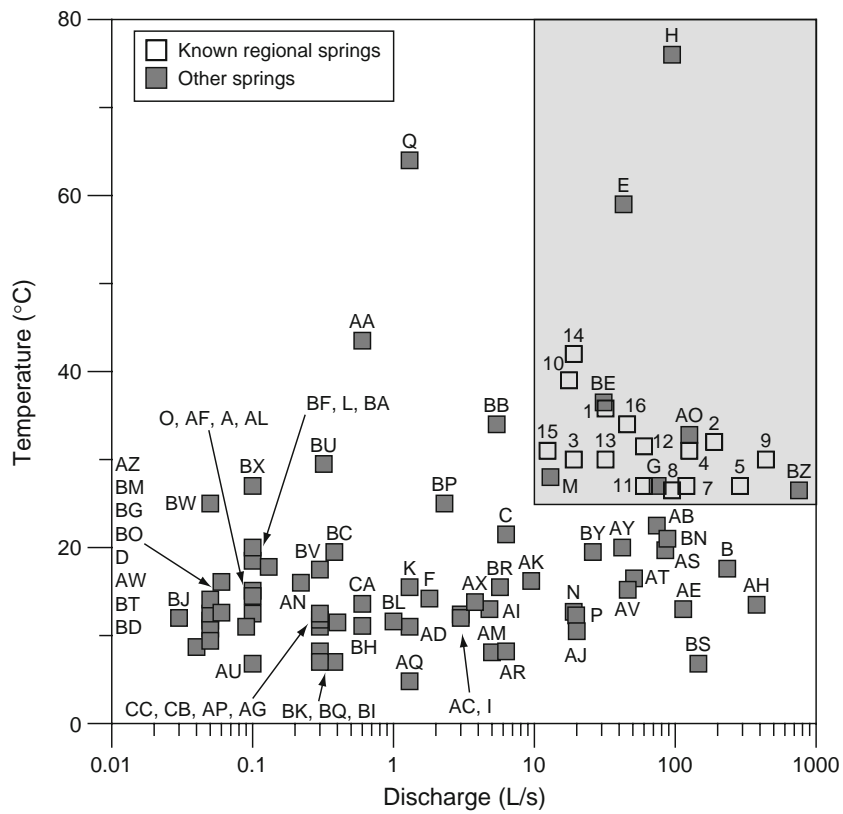


Fig. 4 Plot of spring water temperature (T) vs. spring discharge rate (Q). Known regional springs plot in the grey area

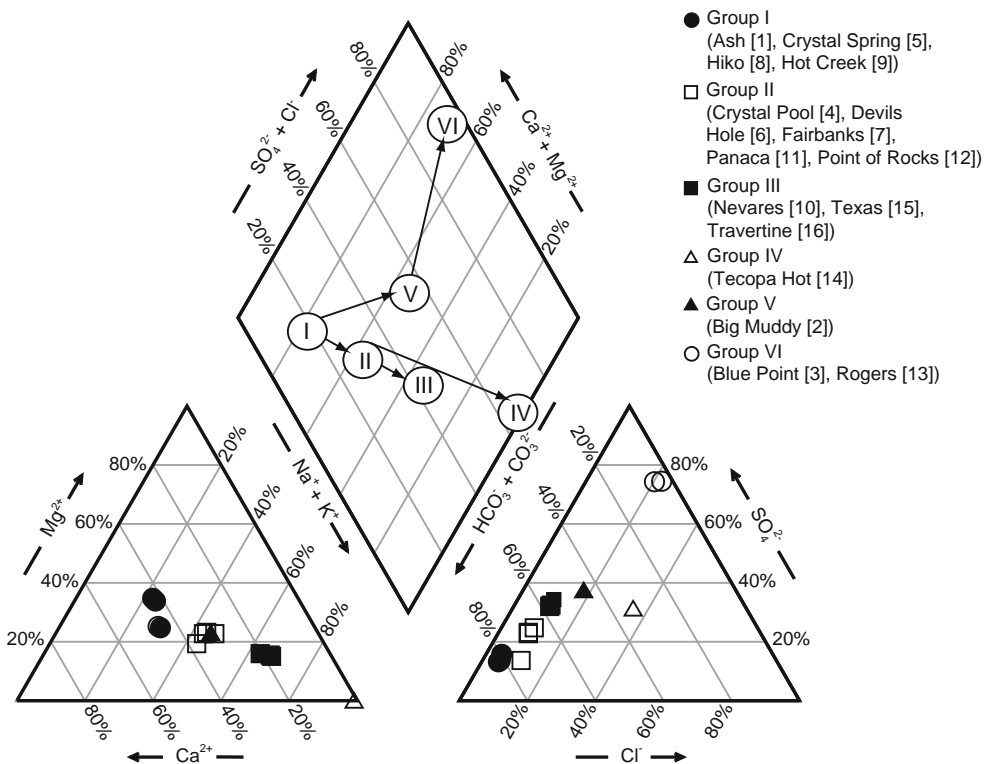


Fig. 5 Piper diagram showing the major-ion evolution of groundwater in regional flow systems

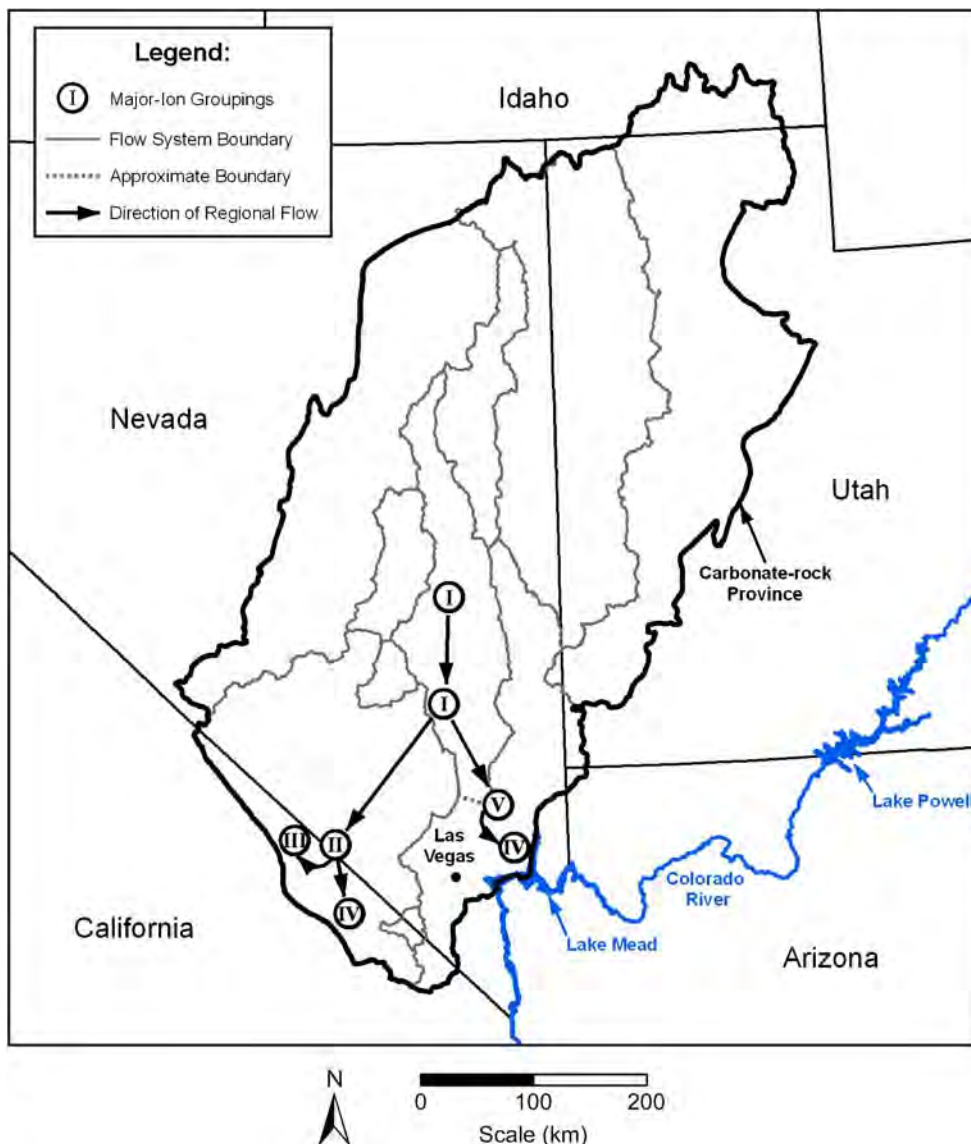


Fig. 6 Map showing major-ion groupings of known regional springs (see Fig. 5) and general direction of groundwater flow in the regional carbonate aquifer

identical major-ion composition, even though these areas are separated by over 30 km. The major ions are dominated by Ca^{2+} and HCO_3^- , indicating the dissolution and precipitation of the predominant carbonate rocks in the central portion of the aquifer. Total dissolved solids (TDS) are moderate, with a mean value of 440 mg/L. From the central portion, groundwater in the regional carbonate aquifer splits into two different flow systems, each with a distinct chemical evolution.

Groundwater from the central portion flows southeastward and evolves chemically to that observed at Big Muddy ([2]; group V). Big Muddy [2] discharge has higher TDS (716 mg/L) than group I and has a molar $\text{Na}^+:\text{Ca}^{2+}:\text{Mg}^{2+}$ ratio of about 4:1:1 and a molar $\text{HCO}_3^-:\text{SO}_4^{2-}:\text{Cl}^-$ ratio of about 2:1:1. From the central portion to Big Muddy [2], groundwater in the regional carbonate aquifer passes through Tertiary silicic volcanic rocks and clastic rocks. Dissolution of the volcanic rocks (under-saturated

primary silicate minerals) adds Na^+ to the groundwater while the clastic rocks composed of sandstone, siltstone, and clay with abundant gypsum beds, add Na^+ , K^+ , and SO_4^{2-} —cation exchange of Na^+ and K^+ for Ca^{2+} , and dissolution of gypsum (under-saturated). From Big Muddy (2), groundwater in the regional carbonate aquifer flows toward Lake Mead and the Colorado River. Another large increase in TDS is observed at Rogers and Blue Point ([13], [3]; group VI; mean TDS \cong 3,500 mg/L)—with increases in the proportion of Ca^{2+} (molar $\text{Na}^+:\text{Ca}^{2+}:\text{Mg}^{2+}$ ratio of about 2:2:1) and SO_4^{2-} (molar $\text{HCO}_3^-:\text{SO}_4^{2-}:\text{Cl}^-$ ratio of about 1:8:4). As in the vicinity of Big Muddy [2], groundwater discharging at Rogers [13] and Blue Point [3] flows through clastic rocks and is greatly affected by the local presence, and dissolution, of gypsum.

Groundwater from the central portion of the regional carbonate aquifer also flows southwestward and evolves chemically to that observed in Ash Meadows ([4], [6], [7];

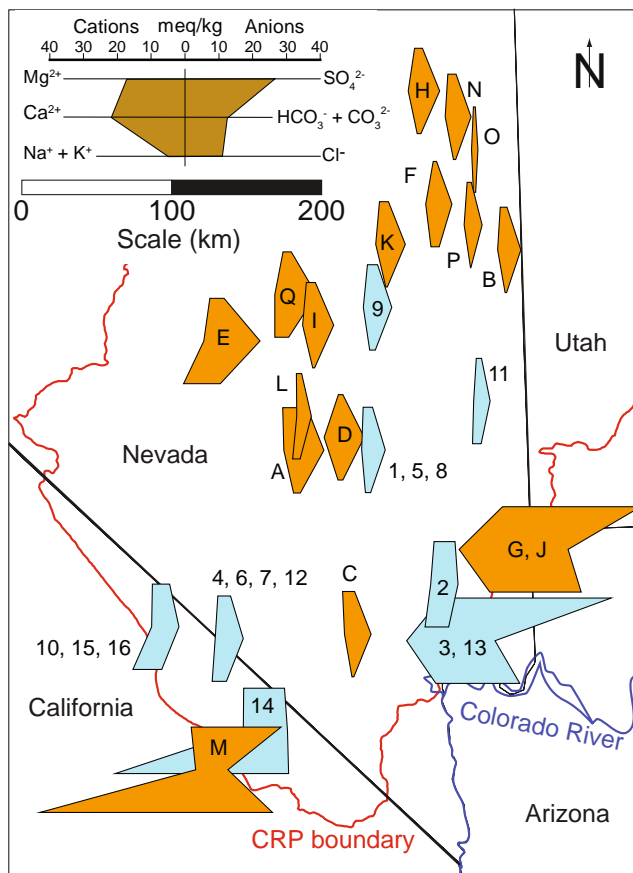


Fig. 7 Stiff diagrams for springs listed in Table 1 plotted on a map for visual observation of spatial variation in water chemistry. The area covered by the map is a subset of that shown in Figs. 1 and 2. Stiff diagrams for known regional springs are light blue; diagrams for other springs are orange. State boundaries are shown in black (the Colorado River, shown in blue, is also a state boundary), and the carbonate rock province (CRP) boundary is shown in red. In four cases where springs were in close proximity and had virtually identical Stiff diagrams, a single diagram is used to represent the group of springs

group II). Ash Meadows springs have increased TDS (mean of ~580 mg/L) compared to the Group I springs, but the chemical evolution from group I to Ash Meadows is markedly different than that from group I to group V. Spring discharge at Ash Meadows has a molar $\text{Na}^+:\text{Ca}^{2+}:\text{Mg}^{2+}$ ratio of about 3:1:1 and a molar $\text{HCO}_3^-:\text{SO}_4^{2-}:\text{Cl}^-$ ratio of about 5:1:1. Schoff and Moore (1964) and Winograd and Thordarson (1975) attribute the change in water chemistry to the weathering of Tertiary silicic volcanic rocks upgradient of Ash Meadows. Dissolution of volcanic rocks (under-saturated primary silicate minerals; see Table 2 in ESM) contributes Na^+ but little SO_4^{2-} and Cl^- . From Ash Meadows, groundwater continues to flow southwestward to Death Valley, which is the terminus of the regional carbonate aquifer in the southwestern part of the carbonate rock province. Spring discharge at the larger springs in Death Valley ([10], [15], [16]; group III) has again increased in TDS (mean of ~780 mg/L) and the proportions of the major ions have changed. Known regional springs from group III have molar $\text{Na}^+:\text{Ca}^{2+}:\text{Mg}^{2+}$ ratios of about 6:1:1 and a molar $\text{HCO}_3^-:\text{SO}_4^{2-}:\text{Cl}^-$ ratio of about 5:1:1.

From Ash Meadows, a portion of groundwater flows southward and evolves chemically somewhat differently than the Death Valley springs. Groundwater discharge at Tecopa Hot ([14]; group IV), thought to be a mixture of flow from Ash Meadows and the Pahrump Valley (Harrill et al. 1988), has very high TDS (~2,500 mg/L); its cation chemistry is dominated by Na^+ (over 99% of cations by molar proportion); and it is a mixed-anion water, having a molar $\text{HCO}_3^-:\text{SO}_4^{2-}:\text{Cl}^-$ ratio of about 2:1:2.

Springs in groups III and IV, and VI, are located at the terminus of the Death Valley and Colorado River regional groundwater flow systems, respectively, and are designated as “end” springs in Table 1. Known regional springs in other groups are situated at intermediate locations in the regional flow systems and are designated “intermediate” springs in Table 1.

From the major-ion content described in the previous section, it is apparent that water chemistry in the southern portion of regional carbonate aquifer is dramatically different from that in the central portion (Fig. 7) and is greatly influenced by the dissolution of volcanic rocks, minerals such as gypsum, and mixing with evaporated shallow groundwater. In many cases, a single characteristic, such as TDS or abundance of an individual ion, is not likely to be a good geochemical indicator of regional flow system discharge. As a result, this study uses a number of criteria for testing ‘regionalness’ based on physical, chemical, and isotopic characteristics of waters. Each of these criteria is supported by empirical observation (i.e., all or most of the known regional springs examined for this study plot as a group, with a narrower range in values than the overall population of waters); however, each criterion is also supported by a theoretical analysis of the likely characteristics of local vs. regional waters.

A plot of $(\text{Na}^+ + \text{K}^+)$ vs. $(\text{Cl}^- + \text{SO}_4^{2-})$ for the springs sampled in this study is shown in Fig. 8a, which is similar to that of Mifflin (1968) except that he used a sloped line as the boundary rather than a vertical or horizontal line for each of the ion pairs. All of the known regional springs plot in the upper right quadrant of the diagram. Regional springs classified as intermediate in the flow system cluster near the center of the graph while those discharging from the end of a regional flow system plot further toward the upper right corner. Seven additional waters plot in the regional spring field. Littlefield [G] and Petrified [J] are located in the Virgin River Valley in the southern part of the study area. Hot [E] and Warm (a) [Q], are in the intermediate portion of the flow system. Saratoga [M] is at the terminus of the flow system in Death Valley. All these springs are located on valley floors. April Fool [A] and Kious [F] also plot in the regional spring field in Fig. 8a. However, the character of these two springs is considerably different from the known regional springs. These springs are situated above the valley floor on bounding mountain blocks, have relatively low temperatures (12.5 and 14.2 °C, respectively) and small discharge (0.1 and 0.5 L/s), and are located in geologic terrains composed of a mixture of basalt, rhyolite, quartzite, carbonates, and/or quartz monzonite/granodiorite.

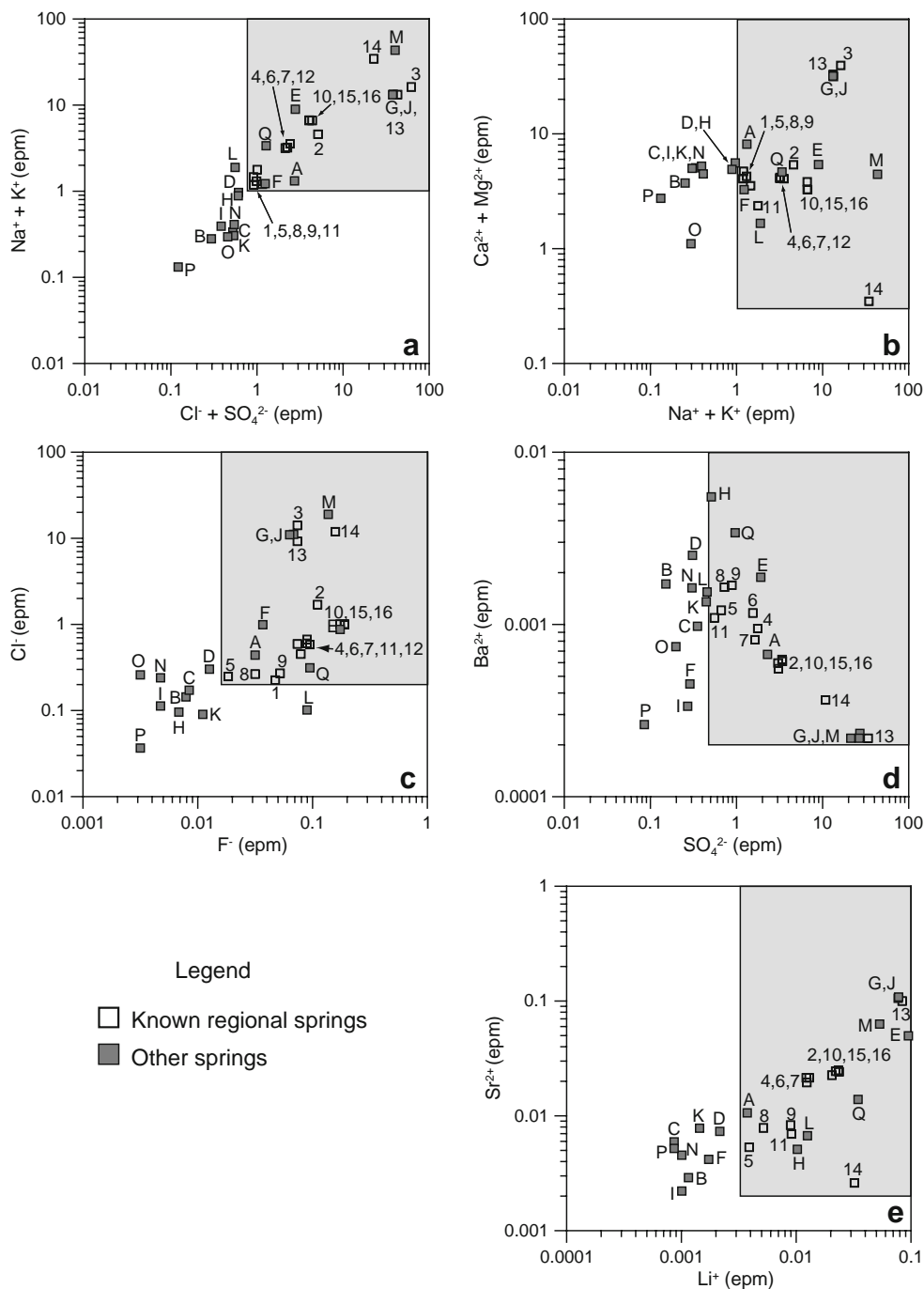


Fig. 8 Plots, in equivalent concentrations, of various chemical constituents in groundwater in regional flow systems. Known regional springs plot in the grey areas. **a** ($\text{Na}^+ + \text{K}^+$) vs. ($\text{Cl}^- + \text{SO}_4^{2-}$), **b** ($\text{Ca}^{2+} + \text{Mg}^{2+}$) vs. ($\text{Na}^+ + \text{K}^+$), **c** Cl^- vs. F^- , **d** Ba^{2+} vs. SO_4^{2-} , **e** Sr^{2+} vs. Li^+ . *epm* equivalents per million

The ratio of equivalent concentrations of ($\text{Ca}^{2+} + \text{Mg}^{2+}$) to ($\text{Na}^+ + \text{K}^+$) for springs sampled in this investigation fell between 0.01 and 32 (Fig. 8b). Known regional springs exhibit ratios from 0.5 to 4 (except Tecopa Hot [14] at 0.01). All known regional springs have values of ($\text{Na}^+ + \text{K}^+$) greater than 1 epm (equivalents per million); known regional springs at the end of the regional flow system have noticeably higher concentrations of ($\text{Na}^+ + \text{K}^+$) than do intermediate regional springs. Winograd and Thordarson (1975) showed a significant difference in the relative

equivalent amounts of ($\text{Ca}^{2+} + \text{Mg}^{2+}$) and ($\text{Na}^+ + \text{K}^+$) between groundwater from carbonate aquifers and those from volcanic aquifers in southern Nevada. Groundwater from carbonate rocks had equivalent concentrations of ($\text{Ca}^{2+} + \text{Mg}^{2+}$) at least three times greater than their equivalent concentrations of ($\text{Na}^+ + \text{K}^+$). Groundwater from volcanic rocks had equivalent concentrations of ($\text{Na}^+ + \text{K}^+$) at least twice that of ($\text{Ca}^{2+} + \text{Mg}^{2+}$). They found that groundwater that flowed through both carbonate and volcanic rocks had similar equivalent concentrations. Eight

additional springs plot in the same area of the graph as the known regional springs. Littlefield [G] and Petrified [J] plot immediately adjacent to Rogers [3] and Blue Point [13]. The remaining six (April Fool [A], Hot [E], Kious [F], Sand [L], Saratoga [M], and Warm (a) [Q]) plot in the lower portion of the 'regional' box along with most of the known regional springs.

In water samples collected for this investigation, F^- and Cl^- concentrations increase in the general direction of groundwater flow through the regional flow systems (Fig. 8c). Because there tends to be little Cl^- in volcanic rocks as compared to F^- , and because there is much less F^- in carbonate rocks than Cl^- , the observed increase of these two ions suggests both mixing of volcanic waters and dissolution of carbonate aquifer minerals. Hem (1992) shows the average $Cl^-:F^-$ ratio in igneous rocks is 0.427—305 parts per million (ppm) Cl^- , 715 ppm F^- —while the average ratio in carbonate rock is 2.72 (305 ppm Cl^- , 112 ppm F^-). The $Cl^-:F^-$ ratio for most of the known regional springs is 5:1 or greater, which indicates that mixing with local evaporated groundwater is also important. Six springs (Rogers [13], Blue Point [3], Tecopa Hot [14], Littlefield [G], Petrified [J], and Saratoga [M]) have ratios in excess of 75:1 indicating that there may be a significant component of evaporated water in these springs. Seven waters not previously recognized as regionally sourced plot in the vicinity of known regional springs. April Fool [A], Hot [E], Kious [F], and Warm [Q] plot in the vicinity of known regional springs at intermediate locations in the flow systems. Littlefield [G], Petrified [J], and Saratoga [M] plot in the general vicinity of known regional springs at the ends of flow systems.

Ba^{2+} and SO_4^{2-} concentrations in known regional springs exhibit an inverse relationship, with Ba^{2+} concentration decreasing as SO_4^{2-} increases (Fig. 8d). Compared to known regional springs at the end of flow systems, known regional springs intermediate within a flow system have higher concentrations of Ba^{2+} and lower concentrations of SO_4^{2-} . The likely source of most of the Ba^{2+} in the regional carbonate aquifer is from the dissolution of carbonate minerals since Ba^{2+} can substitute for Ca^{2+} and Mg^{2+} in the calcite and dolomite crystal structure (Chang et al. 1998) and/or dissolution of small amounts of witherite ($BaCO_3$). Regional carbonate groundwater is saturated with respect to calcite, under-saturated to saturated with respect to dolomite, and under saturated with respect to witherite (see Table 2, ESM). The increasing SO_4^{2-} in the regional carbonate aquifer results from the dissolution of gypsum (or anhydrite) as discussed above. Because the solubility of gypsum ($K_{sp}=10^{-4.6}$) is several orders of magnitude higher than that of barite ($K_{sp}=10^{-10}$), dissolution of gypsum is likely to drive precipitation of barite; regional groundwater is under-saturated with respect to gypsum and at, or near, saturation with respect to barite (see Table 2, ESM). Most of the other waters sampled for this investigation have SO_4^{2-} concentrations below 0.55 epm, the lowest observed value for the known regional springs. Several springs other than

the known regional springs contain SO_4^{2-} concentrations above 0.55 epm. Hot [E], Monte Neva Hot [H], and Warm (a) [Q] have SO_4^{2-} concentrations in the range exhibited by known intermediate regional springs, but have Ba^{2+} concentrations that are significantly higher. April Fool [A] plots on the trend of the regional springs between the intermediate and end springs. Littlefield [G], Petrified [J], and Saratoga [M] plot in the extreme end of the regional end spring field, close to Rogers [13].

Li^+ and Sr^{2+} concentrations in known regional springs exceed 0.003 and 0.002 epm, respectively. A plot of Sr^{2+} vs. Li^+ shows that their equivalent concentrations increase in near-linear fashion along the regional flow paths (Fig. 8e) with known regional springs intermediate in the flow systems having less Li^+ and Sr^{2+} than regional springs at the end of the regional flow paths. The single notable exception to this ratio occurs for Tecopa Hot [14]; this water produced an equivalent $Sr^{2+}:Li^+$ ratio of less than 0.1. The likely source of Li^+ is dissolution of volcanic rocks, although Li^+ also occurs in evaporates and natural brines (Hem 1992). Li^+ is not commonly involved in ion-exchange reactions so it tends to remain in solution once it is introduced by weathering reactions (Hem 1992). Sr^{2+} replaces Ca^{2+} and Mg^{2+} in carbonate minerals so it should increase along the regional carbonate aquifer as carbonate minerals dissolve. Sr^{2+} may also originate from the dissolution of strontianite ($SrCO_3$) and celestite ($SrSO_4$) as both minerals are under-saturated in regional carbonate aquifer water (see Table 2, ESM). Most other springs sampled for this investigation have concentrations of Li^+ lower than the concentrations observed in the known regional springs, but eight of these springs plot among the regional springs. April Fool [A], Monte Neva Hot [H], and Sand [L] plot in the vicinity of intermediate regional springs. Hot [E], Littlefield [G], Petrified [J], Saratoga [M], and Warm (a) [Q] have Li^+ and Sr^{2+} concentrations that plot in the same general area of the diagram as do the known regional springs at the end of the flow system (Table 1).

Intermediate regional springs have $\delta^{18}O$ values from -15.6 to -13.4 ‰, while regional end springs have $\delta^{18}O$ values between -13.7 and -12.4 ‰ (Fig. 9a). The small area of overlap is occupied by the springs of Ash Meadows and Death Valley. All the springs in the northern part of the carbonate rock province (for this purpose, Hot [E] and all springs north of it are considered to be in the northern part of the carbonate rock province, and all springs south of Hot [E] are in the southern portion; see Fig. 3) have $\delta^{18}O$ values in or below the range of the intermediate regional springs. The southern springs have $\delta^{18}O$ values in, or slightly above, the range of the regional end springs. The data show that, in general, spring waters are more enriched in the heavy isotopes in the down-gradient direction of regional groundwater flow. At a gross scale, regional groundwater flow is from north (cooler temperatures) to south (warmer temperatures) and from higher to lower elevation, so the enrichment in heavy isotopes indicates progressive mixing of locally derived recharge with the isotopically light water from the upper

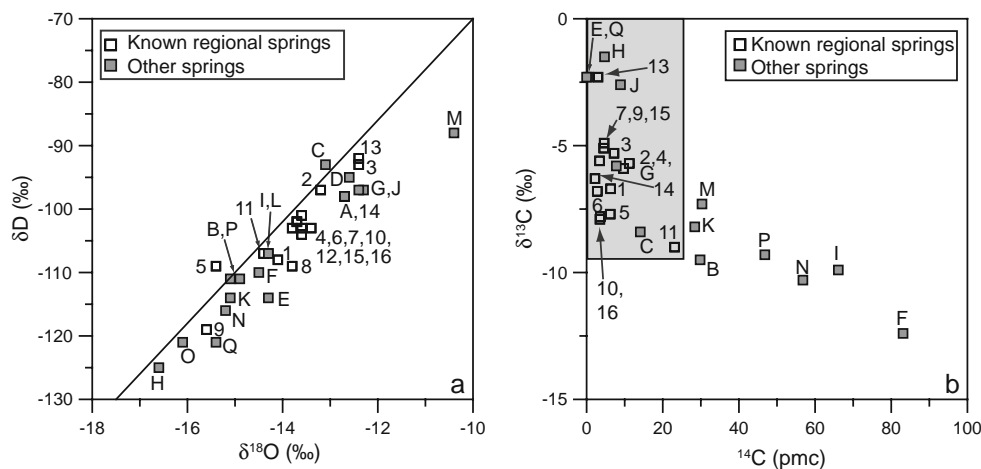


Fig. 9 Plots of isotope values measured in sampled waters. **a** δD vs. $\delta^{18}O$ shown with the global meteoric water line, **b** $\delta^{13}C$ vs. ^{14}C activity as uncorrected percent modern carbon (*pmc*)

portion of the flow system (e.g., Thomas et al. 1996; Rose and Davisson 2003). Monte Neva Hot [H], the northernmost spring sampled, has the lightest isotopic signature, while Saratoga [M], the southernmost spring sampled, has the heaviest isotopic signature and is clearly evaporated.

Many of the springs show some evidence of an isotopic shift to the right of the meteoric water line. The greatest shift occurs for Hiko [8], Hot [E], Littlefield [G], Petrified [J], Saratoga [M], and Warm (a) [Q]. For Warm [Q] and Hot [E], (discharge temperatures of 64 and 59 °C, respectively) this may be the result of kinetically accelerated isotope exchange with the host rock. Hiko [8] and Saratoga [M] were sampled from spring pools because their orifices could not be found, so these waters may have had opportunity to undergo evaporation prior to sampling.

³H activity was determined for 33 springs, including the known regional springs. All the known regional springs and twelve other springs had ³H activity below detection (<10 picocuries per liter, pCi/L), indicating that the waters entered the groundwater system prior to 1952 (Clark and Fritz 1997). Below-detectable ³H activity was shown by Mifflin (1968) to be a good indicator of longer groundwater flow paths and of regionalness. Eight springs were found to have detectable ³H activity (Table 1), indicating that some portion of the waters was recharged after 1952. All eight of the springs with detectable ³H activity are located in the northern portion of the area and most are high elevation springs, which presumably are the endpoints of small local flow systems. Nine springs (Corn Creek [C], Hot [E], Littlefield [G], Monte Neva Hot [H], Petrified [J], Ruppess Boghole [K], Sand [L], Saratoga [M], South Millick [N], and Warm [Q]) had ³H below 10 pCi/L.

For carbon isotopes, the known regional springs cluster in the upper-left portion of Fig. 9b, within the ¹⁴C activity range of 2.8–23.1 pmc (with all but Panaca [11] having ¹⁴C activity below 11.2 pmc) and the δ¹³C range of –9.0 to –3.9‰. In these narrow ranges, there is no pattern that distinguishes intermediate regional and regional end springs. Panaca [11] has higher ¹⁴C activity and lower δ¹³C values, indicating a shorter flow path, less exposure

to carbonate rock along the flow path, mixing with younger waters near the discharge area, exposure to atmospheric carbon in the spring pool, or some combination of these conditions. In addition to the known regional springs, six springs plot in the upper-left portion of the graph. Three are northern springs on the upper-to-intermediate part of the flow systems: Hot [E], Monte Neva Hot [H], and Warm (a) [Q]. They are all thermal springs, and their carbon isotope values were probably affected by their high temperatures, as similar carbon isotope values have been observed for other thermal springs (Mook 1980). Corn Creek [C], Littlefield [G] and Petrified [J] are all at or near the end of a flow system, and have lower temperatures suggesting only normal water–rock interaction has affected their carbon isotope signatures. Springs in the lower-right portion of the plot (¹⁴C pmc values above 40 and δ¹³C values of –9.3‰ or lower) are in the upper to intermediate portion of the flow system: Kious [F], Ox [I], South Millick [N], and unnamed (north of Shoshone) [P]. Together, these data suggest that δ¹³C values increase and the ¹⁴C activity decreases along the general north to south flow path of the regional groundwater systems.

Identification of previously unrecognized regional waters

Classification by examination of physical, chemical, and isotopic data

Because regional springs exhibit a wide range of physical, chemical, and isotopic characteristics, no single test based on these properties would be an accurate indicator of a spring's source (small-local, local, or regional). Results of the chemical, physical, and isotopic tests for regionalness discussed in the previous sections are summarized in Table 2. Some waters have no characteristics in common with the known regional springs (e.g., Ox [I]), indicating they are local in nature. Other springs share some characteristics with the known regional springs, but do not share other important characteristics. For instance,

Table 2 Summary of similarities of spring characteristics to those of known regional springs. *X* indicates that the spring in question meets a given criterion; *NA* indicates that data are not available to test the spring for that criterion. Likelihood that a spring represents a discharge point for a regional flow system is shown by *letters* in the *Regional?* column: *A* very likely to be a regional spring, *B* somewhat likely to be a regional spring, *C* unlikely to be a regional spring

ID	Spring name	T-Q	(Na ⁺ + K ⁺) vs. (Cl ⁻ + SO ₄ ²⁻)	(Ca ²⁺ + Mg ²⁺) vs. (Na ⁺ + K ⁺)	Cl ⁻ vs. F ⁻	Ba ²⁺ vs. SO ₄ ²⁻	Sr ²⁺ vs. Li ⁺	δ ¹³ C vs. ¹⁴ C activity	³ H	Criteria met	Criteria lacking data	Regional?
A	April Fool		X	X	X	X	X	NA		5	1	C
B	Big									0	1	C
C	Corn Creek							X	X	2	0	C
D	Crescent							NA		0	1	C
E	Hot	X	X	X	X	X	X	X	X	8	0	A
F	Kious		X	X	X					3	0	C
G	Littlefield	X	X	X	X	X	X	X	X	8	0	A
H	Monte Neva Hot	X				X	X	X	X	5	0	B
I	Ox									0	0	C
J	Petrified		X	X	X	X	X	X	X	7	0	A
K	Rupes Boghole							NA	X	1	1	C
L	Sand			X			X	NA	X	3	1	B
M	Saratoga	X	X	X	X	X	X		X	7	0	A
N	South Millick									0	0	C
O	Unnamed (east of Piermont Creek)							NA		0	1	C
P	Unnamed (north of Shoshone)									0	0	C
Q	Warm (a)		X	X	X	X	X	X	X	7	0	A

although ³H activity for Corn Creek [C] is below 10 pCi/L, it shares only one other characteristic with the known regional springs (δ¹³C vs. ¹⁴C activity). Exhibiting a few of the characteristics of the known regional springs is inadequate to designate a spring as regional; a spring should meet all or nearly all of the criteria to be designated as a regional spring.

Five springs not previously recognized as regional meet either seven or eight of the eight criteria for being so: Hot [E], Littlefield [G], Petrified [J], Saratoga [M], and Warm (a) [Q]. Hot [E] and Littlefield [G] both meet all eight criteria, and are thus classified as regional. Petrified [J] and Warm (a) [Q] meet all the criteria except for that of temperature and discharge. Petrified [J] and Warm (a) [Q] have diffuse discharge from multiple orifices, which made accurate estimates of discharge difficult. However, visual estimates suggest their total discharge is over 10 L/s. Their discharge temperatures (26 and 64 °C, respectively) also suggest they tap a regional flow system. The physical, chemical and isotopic characteristics of these springs (and, for Petrified [J], its close proximity to Littlefield [G]) merit classification as regional. Saratoga [M] fails only the δ¹³C vs. ¹⁴C test; its δ¹³C value of -7.3‰ is higher than the value of several known regional springs, but its ¹⁴C activity of 30.3 pmc is slightly higher than the highest value observed for a known regional spring.

Monte Neva Hot [H] meets several of the criteria for discharging water from a regional flow system. Its discharge of 95 L/s is higher than many of the known regional springs, and its high temperature is also indicative of deep, regional flow (the water is boiling when it

emerges from the ground; the reported temperature of 76 °C was measured at the closest safe distance from the orifice). It is known that geothermal temperatures can influence ionic composition of waters, especially the ratio of certain ions (e.g., Shikazono 1976); it is possible that Monte Neva Hot [H] is discharging from a regional flow system, but fails to meet two of the chemical criteria because of geothermal effects on water chemistry. It is also worth noting that Monte Neva Hot [H] falls just outside of the regional classification in two of the three tests that suggested it was not a regional spring. Monte Neva Hot's [H] (Na⁺ + K⁺) and (Cl⁻ + SO₄²⁻) concentrations are 0.89 and 0.61 epm (respectively), just below the cutoff values for a regional classification (1.0 and 0.7 epm). In the (Ca²⁺ + Mg²⁺) vs. (Na⁺ + K⁺) test, Monte Neva Hot's [H] (Ca²⁺ + Mg²⁺) concentration of 4.9 epm was higher than many of the known regional springs, but as with the earlier test, its (Na⁺ + K⁺) value was slightly below the threshold for a regional classification. Finally, Monte Neva Hot [H] discharges from a valley floor, supporting the possibility of a regional flow source. On the basis of these tests, Monte Neva Hot [H] is, therefore, likely a regional spring.

April Fool [A] passed five of the eight tests. However, April Fool [A] is a relatively high elevation spring, discharging from an upland area rather than a valley floor and had relatively low temperature and discharge (13.1 °C and 0.1 L/s). It also had ³H activity of 11 pCi/L, which did not meet the <10 pCi/L cutoff for a regional spring. Thus, it is unlikely that April Fool [A] is discharging water from a regional source.

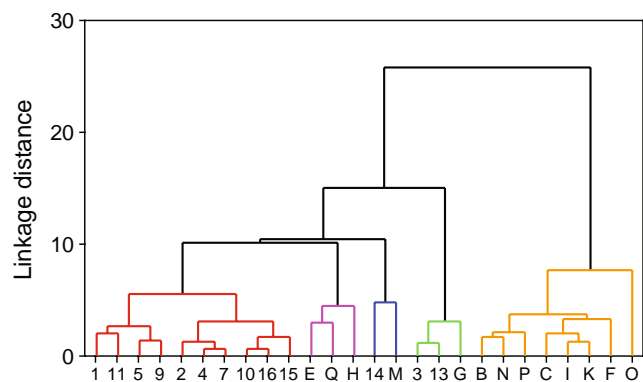


Fig. 10 Dendrogram showing the results of hierarchical cluster analysis (HCA). Letters and numbers represent groundwater sample location names in Table 1

Sand [L] meets only three of the eight criteria for regionalness. Of the three chemical criteria that it failed, it plots extremely close to the quadrant defined by the known regional springs. Its discharge temperature is relatively high (19 °C), suggesting a deep, regional flow system. Although the reported discharge volume is low (0.1 L/s) compared to known regional springs, Sand [L] has extremely diffuse discharge that was impossible to measure; the presence of a large spring pool suggests a much higher discharge. Therefore, Sand [L] is potentially a regional spring, but carbon isotope values should be determined before a final classification is made.

Classification by multivariate statistical analysis of physical, chemical, and isotopic data

The classification above relied on expert analysis of chemical, physical, and isotopic data. However, classification of geochemical data by use of multivariate statistical methods is often considered to be a more robust and objective approach (e.g., Güler et al. 2002; Thyne et

al. 2004). To examine how spring classification using multivariate statistical methods would compare to the ‘by-hand’ classification, hierarchical cluster analysis (HCA) and principal components analysis (PCA), two widely used tools for grouping hydrogeochemical data (e.g., Brown 1998; Cloutier et al. 2008; Davis 1986; Güler et al. 2002; Menció and Mas-Pla 2008; Thyne et al. 2004) were applied to the data. For this classification, the Euclidean distance measure for the observations and Ward’s method for the linkage rule were used. Among the various choices for distance measure and linkage rule that can be used in hierarchical cluster analysis, this combination has been shown to yield the most distinctive groups for hydrogeochemical data (e.g., Cloutier et al. 2008; Güler et al. 2002; Thyne et al. 2004).

First, a subset of variables was selected for the multivariate analysis. Because some variables are strongly correlated (e.g., $\delta^{18}\text{O}$ and δD), performing an analysis using both variables would result in undue influence of a given phenomenon. The variables HCO_3^- , SO_4^{2-} , Ca^{2+} , Mg^{2+} , Na^+ , K^+ , Cl^- , F^- , $\delta^{18}\text{O}$, $\delta^{13}\text{C}$, temperature, and discharge were chosen for use in the analysis. Many regional chemical data sets have asymmetric distributions; in this case, cluster analysis results can be improved by log transforming data to provide more symmetric input (Templ et al. 2008). Values for all variables except those that showed a strong normal distribution (HCO_3^- , $\delta^{18}\text{O}$, and $\delta^{13}\text{C}$) were transformed by taking the base-10 log. A z score was then calculated for the value of each variable using the formula:

$$z_i = \frac{x_i - \bar{x}}{s}$$

where z_i is the standardized score of the sample ‘i’, x_i is the value of the sample ‘i’, \bar{x} is the mean of the data set to which ‘i’ belongs (e.g., Mg^{2+} concentration), and s is the standard deviation of the data set to which ‘i’ belongs.

Table 3 Results of principal components analysis of the data. Upper section shows eigenvalues and the percent of variance explained by each of the first six principal components. Loadings of each variable for the first six principal components are given in the lower section

	PC1	PC2	PC3	PC4	PC5	PC6
Eigenvalue	6.122	2.313	1.123	0.593	0.308	0.204
Proportion	0.471	0.178	0.156	0.086	0.046	0.024
Cumulative proportion	0.471	0.649	0.805	0.891	0.937	0.961
Variable						
Ca^{2+}	0.154	0.547 ^a	-0.214	0.030	0.222	-0.207
Mg^{2+}	0.178	0.481 ^a	-0.306	0.122	0.167	-0.051
Na^+	0.386 ^a	-0.162	-0.031	-0.080	-0.065	-0.030
K^+	0.395	-0.026	0.090	0.050	-0.071	-0.090
HCO_3^-	0.193	-0.317	0.245	0.062	0.803 ^a	0.247
SO_4^{2-}	0.382 ^a	0.014	-0.150	-0.127	-0.115	0.157
Cl^-	0.351	-0.100	-0.205	-0.235	-0.110	0.235
F^-	0.339	-0.215	0.036	0.125	-0.106	-0.628 ^a
pH	-0.146	-0.456 ^a	-0.359	0.130	-0.241	-0.041
$\delta^{18}\text{O}$	0.289	-0.145	-0.396	-0.146	0.051	0.210
$\delta^{13}\text{C}$	0.162	0.233	0.480 ^a	-0.274	-0.367	0.371
Temperature	0.267	-0.007	0.457 ^a	0.217	-0.057	-0.257
Discharge	0.127	0.049	-0.034	0.851 ^a	-0.182	0.405

^a Loadings for variables that are the major contributors to each principal component

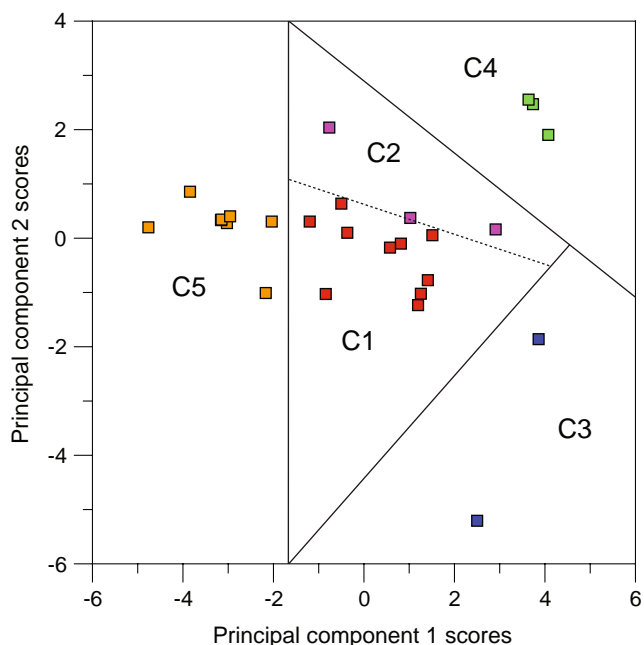


Fig. 11 Plot of scores for principal component 2 vs. scores for principal component 1. Colors of dots used for each sample represent the cluster to which the sample was assigned (see Fig. 10). Together, these two principal components account for ~65% of the variance in the dataset

Data standardization by means of z scores transforms each data set to have a mean of zero, and range of $\sim\pm 3$ standard deviations, giving each variable an equal weight when statistical analysis is performed; in the absence of standardization, variables with high values would have a

greater influence on Euclidean distances than would variables with low values (Güler et al. 2002).

Several variables contain missing values. For instance, two springs do not have measured discharge values, and there are several springs for which no $\delta^{13}\text{C}$ value is known. Many multivariate statistical methods cannot use variables for which observations are missing. There are techniques available for estimating missing hydrogeochemical values (e.g., Güler et al. 2002), but they work well only with specific variables and also are typically more robust the smaller the area of study and the denser the data; given the size of the region covered in this study and the variables with missing observations, missing observations could not be estimated. To determine which parameters were important to include in multivariate statistical analysis in spite of missing observations, a stepwise regression was performed in using the known regional springs and 10 springs from within the study area that were believed to be of local origin. A dummy parameter of 'regionalness' was added; known regional springs were all assigned values of 1,000, and the local springs were assigned values of zero. Using stepwise regression, it was found that temperature is the best single indicator of regionalness; temperature and HCO_3^- are the best pair of indicators, and temperature, HCO_3^- , and $\delta^{13}\text{C}$ are the best trio of indicators; discharge is one of the best quartet of indicators. Based on these results, discharge and $\delta^{13}\text{C}$ are considered important variables to include in spite of missing values.

The results of the cluster analysis are shown in Fig. 10. Five major clusters were found, with four of the five being fairly closely related, and the fifth being the most distinct.

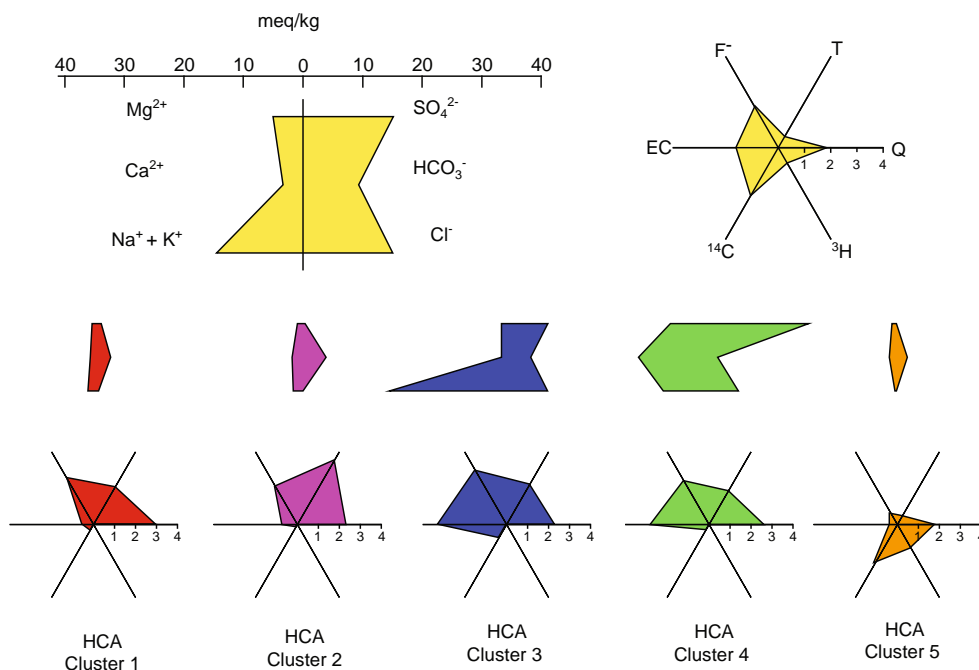


Fig. 12 Stiff diagrams showing mean major-ion composition of groundwater from each cluster, along with radial plots showing mean normalized values for physical, chemical and isotopic characteristics of each cluster. "Key" diagrams at the top showing what parameters are represented in the diagrams are filled in with yellow; other diagrams are filled in using the color representative of their cluster (see Fig. 10)

All the known regional springs and the springs classified as very likely or somewhat likely to be regional on the basis of the analysis in the previous section (see Table 2) are in clusters 1–4; all the springs classified as unlikely to be regional are in cluster 5. A cluster analysis performed without using discharge or $\delta^{13}\text{C}$ values was also performed so that springs missing values for these parameters could also be classified. Devils Hole [6], Hiko [8], Point of Rocks [12], and Sand [L] springs grouped in cluster 1; Petrified Spring [J] grouped in cluster 4, and April Fool [A] and Crescent [D] grouped in cluster 5. These results suggest the groupings made ‘by hand’ using the chemical and isotopic data are valid.

To further test the robustness of the clustering, principal components analysis was applied. The loadings of the principal components are shown in Table 3 along with their eigenvalues and the percentages of variance for which they account. Based on visual examination of break in slope on a scree plot, six principal components (PCs) were used; the six principal components account for ~96% of the variance, while the first two account for a total of ~65% of the variance. PC1 is dominated by Na^+ , K^+ , and SO_4^{2-} , but Cl^- and F^- are also important contributors. Ca^{2+} , Mg^{2+} , and pH are the major contributors to PC2, while $\delta^{13}\text{C}$ and temperature are the primary contributors to PC3. Discharge, HCO_3^- , and F^- are the dominant contributors to PCs 4, 5, and 6 (respectively).

A plot showing the scores for principal component 2 vs. the scores for principal component 1 is shown in Fig. 11, with sample points colored on the basis of their HCA cluster. The distinct grouping of the HCA cluster’s PCA scores supports the robustness of the cluster output. Mean values were calculated for each cluster’s variables; the means of the major ion compositions were plotted on Stiff diagrams (Fig. 12). In addition, radial plots were made using means of adjusted standardized values for chemical, physical and isotopic parameters for each cluster. To allow plotting on the radial diagram, the z scores for each variable were adjusted by adding the absolute value of the minimum sample’s z score to each score, thus converting each variable’s standardized scores from a dataset with a mean of zero to a dataset with a minimum of zero. These plots show some differences in chemical, physical, and isotopic values among clusters 1–4, but a more distinct difference between cluster 5 and the remaining clusters, especially with regard to temperature and isotopic indicators of residence time (^{14}C and ^3H).

Summary and conclusions

The regional carbonate aquifer of the Great Basin is potentially an important resource for meeting future water needs in the area. Large regional springs within an otherwise largely inaccessible flow system are convenient sampling points for establishing baseline data on the quantity and quality of water within the aquifer, as well as for monitoring potential aquifer responses to increased pumping. Towards this purpose, more than a hundred springs were investigated as part of this study. Sixteen of these springs have been previously identified as being

regional in character; the majority, however, had not been investigated prior to this study. The physical, chemical, and isotopic characteristics of the known regional springs were used to identify additional springs that have regional characteristics. Diagnostic physical characteristics of regionally sourced springs include discharges greater than 10 L/s and temperatures exceeding 25 °C; chemical characteristics that can be used to help identify regional springs in the carbonate aquifer are the relative equivalent concentrations of $(\text{Na}^+ + \text{K}^+)$ vs. $(\text{Cl}^- + \text{SO}_4^{2-})$, $(\text{Ca}^{2+} + \text{Mg}^{2+})$ vs. $(\text{Na}^+ + \text{K}^+)$, Cl^- vs. F^- , Ba^{2+} vs. SO_4^{2-} , and Sr^{2+} vs. Li^+ ; finally, $\delta^{13}\text{C}$ vs. ^{14}C and ^3H activity can also be used to diagnose a spring’s regionalness. These tests are all validated empirically, as shown by the similar characteristics of known regional springs. In addition to empirical validation, each of the criteria can be explained theoretically.

Five springs were identified as being regionally sourced (Hot [E], Littlefield [G], Petrified [J], Saratoga [M], and Warm (a) [Q]). Two other springs (Monte Neva Hot [H], and Sand [L]) were identified as potential regional springs, but further data should be obtained to confirm or refute this classification. One spring, April Fool [A] was determined not to be classified as regional because of its topographic location above the valley floor even though it met many of the regionalness criteria. The classification based on the examination of the chemical data is supported by the multivariate statistical methods employed, which suggests that the classification of the springs made ‘by hand’ is robust.

This research suggests that while some individual criteria might be good initial screening tools (e.g., discharge, temperature), no single test appears to provide a good indication of whether or not a spring is part of a regional carbonate aquifer flow system. Identification of regional springs should thus be based on a number of criteria. In other large regional aquifer systems where the geology is complex and diverse, these chemical techniques can also be applied to delineate the extent of the system.

Acknowledgements The authors gratefully acknowledge the support of the Southern Nevada Water Authority; however, the opinions and interpretations discussed in this paper are not necessarily those of the Southern Nevada Water Authority. We appreciate comments on a draft manuscript by W. Howcroft, and the review comments by N. Goldscheider, J. Mudry, and an anonymous reviewer, all of which led to significant improvements in the manuscript. The authors also acknowledge the help with location figures by C. Morton and T. Minor of the Desert Research Institute.

References

- Anderson RE, Zoback ML, Thompson GA (1983) Implications of selected subsurface data on the structural form and evolution of some basins in the northern Basin and Range province, Nevada and Utah. *Geol Soc Am Bull* 94:1055–1072
- Anna LO (1986) Geologic framework of the ground-water system in Jurassic and Cretaceous rocks in the Northern Great Plains, in parts of Montana, North Dakota, South Dakota, and Wyoming. US Geol Surv Prof Pap 1402-B. <http://pubs.er.usgs.gov/usgspubs/pp/pp1402B>. Cited 23 November 2009

- Bredehoeft JD, Belitz K, Sharp-Hansen S (1992) The hydrodynamics of the Big Horn Basin: a study of the role of faults. AAPG Bull 76:530–546
- Brown CE (1998) Applied multivariate statistics in geohydrology and related sciences. Springer, Berlin
- Carpenter E (1915) Ground water in southeastern Nevada. US Geol Surv Water Suppl Pap 365. <http://pubs.er.usgs.gov/usgspubs/wsp/wsp365>. Cited 23 November 2009
- Chang LL, Howie RA, Zussman J (1998) Rock forming minerals, vol 5B: non-silicates, 2nd edn. The Geological Society, Bath, UK
- Clark I, Fritz P (1997) Environmental isotopes in hydrogeology. Lewis, Boca Raton, FL
- Cloutier V, Lefebvre R, Therrien R, Savard MM (2008) Multivariate statistical analysis of geochemical data as indicative of the hydrogeochemical evolution of groundwater in a sedimentary rock aquifer system. J Hydrol 353:294–313
- Coney PJ, Harms TA (1984) Cordilleran metamorphic core complexes: Cenozoic extensional relics of Mesozoic compression. Geology 12:550–554
- Davis JC (1986) Statistics and data analysis in geology, 2nd edn. Wiley, New York
- Dettinger MD (1995) Distribution of carbonate-rock aquifers in southern Nevada and the potential for their development. US Geol Surv Water Resour Invest Rep 91-4146. <http://pubs.er.usgs.gov/usgspubs/wri/wri914146>. Cited 23 November 2009
- Dettinger MD, Schaefer DH (1996) Hydrogeology of structurally extended terrain in the eastern Great Basin of Nevada, Utah, and adjacent states, from geologic and geophysical models. US Geol Surv Hydrol Atlas 694-D
- Dettinger MD, Harrill JR, Schmidt DL, Hess JW (1995) Distribution of carbonate-rock aquifers and the potential for their development, southern Nevada and adjacent parts of California, Arizona, and Utah. US Geol Surv Water Resour Invest Rep 91-4146
- Eakin TE (1962) Ground-water appraisal of Cave Valley in Lincoln and White Pine Counties, Nevada. State of Nevada Department of Conservation and Natural Resources Ground-Water Resources, Reconnaissance Series Report 13, http://images.water.nv.gov/images/publications/recon%20reports/rpt13-cave_valley.pdf. Cited 23 November 2009
- Eakin TE (1963a) Ground-water appraisal of Dry Lake and Delamar Valleys, Lincoln County, Nevada. State of Nevada Department of Conservation and Natural Resources Ground-Water Resources, Reconnaissance Series Report 16. http://images.water.nv.gov/images/publications/recon%20reports/rpt16-dry_lake_delamar_valley.pdf. Cited 23 November 2009
- Eakin TE (1963b) Ground-water appraisal of Garden and Coal Valleys, Lincoln and Nye Counties, Nevada. State of Nevada Department of Conservation and Natural Resources Ground-Water Resources, Reconnaissance Series Report 18. http://images.water.nv.gov/images/publications/recon%20reports/rpt18-garden_coal_valley.pdf. Cited 23 November 2009
- Eakin TE (1966) A regional interbasin groundwater system in the White River area, southeastern Nevada. Water Resour Res 2:251–271
- Eakin TE, Moore DO (1964) Uniformity of discharge of Muddy River Springs, southeastern Nevada and relation to interbasin movement of ground water. Geological Survey Research 1964, US Geol Surv Prof Pap 501-D
- Faunt CC (1997) Effect of faulting on ground-water movement in the Death Valley Region, Nevada and California. US Geol Surv Water Resour Invest Rep. <http://pubs.er.usgs.gov/usgspubs/wri/wri954132>. Cited 23 November 2009
- Fiero B (1986) Geology of the Great Basin. University of Nevada Press, Reno, NV
- Gans PB, Mahood G, Schermer E (1987) Synextensional magmatism in the Basin and Range Province: a case study from the eastern Great Basin. Geol Soc Am Abstr Programs 19:671
- Güler C, Thyne GD, McCray JE, Turner KA (2002) Evaluation of graphical and multivariate statistical methods for classification of water chemistry data. Hydrogeol J 10:455–474
- Hamilton WB (1988) Detachment faulting in the Death Valley region, California and Nevada. In: Carr M D, Yount J C (eds) Geologic and hydrologic investigations of a potential nuclear waste disposal site at Yucca Mountain, southern Nevada. US Geol Surv Bull 1790, pp 51–85
- Harrill JR, Gates JS, Thomas JM (1988) Major ground-water flow systems in the Great Basin region of Nevada, Utah, and adjacent states. US Geol Surv Hydrol Invest Atlas HA-649-C. <http://pubs.er.usgs.gov/usgspubs/ha/ha694C>. Cited 23 November 2009
- Hem JD (1992) Study and interpretation of the chemical characteristics of natural water, 3rd edn. US Geol Surv Water Suppl Pap 2254. <http://pubs.er.usgs.gov/usgspubs/wsp/wsp2254>. Cited 23 November 2009
- Hunt CB (1967) Physiography of the United States. Freeman, San Francisco
- Maxey GB, Eakin TE (1949) Ground water in White River Valley, White Pine, Nye, and Lincoln Counties, Nevada. Bulletin No. 8, Nevada State Engineer Water Resources
- Menció A, Mas-Pla J (2008) Assessment by multivariate analysis of groundwater–surface water interactions in urbanized Mediterranean streams. J Hydrol 352:355–366
- Mifflin MD (1968) Delineation of ground-water flow systems in Nevada. Desert Research Institute Technical Report Series H-W, Hydrology and Water Resources Publication No. 4, Desert Research Institute, Reno, NV
- Mook WG (1980) Carbon-14 in hydrogeological studies. In: Fritz P, Fontes J C (eds) Handbook of environmental isotopes in geochemistry, vol 1: the terrestrial environment, part A, Elsevier, Amsterdam
- Morris HT (1983) Interrelations of thrust and transcurrent faults in the central Sevier orogenic belt near Leamington, Utah. In: Miller DM, Todd VR, Howard KA (eds) Tectonic and stratigraphic studies in the eastern Great Basin. Geol Soc Am Mem 157, pp 75–81
- Nevada Bureau of Mines and Geology (2009) Geothermal resources of Nevada. Nevada Bureau of Mines and Geology, Reno, NV. <http://www.nbmg.unr.edu/geothermal/geochemdata/access/area/chem/AmargosaDesert.xls>. Cited 23 November 2009
- Plume R W (1996) Hydrogeologic framework of the Great Basin region of Nevada, Utah, and adjacent states. US Geol Surv Water Suppl Pap 1409-B. <http://pubs.er.usgs.gov/usgspubs/pp/pp1409B>. Cited 23 November 2009
- Prudic DE, Harrill JR, Burbey TJ (1995) Conceptual evaluation of regional ground-water flow in the carbonate-rock province of the Great Basin, Nevada, Utah, and adjacent states. US Geol Surv Water Suppl Pap 1409-D. <http://pubs.er.usgs.gov/usgspubs/pp/pp1409D>. Cited 23 November 2009
- Rappaport J (2003) U.S. urban decline and growth, 1950 to 2000. Economic Review Third Quarter 2003, Federal Reserve Bank of Kansas City, KS, pp 15–44
- Rose TP, Davisson ML (2003) Isotopic and geochemical evidence for Holocene-age groundwater in regional flow systems of south-central Nevada. In: Enzel Y, Wells SG, Lancaster N (eds) Paleoenvironments and paleohydrology of the Mojave and southern Great Basin Deserts, Geol Soc Am Spec Publ 368, pp 143–163
- Schoff SL, Moore JE (1964) Chemistry and movement of ground water, Nevada Test Site. US Geol Surv Trace Elements Invest Rep TEI-838, <http://pubs.er.usgs.gov/usgspubs/ofr/ofr64139>. Cited 23 November 2009
- Shikazono N (1976) Thermodynamic interpretation of Na-K-Ca geothermometer in the natural water system. Geochemical J 10:47–50
- Stewart J H (1980) Geology of Nevada: a discussion to accompany the geologic map of Nevada. Spec. Publ. 4, Nevada Bureau of Mines and Geology, Reno, NV
- Sweetkind DS, Knochenmus LA, Ponce DA, Wallace AR, Scheirer DS, Watt JT, Plume RW (2007) Hydrogeologic framework. In: Welch AH, Bright DJ, Knochenmus LA (eds) Water resources of the Basin and Range carbonate-rock aquifer system, White Pine County, Nevada, and adjacent areas in Nevada and Utah. US Geol Surv Sci Invest Rep 2007–5261
- Templ M, Filzmoser P, Reimann C (2008) Cluster analysis applied to regional geochemical data: problems and possibilities. Appl Geochem 23:2198–2213

- Thomas JM, Mason JL, Crabtree, JD (1986) Ground-water levels in the Great Basin region of Nevada, Utah, and adjacent states. US Geol Surv Hydrol Invest Atlas HA-694-B
- Thomas JM, Welch AH, Dettinger MD (1996) Geochemistry and isotope hydrology of representative aquifers in the Great Basin region of Nevada, Utah, and adjacent states. US Geol Surv Prof Pap 1409-C. <http://pubs.er.usgs.gov/usgspubs/pp/pp1409C>. Cited 23 November 2009
- Thyne G, Güler C, Poeter E (2004) Sequential analysis of hydrochemical data for watershed characterization. *Ground Water* 42:711–723
- Tooker E W (1983) Variations in structural style and correlation of thrust plates in the Sevier foreland thrust belt, Great Salt Lake area, Utah. In: Miller DM, Todd VR, Howard KA (eds) *Tectonic and stratigraphic studies in the eastern Great Basin*. Geol Soc Am Mem 157, pp 61–73
- Tóth J (1962) A theory of groundwater motion in small drainage basins in central Alberta. *J Geophys Res* 67:4375–4387
- Tóth J (1963) A theoretical analysis of groundwater flow in small drainage basins. *J Geophys Res* 69:4975–4812
- UNLV Center for Business and Economic Research (2008) Clark County and Nevada Populations, 1970–2008. UNLV Center for Business and Economic Research, Las Vegas, NV. <http://cber.unlv.edu/pop.html>. Cited 23 November 2009
- Wernicke B, Axen GJ, Snow JK (1988) Basin and range extensional tectonics at the latitude of Las Vegas, Nevada. *Geol Soc Am Bull* 100:1738–1757
- Western Regional Climate Center (2008) Historic climate information for Nevada. Western Regional Climate Center, Reno, NV. <http://www.wrcc.dri.edu/CLIMATEDATA.html>. Cited 23 November 2009
- Winograd IJ, Thordarson W (1975) Hydrogeologic and hydrochemical framework, south-central Great Basin, Nevada–California, with special reference to the Nevada Test Site. US Geol Surv Prof Pap 712-C. <http://pubs.er.usgs.gov/usgspubs/pp/pp712C>. Cited 23 November 2009

**Empirical Mode Decomposition
Applications to the Muddy River Hydrograph
Preliminary Evaluation and Results**

Cady Johnson
Mifflin & Associates, Inc.

March 23, 2011

"It is difficult to get a man to understand something when his salary depends on his not understanding it." – Upton Sinclair (I, Candidate for Governor: And How I Got Licked)

Preface

Empirical Mode Decomposition (EMD) is a relatively new method for analyzing nonlinear and non-stationary data invented by Huang and others (1998) for decomposing a signal into a finite and often small set of so-called Intrinsic Mode Functions (IMFs) which, with the Hilbert transform (see p. 20), "yield instantaneous frequencies as functions of time that give sharp identifications of imbedded structures" (Huang and others, 1998, p. 904). Application of this method to the Muddy River hydrograph was kindly suggested by Andrew Long of the U.S. Geological Survey (personal communication, 2011), and appears to hold great promise. These preliminary notes document processing steps and results to date, which amplify our long-standing concerns that monitoring must be tailored to an analytical strategy, which until now has revolved around water-balance accounting (reconstitution of flows) in the Muddy River system, and support for a variety of numerical process-response models. With the advent of EMD, prospects for resolving individual influences on measured-discharge records and well hydrographs are much-improved. The power and limitations of EMD provide a framework for re-considering what constitutes comprehensive monitoring of groundwater systems tributary to the Muddy River. Water-balance accounting has still not led to stipulation as to the zero-sum nature of base flow and development in the Muddy River system, perhaps because so many salaries depend on this *not* being the case. Conflicting results from different groundwater models remain unresolved in terms of consensus on fact vs. fiction. Only when the Muddy River hydrograph and associated well hydrographs have been objectively laid bare in terms of the processes and activities that have affected them can water-rights allocations proceed with confidence and integrity. EMD is sure to be an asset, and perhaps a decisive one, in unraveling the historic records of the Muddy River, its tributaries, and associated water levels to support an equitable allocation process consistent with Nevada Water Law.

Part 1. Partial Reconstitution and Base Flow Separation (March 19, 2011)

Pre-processing

For Water Years 1978-82, daily surface-water diversion records are available for the Muddy River, allowing partial reconstitution of flows recorded at the Muddy River Gage to account for power generation activities. Initial EMD trials indicated that storm-related signal components persisted

SE ROA 37399

JA_8905

through most sifting steps (see below), contaminating the intrinsic mode functions (IMFs) with intermittent signal “chirps” that could not be removed in a systematic fashion based on frequency, as Kim and Oh (2009) suggested might be useful in certain circumstances. Therefore, base flows were estimated using the method of Wahl and Wahl (2007) as a precursor to applying EMD (Figure 1).

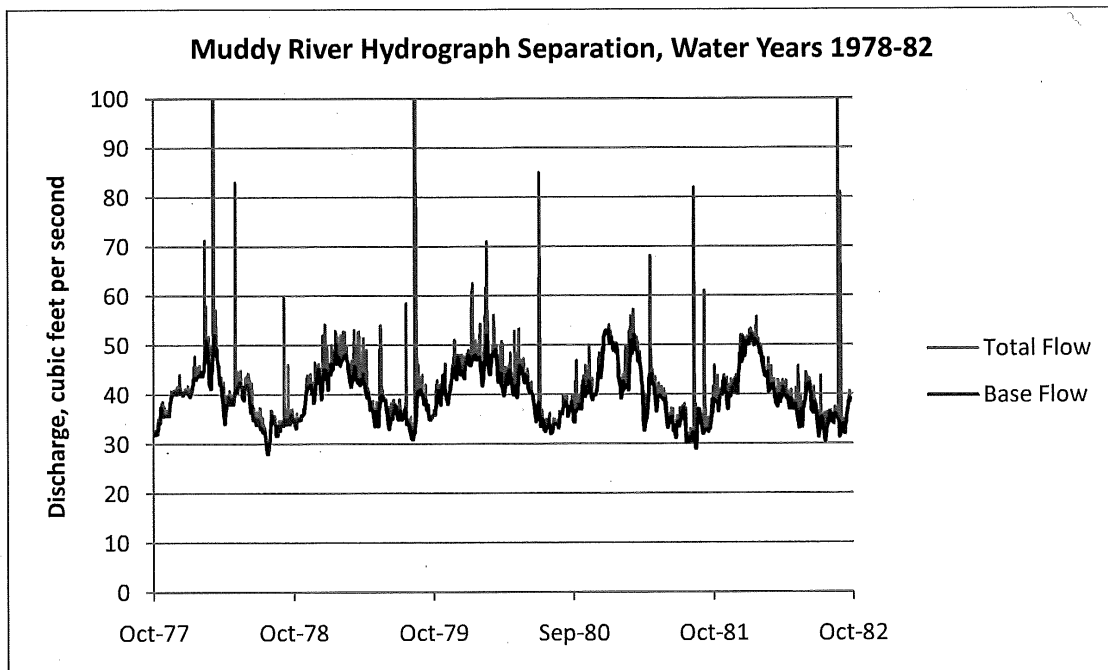


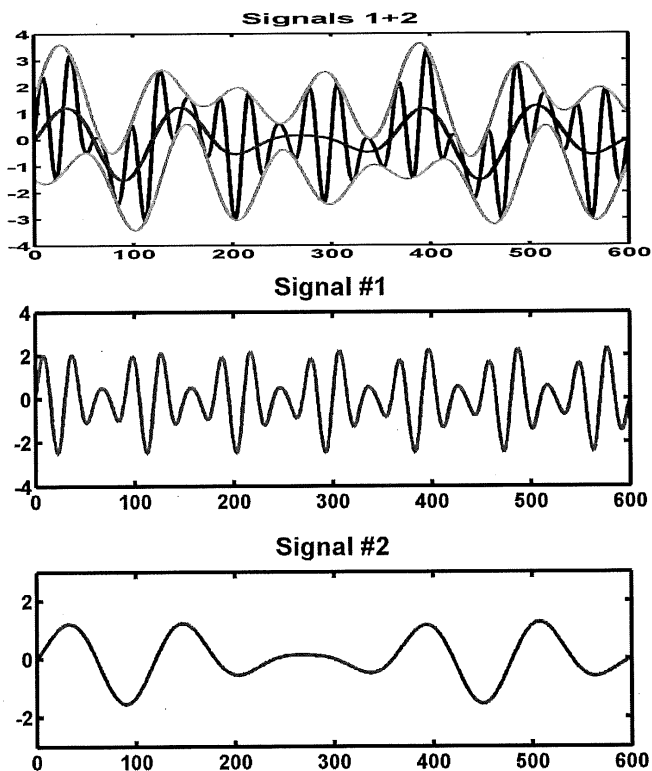
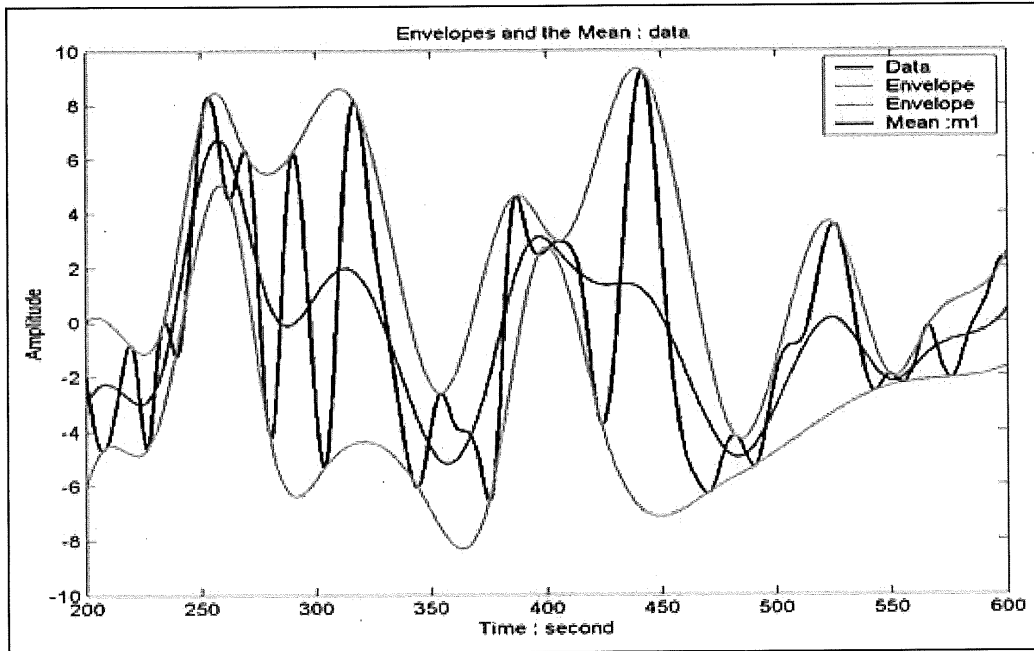
Figure 1. Muddy River hydrograph separation [File MuddyRiver_1977-82.xlsx, 'Sheet BaseFlow']

Sifting

Sifting produces the Intrinsic Mode Functions, defined as any function having the same numbers of zero-crossings and extrema, and also having a symmetric envelope defined by local maxima and minima. EMD is applied by first constructing an envelope defined by a smooth curve (cubic spline) through maxima and minima of the hydrograph (Figure 2), and using the mean of the envelope at each point in time to iteratively create an IMF containing the highest frequencies (Figure 3). Removal of this first IMF from the original signal allows a series of lower-frequency IMFs (Figure 4) and a residue representing the overall trend (Figure 5) to be derived.

Interpretation

The goal of EMD is to extract physically-meaningful signal components from a complex (mixed) signal for subsequent analysis. The Muddy River example above includes the time frame when MX-5 was drilled (April-May of 1981), developed (June of 1981) and tested (July-September of 1981). MX-4 was drilled earlier, reportedly started November 20, 1980 and completed December 12, 1980 (Log # 22449), but no production records are available. Development activities in southeastern Coyote Spring Valley may therefore be responsible for perturbations of the 5th and 6th IMFs during the last two years of the record considered here (Figure 4).



(Huang and Wu, 2008)
 (Wu and Huang, 2009)

Figure 2. Example envelope and envelope mean for a simple signal (top) [file 2a HHT Training Sifting.ppt, Norden E. Huang training slide] and EMD result (bottom) [file EEMDclimate.pdf]

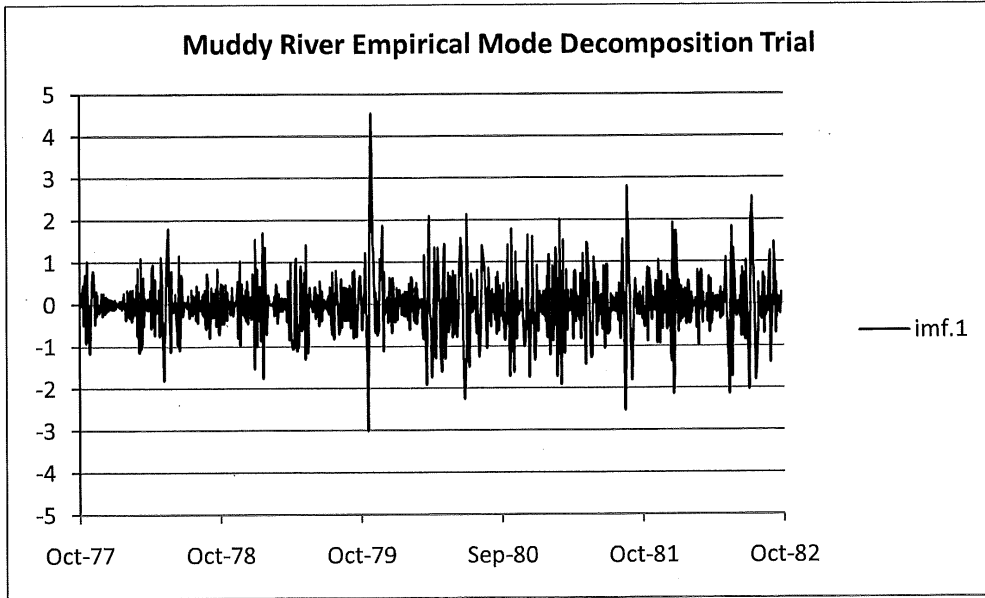


Figure 3. First Intrinsic Mode Function, with amplitude units of cubic feet per second [file MR77-82try2.xlsx, sheet MR77-82try2]

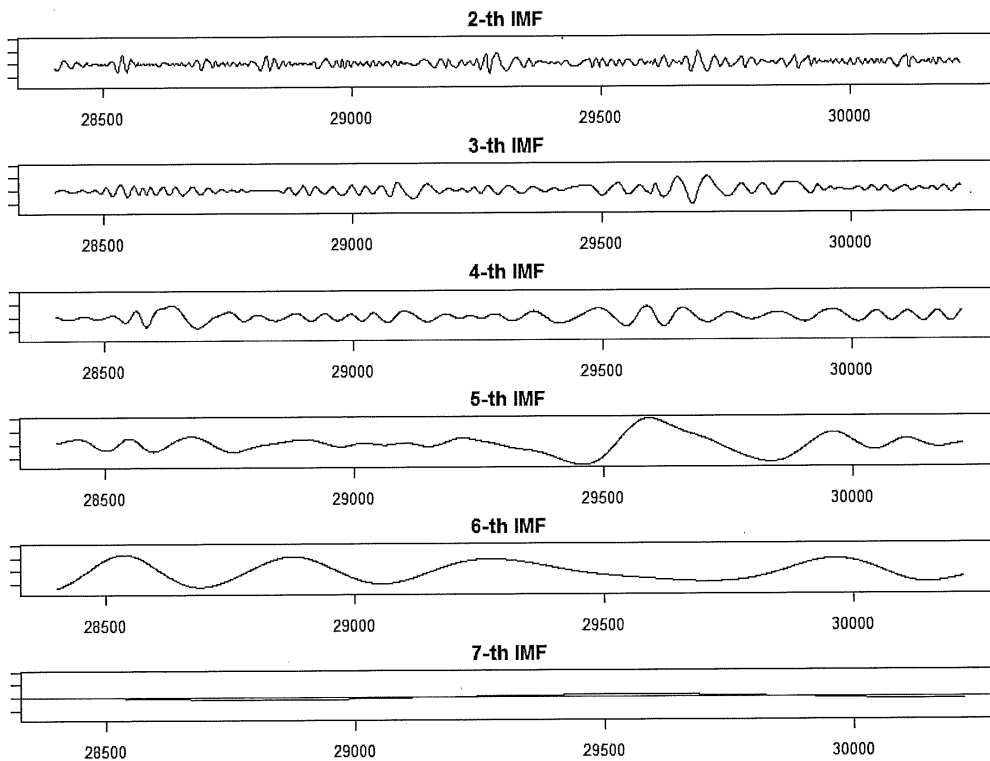


Figure 4. Intrinsic Mode Functions 2 through 7 for base flow component of Muddy River hydrograph, October 1, 1977 through September 30, 1982, adjusted for NPC direct surface-water diversions for power generation [file MRbaseFlow77-82imf2-7.tiff]

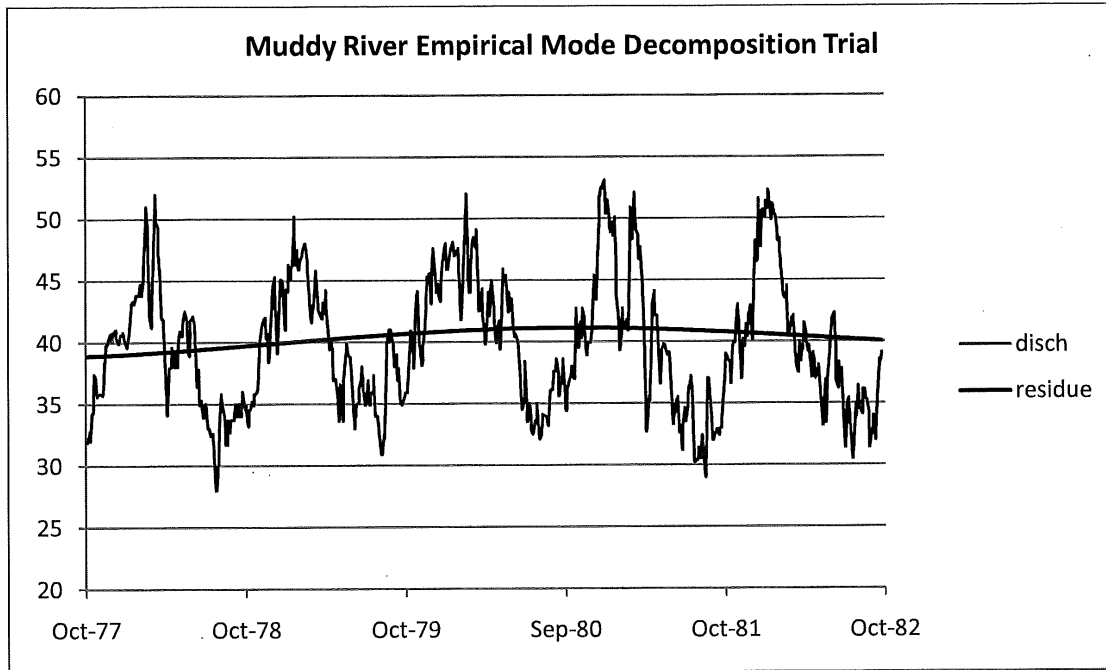


Figure 5. Base flow component of Muddy River hydrograph, with residue (trend) determined by EMD [file MR77-82try2.xlsx, sheet MR77-82try2]

Conclusion to Part 1

Empirical Mode Decomposition (EMD) appears to be a powerful asset with respect to hydrograph interpretation if *daily* surface-water diversions are accounted for, allowing the main-stem hydrograph to be partially reconstituted. In the case of the Muddy River, surface-water diversions by NPC / Nevada Energy are of the same magnitude as the largest IMFs and can occur with highly-variable frequencies, so are capable of contaminating the entire sifting process and subsequent interpretation if not accounted for. From October of 1982 onward, these important monitoring records are absent. However, if we can establish that NPC did not divert water directly from the Muddy River prior to October of 1977 (or obtain records of any such diversions) and improve the scope of current monitoring, EMD analysis of the hydrograph from Water Years 1945 through 1982 will provide important context for evaluating current and future discharge records from the main-stem Muddy River.

Part 2. Evaluate a Longer Record to Include Climate Effects (March 20, 2011)

Water Years 1945-1982

Examining the first 37 years of continuous daily discharge records (Figure 6) from the Muddy River with empirical mode decomposition (EMD) reveals features of the hydrograph that are not evident in shorter records (Figures 7 and 8), and provides some cautionary insights on applying EMD. Importantly, the annually-periodic ET cycle was *not* resolved as a single intrinsic mode function (IMF), likely because of *mode mixing* (see Part 3), as the later half of the hydrograph is affected by delayed effects of groundwater export on River discharge. Removal of the ET signal *a priori* would provide a good comparative analysis.

There appears to be a correspondence between regional climate (Figure 7) and IMF 10 of the decomposition (Figure 8), with a lag of several years. If this finding is correct, base flow fluctuations of plus or minus 1 cfs in response to climate were occurring prior to 1983.

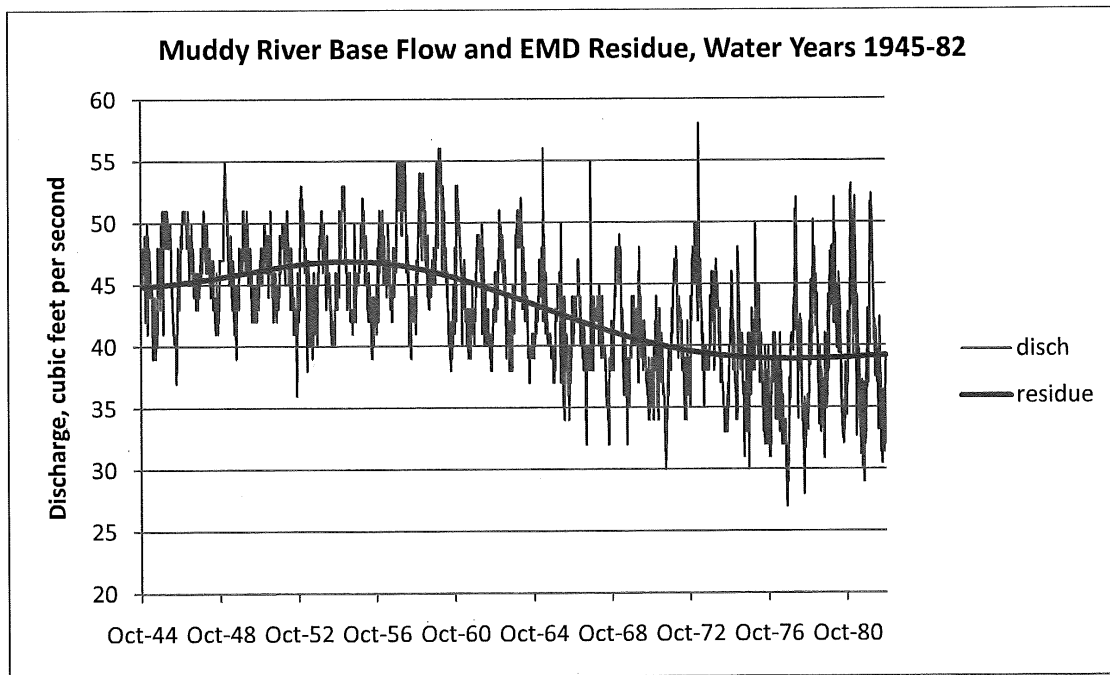


Figure 6. Base flow component of Muddy River hydrograph, adjusted for surface-water diversions above the Gage by Nevada Power Company for Water Years 1978-82 only, and residue from EMD sifting that yielded 10 components. Note that whereas we know groundwater export began in 1965, the residue begins its decline several years earlier. This is an intermittency effect requiring special treatment in the analysis, more complete monitoring records, or both. [file MR44-82try2.xlsx, sheet]

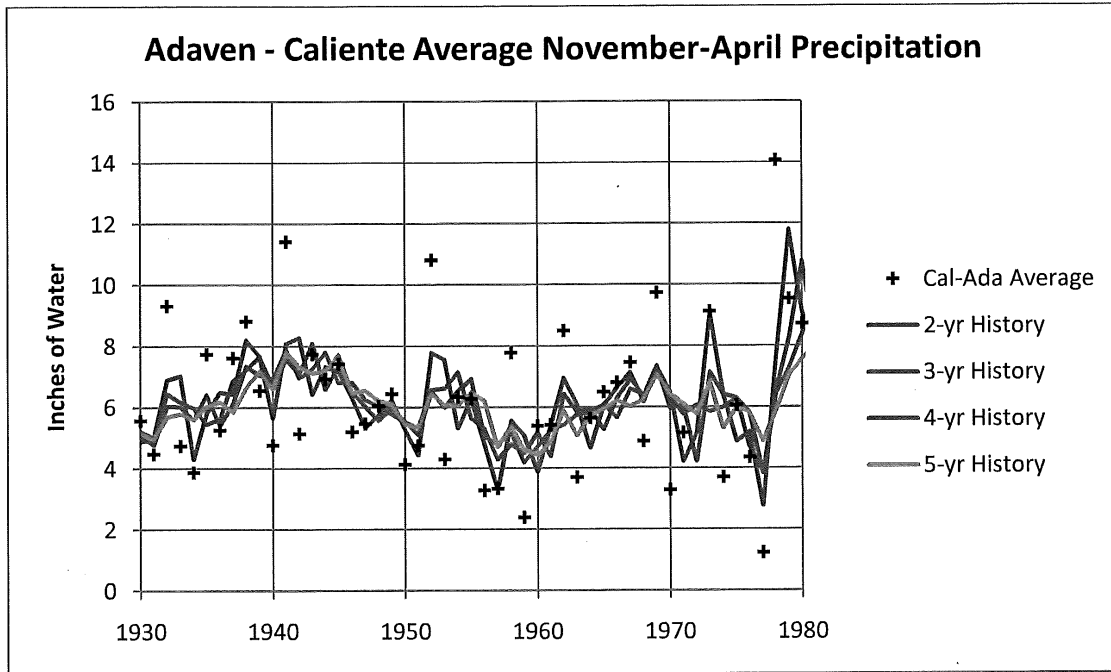


Figure 7. Regional climate from two stations representative (?) of Muddy River groundwater catchment [file CompareCalienteAdaven.xlsx, sheet 'Nov-Apr']

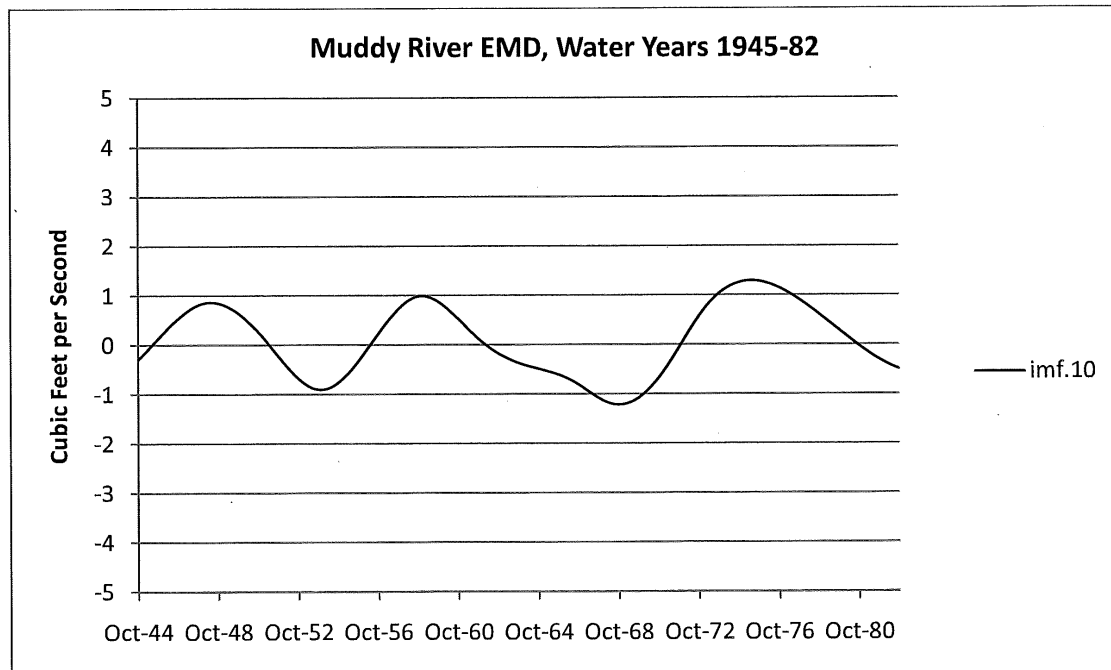


Figure 8. IMF 10 of trial decomposition [file MR44-82try2.clsx]

Part 3. Address the Two-Tone Problem by Removing ET (March 21, 2011)

Mode Mixing

Examination of intrinsic mode functions (IMFs) from the WY 1945-1964 Muddy River hydrograph, before export of groundwater began, reveals a mode with annual periodicity but variable amplitude (IMF 6; Figure 9). There is no apparent correspondence between regional climate (Figure 10), as expressed by various indices, and the variability of IMF 6. It has been established that when two superimposed frequencies are sufficiently close together, a *beat effect* results, and the two contributing signals are difficult or impossible to resolve as individual components (Figure 11). The situation is only unambiguous if there is prior knowledge of one of the signals, which is approximately true for evapotranspiration (ET) in the Muddy River Springs area. The ET signal is likely quite uniform in strength, and its annual periodicity is certain, whereas pumping patterns, though seasonal, can vary considerably from year to year. Having adjusted Muddy River discharge for surface-water diversions, where records exist, and separating the hydrograph to exclude storm runoff, we now investigate further adjusting the base flow of the River to remove the effects of ET before performing empirical mode decomposition (EMD). The goal is to improve the odds of matching the decomposition to physically meaningful processes (groundwater diversions, recharge, etc.) in the hydrologic system.

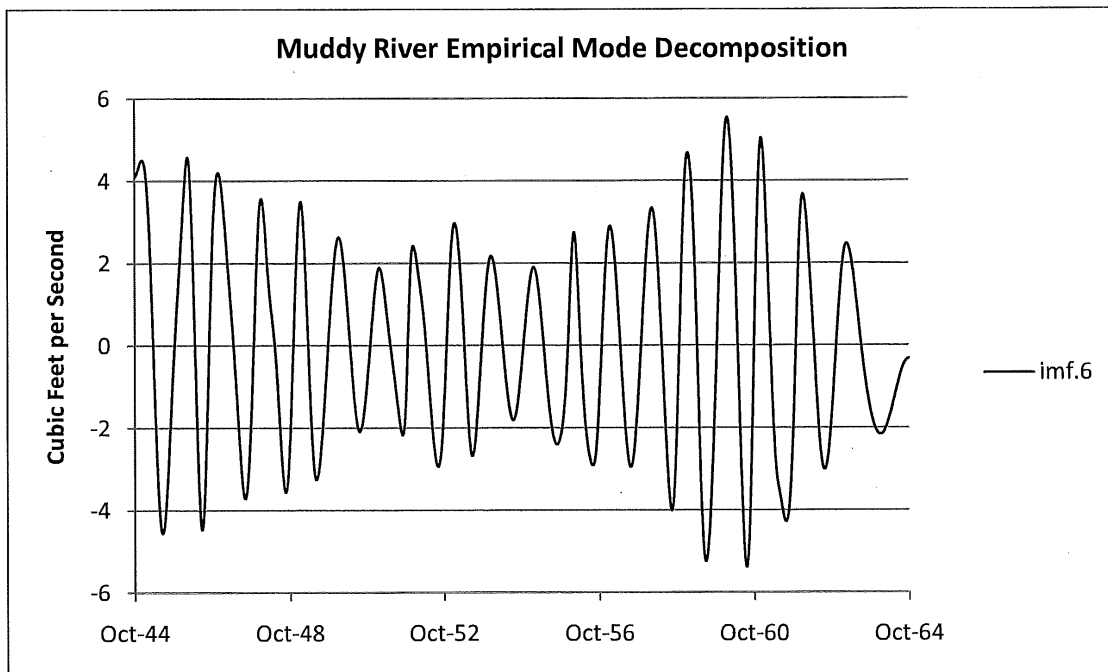


Figure 9. IMF 6 from the Muddy River hydrograph exhibiting *approximate* annual periodicity, Water Years 1945-1964 [file MR44-64try2.xlsx, sheet 'MR44-64try2']

Procedure

The maxima of the IMF given in Figure 9 occur on or about January 10; the standard deviation from January 10 is 25 days. The median date is also January 10, so a sine function with 3.5 cfs amplitude and annual period was used to adjust the Muddy River hydrograph by 7 cfs in summer (July 10), varying systematically to zero each January 10 (Figure 12). The choice of 3.5 cfs as the annualized ET rate was made based on the evaluation of Mifflin and others (1991), and should be revisited at some point.

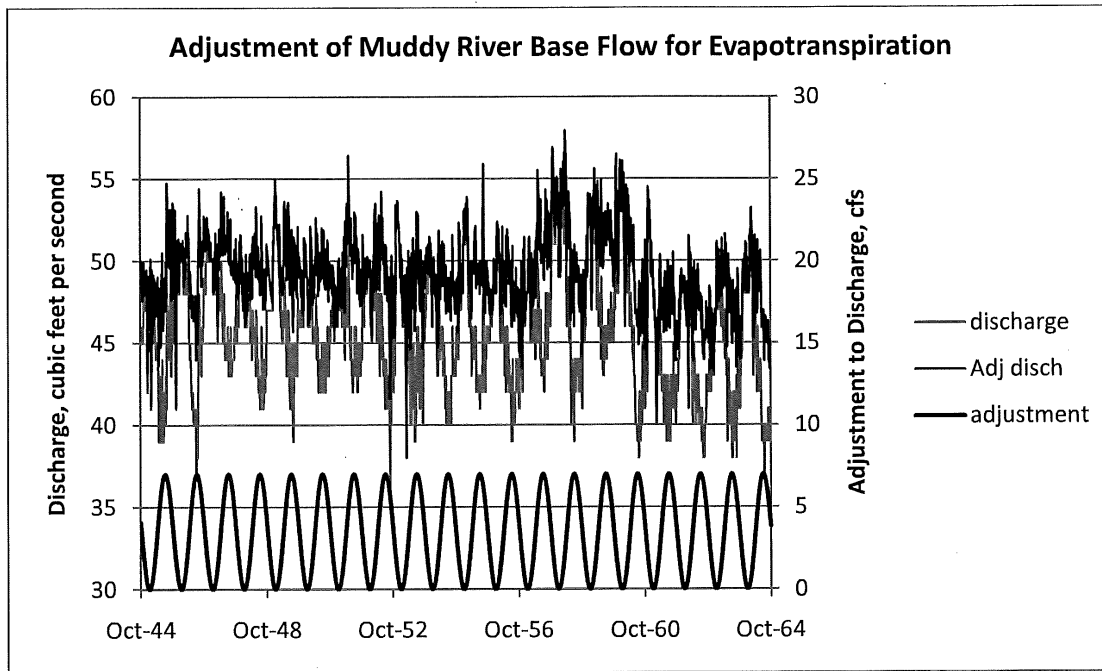


Figure 12. Partial reconstitution of Muddy River base flow to account for evapotranspiration; discharge is increased by 0 to 7 cfs, varying sinusoidally with minima (zero additions) occurring on January 10 of each year, the day of assumed minimum average daily temperature [file MR44-64try2.xlsx, sheet 'FindSinET']

The partially-reconstituted hydrograph (upper, black signal in Figure 12) was processed by EMD, resulting in the set of IMFs and residue shown in Figure 13. Notably, the beat effect has disappeared from IMF #6, presumably revealing processes that were obscured by the ET cycle (Figure 14; compare Figure 9).

Recombining the IMFs, beginning with those with the lowest frequencies allows us to begin describing the Muddy River hydrograph in terms of cause and effect. In Figure 15, the overall trend of the base flow hydrograph is described by a combination of the EMD residue and IMF #9, which together appear to represent climate on a decadal time scale. Adding in IMF #8 to the trend representation (Figure 16) provides additional detail, attributable to more local climatic effects and perhaps early groundwater development in the headwaters area. Either of these approximations of base flow might prove useful as calibration information in groundwater models that incorporate transient recharge.

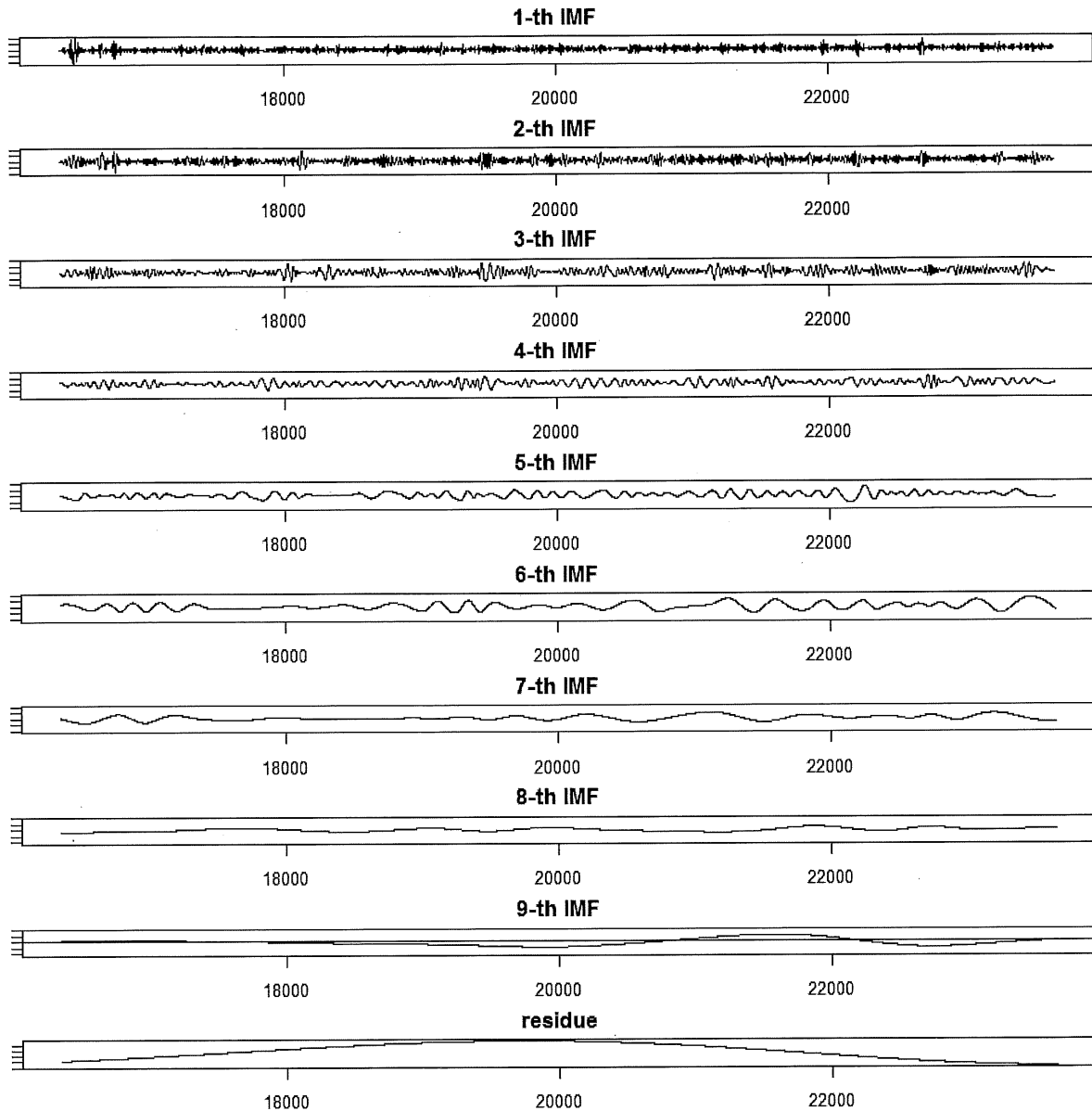


Figure 13. Set of 9 intrinsic mode functions and residue produced by empirical mode decomposition of Muddy River base flow hydrograph, adjusted for ET at annualized rate of 3.5 cfs. Time scale is Excel numerical days, October 1, 1944 through September 30, 1964. [file MR44-64adjET_03.tiff]

The intermediate IMFs combine to illustrate a variety of short-term effects that beg explanation in terms of irrigation schedules, clearing and cropping, hydrologic processes occurring locally in the alluvial aquifer, and introduction of the first irrigation wells (Figure 17). Monitoring records that would allow these associations to be made, however, do not exist.

The higher-frequency IMFs reflect system noise on a daily to weekly basis and are probably not analyzable. Future monitoring strategies should anticipate the power and limitations of EMD, and testing strategies should strive to avoid mode mixing, where possible.

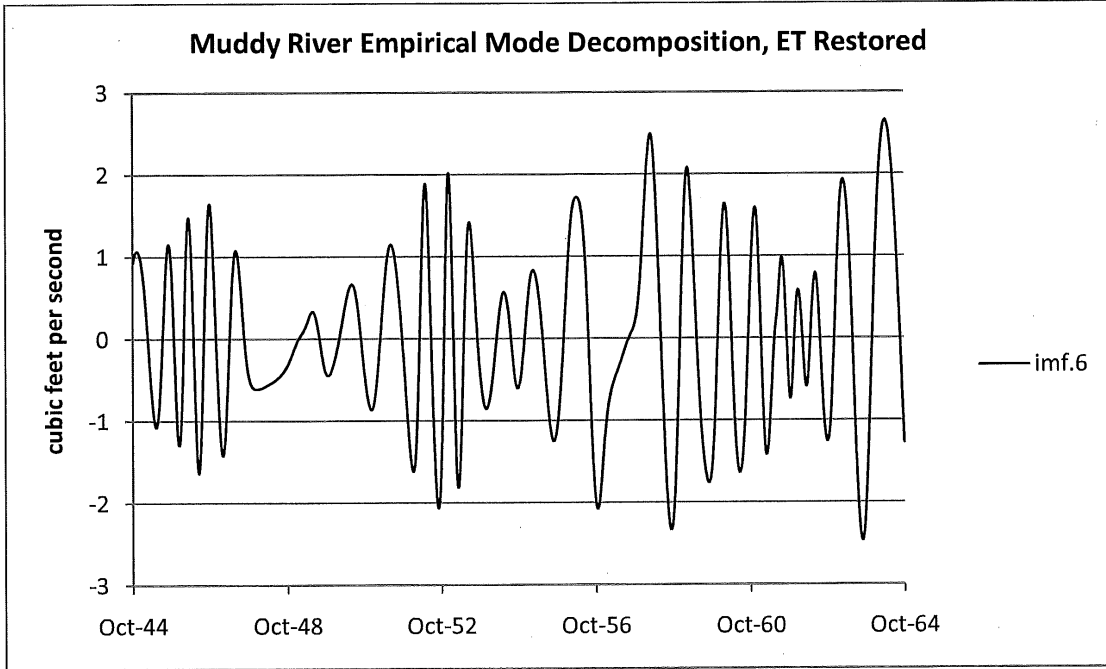


Figure 14. Beat effect disappears from IMF #6 when ET is removed *a priori* [file MR44-64try3.xlsx]

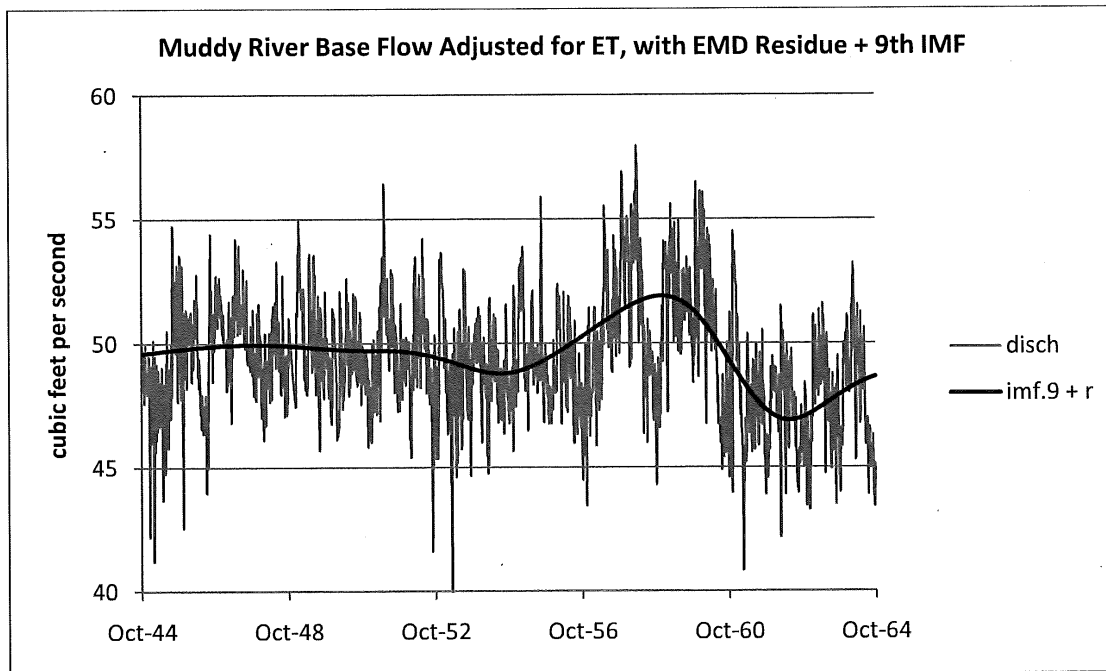


Figure 15. Long-term fluctuations in base flow of the Muddy River, obtained by combining the EMD residue with IMF #9, reflecting climatic influences [file MR44-64try3.xlsx]

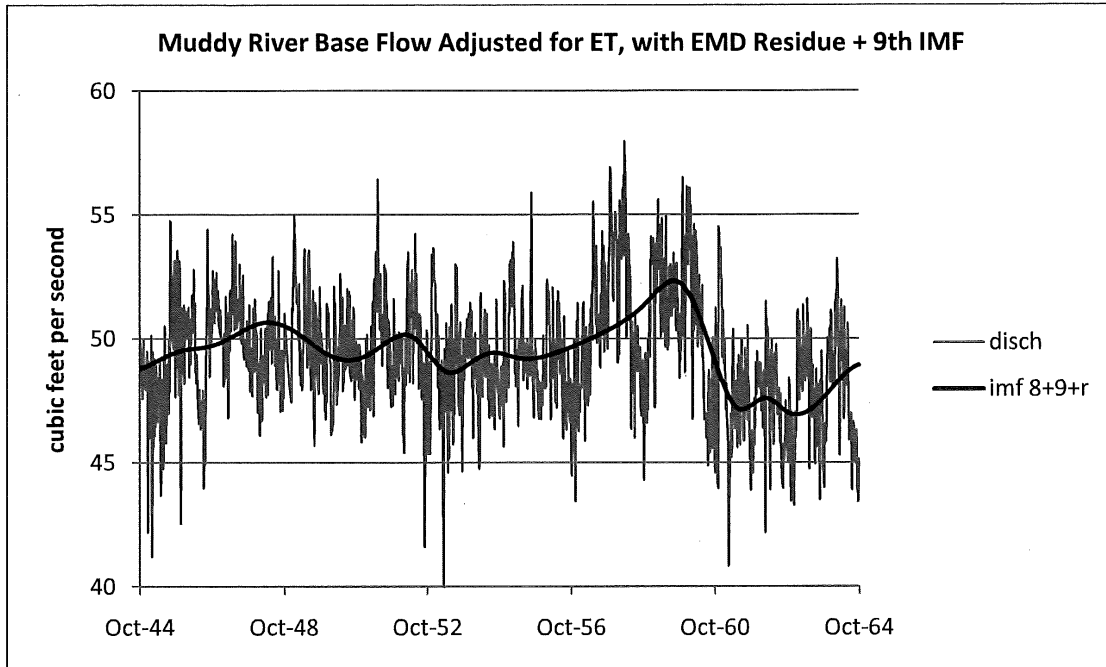


Figure 16. Fluctuations in base flow of the Muddy River, obtained by combining the EMD residue with IMFs #8 and #9, reflecting climatic influences at regional and local scales [file MR44-64try3.xlsx]

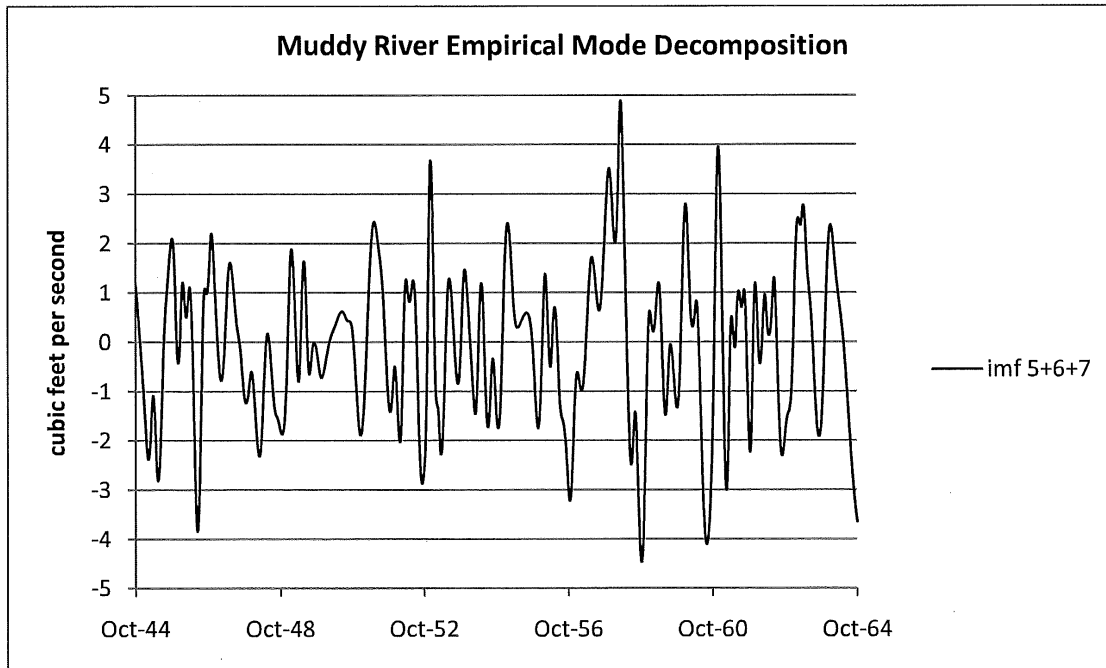


Figure 17. Summation of IMFs 5, 6, and 7 in Muddy River baseflow hydrograph, after compensating for ET. These modes reflect seasonal variability in irrigation/diversion schedules, groundwater recharge and discharge occurring at short time scales in the alluvial aquifer, and introduction of the first irrigation wells after 1949.

Conclusion to Part 3

Recent improvements in EMD methodology appear to be capable of alleviating mode mixing effects in a totally adaptive (non-subjective) fashion (Wu and Huang, 2009). A noise-assisted data analysis method, designated Ensemble EMD (EEMD), promises to define true IMF components as the mean of an ensemble of trials without subjective intervention (like removing the ET component in the present exercise, or defining intermittencies *a priori*). Other unsettled issues with the EMD method remain, however, including selection of an appropriate sifting stoppage criterion and how to manage end effects rationally. Given the broad interdisciplinary interest in EMD, we anticipate rapid progress toward resolving any technical or theoretical issues that might create a reluctance to apply EMD to stream and well hydrographs.

"Should I refuse a good dinner simply because I do not understand the process of digestion?"

– Oliver Heaviside

References

- Huang, N.E., Shen, Z., Long, S.R., Wu, M.C., Shih, H.H., Zheng, Q., Yen, N.C., Tung, C.C., Liu, H.H., 1998: The empirical mode decomposition and the Hilbert spectrum for nonlinear and non-stationary time series analysis. *Proceedings of the Royal Society London A* 454 (1998), 903–995.
- Huang, N.E. and Z. Wu, 2008, A review on Hilbert-Huang transform: method and its applications to geophysical studies: *Reviews of Geophysics*, 46, RG2006/2008, 23 pp.
- Kim, D. and H-S Oh, 2009, EMD: A package for empirical mode decomposition and Hilbert spectrum: *The R Journal*, v. 1 no. 1, May 2009, pp. 40-46.
- Mifflin, M.D., O.A. Adenle, and R.J. Johnson, 1991, Effects of 1989 and 1990 ground-water withdrawals on Muddy River flows, upper Muddy River Valley, Nevada: Mifflin & Associates, Inc., unpublished report prepared for Nevada Power Company and California Department of Water Resources, May, 1991, 136 p.
- Rilling, G. and P. Flandrin, 2008, One or two frequencies? The empirical mode decomposition answers: *IEEE Trans. On Signal Processing*, v. 55, no. 6, pp. 85-95 (Fig. 3 from Nov. 13, 2006 draft)
- Wahl, T.L. and K.L. Wahl, 2007, BFI – A computer program for determining an index to base flow: U.S. Bureau of Reclamation, http://www.usbr.gov/pmts/hydraulics_lab/twahl/bfi/
- Wu, Z. and N.E.Huang, 2009, Ensemble empirical mode decomposition: a noise-assisted data analysis method: *Advances in Adaptive Data Analysis*, v. 1, no. 1, pp. 1-41

The following pages contain a console log from implementation of EMD in the R programming environment, with example input, output, and citations.

NOTE: THE FOLLOWING IS AN ABBREVIATED CONSOLE LOG FROM EMD PROCESSING OF THE DAILY MUDDY RIVER HYDROGRAPH, WATER YEARS 1945-1964. KEYBOARD ENTRIES ARE SHOWN IN RED, SYSTEM OUTPUT IN BLACK, AND PLOTS DRAWN TO THE OUTPUT CONSOLE ARE INSERTED AFTER THE PLOT INSTRUCTIONS. DATA LISTINGS FROM THE `extrema()` COMMAND ARE ABBREVIATED. NOTES LIKE THIS ARE IN BLUE.

THE FOLLOWING MESSAGE IS DISPLAYED WHEN R IS STARTED IN THE WINDOWS™ ENVIRONMENT. THE "R console" WINDOW ACCEPTS TEXT INPUT AND PROVIDES TEXT OUTPUT; AN "R Graphics: Device 2 (ACTIVE)" IS CONFIGURED BY THE `par()` SPECIFICATION AND CONTAINS OUTPUT FROM THE `plot()` COMMAND.

THIS SESSION SUMMARY WAS PREPARED BY CADY JOHNSON ON MARCH 21, 2011

R version 2.12.2 (2011-02-25)
Copyright (C) 2011 The R Foundation for Statistical Computing
ISBN 3-900051-07-0
Platform: i386-pc-mingw32/i386 (32-bit)

R is free software and comes with ABSOLUTELY NO WARRANTY.
You are welcome to redistribute it under certain conditions.
Type `'license()'` or `'licence()'` for distribution details.

Natural language support but running in an English locale

R is a collaborative project with many contributors.
Type `'contributors()'` for more information and
`'citation()'` on how to cite R or R packages in publications.

Type `'demo()'` for some demos, `'help()'` for on-line help, or
`'help.start()'` for an HTML browser interface to help.
Type `'q()'` to quit R.

THE FOLLOWING COMMAND LOADS THE EMPIRICAL MODE DECOMPOSITION AND HILBERT SPECTRAL ANALYSIS PACKAGE <http://dasan.sejong.ac.kr/~dhkim/software/emd.html>

```
> library(EMD)
Loading required package: fields
Loading required package: spam
Package 'spam' is loaded. Spam version 0.23-0 (2010-09-01).
Type demo(spam) for some demos, help(Spam) for an overview
of this package.
Help for individual functions is obtained by adding the
suffix 'spam' to the function name, e.g. 'help(chol.spam)'.
```

Attaching package: 'spam'

The following object(s) are masked from 'package:base':

`backsolve`, `forwardsolve`, `norm`

Use `help(fields)` for an overview of this library

library(fields, keep.source=TRUE) retains comments in the source code.
THE PROCESSING SUMMARY BELOW MIMICS THE SAMPLE SESSION GIVEN BY KIM AND OH
IN THEIR CONTRIBUTED RESEARCH ARTICLE TO THE R JOURNAL, MAY 2009, USING
DAILY BASE FLOW FROM THE MUDDY RIVER MR[date,disch] AS INPUT DATA

```
> ### Process 1944-64 dataset adjusted for ET
> ###
> filepath<-system.file("data","MR44-64adjET.txt",package="EMD")
> MR<-read.table(filepath,header=TRUE)
> ###
> ### Identify extrema and zero-crossings
> extrema(MR$disch)
```

```
$minindex
      [,1] [,2]
[1,]    26    26
[2,]    36    36
[3,]    58    58
      .
      .
      .
```

```
[611,] 7265 7265
[612,] 7276 7276
[613,] 7288 7288
[614,] 7295 7295
```

```
$maxindex
      [,1] [,2]
[1,]    28    28
[2,]    37    37
[3,]    61    61
      .
      .
      .
```

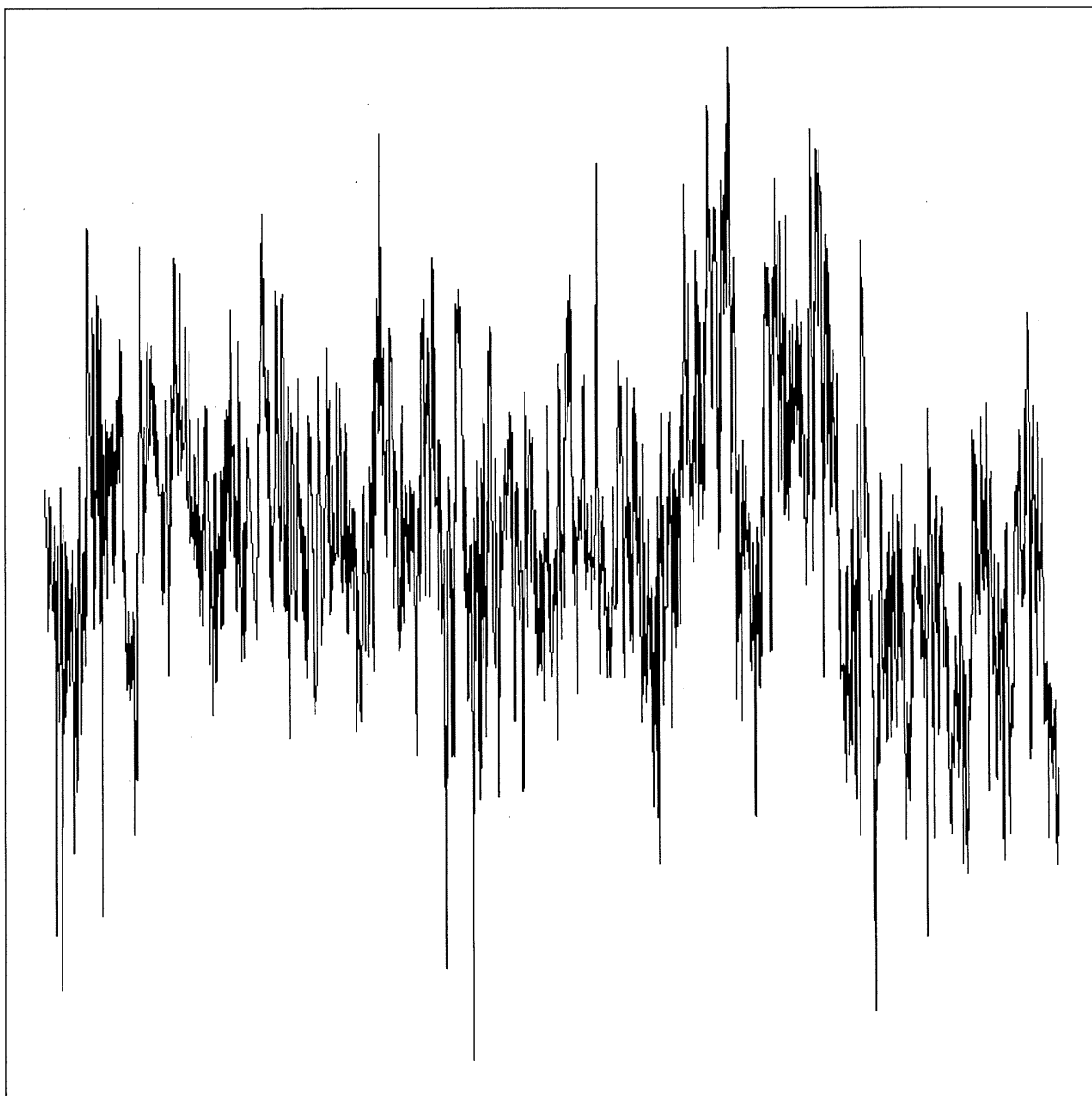
```
[611,] 7267 7267
[612,] 7279 7279
[613,] 7291 7291
[614,] 7300 7300
```

```
$nextreme
[1] 1228
```

```
$cross
NULL
```

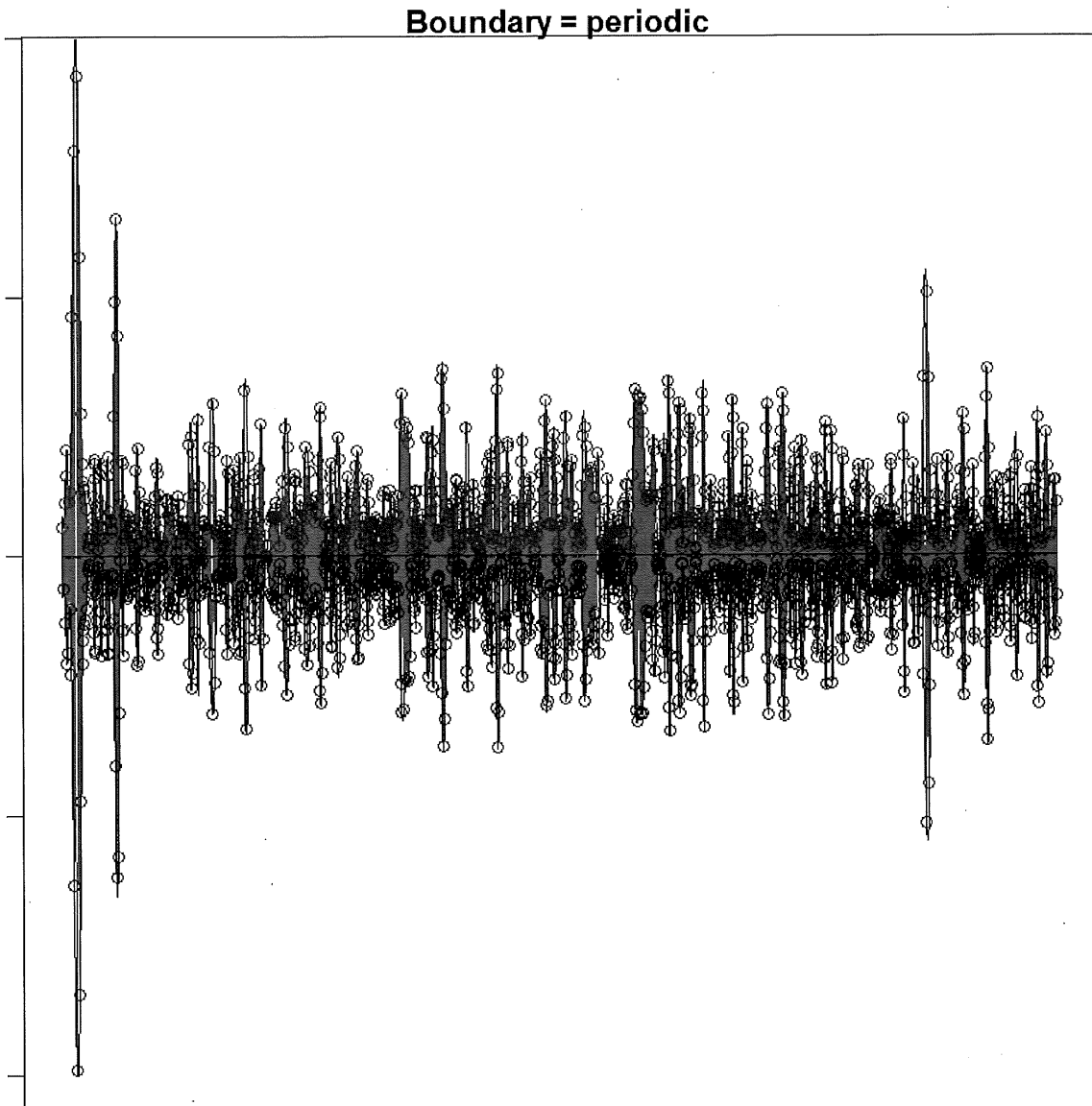
```
$ncross
[1] 0
```

```
> ### Plot the partially-reconstituted hydrograph  
> par(mfrow=c(1,1),mar=c(1,1,1,1))  
> plot(MR$date,MR$disch,xlab="",ylab="",type="l",  
+ axes=FALSE);box()
```



```
> ### saved as MR44-64adjET_01.tiff
```

```
> ###  
> ### Extracting the first IMF by sifting process  
> tryimf<-extractimf(MR$disch,MR$date,check=TRUE,max.sift=500)
```

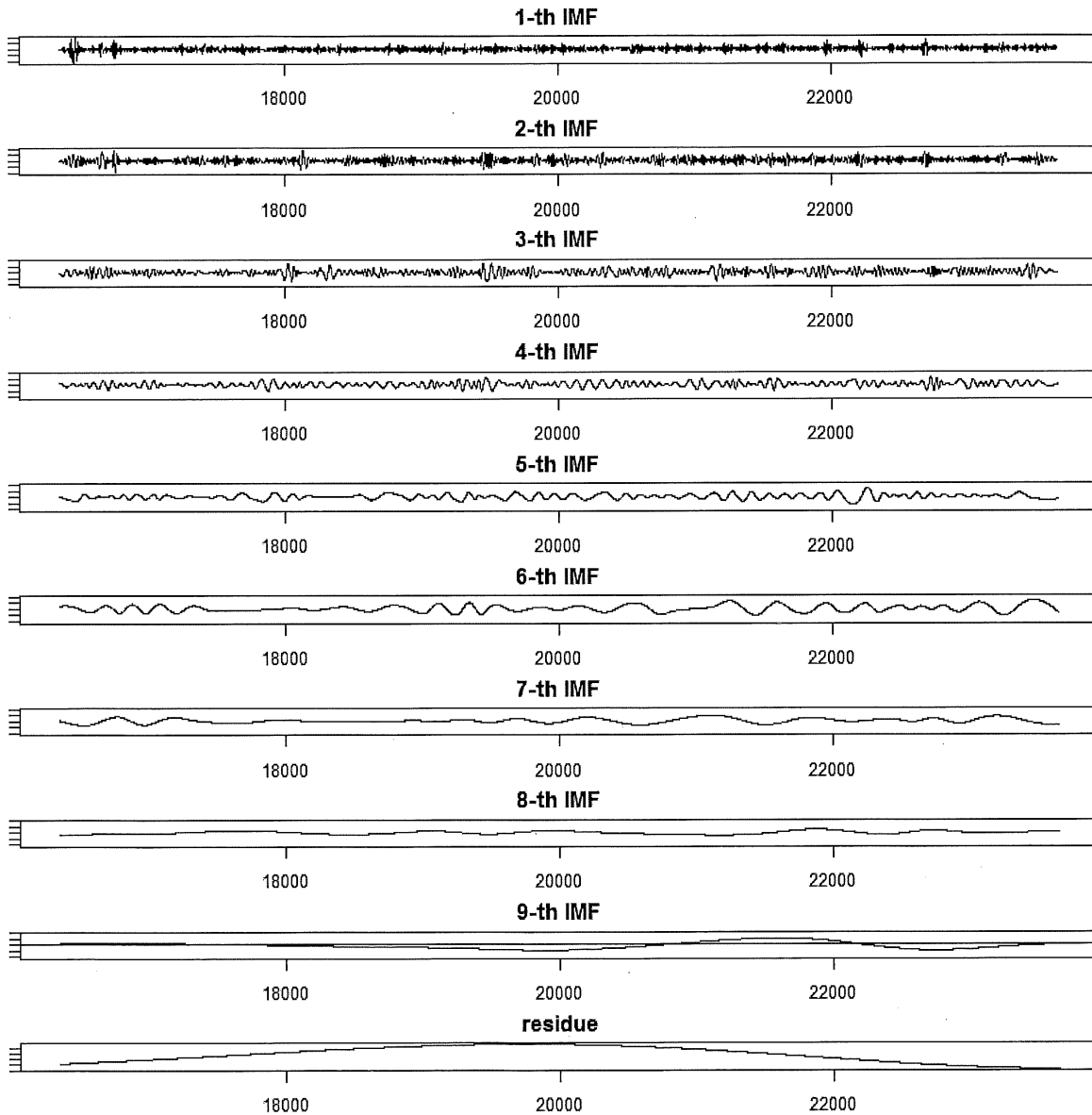


```
> ### sifting result (156 iterations) saved as MR44-64adjET_02.tiff  
> ###  
> ### Empirical Mode Decomposition  
> par(mfrow=c(3,1),mar=c(2,1,2,1))  
> try<-emd(MR$disch,MR$date,boundary="wave")
```

```

> ###
> ### Plotting the IMFs
> par(mfrow=c(3,1),mar=c(2,1,2,1))
> par(mfrow=c(try$nimf+1,1),mar=c(2,1,2,1))
> rangeimf<-range(try$imf)
> for(i in 1:try$nimf)
+ plot(MR$date,try$imf[,i],type="l",xlab="",
+ ylab="",ylim=rangeimf,main=
+ paste(i,"-th IMF",sep="")); abline(h=0)
> plot(MR$date,try$residue,xlab="",ylab="",
+ main="residue",type="l")

```



```

> ### Plot of IMFs from EMD package saved as MR44-64adjET_03.tiff
> ###

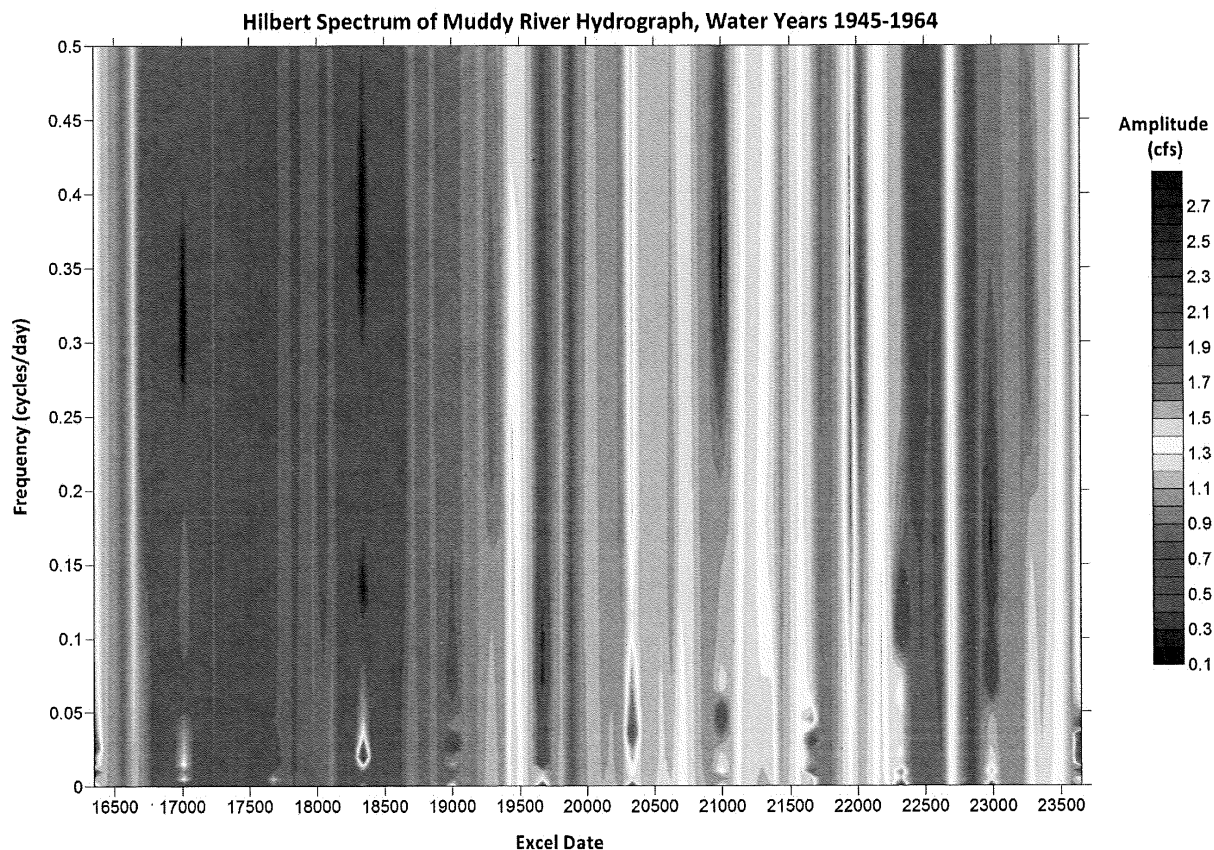
```

```

> ### Write out result to table for Excel input
> write.table(try,file="data/MR44-64try3.txt",sep="\t")
> ### HILBERT SPECTRUM ###
> ###
> ### Spectrogram: X - Time, Y - Frequency,
> ### Z (Image) - Amplitude
> test1<-hilbertspec(try$imf)
> spectrogram(test1$amplitude[,1],
+ test1$instantfreq[,1])
Error: cannot allocate vector of size 407.1 Mb
> spectrogram(test1$amplitude[,2],
+ test1$instantfreq[,2])
Error: cannot allocate vector of size 407.1 Mb
> write.table(test1$instantfreq,file="data/MR44-64freq.txt",sep="\t")
> write.table(test1$amplitude,file="data/MR44-64ampl.txt",sep="\t")
> write.table(test1$energy,file="data/MR44-64energy.txt",sep="\t")
>

```

THE FREQUENCY AND AMPLITUDE TABLES WERE COMBINED IN EXCEL WITH CORRESPONDING DATES, AND THE HILBERT SPECTRUM WAS PLOTTED WITH SURFER USING INVERSE-DISTANCE WEIGHTING ON A 100 X 101 GRID:



CITATIONS

Donghoh Kim <donghoh.kim@gmail.com> and Hee-Seok Oh
<heeseok@stats.snu.ac.kr> (2010). EMD: Empirical Mode Decomposition
and Hilbert Spectral Analysis. R package version 1.2.1.
<http://CRAN.R-project.org/package=EMD>

R Development Core Team (2011). R: A language and environment for
statistical computing. R Foundation for Statistical Computing,
Vienna, Austria. ISBN 3-900051-07-0, URL <http://www.R-project.org/>.

**A Scoping Model of Interbasin Groundwater Flow in Eastern Nevada
Constrained by Anisotropy and Regional Heat Flow,
with Suggestions of Millennial-Scale Climate Memory**

Cady Johnson and Martin Mifflin
Mifflin & Associates, Inc.

April 4, 2019

Nevada’s water-rights seniority justice system, a political growth mantra, waning societal desires to protect endangered species, and climate change have spawned vexing problems for the Nevada State Engineer (NSE). If administrative units (hydrographic basins) are collapsed into larger but no more rational entities such as the 5-basin “Lower White River Flow System” (LWRFS) there is no improvement in analysis potential even as new water-rights disputes are created. Groundwater sustaining the regional springs of southern Nevada is not somehow “extra” water if springflow is fully appropriated, yet the *NSE has consciously allowed time-to-impact to creep into Nevada Water Law* as groundwater models became accepted as evidence. Regional springs are coupled by capture zones to recharge areas in high mountains with appropriate regionally-connected lithology, and significant winter snowfall. In this exercise we select the analysis domain (Figure 1), define a recharge-cutoff surface, assign anisotropy directions, and characterize the Eureka Low (Figures 2 and 3) subjectively but with no intentional bias.



Figure 1 (previous page). Portion of Lower Paleozoic Shelf Domain considered in the MAI groundwater model, with generalized geologic boundaries and anisotropy picks [StructuralGrainInset27V2.jpg]

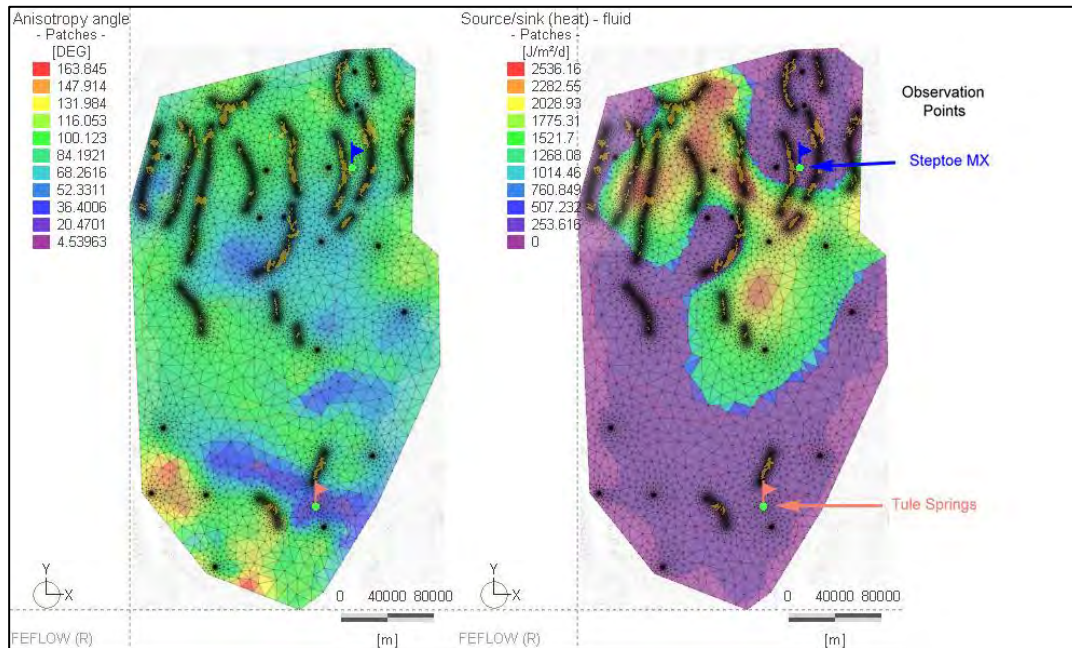


Figure 2. Anisotropy angles as mapped to the finite-element mesh (left) and characterization of the Eureka Low in terms of rate of heat input to the aquifer (right) [AnisotropyAnglesAndEurekaLowV2.jpg]

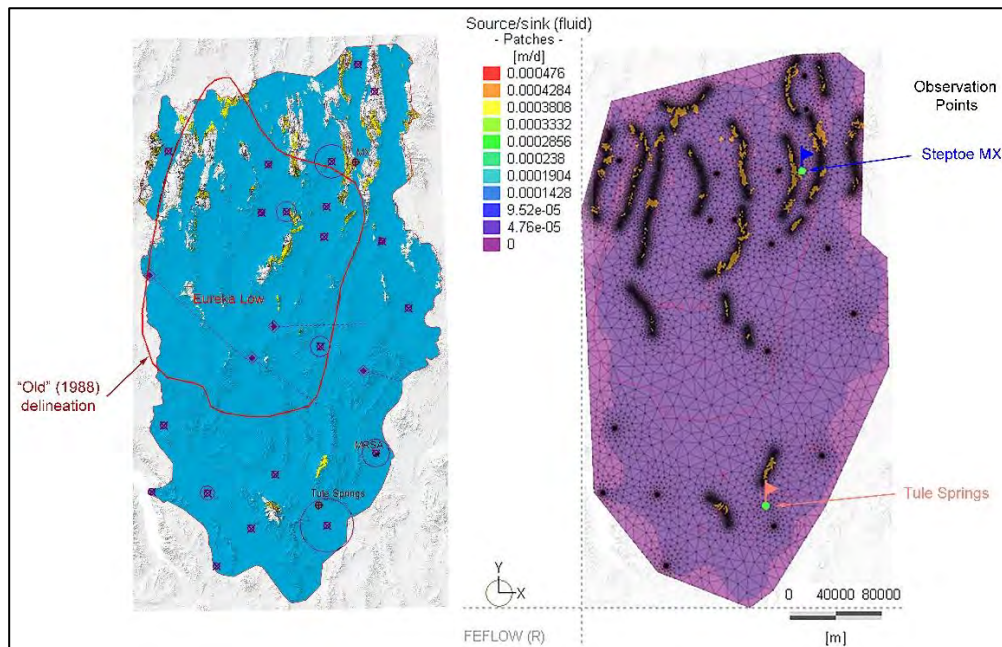


Figure 3. Islands of high terrain above the recharge-cutoff surface (left) and recharge assignment to OSD rocks within those areas (right). The Steptoe Valley MX well (blue flag) and Tule Springs (pink flag) are manual calibration points for hydraulic head and temperature. [RechargeCutoffOSDandRatesV2.jpg]

A north-dipping, planar recharge-cutoff surface isolates terrain ranging from 8,500 feet (2,590 m) at Latitude 36N, down to 7,000 feet (2,134 m) at Latitude 40N (Figure 3). Ordovician, Silurian, and Devonian Lower Paleozoic Shelf Domain rocks, mapped at 1:250,000 in these “islands” of high terrain, are allocated recharge equal to the discharge of regional springs.

Output from the model (Figure 4) is a steady-state solution for head and temperature. Hydraulic head is smoothly distributed in the region, reflecting the southerly fluid-potential gradient driven by regional topography. In contrast, simulated temperatures are highly variable, reflecting complex interplay between distributed recharge and an irregular heat source. With streamlines, the solution for head can be presented to illustrate capture zones of the regional springs (Figure 5).

In this model Las Vegas Valley is a much larger sink (59,000 afy) and the Spring Mountains a much smaller regional source (5,200 afy, based on geologic structure and stratigraphy) than estimated historically. Pahrump and Indian Springs are considered local based on their elevations and locations adjacent to the Spring Mountains, the source of 11,500 afy non-regional recharge to those flanking spring areas. Pahrnagat Valley bypass flow does not reach Ash Meadows in this conceptualization, instead turning southeast toward Las Vegas. Discharge at Oasis Valley, Furnace Creek, Ash Meadows, and Tecopa originates in central, not eastern or southern Nevada.

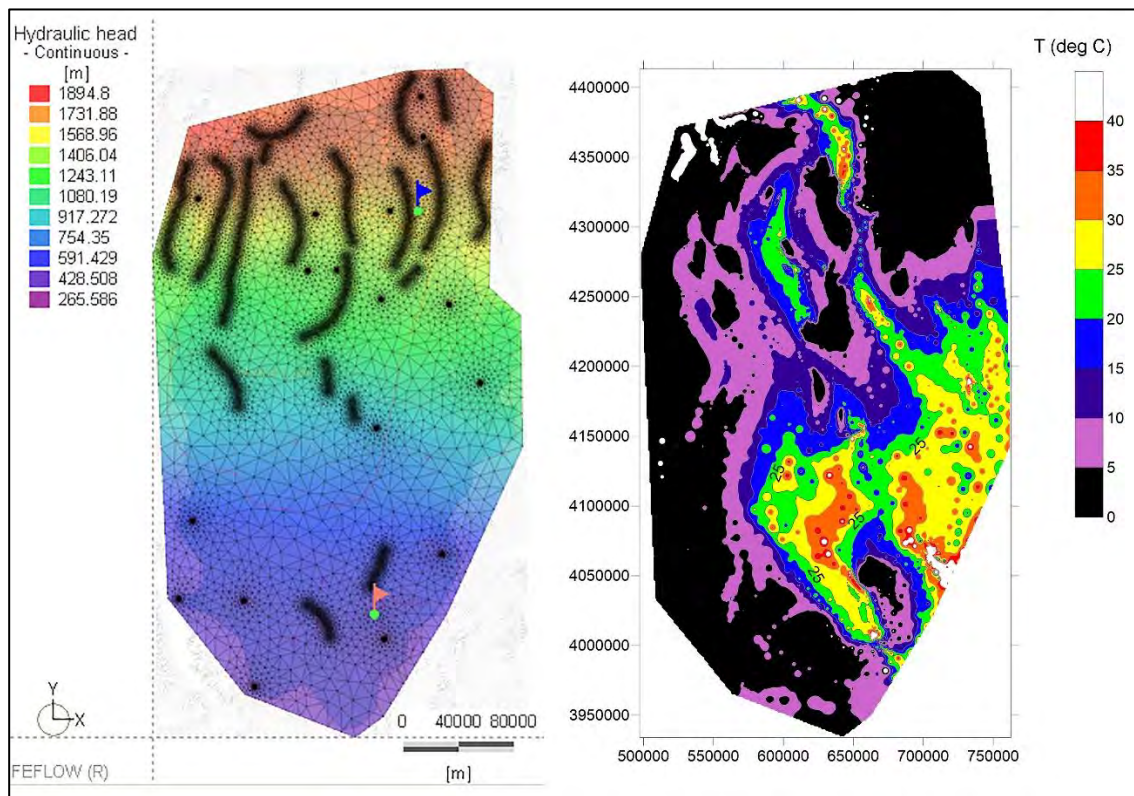


Figure 4. Solutions for hydraulic head and temperature in the base case model. [HeadAndTempSolutions20190310]

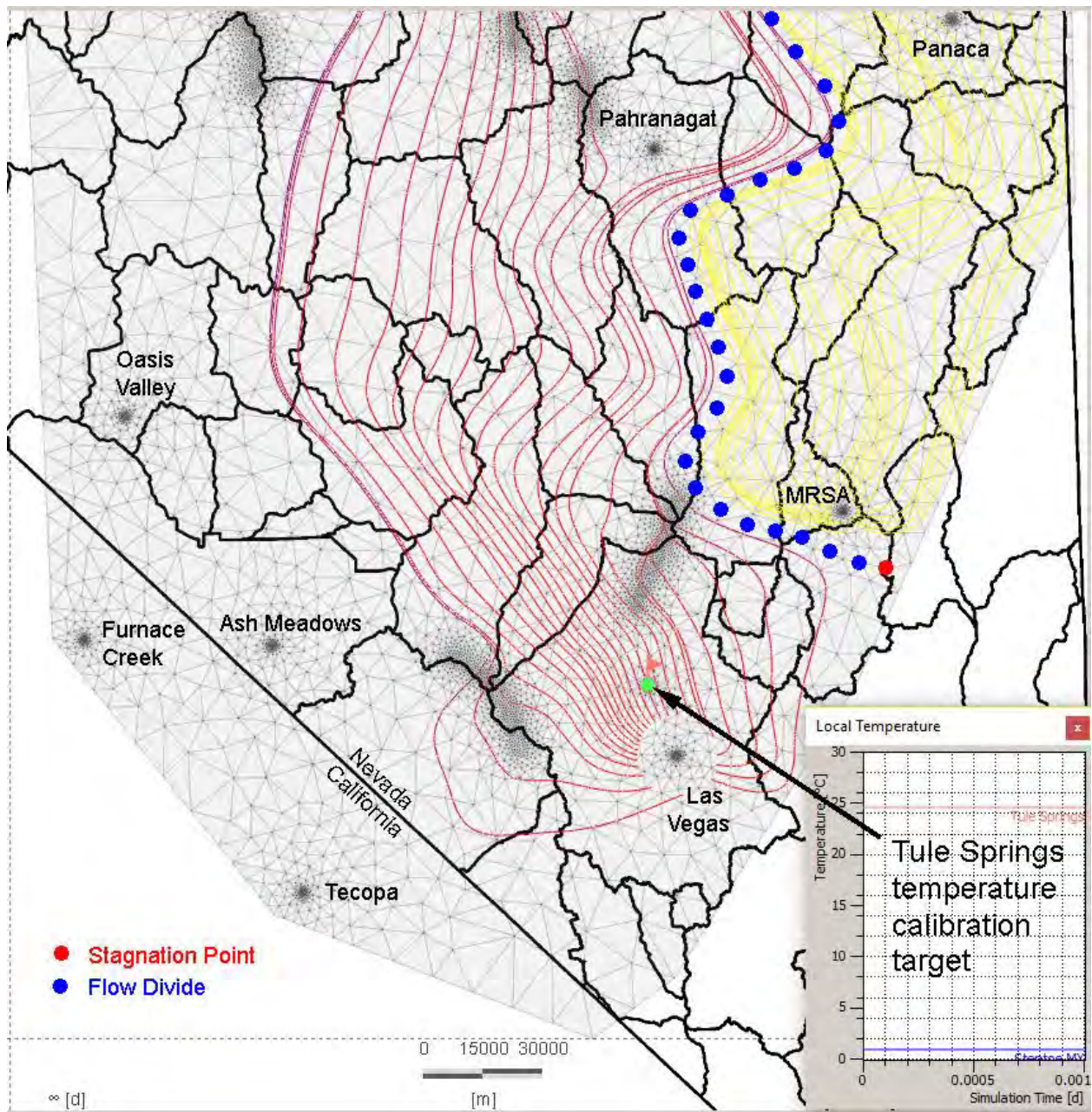


Figure 5. A flow divide between groundwater tributary to the Muddy River Springs and groundwater tributary to Las Vegas Valley is demarcated (blue dots). At the stagnation point the calculated temperature is too high but more importantly the model is numerically stable [FlowDivide20190401.jpg, derived from Supermesh3h.fem]

Thomas and Mihevc (2011, p. 31) state that “Correcting the model ages for diffusion processes is beyond the scope of this report”. From their Executive Summary (Thomas and Mihevc, 2011, p. iii) “Carbon-14 corrected groundwater ages were also estimated for the regional warm spring areas of the WRFS to provide information on recharge timing and groundwater travel times within the WRFS”. This may be an important consideration:

“By plotting the ratio of the rate of diffusion to the rate of decay of carbon-14 over the length scales representative of several common hydrogeologic settings, it is demonstrated that diffusion of carbon-14 should often be not only a significant process, but a dominant one relative to decay”

...Sanford, 1997

Radiocarbon data from regional springs is not diagnostic of groundwater travel time (GWTT), but instead is subject to major uncertainties due to matrix diffusion effectively constituting another ^{14}C decay mechanism along the groundwater flow path, causing ages to appear older than they actually are. However, comparison of percent-modern-carbon analyses in regional springs can be informative, as follows. Preston Big Spring shows 11.2 pmc, Crystal Spring in Pahranaagat Valley has ~ 6.2 pmc for an apparent age difference of 4,941 years. If, however, 200x more matrix water is available to exchange with actively-flowing water the actual groundwater travel time is $4941/200 \approx 25$ years. We’re just missing the radiocarbon lost to the matrix and seeing mostly older radiocarbon released from the matrix (Figure 6). Big Muddy Spring has 9.7 pmc, which is not consistent with a Pahranaagat Valley source without significant local (younger) input, as suggested by Thomas and others (1996). Panaca Valley, given elevated fluoride in several locations, is the more logical source for MRSA discharge with flow paths beneath the Meadow Valley Mountains, Kane Springs Wash, and Coyote Spring Valley. Hershey and others (2010) provide a radiocarbon analysis from Panaca Spring, 23.1 pmc, so the apparent age difference between Panaca Spring and Big Muddy Spring is 7169 years. The ongoing crustal extension in the region and numerous successful production wells in areas of Quaternary faulting suggest that these radiometric age differences are far too large for the system not to be diffusion-dominated.

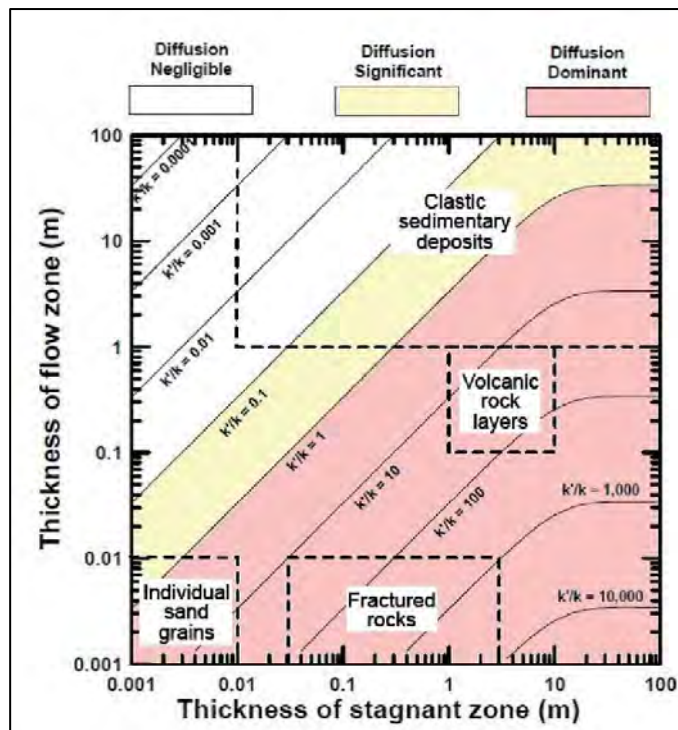


Figure 6. The OSD carbonate-rock aquifer can be characterized as plotting near the lower left corner of the “Fractured rocks” field and even below the x-axis, diffusion-dominated and reflecting the heat-constrained sub-millimeter-diameter active flow zones [SanfordDiffusion.jpg]

Interpretation of stable-isotope analyses should account for matrix storage volume in the region roughly 200 times greater than the volume of active flow zones, with consequent “smearing” of discharge chemistry. This dilution factor is based on 3% porosity for the rock matrix based on laboratory studies (Hershey and others, 2003) and borehole geophysics (Berger, 1992), and from 0.00015 effective (interconnected) regional porosity from the coupled-process finite element model reported here.

When same-day (or within a day) samples were collected more than once from a group of related springs, similar isotopic shifts between times of sampling suggests that analytical uncertainty is not responsible for the temporal difference, in which case the differences would be random. Same-day samples from regional springs in eastern Nevada provide a powerful argument that spring-water compositions are transient on a management time scale of years to decades (Figure 7). Two regional groundwater systems (two primary systems are suggested here, Figure 5) are discharging a once-only record of past climate that should not be ignored or minimized in terms of importance. When the output signals (time-series of isotopic compositions) have been characterized at the main groundwater discharge areas for a sufficiently long monitoring interval those net signals arriving from present *and* past recharge areas will hold the key to groundwater travel times being estimated as mixing with explicit diffusion, where several signals are combined into one in a demonstrable time frame with mathematically defensible error bounds.

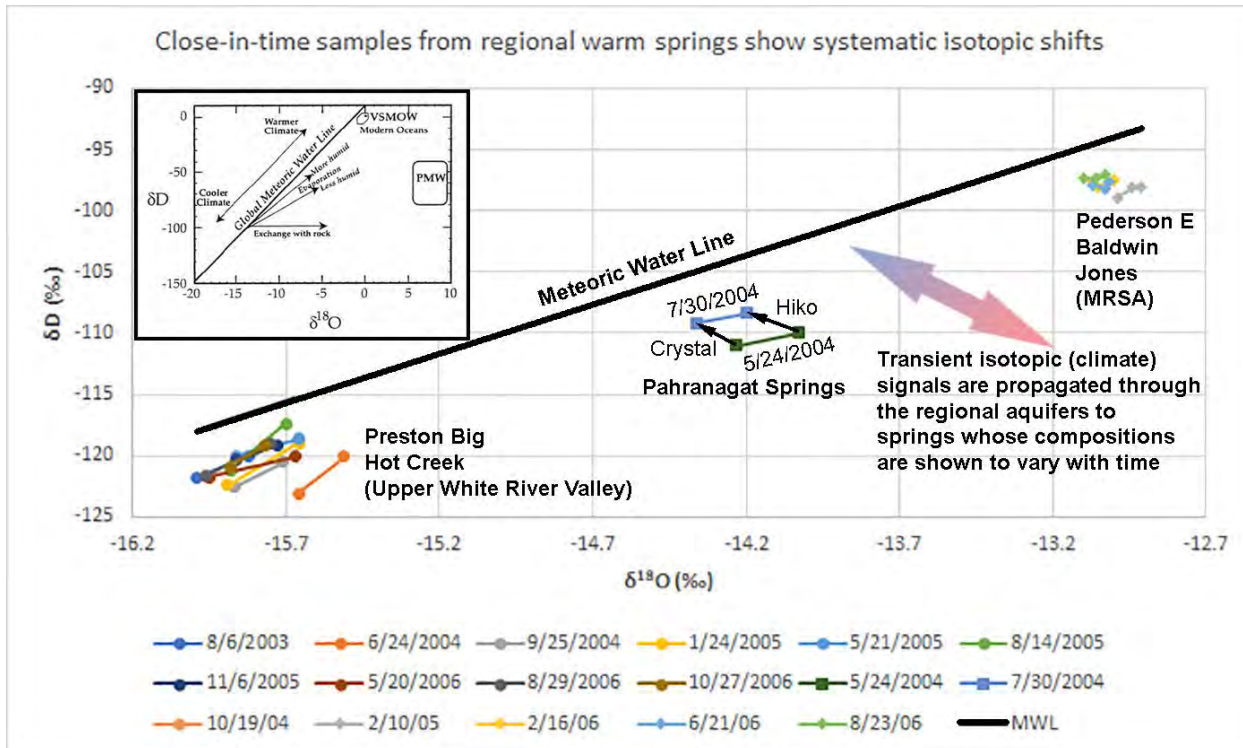


Figure 7. Analytical uncertainty notwithstanding, covariance of isotopic compositions in sub-areas reflects climate, because neither evaporation nor rock-water interactions can produce the observed trends (inset, from Seal and others, 2000) [IsotopicShifts3.jpg]

The high-resolution temperature-anomaly record from bristlecone pine tree-rings (Salzer and others, 2014) reveals by proxy the isotope enrichment- and depletion-producing climate modes that must now be in memory in the regional groundwater system (Figure 8). Unprecedented warming since

1850 is evident in the tree-ring record, preceded by a very cold interval (1827-1833) during which Francisco Garces, a Spanish explorer and missionary, coined the name “Nevada”, which translates precisely as “snow-covered”.

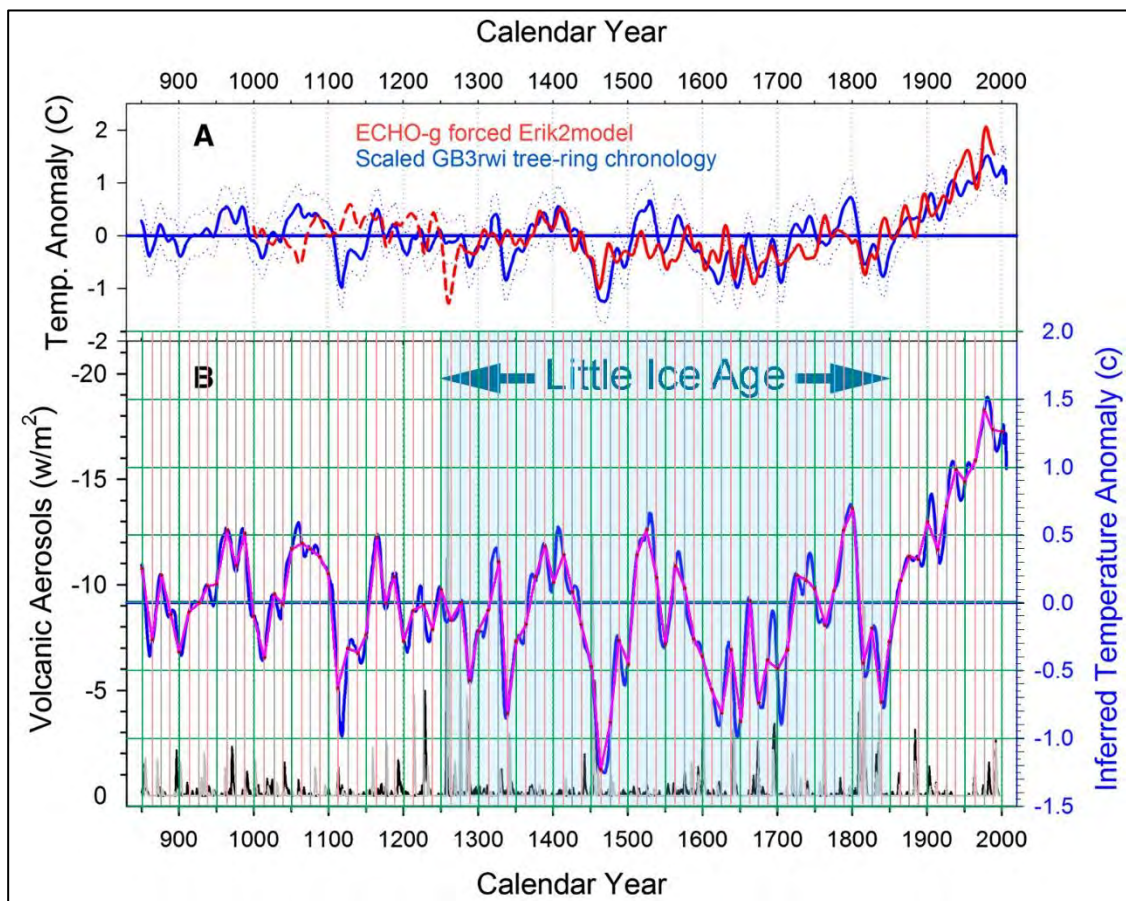


Figure 8. Temperature anomalies in the Great Basin based on long-term average, with model picks by the author at 12.5-year intervals (modified after Salzar and others, 2014) [Salzar2014chronology.jpg]

A diffusion-dominated groundwater system will “smear” the chemical characteristics of the active flow zone through matrix diffusion, with fracture water on relatively long flow paths acquiring the composition of the volumetrically much-larger and relatively stagnant matrix pore water. Matrix diffusion will therefore lessen the amplitude of compositional variations that are propagated to discharge locations, and eliminate the higher-frequency components of the input signal. We would therefore want to model a chemical or isotopic process variable as a “smeared” signal, like what is obtained by a 100-year moving average (Figure 9). In this representation there is an apparent ~200-year periodicity of $\pm 0.2^{\circ}\text{C}$ in an overall thousand-year temperature decline before the recent warming that began with the Industrial Revolution in the mid-1800s. We ask if any of this thermal history of the recharge areas is recognizable in the regional groundwater systems of eastern Nevada, not as temperatures, but expressed as variable stable-isotopic compositions with time at any representative monitoring location.

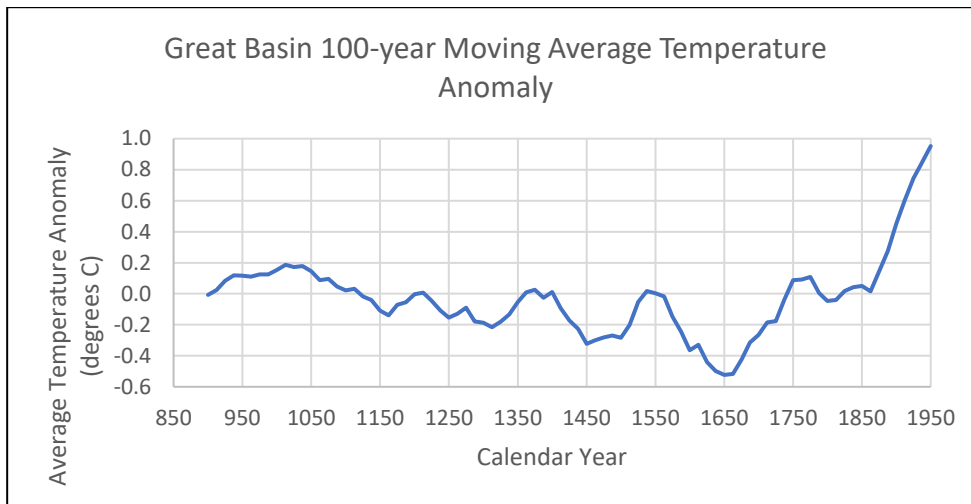


Figure 9. 100-year moving average of 12.5-year-interval picks from Salzar (2014) as shown in Figure 1. Note the apparent 200-year periodicity [AllSameDay.xlsx, sheet 'BristleconeT']

Calculated equilibrium temperatures from springs presumed to represent modern recharge by Thomas and Mihevc (2011) and those near the Fish Hatchery in Ruby Valley follow the same trend with latitude as Panaca and Muddy River Springs. As suggested by Figure 10, the Preston-Pahranagat trend is different and representative of a different recharge temperature regime than Panace-MRSA. If the input signal is smeared to the extent shown in Figure 9 by 100-year averaging, the range between maximum and minimum recharge temperatures is reduced to about 1.5°C. If we are now at about the warmest point since 1850, why are these “modern” waters so light isotopically? Perhaps matrix diffusion is affecting even the “recharge” springs.

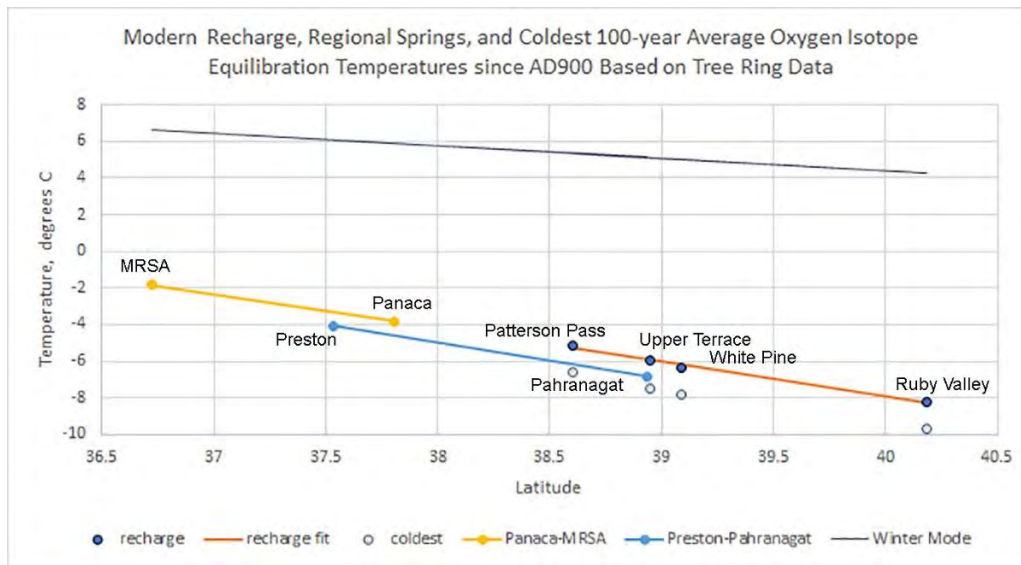


Figure 10. Two regional capture zones, first suggested by a scoping model of heat and fluid transport to balance the Eureka Low, are also indicated by evidence of recharge under colder-than-modern conditions, such that equilibration temperatures in the traditional (Preston to Pahranagat) north-central White River Flow System approach the coldest theoretical input in over a thousand years. [EquilibriumTemperatures.jpg]

The finite-element analysis was instructive in that time-of-travel capture zones for the MRSA were delineated in a minimalist conceptual framework (Figure 11). The anisotropy field used for this base case is experimental and based entirely on professional judgement, as is the operational recharge cutoff surface, OSD-only recharge-area lithology by decree, and characterization of the Eureka Low. All of these assignments could be easily tested for solution sensitivity by another user when there are concerns or disagreements about properties or boundary conditions, because the model executes in about 5 seconds on an i7 laptop. As quickly as users can adjust their input arrays for a new scenario they can test against the base case; there's only a 5-second delay before they can process results.

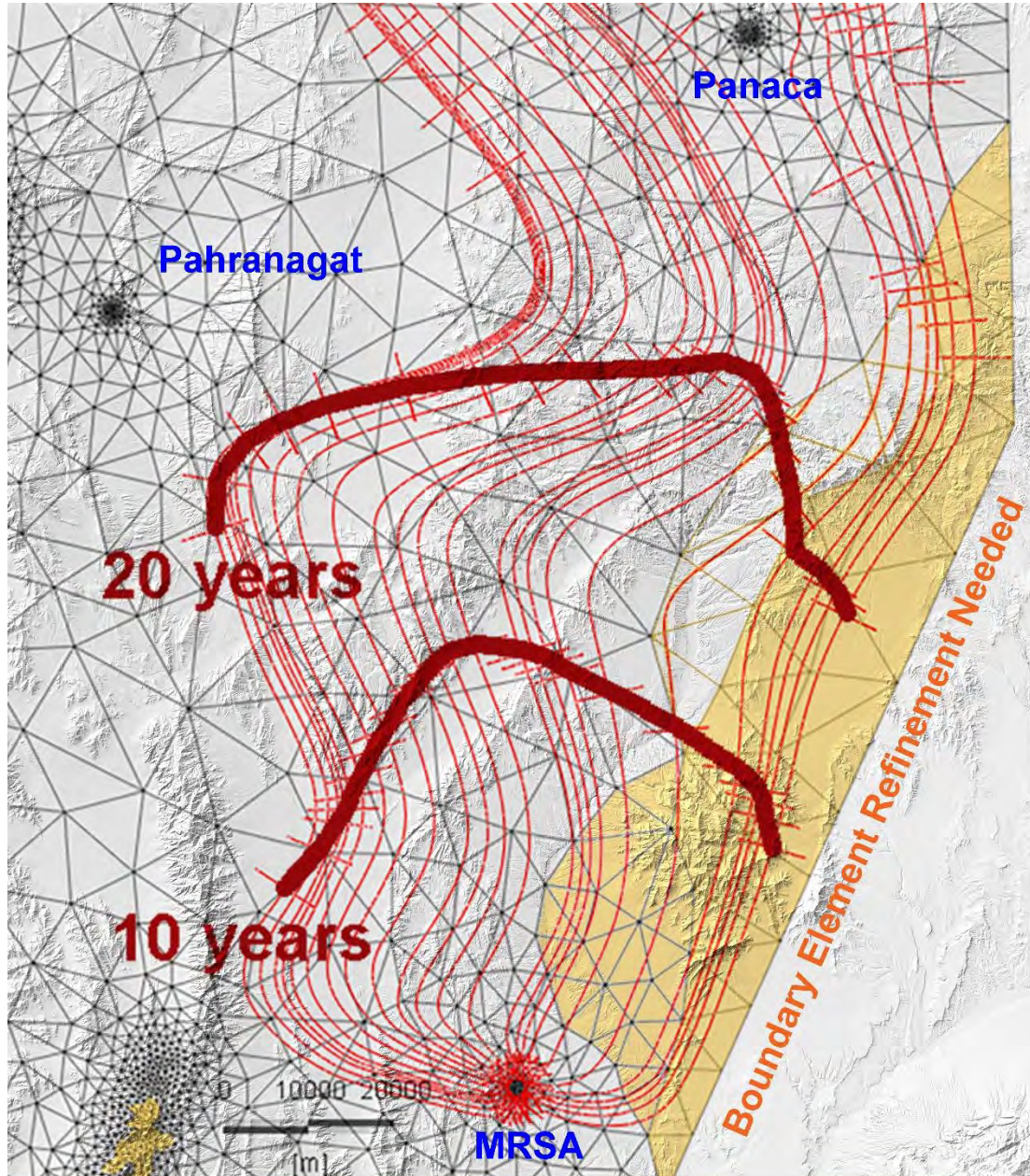


Figure 11. Streamlines and isochrons generated by the FEFLOW program, showing feature-based mesh refinement around regional recharge and discharge areas, where steady-state hydraulic gradients are largest [TimeOfTravelCaptureZonesSR.jpg, derived from Supermesh3h.fem]

The 10- and 20-year time-of-travel capture zones indicate that carbonate-rock aquifer pumping in Kane Springs Valley would impact the MRSA within 10 years, and development impacts from Delamar Valley would be sensed at the MRSA within 20 years.

The meshing process produces some extra elements where straight lines are necessarily used to approximate flow-domain boundaries; as non-participating sub-domains are identified they can be removed by assigning them zero transmissivity and thermal conductivity to improve calibration. Shading in Figure 11 shows a boundary segment that includes the Mormon Mountains that should be removed from the model domain because basement rocks are exposed there. Doing so would compress the streamlines and shift the Panaca-MRSA capture zone slightly westward, producing a new base case model for archival if numerical stability is preserved, which depends on many factors.

In summary, model-derived capture zones of Las Vegas and Muddy River Springs, which envelop the capture zones of Pahranaagat and Panaca Springs, respectively (Figure 5) are supported by stable isotopes and radiocarbon in addition to the simple mass-balance computations of Johnson and others (2001). Groundwater travel time is conceptually complex when matrix diffusion causes climate-driven (decades or less) hydraulic pulses of groundwater to regional springs that are compositionally representative of an integrated pore water composition acquired from the rock matrix, older and with smeared memory of variable climate history, that has largely replaced the soil water molecules and solutes in active-flow zones that began a generally southward journey more recently than spring-water isotopics suggest. Flow in the eastern capture zone (Panaca-MRSA) is more sluggish and/or diffusive than the central (Preston – Las Vegas) zone based on radiocarbon comparisons and relative distances along streamlines.

The information presented here adds support to the idea that Las Vegas Valley is the terminus of a regional groundwater flow system originating north of White River Valley as proposed by Eakin (1966), but not ending at the Muddy River Springs Area, which instead is fed by a separate capture zone that includes Panaca Valley and terminates at the MRSA. The implication for water management is that developments in areas tributary to Las Vegas Valley will likely not cause harm or even be sensed by monitoring, whereas developments in areas tributary to the MRSA, which might exclude alluvial-aquifer systems hydraulically isolated from the carbonate-rock aquifer, would be universally harmful to endangered species and senior water-rights holders in the headwaters area.

Conclusions and Management Implications

- A strongly anisotropic, heat-coupled modeling approach associates known discharge areas of regional, interbasin groundwater flow systems with probable (based on geology) high-elevation recharge areas far to the north, and indicates surprisingly short groundwater travel times when constrained by the regional heat budget
- A finite-element transmissivity model, constrained by physical boundaries, estimated rates of groundwater discharge, and groundwater temperatures, suggests groundwater moves within hydrodynamic flow-domains that do not respect basin physiography in southeastern Nevada.

Instead, primary capture zones (tributary flow fields) of the Muddy River Springs and Las Vegas regional discharge areas are suggested

- Adjustment of radiocarbon ages (residence times) to account for matrix diffusion produces an independent and much larger (than that of Thomas and Mihevc, 2011) estimate of groundwater velocity between Preston Big Spring and Pahrnagat Valley (divide apparent age difference by 200, the matrix:fracture porosity ratio) that supports the thermohydrologic finite-element model
- Two sources of water for the MRSA, suggested by multiple-regression analysis of climate response (prior ADR appendices), appear in this characterization to be associated with northeastern Coyote Spring Valley, and with the Meadow Valley Mountains (bounded by Meadow Valley Wash) to the east
- Radiocarbon analyses suggest groundwater movement between Panaca Valley and the MRSA is more sluggish and/or more diffusive than flow between northernmost White River Valley and Pahrnagat Valley, but “ages” are uncertain
- Big takeaway: The chemical and isotopic compositions of regional springs are transient and therefore rich in climate signals spanning perhaps thousands of years, produced as stagnant but relatively high-volume matrix pore water replaces active flow-zone water along flow paths to and from which diffusion can occur. Conversely, the matrix-water compositions are always seeking equilibrium with fast-moving water in the volumetrically tiny regional flow channels
- In this conceptualization a portion of the groundwater flow field tributary to Las Vegas Valley underlies Delamar and Dry Lake Valleys, following a sinuous boundary with the capture zone of the Panaca-MRSA system to the east
- The southern and westernmost areas of Coyote Spring Valley appear to be tributary to Las Vegas Valley, as is most of California Wash; neither of these is tributary to the MRSA, which appears hydrodynamically isolated from those areas at the present time

References

- Berger, D.L., 1992. Lithologic properties of carbonate-rock aquifers at five test wells in the Coyote Spring Valley area, southern Nevada, as determined from geophysical logs: U.S. Geological Survey Water-Resources Investigations Report 91-4167, 27 p.
- Eakin, T.E., 1966. A regional interbasin ground-water system in the White River area, southeastern Nevada: Water Resources Research, v. 2, no. 2, p. 251-271.
- Fricke, H.C. and J.R. O'Neil, 1999. The correlation between $^{18}\text{O}/^{16}\text{O}$ ratios of meteoric water and surface temperature: its use in investigating terrestrial climate change over geologic time: Earth and Planetary Science Letters, v. 170, pp. 181-196.
- Hershey, R.L., W. Howcroft, and P.W. Reimus, 2003. Laboratory experiments to evaluate diffusion of ^{14}C into Nevada Test Site carbonate aquifer matrix. Desert Research Institute Publication No. 45180.
- Hershey, R.L., S.A. Mizell, and S. Earman, 2010. Chemical and physical characteristics of springs discharging from regional flow systems of the carbonate-rock province of the Great Basin, western United States: Hydrogeology Journal 18(4):1007-1026.
- Johnson, C., M. Mifflin, R.J. Johnson, and H. Haitjema. 2001. Hydrogeologic and groundwater modeling analyses for the Moapa Paiute Energy Center, a Calpine Company project in cooperation with the Moapa Band of Paiute Indians, Moapa Indian Reservation, Clark County, Nevada: 218 p. (unpublished)
- Salzer, M.W., A.G. Bunn, N.E. Graham, and M.K. Hughes, 2014. Five millenia of paleotemperature from tree-rings in the Great Basin, USA: Clim Dyn 42:1517-1526.
- Sanford, W.E., 1997. Correcting for diffusion in carbon-14 dating of groundwater: Groundwater, v. 35, 357-361.
- Seal, R.R.III, C.N. Alpers, and R.O. Rye, 2000. Stable Isotope Systematics of Sulfate Minerals: Chapter 12 in Reviews in Mineralogy and Geochemistry 40 (1): p. 541-602
- Thomas, J.M. and T.M. Mihevc, 2011. Evaluation of Groundwater Origins, Flow Paths, and Ages in East-Central and Southeastern Nevada: University of Nevada, Desert Research Institute, Publication No. 41253, 70 p.
- Thomas, J.M., A.H. Welch, and M.D. Dettinger, 1996. Geochemistry and Isotope Hydrology of Representative Aquifers in the Great Basin Region of Nevada, Utah, and Adjacent States: U.S. Geological Survey Professional Paper 1409-C, 110 p.

Technical Note: Order 1169 Post-Audit Analysis of Pumping Response

Cady Johnson and Martin Mifflin
Mifflin & Associates, Inc.
October 1, 2013

Introduction

Order 1169 monitoring-well databases established before, during, and after the designated MX-5 pumping-test period allow for conventional well-hydraulic analyses, *e.g.*, derivation of aquifer parameters and characterization of boundary conditions. The analytical starting point is to determine the geographic extent and rate at which the cone of depression associated with MX-5 pumping (pumping-induced drawdown) develops over time. To confidently determine drawdown from monitoring-well records, particularly when generally larger forcing agents are affecting regional water levels, it is necessary to separate water-level variations attributable to pumping from those producing background fluctuations. These larger systematic (annual) and multi-year (secular) water-level variations are present in hydrographs of wells finished in carbonate-rock aquifers throughout a large region called the Arrow Canyon Range Cell. A useful analytical strategy to separate out the signal of interest (drawdown) from background forcing effects is to reference a monitoring well record that faithfully records the regional background forcing but does not display any evidence of being influenced by pumping at MX-5.

Background Well

The period between April of 2012 and April of 2013 represented the longest interval of nearly-continuous pumping of MX-5 since the beginning of the Order 1169 test. Reference (background) monitoring wells on the Moapa Indian Reservation were unresponsive to this prolonged pumping episode, based on the absence of any distance-drawdown relationship among the Reservation hydrographs. Instead, the close similarity of the Reservation monitoring-well hydrographs to each other demonstrates that they recorded nearly-identical expressions of environmental forcing agents that produced large water-level changes independent of MX-5 pumping. Application of the method of differences to resolve drawdowns at wells that *were* affected by pumping is therefore a useful analytical strategy to determine the MX-5 – related pumping cone in terms of extent and magnitude. This is the approach utilized by Halford (2006, p.4), who found water levels from “background” wells (those sufficiently removed from pumping effects) can be effective correctors of environmental effects. The large environmental forcing agents producing water-level changes unrelated to MX-5 pumping are filtered out by the difference method using an unaffected control-well hydrograph.

Hydrograph Registration

Hydrographs from the Reservation-area monitoring wells are registered (aligned) by subtracting the average water levels during the interval of 2009 when their records overlap (Figure 1). Notably, there is no systematic divergence of any of the hydrographs in this period of record. Paiutes’ M1 has the most complete record, and is representative of the Reservation area as a whole (Figure 2). The

SE ROA 37432

Reservation monitoring wells range in distance from 14.7 miles (M1) to 21.3 miles (M2) from MX-5, yet the net water-level change is slightly less at M1 than at the other wells. This is the opposite of what would be expected in the presence of a cone of depression resulting from pumping at MX-5. Furthermore, the absence of any systematic divergence of the hydrographs from 2009 until mid-2013, except for the temporary divergence of the ECP-2 hydrograph in late 2012 – early 2013 attributable to intermittent pumping at Paiutes’ ECP-1, indicates that no measurable cone of depression from MX-5 pumping existed in the Reservation area. With the exception of ECP-2, any of the Reservation monitoring wells could have provided adequate control as a background well.

When the hydrograph from MX-4 is compared to that of M1 (the selected background well with no evidence of MX-5 pumping-related responses), it is noteworthy that at times when the pump in MX-5 has been shut off for a month or more, the water level in MX-4 recovers only to the trend defined by M1 (Figure 3). When the difference between the M1 and hydrographs of responding wells are plotted with a logarithmic time scale referenced to the start of pumping (Figure 4), segmented time-drawdown plots typical of bounded aquifers are derived. There is a prominent steepening of the response curves by the end of the first week of pumping (about 10^4 minutes), indicative of the spreading cone of depression encountering a low-permeability boundary. A flattening phase is partly due to interruptions to pumping, but after 10^5 minutes (about 2 months) the response curves steepen again. At the time pumping ceased on April 30 of 2013, drawdown at MX-4 was about one foot, and about 0.3 feet at UMVM-1.

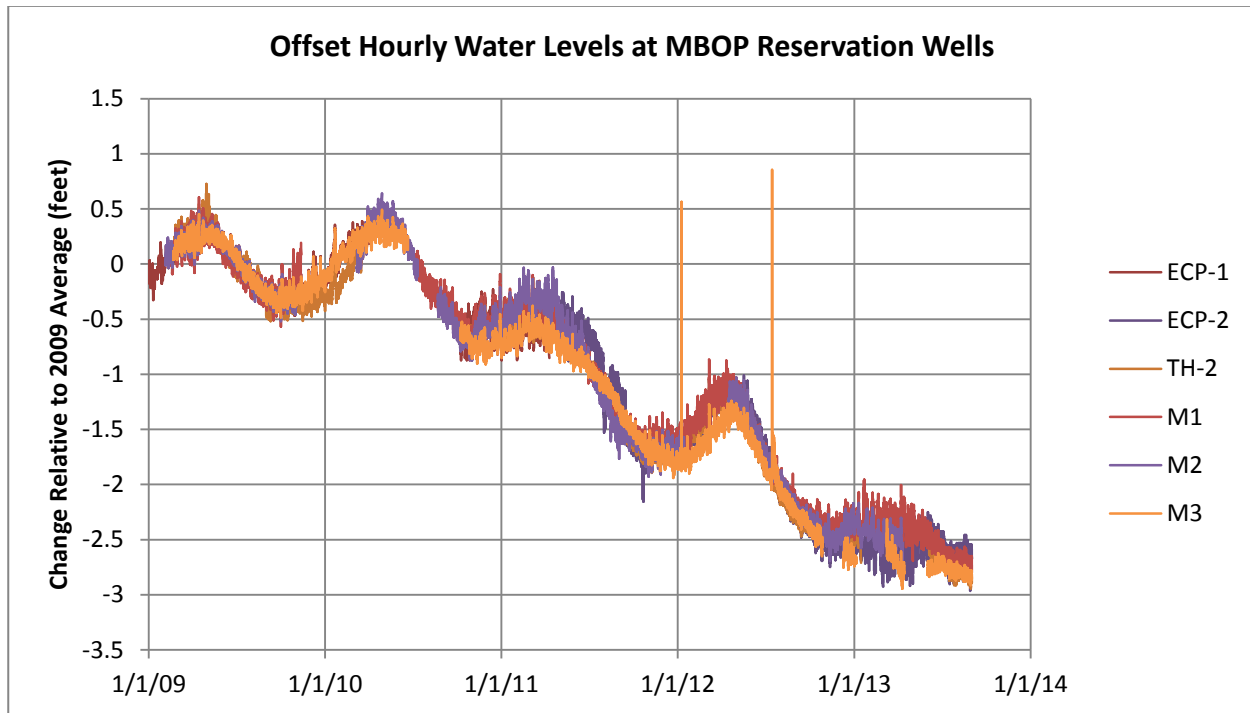


Figure 1. Hourly hydrographs of the Moapa Indian Reservation monitoring wells from January of 2009 to September of 2013. [file OffsetWLS.xlsx, sheet 'OffsetAll']

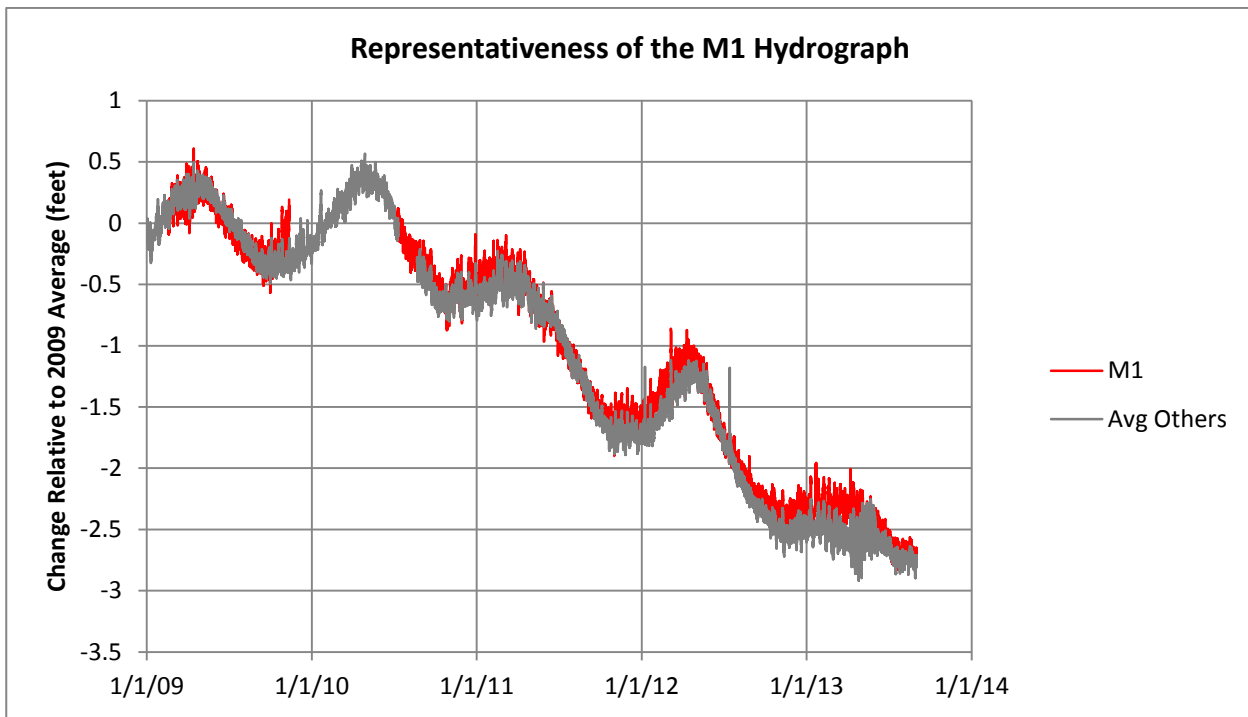


Figure 2. Comparison of the Paiutes' M1 hydrograph with the average of the 5 other Reservation wells that were monitored between 2009 and 2013 [file OffsetWls.xlsx, sheet 'OffsetAll']

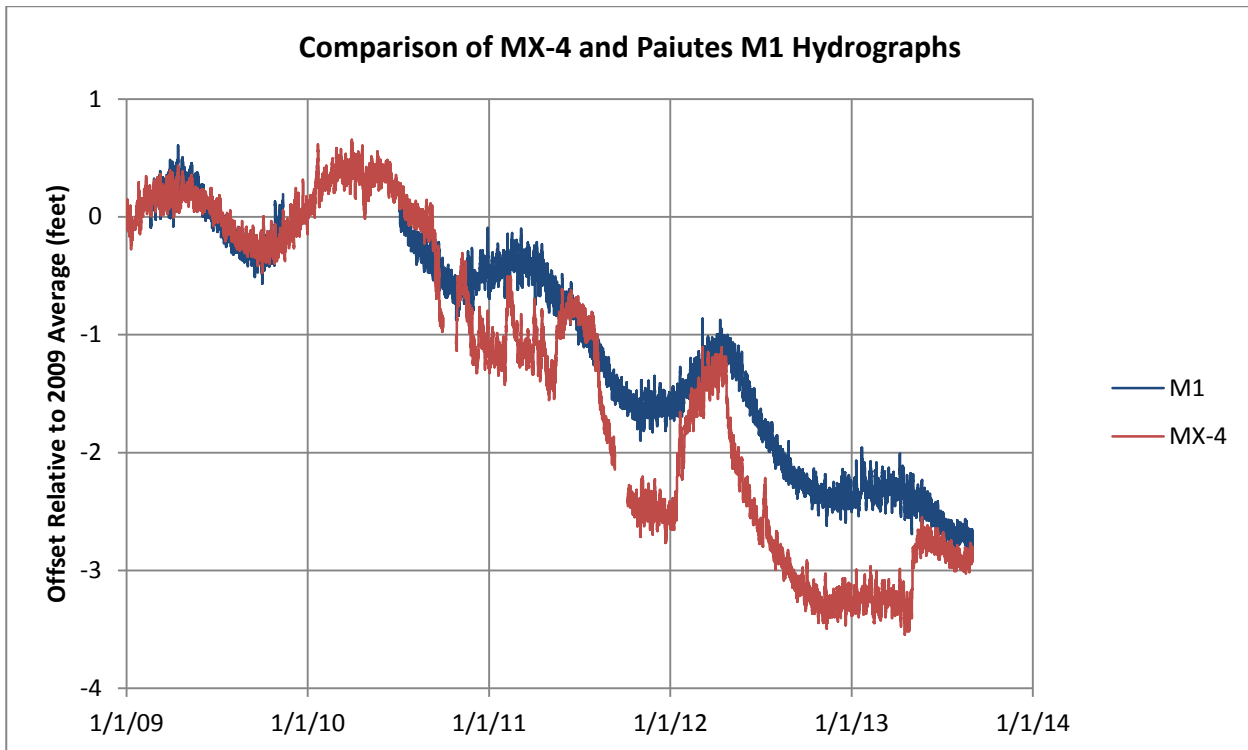


Figure 3. The *difference* between the M1 and MX-4 hydrographs is drawdown; note that MX-4 recovered to the M1 reference level after pumping ceased in 2011, and small residual drawdowns are associated with early 2012 and mid-2013 recoveries. [file OffsetWls.xlsx, sheet 'OffsetAll']

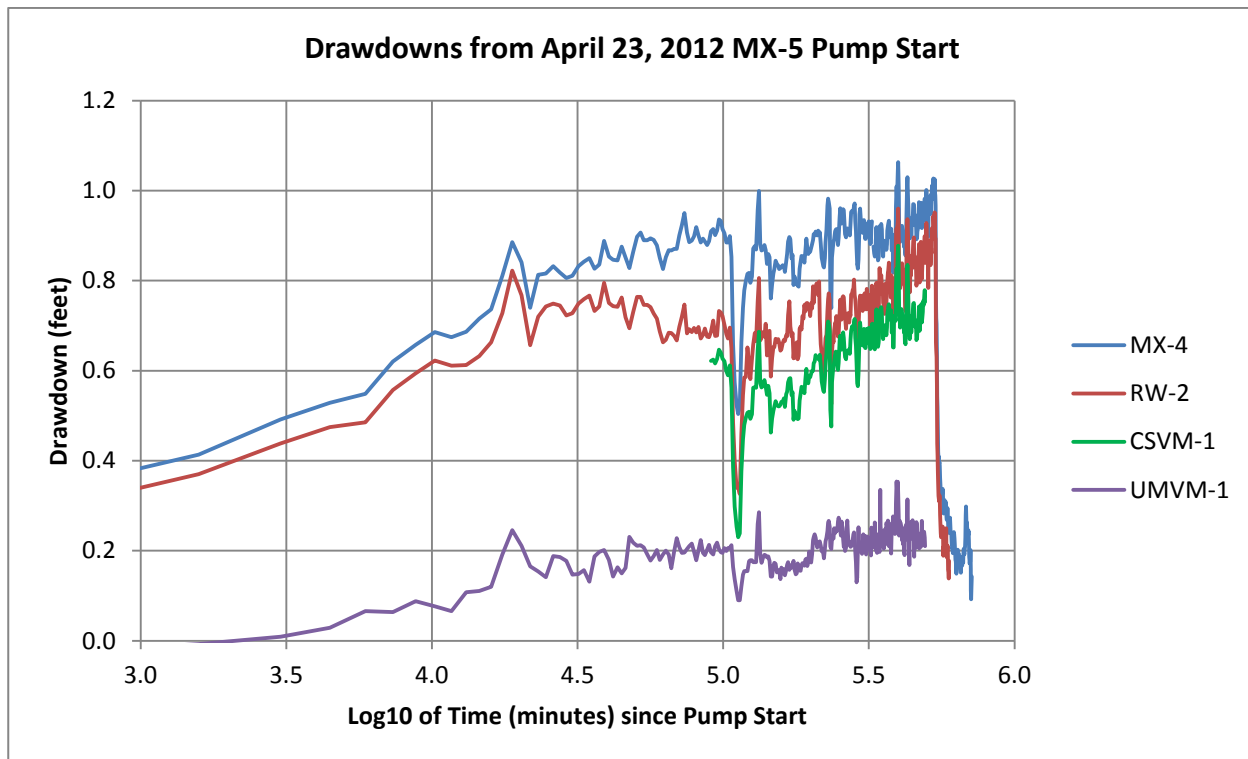


Figure 4. Daily-average drawdowns derived by the method of differences [file Drawdowns.xlsx, sheet 'All']

Conceptual Model of the Carbonate-Rock Aquifer

Geologic mapping by Schmidt and Dixon (1995) strongly suggests a structural discontinuity along the trend of SR 168; Ordovician and Devonian rocks crop out within one mile north of the highway, indicating the absence of the Mississippian Carbonate-Rock Aquifer tapped by MX-5 (Ertec, 1981). Aquifer-test evidence for a near-field low-permeability boundary near MX-5 obtained by Johnson and Mifflin (2012) is therefore consistent with geologic relations. Multiple lines of geologic and hydrologic evidence further suggest that another hydraulic barrier is present to the south (Johnson and Mifflin, 2003), leading to the conclusion that a wedge-shaped aquifer with its apex encompassing the headwaters area is likely an approximate configuration of the Carbonate-Rock Aquifer in southeastern Coyote Spring Valley (Figure 5). The analytical approach of Ferris and others (1962, pp. 154-156) was used to represent the model domain using image wells.

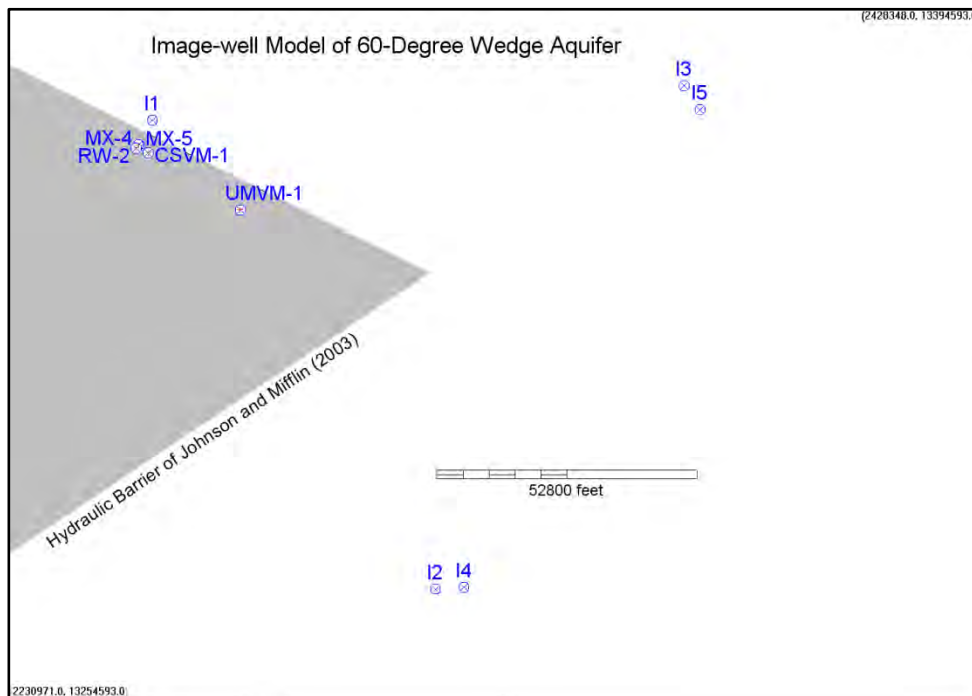


Figure 5. Bounded aquifer (shaded) represented by a 60-degree wedge, image wells (I1 through I5) used to represent pumping in this wedge-shaped model aquifer, and monitoring wells utilized as calibration targets [file WedgeMapCrop.tif, modified after screenshot from model Wedge.aqf]

Optimization of transmissivity (T) and storage coefficient (S) using the wedge-aquifer model and pumping-response data from MX-4 and RW-2 (Figures 6 and 7) produces parameter estimates consistent with those of Johnson and Miffilin (2012) that were based on early-response data only. The optimized T is about 900,000 ft²/day, slightly less than the median T obtained by Johnson and Miffilin (2012) using 5 sets of early pumping-response data. The optimized S is about 0.06, somewhat greater than the median value of 0.04 obtained by Johnson and Miffilin (2012) and strongly indicative of unconfined conditions in the immediate vicinity of the pumping well, MX-5.

Analysis of pumping responses at CSVM-1 and UMVM-1 suggests that confined conditions and substantially higher transmissivities prevail in down-gradient areas (Figures 8 and 9). This is also consistent with the early-response analysis of Johnson and Miffilin (2012), but with caveats. A data gap in the posted daily water-level records from March 22 until June 24 of 2012 in the CSVM-1 record is problematic; Johnson and Miffilin (2012) utilized 30-minute data in their early-time pumping-response analysis, so water-level measurements were being made, but their reliability is now in question since daily averages are absent from the State Engineer's Order 1169 database. In the case of UMVM-1, pumping response was below detection limits in the early interval that was examined. The well log (#90051) indicates "water strata" at 382 feet, yet a surface seal was placed to a depth of 1000 feet in this 1785-foot well. The confined response may be an artifact of well design, which isolates the upper part of the saturated zone from the screened interval below 1000 feet. As a result, model response at UMVM-1 after one year of pumping is greater than what is observed (Figure 10), leaving the representativeness of the UMVM-1 water-level record an open question .

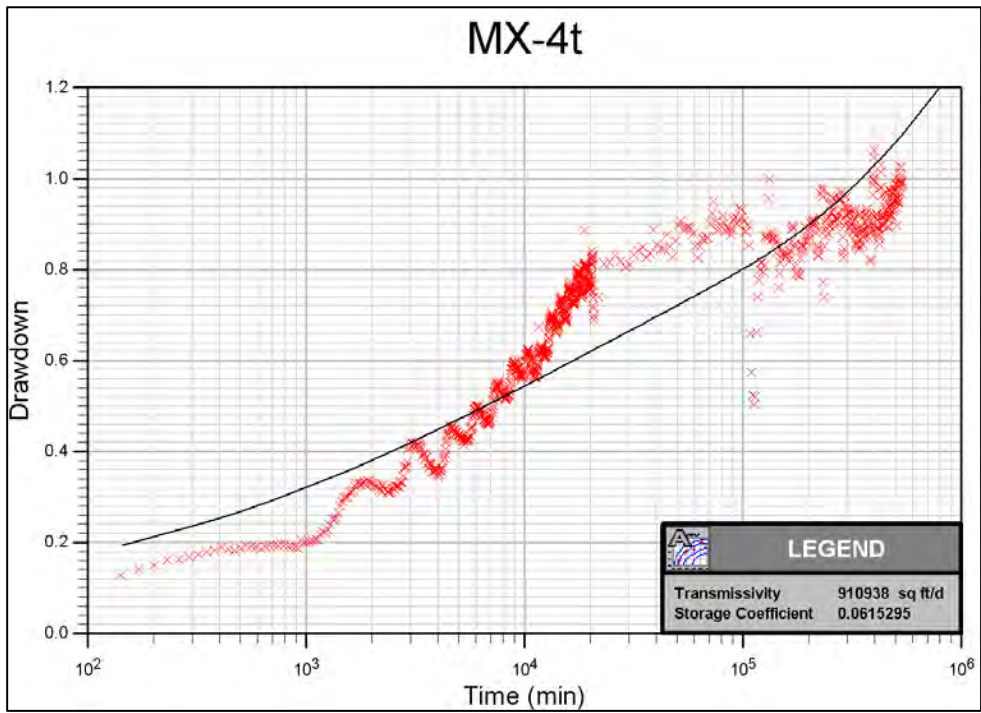


Figure 6. Observed and simulated drawdowns (feet) at MX-4 in response to pumping at MX-5 that began on April 23, 2012. [file Wedge2aMX4crop.tif, obtained with model Wedge2a.aqf]

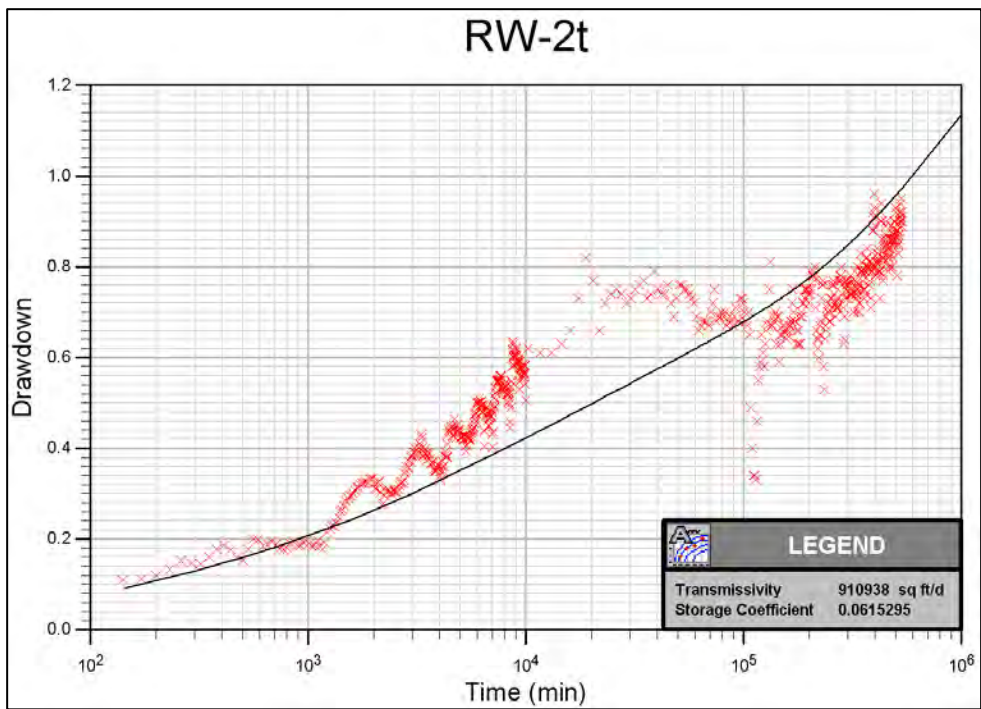


Figure 7. Observed and simulated drawdowns (feet) at RW-2 in response to pumping at MX-5 that began on April 23, 2012. [file Wedge2aRW2crop.tif, obtained with model Wedge2a.aqf]

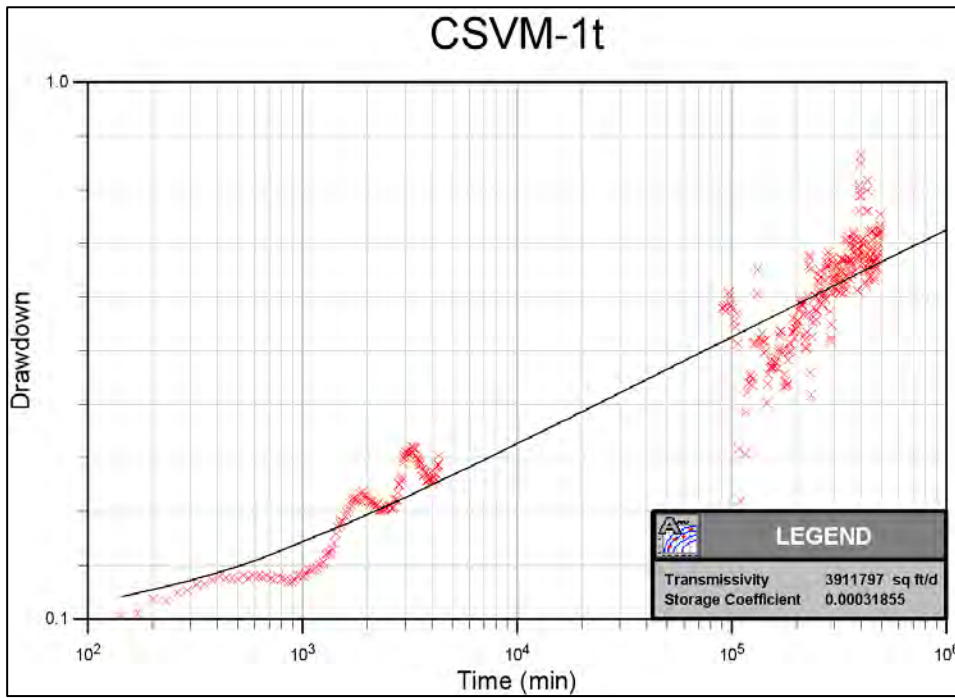


Figure 8. Observed and simulated drawdowns (feet) at CSVM-1 in response to pumping at MX-5 that began on April 23, 2012. [file Wedge2cCSVM1crop.tif, obtained with model Wedge2c.aqf]

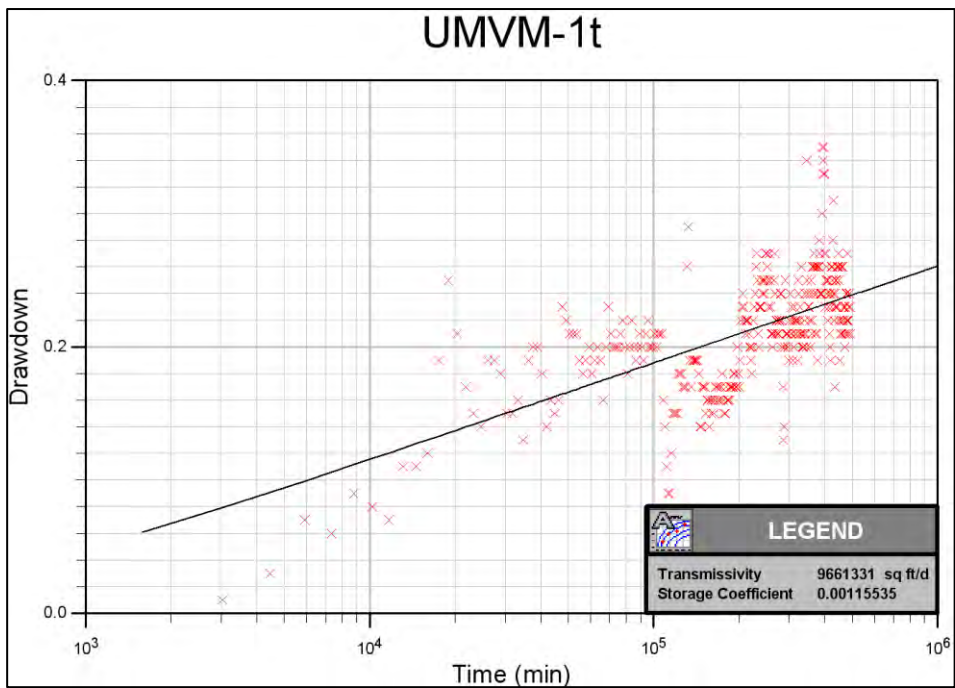


Figure 9. Observed and simulated drawdowns (feet) at UMVM-1 in response to pumping at MX-5 that began on April 23, 2012. [file Wedge2bUMVM1crop.tif, obtained with model Wedge2b.aqf]

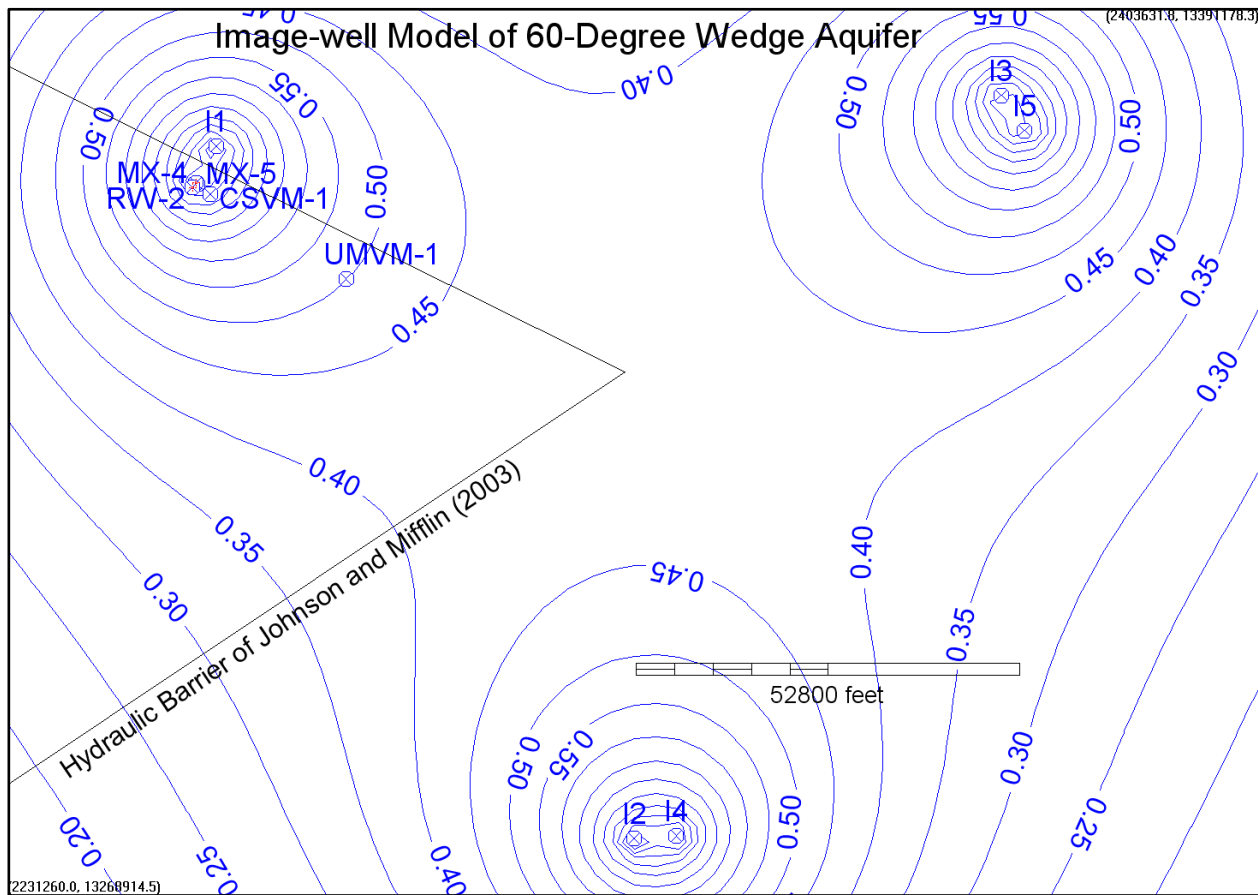


Figure 10. Predicted drawdowns in a 60-degree, wedge-shaped aquifer after one year of pumping 7.43 cfs from MX-5, with T and S based on an optimized solution to MX-4 and RW-2 pumping response as given in Figures 6 and 7. Only the predicted water levels within the wedge are “real”; image wells outside the wedge simulate the effects of 2 impermeable boundaries by assuring there is no hydraulic gradient across the boundaries (see Ferris and others, 1962). The apex of the wedge is 2 km east of Big Muddy Spring. [file WedgeContourMapCrop.tif, derived from model Wedge2a.aqf]

Responses to Comments

Comments in response to the HRT PowerPoint presentation of September 12, 2013 suggest expanded discussion of the relations presented. First, it was suggested that the absence of detectable drawdown beyond about 5 miles from the pumping well (MX-5) could be taken as an indication that SNWA could pump forever and never impact the Springs. This is not likely, since greater drawdown near the pumping well (~1 foot) than mid-way to the Springs (~0.3 feet) reflects a decrease in the regional hydraulic gradient toward the Springs and therefore a decrease in groundwater flux to the headwaters area. The following example calculation quantifies the decrease in flux and compares it with the documented pumping rate:

DateTime	MX-4	UMVM-1	Δ (ft)	dh/dl=i	dist =	24,539 ft
4/23/2012 9:05	1819.75	1815.55	4.20	0.000171	(i1)	
3/17/2013 11:21	1817.81	1814.08	3.73	0.000152	(i2)	

Darcy's Law

$$Q=K*A*i$$

K*A can be assumed constant due to the great thickness of the aquifer;

if Q1 = 55 cfs under non-pumping conditions and gradient i1, K*A= 2.78E+10 ft³/day

under gradient i2 with K*A unchanged, Q2 = 48.8 cfs

The decrease in discharge is	6.15 cfs
-------------------------------------	-----------------

Average MX-5 rate = 7.42 cfs

Water-level measurements before the start of pumping on April 23, 2012, and near the end of the pumping interval on March 17, 2013 indicate nature of impacts from pumping MX-5 on the Springs-area discharge. Each pair of measurements (at MX-4 and UMVM-1) is indicative of the hydraulic gradient along the flow path from Coyote Spring Valley to the headwaters area, and the gradient decreases as MX-5 is pumped. Because of the great thickness of the Carbonate-Rock Aquifer (thousands of feet based primarily on water temperatures) the K*A product would not change significantly in response to 1 foot or less of drawdown, and therefore flux is directly proportional the hydraulic gradient.

Another comment was that forcing agents other than pumping could explain the changing slopes of response curves on the semi-log time-drawdown plots. We disagree, and re-emphasize that the method of differences removes the effects of environmental forcing agents from the response curves, so the observed departures from previous trends on on semi-log drawdown plots are not due to anything other than boundary effects (Ferris and others, 1962) or variable pumping rates. The most reasonable and realistic hydrogeologic model is that of a channelized flow system between Coyote Spring Valley and the headwaters area that responds to pumping in accordance with flow system theory and consistent with parameters estimated from well-hydraulics analyses.

Discussion

It is difficult to confidently identify breakthrough of pumping responses in the Muddy River Springs discharge system due to the relative magnitudes of MX-5 pumping stress, the much greater magnitude of regional flux, heterogeneity, and boundary conditions. Reconstituted Muddy River flows derived by adding groundwater production (with appropriate lag), surface-water diversion, and evapotranspiration rates to measured flow demonstrate large secular variations of natural flux. Nevertheless, traditional methods of well-test analysis and flow-system delineation provide a straightforward logical sequence from parameter estimation to characterization of pumping effects. There is no need, as has been suggested, to abandon traditional methods of analysis due to some unique complexity associated with flow system that sustains the Muddy River. There is complexity, but at the scale of investigation the theory of porous-media flow (Darcy's Law and continuity relations) apply.

Johnson and Mifflin (2012) obtained a median transmissivity (T) of $1.26 \times 10^6 \text{ ft}^2/\text{day}$ and median storage coefficient (S) of 0.045, indicative of a highly transmissive, unconfined aquifer in southeastern Coyote Spring Valley. In conventional notation $T = K*b$, where b represents aquifer thickness and K is the hydraulic conductivity. With T and the K*A product approximately known, possible cross-sectional geometries of the flow domain can be explored. Designating the width of the flow domain as w and the hydraulic gradient as i, $Q = K*A*i = K*b*w*i = T*w*i$. The width of the flow domain is $w = K*A/T$, on the order 4 miles. The distribution of high-yield wells in southeastern Coyote Spring Valley is consistent with a 4-mile-wide transmissive zone in that area, much wider than an individual fault or faults would be likely to produce.

Conclusion

The Order 1169 post-audit study supports and extends our earlier impacts assessments by applying Darcy's Law to non-pumping and quasi-steady pumping conditions that were attained after the formal conclusion of Order 1169 testing. Groundwater production from Coyote Spring Valley carbonate-rock aquifers is registered as equivalent decreases in flux along the groundwater-flow path within several months, impacting Muddy River base flow within a matter of a few years or less.

References

- Ertec Western, Inc., 1981, MX siting investigation, water resources program, results of regional carbonate aquifer testing, Coyote Spring Valley, Nevada: unpublished report dated December 18, 1981.
- Ferris, J.G., D.B. Knowles, R.H. Brown, and R.W. Stallman, 1962. Theory of Aquifer Tests: U.S. Geological Survey Water-Supply Paper 1536-E, 113 p.
- Halford, K.J., 2006. Documentation of a Spreadsheet for Time-Series Analysis and Drawdown Estimation: U.S. Geological Survey Scientific Investigations Report 2006-5024, 48 p.
- Johnson, C. and M.D. Mifflin, 2003. Evidence of a sub-regional hydraulic barrier in southeastern Nevada (abstract): Geological Society of America 115th annual meeting, Seattle, WA.
- Johnson, C. and M.D. Mifflin, 2012. Parameter Estimation for Order 1169: unpublished report distributed to HRT August 27, 2012, 25 p.
- Schmidt, D.L. and G.L. Dixon, 1995. Geology and aquifer system of the Coyote Spring Valley area, southeastern Nevada: U.S. Geological Survey Open-File Report 95-579.

Hydrologic Review Team Presentation

Martin Mifflin and Cady Johnson
Mifflin & Associates, Inc.
September 12, 2013

What is Drawdown?

- Water-level changes and pumping- induced drawdowns are not necessarily equivalent, without supporting evidence.
- We are unaware of any attempt to reconcile the purported uniform, 2-foot “drawdown” over a 2,000-square-mile area with available well-hydraulics analyses from MX-5 and ECP-1.

Order 1169 Refinements

- The Order 1169 pump test and associated water-level, pumping, and stream-gauging records provided key datasets and allowed analyses that lessened uncertainties on the nature of groundwater pumping impacts on discharge of the Muddy River.
- The most important databases stem from monitoring-well water-level changes that allow documentation of the extents and net magnitudes over time of MX-5 pumping-induced drawdowns during the testing period.

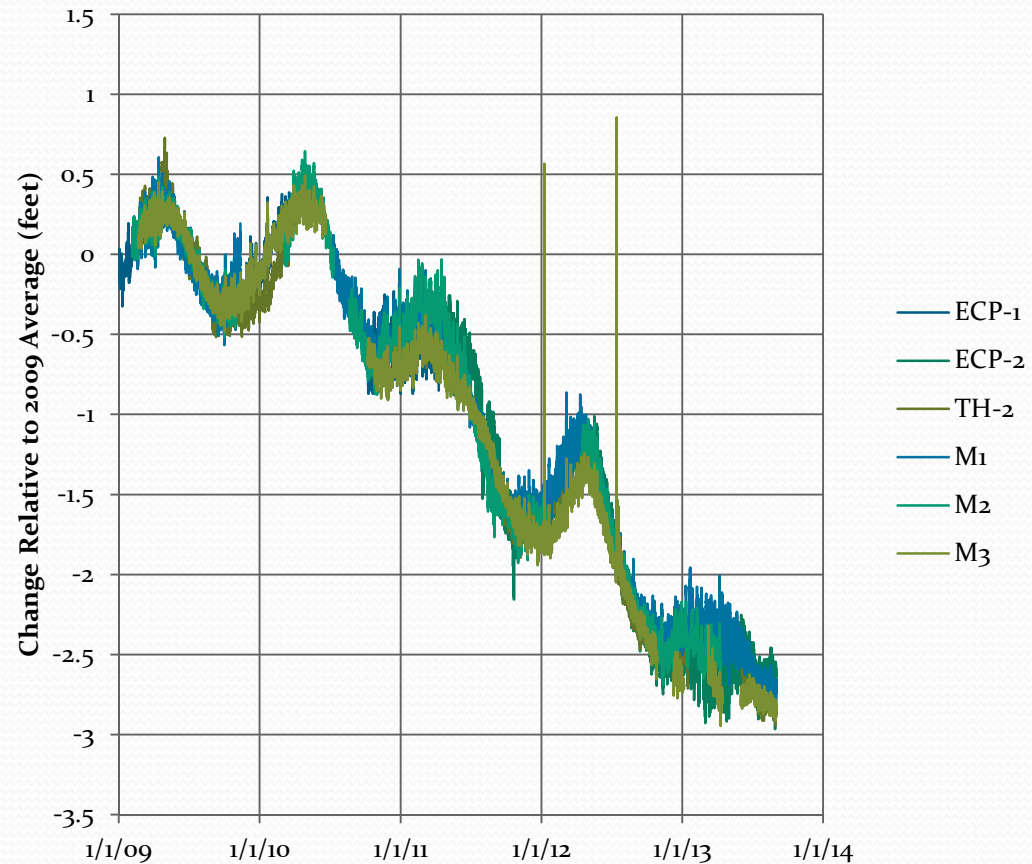
Aquifer Tests

- The extent and magnitude of the MX-5 pumping cone (drawdowns over time in a geographic sense) indicate aquifer parameters and boundary conditions.
- Short-term pumping responses, documented and analyzed in our Order 1169 report, indicate low-permeability boundaries near MX-5.
- Well-hydraulics analyses also indicate how much of the pumping production at any given time has been derived from aquifer storage.

There is no cone of depression (drawdown) evident in the MBOP Reservation area

- Reservation monitoring wells range in distance from 14.7 to 21.3 miles from MX-5.
- There has been no systematic divergence of the Reservation hydrographs since 2009; water-level changes are uniform across the Reservation.

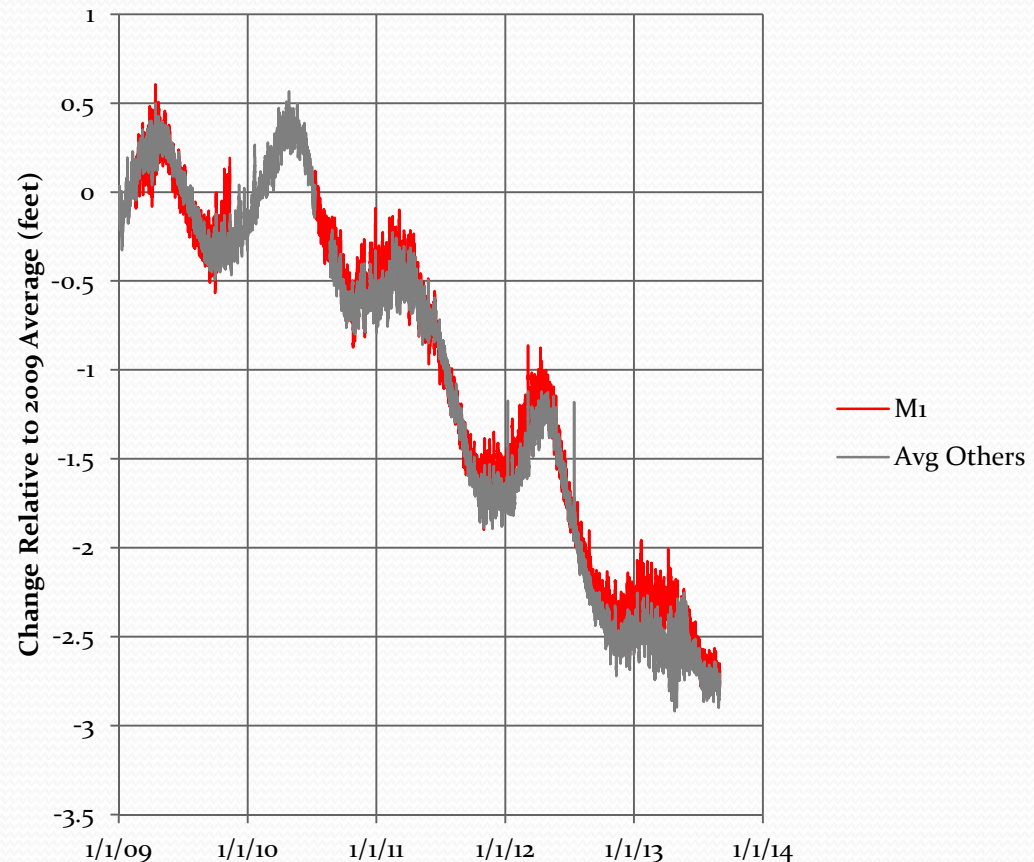
Offset Hourly Water Levels at MBOP Reservation Wells



The Paiutes' M1 well provides an excellent reference hydrograph

- The most complete water-level record is available from monitoring well M1, which is representative of the Reservation area.
- M1 is therefore suitable as a reference (background) well, allowing environmental factors to be filtered from the raw hydrographs of wells affected by pumping.

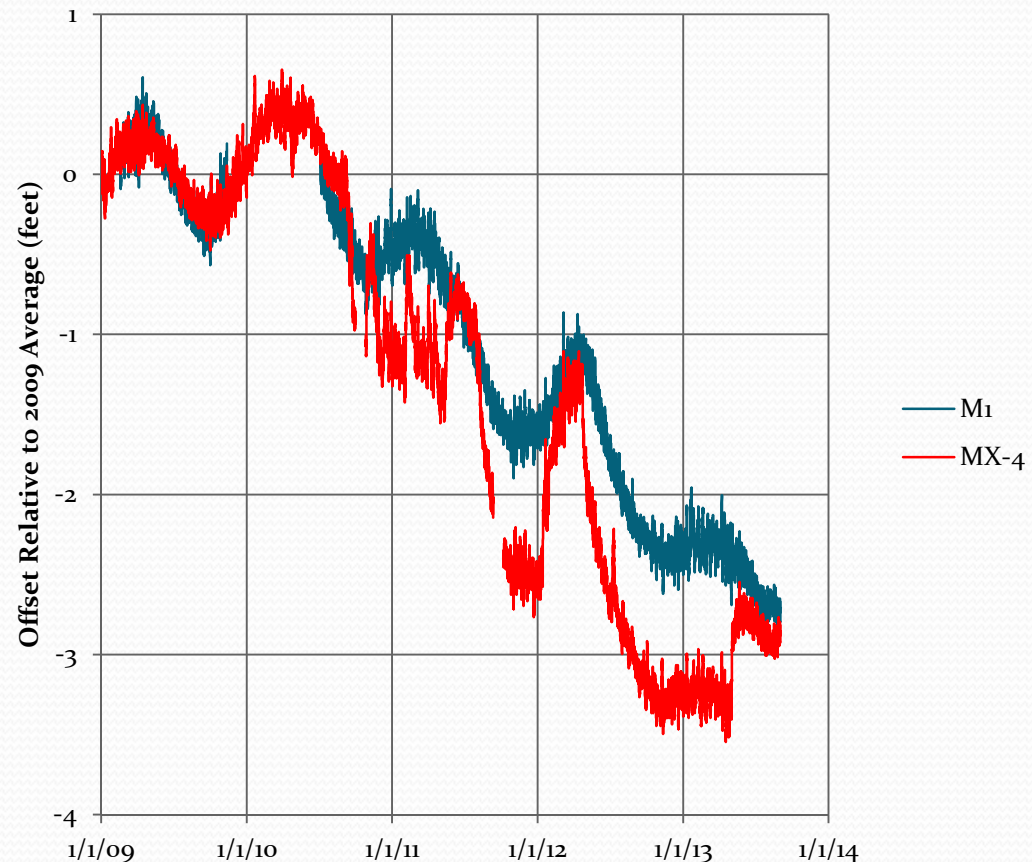
Representativeness of the M1 Hydrograph



Drawdown is obtained by difference

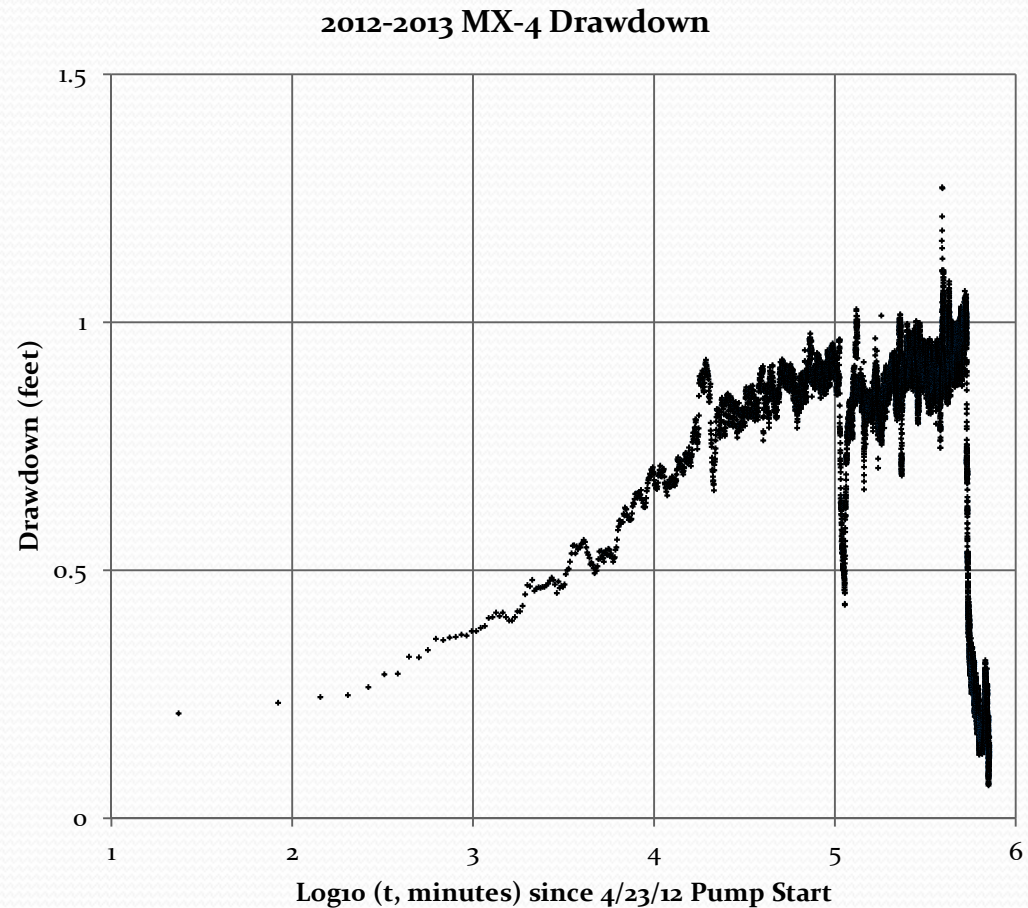
- The M1 hydrograph matches recovery periods in the MX-4 and UMVM-1 hydrographs.
- Drawdown at MX-4, 326 feet from the pumping well MX-5, is the difference between the MX-4 hydrograph and the M1 (reference) hydrograph.

Comparison of MX-4 and Paiutes M1 Hydrographs



Pumping Response at MX-4

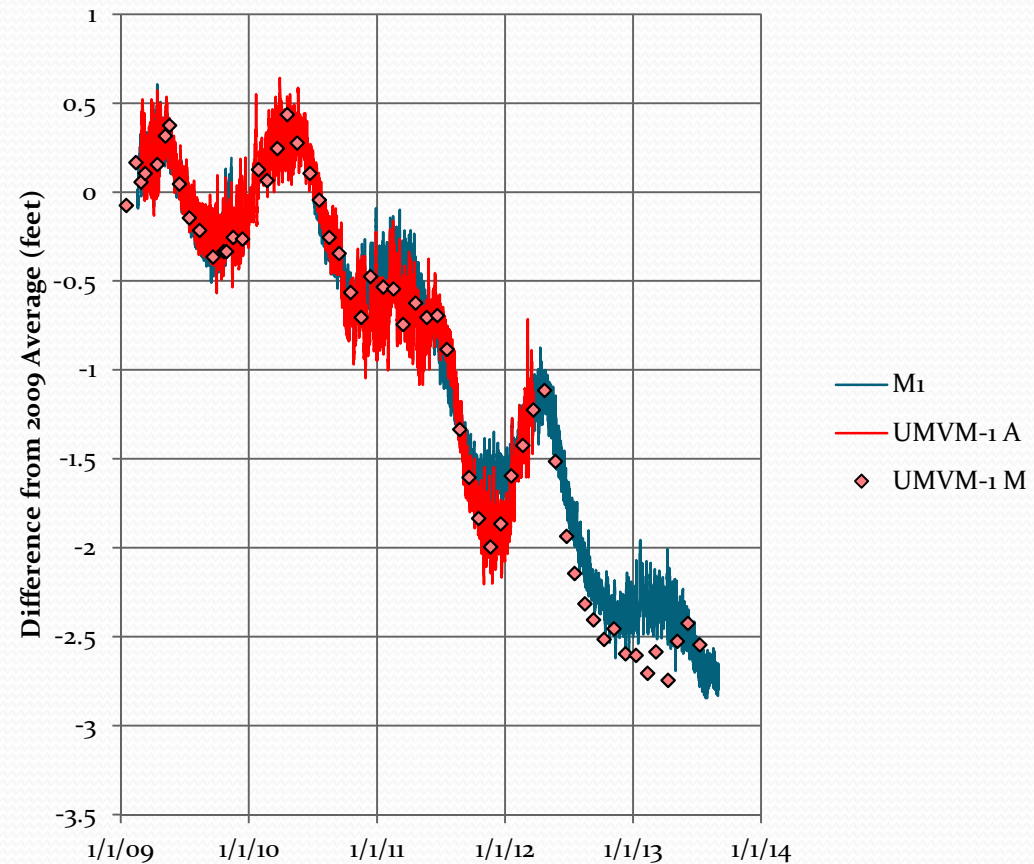
- Drawdown at MX-4 is less than one foot after a year of pumping from MX-5
- Low-permeability boundaries are indicated by steepening of the response curve after about 1 day (1440 minutes or 3.16 on the horizontal axis)



UMVM-1 Hydrograph during Order 1169 Testing

- Automated (transducer) measurements are not available after March of 2013 (not posted on NSE or SNWA websites as of 9/9/2013)
- Reference water levels from M₁ corresponding to manual measurements at UMVM-1 were considered to be the average of the hourly readings that bracket each manual measurement
- Time reference (PST or PDT) differences were not considered since they are undocumented in SNWA datasets

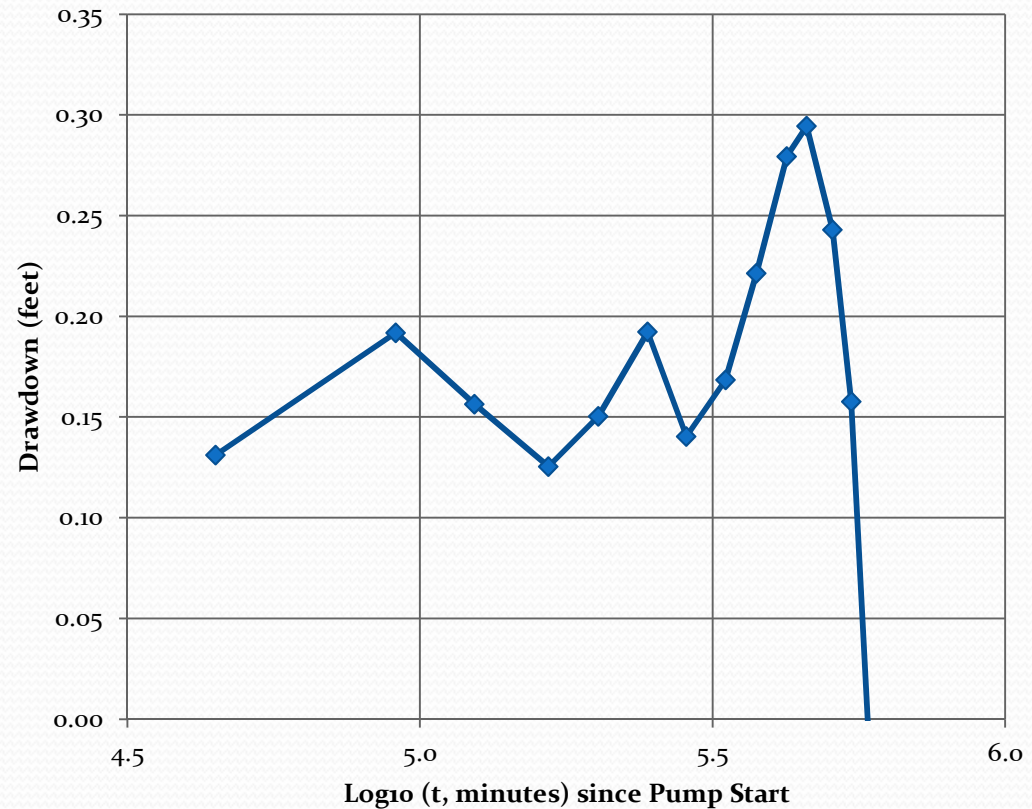
Comparison of UMVM-1 with M₁ Reference Hydrograph



UMVM-1 Drawdown

- Drawdown at UMVM-1, 4.6 miles from MX-5, was less than 0.3 feet.
- The limited pumping cone extent (~ 5 miles to practical detection limit) indicates a very small percentage of production water was derived from aquifer storage.
- MX-5 must therefore intercept groundwater that would otherwise discharge elsewhere.

UMVM-1 Drawdown in Response to 4/23/12 Pump Start at MX-5





There is no shortage of candidate forcing agents other than pumping that explain the net water-level decline since 2010:

1. Local climate
2. Time-lagged effects of regional climate
3. Seasonal loading superimposed on long-term unloading of the Lake Mead Basin
4. Terrestrial moisture loading documented by the GRACE program

The Groundwater Flow System

- There is a broadly based and internally consistent body of evidence that Coyote Spring Valley Carbonate Rock Aquifers are the prime regional source in close hydraulic continuity with the Muddy River discharge system.
- The only internally-consistent explanation for the source of water being produced at MX-5 is that it is being diverted from an outflow boundary, and the only such boundary in evidence is the Muddy River headwaters.

According to Darcy's Law, a decrease in hydraulic gradient is accompanied by a decrease in discharge:

DateTime	MX-4	UMVM-1	Δ (ft)	dh/dl=i	dist =	24,539 ft		
4/23/2012 9:05	1819.75	1815.55	4.20	0.000171 (i1)				
3/17/2013 11:21	1817.81	1814.08	3.73	0.000152 (i2)				
Darcy's Law								
Q=K*A*i where Q=discharge, A=cross-sectional area of flow, and i=hydraulic gradient dh/dl								
K*A can be assumed constant due to the great thickness of the aquifer.								
if Q ₁ = 55 cfs under non-pumping conditions and gradient i ₁ ,						K*A=		
						2.78E+10 ft ³ /day		
under gradient i ₂ with K*A unchanged,						Q ₂ =		
						48.8 cfs		
The decrease in discharge is						6.15 cfs		
Average MX-5 rate =						7.42 cfs		

Discussion

- It is difficult to confidently identify breakthrough in the Muddy River Springs discharge system due to the relative magnitudes of MX-5 pumping stress, the much greater magnitude of regional flux, and localized boundary conditions.
- Reconstituted Muddy River flows derived by adding groundwater production (with appropriate lag), surface-water diversion, and evapotranspiration rates to measured flow demonstrate large secular variations of natural flux.

Conclusion

- All groundwater production from Coyote Spring Valley carbonate-rock aquifers will be registered as equivalent decrease in Muddy River base flow within a matter of a few years or less.

Derivation of Responses to Order 1169 Pumping by the Method of Differences

Cady Johnson
 Martin Mifflin
 Mifflin & Associates, Inc.
 January 6, 2014

Introduction

The Nevada State Engineer (NSE) Order 1169 test “officially” began in November of 2010, and as shown in Figure 1, nearly 2 years of continuous and concurrent water-level and barometric-pressure records are available after the test start for 3 of the 5 wells being monitored on the Moapa Indian Reservation. These monitoring wells have produced hourly records for over 13 years. The barometric-pressure sensor (uppermost trace on Figure 1) failed in July of 2012 and was temporarily removed from service.

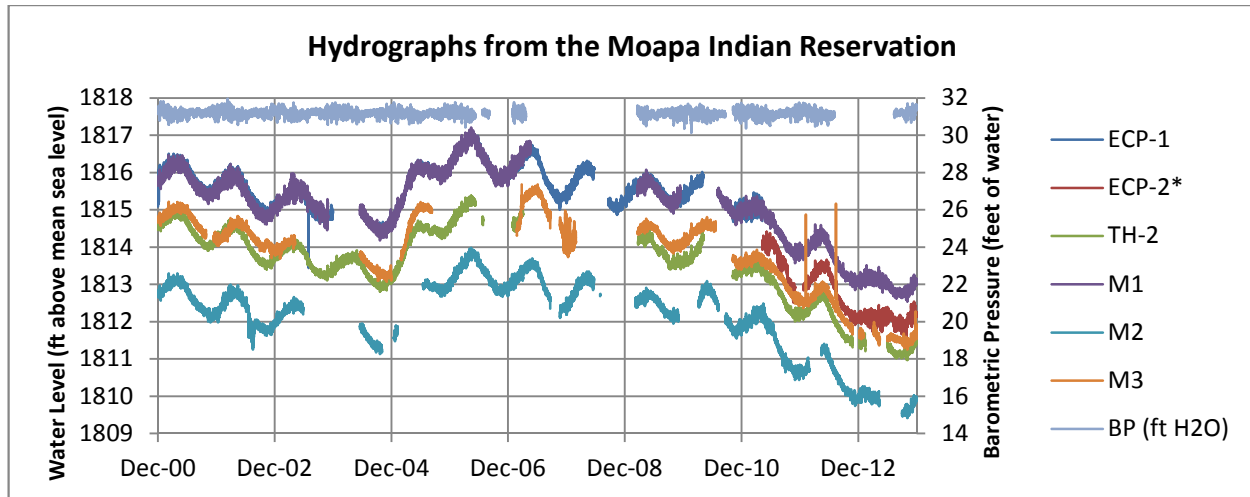


Figure 1. Hourly monitoring data from the Moapa Indian Reservation, collected by Mifflin & Associates on behalf of the Moapa Band of Paiutes (MBOP) [file PaiutesDataThrough2013.xlsx, sheet ‘WLS’]

With Order 1169A, NSE declared the pumping test completed as of December 31, 2012, rescinded the requirement for a Southern Nevada Water Authority (SNWA) update to Exhibit 54 (a SNWA groundwater model that predicted minimal impacts on Muddy River flows from groundwater development in Coyote Spring Valley) and invited Participants in the Order 1169 study to submit reports on information obtained, impacts of pumping, and availability of water pursuant to pending applications. Mifflin & Associates (MAI), on behalf of the Moapa Band of Paiutes (MBOP) submitted their report on June 28, 2013 (Johnson and Mifflin, 2013a), meeting NSE’s deadline with a comprehensive summary of reconstitution of Muddy River flows and well-hydraulic analyses of pumping response, with ancillary discussions of the hydrogeologic setting, groundwater temperatures, and geochemical mass balance on tributary flows. However, the Order 1169A reports submitted by Participants did not benefit from analysis of the full year of pumping between April of 2012 and April of 2013, or of the consequent recovery interval.

Over the years, speculation has persisted that the large seasonal fluctuations of groundwater levels in the region, even at monitoring localities remote (20 miles or more) from major pumping centers, are the result of pumping. MAI shared this interpretation early in involvement with monitoring for the MBOP, but was unable to detect any systematic lag or attenuation of the purported pumping signal in the regional monitoring network and rejected the idea by about 2002. Separation of suspected but unproven pumping effects from the dominant, underlying, natural variation has been an ongoing analytical challenge for over a decade. This report provides timing and quantitative estimates of Order 1169-induced drawdown in monitoring wells beyond 5 miles from MX-5, and of flow reductions in selected springs, using the Method of Differences. The Method, in combination with reconstitution of Muddy River flows updated from Johnson and Mifflin (2013a), also provides resolution of Order-1169-related flow reductions in the River. The Method fundamentally relies on the availability of historical time-series records that are known *not* to contain the signal component (MX-5 pumping responses) that is sought in more recent records; the historical data are used as a basis for comparison by subtracting them, day-by-day or hour-by-hour, from recent data, aligning the time series by corresponding calendar days.

Responses in Monitoring Wells

The extent of the cone of depression resulting from MX-5 pumping is key to the apportionment of pumped waters between release from storage and diversion from system boundaries. This is a key relationship because if lowering of the potentiometric surface in response to pumping is sufficient to yield most or all of the water recently pumped from Coyote Spring Valley (CSV), outflow from the CSV groundwater flow system to the Muddy River headwaters area would not be substantially affected for a considerable period of time. Conversely, a low-volume cone of depression with limited storage capacity demands another source of pumped groundwater, either diversion from outflow boundaries or induced inflow. In a recent analysis report (U.S. Fish and Wildlife Service and others, 2013), several Department of Interior (DOI) agencies concluded that 2 feet of drawdown have occurred over a 2,000 square-mile area, which would attribute the origin of groundwater pumped from CSV primarily to release from storage. In contrast, MAI analyses of transient pumping response, supported by reconstitution of Muddy River discharge, have consistently indicated that groundwater pumped from CSV has been diverted from the Muddy River headwaters-area outflow boundary, where it would otherwise have discharged.

Since 2000, MAI has collected hourly water-level measurements at 5 monitoring wells, and hourly barometric-pressure measurements at one central location on the Moapa Indian Reservation (Figure 1). All station records are intermittent due to a combination of maintenance-related data gaps and culling of record segments judged to be invalid (generally preceding failure of a pressure transducer). Timekeeping in MBOP monitoring records is referenced to Pacific Daylight Time (PDT) throughout the year.

Specific focus is on monitoring wells TH-2 and M1 in the analysis of hourly records that follows; the M2 and M3 records contain short data gaps and perturbations that limit their utility. The analysis is then extended in space and time, using daily-average water-level data from MX-4, UMVM-1, EH-4, EH-

5b, and again, M1. The M1 record provides the basis for evaluating the need for detailed (hourly) barometric-efficiency and well-tide adjustments.

With rejection of the notion that the dominant, annually-periodic mode of the hydrographs shown in Figure 1 is pumping-related, the search for a more subtle pumping signal embedded in these hydrographs might require reduction of noise produced by barometric-pressure fluctuations and well tides. After adjustments (corrections) for these superposed signals were made to the hourly data from M1 and TH-2, records from the time interval between 10/9/10 10:00 and 7/4/12 10:00 were compared to those from 10/9/01 10:00 and 7/5/03 10:00 (note the effect of the 2012 leap year – end dates do not correspond). Figures 2 and 3 show the adjustment results for the analysis (late) and reference (early) intervals, respectively.

To compare the hydrographs, hour-by-hour subtractions of the adjusted, hourly total-head values were performed (Figures 4 and 5). The “Recovery Trend” connecting local maxima in these plots is a smooth, arbitrary function representing the non-pumping potentiometric level that is attained after several months of inactivity at MX-5. The “Apex Δ ” is the *increment* of quarterly pumping from the industrial complex in the Apex area, from the early (2000-2003) to the late (2010-2013) interval, as reported to the State Engineer. The Coyote Springs Investments (CSI) data is reported as weekly averages of daily production, since “daily” meter readings represent more than one day of pumping when they occur after a day (or more) that the meters were not read.

When the total-head differences are referenced to the recovery trend, the magnitude of responses to Order 1169 pumping is revealed to be of the order of 0.3 feet (Figures 6 and 7). M1 and TH-2 are at roughly the same distance from MX-5 (14.7 and 16.2 miles, respectively) and their drawdowns after several months of pumping are substantially the same and close to steady-state. Given this result, pumping response in monitoring wells closer to MX-5 is expected, particularly from the full year of nearly-continuous pumping that began in April of 2012. The same general approach is used, but with daily-average water levels and without adjustments for barometric efficiency or well tides.

For the derivation of long-term pumping response by differences, daily-average water levels from November 1 of 2010 through November 30 of 2013 in monitoring wells M1, EH-4, EH-5b, UMVM-1, and MX-4 were compared with those from November 1 of 2000 through December 1 of 2003 in the same wells, a ten-year offset of corresponding calendar days. The early record from MX-4 was used as a surrogate for that in UMVM-1, using a constant offset, since the latter well was not completed until the summer of 2003. When comparing daily-average water levels, the semi-diurnal component of barometric-pressure-related water-level fluctuations largely cancels, leaving only the synoptic component as residual noise in the water-level signal. Tide predictions are available for wells on the Moapa Indian Reservation, and were incorporated in the daily-average M1 record.

Figure 8 shows the day-by-day differences from the calendar day 10 years prior in the 6 selected observation wells used for this analysis of Order 1169 impacts. The trends of continuous segments of individual hydrographs were derived by Empirical Mode Decomposition (EMD). The “baseline” trend, attributable to greater regional water-level decline in 2010-2013 as compared to 2000-2001, was obtained from the average difference between two-week pre-pumping and post-pumping data segments.

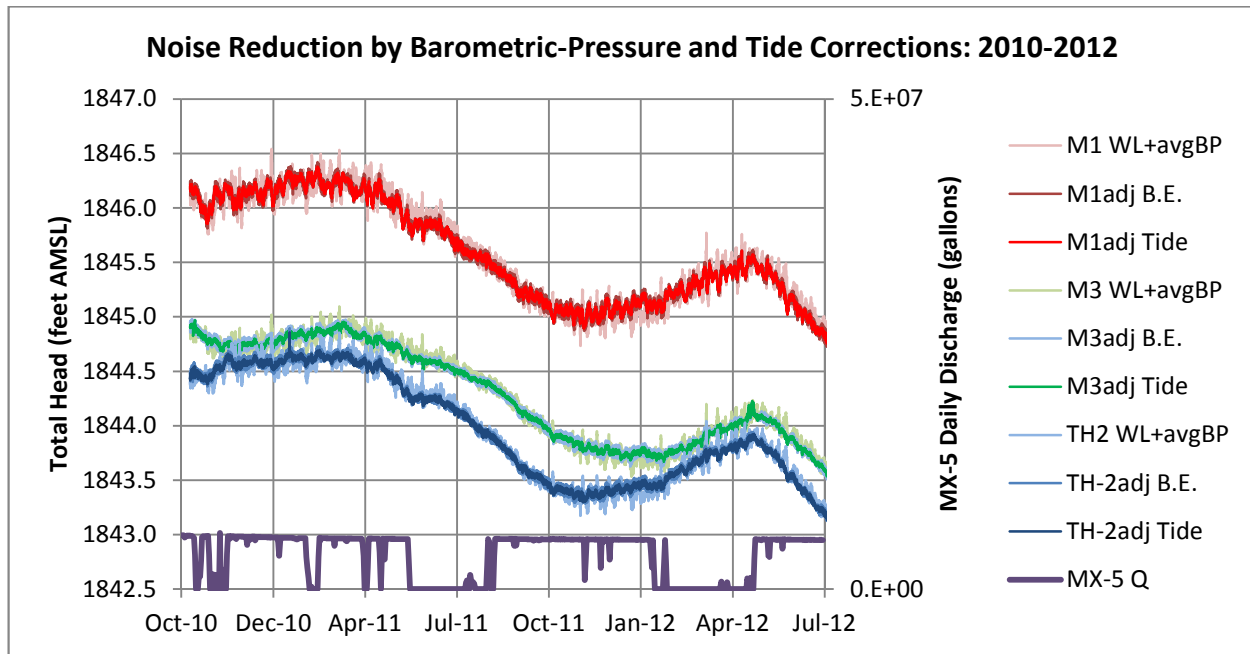


Figure 2. Results of successive total-head adjustments in the Order-1169 time frame based on barometric efficiency and fitting a tide-prediction model to the detrended residuals. For each well, “WL+avgBP” refers to the sum of measured water level and average barometric pressure, “adj B.E.” refers to total head adjusted according to the barometric efficiency of the well, and “adj Tide” incorporates subtraction of the predicted well tide [file TrendsWhilePumping.xlsx, sheet ‘adjTH’]

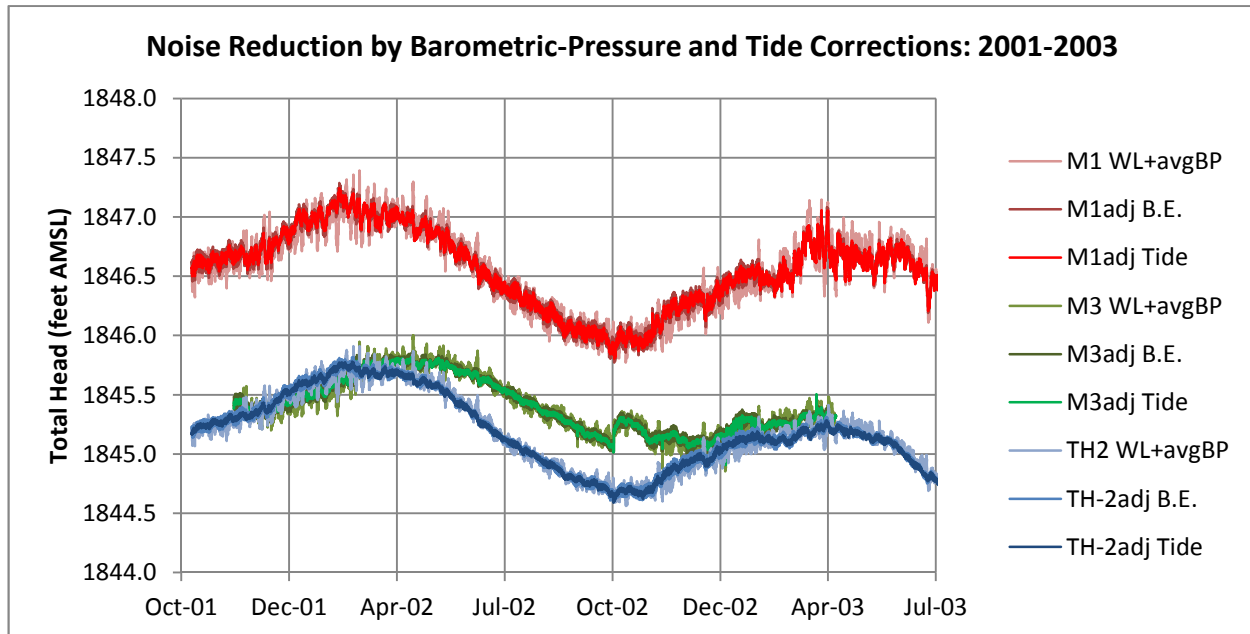


Figure 3. Results of successive total-head adjustments in the pre-Order-1169 time frame based on barometric efficiency and fitting a tide-prediction model to the detrended residuals. Nomenclature in the legend is the same as in Figure 2 [file TrendsBeforePumping.xlsx, sheet ‘adjTH’]

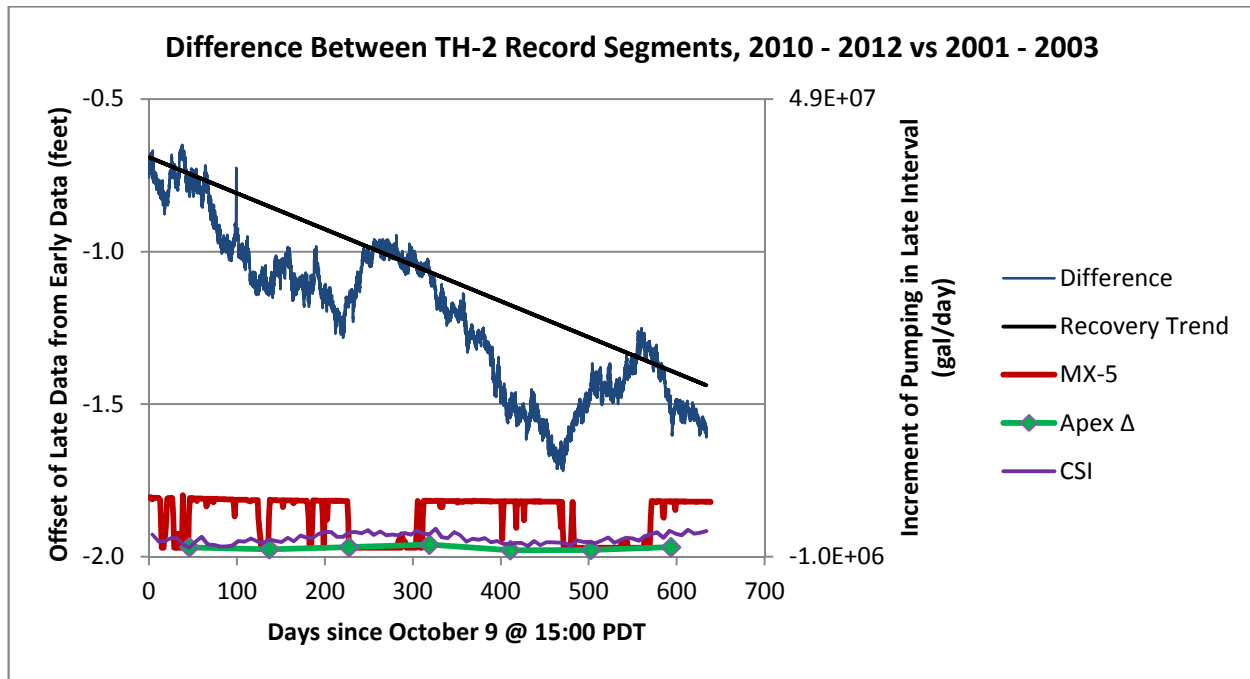


Figure 4. Difference between adjusted, hourly total head in monitoring well TH-2 for record segments beginning in October of 2010 and October of 2001. “Recovery Trend” is an arbitrary, smooth function fitted to the maximum water level (total head) attained at the end of non-pumping intervals [file 1169impactsFromTH2.xlsx, sheet ‘ResidueIN’]

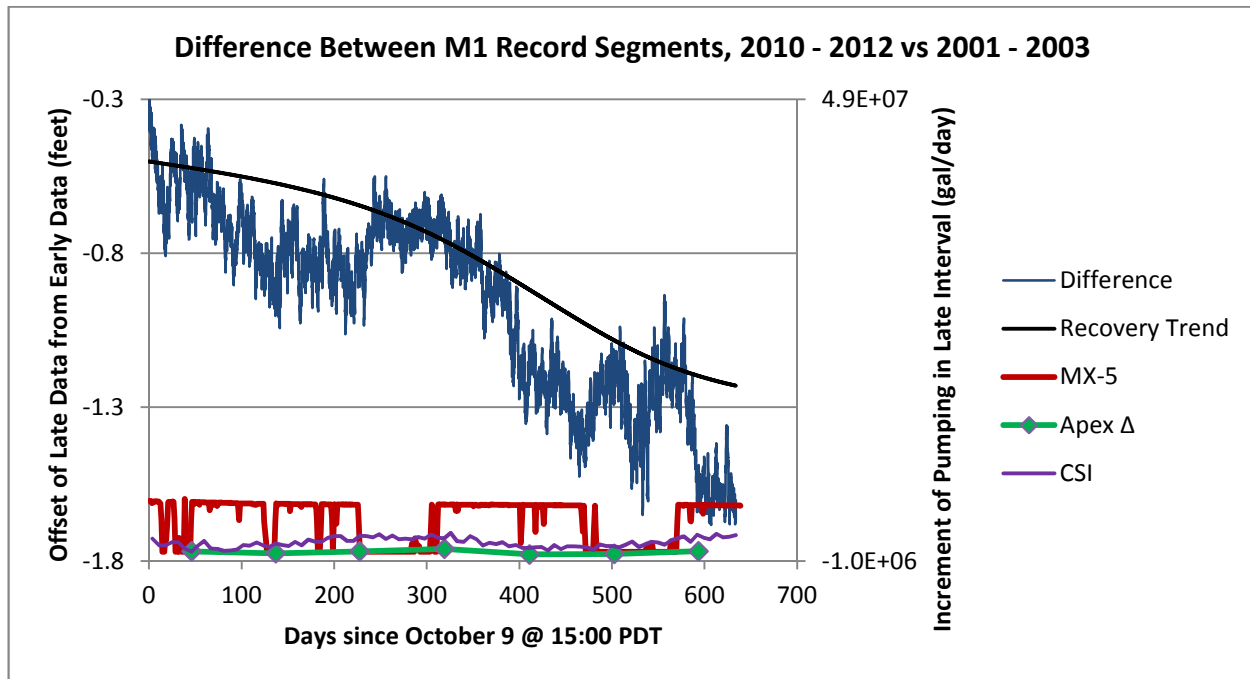


Figure 5. Difference between adjusted, hourly total head in monitoring well M1 for record segments beginning in October of 2010 and October of 2001. “Recovery Trend” is an arbitrary, smooth function fitted to the maximum water level (total head) attained at the end of non-pumping intervals [file 1169impactsFromM1.xlsx, sheet ‘ResidueIN’]

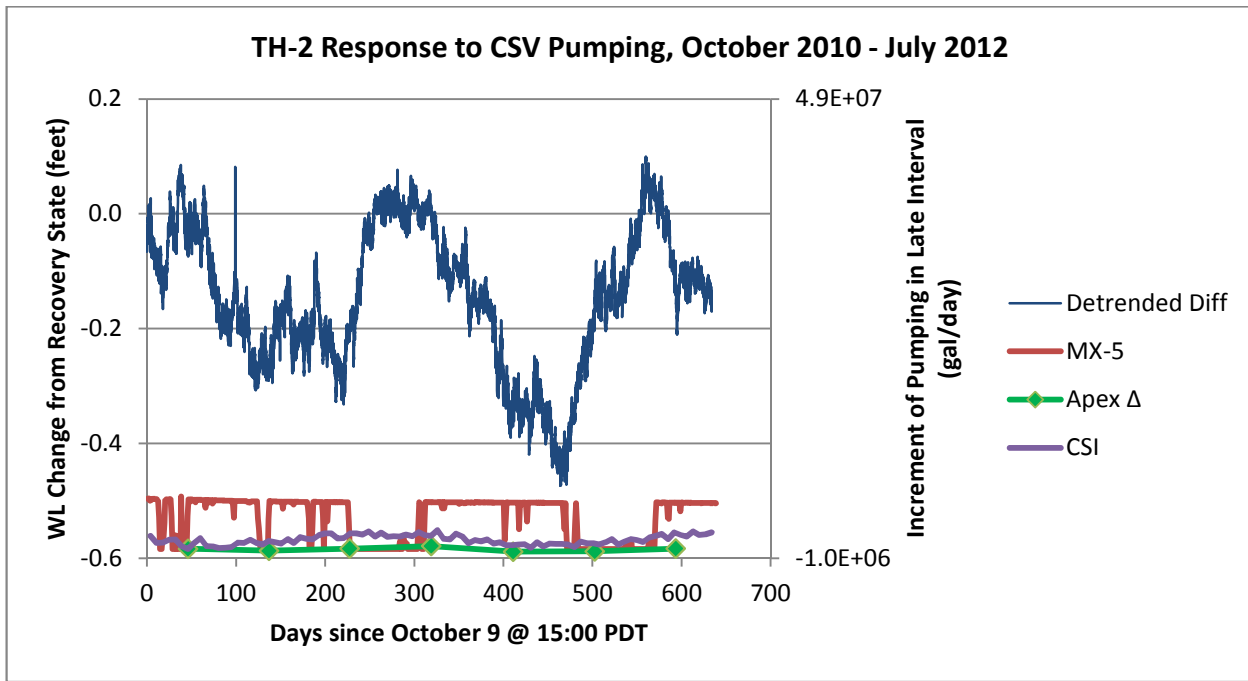


Figure 6. Hourly total-head difference in corresponding hours of 2001-2003 and 2010-2012 at well TH-2, referenced to the recovery trend of Figure 4. Note the correspondence with pumping activity at MX-5, indicative of pumping response [file 1169impactsFromTH2.xlsx, sheet 'ResidueIN']

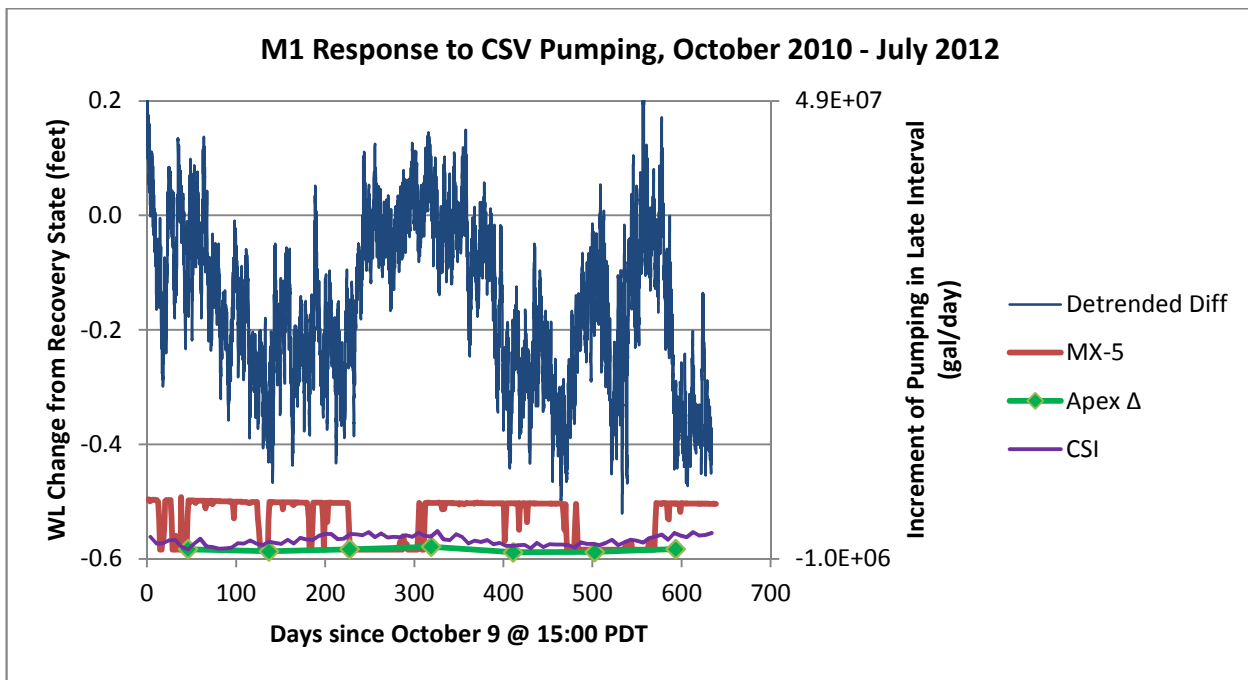


Figure 7. Hourly total-head difference in corresponding hours of 2001-2003 and 2010-2012 at well M1, referenced to the recovery trend of Figure 5. Note the correspondence with pumping activity at MX-5, indicative of pumping response [file 1169impactsFromM1.xlsx, sheet 'ResidueIN']

Figure 9 shows the effect of detrending the hydrographs by subtracting the baseline trend. These residual differences are attributable to pumping, and the effects of both MX-5 and the Lewis Well Field are evident. The correspondence of water-level trend changes with prolonged intervals of activity or inactivity at MX-5 is very clear, particularly at MX-4 and UMVM-1, which are 326 feet and 4.6 miles, respectively, from MX-5. All wells, however, share a prolonged drawdown trend of about 0.00132 feet/day after several months of pumping at MX-5, as illustrated in Figure 9.

The effects of reduced pumping in the Lewis Well Field are also evident, particularly in the EH-5b record. EH-5b is 9.3 miles from MX-5, but only 0.8 miles from LDS-W, the highest-capacity well associated with the Lewis Well Field. Figures 8 and 9 illustrate that in the summer of 2012, pumping from the Lewis Well Field (including LDS-W) was reduced below 2002 levels by nearly as much as the pumping rate from MX-5. As a consequence, the difference hydrographs of EH-5b, EH-4 (11.5 miles from MX-5), M1, and (probably) TH-2 display a prominent bulge or plateau in the summer of 2012. Our long-standing search for evidence of Lewis-area pumping effects in the Reservation area is therefore satisfied, thanks to the fortuitous reduction of pumping by Nevada Energy in the summer of 2012.

An average linear recovery rate of 0.00448 ft/day was established in 5 of the 6 monitoring wells after the cessation of pumping from MX-5 on April 30, 2013, and continued until complete (?) recovery was attained in late September (Figure 9). Only additional record will confirm if complete recovery has occurred. EH-5b was excluded from the regression because a second season of abnormally low pumping was occurring in the Lewis Well Field area, creating a second “hump” in the difference hydrograph for EH-5b during recovery from pumping.

The linearity of the hydrograph segments highlighted on Figure 9 suggests a very simple (conceptually, not geometrically) configuration of boundary conditions. Groundwater naturally enters and discharges from a discrete aquifer volume, where it is temporarily stored. Mass conservation requires that inflow – outflow = rate of accumulation, and the data indicate that the change in storage in this aquifer is linearly proportional to *quantity* pumped. Pumping 650,000 ft³/day from MX-5 eventually creates 0.00132 ft/day of steady drawdown in the bounded aquifer; removal of this pumping stress allows water levels to return to equilibrium at a rate of 0.00448 ft/day. If natural groundwater flux to the headwaters area is of the order of 4.75 X 10⁶ ft³/day (55 cfs), the intermittent MX-5 stress represents about 13.7% of the natural flux. Note that natural discharge to the surface occurs over an elevation range between 1811 feet (Pederson Spring) and 1770 feet (Big Muddy Spring), and storage coefficients derived from aquifer tests vary between those typical of confined and unconfined aquifers.

According to records submitted to the State Engineer by the Southern Nevada Water Authority (SNWA), a total of 847,539,002 gallons were pumped from MX-5 during the first interval of the Order 1169 test, November 15 of 2010 through May 15 of 2011. From August 8 of 2011 through January 14 of 2012, the second interval, a total of 787,913,617 gallons were pumped. In the third and last interval, from April 23 of 2012 through April 30 of 2013, 1.789 billion gallons were pumped. Could these quantities of water have been derived from storage and replenished when pumping ceased, without impacting discharge in the Springs area?

As indicated by the first recovery trend shown on Figure 9 (blue dots), 108 days were required to replenish the 789 million gallons pumped prior to cessation of pumping on January 14, 2012, corresponding to a hypothetical fill rate of about 7.3 million gallons/day (mgd). The second recovery trend (black dots) shows 145 days required to replenish 789 million plus the additional 1 billion gallons

pumped (with respect to the first interval) prior to pump shutdown on April 30, 2013, a hypothetical fill rate of either 12.3 mgd if the entire volume pumped is being considered, or 6.9 mgd if only the *increment* of pumped water is considered. All of these hypothetical fill rates substantially exceed the pumping rate from MX-5, which is about 5 mgd or less. How could this tank-like, bounded aquifer be replenished so quickly, or be impacted at all, if it can be re-supplied more quickly than water is withdrawn? If such an effective recharge boundary for the water-table aquifer exists, then where does the water go in the absence of pumping? The answer is that groundwater storage contributes much less water to the MX-5 pumpage than these trial calculations would suggest. Demonstrable reductions of natural discharge attributable to MX-5 and of the same order of magnitude as the MX-5 pumping rate, as presented below, argue that water-table lowering contributes very little to the water balance.

Apparently, as the hydraulic gradient toward the headwaters area is decreased by pumping (Johnson and Mifflin, 2013b), discharge at the lower elevations is temporarily sustained by release of water from storage. The uniformly-increasing drawdowns that accompany sustained pumping signal an unsustainable, transient state of a system that has not yet been stressed to the point of exhausting its capacity for groundwater storage. Re-filling the storage volume must occur at the expense of groundwater discharge, however.

The footnote to Figure 9 gives an indication of the areas, dewatered at rates corresponding an average of 4.842 million gallons per day (gpd), required to balance MX-5 production by release of groundwater from storage at the observed drawdown rates. Interestingly, at 1% drainable porosity 1,764 square miles would be required, which closely agrees with the conclusions of U.S. Fish and Wildlife and others (2013). In reality, the drainable porosity (on a regional scale) and affected area are likely much less. Johnson and Mifflin (2012) derived an impulse response function that suggests an affected area of the order of 80 square miles, based on response times documented here. The flow domain, which conceptually resembles a tank, must have multiple outlets and some internal heterogeneity.

A conservative estimate of the lateral extent of the dewatered volume is small because 1) thick, down-faulted, low-permeability basin sediments occur east and south of the model cone of depression, 2) basement rocks occur to the northeast in the Mormon Mountains, 3) lower Paleozoic rocks occur within about 2 miles north of MX-5, and 4) low-permeability boundaries are evident in the near-field pumping response (Johnson and Mifflin 2013a, 2013b). Therefore, most of the groundwater diverted at MX-5 (and from up-gradient locations in Coyote Spring Valley) must represent groundwater flux that would otherwise continue flowing southeastward to either discharge in the Muddy River headwaters area or sustain upwelling beneath the Moapa Indian Reservation that is well-documented by paleohydrologic features, water temperatures, stable isotopes, and major-ion chemistry (Johnson and others, 2001).

The results illustrated in Figures 8 and 9 further suggest that the concept of a leaky, northeast-trending hydraulic barrier introduced by Johnson and Mifflin (2006) may be valid. Whereas response to MX-5 pumping is almost instantaneous at UMVM-1, as it is at MX-4, responses in monitoring wells on the Reservation do not occur until about 4 weeks after the pump in MX-5 is turned on or off.

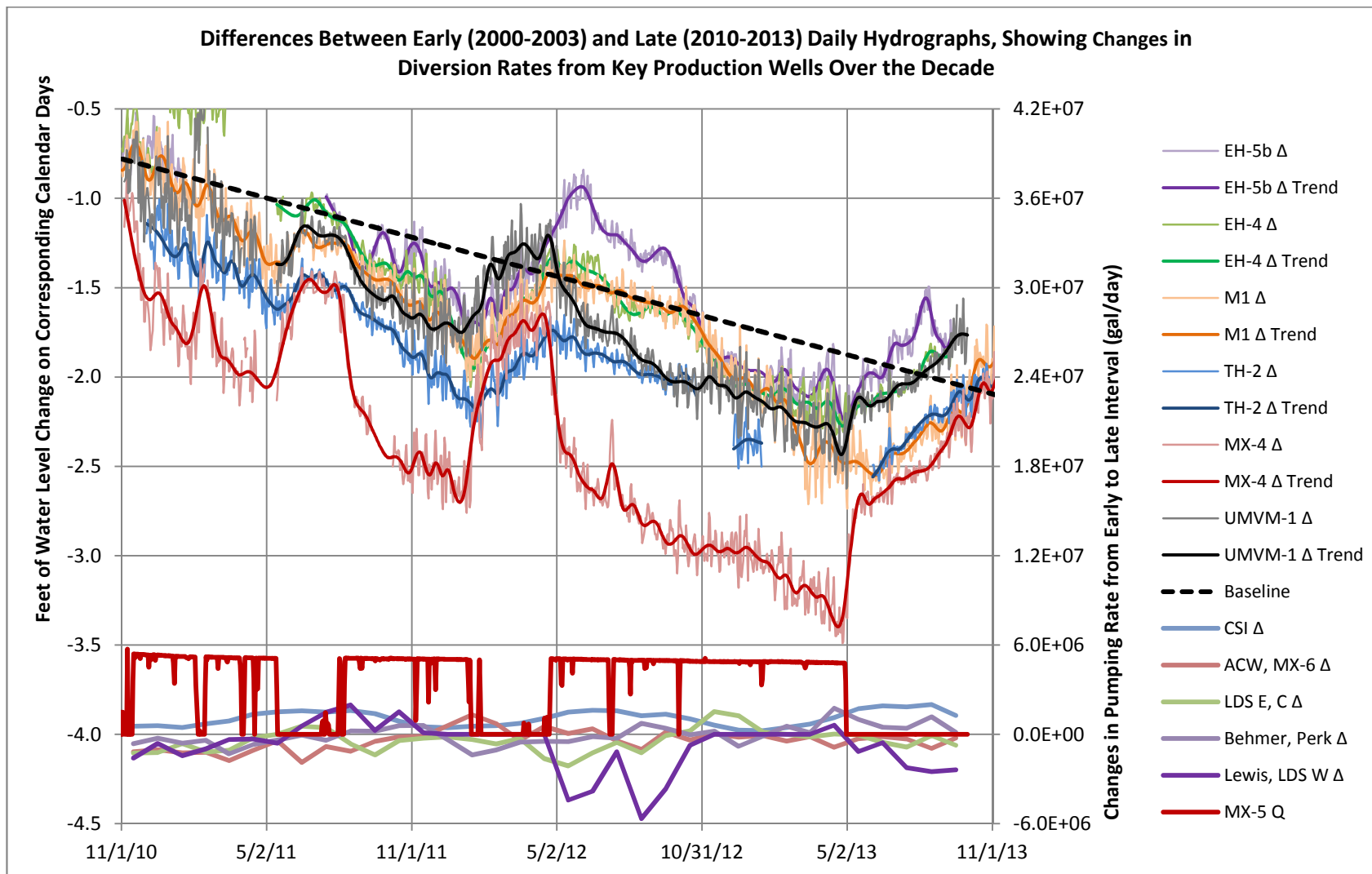


Figure 8. “Baseline” represents the average rate of decline of non-pumping (static) water levels between early November of 2010 and late September of 2013; this is the non-pumping-related component of water-level decline [file 1169differenceTrends.xlsx, sheet ‘Differences’]

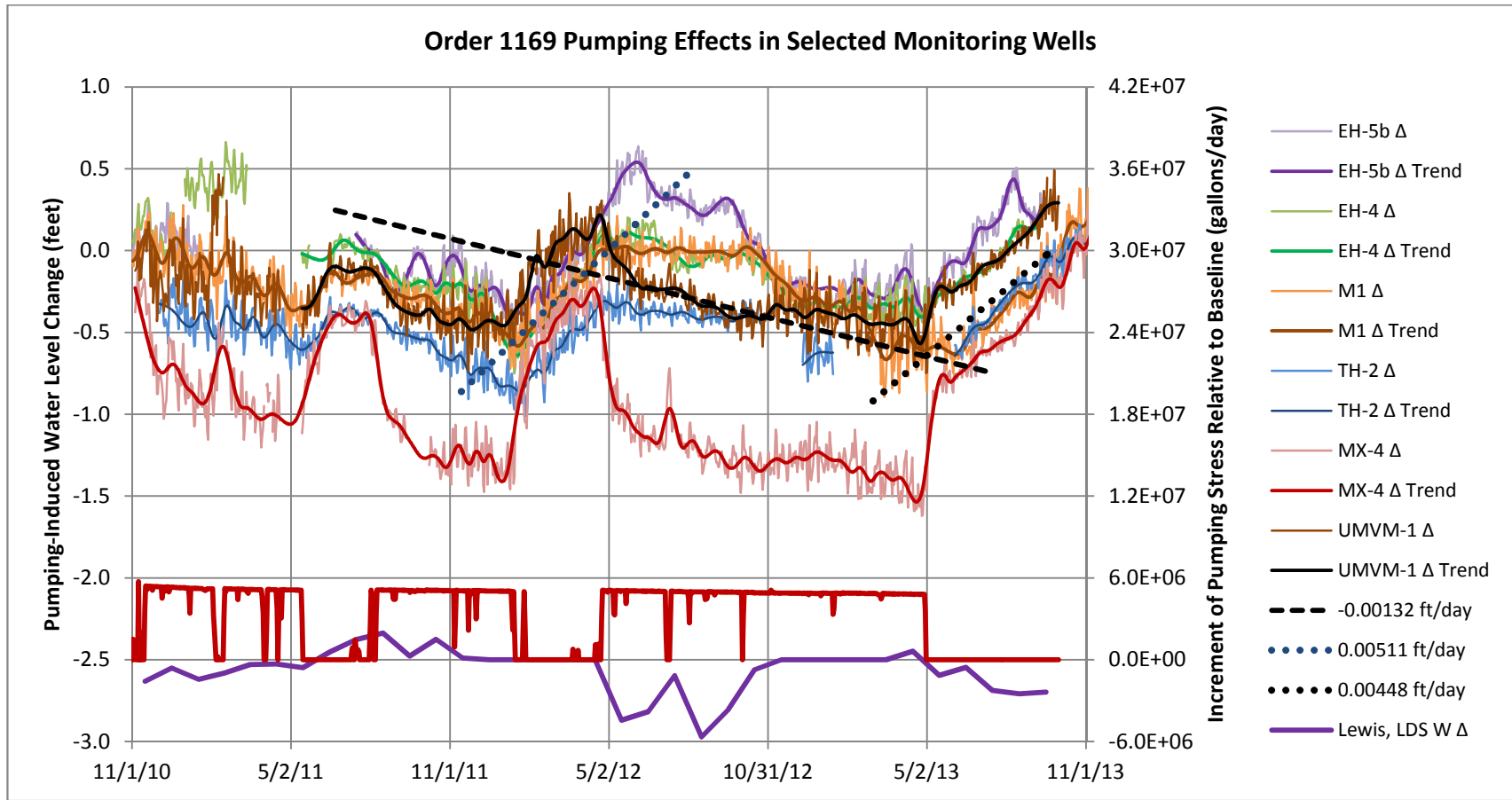


Figure 9. A steady drawdown rate of 0.00132 feet/day characterizes Order 1169 pumping response from December of 2012 through April of 2013, when pumping at MX-5 ceased. Linear response like this is characteristic of a bounded domain, like a tank, and is unsustainable. [file 1169differenceTrends.xlsx, sheet 'Detrend'] Footnote: "Tank" area required to sustain pumping rate for a range of drainable porosities

n	A (ft ²)	A (mi ²)
0.1	4.92E+09	176
0.01	4.92E+10	1,764
0.001	4.92E+11	17,642
0.0001	4.92E+12	176,422

Responses in Springs

Responses at the outflow boundary (headwaters area) seem to mimic the pumping responses derived above. At Pederson Spring, the highest of the headwaters-area springs, daily discharge data are available from November of 1999 through November of 2001, and November of 2010 through November of 2013, providing a basis for comparison of the recent record with a historic baseline. Figure 10 shows day-by-day differences, across an 11-year time span, in the discharge at Pederson Spring. When compared with the water-level differences presented in Figure 8, the discharge hydrograph from the third pumping interval resembles the MX-4 and UMVM-1 records much more closely than EH-4, which is only 1180 feet from Pederson Spring. However, Pederson Spring appears to have been insensitive to the first two, shorter intervals of sustained pumping. This behavior suggests an association between depletion of groundwater storage and decreased response time at the outflow boundary. Johnson and Miffilin (2012) derived an impulse response function with a time constant of 1-2 months, dependent on the areal extent of the model domain that was considered. No such rapid response in the headwaters area was recognized at that time, posing a dilemma; Johnson and Miffilin suggested groundwater storage as the mechanism responsible for delaying the predicted arrival of the pumping signal in the headwaters area. Local recharge from the unusually wet winter of 2010-2011 may also have masked the expected responses by opposing the depletion of groundwater storage that would otherwise have accompanied the new pumping stress from MX-5. The recent (2012-2013) behavior of Pederson Spring is consistent with the predictions of Johnson and Miffilin (2012), at the low end of the range of aquifer areas that were considered.

Discharge records from Big Muddy Spring, the lowest-elevation and largest spring in the headwaters area, were corrupted prior to the summer of 2010 by operations associated with a swimming pool at the spring orifice, complicating any quantitative comparisons of the recent record with a historical baseline (Figure 11). Qualitatively, the record becomes erratic in about 2006, with the present rising trend beginning in 2009. Possible response signatures are evident, with trend reversals occurring at 5 of the 6 major step changes in pumping activity that have occurred during the Order 1169 test (Figure 12).

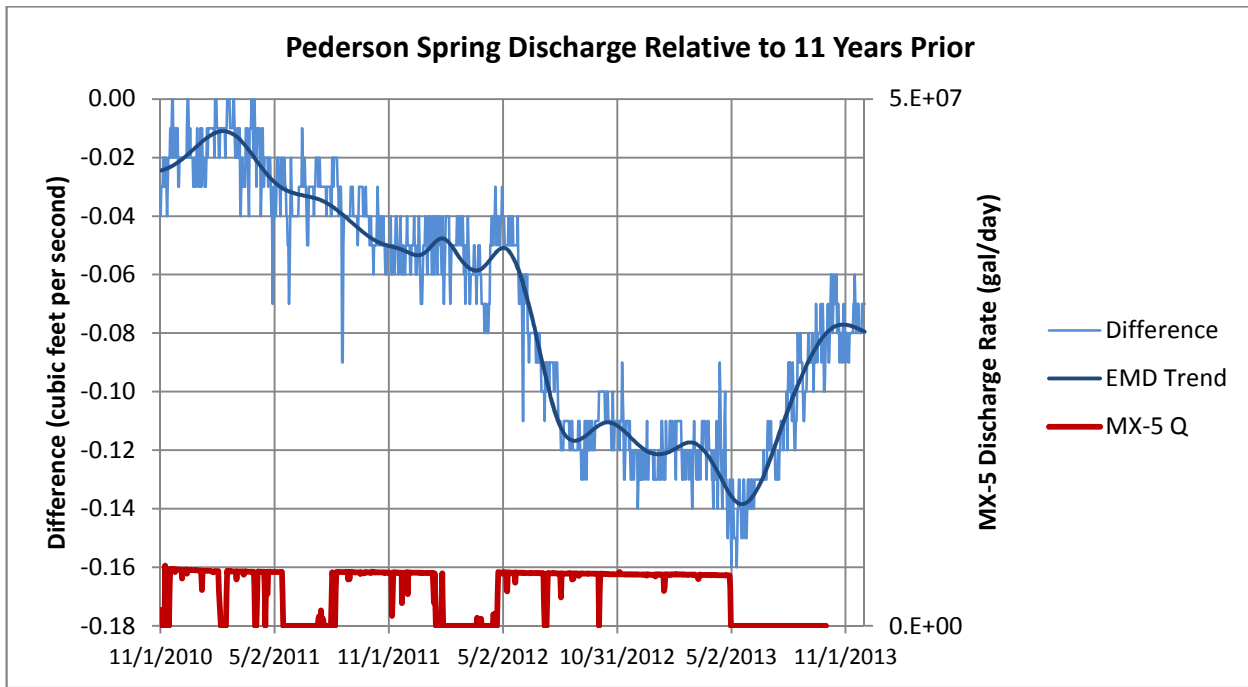


Figure 10. Comparison of recent (2010-2013) daily-average discharge measurements at Pederson Spring compared to corresponding calendar days in 1999-2002 [file PedersonDiffs.xlsx, sheet 'PedersonQ']

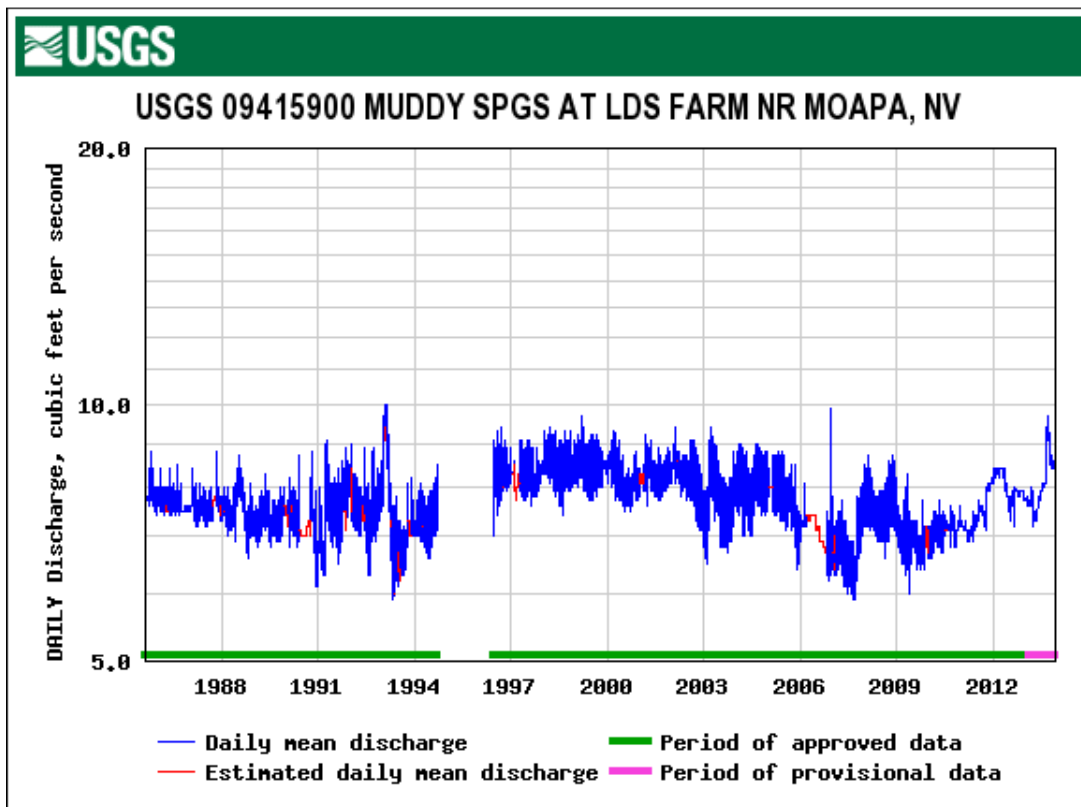


Figure 11. Historic discharge record from Big Muddy Spring [file BigMuddy8513.tif, downloaded from http://waterdata.usgs.gov/nv/nwis/dv/?dd_cd=01_00060_00003&format=img_default&site_no=09415900&begin_date=19850822&end_date=20131212]

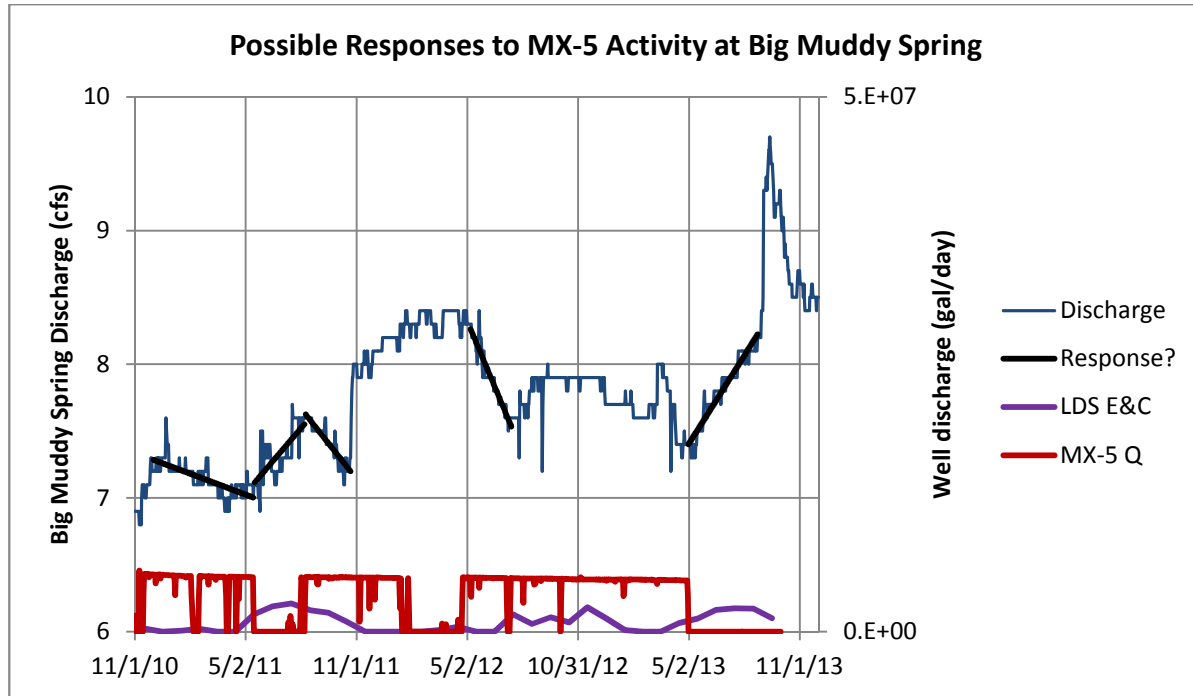


Figure 12. Recent discharge record from Big Muddy Spring, showing trend reversals associated with changes in status of pumping activity at MX-5 [file BigMuddy1013.xlsx]

Muddy River Response

The main-stem Muddy River integrates the many influences from springflow, diffuse seepage discharge, evapotranspiration, groundwater pumping, surface-water diversions, and storm runoff (Figure 13). The discharge record at the Moapa Gage is far too complex to interpret by inspection, and comparison with the record from 10 years prior reveals no obvious correspondence of discharge fluctuations with MX-5 activity (Figure 14). Day-to-day fluctuations in the discharge record are of the same order of magnitude as the pumping stress imposed by MX-5, a signal to noise ratio of 1:1 with respect to the signal we wish to filter from the record. The main-stem Muddy River hydrograph must be *reconstituted* (Johnson and Mifflin, 2013a) to permit meaningful analysis of its individual components. As illustrated in Figure 15, when daily diversions are accounted for and the raw hydrographs are adjusted accordingly there is good correspondence between flow reductions and pumping events. In fact, after several (~5) months of pumping at MX-5 the flow reductions are of about the same magnitude as the pumping rate.

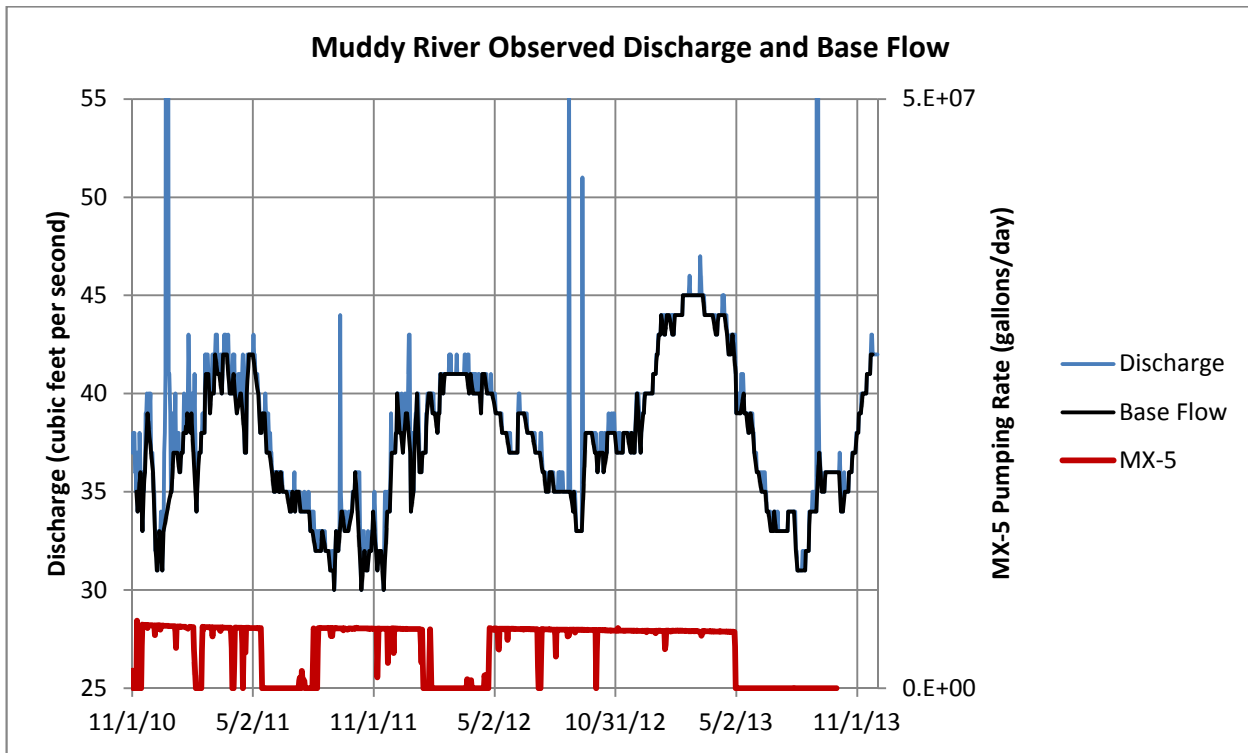


Figure 13. Raw and base flow hydrographs for the Muddy River [file MR1013_BFI_input.xlsx, sheet 'BFI', source data in file mr1013n3.q]

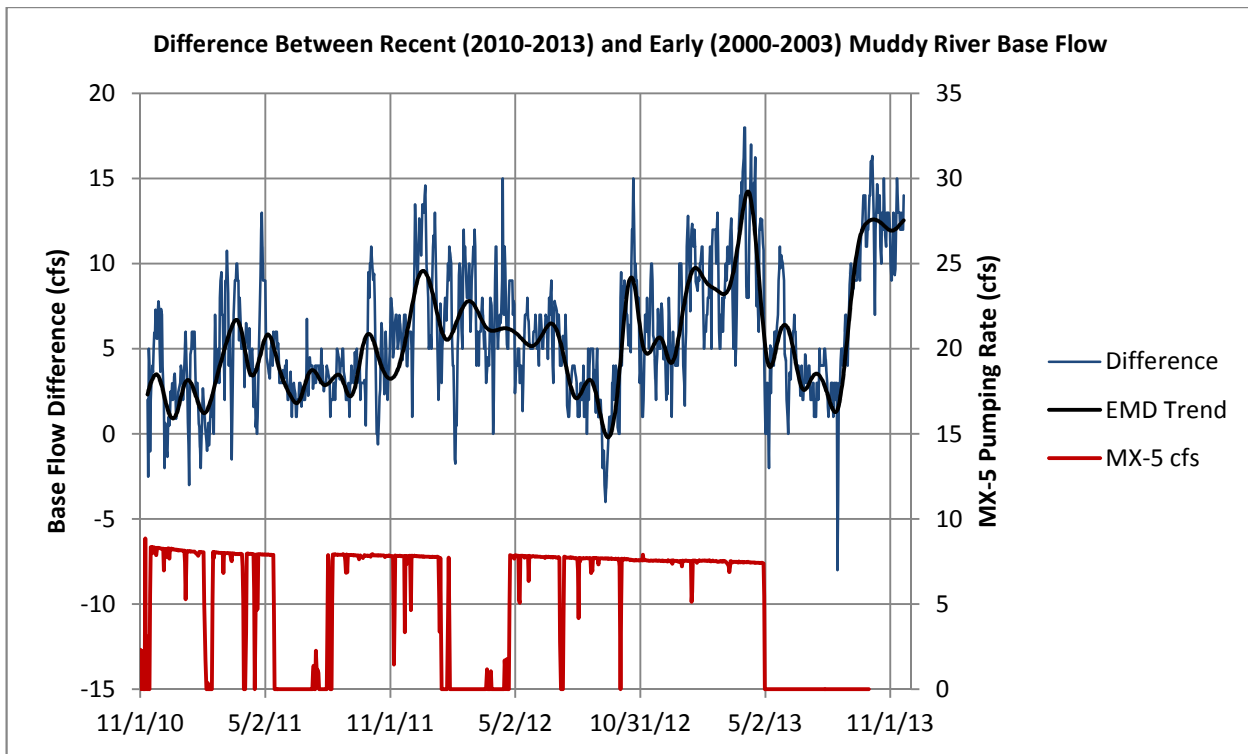


Figure 14. Difference between recent Muddy River base flow hydrograph and that of corresponding calendar days 10 years prior. [file MR1013_BFI_input.xlsx, sheet 'CompareEarly']

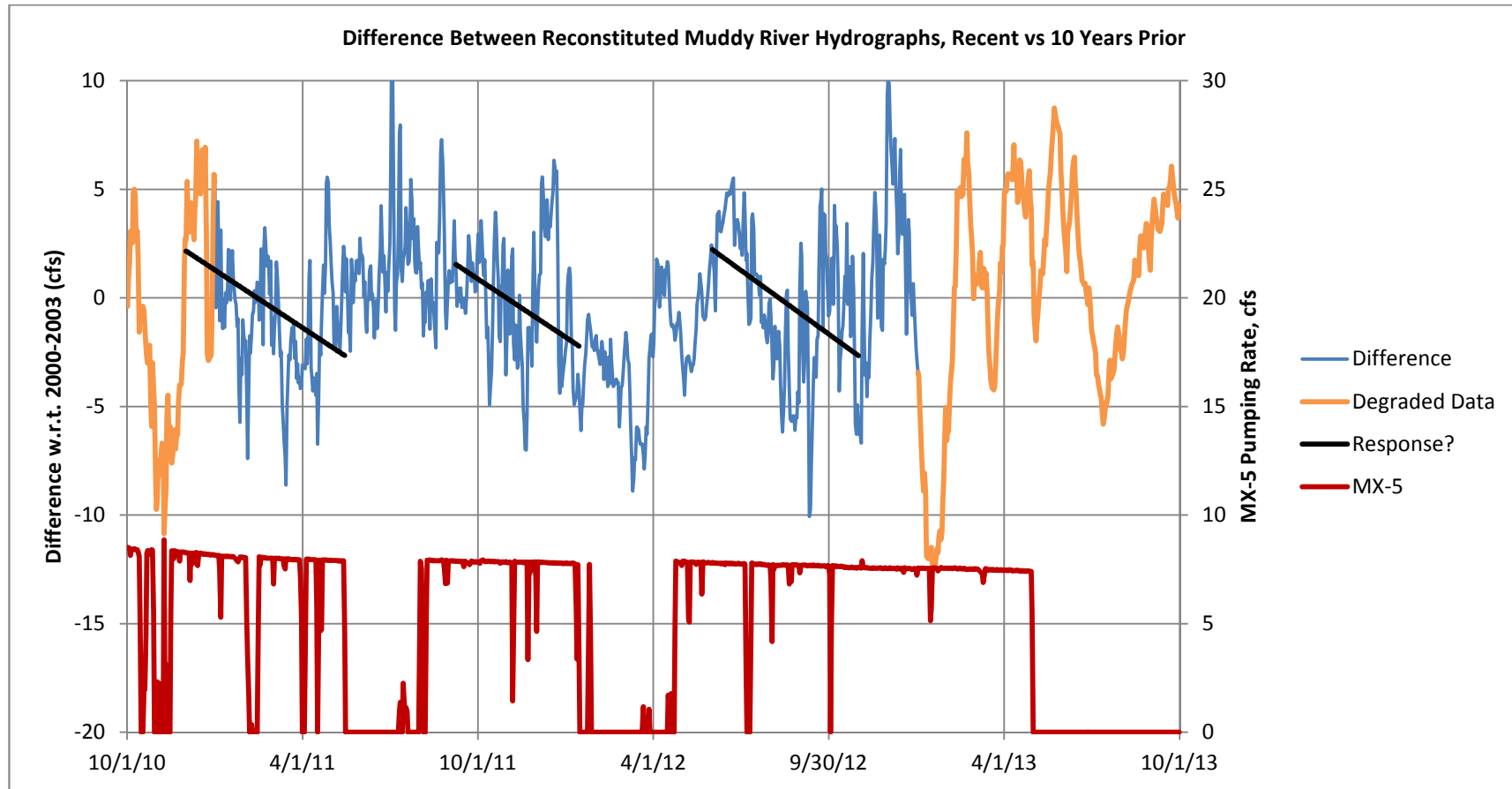


Figure 15. When the daily hydrograph of the Muddy River is reconstituted to account for all diversions *except* those from Coyote Spring Valley, there is correspondence between intervals when MX-5 is pumped and decreases in the 2010-2013 hydrograph with respect to corresponding calendar days in 2000-2003. “Degraded Data” is attributable to NV Energy reporting for 2010 and 2013, when the State Engineer did not require daily monitoring records. Several months are required before groundwater withdrawals in Coyote Spring Valley are fully expressed as flow reductions in the Muddy River. [file MRreconstDiffs2.xlsx, sheet ‘Compare’]

Conclusions

The Order 1169 Test has succeeded in creating measurable impacts on water levels, springflow, and Muddy River Discharge across a large (~80-400 square mile) area down-gradient of Coyote Spring Valley. The most useful aspects of the Test were its long (2-year) duration, availability of monitoring data reported on a daily basis and in many cases hourly or better, baseline data from a decade (or more) prior to the Test, and particularly the intermittent operation of a single, high-capacity well (MX-5). During the 2-year Test, three intervals of pumping lasting 3 months or more were separated by recovery intervals of similar duration, providing an unprecedented opportunity for these step changes in pumping stress to be recognized in a variety of monitoring records.

Seasonal fluctuations of the regional hydrographs and ongoing drought have misled numerous investigators to attribute both the seasonality and intermittent, long-term decline of groundwater levels to pumping stress. For the first time, we have confidently isolated the overprint of pumping effects from the underlying trends, using data from a decade prior as a basis for comparison. This “Method of Differences” is based on the comparison of recent with historic records to isolate the effects of a forcing agent that has only appeared recently; the Method has proved to be highly successful.

Linear time-drawdown trends are diagnostic of a bounded domain being dewatered, and after MX-5 is pumped for a few months an unsustainable, linear trend of water-level decline is established. Although the affected area is large, the amount of water released from storage as groundwater levels are lowered must be very small in proportion to the amount pumped, since springflow reductions in the headwaters area begin within about a month of pump starts and the flow of the Muddy River is impacted by an amount comparable to the pumping rate after just a few months.

These findings indicate that full development of existing permitted groundwater rights (or pending applications) in Coyote Spring Valley, if it is allowed, would not only result in approximately 1:1 reduction of Muddy River flows (in proportion to the pumping rate), but that depletion of groundwater storage in the region would proceed toward an unknown end-state that must follow the observed, unsustainable, pseudo-steady state (in terms of regional drawdown rates) trend that develops within less than a year. As Muddy River drought-period flows, absent of significant groundwater production from Coyote Spring Valley, have been as little as 19 cfs at the Moapa Gage, it's conceivable (we think highly likely) that full development of the existing CSV permitted groundwater rights of 18,100 acre-feet/year (~25 cfs on an annualized basis) would directly cause future periods of little or no flow being registered at the Moapa gage, with most spring-area tributary flows being heavily impacted or eliminated at times as well. The Order 1169 test has therefore produced useful results upon which State and Federal regulators may base further actions.

References

- Johnson, C., M.D. Mifflin, R.J. Johnson, and H. Haitjema, 2001. Hydrogeologic and groundwater modeling analyses for the Moapa Paiute Energy Center: in PBS&J, 2001, Moapa Paiute Draft Environmental Impact Statement, Appendix D., prepared for U.S. Bureau of Indian Affairs and Bureau of Land Management, Case #N66776, March, 2001.
- Johnson, C. and M.D. Mifflin, 2006. The AEM and Regional Carbonate Aquifer Modeling: Groundwater, Vol. 44, Issue 1, pp. 24-34, January-February 2006.
- Johnson, C. and M.D. Mifflin, 2012. Analysis Progress Report – Order 1169 Impacts Assessment: unpublished report to Hydrologic Review Team, March 17, 2012, 15 p.
- Johnson, C. and M.D. Mifflin, 2013a. Summary of Order 1169 Testing Impacts, per Order 1169A: unpublished report to Hydrologic Review Team, June 28, 2013, 77 p.
- Johnson, C. and M.D. Mifflin, 2013b. Technical Note: Order 1169 Post-Audit Analysis of Pumping Response: unpublished report to Hydrologic Review Team, October 1, 2013, 10 p.
- U.S. Fish and Wildlife Service, Bureau of Land Management, and National Park Service, 2013. Test Impacts and Availability of Water Pursuant to Applications Pending Under Order 1169: Presentation to the Office of the Nevada State Engineer, June 28, 2013, 92 p.

A Climate “Sweet Spot” May Refute Groundwater Model Forecasts

Cady Johnson and Martin Mifflin
Mifflin & Associates, Inc.

Devils Hole Workshop
Beatty, Nevada

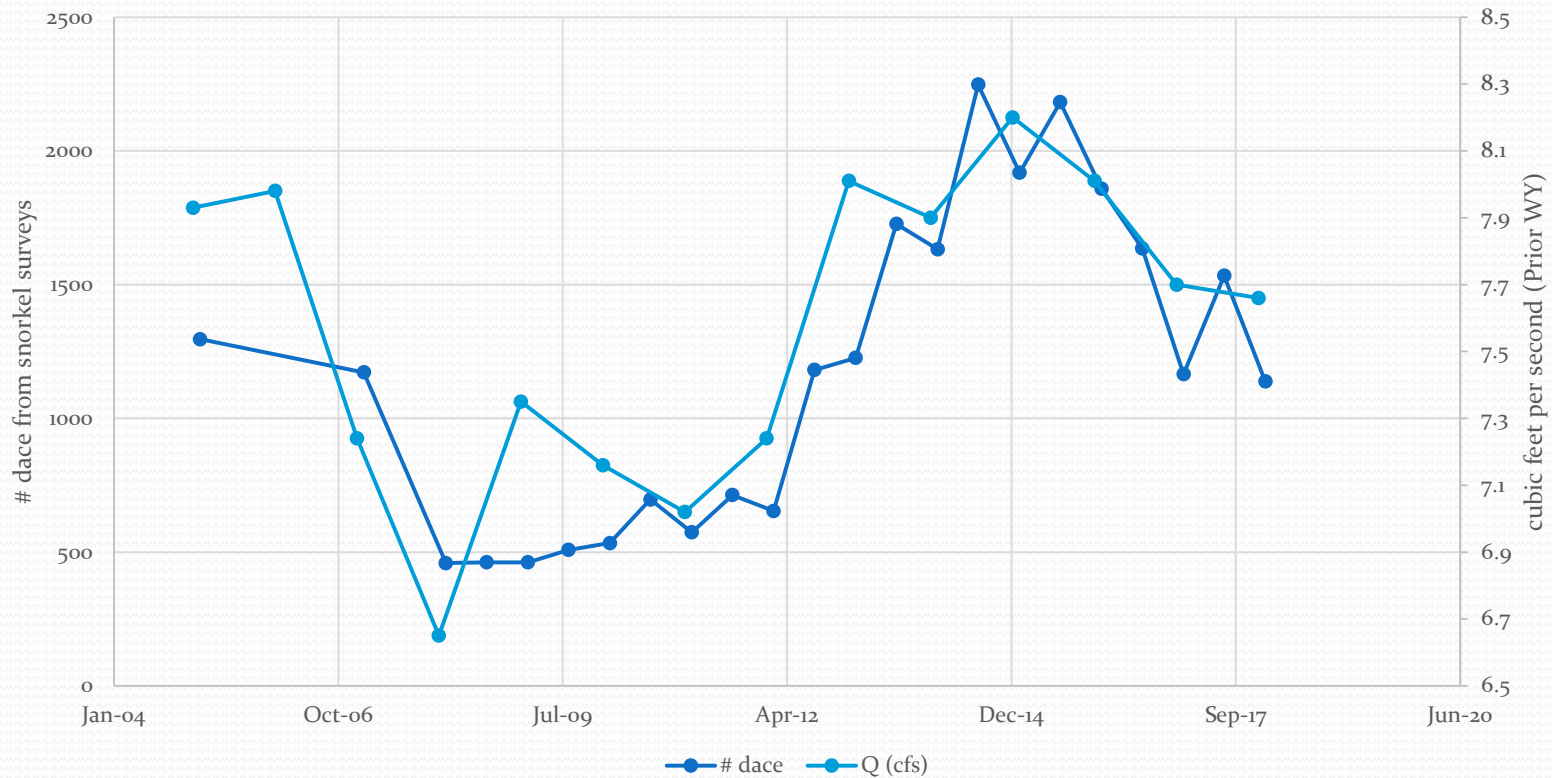
May 3, 2018

SE ROA 37474

JA_8980

Consider a startling observation: the MRSA dace counts closely follow Big Muddy Spring discharge trends!

Moapa Dace Count vs Annualized Big Muddy Spring Discharge



Regional Topography

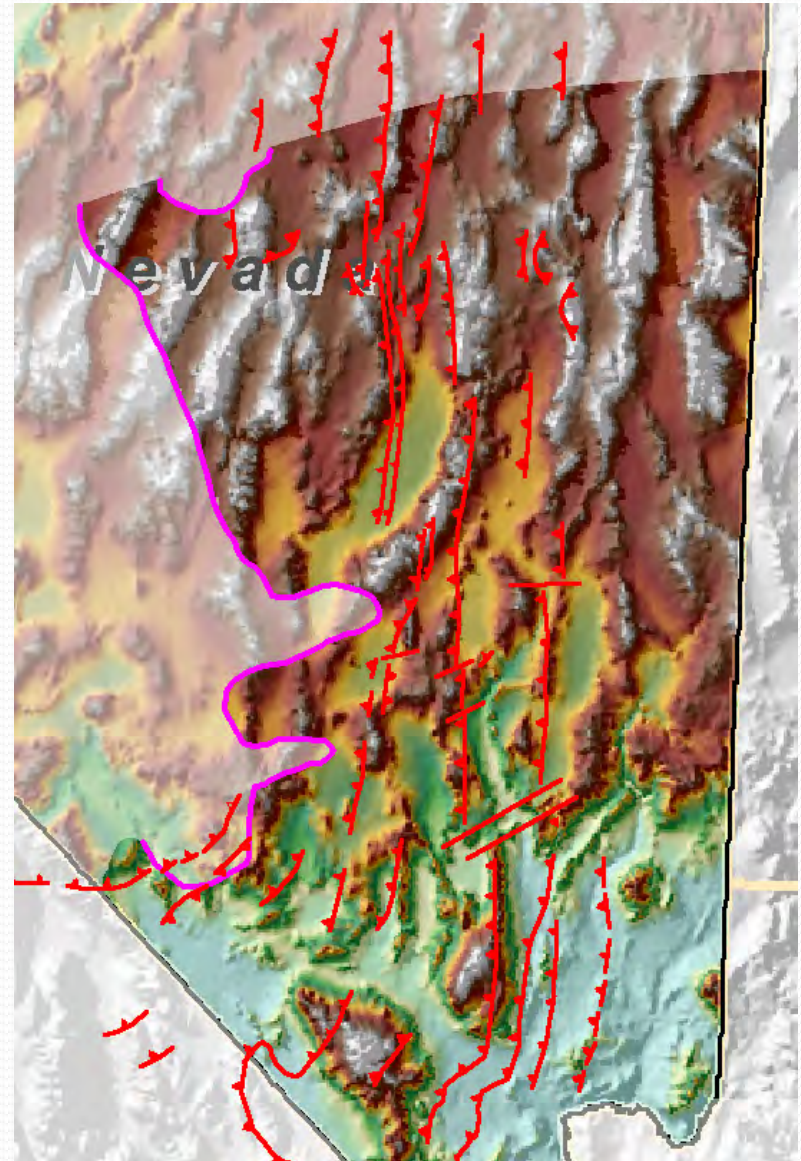
- The color scheme here gives us an excellent base map
- The National Elevation Dataset (NED) is also available at 10-meter resolution
- The “snow capped mountains” area is of particular interest
- Groundwater Discharge Deposits (GWD) are concentrated in the low country of southern Nevada



SE ROA 37476

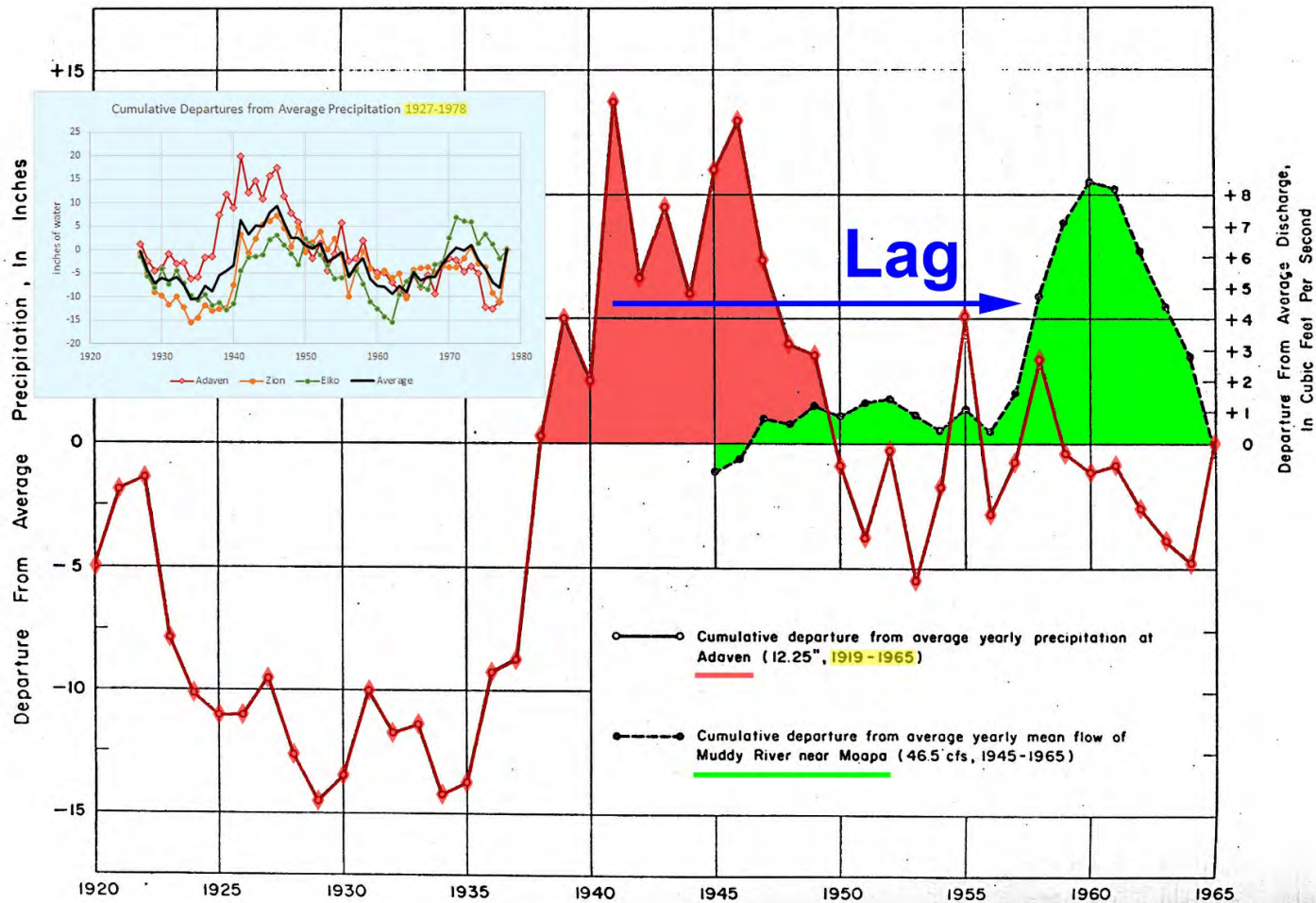
Sevier Faults and Extension within the Lower Paleozoic Shelf Domain

- The Paleozoic Shelf Domain was contracted by faulting of the Cretaceous (?) Sevier Orogeny
- Cenozoic extensional faulting fragmented the belt of thrust faults, which today form important offset markers due to unique characteristics of many of the thrusts
- The magnitude of extension and geometry of normal faults remain topics of active debate
- Are groundwater temperatures suggestive of shallow circulation systems floored by detachment faults?

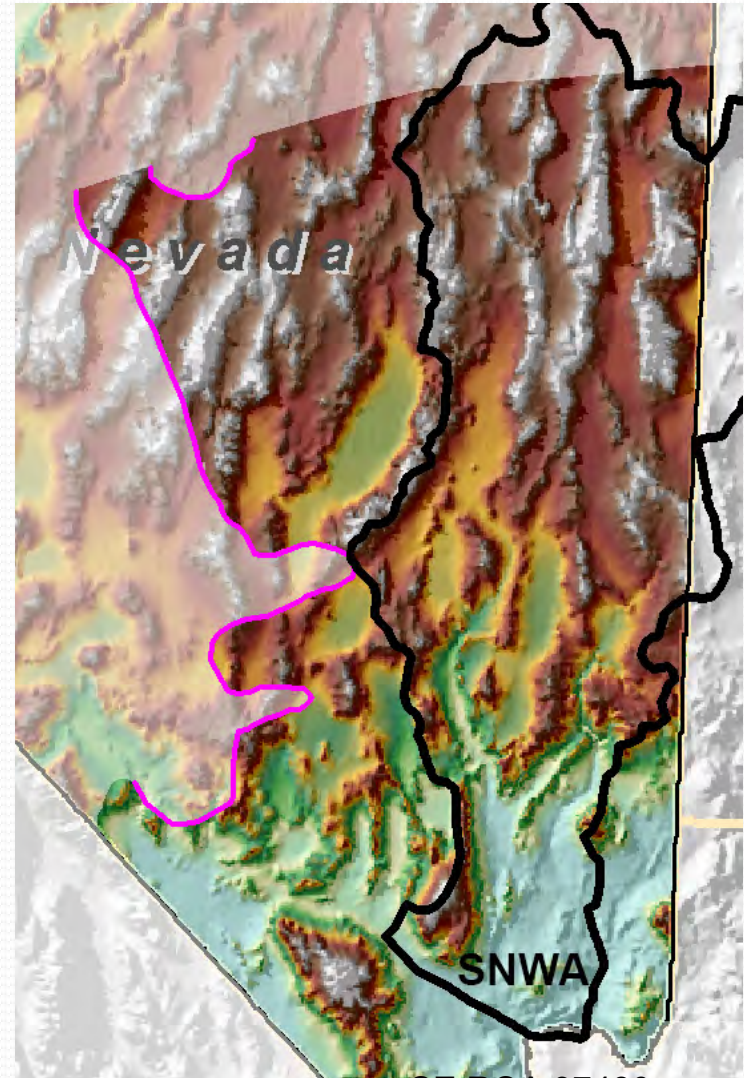
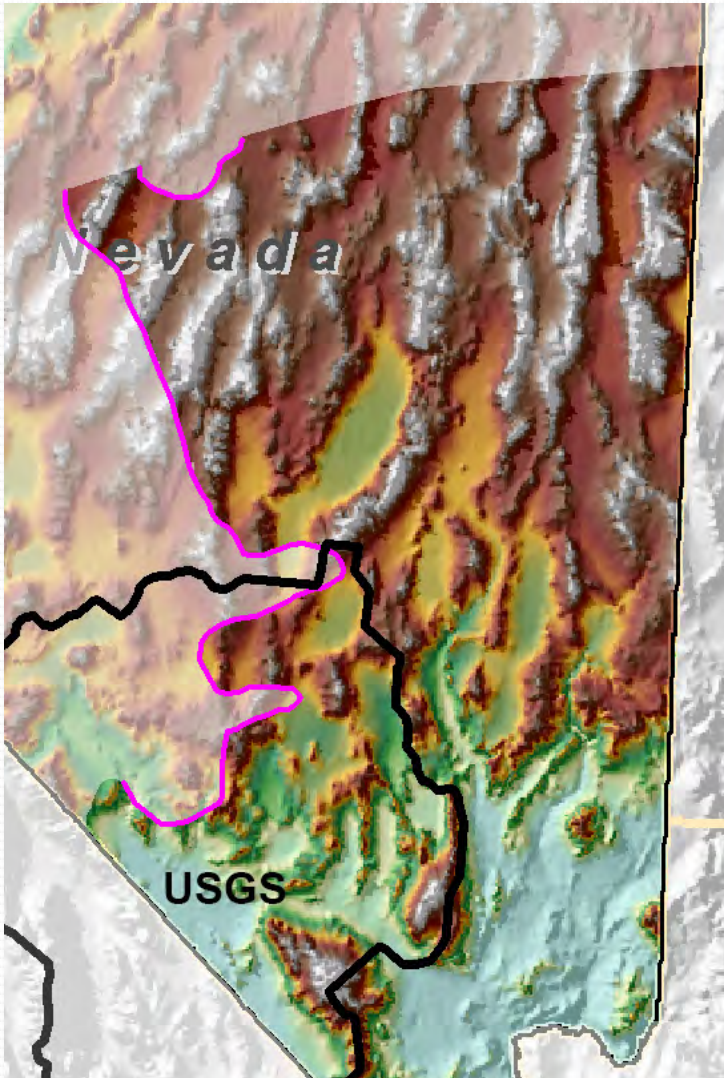


SE ROA 37478

Tom Eakin suggested in 1964 that above-average discharge of the Muddy River during the period 1956-1960 was the response to above-average recharge during the period 1935-1941 based on the Adaven precipitation record. Regional climate trends from 1927-1978 (inset) support the Adaven record as representative of a regional climate cycle

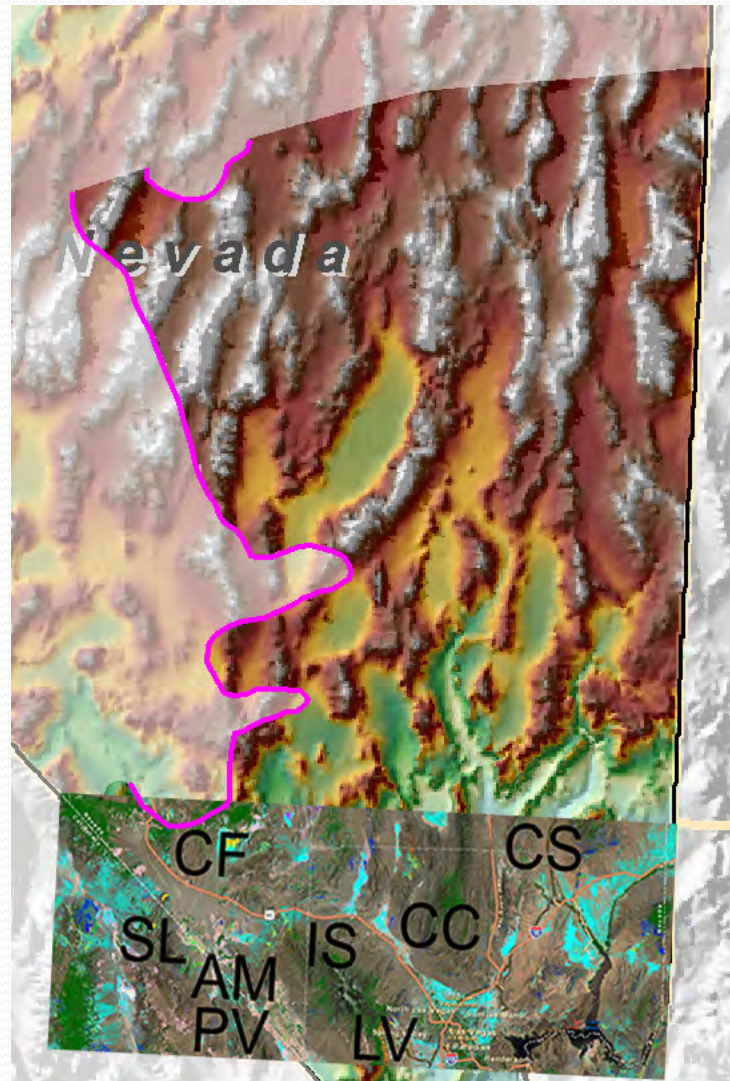
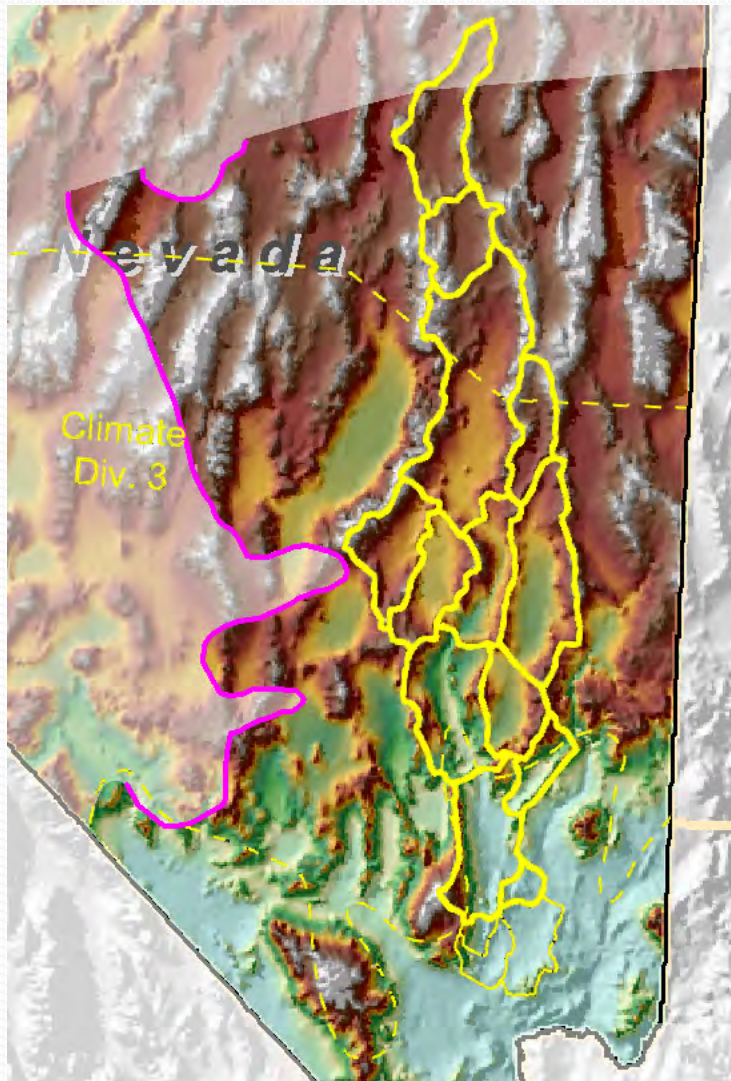


Mission-oriented groundwater models have no crucial validation tests; the pluvial state in the USGS model, transient responses by SNWA still invalid



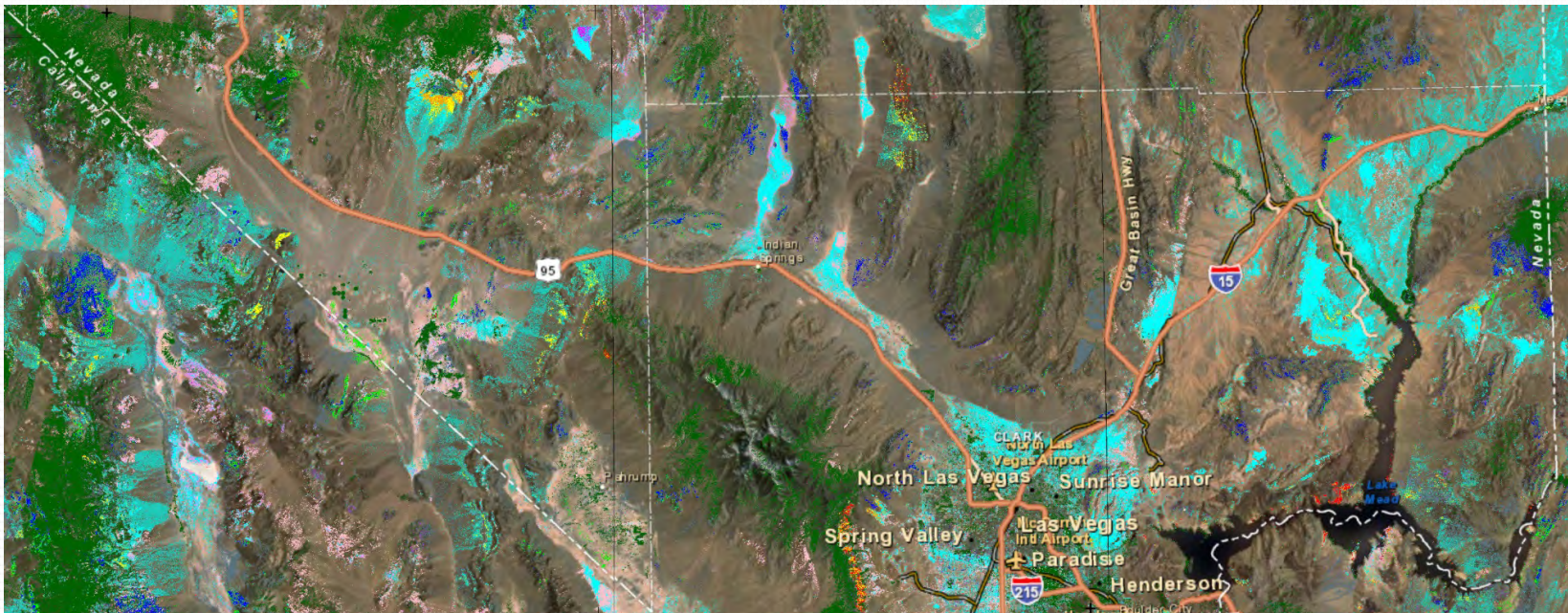
SE ROA 37480

Widespread GWD and evaporation from a ~26 ka DV Lake required LOT of water!



SE ROA 37481

ASTER (Advanced Space-borne Thermal Emission and Reflection Radiometer) imagery reveals fundamentally different GWD chemistries in western (Ash Meadows) and eastern (Las Vegas) paleodischarge deposits, more magnesian (pink) in the west and calcic (blue) in the east



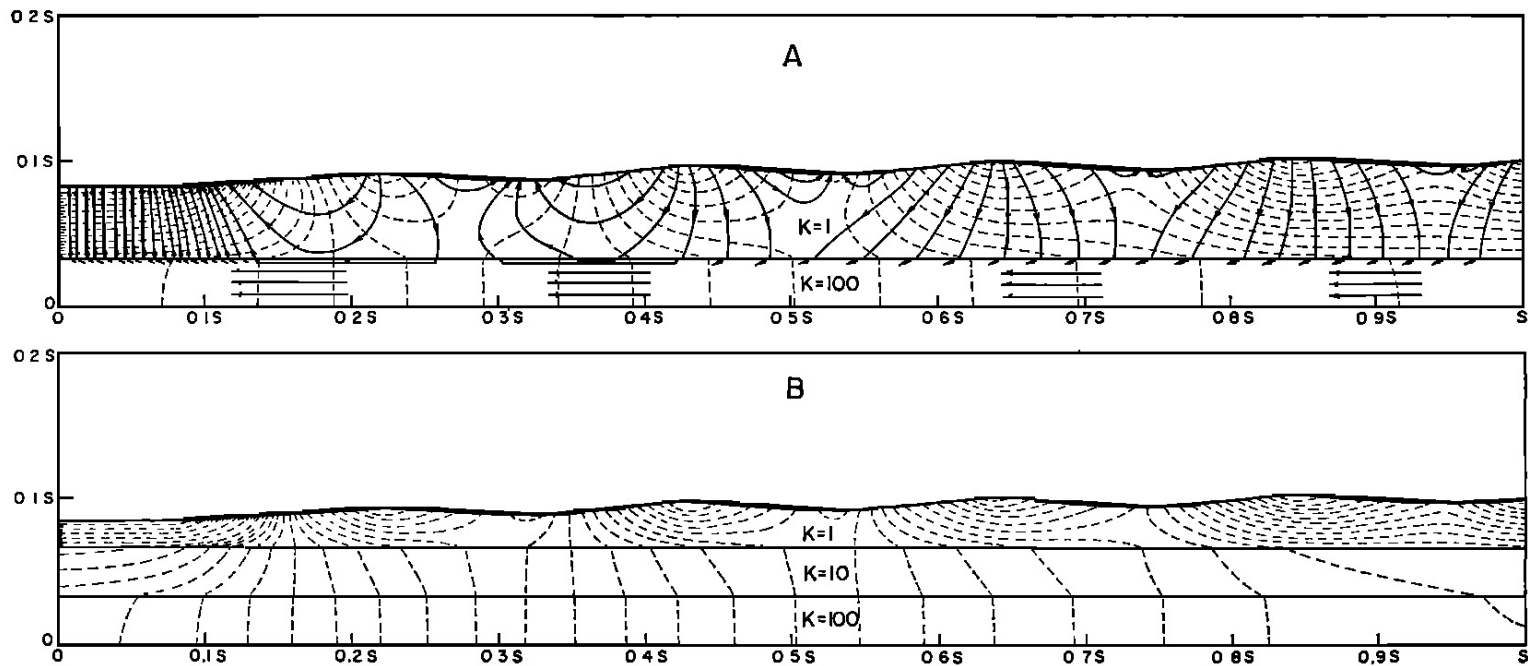
SE ROA 37482

JA_8988

How did all that groundwater get to the paleodischarge areas?

The area over which Pleistocene groundwater discharge occurred is vast, yet discharge areas are typically only a small percentage of their supporting recharge areas.

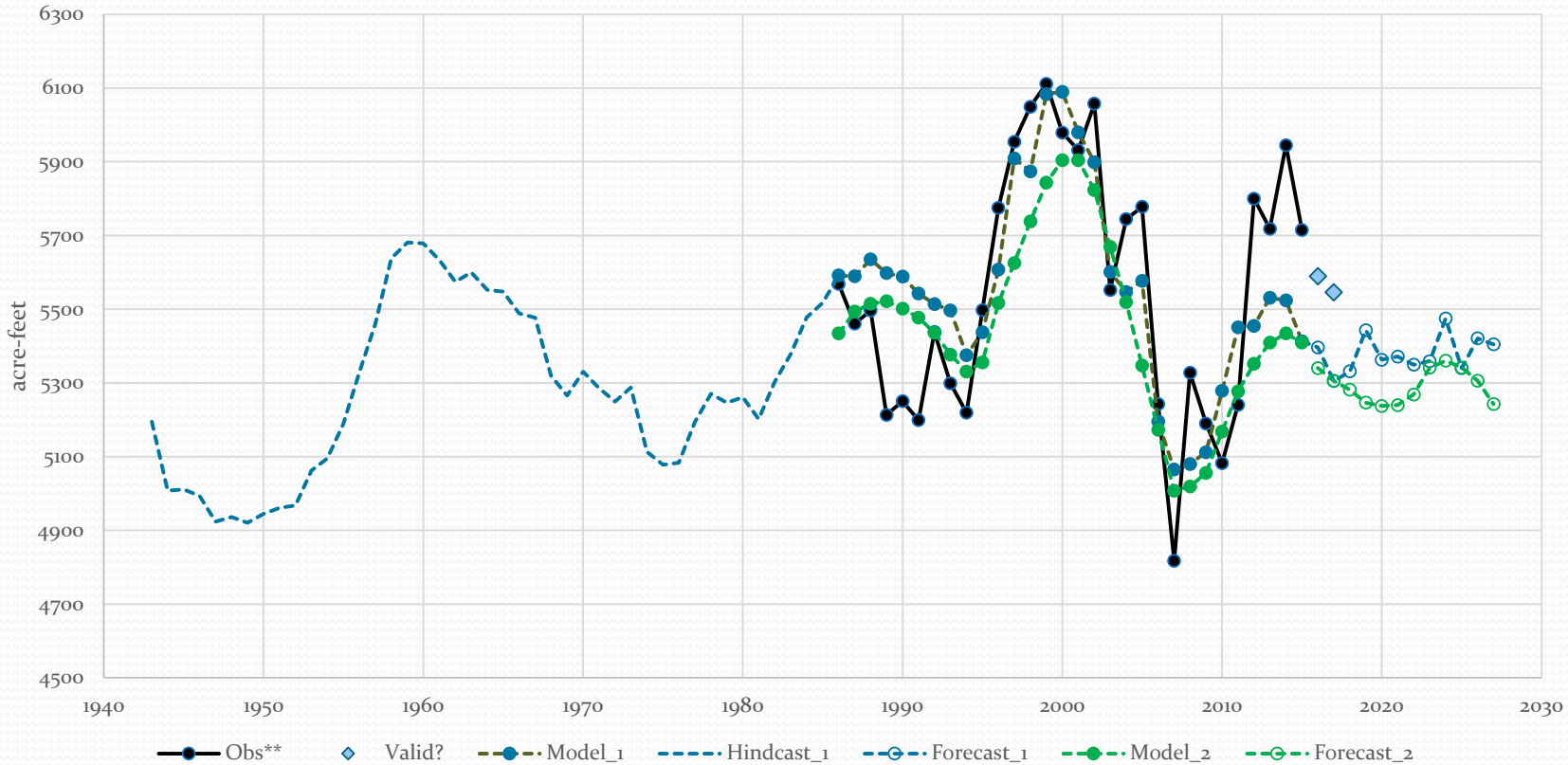
In The Paleozoic Shelf Domain of Nevada, regional groundwater flow is through layered media with a hummocky water-table configuration (Freeze and Witherspoon, 1967, WRR v.3 no.2 pp. 623-634)



SE ROA 37483

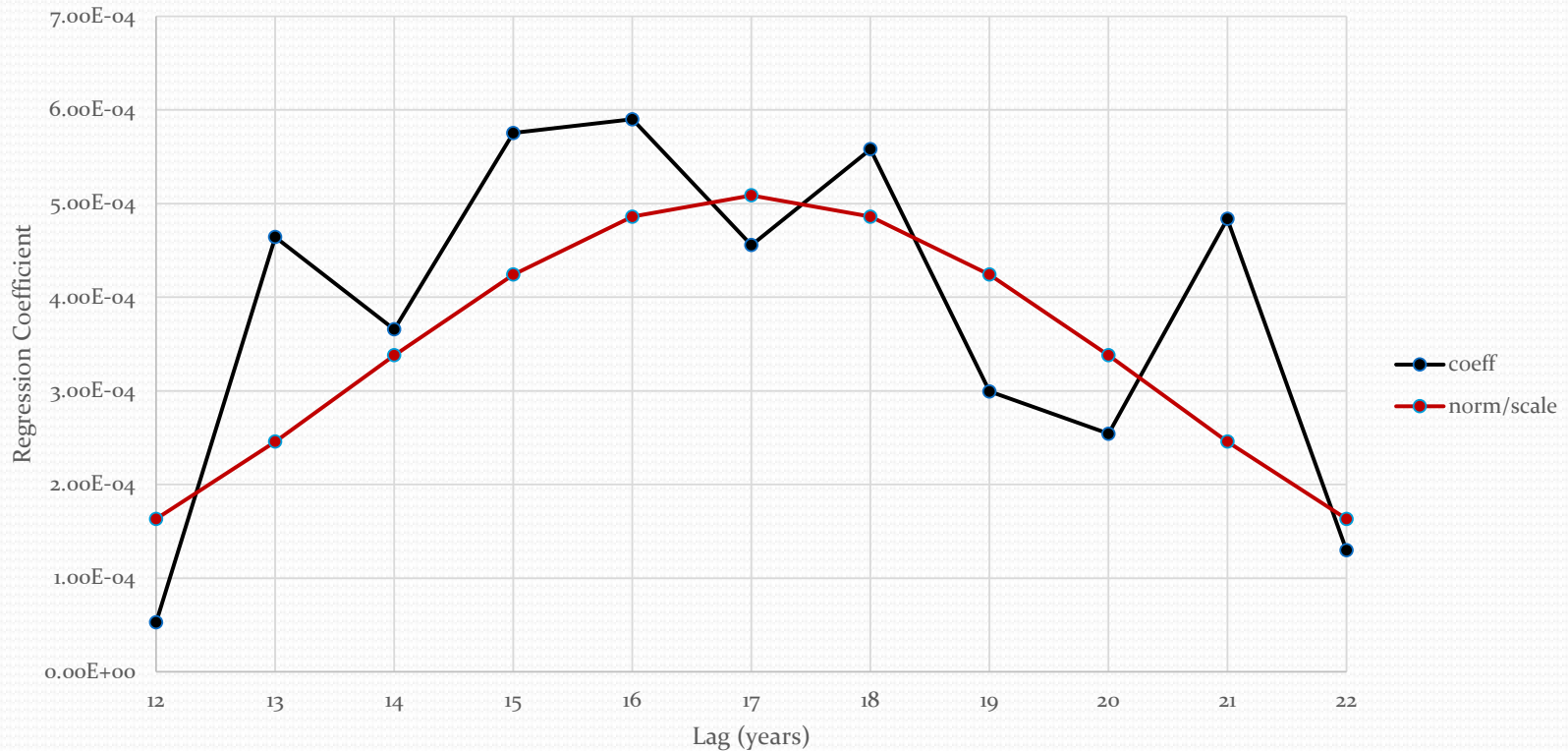
We discovered, by trial-and-error, a multiple-regression model to explain the discharge of Big Muddy Spring in terms of a contiguous set of annual base flows of the Humboldt River at Palisade: the 1960 Muddy River high that Eakin and Maxey noted is also hindcast to have occurred at Big Muddy Spring!

Climate-Response Models for Big Muddy Spring



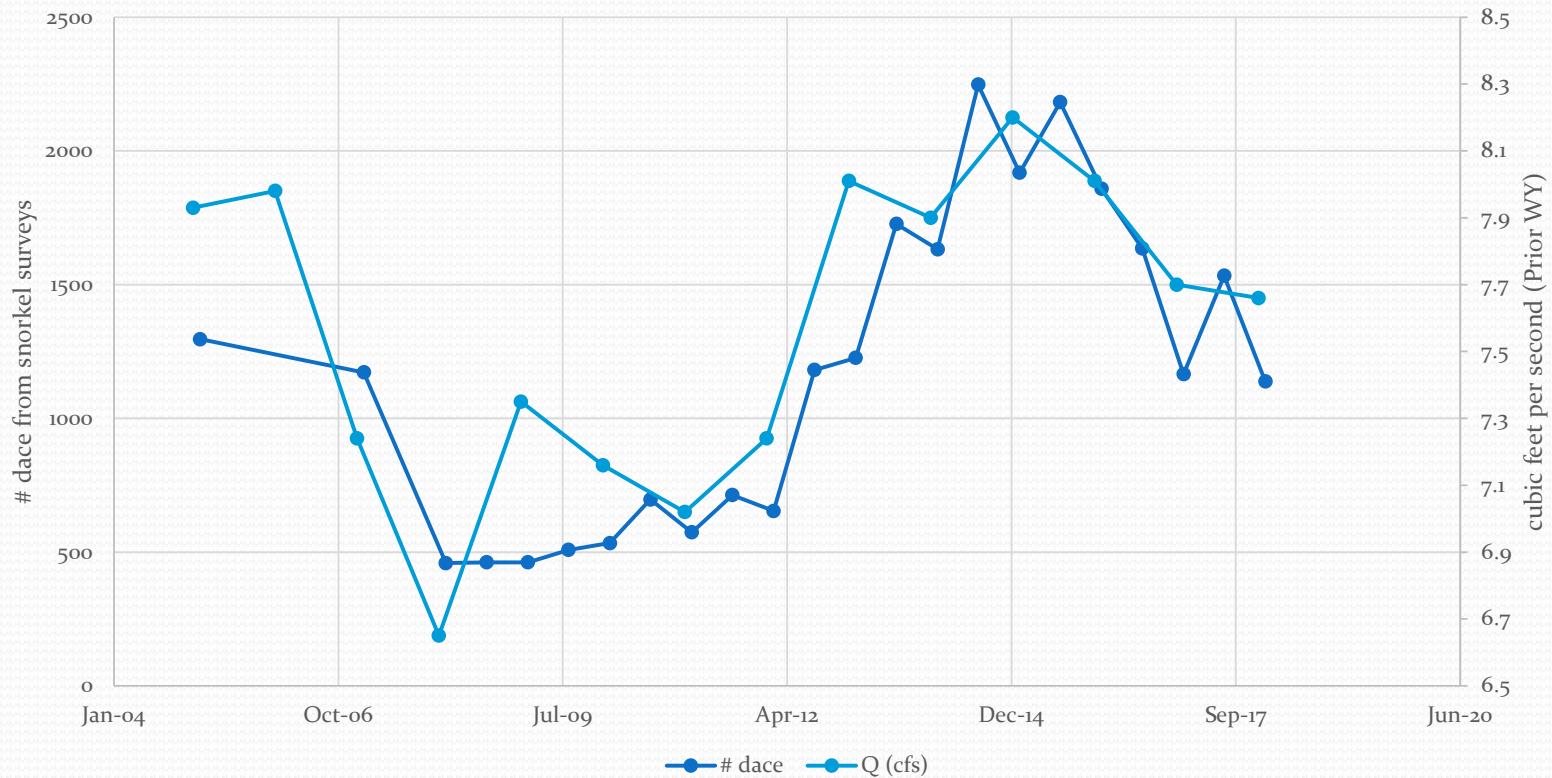
There was only one time window, 12-22 years before a trial response at Big Muddy Spring, that yielded all positive regression coefficients (Spring discharge is rationally explained by River base flow history)

Muddy Spring - Humboldt River Response Functions



Remember this startling observation: the MRSA dace counts closely follow Big Muddy Spring discharge trends!

Moapa Dace Count vs Annualized Big Muddy Spring Discharge



Concluding Observations

- Hydraulic responses of Big Muddy Spring to a northern climate “Sweet Spot” first suggested by Thomas Eakin in 1964 and supported by our work occur within decades, not after centuries
- If the USGS DVRFS model can remove pumping effects to hindcast water levels at Devils Hole, a similar multiple-regression model might be attainable there if adjustments can produce a clean “training” period for the model
- The State Engineer should reconsider his Ruling 6167 in light of these findings, since SNWA failed to appreciate and report our evidence of the climate “Sweet Spot” from 2016. SNWA will be faced with unmanageable problems if transient responses from planned northern developments are as we predict, occurring within two decades at MRSA
- A next-generation of AVIRIS (Airborne Visible InfraRed Imaging Spectrometer) is available and should be directed toward paleodischarge deposits as flux proxies and tracers of the pluvial-state groundwater systems, an elusive aspect of regional groundwater model validation
- A couple of R-code input and output snippets follow to illustrate the implementation of trial-and-error multiple regression in the R programming environment

```

> filepath<-system.file("data","NFvirginBFI2.txt",package="stats")
> WLmodel<-read.table(filepath,header=TRUE)
#
# assign names to columns of complete source data file with water year, EH-4 water level,
# and lagged Virgin River (North Fork) annual base flows as explanatory variables
#
> VarNamesLV <- c("WY", "EH4", "LVo",
+ "LV1", "LV2", "LV3", "LV4", "LV5", "LV6", "LV7", "LV8", "LV9", "LV10",
+ "LV11", "LV12", "LV13", "LV14", "LV15", "LV16", "LV17", "LV18", "LV19", "LV20",
+ "LV21", "LV22", "LV23", "LV24", "LV25", "LV26", "LV27", "LV28", "LV29", "LV30",
+ "LV31", "LV32", "LV33", "LV34", "LV35", "LV36", "LV37", "LV38", "LV39", "LV40",
+ "LV41", "LV42", "LV43", "LV44", "LV45", "LV46", "LV47", "LV48", "LV49", "LV50",
+ "LV51", "LV52", "LV53", "LV54", "LV55", "LV56", "LV57", "LV58")
#
# initialize counters
#
> LagStart <- 2 # first column of lagged climate indices
> LagEnd <- 17 # last column of lagged climate indices
> nCases <- 0 # step in the loop
#
# begin loop to move fixed-width time window containing explanatory variables back in time,
# performing multiple regression to explain EH-4 water levels at each step
#
> while(LagEnd<58){ # number of steps is limited by the width of the lag table WLmodel
+ LagStart <- LagStart+1 # increment counters to move window
+ LagEnd <- LagEnd+1
+ myvars <- c("EH4",VarNamesLV[LagStart:LagEnd]) # assemble the column names to be called
+ LVdata <- WLmodel[myvars] # create temporary data frame for analysis
+ fit <- lm(EH4~.,data=as.data.frame(LVdata)) # perform the multiple regression
+ out <- capture.output(summary(fit)) # multiple regression output for this step
+ nCases <- nCases+1 # count steps of window movement
+ cat(nCases, out,file="data/sumEH4_16x43.txt", sep="\n", append=TRUE) # append output file
+ } # end loop for 16-year windows

```

Call:
lm(formula = EH4 ~ ., data = as.data.frame(LVdata))

Residuals:

Min 1Q Median 3Q Max
-1.3469 -0.4373 0.1067 0.4324 1.3020

Coefficients:

	Estimate	Std. Error	t value	Pr(> t)
(Intercept)	1.800e+03	3.187e+00	564.807	<2e-16 ***
LV1	8.518e-06	1.061e-05	0.802	0.4393
LV2	1.015e-05	1.032e-05	0.984	0.3464
LV3	7.238e-06	1.057e-05	0.685	0.5075
LV4	1.947e-05	1.121e-05	1.737	0.1103
LV5	2.446e-05	1.037e-05	2.359	0.0379 *
LV6	1.710e-05	9.739e-06	1.756	0.1068
LV7	1.624e-05	8.375e-06	1.939	0.0785 .
LV8	1.007e-05	7.695e-06	1.309	0.2174
LV9	1.574e-05	7.604e-06	2.070	0.0628 .
LV10	2.402e-05	8.876e-06	2.707	0.0204 *
LV11	2.008e-05	9.376e-06	2.142	0.0554 .
LV12	2.439e-05	1.098e-05	2.222	0.0482 *
LV13	3.031e-05	1.138e-05	2.663	0.0221 *
LV14	1.858e-05	1.173e-05	1.584	0.1414
LV15	1.182e-05	1.178e-05	1.003	0.3373
LV16	7.169e-06	1.194e-05	0.601	0.5603

Signif. codes: 0 '***' 0.001 '**' 0.01 '*' 0.05 '.' 0.1 ' ' 1

Residual standard error: 0.9487 on 11 degrees of freedom

Multiple R-squared: 0.7694, Adjusted R-squared: 0.434

F-statistic: 2.294 on 16 and 11 DF, p-value: 0.08342

EMD: A Package for Empirical Mode Decomposition and Hilbert Spectrum

by Donghoh Kim and Hee-Seok Oh

Introduction

The concept of empirical mode decomposition (EMD) and the Hilbert spectrum (HS) has been developed rapidly in many disciplines of science and engineering since Huang et al. (1998) invented EMD. The key feature of EMD is to decompose a signal into so-called intrinsic mode function (IMF). Furthermore, the Hilbert spectral analysis of intrinsic mode functions provides frequency information evolving with time and quantifies the amount of variation due to oscillation at different time scales and time locations. In this article, we introduce an R package called **EMD** (Kim and Oh, 2008) that performs one- and two- dimensional EMD and HS.

Intrinsic mode function

The essential step extracting an IMF is to identify an oscillation embedded in a signal from local time scale. Consider the following synthetic signal $x(t), 0 < t < 9$ of the form

$$x(t) = 0.5t + \sin(\pi t) + \sin(2\pi t) + \sin(6\pi t). \quad (1)$$

The signal in Figure 1 consists of several components, which are generated through the process that a component is superimposed to each other.

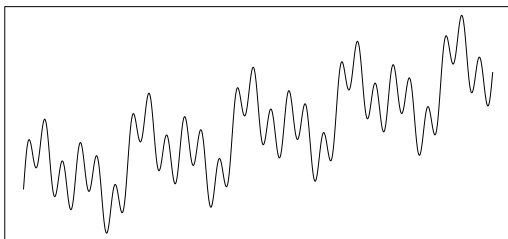


Figure 1: A sinusoidal function having 4 components

An intrinsic oscillation or frequency of a component, for example, $\sin(\pi t), t \in (0, 9)$ in Figure 1 can be perceived through the red solid wave or the blue dotted wave in Figure 2. The blue dotted wave in Figure 2 illustrates one cycle of intrinsic oscillation which starts at a local maximum and terminates at a consecutive local maximum by passing through two zeros and a local minimum which eventually appears between two consecutive maxima. A component for a given time scale can be regarded as the composition of repeated intrinsic oscillation which is symmetric to its local mean, zero.

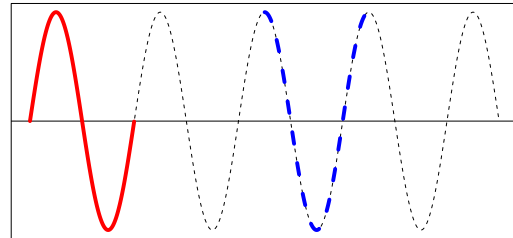


Figure 2: A sinusoidal function

Thus the first step to define intrinsic oscillation is to detect local extrema or zero-crossings. The function `extrema()` identifies local extrema and zero-crossings of the signal in Figure 2.

```
> ### Identify extrema and zero-crossings
> ndata <- 3000
> tt <- seq(0, 9, length=ndata)
> xt <- sin(pi * tt)
>
> library(EMD)
> extrema(xt)
$minindex
  [,1] [,2]
[1,] 501 501
[2,] 1167 1167
[3,] 1834 1834
[4,] 2500 2500

$maxindex
  [,1] [,2]
[1,] 168 168
[2,] 834 834
[3,] 1500 1501
[4,] 2167 2167
[5,] 2833 2833

$nextreme
[1] 9

$cross
  [,1] [,2]
[1,] 1 1
[2,] 334 335
[3,] 667 668
[4,] 1000 1001
[5,] 1333 1334
[6,] 1667 1668
[7,] 2000 2001
[8,] 2333 2334
[9,] 2666 2667

$ncross
[1] 9
```

The function `extrema()` returns a list of followings.

- `minindex` : matrix of time index at which local minima are attained. Each row specifies a starting and ending time index of a local minimum.
- `maxindex` : matrix of time index at which local maxima are attained. Each row specifies a starting and ending time index of a local maximum.
- `nextreme` : the number of extrema.
- `cross` : matrix of time index of zero-crossings. Each row specifies a starting and ending time index of zero-crossings.
- `ncross` : the number of zero-crossings.

Once local extrema is obtained, the intrinsic mode function is derived through the sifting procedure.

Sifting process

Huang et al. (1998) suggested a data-adapted algorithm extracting a sinusoidal wave or equivalently a frequency from a given signal x . First, identify the local extrema in Figure 3(a), and generate the two functions called the upper envelope and lower envelope by interpolating local maxima and local minima, respectively. See Figure 3(b). Second, take their average, which will produce a lower frequency component than the original signal as in Figure 3(c). Third, by subtracting the envelope mean from the signal x , the highly oscillated pattern h is separated as in Figure 3(d).

Huang et al. (1998) defined an oscillating wave as an intrinsic mode function if it satisfies two conditions 1) the number of extrema and the number of zero-crossings differs only by one and 2) the local average is zero. If the conditions of IMF are not satisfied after one iteration of aforementioned procedure, the same procedure is applied to the residue signal as in Figure 3(d), (e) and (f) until properties of IMF are satisfied.

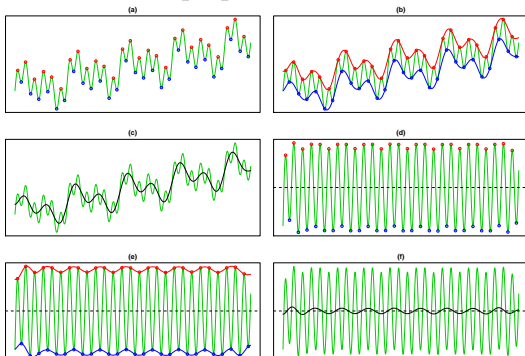


Figure 3: Sifting procedure

This iterative process is called sifting. The following code produces Figure 3, and the function `extractimf()` implements the sifting algorithm by

identifying the local extrema with the `extrema()`. Note that when setting the option `'check=TRUE'`, one must click the plot to proceed to the next step.

```
> ### Generating a signal
> ndata <- 3000
> par(mfrow=c(1,1), mar=c(1,1,1,1))
> tt2 <- seq(0, 9, length=ndata)
> xt2 <- sin(pi * tt2) + sin(2* pi * tt2) +
+ sin(6 * pi * tt2) + 0.5 * tt2
> plot(tt2, xt2, xlab="", ylab="", type="l",
+ axes=FALSE); box()
>
> ### Extracting the first IMF by sifting process
> tryimf <- extractimf(xt2, tt2, check=TRUE)
```

The function `extractimf()` extracts IMF's from a given signal, and it is controlled by the following arguments.

- `residue` : observation or signal observed at time `tt`.
- `tt` : observation index or time index.
- `tol` : tolerance for stopping rule.
- `max.sift` : the maximum number of sifting.
- `stoprule` : stopping rule.
- `boundary` : specifies boundary condition.
- `check` : specifies whether the sifting process is displayed. If `check=TRUE`, click the plotting area to start the next step.

Stopping rule

The sifting process stops when the replication of sifting procedure exceed the predefined maximum number by `max.sift` or satisfies the properties of IMF by stopping rule. The stopping rule `stoprule` has two options – "type1" and "type2". The option `stoprule = "type1"` makes the sifting process stop when the absolute values of the candidate IMF h_i are smaller than tolerance level, that is, $|h_i(t)| < tol$ for all t . Or by the option `stoprule = "type2"`, the sifting process stops when the variation of consecutive candidate IMF's is within the tolerance level,

$$\sum_t \left(\frac{h_i(t) - h_{i-1}(t)}{h_{i-1}(t)} \right)^2 < tol.$$

Boundary adjustment

To eliminate the boundary effect of a signal, it is necessary to adjust a signal at the boundary. Huang et al. (1998) extended the original signal by adding artificial waves repeatedly on both sides of the boundaries. The waves called characteristic waves are constructed by repeating the implicit mode formed from extreme values nearest to boundary. The argument `boundary` specifies the adjusting method of the

boundary. The argument `boundary = "wave"` constructs a wave which is defined by two consecutive extrema at either boundary, and adds four waves at either end. Typical adjusting method extends a signal assuming that a signal is symmetric or periodic. The option `boundary = "symmetric"` or `boundary = "periodic"` extends both boundaries symmetrically or periodically.

Zeng and He (2004) considered two extended signals by adding a signal in a symmetric way and reflexive way called even extension and odd extension, respectively. Even extension and odd extension produce the extended signals so that its average is zero. This boundary condition can be specified by `boundary = "evenodd"`. For each extended signal, upper and lower envelopes are constructed and envelope mean of the extended signals is defined by the average of four envelopes. Then, the envelope mean outside the time scale of the original signal is close to zero, while the envelope mean within the time scale of the original signal is almost the same as the envelope mean of the original signal. On the other hand, the option `boundary = "none"` performs no boundary adjustments.

Empirical mode decomposition

Once the highest frequency is removed from a signal, the same procedure is applied on the residue signal to identify next highest frequency. The residue is considered a new signal to decompose.

Suppose that we have a signal from model (1). The signal in Figure 1 is composed of 4 components from $\sin(6\pi t)$ with the highest frequency to $0.5t$ with the lowest frequency. We may regard the linear component as a component having the lowest frequency. The left panel in Figure 4 illustrates the first IMF and the residue signal obtained by the function `extractimf()`. If the remaining signal is still compound of components with several frequencies as in the left panel in Figure 4, then the next IMF is obtained by taking the residue signal as a new signal in the right panel in Figure 4. The number of extrema will decrease as the procedure continues, so that the signal is sequentially decomposed into the highest frequency component imf_1 to the lowest frequency component imf_n , for some finite n and a residue signal r . Finally, we have n IMF's and a residue signal as

$$x(t) = \sum_{i=1}^n imf_i(t) + r(t).$$

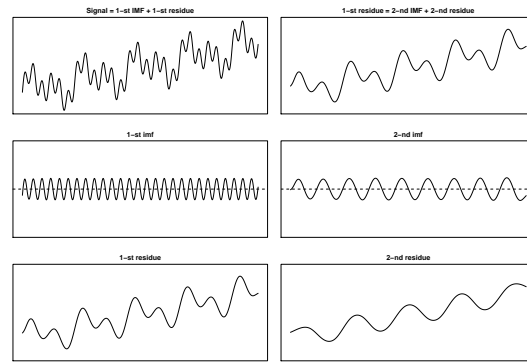


Figure 4: Two IMF's by the sifting algorithm

The above-mentioned decomposition process is implemented by the function `emd()` that utilizes the functions `extractimf()` and `extrema()`. The final decomposition result by the following code is illustrated in Figure 5.

```
> ### Empirical Mode Decomposition
> par(mfrow=c(3,1), mar=c(2,1,2,1))
> try <- emd(xt2, tt2, boundary="wave")
>
> ### Plotting the IMF's
> par(mfrow=c(3,1), mar=c(2,1,2,1))
> par(mfrow=c(try$nimf+1, 1), mar=c(2,1,2,1))
> rangeimf <- range(try$imf)
> for(i in 1:try$nimf)
+ plot(tt2, try$imf[,i], type="l", xlab="",
+ ylab="", ylim=rangeimf, main=
+ paste(i, "-th IMF", sep="")); abline(h=0)
> plot(tt2, try$residue, xlab="", ylab="",
+ main="residue", type="l")
```

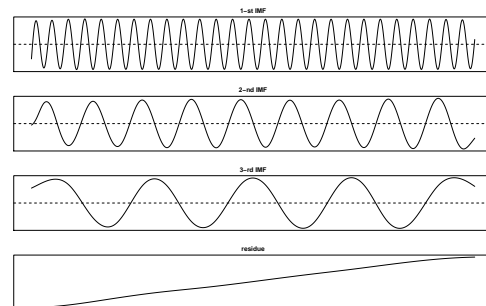


Figure 5: Decomposition of a signal by model (1)

The arguments of `emd()` are similar to those of `extractimf()`. The additional arguments are

- `max.imf`: the maximum number of IMF's.
- `plot.imf`: specifies whether each IMF is displayed. If `plot.imf=TRUE`, click the plotting area to start the next step.

Up to now we have focused on artificial signals without any measurement error. A typical signal in the real world is corrupted by noise, which is not the component of interest and contains no interpretable

information. A remedy to smooth out the noise is to apply smoothing technique not interpolation during the sifting process. Then the first IMF might capture the entire noise effectively. As an alternative, Kim and Oh (Kim and Oh, 2006) proposed an efficient smoothing method for IMF's by combining the conventional cross-validation and thresholding approach. By thresholding, noisy signal can be de-noised while the distinct localized feature of a signal can be kept.

Intermittence

Huang et al. (1998, 2003) pointed out that intermittence raises mode mixing, which means that different modes of oscillations coexist in a single IMF. Since EMD traces the highest frequency embedded in a given signal locally, when intermittence occurs, the shape of resulting IMF is abruptly changed and this effect distorts procedures thereafter.

Huang et al. (2003) attacked this phenomenon by restricting the size of frequency. To be specific, the distance limit of the successive maxima (minima) in an IMF is introduced. Thus, IMF composes of only sinusoidal waves whose length of successive maxima (minima) are shorter than their limit. Equivalently, we may employ the length of the zero-crossings to overcome the intermittence problem. Consider a signal $x(t)$ combined by two sine curves (Deering and Kaiser, 2005),

$$x(t) = \begin{cases} \sin(2\pi f_1 t) + \sin(2\pi f_2 t), & \frac{1}{30} \leq t \leq \frac{2}{30} \\ \sin(2\pi f_1 t), & \text{otherwise.} \end{cases} \quad (2)$$

Figure 6 illustrates the signal $x(t)$ when $f_1 = 1776$ and $f_2 = 1000$ and the corresponding two IMF's. The first IMF absorbs the component that appeared in the second IMF between $\frac{1}{30}$ and $\frac{2}{30}$. Thus, the resulting IMF has a mode mixing pattern.

```
> ### Mode mixing
> tt <- seq(0, 0.1, length = 2001)[1:2000]
> f1 <- 1776; f2 <- 1000
> xt <- sin(2*pi*f1*tt) * (tt <= 0.033 |
+ tt >= 0.067) + sin(2*pi*f2*tt)
>
> ### EMD
> interm1 <- emd(xt, tt, boundary="wave",
+ max.imf=2, plot.imf=FALSE)
> par(mfrow=c(3, 1), mar=c(3,2,2,1))
> plot(tt, xt, main="Signal", type="l")
> rangeimf <- range(interm1$imf)
> plot(tt, interm1$imf[,1], type="l", xlab="",
+ ylab="", ylim=rangeimf, main="IMF 1")
> plot(tt, interm1$imf[,2], type="l", xlab="",
+ ylab="", ylim=rangeimf, main="IMF 2")
```

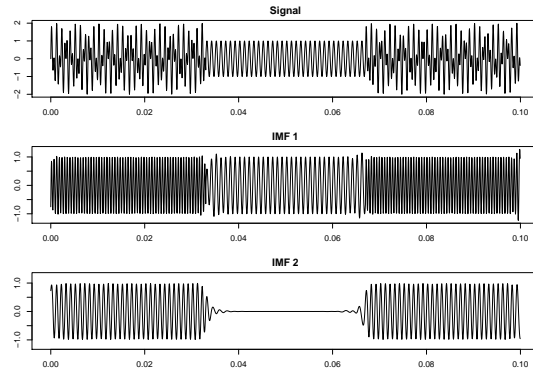


Figure 6: Signal $x(t)$ by model (2) and first two IMF's

By following the approach of Huang et al. (1998, 2003), we can remove waves whose empirical period represented by the distance of other zero-crossings is larger than 0.0007 in the first IMF. The period information obtained by histogram in Figure 7 can be used to choose an appropriate distance. We eliminate the waves with lower frequency in the first IMF with the histogram of other zero-crossings.

```
> ### Histogram of empirical period
> par(mfrow=c(1,1), mar=c(2,4,1,1))
> tmpinterm <- extrema(interm1$imf[,1])
> zerocross <-
+ as.numeric(round(apply(tmpinterm$cross, 1, mean)))
> hist(diff(tt[zerocross[seq(1, length(zerocross),
+ by=2)]]), freq=FALSE, xlab="", main="")
```

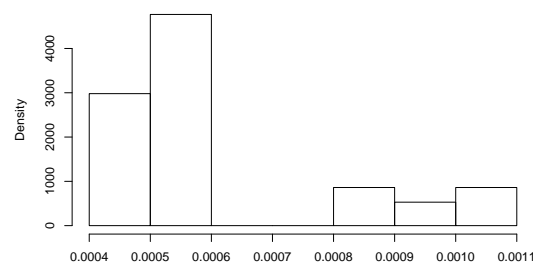


Figure 7: Histogram of the empirical period

Figure 8 shows the resulting IMF's after treating intermittence properly. The argument `interm` of the function `emd()` specifies a vector of periods to be excluded from the IMF's.

```
> ### Treating intermittence
> interm2 <- emd(xt, tt, boundary="wave",
+ max.imf=2, plot.imf=FALSE, interm=0.0007)
>
> ### Plot of each imf
> par(mfrow=c(2,1), mar=c(2,2,3,1), oma=c(0,0,0,0))
> rangeimf <- range(interm2$imf)
> plot(tt, interm2$imf[,1], type="l",
+ main="IMF 1 after treating intermittence",
+ xlab="", ylab="", ylim=rangeimf)
> plot(tt, interm2$imf[,2], type="l",
+ main="IMF 2 after treating intermittence",
+ xlab="", ylab="", ylim=rangeimf)
```

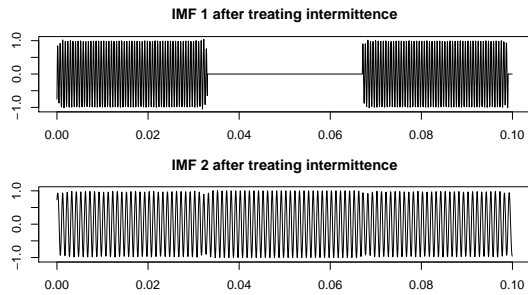


Figure 8: Decomposition of signal $x(t)$ by model (2) after treating the intermittence.

Hilbert spectrum

When a signal is subject to non-stationarity so that the frequency and amplitude change over time, it is necessary to have a more flexible and extended notion of frequency. Huang et al. (1998) used the concept of instantaneous frequency through the Hilbert transform. For a comprehensive explanation of the Hilbert transform, refer to Cohen (1995). For a real signal $x(t)$, the analytic signal $z(t)$ is defined as $z(t) = x(t) + i y(t)$ where $y(t)$ is the Hilbert transform of $x(t)$, that is, $y(t) = \frac{1}{\pi} P \int_{-\infty}^{\infty} \frac{x(s)}{t-s} ds$ where P is the Cauchy principal value. The polar coordinate form of the analytic signal z with amplitude and phase is $z(t) = a(t) \exp(i\theta(t))$ where amplitude $a(t)$ is $\|z(t)\| = \sqrt{x(t)^2 + y(t)^2}$ and phase $\theta(t)$ is $\arctan\left(\frac{y(t)}{x(t)}\right)$. The instantaneous frequency as time-varying phase is defined as $\frac{d\theta(t)}{dt}$. After decomposing a signal into IMF's with EMD thereby preserving any local property in the time domain, we can extract localized information in the frequency domain with the Hilbert transform and identify hidden local structures embedded in the original signal. The local information can be described by the Hilbert spectrum which is amplitude and instantaneous frequency representation with respect to time. Figure 9 describes the Hilbert spectrum for IMF 1 of the signal of model (2) before and after treating the intermittence. The X-Y axis represents time and instantaneous frequency, and the color intensity of the image depicts instantaneous amplitude.

```
> ### Spectrogram : X - Time, Y - frequency,
> ### Z (Image) - Amplitude
> test1 <- hilbertspec(interm1$imf)
> spectrogram(test1$amplitude[,1],
+ test1$instantfreq[,1])
> test2 <- hilbertspec(interm2$imf, tt=tt)
> spectrogram(test2$amplitude[,1],
+ test2$instantfreq[,1])
```

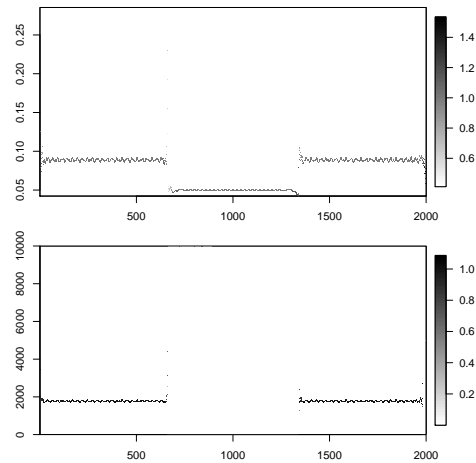


Figure 9: The Hilbert spectrum for IMF 1 of the signal of model (2)

For multiple signals, the function `hilbertspec()` calculates the amplitudes and instantaneous frequency using Hilbert transform. The function has the following arguments,

- `xt` : matrix of multiple signals. Each column represents a signal.
- `tt` : observation index or time index.

The function `hilbertspec()` returns a matrix of amplitudes and instantaneous frequencies for multiple signals. The function `spectrogram()` produces an image of amplitude by time index and instantaneous frequency. The horizontal axis represents time, the vertical axis is instantaneous frequency, and the color of each point in the image represents amplitude of a particular frequency at a particular time. It has arguments as

- `amplitude` : vector or matrix of amplitudes for multiple signals.
- `freq` : vector or matrix of instantaneous frequencies for multiple signals.
- `tt` : observation index or time index.
- `multi` : specifies whether spectrograms of multiple signals are separated or not.
- `nlevel` : the number of color levels used in legend strip
- `size` : vector of image size.

Extension to two dimensional image

The extension of EMD to an image or two dimensional data is straightforward except the identification of the local extrema. Once the local extrema

are identified, the two dimensional smoothing spline technique is used for the sifting procedure.

For the two-dimensional case, we provide four R functions.

- (1) `extrema2d()` for identifying the two dimensional extrema,
- (2) `extractimf2d()` for extracting the IMF from a given image,
- (3) `emd2d()` for decomposing an image to IMF's and the residue image combining two R functions above, and
- (4) `imageEMD()` for displaying the decomposition results.

As in a one-dimensional case, `extractimf2d()` extracts two dimensional IMF's from a given image based on local extrema identified by `extrema2d()`. Combining these functions, `emd2d()` performs decomposition and its arguments are as follows.

- `z` : matrix of an image observed at (x, y) .
- `x`, `y` : locations of regular grid at which the values in `z` are measured.
- `tol` : tolerance for stopping rule of sifting.
- `max.sift` : the maximum number of sifting.
- `boundary` : specifies boundary condition 'symmetric', 'reflexive' or 'none'.
- `boundperc` : expand an image by adding specified percentage of image at the boundary when boundary condition is 'symmetric' or 'reflexive'.
- `max.imf` : the maximum number of IMF.
- `plot.imf` : specifies whether each IMF is displayed. If `plot.imf=TRUE`, click the plotting area to start the next step.

The following R code performs two dimensional EMD of the Lena image. The size of the original image is reduced for computational simplicity.

```
> data(lena)
> z <- lena[seq(1, 512, by=4), seq(1, 512, by=4)]
> lenadecom <- emd2d(z, max.imf = 4)
```

The R function `imageEMD()` plots decomposition results and the argument `extrma=TRUE` illustrates the local maxima (minima) with the white (black) color and grey background. See Figure 10.

```
> imageEMD(z=z, emdz=lenadecom, extrema=TRUE,
+ col=gray(0:100/100))
```

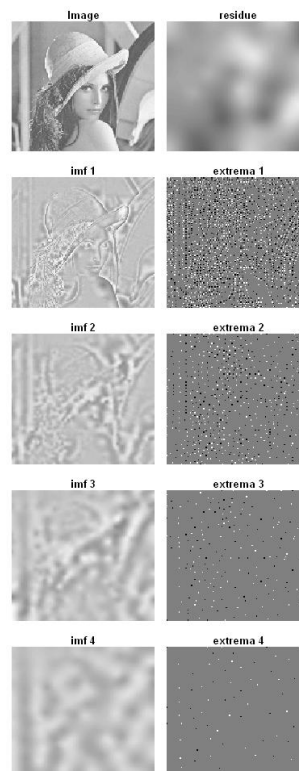


Figure 10: Decomposition of the Lena image

Conclusions

IMF's through EMD provide a multi-resolution tool and spectral analysis gives local information with time-varying amplitude and phase according to the scales. We introduce **EMD**, an R package for the proper implementation of EMD, and the Hilbert spectral analysis for non-stationary signals. It is expected that R package **EMD** makes EMD methodology practical for many statistical applications.

Bibliography

- L. Cohen. *Time-Frequency Analysis*. Prentice-Hall, 1995.
- R. Deering and J. F. Kaiser. The Use of a Masking Signal to Improve Empirical Mode Decomposition. *Proceedings of IEEE International Conference on Acoustics, Speech, and Signal Processing*, 4:485–488, 2005.
- N. E. Huang, Z. Shen, S. R. Long, M. C. Wu, H. H. Shih, Q. Zheng, N.-C. Yen, C. C. Tung, and H. H. Liu. The Empirical Mode Decomposition and Hilbert Spectrum for Nonlinear and Nonstationary Time Series Analysis. *Proceedings of the Royal Society London A.*, 454:903–995, 1998.
- N. E. Huang, M. C. Wu, S. R. Long, S. Shen, W. Qu, P. Gloerson, and K. L. Fan. A Confidence Limit for

- the Empirical Mode Decomposition and Hilbert Spectral Analysis. *Proceedings of the Royal Society London A.*, 31:417–457, 2003.
- D. Kim and H-S. Oh. Hierarchical Smoothing Technique by Empirical Mode Decomposition. *The Korean Journal of Applied Statistics*, 19:319–330, 2006.
- D. Kim and H-S. Oh. **EMD**: Empirical Mode Decomposition and Hilbert Spectral Analysis, 2008. URL <http://cran.r-project.org/web/packages/EMD/index.html>.
- D. Nychka. **fields**: Tools for Spatial Data, 2007. URL <http://cran.r-project.org/web/packages/fields/index.html>.
- K. Zeng and M-X. He. A Simple Boundary Process Technique for Empirical Mode Decomposition. *Proceedings of IEEE International Geoscience and Remote Sensing Symposium*, 6:4258–4261, 2004.

Donghoh Kim
Sejong University, Korea
E-mail: donghoh.kim@gmail.com

Hee-Seok Oh
Seoul National University, Korea
E-mail: heeseok@stats.snu.ac.kr

Analysis and Evaluation of Pumping Test Data

Second Edition (Completely Revised)

G.P. Kruseman

Senior hydrogeologist, TNO Institute of Applied Geoscience, Delft

N.A. de Ridder

Senior hydrogeologist, International Institute for Land Reclamation
and Improvement, Wageningen

and

Professor in Hydrogeology, Free University, Amsterdam

With assistance from

J.M. Verweij

Freelance hydrogeologist

Publication 47



International Institute for Land Reclamation and Improvement,
P.O. Box 45, 6700 AA Wageningen, The Netherlands, 1994.

SE ROA 37497

The first edition of this book appeared as No. 11 in the series of Bulletins of the International Institute for Land Reclamation and Improvement/ILRI. Because the ILRI Bulletins have now been discontinued, this completely revised edition of the book appears as ILRI Publication 47.

The production of the book was made possible by cooperation between the following institutions:

International Institute for Land Reclamation and Improvement, Wageningen

TNO Institute of Applied Geoscience, Delft

Institute for Earth Sciences, Free University/VU, Amsterdam

First Edition 1970

Reprinted 1973

Reprinted 1976

Reprinted 1979

Reprinted 1983

Reprinted 1986

Reprinted 1989

Second Edition

Reprinted 1991

Reprinted 1992

Reprinted 1994

Reprinted 2000

The aims of ILRI are:

- To collect information on land reclamation and improvement from all over the world;
- To disseminate this knowledge through publications, courses, and consultancies;
- To contribute - by supplementary research - towards a better understanding of the land and water problems in developing countries.

© 2000 International Institute for Land Reclamation and Improvement/ILRI. All rights reserved. This book or any part thereof may not be reproduced in any form without written permission of the publisher. Printed in The Netherlands by Veenman drukkers, Ede

ISBN 90 70754 207

SE ROA 37498

Preface

This is the second edition of *Analysis and Evaluation of Pumping Test Data*. Readers familiar with the first edition and its subsequent impressions will note a number of changes in the new edition. These changes involve the contents of the book, but not the philosophy behind it, which is to be a practical guide to all who are organizing, conducting, and interpreting pumping tests.

What changes have we made? In the first place, we have included the step-drawdown test, the slug test, and the oscillation test. We have also added three chapters on pumping tests in fractured rocks. This we have done because of comments from some of our reviewers, who regretted that the first edition contained nothing about tests in fractured rocks. It would be remiss of us, however, not to warn our readers that, in spite of the intense research that fractured rocks have undergone in the last two decades, the problem is still the subject of much debate. What we present are some of the common methods, but are aware that they are based on ideal conditions which are rarely met in nature. All the other methods, however, are so complex that one needs a computer to apply them.

We have also updated the book in the light of developments that have taken place since the first edition appeared some twenty years ago. We present, for instance, a more modern method of analyzing pumping tests in unconfined aquifers with delayed yield. We have also re-evaluated some of our earlier field examples and have added several new ones.

Another change is that, more than before, we emphasize the intricacy of analyzing field data, showing that the drawdown behaviour of totally different aquifer systems can be very similar.

It has become a common practice nowadays to use computers in the analysis of pumping tests. For this edition of our book, we seriously considered adding computer codes, but eventually decided not to because they would have made the book too voluminous and therefore too costly. Other reasons were the possible incompatibility of computer codes and, what is even worse, many of the codes are based on 'black box' methods which do not allow the quality of the field data to be checked. Interpreting a pumping test is not a matter of feeding a set of field data into a computer, tapping a few keys, and expecting the truth to appear. The only computer codes with merit are those that take over the tedious work of plotting the field data and the type curves, and display them on the screen. These computer techniques are advancing rapidly, but we have refrained from including them. Besides, the next ILRI Publication (No. 48, *SATEM: Selected Aquifer Test Evaluation Methods* by J. Boonstra) presents the most common well-flow equations in computerized form. As well, the International Ground-Water Modelling Centre in Indianapolis, U.S.A., or its branch office in Delft, The Netherlands, can provide all currently available information on computer codes.

Our wish to revise and update our book could never have been realized without the support and help of many people. We are grateful to Mr. F. Walter, Director of TNO Institute of Applied Geoscience, who made it possible for the first author and Ms

Hanneke Verwey to work on the book. We are also grateful to Brigadier (Retired) K.G. Ahmad, General Manager (Water) of the Water and Power Development Authority, Pakistan, for granting us permission to use pumping test data not officially published by his organization.

We also express our thanks to Dr J.A.H. Hendriks, Director of ILRI, who allowed the second author time to work on the book, and generously gave us the use of ILRI's facilities, including the services of Margaret Wiersma-Roche, who edited our manuscript and corrected our often wordy English. We are indebted to Betty van Aarst and Joop van Dijk for their meticulous drawings, and to Trudy Pleijsant-Paes for her patience and perseverance in processing the words and the equations of the book. Last, but by no means least, we thank ILRI's geohydrologist, Dr J. Boonstra, for his discussion of the three chapters on fractured rocks and his valuable contribution to their final draft.

We hope that this revised and updated edition of *Analysis and Evaluation of Pumping Test Data* will serve its readers as the first edition did. Any comments anyone would care to make will be received with great interest.

G.P. Kruseman
N.A. de Ridder

Contents

Preface

1	Basic concepts and definitions	13
1.1	Aquifer, aquitard, and aquiclude	13
1.2	Aquifer types	14
1.2.1	Confined aquifer	14
1.2.2	Unconfined aquifer	14
1.2.3	Leaky aquifer	14
1.3	Anisotropy and heterogeneity	14
1.4	Bounded aquifers	17
1.5	Steady and unsteady flow	17
1.6	Darcy's law	18
1.7	Physical properties	19
1.7.1	Porosity (n)	19
1.7.2	Hydraulic conductivity (K)	21
1.7.3	Interporosity flow coefficient (λ)	21
1.7.4	Compressibility (α and β)	22
1.7.5	Transmissivity (KD or T)	22
1.7.6	Specific storage (S_s)	22
1.7.7	Storativity (S)	23
1.7.8	Storativity ratio (ω)	23
1.7.9	Specific yield (S_y)	23
1.7.10	Diffusivity (KD/S)	24
1.7.11	Hydraulic resistance (c)	24
1.7.12	Leakage factor (L)	25
2	Pumping tests	27
2.1	The principle	27
2.2	Preliminary studies	27
2.3	Selecting the site for the well	28
2.4	The well	28
2.4.1	Well diameter	28
2.4.2	Well depth	29
2.4.3	Well screen	29
2.4.4	Gravel pack	30
2.4.5	The pump	30
2.4.6	Discharging the pumped water	31
2.5	Piezometers	31
2.5.1	The number of piezometers	32

2.5.2	Their distance from the well	33
2.5.3	Depth of the piezometers	37
2.6	The measurements to be taken	37
2.6.1	Water-level measurements	38
2.6.1.1	Water-level-measuring devices	40
2.6.2	Discharge-rate measurements	41
2.6.2.1	Discharge-measuring devices	42
2.7	Duration of the pumping test	43
2.8	Processing the data	44
2.8.1	Conversion of the data	44
2.8.2	Correction of the data	44
2.8.2.1	Unidirectional variation	45
2.8.2.2	Rhythmic fluctuations	45
2.8.2.3	Non-rhythmic regular fluctuations	46
2.8.2.4	Unique fluctuations	47
2.9	Interpretation of the data	48
2.9.1	Aquifer categories	48
2.9.2	Specific boundary conditions	51
2.10	Reporting and filing of data	53
2.10.1	Reporting	53
2.10.2	Filing of data	53
3	Confined aquifers	55
3.1	Steady-state flow	56
3.1.1	Thiem's method	56
3.2	Unsteady-state flow	61
3.2.1	Theis's method	61
3.2.2	Jacob's method	65
3.3	Summary	70
4	Leaky aquifers	73
4.1	Steady-state flow	76
4.1.1	De Glee's method	76
4.1.2	Hantush-Jacob's method	77
4.2	Unsteady-state flow	80
4.2.1	Walton's method	81
4.2.2	Hantush's inflection-point method	85
4.2.3	Hantush's curve-fitting method	90
4.2.4	Neuman-Witherspoon's method	93
4.3	Summary	97

5	Unconfined aquifers	99
5.1	Unsteady-state flow	102
5.1.1	Neuman's curve-fitting method	102
5.2	Steady-state flow	106
5.2.1	Thiem-Dupuit's method	107
6	Bounded aquifers	109
6.1	Bounded confined or unconfined aquifers, steady-state flow	110
6.1.1	Dietz's method, one or more recharge boundaries	110
6.2	Bounded confined or unconfined aquifers, unsteady-state flow	112
6.2.1	Stallman's method, one or more boundaries	112
6.2.2	Hantush's method (one recharge boundary)	117
6.3	Bounded leaky or confined aquifers, unsteady-state flow	120
6.3.1	Vandenberg's method (strip aquifer)	120
7	Wedge-shaped and sloping aquifers	125
7.1	Wedge-shaped confined aquifers, unsteady-state flow	125
7.1.1	Hantush's method	125
7.2	Sloping unconfined aquifers, steady-state flow	127
7.2.1	Culmination-point method	127
7.3	Sloping unconfined aquifers, unsteady-state flow	128
7.3.1	Hantush's method	128
8	Anisotropic aquifers	133
8.1	Confined aquifers, anisotropic on the horizontal plane	133
8.1.1	Hantush's method	133
8.1.2	Hantush-Thomas's method	139
8.1.3	Neuman's extension of the Papadopulos method	140
8.2	Leaky aquifers, anisotropic on the horizontal plane	144
8.2.1	Hantush's method	144
8.3	Confined aquifers, anisotropic on the vertical plane	145
8.3.1	Week's method	145
8.4	Leaky aquifers, anisotropic on the vertical plane	147
8.4.1	Week's method	147
8.5	Unconfined aquifers, anisotropic on the vertical plane	148

9	Multi-layered aquifer systems	151
9.1	Confined two-layered aquifer systems with unrestricted cross flow, unsteady-state flow	152
9.1.1	Javandel-Witherspoon's method	152
9.2	Leaky two-layered aquifer systems with crossflow through aquitards, steady-state flow	154
9.2.1	Bruggeman's method	155
10	Partially penetrating wells	159
10.1	Confined aquifers, steady-state flow	159
10.1.1	Huisman's correction method I	162
10.1.2	Huisman's correction method II	162
10.2	Confined aquifers, unsteady-state flow	162
10.2.1	Hantush's modification of the Theis method	162
10.2.2	Hantush's modification of the Jacob method	167
10.3	Leaky aquifers, steady-state flow	169
10.4	Leaky aquifers, unsteady-state flow	169
10.4.1	Weeks's modifications of the Walton and the Hantush curve-fitting methods	169
10.5	Unconfined anisotropic aquifers, unsteady-state flow	170
10.5.1	Streltsova's curve-fitting method	170
10.5.2	Neuman's curve-fitting method	172
11	Large-diameter wells	175
11.1	Confined aquifers, unsteady-state flow	175
11.1.1	Papadopulos's curve-fitting method	175
11.2	Unconfined aquifers, unsteady-state flow	177
11.2.1	Boulton-Streltsova's curve-fitting method	177
12	Variable-discharge tests and tests in well fields	181
12.1	Variable discharge	181
12.1.1	Confined Aquifers, Birsoy-Summer's method	181
12.1.2	Confined aquifers, Aron-Scott's method	185
12.2	Free-flowing wells	187
12.2.1	Confined aquifers, unsteady-state flow, Hantush's method	188
12.2.2	Leaky aquifers, steady-state flow, Hantush-De Glee's method	189
12.3	Well field	189
12.3.1	Cooper-Jacob's method	189

13	Recovery tests	193
13.1	Recovery tests after constant-discharge tests	194
13.1.1	Confined aquifers, Theis's recovery method	194
13.1.2	Leaky aquifers, Theis's recovery method	195
13.1.3	Unconfined aquifers, Theis's recovery method	196
13.1.4	Partially penetrating wells, Theis's recovery method	196
13.2	Recovery tests after constant-drawdown tests	196
13.3	Recovery tests after variable-discharge tests	196
13.3.1	Confined aquifers, Birsoy-Summers's recovery method	196
14	Well-performance tests	199
14.1	Step-drawdown tests	200
14.1.1	Hantush-Bierschenk's method	201
14.1.2	Eden-Hazel's method (confined aquifers)	205
14.1.3	Rorabaugh's method	209
14.1.4	Sheahan's method	212
14.2	Recovery tests	215
14.2.1	Determination of the skin factor	215
15	Single-well tests with constant or variable discharges and recovery tests	219
15.1	Constant-discharge tests	220
15.1.1	Confined aquifers, Papadopulos-Cooper's method	220
15.1.2	Confined aquifers, Rushton-Singh's ratio method	221
15.1.3	Confined and leaky aquifers, Jacob's straight-line method	223
15.1.4	Confined and leaky aquifers, Hurr-Worthington's method	226
15.2	Variable-discharge tests	229
15.2.1	Confined aquifers, Birsoy-Summers's method	229
15.2.2	Confined aquifers, Jacob-Lohman's free-flowing-well method	230
15.2.3	Leaky aquifers, Hantush's free-flowing-well method	231
15.3	Recovery tests	232
15.3.1	Theis's recovery method	232
15.3.2	Birsoy-Summers's recovery method	233
15.3.3	Eden-Hazel's recovery method	233

16	Slug tests	237
16.1	Confined aquifers, unsteady-state flow	238
16.1.1	Cooper's method	238
16.1.2	Uffink's method for oscillation tests	241
16.2	Unconfined aquifers, steady-state flow	244
16.2.1	Bouwer-Rice's method	244
17	Uniformly-fractured aquifers, double-porosity concept	249
17.1	Introduction	249
17.2	Bourdet-Gringarten's curve-fitting method (observation wells)	251
17.3	Kazemi's et al.'s straight-line method (observation wells)	254
17.4	Warren-Root's straight-line method (pumped well)	257
18	Single vertical fractures	263
18.1	Introduction	263
18.2	Gringarten-Witherspoon's curve-fitting method for observation wells	265
18.3	Gringarten et al.'s curve-fitting method for the pumped well	269
18.4	Ramey-Gringarten's curve-fitting method	271
19	Single vertical dikes	275
19.1	Introduction	275
19.2	Curve-fitting methods for observation wells	277
19.2.1	Boonstra-Boehmer's curve fitting method	277
19.2.2	Boehmer-Boonstra's curve-fitting method	279
19.3	Curve-fitting methods for the pumped well	280
19.3.1	For early and medium pumping times	280
19.3.2	For late pumping times	282
	Annexes	289
	References	367
	Author's index	373

1 Basic concepts and definitions

When working on problems of groundwater flow, the geologist or engineer has to find reliable values for the hydraulic characteristics of the geological formations through which the groundwater is moving. Pumping tests have proved to be one of the most effective ways of obtaining such values.

Analyzing and evaluating pumping test data, however, is as much an art as a science. It is a science because it is based on theoretical models that the geologist or engineer must understand and on thorough investigations that he must conduct into the geological formations in the area of the test. It is an art because different types of aquifers can exhibit similar drawdown behaviours, which demand interpretational skills on the part of the geologist or engineer. We hope that this book will serve as a guide in both the science and the art.

The equations we present in this book are from well hydraulics. We have omitted any lengthy derivations of the equations because these can be found in the original publications listed in our References. With some exceptions, we present the equations in their final form, emphasizing the assumptions and conditions that underlie them, and outlining the procedures that are to be followed for their successful application.

'Hard rocks', both as potential sources of water and depositories for chemical or radioactive wastes, are receiving increasing attention in hydrogeology. We shall therefore be discussing some recent developments in the interpretation of pumping test data from such rocks.

This chapter summarizes the basic concepts and definitions of terms relevant to our subject. The next chapter describes how to conduct a pumping test. The remaining chapters all deal with the analysis and evaluation of pumping test data from a variety of aquifer types or aquifer systems, and from tests conducted under particular technical conditions.

1.1 Aquifer, aquitard, and aquiclude

An aquifer is defined as a saturated permeable geological unit that is permeable enough to yield economic quantities of water to wells. The most common aquifers are unconsolidated sand and gravels, but permeable sedimentary rocks such as sandstone and limestone, and heavily fractured or weathered volcanic and crystalline rocks can also be classified as aquifers.

An aquitard is a geological unit that is permeable enough to transmit water in significant quantities when viewed over large areas and long periods, but its permeability is not sufficient to justify production wells being placed in it. Clays, loams and shales are typical aquitards.

An aquiclude is an impermeable geological unit that does not transmit water at all. Dense unfractured igneous or metamorphic rocks are typical aquicludes. In nature, truly impermeable geological units seldom occur; all of them leak to some extent, and must therefore be classified as aquitards. In practice, however, geological units

can be classified as aquicludes when their permeability is several orders of magnitude lower than that of an overlying or underlying aquifer.

The reader will note that the above definitions are relative ones; they are purposely imprecise with respect to permeability.

1.2 Aquifer types

There are three main types of aquifer: confined, unconfined, and leaky (Figure 1.1).

1.2.1 Confined aquifer

A confined aquifer (Figure 1.1A) is bounded above and below by an aquiclude. In a confined aquifer, the pressure of the water is usually higher than that of the atmosphere, so that if a well taps the aquifer, the water in it stands above the top of the aquifer, or even above the ground surface. We then speak of a free-flowing or artesian well.

1.2.2 Unconfined aquifer

An unconfined aquifer (Figure 1.1B), also known as a watertable aquifer, is bounded below by an aquiclude, but is not restricted by any confining layer above it. Its upper boundary is the watertable, which is free to rise and fall. Water in a well penetrating an unconfined aquifer is at atmospheric pressure and does not rise above the watertable.

1.2.3 Leaky aquifer

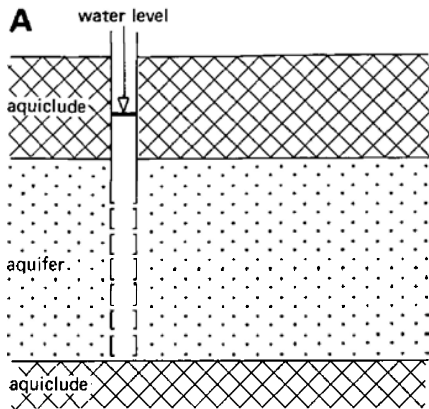
A leaky aquifer (Figure 1.1C and D), also known as a semi-confined aquifer, is an aquifer whose upper and lower boundaries are aquitards, or one boundary is an aquitard and the other is an aquiclude. Water is free to move through the aquitards, either upward or downward. If a leaky aquifer is in hydrological equilibrium, the water level in a well tapping it may coincide with the watertable. The water level may also stand above or below the watertable, depending on the recharge and discharge conditions.

In deep sedimentary basins, an interbedded system of permeable and less permeable layers that form a multi-layered aquifer system (Figure 1.1E), is very common. But such an aquifer system is more a succession of leaky aquifers, separated by aquitards, rather than a main aquifer type.

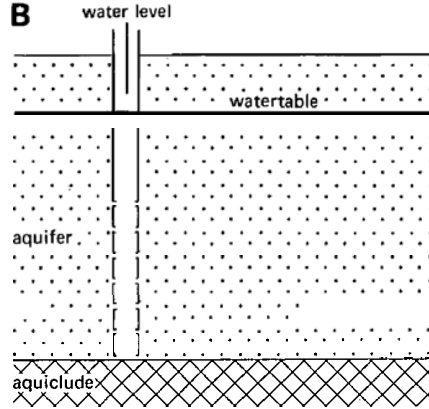
1.3 Anisotropy and heterogeneity

Most well hydraulics equations are based on the assumption that aquifers and aquitards are homogeneous and isotropic. This means that the hydraulic conductivity is the same throughout the geological formation and is the same in all directions (Figure

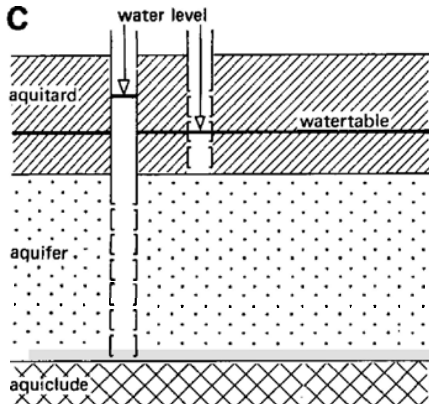
CONFINED AQUIFER



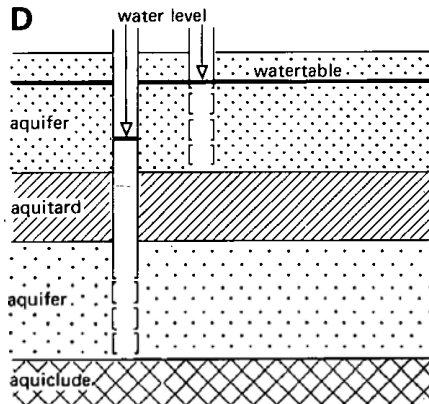
UNCONFINED AQUIFER



LEAKY AQUIFER



LEAKY AQUIFER



MULTI-LAYERED LEAKY AQUIFER SYSTEM

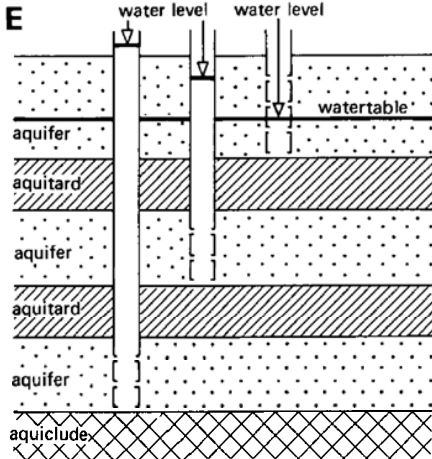


Figure 1.1 Different types of aquifers
A. Confined aquifer
B. Unconfined aquifer
C. and D. Leaky aquifers
E. Multi-layered leaky aquifer

1.2A). The individual particles of a geological formation, however, are seldom spherical so that, when deposited under water, they tend to settle on their flat sides. Such a formation can still be homogeneous, but its hydraulic conductivity in horizontal direction, K_h , will be significantly greater than its hydraulic conductivity in vertical direction, K_v (Figure 1.2B). This phenomenon is called anisotropy.

The lithology of most geological formations tends to vary significantly, both horizontally and vertically. Consequently, geological formations are seldom homogeneous. Figure 1.2C is an example of layered heterogeneity. Heterogeneity occurs not only in the way shown in the figure: individual layers may pinch out; their grain size may vary in horizontal direction; they may contain lenses of other grain sizes; or they may be discontinuous by faulting or scour-and-fill structures. In horizontally-stratified alluvial formations, the K_h/K_v ratios range from 2 to 10, but values as high as 100 can occur, especially where clay layers are present.

Anisotropy is a common property of fractured rocks (Figure 1.2D). The hydraulic conductivity in the direction of the main fractures is usually significantly greater than that normal to those fractures.

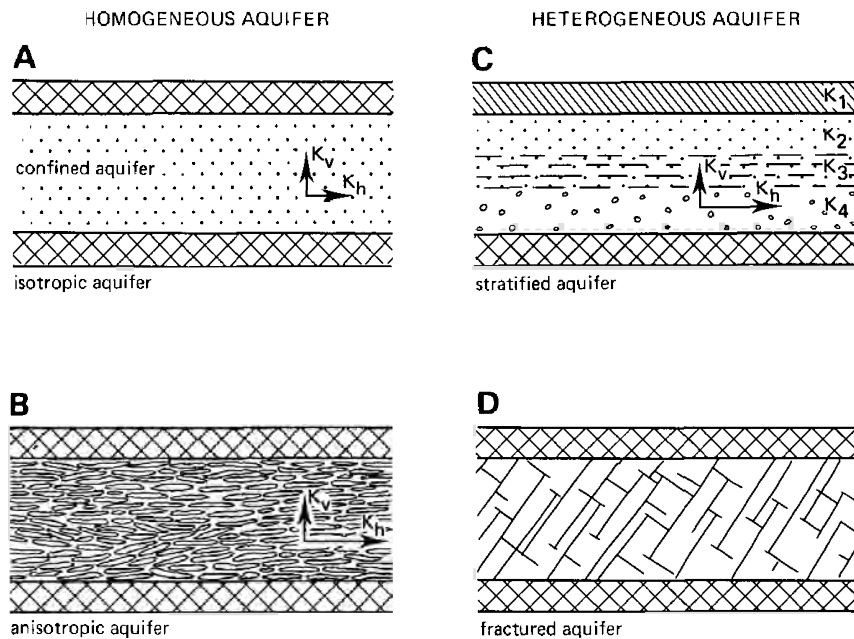


Figure 1.2 Homogeneous and heterogeneous aquifers, isotropic and anisotropic

- A. Homogeneous aquifer, isotropic
- B. Homogeneous aquifer, anisotropic
- C. Heterogeneous aquifer, stratified
- D. Heterogeneous aquifer, fractured

If the principal directions of anisotropy are known, one can transform an anisotropic system into an isotropic system by changing the coordinates. In the new coordinate system, the basic well-flow equation is again isotropic and the common equations can be used.

1.4 Bounded aquifers

Another common assumption in well hydraulics is that the pumped aquifer is horizontal and of infinite extent. But, viewed on a regional scale, some aquifers slope, and none of them extend to infinity because complex geological processes cause interfingering of layers and pinchouts of both aquifers and aquitards. At some places, aquifers and aquitards are cut by deeply incised channels, estuaries, or the ocean. In other words, aquifers and aquitards are laterally bounded in one way or another. Figure 1.3 shows some examples. The interpretation of pumping tests conducted in the vicinity of such boundaries requires special techniques, which we shall be discussing.

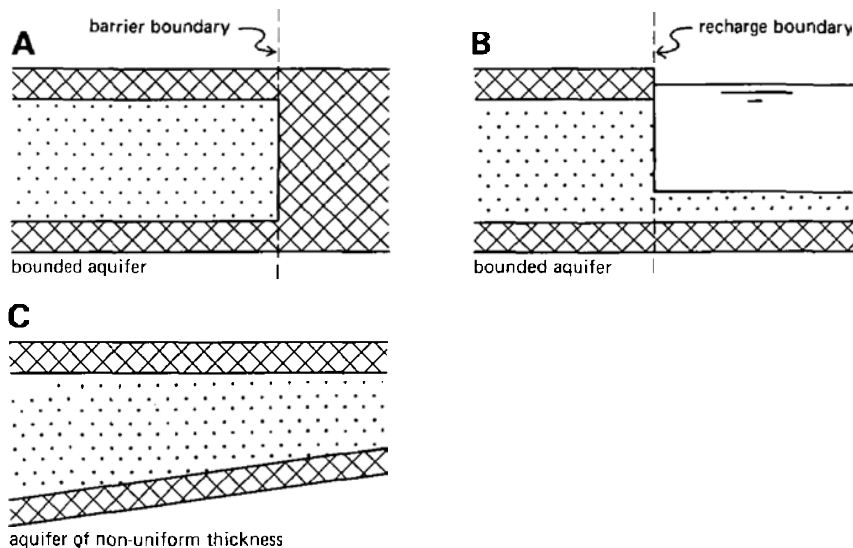


Figure 1.3 Bounded aquifers
A, B, and C

1.5 Steady and unsteady flow

There are two types of well-hydraulics equations: those that describe steady-state flow towards a pumped well and those that describe the unsteady-state flow.

Steady-state flow is independent of time. This means that the water level in the pumped well and in surrounding piezometers does not change with time. Steady-state flow occurs, for instance, when the pumped aquifer is recharged by an outside source, which may be rainfall, leakage through aquitards from overlying and/or underlying unpumped aquifers, or from a body of open water that is in direct hydraulic contact

with the pumped aquifer. In practice, it is said that steady-state flow is attained if the changes in the water level in the well and piezometers have become so small with time that they can be neglected. As pumping continues, the water level may drop further, but the hydraulic gradient induced by the pumping will not change. In other words, the flow towards the well has attained a pseudo-steady-state.

In well hydraulics of fractured aquifers, the term pseudo-steady-state is used for the interporosity flow from the matrix blocks to the fractures. This flow occurs in response to the difference between the average hydraulic head in the matrix blocks and the average hydraulic head in the fractures. Spatial variation in hydraulic head gradients in the matrix blocks is ignored and the flow through the fractures to the well is radial and unsteady.

Unsteady-state flow occurs from the moment pumping starts until steady-state flow is reached. Consequently, if an infinite, horizontal, completely confined aquifer of constant thickness is pumped at a constant rate, there will always be unsteady-state flow. In practice, the flow is considered to be unsteady as long as the changes in water level in the well and piezometers are measurable or, in other words, as long as the hydraulic gradient is changing in a measurable way.

1.6 Darcy's law

Darcy's law states that the rate of flow through a porous medium is proportional to the loss of head, and inversely proportional to the length of the flow path, or

$$v = K \frac{\Delta h}{\Delta l} \quad (1.1)$$

or, in differential form

$$v = K \frac{dh}{dl} \quad (1.2)$$

where $v = Q/A$, which is the specific discharge, also known as the Darcy velocity or Darcy flux (Length/Time), $Q =$ volume rate of flow (Length³/Time), $A =$ cross-sectional area normal to flow direction (Length²), $\Delta h = h_2 - h_1$, which is the head loss, whereby h_1 and h_2 are the hydraulic heads measured at Points 1 and 2 (Length), $\Delta l =$ the distance between Points 1 and 2 (Length), $dh/dl = i$, which is the hydraulic gradient (dimensionless), and $K =$ constant of proportionality known as the hydraulic conductivity (Length/Time).

Alternatively, Darcy's law can be written as

$$Q = K \frac{dh}{dl} A \quad (1.3)$$

Note that the specific discharge v has the dimensions of a velocity, i.e. Length/Time. The concept specific discharge assumes that the water is moving through the entire porous medium, solid particles as well as pores, and is thus a macroscopic concept. The great advantage of this concept is that the specific discharge can be easily measured. It must, however, be clearly differentiated from the microscopic velocities, which are real velocities. Hence, if we are interested in real flow velocities, as in prob-

lems of groundwater pollution and solute transport, we must consider the actual paths of individual water particles as they find their way through the pores of the medium. In other words, we must consider the porosity of the transmitting medium and can write

$$v_a = \frac{v}{n} \text{ or } v_a = \frac{Q}{nA} \quad (1.4)$$

where v_a = real velocity of the flow, and n = porosity of the water-transmitting medium.

In using Darcy's law, one must know the range of its validity. After all, Darcy (1856) conducted his experiments on sand samples in the laboratory. So, Darcy's law is valid for laminar flow, but not for turbulent flow, as may happen in cavernous limestone or fractured basalt. In case of doubt, one can use the Reynolds number as a criterion to distinguish between laminar and turbulent flow. The Reynolds number is expressed as

$$N_R = \rho \frac{vd}{\mu} \quad (1.5)$$

where ρ is the fluid density, v is the specific discharge, μ is the viscosity of the fluid, and d is a representative length dimension of the porous medium, usually taken as a mean grain diameter or a mean pore diameter.

Experiments have shown that Darcy's law is valid for $N_R < 1$ and that no serious errors are created up to $N_R = 10$. This value thus represents an upper limit to the validity of Darcy's law. It should not be considered a unique limit, however, because turbulence occurs gradually. At full turbulence ($N_R < 100$), the head loss varies approximately with the second power of the velocity rather than linearly. Fortunately, most groundwater flow occurs with $N_R < 1$ so that Darcy's law applies. Only in exceptional situations, as in a rock with wide openings, or where steep hydraulic gradients exist, as in the near vicinity of a pumped well, will the criterion of laminar flow not be satisfied and Darcy's law will be invalid.

Darcy's law is also invalid at low hydraulic gradients, as may occur in compact clays, because, for low values of i , the relation between v and i is not linear. It is impossible to give a unique lower limit to the hydraulic gradients at which Darcy's law is still valid, because the values of i vary with the type and structure of the clay, while the mineral content of the water also plays a role (De Marsily 1986).

1.7 Physical properties

In the equations describing the flow to a pumped well, various physical properties and parameters of aquifers and aquitards appear. These will be discussed below.

1.7.1 Porosity (n)

The porosity of a rock is its property of containing pores or voids. If we divide the total unit volume V_T of an unconsolidated material into the volume of its solid portion

V_s and the volume of its voids V_v , we can define the porosity as $n = V_v/V_T$. Porosity is usually expressed as a decimal fraction or as a percentage.

With consolidated and hard rocks, a distinction is usually made between primary porosity, which is present when the rock is formed, and secondary porosity, which develops later as a result of solution or fracturing. As Figure 1.4 shows, fractures

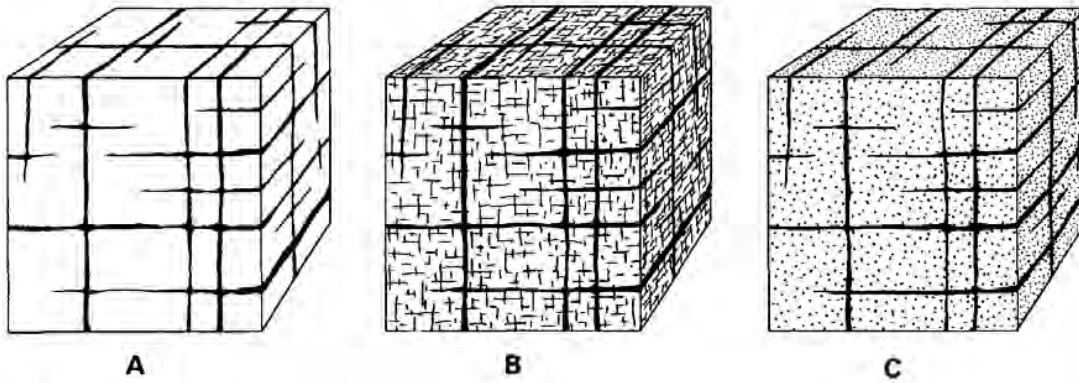


Figure 1.4 Porosity systems
 A. Single porosity
 B. Microfissures
 C. Double porosity

can be oriented in three main directions, which cut the rock into blocks. In theory, the primary porosity of a dense solid rock may be zero and the rock matrix will be impermeable. Such a rock can be regarded as a single-porosity system (Figure 1.4A). In some rocks, notably crystalline rocks, the main fractures are accompanied by a dense system of microfissures, which considerably increase the porosity of the rock matrix (Figure 1.4B). In contrast, the primary porosity of granular geological formations (e.g. sandstone) can be quite significant (Figure 1.4C). When such a formation is fractured, it can be regarded as a double-porosity system because the two types of porosities coexist: the primary or matrix porosity and the secondary or fracture porosity.

Table 1.1 gives some porosity values for unconsolidated materials and rocks.

Table 1.1 Range of porosity values (n) in percentages

Rocks		Unconsolidated materials	
Sandstone	5–30	Gravel	25–40
Limestone	0–20	Sand	25–50
Karstic limestone	5–50	Silt	35–50
Shale	0–10	Clay	40–70
Basalt, fractured	5–50		
Crystalline rock	0–5		
Crystalline rock, fractured	0–10		

1.7.2 Hydraulic conductivity (K)

The hydraulic conductivity is the constant of proportionality in Darcy's law (Equation 1.3). It is defined as the volume of water that will move through a porous medium in unit time under a unit hydraulic gradient through a unit area measured at right angles to the direction of flow. Hydraulic conductivity can have any units of Length/Time, for example m/d.

The hydraulic conductivity of fractured rocks depends largely on the density of the fractures and the width of their apertures. Fractures can increase the hydraulic conductivity of solid rocks by several orders of magnitude.

The significant effect that fractures can have on the hydraulic conductivity of hard rocks has been treated by various authors. Maini and Hocking (1977), for example, as quoted by De Marsily (1986), give the equivalence between the hydraulic conductivity of a fractured rock and that of a porous (granular) aquifer. From their diagram, it follows that the flow through, say, a 100 m thick cross-section of a porous medium with a hydraulic conductivity of 10^{-12} m/d could, in a fractured medium with an impermeable rock matrix, also come from one single fracture only 0.2 mm wide.

For orders of magnitude of K for different materials, see Table 1.2.

Table 1.2 Order of magnitude of K for different kinds of rock (from Bouwer 1978)

Geological classification	K (m/d)	
Unconsolidated materials:		
Clay	10^{-8}	-10^{-2}
Fine sand	1	- 5
Medium sand	5	$- 2 \times 10^1$
Coarse sand	2×10^1	-10^2
Gravel	10^2	-10^3
Sand and gravel mixes	5	-10^2
Clay, sand, gravel mixes (e.g. till)	10^{-3}	-10^{-1}
Rocks:		
Sandstone	10^{-3}	-1
Carbonate rock with secondary porosity	10^{-2}	-1
Shale	10^{-7}	
Dense solid rock	$< 10^{-5}$	
Fractured or weathered rock (Core samples)	Almost 0 - 3×10^2	
Volcanic rock	Almost 0 - 10^3	

1.7.3 Interporosity flow coefficient (λ)

When a confined fractured aquifer of the double-porosity type is pumped, the interporosity flow coefficient controls the flow in the aquifer. It indicates how easily water can flow from the aquifer matrix blocks into the fractures, and is defined as

$$\lambda = \alpha r^2 \frac{K_m}{K_r} \quad (1.6)$$

where α is a shape factor that reflects the geometry of the matrix blocks, r is the distance to the well, K is hydraulic conductivity, f is the fracture, and m is matrix block. The dimension of λ is reciprocal area.

1.7.4 Compressibility (α and β)

Compressibility is an important material and fluid property in the analysis of unsteady flow to wells. It describes the change in volume or the strain induced in an aquifer (or aquitard) under a given stress, or

$$\alpha = \frac{-dV_T/V_T}{d\sigma_e} \quad (1.7)$$

where V_T is the total volume of a given mass of material and $d\sigma_e$ is the change in effective stress. Compressibility is expressed in m^2/N or Pa^{-1} . Its value for clay ranges from 10^{-6} to 10^{-8} , for sand from 10^{-7} to 10^{-9} , for gravel and fractured rock from 10^{-8} to $10^{-10} m^2/N$.

Similarly, the compressibility of water is defined as

$$\beta = \frac{-dV_w/V_w}{dp} \quad (1.8)$$

A change in the water pressure dp induces a change in the volume V_w of a given mass of water. The compressibility of groundwater under the range of temperatures that are usually encountered can be taken constant as $4.4 \times 10^{-10} m^2/N$ (or Pa^{-1}).

1.7.5 Transmissivity (KD or T)

Transmissivity is the product of the average hydraulic conductivity K and the saturated thickness of the aquifer D . Consequently, transmissivity is the rate of flow under a unit hydraulic gradient through a cross-section of unit width over the whole saturated thickness of the aquifer. The effective transmissivity, as used for fractured media, is defined as

$$T = \sqrt{T_{f(x)} T_{f(y)}} \quad (1.9)$$

where f refers to the fractures and x and y to the principal axes of permeability. Transmissivity has the dimensions of $Length^3/Time \times Length$ or $Length^2/Time$ and is, for example, expressed in m^2/d or m^2/s .

1.7.6 Specific storage (S_s)

The specific storage of a saturated confined aquifer is the volume of water that a unit volume of aquifer releases from storage under a unit decline in hydraulic head. This release of water from storage under conditions of decreasing head h stems from the compaction of the aquifer due to increasing effective stress σ_e and the expansion

of the water due to decreasing pressure p . Hence, the earlier-defined compressibilities of material and water play a role in these two mechanisms. The specific storage is defined as

$$S_s = \rho g(\alpha + n\beta) \quad (1.10)$$

where ρ is the mass density of water (M/L^3), g is the acceleration due to gravity (N/L^3), and the other symbols are as defined earlier. The dimension of specific storage is Length^{-1} .

1.7.7 Storativity (S)

The storativity of a saturated confined aquifer of thickness D is the volume of water released from storage per unit surface area of the aquifer per unit decline in the component of hydraulic head normal to that surface. In a vertical column of unit area extending through the confined aquifer, the storativity S equals the volume of water released from the aquifer when the piezometric surface drops over a unit distance. Storativity is defined as

$$S = \rho g D(\alpha + n\beta) = S_s D \quad (1.11)$$

As storativity involves a volume of water per volume of aquifer, it is a dimensionless quantity. Its values in confined aquifers range from 5×10^{-5} to 5×10^{-3} .

1.7.8 Storativity ratio (ω)

The storativity ratio is a parameter that controls the flow from the aquifer matrix blocks into the fractures of a confined fractured aquifer of the double-porosity type. (See also Sections 1.7.1 and 1.7.3.) It is defined as

$$\omega = \frac{S_f}{S_f + S_m} \quad (1.12)$$

where S is the storativity and f is fracture and m is matrix block. Being a ratio, ω is dimensionless.

1.7.9 Specific yield (S_y)

The specific yield is the volume of water that an unconfined aquifer releases from storage per unit surface area of aquifer per unit decline of the watertable. The values of the specific yield range from 0.01 to 0.30 and are much higher than the storativities of confined aquifers. In unconfined aquifers, the effects of the elasticity of the aquifer matrix and of the water are generally negligible. Specific yield is sometimes called effective porosity, unconfined storativity, or drainable pore space. Small interstices do not contribute to the effective porosity because the retention forces in them are greater than the weight of water. Hence, no groundwater will be released from small interstices by gravity drainage.

It is obvious that water can only move through pores that are interconnected. Hard rocks may contain numerous unconnected pores in which the water is stagnant. The most common example is that of secondary dolomite. Dolomitization increases the porosity because the diagenetic transformation of calcite into dolomite is accompanied by a 13% reduction in volume of the rock (Matthess 1982). The porosity of secondary dolomite is high, 20 to 30%, but the effective porosity is low because the pores are seldom interconnected. Water in 'dead-end' pores is also almost stagnant, so such pores are excluded from the effective porosity. They do play a role, of course, when one is studying the mechanisms of compressibility and solute transport in porous media.

In fractured rocks, water only moves through the fractures, even if the unfractured matrix blocks are porous. This means that the effective porosity of the rock mass is linked to the volume of these fractures. A fractured granite, for example, has a matrix porosity of 1 to 2 %, but its effective porosity is less than 1 % because the matrix itself has a very low permeability (De Marsily 1986).

Table 1.3 gives some representative values of specific yields for different materials.

Table 1.3 Representative values of specific yield (Johnson 1967)

Material	S_y	Material	S_y
Coarse gravel	23	Limestone	14
Medium gravel	24	Dune sand	38
Fine gravel	25	Loess	18
Coarse sand	27	Peat	44
Medium sand	28	Schist	26
Fine sand	23	Siltstone	12
Silt	8	Silty till	6
Clay	3	Sandy till	16
Fine-grained sandstone	21	Gravelly till	16
Medium-grained sandstone	27	Tuff	21

1.7.10 Diffusivity (KD/S)

The hydraulic diffusivity is the ratio of the transmissivity and the storativity of a saturated aquifer. It governs the propagation of changes in hydraulic head in the aquifer. Diffusivity has the dimension of Length²/Time.

1.7.11 Hydraulic resistance (c)

The hydraulic resistance characterizes the resistance of an aquitard to vertical flow, either upward or downward. It is the reciprocal of the leakage or leakage coefficient K'/D' in Darcy's law when this law is used to characterize the amount of leakage through the aquitard; K' = the hydraulic conductivity of the aquitard for vertical flow, and D' = the thickness of the aquitard. The hydraulic resistance is thus defined as

$$c = \frac{D'}{K'} \quad (1.13)$$

and has the dimension of Time. It is often expressed in days. Values of c vary widely, from some hundreds of days to several ten thousand days; for aquicludes, c is infinite.

1.7.12 Leakage factor (L)

The leakage factor, or characteristic length, is a measure for the spatial distribution of the leakage through an aquitard into a leaky aquifer and vice versa. It is defined as

$$L = \sqrt{KDc} \quad (1.14)$$

Large values of L indicate a low leakage rate through the aquitard, whereas small values of L mean a high leakage rate. The leakage factor has the dimension of Length, expressed, for example, in metres.

SE ROA 37520

2 Pumping tests

2.1 The principle

The principle of a pumping test is that if we pump water from a well and measure the discharge of the well and the drawdown in the well and in piezometers at known distances from the well, we can substitute these measurements into an appropriate well-flow equation and can calculate the hydraulic characteristics of the aquifer (Figure 2.1).

2.2 Preliminary studies

Before a pumping test is conducted, geological and hydrological information on the following should be collected:

- The geological characteristics of the subsurface (i.e. all those lithological, stratigraphic, and structural features that may influence the flow of groundwater);
- The type of aquifer and confining beds;
- The thickness and lateral extent of the aquifer and confining beds:
 - The aquifer may be bounded laterally by barrier boundaries of impermeable material (e.g. the bedrock sides of a buried valley, a fault, or simply lateral changes in the lithology of the aquifer material);
 - Of equal importance are any lateral recharge boundaries (e.g. where the aquifer is in direct hydraulic contact with a deeply incised perennial river or canal, a lake,

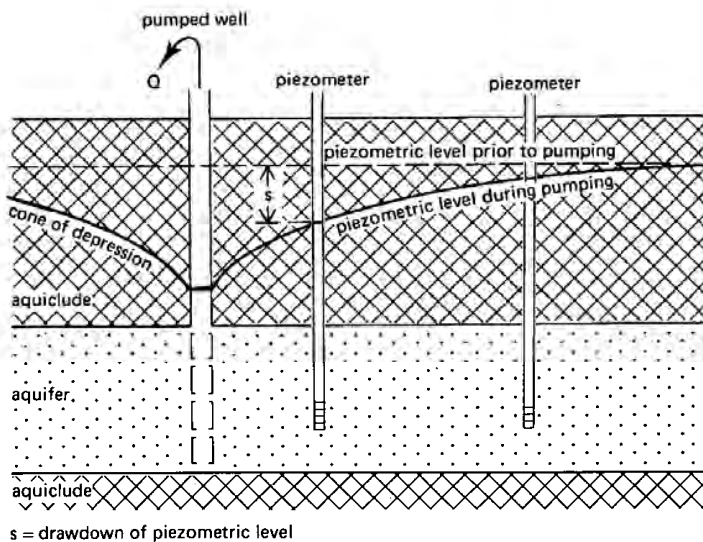


Figure 2.1 Drawdown in a pumped aquifer

- or the ocean) or any horizontal recharge boundaries (e.g. where percolating rain or irrigation water causes the watertable of an unconfined aquifer to rise, or where an aquitard leaks and recharges the aquifer);
- Data on the groundwater-flow system: horizontal or vertical flow of groundwater, watertable gradients, and regional trends in groundwater levels;
 - Any existing wells in the area. From the logs of these wells, it may be possible to derive approximate values of the aquifer's transmissivity and storativity and their spatial variation. It may even be possible to use one of those wells for the test, thereby reducing the cost of field work. Sometimes, however, such a well may produce uncertain results because details of its construction and condition are not available.

2.3 Selecting the site for the well

When an existing well is to be used for the test or when the hydraulic characteristics of a specific location are required, the well site is predetermined and one cannot move to another, possibly more suitable site. When one has the freedom to choose, however, the following points should be kept in mind:

- The hydrogeological conditions should not change over short distances and should be representative of the area under consideration, or at least a large part of it;
- The site should not be near railways or motorways where passing trains or heavy traffic might produce measurable fluctuations in the hydraulic head of a confined aquifer;
- The site should not be in the vicinity of existing discharging wells;
- The pumped water should be discharged in a way that prevents its return to the aquifer;
- The gradient of the watertable or piezometric surface should be low;
- Manpower and equipment must be able to reach the site easily.

2.4 The well

After the well site has been chosen, drilling operations can begin. The well will consist of an open-ended pipe, perforated or fitted with a screen in the aquifer to allow water to enter the pipe, and equipped with a pump to lift the water to the surface. For the design and construction of wells, we refer to Driscoll (1986), *Groundwater Manual* (1981), and Genetier (1984), where full details are given. Some of the major points are summarized below.

2.4.1 Well diameter

A pumping test does not require expensive large-diameter wells. If a suction pump placed on the ground surface is used, as in shallow watertable areas, the diameter of the well can be small. A submersible pump requires a well diameter large enough to accommodate the pump.

The diameter of the well can be varied without greatly affecting the yield of the well. Doubling the diameter would only increase the yield by about 10 per cent, other things being equal.

2.4.2 Well depth

The depth of the well will usually be determined from the log of an exploratory bore hole or from the logs of nearby existing wells, if any. The well should be drilled to the bottom of the aquifer, if possible, because this has various advantages, one of which is that it allows a longer well screen to be placed, which will result in a higher well yield.

During drilling operations, samples of the geological formations that are pierced should be collected and described lithologically. Records should be kept of these lithological descriptions, and the samples themselves should be stored for possible future reference.

2.4.3 Well screen

The length of the well screen and the depth at which it is placed will largely be decided by the depth at which the coarsest materials are found. In the lithological descriptions, therefore, special attention should be given to the grain size of the various materials. If geophysical well logs are run immediately after the completion of drilling, a preliminary interpretation of those logs will help greatly in determining the proper depth at which to place the screen.

If the aquifer consists of coarse gravel, the screen can be made locally by sawing, drilling, punching, or cutting openings in the pipe. In finer formations, finer openings are needed. These may vary in size from some tenths of a millimetre to several millimetres. Such precision-made openings can only be obtained in factory-made screens. To prevent the blocking of well screen openings by spherical grains, long narrow slits are preferable. The slots should retain 30 to 50 per cent of the aquifer material, depending on the uniformity coefficient of the aquifer sample. (For details, see Driscoll 1986; Huisman 1972.)

The well screen should be slotted or perforated over no more than 30 to 40 per cent of its circumference to keep the entrance velocity low, say less than about 3 cm/s. At this velocity, the friction losses in the screen openings are small and may even be negligible.

A general rule is to screen the well over at least 80 per cent of the aquifer thickness because this makes it possible to obtain about 90 per cent or more of the maximum yield that could be obtained if the entire aquifer were screened. Another even more important advantage of this screen length is that the groundwater flow towards the well can be assumed to be horizontal, an assumption that underlies almost all well-flow equations (Figure 2.2A).

There are some exceptions to the general rule:

- In unconfined aquifers, it is common practice to screen only the lower half or lower one-third of the aquifer because, if appreciable drawdowns occur, the upper part

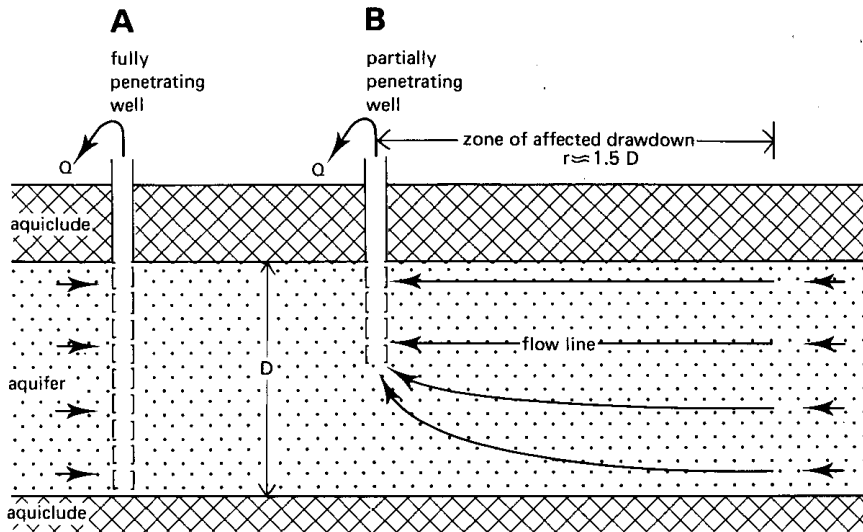


Figure 2.2 A) A fully penetrating well;
 B) A partially penetrating well

of a longer well screen would fall dry;

- In a very thick aquifer, it will be obvious that the length of the screen will have to be less than 80 per cent, simply for reasons of economy. Such a well is said to be a partially penetrating well. It induces vertical-flow components, which can extend outwards from the well to distances roughly equal to 1.5 times the thickness of the aquifer (Figure 2.2B). Within this radius, the measured drawdowns have to be corrected before they can be used in calculating the aquifer characteristics;
- Wells in consolidated aquifers do not need a well screen because the material around the well is stable.

2.4.4 Gravel pack

It is easier for water to enter the well if the aquifer material immediately surrounding the screen is removed and replaced by artificially-graded coarser material. This is known as a gravel pack. When the well is pumped, the gravel pack will retain much of the aquifer material that would otherwise enter the well. With a gravel pack, larger slot sizes can be selected for the screen. The thickness of the pack should be in the range of 8 to 15 cm. Gravel pack material should be clean, smoothly-rounded grains. Details on the gravel sizes to be used in gravel packs are given by Driscoll (1986) and Huisman (1972).

2.4.5 The pump

After the well has been drilled, screened, and gravel-packed, as necessary, a pump has to be installed to lift the water. It is beyond the scope of this book to discuss

the many kinds of pumps that might be used, so some general remarks must suffice:

- The pump and power unit should be capable of operating continuously at a constant discharge for a period of at least a few days. An even longer period may be required for unconfined or leaky aquifers, and especially for fractured aquifers. The same applies if drawdown data from piezometers at great distances from the well are to be analyzed. In such cases, pumping should continue for several days more;
- The capacity of the pump and the rate of discharge should be high enough to produce good measurable drawdowns in piezometers as far away as, say, 100 or 200 m from the well, depending on the aquifer conditions.

After the pump has been installed, the well should be developed by being pumped at a low discharge rate. When the initially cloudy water becomes clear, the discharge rate should be increased and pumping continued until the water clears again. This procedure should be repeated until the desired discharge rate for the test is reached or exceeded.

2.4.6 Discharging the pumped water

The water delivered by the well should be prevented from returning to the aquifer. This can be done by conveying the water through a large-diameter pipe, say over a distance of 100 or 200 m, and then discharging it into a canal or natural channel. The water can also be conveyed through a shallow ditch, but the bottom of the ditch should be sealed with clay or plastic sheets to prevent leakage. Piezometers can be used to check whether any water is lost through the bottom of the ditch.

2.5 Piezometers

A piezometer (Figure 2.3) is an open-ended pipe, placed in a borehole that has been drilled to the desired depth in the ground. The bottom tip of the piezometer is fitted with a perforated or slotted screen, 0.5 to 1 m long, to allow the inflow of water. A plug at the bottom and jute or cotton wrapped around the screen will prevent the entry of fine aquifer material.

The annular space around the screen should be filled with a gravel pack or uniform coarse sand to facilitate the inflow of water. The rest of the annular space can be filled with any material available, except where the presence of aquitards requires a seal of bentonite clay or cement grouting to prevent leakage along the pipe. Experience has taught us that very fine clayey sand provides almost as good a seal as bentonite. It produces an error of less than 0.03 m, even when the difference in head between the aquifers is more than 30 m.

The water levels measured in piezometers represent the average head at the screen of the piezometers. Rapid and accurate measurements can best be made in small-diameter piezometers. If their diameter is large, the volume of water contained in them may cause a time lag in changes in drawdown. When the depth to water is to be measured manually, the diameter of the piezometers need not be larger than 5 cm. If automatic water-level recorders or electronic water pressure transducers are used, larger-diameter piezometers will be needed. In a heterogeneous aquifer with intercalated

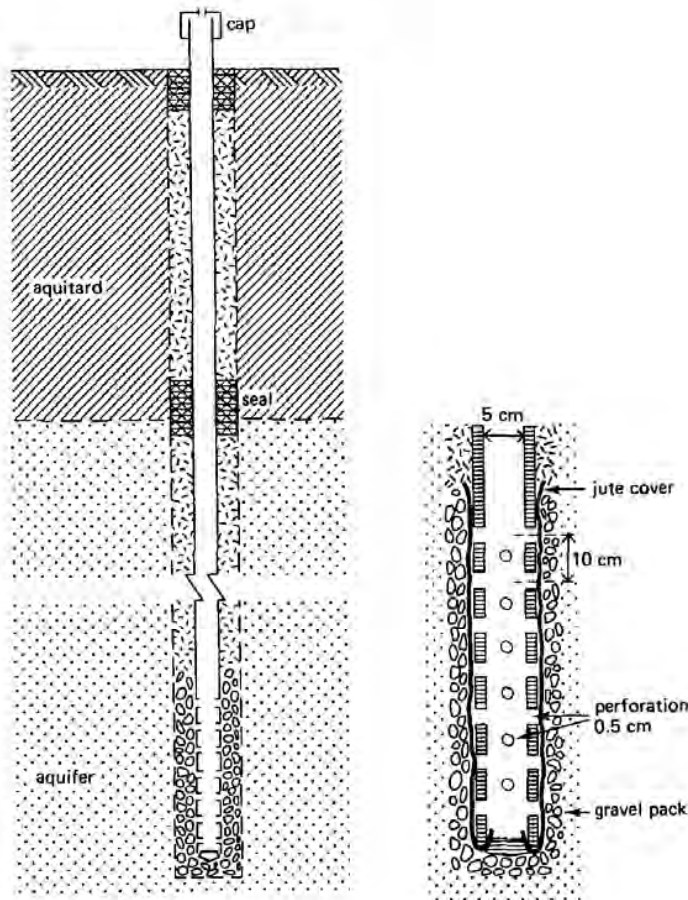


Figure 2.3 A piezometer

aquitards, the diameter of the bore holes should be large enough to allow a cluster of piezometers to be placed at different depths (Figure 2.4).

After the piezometers have been installed, it is advisable to pump or flush them for a short time to remove silt and clay particles. This will ensure that they function properly during the test.

After the well has been completed and its information analyzed, one has to decide how many piezometers to place, at what depths, and at what distances from the well.

2.5.1 The number of piezometers

The question of how many piezometers to place depends on the amount of information needed, and especially on its required degree of accuracy, but also on the funds available for the test.

Although it will be shown in later chapters that drawdown data from the well itself or from one single piezometer often permit the calculation of an aquifer's hydraulic characteristics, it is nevertheless always best to have as many piezometers as conditions

permit. Three, at least, are recommended. The advantage of having more than one piezometer is that the drawdowns measured in them can be analyzed in two ways: by the time-drawdown relationship and by the distance-drawdown relationship. Obviously, the results of such analyses will be more accurate and will be representative of a larger volume of the aquifer.

2.5.2 Their distance from the well

Piezometers should be placed not too near the well, but not too far from it either. This rather vague statement needs some explanation. So, as will be outlined below, the distances at which piezometers should be placed depends on the type of aquifer, its transmissivity, the duration of pumping, the discharge rate, the length of the well screen, and whether the aquifer is stratified or fractured.

The type of aquifer

When a confined aquifer is pumped, the loss of hydraulic head propagates rapidly because the release of water from storage is entirely due to the compressibility of the aquifer material and that of the water. The drawdown will be measurable at great distances from the well, say several hundred metres or more.

In unconfined aquifers, the loss of head propagates slowly. Here, the release of water from storage is mostly due to the dewatering of the zone through which the

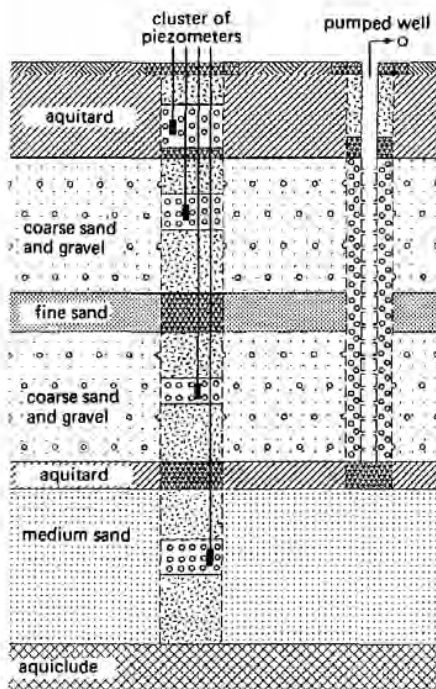


Figure 2.4 Cluster of piezometers in a heterogeneous aquifer intercalated with aquitards

water is moving, and only partially due to the compressibility of the water and aquifer material. Unless pumping continues for several days, the drawdown will only be measurable fairly close to the well, say not much more than about 100 m.

A leaky aquifer occupies an intermediate position. Depending on the hydraulic resistance of its confining aquitard (or aquitards), a leaky aquifer will resemble either a confined or an unconfined aquifer.

Transmissivity

When the transmissivity of the aquifer is high, the cone of depression induced by pumping will be wide and flat (Figure 2.5A). When the transmissivity is low, the cone will be steep and narrow (Figure 2.5B). In the first case, piezometers can be placed farther from the well than they can in the second.

The duration of the test

Theoretically, in an extensive aquifer, as long as the flow to the well is unsteady, the cone of depression will continue to expand as pumping continues. Therefore, for tests of long duration, piezometers can be placed at greater distances from the well than for tests of short duration.

The discharge rate

If the discharge rate is high, the cone of depression will be wider and deeper than if the discharge rate is low. With a high discharge rate, therefore, the piezometers can be placed at greater distances from the well.

The length of the well screen

The length of the well screen has a strong bearing on the placing of the piezometers. If the well is a fully penetrating one, i.e. it is screened over the entire thickness of the aquifer or at least 80 per cent of it, the flow towards the well will be horizontal

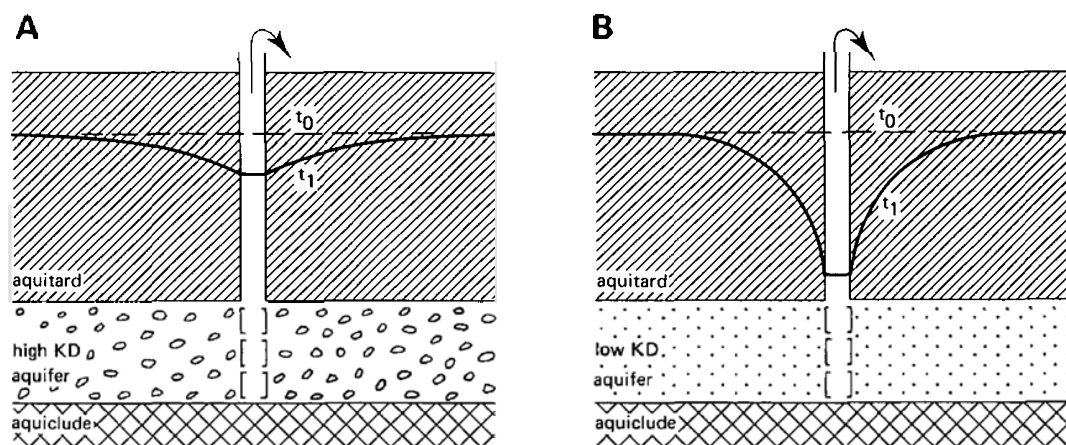


Figure 2.5 Cone of depression at a given time t in:
 A) an aquifer of high transmissivity
 B) an aquifer of low transmissivity

and piezometers can be placed close to the well. Obviously, if the aquifer is not very thick, it is always best to employ a fully penetrating well.

If the well is only partially penetrating, the relatively short length of well screen will induce vertical flow components, which are most noticeable near the well. If piezometers are placed near the well, their water-level readings will have to be corrected before being used in the analysis. These rather complicated corrections can be avoided if the piezometers are placed farther from the well, say at distances which are at least equal to 1.5 times the thickness of the aquifer. At such distances, it can be assumed that the flow is horizontal (see Figure 2.2).

Stratification

Homogeneous aquifers seldom occur in nature, most aquifers being stratified to some degree. Stratification causes differences in horizontal and vertical hydraulic conductivity, so that the drawdown observed at a certain distance from the well may differ at different depths within the aquifer. As pumping continues, these differences in drawdown diminish. Moreover, the greater the distance from the well, the less effect stratification has upon the drawdowns.

Fractured rock

Deciding on the number and location of piezometers in fractured rock poses a special problem, although the rock can be so densely fractured that its drawdown response to pumping resembles that of an unconsolidated homogeneous aquifer; if so, the number and location of the piezometers can be chosen in the same way as for such an aquifer.

If the fracture is a single vertical fracture, however, matters become more complicated. The number and location of piezometers will then depend on the orientation of the fracture (which may or may not be known) and on the transmissivity of the rock on opposite sides of the fracture (which may be the same or, as so often happens, is not the same). Further, the fracture may be open or closed. If it is open, its hydraulic conductivity can be regarded as infinite, and it will resemble a canal whose water level is suddenly lowered. There will then be no hydraulic gradient inside the fracture, so that it can be regarded as an 'extended well', or as a drain that receives water from the adjacent rock through parallel flow. This situation requires that piezometers be placed along a line perpendicular to the fracture. To check whether the fracture can indeed be regarded as an 'extended well', a few piezometers should be placed in the fracture itself.

If the hydraulic conductivity of the fracture is severely reduced by weathering or by the deposition of minerals on the fracture plane, pumping will cause hydraulic gradients to develop in the fracture and in the adjacent rock. This situation requires piezometers in the fracture and in the adjacent rock.

If the fracture is a single vertical open fracture of infinite hydraulic conductivity and known orientation, and if the transmissivity of the rock is the same on both sides of the fracture, two piezometers on the same side of the fracture are required to determine the perpendicular distances between the piezometers and the fracture (Figure 2.6A). In this figure, the piezometer closest to the pumped well is not the piezometer closest to the fracture. Regardless of the distances r_1 and r_2 , the drawdown will be greatest in the piezometer closest to the fracture. To analyze pumping test data from

such a fracture, we must know the distances between the piezometers and the fracture, x_1 and x_2 , which we can calculate from r_1 and r_2 , measured in the field, and the angles θ_1 and θ_2 .

If the precise orientation of the fracture is not known, more than two piezometers will be needed. As can be seen in Figure 2.6B, if x_1 is small relative to x_2 , two orientations are possible because x_1 may be on either side of the fracture. More piezometers must then be placed to find the orientation.

More piezometers are also required if there is geological evidence that the transmissivity of the rock on opposite sides of the fracture is significantly different.

Summarizing

As is obvious from the above, there are many factors to be taken into account in deciding how far from the well the piezometers should be placed. Nevertheless, if one has a proper knowledge of the test site (especially of the type of aquifer, its thickness, stratification or fracturing, and expected transmissivity), it will be easier to make the right decisions.

Although no fixed rule can be given and the ultimate choice depends entirely on local conditions, placing piezometers between 10 and 100 m from the well will give reliable data in most cases. For thick aquifers or stratified confined ones, the distances should be greater, say between 100 and 250 m or more from the well.

One or more piezometers should also be placed outside the area affected by the pumping so that the natural behaviour of the hydraulic head in the aquifer can be

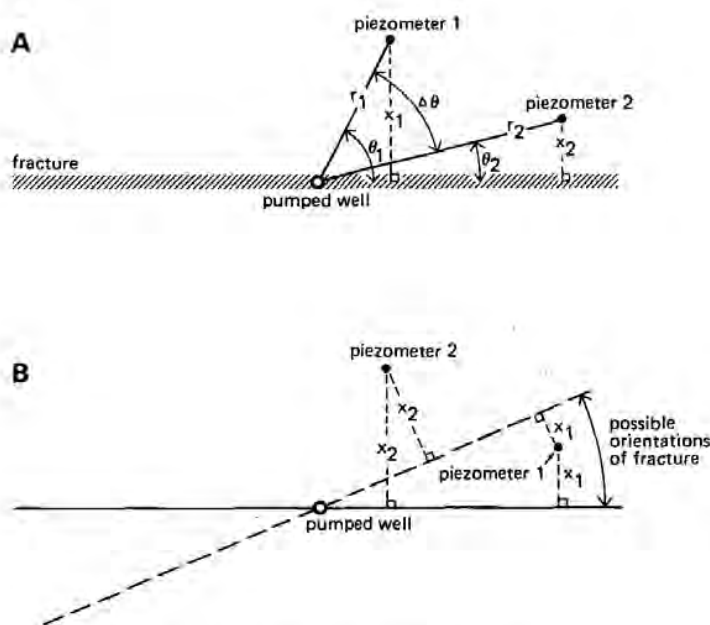


Figure 2.6 Piezometer arrangement near a fracture:
 A) of known orientation
 B) of unknown orientation

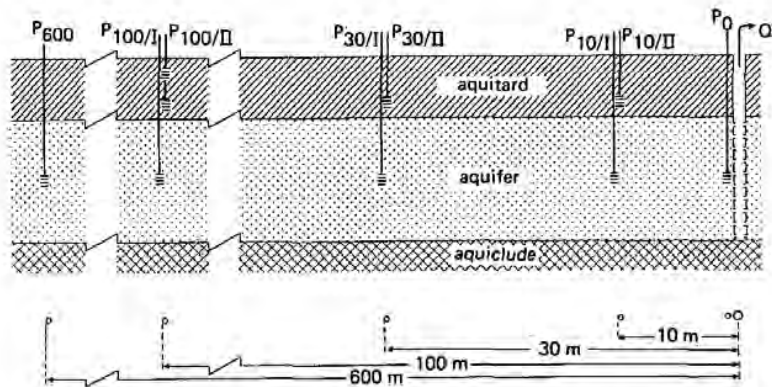


Figure 2.7 Example of a piezometer arrangement

measured. These piezometers should be several hundred metres away from the well, or in the case of truly confined aquifers, as far away as one kilometre or more. If the readings from these piezometers show water-level changes during the test (e.g. changes caused by natural discharge or recharge), these data will be needed to correct the drawdowns induced by the pumping.

An example of a piezometer arrangement in an unconsolidated leaky aquifer is shown in Figure 2.7.

2.5.3 Depth of the piezometers

The depth of the piezometers is at least as important as their distance from the well. In an isotropic and homogeneous aquifer, the piezometers should be placed at a depth that coincides with that of half the length of the well screen. For example, if the well is fully penetrating and its screen is between 10 and 20 m below the ground surface, the piezometers should be placed at a depth of about 15 m.

For heterogeneous aquifers made up of sandy deposits intercalated with aquitards, it is recommended that a cluster of piezometers be placed, i.e. one piezometer in each sandy layer (see Figure 2.4). The holes in the aquitards should be sealed to prevent leakage along the tubes. Despite these precautions, some leakage may still occur, so it is recommended that the screens be placed a few metres away from the upper and lower boundaries of the aquitards where the effect of this leakage is small.

If an aquifer is overlain by a partly saturated aquitard, piezometers should also be placed in the aquitard to check whether its watertable is affected when the underlying aquifer is pumped. This information is needed for the analysis of tests in leaky aquifers.

2.6 The measurements to be taken

The measurements to be taken during a pumping test are of two kinds:

- Measurements of the water levels in the well and the piezometers;

– Measurements of the discharge rate of the well.

Ideally, a pumping test should not start before the natural changes in hydraulic head in the aquifer are known – both the long-term regional trends and the short-term local variations. So, for some days prior to the test, the water levels in the well and the piezometers should be measured, say twice a day. If a hydrograph (i.e. a curve of time versus water level) is drawn for each of these observation points, the trend and rate of water-level change can be read. At the end of the test (i.e. after complete recovery), water-level readings should continue for one or two days. With these data, the hydrographs can be completed and the rate of natural water-level change during the test can be determined. This information can then be used to correct the drawdowns observed during the test.

Special problems arise in coastal aquifers whose hydraulic head is affected by tidal movements. Prior to the test, a complete picture of the changes in head should be obtained, including maximum and minimum water levels in each piezometer and their time of occurrence.

When a test is expected to last one or more days, measurements should also be made of the atmospheric pressure, the levels of nearby surface waters, if present, and any precipitation.

In areas where production wells are operating, the pumping test has to be conducted under less than ideal conditions. Nevertheless, the possibly significant effects of these interfering wells can be eliminated from the test data if their on-off times and discharge rates are monitored, both before and during the test. Even so, it is best to avoid the disturbing influence of such wells if at all possible.

2.6.1 Water-level measurements

The water levels in the well and the piezometers must be measured many times during a test, and with as much accuracy as possible. Because water levels are dropping fast during the first one or two hours of the test, the readings in this period should be made at brief intervals. As pumping continues, the intervals can be gradually lengthened. Table 2.1 gives a range of intervals for readings in the well. For single well tests (i.e. tests without the use of piezometers), the intervals in the first 5 to 10 minutes of the test should be shorter because these early-time drawdown data may reveal well-bore storage effects.

Table 2.1 Range of intervals between water-level measurements in well

Time since start of pumping	Time intervals
0– 5 minutes	0.5 minutes
5– 60 minutes	5 minutes
60– 120 minutes	20 minutes
120–shutdown of the pump	60 minutes

Similarly, in the piezometers, water-level measurements should be taken at brief intervals during the first hours of the test, and at longer intervals as the test continues. Table 2.2 gives a range of intervals for measurements in those piezometers placed in the aquifer and located relatively close to the well; here, the water levels are immediately affected by the pumping. For piezometers farther from the well and for those in confining layers above or below the aquifer, the intervals in the first minutes of the test need not be so brief.

Table 2.2 Range of intervals between water-level measurements in piezometers

Time since start of pumping	Time intervals
0 — 2 minutes	approx. 10 seconds
2 — 5 minutes	30 seconds
5 — 15 minutes	1 minute
15 — 50 minutes	5 minutes
50 — 100 minutes	10 minutes
100 minutes — 5 hours	30 minutes
5 hours — 48 hours	60 minutes
48 hours — 6 days	3 times a day
6 days — shutdown of the pump	1 time a day

The suggested intervals need not be adhered to too rigidly as they should be adapted to local conditions, available personnel, etc. All the same, readings should be frequent in the first hours of the test because, in the analysis of the test data, time generally enters in a logarithmic form.

All manual measurements of water levels and times should preferably be noted on standard, pre-printed forms, with space available for all relevant field data. An example is shown in Figure 2.8. The completed forms should be kept on file.

After some hours of pumping, sufficient time will become available in the field to draw the time-drawdown curves for the well and for each piezometer. Log-log and semi-log paper should be used for this purpose, with the time in minutes on a logarithmic scale. These graphs can be helpful in checking whether the test is running well and in deciding on the time to shut down the pump.

After the pump has been shut down, the water levels in the well and the piezometers will start to rise — rapidly in the first hour, but more slowly afterwards. These rises can be measured in what is known as a recovery test. If the discharge rate of the well was not constant throughout the pumping test, recovery-test data are more reliable than the drawdown data because the watertable recovers at a constant rate, which is the average of the pumping rate. The data from a recovery test can also be used to check the calculations made on the basis of the drawdown data. The schedule for recovery measurements should be the same as that adhered to during the pumping test.

OBSERVATIONS during PUMPING/RECOVERY

Piezometer WI/90; Depth 1.5m-91.5; Distance 90m
 Pumping test by I.C.W.; Directed by H. WITT
 For project ACHTERHOEK
 Location VENNEBULTEN
 Start 28-10-65 10h.27; Stop 29-10-65 11h.59
 Initial water level 1-38.5m
 Final water level 1-58.9m
 Reference level TOP OF PIEZOMETER = 22.322 +m.s.l.*
 Remark TIME IN MINUTES
WATER LEVEL AND DRAWDOWN IN CM
DISCHARGE RATE m³/h

time	water level	draw-down	time	water level	draw-down	discharge rate		
						time	flow-meter	discharge rate
0	138.5							
1.17	138.9	0.4				0	183.54	0
1.34	139.4	0.9				60	219.91	36.37

* mean sea level

Figure 2.8 Example of a pre-printed pumping-test form

2.6.1.1 Water-level-measuring devices

The most accurate recordings of water-level changes are made with fully-automatic microcomputer-controlled systems, as developed, for instance, by the TNO Institute of Applied Geoscience, The Netherlands (Figure 2.9). This system uses pressure transducers or acoustic transducers for continuous water-level recordings, which are stored on magnetic tape (see also Kohlmeier et al. 1983).

A good alternative is the conventional automatic recorder, which also produces a continuous record of water-level changes. Such recorders, however, require large-diameter piezometers.

Fairly accurate measurements can be taken by hand, but then the instant of each reading must be recorded with a chronometer. Experience has shown that it is possible to measure water levels to within 1 or 2 mm with one of the following:

- A floating steel tape and standard with pointer;
- An electrical sounder;
- The wetted-tape method.

For piezometers close to the well where water levels are changing rapidly during the first hours of the test, the most convenient device is the floating steel tape with pointer because it permits direct readings. For piezometers far from the well, conventional automatic recorders are the most suitable devices because only slow water-level changes can be interpreted from their graphs. For piezometers at intermediate distances, either floating or hand-operated water-level indicators can be used, but even when water levels are changing rapidly, accurate observations can be made with a recorder, provided a chronometer is used and the time of each reading is marked manually on the graph.

For detailed descriptions of automatic recorders, mechanical and electrical sounders, and other equipment for measuring water levels in wells, we refer to hand-books (e.g. Driscoll 1986; Genetier 1984; Groundwater Manual 1981).

2.6.2 Discharge-rate measurements

Amongst the arrangements to be made for a pumping test is a proper control of the discharge rate. This should preferably be kept constant throughout the test. During pumping, the discharge should be measured at least once every hour, and any necessary adjustments made to keep it constant.

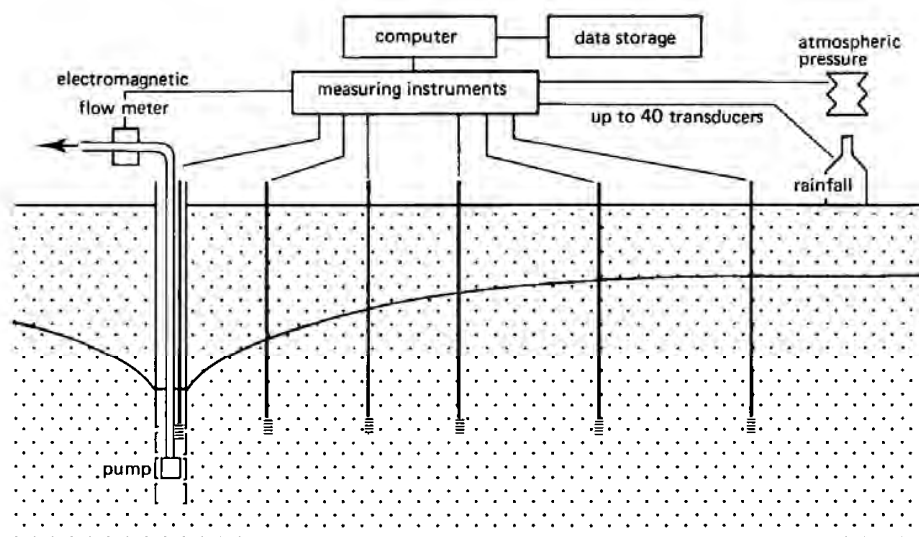


Figure 2.9 A fully-automated micro-computer-controlled recorder

The discharge can be kept constant by a valve in the discharge pipe. This is a more accurate method of control than changing the speed of the pump.

The fully-automatic computer-controlled system shown earlier in Figure 2.9 includes a magnetic flow meter for discharge measurements as part of a discharge-correction scheme to maintain a constant discharge.

A constant discharge rate, however, is not a prerequisite for the analysis of a pumping test. There are methods available that take variable discharge into account, whether it be due to natural causes or is deliberately provoked.

2.6.2.1 Discharge-measuring devices

To measure the discharge rate, a commercial water meter of appropriate capacity can be used. The meter should be connected to the discharge pipe in a way that ensures accurate readings being made: at the bottom of a U-bend, for instance, so that the pipe is running full. If the water is being discharged through a small ditch, a flume can be used to measure the discharge.

If no appropriate water meter or flume is available, there are other methods of measuring or estimating the discharge.

Container

A very simple and fairly accurate method is to measure the time it takes to fill a container of known capacity (e.g. an oil drum). This method can only be used if the discharge rate is low.

Orifice weir

The circular orifice weir is commonly used to measure the discharge from a turbine or centrifugal pump. It does not work when a piston pump is used because the flow from such a pump pulsates too much.

The orifice is a perfectly round hole in the centre of a circular steel plate which is fastened to the outer end of a level discharge pipe. A piezometer tube is fitted in a 0.32 or 0.64 cm hole made in the discharge pipe, exactly 61 cm from the orifice plate. The water level in the piezometer represents the pressure in the discharge pipe when water is pumped through the orifice. Standard tables have been published which show the flow rate for various combinations of orifice and pipe diameter (Driscoll 1986).

Orifice bucket

The orifice bucket was developed in the U.S.A. It consists of a small cylindrical tank with circular openings in the bottom. The water from the pump flows into the tank and discharges through the openings. The tank fills with water to a level where the pressure head causes the outflow through the openings to equal the inflow from the pump. If the tank overflows, one or more orifices are opened. If the water in the tank does not rise sufficiently, one or more orifices are closed with plugs.

A piezometer tube is connected to the outer wall of the tank near the bottom, and a vertical scale is fastened behind the tube to allow accurate readings of the water level in the tank. A calibration curve is required, showing the rate of discharge through

a single orifice of a given size for various values of the pressure head. The discharge rate taken from this curve, multiplied by the number of orifices through which the water is being discharged, gives the total rate of discharge for any given water-level reading. If the orifice bucket is provided with many openings, a considerable range of pumping rates can be measured. A further advantage of the orifice bucket is that it tends to smooth out any pulsating flow from the pump, thus permitting the average pumping rate to be determined with fair accuracy.

Jet-stream method

If none of the above-mentioned methods can be applied, the jet-stream method (or open-pipe-flow method) can be used. By measuring the dimensions of a stream flowing either vertically or horizontally from an open pipe, one can roughly estimate the discharge.

If the water is discharged through a vertical pipe, estimates of the discharge can be made from the diameter of the pipe and the height to which the water rises above the top of the pipe. Driscoll (1986) has published a table showing the discharge rates for different pipe diameters and various heights of the crest of the stream above the top of the pipe.

If the water is discharged through a horizontal pipe, flowing full and with a free fall from the discharge opening, estimates of the discharge can be made from the horizontal and vertical distances from the end of the pipe to a point in the flowing stream of water. The point can be chosen at the outer surface of the stream or in its centre. Another table by Driscoll (1986) shows the discharge rates for different pipe diameters and for various horizontal distances of the stream of water.

2.7 Duration of the pumping test

The question of how many hours to pump the well in a pumping test is difficult to answer because the period of pumping depends on the type of aquifer and the degree of accuracy desired in establishing its hydraulic characteristics. Economizing on the period of pumping is not recommended because the cost of running the pump a few extra hours is low compared with the total costs of the test. Besides, better and more reliable data are obtained if pumping continues until steady or pseudo-steady flow has been attained. At the beginning of the test, the cone of depression develops rapidly because the pumped water is initially derived from the aquifer storage immediately around the well. But as pumping continues, the cone expands and deepens more slowly because, with each additional metre of horizontal expansion, a larger volume of stored water becomes available. This apparent stabilization of the cone often leads inexperienced observers to conclude that steady state has been reached. Inaccurate measurements of the drawdowns in the piezometers – drawdowns that are becoming smaller and smaller as pumping continues – can lead to the same wrong conclusion. In reality, the cone of depression will continue to expand until the recharge of the aquifer equals the pumping rate.

In some tests, steady-state or equilibrium conditions occur a few hours after the start of pumping; in others, they occur within a few days or weeks; in yet others, they never occur, even though pumping continues for years. It is our experience that,

under average conditions, a steady state is reached in leaky aquifers after 15 to 20 hours of pumping; in a confined aquifer, it is good practice to pump for 24 hours; in an unconfined aquifer, because the cone of depression expands slowly, a longer period is required, say 3 days.

As will be demonstrated in later chapters, it is not absolutely necessary to continue pumping until a steady state has been reached, because methods are available to analyze unsteady-state data. Nevertheless, it is good practice to strive for a steady state, especially when accurate information on the aquifer characteristics is desired, say as a basis for the construction of a pumping station for domestic water supplies or other expensive works. If a steady state has been reached, simple equations can be used to analyze the data and reliable results will be obtained. Besides, the longer period of pumping required to reach steady state may reveal the presence of boundary conditions previously unknown, or in cases of fractured formations, will reveal the specific flows that develop during the test.

Preliminary plotting of drawdown data during the test will often show what is happening and may indicate how much longer the test should continue.

2.8 Processing the data

2.8.1 Conversion of the data

The water-level data collected before, during, and after the test should first be expressed in appropriate units. The measurement units of the International System are recommended (Annex 2.1), but there is no fixed rule for the units in which the field data and hydraulic characteristics should be expressed. Transmissivity, for instance, can be expressed in m^2/s or m^2/d . Field data are often expressed in units other than those in which the final results are presented. Time data, for instance, might be expressed in seconds during the first minutes of the test, minutes during the following hours, and actual time later on, while water-level data might be expressed in different units of length appropriate to the timing of the observations.

It will be clear that before the field data can be analyzed, they should first be converted: the time data into a single set of time units (e.g. minutes) and the drawdown data into a single set of length units (e.g. metres), or any other unit of length that is suitable (Annex 2.2).

2.8.2 Correction of the data

Before being used in the analysis, the observed water levels may have to be corrected for external influences (i.e. those not related to the pumping). To find out whether this is necessary, one has to analyze the local trend in the hydraulic head or watertable. The most suitable data for this purpose are the water-level measurements taken in a 'distant' piezometer during the test, but measurements taken at the test site for some days before and after the test can also be used.

If, after the recovery period, the same constant water level is observed as during the pre-testing period, it can safely be assumed that no external events influenced the

hydraulic head during the test. If, however, the water level is subject to unidirectional or rhythmic changes, it will have to be corrected.

2.8.2.1 Unidirectional variation

The aquifer may be influenced by natural recharge or discharge, which will result in a rise or a fall in the hydraulic head. By interpolation from the hydrographs of the well and the piezometers, this natural rise or fall can be determined for the pumping and recovery periods. This information is then used to correct the observed water levels.

Example 2.1

Suppose that the hydraulic head in an aquifer is subject to unidirectional variation, and that the water level in a piezometer at the moment t_0 (start of the pumping test) is h_0 . From the interpolated hydrograph of natural variation, it can be read that, at a moment t_1 , the water level would have been h_1 if no pumping had occurred. The absolute value of water-level change due to natural variation at t_1 is then: $h_0 - h_1 = \Delta h_1$. If the observed drawdown at t_1 is s_1 , where the observed drawdown is defined as the lowering of the water level with respect to the water level at $t = t_0$, the drawdown due to pumping is:

- With natural discharge: $s_1' = s_1 - \Delta h_1$;
- With natural recharge: $s_1' = s_1 + \Delta h_1$.

2.8.2.2 Rhythmic fluctuations

In confined and leaky aquifers, rhythmic fluctuations of the hydraulic head may be due to the influence of tides or river-level fluctuations, or to rhythmic variations in atmospheric pressure. In unconfined aquifers whose watertables are close to the ground surface, diurnal fluctuations of the watertable can be significant because of the great difference between day and night evapotranspiration. The watertable drops during the day because of the consumptive use by the vegetation and recovers during the night when the plant stomata are closed.

Hydrographs of the well and the piezometers, covering sufficiently long pre-test and post-recovery periods, will yield the information required to correct the water levels observed during the test.

Example 2.2

For this example, data from the pumping test 'Dalem' (see Chapter 4 and Figure 4.2) will be corrected for the piezometer at 400 m from the well. The piezometer was located 1900 m from the River Waal, which is under the influence of the tide in the North Sea. The Waal is hydraulically connected with the aquifer; hence the rise and fall of the river level affected the water levels in the piezometers. Piezometer readings covering a few days both prior to pumping and after complete recovery made it possible to interpolate the groundwater time-versus-tide curve for the pumping and recovery periods.

Figure 2.10A shows the curve of the groundwater tide with respect to a reference level, which was selected as the water level at the moment pumping started (08.04 hours). At 10.20 hours, it was low tide and the water levels had fallen 5 mm, independently of pumping. This meant that the water level observed at that moment was 5 mm lower than it would have been if there had been no tidal influence. The drawdown therefore has to be corrected accordingly. The correction term applied is read on the vertical axis of the time-tide curve.

Figure 2.10B shows the uncorrected time-drawdown curve and the same curve after being corrected. It will be noted that different vertical scales have been used in Parts A and B of Figure 2.10.

The same procedure is followed to correct the data from the other piezometers. For each, a time-tide curve, corresponding to the distance between the piezometer and the river, is used. Obviously, the closer a piezometer is to the river, the greater is the influence of the tide on its water levels.

2.8.2.3 Non-rhythmic regular fluctuations

Non-rhythmic regular fluctuations, due, for example, to changes in atmospheric pressure, can be detected on a hydrograph covering the pre-test period. In wells or piezometers tapping confined and leaky aquifers, the water levels are continuously changing as the atmospheric pressure changes. When the atmospheric pressure decreases, the water levels rise in compensation, and vice versa (Figure 2.11). By comparing the atmospheric changes, expressed in terms of a column of water, with the actual changes in water levels observed during the pre-test period, one can determine the barometric efficiency of the aquifer. The barometric efficiency (BE) is defined as the ratio of

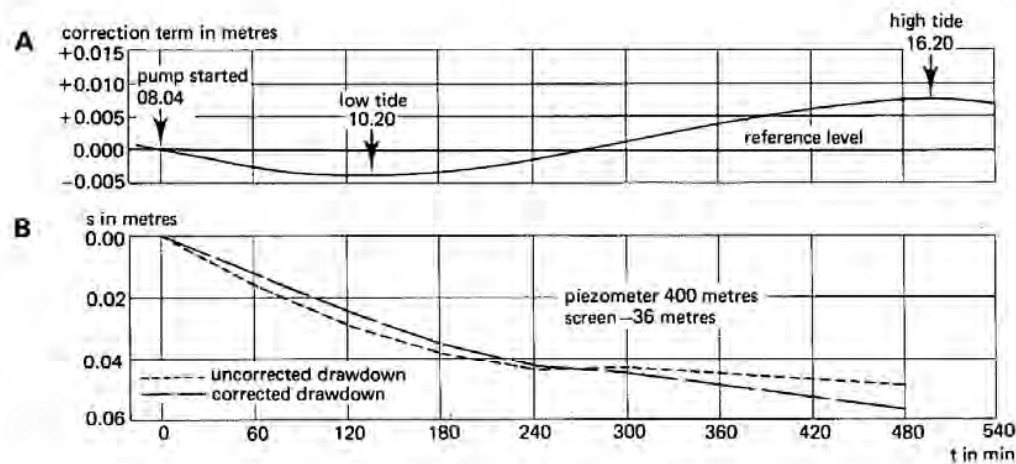


Figure 2.10 Correction of data for tidal influence
 A) The curve of the groundwater tide under non-pumped conditions
 B) Corrected and uncorrected drawdowns
 Note: Vertical scales in upper and lower part of figure are different

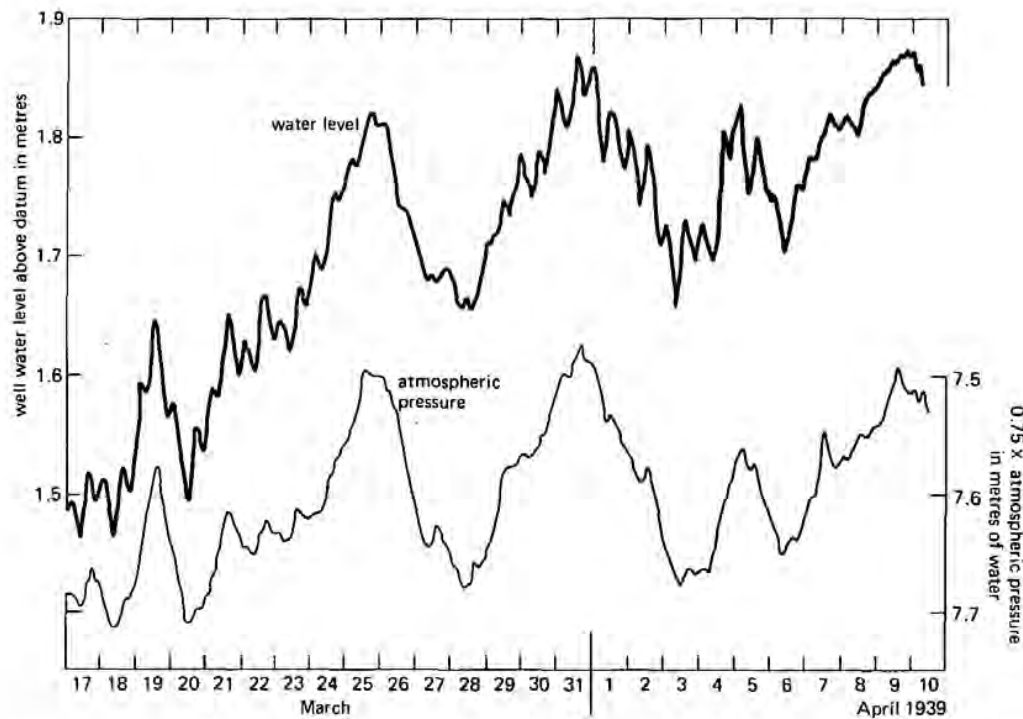


Figure 2.11 Response of water level in a well penetrating a confined aquifer to changes in atmospheric pressure, showing a barometric efficiency of 75 per cent (Robinson 1939)

change in water level (Δh) in a well to the corresponding change in atmospheric pressure (Δp), or $BE = \gamma\Delta h/\Delta p$, in which γ is the specific weight of water. BE usually ranges from 0.20 to 0.75.

From the changes in atmospheric pressure observed during a test, and the known relationship between Δp and Δh , the water-level changes due to changes in atmospheric pressure alone (Δh_p) can be calculated for the test period for the well and each piezometer. Subsequently, the actual drawdown during the test can be corrected for the water-level changes due to atmospheric pressure:

- For falling atmospheric pressures: $s' = s + \Delta h_p$;
- For rising atmospheric pressures: $s' = s - \Delta h_p$.

2.8.2.4 Unique fluctuations

In general, the water levels measured during a pumping test cannot be corrected for unique fluctuations due, say, to heavy rain or the sudden rise or fall of a nearby river or canal that is in hydraulic connection with the aquifer. In certain favourable circumstances, allowance can be made for such fluctuations by extrapolating the data from a control piezometer outside the zone of influence of the well. But, in general, the data of the test become worthless and the test has to be repeated when the situation has returned to normal.

2.9 Interpretation of the data

Calculating hydraulic characteristics would be relatively easy if the aquifer system (i.e. aquifer plus well) were precisely known. This is generally not the case, so interpreting a pumping test is primarily a matter of identifying an unknown system. System identification relies on models, the characteristics of which are assumed to represent the characteristics of the real aquifer system.

Theoretical models comprise the type of aquifer (Section 1.2), and initial and boundary conditions. Typical outer boundary conditions were mentioned in Section 1.4. Inner boundary conditions are associated with the pumped well (e.g. fully or partially penetrating, small or large diameter, well losses).

In a pumping test, the type of aquifer and the inner and outer boundary conditions dominate at different times during the test. They affect the drawdown behaviour of the system in their own individual ways. So, to identify an aquifer system, one must compare its drawdown behaviour with that of the various theoretical models. The model that compares best with the real system is then selected for the calculation of the hydraulic characteristics.

System identification includes the construction of diagnostic plots and specialized plots. Diagnostic plots are log-log plots of the drawdown versus the time since pumping started. Specialized plots are semi-log plots of drawdown versus time, or drawdown versus distance to the well; they are specific to a given flow regime. A diagnostic plot allows the dominating flow regimes to be identified; these yield straight lines on specialized plots. The characteristic shapes of the curves can help in selecting the appropriate model.

In a number of cases, a semi-log plot of drawdown versus time has more diagnostic value than a log-log plot. We therefore recommend that both types of graphs be constructed.

The choice of theoretical model is a crucial step in the interpretation of pumping tests. If the wrong model is chosen, the hydraulic characteristics calculated for the real aquifer will not be correct. A troublesome fact is that theoretical solutions to well-flow problems are usually not unique. Some models, developed for different aquifer systems, yield similar responses to a given stress exerted on them. This makes system identification and model selection a difficult affair. One can reduce the number of alternatives by conducting more field work, but that could make the total costs of the test prohibitive. In many cases, uncertainty as to which model to select will remain. We shall discuss this problem briefly below. The examples we give will illustrate that analyzing a pumping test is not merely a matter of opening a particular page of this book and applying the method described there.

2.9.1 Aquifer categories

Aquifers fall into two broad categories: unconsolidated aquifers and consolidated fractured aquifers. Within both categories, the aquifers may be confined, unconfined, or leaky (Section 1.2, Figure 1.1). We shall first consider all three types of unconsolidated aquifer, and then the consolidated aquifer, but only the confined type.

Figure 2.12 shows log-log and semi-log plots of the theoretical time-drawdown rela-

tionships for confined, unconfined, and leaky unconsolidated aquifers. We present these graphs in pairs because, although log-log plots are diagnostic, as the oil industry states, we believe that semi-log plots can sometimes be even more diagnostic. This becomes clear if we look at Parts A and A' of Figure 2.12. These refer to an ideal, confined, unconsolidated aquifer, homogeneous and isotropic, and pumped at a constant rate by a fully penetrating well of very small diameter. From the semi-log plot (Part A'), we can see that the time-drawdown relationship at early pumping times is not linear, but at later times it is. If a linear relationship like this is found, it should be used to calculate the hydraulic characteristics because the results will be much more accurate than those obtained by matching field data plots with the curve of Part A. (We return to this subject in Sections 3.2.1 and 3.2.2.)

Parts B and B' of Figure 2.12 show the curves for an unconfined, homogeneous, isotropic aquifer of infinite lateral extent and with a delayed yield. These two curves are characteristic. At early pumping times, the curve of the log-log plot (Part B) follows the curve for the confined aquifer shown in Part A. Then, at medium pumping times, it shows a flat segment. This reflects the recharge from the overlying, less permeable aquifer, which stabilizes the drawdown. At late times, the curve again follows a portion of the curve of Part A. The semi-log plot is even more characteristic: it shows two parallel straight-line segments at early and late pumping times. (We return to this subject in Section 5.1.1.)

Parts C and C' of Figure 2.12 refer to a leaky aquifer. At early pumping times, the curves follow those of Parts A and A'. At medium pumping times, more and more water from the aquitard (or aquitards) is reaching the aquifer. Eventually, at late pumping times, all the water pumped is from leakage through the aquitard(s), and the flow towards the well has reached a steady state. This means that the drawdown

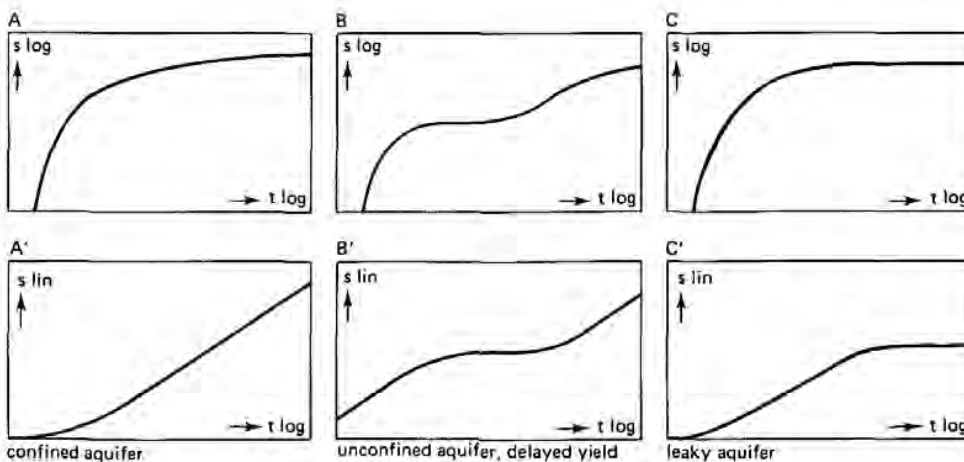


Figure 2.12 Log-log and semi-log plots of the theoretical time-drawdown relationships of unconsolidated aquifers:
 Parts A and A': Confined aquifer
 Parts B and B': Unconfined aquifer
 Parts C and C': Leaky aquifer

in the aquifer stabilizes, as is clearly reflected in both graphs. (We return to this subject in Sections 4.1.1 and 4.1.2.)

We shall now consider the category of confined, consolidated fractured aquifers, some examples of which are shown in Figure 2.13. Parts A and A' of this figure refer to a confined, densely fractured, consolidated aquifer of the double-porosity type. In an aquifer like this, we recognize two systems: the fractures of high permeability and low storage capacity, and the matrix blocks of low permeability and high storage capacity. The flow towards the well in such a system is entirely through the fractures and is radial and in an unsteady state. The flow from the matrix blocks into the fractures is assumed to be in a pseudo-steady state. Characteristic of the flow in such a system is that three time periods can be recognized:

- Early pumping time, when all the flow comes from storage in the fractures;
- Medium pumping time, a transition period during which the matrix blocks feed their water at an increasing rate to the fractures, resulting in a (partly) stabilizing drawdown;
- Late pumping time, when the pumped water comes from storage in both the fractures and the matrix blocks.

(We return to this subject in Chapter 17.)

The shapes of the curves in Parts A and A' of Figure 2.13 resemble those of Parts B and B' of Figure 2.12, which refer to an unconfined, unconsolidated aquifer with delayed yield.

Parts B and B' of Figure 2.13 present the curves for a well that pumps a single plane vertical fracture in a confined, homogeneous, and isotropic aquifer of low permeability. The fracture has a finite length and a high hydraulic conductivity. Characteristic of this system is that a log-log plot of early pumping time shows a straight-line segment of slope 0.5. This segment reflects the dominant flow regime in that period:

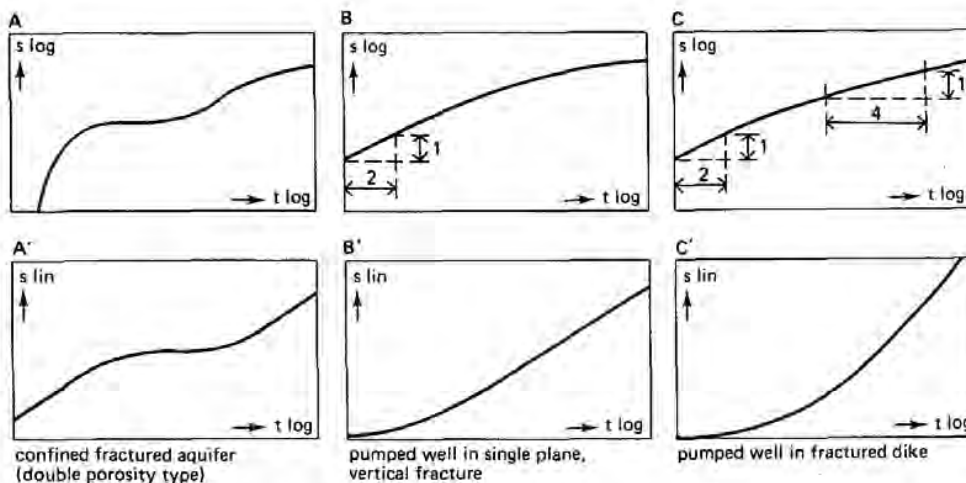


Figure 2.13 Log-log and semi-log plots of the theoretical time-drawdown relationships of consolidated, fractured aquifers:

Parts A and A': Confined fractured aquifer, double porosity type

Parts B and B': A single plane vertical fracture

Parts C and C': A permeable dike in an otherwise poorly permeable aquifer

it is horizontal, parallel, and perpendicular to the fracture. This flow regime gradually changes, until, at late time, it becomes pseudo-radial. The shapes of the curves at late time resemble those of Parts A and A' of Figure 2.12. (We return to this subject in Section 18.3.)

Parts C and C' of Figure 2.13 refer to a well in a densely fractured, highly permeable dike of infinite length and finite width in an otherwise confined, homogeneous, isotropic, consolidated aquifer of low hydraulic conductivity and high storage capacity. Characteristic of such a system are the two straight-line segments in a log-log plot of early and medium pumping times. The first segment has a slope of 0.5 and thus resembles that of the well in the single, vertical, plane fracture shown in Part B of Figure 2.13. At early time, the flow towards the well is exclusively through the dike, and this flow is parallel. At medium time, the adjacent aquifer starts yielding water to the dike. The dominant flow regime in the aquifer is then near-parallel to parallel, but oblique to the dike. In a log-log plot, this flow regime is reflected by a one-fourth slope straight-line segment. At late time, the dominant flow regime is pseudo-radial, which, in a semi-log plot, is reflected by a straight line.

The one-fourth slope straight-line segment does not always appear in a log-log plot; whether it does or not depends on the hydraulic diffusivity ratio between the dike and the adjacent aquifer. (We return to this subject in Section 19.3.)

2.9.2 Specific boundary conditions

When field data curves of drawdown versus time deviate from the theoretical curves of the main types of aquifer, the deviation is usually due to specific boundary conditions (e.g. partial penetration of the well, well-bore storage, recharge boundaries, or impermeable boundaries). Specific boundary conditions can occur individually (e.g. a partially penetrating well in an otherwise homogeneous, isotropic aquifer of infinite extent), but they often occur in combination (e.g. a partially penetrating well near a deeply incised river or canal). Obviously, specific boundary conditions can occur in all types of aquifers, but the examples we give below refer only to unconsolidated, confined aquifers.

Partial penetration of the well

Theoretical models usually assume that the pumped well fully penetrates the aquifer, so that the flow towards the well is horizontal. With a partially penetrating well, the condition of horizontal flow is not satisfied, at least not in the vicinity of the well. Vertical flow components are thus induced in the aquifer, and these are accompanied by extra head losses in and near the well. Figure 2.14 shows the effect of partial penetration. The extra head losses it induces are clearly reflected. (We return to this subject in Chapter 10.)

Well-bore storage

All theoretical models assume a line source or sink, which means that well-bore storage effects can be neglected. But all wells have a certain dimension and thus store some water, which must first be removed when pumping begins. The larger the diameter of the well, the more water it will store, and the less the condition of line source or

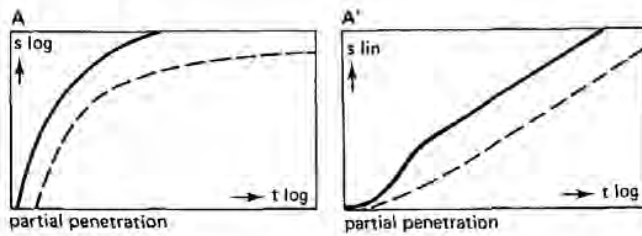


Figure 2.14 The effect of the well's partial penetration on the time-drawdown relationship in an unconsolidated, confined aquifer. The dashed curves are those of Parts A and A' of Figure 2.12

sink will be satisfied. Obviously, the effects of well-bore storage will appear at early pumping times, and may last from a few minutes to many minutes, depending on the storage capacity of the well. In a log-log plot of drawdown versus time, the effect of well-bore storage is reflected by a straight-line segment with a slope of unity. (We return to this subject in Section 15.1.1.)

If a pumping test is conducted in a large-diameter well and drawdown data from observation wells or piezometers are used in the analysis, it should not be forgotten that those data will also be affected by the well-bore storage in the pumped well. At early pumping time, the data will deviate from the theoretical curve, although, in a log-log plot, no early-time straight-line segment of slope unity will appear. Figure 2.15 shows the effect of well-bore storage on time-drawdown plots of observation wells or piezometers. (We return to this subject in Section 11.1.)

Recharge or impermeable boundaries

The theoretical curves of all the main aquifer types can also be affected by recharge or impermeable boundaries. This effect is shown in Figure 2.16. Parts A and A' of that figure show a situation where the cone of depression reaches a recharge boundary. When this happens, the drawdown in the well stabilizes. The field data curve then begins to deviate more and more from the theoretical curve, which is shown in the dashed segment of the curve. Impermeable (no-flow) boundaries have the opposite effect on the drawdown. If the cone of depression reaches such a boundary, the drawdown will double. The field data curve will then steepen, deviating upward from the theoretical curve. This is shown in Parts B and B' of Figure 2.16. (We return to this subject in Chapter 6.)

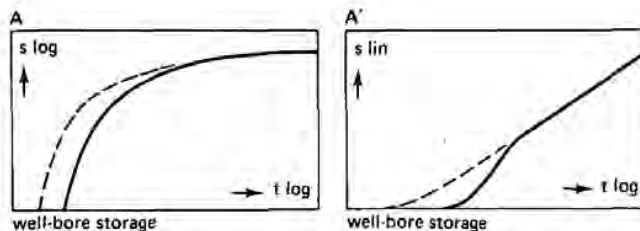


Figure 2.15 The effect of well-bore storage in the pumped well on the theoretical time-drawdown plots of observation wells or piezometers. The dashed curves are those of Parts A and A' of Figure 2.12

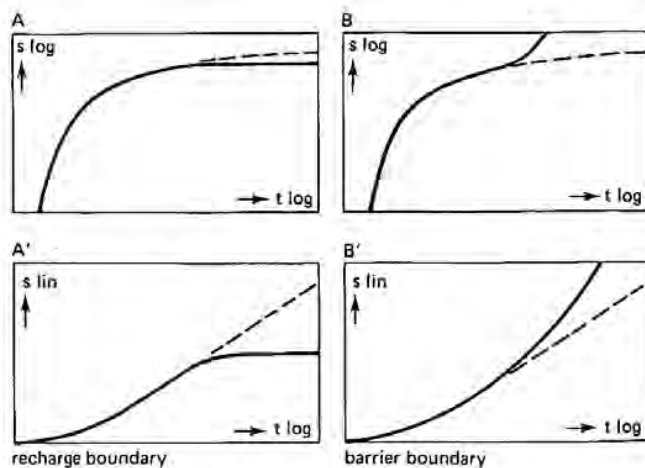


Figure 2.16 The effect of a recharge boundary (Parts A and A') and an impermeable boundary (Parts B and B') on the theoretical time-drawdown relationship in a confined unconsolidated aquifer. The dashed curves are those of Parts A and A' of Figure 2.12

2.10 Reporting and filing of data

2.10.1 Reporting

When the evaluation of the test data has been completed, a report should be written about the results. It is beyond the scope of this book to say what this report should contain, but it should at least include the following items:

- A map, showing the location of the test site, the well and the piezometers, and recharge and barrier boundaries, if any;
- A lithological cross-section of the test site, based on the data obtained from the bore holes, and showing the depth of the well screen and the number, depth, and distances of the piezometers;
- Tables of the field measurements made of the well discharge and the water levels in the well and the piezometers;
- Hydrographs, illustrating the corrections applied to the observed data, if applicable;
- Time-drawdown curves and distance-drawdown curves;
- The considerations that led to the selection of the theoretical model used for the analysis;
- The calculations in an abbreviated form, including the values obtained for the aquifer characteristics and a discussion of their accuracy;
- Recommendations for further investigations, if applicable;
- A summary of the main results.

2.10.2 Filing of data

A copy of the report should be kept on file for further reference and for use in any

later studies. Samples of the different layers penetrated by the borings should also be filed, as should the basic field measurements of the pumping test. The conclusions drawn from the test may become obsolete in the light of new insights, but the hard facts, carefully collected in the field, remain facts and can always be re-evaluated.

Using Hydrogeologic Data to Evaluate Geothermal Potential in the Eastern Great Basin

Melissa D. Masbruch, Victor M. Heilweil, and Lynette E. Brooks

U. S. Geological Survey,
Utah Water Science Center, Salt Lake City, Utah

Keywords

Regional groundwater flow, surficial heat flow, geothermal resources, carbonate aquifer, Great Basin

ABSTRACT

In support of a larger study to evaluate geothermal resource development of high-permeability stratigraphic units in sedimentary basins, this paper integrates groundwater and thermal data to evaluate heat and fluid flow within the eastern Great Basin. Previously published information from a hydrogeologic framework, a potentiometric-surface map, and groundwater budgets was compared to a surficial heat-flow map. Comparisons between regional groundwater flow patterns and surficial heat flow indicate a strong spatial relation between regional groundwater movement and surficial heat distribution. Combining aquifer geometry and heat-flow maps, a selected group of subareas within the eastern Great Basin are identified that have high surficial heat flow and are underlain by a sequence of thick basin-fill deposits and permeable carbonate aquifers. These regions may have potential for future geothermal resources development.

Introduction

Located within the Basin and Range Physiographic Province, the Great Basin carbonate and alluvial aquifer system (GBCAAS) covers an area of approximately 284,900 km² (110,000 mi²) and lies predominantly within eastern Nevada and western Utah (Heilweil et al., 2011). Altitudes range from below sea level to above 4,500 m (14,000 ft). Most of the study area is categorized as having a semi-arid or steppe climate, except for the extreme southwestern basins which have an arid desert climate, and the extreme northeastern mountains which have an alpine/tundra climate (Heilweil et al., 2011). Annual precipitation ranges between 3.8 cm (1.5 inches) in southern Nevada to 178 cm (70 inches) in northern Utah (Heilweil et al., 2011). The physical geography of the study area is characterized by north or northeast trending mountain ranges approximately 8-24 km (5-15 mi) wide separated

by broad basins approximately 8-16 km (5-10 mi) wide (Heilweil et al., 2011). Mountain ranges can be longer than more than 80 km (50 mi); basins are typically 56-112 km (35-70 mi) long, although some are as long as 241 km (150 mi). These longer basins are bordered by multiple mountain ranges. Topographic relief between the mountain crests and basin floors generally ranges from 305 to 1,830 m (1,000 to 6,000 ft).

Interest in the development of geothermal energy includes a national effort to evaluate potential resources. Current installed and utilized power production capacity in the U.S. is more than 2,500 Megawatts-electric (MWe) and the potential for additional conventional geothermal resource development is estimated to be about 9,000 MWe (Williams et al., 2008). Historical geothermal power development has largely focused on hydrothermal system fault-controlled reservoirs. Estimated potential for Enhanced Geothermal System (EGS) development from low-permeability reservoirs adds more than 500,000 MWe to this estimate. In addition, there is significant potential for unconventional geothermal resources associated with deep sedimentary basins in the U.S. Following on this, Allis et al. (2011) noted that there are large areas in the western U.S., especially in the Basin and Range high heat-flow province, where high near-surface temperature gradients indicate the potential for elevated temperatures at relatively shallow depths. There is a particular focus on areas of the Great Basin where significant permeability in consolidated rock exists at depths of 2,000 to 5,000 m and the consolidated rock is blanketed by basin-fill sediments with low thermal conductivity (Allis et al., 2012, in prep.). Such areas may have significant potential for geothermal production where this bedrock permeability is laterally extensive.

This study examines carbonate aquifer thickness, extent, depth beneath sediments and groundwater flow in the context of geothermal resource potential by using recently published data. A hydrogeologic study of the eastern Great Basin (Heilweil and Brooks, 2011) included a three-dimensional hydrogeologic framework (Sweetkind et al., 2011a), evaluation of groundwater flow directions (Sweetkind et al., 2011b), and groundwater budget estimates (Masbruch et al., 2011). The eastern Great Basin study follows upon several previous regional groundwater studies (Welch et al., 2007; Harrill and Prudic, 1998; Prudic et al., 1995).

In addition, a recently published surficial heat-flow map of the conterminous U.S. (Blackwell et al., 2011) improves upon the spatial resolution of previously reported surficial heat flow in the eastern Great Basin (Blackwell, 1983).

Purpose and Scope

The objectives of this study are to (1) evaluate potential effects of groundwater flow on subsurface thermal conditions, and (2) identify areas where carbonate rocks are covered by at least 2 km of basin-fill sediments and are located in high heat-flow areas. These areas may have potential for geothermal resources development in the eastern Great Basin. To meet these objectives, hydrogeologic and thermal data were combined using geographic information system (GIS) techniques to generate maps and cross sections highlighting these areas.

Groundwater Flow

The GBCAAS comprises Cenozoic unconsolidated basin-fill sediments and volcanics, Paleozoic carbonates, and Late Proterozoic and Early Cambrian bedrock. Permeable Cenozoic rocks, which exceed thicknesses of 5,000 m in places, have been divided into three hydrogeologic units: an upper basin-fill aquifer unit (UBFAU), a lower basin-fill aquifer unit (LBFAU) and a volcanic unit (VU) (Sweetkind et al., 2011b). In many areas, these Cenozoic aquifers are underlain by permeable carbonate rocks which form regionally extensive aquifers that are hydraulically connected between basins. These carbonate aquifers have been divided into a

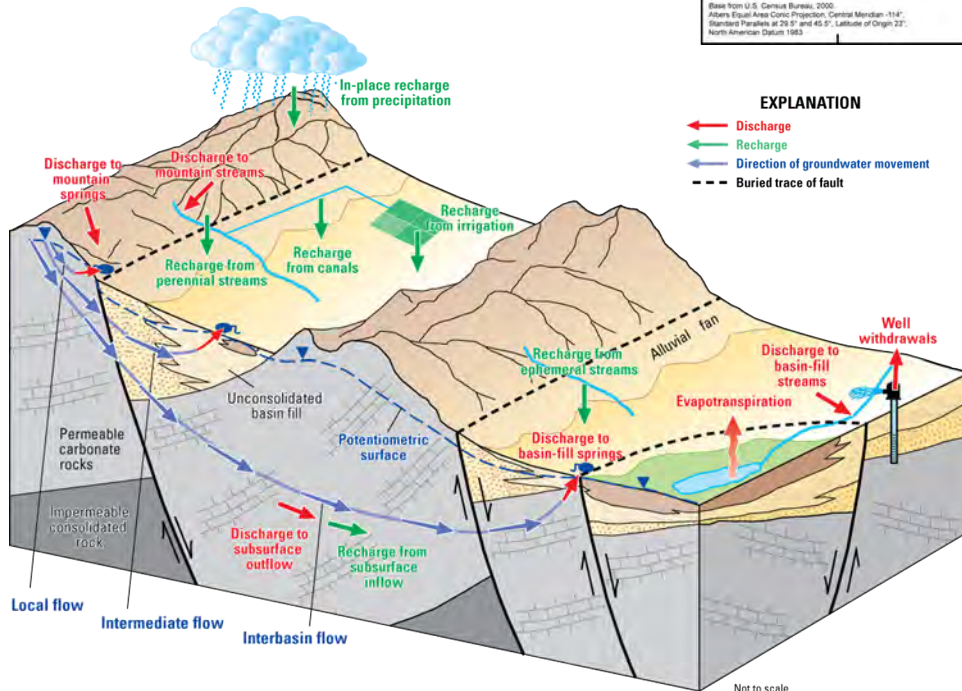


Figure 1. Schematic diagram showing conceptualized groundwater flow in the Great Basin carbonate and alluvial aquifer system study area (from Sweetkind et al., 2011b).

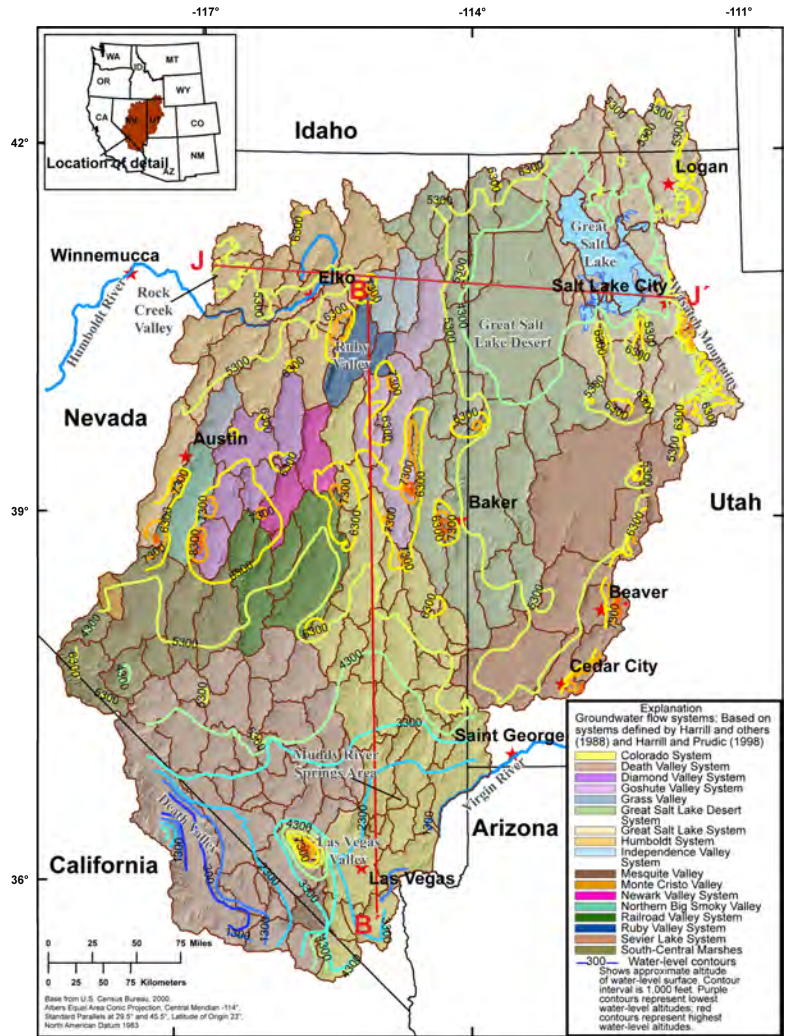


Figure 2. Potentiometric-surface map of the Great Basin carbonate and alluvial aquifer system study area (modified from Heilweil and Brooks, 2011).

lower carbonate aquifer unit (LCAU) and an upper carbonate aquifer unit (UCAU).

Groundwater movement within the GBCAAS typically is from recharge areas in higher- altitude mountains towards lower-altitude discharge areas (figure 1), consistent with previous conceptual models of groundwater flow in areas of high topographic relief (Toth, 1963). Within the study area, most groundwater flow occurs in the UBFAU, the UCAU, and the LCAU.

Figure 2 is a simplified version of a recently published (Heilweil and Brooks, 2011, plate 1) potentiometric-surface map showing contours of equal groundwater-level altitude, indicating generalized hydraulic gradients throughout the GB-CAAS. Groundwater generally flows perpendicular to these contours, moving

from higher to lower groundwater-level altitudes. Because of the large contour interval (1,000 ft), this potentiometric-surface map indicates only regional-scale movement of groundwater. Groundwater flow is indicated from the higher-altitude areas in the center of the area towards the Great Salt Lake Desert, the Muddy River Springs Area, the Virgin River, Death Valley, and the Humboldt River.

It has been previously recognized that regional-scale groundwater flow likely influences the thermal regime of the eastern Great Basin, sweeping heat away from several areas (Lachenbruch and Sass, 1977; 1978). The presence of regionally extensive aquifer units and groundwater flow at depth, such as within the LCAU, likely results in heat transport through advective flow. Heat transport by groundwater flow, therefore, needs to be considered when evaluating the geothermal resource potential.

Carbonate rocks within the GBCAAS study area have relatively high bedrock permeability (geometric mean of 4 ft/d) and underlie 2,000 m of basin-fill sediments in several areas (Sweetkind et al., 2011a). In general, the carbonate units are more continuous in the north-south direction than in the west-east direction, mainly because of structural extension and the existence of intervening mountain ranges and normal faults in the west-east direction (Dettinger and Schaefer, 1996). Figure 3 shows both north-south and west-east cross sections through the study area. Cross-section B-B' extends from Ruby Valley in the north to Las Vegas Valley in the south and shows continuity of LCAU along this north-south profile. Cross-section J-J', extending east from Rock Creek Valley in north-central Nevada to the Wasatch Mountains of Utah, illustrates the disconnected nature of LCAU along this west-east profile.

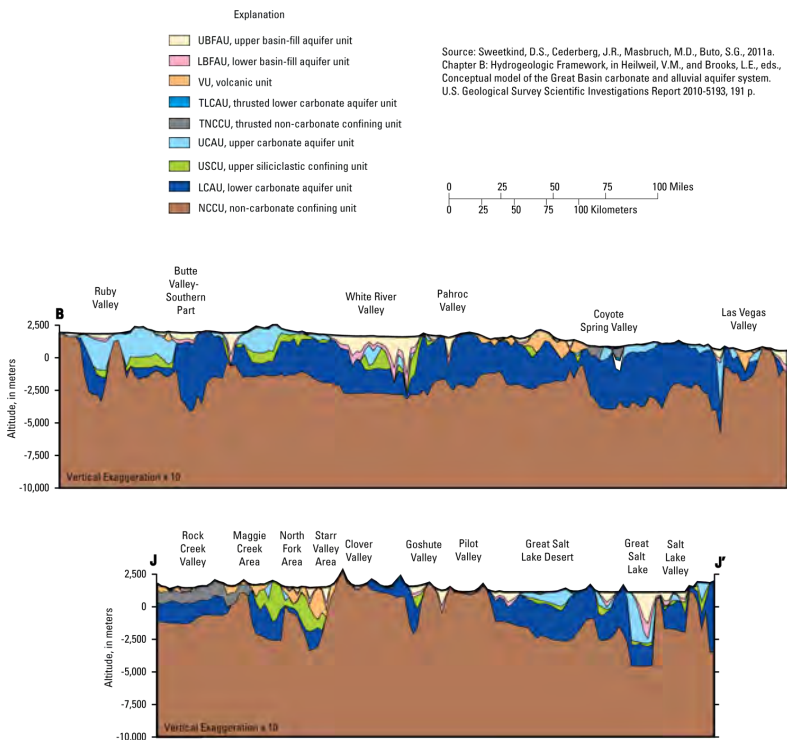


Figure 3. Cross sections B-B' (north-south) and J-J' (west-east) representing the three-dimensional hydrogeologic framework developed for the Great Basin carbonate and alluvial aquifer system study area (from Sweetkind et al., 2011a). See figure 2 for cross-section locations.

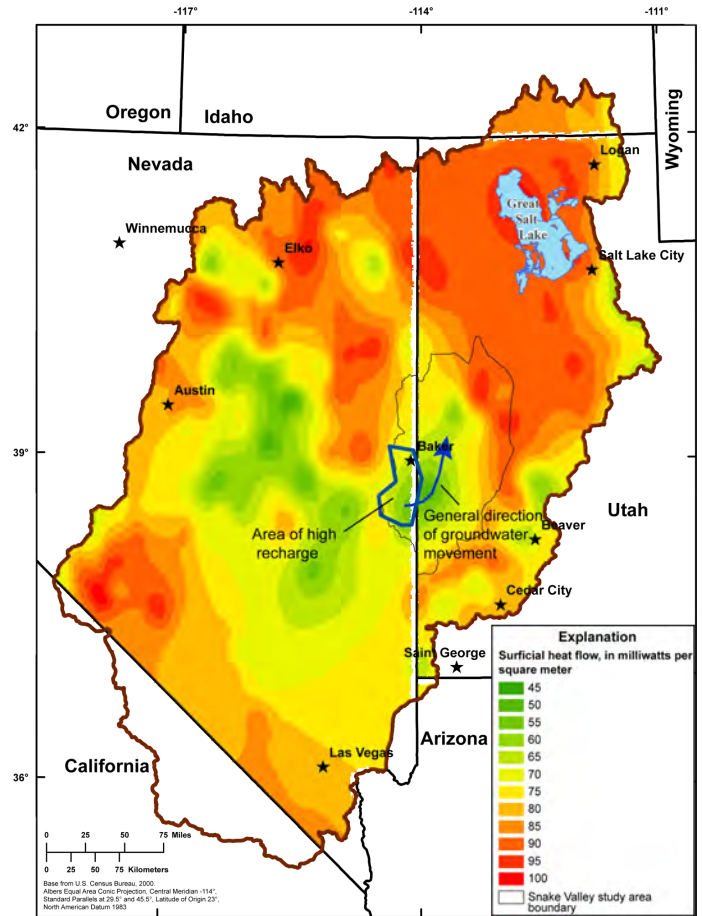


Figure 4. Surficial heat flow in the Great Basin carbonate and alluvial aquifer system study area and an area of high recharge in the Snake Valley study area (modified from Blackwell et al., 2011).

Heat Flow

The Great Basin portion of a surficial heat-flow map recently updated by Blackwell et al. (2011) is reproduced in figure 4. Heat flow within the Basin and Range province is complicated by a combination of extension (including volcanism and intrusion), effects of thermal refraction, variations in radioactive heat production, erosion and sedimentation, and advective effects of groundwater flow (Blackwell, 1983). Surficial heat-flow values in the study area range from 45 to 100 milliwatts per square meter (mW/m^2) (Blackwell et al., 2011); values of less than 70 mW/m^2 might be the result of groundwater movement flushing heat from the subsurface, as proposed by Lachenbruch and Sass (1977; 1978). One area of low surficial heat flow that has undergone detailed hydrological study in recent years is the Snake Valley area along the Utah-Nevada border. It is likely that groundwater is significantly affecting surficial heat flow in this area. Results of a groundwater flow and heat transport numerical model (Melissa Masbruch, U.S. Geological Survey, written commun., May 2012), recent temperature measurements (Blackett, 2011), and analysis of groundwater geochemical

data (Phil Gardner, U.S. Geological Survey, written commun., May 2012) indicate that low surficial heat flow south of Baker, Nevada, corresponds to an area with high groundwater recharge rates and active groundwater flow from southwest to northeast.

On the basis of these Snake Valley area findings, it is possible that similar areas of low surficial heat flow in a large portion of east-central Nevada are also caused by the flushing of heat by groundwater flow. Figure 5 shows groundwater-budget imbalances and possible subsurface flow between groundwater flow systems and subareas within the GBCAAS study area (Masbruch et al., 2011), and areas of low surficial heat flow (less than 70 mW/m²) (Blackwell et al., 2011). This suggests that heat is being swept by regional groundwater flow, particularly by subsurface outflow from the Diamond Valley, Newark Valley, and the northern part of the Colorado groundwater flow systems. Additionally, these areas of low surficial heat flow contain thick, continuous deposits of permeable carbonates (Cederberg et al., 2011) which are likely conduits for groundwater flow.

Use of Hydrogeologic and Surficial Heat-Flow Data to Highlight Areas of Potential Geothermal Development

A study by Allis et al. (2012, in prep.) indicates that at least 2,000 m of sediments and high surficial heat flow (greater than 80 mW/m²) are needed to produce temperatures of more than

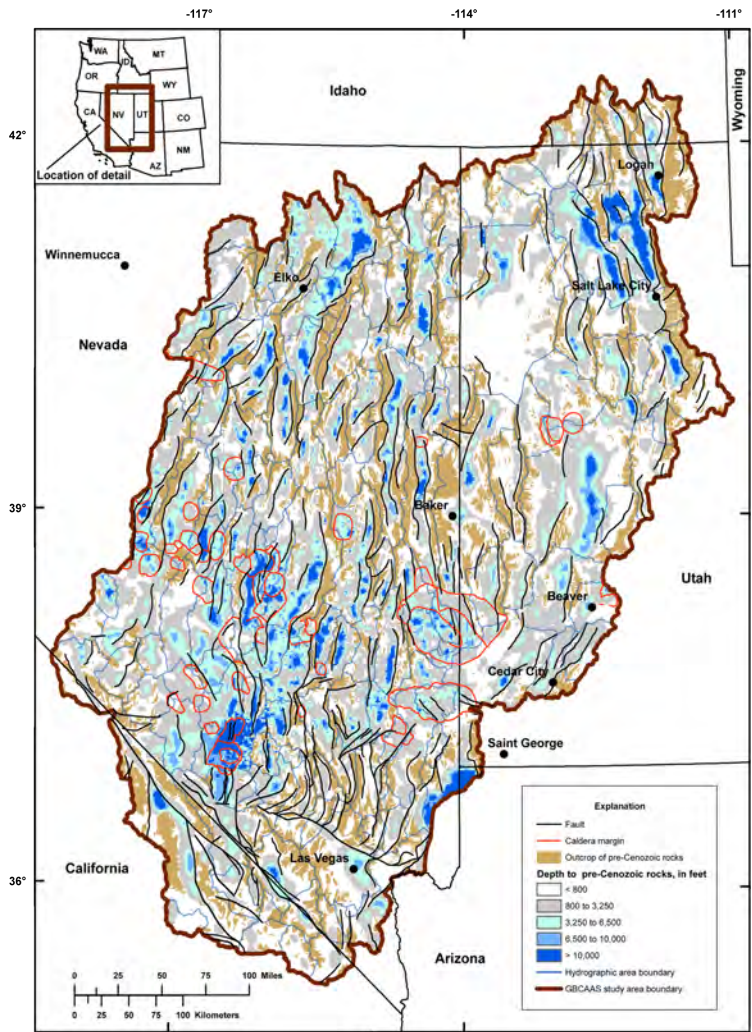
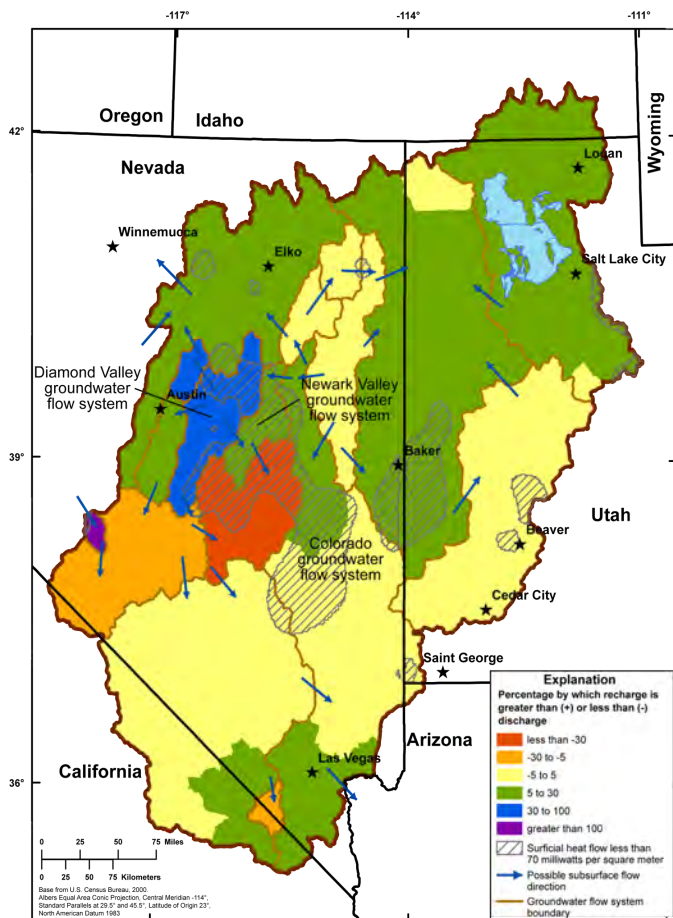


Figure 6. Surface exposure and depth to pre-Cenozoic rocks in the Great Basin carbonate and alluvial aquifer system study area (from Sweetkind et al., 2011a).

150 °C at about 3,000 m depth; this combination of high temperature at relatively shallow depths is preferred for geothermal development. Figure 6 shows locations within the GBCAAS where pre-Cenozoic rocks underlie sequences of Cenozoic units (UBFAU, LBFAU, VU) that have thickness greater than 2,000 m. Where thick sequences of Cenozoic units overlie permeable bedrock, a geothermal resource may occur at depths of 2,000 to 3,000 m.

GIS techniques were used to combine areas of high surficial heat flow (greater than 80 mW/m²) and areas of thick (greater than 2,000 m) Cenozoic units (figure 7) in the GBCAAS study area. Areas with high potential for geothermal development include

Figure 5. Possible subsurface flow between groundwater flow systems and groundwater budget imbalances in groundwater flow systems and subareas in the Great Basin carbonate and alluvial aquifer system study area and areas of low surficial heat flow (modified from Masbruch et al., 2011).

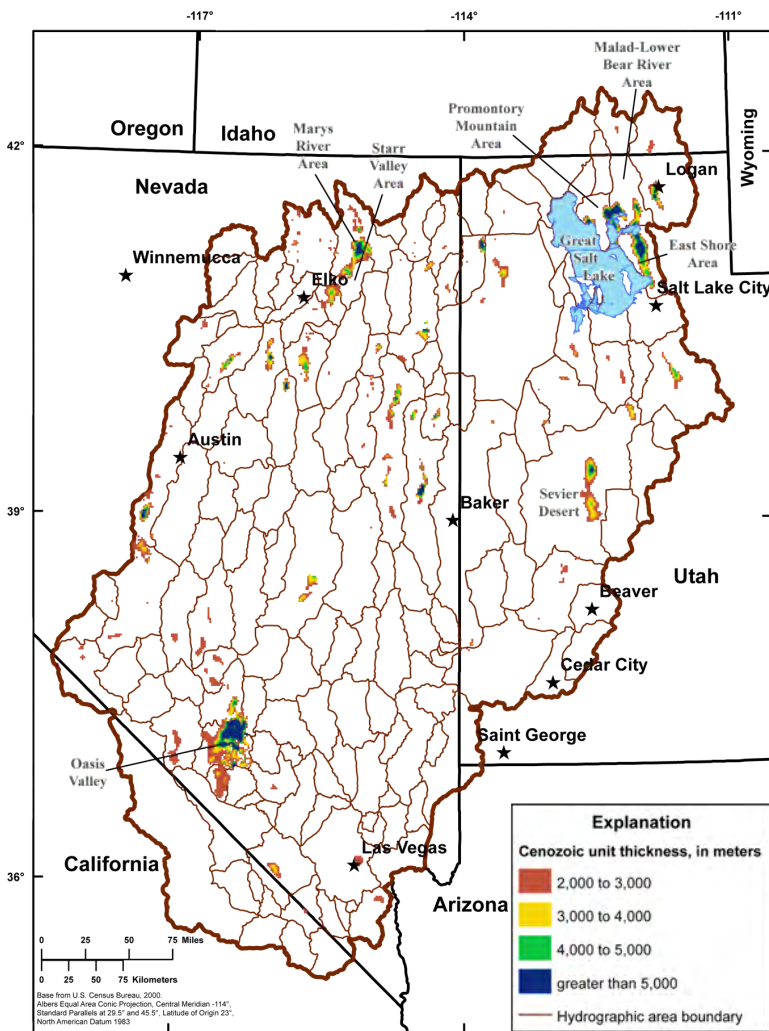


Figure 7. Areas of Cenozoic units greater than 2,000 meters thick and surficial heat flow greater than 80 mW/m² within the Great Basin carbonate and alluvial aquifer system study area.

(1) Oasis Valley, Nevada, in the Death Valley groundwater flow system; (2) Sevier Desert, Utah, in the Sevier Lake groundwater flow system; (3) East Shore, Promontory Mountain, and Malad-Lower Bear River areas, Utah, in the Great Salt Lake groundwater flow system; and (4) Marys River and Starr Valley areas, Nevada, in the Humboldt groundwater flow system.

Conclusions

The following conclusions can be drawn from recently published hydrogeologic concepts of the Great Basin carbonate and alluvial aquifer system and surficial heat flow, as presented in this paper:

The continuity of thick, permeable carbonates at depth allow for regional-scale groundwater flow within the study area.

The existence of areas of low surficial heat flow (less than 70 mW/m²) within the study area may indicate flushing of heat by groundwater flow. Such areas may not be ideal targets for geothermal resources development because of the likelihood of cooler groundwater temperatures and lower geothermal gradients.

The existence of thick sequences of low thermal conductivity Cenozoic units in areas of high surficial heat flow such as Marys River and Starr Valley areas, and Oasis Valley, Nevada, and East Shore, Promontory Mountain, and Malad-Lower Bear River areas, and Sevier Desert, Utah, indicate potential areas that may warrant further investigation of geothermal resources development within the study area.

Future Work

We recommend a more detailed study than has been possible for this paper on groundwater flow and surficial heat-flow relations. This is likely to provide more insight regarding effects of groundwater movement on lateral heat-flow variations.

Acknowledgements

This study was funded by the Department of Energy. Previous hydrogeologic and water-budget analyses were funded by the U.S. Geological Survey Groundwater Availability Project. Much of the hydrogeologic characterization is based on work by Donald S. Sweetkind, U.S. Geological Survey, Lakewood, Colorado.

References

- Allis, R., Blackett, R., Gwynn, M., Hardwick, C., Moore, J., Morgan, C., Schelling, D., and Sprinkel, D., 2012. Stratigraphic reservoirs in the Great Basin—the bridge to development of enhanced geothermal systems in the U.S. Geothermal Resources Council Transactions, 36, in prep.
- Allis, R., Moore, J., Blackett, R., Gwynn, M., Kirby, S., and Sprinkel, D., 2011. The potential for basin-centered geothermal resources in the Great Basin. GRC Transactions, 35, 683-688.
- Blackett, R.E., 2011. Temperature profiles of water monitoring wells in Snake Valley, Tule Valley, and Fish Springs Flat, Millard and Juab Counties, Utah. Utah Geological Survey Open-File Report 578, 13 p.
- Blackwell, D.D., 1983. Heat flow in the northern Basin and Range province. Geothermal Resources Council Special Report no. 13, 81-92.
- Blackwell, D.D., et al., 2011. Heat flow map of the conterminous United States, Google.org/egs, 2011.
- Cederberg, J.R., Sweetkind, D.S., Buto, S.G., and Masbruch, M.D., 2011. Three-dimensional hydrogeologic framework. Appendix 1 in Heilweil, V.M., and Brooks, L.E., eds., 2011. Conceptual model of the Great Basin carbonate and alluvial aquifer system. U.S. Geological Survey Scientific Investigations Report 2010-5193, 127-142.
- Dettinger, M.D., and Schaefer, D.H., 1996. Hydrogeology of structurally extended terrain in the eastern Great Basin of Nevada, Utah, and adjacent states, from geologic and geophysical models. U.S. Geological Survey Hydrologic Investigations Atlas HA-694-D, 1 sheet, scale 1:1,000,000.
- Harrill, J.R., Gates, J.S., and Thomas, J.M., 1988. Major ground-water flow systems in the Great Basin region of Nevada, Utah, and adjacent states. U.S. Geological Survey Hydrologic Investigations Atlas HA-694-C, 2 sheets, scale 1:1,000,000.
- Harrill, J.R., and Prudic, D.E., 1998. Aquifer systems in the Great Basin region of Nevada, Utah, and adjacent states—Summary Report. U.S. Geological Survey Professional Paper 1409-A, 66 p.
- Heilweil, V.M., and Brooks, L.E., eds., 2011. Conceptual model of the Great Basin carbonate and alluvial aquifer system. U.S. Geological Survey Scientific Investigations Report 2010-5193, 191 p.

- Heilweil, V.M., Sweetkind, D.S., and Susong, D.D., 2011. Introduction. Chapter A in Heilweil, V.M., and Brooks, L.E., eds., Conceptual model of the Great Basin carbonate and alluvial aquifer system. U.S. Geological Survey Scientific Investigations Report 2010-5193, 3-14.
- Lachenbruch, A.J., and Sass, J.H., 1977. Heat flow in the United States and the thermal regime of the crust. In Heacock, J.G., ed. The Earth's crust, its nature and physical properties. Geophysical Monograph 20, Washington, D.C., American Geophysical Union, 626-675.
- Lachenbruch, A.J., and Sass, J.H., 1978. Models of extending lithosphere and heat flow in the Basin and Range province. In Smith, R.B., and Eaton, G.P., eds. Cenozoic tectonics and regional geophysics of the western Cordillera. Memoir 152, 209-250.
- Masbruch, M.D., Heilweil, V.M., Buto, S.G., Brooks, L.E., Susong, D.D., Flint, A.L., Flint, L.E., and Gardner, P.M., 2011. Estimated groundwater budgets. Chapter D in Heilweil, V.M., and Brooks, L.E., eds., Conceptual model of the Great Basin carbonate and alluvial aquifer system. U.S. Geological Survey Scientific Investigations Report 2010-5193, 73-126.
- Prudic, D.E., Harrill, J.R., and Burbey, T.J., 1995. Conceptual evaluation of regional ground-water flow in the carbonate-rock province of the Great Basin, Nevada, Utah, and adjacent states. U.S. Geological Survey Professional Paper 1409-D, 102 p.
- Sweetkind, D.S., Cederberg, J.R., Masbruch, M.D., and Buto, S.G., 2011a. Hydrogeologic framework. Chapter B in Heilweil, V.M., and Brooks, L.E., eds., Conceptual model of the Great Basin carbonate and alluvial aquifer system. U.S. Geological Survey Scientific Investigations Report 2010-5193, 15-50.
- Sweetkind, D.S., Masbruch, M.D., Heilweil, V.M., and Buto, S.G., 2011b. Groundwater flow. Chapter C in Heilweil, V.M., and Brooks, L.E., eds., Conceptual model of the Great Basin carbonate and alluvial aquifer system. U.S. Geological Survey Scientific Investigations Report 2010-5193, 51-72.
- Toth, J., 1963. A theoretical analysis of groundwater flow in small drainage basins. *Journal of Geophysical Research*, 68, 2354-2356.
- Welch, A.H., Bright, D.J., and Knochenmus, L.A., eds., 2007. Water resources of the Basin and Range carbonate-rock aquifer system, White Pine County, Nevada, and adjacent areas in Nevada and Utah. U.S. Geological Survey Scientific Investigations Report 2007-5261, 96 p.
- Williams, C.F., Reed, M.J., Mariner, R.H., DeAngelo, J., and Galanis S.P., 2008. Assessment of moderate- and high-temperature geothermal resources of the United States. U.S. Geological Survey Fact Sheet 2008-3082.

An animated tectonic reconstruction of southwestern North America since 36 Ma

Nadine McQuarrie*

Brian P. Wernicke

Division of Geological and Planetary Sciences, MS 100-23, California Institute of Technology, Pasadena, California 91125, USA

ABSTRACT

We present tectonic reconstructions and an accompanying animation of deformation across the North America–Pacific plate boundary since 36 Ma. Intraplate deformation of southwestern North America was obtained through synthesis of kinematic data (amount, timing, and direction of displacement) along three main transects through the northern (40°N), central (36°N–37°N), and southern (34°N) portions of the Basin and Range province. We combined these transects with first-order plate boundary constraints from the San Andreas fault and other areas west of the Basin and Range. Extension and strike-slip deformation in all areas were sequentially restored over 2 m.y. (0–18 Ma) to 6 m.y. (18–36 Ma) time intervals using a script written for the ArcGIS program. Regions where the kinematics are known constrain adjacent areas where the kinematics are not well defined. The process of sequential restoration highlighted misalignments, overlaps, or large gaps in each incremental step, particularly in the areas between data transects, which remain problematic. Hence, the value of the reconstructions lies primarily in highlighting questions that might not otherwise be recognized, and thus they should be viewed more as a tool for investigation than as a final product.

The new sequential reconstructions show that compatible slip along the entire north-south extent of the inland right-lateral shear zone from the Gulf of California to the northern Walker Lane is supported by available data and that the east limit of active shear has migrated westward with respect to North America since ca. 10 Ma. The reconstructions also highlight new problems regarding strain-compatible ex-

tension east and west of the Sierra Nevada–Great Valley block and strain-compatible deformation between southern Arizona and the Mexican Basin and Range. Our results show ~235 km of extension oriented ~N78°W in both the northern (50% extension) and central (200% extension) parts of the Basin and Range. Following the initiation of east-west to southwest-northeast extension at 15–25 Ma (depending on longitude), a significant portion of right-lateral shear associated with the growing Pacific–North America transform jumped into the continent at 10–12 Ma, totaling ~100 km oriented N25°W, for an average of ~1 cm/yr since that time.

Keywords: Basin and Range, kinematic reconstruction, extension, plate tectonics, velocity field.

INTRODUCTION

The large-scale horizontal velocity field at Earth's surface is one of the main predictions of physical models of lithospheric deformation (e.g., England and McKenzie, 1982). Two-dimensional, cross-sectional models of finite deformation of mountain belts incorporating strong heterogeneity in rheologic parameters have been developed over the last decade (e.g., Lavier and Buck, 2002; Braun and Pauselli, 2004). Owing to advances in computation, fully three-dimensional models of plate boundary deformation zones, incorporating both horizontal and vertical variations in lithospheric rheology, will soon become common. Thus, a key observational frontier will be the determination of precise displace-

*Current address: Department of Geosciences, Guyot Hall, Princeton University, Princeton, New Jersey 08544, USA.

ment vector fields of continental deformation in order to test these models. The most dramatic recent improvement in obtaining such velocity fields has been the advent of space-based tectonic geodesy (especially using continuous global positioning systems [GPS]), which is yielding velocity fields that are unprecedented in terms of both the scale of observation and the accuracy of the velocities. These data have already been used as tests for physical models in southwestern North America (e.g., Bennett et al., 1999, 2003; Flesch et al., 2000) and elsewhere (e.g., Holt et al., 2000). Substantial progress has also occurred over the last decade in determining longer-term velocity fields using the methods of plate tectonics and regional structural geology.

These longer-term displacement histories are essential for addressing the question of how the lithosphere responds to major variations in plate geometry and kinematics (e.g., Houseman and England, 1986; England and Houseman, 1986; Bird, 1998) because such variations occur on the million-year time scale. Plate tectonics is a precise method for constraining the overall horizontal kinematics of plate boundaries, using seafloor topographic and magnetic data in concert with the geomagnetic time scale. For the diffuse deformation that characterizes the continental lithosphere along plate boundaries, however, tectonic reconstruction at scales in the 100 km to 1000 km range is not as straightforward. It is based primarily on structural geology and paleomagnetic studies and requires the identification of large-scale strain markers and consideration of plate tectonic constraints (e.g., Wernicke et al., 1988; Snow and Wernicke, 2000; McQuarrie et al., 2003). Regional strain markers within the continents may not exist in any given region, and even if they do, they may not be amenable to accurate reconstruction at large scales.

Geosphere; December 2005; v. 1; no. 3; p. 147–172; doi: 10.1130/GES00016.1; 11 figures; 6 tables, 1 animation.

For permission to copy, contact editing@geosociety.org
© 2005 Geological Society of America

SE ROA 37555

147

JA_9061

In southwestern North America, a zone of plate boundary deformation on the order of 1000 km wide is developed along the plate boundary. In mid-Tertiary time (36 Ma), this boundary was strongly convergent, with the Farallon plate subducting eastward beneath the North American plate. Beginning at ca. 30 Ma, the Pacific-Farallon ridge came in contact with the North American plate. Since then, the Pacific-North America boundary has grown through the migration of triple junctions along the coast. Now, the entire margin from southern Baja California to Cape Mendocino is a transform Pacific-North America boundary, rather than a convergent Farallon-North America boundary (Atwater, 1970). This change in the configuration of the plate boundary is both relatively simple and profound, making southwestern North America an ideal laboratory for investigating how continental lithosphere responds to changes in relative plate motion.

Refined plate tectonic reconstructions have provided an improved kinematic model of the change from convergent to transform motion and have shown that there were significant variations in the obliquity of the transform after it developed. In particular, during the interval ca. 16 to ca. 8 Ma, Pacific-North America motion was highly oblique and included a margin-normal extensional component of as much as 2 cm/yr, coeval with a rapid pulse of Miocene extension that formed the Basin and Range province (Atwater and Stock, 1998; Wernicke and Snow, 1998). At ca. 8 Ma, Pacific-North America motion changed to more purely coastwise motion, which appears to have changed the intraplate tectonic regime from profound extension to a more complex mixture of extension, shortening, and transform motion, responsible for the opening of the Gulf of California, thrust faulting of the western Transverse Ranges, and development of the San Andreas fault-eastern California shear zone-Walker Lane, respectively.

Over the last several years, high-quality, large-scale kinematic constraints, many of which resulted from decades of field work and attending debate, have become available, reaching the point where synthesis into a large-scale velocity field is feasible. A rudimentary kinematic model using many of the constraints along the plate boundary and in the plate interior was incorporated into a publicly available animation of the post-38 Ma evolution of the entire Pacific-Farallon-North America system (Atwater and Stock, 1998; animation available at <http://emvc.geol.ucsb.edu/download/nepac.php>).

In this paper, we synthesize the current state

of information on the kinematics of the diffusely deforming North American plate since 36 Ma, based on offsets of regional structural markers, and construct a strain-compatible kinematic model of the horizontal motions at 2 m.y. (0–18 Ma) and 6 m.y. (18–36 Ma) intervals, presented as a continuous animation. The model is by no means a final product, as new kinematic information and testing will require significant modifications of the model. Rather, the model is an attempt to be quantitatively rigorous in a way that will be useful for comparison with large-scale, three-dimensional physical models and for the identification of issues regarding the structural kinematics that might not otherwise be detected. Thus, in addition to the animation, we have constructed “instantaneous” velocity fields based on 2 m.y. averages from 0 Ma to 18 Ma and 6 m.y. averages from 18 Ma to 36 Ma. These results are our best attempt at “paleogeodesy,” presenting the geology-based kinematic model in a format similar to modern GPS velocity fields, which in turn may be quantitatively compared to physically based model velocity fields.

METHODS

By combining regional structural constraints into a single model, the self-consistency of the model (i.e., its strain compatibility through time) provides powerful additional constraints on the kinematics in at least three ways. The first and most important is the fact that high-quality local kinematic information imposes severe constraints on its surroundings where information may not be available. As a hypothetical example, consider a large region of oblique extension between two undeformed blocks (Fig. 1). The strain and strain path need not be known for each geological element in the deforming region in order to constrain the large-scale kinematics. If the sum of fault displacements across just a single reconstruction path (**p**) is known, restoring point A to a position at point B, and it is known that the blocks have not rotated, then the single path imposes a strong constraint on the overall kinematics of all of the other paths between the blocks (Fig. 1A).

The second additional constraint is on errors in reconstructions. In the example in Figure 1, let us suppose that the minimum value of all fault displacements along reconstruction path **p** restores the block to point B, but there is no constraint on the maximum value along the path itself. The side of the block containing A would overlap the block on the other side of the rift if the displacement along the

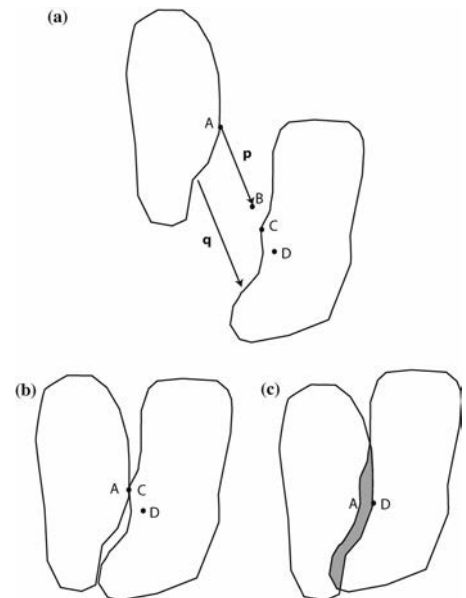


Figure 1. Schematic diagram illustrating the method of using regional structural constraints to limit possible displacement paths in tectonic reconstructions. See text for discussion and explanation of letters.

path were in excess of AC (Fig. 1B), violating the condition of strain compatibility. Therefore, the displacement is constrained to be between AB and AC, rather than some value greater than AB.

A third and perhaps most useful additional constraint arises when local constraints contradict one another. For example, if reconstruction along path **q** (Fig. 1A) required that point A restore to a position D, which is well within the other block, then the violation of strain compatibility forces reevaluation of the geological constraints. The geological reconstruction for displacement along **q**, the paleomagnetic constraints on the blocks, and the presumed rigidity of the blocks cannot all be correct. Thus, the exercise of regional reconstruction focuses attention on information that is most critical for improving the accuracy of the reconstruction. For southwestern North America, there is now enough high-quality local kinematic information that large-scale self-consistency of the model imposes useful additional constraints in all of these ways.

In making the reconstruction, the methods used in the local study of Wernicke et al. (1988) and Snow and Wernicke (2000) in the Death Valley region of the central Basin and Range province were applied at large scale. In Snow and Wernicke (2000), each step in the reconstruction showed the paleoposition of existing mountain ranges. Although the recon-

struction allowed for the ranges to change shape as extension is restored (i.e., the ranges may decrease in area), in our reconstruction, the mountain ranges are shown as digitized polygons that approximate: (1) the modern bedrock-alluvium contact (e.g., a typical range in the Basin and Range), (2) faults bounding individual crustal blocks (e.g., the Santa Ynez Mountains block in the western Transverse Ranges), or (3) the physiographic boundaries of large, intact crustal blocks (e.g., the Colorado Plateau). In some cases, especially where large extensional strains are involved, the reconstruction overlaps individual polygons to account for extension, essentially using the modern bedrock-alluvium contact as a geographical reference marker. Because the strain is extensional, and in the case of metamorphic core complexes, one range has literally moved off of the top of another, these overlaps do not violate strain compatibility.

The individual positions of polygons were restored in each 2 m.y. time frame through an ArcGIS script that reads and updates a table listing the kinematic data for each range. The script, created by Melissa Brenneman of the Redlands Institute at the University of Redlands, is written in Visual Basic and is incorporated as a tool in a custom ArcMap document. The script reads a dBASE 4 table that contains the movement parameters (direction, distance, rotation, and time interval) for each range (Appendix 1).¹ The movement parameters listed in the table include both the available data (Figs. 2–5), as well as the motion required for strain compatibility. For the regions where kinematic data are not available, the kinematics could be defined by inserting data from proximal areas, or individual ranges could be moved by hand with the motion updated and recorded in the dBASE table using the ArcGIS script. The ArcGIS format and accompanying script allows for exact displacements to be incorporated into the model, as well as the individual adjustment of ranges to ensure strain compatibility. The GIS script records the geographical position of the centroid of each range at each 2 m.y. or 6 m.y. epoch. This allows for the data to be displayed in a variety of ways, including palinspastic maps for each 2 m.y. or 6 m.y. epoch, instantaneous velocity vectors at each 2 m.y. or 6 m.y. epoch, “paths” that individual ranges take over

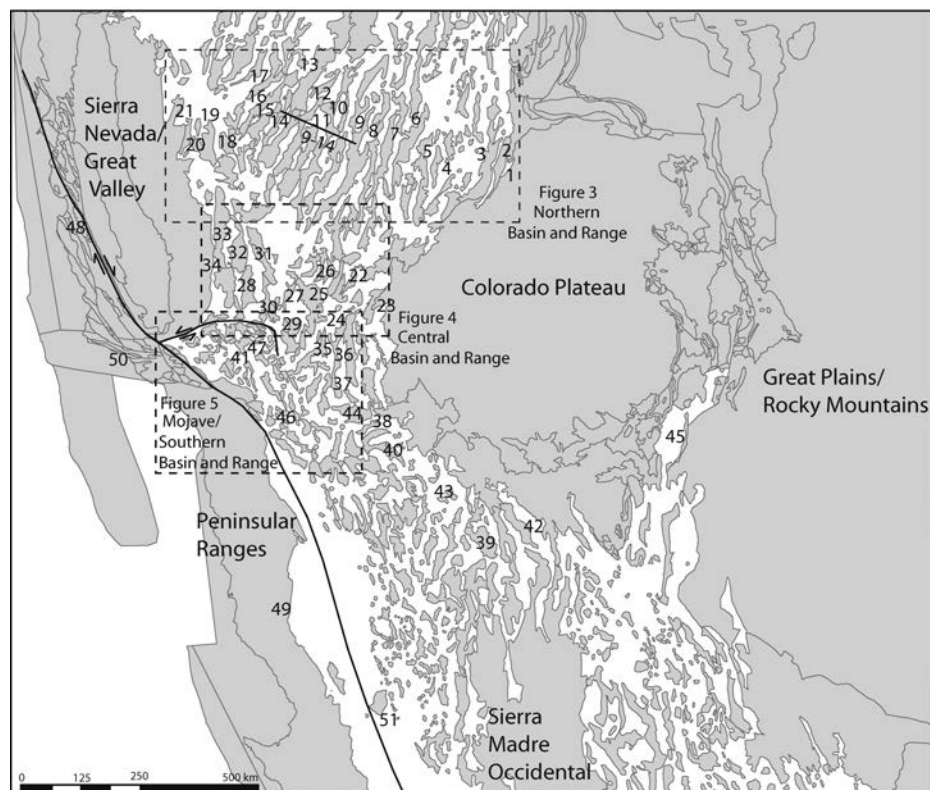


Figure 2. Map of western North America showing the primary tectonic elements in the reconstruction. The gray shaded polygons represent the physiographic or geologic expression of mountain ranges, which in the Basin and Range are fault bounded and separated by alluvial valleys. Dashed boxes are the locations of Figures 3–5. The numbers refer to specific mountain ranges identified in Tables 1–6.

the 36 m.y. span of the reconstruction, or an animation that shows the integrated motion over 36 m.y. Instantaneous geology velocity fields are obtained from connecting the centroids of specific ranges at one time with the centroid of the same range in a later time.

DATA

The primary tectonic elements in the reconstruction are large crustal blocks comprising flat-lying pre-36 Ma strata, or geologic elements that are otherwise little deformed, and the straining areas in between them. The large unstrained blocks include the Great Plains–Rocky Mountains region (nominal North America reference frame), the Sierra Madre Occidental, the Colorado Plateau, the Sierra Nevada–Great Valley block, and Peninsular Ranges block (Fig. 2). The strained areas around them include the Rio Grande rift and Basin and Range province, the Gulf of California, the Transverse Ranges, the Coast Ranges, and the Continental Borderlands province offshore of southern California and Baja California.

The constraints used in the reconstruction are organized into six major categories (Tables 1–6). The first covers a range-by-range reconstruction path across the northern Basin and Range near latitude 40°N (Fig. 3 and Table 1). The second includes a similar reconstruction path across the central Basin and Range near latitude 37°N (Fig. 4 and Table 2). These two reconstructions collectively constrain the motion of the Sierra Nevada–Great Valley block. The third includes constraints from the southern Basin and Range, mainly the mid-Tertiary metamorphic core complexes of the Colorado River corridor and southern Arizona, west of the Sierra Madre Occidental, and extension across the Rio Grande rift north and east of the Sierra Madre Occidental (Table 3). The fourth includes the complex Oligocene to recent strike-slip and extensional displacements of the Mojave region, which connect the Sierran displacement to regions farther south (Fig. 5 and Table 4). The fifth includes paleomagnetic and geologic constraints on vertical axis rotations of large crustal blocks, including the Sierra Nevada and Colorado Plateau, as well as small, individual ranges within the

¹GSA Data Repository item 2005200, Appendix 1, Movement Table, paleogeographic maps, and ArcGIS files (shape files for each reconstructed time step), is available online at www.geosociety.org/pubs/ft2005.htm, or on request from editing@geosociety.org or Documents Secretary, GSA, P.O. Box 9140, Boulder, CO 80301-9140, USA

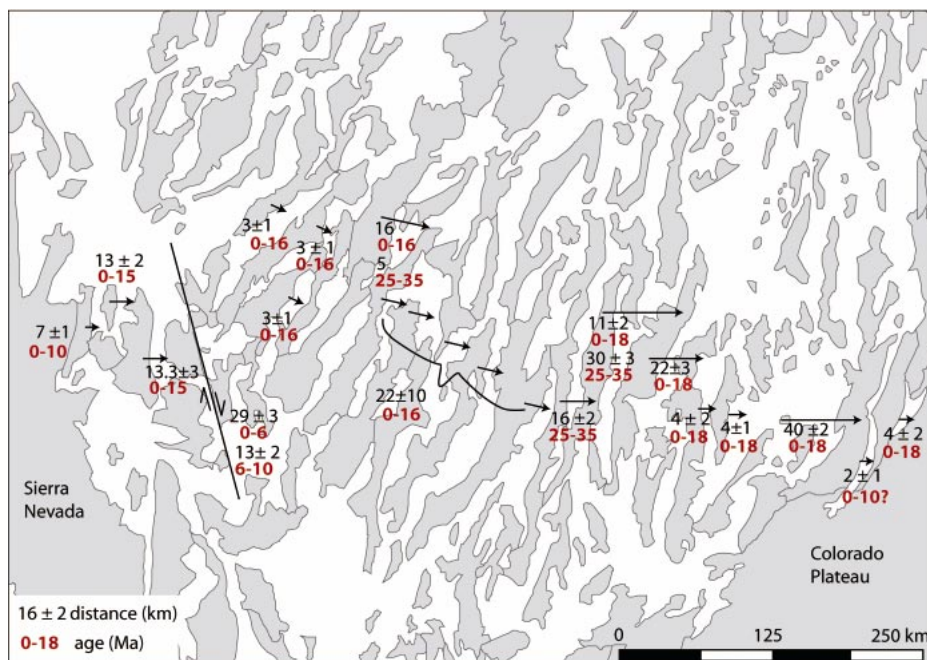


Figure 3. Map of the northern Basin and Range showing the kinematic data incorporated into the model. Black numbers indicate horizontal displacement amount, red bold numbers indicate age range of motion. Arrows indicate approximate magnitude and direction of individual relative displacements between polygons. Data compiled from Allmendinger et al., 1986; Armstrong et al., 2004; Bartley and Wernicke, 1984; Coogan and DeCelles, 1996; DeCelles et al., 1995; Dilles and Gans, 1995; Faulds et al., 2003; Hardyman et al., 1984; Hintzi, 1973; Hudson and Oriol, 1979; Lee, 1999; Miller et al., 1999; Niemi, 2002; Niemi et al., 2004; Smith, 1992; Smith et al., 1990; Smith and Bruhn, 1984; Stockli, 2000, 2001; Surpress, 1999.

central Basin and Range and Mojave regions (Table 5). Lastly, constraints on the large displacements along the San Andreas fault–Gulf of California shear system, and strains and rotations within the Continental Borderlands, including the large clockwise rotation of the Santa Ynez Mountains block, are included in Figure 6 and Table 6.

Northern Basin and Range

The extensional kinematics of the northern Basin and Range are dominated by two large-offset normal fault systems, the Snake Range detachment system (78 km of total offset) and the Sevier Desert detachment (40 km of total offset). The Snake Range detachment system affects the Egan, Schell Creek, and Snake Ranges (Fig. 2, ranges 6–8). Although the coupling of this system of faults to deep crustal extension has been debated (e.g., Gans and Miller, 1983; Miller et al., 1983; Bartley and Wernicke, 1984; Miller et al., 1999; Lewis et al., 1999), a magnitude of upper crustal extension of $78 \text{ km} \pm 10 \text{ km}$, as determined through mapped and restored stratigraphic

markers, is not controversial (Gans and Miller, 1983; Bartley and Wernicke, 1984). More controversial is the geometry of the extensional faults in the Sevier Desert basin (between ranges 3 and 4, Fig. 2), including the very existence of the Sevier Desert detachment, which is known only from interpretations of seismic reflection profiles and well data (Anders and Christie-Blick, 1994; Wills et al., 2005). The 40-km offset along the Sevier Desert detachment used in this paper is based on restoring Sevier fold-thrust belt structures that are offset by the detachment, and high-angle normal faults in the hanging wall imaged in the Consortium for Continental Reflection Profiling (COCORP) and industry seismic reflection lines (Allmendinger et al., 1986; Allmendinger et al., 1995; Coogan and DeCelles, 1996). An opposing view to the large-offset kinematics of a shallow detachment suggests that the imaged reflection surface is a composite of aligned features that includes basin-bounding high-angle normal faults, a subhorizontal thrust fault, and an evaporite horizon (Anders and Christie-Blick, 1994). According to this interpretation, exten-

sion across ranges within and around the Sevier Desert basin could be as little as 10 km (versus 40 km), which would subtract $\sim 15\%$ from our overall estimate of extension along the transect.

To the west of the Egan Range area, the remainder of the northern Basin and Range deformation is partitioned into extensional and right-lateral strike-slip offsets, both of which accommodate translation of the Sierra–Great Valley block away from the interior of North America. The extension (94 km) is accommodated by several systems of steeply tilted normal fault blocks in the western Basin and Range, with individual fault systems accommodating up to 16 km of extension (Fig. 2, ranges 13, 19, and 20) (Surpress, 1999; Dilles and Gans, 1995; Smith, 1992), and a number of high-angle, presumably modest-offset normal faults that define the Basin and Range physiography across the central part of the reconstruction path, which we assume have 3–4 km of horizontal offset each.

Right-lateral shear is accommodated predominantly through northwest-trending faults concentrated near the western edge of the northern Basin and Range in the northern Walker Lane Belt (Fig. 2, range 18). Right-lateral offset on a series of faults, which individually have 5–15 km of offset, totals 20–56 km (Faulds et al., 2005; Hardyman et al., 1984). Because the faults strike more westerly than the North American margin, their motion accommodates a component of westward motion of the plate boundary.

Timing of extension in the northern Basin and Range is constrained by a large body of work on the ages of faulted Cenozoic volcanic and sedimentary units and cooling ages of uplifted footwall blocks. For example, the early “core complex”–related extension (ca. 35–25 Ma) is seen in coeval faulting and volcanism at 35 Ma in the Egan Range (Gans and Miller, 1983) and $^{40}\text{Ar}/^{39}\text{Ar}$ cooling ages indicative of rapid cooling from 30 to 25 Ma in the western portion of the northern Snake Range and from 20 to 15 Ma in the eastern portion of the range (Lee, 1995). Apatite fission track (AFT) cooling ages from the northern Snake Range indicate 10–13 km of fault slip from 18 to 14 Ma. Initiation of later “Basin and Range” extension is seen predominantly in the fission-track and helium cooling ages of apatite and zircon. The cooling ages across the width of the extending zone cluster ca. 15 Ma (Stockli, 1999), with 18 Ma ages in the footwall of the Snake Range detachment (Miller et al., 1999) (Fig. 2, range 6) and Sevier Desert detachment (Stockli et al., 2001) (Canyon Range, Figure 2, range 3).

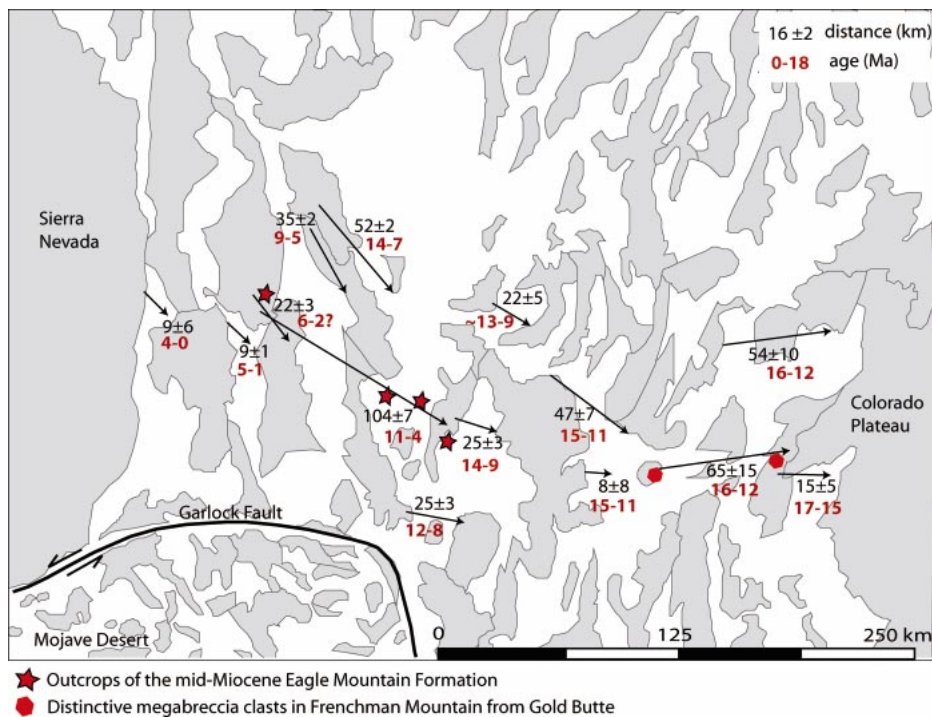


Figure 4. Map of the central Basin and Range showing the kinematic data incorporated into the model. Motion of the Sierra Nevada with respect to the Colorado Plateau in this region is predominantly constrained by two distinctive sedimentary deposits (indicated as stars and hexagons) offset along extensive normal and strike-slip fault systems. Arrows indicate approximate magnitude and direction of individual relative displacements between polygons. Black numbers indicate horizontal displacement amount, bold red numbers indicate age range of displacement. Data from Axen et al., 1990; Brady et al., 2000; Burchfiel, 1968; Burchfiel et al., 1987; Cemen et al., 1985; Duebendorfer et al., 1998; Fitzgerald et al., 1991; Fowler and Calzia, 1999; Guth, 1989; Holm and Dokka, 1991, 1993; Hoisch and Simpson, 1993; Niemi et al., 2001; Snow and Lux, 1999; Snow and Wernicke, 1989, 2000; and Wernicke et al., 1988.

Central Basin and Range

The central Basin and Range province is in many respects an ideal location for a province-wide restoration of Basin and Range extension (Snow and Wernicke, 2000, and references therein). A regionally conformable miogeocline, Mesozoic thrust structures and distinctive Tertiary sedimentary deposits tightly limit the extensional history of both the Lake Mead (Fig. 2, ranges 22–25) and the Death Valley (Fig. 2, ranges 27–34) extensional systems (Wernicke et al., 1988; Wernicke, 1992). Motion of the Sierra Nevada with respect to the Colorado Plateau in this region is primarily constrained by displacements of two distinctive Miocene basins developed early in the history of the extension of each system (Fig. 4).

In the Lake Mead system, restoring numerous proximal landslide breccias at Frenchman Mountain (Fig. 2, range 24) to their source

areas in the Gold Butte block (Fig. 2, range 23) also restores piercing lines defined by the southward truncation of Triassic formational boundaries by the basal Tertiary unconformity in both areas. The correlation of these features in the Frenchman Mountain and Gold Butte areas suggests 65 km \pm 15 km of extension between the two blocks (Fig. 4).

In the Death Valley system, Wernicke et al. (1988) initially proposed that the Panamint thrust at Tucki Mountain (Panamint Range, Figure 2, range 28) is correlative with the Chicago Pass thrust in the Nopah–Resting Springs Range (Fig. 2, range 27) and the Wheeler Pass thrust in the Spring Mountains (Fig. 2, range 25), suggesting a total of 125 km \pm 7 km of post-Cretaceous, west-northwestern extension has separated them (Table 2). This offset is strengthened by correlations of additional contractile structures exposed across the Death Valley extensional system (Snow and Wernicke, 1989; Snow,

1992; Snow and Wernicke, 2000) and distinctive middle Miocene sedimentary deposits that occur along the extensional path (Niemi et al., 2001). These include proximal conglomeratic strata of the Eagle Mountain Formation, which were derived from the northeastern margin of the Hunter Mountain batholith in the southern Cottonwood Mountains (Fig. 2, range 32). Recognition and correlation of this dismembered early extensional basin, in conjunction with stratigraphic constraints from other Tertiary deposits in the region, indicates that its fragmentation occurred mainly from 12 Ma to 2 Ma (Fig. 4). The correlation of these deposits yields a displacement vector of 104 km \pm 7 km oriented N67°W between the Nopah–Resting Springs Range (Fig. 2, range 27) and the Cottonwood Mountains (Fig. 2, range 32).

To the \sim 170 km of displacement from these constraints, we add four additional estimates to complete the reconstruction path. In the Lake Mead system, 15 km of extension between the Gold Butte area and the Colorado Plateau (Fig. 2, range 23) (Brady et al., 2000) and a maximum of 8 km of extension between the Spring Mountains (Fig. 2, range 25) and Frenchman Mountain (Fig. 2, range 24) (Wernicke et al., 1988) increases the total displacement of the Spring Mountains relative to the Colorado Plateau to \sim 88 km. In the Death Valley system, an addition of 9 km of displacement in both the Panamint and Owens Valleys increases the total displacement to \sim 147 km between the Spring Mountains and the Sierra Nevada.

The sum of all displacements along the path is therefore 235 km \pm 20 km (Table 2), which represents a combination of areal dilation (crustal thinning) and plane strain (strike-slip faulting). Approximately 80% of the elongation is accommodated by vertical thinning and \sim 20% by north-south contraction (Wernicke et al., 1988; Snow and Wernicke, 2000). In addition to this path, there are a number of more local offsets that were used to position polygons to the north and south, which are shown in Figure 4 and summarized in Table 2.

Southern Basin and Range–Rio Grande Rift

Extension in the southern Basin and Range is almost completely dominated by the formation of large-offset normal faults that form the metamorphic core complexes (Coney, 1980; Spencer and Reynolds, 1989; Dickinson, 2002). The core complexes ring the southwestern margin of the Colorado Plateau (Fig. 2, ranges 37–44), and estimates of the

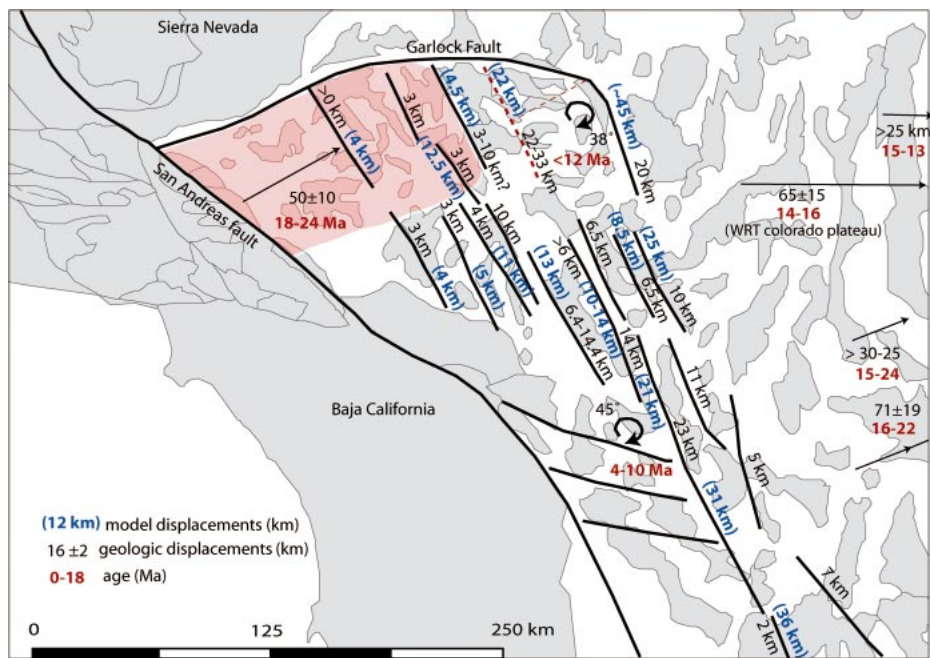


Figure 5. Map of the Mojave and Southern Basin and Range region showing distribution of strike-slip faults (bold lines), vertical axis rotation data (curved arrows), and extensional offsets (straight arrows). For strike-slip faults, reported slip amounts (black numbers) are contrasted with model slip (bold blue numbers). For extension and rotation constraints, black numbers indicate horizontal displacement or amount of rotation, bold red numbers indicate age range of deformation. Red shaded area is the area of the model that undergoes 24–18 Ma core complex extension in the Mojave region. WRT indicates measured displacement is “with respect to” the Colorado Plateau. Data from Ballard, 1990; Bassett and Kupfer, 1964; Dokka, 1983, 1989; Foster et al., 1993; John and Foster, 1993; Hamilton, 1987; Howard and Miller, 1992; Miller, 1980; Miller and Morton, 1980; Powell, 1981; Richard et al., 1992; Richard, 1993; Richard and Dokka, 1992; Spencer and Reynolds, 1989; Spencer et al., 1995; Schermer et al., 1996; Walker et al., 1995.

total extension they represent are remarkably systematic in magnitude, direction, and rate (Table 3). The timing of extension varies in age from 28 Ma to 14 Ma as the extension migrates from southeast to northwest. The migration of extension has been related to a similar migration in volcanism. Both extension and volcanism have been proposed to be a result of the northwestward foundering of the Farallon plate (e.g., Humphreys, 1995; Dickinson, 2002).

In a similar time frame (ca. 26 Ma), volcanoclastic sediments deposited east of the Colorado Plateau in the Rio Grand Rift (Fig. 2, location 45) have been interpreted as representing the onset of extension (Chapin and Cather, 1994). Ingersoll (2001) counters that the early sediments are broad volcanoclastic aprons that show no evidence of syndepositional faulting. He places the initiation of rifting slightly later (ca. 21 Ma). Based on initiation of half-graben sedimentation and stratal tilting, rapid extension occurred between 17

and 10 Ma (Ingersoll, 2001; Chapin and Cather, 1994). The total magnitude of extension is small and ranges from 6 km in the northern part of the rift to 17 km in the south, consistent with the 1.5° clockwise rotation of the Colorado Plateau (Chapin and Cather, 1994; Russell and Snelson, 1994).

Extension within the Rio Grande rift is contiguous with the broad extended region farther south, east of the Sierra Madre Occidental (in Chihuahua), the magnitude of which is poorly understood (Dickinson, 2002). Generally, extension in the Mexican Basin and Range is partitioned both in time and space. Early core complex extension is documented in northwestern Mexico (in Sonora), just west of the Sierra Madre Occidental (Nourse et al., 1994; Gans, 1997) (Fig. 2). Palinspastic reconstructions over small regions in Sonora suggest cumulative extension of 90%, mostly between 26 and 20 Ma, and more modest extension (10%–15%) between 20 and 17 Ma (Gans, 1997). Limited crustal extension is also doc-

umented east of the Sierra Madre Occidental during the same time period (Dickinson, 2002). Major extension occurred in both Chihuahua (Henry and Aranda-Gomez, 2000; Dickinson, 2002) and Sonora Mexico (e.g., Stock and Hodges, 1989; Henry, 1989; Lee et al., 1996) from ca. 12 Ma to 6 Ma as a prelude to the opening of the Gulf of California at 6 Ma (Oskin et al., 2001). During the 12 Ma to 6 Ma interval, very small magnitude east-west “Basin and Range” extension affected Arizona (Spencer and Reynolds, 1989; Spencer et al., 1995).

Mojave Region

Cenozoic deformation of the Mojave region occurred in two main stages. Deformation began in the late Oligocene–early Miocene with the formation of large-offset normal faults and associated core complexes (Glazner et al., 1989; Dokka, 1989; Walker et al., 1990). Extension in the Mojave region (Fig. 2, location 41, and Fig. 5) may be linked to core complex extension in the southern Basin and Range corridor (Fig. 2, ranges 38 and 44) through a diffuse transfer zone that involves both rotation and strike-slip faulting (Bartley and Glazner, 1991; Martin et al., 1993). The magnitude of extension is determined through alignment of pre-extensional markers that include facies trends in Paleozoic strata, a unique gabbro-granite complex, and late Jurassic dikes, indicating a total of 40–70 km of offset (Glazner et al., 1989; Walker et al., 1990; Martin et al., 1993). Extension began in synchronism with the eruption and emplacement of 24–23 Ma igneous rocks (Walker et al., 1995) and is capped by the flat-lying, 18.5 Ma Peach Springs Tuff (Glazner et al., 2002). The fraction of the Mojave Desert region that was affected by mid-Tertiary extension is controversial (e.g., Dokka, 1989; Glazner et al., 2002). Glazner et al. (2002) propose that only a small region north of Barstow (Fig. 2, location 41) was affected by the early extension, with the southern boundary of this extensional domain linked to core complex extension to the southeast through diffuse right-lateral shear. The northern boundary of the extensional domain is more problematic; however, regional kinematic compatibility requires a northern transfer zone that links Mojave extension to similar age extension to the north or west. Rotation of the Tehachapi Mountains and/or extension in the southern San Joaquin Valley may represent the northern portion of this system (McWilliams and Li, 1985; Plescia and Calderone, 1986; Tennyson, 1989; Goodman and

TABLE 1. DATA USED FOR RESTORING EXTENSION IN NORTHERN BASIN AND RANGE LATITUDE 40° N

Range/fault	Horizontal displacement of range block (model polygon)	Horizontal component of fault slip (data)	Timing of slip	Rate of deformation (horizontal component of fault slip/duration)	Direction of motion	Data used	Source	Cumulative path displacement (\pm cumulative error)	Long. (X)	Lat. (Y)
San Pitch/Gunnison (1) [346]	4 km	4 km \pm 2	~18-0 Ma	0.22 km/m.y.	E-W	Stratigraphic separation	Hintze, 1973	4 km \pm 2 km	-111.78879	39.50297
Canyon/Levan and Fayette segments, Wasatch fault (2) [358]	5 km	5 km \pm 2 km	~10-0 Ma	0.5 km/m.y.	E-W	Holocene vertical offset rates and Miocene exhumation rates, assume ~30° dip	Neimi et al., 2004; Machette et al., 1992; Jackson, 1991; Smith and Brumm, 1984;	6 km \pm 3 km	-112.15421	39.56082
Cricket Range/Sevier Desert Detachment (3) [300]	34 km	40 km \pm 2 km	~18-0 Ma	2.22 km/m.y. (total)	E-W	Matching CR culmination in surface and subsurface. AFT cooling ages assuming a 34-40 degree fault	Coogan and DeCelles, 1996; Coogan et al., 1995; Stockli et al., 2001	46 km \pm 3.5 km	-112.75582	39.21301
House Range/Reflection F" fault (4) [350]	22 km	12-10 km	~19-15 Ma	3 km/m.y.	E-W	Offset reflector on seismic line	Stockli et al., 2001	50 km \pm 3.6 km	-113.34716	39.23402
Confusion Range/House Range fault (5) [359]	3.33 km	16-30 km	15-0 Ma	1 km/m.y.	E-W	AFT cooling age	Almendinger et al., 1986	113.61446	38.88285	
Snake Range/northern Snake Range decollement (6) [366]	4.66 km	4 km (2-3 km exhumation)	~15 Ma	.267 km/m.y.	E-W	Map relations stratigraphic offset, Aft/Ar cooling ages and AFT data (suggests 10.5-13 km of slip between 18-14 Ma)	Stockli, 1999	102 km \pm 5.5 km	-114.11642	39.43517
Schell Creek Range/Spring Valley fault (7) [362]	30 km (25-35), 22 km (0-18)	30 km \pm 3 km (0) 22 \pm 3 km	35-25 Ma, (pause 25-18Ma) 18-0 Ma	3 km/m.y. from 35-25 Ma, 2 km/m.y. from 18-0 Ma, 3 km/m.y. from 18-14 Ma, 1.7 km/m.y. from 14-0 Ma	E-W	Map relations, AFT, ZFT, Ar/Ar	Gans and Miller, 1983; Bartley and Wernicke, 1984; Lee 1995; Miller et al., 1999; Lewis et al., 1999	113 km \pm 6 km	-114.63925	39.22082
Butte Mtns./Egan Range low-angle faults (8) [80]	11 km (0-18)	11 km \pm 2 km	18-0 Ma	1.6 km/m.y. from 35-25 Ma, 6 km/m.y. from 18-0 Ma	E-W	Map relations, AFT, ZFT, Ar/Ar	Bartley and Wernicke, 1984; Gans et al., 1985; Lee, 1995; Miller et al., 1999; Lewis et al., 1999	129 km \pm 6 km	-114.91863	39.07945
Egan Range to Shoshone Mountains (9-14)	16 km (25-35)	16 km \pm 2 km, 5 km exhumation	35-25 Ma 16-17 Ma	26 km/16 m.y./5 ranges	E-W	Map relations and cross section restoration.	Bartley and Wernicke, 1984; Gans et al., 1985; Lee, 1995; Stockli, 1999	176 km \pm 11.8 km	-116.82368	39.15694
Pine Range/Grant Range and Buck Range faults (9) [348]	45.6 km	47 km \pm 10 km (26 excluding Toyabe range)	16-0 Ma	.325 km/m.y.	E-W	Map relations and cross section restoration.	Smith et al., 1991	176 km \pm 11.8 km	-116.81732	40.33706
Diamond Range/Pancake Range/Mahogany Hills faults (10) [360]	5 km	6 km \pm 1.5 km, ~5 km exhumation	~15 km	.325 km/m.y.	E-W	Map relations and cross section restoration.	Lund et al., 1993; Taylor et al., 1989	115.37732	40.39933	
Sulfur Springs Range faults (11)	5 km	5 km of 26 total	unknown, assumed ~16-0 Ma	.325 km/m.y.	E-W	Map relations and cross section restoration.	Smith et al., 1991	115.82060	39.83001	
Toquima Range/Simpson Park Mountains fault (12) [364]	5 km	5 km of 26 total	assumed ~16-0 Ma	.325 km/m.y.	E-W	Map relations and cross section restoration.	Smith et al., 1991	116.82368	39.15694	
Toiyabe Range faults (13)	5 km (25-35), 16 km (0-16)	21 km extension, ~5 km exhumation	35-25 Ma, 16-0 Ma	.5 km/m.y. (35-25), 1 km/m.y. (16-0)	E-W	Map relations and cross section restoration.	Smith, 1992; Stockli, 1999	176 km \pm 11.8 km	-116.81732	40.33706
Shoshone Mountain faults (14) [363]	4.6 km	5 km of 26 total	assumed ~16-0 Ma	.325 km/m.y.	E-W	Map relations and cross section restoration.	Smith et al., 1991	117.37972	39.47125	
Paradise Range fault (15) [351]	3.5 km	3 km \pm 1	assumed ~16-0 Ma	.188 km/m.y.	N 64 W	Map relations and cross section restoration.	Smith et al., 1991	179 km \pm 11.8 km	-117.56178	39.32198
C. Alpine Range fault (16) [349]	3 km	3 km \pm 1	assumed ~16-0 Ma	.188 km/m.y.	N 65 W	Paradise, C. Alpine and Stillwater Ranges represent 100 km area that has geographical extent on map	Faulds et al., 2003	182 km \pm 11.8 km	-117.70814	39.75161
Stillwater Range fault (17) [354]	1.5 km	3 km \pm 1	assumed ~16-0 Ma	.188 km/m.y.	N 65 W	Extended an unknown amount	Surplus, 1999; Stockli et al., 2002	185 km \pm 11.8 km	-117.85557	40.26451
Gillis/Gabbs Valley Range, Gumdrops hills, Indian head, Benton spring, Petrified Spring faults. (18) [326]	-117.85557	40.26451	younger than 25 Ma	6.75 km/m.y. (if since 8 Ma)	N 14 W	Unknown/best estimate	Hardyman et al., 1984	203 km \pm 13.3 km	-118.46915	38.81173
Northern Walker Lane fault system (18)	29 (0-6), 13 (8-10)	35 \pm 5 km right lateral	younger than 25 Ma	5-10 km/m.y. (if since 5 Ma)	N 37 W	Offset segments of East trending Oligocene paleovalley	Faulds et al., 2003	215 km \pm 13.6 km	-118.88407	38.66236
Wasatch Range fault system (19) [354]	16 km	11.76 \pm 1 km (13.3 \pm 3 km)	15-0 Ma	4.3 km/m.y.	E-W	Cross section restoration plus unroofing of granite from valley between Singatse and Wassack ranges	Surplus, 1999; Stockli et al., 2002	228 km \pm 13.8 km	-119.25357	38.95920
Singatse Range fault system (20) [365]	10.5 km	8.71 km	14-15 Ma	1.05 km/m.y.	E-W	Offset volcanic and sedimentary rocks, Ar/Ar isotope ages	Dilles and Gans, 1995	231 km \pm 14 km	-119.45646	38.71853
	2 km	2.1 km	9-7 Ma	.3 km/m.y.	E-W					
	3.4 km	0.5 km (0 \pm 2), 2.5 \pm 2	7-0 Ma		E-W					
	15.66 km	13 \pm 2	15 to 0 Ma		E-W					
	7.66 km	Main phase 7.26	14-12 Ma	3.63 km/m.y.	E-W					
	4.4 km	1.7 km	11-8 Ma	.56 km/m.y.	E-W					
	3.6 km	4.1 km	7-0 Ma	.58 km/m.y.	E-W					
	5 km	7 \pm 2, 2-3 km of exhumation	10-0 Ma	.7 km/m.y.	E-W					
Buckskin Mtns./Pine Nut Valley/Pine Nut Range Faults (21) [362]	5 km	7 \pm 2, 2-3 km of exhumation	10-0 Ma	.7 km/m.y.	E-W	Offset from mapped units; timing (10-5 Ma) from Surplus	Hudson and Oriol, 1979; Stockli, 1999	231 km \pm 14 km	-119.45646	38.71853
Total extension	236 km	235 \pm 14 km			N 78° W					

Note: Long.—longitude; Lat.—latitude. CR—Canyon Range; AFT—Apatite Fission Track cooling age. Numbers in parentheses refer to specific ranges identified on Fig. 2; numbers in brackets refer to the RAINDRUMBER for individual ranges in the ArcGIS shape files and the Movement Table (ArcGIS files, Movement Table [see footnote 1]). The cumulative error reported in column 9 equals the square root of the sum of the squares for individual vectors.

TABLE 2. DATA USED FOR RESTORING EXTENSION IN CENTRAL BASIN AND RANGE LATITUDE OF 38° N

Range/fault	Horizontal displacement of range block (model polygon)	Horizontal component of fault slip (data)	Timing of slip	Rate of deformation (horizontal component of fault slip/duration)	Direction of motion	Data used	References	Cumulative displacement of fault slip data (\pm cumulative error)	Long. (x)	Lat. (y)
Mormon Mountains area/Mormon Peak, Tule Springs and Castle Cliff detachments (22) [73]	68 km	54 \pm 10	16–12 Ma	13.5 km/m.y.	S 60 E	Cross section reconstruction through Beaver Dam/Tule Springs and Mormon Peak detachment systems	Aven et al., 1990	54 km \pm 10 km	-114.24552	37.09463
Gold Butte/South Virgin Mountains detachment (23)	18 km	15 \pm 5	~17–15 Ma	7.5 km/m.y.	E-W	Cross section reconstruction, AFT cooling ages, overlapping 15 Ma basal	Wernicke et al., 1988; Brady et al., 2000; Fitzgerald et al., 1991	15 km \pm 5 km	-114.20920	36.38748
Frenchman Mountain/Lake Mead fault system (24) [47]	60 km	60 min 90 max 65 \pm 15	16–12 Ma	16.25 km/m.y.	N 75 E	Megabreccia from Gold Butte, pinchout of Mz formations, Virgin Mountains detachment system	Snow and Wernicke, 2000; Duebendorfer and Black, 1992; Duebendorfer et al., 1998; Wernicke et al., 1988	80 km \pm 16 km	-114.96999	36.20312
Spring Mountains/Las Vegas fault system (25) [53]	8 km	8 km \pm 8	15–11 Ma		N 75 E	Unknown amount of extension between Spring Mountain and Frenchman Mtn.	Wernicke et al., 1988	88 km \pm 18 km	-115.60912	36.06631
Las Vegas shear zone	Undetermined	47 \pm 7 km	15–11 Ma	11.75 km/m.y.		Alignment of Gass Peak thrust (Sheep Range) with Wheeler Pass thrust (Spring Mt.).	Snow and Wernicke, 2000; Burchfiel et al., 1987; Wernicke et al., 1988			
Sheep Range, Pintwater Range, Spotted Range detachment (26) [59, 61, 64]	23 km	20 \pm 5 km	13 Ma–7 (9 Ma)	3.67 km/m.y.	N 63 W	Extension associated with the Sheep Range detachment, extension amount based on cross section restoration	Guth, 1989; Snow and Wernicke, 2000; Snow, 1992	74 km \pm 11 km	-114.91820	36.63221
Nopah Range, Resting Spring Range, Spring Mtns. detachment (27) [50]	26 km	~25 \pm 3 km	14–9 Ma	5 km/m.y.	N 63 W	Alignment of the trace of the Wheeler Pass thrusts with respect to other thrusts in the system	Wernicke et al., 1988, Snow and Wernicke, 2000	113 km \pm 18 km	-116.18892	36.27185
Cottonwood, Panamint, Black Mountains/Amargosa, central Death Valley, Emigrant detachments (28, 30, 32) [54]	102 km	104 km \pm 7	11–2 (?) Ma	11.5 km/m.y.	N 67 W	The original extent of Eagle Mountain Formation must have been within 20 km of source area in southern Cottonwoods.	Neimi et al., 2001	217 km \pm 19 km	-117.15952	36.20316
Resting Springs, Nopah Ranges and Black, Panamint Mountains/ Grapevine, Amargosa, central Death Valley area detachments (27, 28, 30)	105 km	100 \pm 7	9–5 Ma	22.5 km/m.y.	N 78 W	Willow Spring pluton intruded (10–12 km) at 11.6 cooled rapidly (6–7 Ma) and appears in boulders at ~5 Ma. (Amargosa chaos). Alignment of thrust-belt structures	Wernicke et al., 1988; Snow and Wernicke, 2000; Holm et al., 1992; Holm and Dokka, 1993; Snow, 1992			
Kingston Range/Kingston Range detachment (29) [38]	6 km	6 km	13.1–12 Ma	6 km/m.y.	E-W	Deposition in the Shadow Valley Basin	Fowler and Calzia, 1999	-115.88365	35.68015	
Southern Black Mountains/ Kingston Range, Amargosa detachments (30) [52]	25 km	25 \pm 3 km	12–8 Ma	6.25 km/m.y.	E-W	Granite megabreccias (in the greater Amargosa basin) possibly derived from a displaced portion of Kingston Range pluton (west of basin).	Snow and Wernicke, 2000	-116.59671	36.03965	
Funeral, Grapevine Mountains/ Point of Rocks detachment (31) [60]	Undetermined	~10 km	14–10 Ma	2.5 km/m.y.	N 45 E	Opening of the extensional Bullfrog Basin	Cemen et al., 1985; Snow and Lux, 1999	-116.87030	36.68789	
Grapevine Mountains, Bare Mountain/Bullfrog detachments (31) [72, 58]	60 km	52 \pm 2	14–7 Ma	7.43 km/m.y.	S 68 E	Cordillera fold-thrust belt reconstructions	Snow and Wernicke, 2000, 1989	-116.67924	36.87579	
Grapevine Mountains, Funeral Mountains/Boundary Canyon detachment (31) [72]	32 km	35 \pm 2 km	9–5 Ma	8.75 km/m.y.	S 37 E	Cordillera fold-thrust belt reconstructions, AFT, ZFT and sphene FT cooling ages	Snow and Wernicke, 2000, 1989; Snow, 1992; Hoisch and Simpson, 1993; Holm and Dokka, 1991	-117.21776	37.12056	
Northern Death Valley		20 \pm 10	5–0 Ma	2–6 km/m.y.	E-W	Offset thrust fault and Quaternary markers	Reheis 1993, Reheis and Sawyer, 1997			
Cottonwood Mountains/ Emigrant fault system (32)	22 km	22 \pm 3 km	6–3.2 Ma	5.5 km/m.y.	S 45 E	Correlation of White Top backfold in Cottonwood, Funeral Mountains and Specter Range	Wernicke et al., 1988; Snow, 1992; Snow and Lux, 1999; Snow and Wernicke, 2000	-117.57841	36.87160	
Darwin Plateau, Inyo Mountains/Hunter fault (33) [51, 66]	9 km	9 \pm 1	4.8–0.6 Ma	2.25 km/m.y.	S 55 E	Correlation of Saline Range volcanics	Burchfiel et al., 1987	226 km \pm 19 km	-117.66132	36.17492
Sierra Nevada/Owens Valley fault system (34) [65]	~9 km	9 \pm 6	0–4 Ma	2.25 km/m.y.	S 60 E	Estimate of 15% \pm 10% extension	Wernicke et al., 1988	235 km \pm 20 km	-119.80163	37.88503
Total extension	232 km		235 \pm 20 km		N 78° W					

Note: Long.—longitude; Lat.—latitude; AFT—Apatite Fission Track cooling age; ZFT—Zircon fission track age; FT—Fission Track. Numbers in parentheses refer to the number for individual ranges in the ArcGIS shape files and the Movement Table (see footnote 1). The cumulative error reported in column 9 equals the square root of the sum of the squares for individual vectors.

TABLE 3. DATA USED FOR RESTORING EXTENSION IN SOUTHERN BASIN AND RANGE

Range/fault	Horizontal displacement of range block (model polygon)	Horizontal component of fault slip (data)	Timing of slip	Rate of deformation (horizontal component of fault slip/duration)	Direction of motion	Data used	References	Long. (x)	Lat. (y)
McCullough Range to Colorado Plateau (35) [37]	80 km	50-80 km	14-16 Ma (24)	8 km/m.y.	S 75 W	Restoration of strike slip fault offsets, tilted volcanic rocks, porphyry copper emplacement depths	Spencer and Reynolds, 1989; John and Foster, 1993	-115.34595	35.17415
Black Mountains (36) [46]	36 km (total)	>25 km	15-13.4 Ma	2.5 km/m.y.	N 70 E	Tilted volcanic rocks.	Foster et al., 1993; Spencer et al., 1995; Spencer and Reynolds, 1989	-114.49030	35.47688
Sacramento, Chemehuevi	36 km	>25-30 km	21-15 Ma	5 km/m.y.	S 60 W	Ar/Ar, AFT cooling ages	John and Foster, 1993	-114.76854	35.31117
Eldorado Mountains (37) [44]	66 km	66 km ± 8 km	27-13 Ma	4.7 km/m.y.	S 57 W	Timing indicated by tilted volcanic strata, magnitude determined by offset necessary to expose lower plate	Scott et al., 1998; Foster et al., 1993; Spencer et al., 1995; Spencer and Reynolds, 1991	-113.74331	34.09275
Buckskin, Rawhide Mountains (38) [629]	66 km	66 km ± 17 km	26-14 Ma	5.6 km/m.y.	S 57 W	Displaced breccias (55 km) plus additional extension in volcanic and Precambrian rocks (12 ± 7)	Richard et al., 1990; Spencer and Reynolds, 1991	-113.51995	33.86443
Catalina, Rincon Mountains (39) [648]	28 km	20-30 km, could be up to 40 km	27-20 Ma	4 km/m.y.	S 60 W	Correlation of Precambrian granite and pre-mid Tertiary thrusting	Dayi et al. 1989; Dickinson, 1991; Fayon et al., 2000	-110.71584	32.35001
Harquahala, Harcuvar Mountains (40) [657]	66 km	67 km ± 17 km	26-14 Ma	5.6 km/m.y.	S 57 W	Displaced breccias (55 km) plus additional extension in volcanic and Precambrian rocks (12 ± 7)	Richard et al., 1990; Spencer and Reynolds, 1991	-113.51995	33.86443
Pinaleno Mountains (41) [647]	22 km	20-30? km	29-19 Ma	2.5 km/m.y.	S 60 W	Ar/Ar cooling ages, approximate amount of displacement necessary to expose lower plate	Long et al., 1995	-110.01163	32.77288
South Mountain (43) [653, 654]	50 km	71 km ± 19 km	25-19 Ma	11.8 km/m.y.	S 60 W	Offset of dike swarm, tilted sedimentary strata	Reynolds, 1985	-111.60311	33.13175
Whipple Mountain (44) [665]	63 km	6 km	22-16 Ma	.875 km/m.y.	S 57 W	palinspastic restoration of seismic controlled cross section, and growth strata in basin	Davis and Lister, 1988; Spencer and Reynolds, 1991	-114.10627	34.31624
Rio Grand extension (45)	7 km	10 km	12-18 Ma	1.625 km/m.y.	38°N		Chapin and Cather, 1994; Ingersoll, 2001; Russell and Snelson, 1994		
	13 km	17 km	12-18 Ma	2 km/m.y.	36°N		Chapin and Cather, 1994; Ingersoll, 2001; Russell and Snelson, 1994		
	17 km		12-18 Ma		35°N		Chapin and Cather, 1994; Ingersoll, 2001; Russell and Snelson, 1994		

Note. Long.—longitude; Lat.—latitude; AFT—Apatite Fission Track cooling age. Numbers in parentheses refer to specific ranges identified on Fig. 2; numbers in brackets refer to the RANGE number for individual ranges in the ArcGIS shape files and the Movement Table (ArcGIS files, Movement Table [see footnote 1]).

Malin, 1992; Walker et al., 1995; Glazner et al., 2002).

Following this early phase of extensional deformation, a system of right- and left-lateral strike-slip faults similar to those active today was established, with right-lateral shear along a series of northwest-striking faults predominant (Fig. 5). The total accumulated shear across the Mojave, as documented by field studies, is 53 km ± 6 km (Table 4). The timing of right-lateral shear is not well constrained. Motion on the faults is inferred to be post-10 Ma based on strain compatibility with deformation directly north and south (Tables 2 and 5).

Vertical Axis Rotations East of the San Andreas Fault

There are two zones of vertical-axis rotation east of the San Andreas fault: the Eastern Transverse Ranges located immediately south of the Mojave block and the northeastern Mojave rotational block (Carter et al., 1987; Schermer et al., 1996; Dickinson, 1996) (Fig. 5 and Table 4).

The Eastern Transverse Ranges include a series of structural panels separated by east-west-oriented, left-lateral faults (Dickinson, 1996). Paleomagnetic studies show that 10 ± 2 Ma rocks within this zone record the entire 45° rotation (Carter et al., 1987), while 4.5 Ma volcanic rocks are unrotated (Richard, 1993). These constraints imply that all of the rotation and most of the right-lateral strike-slip motion in the Mojave region immediately to the north are ca. 10 Ma and younger.

The northeastern corner of the Mojave region is another area of pronounced clockwise rotation. Schermer et al. (1996) proposed that the northeastern Mojave underwent 23° of rotation accompanied by 5 km of left-lateral slip on faults within the rotating region and 15° of "rigid body" rotation. Total right-lateral shear predicted by this model is 33 km.

San Andreas System and Areas to the West

Deformation west of the San Andreas fault is defined by four first-order constraints (Fig. 6 and Table 6). The first is motion on the San Andreas fault itself, which is tightly constrained in central California at 315 km ± 10 km by restoring the Pinnacles volcanics west of the fault to the Neenach volcanics to the east of it (Matthews, 1976; Graham et al., 1989; Dickinson, 1996). The offset volcanics were extruded from 22 Ma to 24 Ma, but tentatively correlative late Miocene strata (7-8

TABLE 4. DATA USED FOR RESTORING STRIKE-SLIP DISPLACEMENTS IN THE MOJAVE REGION

Fault	Horizontal displacement of range block (model polygon)	Horizontal component of fault slip (data)	Timing of slip	Data used (offset features)	References	Cumulative displacement of right-lateral fault slip data (\pm cumulative error)
Central Mojave (41)	63 km	40–50 km	24–18 Ma	Offset features that include Jurassic dikes, intrusive rocks, and shelf to ocean facies transition	Glazner et al., 1989; Martin et al., 1993; Fletcher et al., 1995; Ingersoll et al., 1996	
Aztec Mines Wash fault	8 km	8 km LL	post lower Miocene	Intrusive contact between San Gabriel terrane and Cretaceous pluton	Powell, 1981	
Blue Cut fault	4 km	6–9–9 km		Antiform in gneissic foliation	Hope, 1966	
Bullion/Rodman/Pisgah fault	13 km	6.4–14.4 km RL		Kane springs fault	Dokka, 1983	10.4 km \pm 4 km
Chiniasco fault	7–16 km	11 km LL		Dacite dike, and steeply dipping Red Cloud thrust fault	Powell, 1981	
Chuckwalla Valley basin	31 km (RL)	gravity low		Gravity data indicate complex basin structure	Rotstein et al., 1976; Richard, 1993	
Cibola fault	7 km	7 km RL		West dipping normal faults, and east dipping contact between lavas	Richard et al., 1992	
Ford Lake North basin	5 km	3.5 km RL		Base of McCoy Mountains formation	Stone and Pelka, 1989	
Indian Wash Basin	7 km	7 km RL		Stratigraphic separation	Richard, 1993	
Iron Mountains fault	5 km	5.5 km RL		Rock units (unspecified)	Howard and Miller, 1992	
Laguna fault system	36 km	2 km RL		Slip estimated by estimating extension necessary for 20° dip in conglomerate	Richard, 1993	
Mammoth Wash fault	~12 km	~9 km LL		Intersection of greenschist with Chocolate Mountain Thrust	Dillon, 1975	
Maria fault		4.5 km RL		Thrust faults and syncline	Hamilton, 1987; Ballard, 1990	
Mesquite Lake fault		3.5 km RL		Folds in Pleistocene sediments	Bassett and Kupfer, 1964	
Packard Well fault	16 km	16 km RL		Mesozoic rocks and structures	Powell, 1981; Richard and Dokka, 1992	
Pinto Mountain fault	not available	18–22 km LL		Intrusive contacts	Hope, 1966; Dibblee, 1982	
Salton Creek fault	8 km	8 km LL		Correlation with Aztec mines fault	Powell, 1981	
Sheep Hole, Dry Lakes fault	31 km	23 km RL/11 km RL	to early Pleistocene	Photo interpretation	Powell, 1981; Howard and Miller, 1992	
Valley Mountain fault	21 km	6.5–14.4 km RL		Intrusive contacts	Dokka, 1983; Richard, 1993	
Cleghorn Pass fault	valley mt offset	12 km RL	to early Pleistocene		Howard and Miller, 1992	
Cleghorn Lakes fault	"	3 km RL	to early Pleistocene	Intrusive contacts	Howard and Miller, 1992	
Cadiz Lake fault	16–25 km	25 km RL	Pleistocene to early Pleistocene	Roof pendants with distinctive lithology	Howard and Miller, 1992	
Broadwell Lake fault	6 km	6 km RL	Pleistocene to early Pleistocene	Miocene strata	Howard and Miller, 1992	16 km \pm 4 km
South Bristol fault	9 km	6.5 km RL	Pleistocene to late Pleistocene	Mesozoic granitites, metavolcanics	Howard and Miller, 1992	22.5 km \pm 4 km
Bristol, Granite Mountain fault	27 km	10 km RL (0-10)		Unknown, or plutons and volcanic rocks	Howard and Miller, 1992; Dokka and Travis, 1990	27.5 km \pm 6.4 km
Ludlow	14 km	>6 km RL	to early Pleistocene	Source area for Pleistocene conglomerate	Howard and Miller, 1992	33.5 km \pm 6.4 km
Calico	10 km	9.6 km RL		Offset early Miocene fault	Dokka, 1989; Glazner et al., 2002	43.1 km \pm 6.4 km
Blackwater	4.5 km	1.8 km	last 3.77 m.y.	Offset volcanics, basement lithologies	Oskin et al., 2004	
Gravel Hills + Harper Lake	12.5 km	3.2 km RL + 3 km RL		Offset lithologies	Dokka and Travis, 1990; Dibblee, 1968	47.1 km \pm 6.4 km
Camp rock	11 km	4 km RL		Offset basement lithologies	Dokka, 1983; Dibblee, 1964	50.1 km \pm 6.4 km
Hendale	4 km	3 km RL		Offset lithologies	Miller and Morton, 1980	
Lockheart	4 km	>0 RL			Dokka and Travis, 1990	
Lenwood	5 km	2 km RL		Offset volcanics, graben width	M. Strane, Pers. Comm, 2005	53 km \pm 6.4 km
NE Mojave rotation	23 km	22–23 km RL		Paleomagnetic rotations	Schermer, 1996; Miller and Yount, 2002	
Total shear in the Mojave	99 km	53 \pm 6.4 km				

Note: RL and LL indicate right-lateral motion and left-lateral motion, respectively.

TABLE 5. DATA USED FOR RESTORING VERTICAL AXIS ROTATION IN RECONSTRUCTION

Rotations	Rotation in model	Measured rotations from data	Age	Rate	Direction	References	Long. (x)	Lat. (y)
Colorado Plateau (45) [74]	1.5°	1°–1.5°	12–18 Ma	.1875°/m.y.	Paleomagnetism, extension determined through cross section restoration	Chapin and Cather, 1994	–110.14435	37.26894
Eastern Transverse Ranges (46) [90–99]	45°	41.4° ± 7.7	after 10.4 Ma	cw	Paleomagnetic data	Carter et al., 1987		
Northeastern Mojave (47) [mojave 6]	36°–38°	23° locally 63°	after 10.4 Ma	cw	Paleomagnetic data	Schermer et al., 1996		
Jurassic dikes in NE Mojave (47) Mojave rotations (47)		40–50° 30°	21–48 Ma	cw	Paleomagnetic data	Ron and Nur, 1996 Dokka and Travis, 1990;		
Cottonwood and Funeral Mtns. (31, 32) [70, 60]		40°	mid Miocene or later	cw	Paleomagnetic data	Snow and Lux, 1999; Snow and Wernicke, 2000	–117.57841	36.87160
Black Mountains (30) [52]		50–80°	after mid Miocene pluton	ccw	Paleomagnetic data	Holm et al., 1993	–116.59671	36.03965
Grapevine Mountains (31) [72]		~20°			Paleomagnetic data	Niemi, 2002; Snow and Wernicke, 2000	–117.21776	37.12056
Bare Mountain (31) [58]	80°	80°	pre mid-Miocene	cw	Paleomagnetic data	Snow and Prave, 1994	–116.67924	36.87579
Pinwater, Spotted and Specter Range and Stripped Hills (26) [56]		Oroclinal flexure (75–90°)	between 16 and 14 Ma	cw		Carr et al., 1986; Hudson et al., 1994; Niemi, 2002	–116.78407	36.62382
Northern Walker Lane (18–19) [326, 355]		35°–51°	9–13 Ma	cw	Paleomagnetic data on volcanic rocks	Cashman and Fontaine, 2000		
Sierra Nevada (34) [65]	2° (ccw)	6° ± 8°	post Cretaceous	cw	Paleomagnetic data	Frei et al., 1984; Frei, 1986; Bogen and Schweickert, 1985; Gilder and McNulty, 1999	–119.80163	37.98503
Western Transverse Ranges (50)	117°	90°–110°	~15 Ma	6°/m.y.	Paleomagnetic data	Hornafius et al., 1986; Luyendyk, 1991		

Note: Table 5 is an incomplete listing of an extensive paleomagnetic data set for western North America. Long.—longitude; Lat.—latitude; cw—clockwise rotations; ccw—counterclockwise rotations. Numbers in parentheses refer to specific ranges identified on Fig 2; numbers in brackets refer to the RANGE.ID number for individual ranges in the ArcGIS shape files and the Movement Table (ArcGIS files, Movement Table [see footnote 1]).

Ma) are apparently offset 255 km (Graham et al., 1989; Dickinson, 1996).

The second constraint is the ~110° clockwise rotation of major fault-bounded blocks in the western Transverse Ranges (Hornafius et al., 1986; Luyendyk, 1991). Because of the length and structural integrity of these blocks (in particular, the Santa Ynez Mountains), this rotation requires a coast-parallel displacement of ~270 km (Hornafius et al., 1986).

The shear and rotation of these blocks are confirmed by the third major constraint, reconstruction of now-scattered outcrops of the distinctive Eocene Poway Group. Exposures along the Channel Islands were rifted away from counterparts in southernmost California, which are in turn offset from their source area in northern Sonora, Mexico, by the southern San Andreas fault system (Abbott and Smith, 1989). Rifting and rotation of the western Transverse Ranges away from the Peninsular Ranges formed the strongly attenuated crust of the Continental Borderlands on their trailing edge. The magnitude of this extension is proposed to be ~250 km based on seismic reflection data delineating the geometry of extensional fault systems and correlation of “mega key beds” or lithotectonic belts (fore-arc basin sediment, Franciscan subduction complex) (Crouch and Suppe, 1993; Bohannon and Geist, 1998).

The final first-order constraint is the opening of the Gulf of California. Although offset of the Poway Group suggests roughly 250 km of displacement, recognition of correlative pyroclastic flows on Isla Tiburon and near Puerrecitos on the Baja Peninsula dated at 12.6 Ma and 6.3 Ma constrains the full transfer of Baja California to the Pacific plate to have occurred no earlier than ca. 6 Ma, with 255 km ± 10 km of displacement along the plate boundary since then (Oskin et al., 2001). Including additional deformation of the adjacent continental margins increases the magnitude of displacement to as much as 276 km ± 10 km (Oskin and Stock, 2003).

WESTERN NORTH AMERICA ANIMATION

The western North America animation (Animation 1) combines 13 individual paleogeographic maps (Figs. 7–9) (Appendix 1, paleogeographic maps [see footnote 1])² generated by ArcGIS into a digital animation illustrating a model of how extension and right lateral shear evolved in the region. The color scheme

²If you are reading this offline, please visit www.gsa-journals.org to view Animation 1.

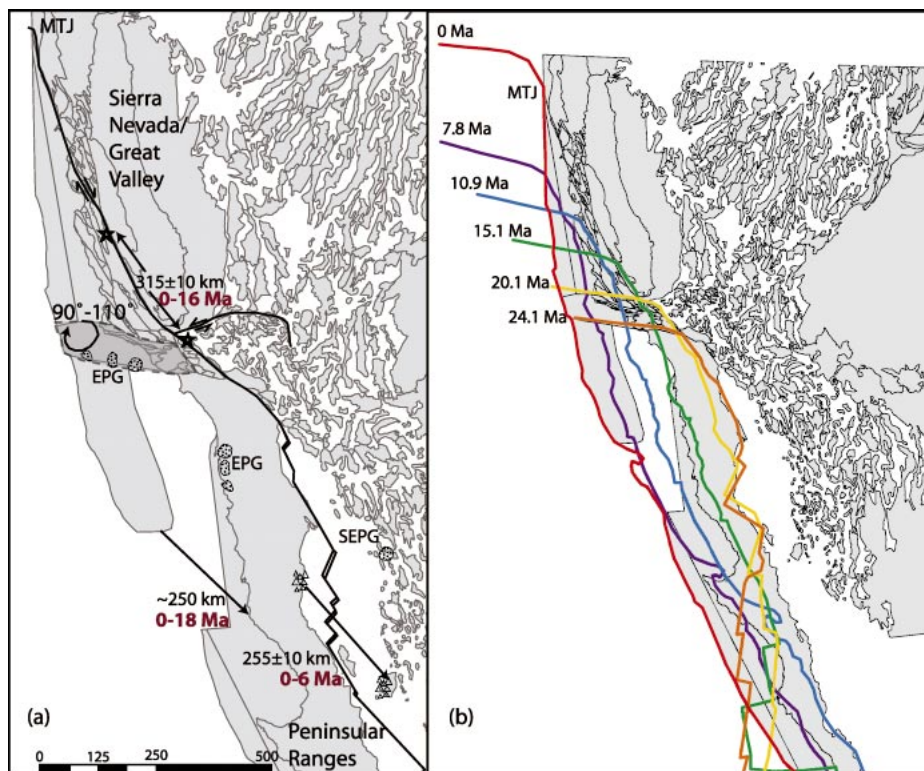


Figure 6. A: First-order constraints for displacement along the San Andreas fault and associated displacements to the west. Arrows indicate approximate magnitude and direction of individual relative displacements between polygons. Black numbers indicate horizontal displacement amount, bold red numbers indicate age range of displacement. Stippled areas labeled EPG show distribution of Eocene Poway Group and equivalents. Stippled area labeled SEPG marks the location of the source area for the Eocene Poway Group. Triangle pattern (Gulf of California), and stars (central California) show distribution of correlative volcanic units offset by the San Andreas–Gulf of California rift system. MTJ is modern location of the Mendocino triple junction. Data from Abbott and Smith, 1989; Bohannon and Geist, 1998; Crouch and Suppe, 1993; Dickinson and Wernicke, 1997; Dickinson, 1996; Graham et al., 1989; Hornafius et al., 1986; Luyendyk, 1991; Matthews, 1979; Oskin et al., 2001. **B:** Successive locations of the eastern edge of Pacific plate oceanic lithosphere relative to stable North America. The thick colored lines represent minimum extent of oceanic lithosphere at the times shown (from Atwater and Stock, 1998). These positions constrain the maximum westward extent of continental North America through time.

for the animation includes yellow, orange, and red polygons on a white background. The polygon shape reflects the modern bedrock-alluvium contact, fault-bounded crustal blocks or the physiographic boundaries of large, intact crustal blocks. Yellow polygons indicate areas where there are no data for how the region is deforming. Orange polygons (ranges) are ranges whose motion is directly constrained by kinematic data. These polygons turn red during the time period of motion (i.e., Baja California turns red from 6 to 0 Ma as it separates from North America and moves northward on the Pacific Plate). A notable exception to this is the Colorado Plateau–Rio

Grand rift area. Neither the Colorado Plateau, nor the Rio Grande rift turn red during rotation and extension even though there are data that describe this deformation (Table 5). The space created (additional white space between the colored polygons) as the movie progresses in time indicate areas of extension. The removal of white space (as polygons move closer together) indicates areas of compression. The thick blue line on the left of the animation represents successive locations of the eastern edge of Pacific plate oceanic lithosphere relative to stable North America at the time period annotated on the upper left edge of the line (from Atwater and Stock, 1998). The po-

sition of this line constrains the maximum westward extent of continental North America at the time indicated because it shows the minimum east limit of extant oceanic crust. Details of the reconstruction can be seen by moving the slider bar on the animation. To move back and forth over a narrow window of time, just hold the mouse key down over the triangle on the slider bar and move it back and forth over the time window of interest.

DISCUSSION

The exercise of developing a self-consistent, strain-compatible model has raised a number of issues that are difficult to resolve satisfactorily in the reconstruction and require further investigation. The most apparent (among many!) are (1) the need for middle to late Miocene right-lateral shear in the eastern Mojave region to make room for the northerly motion of the Sierra Nevada determined from the central and northern Basin and Range reconstruction paths; (2) the need for large amounts of relatively young extension in northern Mexico both east and west of the Sierra Madre Occidental to reconcile core complex extension in Arizona and the late Miocene–Pliocene opening of the Gulf of California; (3) the apparent rotational history of the Sierra Nevada–Great Valley block; and (4) generally large amounts of Miocene–Pliocene shortening and extension in the Transverse Ranges, Coast Ranges, and Borderlands provinces, which arise from the need to reconcile San Andreas offset with the position of oceanic crust offshore, differences in the age of extension north and south of the Garlock fault, and large clockwise rotation of the Santa Ynez Mountains block (Animation 1).

Eastern Mojave Region

The eastern California shear zone–Walker Lane belt is an ~120-km-wide zone of right-lateral, intraplate shear east of the Sierra Nevada and San Andreas fault. Geodetically this shear zone accommodates up to 25% of the Pacific–North America relative plate motion (Bennett et al., 2003; McClusky et al., 2001; Miller et al., 2001; Sauber et al., 1994). Geologic estimates of displacements vary along the north-south extent of the eastern California shear zone. Proposed net displacement along the eastern California shear zone (oriented ~N20°W) varies from 65 km in the Mojave region (Dokka and Travis, 1990) to 133 km in the central Basin and Range (Snow and Wernicke, 2000; Wernicke et al., 1988). In the northern Walker Lane region, shear estimates

TABLE 6. DATA USED FOR RESTORING HORIZONTAL DISPLACEMENTS WEST OF THE SAN ANDREAS FAULT

Range/fault	Horizontal displacement of range block (model polygon)	Horizontal component of fault slip (data)	Timing of slip	Rate of deformation (horizontal component of fault slip/duration)	Direction of motion	Data used	References
San Andreas motion (48)	310 km: 0–6 Ma, 174 km; 8–12 Ma, 89 km; 14–16 Ma, 47 km	315 km ± 10 km	0–5 Ma, 170 km ± 5; 0–10 Ma, 289 km ± 9; 0–16 Ma, 315 km ± 10	0–5 Ma, 34 km/yr; 0–10 Ma, 24 km/yr; 0–16 Ma, 4.3 km/yr	N 30 W	Offset of Holocene geological features, early Miocene volcanic and sedimentary rocks and Miocene sedimentary breccias	Atwater and Stock, 1998; Dickinson and Wernicke, 1997; Dickenson, 1996; Graham et al., 1989; Sieh and Jahns, 1984; Matthews, 1979
Baja/Isla de Tibron (49)	300 km	276 km ± 13 km	6–0 Ma	43.5 km/yr	N 50 W	Correlating Miocene volcanoclastic strata	Oskin et al., 2001; Oskin and Stock, 2003
Isla de Tibron/Sonora (51)	50 km	20 km ± 10 km	pre-12 Ma		N 50 W	Correlating Miocene volcanoclastic strata	Oskin and Stock, 2003
Transverse Ranges (50)							
Eocene Poway Group							
Borderland extension	305 km at N 67 W	~250 km	~18 Ma	14 km/m.y.	~N 40 W	Correlation of distinctive volcanic clasts with source area in Sonora Mexico	Abbott and Smith, 1989
						Seismic reflection data, correlation of "mega keybeds"	Crouch and Suppe, 1993; Bohannon and Geist, 1998

Note: Numbers in parentheses refer to specific ranges identified on Fig. 2; numbers in brackets refer to the RANGE_ID number for individual ranges in the ArcGIS shape files and the Movement Table (ArcGIS files, Movement Table [see footnote 1]).

range from 20 km to 54 km (Faulds et al., 2005; Hardyman et al., 1984), plus an additional component of northwest-directed extension due to a change in extension direction in the northern Basin and Range from east-west in the east to northwest-southeast in the west.

One of the goals of this study was to develop a kinematically consistent model of the eastern California shear zone that fits within the errors provided by both local and regional studies. We found 100 km ± 10 km right-lateral shear oriented N25°W was compatible with data in both the northern and central Basin and Range (Animation 1). In the Mojave region of the eastern California shear zone, however, available data suggest no more than 53 km ± 6 km of right-lateral shear oriented N25°W, about half of what is required to the north. Kinematic compatibility with the magnitude of deformation north of the Garlock fault requires ~100 km of right-lateral shear though the Mojave region, with the majority of additional shear located on the eastern edge of the shear zone during its early (12–6 Ma) history (Figs. 5,7,8, Animation 1). The 27 km and 45 km of right-lateral offset along the Bristol Mountains–Granite Mountain and southern Death Valley fault zones is significantly greater than previous estimates (0–10 km and 20 km, respectively), but solid piercing points that limit the net offset are scarce and debatable (Howard and Miller, 1992; Dokka and Travis, 1990; Davis, 1977). The ~30 km of displacement along the eastern edge of the Mojave must be transferred southward along the Sheep Hole fault to the Laguna Fault system of Richard (1993). The 36 km of model offset is significantly greater than the 2 km of right-lateral offset proposed by Richard (1993) (Table 4, Fig. 5). Additional faults with significantly greater offsets than that documented by geology are the 11–13 km model offsets on the Camp Rock, Gravel Hills, and Harper Lake fault systems, where current estimates suggest no more than 3 km of offset on any of these faults (Dibblee, 1964; Oskin and Iriondo, 2004; M. Strane, 2005, personal commun.). The difference between the model and data requires that the slip discrepancy must be taken up on other faults (most likely to the east) in the Mojave shear system. Although the details concerning both timing and distribution of shear within the eastern California shear zone will continue to evolve with time, the strength of the central Basin and Range offsets combined with kinematic compatibility constraints require reevaluation of geologic evidence for total magnitude of right-lateral shear through the Mojave. Therefore, we have modeled many of the faults in the

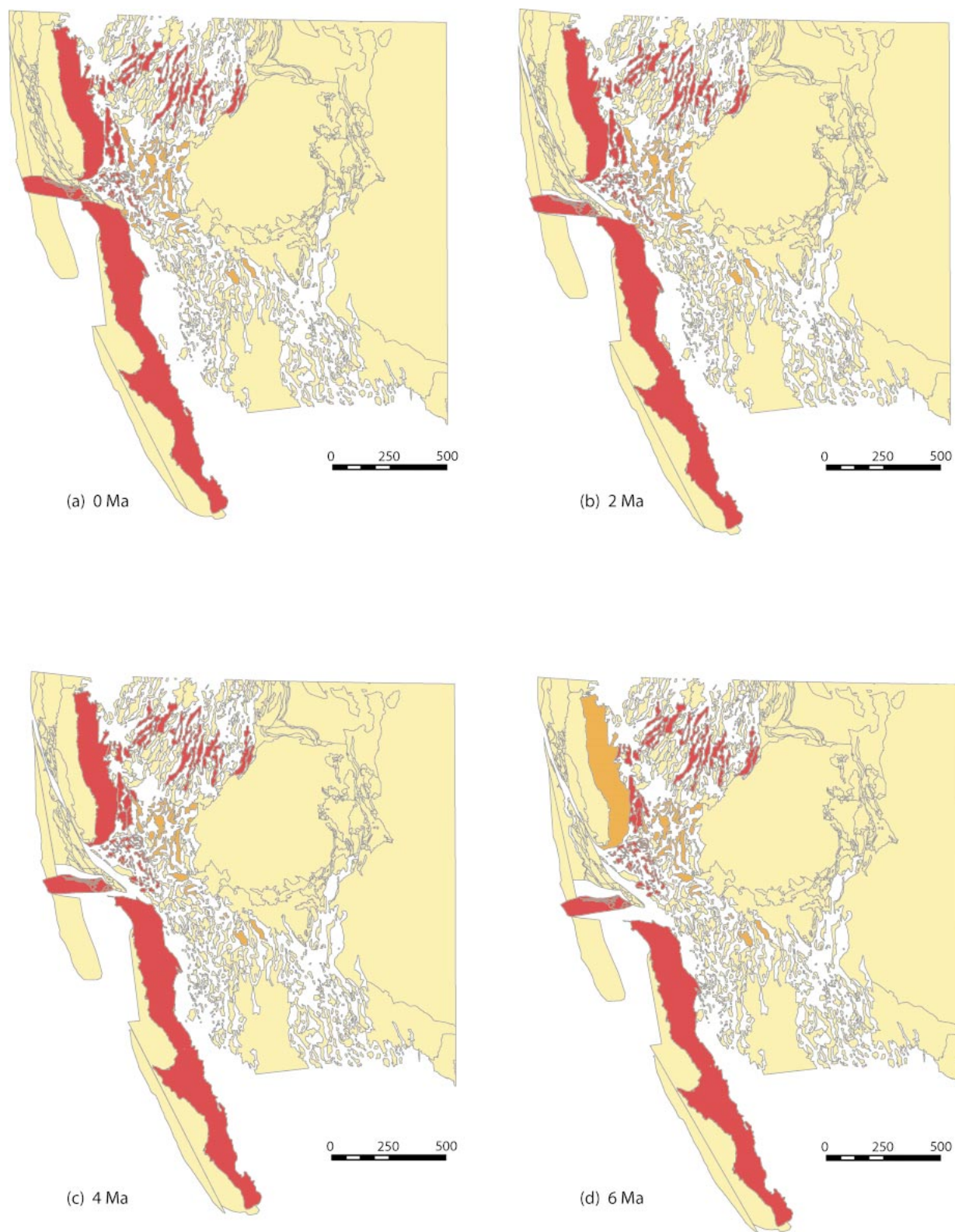


Figure 7. Reconstructed paleogeographic maps (from 0–6 Ma) used in the reconstruction. The color scheme is the same as that for the animation, yellow polygons on a white background. Yellow polygons indicate areas where there are no data for how the region is deforming. Polygons (ranges) that have data associated with their motion are orange when associated faulting is inactive and red during fault activity. Panels represent different time slices: (a) 0 Ma, (b) 2 Ma, (c) 4 Ma, and (d) 6 Ma.

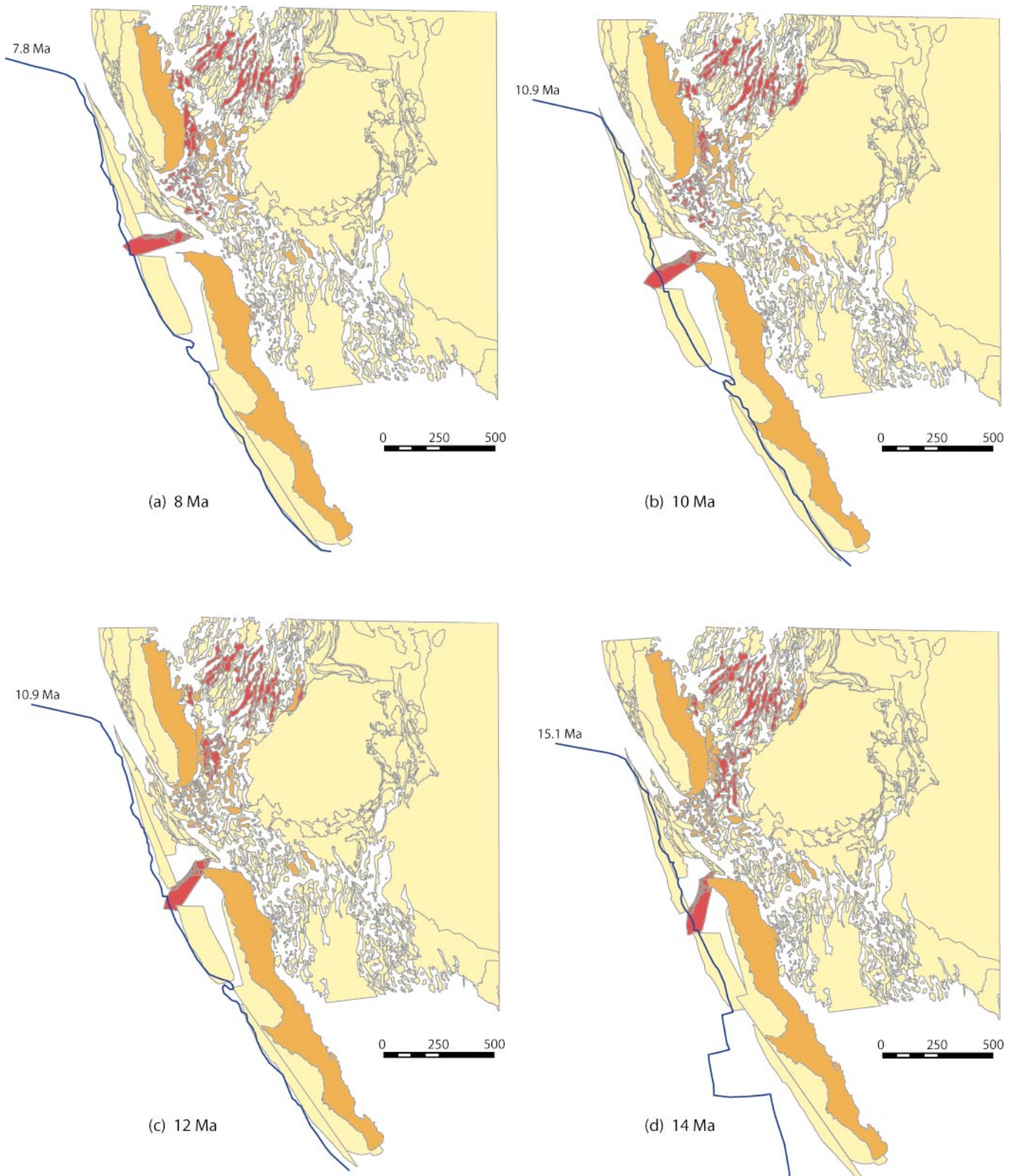


Figure 8. Reconstructed paleogeographic maps (from 8 to 14 Ma) used in the reconstruction. The color scheme is the same as Figure 7. Panels represent different time slices: (a) 8 Ma, (b) 10 Ma, (c) 12 Ma, and (d) 14 Ma.

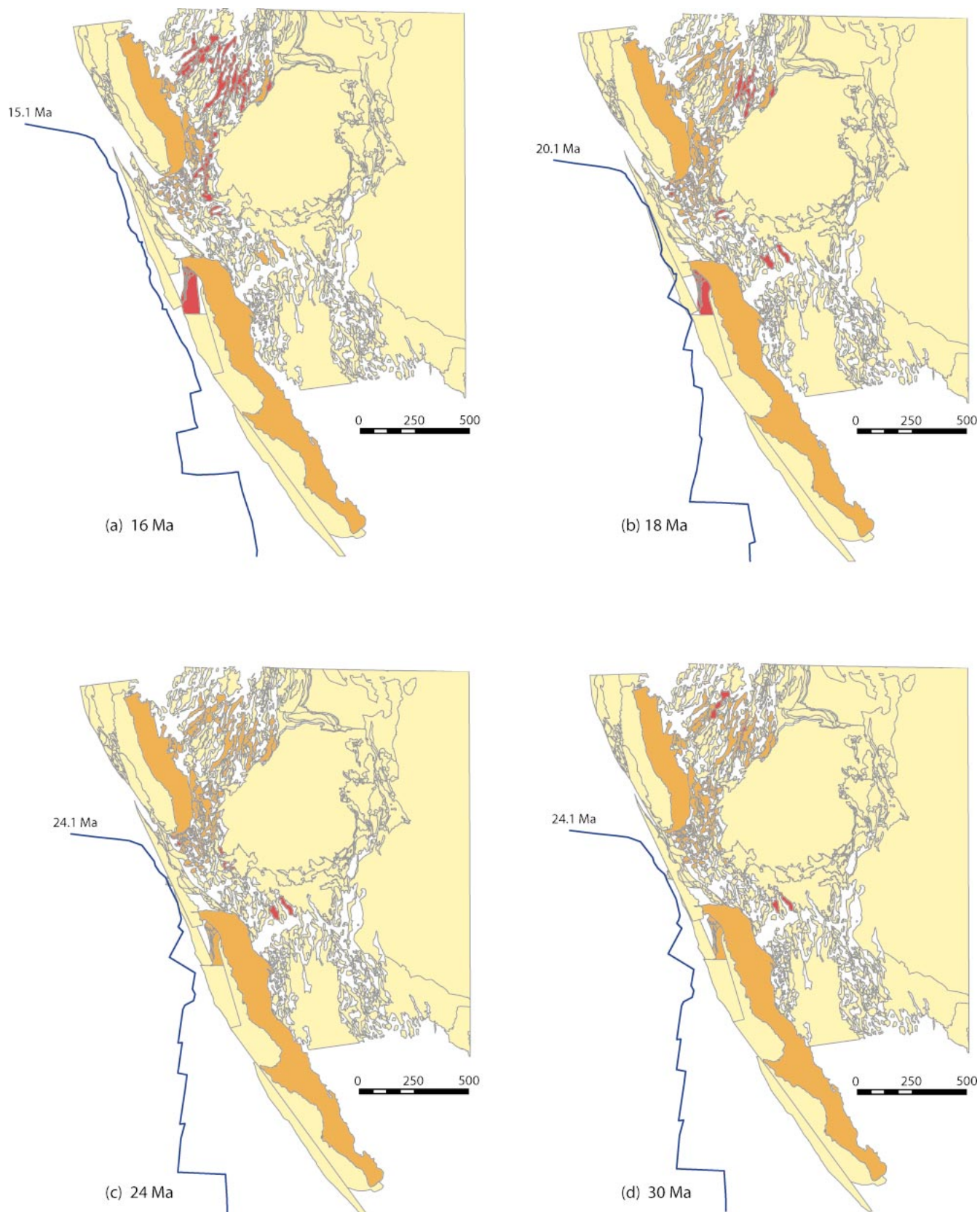


Figure 9. Reconstructed paleogeographic maps (from 16 to 36 Ma) used in the reconstruction. The color scheme is the same as Figure 7. Panels represent different time slices: (a) 16 Ma, (b) 18 Ma, (c) 24 Ma, (d) 30 Ma, and (e) 36 Ma.

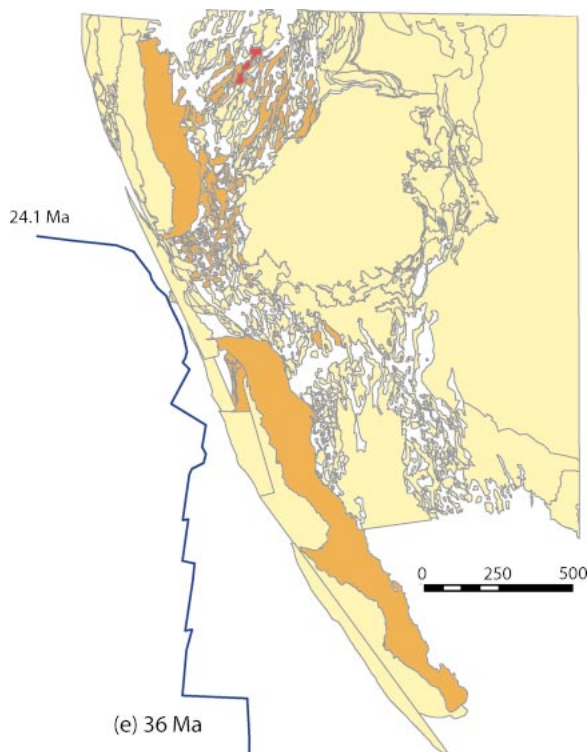


Figure 9. (continued).

Mojave with greater net offset than suggested by offset markers. From the model slip amounts shown on Figure 5, we obtain 100 km of right-lateral shear oriented N25°W since 12 Ma, at a long-term rate of 8.3 mm/yr \pm 1 mm/yr. We suggest that the discrepancy may be due to penetrative shear in the largely granitic crust between the strike-slip faults (e.g., Miller and Yount, 2002).

Increasing right-lateral shear in the eastern Mojave has implications on how shear is distributed along the entire plate boundary. Since much of the additional shear predates the opening of the Gulf of California (Oskin et al., 2001), it implies \sim 50 km of dextral shear between 6 and 12 Ma in the Sonora region. The total magnitude of separation of the Baja Peninsula from Sonora predicted from the model is 350 km, 300 km of which is post 6 Ma. This is slightly greater than the 296 ± 20 km, 276 ± 10 km of which is post 6 Ma measured by Oskin and Stock (2003), but still significantly less than the 450 km total continental separation proposed by Fletcher (2003).

Dokka and Travis (1990) proposed that the eastern California shear zone accommodated 9%–14% of total predicted relative motion between plates if shear initiated at 10 Ma. The model of eastern California shear zone deformation that we propose here (Animation 1) suggests that eastern California shear zone de-

formation is \sim 28% of San Andreas motion averaged since 12 Ma and 15% of total plate motion since 16 Ma.

Arizona–Mexican Basin and Range

The geographic region that has the fewest local kinematic constraints is Sonora–Chihuahua Mexico. However, the kinematics of Baja California, based on plate tectonic reconstructions (Atwater and Stock, 1998), is an especially powerful constraint on intraplate deformation in this region. The constraint arises from the simple fact that oceanic and continental lithosphere cannot occupy the same surface area at the same time (Atwater and Stock, 1998) (Fig. 6B). The plate tectonic constraint suggests \sim 330 km \pm 50 km of extension between 6 Ma and 24 Ma, because after restoring the offset across the Gulf of California (Oskin et al., 2001; Oskin and Stock, 2003), this is the total overlap between continent and ocean. In concert with strong northeast-southwest extension in Arizona, we suggest similar magnitudes of extension (44 km and 86 km) occurred from 16 Ma to 24 Ma and was oriented N50°E–N60°E (making room for the brown and green curves in Fig. 6B). We show another pulse from 12 Ma to 8 Ma oriented N65°W–N78°W, reflecting the growing influence of the Pacific plate's northerly motion on

intraplate deformation, as appears to be the case to the north (Animation 1).

Restoring 330 km of extension, however, particularly the northwesterly extension in the window of time from 16 Ma to 8 Ma, opens up a large northeast-trending gap in southern Arizona and northern Sonora. This gap is a result of differences in both magnitude and timing of extension between southern Arizona and northern Sonora and suggests (incorrectly) that there is \sim 60 km of NW-SE compression between 16 and 8 Ma (Figs. 8–9). Large magnitude core complex extension in southern Arizona initiates at ca. 28 Ma and wanes from 16 Ma to 14 Ma (Table 3). Significant extension in Sonora occurs over a similar time range (Nourse et al., 1994; Gans, 1997). At ca. 12 Ma, however, significant extension is recorded in both the Gulf extensional province west of the Sierra Madre Occidental (e.g., Stock and Hodges, 1989; Henry, 1989; Lee et al., 1996; Gans et al., 2003) and east of the Sierra Madre Occidental (Henry and Aranda-Gomez, 2000), while only minimal magnitudes of east-west extension are recorded in southern Arizona. This problem is similar to that arising from the difference in timing of extension north of the Colorado River extensional corridor between the Mojave Desert and central Basin and Range. Here, the Garlock fault accommodates different amounts of extension, not only from 10 Ma to the present (Davis and Burchfiel, 1973), but potentially throughout the history of extension in the region (24–0 Ma). Although the difference in timing and magnitude of extension between the Mojave region and the southern Arizona Basin and Range versus the Mexican Basin and Range in Sonora and Chihuahua is generally recognized (e.g., Henry and Aranda-Gomez, 2000; Dickinson, 2002), the geometry and genetic relationship of the transfer system that must separate them is problematic.

In the model presented here, the amount of extension in the Mexican Basin and Range is partitioned between the extending regions east (\sim 134 km) and west (\sim 180 km) of the unstrained Sierra Madre Occidental block. Although both regions display numerous extensional structures, the exact magnitude of extension is unknown. Because of the difference in post-16 Ma extension in Chihuahua and the Rio Grande rift (90 and 20 km, respectively) after ca. 16 Ma, the model includes a zone of right-lateral shear that extends through southeastern Arizona between the two provinces (Animation 1). The existence of this shear zone is unlikely, leaving two possible solutions. The first is that extension systematically increases from the Rio Grande rift to

Chihuahua Mexico due to clockwise rotation of the Sierra Madre Occidental (rotation would need to be greater than the 1.5° rotational opening of the Rio Grande rift). Another solution would be partitioning a much greater magnitude of extension in the Gulf extensional province (~ 270 – 300 km), but this is thus far not supported by mapping in the region (Henry and Aranda-Gomez, 2000). Most likely some combination of these factors is necessary to match the first-order geologic constraints of the region.

Sierra Nevada–Great Valley Block Rotation

The reconstruction presented here shows significant extension in the northern Basin and Range between 36 Ma and 24 Ma, with essentially no extension occurring over this time period in the central Basin and Range. To accommodate this difference, the Sierra Nevada–Great Valley Block must rotate or deform internally. We propose that the block behaves fairly rigidly and rotates counterclockwise (Animation 1). After initiation of extension in the central Basin and Range at ~ 16 Ma, the Sierra Nevada–Great Valley Block rotates clockwise for a final net rotation of 2° (Table 5, Appendix 1, Movement Table [see footnote 1]). The animation shows the early 36–24 Ma rotation accommodated by ~ 35 km of dextral shear along the proto–Garlock fault and accompanying compression in the southeastern Sierra Nevada region (Animation 1). The actual effects of this rigid body rotation on the deformation of surrounding regions (particularly to the north and south) are highly dependent on the axis of rotation and how rigidly the block behaved, both of which are unknown. The rotation of the Tehachapi Mountains may include this early counterclockwise rotation of the Sierras, as well as potentially being linked to southern Basin and Range core-complex formation, which immediately followed (McWilliams and Li, 1985; Plescia and Calderone, 1986; Walker et al., 1995; Glazner et al., 2002).

Areas West of the San Andreas Fault

Based on the timing and magnitude of displacement on a few fault systems (San Andreas, northern Gulf of California, Mojave, central Basin and Range, and the Santa Ynez Mountains), continental basins must open (creation of white spaces in the movie [Animation 1, Figs. 7–9] suggesting pulses of extension) and close (closing of spaces or overlap of polygons suggesting pulses of

contraction) from 24 Ma to 0 Ma. Even at this large and relatively simplified scale, extension and contraction are spatially and temporally complex throughout the region west of the San Andreas fault, and we expect even greater complexities in timing and magnitude at a more detailed level. The following discussion highlights the magnitudes of displacement and summarizes data that either support or conflict with the model displacements.

Transverse Ranges

The clockwise rotation of the Western Transverse Ranges (Hornafius et al., 1986; Luyendyk, 1991) suggests regions of extension and subsequent compression both north and south of the rotating Santa Ynez Mountains block (Fig. 2, range 50) (Animation 1). The magnitude of predicted extension (Fig. 8) and contraction (Fig. 7) (oriented \sim north-south) is as great as 130 km to the north of the western side of the block from ca. 12 Ma to the present. Motion of Baja California northward from 6 Ma to the present suggests as much as 90 km of shortening in the southern Transverse Ranges (Santa Ynez and San Gabriel Mountains blocks) (Fig. 7, Animation 1). Transpressive motion involving the San Gabriel Mountains, San Bernardino Mountains, and Mojave blocks implies ~ 40 km of north-south shortening immediately north of the Peninsular Ranges block. Balanced cross sections through the San Emigdio, Santa Ynez, and San Gabriel Ranges indicate 53 km of shortening since 3 Ma (Namson and Davis, 1988a). Although the shortening estimate is strongly dependent on the details of how the Santa Ynez and Peninsular Ranges–Baja California blocks move, the reconstruction presented here suggests ~ 60 km of north-south shortening at the longitude of the eastern Santa Ynez Mountains block since 6 Ma. As suggested by Namson and Davis (1988a), shortening of this magnitude in the upper mantle lithosphere is supported by a large volume of high-velocity material imaged tomographically beneath the region (e.g., Humphreys et al., 1984).

Coast Ranges

Differences in the timing of extension within the Mojave and Basin and Range north and south of the Garlock fault, in conjunction with plate tectonic constraints on the westernmost limit of the North America continental edge (Atwater and Stock, 1998), indicate a period of extension (20–16 Ma) and subsequent compression (14–0 Ma) to the west of the Sierra–Great Valley block (Figs. 7–9, Animation 1). Approximately 80 km of core-complex exten-

sion south of the Garlock fault occurred prior to significant extension in the central Basin and Range. In order to maintain a quasilinear ocean-continent boundary, a zone of extension roughly equal in magnitude to the core-complex extension is required north of the Garlock fault and west of the Sierra Nevada–Great Valley block. This becomes most visible in the reconstruction at 16 Ma (Fig. 9A). As extension evolves in the central Basin and Range, this same zone undergoes contraction to maintain the quasilinear plate boundary suggested by the extant distribution of oceanic crust from 16 Ma to the present.

The Neogene tectonic and volcanic history from the Great Valley to the edge of the continent is broadly consistent with the model (data summarized in Tennyson, 1989). Although the model and geologic data are difficult to compare quantitatively because there are no obvious normal faults with measurable offsets, the magnitude of extension (and subsequent compression) is significantly less than that predicted by the model. Development of local nonmarine basins and eroded highs, followed by significant subsidence at ~ 16 – 18 Ma and the development of the relatively deep marine Monterey basin strongly suggests an extensional event. Rotation of the Tehachapi Mountains and/or extension in the southern San Joaquin Valley (McWilliams and Li, 1985; Plescia and Calderone, 1986; Tennyson, 1989; Goodman and Malin, 1992) may be indicative of this extension but may represent far less than the ~ 80 km predicted by the model.

The subsequent compression in the Coast Ranges is more quantifiable and appears to be significantly less than that suggested by the model. Estimates of compression in the Coast Ranges east and west of the San Andreas fault range from 20 km to 48 km (Page et al., 1998; Namson and Davis, 1990, 1988b), with all of the known shortening occurring post-10 Ma, and most of it post-4 Ma (Page et al., 1998; Namson and Davis, 1990). Therefore, the model predicts an additional 32–50 km of shortening prior to 10 Ma, for which there is (thus far) no evidence in the Coast Ranges.

Pausing Animation 1 at 15 Ma highlights the crux of the problem (Fig. 9a). To eliminate the need of early 24–16 Ma extension in the Coast Ranges (and subsequent compression), the continental edge would need to bend eastward north of the Mojave and then continue north along the western edge of the Great Valley (Animation 1). This bend in the continental edge would create an ~ 80 -km-wide, ~ 300 -km-long section of oceanic crust that would have to be subducted south of the

northward migrating triple junction during the period of central Basin and Range extension. The solution to the space problem that the model highlights may rest in a combination of several possibilities which include allowing for a warping of the North America coast line, finding greater magnitudes of deformation in the region of the Coast Ranges, and less extension in the central Basin and Range. However, to truly evaluate the magnitude of each of these options requires more detailed reconstruction of crustal blocks west of the San Andreas fault.

Uncertainties in the Reconstruction

Statistically rigorous uncertainties are notoriously difficult to quantify in geological reconstructions, largely because estimates of geologic offset do not have Gaussian or other standard probability distribution functions. The condition of strain compatibility or “no overlap” sets a hard limit on the displacement estimate but does not distinguish higher or lower probability of any given position within those limits. Hence, the variance of any given estimate cannot be rigorously quantified.

In map view, any given displacement estimate will have an irregularly shaped uncertainty region. Under the assumption of a uniform probability distribution within these uncertainty regions, Wernicke et al. (1988) used a Monte Carlo method to estimate the total uncertainty on the sum of displacement vectors for a path across the central Basin and Range. This method repeatedly summed randomly selected vectors from each uncertainty region to generate a probability distribution for the net offset. The contour that excluded the outermost 5% of the model runs was taken as an estimate of two standard deviations of the measurement. The estimate of total Sierran motion thus derived was $247 \text{ km} \pm 56 \text{ km}$, $S 75^\circ \pm 12^\circ E$, and therefore a reasonable estimate of the standard deviation would be 28 km. For this same estimate, the square root of the sum of the squares for individual vectors (in the direction of displacement, using values from Table 1 and Figure 10 in Wernicke et al., 1988) is only 15 km. This is perhaps not surprising because the Monte Carlo approach does not place greater weight on values near the center of the uncertainty polygon than on values at the edges.

Our revised displacement estimate for the central Basin and Range, $235 \text{ km} \pm 20 \text{ km}$ (again the error is equal to the square root of the sum of the squares for individual vectors), is similar to that of Wernicke et al. (1988) if one considers the 20 km figure as a crude es-

timate of the standard deviation (1-sigma). However, given the results from Wernicke et al. (1988), the real error may scale upward by as much as a factor of two, depending on the degree to which our best estimate is more probable than values at the extremes. A simple sum of each uncertainty along a given path from Table 1 and Table 2 gives an error estimate of 47 km and 45 km, respectively. Thus, as a rule of thumb, the uncertainty in position of any given range or set of ranges at any given time is on the order of 20–40 km at one standard deviation.

Because the reconstruction involves temporal information (which is also uncertain), the problem of rigorously estimating errors becomes even more difficult and is clearly beyond the scope of this paper. Even though temporal information adds to the uncertainty of position at any given time, the self-consistency of the reconstruction mitigates these uncertainties to a substantial degree.

EVOLUTION OF THE REGIONAL VELOCITY FIELD

Tracking the restored positions of the ranges from the palinspastic maps, we have created “instantaneous” velocity fields based on 2 m.y. averages from 0 Ma to 18 Ma and 6 m.y. averages from 18 to 36 Ma. These paleogeodetic velocity fields depict how deformation has evolved in space and time across the plate boundary deformation zone (Figs. 10A–10G).

Figures 10F and 10G (30–18 Ma) illustrate the collapse of the Basin and Range away from the stable Colorado Plateau through the formation of metamorphic core complexes at a time of active ignimbrite volcanism and Pacific–Farallon convergence. Extension initiated first in the northern Basin and Range and then in the southern Basin and Range. This pulse of large-magnitude extension migrated south and north, respectively, until it converged in the central Basin and Range at ca. 16 Ma. Figure 10E (14–16 Ma) emphasizes the large extensional strains in the central Basin and Range especially with respect to the concurrent faulting to the north and south. The 14–16 Ma time slice also shows the impact of the evolving plate boundary on the North American continent as right-lateral shear is accommodated through the rotation of the Western Transverse Ranges and accompanying shear and extension. The 10–12 Ma time slice (Fig. 10D) illustrates the uniform (systematically increasing) strain in the northern Basin and Range and, in contrast, the westward-migrating extension in the central Basin and

Range. Significant extension is also necessary in the Mexican Basin and Range due to plate-boundary constraints. It is during this time period that right-lateral shear migrates farther inboard into the continent through the development of the eastern California shear zone. South of the Garlock fault, the shear is oriented nearly parallel to the plate boundary ($N25^\circ W$). North of the Garlock fault, the shear plus extension creates a more oblique orientation of shear ($\sim N67^\circ W$). From 6 Ma to 8 Ma, this same pattern of intracontinental right-lateral shear strengthens with shear partitioned differently south of the Garlock fault than in the central Basin and Range and northern Basin and Range portions of the eastern California shear zone (Fig. 10C). In the Mexican Basin and Range, deformation wanes and extension and right-lateral shear become concentrated in the proto-Gulf of California.

The differences in the velocity fields from the 2–4 Ma average to the 0–2 Ma average is most likely a function of limitations in the data, rather than a significant slowing in the rate of deformation over the last 2 m.y. (i.e., the Mojave region) (Figs. 10A and 10B). Within the model, the lack of timing constraints for right-lateral faults through the Mojave means that the rate of deformation there becomes a function of the rate of deformation to the north and south. North of the Garlock fault, large magnitudes (104 km) of oblique extension are focused predominately from 11 Ma to 3 Ma (Niemi et al., 2001; Snow and Wernicke, 2000; Snow and Lux, 1999). South of the Mojave, the timing of deformation is partially bracketed by the age of rotation of the Eastern Transverse Ranges (as mentioned earlier, ca. 10 Ma rocks record the entire 45° of rotation whereas ca. 4 Ma rocks indicate no rotation; Carter et al., 1987; Richard, 1993). These timing constraints suggest most of the deformational shear in the Mojave occurred between 10 Ma and 2 Ma. However, the total displacement across the eastern California shear zone ($100 \text{ km} \pm 10 \text{ km}$) averaged over the last 12 m.y. suggests a long-term rate of $8.3 \text{ mm/yr} \pm 1 \text{ mm/yr}$. This rate is similar to or slightly less than the 8–12 mm/yr rate suggested by geodetic studies (McClusky et al., 2001; Miller et al., 2001; Sauber et al., 1994; Savage et al., 1990).

Another way to look at the evolution of the velocity field and provide a direct comparison between geologic data and geodynamical model results is by mapping the paths that individual ranges take over the deformational interval of interest (Fig. 11). Note that the bend in the path of the Pacific plate does not appear to be related to changes in the paths of

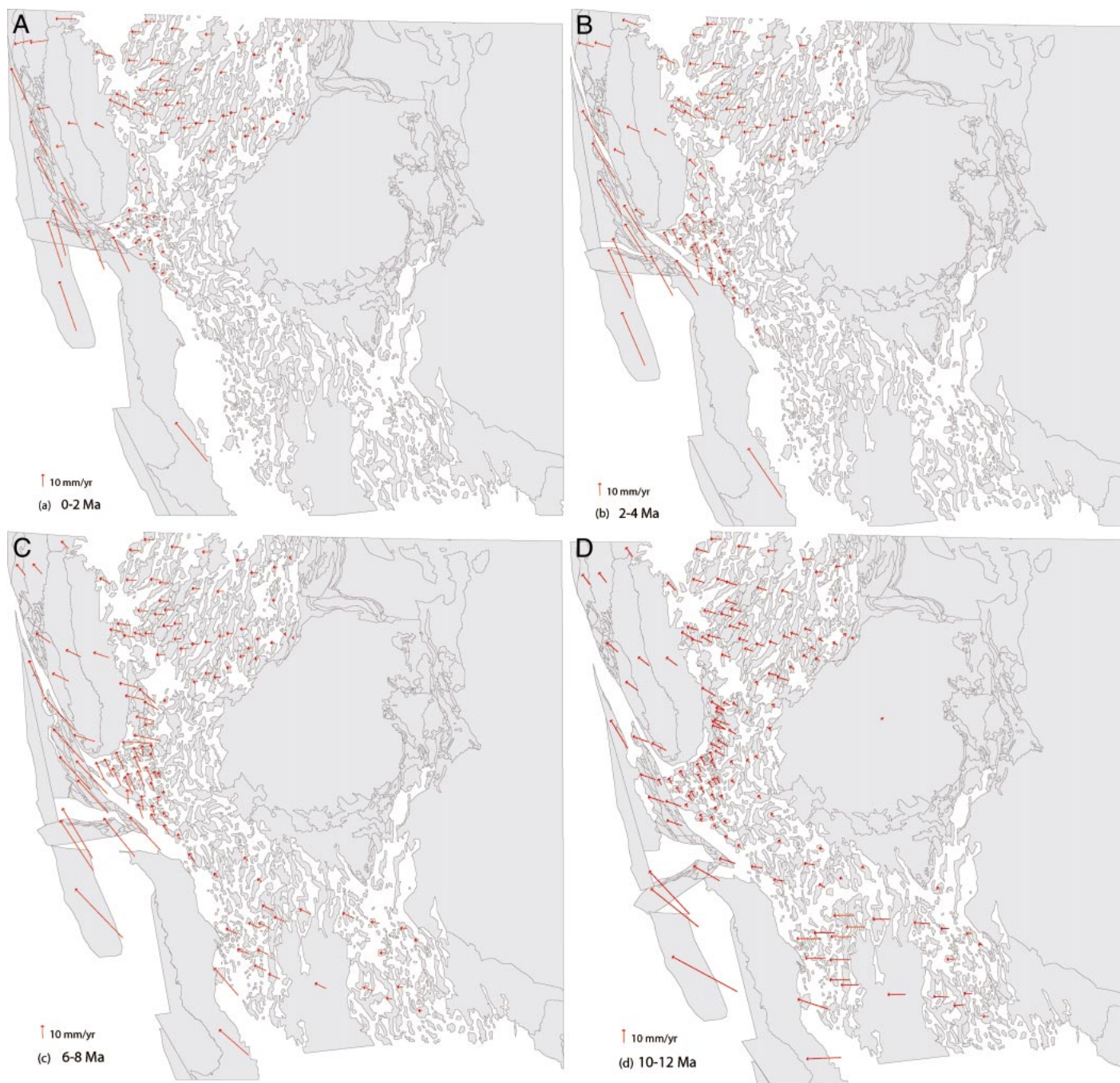


Figure 10. “Instantaneous” velocity fields based on 2 m.y. averages from 0 to 18 Ma, and 6 m.y. averages from 18 to 36 Ma. Arrows show displacement with respect to stable North America and were determined by connecting the centroids of specific ranges at one time with the centroid of the same range in a later time. Because the motion of individual ranges can be very slight at the eastern edge of the model, the line lengths representing each incremental offset were uniformly doubled. Map base is the palinspastic map from the youngest time in the 2 or 6 m.y. interval.

the Sierra Nevada with respect to the Colorado Plateau or changes in the paths of individual ranges within the continent. The most significant continental change in direction occurs at 12 Ma. Because the plate constraints do not require the bend to occur at that time (it is

only a function of the times at which magnetic anomalies constrain the position), it is possible within the uncertainties of both the plate reconstruction and geological reconstruction (Atwater and Stock, 1998; Wernicke and Snow, 1998) that these events more closely

correlate. As stated previously, the timing of development of right-lateral shear depends on the orientation and timing of early extension in the Death Valley region, which if relatively minor prior to 11 Ma would point toward a later time of onset of right-lateral shear in-

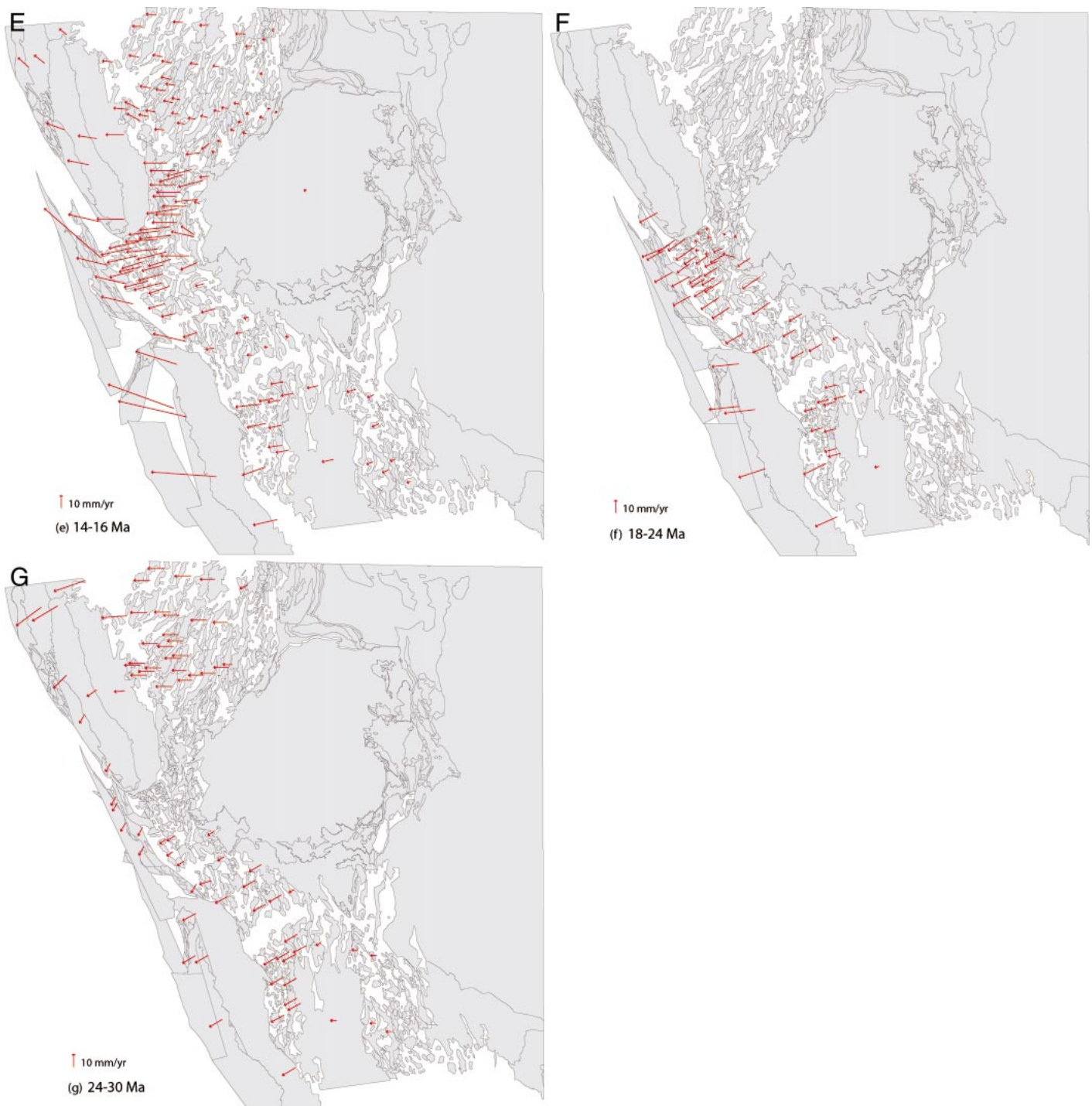


Figure 10. (continued).

board of the Sierra Nevada. The distribution of north-northwest shear through the Mojave is kinematically linked to the northwesterly motion of the Sierra Nevada–Great Valley block, in turn requiring at least some amount of right-lateral shear within the Mojave region between 12 Ma and 8 Ma.

CONCLUSIONS

Although orogen-scale reconstructions of the Basin and Range will continue to evolve with time and adjust as more data is acquired, the exercise in kinematic compatibility we present here highlights what we understand

and more importantly what we still do not understand regarding the evolution of the plate boundary.

Results that are robust and highlight what we do understand include: (1) $235 \text{ km} \pm 20 \text{ km}$ of extension oriented $\text{N}78^\circ\text{W}$ in both the northern (50% extension) and central (200%

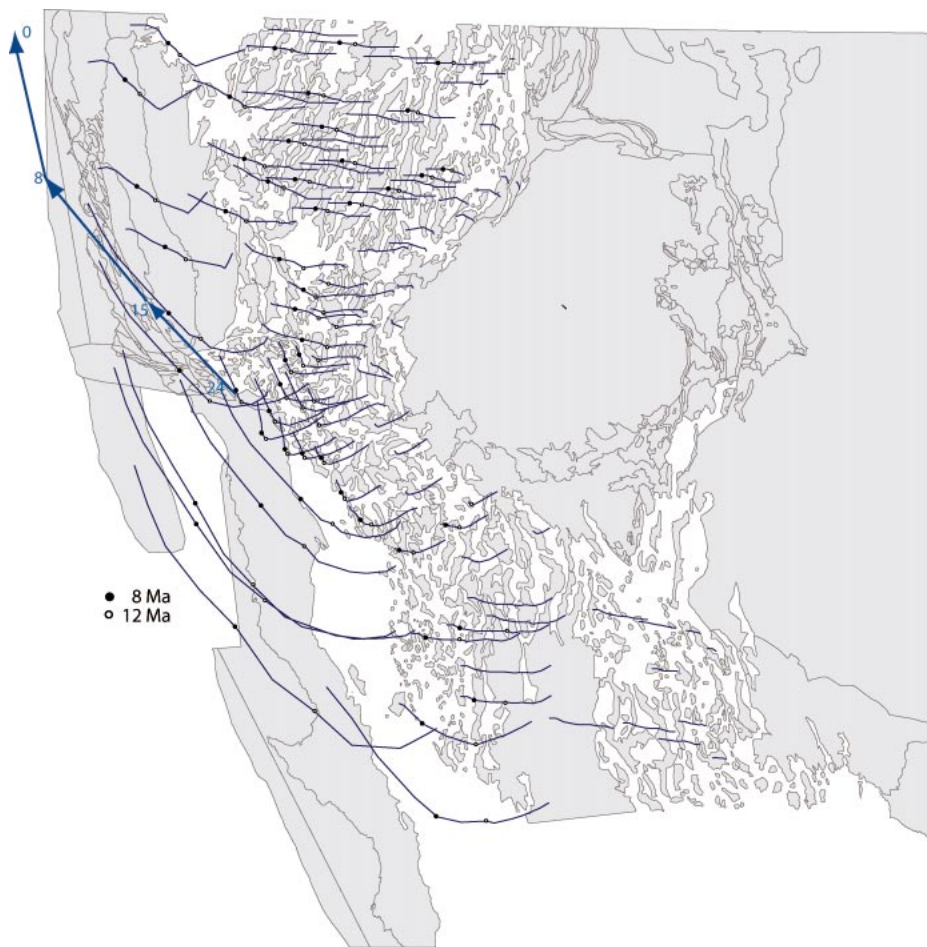


Figure 11. Map illustrating paths of various ranges from 0 to 36 Ma. Solid black circles indicate the positions of the ranges at 8 Ma, and open circles represent the positions of the ranges at 12 Ma. The westernmost point on each line represents the current location of each range. The easternmost point on the path represents the location of the range at 36 Ma. The blue arrows represent the motion of the Mendicino triple junction, with its position shown at 24, 15, 8, and 0 Ma (Atwater and Stock, 1998).

extension) parts of the province. An important implication of the model is that any significant change in extension amount in a portion of the region (i.e., a range on the path between the Colorado Plateau and the Sierra Nevada) must be evaluated in light of how that change affects coevolving regions to the north and south. (2) A significant portion of boundary-parallel shear (in contrast to earlier extension) jumped into the continent at ca. 10–12 Ma, and once established, appears to have migrated westward with time. (3) The magnitude of slip on the eastern California shear zone appears to be $100 \text{ km} \pm 10 \text{ km}$, although the exact structures that accommodate this shear in the Mojave, or how much of the relative motion is accommodated by distributed shear, is not known.

Problems with the current reconstructions

are highlighted by large gaps in the model. These zones emphasize areas where more work is needed in refining our ideas about how intraplate deformation is accommodated through time. Salient aspects of the model that we do not understand include: (1) compatibility between timing of extension north and south of the Garlock fault and a smooth north-northwest-trending continental edge as implied by plate tectonic reconstructions. To maintain a relatively smooth continental edge with different periods of extension across the Garlock fault, a triangular window of significant extension ($>50 \text{ km}$; 24–16 Ma) followed by an equal amount of shortening (14–0 Ma) would have occurred in the Coast Range–Great Valley region. While known geology supports extension and subsequent compression in these time windows, the magnitude is

~25% of what is needed; and (2) differences in magnitude and timing of extension between southern Arizona and northern Sonora, Mexico, require a transfer zone or large lateral displacement gradient. The model displays this zone as a gap that opens up (going backward with time) between the two provinces. Timing and magnitude of extension in the Sonora region were constrained only by plate motions to the west and broad assumptions as to similarities in timing and direction with areas to the north. Data detailing the magnitude, timing, and direction of extension through the Mexican Basin and Range is necessary to resolve this problem.

ACKNOWLEDGMENTS

This paper has benefited greatly from many conversations with scientists familiar with western North America geology. We specifically want to acknowledge Tanya Atwater, Bill Dickinson, Allen Glazner, Steve Graham, Jon Spencer, Joann Stock, Nathan Niemi, Mike Oskin, Jason Saleeby, and John Suppe. We are grateful to Melissa Brenneman at the University of Redlands for creating the ArcMap document and script used for the reconstruction. The movie would not exist without the help of the University of California, Santa Barbara, Educational Multimedia Visualization Center, specifically Carrie Glavich and Grace Giles. Gary Axen, Doug Walker, Craig Jones, and Randy Keller all provided insightful feedback through the review processes that greatly improved the clarity of presentation. This project was funded by the Caltech Tectonics Observatory.

REFERENCES CITED

- Abbott, P.L., and Smith, T.E., 1989, Sonora Mexico, source for the Eocene Poway conglomerate of southern California: *Geology*, v. 17, p. 329–332, doi: 10.1130/0091-7613(1989)017<0329:SMSFTE>2.3.CO;2.
- Allmendinger, R.W., Farmer, H., Hauser, E.C., Sharp, J., Von Tish, D., Oliver, J., and Kaufman, S., 1986, Phanerozoic tectonics of the Basin and Range—Colorado Plateau transition from COCORP data and geologic data, in Barazangi, M., and Brown, L.D., eds., *Reflection seismology: The continental crust*: American Geophysical Union Geodynamics Series, v. 14, p. 257–268.
- Allmendinger, R.W., Royse, F., Anders, M.H., Christie-Blick, N., and Wills, S., 1995, Is the Sevier Desert reflection of west-central Utah a normal fault?: *Comment: Geology*, v. 23, p. 669–670, doi: 10.1130/0091-7613(1995)023<0669:ITSDRO>2.3.CO;2.
- Anders, M.H., and Christie-Blick, N., 1994, Is the Sevier Desert reflection of west-central Utah a normal fault?: *Geology*, v. 22, p. 771–774, doi: 10.1130/0091-7613(1994)022<0771:ITSDRO>2.3.CO;2.
- Atwater, T., 1970, Implications of plate tectonics for the Cenozoic tectonic evolution of western North America: *Geological Society of America Bulletin*, v. 81, p. 3513–3536.
- Atwater, T., and Stock, J., 1998, Pacific–North America Plate tectonics of the Neogene southwestern United States; an update, in Ernst, W.G., and Nelson, C.A., eds., *Integrated Earth and environmental evolution of the southwestern United States: The Clarence A. Hall, Jr. volume*: Columbia, Bellwether Publishing, p. 393–420.
- Axen, G.J., Wernicke, B.P., Skelly, M.J., and Taylor, W.J., 1990, *Mesozoic and Cenozoic tectonics of the Sevier*

- thrust belt in the Virgin River Valley area, southern Nevada, *in* Wernicke, B., ed., Basin and Range extensional tectonics near the latitude of Las Vegas, Nevada: Boulder, Colorado, Geological Society of America Memoir 176, p. 123–153.
- Ballard, S.N., 1990, The structural geology of the Little Maria Mountains, Riverside County, California [Ph.D. thesis]: Santa Barbara, University of California, 206 p.
- Bartley, J.M., and Glazner, A.F., 1991, En echelon Miocene rifting in the southwestern United States and model for vertical-axis rotation in continental extension: *Geology*, v. 19, p. 1165–1168, doi: 10.1130/0091-7613(1991)019<1165:EEMRIT>2.3.CO;2.
- Bartley, J.M., and Wernicke, B.P., 1984, The Snake Range decollement interpreted as a major extensional shear zone: *Tectonics*, v. 3, p. 647–657.
- Bassett, A.M., and Kupfer, D.H., 1964, A geologic reconnaissance in the southeastern Mojave Desert, California: Special report: California Division of Mines and Geology, v. 83, p. 1–43.
- Bennett, R.A., Davis, J.L., and Wernicke, B.P., 1999, Present-day pattern of Cordilleran deformation in the western United States: *Geology*, v. 27, p. 371–374, doi: 10.1130/0091-7613(1999)027<0371:PDPOCD>2.3.CO;2.
- Bennett, R.A., Wernicke, B.P., Niemi, N.A., Friedrich, A.M., and Davis, J.L., 2003, Contemporary strain rates in the northern Basin and Range province from GPS data: *Tectonics*, v. 22, p. 1008, doi: 10.1029/2001TC001355.
- Bird, P., 1998, Kinematic history of the Laramide orogeny in latitudes 35–49 N, western United States: *Tectonics*, v. 17, p. 780–801, doi: 10.1029/98TC02698.
- Bogen, N.L., and Schweickert, R.A., 1985, Magnitude of crustal extension across the northern Basin and Range Province; constraints from paleomagnetism: *Earth and Planetary Science Letters*, v. 75, no. 1, p. 93–100, doi: 10.1016/0012-821X(85)90054-8.
- Bohannon, R.G., and Geist, E., 1998, Upper crustal structure and Neogene tectonic development of the California continental borderland: *Geological Society of America Bulletin*, v. 110, p. 779–800, doi: 10.1130/0016-7606(1998)110<0779:UCSANT>2.3.CO;2.
- Brady, R., Wernicke, B., and Fryxell, J., 2000, Kinematic evolution of a large-offset continental normal fault system, South Virgin Mountains, Nevada: *Geological Society of America Bulletin*, v. 112, p. 1375–1397, doi: 10.1130/0016-7606(2000)112<1375:KEOALO>2.0.CO;2.
- Braun, J., and Pauselli, C., 2004, Tectonic evolution of the Lachlan Fold Belt, southeastern Australia: Constraints from coupled numerical models of crustal deformation and surface erosion driven by subduction of the underlying mantle: *Physics of the Earth and Planetary Interiors*, v. 141, p. 281–301, doi: 10.1016/j.pepi.2003.11.007.
- Burchfiel, B.C., Hodges, K.V., and Royden, L.H., 1987, Geology of Panamint Valley–Saline Valley pull apart system, California: Palinspastic evidence for low-angle geometry of a Neogene range-bounding fault: *Journal of Geophysical Research*, v. 92, p. 10,422–10,426.
- Carr, W.J., Byers, F.M., Jr., and Orkild, P.P., 1986, Stratigraphic and volcano-tectonic relations of Crater Flat Tuff and some older volcanic units, Nye County, Nevada: Reston, Virginia, U.S. Geological Survey, U.S. Geological Survey Professional Paper 1323, 28 p.
- Carter, J.N., Luyendyk, B.P., and Terres, R.R., 1987, Neogene clockwise tectonic rotation of the eastern Transverse Ranges, California, suggested by paleomagnetic vectors: *Geological Society of America Bulletin*, v. 98, p. 199–206, doi: 10.1130/0016-7606(1987)98<199:NCTROT>2.0.CO;2.
- Cashman, P.H., and Fontaine, S.A., 2000, Strain partitioning in the northern Walker Lane, western Nevada and northeastern California: *Tectonophysics*, v. 326, p. 111–130, doi: 10.1016/S0040-1951(00)00149-9.
- Cemen, I., Wright, L.A., Drake, R.E., and Johnson, F.C., 1985, Cenozoic sedimentation and sequence of deformational events at the southeastern end of Furnace Creek strike-slip fault-zone, Death Valley region, California, *in* Biddle, K.T., and Christie-Blick, N., eds., Strike-slip deformation, basin formation, and sedimentation: Tulsa, Oklahoma, Society for Sedimentary Geology (SEPM), Society of Economic Paleontologists and Mineralogists Special Publication 37, p. 127–139.
- Chapin, C.E., and Cather, S.M., 1994, Tectonic setting of the axial basins of the northern and central Rio Grande rift, *in* Keller, G.R., and Cather, S.M., ed., Basins of the Rio Grande rift: Structure, stratigraphy, and tectonic setting: *Geological Society of America Special Paper* 291, p. 5–25.
- Coney, P.J., 1980, Cordillera metamorphic core complexes: An overview, *in* Crittenden, M.D., Coney, P.J., and Davis, G.H., eds., Cordilleran metamorphic core complexes: *Geological Society of America Memoir* 153, p. 7–31.
- Coogan, J.C., and DeCelles, P.G., 1996, Seismic architecture of the Sevier Desert detachment basin: Evidence for large-scale regional extension: *Geology*, v. 24, p. 933–936, doi: 10.1130/0091-7613(1996)024<0933:ECATSD>2.3.CO;2.
- Coogan, J.C., DeCelles, P.G., Mitra, G., and Sussman, A.J., 1995, New regional balanced cross section across the Sevier Desert region and central Utah thrust belt: *Geological Society of America Abstracts with Programs*, v. 27, no. 4, p. 7.
- Crouch, J.K., and Suppe, J., 1993, Late Cenozoic tectonic evolution of the Los Angeles basin and inner California borderland: A model for core-complex-like crustal extension: *Geological Society of America Bulletin*, v. 105, p. 1415–1434, doi: 10.1130/0016-7606(1993)105<1415:LCTEOT>2.3.CO;2.
- Davis, G.A., 1977, Limitations on displacement and south-eastward extent of the Death Valley fault zone, California: Short contributions to California Geology: Special report: California Divisions of Mines and Geology, v. 129, p. 27–33.
- Davis, G.A., and Burchfiel, B.C., 1973, Garlock Fault: An intracontinental transform structure, southern California: *Geological Society of America Bulletin*, v. 84, p. 1407–1422, doi: 10.1130/0016-7606(1973)84<1407:GFAITS>2.0.CO;2.
- Davis, G.A., and Lister, G.S., 1988, Detachment faulting in continental extension: Perspectives from the southwestern U.S. Cordillera, *in* Clark, S.P., Jr., Burchfiel, B.C., and Suppe, J., eds., Processes in continental lithospheric deformation: *Geological Society of America Special Paper* 218, p. 133–159.
- Davy, P., Guerin, G., and Brun, J.-P., 1989, Thermal constraints on the tectonic evolution of a metamorphic core complex (Santa Catalina Mountains), Arizona: *Earth and Planetary Science Letters*, v. 94, p. 425–440, doi: 10.1016/0012-821X(89)90159-3.
- Dibblee, T.W., Jr., 1964, Geologic map of the Ord Mountains quadrangle, San Bernardino County, California: U.S. Geological Survey Miscellaneous Geologic Investigations Map I-427, 1 sheet, scale: 1:62,500.
- Dibblee, T.W., Jr., 1968, Geologic map of the Twentynine Palms quadrangle, San Bernardino and Riverside counties, California: U.S. Geological Survey Miscellaneous Geologic Investigations Map I-561, 1 sheet, scale: 1:62,500.
- Dibblee, T.W., Jr., 1982, Regional geology of the Transverse Ranges Province of southern California, *in* Fife, D., ed., Geology and mineral wealth of the California Transverse Ranges: Santa Ana, California: Santa Ana, South Coast Geological Society, Inc., p. 7–26.
- Dickinson, W.R., 1991, Tectonic setting of faulted Tertiary strata associated with the Catalina core complex in southern Arizona: *Geological Society of America Special Paper* 264, p. 106.
- Dickinson, W.R., 1996, Kinematics of transrotational tectonism in the California Transverse Ranges and its contribution to cumulative slip along the San Andreas transform fault system: *Geological Society of America Special Paper* 305, p. 46.
- Dickinson, W.R., 2002, The Basin and Range province as a composite extensional domain: *International Geology Review*, v. 44, no. 1, p. 1–38.
- Dickinson, W.R., and Wernicke, B.P., 1997, Reconciliation of San Andreas slip discrepancy by a combination of interior basin-range extension and transrotation near the coast: *Geology*, v. 25, p. 663–665, doi: 10.1130/0091-7613(1997)025<0663:ROSASD>2.3.CO;2.
- Dilles, J.H., and Gans, P.B., 1995, The chronology of Cenozoic volcanism and deformation in the Yerington area, western Basin-and-Range and Walker Lane: *Geological Society of America Bulletin*, v. 107, p. 474–486, doi: 10.1130/0016-7606(1995)107<0474:TCOCVA>2.3.CO;2.
- Dillon, J.T., 1975, Geology of the Chocolate and Cargo Muchacho Mountains, southeasternmost California [Ph.D. thesis]: Santa Barbara, University of California, 405 p.
- Dokka, R.K., 1983, Displacements on late Cenozoic strike-slip faults of the central Mojave Desert, California: *Geology*, v. 11, p. 305–308, doi: 10.1130/0091-7613(1983)11<305:DOLCSF>2.0.CO;2.
- Dokka, R.K., 1989, The Mojave extensional belt of southern California: *Tectonics*, v. 8, p. 363–390.
- Dokka, R.K., and Travis, C.J., 1990, Late Cenozoic strike-slip faulting in the Mojave Desert, California: *Tectonics*, v. 9, no. 2, p. 311–340.
- Dokka, R.K., Ross, T.M., and Lu, G., 1998, The Trans Mojave-Sierran shear zone and its role in early Miocene collapse of southwestern North America, *in* Holdsworth, B., Dewey, J., and Strachan, R., eds., Continental transpressional and transtensional tectonics: *Geological Society Special Publication* 135, p. 183–202.
- Duebendorfer, E.M., and Black, R.A., 1992, The kinematic role of transverse structures in continental extension: An example from the Las Vegas Valley shear zone, Nevada: *Geology*, v. 20, p. 1107–1110, doi: 10.1130/0091-7613(1992)020<1107:KROTSI>2.3.CO;2.
- Duebendorfer, E.M., Beard, L.S., and Smith, E.I., 1998, Restoration of Tertiary deformation in the Lake Mead region, southern Nevada; the role of strike-slip transfer faults, *in* Faulds, J.E., and Stewart, J.H., eds., Accommodation zones and transfer zones; the regional segmentation of the Basin and Range province: *Geological Society of America Special Paper* 323, p. 127–148.
- England, P., and Houseman, G., 1986, Finite strain calculations of continental deformation. 2. Comparison with the India-Asia collision zone: *Journal of Geophysical Research*, v. 91, p. 3664–3676.
- England, P., and McKenzie, D., 1982, A thin viscous sheet model for continental deformation: *Geophysical Journal of the Royal Astronomical Society*, v. 70, p. 295–321.
- Faulds, J.E., Henry, C.D., and Hinz, N.H., 2005, Kinematics of the northern Walker Lane; an incipient transform fault along the Pacific-North American Plate boundary: *Geology*, v. 33, p. 505–508, doi: 10.1130/G21274.1.
- Fayon, A.K., Peacock, S.M., Stump, E., and Reynolds Stephen, J., 2000, Fission track analysis of the footwall of the Catalina detachment fault, Arizona: Tectonic denudation, magmatism and erosion: *Journal of Geophysical Research*, v. 105, p. 11,047–11,062, doi: 10.1029/1999JB900421.
- Fitzgerald, P.G., Fryxell, J.E., and Wernicke, B.P., 1991, Miocene crustal extension and uplift in southeastern Nevada: Constraints from apatite fission track analysis: *Geology*, v. 19, p. 1013–1016, doi: 10.1130/0091-7613(1991)019<1013:MCEAU1>2.3.CO;2.
- Flesch, L.M., Holt, W.E., Haines, A.J., and Shen-Tu, B., 2000, Dynamics of the Pacific-North American plate boundary in the western United States: *Science*, v. 287, p. 834–836, doi: 10.1126/science.287.5454.834.
- Fletcher, J.M., 2003, Tectonic restoration of the Baja California microplate and the geodynamic evolution of the Pacific-North American plate margin: *Geological Society of America Abstracts with Programs*, v. 35, no. 4, p. 9.
- Fletcher, J.M., Bartley, J.M., Martin, M.W., Glazner, A.F., and Walker, J.D., 1995, Large-magnitude continental extension: An example from the central Mojave metamorphic core complex: *Geological Society of America Bulletin*, v. 107, no. 12, p. 1468–1483, doi: 10.1130/0016-7606(1995)107<1468:LMCEAE>2.3.CO;2.
- Foster, D.A., Gladow, A.J.W., Reynolds, S.J., and Fitzgerald,

- ald, P.G., 1993, Denudation of metamorphic core complexes and the reconstruction of the Transition Zone, west-central Arizona: constraints from apatite fission track thermochronology: *Journal of Geophysical Research*, v. 98, p. 2167–2185.
- Fowler, T.K., Jr., and Calzia, J.P., 1999, Kingston Range detachment fault, southeastern Death Valley region, California; relation to Tertiary deposits and reconstruction of initial dip, in Wright, L.A., and Troxel, B.W., eds., Cenozoic basins of the Death Valley region: Geological Society of America Special Paper 333, p. 245–257.
- Frei, L.S., 1986, Additional paleomagnetic results from the Sierra Nevada: Further constraints on Basin and Range extension and northward displacement in the western United States: *Geological Society of America Bulletin*, v. 97, p. 840–849, doi: 10.1130/0016-7606(1986)97<840:APRFTS>2.0.CO;2.
- Frei, L.S., Magill, J.R., and Cox, A., 1984, Paleomagnetic results from the central Sierra Nevada: Constraints on reconstructions of the western United States: *Tectonics*, v. 3, p. 157–177.
- Gans, P.B., 1997, Large-magnitude Oligo-Miocene extension in southern Sonora: Implications for the tectonic evolution of northwest Mexico: *Tectonics*, v. 16, p. 388–408, doi: 10.1029/97TC00496.
- Gans, P.B., and Miller, E.L., 1983, Style of mid-Tertiary extension in east-central Nevada: *Utah Geology and Mineral Survey Special Studies*, v. 59, p. 107–160.
- Gans, P.B., Blair, K., MacMillan, I., Wong, M., and Roldan, J., 2003, Structural and magmatic evolution of the Sonoran rifted margin: A preliminary report: *Geological Society of America Abstracts with Programs*, v. 35, no. 4, p. 21.
- Gans, P.B., Miller, E.L., McCarthy, J., and Oldcott, M.L., 1985, Tertiary extensional faulting and evolving ductile-brittle transition zones in the northern Snake Range and vicinity: new insights from seismic data: *Geology*, v. 13, p. 189–193, doi: 10.1130/0091-7613(1985)13<189:TEFAED>2.0.CO;2.
- Gilder, S., and McNulty, B.A., 1999, Tectonic exhumation and tilting of the Mount Givens pluton, central Sierra Nevada, California: *Geology*, v. 27, p. 919–922, doi: 10.1130/0091-7613(1999)027<0919:TEATOT>2.3.CO;2.
- Glazner, A.F., Bartley, J.M., and Walker, J.D., 1989, Magnitude and significance of Miocene crustal extension in the central Mojave Desert, California: Reply: *Geology*, v. 17, p. 1061–1062, doi: 10.1130/0091-7613(1989)017<1061:CAROMA>2.3.CO;2.
- Glazner, A.F., Walker, J.D., Bartley, J.M., and Fletcher, J.M., 2002, Cenozoic evolution of the Mojave Block of southern California, in Glazner, A.F., Walker, J.D., and Bartley, J.M., eds., *Geologic evolution of the Mojave Desert and southwestern Basin and Range*: Geological Society of America Memoir 195, p. 19–41.
- Goodman, E.D., and Malin, P.E., 1992, Evolution of the southern San Joaquin Basin and mid-Tertiary “transitional” tectonics, central California: *Tectonics*, v. 11, p. 478–498.
- Graham, S.A., Stanley, R.G., Bent, J.V., and Carter, J.R., 1989, Oligocene and Miocene paleogeography of central California and displacement along the San Andreas fault: *Geological Society of America Bulletin*, v. 101, p. 711–730, doi: 10.1130/0016-7606(1989)101<0711:OAMPOC>2.3.CO;2.
- Guth, P.L., 1989, Day 4. Tertiary extension in the Sheep Range Area, northwestern Clark County, Nevada, in Wernicke, B.P., Snow, J.K., Axen, G.J., Burchfiel, B.C., Hodges, K.V., Walker, J.D., and Guth, P.L., eds., *Extensional tectonics in the Basin and Range Province between the southern Sierra Nevada and the Colorado Plateau*: Washington D.C., Field Trip Guidebook T138, 28th International Geological Congress, American Geophysical Union, p. 33–39.
- Hamilton, W.B., 1987, Mesozoic geology and tectonics of the Big Maria Mountains region, southeastern California, in Dickinson, W.R., and Klute, M.A., eds., *Mesozoic rocks of southern Arizona and adjacent areas*: Arizona Geological Society Digest, v. 18, p. 33–47.
- Hardyman, R.F., Ekren, E.B., and Proffett, J., 1984, Tertiary tectonics of west-central Nevada—Yerington to Gabbs Valley, Western Geological Excursions, Guidebook, volume 4: Reno, Mackay School of Mines, Department of Geological Sciences, p. 160–231.
- Henry, C.D., 1989, Late Cenozoic Basin and Range structure in western Mexico adjacent to the Gulf of California: *Geological Society of America Bulletin*, v. 101, p. 1147–1156, doi: 10.1130/0016-7606(1989)101<1147:LCBARS>2.3.CO;2.
- Henry, C.D., and Aranda-Gomez, J.J., 2000, Plate interactions control middle–late Miocene, proto-Gulf and Basin and Range extension in the southern Basin and Range province: *Tectonophysics*, v. 318, p. 1–26, doi: 10.1016/S0040-1951(99)00304-2.
- Hintze, L.F., 1973, Geologic road logs of western Utah and eastern Nevada: Brigham Young University Research Studies, *Geology Series*, v. 20, part 2, no. 7, 66 p.
- Hoisch, T.D., and Simpson, C., 1993, Rise and tilt of metamorphic rocks in the lower plate of a detachment fault in the Funeral Mountains, Death Valley, California: *Journal of Geophysical Research*, v. 98, no. 4, p. 6805–6827.
- Holm, D.K., and Dokka, R.K., 1991, Major late Miocene cooling of the middle crust associated with extensional orogenesis in the Funeral Mountains, California: *Geophysical Research Letters*, v. 18, no. 9, p. 1775–1778.
- Holm, D.K., and Dokka, R.K., 1993, Interpretation and tectonic implications of cooling histories; an example from the Black Mountains, Death Valley extended terrane, California: *Earth and Planetary Science Letters*, v. 116, no. 1–4, p. 63–80, doi: 10.1016/0012-821X(93)90045-B.
- Holm, D.K., Snow, J.K., and Lux, D.R., 1992, Thermal and barometric constraints on the intrusive and unroofing history of the Black Mountains; implications for timing, initial dip, and kinematics of detachment faulting in the Death Valley region, California: *Tectonics*, v. 11, no. 3, p. 507–522.
- Holm, D.K., Geissman, J.W., and Wernicke, B., 1993, Tilt and rotation of the footwall of a major normal fault system: Paleomagnetism of the Black Mountains, Death Valley extended terrane, California: *Geological Society of America Bulletin*, v. 105, no. 10, p. 1373–1387, doi: 10.1130/0016-7606(1993)105<1373:TAROTF>2.3.CO;2.
- Holt, W.E., Chamot-Rooke, N., Le Pichon, X., Haines, A.J., Shen, T.B., and Ren, J., 2000, Velocity field in Asia inferred from Quaternary fault slip rates and global positioning system observations: *Journal of Geophysical Research*, v. 105, p. 19,185–19,210, doi: 10.1029/2000JB900045.
- Hope, R.A., 1966, *Geology and structural setting of the eastern Transverse Ranges, southern California* [Ph.D. thesis]: Los Angeles, University of California, 201 p.
- Hornafius, J.S., Luyendyk, B.P., Terres, R.R., and Kamberling, M.J., 1986, Timing and extent of Neogene tectonic rotation in the western Transverse Ranges, California: *Geological Society of America Bulletin*, v. 97, p. 1476–1487, doi: 10.1130/0016-7606(1986)97<1476:TAEONT>2.0.CO;2.
- Houseman, G., and England, P., 1986, Finite strain calculations of continental deformation. 1. Method and general results for convergent zones: *Journal of Geophysical Research*, v. 91, p. 3651–3663.
- Howard, K.A., and Miller, D.M., 1992, Late Cenozoic faulting at the boundary between the Mojave and Sonoran blocks; Bristol Lake area, California, in Richard, S.M., ed., *Deformation associated with the Neogene, eastern California shear zone, southeastern California and southwestern Arizona*; proceedings: Redlands, California, San Bernardino County Museum Association, San Bernardino County Museum Association Special Publication 92–1, p. 37–47.
- Hudson, D.M., and Oriol, W.M., 1979, Geologic map of the Buckskin Range, Nevada, Nevada Bureau of Mines and Geology, no. 64, 1 sheet, scale 1:18,000.
- Hudson, M.R., Sawyer, D.A., and Warren, R.G., 1994, Paleomagnetism and rotation constraints for the middle Miocene southwestern Nevada volcanic field: *Tectonics*, v. 13, no. 2, p. 258–277, doi: 10.1029/93TC03189.
- Humphreys, E.D., 1995, Post-Laramide removal of the Farallon slab, western United States: *Geology*, v. 23, p. 987–990, doi: 10.1130/0091-7613(1995)023<0987:PLROTF>2.3.CO;2.
- Humphreys, E.D., Clayton, R.W., and Hager, B.H., 1984, A tomographic image of mantle structure beneath southern California: *Geophysical Research Letters*, v. 11, no. 7, p. 625–627.
- Ingersoll, R.V., 2001, Structural and stratigraphic evolution of the Rio Grande Rift, northern New Mexico and southern Colorado: *International Geology Review*, v. 43, no. 10, p. 867–891.
- Ingersoll, R.V., Devaney, K.A., Geslin, J.K., Cavazza, W., Diamond, D.S., Heins, W.A., Jagiello, K.J., Marsaglia, K.M., Paylor, E.D., II, and Short, P.F., 1996, The Mud Hills, Mojave Desert, California: Structure, stratigraphy, and sedimentology of a rapidly extended terrane: *Geological Society of America Special Paper* 303, p. 61–84.
- Jackson, M., 1991, *Paleoseismology of Utah*, volume 3: The number and timing of Holocene paleoseismic events on the Nephi and Levan segments, Wasatch fault zone, Utah: *Utah Geological Survey Special Study* 78, 23 p.
- John, B.E., and Foster, D.A., 1993, Structural and thermal constraints on the initiation angle of detachment faulting in the southern Basin and Range: The Chemehuevi Mountains case study: *Geological Society of America Bulletin*, v. 105, p. 1091–1108, doi: 10.1130/0016-7606(1993)105<1091:SATCOT>2.3.CO;2.
- Lavier, L.L., and Buck, W.R., 2002, Half graben versus large-offset low-angle normal fault: Importance of keeping cool during normal faulting: *Journal of Geophysical Research*, v. 107, p. 2122, doi: 10.1029/2001JB000513.
- Lee, J., 1995, Rapid uplift and rotation of mylonitic rocks from beneath a detachment fault: Insights from potassium feldspar ⁴⁰Ar/³⁹Ar thermochronology, northern Snake Range, Nevada: *Tectonics*, v. 14, p. 54–77, doi: 10.1029/94TC01508.
- Lee, J., Miller, M.M., Crippen, R., Hacker, B., and Ledesma Vazquez, J., 1996, Middle Miocene extension in the Gulf Extensional Province, Baja California: Evidence from the southern Sierra Juarez: *Geological Society of America Bulletin*, v. 108, p. 505–525, doi: 10.1130/0016-7606(1996)108<0505:MMEITG>2.3.CO;2.
- Lewis, C.J., Wernicke, B.P., Selverstone, J., and Bartley, J.M., 1999, Deep burial of the footwall of the northern Snake Range decollement, Nevada: *Geological Society of America Bulletin*, v. 111, p. 39–51, doi: 10.1130/0016-7606(1999)111<0039:DBOTFO>2.3.CO;2.
- Long, K.B., Baldwin, S.L., and Gehrels, G.E., 1995, Tectonothermal evolution of the Pinaleno-Jackson Mountain core complex, southeast Arizona: *Geological Society of America Bulletin*, v. 107, p. 1231–1240, doi: 10.1130/0016-7606(1995)107<1231:TEOTPO>2.3.CO;2.
- Lund, K., Beard, S.L., and Perry, W.J., 1993, Relation between extensional geometry of the northern Grant Range and oil occurrences in Railroad Valley, east-central Nevada: *AAPG Bulletin*, v. 77, p. 945–962.
- Luyendyk, B.P., 1991, A model for Neogene crustal rotations, transtension, and transpression in southern California: *Geological Society of America Bulletin*, v. 103, p. 1528–1536, doi: 10.1130/0016-7606(1991)103<1528:AMFNCR>2.3.CO;2.
- Machette, M.N., Personius, S.F., and Nelson, A.R., 1992, Paleoseismology of the Wasatch fault zone; a summary of recent investigations, interpretations, and conclusions, in Gori, P.L., and Hays, W.W., eds., *Assessment of regional earthquake hazards and risk along the Wasatch Front, Utah*: U.S. Geological Survey Professional Paper, v. 1500-A, p. A1–A71.
- Martin, M.W., Glazner, A.F., Walker, J.D., and Schermer, E.R., 1993, Evidence for right-lateral transfer faulting accommodating an echelon Miocene extension, Mojave Desert, California: *Geology*, v. 21, p. 355–358, doi: 10.1130/0091-7613(1993)021<0355:EFRLTF>2.3.CO;2.
- Matthews, V., III, 1976, Correlation of Pinnacles and Neenach volcanic formations and their bearing on the San Andreas problem: *American Association of Petroleum Geologists Bulletin*, v. 51, p. 2128–2141.

- McClusky, S.S., Bjornstad, S., Hager, B., King, R., Meade, B., Miller, M., Monastero, F., and Souter, B., 2001, Present-day kinematics of the Eastern California Shear Zone from a geodetically constrained block model: *Geophysical Research Letters*, v. 28, p. 3369–3372, doi: 10.1029/2001GL013091.
- McQuarrie, N., Stock, J.M., Verdel, C., and Wernicke, B.P., 2003, Cenozoic evolution of Neotethys and implications for the causes of plate motions: *Geophysical Research Letters*, v. 30, p. 2036, doi: 10.1029/2003GL017992.
- McWilliams, M.O., and Li, Y., 1985, Oroclinal folding of the southern Sierra Nevada batholith: *Science*, v. 230, p. 172–175.
- Miller, D.M., and Yount, J.C., 2002, Late Cenozoic tectonic evolution of the north-central Mojave Desert inferred from fault history and physiographic evolution of the Fort Irwin area, in Glazner, A.F., Walker, J.D., and Bartley, J.M., eds., *Geologic evolution of the Mojave Desert and southwestern Basin and Range*: Geological Society of America Memoir 195, p. 173–198.
- Miller, E.L., Gans, P.B., and Garing, J., 1983, The Snake Range decollement: An exhumed mid-Tertiary ductile-brittle transition: *Tectonics*, v. 2, p. 239–263.
- Miller, E.L., Dumitru, T.A., Brown, R.W., and Gans, P.B., 1999, Rapid Miocene slip on the Snake Range–Deep Creek Range fault system, east-central Nevada: *Geological Society of America Bulletin*, v. 111, no. 6, p. 886–905, doi: 10.1130/0016-7606(1999)111<0886:RMSOTS>2.3.CO;2.
- Miller, F.K., and Morton, D.M., 1980, Potassium-argon geochronology of the eastern Transverse Ranges and southern Mojave Desert, southern California, U.S.: Reston, Virginia, U.S. Geological Survey, Geological Survey Professional Paper 1152, 30 p.
- Miller, M., Johnson, D., Dixon, T., and Dokka, R.K., 2001, Refined kinematics of the eastern California shear zone from GPS observations, 1993–1998: *Journal of Geophysical Research*, v. 106, p. 2245–2263, doi: 10.1029/2000JB900328.
- Namson, J.S., and Davis, T.L., 1988a, Structural transect of the western Transverse Ranges, California: Implications for lithospheric kinematics and seismic risk evaluation: *Geology*, v. 16, p. 675–679, doi: 10.1130/0091-7613(1988)016<0675:STOTWT>2.3.CO;2.
- Namson, J.S., and Davis, T.L., 1988b, Seismically active fold-thrust belt in the San Joaquin Valley, central California: *Geological Society of America Bulletin*, v. 100, p. 257–273, doi: 10.1130/0016-7606(1988)100<0257:SAFATB>2.3.CO;2.
- Namson, J.S., and Davis, T.L., 1990, Late Cenozoic fold and thrust belt of the southern Coast Ranges and Santa Maria Basin, California: *American Association of Petroleum Geologists Bulletin*, v. 74, p. 467–492.
- Niemi, N.A., 2002, Extensional tectonics in the Basin and Range Province and the geology of the Grapevine Mountains, Death Valley Region, California and Nevada [Ph.D. thesis]: Pasadena, California, California Institute of Technology, 344 p.
- Niemi, N.A., Wernicke, B.P., Brady, R.J., Saleeby, J.B., and Dunne, G.C., 2001, Distribution and provenance of the middle Miocene Eagle Mountain Formation, and implications for regional kinematic analysis of the Basin and Range province: *Geological Society of America Bulletin*, v. 113, p. 419–442, doi: 10.1130/0016-7606(2001)113<0419:DAPOTM>2.0.CO;2.
- Niemi, N.A., Wernicke, B.P., Friedrich, A.M., Simons, M., Bennett, R.A., and Davis, J.L., 2004, BARGEN continuous GPS data across the eastern Basin and Range province, and implications for fault system dynamics: *Geophysical Journal International*, v. 159, p. 842–862, doi: 10.1111/j.1365-246X.2004.02454.x.
- Nourse, J.A., Anderson, T.H., and Silver, L.T., 1994, Tertiary metamorphic core complexes in Sonora, northwestern Mexico: *Tectonics*, v. 13, p. 1161–1182, doi: 10.1029/93TC03324.
- Oskin, M., and Stock, J., 2003, Pacific-North America plate motion and opening of the Upper Delfin basin, northern Gulf of California, Mexico: *Geological Society of America Bulletin*, v. 115, no. 10, p. 1173–1190, doi: 10.1130/B25154.1.
- Oskin, M., and Iriondo, A., 2004, Large magnitude transient strain accumulation on the Blackwater fault, Eastern California shear zone: *Geology*, v. 32, p. 313–316, doi: 10.1130/G20223.1.
- Oskin, M., Stock, J., and Martin-Barajas, A., 2001, Rapid localization of Pacific-North America plate motion in the Gulf of California: *Geology*, v. 29, p. 459–462, doi: 10.1130/0091-7613(2001)029<0459:RLOPNA>2.0.CO;2.
- Page, B.M., Thompson, G.A., and Coleman, R.G., 1998, Late Cenozoic tectonics of the central and southern ranges of California: *Geological Society of America Bulletin*, v. 110, p. 846–876, doi: 10.1130/0016-7606(1998)110<0846:OLCTOT>2.3.CO;2.
- Plescia, J.B., and Calderone, G.J., 1986, Paleomagnetic constraints on the timing and extent of rotation of the Tehachapi Mountains, California: *Geological Society of America Abstracts with Programs*, v. 18, p. 171.
- Powell, R.E., 1981, *Geology of the crystalline basement complex, eastern Transverse Ranges, southern California: Constraints on regional tectonic interpretation* [Ph.D. thesis]: Pasadena, California, California Institute of Technology, 441 p.
- Reheis, M.C., 1993, Neogene tectonism from the south-western Nevada volcanic field to the White Mountains, California; part II, Late Cenozoic history of the southern Fish Lake Valley fault zone, Nevada and California, in Lahren, M.M., Trexle, J.H., Jr., and Spinosa, C., eds., *Crustal evolution of the Great Basin and the Sierra Nevada*: Reno, University of Nevada, p. 370–382.
- Reheis, M.C., and Sawyer, T.L., 1997, Late Cenozoic history and slip rates of the Fish Lake Valley, Emigrant Peak, and Deep Springs fault zones, Nevada and California: *Geological Society of America Bulletin*, v. 109, no. 3, p. 280–299, doi: 10.1130/0016-7606(1997)109<0280:LCHASR>2.3.CO;2.
- Reynolds, S.J., 1985, *Geology of the South Mountains, central Arizona*: Arizona Bureau of Geology and Mineral Technology Bulletin, v. 195, 61 p.
- Richard, S.M., 1993, Palinspastic reconstruction of southeastern California and southwestern Arizona for the middle Miocene: *Tectonics*, v. 12, p. 830–854.
- Richard, S.M., and Dokka, R.K., 1992, *Geology of the Packard Well fault zone, southeastern California*, in Richard, S.M., ed., *Deformation associated with the Neogene, eastern California shear zone, southeastern California and southwestern Arizona*; proceedings: Redlands, California, San Bernardino County Museum Association, San Bernardino County Museum Association Special Publication 92–1, p. 71–74.
- Richard, S.M., Fryxell, J.E., and Sutter, J.F., 1990, Tertiary structure and thermal history of the Harquahala and Buckskin Mountains, west central Arizona: Implications for denudation by a major detachment fault system: *Journal of Geophysical Research*, v. 95, p. 19,973–19,987.
- Richard, S.M., Sherrod, D.R., and Tosdal, R.M., 1992, Cibola Pass fault, southwestern Arizona, in Richard, S.M., ed., *Deformation associated with the Neogene, eastern California shear zone, southeastern California and southwestern Arizona*; proceedings: Redlands, California, San Bernardino County Museum Association, San Bernardino County Museum Association Special Publication 92–1, p. 66–70.
- Ron, H., and Nur, A., 1996, Vertical axis rotation in the Mojave: Evidence from the Independence dike swarm: *Geology*, v. 24, no. 11, p. 973–976, doi: 10.1130/0091-7613(1996)024<0973:VARITM>2.3.CO.
- Rotstein, Y., Combs, J., and Biehler, S., 1976, Gravity investigation in the southern Mojave Desert, California: *Geological Society of America Bulletin*, v. 87, p. 981–993, doi: 10.1130/0016-7606(1976)87<981:GIITSM>2.0.CO;2.
- Russell, L.R., and Snelson, S., 1994, Structure and tectonics of the Albuquerque Basin segment of the Rio Grande Rift; insights from reflection seismic data, in Keller, G.R., and Cather, S.M., eds., *Basins of the Rio Grande Rift: Structure, stratigraphy, and tectonic setting*: Geological Society of America Special Paper 291, p. 83–112.
- Sauber, J., Thatcher, W., Solomon, S., and Lisowski, M., 1994, Geodetic slip rate for the eastern California shear zone and the recurrence time of Mojave desert earthquakes: *Nature*, v. 367, p. 264–266, doi: 10.1038/367264a0.
- Savage, J.C., Lisowski, M., and Prescott, W., 1990, An apparent shear zone trending north-northwest across the Mojave Desert into Owens Valley, eastern California: *Geophysical Research Letters*, v. 17, p. 2113–2116.
- Schermer, E.R., Luyendyk, B.P., and Cisowski, S., 1996, Late Cenozoic structure and tectonics of the northern Mojave Desert: *Tectonics*, v. 15, no. 5, p. 905–932, doi: 10.1029/96TC00131.
- Scott, R.J., Foster, D.A., and Lister, G.S., 1998, Tectonic implications of rapid cooling of lower plate rocks from the Buckskin-Rawhide metamorphic core complex, west-central Arizona: *Geological Society of America Bulletin*, v. 110, p. 588–614, doi: 10.1130/0016-7606(1998)110<0588:TIORCO>2.3.CO;2.
- Sieh, K., and Jahns, R.H., 1984, Holocene activity of the San Andreas fault at Wallace Creek, California: *Geological Society of America Bulletin*, v. 95, p. 883–896, doi: 10.1130/0016-7606(1984)95<883:HAOTSA>2.0.CO;2.
- Smith, D.L., 1992, History and kinematics of Cenozoic extension in the northern Toiyabe Range, Lander County, Nevada: *Geological Society of America Bulletin*, v. 104, p. 789–801, doi: 10.1130/0016-7606(1992)104<0789:HAKOBE>2.3.CO;2.
- Smith, D.L., Gans, P.B., and Miller, E.L., 1991, Palinspastic restoration of Cenozoic extension in the central and eastern Basin and Range Province at latitude 39–40 degrees N, in Raines, G.L., Lisle, R.E., Schafer, R.W., and Wilkinson, W.H., eds., *Geology and ore deposits of the Great Basin*; symposium proceedings: Reno, Nevada, Geological Society of Nevada, p. 75–86.
- Smith, R.B., and Bruhn, R.L., 1984, Intraplate extensional tectonics of the western U.S. Cordillera—Inferences on structural style from seismic-reflection data, regional tectonics and thermal-mechanical models of brittle ductile deformation: *Journal of Geophysical Research*, v. 89, p. 5733–5762.
- Snow, J.K., 1992, Large-magnitude Permian shortening and continental margin tectonics in the southern Cordillera: *Geological Society of America Bulletin*, v. 104, no. 1, p. 80–105, doi: 10.1130/0016-7606(1992)104<0080:LMPASAC>2.3.CO;2.
- Snow, J.K., and Lux, D.R., 1999, Tectono-sequence stratigraphy of Tertiary rocks in the Cottonwood Mountains and northern Death Valley area, California and Nevada, in Wright, L.A., and Troxel, B.W., eds., *Cenozoic basins of the Death Valley region*: Geological Society of America Special Paper 333, p. 17–64.
- Snow, J.K., and Prave, A.R., 1994, Covariance of structural and stratigraphic trends; evidence for anticlockwise rotation within the Walker Lane Belt, Death Valley region, California and Nevada: *Tectonics*, v. 13, no. 3, p. 712–724, doi: 10.1029/93TC02943.
- Snow, J.K., and Wernicke, B.P., 1989, Uniqueness of geological correlations; an example from the Death Valley extended terrain: *Geological Society of America Bulletin*, v. 101, no. 11, p. 1351–1362, doi: 10.1130/0016-7606(1989)101<1351:UOGCAE>2.3.CO;2.
- Snow, J.K., and Wernicke, B.P., 2000, Cenozoic tectonism in the central Basin and Range: Magnitude, rate and distribution of upper crustal strain: *American Journal of Science*, v. 300, p. 659–719.
- Spencer, J.E., and Reynolds, S.J., 1989, Middle Tertiary tectonics of Arizona and adjacent areas, in Jenney, J.P., and Reynolds, S.J., eds., *Geologic evolution of Arizona*: Tucson, Arizona, Arizona Geological Society, Arizona Geological Society Digest, v. 17, p. 539–574.
- Spencer, J.E., and Reynolds, S.J., 1991, Tectonics of mid-Tertiary extension along a transect through west-central Arizona: *Tectonics*, v. 10, no. 6, p. 1024–1221.
- Spencer, J.E., Richard, S.M., Reynolds, S.J., Miller, R.J., Shafiqullah, M., Gilbert, W.G., and Grubensky, M.J., 1995, Spatial and temporal relationships between mid-Tertiary magnetism and extension in southwestern Arizona: *Journal of Geophysical Research, Solid Earth and Planets*, v. 100, no. B6, p. 10,321–10,351, doi: 10.1029/94JB02817.
- Stock, J.M., and Hodges, K.V., 1989, Pre-Pliocene extension around the Gulf of California and the transfer of

- Baja California to the Pacific Plate: *Tectonics*, v. 8, p. 99–115.
- Stockli, D.F., 1999, Regional timing and spatial distribution of Miocene extension in the northern Basin and Range Province [Ph.D. thesis]: Stanford, California, Stanford University, 239 p.
- Stockli, D.F., Linn, J.K., Walker, J.D., and Dumitru, T.A., 2001, Miocene unroofing of the Canyon Range during extension along the Sevier Desert Detachment, west-central Utah: *Tectonics*, v. 20, p. 289–307, doi: 10.1029/2000TC001237.
- Stockli, D. F., Surpless, B.E., Dumitru, T.A., and Farley, K.A., 2002, Thermochronological constraints on the timing and magnitude of Miocene and Pliocene extension in the central Wassuk Range, western Nevada: *Tectonics*, v. 21, no. 4, p. 10–1–10–17, doi: 10.1029/2001TC001295.
- Stone, P., and Pelka, G.J., 1989, Geologic map of the Palen–McCoy Wilderness study area and vicinity: Riverside County, California, Geological Survey Miscellaneous Field Investigations Map MF-2070, 1 sheet, scale: 1:62,500.
- Surpless, B., 1999, Tectonic evolution of the Sierra Nevada–Basin and Range transition zone: A study of crustal evolution in extensional provinces [Ph.D. thesis]: Stanford, California, Stanford University, 186 p.
- Taylor, W.J., Bartley, J.M., Lux, D.R., and Axen, G.J., 1989, Timing of Tertiary extension in the Railroad Valley–Pioche Transect, Nevada: Constraints from $^{40}\text{Ar}/^{39}\text{Ar}$ ages of volcanic rocks: *Journal of Geophysical Research*, v. 94, p. 7757–7774.
- Tennyson, M.E., 1989, Pre-transform early Miocene extension in western California: *Geology*, v. 17, p. 792–796, doi: 10.1130/0091-7613(1989)017<0792:PTEMEI>2.3.CO;2.
- Walker, J.D., Bartley, J.M., and Glazner, A.F., 1990, Large-magnitude Miocene extension in the central Mojave Desert; implications for Paleozoic to Tertiary paleogeography and tectonics: *Journal of Geophysical Research*, v. 95, p. 557–569.
- Walker, J.D., Fletcher, J.M., Fillmore, R.P., Martin, M.W., Taylor, W.J., Glazner, A.F., and Bartley, J.M., 1995, Connection between igneous activity and extension in the central Mojave metamorphic core complex, California: *Journal of Geophysical Research*, v. 100, p. 10,477–10,494, doi: 10.1029/94JB03132.
- Wernicke, B., 1992, Cenozoic extensional tectonics of the U.S. Cordillera, in Burchfiel, B.C., Lipman, P.W., and Zoback, M.L., eds., *The Cordilleran Orogen: Continuous U.S.: Boulder, Colorado, Geological Society of America, The Geology of North America*, v. G-3, p. 553–581.
- Wernicke, B., and Snow, J.K., 1998, Cenozoic tectonism in the central Basin and Range: Motion of the Sierran–Great Valley Block: *International Geology Review*, v. 40, p. 403–410.
- Wernicke, B., Axen, G.J., and Snow, J.K., 1988, Basin and Range extensional tectonics at the latitude of Las Vegas, Nevada: *Geological Society of America Bulletin*, v. 100, p. 1738–1757, doi: 10.1130/0016-7606(1988)100<1738:BARETA>2.3.CO;2.
- Wills, S., Anders, M.H., and Christie-Blick, N., 2005, Pattern of Mesozoic thrust surfaces and Tertiary normal faults in the Sevier Desert subsurface, west-central Utah: *American Journal of Science*, v. 305, p. 42–100.

MANUSCRIPT RECEIVED BY THE SOCIETY 5 APRIL 2005

REVISED MANUSCRIPT RECEIVED 29 AUGUST 2005

MANUSCRIPT ACCEPTED 23 SEPTEMBER 2005

Printed in the USA

MBOP Ex. No. 19b McQuarrieWernicke animation

**MBOP Ex. No. 19b is available on the
Nevada State Engineer's website at:**

<http://water.nv.gov/news.aspx?news=LWRFS>

Research Question

How do local meteoric water lines and seasonal signals in precipitation isotopes change regionally and between event and monthly sampling intervals?



We collected data in Kent, OH and compared it to the records in the GNIP database. The sites Coshocton and Simcoe were the closest sites. Coshocton collected samples from 1966-1975 and Simcoe collected samples monthly from 1975-1982.

Seasonal Signals

The best-fit seasonal signal (Figure 3, Table 2) for Kent, OH is more similar isotopically to Simcoe (206 km north from Kent) than Coshocton (106 km south).

For the Kent dataset (Figure 4), the event-based data produced a sine wave with greater amplitude of 6.1‰, than that fit to the monthly data.

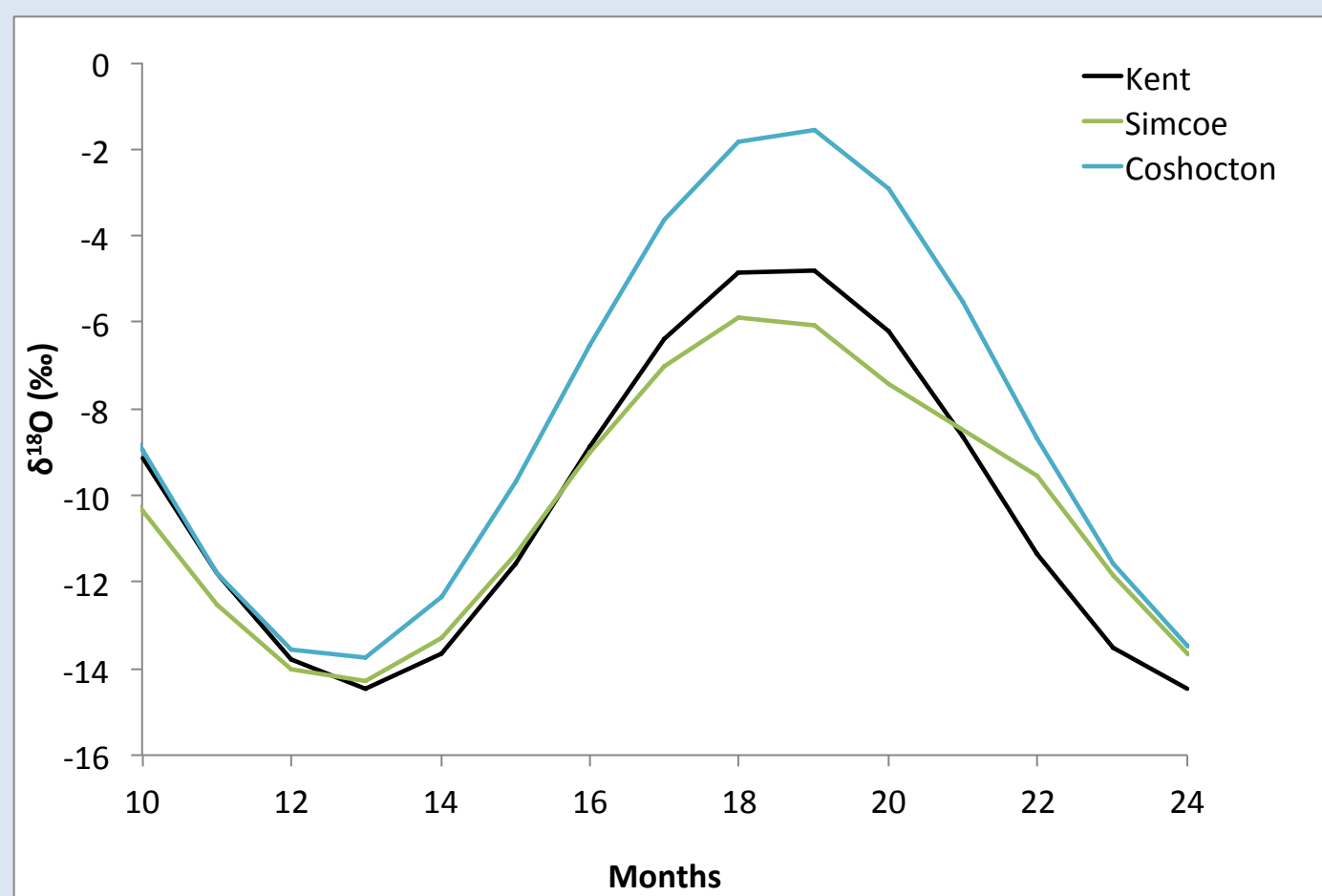


Figure 3. Kent, Coshocton, and Simcoe sinewaves compared

Methods

- Precipitation samples were collected in Kent, Ohio in a residential yard.
- Rain was collected in a 10.16 cm diameter rain gage, and snow was collected in a 15 by 30 cm box. Samples were collected daily at 8 am local time, and some events were also sampled at 8 pm.
- Samples were filtered and analyzed by a Picarro L-2130i at Kent State University and the data was processed following the protocols in van Geldern and Barth (2012).
- The closest GNIP sites are Coshocton, Ohio, USA and Simcoe, Ontario, Canada. Monthly data were downloaded from the IAEA WISER database (http://www-naweb.iaea.org/napc/ih/IHS_resources_isohis.html).



Kent, OH sampling site is indicated by the red dot.

Instrument Performance

Repeat analyses show a standard error of 0.01‰ for δ18O and 0.04‰ for δ2H. Approximately 27% of samples had multiple analyses, and for these we report average values.

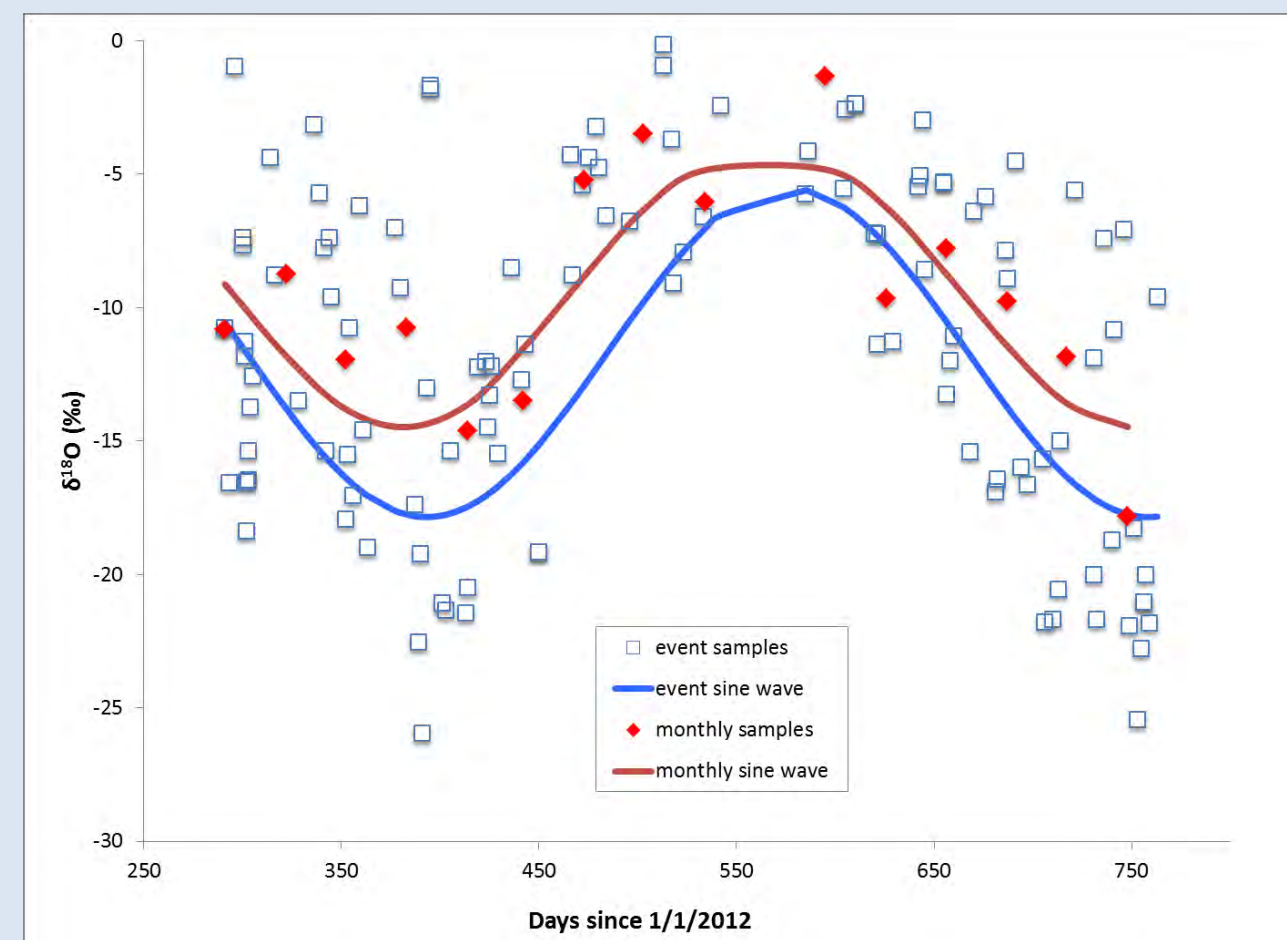


Figure 4. Time series of event (blue squares) and monthly samples (red diamonds) for Kent, OH showing fitted sine waves.

Table 2. Best-fit sine waves. The amplitude of the seasonal signal is represented by the first term, and average δ18O is the last term.

Location	Equation for δ18O
Coshocton	$6.2 * \sin(0.52 * t - 1.33) - 7.672$, where t = months
Simcoe	$4.3 * \sin(0.55 * t - 4.18) - 10.07$, where t = months
Kent (monthly)	$4.9 * \sin(0.56 * t - 3.23) - 9.56$, where t = months
Kent (event)	$6.14 * \sin(0.017 * t - 291) - 11.69$, where t = days

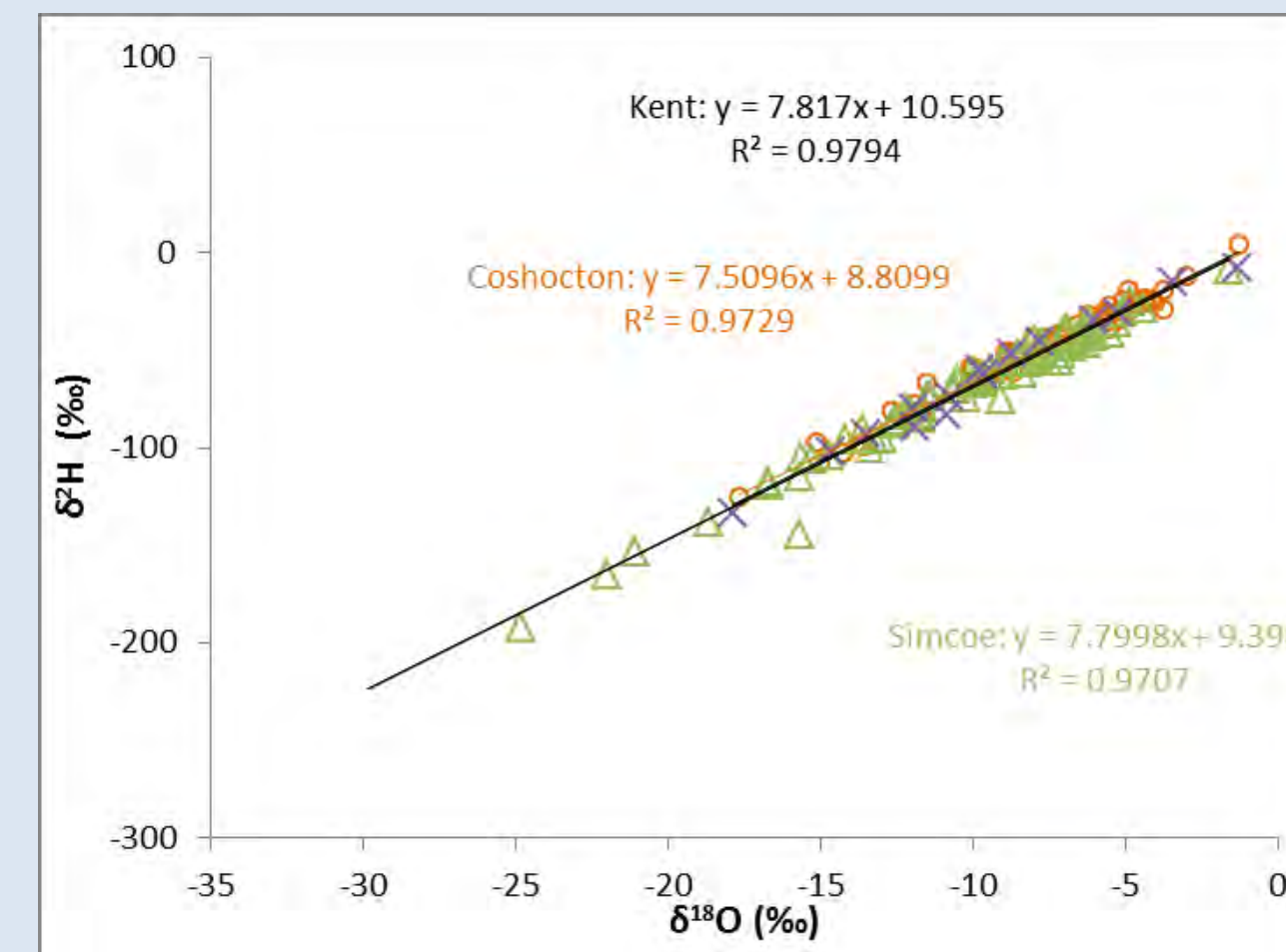


Figure 1. LMWL for Kent, Coshocton, and Simcoe, based on monthly data

Table 1. Comparison of the range of isotopic values for event samples versus monthly composites for Kent.

Kent	Event	Monthly
Minimum δ18O	-26.0	-17.8
Maximum δ18O	-0.1	-1.3

Conclusions and Implications

- LMWLs and seasonal signals derived from monthly samples were broadly similar along a 300 km north-south transect in the US eastern Great Lakes Region. Mean isotopic values are more depleted at the northern end of the transect.
- Composite samples on monthly basis under-represent event scale variability in precipitation isotopes, based on samples from Kent, Ohio.
- Monthly sampling reduces the apparent d-excess. The d-excess values have a bigger difference between Kent event sampling and Kent monthly sampling than is observed between monthly samples across sites.
- There is substantial diversity in precipitation isotopes in winter months. Isotopically depleted events are frequent but do not produce large amounts of precipitation. This may reflect different air mass sources and trajectories.
- Understanding the amount and source of variability in precipitation isotopes in space and time is important for correctly using them in watershed hydrology applications.

Local Meteoric Water Lines (LMWLs)

LMWLs for each site were similar (Figure 1).

Comparing the LMWLs generated from the event samples and the monthly data (Figure 2), the monthly data had a slightly lower slope and d-excess.

Transforming from event to monthly samples also reduced the range of variability in isotopic signatures in Kent (Figure 2, Table 1).

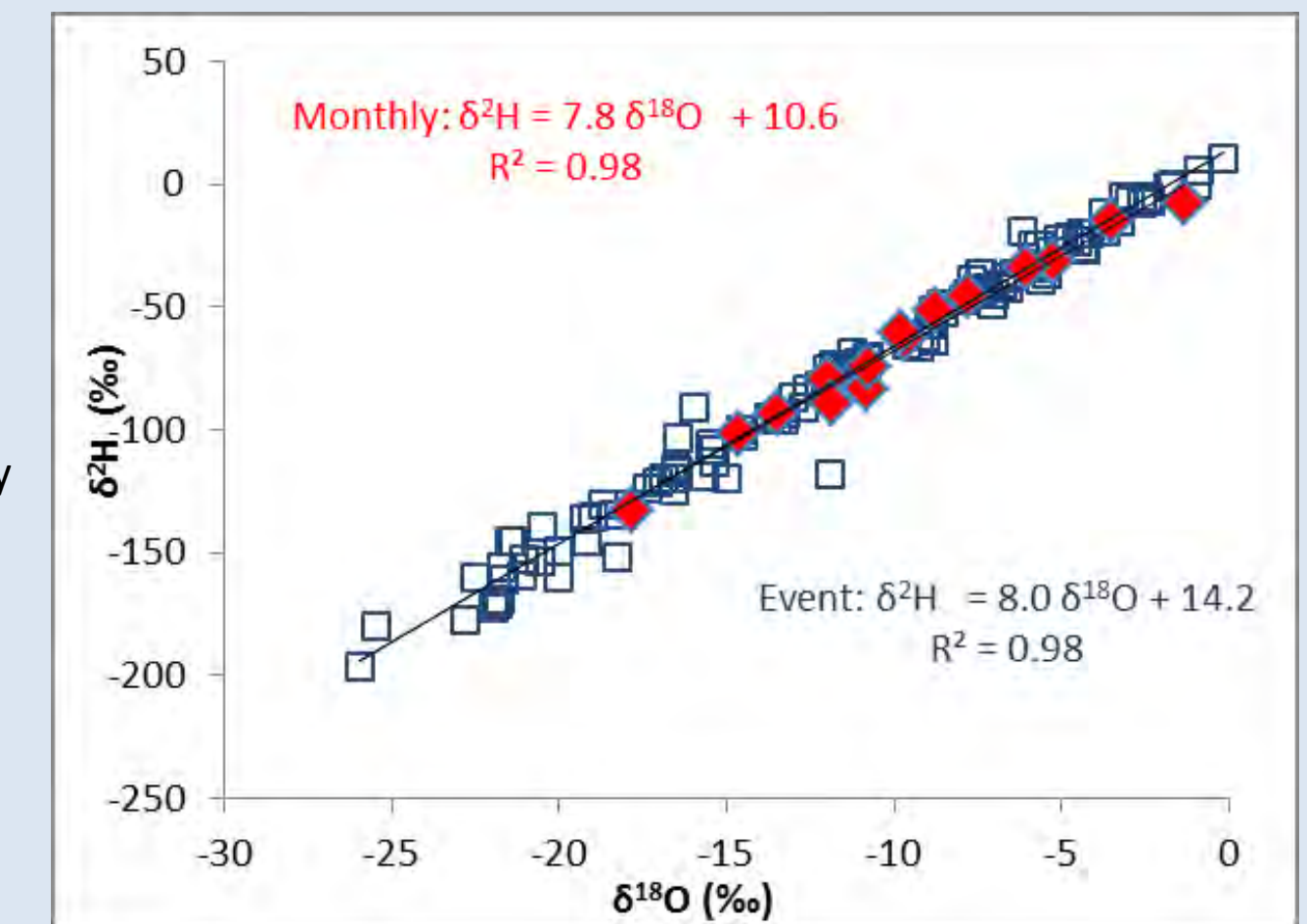


Figure 2. LMWLs calculated from event and monthly samples at Kent, Ohio.

Future plans

- Continued event sampling to assess inter-annual variability
- Sub-event sampling to assess variability within events
- Correlating isotopes with air masses trajectories and histories
- Comparison with other existing precipitation isotope datasets in the region
- Establish Kent as a GNIP station with better sample collection location and monthly sampling

Five millennia of paleotemperature from tree-rings in the Great Basin, USA

Matthew W. Salzer · Andrew G. Bunn ·
Nicholas E. Graham · Malcolm K. Hughes

Received: 6 November 2012 / Accepted: 8 August 2013 / Published online: 21 August 2013
© The Author(s) 2013. This article is published with open access at Springerlink.com

Abstract The instrumental temperature record is of insufficient length to fully express the natural variability of past temperature. High elevation tree-ring widths from Great Basin bristlecone pine (*Pinus longaeva*) are a particularly useful proxy to infer temperatures prior to the instrumental record in that the tree-rings are annually dated and extend for millennia. From ring-width measurements integrated with past treeline elevation data we infer decadal- to millennial-scale temperature variability over the past 4,500 years for the Great Basin, USA. We find that twentieth century treeline advances are greater than in at least 4,000 years. There is also evidence for substantial volcanic forcing of climate in the preindustrial record and considerable covariation between high elevation tree-ring widths and temperature estimates from an atmosphere–ocean general circulation model over much of the last millennium. A long-term temperature decline of ~ -1.1 °C since the mid-Holocene underlies substantial volcanic forcing of climate in the preindustrial record.

Keywords Dendroclimatology · Bristlecone Pine · Treeline · Holocene · Tree-Rings · Paleotemperature

1 Introduction

Multiple lines of evidence, including comparisons with instrumental climate data over the last century, show that patterns in the ring widths of upper treeline bristlecone pine are strongly influenced by temperature variability, particularly at decadal to centennial scales (LaMarche 1974; Hughes and Funkhouser 2003; Salzer and Kipfmueller 2005; Salzer and Hughes 2007; Salzer et al. 2009; Kipfmueller and Salzer 2010; Towlinski-Ward et al. 2010; Bunn et al. 2011). Some of the most recent bristlecone pine research has focused on the contrasting signals present in the ring widths of trees at the upper treeline (positive growth correlations with temperature) and in trees below upper treeline (negative or no correlation with temperature; e.g. Salzer et al. 2009; Kipfmueller and Salzer 2010; Bunn et al. 2011). These studies suggest that upper treeline ring widths contain an appreciable temperature signal at decadal to multi-centennial timescales, whereas trees below the treeline do not. However, using bristlecone pine ring widths to infer paleotemperature has been complicated by the discovery that trees somewhat below, yet still very near the upper treeline environment, as close as 150 vertical m, do not contain the same temperature signal as trees within ~ 100 m of treeline. For example, we have shown in the White Mountains of California, that the growth patterns of *Pinus longaeva* trees growing at treeline are quite different from growth patterns of the same species of tree growing only 150 m below treeline (see Salzer et al. 2009, Fig. 4a). The elevational threshold for bristlecone temperature-sensitivity is unknown and has not been widely studied. Also,

Electronic supplementary material The online version of this article (doi:10.1007/s00382-013-1911-9) contains supplementary material, which is available to authorized users.

M. W. Salzer (✉) · M. K. Hughes
Laboratory of Tree-Ring Research,
University of Arizona, Tucson, AZ 85721, USA
e-mail: msalzer@ltrr.arizona.edu

A. G. Bunn
Department of Environmental Sciences,
Western Washington University, Bellingham, WA 98225, USA

N. E. Graham
Hydrologic Research Center, 12780 High Bluff Drive,
Suite 250, San Diego, CA 92130-2069, USA

it has been argued that microtopographical features such as cold air pooling, for example, could complicate defining temperature-sensitive trees based solely on elevation or distance from treeline (Bunn et al. 2011).

In spite of these challenges, we suggest the most accurate estimates of past temperature will come from ring widths formed in trees within ~ 100 m of the species upper elevation ecotonal boundary. This elevational sector corresponds to a cold zone where temperatures are most limiting to growth (Fritts 1976) and above which cold temperatures preclude tree establishment entirely. However, these ecotonal boundaries have changed with time as climate has evolved, and quantifying the narrow elevation band occupied by trees with a ring-width temperature signal can be particularly problematic when working with material that predates the age of modern, established treeline. Due to past climatic change and the fluctuation of past treeline elevations, it becomes necessary to first determine the elevation of past treelines, and then, when developing temperature-sensitive ring-width chronologies, it is important to use only those trees that were growing within the cold zone (~ 100 m of treeline) during their lifetimes. We systematically avoid the use of rings formed in a past warmer era of higher treeline if these rings were sampled from wood at a location much lower than the remnant treeline. For example, old deadwood samples taken near modern upper treeline elevation or just below are avoided, as these rings would have been below the 100 m cold zone during their time of formation, and thus are inappropriate for paleotemperature inference. This line of reasoning is based on the assumption that the same, or a very similar, temperature-growth threshold relationship existed in past eras as exists currently. The existence of temperature-sensitive trees near treeline at the upper-elevational limit of their distribution has been confirmed in our previous work on bristlecone pine (Salzer et al. 2009). In this study, we first derive estimates of past treeline elevations, and then use samples collected within ~ 100 vertical m of these elevations to create a 4,582-year regional ring-width index chronology (2575 BC-AD 2006), hereafter referred to as GB3rwi. We then estimate millennial-scale temperature variability based on treeline elevational change, and estimate decadal to multicentennial-scale temperature variability using the regional ring-width index chronology scaled to regional temperature output from a climate model millennium run.

2 Materials and methods

2.1 Chronology construction

We use samples from bristlecone pine living trees and remnant wood in the upper treeline zone (within 100 m of

known treeline or estimated past treeline) in three separate mountain ranges in western North America: (1) Sheep Mountain, White Mountains, CA (SHP, 37.52 N. lat., 118.20 W. long.); (2) Mt. Washington, Snake Range, NV (MWA, 38.91 N. lat., 114.31 W. long.); and (3) Pearl Peak, Ruby Mountains, NV (PRL, 40.23 N. lat., 115.54 W. long.) (Fig. 1). Previous work at these sites has revealed strong correspondence in growth patterns, despite lengthy distances between sites (500 + km) and strong replication for millennia (Fig. 1, S1, S2) (Salzer and Hughes 2007; Salzer et al. 2009). The high correlation between the three chronologies over long intervals is indicative of similar biological responses by the trees to the same factor or factors limiting growth at all three sites.

Mean ring-width index chronologies were developed both for individual sites, and also for the region (GB3rwi) using samples from all three sites: SHP, MWA, and PRL. To gain maximum temporal coverage, we used dendrochronologically-dated materials from both living trees and from relict wood. We standardized each of the individual tree-ring width series to eliminate tree age/size related influences on ring width. Low-frequency variability was retained by limiting the minimum series length allowed to 100 years and standardizing with a negative exponential curve, a trend line with negative slope, or a mean line as determined by standardization option two in the dendrochronological software ARSTANL (Cook 1985; available at <http://www.ltr.arizona.edu/pub/dpl/>). This standardization approach is designed to retain decadal to multi-centennial scale variability and to minimize the

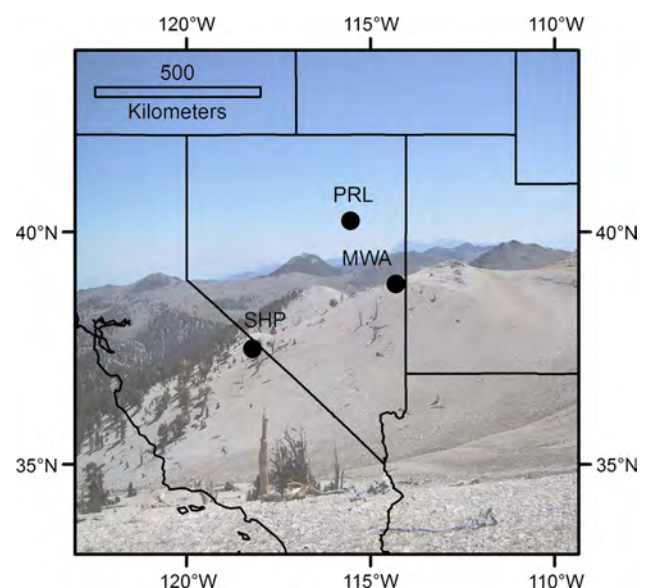


Fig. 1 Three upper forest border sites where samples were collected for the GB3rwi ring-width chronology. The background image shows living *Pinus longaeva* and remnant wood from upper treeline near Sheep Mountain in the White Mountains of California

“segment length curse” (Cook et al. 1995). The individual series lengths were typically between 500 and 800 years from 2000 BC on, suggesting that the chronology should retain variations whose wavelength is a few to several centuries. Samples were dated and measured using established dendrochronological methods (Stokes and Smiley 1968). The GB3rwi chronology was created by using the same dating, measuring, and standardization techniques described above. The GB3rwi chronology differs in that each individual index series after standardization was smoothed with a 20-year cubic smoothing spline to emphasize decadal- to centennial-scale variability prior to averaging the smoothed index series into a chronology of low-frequency variation. This approach allows for the calculation of 95 % confidence intervals for each mean value of the low-frequency chronology (Sheppard 1991). A non-standardized “raw” chronology (GB3raw) was similarly constructed, but without any standardization procedures—using instead the raw growth measurements. An additional step was taken with GB3raw to eliminate some juvenile growth; each growth curve that resembled a negative exponential as determined by ARSTANL (Cook 1985) was truncated for its first 100 years. However, all analyses in the main paper are based on the standardized version (GB3rwi) to eliminate as much potential bias from non-climatic tree-growth influences as possible. The GB3rwi ring-width chronology is built from series at all three mountain ranges, and extends 4,582 years, from 2575 BC to AD 2006.

2.2 Treeline elevation change

Climatic-treeline elevation is primarily controlled by minimum summer temperature at large spatial scales (Körner and Paulson 2004; Körner 2012). Both SHP and MWA sites contain extensive amounts of deadwood above modern treeline, while PRL contains less due to limited available elevation gain above modern treeline (Figs. S3–S5). Older higher treelines have been documented previously in both the White Mountains of California (LaMarche 1973) and in the Sierra Nevada (Lloyd and Graumlich 1997). We estimated the elevation of past treelines at SHP and MWA based on the elevation of the highest living trees sampled at that point in time (Figs. S3, S4). Past treeline at PRL was estimated based on the data from MWA (Fig. S5). The estimates of past treeline elevations serve a dual purpose. First, they allow for identification of three ~ 100 m elevational zones (one for each site), which have varied through time, and within which temperature-sensitive trees can be expected to have grown. We use only these trees for our regional ring-width chronology (GB3rwi). Second, independent of the growth records of the rings, the treeline

elevation through time is also a record of past environmental change. We use the changing upper treeline at SHP and a local lapse rate to estimate long-term temperature change (see Sect. 3.1).

2.3 Ring-width index and model output

The GCMs used for comparisons to the GB3rwi tree-ring chronology include the Max Planck Institute ECHO-G model (ERIK2, AD 1,000–1,990, single simulation; Legutke and Voss 1999; Stevens et al. 2008), the Max Planck Institute COSMOS system (MPI, AD 800–2005, 5 simulations; Jungclaus et al. 2010), and the National Centers for Atmospheric Research Community Climate Model (CSM, AD 850–1999, single simulation) (Ammann et al. 2007). Two important differences between these simulations are (1) the amplitude of the changes in total solar irradiance (Maunder Minimum to present) used in the ERIK2 and CSM ($\sim 4 \text{ W m}^{-2}$) simulations is about 3 times the 1.3 W m^{-2} that was used in the MPI (COSMOS) simulations, and (2) the ERIK2 and CSM models use prescribed greenhouse gas concentrations while the MPI (COSMOS) model uses a full carbon cycle model. We use area-averaged near-surface temperature from the GCM grid points over the western USA (40° – 34°N and from 104° to 124°W) for comparison with the ring-width data.

The scaling of GB3rwi to the GCM output can be formally expressed as follows:

$T(t) = f \cdot R(t) + c$, where T is the modeled temperature data, R is the ring-width index chronology, f is a variance scaling factor, c is a constant that adjusts the mean, and t is time. The factor f and constant c are derived by: $f = S_T/S_R$ and $c = T_{(mean)} - f \cdot R_{(mean)}$ where S_T and S_R are the respective standard deviations of the modeled temperature data and the ring-width index chronology in the AD 1276 to 1990 interval, and $T_{(mean)}$ and $R_{(mean)}$ are the corresponding means. Error bars are the RMSE statistic. Temperature anomalies were originally computed based on the AD 1000–1990 July–September mean of $20.32 \text{ }^\circ\text{C}$ ‘near surface’ from the ERIK2 model. They were then adjusted for the preindustrial period of 2575 BC to AD 1328 by adding a negative trend of $1.102 \text{ }^\circ\text{C}$ based on the empirical data from treeline elevation change. There were no adjustments made to the period after AD 1328. The results are a 4,000 + year record of decadal- to millennial-scale variability in past summer temperature. We acknowledge a high level of uncertainty in these past temperature estimates. This is unavoidable, given the multiple sources contributing to the uncertainty: (1) the ring-width chronology itself, (2) the ECHO-g modeling effort (3) the scaling of the tree rings to the modeled data, and (4) the trend adjustment.

3 Results and discussion

3.1 Treeline elevation and temperature inference

Past treeline estimates from the SHP site extend into the mid-Holocene (Fig. 2a). The SHP estimated treeline is broadly similar to that from MWA, roughly 400 km distant, for their period of overlap (Fig. 2b). Both mountains show substantially higher past treelines, greater than 100 m relative to recent levels, and both decline to modern levels in the fourteenth century AD. At SHP, treeline reaches its maximum elevation approximately 5,000 years ago. Prior to that, estimated treelines range from 45 m above modern level in 4410 BC at the beginning of the record, to 76 m above modern levels in 3755 BC. Treeline reaches its highest point, at 116 m above modern levels, in 2997 BC (Fig. 2a). We are less confident in the completeness of the record prior to 3000 BC and so concentrate our interpretations on the last 5,000 years.

Estimated past treelines are generally slightly higher at MWA than at SHP. This could result from a variety of reasons. Possibilities include a more complete record or a different lapse rate at MWA. It is worth noting that all the estimates are necessarily the minimum past treeline elevations, as we can never be sure we have found the highest trees that were growing at any particular time. Also, it is difficult to determine the precise timing of climate change by treeline movement for several reasons. Most notably because remnant wood samples often crack and erode over time obliterating many rings. In addition, reproductive lags cause treeline change to unavoidably lag behind climate change. While many different phenomena, such as fragmentation by disturbance, might contribute to local treeline positions, there is abundant evidence on a global scale that climatic treeline positions occur where growing season temperatures are 5–7 °C, with a global mean of 6.4 ± 0.7 (Körner 2012). This global correlation between treeline position and temperature demonstrates that temperature is a primary driver of treeline position and challenges the concept that treeline position is a multifaceted phenomenon with complex interactions between multiple environmental drivers (Körner 1998). If the latter were correct, global mountain treeline positions would not correlate with one explicit climatic parameter, which they do (Paulsen et al. 2000).

Two meteorological stations have at times operated at the SHP site simultaneously, but at differing elevations. From these station data we know that the summer surface air temperature gradient at SHP varies at 0.95 °C per 100 m—very near the dry adiabatic lapse rate of 0.98 °C per 100 m (LaMarche 1973). From the 0.95 °C lapse rate and the treeline data we can infer a temperature decline during the growing season (summer) of approximately

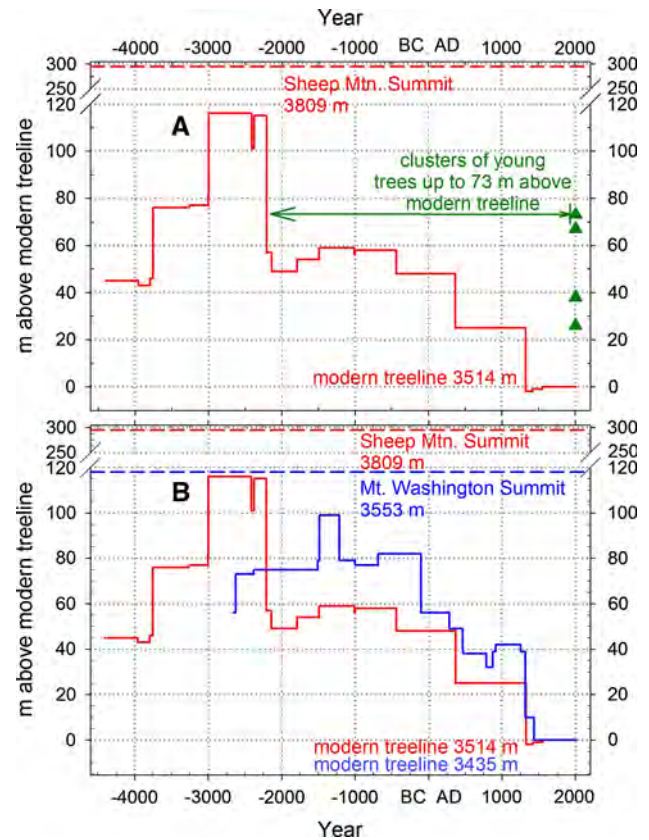


Fig. 2 Upper treeline elevation and past estimated treeline elevations. **a** White Mountains, CA (SHP). Green triangles represent the elevations of clusters of juvenile *Pinus longaeva* establishing above established modern upper treeline. **b** Upper treeline elevation and past estimated upper treeline elevations in White Mountains, CA (SHP, red) and Snake Range, NV (MWA, blue)

1.1 °C from 2209 BC to AD 1328, from the time of the highest treeline elevations to when treeline stabilized and persisted near modern levels until the late twentieth century (Fig. 2a). Modern treeline also stabilized in the early AD 1300 s at MWA (Fig. 2b). Trees were growing at least 25 m above modern treeline in both mountain ranges prior to AD 1300, suggesting warmer temperatures of at least 0.24 °C during this interval before subsequent cooling and treeline decline.

Earlier in the SHP record there is a very sharp treeline decline of about 65 m (0.6 °C) between 2209 and 2139 BC. This decline is not in the MWA treeline record most likely because the MWA summit is only 118 m above modern treeline, whereas the summit at SHP is 295 m above modern treeline. The MWA summit is a very harsh and inhospitable environment that precludes seedling establishment. Without the suitable and available high elevation habitat during the warmest mid-Holocene interval the MWA trees were unable to move up the mountainside. Hence, there is no record of a substantial treeline drop around 2200 BC at MWA. The 2209 BC treeline

decline at SHP corresponds temporally to the apparent 4.2–3.9 ka BP abrupt climate change event indicated in many widely distributed proxy records (Zhang and Hebda 2005; Booth et al. 2006; Fischer et al. 2008; Menounos et al. 2008; Baker et al. 2009). This “event” may have been a major contributing factor for massive old-world cultural change (Stanley et al. 2003; An et al. 2005; Staubwasser and Weiss 2006).

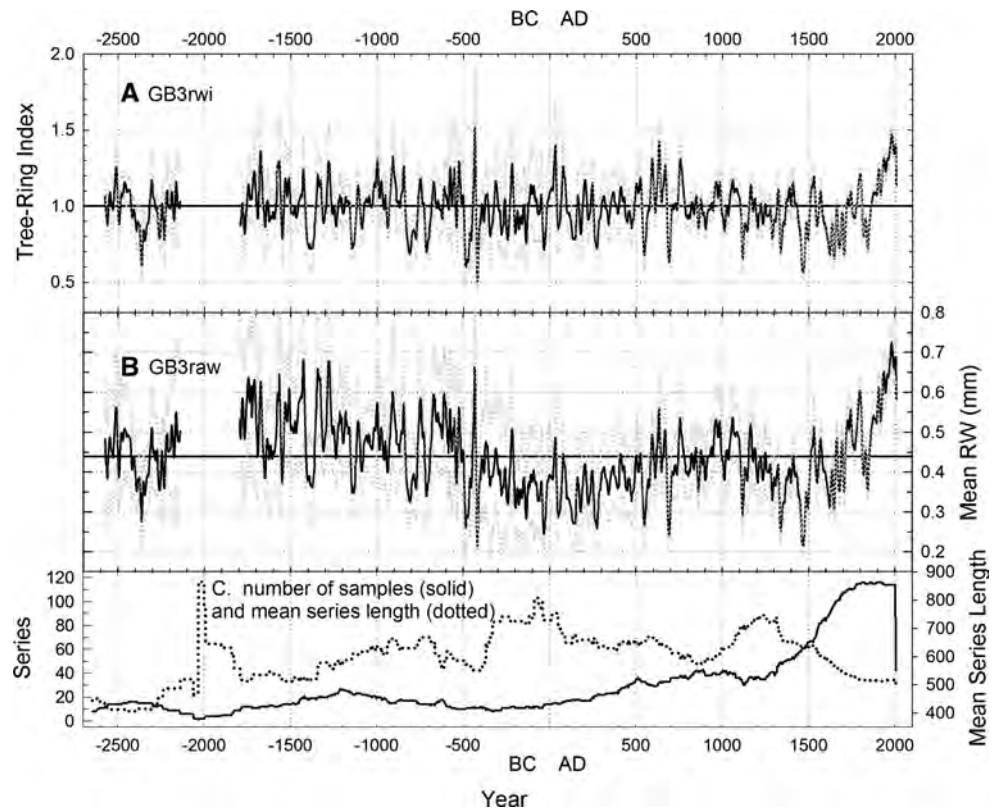
At the SHP site at least four clusters of juvenile trees are growing well above modern treeline. The highest of these clusters is 73 m above treeline and contains at least one tree which has reached reproductive maturity. To avoid injury to these young trees they were not cored to determine exact age. However, counting the number of needle whorls suggested an approximate age of 35–50 years in 2012. It is possible that we are witnessing the incipient stages of treeline advance due to modern warming. A 73 m treeline advance is indicative of a modern warming of 0.7 °C, and local PRISM (Daly et al. 2008) modeled summer temperature for this elevation since AD 1895, is consistent with a mid-twentieth century establishment period. There is no evidence that treelines at SHP have established at these altitudes since before the 2200 BC treeline drop. The nature of the treeline-change data precludes us from knowing exactly how long it has been since trees established at this elevation, as it is possible that some smaller remnant material from more

recent incipient treeline advances has eroded away or not been found. Yet, it is likely that full-size trees have not grown at this elevation since before 2200 BC and quite possible that high elevation ecosystems are now responding in a manner unprecedented in approximately 4,200 years.

3.2 Ring-width variability and temperature inference

To complement the millennial-scale treeline-change information, we used the GB3rwi ring-width index chronology that spans much of the last five millennia (Fig. 3). We do not interpret GB3rwi from 2140 to 1795 BC due to poor agreement and low sample size during that period (SSS <0.85) (Wigley et al. 1984) (Fig. S2). This “gap” occurs immediately following the 65 m treeline decline at SHP. It coincides with both the 4.2–3.9 ka BP abrupt climate event and with a severely frost-damaged ring that occurs in trees at all three sites in 2036 BC. Cold-damaged high-elevation tree rings (“frost rings”) have been shown to be associated with volcanically-forced short-term cooling events (LaMarche and Hirschboeck 1984; Salzer and Hughes 2007). The event at 2036 BC is the most visually severe in our period of record. The wood has often fractured along the 2036 BC latewood annual boundary and eroded along both sides. This cracking and subsequent erosion has, in many cases, effectively erased the ring-

Fig. 3 Time-series plots of Great Basin 3 (GB3rwi) low-frequency tree-ring chronologies with 95 % confidence intervals (grey dotted lines). Included are **a** the standardized ring-width index chronology (GB3rwi); **b** the non-standardized raw ring-width chronology (GB3raw); and **c** the number of samples used in GB3rwi and the mean length of those segments over the length of the chronology



width record for decades to centuries around the 2036 BC ring, which contributes to the “gap” in the record.

Past work has demonstrated significant correspondence between ring-widths from trees at these sites and meteorological temperatures over the relatively short period of overlap provided by the instrumental record (Salzer et al. 2009; Bunn et al. 2011). We expanded on this by comparing the GB3rwi chronology to results from forced coupled global climate model (GCM) simulations for the past millennium. These models simulate past changes in climate in response to estimated changes in external forcing such as solar variability, volcanic activity, and greenhouse gas concentrations.

The tree-ring data agree much more closely with the ECHO-G (ERIK2) results than with those from the MPI (COSMOS) model; the CSM results fall somewhere in between (Fig. 4). The correlations over 991 years between non-smoothed monthly-modeled data and non-smoothed ring-width indices are highest using ERIK2 and for the summer months (July–September, $r = 0.32$, $n = 991$, $N_{\text{eff}} = 589$, $p < 0.001$). The correlation increases to 0.64 when the GB3rwi chronology is compared to the July–September ERIK2 data smoothed in a similar manner to GB3rwi over the common interval of the two data sets, AD 1000–1990 (Fig. 4a). For comparison, the AD 1000–1990 correlations using a mean of the five MPI (COSMOS) ensemble members (20-year smooth) is 0.08 (Fig. 4c), while the CSM results give a value of 0.41 (Fig. 4b). The better agreement between the proxy data and the ERIK2 and CSM models is possibly a result of the larger solar variability used in those simulations. [We note that the difference between the ERIK2 and the MPI (COSMOS) temperature records, both for the Great Basin and for the Northern Hemisphere, closely resembles the solar irradiance record (Crowley 2000) used as forcing for the ERIK2 simulation (not shown)]. ERIK2 and GB3rwi, two completely independent records, show some strong similarities, particularly after AD 1275 ($r = 0.75$, $n = 716$); in contrast, the first 276 years show no correspondence (AD 1000–1275, $r = -0.13$). The lack of agreement in the 11th through late-thirteenth centuries may be due to shortcomings in the forcing data used in the models. It is not uncommon for tree-ring temperature proxy records and model results to disagree during the medieval period, particularly with regard to volcanic signals (Mann et al. 2012). To obtain estimates of temperature from the ring-widths, we scaled the GB3rwi chronology to the smoothed July–September ERIK2 temperature data over the 716-year period from AD 1276–1990 where the two data sets show strong agreement (Fig. 5a). If the entire overlap period (AD 1000–1990) were used in the scaling, the temperature scale would be similar to what was found using the more highly correlated AD 1276–1990 scaling interval. The

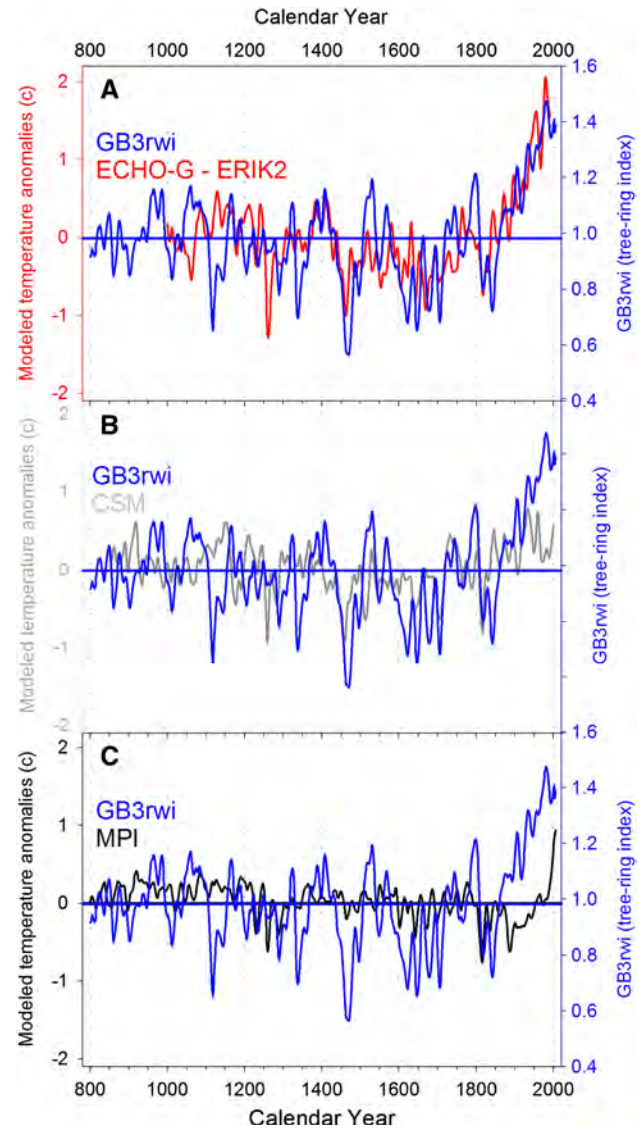
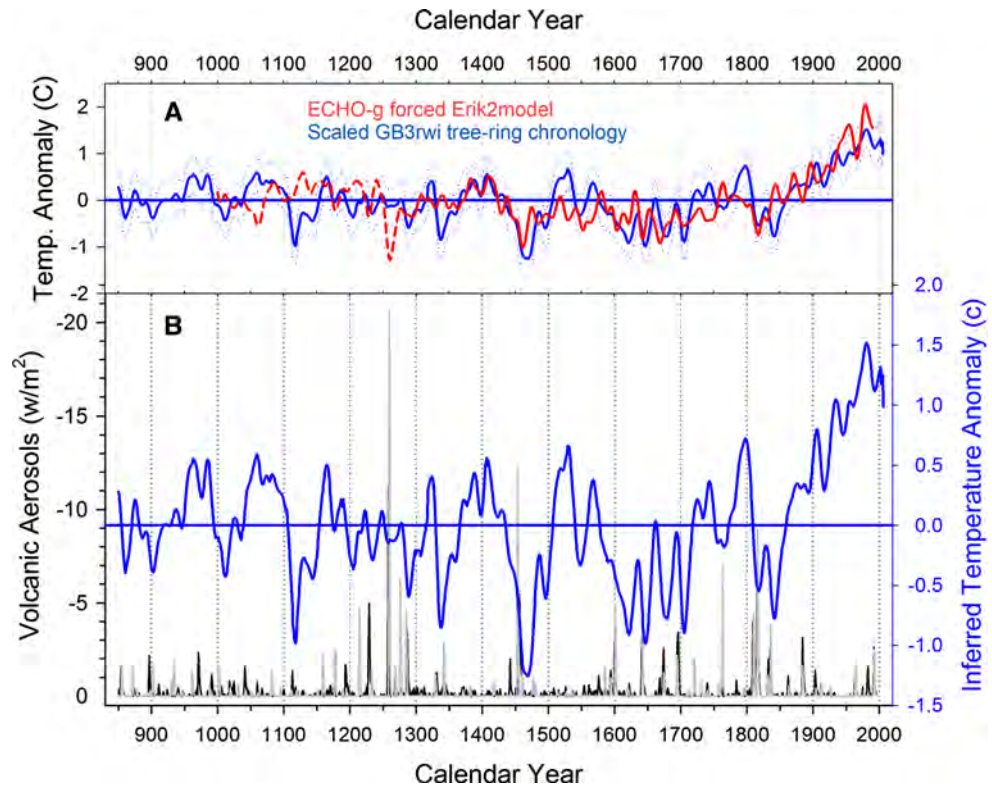


Fig. 4 GB3rwi (blue) and July–September Great Basin temperature from three millennial-run climate models. The tree-ring data agrees most strongly with the ECHO-g model (a red), and less well with the CSM model (b grey) and the MPI model (c black). Modeled temperature anomalies are based on the period AD 1000–1990 with respective mean values in degree celsius of: ECHO-g = 20.32, MPI = 23.33, CSM = 19.03

mean difference between estimates when using the two different scaling intervals is only 0.014 °C; the maximum difference, found in years with larger ring-widths and as a result higher estimated temperature, is only 0.040 °C. Scaling allows estimates of decadal to multi centennial variability for past summer temperature in degrees C for years prior to the model (before AD 1000). Hence, we can interpret the paleoclimatic record for much of the second half of the Holocene based on both the GB3rwi tree-ring data and on the treeline elevation change data discussed above.

Fig. 5 GB3rwi chronology scaled to ECHO-G climate modeled temperature data (Legutke and Voss 1999; Stevens et al. 2008) for period AD 850–2006. Temperature anomalies are based on the AD 1000–1990 July–September mean of 20.32 °C and no trend adjustment is used. **a** Red is the modeled temperature anomaly data, the solid red line indicates the interval used in the scaling (1276–1990). Blue is the scaled tree-ring data with error bars (± 1 RMSE). **b** GB3rwi inferred temperature anomalies (blue) with no trend adjustment compared to volcanic data (black and grey, Gao et al. 2008; Crowley et al. 2008)



3.3 Inferred paleotemperature record

The negative trend of 1.1 °C, derived from the treeline decline data, equates to a long-term preindustrial Holocene cooling rate of -0.31 °C per 1,000 years over the length of the tree ring record prior to treeline stabilization (2575 BC to AD 1328) (Fig. 6). This is greater than the -0.23 °C per 1,000 years (AD 300–1900) reported for the northern Hemisphere (Mann et al. 2008) and the -0.21 °C per 1,000 years (AD 1–1900) reported for the Arctic (Kaufman et al. 2009). The exact same rate of temperature decline, -0.31 °C per 1,000 years, was recently reported over the last $\sim 2,000$ years from high latitude Scandinavia on the basis of tree-ring maximum latewood density (MXD) (Esper et al. 2012).

The overall range of summer temperature variability over 4,582 years is approximately 3.44 °C, with departures from -1.25 °C to $+2.19$ °C (Fig. 6). A similar scale of temperature change (~ 3.1 °C) is produced using PRISM (Daly et al. 2008) modeled instrumental temperature data, unadjusted “raw” ring widths, and regression-based techniques (not shown). The magnitude of temperature anomalies depends on the detail of the scaling of the GB3rwi chronology and partly, prior to AD 1328, on the fact that the chronology has been adjusted using the trend calculated from the tree line changes. The negative trend of 1.1 °C is superimposed upon decadal to century timescale positive departures that exceed $+2$ °C in the fifth century BC, the

warmest period at $+2.19$ °C, and in the seventeenth century BC at $+2.11$ °C. There is a strong upward excursion of $+1.52$ °C in the twentieth century AD. However, the inferred temperature of the modern period was exceeded twice in the Common Era: $+1.69$ °C in the mid first century AD (centered on AD 33) and $+1.58$ °C in the mid seventh century (centered on AD 634). The coldest interval is in the mid to late fifteenth century AD (centered on AD 1469) with a temperature departure of -1.25 °C. Consistent with these results and suggesting that some of the departures from mean conditions are at least hemispheric in scale, the MXD estimates of northern Scandinavian summer temperatures indicate nearly identical dates for their warmest and coldest 30-year periods over the last $\sim 2,000$ years, at AD 21–50 and AD 1451–1480 respectively (Esper et al. 2012). These similar results are derived from different methods (MXD and ring-width), from different species (*Pinus sylvestris* and *Pinus longaeva*) from different ecosystems (lakeshore and alpine/subalpine), and from two distant regions, northern Europe and western North America.

The GB3rwi temperature estimates are likely “missing” some variance in the multi-century part of the variance spectrum because variance at that scale is less evident in the treeline changes and is not as well preserved in the standardized chronology as it is in the “raw” chronology (Fig. 3b). The decadal- to centennial-scale variability in the temperature estimates is likely mainly a result of volcanic

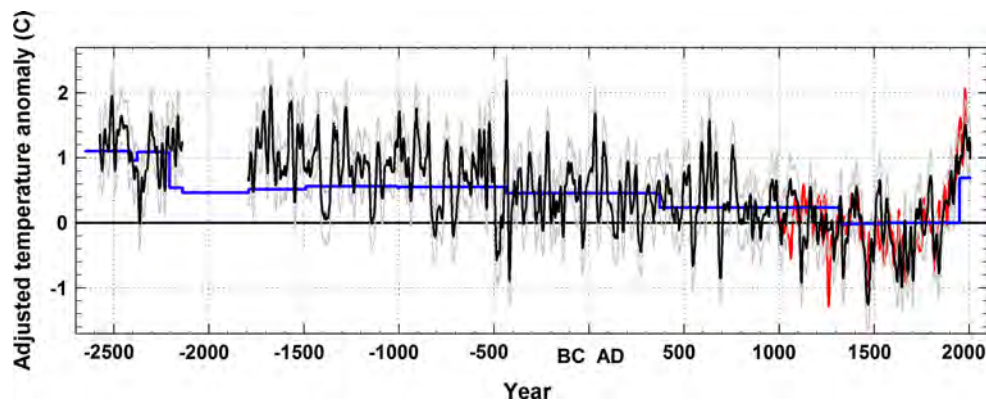


Fig. 6 Scaled paleotemperature from Great Basin, USA with a millennial-scale trend adjustment for the period before AD 1328. The negative trend is based on empirical data from treeline elevation change. *Blue* is inferred past temperature from treeline position (July); *black* is adjusted temperature anomaly from ring-widths (July–September GB3rwi, see “Materials and methods”); *grey* is error

component from scaling (± 1 RMSE); *red* is ECHO-g ERIK2 climate model (Legutke and Voss 1999; Stevens et al. 2008). The *black* and *blue* lines are not independent as trend has been added to the portion of the *black* curve before AD 1328 based on estimated change in temperature from treeline elevation change (*blue* curve). No trend has been added after AD 1328

and/or solar forcing and of internal climate variability. Direct comparisons between scaled GB3rwi and estimates of volcanic (Crowley et al. 2008; Gao et al. 2008) forcing since AD 850 show an association between volcanic forcing and periods of low temperature (Fig. 5b). It is interesting to note four episodes when volcanic activity is high that correspond with periods of inferred low temperature in the late-thirteenth, mid-fifteenth, late-seventeenth, and early-nineteenth centuries. Moreover, the period with the lowest inferred temperature since AD 850 (mid-fifteenth century; -1.25 °C) is associated with very high volcanic activity. In fact, many of the negative departures in temperature coincide with known periods of climatically effective volcanic eruptions (Salzer and Hughes 2007). This is particularly apparent for the five cool temperature episodes between AD 1280 and 1850 (Fig. 5b). Many of the dips earlier in the record are most likely the result of currently unknown and undated eruptions. It is interesting to note that the large volcanic peak of AD 1258 is not associated with inferred cooling. Warm temperature anomalies of $\sim +0.7$ °C are found for several decades in the second half of the tenth and mid eleventh centuries. The Medieval period is a fairly minor warm interval in our record compared to some earlier periods with higher inferred temperatures.

Other paleotemperature proxy records from the Great Basin region often extend farther back into the Holocene than our record, but with less than annual resolution. These proxy archives, such as lacustrine and meadow sediment cores, packrat middens, and glacial moraine dynamics (Thompson et al. 1994; Clark and Gillespie 1997; Smith and Betancourt 2006; Reinemann et al. 2009) are in general agreement with our results, recording higher temperatures during the middle Holocene. Unfortunately, the other proxy archives lack the resolution to be effectively

compared to our results in detail. Additionally, the estimates presented here are in agreement with a high-resolution regional-climate model (Diffenbaugh and Sloan 2004). This model uses mid-Holocene orbital forcing and simulates a mid-Holocene summer warming of 1–2.5 °C over most of western USA.

Annually dated multi-millennial length proxy records that contain information about past temperature are extremely rare. We have combined information from two separate aspects of the biological system of long-lived bristlecone pine trees: (1) reproduction and survival at the upper elevational limit of tree distribution resulting in temporal variability in treeline elevation and (2) radial growth measurements of annual rings from trees at their upper elevational limit. This combination allows us to include millennial-scale variability, in addition to decadal to multi-centennial scale, in our estimates of past summer temperatures over several millennia. This is a promising approach for high resolution paleoclimatology that could provide ring-width-based temperature estimates of summer temperature with improved fidelity at millennial time-scales. Using this approach we have found: (1) covariation between upper treeline *Pinus longaeva* ring widths and regional GCM surface temperature data, (2) treeline evidence of a long-term temperature decline of approximately -1.1 °C since the mid-Holocene, (3) abrupt treeline decline (cooling) around 2200 BC coincident with the 4.2 k climate event reported in many proxy data-sets globally, (4) substantial volcanic forcing of climate in the pre-industrial record, (5) severe frost damage recorded in the 2036 BC upper treeline rings with few extant treeline samples covering this time, and (6) initial evidence of twentieth century treeline advances greater than in approximately 4,000 years.

Acknowledgments We gratefully acknowledge support from the National Science Foundation's Paleo Perspectives on Climate Change (P2C2) Program (Grants ATM-090227 and ATM-1203749). We thank the US Forest Service, the US National Park Service, and the Long Now Foundation for site access, and Kurt Kipfmüller, Evan Larson, and Jim Parks for their assistance.

Open Access This article is distributed under the terms of the Creative Commons Attribution License which permits any use, distribution, and reproduction in any medium, provided the original author(s) and the source are credited.

References

- Ammann CM, Joos F, Schimel D, Otto-Bliesner BL, Tomas R (2007) Solar influence on climate during the Last Millennium. *Proc US Natl Acad Sci* 104:3713–3715
- An CB, Tang L, Barton L, Chen FH (2005) Climate change and cultural response around 4,000 cal year B.P. in the western part of Chinese loess plateau. *Quat Res* 63:347–352
- Baker PA, Fritz SC, Burns SJ, Ekdahl E, Rigsby CA (2009) The Nature and Origin of Decadal to Millennial Scale Climate Variability in the Southern Tropics of South America: The Holocene Record of Lago Umayo, Peru. In: Vimeux F, Sylvestre F, Khodri M (eds) Past climate variability in South America and surrounding regions: from the Last Glacial Maximum to the Holocene, Developments in Paleoenvironmental Research vol 14. Springer, pp 301–322
- Booth RK, Jackson ST, Forman SL, Kutzbach JE, Bettis EA III, Kreig J, Wright DK (2006) A severe centennial-scale drought in mid-continental North America 4,200 years ago and apparent global linkages. *Holocene* 15:321–328
- Bunn AG, Hughes MK, Salzer MW (2011) Topographically modified tree-ring chronologies as a potential means to improve paleoclimate inference. *Clim Change* 105:627–634
- Clark DH, Gillespie AR (1997) Timing and significance of late-glacial and Holocene cirque glaciation in the Sierra Nevada, California. *Quat Int* 38(39):21–38
- Cook ER (1985) A time series approach to tree-ring standardization. University of Arizona, Dissertation
- Cook ER, Briffa KR, Meko DM, Graybill DA, Funkhouser GS (1995) The 'segment length curse' in long tree-ring chronology development for palaeoclimatic studies. *Holocene* 5:229–237
- Crowley TJ (2000) Causes of climate change over the past 1,000 years. *Science* 289:270–277
- Crowley TJ, Zielinski G, Vinther B, Udisti R, Kreutz K, Cole-Dai J, Castellano E (2008) Volcanism and the little ice age. *PAGES Newsl* 16:22–23
- Daly C et al (2008) Physiographically-sensitive mapping of temperature and precipitation across the conterminous United States. *Int J Clim* 28:2031–2064
- Diffenbaugh NS, Sloan LC (2004) Mid-Holocene orbital forcing of regional-scale climate: a case study of western North America using a high-resolution RCM. *J Clim* 17:2927–2937
- Esper J et al (2012) Orbital forcing of tree-ring data. *Nat Clim Change*. doi:10.1038/nclimate1589
- Fischer D et al (2008) The Mt Logan Holocene-late Wisconsinan isotope record: tropical Pacific–Yukon connections. *Holocene* 18:667–677
- Fritts HC (1976) Tree rings and climate. Academic, New York
- Gao C, Robock A, Ammann CM (2008) Volcanic forcing of climate over the past 1,500 years: An improved ice core-based index for climate models. *J Geophys Res* (D23111). doi:10.1029/2008JD010239113
- Hughes MK, Funkhouser GS (2003) Frequency-dependent climate signal in upper and lower forest border tree rings in the mountains of the Great Basin. *Clim Change* 59:233–244
- Jungclaus JH et al (2010) Climate and carbon-cycle variability over the last millennium. *Clim Past Discuss* 6:1009–1044
- Kaufman DS et al (2009) Recent warming reverses long-term arctic cooling. *Science* 325:1236–1239
- Kipfmüller KF, Salzer MW (2010) Linear trend and climate response of five-needle pines in the western United States related to treeline proximity. *Can J For Res* 40:134–142
- Körner C (1998) A reassessment of high elevation tree line positions and their explanation. *Oecologia* 115:445–459
- Körner C (2012) Alpine treelines. Springer, Basel
- Körner C, Paulsen JA (2004) World-wide study of high altitude treeline temperatures. *J Biogeogr* 31:713–732
- LaMarche VC Jr (1973) Holocene climatic variations inferred from treeline fluctuations in the White Mountains, California. *Quat Res* 3:632–660
- LaMarche VC Jr (1974) Paleoclimatic inferences from long tree-ring records. *Science* 183:1043–1048
- LaMarche VC Jr, Hirschboeck KK (1984) Frost rings in trees as records of major volcanic eruptions. *Nature* 307:121–126
- Legutke S, Voss R (1999) The Hamburg atmosphere-ocean coupled circulation model ECHO-g. Technical Report 18, German Climate Computing Center, Hamburg
- Lloyd AH, Graumlich LJ (1997) Holocene dynamics of treeline forests in the Sierra Nevada. *Ecol* 4:1199–1210
- Mann ME et al (2008) Proxy-based reconstructions of hemispheric and global surface temperature variations over the past two millennia. *Proc US Natl Acad Sci* 105:13252–13257
- Mann ME, Fuentes JD, Rutherford S (2012) Underestimation of volcanic cooling in tree-ring-based reconstructions of hemispheric temperatures. *Nat Geosci* 5:202–205
- Menounos B, Clague JJ, Osborn G, Luckman BH, Lakeman TR, Minkus R (2008) Western Canadian glaciers advance in concert with climate change. *Geophys Res Lett* 35 (L07501). doi:10.1029/2008GL033172
- Paulsen JA, Weber UM, Körner C (2000) Tree growth near treeline: abrupt or gradual reduction with altitude? *Arc Antarct Alp Res* 32:14–20
- Reinemann SA, Porinchu DF, Bloom AM, Mark BG, Box JE (2009) A multi-proxy paleolimnological reconstruction of Holocene climate conditions in the Great Basin, United States. *Quat Res* 72:347–358
- Salzer MW, Hughes MK (2007) Bristlecone pine tree rings and volcanic eruptions over the last 5,000 year. *Quat Res* 67:57–68
- Salzer MW, Kipfmüller KF (2005) Reconstructed temperature and precipitation on a millennial timescale from tree-rings in the southern Colorado Plateau. *Clim Change* 70:465–487
- Salzer MW, Hughes MK, Bunn AG, Kipfmüller KF (2009) Recent unprecedented tree-ring growth in bristlecone pine at the highest elevations and possible causes. *Proc US Natl Acad Sci* 106:20348–20353
- Sheppard PR (1991) Identifying low frequency tree-ring variation. *Tree-Ring Bull* 51:29–38
- Smith FA, Betancourt JL (2006) Predicting woodrat (*Neotoma*) responses to anthropogenic warming from studies of the palaeomidden record. *J Biogeogr* 33:2061–2076
- Stanley JD, Krom MD, Cliff RA, Woodward JC (2003) Nile flow failure at the end of the Old Kingdom, Egypt: strontium isotopic and petrologic evidence. *Geoarchaeology* 18:395–402
- Staubwasser M, Weiss H (2006) Holocene climate and cultural evolution in late prehistoric-early historic West Asia. *Quat Res* 66:372–387
- Stevens MB, González-Rouco JF, Beltrami H (2008) North American climate of the last millennium: underground temperatures and model comparison. *J Geophys Res*. doi:10.1029/2006JF000705

- Stokes M, Smiley T (1968) *An Introduction to Tree-Ring Dating*. University of Arizona Press, Tucson
- Thompson RS, Whitlock C, Bartlein PJ, Harrison SP, Spaulding WG (1994) Climatic changes in the western United States since 18,000 yr B.P. In: Wright HE, Kutzbach T, Webb TI, Ruddiman WF, Street-Perrott FA, Bartlein PJ (eds) *Global climates since the Last Glacial Maximum*. University of Minnesota Press, Minneapolis, pp 468–513
- Tolwinski-Ward SE, Evans MN, Hughes MK, Anchukaitis KJ (2010) An efficient forward model of the climate controls on interannual variation in tree-ring width. *Clim Dyn* 36:2419–2439
- Wigley TML, Briffa KR, Jones PD (1984) On the average value of correlated time series, with applications in dendroclimatology and hydrometeorology. *J Clim Appl Meteorol* 23:201–213
- Zhang QB, Hebda RJ (2005) Abrupt climate change and variability in the past four millennia of the southern Vancouver Island, Canada. *Geophys Res Lett* 32 (L16708). doi:[10.1029/2005GL022913](https://doi.org/10.1029/2005GL022913)

The thesis of Brian Schroth is approved

Robert L. Jacobson

Head, Graduate School

**Water Chemistry Reconnaissance
And
Geochemical Modeling In The Meadow Valley Wash Area,
Southern Nevada**

Brian K. Schroth
iii

University of Nevada

Reno

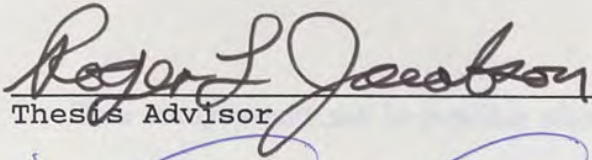
April 1987

**In requirement for the degree of Master of Science in
Hydrology/Hydrogeology
University of Nevada Reno
20 April, 1987**

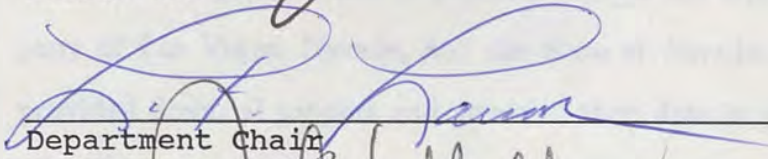
SE ROA 37593

thesis
2218

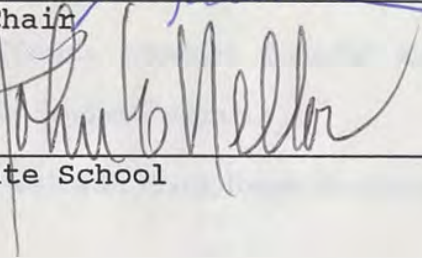
The thesis of Brian Schroth is approved:



Thesis Advisor



Department Chair



Dean, Graduate School

University of Nevada

Reno

April 1987

ACKNOWLEDGEMENTS

This study would not be possible without the input of Nevada Power Company of Las Vegas, Nevada, and the State of Nevada. Nevada Power Company provided financial support and access to their data in preparation for this study. The State of Nevada provided financial support as part of the Nevada Carbonate-Aquifer Studies Program.

The author wishes to thank Roger Jacobson for his advisement and countless ideas.

A very special thanks goes to Alan McKay, who was always there with opinions, thoughts and general good cheer. The task would be much longer and more painful if not for his support.

And of course, immeasurable thanks to Leslie for making it easy.

Table of Contents

ACKNOWLEDGEMENTS	11
ABSTRACT	12
LIST OF FIGURES	13
LIST OF TABLES	14
INTRODUCTION	15
Purpose	15
Scope	15
The study area groundwater system encompasses Coyote Springs, Kane Springs, Moapa and Meadow Valleys. The geology is dominated by Paleozoic carbonates to the north, and younger alluvium and lacustrine deposits to the south. Underflow from Pahrnagat Valley mixes with groundwater from Kane Springs Wash and recharge from the Sheep Range to produce the final discharge of Muddy Springs at the head of Moapa Valley. It is possible that at least 4,000 acre-ft/yr of underflow from Meadow Valley Wash contributes to Muddy Spring discharge. The use of BALANCE, WATEQ, and PHREEQE chemically verifies these proposed flowpaths. Volcanic rocks are the probable explanation of sodium-dominated waters in the south. In lower Moapa Valley and Meadow Valley Wash, the Muddy Creek Formation produces saline, generally sodium-sulfate waters (up to 4500 mg/l TDS) by dissolution of evaporite minerals, primarily gypsum and thenardite. Flow is complex due to local geology and thus geochemical simulation was limited.	15
Major ions	16
Cations and Volcanic Source	17
Muddy Creek Formation Water Conductivity Variation	18
The Base Analysis	19
Ground Flowing	20
GROUNDWATER FLOW AND INTERFACES	21
COMPUTER SIMULATIONS	22
SUMMARY AND CONCLUSIONS	23
REFERENCES	24
APPENDIX	25

Table of Contents

signature page	i
ACKNOWLEDGEMENTS	ii
ABSTRACT	iii
List of Figures	v
List of Tables	vi
INTRODUCTION	1
Purpose	3
Geology	3
HYDROGEOLOGY	5
The White River Drainage System	5
Moapa Valley and Meadow Valley Wash	14
Water Chemistry Overview	16
SOURCES OF DATA	19
MODELS USED	22
SOURCES OF DISSOLVED SALTS	24
The Muddy Creek Formation	24
Sodium Sources	25
Magnesium Sources	31
Carbonate and Volcanic Source Rocks	32
MUDDY CREEK FORMATION WATER CHEMISTRY VARIATION	35
Time Series Analysis	39
Chemical Groupings	41
DRI EXPLORATION HOLES AND ISOTOPES	55
COMPUTER SIMULATIONS	66
SUMMARY AND CONCLUSIONS	75
REFERENCES	78
APPENDIX	80

List of Figures

Figure 1. Study area and surrounding region.	2
Figure 2. Locations of previous work data points.	6
Figure 3. Study area data points.	7
Figure 4. Moapa Valley data points.	8
Figure 5. Meadow Valley Wash data points.	9
Figure 6. The White River Drainage System.	11
Figure 7. Study area water levels.	13
Figure 8. Meadow Valley Wash water levels.	17
Figure 9. General water quality of thesis area.	18
Figure 10. Moapa Valley water quality.	20
Figure 11. Silica vs. sodium/sulfate in Meadow Valley Wash.	28
Figure 12. Simplified surface geology map of the junction between Pahranagat and Coyote Springs Valleys.	34
Figure 13. Well depth vs. conductivity in Meadow Valley Wash.	37
Figure 14. Withdrawl vs. conductivity in Meadow Valley Wash.	38
Figure 15. TDS vs. time: Moapa Valley and Meadow Valley Wash.	40
Figure 16. Piper representation of thesis area waters.	42
Figure 17. Location of chemical groups 1-7.	43
Figure 18 (a-g). Stiff representation of chemical groups 1-7.	44-50
Figure 19 (a-g). Lithologic logs and chemical profiles of EH1-8.	56-62
Figure 20. Deuterium vs. oxygen-18: EH1-8.	64
Figure 21. Deuterium vs. oxygen-18: EH1-8 and regional waters.	65
Figure 22. Map view of oxygen-18 and deuterium.	67
Figure 23. Map view of flowpath simulations.	68
Figure A-1 (a-b). XRD output: salt crust #3.	93-94
Figure A-2 (a-b). XRD output: EH6 well cuttings.	95-96

List of Tables

Table 1. Results of cation exchange experiment.	30
Table 2. Comparison of gypsum saturation indices and TDS in groups 1-7.	54
Table 3 (a-b). PHREEQE simulation results.	70-71
Table A-1. Chemical data from data points shown in Figure 3.	81
Table A-2 (a-b). Chemical data from data points shown in Figure 4.	82-83
Table A-3 (a-c). Chemical data from data points shown in Figure 5.	84-86
Table A-4. Supplemental chemical data.	87
Table A-5. Sources of data in previous work.	88
Table A-6 (a-d). XRD peaks for SC1, SC2, SC3, and EH6.	89-92
Table A-7. PHREEQE sensitivity analysis.	97

INTRODUCTION

The region under study consists of the southern ends of the Meadow Valley Wash and White River drainage system (see Figure 1). The latter may be broken down into three drainage areas: (1) Kane Springs Valley, (2) Coyote Springs Valley, and (3) Moapa Valley. The Muddy River flows through Moapa Valley and intersects the Meadow Valley Wash at Glendale. It continues flowing to the Overton arm of Lake Mead, about 15 miles away. Glendale is on Interstate 15 about 50 miles northeast of Las Vegas.

Several mountain ranges border these valleys. Kane Springs Valley runs NE-SW and is bordered on the northwest by the Delamar Mountains and on the southeast by the Meadow Valley Mountains. Coyote Springs Valley is bordered on the west by the Sheep Range, on the northeast and east by the Delamar and Meadow Valley Mountains, and on the south by the Las Vegas and Arrow Canyon Ranges. Groundwater flows into Moapa Valley through Arrow Canyon, which cuts through the Meadow Valley Mountains and the Arrow Canyon Range. Meadow Valley Wash runs parallel to Coyote Springs Valley, with the Meadow Valley Mountains to the west and the Mormon Mountains to the east.

This is an arid region, with annual precipitation less than 10 inches and a temperature range from less than 20 to 120 degrees Fahrenheit (Longwell et al., 1965). Elevation ranges from about 1500 feet at Glendale to the 9912-foot Hayford peak in the Sheep Range.

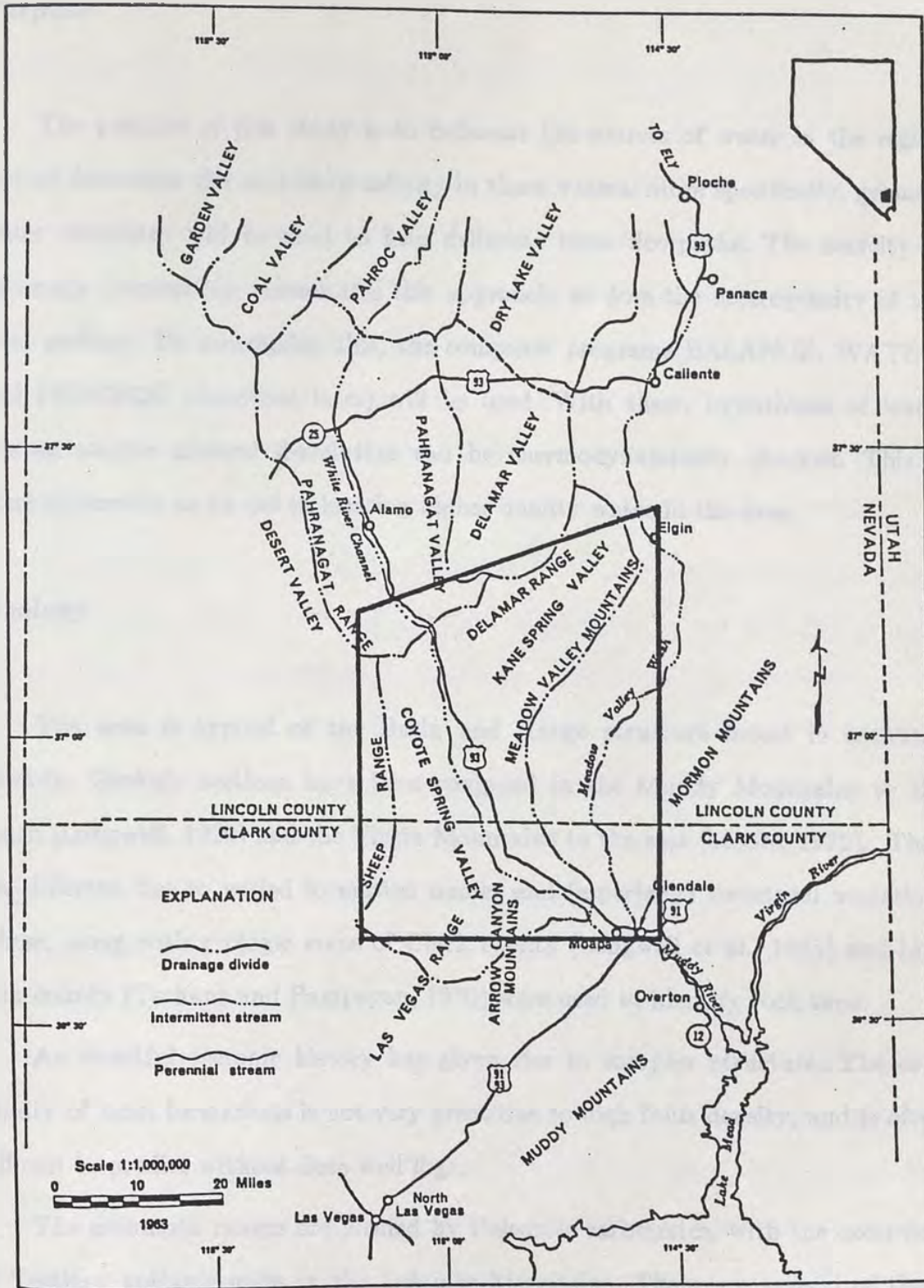


Figure 1. Study area (outlined) and surrounding region. After Eakin (1964). Drainage divide locations are controversial.

Purpose

The purpose of this study is to delineate the sources of water in the region and to determine the sources of salinity in these waters. More specifically, groundwater chemistry will be used to help delineate these flowpaths. The scarcity of hydraulic information necessitates this approach, as does the heterogeneity of the local geology. To accomplish this, the computer programs BALANCE, WATEQ, and PHREEQE (described later) will be used. With these, hypotheses of water mixing and/or mineral dissolution can be thermodynamically checked. This is done ultimately as an aid to locating higher quality water in the area.

Geology

The area is typical of the Basin and Range structure found in southern Nevada. Geologic sections have been compiled in the Muddy Mountains to the south (Longwell, 1928) and the Virgin Mountains to the east (Moore, 1972). They are different due to varied formation names and (especially) structural variation. These, along with geologic maps of Clark county (Longwell et al., 1965) and Lincoln county (Tschanz and Pampeyan, 1970) were used to identify rock type.

An eventful tectonic history has given rise to complex structure. The continuity of most formations is not very great due to high fault density, and is often difficult to predict without deep well logs.

The mountain ranges are formed by Paleozoic carbonates, with the exception of Tertiary volcanic units in the Delamar Mountains. There are several of these formations mapped in the area. An important water-bearing rock is the Mississippian-Permian Bird Springs Formation. Recently drilled wells in the lower

Coyote Springs Valley are believed to penetrate this formation (Dettinger, personal comm., 1986). The Bird Springs Formation is an impure carbonate, containing significant amounts of sandstone, shale, and chert (Longwell et al., 1965). Underneath is the more resistant Monte Cristo Limestone, consisting of purer limestones and dolomites. As with the Bird Springs, chert is an important minor member. These formations form the bulk of the Mormon Mountains, the southern Meadow Valley Mountains, and the northern Las Vegas Range.

Further east and north, thrusting has resulted in Cambrian-Silurian rocks dominating the Arrow Canyon and Sheep Ranges as well as the northern Meadow Valley Mountains. These are similar impure carbonates with associated cherts.

Younger alluvium and Tertiary deposits fill the valleys. In Kane and Coyote Springs Valleys, the thickness of alluvium is small, as is the case in the upper Moapa Valley. In the rest of Moapa Valley and throughout Meadow Valley Wash, however, the thickness is very large.

The Muddy Creek Formation dominates the lithology in these areas. Originally named by Stock (1921) and further described by Longwell (1928), it is a Tertiary (Pliocene?) deposit associated with alluvial, fluvial, and lacustrine environments (Bohannon, 1984). It shows a high degree of variation in thickness, facies, and mineralogy. Thickness ranges from over 1200 feet in the central part of Moapa Valley to near zero in the upper part. It is typically found as zones of clay, silt, sand, and gravel that do not show a high degree of continuity. Since the depositional environment was mostly that of a lakebed, there are associated evaporites. The most commonly reported is gypsum. The presence of gypsum increases southward, and extensive outcrops are found near Lake Mead (Longwell et al., 1965). In the study area, it is most common to find gypsiferous clay rather than gypsum outcrops.

In Moapa Valley, the Muddy Creek is underlain by an ash flow tuff that contains an upper green member and a lower white member. This is believed to be the upper part of the Horse Spring Formation. Well EH2a, drilled near the Nevada Power Company power plant, is the basis for this conclusion. Twenty-five hundred feet of water-lain ash with numerous tan limestone interbeds were penetrated. Gypsum and clastics were also noted, and this correlates reasonably well with the description of the Horse Spring in Longwell et al. (1965). It is assigned a Miocene age. Rocks believed to be Mesozoic "red beds" were found in the last 100 feet of the same well, at a depth of 4000 feet.

HYDROGEOLOGY

In terms of hydrogeology, the study area may be split into two subregions. As mentioned before, Kane Springs Valley and Coyote Springs Valley are considered part of the White River drainage system, a regional deep carbonate groundwater flow system extending over 230 miles in length. The final discharge point of this southward flowing system is the Muddy Springs at the head of Moapa Valley. The remainder of Moapa Valley and Meadow Valley Wash consist of local shallow aquifers in more recent sediments (i.e. the Muddy Creek Formation). Figure 2 shows the collection sites of previous reports, and Figures 3-5 give data points used in this thesis.

The White River Drainage System

In an effort to gain an overall knowledge of groundwater resources in Nevada, a joint effort was made by the Department of Conservation and Natural

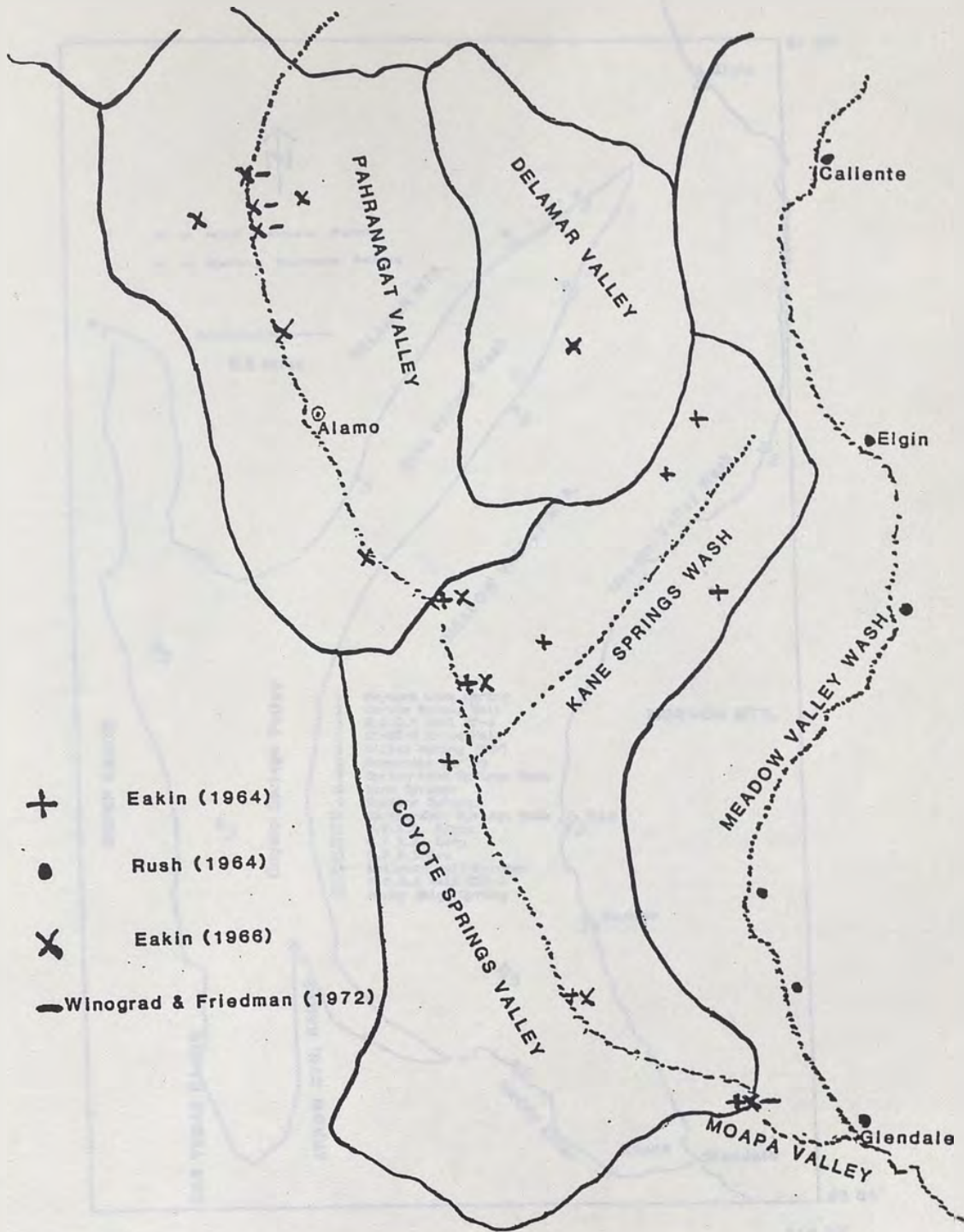


Figure 2. Map of data points used in previous hydrologic reports. See Table A-4 for listing.

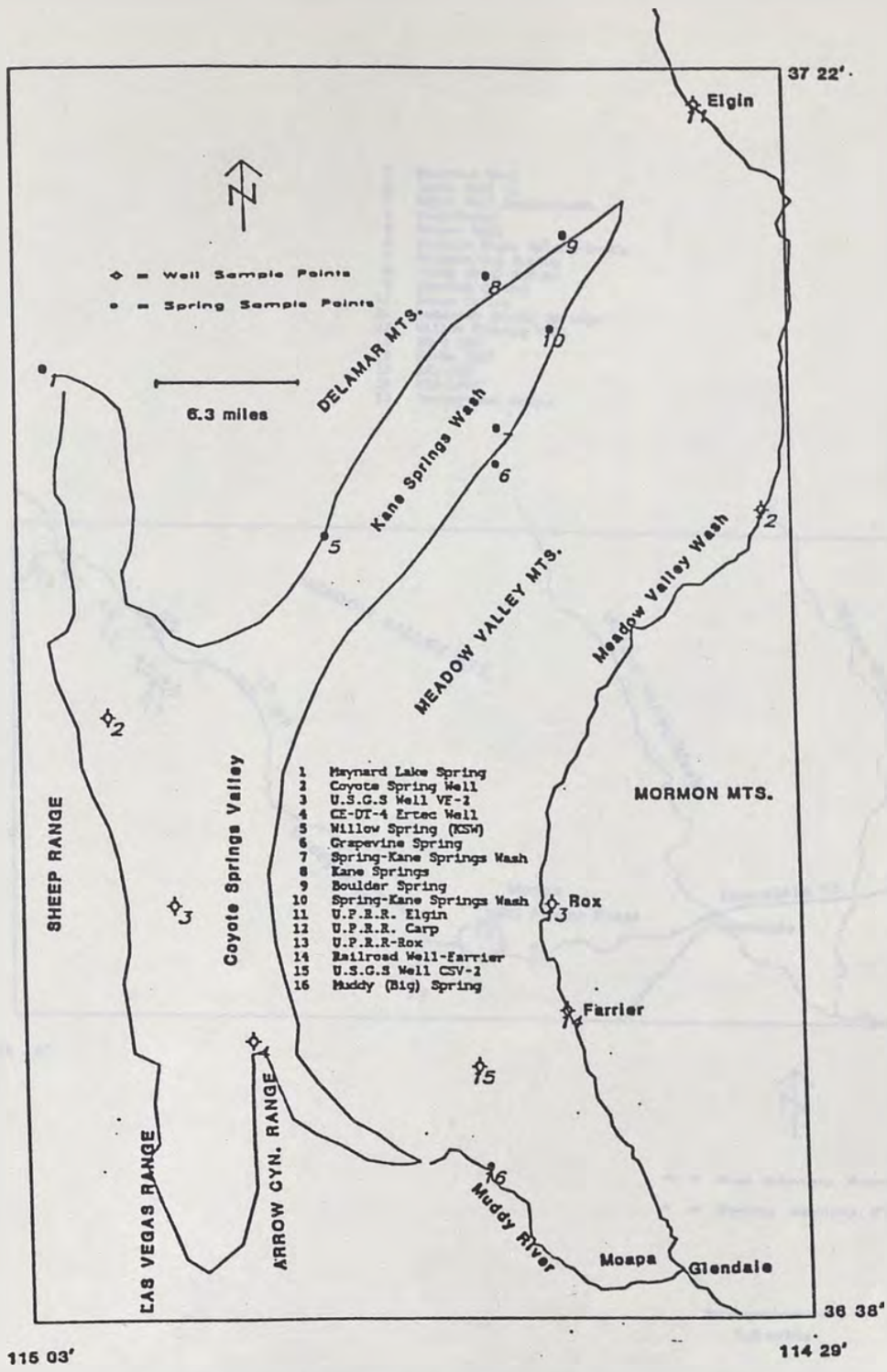


Figure 3. Data points within thesis area. Numbers correspond to chemical analyses in Table A-1. Detail of Moapa Valley and lower Meadow Valley Wash shown in Figures 4 and 5.

SE ROA 37606

- 1 Anderson Well
- 2 Lewis Well #1
- 3 Abbot Well Replacement
- 4 Well-Moapa
- 5 Bremer Well
- 6 Baldwin House Spring-South
- 7 Baldwin Curt Spring
- 8 Muddy (Big) Spring
- 9 Iverson Spring
- 10 Jones Spring
- 11 Pederson (Warm) Springs
- 12 Willow Flowing Well
- 13 EH-4 285'
- 14 EH-5a 205'
- 15 EHL-295'
- 16 EHL-1095'
- 17 Spring-Near Moapa

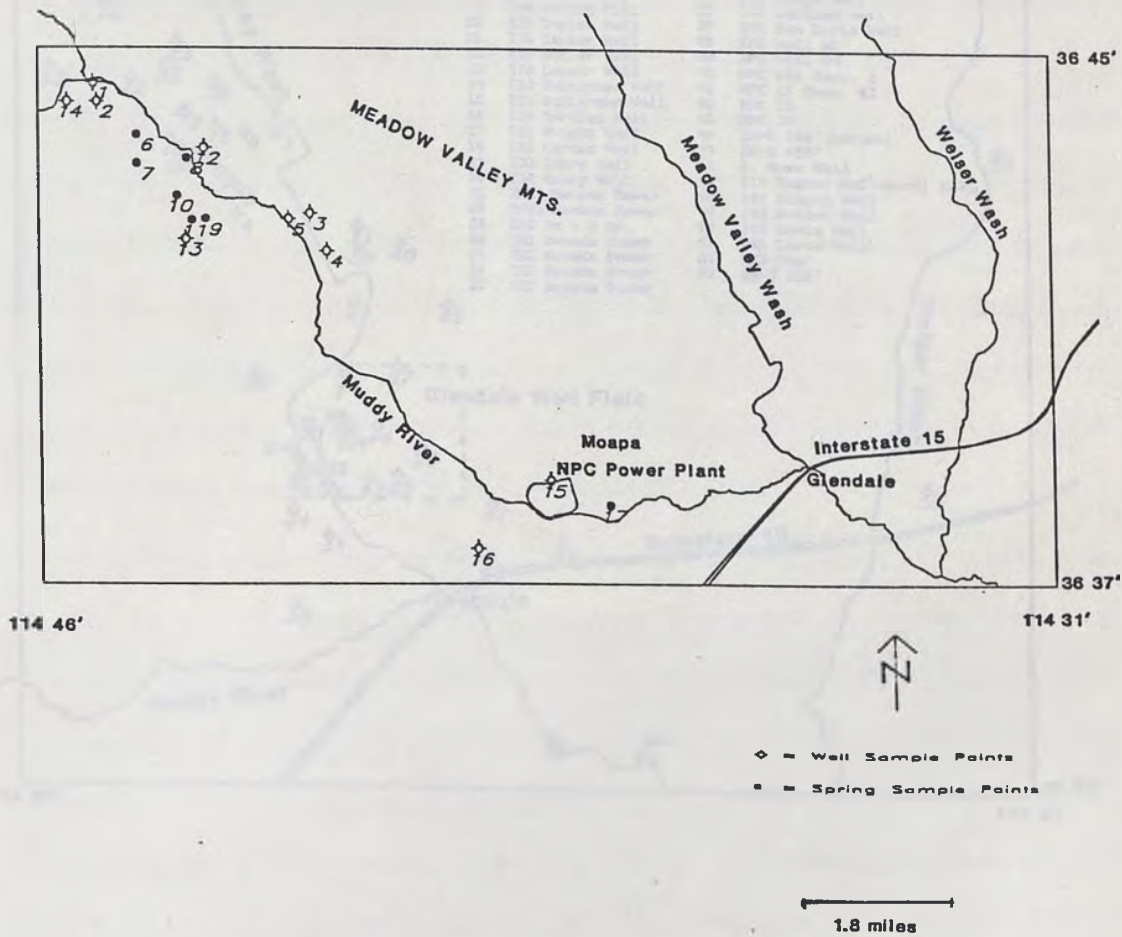


Figure 4. Moapa Valley data points. Numbers correspond to chemical analyses in Table A-2.

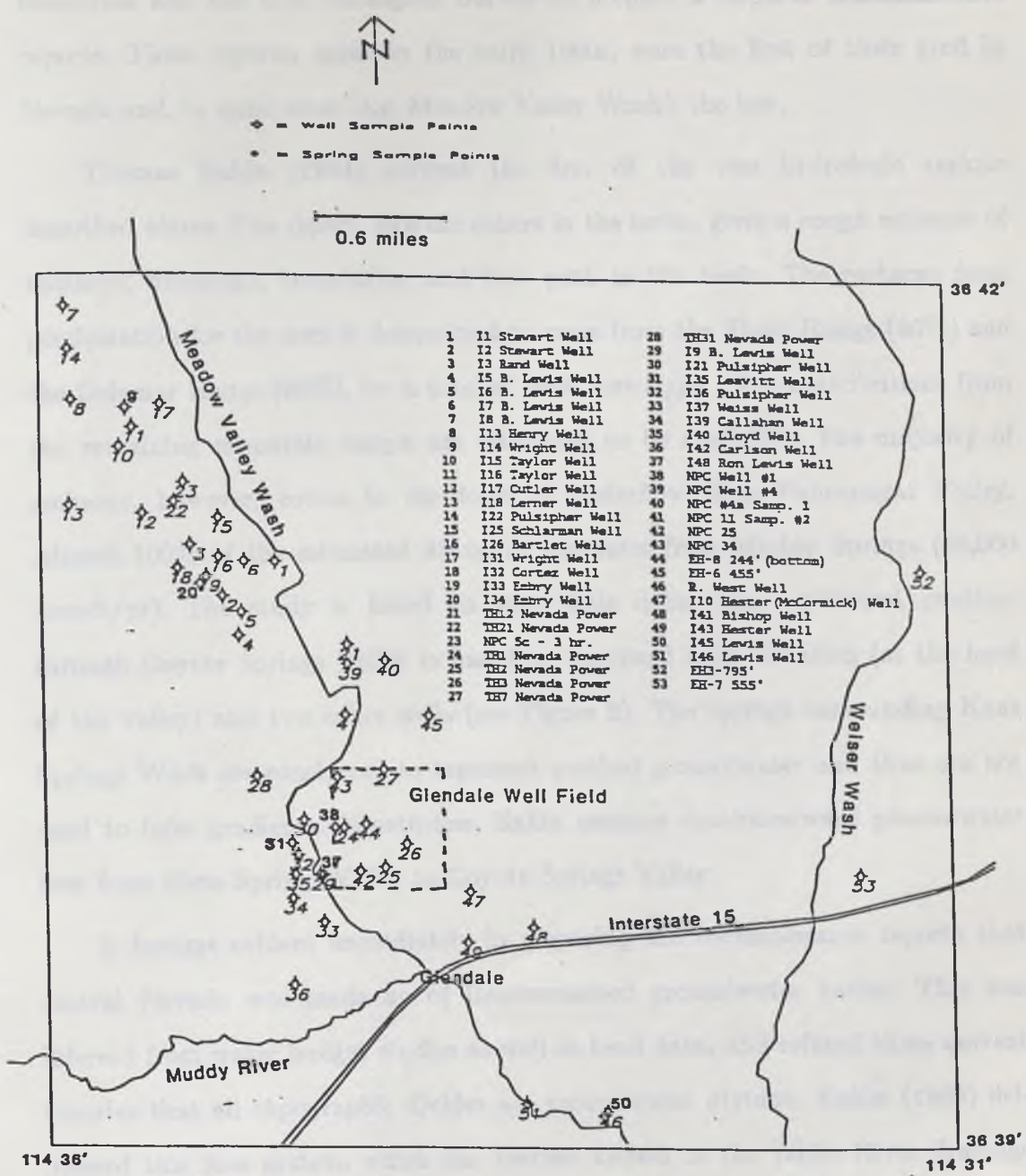


Figure 5. Data points in Meadow Valley Wash and Weiser Wash. Numbers correspond to chemical analyses in Table A-3.

SE ROA 37608

Resources and the U.S. Geological Survey to prepare a series of reconnaissance reports. These reports, made in the early 1960s, were the first of their kind in Nevada and, in some areas (e.g. Meadow Valley Wash), the last.

Thomas Eakin (1964) covered the first of the two hydrologic regions described above. The report, like the others in the series, gives a rough estimate of recharge, discharge, boundaries, and flow path in the basin. The recharge from precipitation for the area is determined to come from the Sheep Range (80%) and the Delamar Range (20%), for a total of 2600 acre-ft/yr. The contributions from the remaining mountain ranges are estimated to be negligible. The majority of recharge, however, comes in the form of underflow from Pahrnagat Valley. Almost 100% of the estimated discharge emanates from Muddy Springs (36,000 acre-ft/yr). The study is based on very little data. The southward gradient through Coyote Springs Valley is based on Maynard Lake elevation (at the head of the valley) and two other wells (see Figure 2). The springs surrounding Kane Springs Wash are considered to represent perched groundwater and thus are not used to infer gradients. Nonetheless, Eakin assumes southwestward groundwater flow from Kane Springs Valley to Coyote Springs Valley.

It became evident immediately in preparing the reconnaissance reports that central Nevada was made up of interconnected groundwater basins. This was inferred from water budget studies as well as head data, and refuted then-current theories that all topographic divides are groundwater divides. Eakin (1966) delineated this flow system, which has become known as the White River drainage system (Figure 6). Though the White River ends in Pahrnagat Valley in present time, it flowed through Coyote Springs and Moapa Valleys during the Pleistocene. This, Eakin claims, is still the groundwater flow path. The report is similar in methodology, but larger in scope than the 1964 paper. Hydraulic heads, spring

Interbasin Groundwater System

Estimated average annual recharge to and discharge (-) from the regional ground-water systems, in thousands of acre-feet per year.

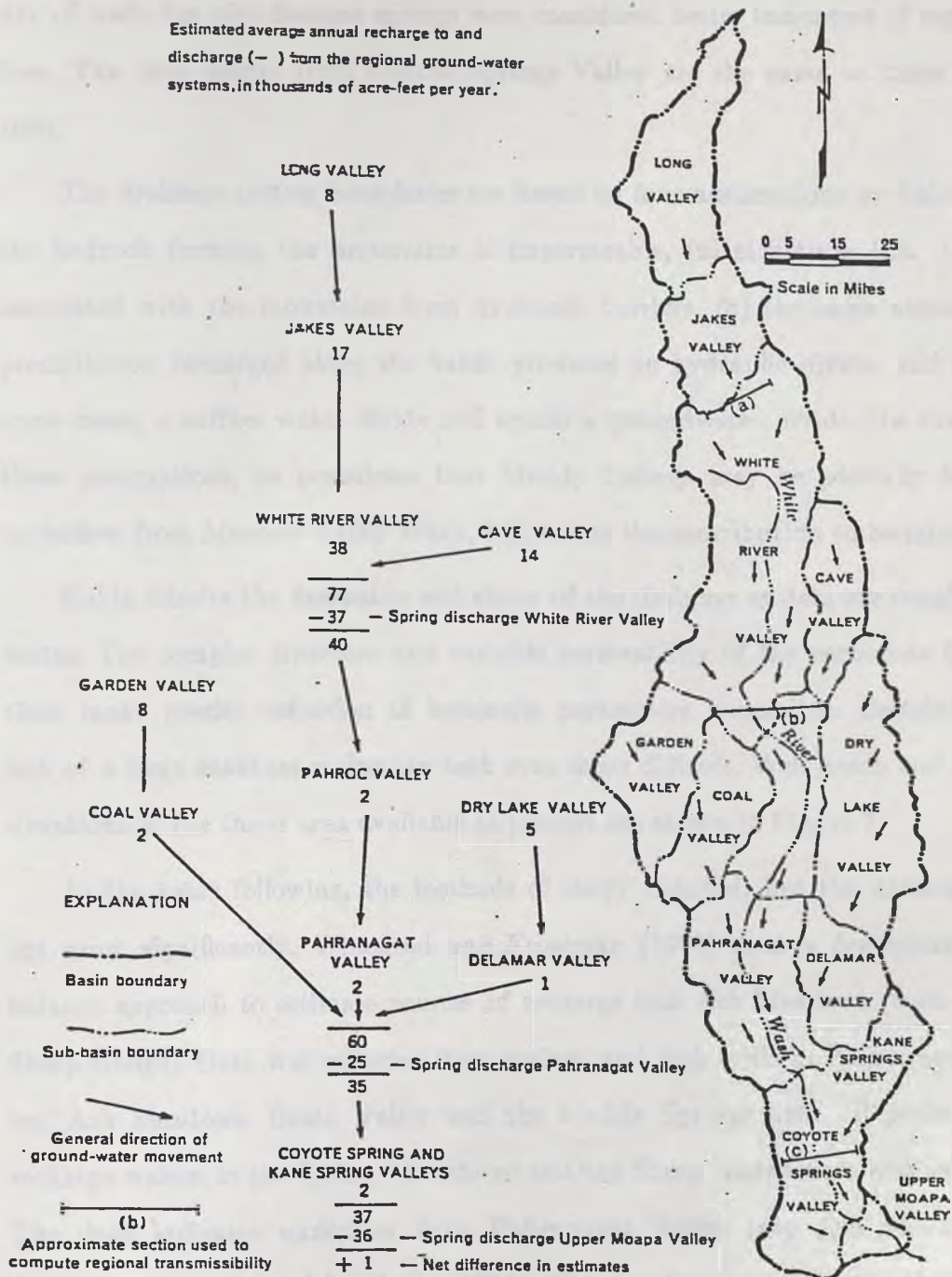


Figure 6. The White River Drainage System, from Eakin (1966).

elevations and regional topography are used to indicate the southward regional gradient. A far greater number of springs were used, mostly because of the scarcity of wells but also because springs were considered better indicators of regional flow. The data points from Coyote Springs Valley are the same as those from 1964.

The drainage system boundaries are based on four assumptions by Eakin: (1) the bedrock forming the mountains is impermeable, (2) structures (i.e. faults) associated with the mountains form hydraulic barriers, (3) the large amount of precipitation recharged along the flanks produces an hydraulic divide, and (4) in some cases, a surface water divide still equals a groundwater divide. On checking these assumptions, he postulates that Muddy Springs may be partially fed by underflow from Meadow Valley Wash, but claims the contribution to be minor.

Eakin admits the flowpaths and shape of the drainage system are rough estimates. The complex structure and variable permeability of the carbonate formations make precise definition of hydraulic parameters impossible. Certainly the lack of a large database makes the task even more difficult. Well heads and spring elevations in the thesis area available at present are shown in Figure 7.

In the years following, the methods of study changed, but the database did not grow significantly. Winograd and Friedman (1972) used a deuterium mass balance approach to estimate sources of recharge into Ash Meadows (west of the Sheep Range). Data was collected from springs and deep wells in Pahrangat Valley, Ash Meadows, Death Valley and the Muddy Springs area. Representative recharge waters in the Spring Mountains and the Sheep Range were also sampled. The data indicates underflow from Pahrangat Valley into Ash Meadows, a flowpath not considered by Eakin (1966). This has importance in the thesis area because it alters Eakin's (1966) water budget. It implies that, given no other

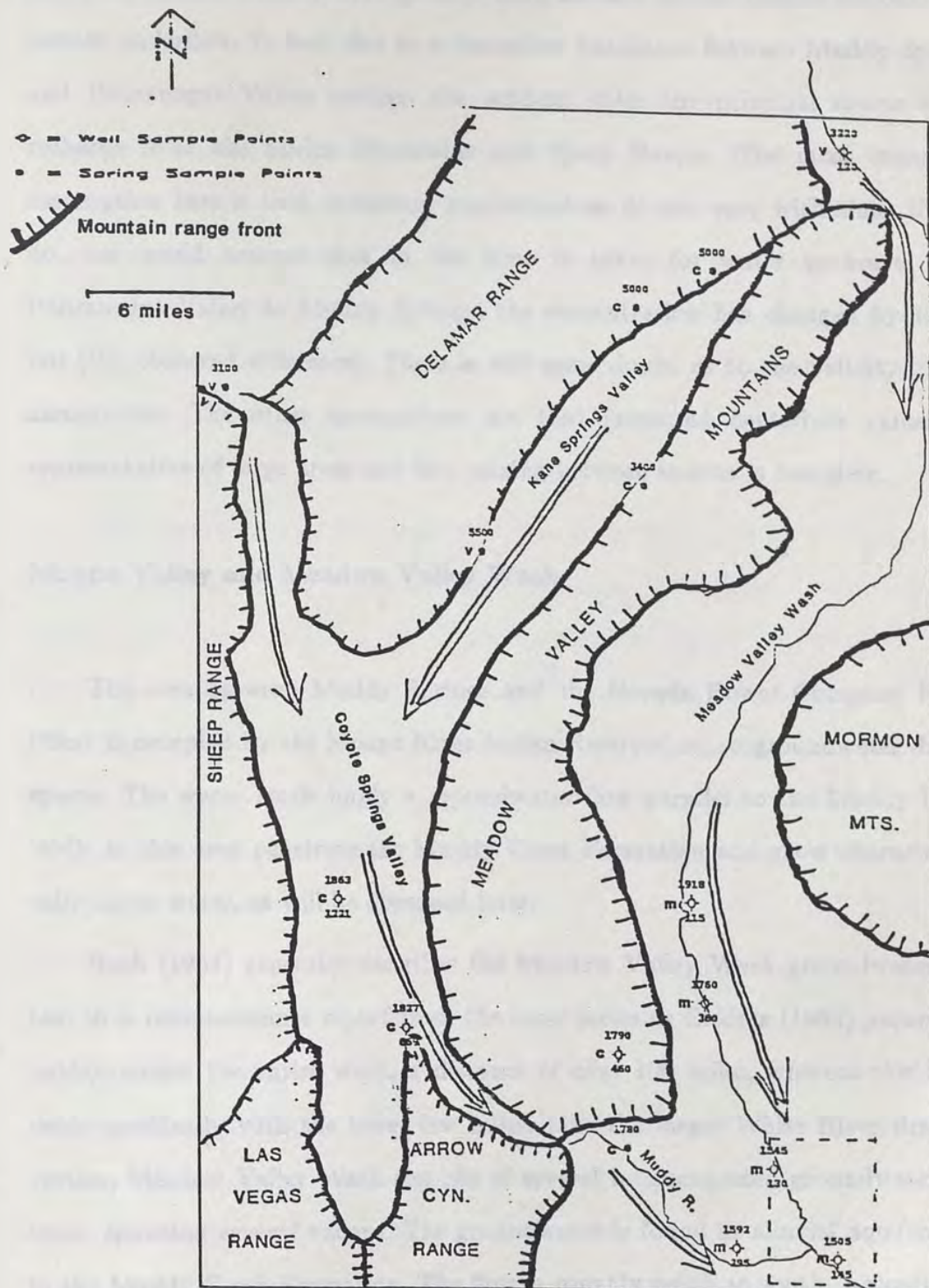


Figure 7. Water levels (above) and well depth (below) for data points in thesis area. Arrows show inferred flowpath. See Figure 8 for detail of Meadow Valley Wash (dashed area). Rock types: c= carbonate, v= volcanic, m= Muddy Creek Fm.

SE ROA 37612

errors by Eakin, Muddy Springs may have another source besides regional carbonate underflow. In fact, due to a deuterium imbalance between Muddy Springs and Pahrnagat Valley springs, the authors claim the principal source to be recharge from the Spring Mountains and Sheep Range. The most important assumption here is that deuterium concentrations do not vary with time. If they do, one could assume that in the time it takes for water to travel from Pahrnagat Valley to Muddy Springs, the concentration has changed by 13 per mil (the observed difference). There is still some doubt as to the validity of this assumption. The other assumptions are that measured deuterium values are representative of large areas and that mixing between sources is complete.

Moapa Valley and Meadow Valley Wash

The area between Muddy Springs and the Nevada Power Company Power Plant is occupied by the Moapa River Indian Reservation, so groundwater data is sparse. The water levels imply a groundwater flow parallel to the Muddy River. Wells in this area penetrate the Muddy Creek Formation and show characteristically saline water, as will be discussed later.

Rush (1964) generally describes the Meadow Valley Wash groundwater system in a reconnaissance report from the same series as Eakin's (1964) paper. The author covers the entire wash, a distance of over 100 miles, whereas this thesis deals specifically with the lower few miles. Like the larger White River drainage system, Meadow Valley Wash consists of several interconnected groundwater systems, spanning several valleys. The groundwater is found in alluvial aquifers and in the Muddy Creek Formation. The flow is roughly north to south. According to Rush's budget, precipitation is the largest contributor of recharge (24,000 acre-

ft/yr), while underflow from Lake Valley at the head of the system is a distant second (3,000 acre-ft/yr). The discharge is in the form of pumping, evapotranspiration, and underflow (20,000 acre-ft/yr). The budget dictates 7,000 acre-ft/yr leaves as a combination of evaporation and underflow to Moapa Valley. Unfortunately, no follow-up studies of this type have been performed in Meadow Valley Wash. Rush's report was a rough overview, and the pumping rate estimates, an integral part of the water budget, are sadly outdated. In the part of the wash contained in the thesis area, most domestic wells were drilled in the early 1970's and Nevada Power Company has significantly increased its groundwater use since 1964.

The only remaining information on the lower Meadow Valley Wash is contained in Desert Research Institute (DRI) reports to Nevada Power Company (NPC). NPC constructed a power plant in central Moapa Valley in the early 1960's. To supply water for their cooling towers, a well field was set up in the lower Meadow Valley Wash. All wells pump water from the Muddy Creek, so poor water quality has always been a problem. In many places the Muddy Creek is not well consolidated, and sanding and/or formation collapse has occurred in many wells. There has also been a tendency for water quality to decrease with time.

DRI is currently solving these problems by finding better water quality and by carefully constructing wells. Many exploration and pumping wells were constructed in the Meadow Valley Wash under DRI supervision and many of the same problems were experienced. Transmissivity values range from 20,000 to 90,000 gpd/ft in isolated gravel zones. Several unpublished reports to NPC contain much of the water quality information used in this paper. In addition to the NPC wells, many privately owned wells were inventoried in Meadow Valley Wash

during 1981-1982 (Mifflin et al., 1982). The recent conclusion is to seek water elsewhere in the area because the above problems cannot be completely avoided. A series of exploration holes have been drilled in Moapa Valley and Meadow Valley Wash as well as Weiser Wash to the east.

The bulk of these reports deal with individual well data (pump tests, water level fluctuations, water chemistry). This provides an amazingly dense database, but little regional insight. Zimmerman et al. (1982) describe Meadow Valley Wash as a complex multiple aquifer system that fluctuates between confined and unconfined conditions. In the Glendale well field (Figure 5) the producing zone is a variable thickness gravel zone at the base of the recent alluvial sediments. However, pumping from this zone draws water from above (fine-grained alluvium) and below (Muddy Creek Formation). The amount of leakage is difficult to determine but is assumed to be high. An upward gradient was observed in one part of the Muddy Creek Formation, but this is not commonly found. Without surprise, transmissivity values vary widely (23,000-630,000 gpd/ft). As leakage is occurring, measurements will increase away from the pumping well. The facies variability in the Muddy Creek as well as pumping influences make flowpath determination difficult, but it is generally north to south as shown in Figure 8.

Water Chemistry Overview

There is a southward trend of increased salinity in the study area (Figure 9). Salinity is commonly reported as total dissolved solids (TDS). In Kane Springs Wash, the springs show a direct limestone source with a low TDS calcium-bicarbonate water. The exception is Willow Spring, which has a sodium dominance due to its location in volcanic rocks of the Delamar Mountains. Maynard

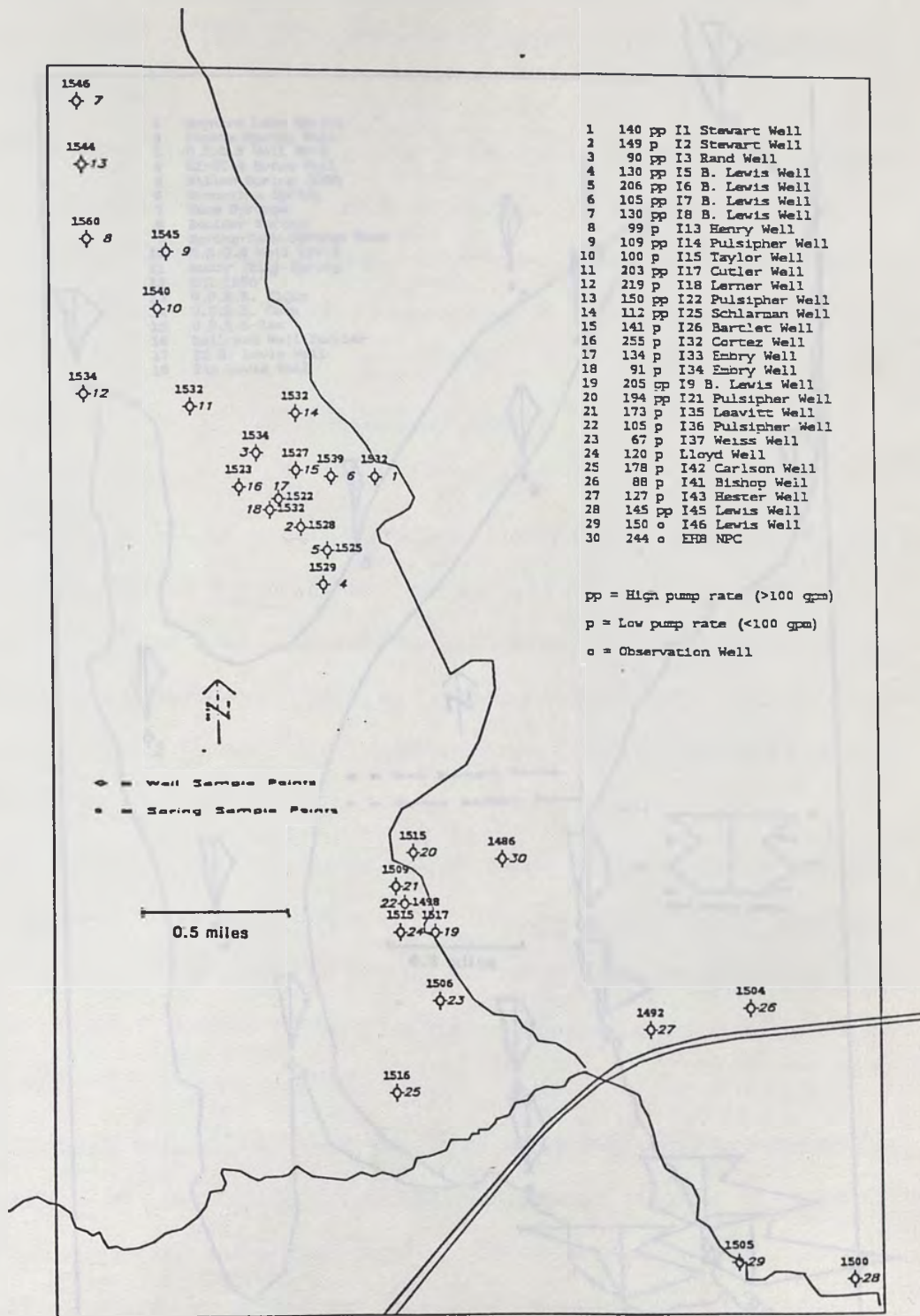


Figure 8. Static water levels in Meadow Valley Wash (ft). Lack of consistent elevations in southern area is due to pumping. Well depths are given before each data point in the list.

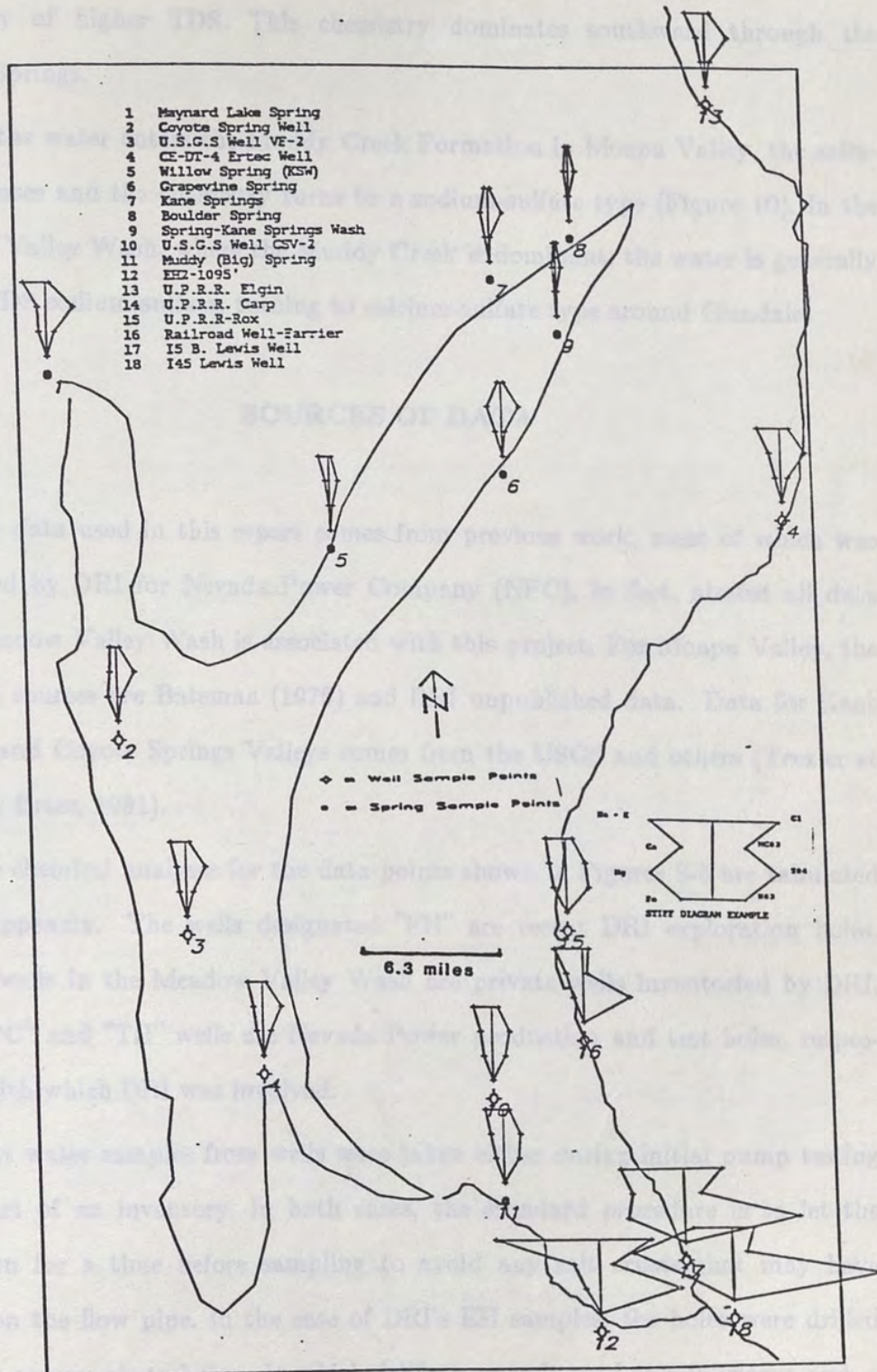


Figure 9. General water quality of thesis area.

SE ROA 37617

Lake Spring, at the head of Coyote Springs Valley, shows a sodium-bicarbonate chemistry of higher TDS. This chemistry dominates southward through the Muddy Springs.

As the water enters the Muddy Creek Formation in Moapa Valley, the salinity increases and the chemistry turns to a sodium-sulfate type (Figure 10). In the Meadow Valley Wash, where the Muddy Creek is dominant, the water is generally a high TDS sodium-sulfate, turning to calcium-sulfate type around Glendale.

SOURCES OF DATA

The data used in this report comes from previous work, most of which was performed by DRI for Nevada Power Company (NPC). In fact, almost all data from Meadow Valley Wash is associated with this project. For Moapa Valley, the principal sources are Bateman (1976) and DRI unpublished data. Data for Kane Springs and Coyote Springs Valleys comes from the USGS and others (Trexler et al., 1982; Ertec, 1981).

The chemical analyses for the data points shown in Figures 3-5 are tabulated in the appendix. The wells designated "EH" are recent DRI exploration holes. The "T" wells in the Meadow Valley Wash are private wells inventoried by DRI. The "NPC" and "TH" wells are Nevada Power production and test holes, respectively, with which DRI was involved.

Most water samples from wells were taken either during initial pump testing or as part of an inventory. In both cases, the standard procedure is to let the water run for a time before sampling to avoid any salt crusts that may have formed on the flow pipe. In the case of DRI's EH samples, the holes were drilled using the reverse air technique in which drilling water is used as a lubricant and

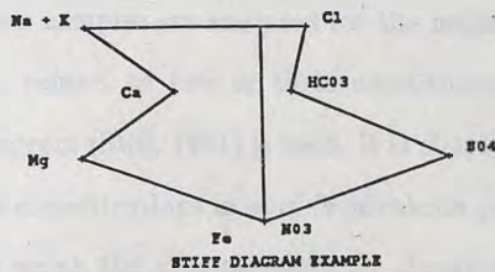
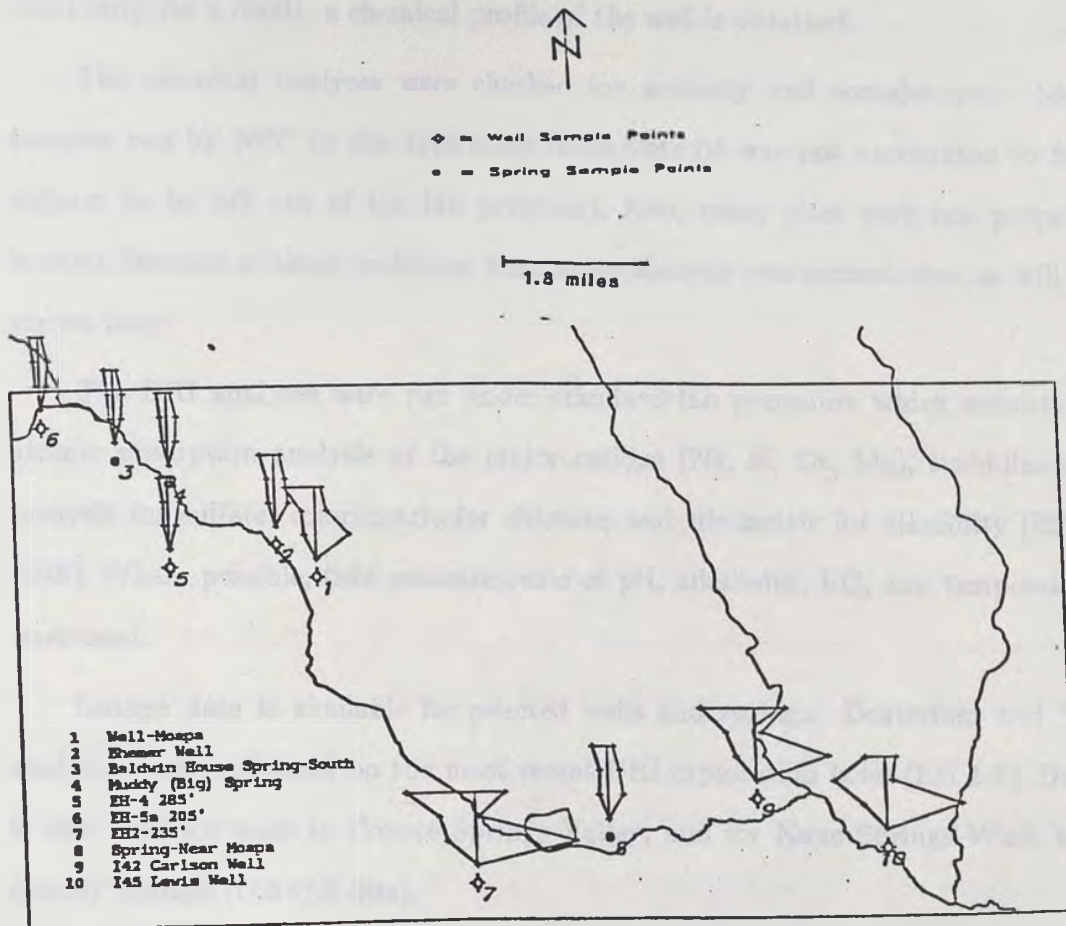


Figure 10. Selected water chemistries in southern part of study area. Sodium-sulfate wells mark extent of Muddy Creek Formation.

compressed air forces circulation (Driscoll, 1986, p. 289-295). With this method, drilling may be stopped at any time, and the compressed air is used to bring formation water to the surface for sampling (after the drilling water has been circulated out). As a result, a chemical profile of the well is obtained.

The chemical analyses were checked for accuracy and completeness. Most samples run by NPC in the 1960's are incomplete (it was not uncommon to find sodium to be left out of the lab program). Also, many sites were not properly located. Because of these problems, time series analysis was inconclusive, as will be shown later.

The DRI analyses were run under standard lab procedure which consists of atomic absorption analysis of the major cations (Na, K, Ca, Mg), turbidimetric analysis for sulfate, colorimetric for chloride, and titrimetric for alkalinity (EPA, 1979). Where possible, field measurements of pH, alkalinity, EC, and temperature were used.

Isotope data is available for selected wells and springs. Deuterium and ¹⁸O analyses were performed on the most recent DRI exploration holes (EH 1-8). Data is also used for wells in Coyote Springs Valley, and for Kane Springs Wash and Muddy Springs (U.S.G.S files).

When groundwater samples are analyzed for the major cations and anions, a strong character with respect to two or three constituents emerges. To see this more easily, a Stiff diagram (Stiff, 1951) is used. It is simply a plot of the common constituents and their concentrations in epm (equivalents per million). Equivalents per million is used to weigh the concentrations by charge and atomic (or molecular) weight, so that it is a measure of abundance of ions and not simply weight percentage. The calculation is made using the equation

$$\text{epm} = \frac{(\text{measured mg/l of constituent})(\text{absolute value of ion charge})}{(\text{atomic or molecular wt.})}$$

The most abundant ions are easily seen as the biggest "bulges" in the plot. Also, relative TDS may be seen by comparing sizes of plots. Stiff diagrams are used extensively in this study.

Another important chemical grouping tool is the Piper diagram (Piper, 1944). Cations and anion molar concentrations are plotted on separate triangular diagrams. They are combined by projecting the points onto a diamond-shaped field. This is useful in graphically presenting groups of waters, as different waters will occupy different regions of the diamond field.

MODELS USED

When mixing and/or mineral dissolution scenarios are hypothesized, BALANCE is the simplest check used. Developed by Parkhurst et al. (1982), it is simply a mass balance program that solves simultaneous equations. For example, if an initial and final water chemistry are input along with a mineral assemblage, BALANCE will determine how much each mineral must precipitate or dissolve in the path between initial and final. The major shortcoming of the program is that the number of minerals must equal the number of phases (Na, Ca, SO₄, etc.) in order for the unknowns and equations to balance. This is an unrealistic approach for natural systems. Also, it does not consider thermodynamics, so the output may be mathematically correct, but chemically impossible. However, other tools may be used to check this, and it gives a good first estimation which can act as input to more sophisticated chemical simulation programs.

WATEQDR (Bohm and Jacobson, 1981) is a modified version of WATEQF (Plummer et. al., 1976), which in turn was developed from the original WATEQ (Truesdell and Jones, 1973). Though WATEQDR was actually used for this

thesis, WATEQ will be used in the discussions for simplicity. Short for WATER Equilibrium, WATEQ is not a mixing model. It gives a rigorous thermodynamic description of an input water chemistry using a large data base. Among its calculations are activity coefficients, partial pressures of gasses, ion activity products, and, most importantly, saturation indices.

The saturation index (SI) of a mineral in a solution determines whether that mineral should precipitate or dissolve. A negative SI indicates undersaturation (dissolution favored), positive indicates supersaturation (precipitation favored) and zero shows an equilibrium (Drever, 1982, chapter 2). This is an important parameter because it acts as a check on BALANCE output. For example, if BALANCE reports a dissolution of gypsum, yet WATEQ shows the input water to be saturated with respect to gypsum, then the BALANCE output is invalid.

PHREEQE (Parkhurst et al., 1980) is a versatile, powerful geochemical modeling program that combines the qualities of both WATEQ and BALANCE. It uses mass balance to evolve an input water while obeying thermodynamic laws. The program calculates all properties of the final water, including pH and the saturation indices, in order to check the simulation against WATEQ output.

The way in which the three programs are typically used together is as follows: (1) A water passes through a proposed mineral assemblage to attain a final chemistry; (2) to test this, BALANCE is run and the molar amounts of each mineral dissolving or precipitating is given; (3) separately, WATEQ is run on the initial and final water chemistry; (4) if the BALANCE results do not conflict with the SI values for the initial water, these results are input into PHREEQE; (5) the thermodynamic properties from the PHREEQE solution are then compared to those of the actual final water; and (6) if there is a reasonable agreement, the reaction hypothesis may be viable.

This is not the definitive method for explaining water chemistry changes, but only a way to list possibilities. WATEQ and PHREEQE use precise values (generated in a quantitative lab) on sometimes questionable data. The value of pH, for example, is an integral part of carbonate equilibria, and hence strongly influences the SI for calcite and dolomite. This parameter is either measured in the field by meters prone to errors (poor electrode, inaccurate calibration, temperature influences, etc.) or in the lab, by which time the actual pH has changed. In the range of pH found in these waters (7.0-8.0+), an error of a few tenths causes a significant error in SI. In fact, an error of 0.6 would cause the SI of calcite to change by 150 percent for one of the waters of the region. Since pH and alkalinity are the most changeable of parameters (and the most difficult to measure accurately), a greater emphasis is placed on the SI for gypsum in checking the simulations. Also, care must be taken to use reasonable hypotheses and trusted data. This may seem obvious, but any hypothesis may be "verified" if the input parameters are strategically used. Supporting data of another type is always helpful.

SOURCES OF DISSOLVED SALTS

The Muddy Creek Formation

Before any explanations can be proposed concerning chemical evolution of the regional water, mineralogy of the flow environment must be explored. As stated before, every source in the literature notes gypsum in the Muddy Creek Formation. Rock salt (halite) is also a common observation (Longwell et al., 1965). These two are mentioned more because they are familiar, rather than dominant.

Gypsum or anhydrite certainly must be considered the most important mineral, as implied by high sulfate water chemistry. Though there are high concentrations of sodium in Meadow Valley Wash waters (up to 785 mg/l), these are not matched by chloride: the molar ratio of sodium to chloride ranges to over 10:1. Chloride is a conservative ion, and halite is its only common source mineral. Sodium, on the other hand, has a few more sources, including cation exchange. Therefore, the concentration of chloride, not sodium, indicates the abundance of halite. Chloride is occasionally found at high concentrations, though it is often third behind sulfate and bicarbonate. The importance of halite, therefore, is not as great as that of gypsum.

SODIUM SOURCES

If gypsum is the dominant mineral in the area, then why are the waters more often a sodium-sulfate type? It is not uncommon to find calcium the least abundant of the three major cations. The waters of Muddy Springs issue from carbonate rock (a calcite/dolomite mineralogy), yet sodium is dominant, not calcium or magnesium. Clearly there is a major source of sodium, and halite is not the answer.

In the literature, most high sodium waters are explained by cation exchange without a rigorous treatment, or else left unexplained. The latter is the case concerning the sodium-bicarbonate Muddy Springs in the Ertec (1981) report, and no known attempt has been made to explain the sodium-sulfate chemistry of Muddy Creek Formation waters.

Cation exchange does appear to be an attractive explanation. In this case, the clay would exchange two sodium ions for one calcium ion in order to maintain

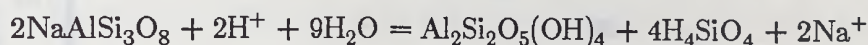
charge balance. Many clays prefer divalence over monovalence at their exchange sites (Bohn et al., 1979). In the case of the sodium-sulfate waters, the sulfate concentration exceeds that of calcium. One could reason that a given amount of gypsum (equal to the sulfate concentration) could dissolve and part or most of the calcium could be exchanged for sodium. Therefore a sodium-sulfate water could result simply from gypsum dissolution with cation exchange.

Unfortunately, this theory does not hold up. As an example, consider the water from the bottom of EH6 in Meadow Valley Wash. It is a calcium-sulfate water from group 1, defined earlier. The total sulfate epm is 38.3, while the combined epm of sodium and calcium is 30.0. If the above theory was correct, the two numbers should be nearly equal. This might be partially explained by gypsum dissolution with calcite precipitation. Gypsum is more soluble than calcite, so calcium ions liberated by gypsum dissolution may be removed immediately by calcite precipitation. In this way, sulfate will accumulate in solution, while calcium will not. WATEQ shows this water to be saturated with calcite (this is true of almost all waters of the region), so any calcium introduced into the water should be precipitated.

Another possible sulfate input is the dissolution of sodium sulfate. Jones (1965) describes a significant amount of thenardite (Na_2SO_4) in Deep Springs Lake, Inyo County, California. The dry lake environment is similar to that of the Muddy Creek Formation in the early Tertiary. More locally, a large deposit of glauberite ($\text{Na}_2\text{Ca}(\text{SO}_4)_2$) was found in the Muddy Creek at a site now under Lake Mead, and in White Basin to the west (Longwell et al., 1965). The presence of the mineral is therefore a viable assumption. Sulfate so dominates the anion concentrations in this EH6 water (as well as others) that if one wanted to eliminate cation exchange as a possibility, one must assume sulfate mineral sources for all

cations. This is impossible because the principal source of magnesium is dolomite, not epsomite ($\text{MgSO}_4 \cdot 7\text{H}_2\text{O}$).

Still another sodium source is the alteration of silicate minerals. Dissolved silica concentrations vary in Meadow Valley Wash to the extent that trends are unclear. However, if silica is plotted against sodium/sulfate, a relationship emerges (Figure 11). It seems that waters below the dashed line exhibit a linear relationship between silica and "extra" sodium content. Extra sodium means sodium not associated with thenardite dissolution, which is why the sulfate divisor is included. The most likely reaction taking place to give this relationship is the weathering of sodium-rich silicates. As an example of this type of reaction, consider the weathering of albite to kaolinite:



Waters containing greater than 2.0 mmol/l (120 mg/l) dissolved silica are said to be saturated with amorphous silica. These waters lie above the horizontal line in Figure 11, and the linear relationship is upset by the saturation. Similar plots using calcium and magnesium instead of sodium did not show a relationship.

In some areas of Moapa Valley and Meadow Valley Wash, salt crusts are visible on the surface. These are believed to be indicative of the evaporite mineralogy of the Muddy Creek. Three samples were collected: the first from the NPC power plant area, the second about 1.5 miles east of Muddy Springs, and the third from the Glendale well field in Meadow Valley Wash. The samples were powdered and run on the DRI X-ray diffractometer (XRD), which identifies minerals based on their individual capacities to diffract X-rays. The XRD output is given in the appendix.

As expected, the dominant minerals are gypsum, thenardite, and calcite. The gypsum peaks were checked by baking the sample to drive the water off. When

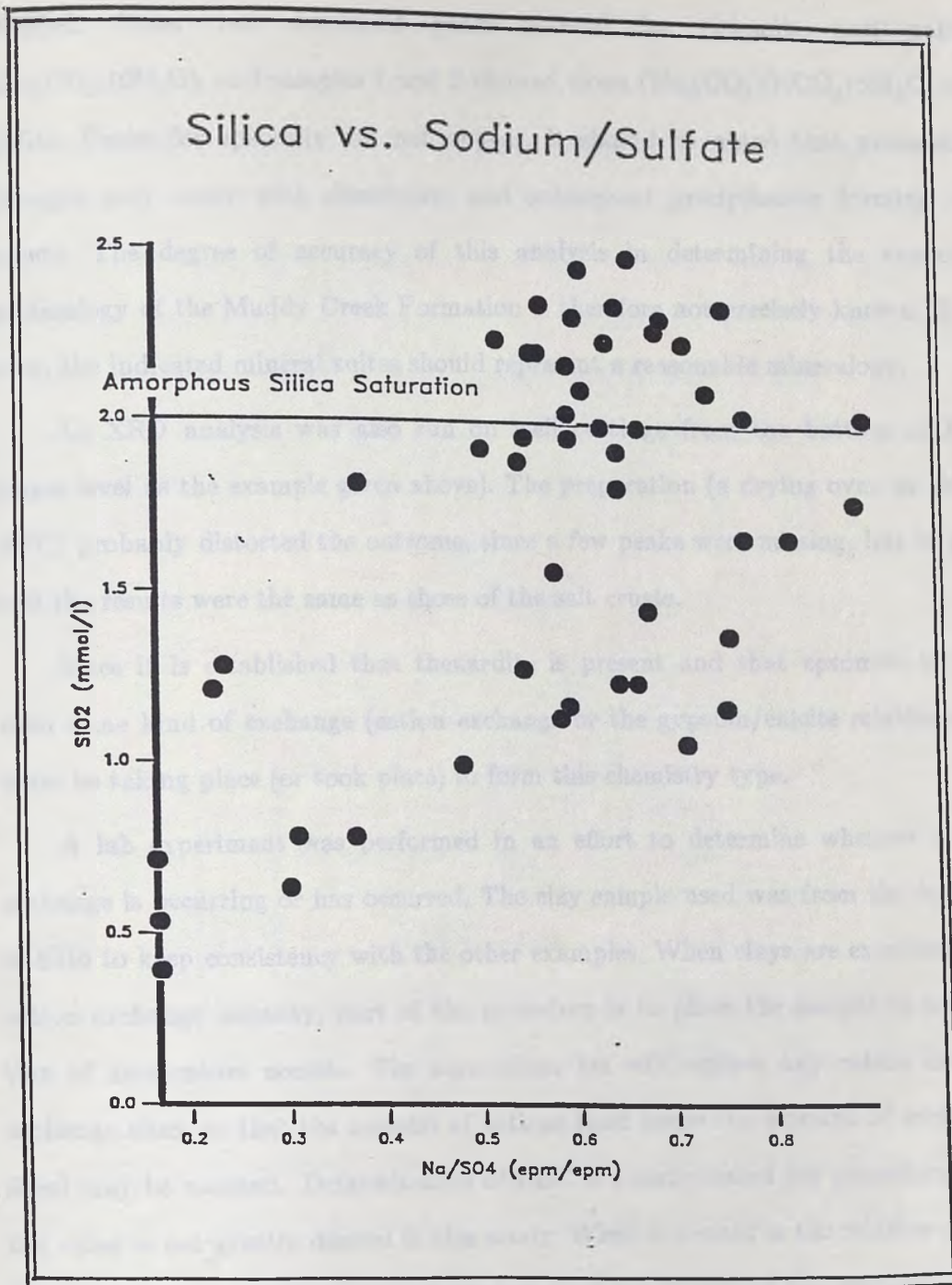


Figure 11. Silica vs. Sodium/sulfate. Waters undersaturated with amorphous silica seem to show a strong correlation.

the baked sample showed anhydrite peaks instead, the presence of gypsum was verified. Other less developed peaks showed for dolomite and natron ($\text{Na}_2\text{CO}_3 \cdot 10\text{H}_2\text{O}$), and samples 1 and 2 showed trona ($\text{Na}_3(\text{CO}_3)(\text{HCO}_3) \cdot 2\text{H}_2\text{O}$) and halite. Peaks for epsomite did not appear. It should be noted that mineralogy changes may occur with dissolution and subsequent precipitation forming salt crusts. The degree of accuracy of this analysis in determining the evaporite mineralogy of the Muddy Creek Formation is therefore not precisely known. However, the indicated mineral suites should represent a reasonable mineralogy.

An XRD analysis was also run on well cuttings from the bottom of EH6 (same level as the example given above). The preparation (a drying oven at about 57°C) probably distorted the outcome, since a few peaks were missing, but in general the results were the same as those of the salt crusts.

Since it is established that thenardite is present and that epsomite is not, then some kind of exchange (cation exchange or the gypsum/calcite relationship) must be taking place (or took place) to form this chemistry type.

A lab experiment was performed in an effort to determine whether cation exchange is occurring or has occurred. The clay sample used was from the bottom of EH6 to keep consistency with the other examples. When clays are examined for cation exchange capacity, part of the procedure is to place the sample in a solution of ammonium acetate. The ammonium ion will replace any cation on the exchange sites, so that the amount of cations (and hence the amount of exchange sites) may be counted. Determination of CEC is a complicated lab procedure, and the value is not greatly desired in this study. What is desired is the relative abundances of sodium, calcium, and magnesium that are occupying the exchange sites. After mixing thoroughly with ammonium acetate, the solution was centrifuged and examined for Na, Ca, and Mg via atomic absorption. This will prove or

disprove the contention that sodium has been exchanged for calcium. Unfortunately, only one well cuttings sample was run, so a conclusion cannot be made for the entire area.

The results of this experiment are given in Table 1. Shown also is a "blank" run in which water was used instead of ammonium acetate. This was done to differentiate between water soluble sources and exchange site sources. Results from the blank run should be subtracted from the acetate run to obtain correct exchange site concentrations. The higher amount of magnesium may be indicative of vermiculite among the clay minerals. Vermiculite has a special preference for magnesium in ion exchange reactions (Bohn et al., 1979).

Table 1. Results of cation exchange experiment.

	Water Run		Ammonium Acetate Run	
	mg/l	epm	mg/l	epm
Na	2.67	0.12	9.85	0.43
Ca	5.56	0.28	195	9.31
Mg	3.30	0.27	157	12.91

Assuming the exchange sites were originally dominated by sodium, cation exchange has virtually gone to completion. This leaves thenardite as the principal source of sodium. If the abundance of thenardite in the Muddy Creek is not thought to be large enough to account for the observed sodium in groundwater, then the only remaining explanation is that the waters are very old and still contain sodium from exchange sites. That is, the sodium derived from cation

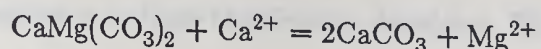
exchange has not yet been flushed out. If this is true, an increase in calcium/magnesium percentages would be expected with time. It is more likely however that the observed sodium is derived from thenardite. If the waters are young, cation exchange must be ruled out. Claiming cation exchange is a common mistake made in studies where an explanation is needed and not enough attention is paid to age of water/sediment interaction.

MAGNESIUM SOURCES

The source of magnesium in all waters of the region is assumed to be dolomite. The Paleozoic carbonates are either classified as dolomite or at least have significant dolomitic character. Dolomite shows up in the Muddy Creek Formation, as the rock is derived in part from the older sediments. There are little or no epsomite present, and the other possible sources-clay minerals, igneous and volcanic rock minerals-are far less soluble (Drever, 1982). Other magnesium carbonate species, such as magnesite (MgCO_3), nesquehonite ($\text{MgCO}_3 \cdot 3\text{H}_2\text{O}$), lansfordite ($\text{MgCO}_3 \cdot 5\text{H}_2\text{O}$) and hydromagnesite ($\text{Mg}_4(\text{CO}_3)_3(\text{OH})_2 \cdot 3\text{H}_2\text{O}$), are rarely important species influencing magnesium in natural water (Hem, 1985).

The random mineralogy of the Muddy Creek Formation described earlier also applies to magnesium sources. In waters where magnesium epm equals or exceeds calcium epm (Coyote Springs Valley, Muddy River Springs, groups 3, 4, 5, and 7), it is likely that dolomite is the major carbonate. When dolomite dissolves, it is most common that the precipitate from such a solution is pure calcite. This is true even with dolomite supersaturation (Hem, 1985). Hem maintains dolomite precipitation will not occur until "a rather high $[\text{Mg}]:[\text{Ca}]$ ratio is reached". This ratio does not exceed 1.6 in the study area. Drever (1982) calls this process the

incongruent dissolution of dolomite, and it explains why magnesium concentration is similar to or exceeding calcium:



As long as there are significant amounts of calcium present (a viable assumption remembering the ubiquitous gypsum), magnesium will stay in solution.

Carbonate and Volcanic Source Rocks

Turning to the Muddy Springs area and southern Coyote Springs Valley, the waters are different but the mysteries are similar. The sodium dominance of the cations is confusing since the Muddy Creek Formation is absent in these areas. As in the Meadow Valley Wash area, sodium outweighs chloride by a significant amount. There is a thin layer of alluvium overlying the carbonates, but it is not considered important since the same chemistry is present in wells hundreds of feet deep. It has been shown that the carbonates are impure, so the associated sediments may have an influence on water chemistry. Evaporite minerals would not be expected in marine sediments, but not only sodium but also sulfate is found in significant concentrations, rivaling bicarbonate. Hem (1985) claims most fine-grained sediments contain abundant sulfides when raised above sea level, and once uplift occurs, they may be readily oxidized to sulfate. Similarly, sodium may be found in these sediments in various forms - in unaltered mineral grains, as an impurity in cementing material, or in soluble salts (Hem, 1985). Though these sediments make up only a small fraction of the Paleozoic sequence, the sodium will accumulate in solution whereas calcium will not.

In Kane Springs Wash, the situation is much simpler. The springs issue from carbonate rocks and show strong calcium-bicarbonate dominance. The

concentrations of other species are practically at background levels. All data point to a very pure limestone source. Willow Spring discharges from undivided Tertiary volcanics, and carries a sodium-bicarbonate chemistry. This is expected from a water issuing from sodium-rich igneous rocks.

Maynard Lake Spring at the head of Coyote Springs Valley has a sodium-bicarbonate chemistry, but with different proportion from Muddy Springs waters. Sodium and bicarbonate are higher, and the other constituents are lower. The geologic map shows a high proportion of volcanic rock in this area (Figure 12), and this may explain the unique chemistry. The only other waters with similar chemistry are well waters near Elgin and Carp in the Meadow Valley Wash north of the study area. These wells are also located in or about the Tertiary volcanics, so this may be a fingerprint chemistry for the geologic unit.

This brings up an important point concerning the regional flow system. If this spring is assumed to be issuing from volcanic rock and is considered a representative regional spring, then Tertiary volcanics, in addition to Paleozoic carbonates, are a contributing factor to the regional water chemistry. There is a high fault density around this spring. By virtue of this faulting, the "deep carbonate" flow system may contain a region of volcanic rock, thus altering the water chemistry. Though one data point hardly verifies a hypothesis, it is another possible explanation for the sodium dominance of Coyote Spring Valley and Muddy Spring waters. North of the volcanic area, springs of Pahrangat Valley show the expected calcium-magnesium-bicarbonate chemistry. Sodium-bicarbonate water is not found on the flowpath until the area in question is reached. South of this zone, all waters are of this type. Unfortunately, there are no wells in this crucial zone, so pump test data and well logs cannot verify this hypothesis.

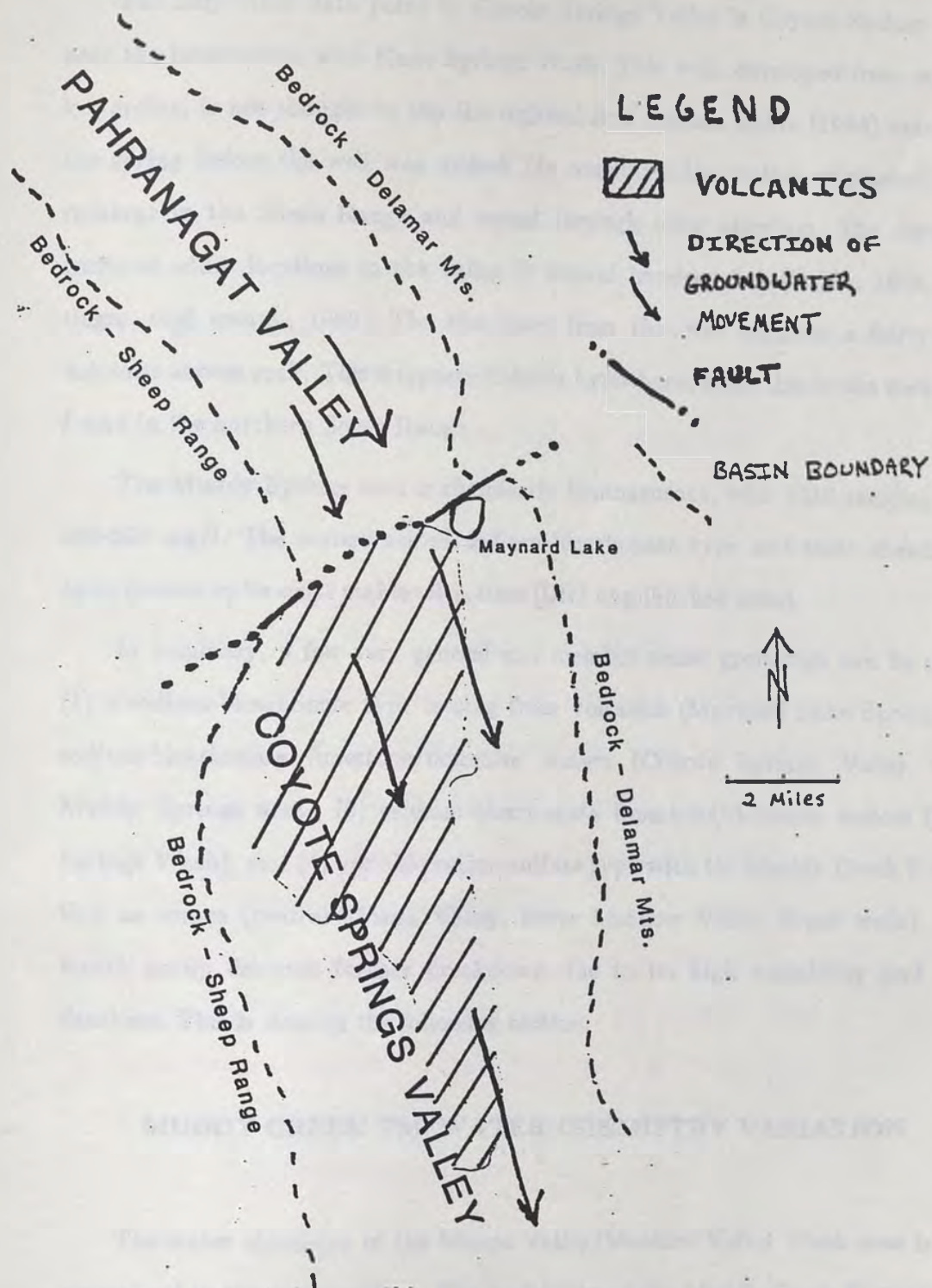


Figure 12. Simplified surface geology map of the junction between Pahranaagat and Coyote Springs Valleys. Only the essential fault is shown: there are many more. Waters passing through this zone are believed to gain sodium, thus explaining the down-gradient chemistry.

The only other data point in Coyote Springs Valley is Coyote Springs Well near the intersection with Kane Springs Wash. This well, developed from a shallow spring, is not thought to tap the regional flow system. Eakin (1964) examined the spring before the well was drilled. He concluded the waters originated from recharge in the Sheep Range and issued through older alluvium. The depth to water at other locations in the valley is several hundred feet (Eakin, 1964, Dettinger, oral comm., 1986). The chemistry from this well suggests a fairly pure dolomite source rock. This supports Eakin's hypothesis, since this is the rock type found in the northern Sheep Range.

The Muddy Springs area is chemically homogeneous, with TDS ranging from 500-650 mg/l. The waters are of sodium-bicarbonate type and their chemistries have proven to be quite stable with time (DRI unpublished data).

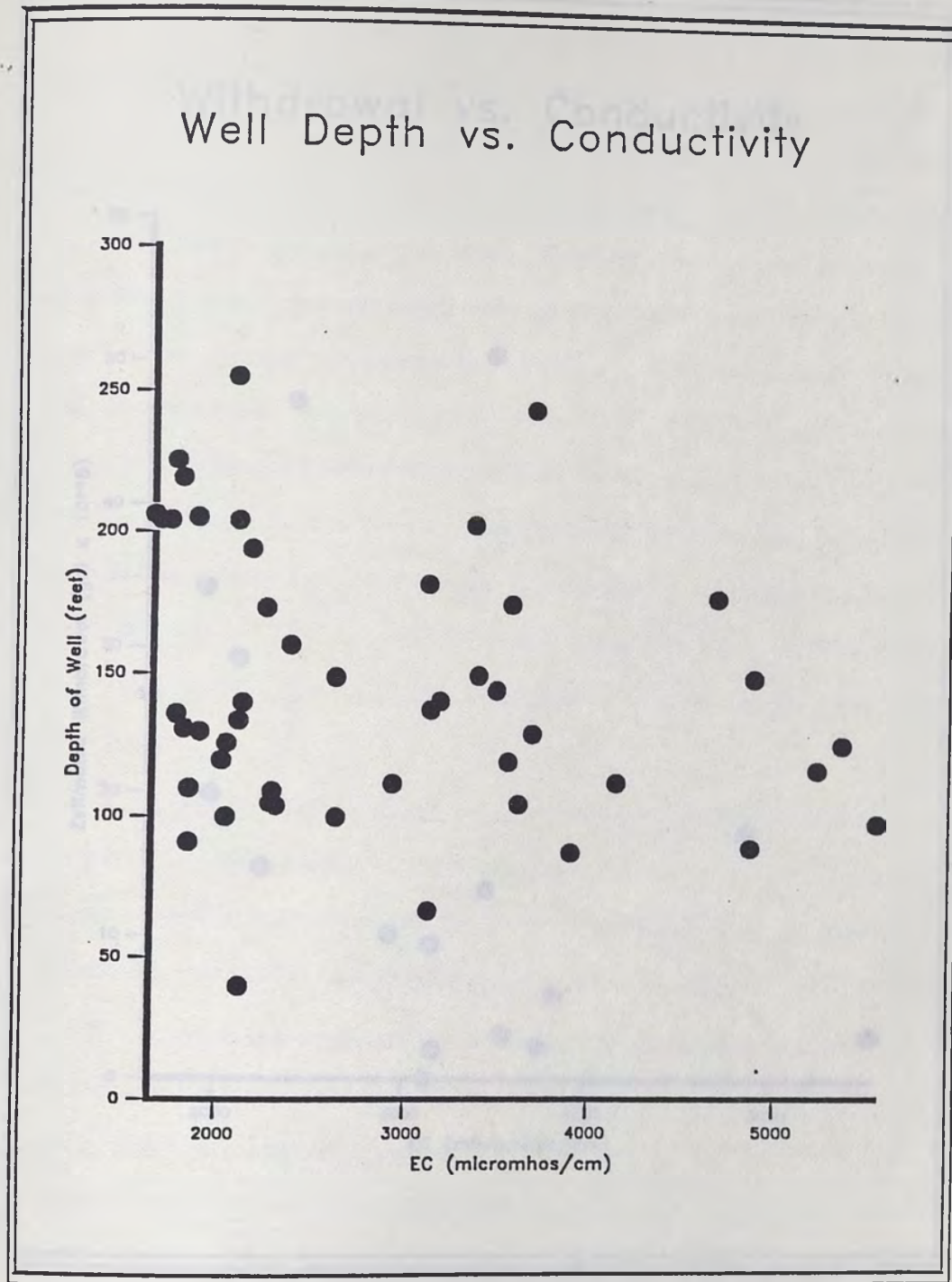
In summary, a few very general end member water groupings can be made: (1) a sodium-bicarbonate type issuing from volcanics (Maynard Lake Spring), (2) sodium-bicarbonate limestone/dolomite waters (Coyote Springs Valley wells, Muddy Springs area), (3) calcium-bicarbonate limestone/dolomite waters (Kane Springs Wash), and (4) variable cation-sulfate type with the Muddy Creek Formation as source (central Moapa Valley, lower Meadow Valley Wash wells). The fourth group deserves further breakdown due to its high variability and large database. This is done in the following section.

MUDDY CREEK FM. WATER CHEMISTRY VARIATION

The water chemistry of the Moapa Valley/Meadow Valley Wash area is very generalized in the introduction. The variability of the Muddy Creek Formation is evident in well logs from Meadow Valley Wash wells. Grain size, consolidation,

mineralogy and color all vary more than might be expected in a six-square mile area. Water chemistry will vary for a given alluvial rock type, and when different rock types are mixed, the chemistry becomes complex.

In the absence of obvious geographic trends in water chemistry, the relationships between electrical conductivity (EC, a salinity indicator) and well depth as well as total well withdrawal were examined. There is very little correlation with well depth, as shown in Figure 13. There is an EC range of 3500 $\mu\text{mhos/cm}$ for wells ranging in depth from 50 to 250 feet. Figure 14 indicates a relationship between conductivity and total withdrawal. Withdrawal was estimated by multiplying average pumping rates by the age of the well. Of course, pumping rates could vary a great deal (especially with old wells). As EC increases, withdrawal decreases logarithmically. This is probably due to the fact that higher pumping rates will tend to flush the sediments of salts rather than allowing for salt accumulation. A steady state seems to occur in the area of 2000 $\mu\text{mhos/cm}$. There are two wells that do not follow this trend: Lewis Well (I45), shown in the upper center of Figure 14, and the Hester/McCormick Well (I10), which was not included in the plot because its high withdrawal (183×10^8 gallons) dwarfs the scale. These wells have the highest values of withdrawal. It is possible that extended pumping results in a reduction of water quality, as Nevada Power Company claims. When a higher quality zone of the Muddy Creek Formation is exhausted, water from a poor quality zone may be pumped. This process would result in a sine wave of water quality over a long period of time. Only an extended time series analysis could prove this.



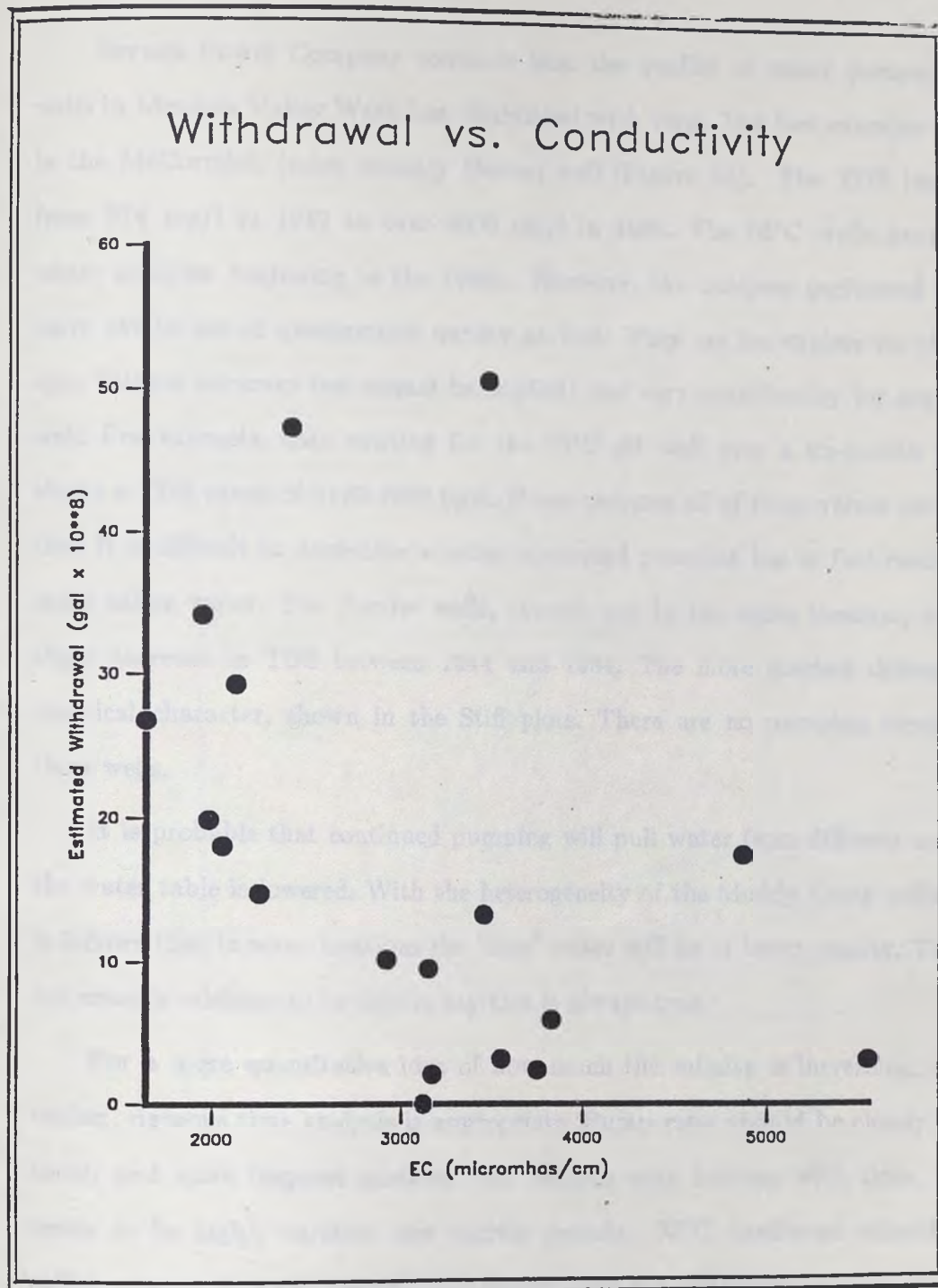


Figure 14. Estimated total withdrawal versus water quality. The graph shows an increase in quality with pumping.

Time Series Analysis

Nevada Power Company contends that the quality of water pumped from wells in Meadow Valley Wash has diminished with time. The best example of this is the McCormick (more recently Hester) well (Figure 15). The TDS increased from 974 mg/l in 1949 to over 4000 mg/l in 1982. The NPC wells have good water analyses beginning in the 1980s. However, the analyses performed in the early 1960's are of questionable quality at best. They are incomplete (so that an epm balance accuracy test cannot be applied) and vary considerably for any given well. For example, data existing for the NPC #1 well over a six-month period shows a TDS range of 1160-1900 ppm. If one assumes all of these values are valid, then it is difficult to determine whether continued pumping has in fact resulted in more saline water. The Farrier wells, though not in the same location, show a slight increase in TDS between 1944 and 1984. The more marked difference is chemical character, shown in the Stiff plots. There are no pumping records on these wells.

It is probable that continued pumping will pull water from different zones as the water table is lowered. With the heterogeneity of the Muddy Creek sediments, it follows that in some locations the "new" water will be of lower quality. There is not enough evidence to be able to say this is always true.

For a more quantitative idea of how much the salinity is increasing, a controlled, rigorous time analysis is appropriate. Pump rates should be closely monitored, and more frequent analyses run. Salinity may increase with time, but it seems to be highly variable over shorter periods. NPC monitored chloride and sulfate over a 5 month period. The results were not conclusive, though the test period was short. With this in mind, it becomes difficult to predict future water

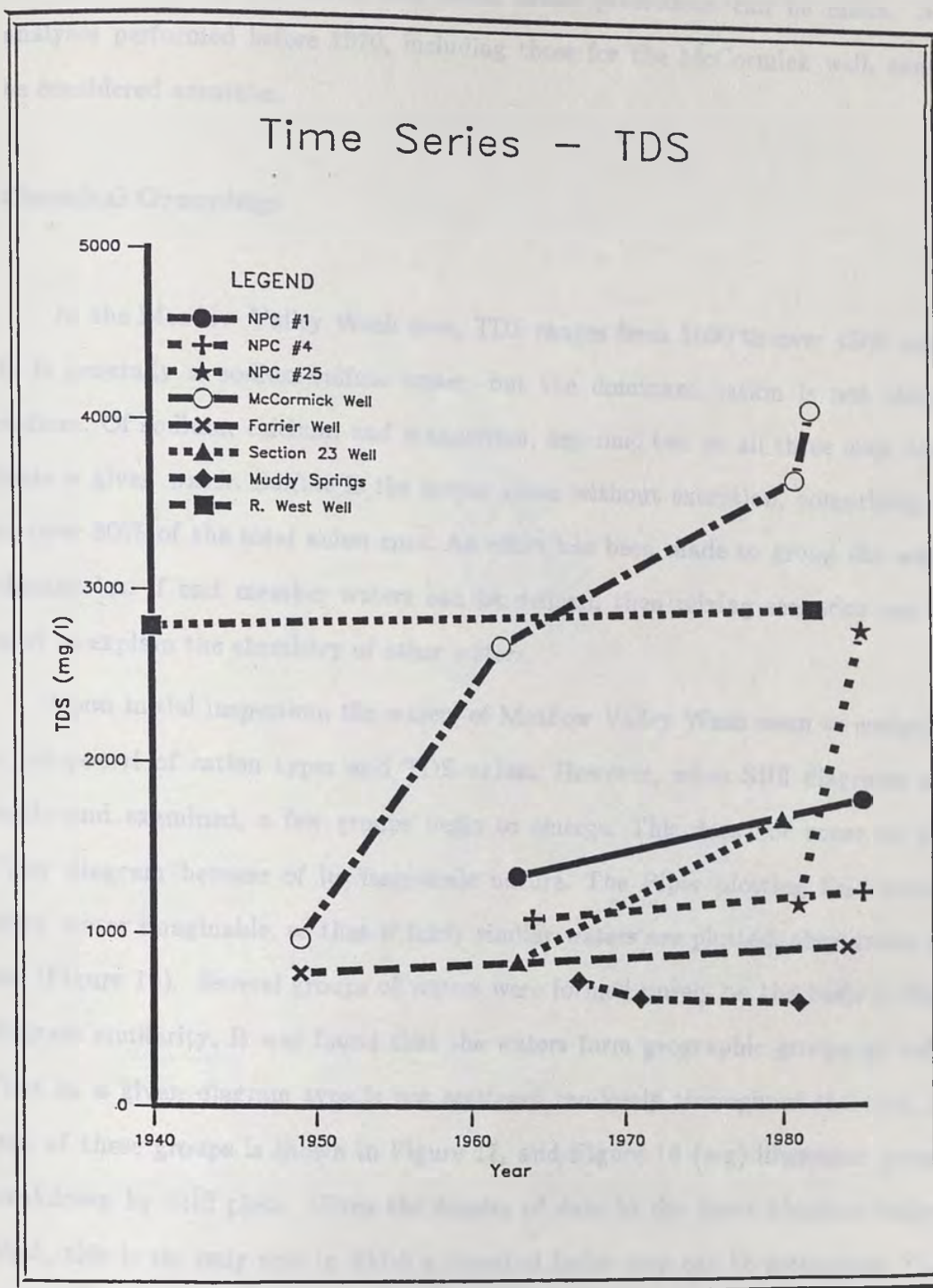


Figure 15. Time series analysis of salinity in Meadow Valley Wash waters.

chemistries. That is, the amount of increase expected in the future is unknown. With more closely monitored well fields, better predictions can be made. Any analyses performed before 1970, including those for the McCormick well, cannot be considered accurate.

Chemical Groupings

In the Meadow Valley Wash area, TDS ranges from 1000 to over 4500 mg/l. It is generally a sodium-sulfate water, but the dominant cation is not always sodium. Of sodium, calcium, and magnesium, any one, two or all three may dominate a given water. Sulfate is the major anion without exception, comprising 65 to over 80% of the total anion epm. An effort has been made to group the water chemistries. If end member waters can be defined, then mixing scenarios can be used to explain the chemistry of other waters.

Upon initial inspection, the waters of Meadow Valley Wash seem to comprise a pot-pourri of cation types and TDS values. However, when Stiff diagrams are made and examined, a few groups begin to emerge. This does not occur on the Piper diagram because of its large-scale nature. The Piper plotting field covers every water imaginable, so that if fairly similar waters are plotted, they group as one (Figure 16). Several groups of waters were formed purely on the basis of Stiff diagram similarity. It was found that the waters form geographic groups as well. That is, a given diagram type is not scattered randomly throughout the area. A map of these groups is shown in Figure 17, and Figure 18 (a-g) illustrates group breakdown by Stiff plots. Given the density of data in the lower Meadow Valley Wash, this is the only area in which a chemical facies map can be attempted. The differences are more subtle, yet repetition of precise geometric form of the Stiff

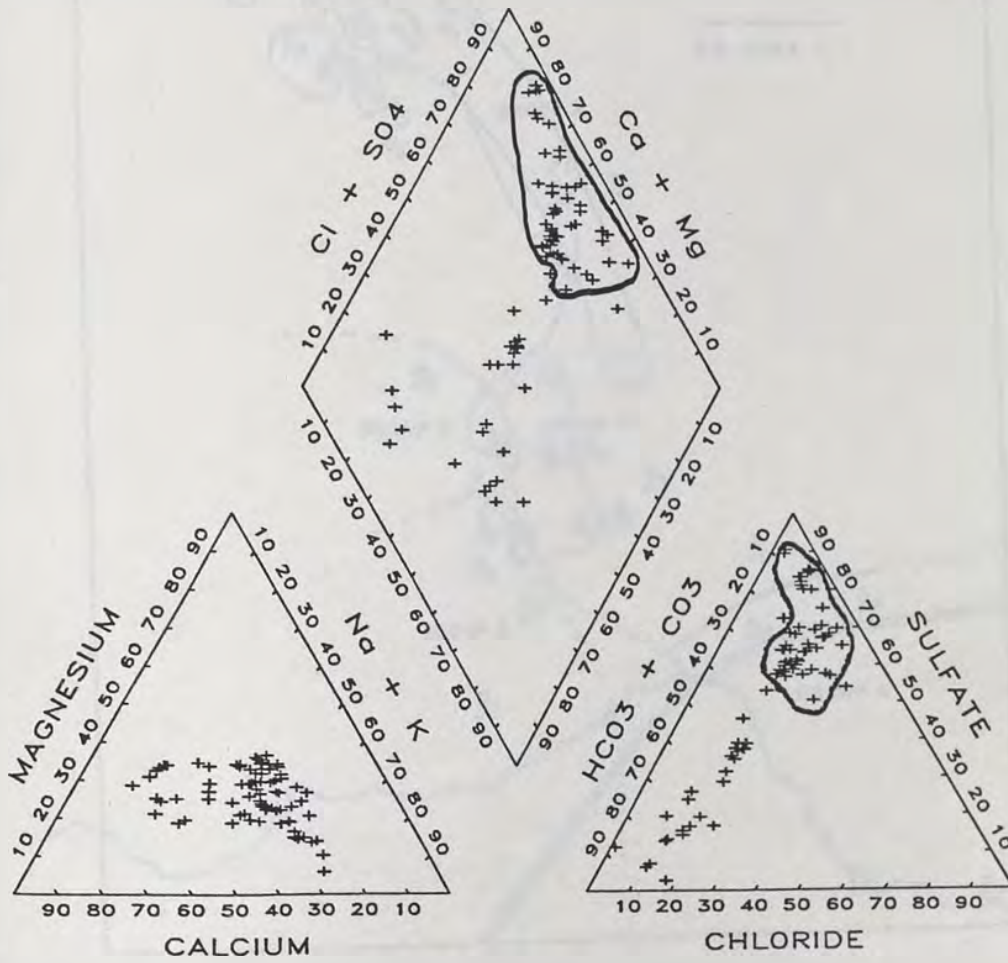


Figure 16. Piper representation of thesis area waters. Waters from Meadow Valley Wash are circled.

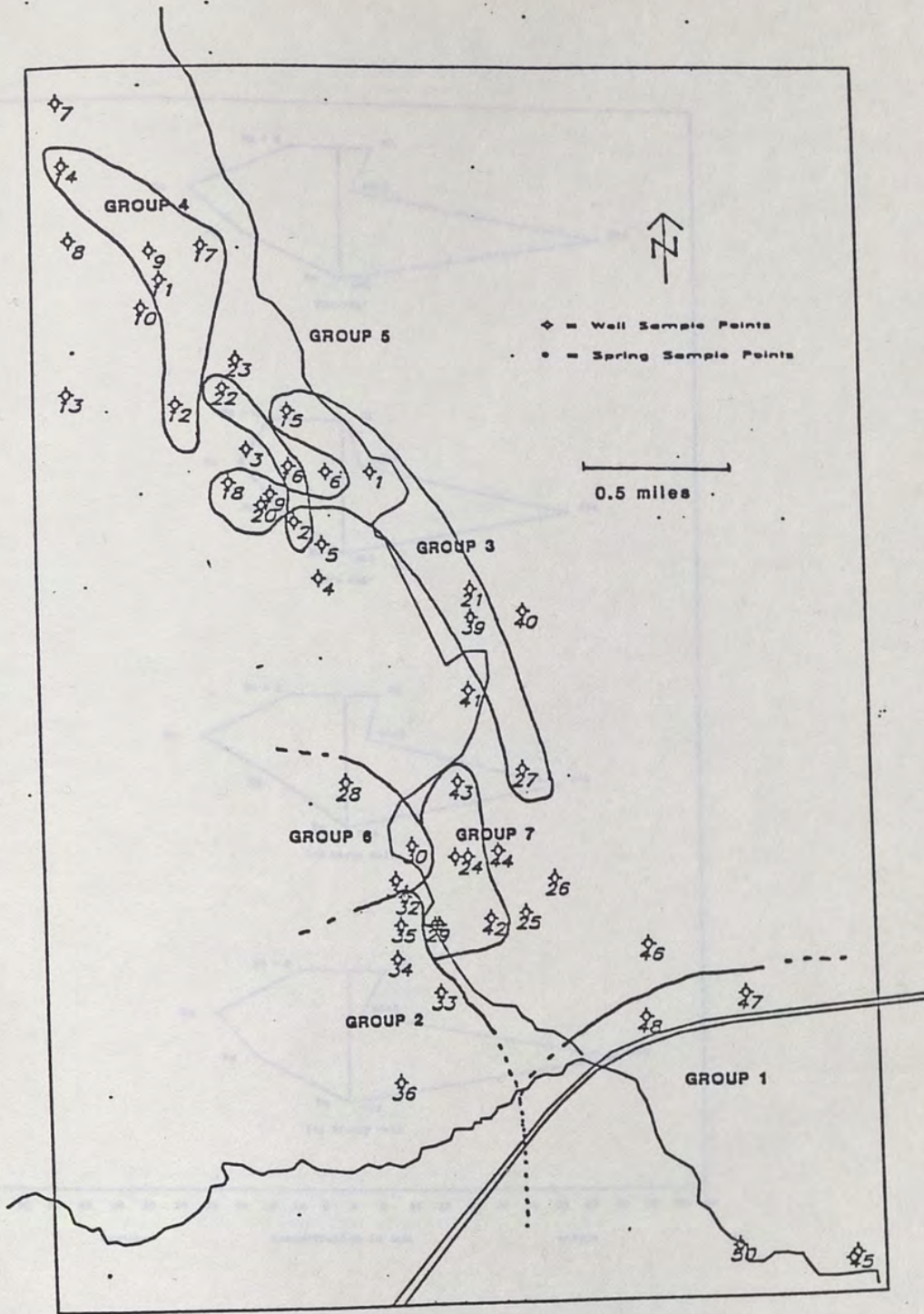


Figure 17. Location of chemical groups 1-7. Groups are based on Stiff diagram type shown in Figure 18.

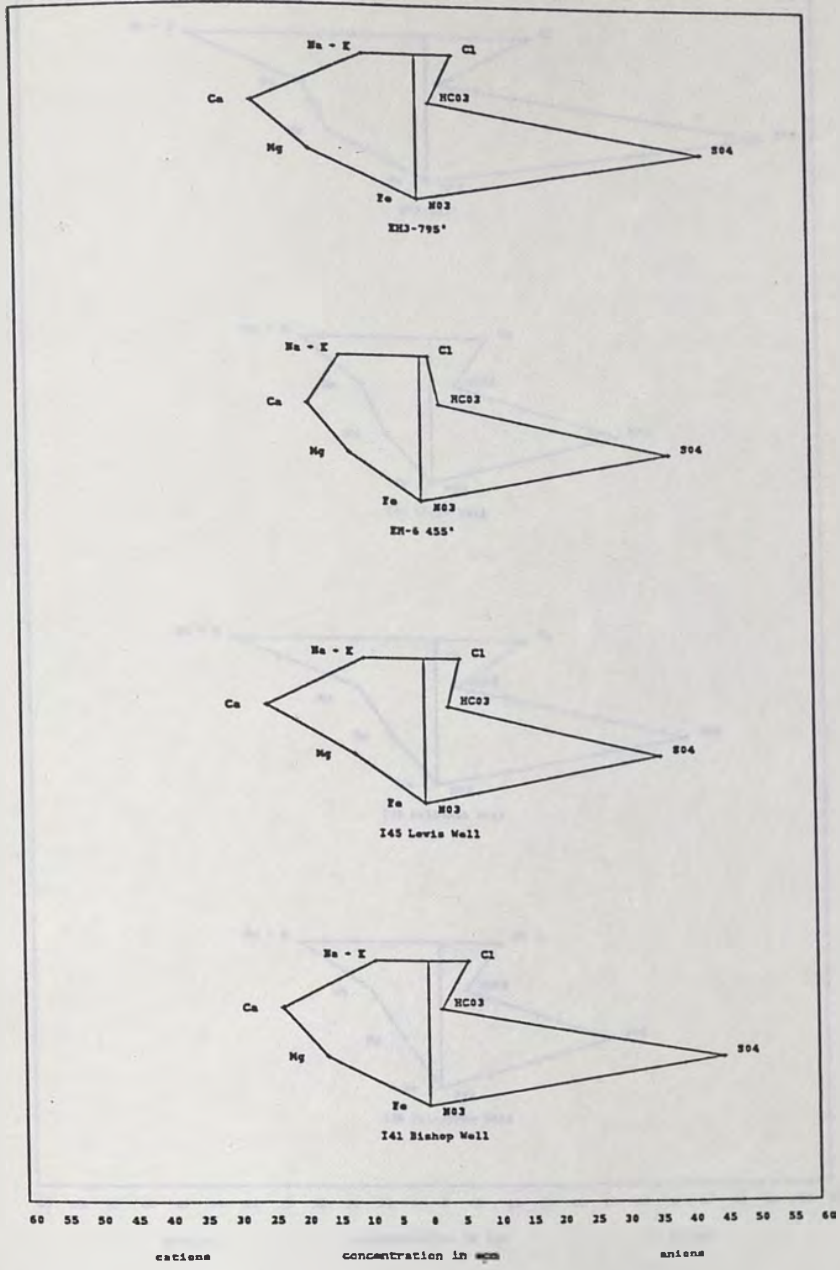


Figure 18 (a). Group 1: high TDS calcium-sulfate type. Waters of this type are found only east of Meadow Valley Wash (excepting EH1).

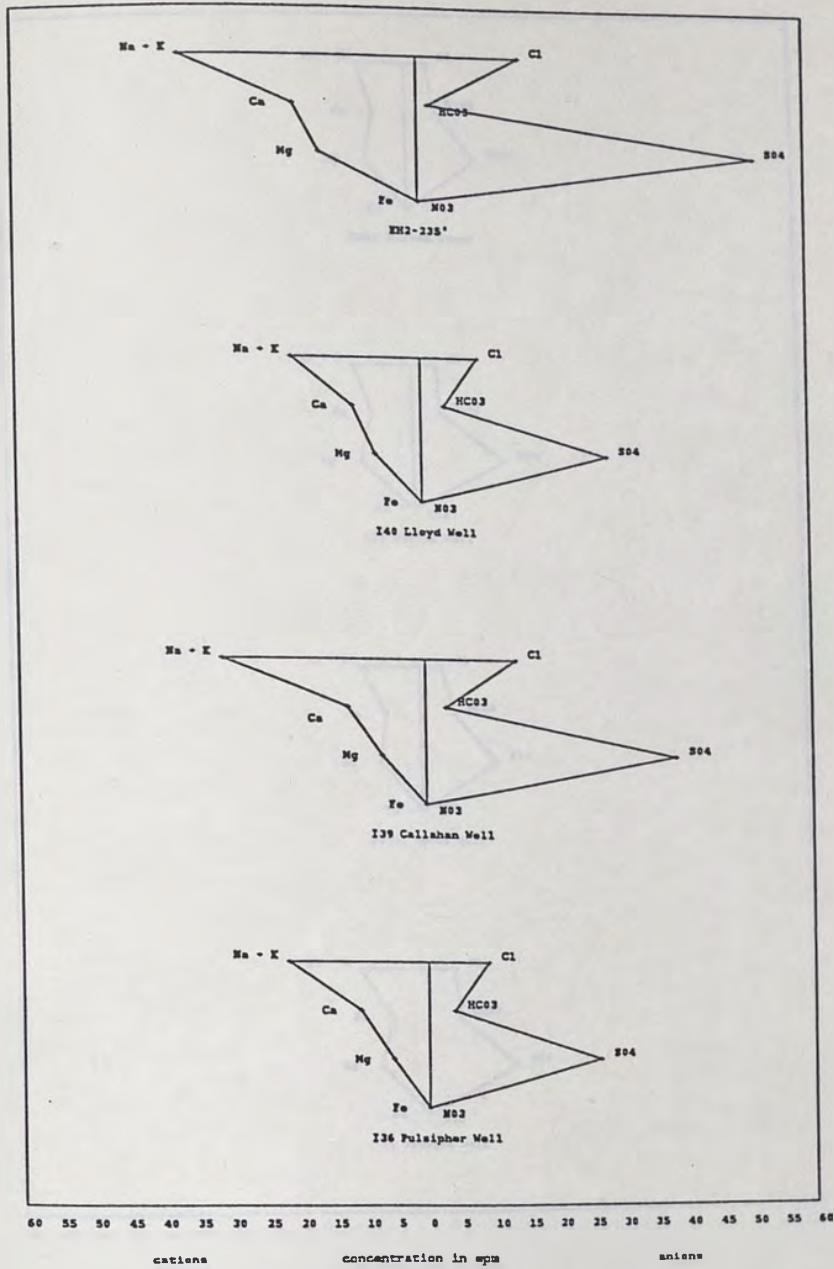


Figure 18 (b). Group 2: high TDS sodium-sulfate type. This water type is common only west of Meadow Valley Wash.

SE ROA 37644

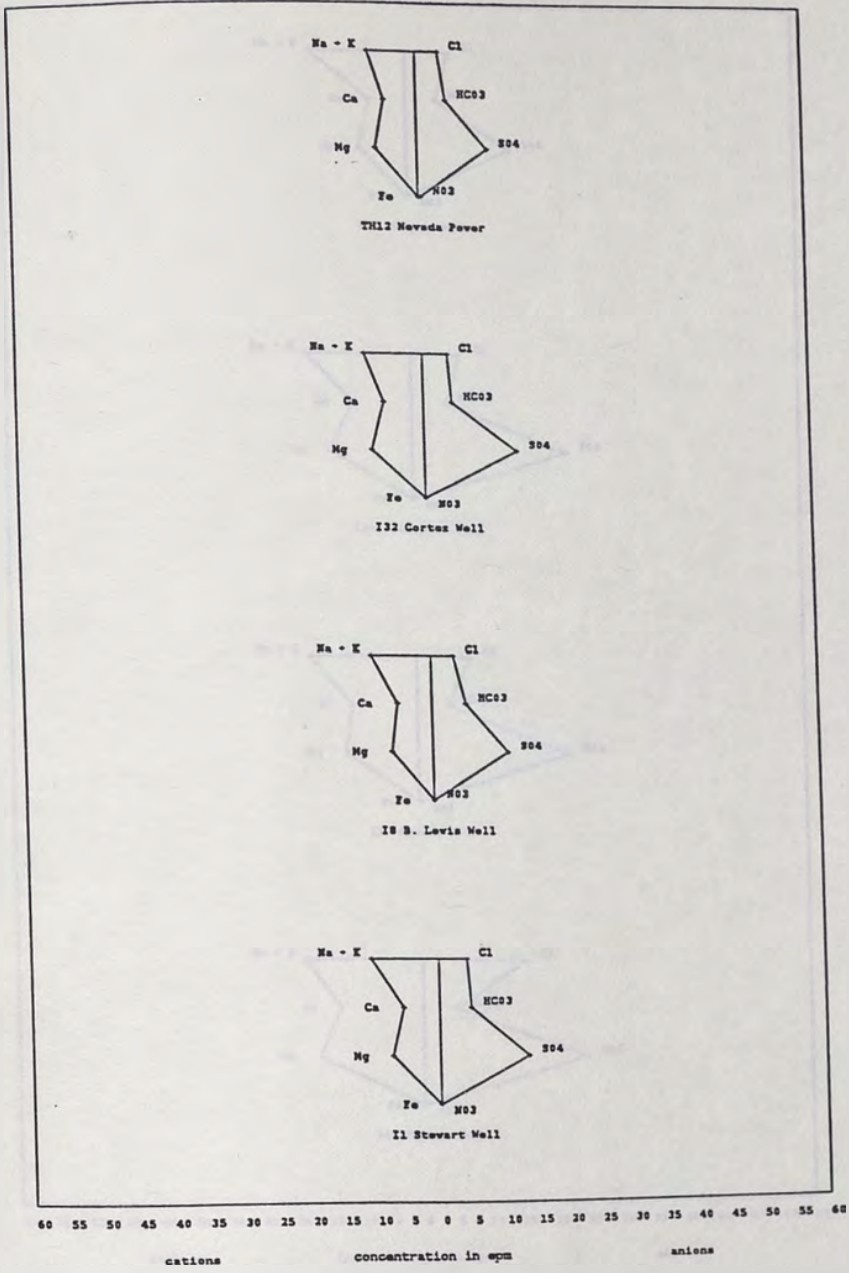


Figure 18 (c). Group 3: A lower (~1200 mg/l) TDS water, with Na>Mg>Ca. Also note that HCO₃>Cl.

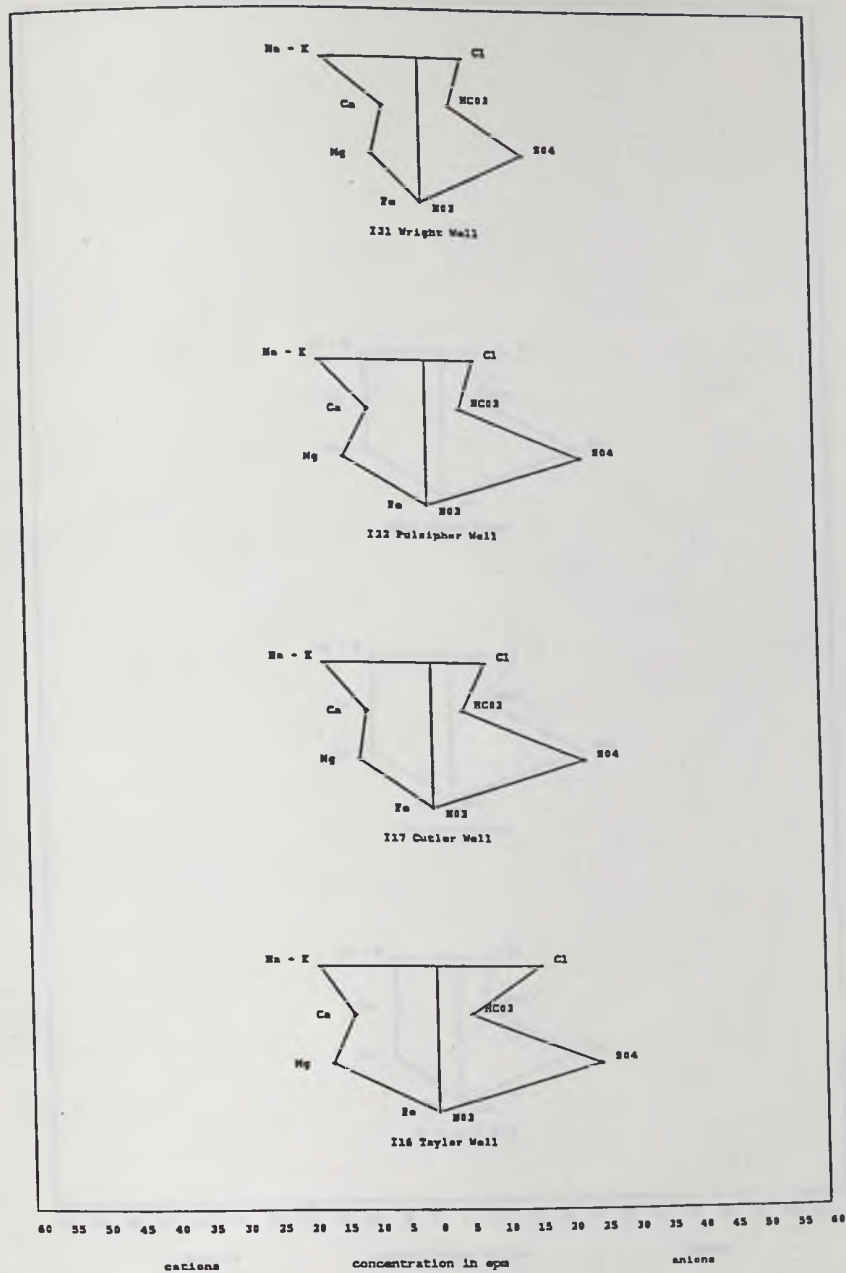


Figure 18 (d). Group 4: Similar to group 3 only with higher TDS (compare diagram sizes) and $Cl > HCO_3$.

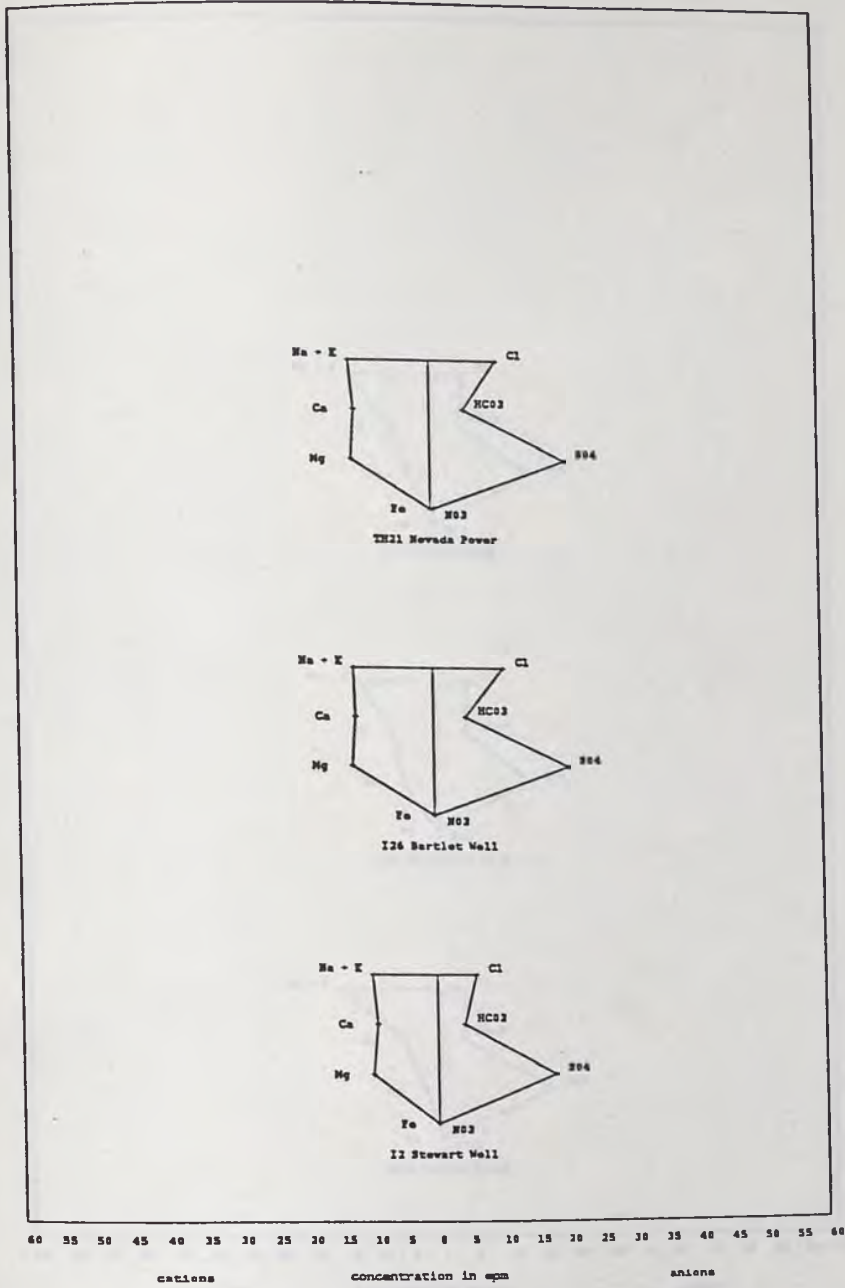


Figure 18 (e). Group 5: No clear cation dominance. TDS similar to Group 4.

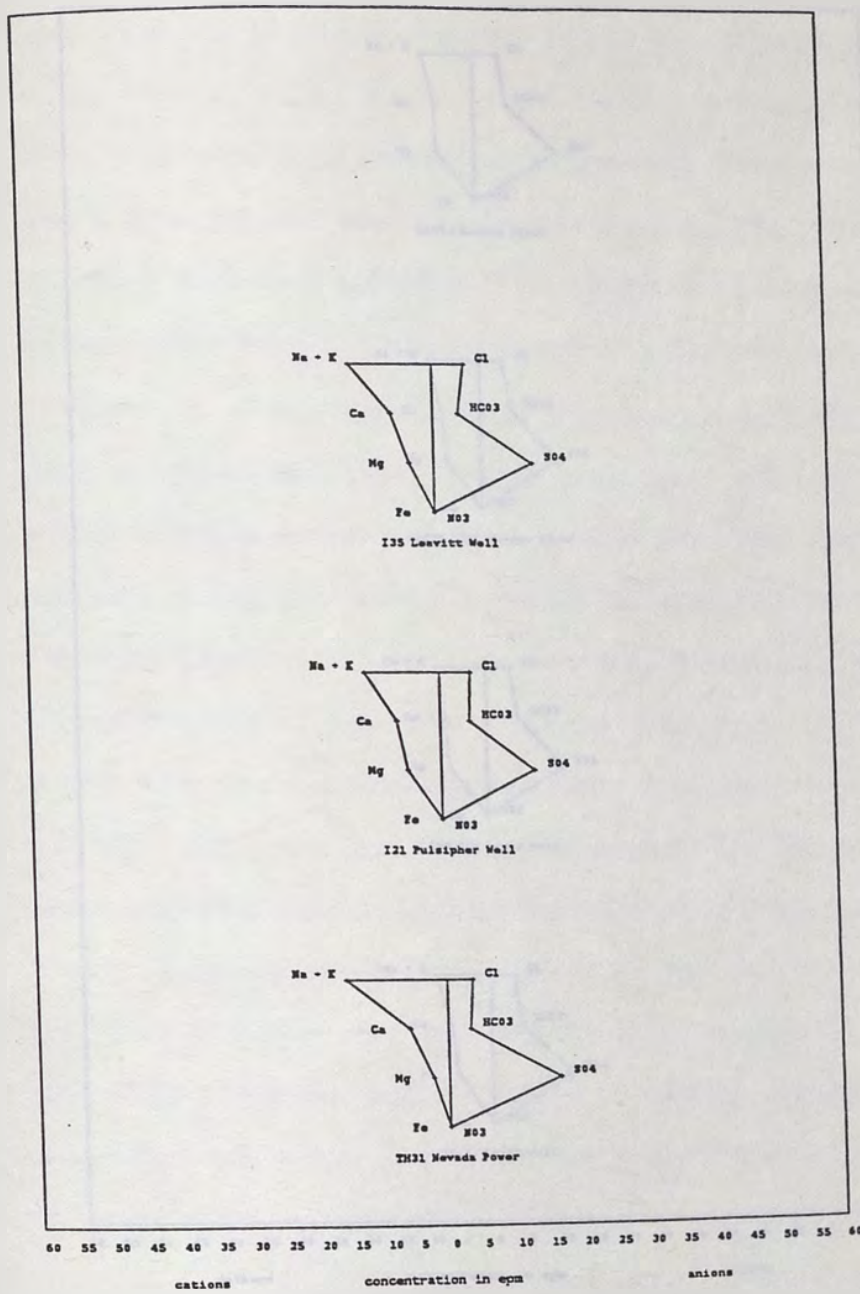


Figure 18 (f). Group 6: Distinguished by $\text{Na} > \text{Ca} > \text{Mg}$, and $\text{Cl} > \text{HCO}_3$.
 This group shows a stronger sodium dominance than Group 7,
 as well as a slightly higher TDS.

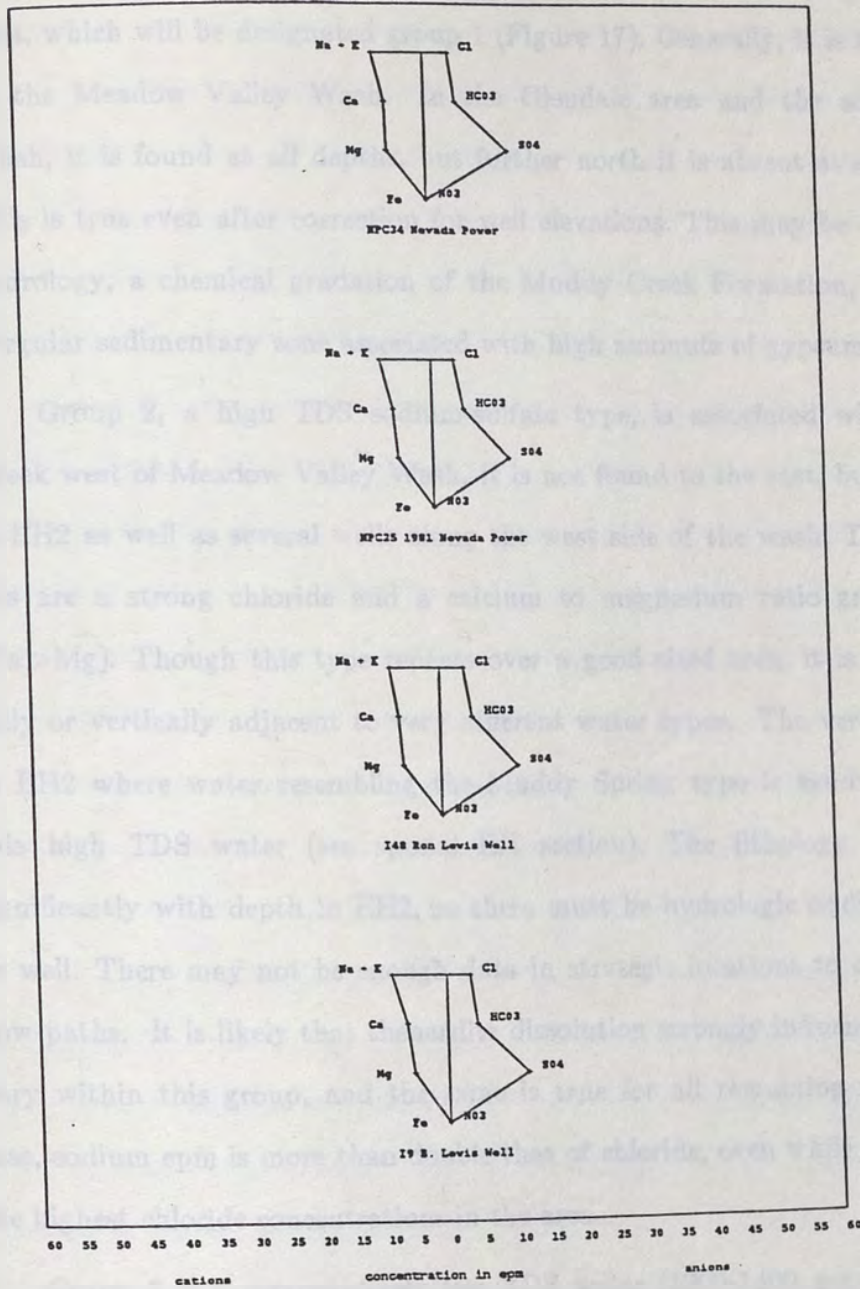


Figure 18 (g). Group 7: Similar to, but distinguished from Group 6 by $Na > Ca = Mg$, and $HCO_3 > Cl$. The groups are located adjacent to one another (Figure 17), and differences are subtle.

diagrams cannot go unnoticed.

An important group is a high TDS, calcium-sulfate water in the Glendale area, which will be designated group 1 (Figure 17). Generally, it is found only east of the Meadow Valley Wash. In the Glendale area and the southern Weiser Wash, it is found at all depths, but further north it is absent at shallow depths. This is true even after correction for well elevations. This may be due to complex hydrology, a chemical gradation of the Muddy Creek Formation, or possibly an irregular sedimentary zone associated with high amounts of gypsum.

Group 2, a high TDS sodium-sulfate type, is associated with the Muddy Creek west of Meadow Valley Wash. It is not found to the east, but has appeared in EH2 as well as several wells along the west side of the wash. Two characteristics are a strong chloride and a calcium to magnesium ratio greater than one ($Ca > Mg$). Though this type repeats over a good sized area, it is found horizontally or vertically adjacent to very different water types. The vertical example is in EH2 where water resembling the Muddy Spring type is sandwiched between this high TDS water (see special EH section). The lithology does not vary significantly with depth in EH2, so there must be hydrologic oddities in the area as well. There may not be enough data in strategic locations to define the many flow paths. It is likely that thenardite dissolution strongly influences water chemistry within this group, and the same is true for all remaining groups. In each case, sodium epm is more than double that of chloride, even while the waters have the highest chloride concentrations in the area.

Group 3 is a comparatively low TDS water (1200-1400 mg/l) distinguished by $Na > Mg > Ca$ order of cation concentration and that $HCO_3 > Cl$. Whether HCO_3 is greater or less than Cl concentration seems to be dependent on TDS. Due to solubility constraints of calcite, bicarbonate concentrations occupy a smaller

range. Since mineral precipitation does not stop chloride from accumulating in solution, a high $\text{Cl}:\text{HCO}_3$ ratio generally indicates greater amounts of evaporite minerals in a given group area. Since the TDS is low in this group, the ratio is low. The ratio of calcium to magnesium probably parallels the gypsum to carbonate ratio in the sediments. In the absence of high amounts of gypsum, calcium will be more limited than magnesium in solution due to the incongruent dissolution of dolomite (discussed in the SOURCES OF DISSOLVED SALTS section). The ratio will increase, however, as gypsum begins to dominate the mineralogy.

Group 4 has a similar cation relationship to group 3, but the TDS is higher (1700-2400mg/l). With the higher TDS, chloride is greater than bicarbonate as predicted in the above discussion. Based on water chemistry inferences, the mineralogy contains a greater amount of evaporites, with carbonates dominating gypsum and, as always, thenardite present in significant amounts, giving a sodium-sulfate character to the water.

Group 5 is distinguished by its mixed cation nature ($\text{Na}=\text{Ca}=\text{Mg}$). The chemistry implies that this small zone contains more gypsum and less thenardite than group 4, while the salinity of the water remains constant.

In Group 6, $\text{Na} > \text{Ca} > \text{Mg}$ and the TDS range is intermediate (1500-1700mg/l). The mineralogy implied by this chemistry seems the same as that of group 2, only the TDS is much lower. Since group 2 lies immediately to the south, it would seem logical to assume this evaporite suite increases its dominance of the lithology in a southward direction.

Group 7 is similar to group 3 in almost every way, except that calcium nearly equals magnesium in this case. By the previously defined line of thinking, this indicates an increased gypsum presence. A southern trend is again noted, as gypsum completely takes over in group 1 to the south. EH8 was drilled in this

group's region, as was NPC well number 1. These deeper wells (244 ft. and 480 ft., respectively) show a greater gypsum influence, and it is assumed that the same chemistry would emerge if NPC 25 and 34 were drilled deeper. A typical group 7 chemistry shows up in EH8 at 115 ft. and Ca-SO₄ water takes over at 175 ft. (see EH section).

Figure 17 resembles a geologic map more than a hydrologic map, with overlapping groups and no definite evolutionary trend. This is explained by the history of the Muddy Creek Formation. These water groups may be indicative of superimposed sedimentary zones (and respective mineralogies).

As a different form of classification, saturation indices were calculated for each group using WATEQ (Table 2). As stated before, the SI values for calcite and dolomite varied with pH/alkalinity and were determined to be unreliable. The gypsum SI values were more stable. Generally, the groups show distinct ranges that further support the breakdown. The values are shown not for their geochemical significance, but as a way to further delineate the groupings.

These groups are not designed to show a flowpath. On the contrary, they give further insight into how complex the flow may be. A strong argument is made for local water mixing with the principal southward-flowing groundwater of the Meadow Valley Wash. The amount of mixing is difficult to determine. Several small ephemeral streams flow into the wash, suggesting a similar groundwater movement. Saline waters from isolated beds to the east and west could be mixing. The facts that group 1 occurs only to the east and group 2 only to the west support this idea. An attempt was made to simulate water chemistry evolution between the groups, but no computer-generated scenario was chemically possible.

Another scenario that may be just as valid is sluggish southward flow through highly variable mineralogy. The complex bedding in the Muddy Creek

Table 2. Comparison of gypsum saturation indices and TDS among chemical groups.

	SI(gypsum)	TDS
Group 1		
I45	-.09	2935
I46	-.16	2560
I41	-.07	3333
EH7(555')	-.12	2930
EH6(455')	-.20	2765
Average	-.13	2905
Group 2		
I39	-.35	3534
I42	-.32	3402
I13	-.16	4513
EH2(235')	-.14	4528
I38	-.43	2714
I40	-.45	2594
Average	-.31	3548
Group 3		
I8	-.91	1342
I15	-.83	1432
I25	-.85	1936
I1	-.87	1484
I32	-.85	1445
I33	-.81	1459
I34	-1.00	1325
TH12	-.99	1170
TH7	-.91	1245
Average	-.89	1426

	SI(gypsum)	TDS
Group 4		
I22	-.70	2351
I31	-.86	1743
I16	-.58	2437
I17	-.61	2170
Average	-.69	2175
Group 5		
TH21	-.53	2249
I26	-.53	2263
I2	-.50	2220
Average	-.52	2244
Group 6		
TH31	-.77	1617
I21	-.77	1541
I35	-.71	1725
Average	-.75	1628
Group 7		
I9	-.81	1377
I48	-.86	1276
NPC25(1981)	-.88	1194
NPC34	-.86	1323
Average	-.85	1293

Formation has already been discussed. If flow rates are assumed to be low, then water chemistry from a given well will reflect only local mineralogy. This is not an unrealistic assumption given the low gradients and hydraulic conductivities.

The matter is further complicated by the fact that an upward gradient has been observed in one part of the formation (Zimmerman et al., 1982). Though vertical flow has certainly not been the case in all wells penetrating the Muddy Creek, it may explain chemical anomalies in certain areas.

There are some wells that do not fall into any of these categories. This should not be surprising, since the system's complexity has already been established. Some of these wells are located adjacent to ponds and corrals, which may influence the well water chemistry if the depth is not too great. Also, the wells were constructed differently and to varying degrees of success. The amount of water pumped from a given well varies substantially. All of these factors could partially explain water chemistry variations.

DRI EXPLORATION HOLES AND ISOTOPES

A special section will be given for the exploration holes (EH 1-8) drilled by DRI. They are unique in that they provide a vertical chemical profiles and that they make up the bulk of the regional isotope data. The logs and chemical profiles are shown in Figures 19 a-g.

EH1 and 2, drilled around the NPC power plant and separated by less than 1.5 miles, are testimony to the vertical and horizontal variability of the Muddy Creek Formation. EH1 was drilled to a depth of 295' and the water sample from this depth shows a group 1 (Ca-SO₄) type. Samples from a similar elevation in EH2 are group 2 (Na-SO₄) waters, a significant difference. As mentioned before, a

DEPTH

0'

Qal: Fine tan sand with a few clay chunks. Turns to reddish brown silty clay at 25'.

65'

Tmc: Muddy Creek Formation. Claystone, sandstone, siltstone; mostly claystone with sand, becoming 100% fine/med. sand at 275'.

T.D. 295'

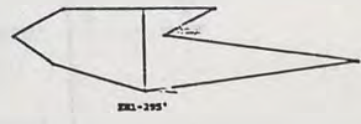
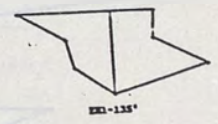
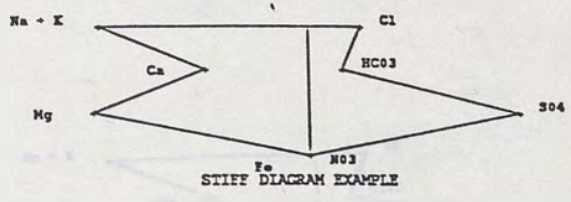


Figure 19 (a). Generalized lithologic log and chemical profile of EHL, Moapa Valley.

Tmc: Red-brown claystone with varying amounts of sand, silt, and clay.

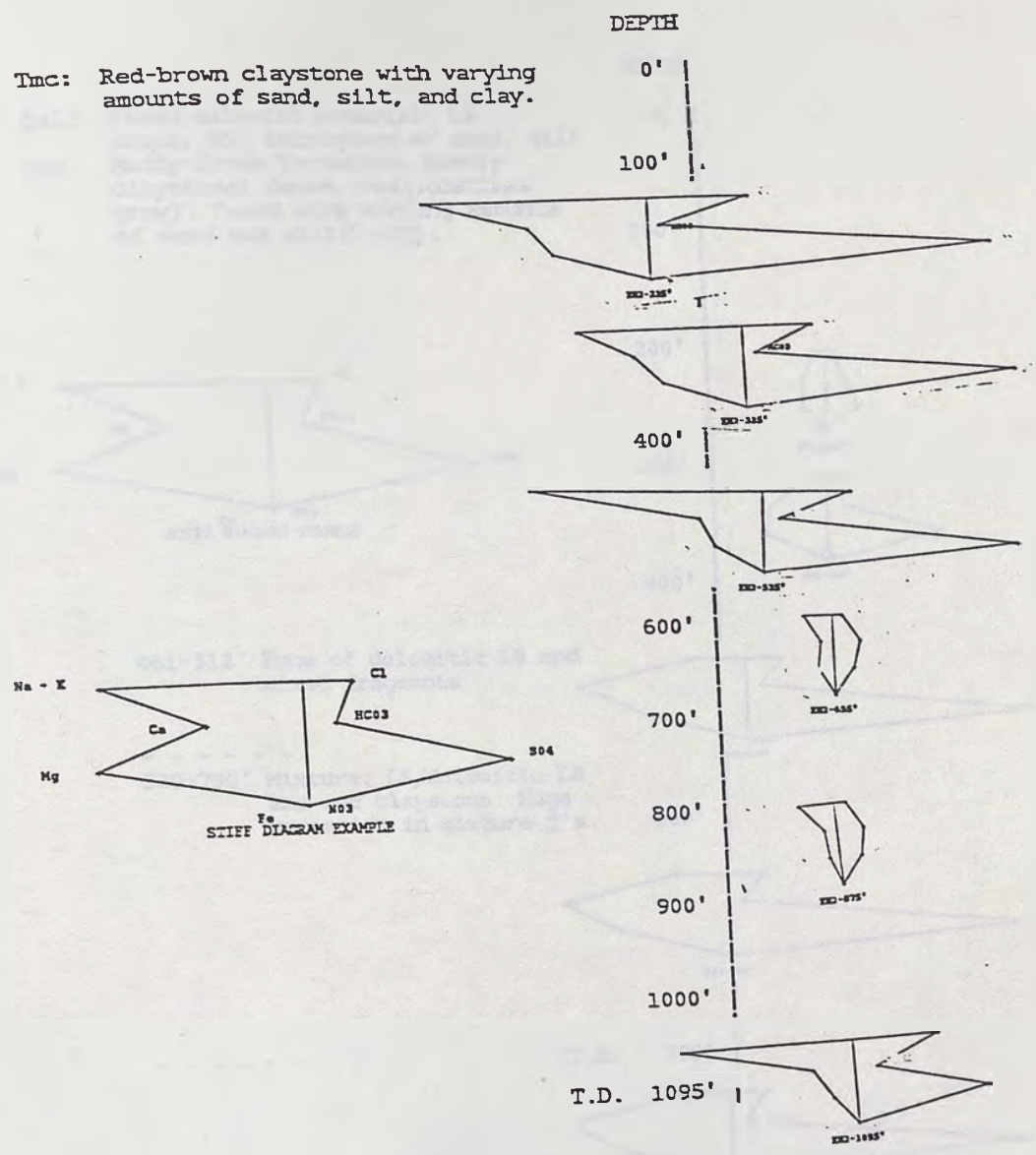


Figure 19 (b). Generalized lithologic log and chemical profile of EH2, Moapa Valley.

Qal: Mixed alluvial material- LS chips, SS, intrusives w/ sand, silt
 Tmc: Muddy Creek Formation. Mostly claystone: dense, red (sometimes gray). Found with varying amounts of sand and silt (5-40%).

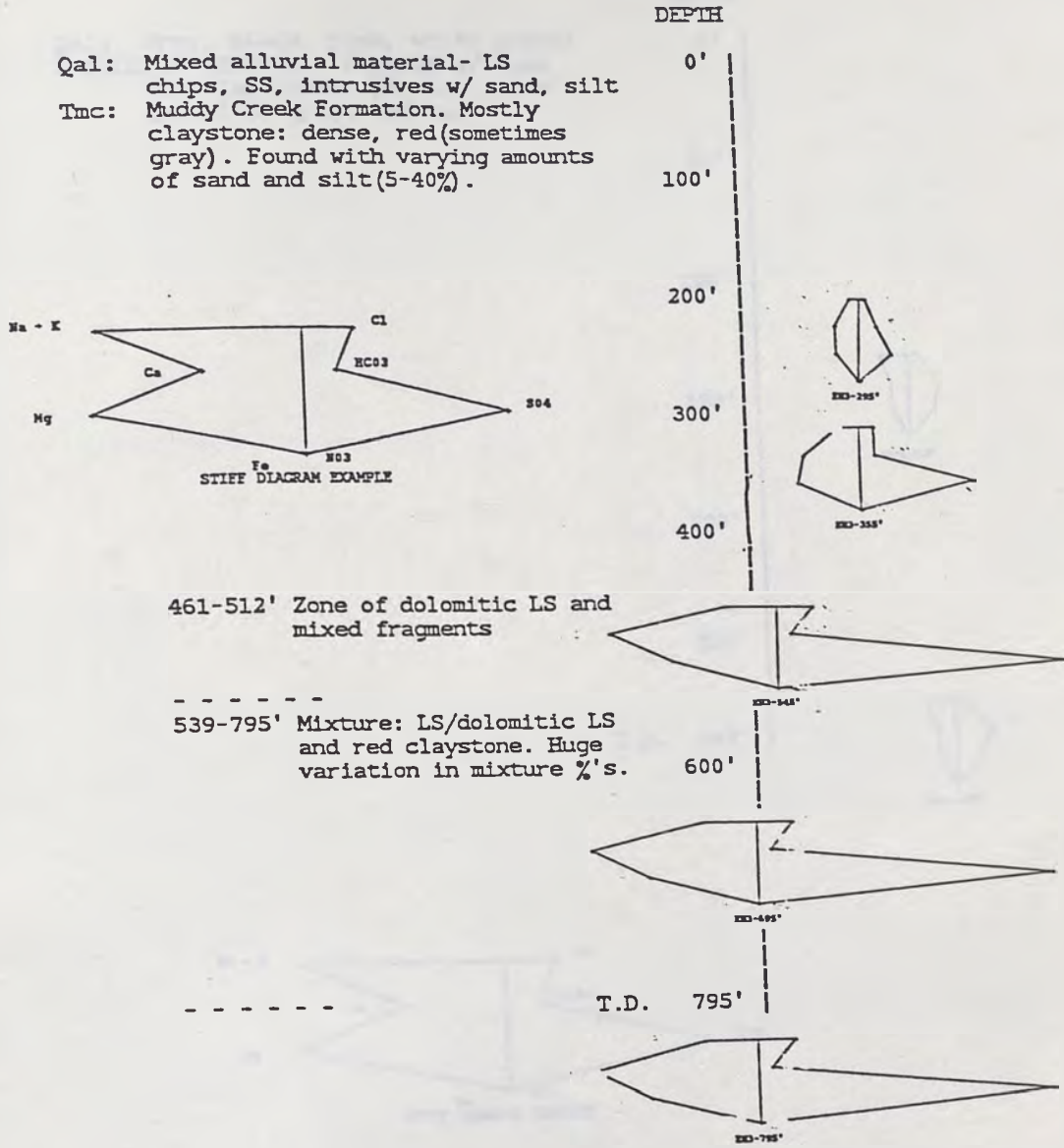


Figure 19 (c). Generalized lithologic log and chemical profile of EH3, Weiser Wash.

Qal: Gray, black, pink, white gravel
 PALEOZOIC BEDROCK: Pink LS w/ some
 red clay zones. LS also found
 in white, gray, and tan.

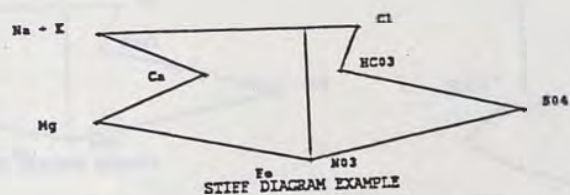
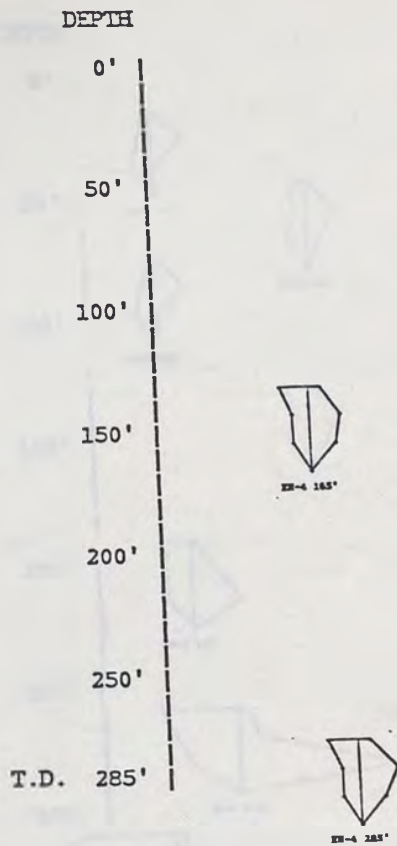


Figure 19 (d). Generalized lithologic log and chemical profile of EH4, Muddy Springs area.

Tmc: Fine sand and silt with clay and occasional gravel.

coarse sand also included

LS chips included (red-gray)

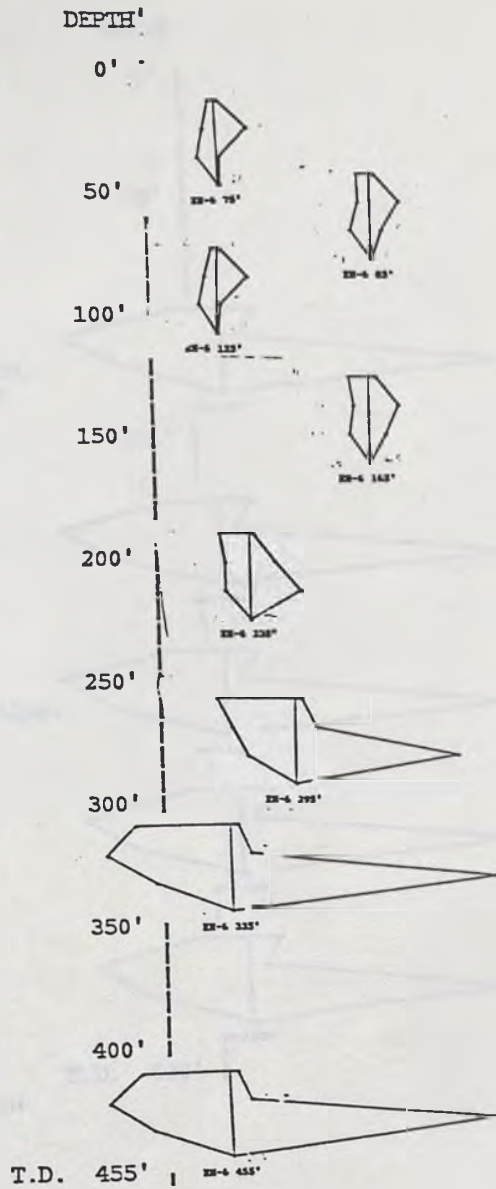
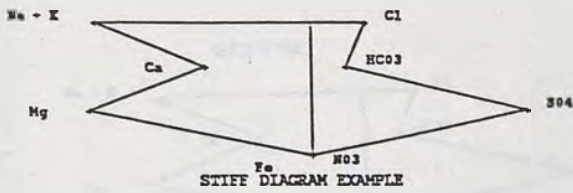


Figure 19 (e). Generalized lithologic log and chemical profile of EH6, Meadow Valley Wash.

Qal: LS gravels, silt, clay.
 Tmc: sand, silt, clay
 70-80% clay

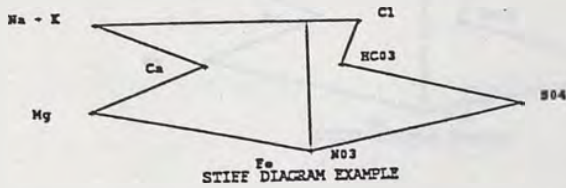
60-90% sand

Pink-gray LS/dolomite with sand,
 silt, and clay. Isolated chert
 and calcite beds.

80% red clay, 20% mudstone chips.

LS/mudstone mixtures to 555'

shales



DEPTH

0'

75'

225'

EH-7 175'

EH-7 348'

EH-7 443'

EH-7 545'

EH-7 555'

T.D. 620'

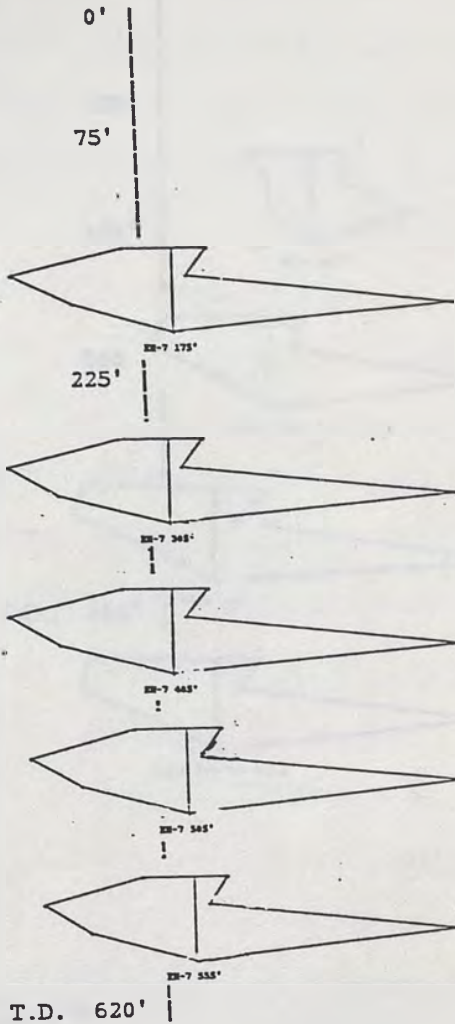


Figure 19 (f). Generalized lithologic log and chemical profile of EH7, Weiser Wash.

Qal: Alluvium- mostly clay(80-100%)
with some sand and silt

Tmc: sand, silt, and clay with LS/
volcanic gravel

predominantly LS/volcanic gravel
with sand and clay

T.D. 244'

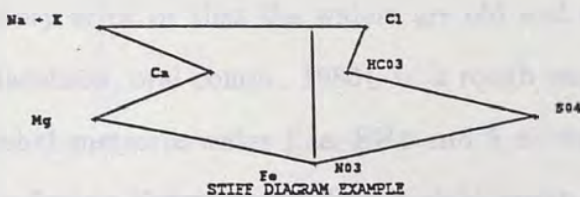
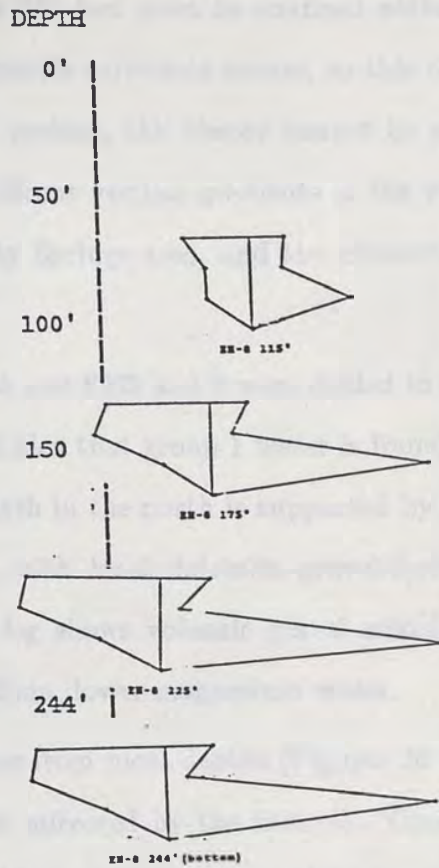


Figure 19 (g). Generalized lithologic log and chemical profile of EHS, Meadow Valley Wash.

low TDS water similar to Muddy Springs type is found vertically between group 2 waters in EH2. This is believed to come laterally from carbonate rocks to the west. For this to be true, a thickness of about 250 feet must be confined without vertical gradients. EH2 is two miles from a possible carbonate source, so this condition must be present over that distance. At present, this theory cannot be proven nor refuted. Obviously there are not significant vertical gradients in the well. EH4, 5a, and 5b were all drilled in the Muddy Springs area, and the chemistries all reflect this water type.

EH6 and 8 are from Meadow Valley Wash and EH3 and 7 were drilled to the east in Weiser Wash. The previously described idea that group 1 water is found at all depths in the south and only at greater depth in the north is supported by the Weiser Wash data. EH6 also supports this, with local dolomite gravel-derived water overlying more saline water. The EH8 log shows volcanic gravel mixed in, which is a possible explanation of the high sodium, lower magnesium water.

Deuterium and ^{18}O were run on EH waters from most depths (Figures 20 and 21). The chemical complexity of the region is mirrored by the isotopes. There is some doubt concerning the accuracy of the data, as some points plot above the meteoric water line. This is beyond normal scatter, and may be explained by laboratory error or that the waters are old and scatter around an ancient water line (Jacobson, oral comm., 1986). In a rough sense, EH3, 7, and 8 group around the global meteoric water line. EH4 and 5 as well as Muddy Springs and lower Coyote Spring Valley waters form a tight group, as expected (excepting EH5b at 265'). There is a great deal of inconsistency with the remaining waters. EH1 at 295' is a group 1 water, and accordingly plots with EH3, 7, and 8. However, group 1 waters from EH6 do not. The two samples (335' and 455') have identical bulk chemistries, yet show a 1.1 parts per mil difference in ^{18}O . The expected lab

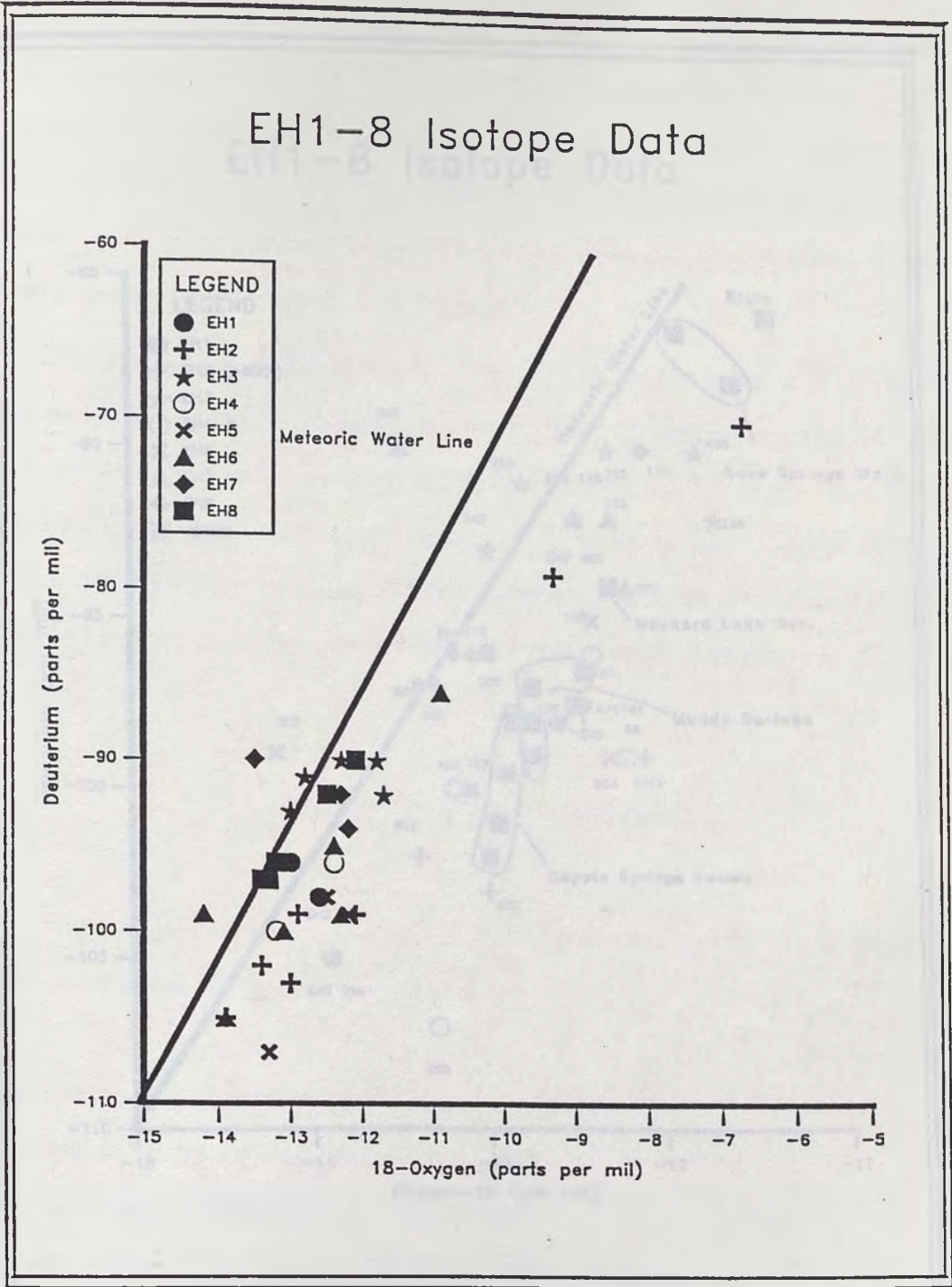


Figure 20. Deuterium and Oxygen-18 from DRI's exploration holes.

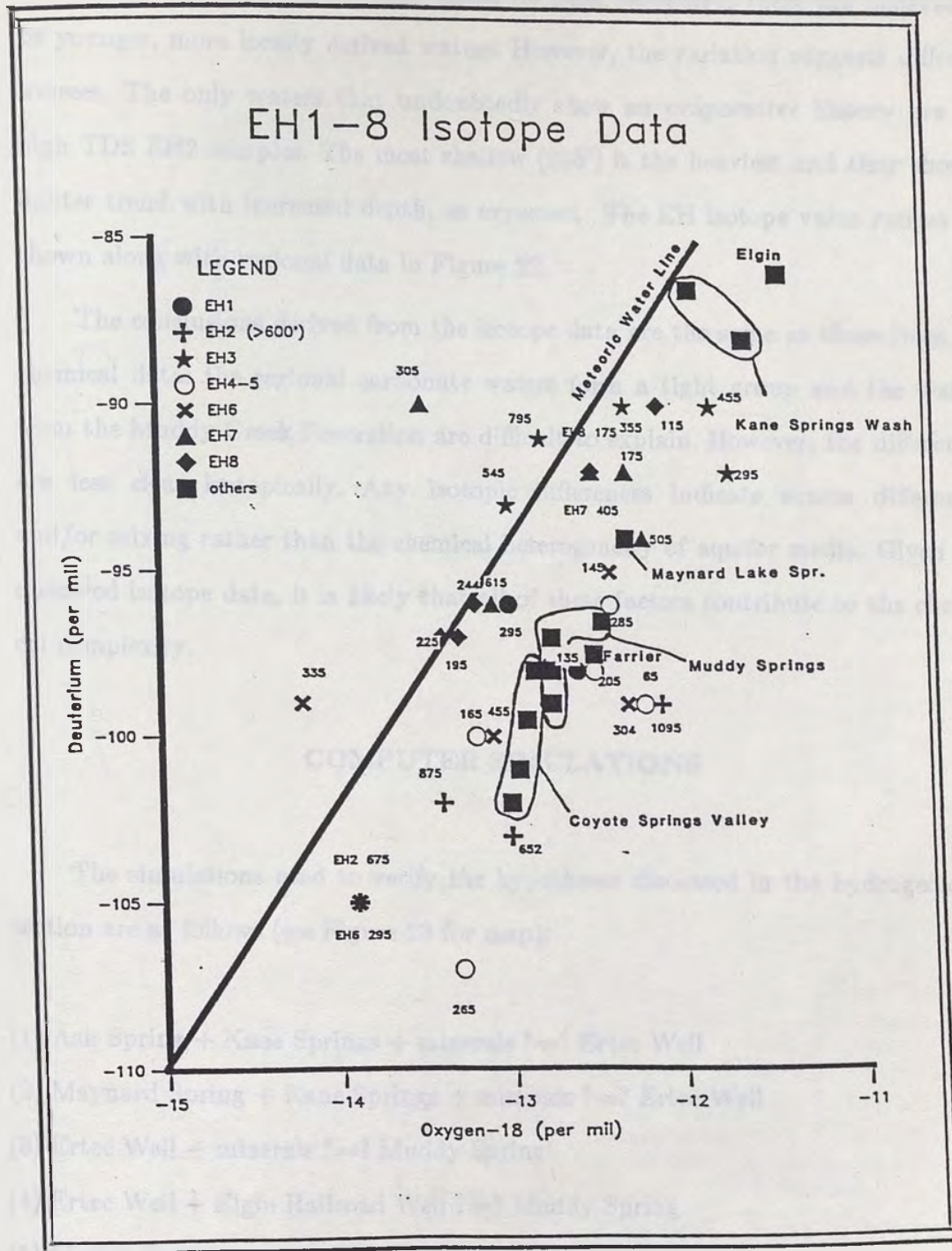


Figure 21. Deuterium and Oxygen-18 for EH1-8, not including poor quality water from EH2. Numbers represent sampling depth. Regional samples are also included.

error is no greater than 0.4 (Jacobson, oral comm., 1986). The remaining samples from EH6 are widely distributed. Based on bulk chemistry, these are believed to be younger, more locally derived waters. However, the variation suggests different sources. The only waters that undoubtedly show an evaporative history are the high TDS EH2 samples. The most shallow (235') is the heaviest and they show a lighter trend with increased depth, as expected. The EH isotope value ranges are shown along with regional data in Figure 22.

The conclusions derived from the isotope data are the same as those from the chemical data: the regional carbonate waters form a tight group and the waters from the Muddy Creek Formation are difficult to explain. However, the differences are less clear isotopically. Any isotopic differences indicate source differences and/or mixing rather than the chemical heterogeneity of aquifer media. Given the observed isotope data, it is likely that all of these factors contribute to the chemical complexity.

COMPUTER SIMULATIONS

The simulations used to verify the hypotheses discussed in the hydrogeology section are as follows (see Figure 23 for map):

- (1) Ash Spring + Kane Springs + minerals ?=? Ertec Well
- (2) Maynard Spring + Kane Springs + minerals ?=? Ertec Well
- (3) Ertec Well + minerals ?=? Muddy Spring
- (4) Ertec Well + Elgin Railroad Well ?=? Muddy Spring
- (5) Muddy Spring + minerals ?=? Bhemer Well
- (6) Bhemer Well + minerals ?=? EH2(235')

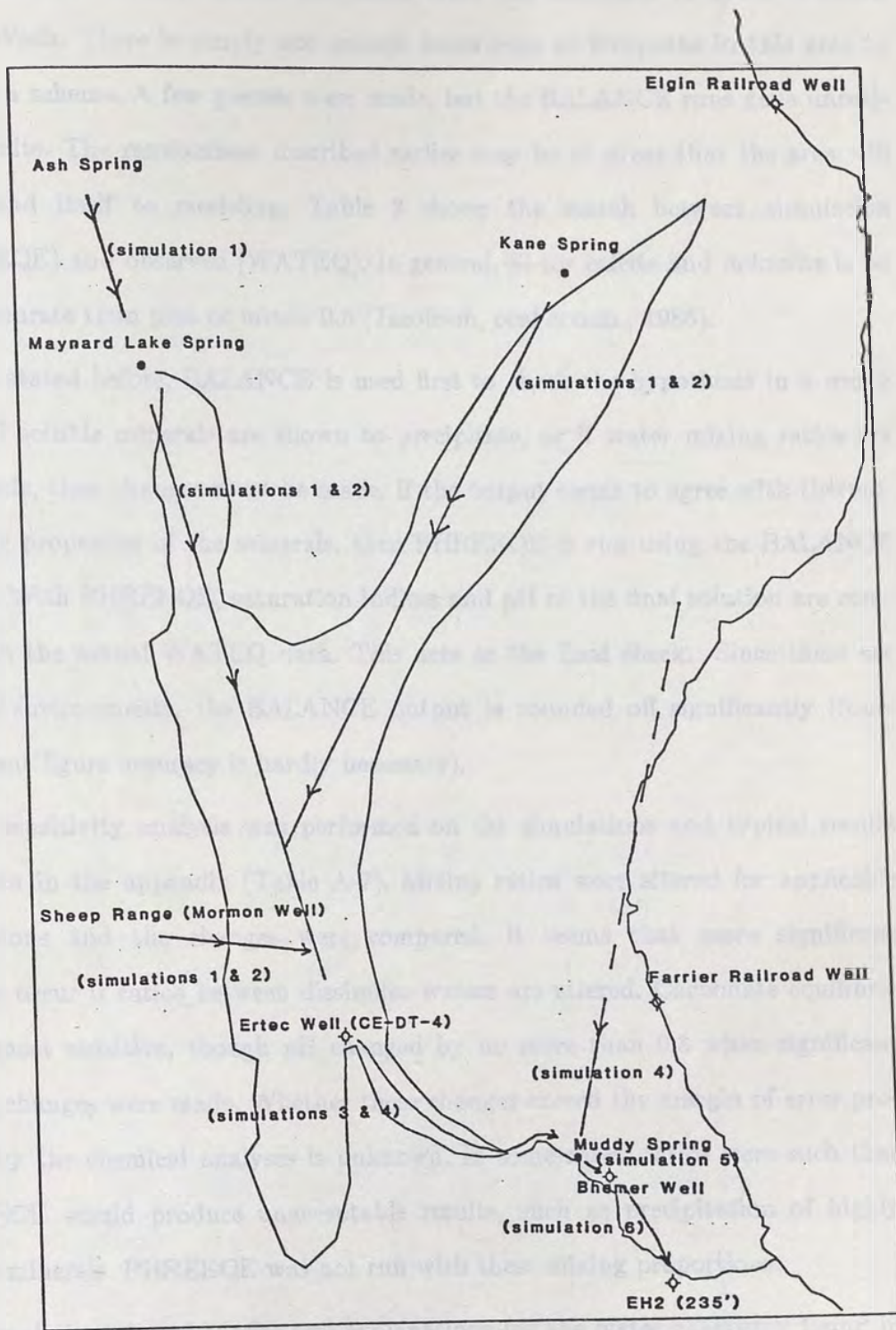


Figure 23. Map view of flowpath simulations.

These cover the proposed flowpaths, with the exception of lower Meadow Valley Wash. There is simply not enough knowledge of flowpaths in this area to propose a scheme. A few guesses were made, but the BALANCE runs gave unrealistic results. The randomness described earlier may be so great that the area will never lend itself to modeling. Table 3 shows the match between simulation (PHREEQE) and observed (WATEQ). In general, SI for calcite and dolomite is no more accurate than plus or minus 0.5 (Jacobson, oral comm., 1986).

As stated before, BALANCE is used first to check the hypothesis in a rough sense. If soluble minerals are shown to precipitate, or if water mixing ratios are unrealistic, then changes must be made. If the output seems to agree with thermodynamic properties of the minerals, then PHREEQE is run using the BALANCE output. With PHREEQE, saturation indices and pH of the final solution are compared to the actual WATEQ data. This acts as the final check. Since these are natural environments, the BALANCE output is rounded off significantly (four-significant figure accuracy is hardly necessary).

A sensitivity analysis was performed on the simulations and typical results are given in the appendix (Table A-7). Mixing ratios were altered for applicable simulations and the changes were compared. It seems that more significant changes occur if ratios between dissimilar waters are altered. Carbonate equilibria is the most sensitive, though pH changed by no more than 0.3 when significant mixing changes were made. Whether these changes exceed the margin of error produced by the chemical analyses is unknown. In some cases, ratios were such that BALANCE would produce unacceptable results, such as precipitation of highly soluble minerals. PHREEQE was not run with these mixing proportions.

Simulations 1 and 2 offer two explanations for the water chemistry found in southern Coyote Springs Valley, exemplified by the Ertec well. The first is the

Table 3 (a). PHREEQE simulation results. Input water(s) given on left.
Final water and PHREEQE product given on right.

Simulation 1					
	Ash Spring	Kane Spring	Mormon Well	Ertec Well	PHREEQE
pH	7.0	7.2	7.6	7.7	7.7
log PCO ₂	-1.5	-1.9	-2.1	-2.2	-2.2
SI(calcite)	-.27	-.41	.28	.46	.46
SI(dolomite)	-.64	-1.2	.48	.95	.89
SI(gypsum)	-2.2	-2.5	-2.3	-1.8	-1.8

Mineral Suite: calcite, dolomite, gypsum, halite, sylvite, albite.

Mixing Ratios: Ash:Kane:Mormon = 23:2:9

Simulation 2					
	Maynard Lake Spring	Kane Spring	Mormon Well	Ertec Well	PHREEQE
pH	7.9	7.2	7.6	7.7	7.8
log PCO ₂	-2.4	-1.9	-2.1	-2.2	-2.3
SI(calcite)	.39	-.41	.29	.46	.62
SI(dolomite)	.62	-1.2	.48	.95	1.19
SI(gypsum)	-1.9	-2.5	-2.3	-1.8	-1.8

Mineral suite: calcite, dolomite, gypsum, halite, sylvite, thenardite.

Mixing Ratios: Maynard Lake:Kane:Mormon = 23:2:9

Simulation 3			
	Ertec Well	Muddy Spring	PHREEQE
pH	7.7	7.7	7.9
log PCO ₂	-2.2	-2.25	-2.5
SI(calcite)	.46	.48	.70
SI(dolomite)	.95	.92	1.32
SI(gypsum)	-1.8	-1.4	-1.4

Mineral suite: calcite, dolomite, gypsum, halite, sylvite, thenardite.

Simulation 4				
	Ertec Well	Elgin Well	Muddy Spring	PHREEQE
pH	7.7	7.6	7.7	7.7
log PCO ₂	-2.2	-2.19	-2.25	-2.3
SI(calcite)	.46	.07	.48	.50
SI(dolomite)	.95	-.16	.92	.92
SI(gypsum)	-1.8	-2.00	-1.4	-1.4

Mineral suite: calcite, dolomite, gypsum, halite, sylvite, thenardite.

Mixing Ratios: Ertec:Farrier = 32:4

Table 3 (b). Continuation of simulation results.

Simulation 5			
	Muddy Spring	Bhemer Well	PHREEQE
pH	7.7	7.6	7.4
log PCO2	-2.25	-2.13	-2.0
SI(calcite)	.48	.38	.20
SI(dolomite)	.92	.78	.42
SI(gypsum)	-1.4	-1.2	-1.2

Mineral suite: calcite, dolomite, gypsum, halite, sylvite, thenardite, trona.

Simulation 6			
	Bhemer Well	EH2(235')	PHREEQE
pH	7.6	8.1	9.2
log PCO2	-2.13	-3.22	-4.3
SI(calcite)	.38	.68	1.83
SI(dolomite)	.78	1.3	3.6
SI(gypsum)	-1.2	-1.4	-1.4

Mineral Suite: calcite, dolomite, gypsum, halite, sylvite, thenardite.

widely held view, where water of Ash Springs type (calcite/dolomite source) mixes with Kane Springs Valley water and recharge from the Sheep Range. The Mormon Well, though south of the recharge area, is believed to be an accurate representation of groundwater from the eastern slopes of the Sheep Range. The chemistries were mixed in the proportions estimated from Harrill (1976) and Eakin (1964, 1966). Harrill (1976) estimates 1600 of the 11,000 acre-ft/yr of Sheep Range recharge flows into Las Vegas Valley to the west. Rounding the figure, that leaves a 9,000 acre-ft/yr contribution to Coyote Springs Valley. Input from Kane Springs Valley is thought to be minor, though no direct measurements have been made. A value of 2,000 acre-ft/yr is used in this study. Eakin (1964) estimates between 2,000 and 3,000 acre-ft/yr of the 36,000 acre-ft/yr discharge at Muddy Springs is derived from local recharge. Subtracting 2,000 (down-gradient recharge) along with 9,000 (Sheep Range) and 2,000 (Kane Springs Valley) from 36,000 gives 23,000 acre-ft/yr contribution of White River Drainage System water to southern Coyote Springs Valley. Thus, Ash Spring, Kane Spring, and Mormon Well waters are mixed in the ratio 23:2:9.

The mineral assemblage used in simulation 1 is thought to be associated with the deep carbonate flow system: calcite, dolomite, gypsum, halite, sylvite, and albite. Albite contributes sodium not by dissolving, but by the weathering process mentioned earlier. This is probably the largest flaw in the simulation. With the proportions used, the only way to evolve a calcium-bicarbonate water like Ash Spring to a sodium-bicarbonate water (Ertec Well) is to provide a sodium source from the local mineralogy. Halite is not the only answer, since sodium outweighs chloride in the Ertec Well. Sodium silicates may exist in the impure beds of the Paleozoic carbonates, but their role as a major sodium source is questionable. Sodium salts such as thenardite and trona are equally rare and in addition produce unacceptable simulation results because of the associated sulfate and

carbonate. The requirement in BALANCE is a sodium source unassociated with the major anions.

Simulation 2 differs from 1 only in that Maynard Lake Spring is used rather than Ash Spring. This spring has not been mentioned in the literature, though Eakin (1964, 1966) used Maynard Lake's elevation in determination of the flow system head gradients. The chemistry of this spring water indicates a volcanic rock influence, as discussed before. Despite the use of Maynard Lake, Eakin claims spring waters emanating from volcanic rock represent a perched aquifer. However, in the case of the Maynard Lake area this has not been proven. This may be a more attractive source of sodium than the Paleozoic carbonates.

The results of both simulations are shown in Table 3. By any standard, both produce acceptable results. Though the simulation 1 numbers look more accurate, it is flawed by the mineral suite used. Only subsurface exploration near Maynard Lake will determine which approach is correct.

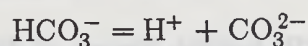
Simulations 3 and 4 show two possible evolution theories for Muddy Springs. The first is the more traditional, again based on Eakin's (1964, 1966) theories. Here, the Ertec well water passes through a mineral assemblage and emerges at Muddy Springs. Simulation 4 is based on Rush's (1964) theory that Meadow Valley Wash water also contributes. Recalling the head data from Figure 7, water must exit the Meadow Valley Wash basin north of Farrier. Unfortunately, no complete analysis exists in the database between Elgin and Farrier. The Farrier water chemistry was used initially, but BALANCE would not produce acceptable results for any realistic mineral assemblage. Instead, the railroad well from Elgin was used, with much more attractive results. At first, the proportions used were 29:7 (Ertec well:Elgin well), based on Rush's estimation of 7,000 acre-ft/yr underflow. However, a ratio of 32:4 produced better chemical results (compare in

Table A-7). Since Rush's (1964) study may be outdated, this is believed to be a more correct proportion. If flowpath simulations 3 and 4 are evaluated on a purely chemical basis, then Meadow Valley Wash underflow is most likely occurring.

The mineral assemblage used is based on Muddy Creek Formation mineralogy. Its influence here is probably not as strong as in lower Moapa Valley, but it is indeed present.

The next step is the Muddy Spring water evolving to the sodium-sulfate type (simulation 5). The Bhemer well was chosen as an end member because it is the first known water of this type away from the springs. A Muddy Creek Formation mineral assemblage is used again, as it is in all subsequent runs.

In general, the salinity increases southeastward, as shown by the high TDS waters of EH2. The Bhemer well water is evolved to this state using simulation 6. An increase in pH coupled with a decrease in P_{CO_2} is not expected in an environment of calcite precipitation. As shown by the carbonate equilibria,



this type of change may be brought about by CO_2 degassing, thus shifting the equilibrium to the left. Calcite precipitation removes CO_3^{2-} from solution, which would move the equilibrium to the right. However, if large amounts of Ca^{2+} are supplied by gypsum dissolution, then precipitation of calcite may occur along with degassing. There is less agreement in this simulation than any of the others, implying that other waters are mixing along the flowpath. The heterogeneity of the Muddy Creek Formation along with the observed water chemistry supports this hypothesis. A spring farther down the Muddy River (Spring-near Moapa in the appendix) shows a chemistry quite similar to Bhemer well. The water in EH2

may therefore be from a different source without any mixing with Bhemer type water.

SUMMARY AND CONCLUSIONS

The Coyote Springs-Moapa-Meadow Valley area is one in which hydrogeology is still a mystery. Not only is there very little hydraulic data, but the geochemistry and isotopes have shown unexpected relationships. Sources of salts have not previously been described in detail and the geochemistry has not been used to check flowpath hypotheses.

The groundwater flow in Coyote Springs Valley is north to south, with input from Kane Springs Wash (2,000 acre-ft/yr) and recharge from the Sheep Range (9,000 acre-ft/yr). A bedrock high at the southern end of the valley diverts the groundwater eastward through Arrow Canyon, leading to a major discharge at Muddy Springs. The springs may have a contribution from Meadow Valley Wash underflow (4,000 acre-ft/yr), though this is not certain.

South of the springs, the flowpath is poorly defined. Results of the Bhemer Well-EH2 simulation imply local water mixing and (possibly) perched water bodies. This is even more prevalent in lower Meadow Valley Wash, where no obvious water evolution scenario is detectable. In general, groundwater flows north to south in Meadow Valley Wash, but water chemistry type and TDS vary to such a degree that a more precise evolutionary path cannot be defined.

As might be expected, water in the carbonate aquifers of the White River drainage system is a calcium/magnesium-bicarbonate type. This is evident in Pahranaagat Valley (north of the study area) and Kane Springs valley, but not in Coyote Springs Valley. A possible explanation is the presence of volcanic rock at

the Maynard Lake area. This rock gives additional sodium to the water, thus altering the chemistry to the observed sodium-bicarbonate type. Whether the drainage system waters flow through the volcanic unit or not remains a mystery. The sodium-bicarbonate chemistry extends to the Muddy Springs.

The Muddy Creek Formation dominates the geology in Moapa Valley and lower Meadow Valley Wash, and its effect on groundwater chemistry is evidenced by high salinity (a TDS range of 1000-4500 mg/l) and a sulfate character (up to 80% of total anion eqm). The numerous evaporite minerals (mainly gypsum and thenardite) in these sediments are the principal cause of these characteristics.

Geochemical modeling techniques show that groundwater from Kane Springs Wash and the Sheep Range mix with regional flow from the north to form the observed water chemistry in southern Coyote Springs Valley. It is universally agreed that Ash Spring in Pahrnagat Valley is representative of regional flow, while this is not true for Maynard Lake Spring. Using the same mineral assemblage, both produce acceptable results in the simulations. The requirement in the Ash Spring scenario is that significant amounts of sodium silicate must be present in the carbonate formations to give the sodium values observed down gradient. Because of its location in volcanic rocks, Maynard Lake Spring chemistry already shows the sodium spike, and so sodium silicate contribution along the flowpath is not required.

In testing the theory that Meadow Valley Wash groundwater contributes to Muddy Springs discharge, acceptable results were obtained when Elgin groundwater was used in the simulations. However, no realistic mineral assemblage would produce a mass balance when a Farrier sample was used. It is likely that underflow is occurring between the two sites, but no complete data is available here. The traditional theory that Meadow Valley Wash does not contribute was

tested and also produced good results. The lack of regional hydraulic data from Meadow Valley Wash makes the conclusion untenable.

Simulations support some Muddy Spring water evolution into the Muddy Creek Formation, but other unsuccessful runs point to complex hydrogeology in Moapa Valley. It is evident that water from Farrier passes through the Muddy Creek Formation and evolves to the general type found in lower Meadow Valley Wash, but the precise flowpath is unclear.

Allen, H., 1954. *Geology of the Moapa Valley, Utah*. U.S. Geol. Surv. Prof. Paper 284, 104 p.

Allen, H., 1955. *Geology of the Moapa Valley, Utah*. U.S. Geol. Surv. Prof. Paper 304, 104 p.

Allen, H., 1956. *Geology of the Moapa Valley, Utah*. U.S. Geol. Surv. Prof. Paper 324, 104 p.

Allen, H., 1957. *Geology of the Moapa Valley, Utah*. U.S. Geol. Surv. Prof. Paper 344, 104 p.

Allen, H., 1958. *Geology of the Moapa Valley, Utah*. U.S. Geol. Surv. Prof. Paper 364, 104 p.

Allen, H., 1959. *Geology of the Moapa Valley, Utah*. U.S. Geol. Surv. Prof. Paper 384, 104 p.

Allen, H., 1960. *Geology of the Moapa Valley, Utah*. U.S. Geol. Surv. Prof. Paper 404, 104 p.

Allen, H., 1961. *Geology of the Moapa Valley, Utah*. U.S. Geol. Surv. Prof. Paper 424, 104 p.

Allen, H., 1962. *Geology of the Moapa Valley, Utah*. U.S. Geol. Surv. Prof. Paper 444, 104 p.

Allen, H., 1963. *Geology of the Moapa Valley, Utah*. U.S. Geol. Surv. Prof. Paper 464, 104 p.

Allen, H., 1964. *Geology of the Moapa Valley, Utah*. U.S. Geol. Surv. Prof. Paper 484, 104 p.

Allen, H., 1965. *Geology of the Moapa Valley, Utah*. U.S. Geol. Surv. Prof. Paper 504, 104 p.

Allen, H., 1966. *Geology of the Moapa Valley, Utah*. U.S. Geol. Surv. Prof. Paper 524, 104 p.

Allen, H., 1967. *Geology of the Moapa Valley, Utah*. U.S. Geol. Surv. Prof. Paper 544, 104 p.

Allen, H., 1968. *Geology of the Moapa Valley, Utah*. U.S. Geol. Surv. Prof. Paper 564, 104 p.

Allen, H., 1969. *Geology of the Moapa Valley, Utah*. U.S. Geol. Surv. Prof. Paper 584, 104 p.

Allen, H., 1970. *Geology of the Moapa Valley, Utah*. U.S. Geol. Surv. Prof. Paper 604, 104 p.

Allen, H., 1971. *Geology of the Moapa Valley, Utah*. U.S. Geol. Surv. Prof. Paper 624, 104 p.

Allen, H., 1972. *Geology of the Moapa Valley, Utah*. U.S. Geol. Surv. Prof. Paper 644, 104 p.

Allen, H., 1973. *Geology of the Moapa Valley, Utah*. U.S. Geol. Surv. Prof. Paper 664, 104 p.

Allen, H., 1974. *Geology of the Moapa Valley, Utah*. U.S. Geol. Surv. Prof. Paper 684, 104 p.

Allen, H., 1975. *Geology of the Moapa Valley, Utah*. U.S. Geol. Surv. Prof. Paper 704, 104 p.

Allen, H., 1976. *Geology of the Moapa Valley, Utah*. U.S. Geol. Surv. Prof. Paper 724, 104 p.

Allen, H., 1977. *Geology of the Moapa Valley, Utah*. U.S. Geol. Surv. Prof. Paper 744, 104 p.

Allen, H., 1978. *Geology of the Moapa Valley, Utah*. U.S. Geol. Surv. Prof. Paper 764, 104 p.

Allen, H., 1979. *Geology of the Moapa Valley, Utah*. U.S. Geol. Surv. Prof. Paper 784, 104 p.

Allen, H., 1980. *Geology of the Moapa Valley, Utah*. U.S. Geol. Surv. Prof. Paper 804, 104 p.

Allen, H., 1981. *Geology of the Moapa Valley, Utah*. U.S. Geol. Surv. Prof. Paper 824, 104 p.

Allen, H., 1982. *Geology of the Moapa Valley, Utah*. U.S. Geol. Surv. Prof. Paper 844, 104 p.

Allen, H., 1983. *Geology of the Moapa Valley, Utah*. U.S. Geol. Surv. Prof. Paper 864, 104 p.

Allen, H., 1984. *Geology of the Moapa Valley, Utah*. U.S. Geol. Surv. Prof. Paper 884, 104 p.

Allen, H., 1985. *Geology of the Moapa Valley, Utah*. U.S. Geol. Surv. Prof. Paper 904, 104 p.

Allen, H., 1986. *Geology of the Moapa Valley, Utah*. U.S. Geol. Surv. Prof. Paper 924, 104 p.

Allen, H., 1987. *Geology of the Moapa Valley, Utah*. U.S. Geol. Surv. Prof. Paper 944, 104 p.

Allen, H., 1988. *Geology of the Moapa Valley, Utah*. U.S. Geol. Surv. Prof. Paper 964, 104 p.

Allen, H., 1989. *Geology of the Moapa Valley, Utah*. U.S. Geol. Surv. Prof. Paper 984, 104 p.

Allen, H., 1990. *Geology of the Moapa Valley, Utah*. U.S. Geol. Surv. Prof. Paper 1004, 104 p.

SE ROA 37676

BIBLIOGRAPHY

- Bateman, R.L., 1976, "Inventory and Chemical Quality of Ground Water in the White River-Muddy River-Meadow Valley Wash Area, Southeastern Nevada," *Water Resources Center, Desert Research Institute, University of Nevada System*. Project Report 40. 44 p.
- Bohannon, R.G., 1984, "Nonmarine Sedimentary Rocks of Tertiary Age in the Lake Mead Region, Southeastern Nevada and Northwestern Arizona," *USGS Prof. Paper 1259*. 72 p.
- Bohm, B. and Jacobson, R.L., 1981, *WATEQDR, An Updated Version of WATEQF - A Computerized Chemical Model of Natural Waters*. (DRI/WRC files) 55 p.
- Bohn, H., McNeal, B., and O'Connor, G., 1985, *Soil Chemistry, 2nd ed.*, John Wiley & Sons, New York. 341 p.
- Dettinger, M., 1986. personal communication, U.S.G.S., Carson City, Nevada
- Drever, J.L., 1982, *The Geochemistry of Natural Waters*, Prentice-Hall, Englewood Cliffs, N.J.. 388 p.
- Driscoll, F.G., 1986, *Groundwater and Wells, 2nd ed.*, Johnson Division, St. Paul. 1089 p.
- Eakin, T.E., 1964, "Ground-Water Appraisal of Coyote Spring and Kane Spring Valleys and Muddy River Springs Area, Lincoln and Clark Counties, Nevada," *Ground-Water Resources - Reconnaissance Series Report 25*. 40 p.
- Eakin, T.E., 1966, "A Regional Interbasin Groundwater System in the White River Area, Southeastern Nevada," *Water Resources Research*, vol. 2, pp. 251-271.
- EPA, 1979, "Methods for Chemical Analysis of Water and Wastes," *EPA-600/4-79-020*.
- Ertec, 1981, *MX Siting Investigation WR Program. Results of Regional Carbonate Aquifer Testing, Coyote Spring Valley, Nevada*. (Ertec files) 65 p.
- Hem, J.D., 1985, "Study and Interpretation of the Chemical Characteristics of Natural Water, 3rd ed.," *USGS Water Supply Paper 2254*. 263 p.
- Jacobson, R.L., 1986. personal communication, D.R.I./W.R.C., Reno, Nevada
- Longwell, C.R., Pampeyan, E.H., Bowyer, B., and Roberts, R.J., 1965, "Geology and Mineral Deposits of Clark County, Nevada," *Nev. Bur. Mines Bull. 62*. 218 p.
- Longwell, C.R., 1928, "Geology Of The Muddy Mountains, Nevada," *USGS Bull.*, vol. 798. 152 p.
- Mifflin, M.D., Zimmerman, D.E., Sullivan, K.E., and Elliott, B., 1982, *Lower Meadow Valley Wash Well Inventory 1981-1982*. (Report to Nevada Power Company by DRI/WRC Las Vegas, NV)
- Moore, R.T., 1972, "Geology of the Virgin and Beaverdam Mountains, Arizona," *Ariz. Bur. Mines Bull. 186*.
- Parkhurst, D.L., Plummer, L.N., and Thorstenson, D.C., 1982, "BALANCE - A Computer Program for Calculating Mass Transfer for Geochemical Reactions in Ground Water," *USGS/WRI 82-14*. 29 p.
- Parkhurst, D.L., Thorstenson, D.C., and Plummer, L.N., 1980, "PHREEQE - A Computer Program for Geochemical Calculations," *USGS Water-Resources Investigations 80-96*. 210 p.
- Piper, A.M., 1944, "A Graphic Procedure in the Geochemical Interpretation of Water-Analyses," *Am. Geophys. Union Trans.*, vol. 25. pp. 914-923.
- Plummer, L.N., Jones, B.F., and Truesdell, A.H., 1976, "WATEQF - A FORTRAN IV Version of WATEQ, a Computer Program for Calculating Chemical Equilibrium of Natural Waters," *U.S.G.S. WRI*, vol. 76-13. 61 p.

- Rush, F.E., 1964, "Ground-Water Appraisal of the Meadow Valley Area, Lincoln and Clark Counties, Nevada," *Ground-Water Resources - Reconnaissance Series Report 27*. 43 p.
- Stiff, H.A., Jr., 1951, "The Interpretation of Chemical Water Analyses by Means of Patterns," *Jour. Petroleum Technology*, vol. 3. No. 10, Section 1, 15-16; Section 2, 3
- Stock, C., 1921, "Later Cenozoic Mammalian Remains from the Meadow Valley Region, Southeastern Nevada," *Am. Jour. Sci., 5th ser.*, vol. 2. p. 250-264
- Trexler, A., Bruce, B., Cates, C., and Covington, D., 1982, "Geothermal Assessment of the MX Deployment Area," *DOE/NV 10187-1 Dist. Cat. UC-66a*.
- Truesdell, A.H. and Jones, B.F., 1973, "WATEQ, a Computer Program for Calculating Chemical Equilibria of Natural Waters," *Journal of Research, U.S.G.S.*, vol. 2. p. 233-274.
- Tschanz, C.M. and Pampeyan, E.H., 1970, "Geology and Mineral Deposits of Lincoln County, Nevada," *Nev. Bur. Mines. Geol. Bull 78*. 188 p.
- Winograd, I.J. and Friedman, I., 1972, "Deuterium As A Tracer Of Regional Ground-Water Flow, Southern Great Basin, Nevada And California," *Geol. Soc. Am. Bull.*, vol. 83, pp. 3691-3708.
- Zimmerman, D.E., Mifflin, M.D., and Sullivan, K.E., 1982, and B.F., Jones, 1965, "The Hydrology and Mineralogy of Deep Springs Lake, Inyo County, California," *USGS Prof. Paper 502-A*. (DRI unpublished report to Nevada Power Company) 123 p.

map no.	Site Name	LONG. dms	LAT. dms	Date mdy	Temp (C)	EC u-mhos	TDS mg/l	pH	Ca mg/l	Mg mg/l	Na mg/l	K mg/l	Cl mg/l	SO4 mg/l	HCO3 mg/l	SiO2 mg/l
1	Maynard Lake Spring	1150202	371130	1-14-85	9.6	905.0	515.5	7.90	43.1	23.4	114.0	13.7	30.4	88.3	405.0	0.
2	Coyote Spring Well	1145929	365908	11-0-80	0.	563.0	299.0	7.70	37.4	27.0	32.1	2.9	16.4	35.4	257.7	18.9
3	Coyote Spring Well	1145929	365908	11-0-81	15.3	0.	325.1	7.80	37.5	30.0	36.0	3.1	22.0	46.0	259.0	21.0
3	U.S.G.S Well VE-2	1145644	365230	2-5-86	34.0	800.0	469.5	7.40	47.0	21.0	81.0	11.0	34.0	90.0	303.0	34.0
4	CE-DT-4 Ertec Well	1145332	364744	11-0-80	0.	0.	491.0	0.	51.0	20.0	83.0	10.7	37.1	102.0	306.4	34.0
4	CE-DT-4 Ertec Well	1145332	364744	7-0-81	35.5	0.	472.3	7.70	46.0	20.3	78.0	11.0	34.0	100.0	300.0	33.0
5	Willow Spring (KSW)	1144952	370534	7-17-75	25.5	385.0	266.5	7.70	19.0	3.0	50.0	3.0	21.0	34.0	135.0	69.0
5	Willow Spring (KSW)	1144952	370534	11-0-80	0.	380.0	246.6	7.20	17.0	4.0	47.6	4.5	23.0	26.7	130.3	58.6
5	Willow Spring (KSW)	1144952	370534	11-0-81	17.4	0.	275.3	7.50	20.5	2.7	56.0	4.6	22.3	34.0	140.3	65.0
6	Grapevine Spring	1144202	370808	11-0-81	18.4	0.	342.9	7.30	75.0	22.0	17.0	2.3	26.9	40.0	275.5	22.0
7	Spring-Kane Springs Wa	1144157	370924	7-17-75	30.5	180.0	88.0	7.90	19.0	4.0	10.0	2.0	0.5	9.0	87.0	0.
8	Kane Springs	1144221	371446	11-0-81	16.4	0.	275.6	7.20	43.5	13.0	20.0	5.9	16.6	14.0	205.3	60.0
9	Boulder Spring	1143844	371612	11-0-81	16.8	0.	146.0	7.90	21.5	4.9	12.2	2.3	7.8	6.0	102.2	41.0
10	Spring-Kane Springs Wa	1143924	371255	7-17-75	31.0	160.0	81.5	7.90	18.0	4.0	7.0	1.0	10.0	2.0	79.0	0.
11	Railroad Well, Elgin	1143241	372047	1-31-84	16.0	0.	414.8	7.60	42.0	14.0	98.0	8.8	42.0	60.0	300.0	0.
11	Bradshaw Well, Elgin	1143235	372015	2-1-84	14.8	0.	647.0	7.30	85.0	28.0	120.0	11.0	52.0	76.0	550.0	0.
11	Randono Well, Elgin	0	0	2-3-84	17.2	0.	450.4	7.60	46.0	14.0	100.0	8.4	44.0	63.0	350.0	0.
11	U.P.R.R. Elgin	1143243	372047	6-1-44	0.	847.0	427.4	0.	40.8	13.0	109.0	0.	42.9	55.2	333.0	0.
12	U.P.R.R. Carp	1143006	370634	10-12-45	0.	1027.0	536.1	0.	57.0	17.6	125.0	0.	74.8	79.7	364.0	0.
13	U.P.R.R-Rox	1143950	365235	1-12-44	0.	1191.0	712.3	0.	83.5	38.2	112.5	0.	63.8	266.6	295.3	0.
14	Meadow Valley Wash, Fa	1143845	364955	10-14-49	0.	1260.0	776.2	0.	77.3	46.5	135.0	0.	74.8	324.2	236.8	0.
14	Meadow Valley Wash, Fa	1143900	364900	10-14-49	0.	1220.0	723.3	0.	60.2	46.5	133.9	0.	79.1	317.5	172.1	0.
14	Farrier Railroad Well	1143914	364849	2-4-84	22.8	1300.0	909.0	8.00	84.0	31.0	150.0	19.0	52.0	550.0	0.	23.0
15	U.S.G.S Well CSV-2	1144320	364650	1-26-86	27.0	995.0	586.0	7.40	60.0	27.0	100.0	10.0	61.0	160.0	276.0	30.0
16	Muddy (Big) Spring	1144257	364319	7-22-81	32.5	930.0	478.0	7.24	66.0	26.0	96.0	10.0	61.0	190.0	0.	29.0

Table A-1. Data from Coyote, Kane Springs, and Meadow Valleys (see Figure 3). A map number of zero indicates the data point was not included on the map. A value of zero for a given constituent indicates there was no analysis.

map no.	Site Name	LONG. dms	LAT. dms	Date mdy	Temp (C)	EC u-mhos	TDS mg/l	pH	Ca mg/l	Mg mg/l	Na mg/l	K mg/l	Cl mg/l	SO4 mg/l	HCO3 mg/l	S102 mg/l
1	Anderson Well	1144414	364411	10-28-69	0.	0.	525.0	7.70	69.0	22.0	92.0	0.	58.0	140.0	288.0	0.
2	Lewis Well #1	1144411	364358	10-28-69	0.	0.	499.0	7.60	67.0	23.0	84.0	0.	58.0	123.0	288.0	0.
0	Lewis Well #2	1144359	364358	10-28-69	0.	0.	501.0	7.70	69.0	21.0	86.0	0.	57.0	123.0	290.0	0.
0	Lewis Well #3	1144357	364357	10-28-69	0.	0.	585.5	7.70	77.0	27.0	98.0	0.	60.0	165.0	317.0	0.
3	Abbot Well	1144115	364241	9-25-74	20.0	1575.0	1071.5	8.40	90.0	54.0	153.0	15.0	117.0	429.0	297.0	65.0
3	Abbot Well Replacement	1144115	364241	3-19-86	0.	1860.0	1270.4	7.64	120.0	67.9	184.0	19.5	157.0	515.0	316.0	49.0
0	Spring	114	36	11-0-80	31.0	1100.0	1289.5	8.10	115.0	60.0	225.0	25.0	143.0	394.0	579.0	38.0
0	Spring	114	36	11-0-80	28.5	1100.0	598.0	8.20	65.0	27.0	95.0	14.0	61.0	172.0	278.0	25.0
0	Spring	114	36	11-0-80	26.8	2100.0	603.0	7.90	65.0	27.0	95.0	15.0	68.0	172.0	274.0	24.0
4	Well-Moapa	1144101	364215	5-27-63	0.	0.	848.0	7.50	90.0	29.0	156.0	0.	109.0	320.0	288.0	0.
4	Well-Moapa	1144101	364215	11-0-80	17.0	2600.0	1692.0	8.10	136.0	69.0	315.0	30.0	120.0	819.0	360.0	23.0
5	Bhamer Well	1144133	364237	12-10-74	27.0	1460.0	904.0	7.60	76.0	40.0	157.0	11.0	104.0	318.0	316.0	40.0
6	Baldwin House Spring-S	1144338	364335	6-28-71	32.0	853.9	598.8	8.15	62.5	27.0	91.3	11.5	65.7	177.5	262.2	32.3
6	Baldwin Spring	1144338	364336	6-5-81	0.	870.0	595.5	7.80	65.0	29.0	95.0	11.0	61.0	170.0	267.0	31.0
6	Baldwin Spring	1144338	364335	9-30-81	0.	930.0	588.0	7.30	63.0	28.0	90.0	11.0	64.0	170.0	268.0	28.0
6	Baldwin House Spring-N	1144338	364336	6-28-71	32.0	849.8	598.0	8.05	62.5	26.9	91.8	11.3	62.8	178.8	265.8	31.2
7	Baldwin Cut Spring	1144338	364315	6-28-71	31.5	877.8	614.5	8.20	63.0	27.5	96.3	11.3	66.3	183.8	269.3	31.8
7	Baldwin Cut Spring	1144338	364315	6-5-81	0.	837.0	615.5	7.80	66.0	28.0	94.0	11.0	64.0	190.0	267.0	29.0
7	Baldwin Cut Spring	1144338	364315	9-30-81	0.	950.0	599.0	7.20	64.0	28.0	90.0	11.0	63.0	180.0	268.0	29.0
8	Muddy(Big) Spring	1144257	364319	6-28-71	31.5	908.7	633.6	8.12	65.0	28.1	97.8	11.8	69.5	196.3	270.5	30.0
8	Muddy (Big) Spring	1144257	364319	7-22-81	32.5	930.0	478.0	7.24	66.0	26.0	96.0	10.0	61.0	190.0	0.	29.0
8	Muddy Spring	1144257	364319	6-5-81	0.	930.0	597.5	7.80	66.0	28.0	99.0	11.0	65.0	170.0	255.0	31.0
8	Muddy Spring	1144257	364319	9-30-81	0.	910.0	607.0	7.40	63.0	28.0	96.0	12.0	66.0	180.0	268.0	28.0
9	Iverson Spring	1144242	364237	6-28-71	31.5	883.9	613.5	8.08	63.8	26.5	97.0	11.5	67.7	182.5	270.5	29.3
10	Jones Spring	1144305	364253	6-28-71	33.0	830.0	606.5	8.20	62.0	27.0	94.0	12.0	66.0	181.0	267.0	31.0
11	Pederson (Warm) Spring	1144253	364236	7-2-75	32.0	1045.0	626.5	8.00	65.0	29.0	101.0	10.0	61.0	193.0	277.0	29.0
11	Pederson Spring	1144253	364236	6-5-81	0.	841.0	619.0	7.70	66.0	28.0	100.0	11.0	57.0	190.0	274.0	30.0
11	Pederson Spring	1144253	364236	9-30-81	0.	950.0	617.0	7.60	66.0	28.0	96.0	11.0	64.0	190.0	268.0	28.0
12	Willow Flowing Well	1144243	364326	4-17-69	32.5	939.1	612.4	7.75	62.2	26.8	97.5	10.0	67.4	182.8	274.0	28.7
0	NPC Well #1	114	36	12-12-85	0.	844.0	585.0	8.03	59.0	27.1	89.8	11.2	55.4	159.0	291.0	38.0
0	NPC Well #2	114	36	12-12-85	0.	834.0	619.0	8.22	62.6	29.2	93.6	10.4	58.7	180.0	293.0	38.0
0	NPC Well #3	114	36	12-12-85	0.	801.0	604.9	8.10	60.0	27.3	94.6	11.0	58.5	169.0	285.0	42.0
0	NPC Well #4	114	36	12-12-85	0.	798.0	581.0	8.10	58.4	28.3	91.9	10.2	52.2	162.0	286.0	35.0
0	NPC Well #5	114	36	12-12-85	0.	915.0	573.0	8.08	57.9	26.1	93.1	11.3	54.1	156.0	279.0	35.0
13	EH-4 165'	1144258	364223	3-18-86	21.4	921.0	561.5	8.46	50.3	30.0	89.4	11.6	57.7	175.0	241.0	27.0
13	EH-4 285'	1144258	364223	3-18-86	24.1	916.0	555.6	8.15	47.8	29.3	90.8	11.5	56.7	167.0	249.0	28.0
14	EH-5a 65'	1144436	364358	3-5-86	27.0	888.0	544.5	8.32	40.4	26.1	100.0	12.2	54.8	156.0	252.0	29.0
14	EH-5a 205'	1144436	364358	3-5-86	29.0	881.0	552.9	8.10	58.0	26.0	92.1	11.9	52.9	152.0	258.0	31.0
14	EH-5b 265'	1144436	364358	3-12-86	29.0	899.0	551.2	8.29	49.6	26.4	95.9	11.8	51.5	145.0	276.0	33.0
15	EH1-135'	1143752	363937	10-2-85	0.	2360.0	1620.8	8.25	137.0	70.4	306.0	19.9	219.0	670.0	361.0	18.0
map no.	Site Name	LONG. dms	LAT. dms	Date mdy	Temp (C)	EC u-mhos	TDS mg/l	pH	Ca mg/l	Mg mg/l	Na mg/l	K mg/l	Cl mg/l	SO4 mg/l	HCO3 mg/l	S102 mg/l

Table A-2 (a). Data from Moapa Valley (see Figure 4).
A map number of zero indicates the data point was not included
on the map. A value of zero for a given constituent indicates
there was no analysis.

Table A-2 (b). Continuation of data from Figure 4.

map Site Name no.	LONG. dms	LAT. dms	Date mny	Temp (C)	EC u-mhos	TDS mg/l	pH	Ca mg/l	Mg mg/l	Na mg/l	K mg/l	Cl mg/l	SO4 mg/l	HCO3 mg/l	SiO2 mg/l
15 EH2-295'	1143752	363937	10-3-85	0.	3640.0	2806.2	8.13	387.0	162.0	249.0	32.2	370.0	1500.0	178.0	17.0
16 EH2-235'	1143855	363850	10-5-85	23.0	6600.0	4528.3	8.06	381.0	184.0	769.0	80.3	554.0	2500.0	102.0	9.0
16 EH2-335'	1143855	363850	10-5-85	0.	4580.0	3526.0	8.10	343.0	154.0	556.0	65.0	374.0	1970.0	110.0	9.0
16 EH2-535'	1143855	363850	10-6-85	0.	4870.0	3553.4	8.27	197.0	90.5	815.0	41.4	473.0	1850.0	155.0	9.0
16 EH2-655'	1143855	363850	10-6-85	0.	851.0	508.6	8.51	38.5	29.7	90.9	16.3	51.2	143.0	248.0	15.0
16 EH2-675'	1143855	363850	10-6-85	24.0	895.0	514.6	7.90	36.8	29.7	95.4	16.0	52.2	145.0	253.0	13.0
16 EH2-875'	1143855	363850	10-8-85	0.	915.0	549.0	8.29	38.9	19.4	116.0	14.5	61.2	158.0	250.0	16.0
16 EH2-1095'	1143855	363850	11-14-85	0.	3400.0	2319.5	8.17	128.0	42.8	588.0	25.7	459.0	962.0	206.0	11.0
17 Spring-Hear Hoopa	1143652	363842	10-13-49	19.0	1550.0	995.0	0.	85.0	55.0	174.0	0.	110.0	355.0	354.0	39.0

map Site Name no.	LONG. dms	LAT. dms	Date mny	Temp (C)	EC u-mhos	TDS mg/l	pH	Ca mg/l	Mg mg/l	Na mg/l	K mg/l	Cl mg/l	SO4 mg/l	HCO3 mg/l	SiO2 mg/l
15 EH2-295'	1143752	363937	10-3-85	0.	3640.0	2806.2	8.13	387.0	162.0	249.0	32.2	370.0	1500.0	178.0	17.0
16 EH2-235'	1143855	363850	10-5-85	23.0	6600.0	4528.3	8.06	381.0	184.0	769.0	80.3	554.0	2500.0	102.0	9.0
16 EH2-335'	1143855	363850	10-5-85	0.	4580.0	3526.0	8.10	343.0	154.0	556.0	65.0	374.0	1970.0	110.0	9.0
16 EH2-535'	1143855	363850	10-6-85	0.	4870.0	3553.4	8.27	197.0	90.5	815.0	41.4	473.0	1850.0	155.0	9.0
16 EH2-655'	1143855	363850	10-6-85	0.	851.0	508.6	8.51	38.5	29.7	90.9	16.3	51.2	143.0	248.0	15.0
16 EH2-675'	1143855	363850	10-6-85	24.0	895.0	514.6	7.90	36.8	29.7	95.4	16.0	52.2	145.0	253.0	13.0
16 EH2-875'	1143855	363850	10-8-85	0.	915.0	549.0	8.29	38.9	19.4	116.0	14.5	61.2	158.0	250.0	16.0
16 EH2-1095'	1143855	363850	11-14-85	0.	3400.0	2319.5	8.17	128.0	42.8	588.0	25.7	459.0	962.0	206.0	11.0
17 Spring-Hear Hoopa	1143652	363842	10-13-49	19.0	1550.0	995.0	0.	85.0	55.0	174.0	0.	110.0	355.0	354.0	39.0

map no.	Site Name	LONG. dms	LAT. dms	Date mdy	Temp (C)	EC u-mhos	TDS mg/l	pH	Ca mg/l	Mg mg/l	Na mg/l	K mg/l	Cl mg/l	SO4 mg/l	HCO3 mg/l	SI02 mg/l
1	I1 Stewart Well	1143501	364133	7- 1-81	23.0	1965.0	1476.3	7.45	111.0	88.4	229.0	13.9	154.0	667.0	300.0	63.0
1	I1 Stewart Well	1143501	364133	4-19-82	21.0	1940.0	1483.6	7.67	114.0	85.8	231.0	14.3	161.0	669.0	299.0	59.0
2	I2 Stewart Well	1143518	364124	7- 1-81	23.0	2496.0	1822.0	6.92	186.0	121.0	219.0	16.0	212.0	878.0	254.0	63.0
2	I2 Stewart Well	1143518	364124	4-22-82	21.0	2916.0	2220.1	7.11	226.0	151.0	252.0	17.6	265.0	1120.0	249.0	64.0
3	I3 Rand Well	1143528	364137	7- 7-81	21.0	4390.0	3668.5	7.18	268.0	238.0	548.0	19.5	482.0	1880.0	328.0	69.0
3	I3 Rand Well	1143528	364137	4-22-82	21.0	4661.0	3800.2	7.20	262.0	244.0	596.0	20.7	513.0	1930.0	333.0	68.0
4	I5 B. Lewis Well	1143513	364114	7- 7-81	22.0	3452.0	2643.5	7.23	256.0	168.0	348.0	16.5	334.0	1340.0	256.0	53.0
4	I5 B. Lewis Well	1143513	364114	4-22-82	21.5	3695.0	2931.4	7.08	260.0	175.0	391.0	17.9	368.0	1540.0	255.0	52.0
5	I6 B. Lewis Well	1143512	364120	7- 8-81	22.0	1593.0	1123.7	7.30	138.0	44.9	158.0	12.8	108.0	510.0	234.0	35.0
6	I7 B. Lewis Well	1143511	364133	7- 8-81	21.0	2168.0	1591.7	7.34	149.0	90.1	228.0	14.6	173.0	737.0	292.0	54.0
6	I7 B. Lewis Well	1143511	364133	4-22-82	21.0	2450.0	1783.8	7.12	156.0	106.0	249.0	15.3	228.0	814.0	311.0	60.0
7	I8 B. Lewis Well	1143607	364238	7- 9-81	22.0	1827.0	1305.2	7.60	107.0	75.8	203.0	11.9	121.0	560.0	321.0	66.0
7	I8 B. Lewis Well	1143607	364238	4-19-82	19.0	1829.0	1342.0	7.40	113.0	75.9	209.0	12.6	126.0	578.0	325.0	65.0
8	I13 Henry Well	1143605	364214	7-16-81	30.0	4737.0	4513.4	7.25	348.0	188.0	785.0	13.9	231.0	2760.0	309.0	33.0
9	I14 Wright Well	1143548	364212	7-16-81	22.0	2177.0	1615.9	7.25	149.0	97.2	216.0	14.2	210.0	710.0	313.0	63.0
9	I14 Wright Well	1143548	364212	4-26-82	24.0	2193.0	1674.7	7.30	145.0	100.0	242.0	14.7	207.0	744.0	316.0	64.0
10	I15 Taylor Well	1143550	364202	7-16-81	32.0	1927.0	1431.6	7.15	126.0	85.7	198.0	13.4	121.0	696.0	269.0	57.0
11	I16 Taylor Well	1143546	364207	7-16-81	22.0	3823.0	2895.3	6.95	254.0	195.0	402.0	17.8	578.0	1220.0	329.0	64.0
11	I16 Taylor Well	1143546	364207	4-26-82	22.5	3048.0	2436.6	7.37	195.0	154.0	377.0	17.1	366.0	1100.0	329.0	63.0
12	I17 Cutler Well	1143543	364145	7-17-81	23.0	3120.0	2334.5	7.17	199.0	135.0	368.0	14.5	297.0	1134.0	292.0	41.0
12	I17 Cutler Well	1143543	364145	5- 4-82	23.0	2900.0	2169.9	7.13	179.0	124.0	349.0	13.9	269.0	1050.0	290.0	40.0
13	I18 Lerner Well	1143606	364147	7-17-81	25.0	1750.0	1213.2	7.56	151.0	78.2	113.0	12.0	136.0	637.5	127.0	22.0
14	I22 Pulsipher Well	1143606	364227	7-20-81	23.0	3120.0	2350.9	7.18	178.0	153.0	363.0	14.4	264.0	1148.0	321.0	70.0
14	I22 Pulsipher Well	1143606	364227	5- 4-82	22.5	2625.0	2081.5	7.19	145.0	124.0	336.0	14.0	240.0	996.0	321.0	66.0
15	I25 Schlarman Well	1143519	364144	7-22-81	23.0	2600.0	1935.9	7.41	172.0	136.0	262.0	17.9	170.0	971.0	290.0	62.0
15	I25 Schlarman Well	1143519	364144	4-26-82	21.0	1973.0	1442.2	7.60	125.0	85.8	201.0	14.4	166.0	638.0	306.0	59.0
16	I26 Bartlet Well	1143519	364134	4-26-82	21.5	3052.0	2262.9	7.62	238.0	150.0	266.0	17.4	380.0	999.0	301.0	62.0
17	I31 Wright Well	1143537	364213	7-23-81	27.0	1732.0	1742.7	7.47	113.0	89.1	329.0	12.1	236.0	765.0	283.0	57.0
18	I32 Cortez Well	1143532	364131	7-23-81	37.0	1960.0	1445.3	7.11	122.0	97.0	196.0	13.8	134.0	689.0	265.0	61.0
19	I33 Embry Well	1143523	364129	7-23-81	27.0	1943.0	1459.3	7.09	111.0	84.2	229.0	13.6	123.0	689.0	289.0	65.0
19	I33 Embry Well	1143523	364129	5- 4-82	0.	2050.0	1380.7	7.51	109.0	78.4	223.0	12.8	120.0	629.0	289.0	64.0
20	I34 Embry Well	1143525	364127	7-23-81	22.0	2761.0	1271.3	7.70	101.0	77.7	177.0	14.1	124.0	572.0	279.0	66.0
20	I34 Embry Well	1143525	364127	5- 4-82	22.0	1930.0	1325.1	7.26	85.6	66.5	256.0	11.0	135.0	575.0	278.0	57.0
21	TH12 Nevada Power	1143438	364112	11-21-80	21.0	1691.0	1170.1	7.14	99.3	76.7	160.0	9.6	120.0	517.0	273.0	51.0
22	TH21 Nevada Power	1143533	364148	11-21-80	20.2	3210.0	2248.8	7.01	232.0	146.0	271.0	17.3	361.0	998.0	315.0	66.0
23	NPC 5c - 3 hr.	1143530	364153	1-27-80	0.	2015.0	1362.7	7.75	120.0	78.0	211.0	11.2	155.0	615.0	285.0	30.0
23	NPC 5c - 28 hr.	1143530	364153	1-28-80	0.	2015.0	1339.7	7.80	117.0	78.0	206.0	11.2	148.0	607.0	285.0	30.0
23	NPC 5c - 75 hr.	1143530	364153	1-29-80	0.	2015.0	1330.8	7.76	118.0	76.0	204.0	10.8	157.0	609.0	254.0	29.0
24	TH1 Nevada Power	1143440	364025	12-24-80	20.0	1925.0	1480.3	7.37	118.0	96.4	207.0	17.4	246.0	584.0	305.0	59.0
25	TH2 Nevada Power	1143427	364015	11-20-80	21.4	2455.0	1794.1	6.95	211.0	79.3	222.0	15.3	145.0	921.0	293.0	54.0
map no.	Site Name	LONG. dms	LAT. dms	Date mdy	Temp (C)	EC u-mhos	TDS mg/l	pH	Ca mg/l	Mg mg/l	Na mg/l	K mg/l	Cl mg/l	SO4 mg/l	HCO3 mg/l	SI02 mg/l

Table A-3 (a). Data from lower Meadow Valley and Weiser Wash (see Figure 5). A map number of zero indicates the data point was not included on the map. A value of zero for a given constituent indicates there was no analysis.

map no.	Site Name	LONG. dms	LAT. dms	Date mdy	Temp (C)	EC u-mhos	TDS mg/l	pH	Ca mg/l	Mg mg/l	Na mg/l	K mg/l	Cl mg/l	SO4 mg/l	HCO3 mg/l	SiO2 mg/l
26	TH3 Nevada Power	1143420	364021	11-20-80	22.0	2119.0	1621.6	7.14	205.0	87.3	157.0	17.3	100.0	876.0	256.0	51.0
27	TH7 Nevada Power	1143427	364040	11-20-80	20.2	1793.0	1244.5	7.25	106.0	76.7	168.0	11.3	104.0	606.0	257.0	44.0
28	TH31 Nevada Power	1143508	364038	11-21-80	22.0	2336.0	1617.2	7.29	119.0	29.4	347.0	13.3	138.0	815.0	211.0	50.0
29	19 B. Lewis Well	1143448	364013	7-9-81	23.0	1851.0	1301.1	7.26	127.0	64.5	108.0	15.1	124.0	588.0	277.0	56.0
29	19 B. Lewis Well	1143448	364013	4-20-82	21.0	1897.0	1377.3	7.46	137.0	69.2	201.0	15.6	139.0	623.0	275.0	55.0
30	I21 Pulsipher Well	1143453	364027	7-20-81	23.0	2028.0	1506.1	7.36	134.0	62.7	253.0	16.7	166.0	679.7	274.0	57.0
30	I21 Pulsipher Well	1143453	364027	4-20-82	21.5	2142.0	1541.4	7.13	143.0	66.3	252.0	16.6	187.0	684.0	271.0	57.0
31	I35 Leavitt Well	1143457	364021	7-28-81	23.0	2007.0	1518.8	7.40	130.0	45.6	280.0	16.7	170.0	711.5	236.0	47.0
31	I35 Leavitt Well	1143457	364021	4-20-82	21.0	2385.0	1724.8	7.49	146.0	47.4	333.0	19.4	206.0	805.0	238.0	49.0
32	I36 Pulsipher Well	1143455	364018	7-28-81	23.0	3276.0	2558.0	6.97	213.0	68.7	476.0	27.8	325.0	1280.0	241.0	47.0
32	I36 Pulsipher Well	1143455	364018	4-20-82	21.0	3577.0	2713.7	7.14	228.0	77.7	517.0	29.0	335.0	1360.0	240.0	47.0
33	I37 Weiss Well	1143447	364001	10-19-81	22.0	2390.0	2274.4	7.40	220.0	102.0	328.0	19.9	288.0	1151.0	221.0	55.0
34	I39 Callahan Well	1143457	364007	10-20-81	23.0	3640.0	3533.5	7.56	243.0	83.7	681.0	31.8	491.0	1870.0	188.0	39.0
35	I40 Lloyd Well	1143456	364013	10-20-81	23.5	2780.0	2593.7	7.14	214.0	87.6	440.0	24.1	305.0	1380.0	216.0	35.0
36	I42 Carlson Well	1143457	363945	10-21-81	25.0	3200.0	3401.5	7.32	290.0	118.0	609.0	22.5	540.0	1680.0	218.0	33.0
37	I48 Ron Lewis Well	1143447	364013	11-10-81	22.0	1460.0	1275.7	7.53	130.0	70.4	169.0	13.8	128.0	561.0	295.0	56.0
38	NPC Well #1	1143443	364025	3-29-85	0.	2420.0	1811.8	7.77	193.0	99.1	229.0	16.2	210.0	871.0	277.0	55.0
39	NPC Well #4	1143438	364107	3-29-85	0.	1770.0	1267.1	7.98	111.0	88.3	165.0	9.3	146.0	589.0	253.0	32.0
40	NPC #4a Samp. 1	1143426	364108	3-27-80	0.	3327.0	2570.1	7.75	321.0	111.0	248.0	24.9	40.9	1713.0	187.0	17.8
40	NPC #4a Samp. 2	1143430	364108	3-27-80	0.	3186.0	2424.1	7.97	312.0	110.0	250.0	22.3	34.0	1583.0	190.0	17.8
40	NPC #4a Samp. 3	1143430	364108	3-27-80	0.	2605.0	2110.4	7.96	363.0	133.0	264.0	25.0	54.9	1150.0	199.0	21.0
40	NPC #4a Samp. 4	1143430	364108	3-28-80	0.	2244.0	1570.6	8.07	181.0	86.0	200.0	12.4	61.1	905.0	210.0	20.1
40	NPC #4a Samp. 5	1143430	364108	3-28-80	0.	2154.0	1552.3	8.10	181.0	80.0	200.0	11.7	50.6	905.0	212.0	18.0
41	NPC 11 Samp. #1	1143439	364054	9-10-81	21.0	2150.0	1395.0	7.63	135.0	76.0	190.0	15.0	140.0	639.0	284.0	58.0
41	NPC 11 Samp. #2	1143439	364054	9-10-81	21.0	2040.0	1408.0	7.68	139.0	78.0	188.0	14.0	144.0	644.0	284.0	59.0
42	NPC 25 1981 Nevada Pow	1143435	364014	6-24-81	21.0	1780.0	1194.0	7.80	122.0	65.0	174.0	14.0	119.0	553.0	294.0	0.
42	NPC 25 1985 Nevada Pow	1143435	364014	3-29-85	0.	3350.0	2818.3	7.85	329.0	179.0	264.0	19.8	295.0	1560.0	237.0	53.0
43	NPC 34 Nevada Power	1143442	364038	3-27-81	21.0	1820.0	1323.5	7.81	133.0	72.0	173.0	14.0	131.0	600.0	291.0	65.0
0	NPC 2 Samp. #1	1143444	364014	9-28-81	22.0	1750.0	1229.5	7.55	118.0	64.0	180.0	14.0	112.0	541.0	285.0	58.0
0	NPC 2 Samp. #2	1143444	364014	9-28-81	22.0	1730.0	1187.0	7.65	116.0	63.0	177.0	13.0	112.0	505.0	286.0	58.0
44	EH-8 115'	1143433	364026	5-10-86	0.	1753.0	1372.2	8.05	125.0	73.6	200.0	16.6	162.0	633.0	248.0	38.0
44	EH-8 175'	1143433	364026	5-10-86	0.	3400.0	2425.8	7.56	320.0	80.8	317.0	20.0	177.0	1390.0	172.0	35.0
44	EH-8 195'	1143433	364026	5-10-86	0.	4250.0	3045.3	7.74	358.0	107.0	436.0	22.8	240.0	1780.0	161.0	21.0
44	EH-8 225'	1143433	364026	5-10-86	0.	3640.0	3118.0	7.61	394.0	103.0	415.0	22.0	236.0	1840.0	158.0	29.0
44	EH-8 244' (bottom)	1143433	364026	5-10-86	0.	3580.0	2950.4	7.62	374.0	102.0	397.0	21.9	224.0	1720.0	167.0	28.0
45	EH-6 75'	1143412	364054	3-24-86	21.2	515.0	288.3	7.99	38.8	34.7	19.0	4.8	12.3	16.2	283.0	21.0
45	EH-6 85'	1143412	364054	3-24-86	21.4	548.0	346.0	8.14	34.8	34.4	37.2	6.7	19.5	76.9	251.0	11.0
45	EH-6 95'	1143412	364054	3-24-86	21.8	552.0	284.3	8.24	38.2	35.0	15.7	5.0	10.6	18.8	282.0	20.0
45	EH-6 105'	1143412	364054	3-24-86	22.4	520.0	284.5	8.18	37.5	34.0	19.4	7.4	14.8	26.8	263.0	13.0
45	EH-6 115'	1143412	364054	3-24-86	22.4	557.0	278.5	8.22	38.4	33.2	16.4	5.3	11.5	20.2	269.0	19.0
map no.	Site Name	LONG. dms	LAT. dms	Date mdy	Temp (C)	EC u-mhos	TDS mg/l	pH	Ca mg/l	Mg mg/l	Na mg/l	K mg/l	Cl mg/l	SO4 mg/l	HCO3 mg/l	SiO2 mg/l

Table A-3 (b). Continuation of data from Figure 5.

map no.	Site Name	LONG. dms	LAT. dms	Date mdy	Temp (C)	EC u-mhos	TDS mg/l	pH	Ca mg/l	Hg mg/l	Na mg/l	K mg/l	Cl mg/l	SO4 mg/l	HCO3 mg/l	SiO2 mg/l
45	EH-6 125'	1143412	364054	3-24-86	22.4	550.0	275.0	8.17	36.3	31.6	16.8	5.6	11.1	24.6	260.0	19.0
45	EH-6 135'	1143412	364054	3-24-86	24.2	1022.0	433.8	8.17	41.9	36.6	55.2	8.4	37.7	112.0	252.0	16.0
45	EH-6 145'	1143412	364054	3-24-86	22.4	510.0	273.8	8.19	35.3	29.7	21.2	5.4	11.1	27.6	249.0	19.0
45	EH-6 155'	1143412	364054	3-24-86	0.	471.0	271.9	8.16	31.3	29.6	22.1	5.8	11.0	27.6	251.0	19.0
45	EH-6 165'	1143412	364054	3-24-86	0.	520.0	449.1	8.06	43.9	33.8	61.0	7.8	36.6	113.0	258.0	24.0
45	EH-6 175'	1143412	364054	3-24-86	22.6	510.0	288.3	8.16	36.5	28.1	26.5	4.8	9.0	40.9	245.0	20.0
45	EH-6 235'	1143412	364054	3-24-86	23.9	1090.0	714.3	7.64	70.1	42.8	89.7	9.7	19.5	350.0	221.0	22.0
45	EH-6 295'	1143412	364054	3-25-86	24.0	3100.0	1799.4	8.07	183.0	84.5	245.0	21.8	36.6	1120.0	187.0	15.0
45	EH-6 304'	1143412	364054	3-25-86	0.	1178.0	794.1	7.63	80.0	46.8	102.0	10.9	12.9	417.0	209.0	20.0
45	EH-6 335'	1143412	364054	3-26-86	24.8	3680.0	2808.8	7.52	362.0	131.0	292.0	34.7	40.1	1850.0	172.0	13.0
45	EH-6 435'	1143412	364054	3-26-86	24.5	2260.0	2585.3	7.84	310.0	129.0	264.0	27.3	41.5	1710.0	183.0	12.0
45	EH-6 455'	1143412	364054	3-26-86	25.1	3140.0	2765.1	7.64	350.0	134.0	267.0	31.2	40.9	1840.0	178.0	13.0
46	R. West Wall	1143315	363913	1-22-40	0.	4100.0	2788.5	0.	474.0	164.0	153.0	0.	156.0	1750.0	183.0	0.
47	McCormick Wall	1143403	364005	10-10-49	0.	1450.0	974.0	0.	132.0	80.0	62.0	0.	32.0	516.0	250.0	27.0
47	I10 Hester (McCormick)	1143359	364009	7- 9-81	21.0	4390.0	3698.5	6.87	320.0	259.0	474.0	17.0	482.0	1960.0	301.0	36.0
47	I10 Hester (McCormick)	1143359	364009	4-22-82	20.0	5092.0	4119.4	7.03	320.0	287.0	568.0	19.9	557.0	2170.0	323.0	36.0
48	I41 Bishop Wall	1143338	364000	10-21-81	25.0	2650.0	3332.5	7.19	454.0	192.0	178.0	17.5	218.0	2190.0	126.0	20.0
49	I43 Hester Wall	1143400	363956	10-21-81	22.0	3664.0	4587.7	7.00	594.0	299.0	356.0	21.2	476.0	2690.0	265.0	19.0
49	I43 Hester Wall	1143400	363956	4-22-82	21.0	5203.0	4549.7	7.07	596.0	302.0	387.0	24.7	486.0	2600.0	264.0	22.0
50	I45 Lewis Wall	1143316	363912	5- 4-82	23.5	3275.0	2934.8	6.98	488.0	132.0	198.0	25.8	193.0	1750.0	224.0	36.0
51	I46 Lewis Wall	1143341	363915	10-22-81	25.0	2350.0	2389.6	7.40	296.0	116.0	161.0	18.1	147.0	1520.0	197.0	33.0
51	I46 Lewis Wall	1143341	363915	5- 4-82	25.0	2900.0	2560.0	6.95	438.0	121.0	165.0	21.5	155.0	1530.0	191.0	34.0
52	EH3-295'	1143132	364132	2- 2-86	18.9	829.0	508.5	7.96	73.3	41.2	28.5	7.7	31.8	235.0	160.0	11.0
52	EH3-355'	1143132	364132	2- 2-86	18.1	1800.0	1341.5	7.98	172.0	115.0	67.3	9.6	75.6	813.0	144.0	17.0
52	EH3-455'	1143132	364132	2- 2-86	21.2	3080.0	2442.1	7.74	273.0	159.0	254.0	13.1	158.0	1500.0	140.0	15.0
52	EH3-475'	1143132	364132	2- 2-86	21.2	2880.0	2334.9	7.84	302.0	174.0	155.0	12.4	138.0	1470.0	135.0	16.0
52	EH3-545'	1143132	364132	2- 2-86	24.1	3690.0	3243.3	7.81	519.0	197.0	166.0	21.3	193.0	2070.0	124.0	15.0
52	EH3-655'	1143132	364132	2- 4-86	24.0	3700.0	3279.4	7.76	510.0	201.0	168.0	20.9	193.0	2110.0	123.0	15.0
52	EH3-695'	1143132	364132	2- 5-86	24.2	3750.0	3286.5	7.75	510.0	203.0	175.0	22.0	190.0	2110.0	123.0	15.0
52	EH3-795'	1143132	364132	2- 5-86	0.	3740.0	3286.8	7.72	505.0	202.0	173.0	22.3	198.0	2110.0	123.0	15.0
53	EH-7 175'	1143153	364014	4- 5-86	0.	5380.0	3083.4	7.77	494.0	188.0	162.0	22.9	184.0	1960.0	123.0	11.0
53	EH-7 305'	1143153	364014	4- 6-86	22.3	3260.0	3147.7	7.52	488.0	206.0	163.0	20.7	182.0	2020.0	114.0	11.0
53	EH-7 405'	1143153	364014	4- 9-86	23.5	3650.0	3170.9	7.82	494.0	209.0	161.0	20.9	192.0	2020.0	120.0	14.0
53	EH-7 505'	1143153	364014	4- 9-86	23.1	3570.0	3057.2	7.63	474.0	195.0	166.0	27.2	185.0	1930.0	132.0	14.0
53	EH-7 555'	1143153	364014	4- 9-86	24.1	3500.0	2930.3	7.86	455.0	191.0	163.0	27.3	175.0	1840.0	132.0	13.0

map no.	Site Name	LONG. dms	LAT. dms	Date mdy	Temp (C)	EC u-mhos	TDS mg/l	pH	Ca mg/l	Hg mg/l	Na mg/l	K mg/l	Cl mg/l	SO4 mg/l	HCO3 mg/l	SiO2 mg/l
---------	-----------	-----------	----------	----------	----------	-----------	----------	----	---------	---------	---------	--------	---------	----------	-----------	-----------

Table A-3 (c). Continuation of data from Figure 5.

samp Site Name no.	LONG. dms	LAT. dms	Date mdy	Temp (C)	EC u-mhos	TDS mg/l	pH	Ca mg/l	Mg mg/l	Na mg/l	K mg/l	Cl mg/l	SO4 mg/l	HCO3 mg/l	SiO2 mg/l
1 Hiko Spring-Bateman	0	0	3-10-62	26.5	0.	313.0	8.00	44.0	23.0	29.0	7.0	11.0	36.0	260.0	33.0
2 Hiko Spring-USGS	0	0	0-0-0	26.0	0.	324.4	7.45	49.0	23.0	26.0	7.4	11.0	37.0	282.0	30.0
3 Hiko Spring-DRI	0	0	1-14-85	0.	502.0	319.9	8.04	46.1	24.0	25.6	7.0	9.6	36.6	276.0	33.0
4 Crystal Spring-Bateman	0	0	5-1-73	27.0	0.	276.0	8.30	45.0	24.0	30.0	0.	10.0	44.0	246.0	0.
5 Crystal Spring-USGS	0	0	0-0-0	27.5	408.0	288.9	7.30	43.0	21.0	22.0	5.0	8.9	34.0	260.0	25.0
6 Crystal Spring-DRI	0	0	1-14-85	0.	476.0	296.9	8.08	44.6	22.9	24.0	5.3	9.1	34.0	264.0	25.0
7 Ash Spring-Bateman	0	0	1-16-73	0.	0.	280.0	7.80	56.0	14.0	33.0	0.	10.0	35.0	264.0	0.
8 Ash Spring-USGS	0	0	0-0-0	36.0	460.0	288.9	7.00	43.0	14.0	27.0	7.4	8.5	34.0	250.0	30.0
9 Mormon Well	1150542	363840	9-5-83	10.0	0.	363.0	7.60	65.0	41.0	12.0	1.0	12.0	21.0	390.0	16.0

samp Site Name no.	LONG. dms	LAT. dms	Date mdy	Temp (C)	EC u-mhos	TDS mg/l	pH	Ca mg/l	Mg mg/l	Na mg/l	K mg/l	Cl mg/l	SO4 mg/l	HCO3 mg/l	SiO2 mg/l
-----------------------	--------------	-------------	-------------	-------------	--------------	-------------	----	------------	------------	------------	-----------	------------	-------------	--------------	--------------

Table A-1. Supplemental data used in simulations.

Table A-5. Sources of data in previous work.

Author (year)	Valley	Data Point	Water Level	Chem.	Iso.	
Eakin (1964)	Coyote Springs	14a1	*			
		24b1	*			
		Coyote Spring	*			
		25a1	*			
	Kane Springs	Cabin Spring				
		Kane Spring				
		Roy Spring				
		No Name Spring				
		Willow Spring				
		Grapevine Spring				
		Muddy Spring	*	*		
	Moapa	Iverson Spring	*	*		
		Pederson Spring	*	*		
		8ab1	*			
		8ac1	*			
		8db1	*			
		8db2	*			
		9cc1	*			
		9dd1	*			
		9dd2	*			
15bb1	*					
16aa1	*					
23ab1	*					
23ac1	*					
23bb1	*					

Author (year)	Valley	Data Point	Water Level	Chem.	Iso.	
Eakin (1966)	Coyote Springs	14a1	*			
		25a1	*			
	Moapa	Maynard Lake	*			
		Muddy Springs	*		*	
	Pahrnagat	Hiko Spring	*		*	
		Crystal Spring	*		*	
		Ash Spring	*		*	
		Well 4s/60-2a1	*			
		Well 4s/61-15b1	*			
		Well 5s/60-6c1	*			
		Well 3s/60-24d1	*			
Win. & Fried. (1972)	Pahrnagat	Hiko Spring			*	
		Crystal Spring			*	
		Ash Spring			*	
	Moapa	Muddy Springs			*	
Rush (1964)	Meadow	Well 4s/67-7d1	*			
		Schlarman Well	*			
		Bradshaw Well	*			
		Breedlove Well	*			
		Cole Well	*			
		G.S. Glendale	*			

Table A-6 (a). X-ray diffraction peaks for SC1, from the NPC power plant.

2θ	d-spacing	intensity	mineral	peak order
18.8	4.72	14	?	
19.1	4.65	15	thenardite	2
20.9	4.25	20	gypsum	3
			quartz	2
26.7	3.34	100	quartz	1
27.8	3.21	14	mirabilite	2
28.0	3.19	17	thenardite	3
28.1	3.18	16	?	
29.1	3.07	38	trona	2
29.2	3.06	32	gypsum	2
29.4	3.04	35	natron	1
29.5	3.03	42	calcite	1
31.6	2.83	31	?	
31.7	2.82	33	halite	1
31.8	2.81	36	?	
32.2	2.78	27	thenardite	1
33.9	2.64	34	trona	1

Table A-6 (b). X-ray diffraction peaks for SC2, from the Muddy Springs area.

2 θ	d-spacing	intensity	mineral	peak order
19.1	4.65	13	thenardite	2
20.0	4.44	13	?	
20.6	4.31	18	?	
20.8	4.27	22	gypsum	3
20.9	4.25	22	quartz	2
23.2	3.83	10	calcite	3
26.8	3.33	85	quartz	1
27.7	3.22	12	?	
29.1	3.07	15	trona	2
29.3	3.05	17	gypsum	2
29.4	3.04	18	natron	1
29.5	3.03	21	calcite	1
29.6	3.02	24	?	
30.9	2.89	11	natron	3
31.0	2.88	13	dolomite	1
32.2	2.78	18	thenardite	1
32.3	2.77	20	?	
33.9	2.64	11	trona	1

Table A-6 (c). X-ray diffraction peaks for SC3, from the Glendale well field.

2 θ	d-spacing	intensity	mineral	peak order
19.1	4.65	12	thenardite	2
20.7	4.29	29	?	
20.8	4.27	36	gypsum	3
20.9	4.25	32	quartz	2
23.5	3.79	13	?	
26.7	3.34	55	quartz	1
27.8	3.21	17	mirabilite	2
28.1	3.18	16	thenardite	3
29.0	3.08	18	?	
29.1	3.07	20	trona	2
29.2	3.06	19	gypsum	2
29.3	3.05	17	?	
29.5	3.03	12	natron	1
31.1	2.88	15	dolomite	1
32.1	2.79	16	?	
32.2	2.78	20	thenardite	1
32.3	2.77	16	?	
36.5	2.46	12	?	

Table A-6 (d). X-ray diffraction peaks for EH6 well cuttings.

2θ	d-spacing	intensity	mineral	peak order
20.9	4.25	26	gypsum	3
24.9	3.58	11	?	
26.7	3.34	91	quartz	1
27.1	3.29	12	?	
27.3	3.27	14	?	
27.5	3.24	15	?	
27.6	3.23	13	?	
29.3	3.05	13	gypsum	2
29.5	3.03	13	natron	1
29.6	3.02	20	calcite	1
35.2	2.55	12	?	
36.7	2.45	17	?	
39.6	2.28	11	?	
45.8	1.98	13	?	

XRD Output: Salt Crust #3

Z. A. Datta

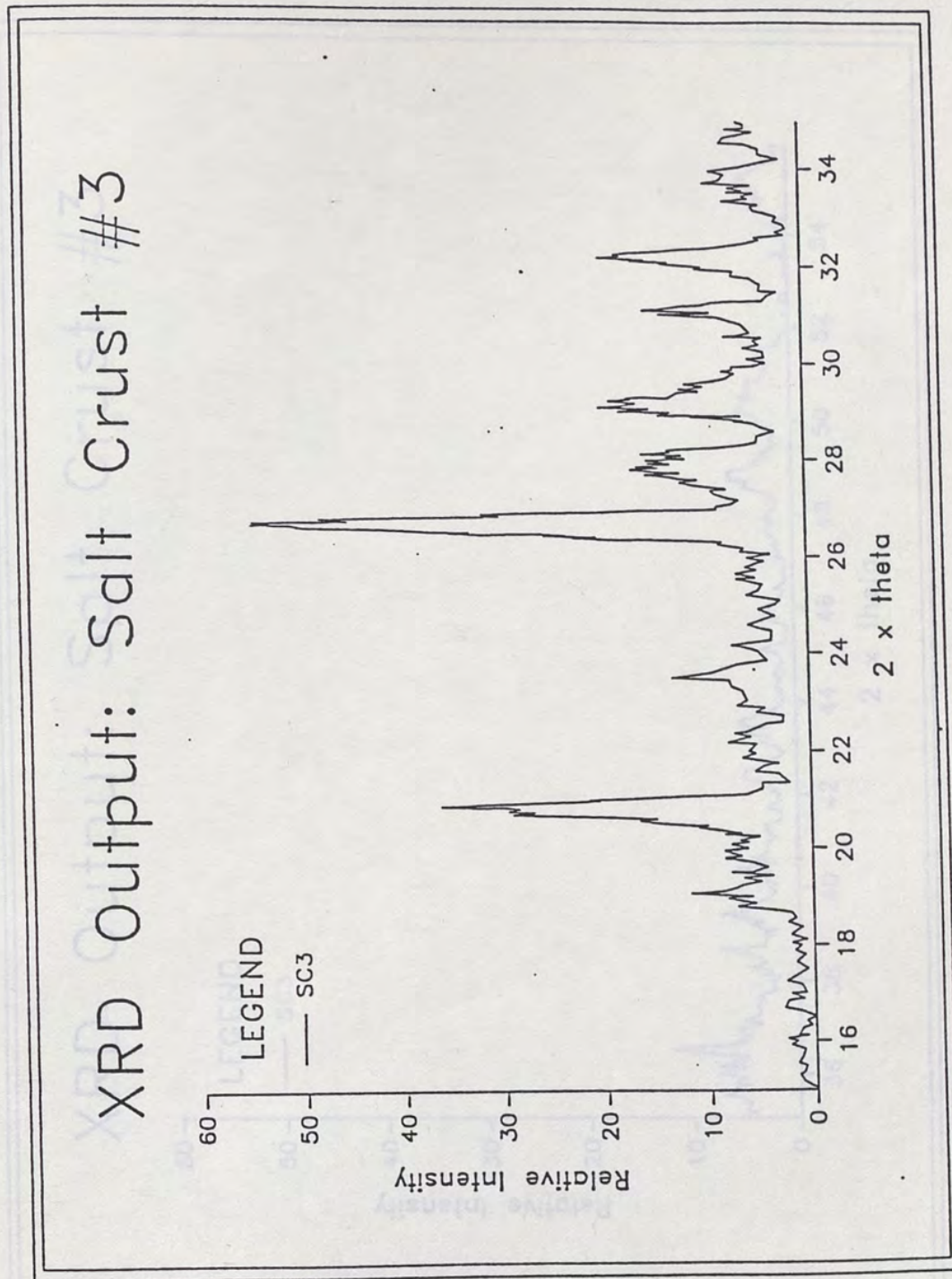


Figure A-1 (a). X-ray diffractogram for salt crust #3, from the Glendale well field. Salt Crusts 1 and 2 are similar.

XRD Output: Salt Crust #3

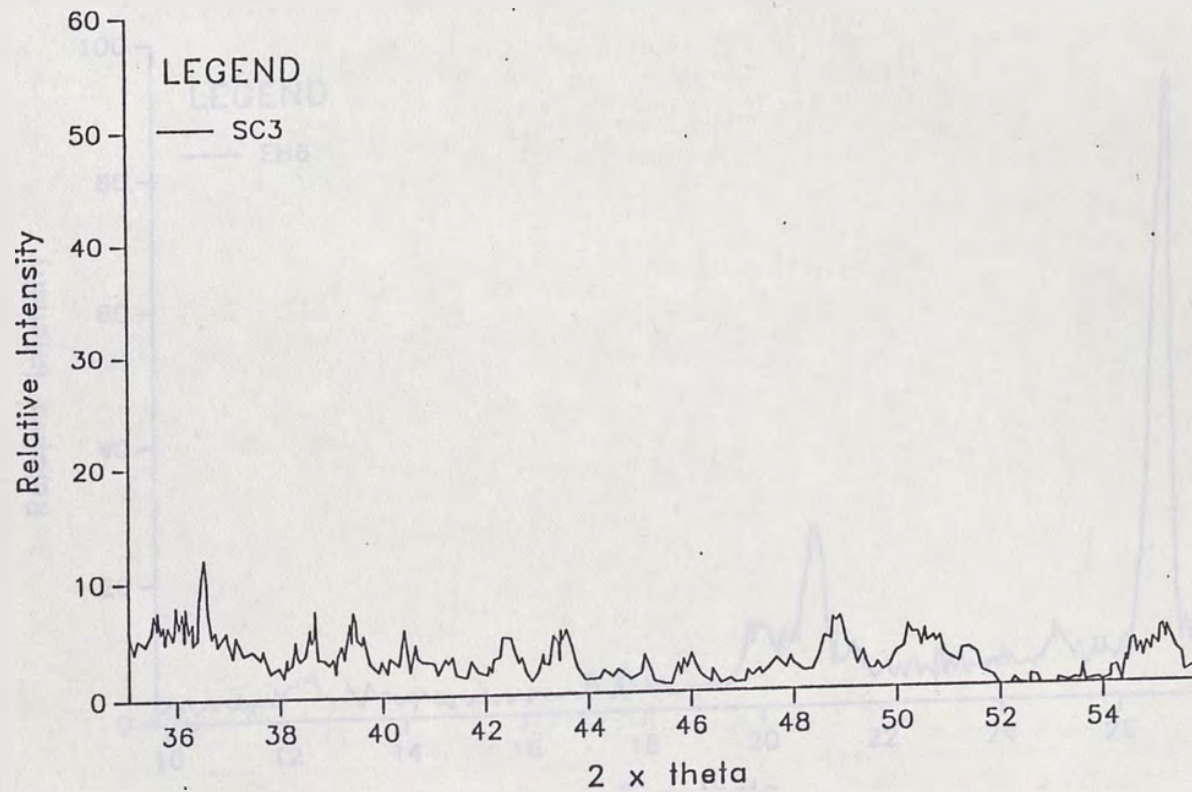


Figure A-1 (b). Continuation of XRD output for SC3.

XRD Output: EH6 Cuttings

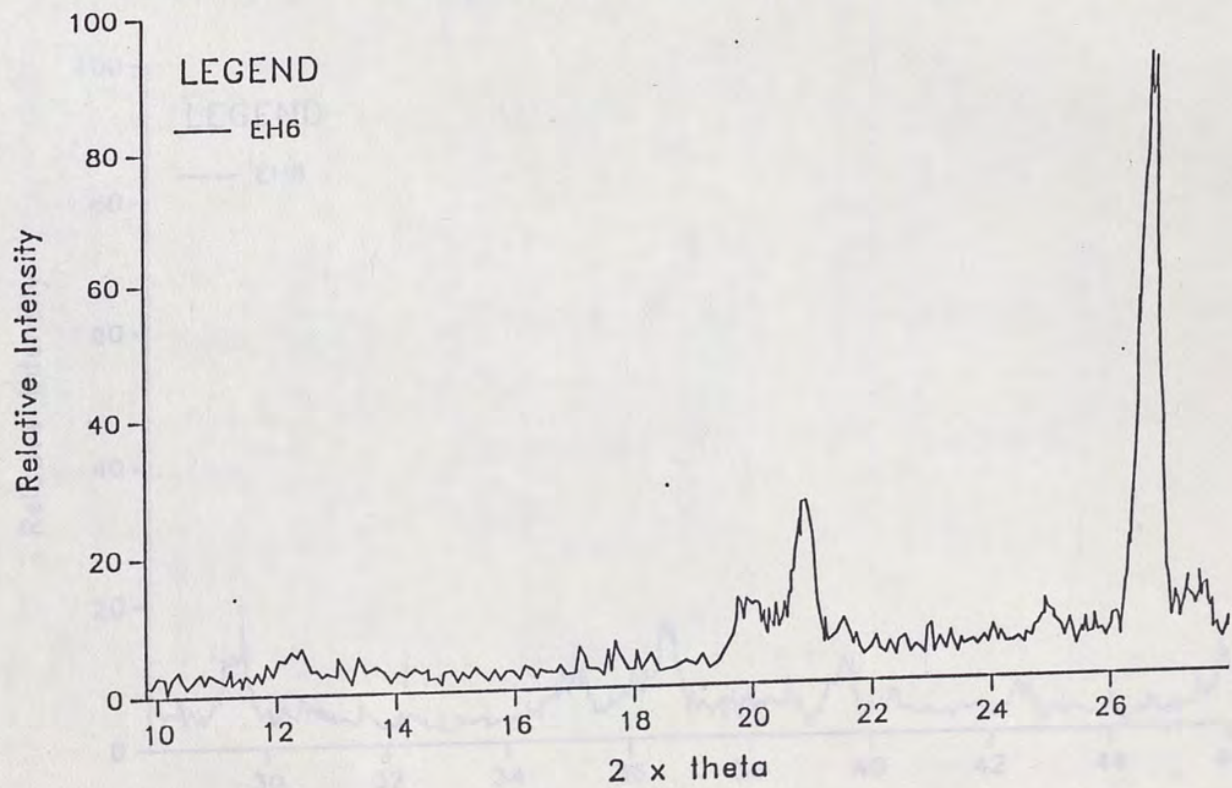


Figure A-2 (a). X-ray diffractogram for EH6 well cuttings.

XRD Output: EH6 Cuttings

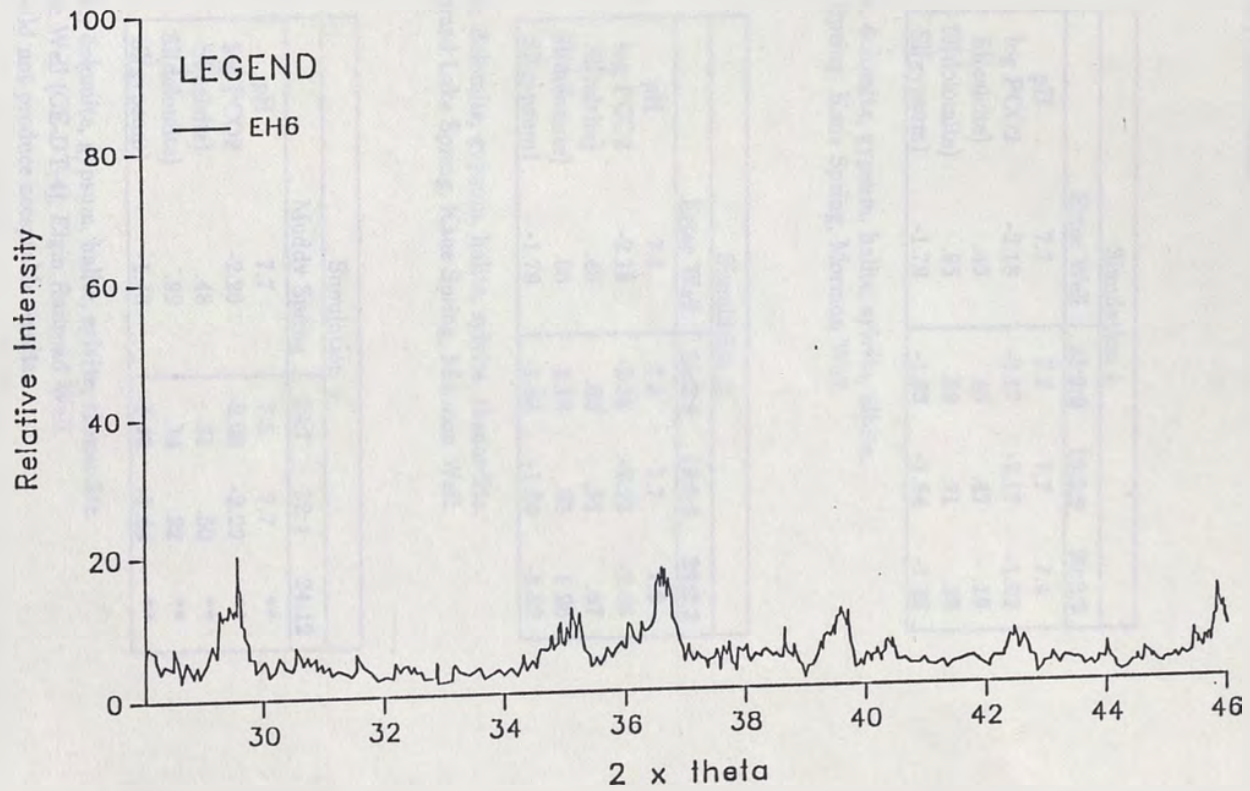


Figure A-2 (b). Continuation of XRD output for EH6.

Table A-7. PHREEQE sensitivity analysis. Final water followed by simulation results for different mixing ratios are given for applicable simulations.

Simulation 1				
	Ertec Well	23:2:9	19:6:9	29:2:3
pH	7.7	7.7	7.7	7.4
log PCO ₂	-2.18	-2.17	-2.17	-1.92
SI(calcite)	.46	.46	.47	.16
SI(dolomite)	.95	.89	.91	.33
SI(gvpsum)	-1.79	-1.83	-1.84	-1.86

Mineral Suite: calcite, dolomite, gypsum, halite, sylvite, albite.
Mixed Waters: Ash Spring, Kane Spring, Mormon Well.

Simulation 2				
	Ertec Well	23:2:9	19:6:9	29:2:3
pH	7.7	7.8	7.7	7.9
log PCO ₂	-2.18	-2.28	-2.23	-2.36
SI(calcite)	.46	.62	.51	.67
SI(dolomite)	.95	1.19	.95	1.26
SI(gypsum)	-1.79	-1.83	-1.86	-1.82

Mineral suite: calcite, dolomite, gypsum, halite, sylvite, thenardite.
Mixed Waters: Maynard Lake Spring, Kane Spring, Mormon Well.

Simulation 4				
	Muddy Spring	29:7	32:4	24:12
pH	7.7	7.5	7.7	**
log PCO ₂	-2.26	-2.03	-2.29	**
SI(calcite)	.48	.21	.50	**
SI(dolomite)	.92	.34	.92	**
SI(gvpsum)	-1.43	-1.43	-1.44	**

Mineral suite: calcite, dolomite, gypsum, halite, sylvite, thenardite.
Mixed Waters: Ertec Well (CE-DT-4), Elgin Railroad Well.
**= BALANCE could not produce acceptable results.